NODYCON Conference Proceedings Series

Walter Lacarbonara *Editor*

Advances in Nonlinear Dynamics, Volume III

Proceedings of the Third International Nonlinear Dynamics Conference (NODYCON 2023)

Springer

NODYCON Conference Proceedings Series

Series Editor

Walter Lacarbonara, Sapienza University of Rome, Rome, Italy

The NODYCON Conference Proceedings Series presents early findings and case studies from a wide range of fundamental and applied work across the range of multidisciplinary fields that encompass Nonlinear Dynamics. Series volumes follow the principle tracks or focus topics featured in the biennial International Nonlinear Dynamics Conference. Volumes in the series feature both well-established streams of research as well as novel areas and emerging fields of investigation.

Walter Lacarbonara
Editor

Advances in Nonlinear Dynamics, Volume III

Proceedings of the Third International Nonlinear Dynamics Conference (NODYCON 2023)

Springer

Editor
Walter Lacarbonara
Department of Structural and Geotechnical
Engineering
Sapienza University of Rome
Rome, Italy

ISSN 2730-7689 ISSN 2730-7697 (electronic)
NODYCON Conference Proceedings Series
ISBN 978-3-031-50634-5 ISBN 978-3-031-50635-2 (eBook)
https://doi.org/10.1007/978-3-031-50635-2

© The Editor(s) (if applicable) and The Author(s), under exclusive license to Springer Nature Switzerland AG 2024
This work is subject to copyright. All rights are solely and exclusively licensed by the Publisher, whether the whole or part of the material is concerned, specifically the rights of translation, reprinting, reuse of illustrations, recitation, broadcasting, reproduction on microfilms or in any other physical way, and transmission or information storage and retrieval, electronic adaptation, computer software, or by similar or dissimilar methodology now known or hereafter developed.
The use of general descriptive names, registered names, trademarks, service marks, etc. in this publication does not imply, even in the absence of a specific statement, that such names are exempt from the relevant protective laws and regulations and therefore free for general use.
The publisher, the authors, and the editors are safe to assume that the advice and information in this book are believed to be true and accurate at the date of publication. Neither the publisher nor the authors or the editors give a warranty, expressed or implied, with respect to the material contained herein or for any errors or omissions that may have been made. The publisher remains neutral with regard to jurisdictional claims in published maps and institutional affiliations.

This Springer imprint is published by the registered company Springer Nature Switzerland AG
The registered company address is: Gewerbestrasse 11, 6330 Cham, Switzerland

Paper in this product is recyclable.

Preface

This volume is part of three volumes collecting the *Proceedings of the Third International Nonlinear Dynamics Conference (NODYCON 2023)* held in Rome from June 18 to 22, 2023. NODYCON originated in 2019 with the purpose of continuing the tradition of a conference series initiated by Prof. Ali H. Nayfeh in 1986 at Virginia Tech, known as the Nonlinear Vibrations, Stability, and Dynamics of Structures Conference. After the passing of Prof. Nayfeh in 2017, NODYCON 2019 evolved into a collective tribute to his enduring contributions. The conference received an outstanding response from the community, with 450 submissions and around 400 participants representing 68 countries.

Following the launch of NODYCON in 2019, NODYCON 2021, originally scheduled to take place in Rome on February 16–19, 2021, underwent a transformation into a virtual (online) conference in response to the widespread uncertainties arising from the global pandemic.

In June 2023, NODYCON 2023 reconvened in Rome after four years from the inaugural event, providing participants with both in-person and online presentation formats. Driven by a strong commitment to promoting personal connections and the exchange of scientific ideas together with meaningful social interactions, the conference successfully brought together a diverse community of over 600 participants. The Organizing Committee, comprised of 21 members, reviewed 577 abstracts, ultimately approving the presentation and publication of 557 one-page abstracts, accompanied by posters, into the Conference Book of Abstracts, following standard review cycles.

To structure the technical sessions, the diverse topics explored in the papers were categorized into four overarching themes:

A – Concepts and methods in nonlinear dynamics
B – Nonlinear dynamics of mechanical and structural systems
C – Nonlinear dynamics and control
D – Recent trends in nonlinear dynamics

The authors of a selection of approximately 50 papers were invited to publish in the Special Issue of *Nonlinear Dynamics* entitled “NODYCON 2023 Third

International Nonlinear Dynamics Conference". At the same time, about 171 full papers were submitted to *Advances in Nonlinear Dynamics – Proceedings of the Third International Nonlinear Dynamics Conference (NODYCON 2023)* within the *NODYCON Conference Proceedings Series*. After a rigorous peer review process, 146 papers were accepted. These papers have been collected into three volumes, which are listed below together with a sub-topical organization.

Volume 1: Nonlinear Dynamics of Structures, Systems and Devices

(i) Fluid-structure interactions
(ii) Mechanical systems and structures
(iii) Computational nonlinear dynamics
(iv) Analytical techniques
(v) Bifurcation and dynamic instability
(vi) Rotating systems
(vii) Nonsmooth systems
(viii) Experimental dynamics

Volume 2: Nonlinear Dynamics and Control

(i) Control of nonlinear systems
(ii) Synchronization
(iii) Nonlinear vibration control
(iv) Sensors and actuators
(v) Passive energy damping

Volume 3: New Trends in Nonlinear Dynamics

(i) MEMS/NEMS
(ii) Chaotic systems and uncertainty
(iii) Energy harvesting
(iv) Constitutive and phenomenological models
(v) Fractional-order systems
(vi) System identification and SHM
(vii) Nonlinear wave propagation
(viii) Nonlinear phenomena in bio- and eco-systems dynamics

The success of NODYCON 2023 can be attributed to the collective efforts, talent, energy, and enthusiasm of the entire community of researchers in the field of nonlinear dynamics. Their dynamic contributions were reflected in the vibrant writing, submission, and presentation of papers. Special praise is also extended to the handling editors, drawn from the Organizing, Steering, and Advisory Boards, and the hardworking reviewers. Their dedicated commitment to reading, examining, and evaluating numerous papers played a pivotal role in ensuring a high standard of quality for the conference proceedings.

Rome, Italy
December 2023

Walter Lacarbonara

Preface for Volume 3: New Trends in Nonlinear Dynamics

Volume 3 of the NODYCON 2023 Proceedings is composed of 59 papers, which are spread across the following groupings: (i) MEMS/NEMS (5 papers), (ii) chaotic systems and uncertainty (13 papers), (iii) energy harvesting (5 paper), (iv) constitutive and phenomenological models (8 papers), (v) fractional-order systems (5 papers), (vi) system identification and SHM (12 papers), (vii) nonlinear wave propagation (5 papers), (viii) nonlinear phenomena in bio- and eco-systems dynamics (6 papers).

Given the interdisciplinary nature of the subjects covered, the editor recognizes that a paper assigned to one category could equally fit into another grouping. As readers delve into these 59 contributions, they will observe the utilization of diverse experimental, analytical, and numerical methodologies to explore the nonlinear dynamics of various systems, ranging from new material systems to complex ecosystems, and spanning different length and time scales.

In Part I tackling *MEMS/NEMS*, the intersection of noise, amplitude, and nonlinearity in a high-Q micromechanical torsion pendulum is explored by J. Pratt. A comparative study of two types of bifurcation-based MEMS sensors is conducted by Y. Shama et al. S. Rahmanian et al. discuss how to excite anti-symmetric modes in a symmetric MEMS. Control of an electrostatically actuated micro portal frame with 2:1 internal resonance subjected to damping disturbances is investigated by W. B. Lenz et al. Vibration mitigation by two parametric anti-resonances in high-Q resonators is explored in a preliminary case study by M. R. Barrios and F. Dohnal.

In Part II dealing with *chaotic systems and uncertainty*, self-supervised contrastive learning for chaotic time-series classification is investigated by S. Hassona and W. Marszalek. A comprehensive study of electrical power grid stability issues using bifurcation and chaos theory is conducted by A. Harb. Multidimensional nonlinearity time series forecasting based on a multi-reservoir echo state network is explored by J. Sun et al. M. Messias analyzes time-periodic perturbation leading to chaos in a planar memristor oscillator with a Bogdanov-Takens bifurcation. C. Mazzilli and G. Franzini present a structural reliability analysis based on the dynamic integrity of an attractor. Chaotic dynamic induced by PI control in offshore oil production plants is discussed by N.A. Clavijo et al. The jerk dynamics of

the Lorenz model are explored by J.-M. Ginoux et al. The nonlinear dynamics of spiral bevel gears are explored by M. Molaie Emamzadeh et al., focusing on the existence of chaotic response in multi-dof systems. E. Campos-Canton et al. study the coexistence of hidden attractors and self-excited attractors on the plane. Compact multiplier-less FPGA implementation of sine and modified sine chaotic maps is developed by H. Elrefai and L. Said. Fixed-time adaptive neural tracking control for a helicopter-like twin rotor MIMO system is proposed by A. Bacha et al. A new key generator based on an auto-switched hybrid chaotic system and its FPGA implementation is introduced by S. Hichem et al. Finally, H. Chen explores the two-dimensional critical dynamics of the Kuramoto model on Erdős-Rényi random graphs.

Part III discusses *energy harvesting* in various systems. Numerical simulations of energy harvesting in a portal frame coupled with a nonlinear energy sink are conducted by A.M. Tusset et al. The leveraging of 2:1 parametric resonance in a notional wave energy harvester is explored by G. Giorgi. Experimental testing of a bi-stable point wave energy absorber under harmonic waves is performed by M. Khasawneh and M. Daqaq. P. Kumar and S. Narayanan focus on the optimization of energy harvesting from a nonlinear energy sink. The enhancement of aeroelastic wind energy harvesting using quasi-zero stiffness is studied by S. Chen and L. Zhao.

In Part IV, *constitutive and phenomenological models* are analyzed for various systems and nonconventional materials. Stochastic delay modeling of landslide dynamics is conducted by S. Kostic et al. A new methodology for the nonlinear analysis of magneto-rheological elastomers' behavior under large amplitude oscillatory axial loadings is presented by H. Vatandoost et al. The magneto-dynamic characterization of a silicone filament embedded with magnetic composite micro-spheres is explored by G. Lanzara. Asymmetric hysteresis is modeled with continuous development using experimental data by J-S. Pei et al. Preliminary results on simulating pressurized sand dampers using the Vaiana-Rosati model are shared by N. Vaiana et al. A modified Bouc-Wen model with damage and flexibility increase for the dynamic analysis of masonry walls is proposed by A. Paoloni et al. A constrained Green's function for a beam with an arbitrary spring and nonlinear spring foundation is developed by X. Zhao et al. Experimental characterization and identification of the shear hysteretic behavior of a helical wire rope isolator are carried out by R. Capuano et al.

Fractional order systems are discussed in Part V. The reliability problem of a fractional stochastic dynamical system is addressed by Y. Guan et al. using the stochastic averaging method and a data-driven deep learning algorithm. The dynamic analysis of a fractional-type microresonator system is discussed by J. Xie et al. M. A. Qureshi explores bird-like trajectories in a 6D chaotic system integrated with fractional-order derivatives, memristors, and encryption. A generalized fractional-order complex logistic map and fractals on FPGA are presented by S. Mustafa et al. P. Chaber and P. Domanski conduct a fractional control performance assessment of nonlinear mechanical systems.

Part VI tackles *system identification and SHM* from various standpoints. The nonlinear system identification of a multi-story building with geometrical nonlinear-

ity is conducted by A. Sadeqi et al. using a deterministic output-only data approach. An approach for monitoring bolt faults in two-dimensional structures without reference is proposed by Q. Li et al. The physics-informed sparse identification of a bistable nonlinear energy sink is presented by Q. Liu and J. Cao. Simultaneous estimation of multiple backbone curves using smooth coordinate tracking is performed by D. Stein and D. Chelidze. Multilayer perceptrons are optimized by A. Buscarino et al. to approximate nonlinear quaternion functions. Experimental characterization and phenomenological modeling of wire rope isolators are presented by P. Neri and J. Holzbauer. G. Hausherr and G. Lanzara present a bimaterial structure that provides substantial shape changes at given control temperatures and discuss the vibrational features of the morphing modes. A novel vibration response-based approach to monitor faults in bolted complex structures is introduced by Q. Li et al. Data-driven delay identification is explored by A. T. Köpeczi-Bócz et al. Uncertainty quantification in parameter estimation using physics-integrated machine learning is addressed by Z. Liu et al. Physics-enhanced sparse identification of a nonlinear oscillator with Coulomb friction is presented by C. Lathourakis and A. Cicirello. Recycled smart devices for real-time monitoring of civil infrastructures are proposed by A. Buscarino et al.

Nonlinear wave propagation is discussed in Part VII. Distorted magnetosonic lump waves are examined in ionospheric plasma, excited by orbital charged space debris objects, by S. P. Acharya et al. Harmonic and superharmonic components in periodic waves propagating through mechanical metamaterials with inertia amplification are studied by M. Lepidi and V. Settimi. M. Lavrentiev et al. present a fast numerical solution to the nonlinear shallow water system. The asymptotic description of soliton solutions to the matrix modified Korteweg-de Vries equation is discussed by S. Carillo and C. Schiebold. Chirped optical solitons in fiber Bragg gratings with dispersive reflectivity are explored by K. Al-Ghafri et al.

Lastly, diverse works on *nonlinear phenomena in bio- and eco-systems dynamics* are discussed in Part VIII. An overview of the time-frequency effects of ECG signals is provided by M. Varanis et al. using the synchroextracting transform. A Hopf bifurcation analysis of the BVAM model for the electrocardiogram is performed by A. Naseer et al.

The stability and instability of a complex biodynamical discrete structure on a cantilever coupled to nonlinear springs are investigated by A. Hedrih et al. The effects of rising sea surface temperature on the dynamics of coral-algal interactions are examined by S. Pal et al. The bifurcations of a non-smooth Filippov predator-prey system with harvesting are analyzed and explored by U. Yadav and S. Gakkhar. The effect of different control strategies on the dynamics of a dengue model is studied by C. Pinto et al.

In conclusion, this volume presents studies reflecting recent advances in a variety of fields and using a plethora of distinct tools and perspectives. We hope that the rich work presented on new trends in nonlinear dynamics will spur and inspire new ideas and future contributions.

Rome, Italy
December 2023

Walter Lacarbonara

Contents

Part I MEMS/NEMS

The Intersection of Noise, Amplitude, and Nonlinearity in a High-Q Micromechanical Torsion Pendulum 3
Jon R. Pratt, Stephan Schlamminger, Aman R. Agrawal, Charles A. Condos, Christian M. Pluchar, and Dalziel J. Wilson

A Comparative Study of Two Types of Bifurcation-Based MEMS Sensors 15
Yasser S. Shama, Rana Abdelrahman, Mohamed Arabi, Resul Saritas, Sasan Rahmanian, Ahmet Gulsaran, Samed Kocer, Alaa Elhady, Hamza Mouharrar, and Eihab M. Abdel-Rahman

How to Excite Anti-symmetric Modes in a Symmetric MEMS? 25
Sasan Rahmanian, Ayman Alneamy, Yasser S. Shama, Samed Kocer, Eihab M. Abdel-Rahman, and Mustafa Yavuz

Control of an Electrostatically Actuated Micro Portal Frame with 2:1 Internal Resonance Subjected to Damping Disturbances 35
Wagner B. Lenz, Rodrigo T. Rocha, Fahimullah Khan, Yousef Algoos, and Mohammad I. Younis

Vibration Mitigation by Two Parametric Anti-resonances in High-Q Resonators: A Preliminary Case Study 45
Miguel Ramírez-Barrios and Fadi Dohnal

Part II Chaotic Systems and Uncertainty

Self-supervised Contrastive Learning for Chaotic Time-Series Classification 59
Salama Hassona and Wieslaw Marszalek

Comprehensive Study of Electrical Power Grid Stability Issues Using Bifurcation and Chaos Theory 71
Ahmad Harb

Multidimensional Nonlinearity Time Series Forecasting Based on Multi-reservoir Echo State Network 81
Jingyu Sun, Lixiang Li, Haipeng Peng, and Shengyu Liu

Time-Periodic Perturbation Leading to Chaos in a Planar Memristor Oscillator Having a Bogdanov-Takens Bifurcation 91
Marcelo Messias and Paulo C. Rech

Structural Reliability Analysis Based on the Dynamic Integrity of an Attractor: Part I 101
Carlos Eduardo Nigro Mazzilli and Guilherme Rosa Franzini

Chaotic Dynamic Induced by PI Control in Offshore Oil Production Plants 111
Nayher A. Clavijo, Giovani G. Gerevini, Fabio C. Diehl, Príamo A. Melo, and José Carlos Pinto

The Jerk Dynamics of Lorenz Model 121
Jean-Marc Ginoux, Riccardo Meucci, Jaume Llibre, and Julien Clinton Sprott

Spiral Bevel Gears Nonlinear Dynamics: Chaotic Response Existence in Multi Degree of Freedom Systems 131
Moslem Molaie, Farhad S. Samani, Giovanni Iarriccio, Antonio Zippo, and Francesco Pellicano

Coexistence of Hidden Attractor and Self-Excited Attractors on the Plane 143
Eric Campos-Cantón, R. de J. Escalante González, Hector E. Gilardi-Velázquez, and Guillermo Huerta-Cuellar

Compact Multiplier-less CORDIC-Based FPGA Implementation of Sine and Modified Sine Chaotic Maps 153
Hisham M. Elrefai, Sara S. Abou Zeid, Wafaa S. Sayed, Lobna A. Said, and Ahmed G. Radwan

Fixed-Time Adaptive Neural Tracking Control for a Helicopter-Like Twin Rotor MIMO System 163
Aymene Bacha, Abdelghani Chelihi, and Chouki Sentouh

A New Key Generator Based on an Auto-Switched Hybrid Chaotic System and Its FPGA Implementation 175
Sid Hichem, Azzaz Mohamed Salah, and Sadoudi Saïd

Critical Dynamics of Kuramoto Model on Erdös–Rényi Random Graphs 185
H. Chen

Part III Energy Harvesting

Numerical Simulations of Energy Harvesting in a Portal Frame Coupled with a Nonlinear Energy Sink 197
Angelo M. Tusset, Alisson L. Agusti, Maria E. K. Fuziki, and Giane G. Lenzi

Leveraging 2:1 Parametric Resonance in a Notional Wave Energy Harvester 207
Giuseppe Giorgi

Experimental Testing of a Bi-stable Point Wave Energy Absorber Under Harmonic Waves 217
Mohammad A. Khasawneh and Mohammed F. Daqaq

Optimization of Energy Harvesting from a Nonlinear Energy Sink 227
Pankaj Kumar and S. Narayanan

Enhancing Aeroelastic Wind Energy Harvesting Using Quasi-Zero Stiffness 239
Shun Chen and Liya Zhao

Part IV Constitutive and Phenomenological Models

Stochastic Delay Modeling of Landslide Dynamics 251
Srđan Kostić and Nebojša Vasović

A New Methodology for Nonlinear Analysis of Magneto-Rheological Elastomers Behavior Under Large Amplitude Oscillatory Axial (LAOA) Loadings 261
Hossein Vatandoost, Ramin Sedaghati, and Subhash Rakheja

Magneto-Dynamic Characterization of a Silicone Filament Embedded with Magnetic Composite Microspheres 271
Luís Pedro Vieira Alexandrino, Alessandro Porrari, and Giulia Lanzara

Modeling Asymmetric Hysteresis: Continuous Development Using Experimental Data 279
Jin-Song Pei, Biagio Carboni, and Walter Lacarbonara

Preliminary Results on the Simulation of Pressurized Sand Dampers by Using the Vaiana-Rosati Model 289
Nicolò Vaiana, Luciano Rosati, Xenofon Palios, and Nicos Makris

Modified Bouc-Wen Model with Damage and Flexibility Increase for the Dynamic Analysis of Masonry Walls 301
Alessandra Paoloni, Domenico Liberatore, and Daniela Addessi

Constrained Green's Function for a Beam with Arbitrary Spring and Nonlinear Spring Foundation 311
X. Zhao, Q. Wang, W. D. Zhu, and Y. H. Li

Experimental Characterization and Identification of the Shear Hysteretic Behavior of a Helical Wire Rope Isolator 325
Raffaele Capuano, Nicolò Vaiana, and Biagio Carboni

Part V Fractional-Order Systems

Reliability Problem of a Fractional Stochastic Dynamical System Based on Stochastic Averaging Method and Data-Driven Deep Learning Algorithm 337
Yu Guan, Wei Li, Dongmei Huang, and Natasa Trisovic

On the Dynamics Analysis of Fractional-Type Microresonator System ... 349
Tao Xi, Jin Xie, and Zhaohui Liu

Bird-Like Trajectories in 6D Chaotic System Integrated with Fractional Order Derivative, Memristor, and Encryption 359
Muhammad Ali Qureshi

Generalized Fractional-Order Complex Logistic Map and Fractals on FPGA 371
Sara M. Mohamed, Wafaa S. Sayed, Lobna A. Said, and A. G. Radwan

Fractional Control Performance Assessment of the Nonlinear Mechanical Systems 381
Patryk Chaber and Paweł D. Domański

Part VI System Identification and SHM

Nonlinear System Identification of a Multi-story Building with Geometrical Nonlinearity Using a Deterministic Output-Only-Data Approach 395
Amirali Sadeqi, Dario Anastasio, and Stefano Marchesiello

An Approach to Monitor Bolt Faults in Two-Dimensional Structures Without Reference 407
Quankun Li, Qingzhou Zhao, Mingfu Liao, and Fali Yang

Physics-Informed Sparse Identification of a Bistable Nonlinear Energy Sink 419
Qinghua Liu and Junyi Cao

Simultaneous Estimation of Multiple Backbone Curves Using Smooth Coordinate Tracking 429
Dalton L. Stein and David Chelidze

Optimizing Multilayer Perceptrons to Approximate Nonlinear Quaternion Functions 441
Arturo Buscarino, Luigi Fortuna, and Gabriele Puglisi

Experimental Characterization and Phenomenological Modeling of Wire Rope Isolators 451
Paolo Neri and Jeremiah Holzbauer

Multilayer Radical Morphing: Shape Transitions and Vibration 463
Ginevra Hausherr and Giulia Lanzara

A Novel Vibration Response-Based Approach to Monitor Faults in Bolted Complex Structures 471
Quankun Li, Qingzhou Zhao, Mingfu Liao, and Xiaobo Lei

Data-Driven Delay Identification with SINDy 481
Ákos Tamás Köpeczi-Bócz, Henrik Sykora, and Dénes Takács

Uncertainty Quantification in Parameter Estimation Using Physics-Integrated Machine Learning 493
Zihan Liu, Amirhassan Abbasi, Prashant N. Kambali, and C. Nataraj

Physics Enhanced Sparse Identification of Nonlinear Oscillator with Coulomb Friction 507
Christos Lathourakis and Alice Cicirello

Recycled Smart Devices for Real-Time Monitoring of Civil Infrastructures 519
Arturo Buscarino, Carlo Famoso, and Luigi Fortuna

Part VII Nonlinear Wave Propagation

Excitations of Distorted Magnetosonic Lump Waves by Orbital Charged Space Debris Objects in Ionospheric Plasma 531
Siba Prasad Acharya, Abhik Mukherjee, and M. S. Janaki

Harmonic and Superharmonic Components in Periodic Waves Propagating Through Mechanical Metamaterials with Inertial Amplification 541
Marco Lepidi and Valeria Settimi

Fast Numerical Solution to Nonlinear Shallow Water System 553
Mikhail Lavrentiev, Andrey Marchuk, Konstantin Oblaukhov, and Mikhail Shadrin

On the Asymptotical Description of Soliton Solutions to the Matrix Modified Korteweg-de Vries Equation 565
Sandra Carillo and Cornelia Schiebold

Chirped Optical Solitons in Fiber Bragg Gratings with Dispersive Reflectivity 577
Khalil S. Al-Ghafri and Mani Sankar

Part VIII Nonlinear Phenomena in Bio- and Eco-systems Dynamics

An Overview on Time-Frequency Effects of ECG Signals Using Synchroextracting Transform 591
Marcus Varanis, Sadra Hemmati, Murilo Cesar Filipus, Felipe Lima de Abreu, Jose M. Balthazar, and C. Nataraj

Hopf Bifurcation Analysis of the BVAM Model for Electrocardiogram ... 601
Ahsan Naseer, Imran Akhtar, and Muhammad R. Hajj

Stability and Instability of a Complex Biodynamical Discrete Structure on a Cantilever Coupled to Nonlinear Springs 613
Katica Hedrih [Stevanović] and Andjelka Hedrih

Effects of Rising Sea Surface Temperature on the Dynamics of Coral-Algal Interactions..... 623
Sasanka Shekhar Maity, Joydeb Bhattacharyya, and Samares Pal

Analysis and Bifurcations of Non-smooth Filippov Predator Prey System with Harvesting 637
U. Yadav, S. Gakkhar, and A. K. Nayak

The Effect of Different Control Strategies on the Dynamics of a Dengue Model 651
Carla M. A. Pinto, Dumitru Baleanu, and Amin Jajarmi

Index..... 661

Part I
MEMS/NEMS

The Intersection of Noise, Amplitude, and Nonlinearity in a High-Q Micromechanical Torsion Pendulum

Jon R. Pratt, Stephan Schlamminger, Aman R. Agrawal, Charles A. Condos, Christian M. Pluchar, and Dalziel J. Wilson

1 Introduction

The variation of gravity with latitude was originally detected in 1671 when a meter-long pendulum clock set to astronomical references ran 2.5 minutes slower per day in Cayenne, French Guiana, than in Paris, France [1]. Later centuries proved the pendulum clock to be a reliable, if burdensome, tool for measuring local gravity, ultimately replaced by compact mass-spring systems; nevertheless, the simplicity and absolute nature of clock gravimetry remain attractive, and recent developments in low loss micromechanical resonators have inspired a revisiting of their potential.

We explore here a device reported in [2] and sketched in Fig. 1. This torsion pendulum has a length of only 50 μm, but its 34 Hz natural frequency changed by 10 Hz when inverted in the gravitational field. It is tempting to contemplate deploying such a device in everything from cell phones to satellites; we therefore seek refinements that might enable the pendulum frequency to track shifts in gravity below a micro-g, aiming for as low as 10 nano-g to compete with state of the art, chip scale gravimeters [3–5].

To resolve local gravity to within 10 nano-g in a reasonable time (< 1000 s) may require driving the pendulum to amplitudes that exceed its thermal noise by 3 orders of magnitude. Unfortunately, we find thermal noise scales inversely with pendulum length, implying our microscale pendulum must be driven to amplitudes where the frequency-amplitude coupling (anisochronous pendulation) is well-known to limit the performance of pendulum clocks [6]. However, the high aspect ratio and

J. R. Pratt (✉) · S. Schlamminger
National Institute of Standards and Technology, Gaithersburg, MD, USA
e-mail: jon.pratt@nist.gov

A. R. Agrawal · C. A. Condos · C. M. Pluchar · D. J. Wilson
Wyant College of Optical Sciences, University of Arizona, Tucson, AZ, USA

© The Author(s), under exclusive license to Springer Nature Switzerland AG 2024

W. Lacarbonara (ed.), *Advances in Nonlinear Dynamics, Volume III*, NODYCON Conference Proceedings Series, https://doi.org/10.1007/978-3-031-50635-2_1

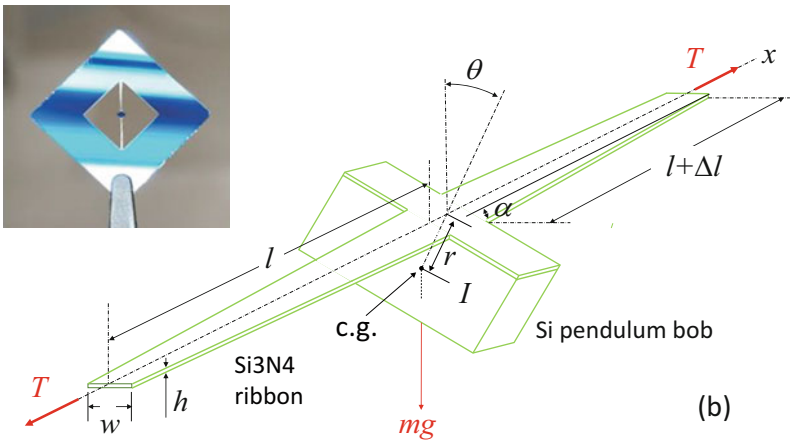

Fig. 1 Microtorsion pendulum (**a**) photograph of the typical device (**b**) schematic illustrating salient features of the model

tensile stress of our nanoribbon suspension may offer a work-around. Exploiting its nonlinear torsional stiffness, we find geometries that counteract the gravitational nonlinearity and preserve the isochronous pendulation through angles approaching 1 radian.

2 Sensitivity of a Torsion Pendulum to Gravity

The device shown in Fig. 1 consists of a small paddle of silicon having a moment of inertia I and mass m, suspended from a ribbon of silicon nitride.

2.1 Parametric Frequency-Gravity Coupling

The ribbon has effective torsional stiffness κ and the paddle of mass m and inertia I experiences gravitational stiffness $\kappa_g = mgr$, where g is the acceleration due to gravity and r the offset of the center of gravity from the torsion (x) axis. Assuming damping coefficient Γ, the equation of motion for vibrations driven by random thermal torque $\tau_{th}(t)$ and coherent drive torque $\tau_{PLL}(t)$ is

$$I\ddot{\theta} + \Gamma\dot{\theta} + \kappa\theta + mgr\sin\theta = \tau_{th}(t) + \tau_{PLL}(t), \tag{1}$$

so the natural frequency for small oscillations ($\sin\theta \approx \theta$) is

$$f_0 = \frac{1}{2\pi}\omega_0 = \frac{1}{2\pi}\sqrt{\frac{\kappa + mgr}{I}}. \tag{2}$$

The natural frequency is thus a parametric function of gravity, where a change in gravity produces a change in frequency

$$\Delta f = \frac{1}{8\pi^2 f_0}\frac{mr}{I}\Delta g. \tag{3}$$

2.2 Thermal Noise

The position of the device fluctuates by small amounts due to energy dissipated at thermodynamic equilibrium and due to the forces of detection (i.e., back action) that perturb the device. Optical techniques can be used to measure the angular displacement θ of a microscale pendulum with negligible back action and exceptional precision [2]. The remaining thermal torque τ_{th} disturbs the pendulum with a characteristic white spectral density [7]

$$\tau_{\text{th}}^2(\omega) = 4k_{\text{B}}\mathscr{T}\Gamma, \tag{4}$$

where k_{B} is the Boltzmann constant and $\mathscr{T}$ is the temperature.

Pendulums typically dissipate energy through friction at the pivot, here a silicon nitride ribbon in tension. As we have shown in [2], tension creates a restoring torque that dilutes anelastic shear [8], making for an effectively lossless pivot. In fact, pivot loss is negligible compared to gas damping in all but ultrahigh vacuum environments, similar to findings in other low-loss torsion systems [9, 10].

Anticipating the limitations of chip-scale vacuum packaging [11], we consider the thermodynamic noise floor of a viscous-damped pendulum where the loss due to gas damping is characterized using a quality factor Q,

$$\Gamma = \frac{\omega_0 I}{Q}. \tag{5}$$

We are interested in measuring the frequency of this resonator by recording a convenient, characteristic periodic event—zero crossings of the optical lever when the device is driven on resonance using a small amplitude phase-locked drive τ_{PLL}. For low-level coherent excitation, the response is approximately linear ($\theta < 0.1$ rad), and the thermal torque of Eq. (4) will drive fluctuations of the pendulum in linear superposition with the resulting phase-locked motion $\theta_{PLL} = \theta_0 \sin\omega_{\text{n}}t$, giving rise to the mean squared variance $\sigma_\theta^2 = \langle(\theta - \theta_{PLL})^2\rangle$.

The average thermal amplitude can be quantified from the equipartition of energy

$$\langle \sigma_\theta^2 \rangle = \frac{k_B \mathscr{T}}{I\omega_0^2} \approx \frac{k_B \mathscr{T}}{mgr}, \tag{6}$$

where the final approximation assumes ($\kappa << mgr$), since this would seem to give the greatest sensitivity to gravity. The thermal noise motion is the limiting uncertainty associated with the observation of a zero crossing event and scales poorly for our purposes; it is inversely proportional to pendulum length r and mass m. Nevertheless, a frequency based detection scheme for gravity remains alluring, since exceedingly accurate time bases (e.g., GPS) are readily accessible, and a small signal can be recovered from noise using averaging techniques, provided that the base resonator is sufficiently stable.

State-of-the-art chip-scale mechanical clocks [12] now achieve part per billion frequency stability over a period of a week, so we will assume stabilization is difficult, but possible.

2.3 Timing Uncertainty Due to Thermal Noise

The determination of a zero crossing from the optical lever readout can be no more precise than the projection of noise (taken here as σ_θ) onto the time axis, which depends on the slope of the coherent response $\theta_0\omega_0$. We thus anticipate that temporal deviations Δt of a zero crossing event with respect to a reference clock will have root mean squared variance

$$\sigma_{\Delta t} = \frac{\sigma_\theta}{\theta_0\omega_0}. \tag{7}$$

The timing of the next zero crossing is correlated with the previous, to an amount dependent on dissipation [13], so deviations of periods measured in this fashion are

$$\sigma_{1/f_0,1} \approx \frac{\sigma_\theta}{\theta_0\omega_0}\sqrt{\frac{2\pi}{Q}}. \tag{8}$$

Averaging across a number of positive(negative) going zero crossings $N << Q\pi$, the relative uncertainty u_{rel} defined as the standard deviation divided by the mean, is

$$u_{\text{rel}} = \frac{\sigma_{1/f_0,N}}{T_0} \approx \frac{\sigma_\theta}{\theta_0}\sqrt{\frac{1}{2\pi N Q}}, \tag{9}$$

so that the precision with which the period can be observed in the presence of amplitude noise depends on the quality factor Q, the number of periods averaged N, and the amplitude of the motion θ_0. Here, the underlying mechanical frequency of

the resonator is constant, but the observations are obscured by the random amplitude deviations.

The choice of N is limited by the mechanical stability of the system, often determined by factors such as temperature drift or material creep, and the maximum frequency of gravitational variations to be observed, typically on the order of minutes to hours. The choice of θ_0 for a pendulum has been limited since the time of [1] by the nonlinear response, since the frequency of the resonance is weakly dependent on amplitude, which then depends on the precision of the phase-locked drive. Consideration of drive noise is beyond the scope of this rudimentary analysis. For now, we assume drive noise is less than the thermal energy.

Introducing some physical numbers, we first consider the nominal sensitivity of the microscale silicon paddle shown in Fig. 1. Given the device has $m \approx 1\times10^{-7}$ kg, $r = 5 \times 10^{-5}$ m, $I = 6 \times 10^{-15}$ kg m^{-2}, and $f_0 = 35$ Hz, a change in gravity of 10^{-7}ms^{-2} should yield a change in its frequency of $\Delta f = 3 \times 10^{-8}$ Hz. Next, we assume $T = 300$ K and find the amplitude noise is on the order of $\sigma_\theta = 4\times10^{-6}$ rad and that the relative precision on a period is $u_{\text{rel}} \leq \frac{1}{\theta_0\sqrt{N}} \times 10^{-8}$ provided $Q \geq 10^4$. Our goal is $u_{\text{rel}} \approx 10^{-8}$ for $N \approx \mathcal{O}(10^4)$, so that it appears that an amplitude $\theta_0 \geq 0.01$ rad would be minimally adequate. But the period of a pendulum is dependent on amplitude, and we must now assess the additional frequency noise resulting from this nonlinear behavior.

3 Nonlinear Equation of Motion

In this section, we derive an equation of motion for pendulation incorporating the first-order nonlinearity of the gravitational and ribbon suspension restoring torques. For the weak ribbon suspension shown in Fig. 1, the gravitational torque acting on the paddle is on the order of the suspension torque, with the balance of these two effects tuned by the placement of the paddle's center of mass, here centered below the torsion axis. To begin, we develop an expression for the stiffness of the nanoribbon suspension.

3.1 Torques Arising from Bifilar Effect

Quinn et al. [10] used a ribbon as the torsion fiber in a balance apparatus designed for measurement of the universal gravitation constant. The Q of this torsion pendulum was enhanced via the bifilar effect described by Buckley [14]. Summarizing, the restoring torque τ for each ribbon of Fig. 1 is known from torsion balance experiments (e.g., [10]) to consist of two components

$$\tau = \tau_E + \tau_\sigma \quad \text{with} \quad \tau_E = \frac{Eh^3 w}{6l}\theta \quad \text{and} \quad \tau_\sigma = \frac{\sigma h w^3}{12l}\theta. \tag{10}$$

The first component, τ_E, attributable to Saint-Venant [15, 16], is due to shear deformation of the ribbon and is a source of loss. The second component, τ_σ, attributable to Buckley [14], is due to the tensile load $T = \sigma h w$ and is lossless.

3.2 Torques Arising from Midplane Stretching

We now consider a horizontal torsion balance that uses fully constrained ribbons (clamped on each end) whose tensile load is due to thin-film residual stress, as in Fig. 1.

Heuristically, we follow [14] and consider each ribbon to be composed of parallel infinitesimal strings of length l and infinitesimal width $\mathrm{d}y$, located at a distance y from the center line. Each string is fastened at one end to the fixed frame and at the other end to the torsion paddle, which is free to rotate through angle θ.

The strings represent a very high aspect ratio ($l/h > 10^4$) membrane of thickness h and width w loaded in tension from residual stress $\sigma = T/(hw)$. The tensile force per breadth of ribbon $T_0 = T/w$ imposes a tensile load $T_0\,\mathrm{d}y$ on each infinitesimal string.

To analyze the torsional stiffness of the ribbon, we consider rotating the paddle through an angle θ. Shown in Fig. 1, each infinitesimal string displaces vertically from equilibrium a distance $\Delta z \approx y\theta$ at the paddle end to form angle α with horizontal. It also elongates by an amount $\Delta l \approx \Delta z^2/(2l)$, yielding a (longitudinal) strain

$$s = \frac{\Delta l}{l} \approx \frac{1}{2}\frac{y^2\theta^2}{l^2}. \tag{11}$$

The quadratic dependence of strain on rotation angle suggests that the restoring torque due to tension contains a negligible contribution from deformation, i.e., approximately "lossless." Continuing, note that the longitudinal stiffness per breadth of the ribbon is $k = Eh/l$, where E is the modulus of elasticity. The change in tension per breadth of the ribbon is then $\Delta T_0 = k\Delta l = Ehs$, and the vertical restoring force applied by each string to the paddle (containing contributions from both tension T_0 and elongation ΔT_0) is

$$\begin{aligned} F_z &= (T_0 + \Delta T_0)\mathrm{d}y \sin\alpha \approx (T_0 + Ehs)\frac{y\theta}{l(1+s)}\,\mathrm{d}y \\ &\approx T_0\frac{y\theta}{l}\mathrm{d}y + \frac{1}{2}\left(Eh - T_0\right)\frac{y^3\theta^3}{l^3}\mathrm{d}y, \end{aligned} \tag{12}$$

where α is the angle of each string from horizontal and $\sin\alpha \approx \frac{y\theta}{l(1+s)} \approx \frac{y\theta}{l}(1-s)$.

To compute the total restoring torque on the paddle, we sum the contribution $\tau_0 \approx F_z y$ from each string, remembering they occur in pairs, one on each side of the neutral line, and mirrored across the paddle

$$\tau_\sigma \approx \int_0^{w/2} 4F_z y dy = \frac{\sigma h w^3 \theta}{6l} + \frac{1}{80}\left(E-\sigma\right)\frac{h w^5 \theta^3}{l^3}. \tag{13}$$

We have recovered the result due to [14], with an additional term due to the linear longitudinal strain that is nonlinear in the displacement θ.

3.3 Free Oscillations Without Damping

Our interest is in quantifying the nonlinear dependence of the natural frequency on amplitude. The motion in the absence of dissipation and excitation is sufficient to determine conditions for isochronous behavior.

First, we need an expression for the restoring torque due to gravity. This is simply $\tau_g = mgr\sin\theta \approx mgr(\theta - \theta^3/6 + \cdots)$. Summing the torques that act on the paddle and setting them equal to the product of inertia and angular acceleration, we have

$$I\ddot{\theta} = -\tau_g - \tau_E - \tau_\sigma. \tag{14}$$

Collecting and grouping terms linear and nonlinear in θ gives

$$\ddot{\theta} = -\alpha_1\theta - \alpha_3\theta^3, \tag{15}$$

where

$$\alpha_1 = \frac{Eh^3 w}{3lI} + \frac{\sigma h w^3}{6lI} + \frac{mgr}{I} = \omega_0^2 \;\text{ and }\; \alpha_3 = \frac{1}{80I}\left(E-\sigma\right)\frac{h w^5}{l^3} - \frac{mgr}{6I}. \tag{16}$$

We make the following observations concerning α_3. First, the difference $(E-\sigma)$ is always positive since the residual stress cannot exceed a small fraction of the modulus. Second, there is an opportunity to null this term since the contribution from mid-plane stretching is of the opposite sign to that of the first-order nonlinear gravitational torque. Supposing we can neglect σ in the expression for α_3, then we seek a geometry such that

$$\frac{E}{80} h w^5 / l^3 \approx mgr/6. \tag{17}$$

To test if a suitable geometry is feasible, we pick a convenient nitride layer thickness $h = 100\,\text{nm}$ and substitute $E = 280 \times 10^9\,\text{Nm}^{-2}$ and $g = 9.81\,\text{m}\,\text{s}^{-2}$,

yielding

$$\frac{w^5}{l^3} \cdot 214\,\mathrm{kg\,m^{-1}} \approx mr. \tag{18}$$

Assuming the suspended mass is a cube of silicon with density $\rho = 2700\,\mathrm{kg\,m^{-3}}$ and that each side has length $\approx 2r$, then $m = \rho(2r)^3 \approx 2.2 \times 10^4\,\mathrm{kg/m^3}\,r^3$ so that the dimensional relationships between the ribbon and suspended mass required to null the first order nonlinearity are

$$\left(\frac{w}{l}\right)^3 w^2 = r^4 \cdot 103\,\mathrm{m^{-2}}. \tag{19}$$

Choosing $w/l \approx 0.02$ and $r \approx 125\,\mu\mathrm{m}$, we find that a ribbon suspension with $w \approx 52\,\mu\mathrm{m}$, $l \approx 2.6\,\mathrm{mm}$, and $h \approx 100\,\mathrm{nm}$ might yield isochronous pendulation of a cube of silicon, $\approx 440\,\mu\mathrm{m}$ on a side, weighing $\approx 60\,\mu\mathrm{g}$.

In summary, the general form of the equation of motion is

$$\ddot{\theta} + \omega_0^2\theta + \epsilon\alpha_3\theta^3 = 0, \tag{20}$$

where we employ the variable ϵ as a small parameter introduced as a bookkeeping term. The equation has the form of a Duffing equation. In the next section, we employ the method of multiple scales [17] to determine its first-order uniform expansion.

4 Analytical Approximation for Frequency-Amplitude Coupling

Following Nayfeh, [17], we seek a uniform expansion of (20) using the substitution

$$\theta(t;\epsilon) = u(T_0, T_1, T_2 \cdots;\epsilon), \tag{21}$$

where $T_n = \epsilon^{n-1}t$. Letting $u = u_0(T_0, T_1, T_2, \cdots) + \epsilon u_1(T_0, T_1, T_2, \cdots) + \cdots$, substitute for θ in the equation of motion, and equate coefficients of ϵ^0 and ϵ^1 to zero, finding

$$D_0^2 u_0 + \omega_0^2 u_0 = 0, \text{ and} \tag{22}$$

$$D_0^2 u_1 + \omega_0^2 u_1 = -2D_0 D_1 u_0 - \alpha_3 u_0^3. \tag{23}$$

The general solution of Eq. (22) can be written as

$$u_0 = U(T_1)e^{i\omega_0 T_0} + \bar{U}(T_1)e^{-i\omega_0 T_0} \text{ with } U = \frac{1}{2}ae^{i\beta} \tag{24}$$

and $\bar{U}$ is its complex conjugate. Plugging this solution into Eq. (23) yields

$$D_0^2 u_1 + \omega_0^2 u_1 = -2i\omega_0 U' e^{i\omega_0 T_0} - \alpha_3 U^3 e^{i3\omega_0 T_0} - 3\alpha_3 U^2 \bar{U} e^{i\omega_0 T_0} + cc, \tag{25}$$

where the prime denotes differentiation with respect to T_1 and cc are the complex conjugates of the preceding terms.

Collecting secular terms and setting them equal to zero

$$2i\omega_0 U' = -3\alpha_3 U^2 \bar{U}, \tag{26}$$

which in polar form is

$$2i\omega_0\left(\frac{1}{2}a'e^{i\beta} + \frac{1}{2}ia\beta' e^{i\beta}\right) = -\alpha_3 \frac{3}{8}a^3 e^{i\beta}. \tag{27}$$

Collecting real and imaginary terms and setting them equal to zero yields

$$a' = 0 \text{ and } \beta' = \frac{\alpha_3}{\omega_0}\frac{3}{8}a^2. \tag{28}$$

By inspection, Eq. (28) suggests that the amplitude is constant. The phase modulation is determined by integrating β'. The final form of the approximate solution is

$$\theta(t) \approx \theta_0 \cos(\omega_n t + \beta_0) \text{ with } \omega_n \approx \omega_0 + \frac{3}{8}\frac{\alpha_3}{\omega_0}\theta_0^2. \tag{29}$$

This reveals that the natural frequency of a pendulum suspended from a torsion ribbon, ω_n, depends in a parametric fashion on the amplitude squared. This coupling provides a conduit for amplitude noise to project onto the resonator frequency, as we explore next.

4.1 Parametric Frequency Noise

To approximate self-sustaining oscillation, assume a noiseless phase locked torque creates a closed loop system on the boundary of linear stability, or effectively free oscillation subject to a weak thermal drive, similar to approaches in the past [18]. We then consider fluctuations due to noise about a given amplitude θ_0 and employ the derivative of ω_n with respect to amplitude as a measure of the resonant frequency's sensitivity to amplitude variations

$$\frac{d\omega_n}{d\theta_0} = \frac{\alpha_3}{\omega_0}\frac{3}{4}\theta_0. \tag{30}$$

By taking the modulus of this sensitivity, we may approximate the root mean squared parametric frequency noise as

$$\sigma_{\omega_n} \approx \left|\frac{\alpha_3}{\omega_0}\frac{3}{4}\theta_0\right|\sigma_\theta \implies \sigma_{1/f_n,1} \approx 2\pi\frac{\sigma_{\omega_n}}{\omega_n^2}, \tag{31}$$

where the right equation gives the uncertainty in the period.

In contrast to the discussion of Eq. (8), the resonance frequency now varies as a consequence of the random thermal motions. Formerly, the mechanical frequency was constant, and noise limited our ability to resolve periodic events. Here, the period itself is altered by the noise. Summing Eqs. (8) and (31) in quadrature, an approximation of the rms frequency noise is

$$\sigma_{1/f_n} = \frac{\sqrt{2\pi}\sigma_\theta}{\omega_0\theta_0}\sqrt{\frac{1}{Q^2} + \frac{9\pi}{8}\frac{\alpha_3^2\theta_0^4}{\omega_n^4}}. \tag{32}$$

5 Comparison of Analytical Results and Simulations

The previous derivations suggest the device is a classical pendulum and achieves maximum sensitivity to gravity when $\kappa << \kappa_g$, resulting in $\alpha_3 \approx \omega_0^2/6$. In this case, Eq. (32) suggests parametric phase noise becomes the limiting factor in devices where Q exceeds 10^6 and amplitude approaches 10 mrad, as in our previous investigation [2]. Now, consider a suspension where $\kappa \geq \kappa_g$. The phase noise is predicted to be reduced for these devices and completely eliminated once the isochronous condition $\alpha_3 \approx 0$ is met. From Eqs. (2) and (3), we conclude that the isochronous condition will cost us gravitational sensitivity. Nevertheless, isochronous behavior appears worth pursuing in order to inoculate the device from as yet unconsidered drive noise, as discussed in [6].

We perform numerical simulations (fourth-order fixed step Runge Kutta) using the equation of motion (Eq. 20) to examine the dependence of the period on the amplitude of the initial deflection and to validate the multiple scales solution. The motion is integrated for $N \approx 3 \times 10^5$, and the frequency is determined from a fast Fourier transform of the resulting time series, so that we resolve the frequency to several parts per million.

In Fig. 2, we highlight geometries that yield softening, isochronous, and hardening behaviors, respectively. We assume a Si paddle 125 μm thick ($r = 50$ μm) and 425 μm × 425 μm wide (mass $m_{pad} \approx 0.06$ mg) suspended from a silicon nitride nanoribbon having dimensions $l = 2.6$ mm, $h = 75$ nm, and $w = 35$ μm, 53 μm, or 75 μm, with mechanical properties $\sigma = 0.85$ GPa and $E = 250$ GPa. The results

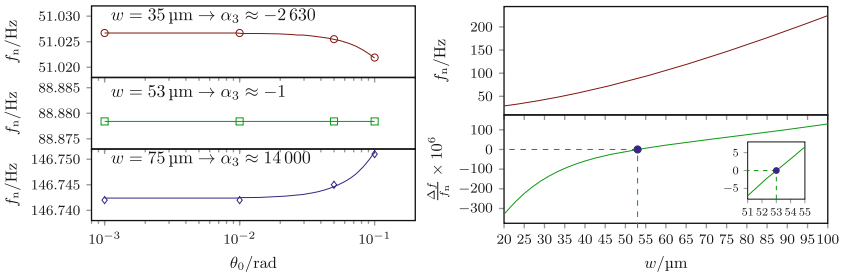

Fig. 2 Left: Frequency obtained by simulation for three oscillators with different strip width w as a function of initial excursion θ_o. The points are obtained by numerical simulations discussed above, and the lines are calculated using Eq. (29). At $w = 53\,\mu\text{m}$, the frequency of the oscillator is independent of θ_o. Right: The top panel shows the frequency of the oscillator driven with an amplitude of $\theta_o = 1$ mrad. The bottom panels show the relative frequency difference for the pendulum driven at 100mrad and 1 mrad. The isochronous case is reached when the frequency does not depend on amplitude, at $w = 53\,\mu\text{m}$

are plotted as open circles along with solid lines representing the analytical solution (Eq. 33). The agreement between simulation and analytic results is excellent.

Finally, we employ the multiple scales solution to explore the sensitivity of the isochronous condition to variations in the beam width, plotting the difference between small (1 mrad) and large (100 mrad) amplitude natural frequencies computed as a function of ribbon width in Fig. 2. The figure inset suggests an approximately isochronous state with $\Delta f/f < 5 \times 10^{-6}$ that can be maintained in the presence of large amplitude noise, as long as w can be manufactured to within approximately $2\,\mu\text{m}$ of the desired width. Such a tolerance is challenging within the bounds of conventional photolithography but easily achieved using e-beam lithography.

6 Conclusions

We have modeled the weakly nonlinear behavior of micropendulum devices from [2] considering their phase-locked driven performance in the presence of room temperature thermomechanical noise and find no fundamental impediments to achieving micro-g resolution at averaging times $< 1000\,\text{s}$. We find that nonlinear torques due to gravity and midplane stretching of the torsion fiber cause the resonant frequency of the device to depend on driven amplitude. Interestingly, the model suggests that the two nonlinearities can compensate one another to yield an isochronous motion. Simulated behavior using both the equation of motion and an analytical multiple scales perturbation solution agree for amplitudes up to 100 mrad, and the perturbation solution suggests an approximately isochronous micropendulum should be manufacturable. Next steps are to fabricate new devices, develop a

detection scheme for monitoring the large amplitude motion, and characterize the amplitude dependence of frequency experimentally.

References

1. Richer, J.: Observations Astronomiques et Physiques faites en L'isle de Caïenne. Mémoires de l'Académie Royale des Sciences **7**, 231 (1729)
2. Pratt, J.R., et al.: Nanoscale torsional dissipation dilution for quantum experiments and precision measurement. Phys. Rex X **13**, 011018 (2022)
3. Pike, W.T., et al.: A broad-band silicon microseismometer with 0.25 ng/rt-Hz performance. Proc. IEEE MEMS (2018). https://doi.org/10.1109/MEMSYS.2018.8346496
4. Middlemiss, R.P., et al.: Measurement of the Earth tides with a MEMS gravimeter. Nature **531**, 614 (2016)
5. Mustafazade, A., et al.: A vibrating beam MEMS accelerometer for gravity and seismic measurements. Sci. Rep. **10**, 10415 (2020)
6. Agnew, D.C.: Time and tide: pendulum clocks and gravity tides. Hist. Geo Space. Sci. **11**, 215 (2020)
7. Saulson, P.M.: Thermal noise in mechanical experiments. Phys. Rev. D **42**, 2437 (1990)
8. Zener, C.M.: Elasticity and Anelasticity of Metals. The University of Chicago Press, Chicago (1948)
9. Braginsky, V.B., Manukin, A.B.: Measurement of Weak Forces in Physics Experiments. Chicago U.P., Chicago (1977)
10. Quinn, T.J., et al.: Novel torsion balance for the measurement of the Newtonian gravitational constant. Metrologia **34**, 245 (1997)
11. Lin, D., et al.: Polaris - A Low Cost MEMS Fabrication Platform for Navigation-Grade Inertial Sensors, 2021. In: IEEE International Symposium on Inertial Sensors and Systems (INERTIAL), Kailua-Kona, HI, USA (2021)
12. Ortiz, L.C., et al.: Low-power dual mode MEMS resonators with PPB stability over temperature. J. Microelectromech. Syst. **29**, 190 (2020)
13. Wang, M., et al.: Fundamental limits and optimal estimation of the resonance frequency of a linear harmonic oscillator. Commun. Phys. **4**, 207 (2021)
14. Buckley, J.C.: The bifilar property of twisted strips. Philos. Mag. Ser. 1 **28**, 778 (1914)
15. de Saint-Venant, M.: Mémoire sur la torsion des prismes. Imprimerie nationale, Paris (1856)
16. Timoshenko, S.P., Goodier, J.N.: Theory of Elasticity. Citeseer, New York (1951)
17. Nayfeh, A.H.: Introduction to Perturbation Techniques. Wiley, New York (1981)
18. Miller, N.J., et al.: Suppressing frequency fluctuations of self-sustained vibrations in underdamped nonlinear resonators. Phys. Rev. Appl. **15**, 014024 (2021)

A Comparative Study of Two Types of Bifurcation-Based MEMS Sensors

Yasser S. Shama, Rana Abdelrahman, Mohamed Arabi, Resul Saritas, Sasan Rahmanian, Ahmet Gulsaran, Samed Kocer, Alaa Elhady, Hamza Mouharrar, and Eihab M. Abdel-Rahman

1 Introduction

Urban sprawl and industrial expansion are massive sources of pollution as they release large quantities of hazardous waste. Detecting and monitoring pollutants are essential in environmental management and control. Therefore, we need to deploy highly sensitive sensor arrays that can detect low concentrations of hazardous gases. Micro electromechanical system (MEMS) gas sensors have been a leading technology in this field for the last two decades due to their small size, lightweight, low power consumption, and high functionality in real-time applications [1]. Researchers have recently pursued bifurcation-based sensing as a means to enhance the sensitivity and robustness of MEMS sensors by exploiting the sudden, typically large, jump in vibration amplitude experienced through bifurcations [1–6].

Y. S. Shama (✉)
Department of Systems Design Engineering, University of Waterloo, Waterloo, ON, Canada
Waterloo Institute of Nanotechnology, University of Waterloo, Waterloo, ON, Canada
Benha Faculty of Engineering, Department of Mechanical Engineering, Benha University, Benha, Egypt
e-mail: Ys2shama@uwaterloo.ca

R. Abdelrahman · R. Saritas · S. Rahmanian · S. Kocer · A. Elhady · H. Mouharrar · E. M. Abdel-Rahman
Department of Systems Design Engineering, University of Waterloo, Waterloo, ON, Canada
Waterloo Institute of Nanotechnology, University of Waterloo, Waterloo, ON, Canada

M. Arabi
Department of Electrical and Mechanical Engineering, Applied Science University (ASU), Al Eker, Kingdom of Bahrain

A. Gulsaran
Waterloo Institute of Nanotechnology, University of Waterloo, Waterloo, ON, Canada
Department of Mechanical and Mechatronics Engineering, University of Waterloo, Waterloo, ON, Canada

© The Author(s), under exclusive license to Springer Nature Switzerland AG 2024

W. Lacarbonara (ed.), *Advances in Nonlinear Dynamics, Volume III*, NODYCON Conference Proceedings Series, https://doi.org/10.1007/978-3-031-50635-2_2

Younis and Alsaleem [1] proposed mass sensing techniques using harmonically excited electrostatic MEMS. Their results demonstrate the feasibility of using bifurcations in the vicinity of primary resonance and the subharmonic resonance of order one-half to detect mass changes. They also found the latter bifurcation to provide a higher detection signal than the former.

Khater et al. [2] presented a technique to improve the sensitivity of inertial electrostatic MEMS sensors by driving them near a static or dynamic bifurcation resulting in a large detection signal upon mass change.

Kumar et al. [3] utilized a piezoelectrically actuated MEMS sensor to detect methanol vapor by monitoring the changes in its response amplitude in the vicinity of a cyclic-fold bifurcation. Li et al. [4] presented a di-nitro toluene (DNT) gas sensing system using a piezoelectrically actuated MEMS resonator. The sensor uses two detection mechanisms based on a primary Hopf and a reverse Hopf bifurcations at the edges of the nontrivial region of a parametric resonator. They were able to detect 0.93 ppb of DNT.

Al-Ghamdi et al. [5] developed binary inertial gas sensors using electrostatic MEMS resonators. Their detection mechanism was based on a cyclic-fold bifurcation in the vicinity of primary resonance to detect ethanol vapor. Their results show a detection limit lower than 5 ppm.

Meesala et al. [6] proposed two bifurcation-based sensing mechanisms for inertial electromagnetic MEMS sensors. In the first, a subcritical Hopf changes to a supercritical Hopf upon addition of a mass while in the second the location of a subcritical Hopf resulting in a large nontrivial detection signal.

In this paper, we experimentally compare the sensitivity of an electrostatic MEMS methane sensor employing a Hopf bifurcation to that of the sensor when employing a cyclic-fold bifurcation in terms of the size of the detection signal and the shift in the bifurcation frequency.

2 Sensor

2.1 Design

The sensor was fabricated in the PolyMUMPs process [7]. The sensor comprises a ($35 \times 120 \times 1.5$ μm) sense-plate supported by two (110 μm long × 10 μm wide × 1.5 μm thick) cantilever beams fabricated in the second structural polysilicon layer (Poly 2). They lie above a central actuation electrode fabricated in the first polysilicon layer (Poly 0) and two side landing electrodes fabricated in the first structural layer (Poly 1), Fig. 1. The stepped-up landing electrodes are designed to prevent direct contact between the resonator and the actuation electrode to protect against short circuits, stiction, and dielectric charging. A gold layer, 5 μm wide and 500 nm thick, is deposited along the two cantilever beams to produce upward curvature in those beams, thereby increasing the capacitive gap and reducing

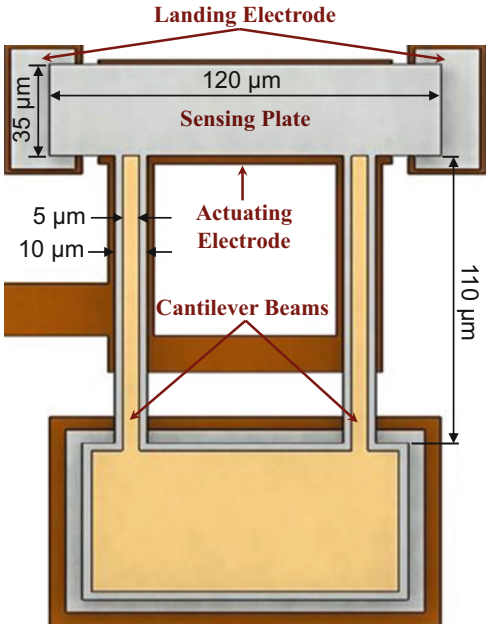

Fig. 1 A schematic of the sensor under test

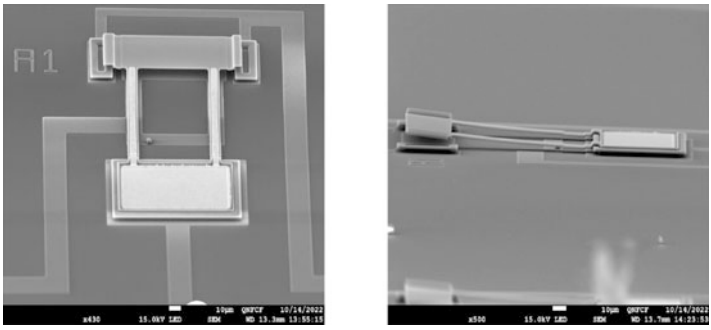

Fig. 2 The Scanning Electron Microscope (SEM) images of the sensor

damping due to squeeze-film. Figure 2 shows Scanning Electron Microscope (SEM) top and side images of the fabricated sensor.

2.2 Modal Analysis

Thermal noise, a stochastic excitation force with a uniform frequency spectrum, is deployed to capture the structure's resonant frequencies. To increase the signal-to-noise ratio (SNR), the sensor was placed inside a vacuum chamber at a pressure of 6 mbar. All experiments were conducted at room temperature $T = 23\,^{\circ}\mathrm{C}$. A glass port

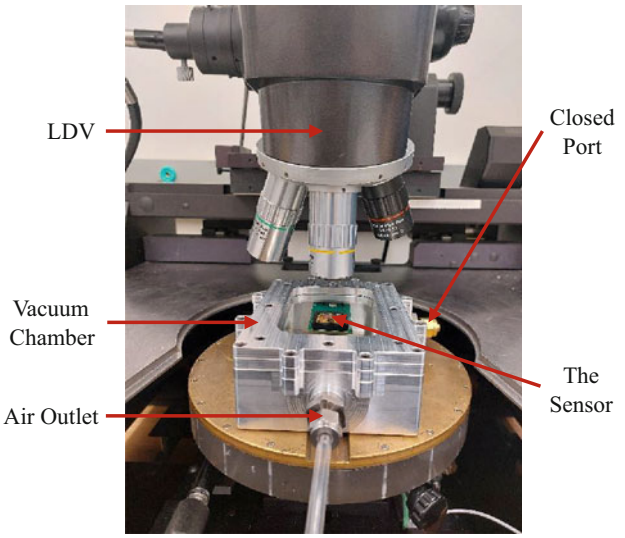

Fig. 3 The Experimental setup for thermal noise excitation

in the chamber was used to optically measure the velocity at the tip of the sense-plate right edge via a laser Doppler Vibrometer (LDV), Polytec Inc.'s MSV400 [8]. The experimental setup is shown in Fig. 3.

The Fast Fourier Transform (FFT) of the plate center point velocity was evaluated and inspected for peaks in the first 400 kHz of the frequency spectrum. The peaks were found to correspond to the first out-of-plane bending mode at $\omega_\circ = 39.339$ kHz, the first torsional mode at 120.587 kHz, and the second out-of-plane bending mode at 304.831 kHz.

2.3 Functionalization

In this process, the sensor becomes functional by depositing a sensing material on its sense-plate. Polyaniline (PANI) doped with 5% SnO_2 was deposited on the sensor plate for methane absorption. Since this mixture is a solid powder, a liquid solution that contains ethylene glycol (solvent) and the solid powder was prepared with a concentration of 10–15% to ease the deposition process. The idea of using a liquid solution is that it acts as a transportation agent to locate the functional powder on its target location, and then the solvent is allowed to evaporate, leaving the solid powder on the sense-plate. Considering that, a semi-automated deposition system that consists of a nanostage with a glass micropipette of 20 μm tip attached to a microplotter from Sonoplot [9] was employed for deposition. Figure 4 shows the Scanning Electron Microscope (SEM) image of the sensor after functionalization.

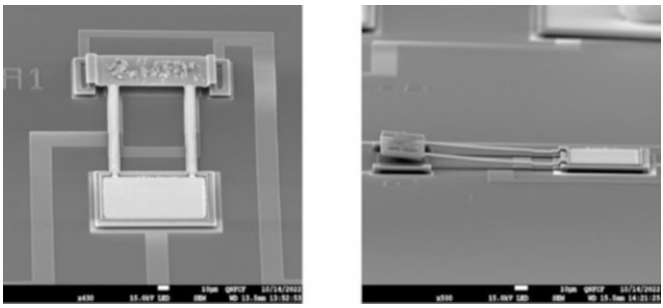

Fig. 4 The Scanning Electron Microscope (SEM) images of the functionalized sensor

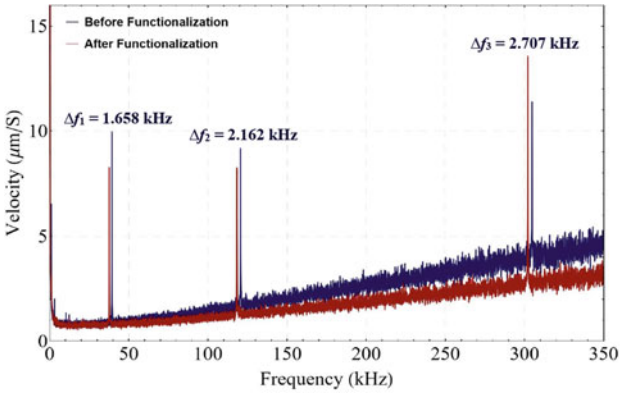

Fig. 5 The frequency response of the sensor before and after functionalization

Using the experimental setup and procedure described above, the first three natural frequencies of the functionalized sensor were obtained under thermal noise excitation, Fig. 5. The first three natural frequencies were found to have dropped by 1.658, 2.162, and 2.707 kHz, respectively. Based on linear vibration theory and using the drop in the fundamental natural frequency, the fractional mass of the deposited material m_d was estimated as

$$N = \frac{m_d}{m_s} = \left(\frac{f_{\text{before}}}{f_{\text{after}}}\right)^2 - 1 \tag{1}$$

and was found to be 9% of the sensor's effective mass m_s.

2.4 Bifurcations

The sensor was actuated electrostatically using a biased voltage waveform

$$V(t) = V_{\mathrm{DC}} + V_{\mathrm{AC}} \cos(\Omega t) \tag{2}$$

where Ω is the signal frequency. The resulting electrostatic force

$$F_e(t) = \alpha\left(V_{\mathrm{DC}}^2 + \tfrac{1}{2}V_{\mathrm{AC}}^2 + 2V_{\mathrm{DC}}V_{\mathrm{AC}}\cos(\Omega t) + \tfrac{1}{2}V_{\mathrm{AC}}^2\cos(2\Omega t)\right) \tag{3}$$

has two harmonics. The voltage waveform was generated using a function generator (Tectronix AFG3022B) [10] and a voltage amplifier. In the current work, we set $V_{\mathrm{AC}} = V_{\mathrm{DC}}$ throughout our experiments, thereby minimizing the impact of the second harmonic at 2Ω and leaving the first harmonic at Ω as the dominant excitation frequency. Forward frequency sweeps of Ω were employed to detect bifurcations in the response of the sensor in the vicinity of its primary resonance and subharmonic resonance of order one-half.

To obtain the frequency response of the sensor at primary resonance, the excitation amplitude was set to a constant value while the frequency Ω was increased past the fundamental resonant frequency $\omega_\circ$ at a slew rate of 5 kHz/s. The sense-plate center velocity was measured using a Laser Doppler vibrometer (LDV) (Polytec MSV 400) [8]. A trigger signal was introduced by the function generator to synchronize the input (applied voltage) and the output (MEMS velocity) signals. The output signal was discretized using an oscilloscope (Keysight DSOS204A) [11]. Finally, the frequency-response curve was obtained by evaluating the RMS of the time-domain response using an in-house software. Figure 6 shows the frequency-response curves of the sensor in the vicinity of primary resonance for four voltage waveforms. As the amplitude of the first harmonic increases from $V_{\mathrm{AC}} = V_{\mathrm{DC}} =$ 22.5 to 24.75V, the sensor response becomes multivalued. This is exhibited in a sudden jump from a low branch to a high branch at a cyclic-fold bifurcation.

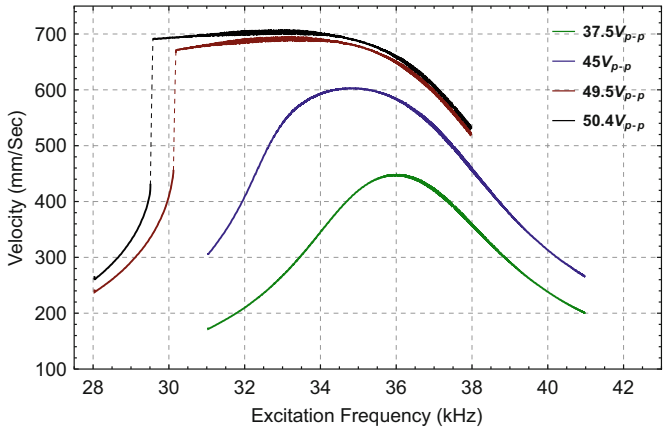

Fig. 6 The frequency-response curves of the functionalized sensor under four voltage waveform with $V_{\mathrm{AC}} = V_{\mathrm{DC}}$

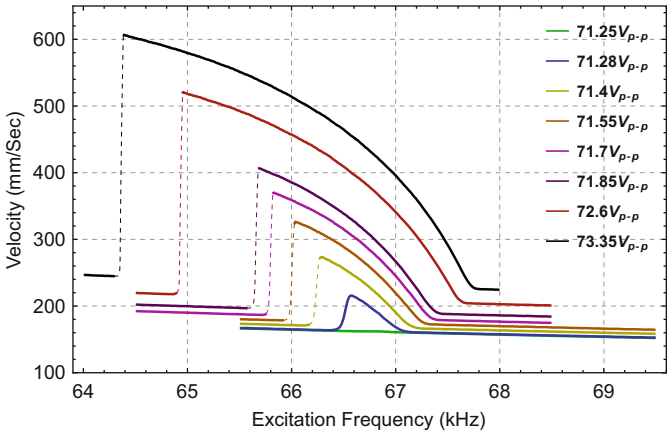

Fig. 7 The frequency-response curves of the functionalized sensor in the vicinity of its subharmonic resonance under eight voltage waveform with $V_{AC} = V_{DC}$

The same setup was used to obtain the frequency-response curves in the vicinity of the subharmonic resonance of order one-half. The excitation amplitude was set to a constant value while the frequency Ω was increased past twice the fundamental resonant frequency $2\omega_o$ at a slew rate of 2.5 kHz/s. The amplitude of the first harmonic $2V_{\mathrm{DC}}V_{\mathrm{AC}}$ was increased until it crossed the activation level of the subharmonic resonance beyond $V_{\mathrm{AC}} = V_{\mathrm{DC}} = 35.625$ V.

Figure 7 shows eight frequency-response curves in the vicinity of the subharmonic resonance of order one-half. For excitations above the activation level, the sensor experiences a subcritical Hopf bifurcation at the left-end of a nontrivial region, Fig. 7, marked by a sudden jump from a small branch of forced oscillations to a large resonant branch. The location of this bifurcation moves to lower frequencies as the excitation level increases. A corresponding supercritical Hopf bifurcation marks the merger of the resonant and forced branches at the other end of the nontrivial region.

3 Experiment

The experiment was designed to compare bifurcation sensing using the cyclic-fold bifurcation, appearing in the vicinity of the primary resonance, to the Hopf bifurcation, appearing in the neighbor of the subharmonic resonance of order one-half, on the same sensor platform. The baseline location (frequency) of each bifurcation was obtained first in nitrogen then in the presence of 50 ppm methane mixed with nitrogen. The sensing metric is the difference between the locations of the bifurcation before and after introduction of methane for each resonance type.

The experimental setup is the same as that described above except that the inlet of the test chamber was attached to a nitrogen and 50 ppm methane/nitrogen balance cylinders via a mass flow control unit (MKS Series 946) [12]. A water bubbler was attached to the outlet to prevent back flow. First, nitrogen was introduced at a flow rate of 100 SCCM. The chamber conditions were monitored by an environmental sensor (SensorPush) [13] until its relative humidity level has stabilized at $RH = 6\%$. The baseline location of the cyclic-fold bifurcation was obtained under the voltage waveform $V_{AC} = V_{DC} = 25.2\,\text{V}$ by sweeping the excitation frequency past its previously measured location, Fig. 6. The baseline location of the subcritical Hopf bifurcation was obtained under the voltage waveform $V_{AC} = V_{DC} = 36.75\,\text{V}$ by sweeping the excitation frequency past its previously measured location, Fig. 7. The locations of the baseline bifurcations were found using the same procedure described above.

The nitrogen flow line was then closed, and the methane/nitrogen line was opened introducing the target gas mixture into the chamber at the same flow rate for 20 min. The same procedure described above was used to obtained the locations of the cyclic-fold and subcritical Hopf bifurcations in the presence of methane. Finally, another cycle of nitrogen was introduced into the chamber to refresh the sensor.

4 Results and Discussion

Figure 8 compares the frequency-response curve of the sensor in the vicinity of primary resonance before exposure to methane to that after exposure. The location of the cyclic-fold bifurcation, marked by the jump from the low to the high branch, shifts to the left by 34 Hz upon exposure to 50 ppm of methane, which is highlighted in the figure inset. The frequency-response curves of the sensor in the vicinity of subharmonic resonance of order one-half before and after exposure to 50 ppm methane, Fig. 9, show a downward shift in the location of the subcritical Hopf bifurcation of 48 Hz.

To examine the sensor repeatability, we refreshed the functional material by purging the chamber with nitrogen for 20 min then repeated the procedure described

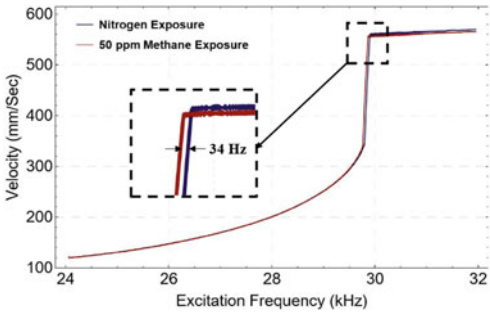

Fig. 8 Detection of 50 ppm methane using the cyclic-fold bifurcation

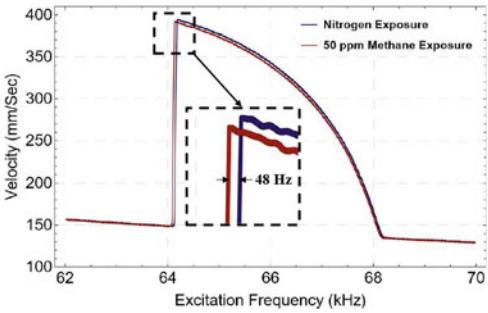

Fig. 9 Detection of 50 ppm methane using the subcritical Hopf bifurcation

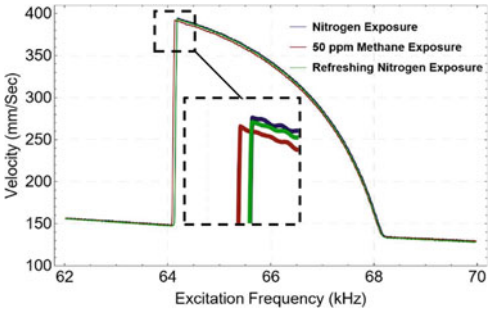

Fig. 10 The frequency-response curves of the sensor during a sequence of exposure to nitrogen only, 50 ppm of methane in nitrogen, and nitrogen again

above to obtain the frequency-response curve in the vicinity of the subharmonic resonance of order one-half. Figure 10 compares refreshed curve to those before and after first exposure to methane. The curves obtained during the first and second cycles of nitrogen are almost indistinguishable which shows that the sensor is reversible.

5 Conclusions

This paper compares experimentally the sensitivity of bifurcation sensors employing two types of bifurcations, namely a cyclic-fold bifurcation and a subcritical Hopf bifurcation. The platform used in the comparison is an electrostatic MEMS methane sensor fabricated in the PolyMUMPs process and functionalized by depositing a methane sensitive polymer, Polyaniline (PANI) doped with 5% SnO_2, on its sense-plate. The frequency response of the sensor in the vicinity of its primary resonance and subharmonic resonance of order one-half were used to measure the locations of the bifurcations, respectively, before and after exposure to methane. The results demonstrate that utilizing the subcritical Hopf bifurcation is more effective compared to the cyclic-fold bifurcation, with a sensitivity improvement of over 40%. Moreover, the signal amplitude upon detection is 25% larger. However, the subcritical Hopf was found to be more sensitive to variability in environmental conditions which can affect the performance of sensors using it as a detection mechanism.

References

1. Younis, M.I., Alsaleem, F.: Exploration of new concepts for mass detection in electrostatically-actuated structures based on nonlinear phenomena. J. Comput. Nonlinear Dyn. **4**(2), 021010 (1–15) (2009)
2. Khater, M.E., Abdel-Rahman, E.M., Nayfeh, A.H.: A mass sensing technique for electrostatically-actuated MEMS. In: International Design Engineering Technical Conferences and Computers and Information in Engineering Conference, vol. 49033, pp. 655–661 (2009)
3. Kumar, V., Yang, Y., Boley, J.W., Chiu, G.T.-C., Rhoads, J.F.: Modeling, analysis, and experimental validation of a bifurcation-based microsensor. J. Microelectromech. Syst. **21**(3), 549–558 (2012)
4. Li, L.L., Holthoff, E.L., Shaw, L.A., Burgner, C.B., Turner, K.L.: Noise squeezing controlled parametric bifurcation tracking of MIP-coated microbeam MEMS sensor for TNT explosive gas sensing. J. Microelectromech. Syst. **23**(5), 1228–1236 (2014)
5. M. Al-Ghamdi, Khater, M., Stewart, K., Alneamy, A., Abdel-Rahman, E.M., Penlidis, A.: Dynamic bifurcation "MEMS" gas sensors. J. Micromech. Microeng. **29**(1), 015005 (2018)
6. Meesala, V.C., Hajj, M.R., Abdel-Rahman, E.: Bifurcation-based MEMS mass sensors. Int. J. Mech. Sci. **180**, 105705 (2020)
7. Cowen, A., Hardy, B., Mahadevan, R., Wilcenski, S.: PolyMUMPs Design Handbook, vol. 13. Memscap Inc. (2003). https://people.eecs.berkeley.edu/~poster/245/polymumps.dr.v10%5B1%5D.pdf
8. Polytec Inc.: OFV-5000 Vibrometer Controller User Manual. www.Polytec.com
9. Sonoplot: GIX Microplotter Desktop User Manual. www.sonoplot.com
10. Tektronix: AFG3000 Series Quick Start User Manual. www.Tek.com
11. Keysight: DSOS204A High-Definition Oscilloscope User Manual. www.Keysight.com
12. MKS: MKS Series 946 Vacuum System Controller User Manual. www.MKS.com
13. SensorPush: HTP Extreme Accuracy Water-Resistant Temperature/Humidity/Barometric Pressure Smart Sensor User Manual. www.sensorpush.com

How to Excite Anti-symmetric Modes in a Symmetric MEMS?

Sasan Rahmanian, Ayman Alneamy, Yasser S. Shama, Samed Kocer, Eihab M. Abdel-Rahman, and Mustafa Yavuz

1 Introduction

The nonlinear dynamics of Micro-Electro-Mechanical Systems (MEMS) feature interesting phenomena that can be employed to improve the performance of MEMS actuators and sensors, such as modal interactions [1–11]. This phenomenon leads to energy exchange between two vibration modes of a structure having a commensurate ratio between their natural frequencies and an energy channel. The vibrations of the two modes may occur along the same degree-of-freedom [1] or two or more linearly independent degrees-of-freedom [12].

Several researchers have observed the activation of one-to-two modal interactions between the symmetric modes of symmetrically designed MEMS and NEMS. For example, Hajjaj et al. [13] found interaction between the first two

S. Rahmanian (✉) · S. Kocer · E. M. Abdel-Rahman
Systems Design Engineering, University of Waterloo, Waterloo, ON, Canada

Waterloo Institute for Nanotechnology (WIN), University of Waterloo, Waterloo, ON, Canada
e-mail: s223rahm@uwaterloo.ca

A. Alneamy
Department of Mechanical Engineering, Jazan University, Jazan, Saudi Arabia

Y. S. Shama
Systems Design Engineering, University of Waterloo, Waterloo, ON, Canada

Waterloo Institute for Nanotechnology (WIN), University of Waterloo, Waterloo, ON, Canada

Mechanical Engineering Department, Benha Faculty of Engineering, Benha University, Benha, Egypt

M. Yavuz
Waterloo Institute for Nanotechnology (WIN), University of Waterloo, Waterloo, ON, Canada

Mechanical and Mechatronics Engineering Department, University of Waterloo, Waterloo, ON, Canada

© The Author(s), under exclusive license to Springer Nature Switzerland AG 2024

W. Lacarbonara (ed.), *Advances in Nonlinear Dynamics, Volume III*, NODYCON Conference Proceedings Series, https://doi.org/10.1007/978-3-031-50635-2_3

symmetric modes of an electrostatically actuated arch microbeam. Ruzziconi et al. [1] also observed interactions between the second and third symmetric modes of an electrostatically actuated straight microbeam. Gobat et al. [14, 15] reported on modal interactions between the first and second symmetric modes of an arch microstructure and studied the emergence of quasiperiodicity due to that. Keşkekler et al. [16] reported modal interaction between the first axisymmetric mode and a higher mode of a thermally actuated circular graphene membrane. To the best of our knowledge, modal interactions between symmetric and anti-symmetric modes in symmetrically designed MEMS resonators have yet to be addressed.

Lacarbonara et al. [17] examined one-to-one modal interactions between the first symmetric and first anti-symmetric modes of imperfect arch beams and found that once symmetry is broken by changing the flexibility of one of the two supports, the only available response involved modal interaction. Since MEMS beams are by definition imperfect, even when they follow a symmetric design, we hypothesize that modal interactions can be activated between the symmetric and anti-symmetric modes of those beams.

In this study, we demonstrate a two-to-one modal interaction between the first anti-symmetric and second symmetric in-plane bending modes of an arch microbeam. We find an internal resonance mechanism that allows for energy transfer between the two modes. The steady-state dynamics of the MEMS are measured optically using a Laser Doppler Vibrometer (LDV), finding M-shaped frequency-response curves composed of trivial and stable nontrivial branches, where the two modes contribute to the response.

2 MEMS Resonator and Experimental Set-Up

The electrostatic MEMS resonator was fabricated in the PiezoMUMPs process [18]. It is made of a clamped-clamped curved microbeam, as shown in Fig. 1, which is fabricated into the single-crystal silicon layer (with a Young's modulus of E = 129GPa) of a silicon-on-insulator (SOI) wafer. The thickness of the structural layer is 10 μm. The silicon is boron-doped to enhance its conductivity. The beam is sandwiched between two actuation electrodes. The microbeam's dimensions were determined to be as follows: a length of 1000 μm, a thickness of 3.5 μm, and a width of 10 μm. Electrostatic actuation is created by applying a potential difference between the beam and the stationary electrode on its concave side.

Figure 1a, b depicts 10X and 20X microscopic top views of the arch microbeam, respectively. The small bump on the counter electrode, shown in Fig. 1b, marks the beam's mid-point. A profilometer image under 10X magnification is shown in Fig. 1c. The dimensions of the MEMS as designed are listed in Table 1. The image profilometer and the profilometer's built-in geometry tools were used to measure the initial rise and gap distance, which are 3.55 μm and 10.51 μm, respectively.

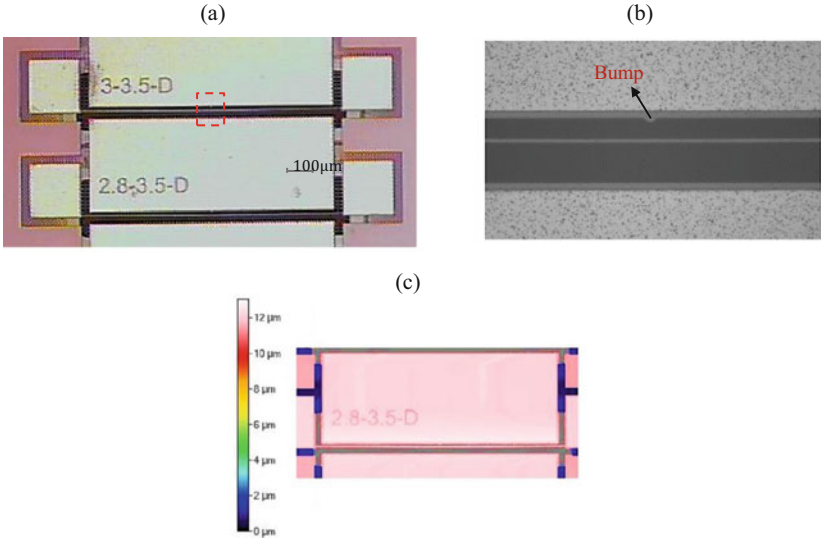

Fig. 1 (**a**) Optical microscope image (10X) of two curved beams and their side electrodes, (**b**) zoomed image (20X) of the area marked by the red dashed line in (**a**) showing the bump, and (**c**) profilometer image of the curved beam and its actuation electrode

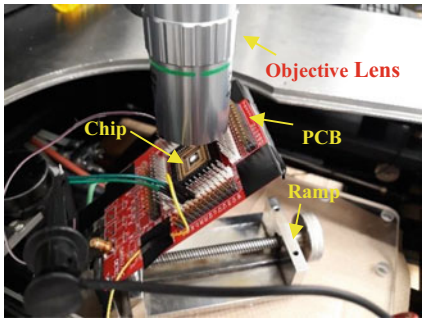

Fig. 2 The electrostatic MEMS resonator mounted to a 45° platform

This study employs optical measurement to observe the dynamic response of the MEMS resonator. The wire-bonded MEMS chip is placed in a chip carrier, which is positioned under the objective lens of a Laser Doppler Vibrometer (LDV). The spot of the measurement laser beam is focused on the side wall of the arch resonator to observe its in-plane motions [19]. Towards that end, the chip carrier is placed on a 45-degree ramp, as shown in Fig. 2. A function generator (Tektronix AFG3022B) and a high-voltage amplifier (Tabor Electronics) are used to produce the voltage waveform. The velocity signal measured by the LDV is sampled using an oscilloscope. A trigger signal is generated by the function generator, which is used to synchronize the input and output signals.

3 MEMS Characterization

A FEM model was constructed in COMSOL to investigate the modal response of the resonator. Using eigenvalue analysis, we obtained the first three in-plane and the first out-of-plane bending mode shapes and their natural frequencies, among which the third in-plane mode's free-vibration characteristics are shown in Fig. 3.

The linear dynamic response of the MEMS resonator was measured under pulse excitation to locate the natural frequencies of the first three in-plane bending modes. The resonator is actuated in-plane using electrostatic force. The beam is grounded, and pulse voltage is applied to the side electrode. The frequency and amplitude of the pulse excitation are set to $f = 15$ Hz and A = 15 V with a duty cycle of 0.1%. The FFT of the curved beam *mid-point* velocity under pulse excitation was obtained for a single pulse, averaged 100 times in the frequency domain. It is depicted in Fig. 4a.

The figure demonstrates three peaks. Comparing those frequencies to the results of the modal analysis carried out using FEM shows that the first and third peaks correspond to the first and the second symmetric in-plane bending modes located at f_1^i=33.22 kHz and $f_3^i = 111.6$ kHz, respectively. However, the second peak corresponds to the first symmetric out-of-plane bending mode at f_1^o =67.41 kHz. Inspecting the half-power bandwidth of the frequency-response curve, the Q-factor of the first and second symmetric modes were found to be Q_1^i =53.67 and Q_3^i =130.543, respectively.

To capture the first anti-symmetric in-plane mode, the response of the curved beam was captured at the quarter-length point, as shown in Fig. 4b. The previously identified modes appear in the response, as well as a new peak corresponding to the first anti-symmetric in-plane bending mode at $f_2^i = 56.78$ kHz. Due to its shape, this

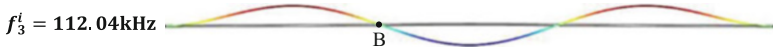

Fig. 3 FEM result depicting the natural frequency and mode shape of the resonator's third in-plane bending modes

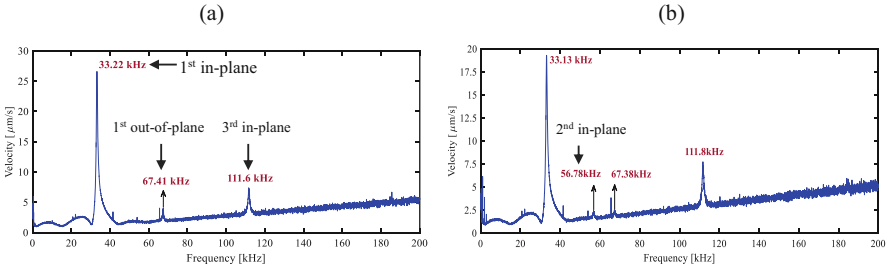

Fig. 4 The measured FFT of the curved beam at (**a**) mid-point and (**b**) quarter-length under a pulse excitation with a frequency and amplitude of 15 Hz and 15 V and a duty cycle of 0.1%

mode does not contribute to the structural response at the mid-point. The Q-factor of the mode was determined to be Q_2^i =91.98 by examining the mode's half-power bandwidth in the FFT plot.

Parameter identification was carried out to match the natural frequencies obtained from FEM and experiment. This resulted in identifying beam width and thickness as b = 9.2μm, the $h = 2.7\mu$m, and the initial rise at the mid-point as 3.2μm. As observed in Fig. 4, there is a close two-to-one ratio between the natural frequencies of the second symmetric and the first anti-symmetric in-plane bending modes $\frac{f_3^i}{f_2^i} = 2.036$.

Alneamy et al. [18] derived the nondimensional equation of motion of this resonator as:

$$\ddot{w} + \left(c_v + c_{sf}\right)\dot{w} + w'''' - \alpha_1\left(w_o'' - w''\right)\int_0^1 \left(w'^2 - 2w_o'w'\right)dx = \alpha_2 V(t)^2 \frac{1}{(1 + w_o - w)^2} \tag{1}$$

subject to the following boundary conditions:

$$w(0) = w'(0) = 0, w(1) = w'(1) = 0 \tag{2}$$

where the nondimensional coefficients appearing in Eq. (1) are defined as:

$$\alpha_1 = 6\left(\frac{g_0}{h}\right)^2, \alpha_2 = \frac{\epsilon b L^4}{2EIg_0^3}, c_v = \frac{cL^4}{EIt^*}, c_{sf} = \left(\frac{b}{g_0}\right)^3 \frac{t^*}{m} \frac{\mu}{(1+6Kn)\,(1+w_o-w)^3} \tag{3}$$

where L is the length of the microbeam, $I = \frac{bh^3}{12}$ is the second moment of area of the beam's cross section, and m is the beam mass. Moreover, c represents the viscous damping coefficient, μ is air viscosity, $Kn = \frac{\lambda}{g_0}$ is the Knudsen number, and λ is the mean free path of air molecules at ambient pressure. g_0 is the initial gap between the microbeam and the actuation electrode, and $V(t)$ is the electrical potential applied across the MEMS capacitor. The initial configuration of the beam middle-axis is denoted as $w_o(x)$ [18]. Finally, t^* is a timescale defined as $t^* = \sqrt{\frac{\rho b h L^4}{EI}}$.

The equation accounts for both the linear viscous damping c_v as well as the nonlinear, displacement-dependent, squeeze film damping c_{sf} developed in the narrow gap between the curved beam and the stationary electrode. The electrostatic force and squeeze film damping provide strong quadratic and cubic nonlinearities when the resonator undergoes large-amplitude motions. Quadratic nonlinearities also appear in the equation of motion due to the beam's initial curvature, namely $\alpha_1 w_o'' \int_0^1 w'^2 dx$ and $2\alpha_1 w'' \int_0^1 w_o' w' dx$. These nonlinearities provide possible energy channels for two-to-one modal interactions.

4 Symmetric–Anti-symmetric Modal Interaction

An almost two-to-one ratio was observed between the natural frequencies of the first anti-symmetric and the second symmetric in-plane bending modes, $f_3^i \approx 2f_2^i$. To investigate the coupling between these two modes, the laser spot was pointed at a node of the second symmetric mode. Excitation voltage of the form $V(t) = V_{ac} \cos(2\pi f\, t)$ was applied to the actuation electrode while the beam is grounded. The signal frequency was varied in the vicinity of $\frac{1}{2} f_3^i$ resulting in an excitation frequency at $2f$ that directly excites the second symmetric mode. Figure 5a displays the measured velocity at two points along the beam span: the mid-point (black line) and a node of the second symmetric mode (yellow line), dubbed point B in Fig. 3, as the frequency is varied from $f = 54.2$ kHz to 58 kHz at a constant slew rate in 20 ms while the amplitude is set to $V_{ac} = 52.5$ V. The response at the node, point B, remains constant at a level comparable to the noise floor throughout the frequency sweep. On the other hand, the response at the mid-point increases as the frequency of excitation approaches the resonance of the second symmetric mode and drops as it sweeps beyond it. This confirms that point B is a node of the second symmetric mode and that the response of other modes is negligible at this excitation level.

Increasing the voltage amplitude to $V_{ac} = 53.25$ V, a nontrivial response emerges at point B, as illustrated in Fig. 5b, close to the resonance of the second symmetric mode f_3^i, indicating activation of energy channel from that mode to the first anti-symmetric mode. Therefore, it can be concluded that the activation level for modal interaction is at about $V_{ac} = 53$ V.

To examine the evolution of this modal interaction, we obtained the frequency response of the velocity of point B during similar frequency sweeps for increasing levels of the voltage amplitude beyond the activation level. For example, the time-history of point B at a voltage amplitude of $V_{ac} = 90$ V is shown in Fig. 6a. The

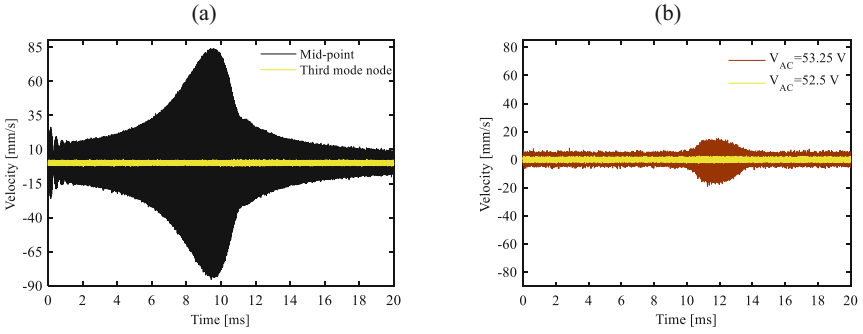

Fig. 5 The measured velocity (**a**) at the beam mid-point (black line) and the second symmetric mode node (yellow line) under an excitation with a voltage amplitude of V_{ac}= 52.5 V and (**b**) at the second symmetric mode node for voltage amplitudes of V_{ac}= 52.5 V (yellow line) and V_{ac}= 53.25 V (brown line). The frequency is swept from 54.2 kHz to 58 kHz in both cases

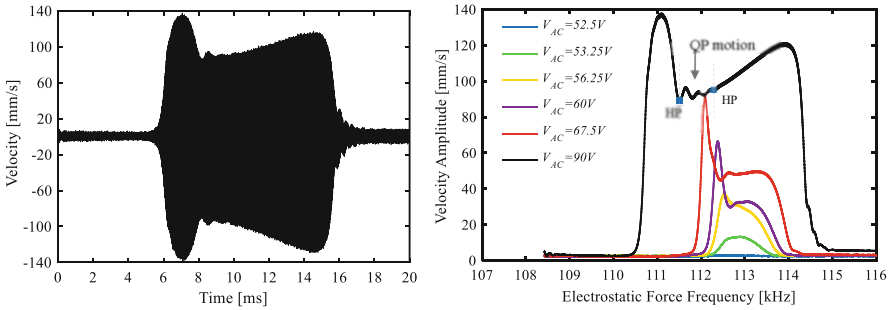

Fig. 6 (**a**) The measured velocity time-history of point B under a voltage amplitude of V_{ac}= 90 V, (**b**) The frequency-response curves of the velocity RMS at point B for 6 values of the voltage amplitude V_{ac}. The solid blue markers demarcate the locations of secondary Hopf bifurcations

time-histories were used to construct the frequency response of the resonator at point B by evaluating the RMS of the velocity in a moving time-window and assigning that value to the excitation frequency at the mid-point of the window.

Figure 6b shows the frequency-response curves for voltage amplitudes of V_{ac} = 52.5, 53.25, 56.25, 60, 67.5, and 90 V. No motion is observed below the activation level (V_{ac} = 52.5 V). As the voltage amplitude crosses that level, a nontrivial branch appears at V_{ac} = 53.25 between the excitation frequencies 112.2 and 113.7 kHz. The energy exchange intensifies as the voltage amplitude increases, resulting in an expansion of the region where the trivial solution is unstable and an M-shaped frequency-response curve, which are the main characteristics of nonlinear modal interactions.

For the highest excitation level V_{ac} = 90 V, the steady-state dynamics are a trivial response until a primary Hopf bifurcation occurs at 110.2 kHz where the trivial solution loses stability. At this point, the nontrivial response emerges, and its amplitude grows swiftly up to a maximum as the excitation frequency increases. Increasing the excitation frequency, the velocity drops down to a minimum gradually, forming the left side of the M-shaped curve. The curves encounter an irregular region marked by two solid blue markers in Fig. 6b, suggesting the existence of secondary Hopf bifurcations along the mid-section of the nontrivial branch before growing smoothly towards another maximum that forms the right side of the M-shaped curve. It drops from there swiftly to merge via another Hopf bifurcation with the trivial solution at 114.9 kHz. The experimental results reveal that the response of the anti-symmetric mode experiences rapid growth with only a small change in the excitation frequency, which can significantly enhance the sensitivity of electrostatic MEMS sensors that rely on changes in resonance amplitude.

Figure 7 compares the frequency spectrum of point B velocity for an excitation frequency of $2f$ =109.8 kHz, just below the left Hopf bifurcation, to that at an excitation frequency of $2f$ =110.2 kHz, beyond the Hopf bifurcation. Both FFTs were obtained under excitation with a voltage amplitude of V_{ac} = 90 V. The figure shows that when the excitation frequency is below the bifurcation frequency, the

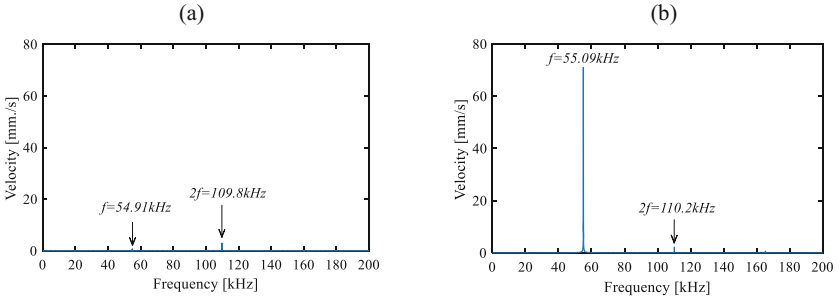

Fig. 7 The FFT of point B velocity under an excitation amplitude of V_{ac}= 90 V and frequency of (**a**) $2f$ =109.8 kHz, (**b**) $2f$ =110.2 kHz

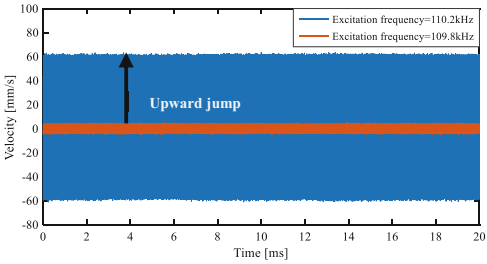

Fig. 8 The time-history of the point B velocity under an excitation amplitude of V_{ac}= 90 V and frequency of (**a**) $2f$ =109.8 kHz (orange line), (**b**) $2f$ =110.2 kHz (blue line)

dominant peak occurs at the forcing frequency $2f$. However, the peak at f grows tremendously beyond the bifurcation, as shown in Fig. 7b, from 0.5 mm/s to 74 mm/s and dominates the response.

Figure 8 shows the time-domain measurements of point B velocity corresponding to the FFTs shown in Fig. 7. The measured velocity for $2f$ =109.8 kHz is shown in the orange line, and that for $2f$ =110.2 kHz is shown in the blue line.

We used a Lock-in-Amplifier (Zurich Instruments HF2LI 50 MHz) to study the relationship between the amplitude and phase of the first anti-symmetric mode during its modal interactions with the second symmetric mode. In this experiment, the time-domain velocity of point B, measured optically using the LDV, was fed to the Lock-in-Amplifier to track the response at f only. The response was measured for nine values of the voltage amplitude applied to another resonator specimen on the same chip, as shown in Fig. 9, while the excitation frequency was swept up in the range of 108 to 114.3 kHz. In this case, the activation level was found to be larger than V_{ac} = 15 V, where only the trivial response prevailed throughout the frequency range but less than V_{ac} = 15.75 V, where a nontrivial response appeared in the excitation frequency range of $2f$ =111 to 111.65 kHz. Increasing the voltage amplitude expands the nontrivial region and magnitude of the nontrivial branch. For the voltage amplitudes of V_{AC}= 33 and 34.5 V, we found a jump down along the nontrivial branch during frequency upsweep at $2f$ =110.65 and 110.8 kHz, respectively. At the highest excitation level (V_{AC}= 34.5 V), the nontrivial branch extended over the frequency range $2f$ = 109.1 and 113.3 kHz. Moreover, the phase-

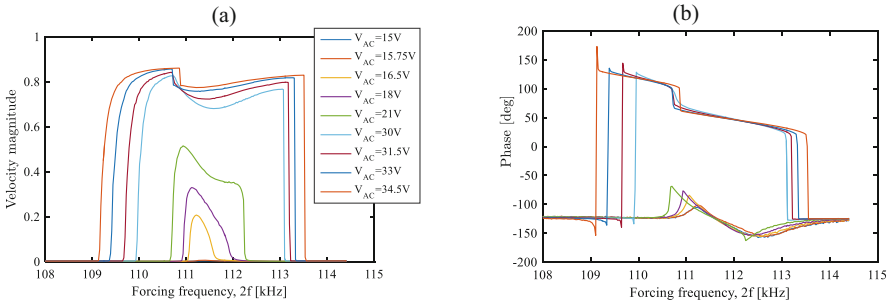

Fig. 9 The measured (**a**) amplitude- and (**b**) phase-frequency behavior of the MEMS illustrating the second (first anti-symmetric) mode contribution, for different values of the AC voltage amplitude

frequency diagram shows a sharp drop right before the bifurcation point, as shown in Fig. 9b, unlike the frequency-response curve, thereby proving that the phase-frequency diagram has higher sensitivity than frequency response to an impending bifurcation.

5 Conclusions

This study demonstrates the actuation of the first anti-symmetric bending mode of a symmetric electrostatic microresonator via a two-to-one modal interaction between this mode and the second symmetric bending mode. The underlying arch microbeam geometry was measured using white light profilometry. The natural frequencies of the first three in-plane bending modes were determined, and a two-to-one ratio was found between the second symmetric and the first anti-symmetric modes. The steady-state dynamic response of the system was captured under unbiased voltage excitation in the vicinity of the second symmetric mode's primary resonance. This direct excitation of the mode led to indirect excitation for the first anti-symmetric mode. The experimental results demonstrate significant energy exchange between the two engaged modes resulting in an M-shaped frequency-response curve with trivial and large-amplitude nontrivial branches.

References

1. Ruzziconi, L., Jaber, N., Kosuru, L., Bellaredj, M.L., Younis, M.I.: Experimental and theoretical investigation of the 2: 1 internal resonance in the higher-order modes of a MEMS microbeam at elevated excitations. J. Sound Vib. **499**, 115983 (2021)
2. Hajjaj, A., Jaber, N., Hafiz, M.A.A., Ilyas, S., Younis, M.I.: Multiple internal resonances in MEMS arch resonators. Phys. Lett. A. **382**(47), 3393–3398 (2018)

3. Wang, Z., Ren, J.: Nonlinear modal interaction of an electrically actuated microbeam with flexible support. Nonlinear Dyn. **99**(3), 1871–1891 (2020)
4. Czaplewski, D.A., Strachan, S., Shoshani, O., Shaw, S.W., López, D.: Bifurcation diagram and dynamic response of a MEMS resonator with a 1: 3 internal resonance. Appl. Phys. Lett. **114**(25), 254104 (2019)
5. Czaplewski, D.A., et al.: Bifurcation generated mechanical frequency comb. Phys. Rev. Lett. **121**(24), 244302 (2018)
6. Xia, C., Wang, D.F., Ono, T., Itoh, T., Maeda, R.: A mass multi-warning scheme based on one-to-three internal resonance. Mech. Syst. Signal Process. **142**, 106784 (2020)
7. Sarrafan, A., Azimi, S., Golnaraghi, F., Bahreyni, B.: A nonlinear rate microsensor utilising internal resonance. Sci. Rep. **9**(1), 1–9 (2019)
8. Sarrafan, A., Bahreyni, B., Golnaraghi, F.: Analytical modeling and experimental verification of nonlinear mode coupling in a decoupled tuning fork microresonator. J. Microelectromech. Syst. **27**(3), 398–406 (2018)
9. Noori, N., Sarrafan, A., Golnaraghi, F., Bahreyni, B.: Utilization of 2: 1 internal resonance in microsystems. Micromachines. **9**(9), 448 (2018)
10. Sarrafan, A., Bahreyni, B., Golnaraghi, F.: Development and characterization of an H-shaped microresonator exhibiting 2: 1 internal resonance. J. Microelectromech. Syst. **26**(5), 993–1001 (2017)
11. Wang, Z., Ren, J.: Three-to-one internal resonance in MEMS arch resonators. Sensors. **19**(8), 1888 (2019)
12. Wang, R., Xia, C., Wang, D.F., Ono, T.: A high-frequency narrow-band filtering mechanism based on auto-parametric internal resonance. In: 2021 IEEE 16th International Conference on Nano/Micro Engineered and Molecular Systems (NEMS), pp. 670–675. IEEE (2021)
13. Hajjaj, A., Alfosail, F., Younis, M.I.: Two-to-one internal resonance of MEMS arch resonators. Int. J. Non-Linear Mech. **107**, 64–72 (2018)
14. Gobat, G., Guillot, L., Frangi, A., Cochelin, B., Touzé, C.: Backbone curves, Neimark-Sacker boundaries and appearance of quasi-periodicity in nonlinear oscillators: application to 1: 2 internal resonance and frequency combs in MEMS. Meccanica. **56**(8), 1937–1969 (2021)
15. Gobat, G., Zega, V., Fedeli, P., Touzé, C., Frangi, A.: Frequency combs in a MEMS resonator featuring 1: 2 internal resonance: ab initio reduced order modelling and experimental validation. Nonlinear Dyn. **111**(4), 2991–3017 (2023)
16. Keşkekler, A., Arjmandi-Tash, H., Steeneken, P.G., Alijani, F.: Symmetry-breaking-induced frequency combs in graphene resonators. Nano Lett. **22**(15), 6048–6054 (2022)
17. Lacarbonara, W., Arafat, H.N., Nayfeh, A.H.: Non-linear interactions in imperfect beams at veering. Int. J. Non-Linear Mech. **40**(7), 987–1003 (2005)
18. Alneamy, A., Khater, M., Al-Ghamdi, M., Abdel-Aziz, A., Heppler, G., Abdel-Rahman, E.: Large oscillation of electrostatically actuated curved beams. J. Micromech. Microeng. **30**(9), 095005 (2020)
19. Arabi, M., Gopanchuk, M., Abdel-Rahman, E., Yavuz, M.: Measurement of in-plane motions in MEMS. Sensors. **20**(12), 3594 (2020)

Control of an Electrostatically Actuated Micro Portal Frame with 2:1 Internal Resonance Subjected to Damping Disturbances

Wagner B. Lenz, Rodrigo T. Rocha, Fahimullah Khan, Yousef Algoos, and Mohammad I. Younis

1 Introduction

The dynamics of MEMS have been extensively investigated due to the presence of many nonlinear behaviors arising from transduction techniques and geometric nonlinearities. One of the most reported behaviors is the jump phenomenon, which is very common in microresonators due to, for example, nonlinear mid-plane stretching and electrostatic force. This phenomenon can appear in softening or hardening behaviors depending on the dominant nonlinearities [1–4].

One of the most intriguing nonlinear phenomena observed in MEMS resonators is the internal or the autoparametric resonance, which occurs when there is a commensurate ratio of the resonance frequencies between two modes of vibration [1, 2]. To achieve such conditions, single-element structures need to have very specific design requirements. On the other hand, compound structures composed of more than one structure have shown more flexibility in fulfilling the conditions for

W. B. Lenz · Y. Algoos
King Abdullah University of Science and Technology, Thuwal, Saudi Arabia
e-mail: barthlenz.wagner@kaust.edu.sa

R. T. Rocha
King Abdullah University of Science and Technology, Thuwal, Saudi Arabia
Silicon Austria Labs Gmbh, Villach, Kärnten, Austria

F. Khan
King Abdullah University of Science and Technology, Thuwal, Saudi Arabia
International Iberian Nanotechnology Laboratory, Braga, Portugal

M. I. Younis (✉)
King Abdullah University of Science and Technology, Thuwal, Saudi Arabia
State University of New York, Binghamton, NY, USA
e-mail: Mohammad.Younis@kaust.edu.sa

© The Author(s), under exclusive license to Springer Nature Switzerland AG 2024

W. Lacarbonara (ed.), *Advances in Nonlinear Dynamics, Volume III*, NODYCON Conference Proceedings Series, https://doi.org/10.1007/978-3-031-50635-2_4

internal resonance due to their multiple ports for input excitations and their unique geometrical features.

Nevertheless, compound structures have not been thoroughly studied. A few examples have been reported involving linear static behaviors for applications of actuators, logic devices, and RF switches [5, 6]. However, these structures can exhibit rich dynamics, where such applications can be enhanced. L-shape, H-shape, U-shape (portal frame) structures, and trusses are the most commonly employed compound structures [7]. Recently, Rocha and Younis [8] have demonstrated the activation of the saturation phenomenon due to a 2:1 internal resonance in a micro portal frame resonator, both theoretically and experimentally.

However, this nonlinear dynamic phenomenon is strongly affected by damping [8], either being suppressed or leading to irregular behaviors due to environmental pressure variations, which weakens the potential practical usage of the device.

Therefore, this work aims to electrostatically control a micro portal frame, modeled as a two-degrees-of-freedom (2DOFs) system, with 2:1 internal resonance between the second (Y-direction motion) and first (X-direction motion) modes. To avoid irregular behaviors under the saturation phenomenon within the internal resonance, we propose to use the Linear Quadratic Regulator (LQR) control technique to create an electrostatic force that alleviates the damping effect. For the effectiveness evaluation of the control, an ideal control strategy is compared to limited voltage actuation.

2 The Micro Portal Frame Resonator

2.1 Design and Fabrication

The device is fabricated in-house using a bulk micromachining process with an SOI wafer, as shown in Fig. 1a. The substrate has an electrical sheet resistance of 10–30 ohm-cm, and the device layer has a resistivity of 0.1 ~ 0.2 ohm-cm. The process starts with the sputtering of 50 nm of Cr and 200 nm of Au layers on an SOI wafer, as shown in Fig. 1b. The wafer is patterned using the first mask layer for fabricating device pads, as shown in Fig. 1c. Afterward, the wafer is spin-coated with the 4 μm thick photoresist ECI 3027 and patterned with the second mask layer, as shown in Fig. 1d. The 25 μm device layer is anisotropically etched using deep reactive ion etching (DRIE) (see Fig. 1d). Finally, the photoresist is removed, and the microresonator is released using HF vapor etching. The fabricated micro portal frame is shown in Fig. 1a.

The microstructure has a Young Modulus of $E = 145\text{GPa}$. It consists of the short beam elements (columns) of length $L_1 = 196$ μm and the long beam element (supported beam) of length $L_2 = 311.5$ μm. The columns and beam widths are designed, respectively, as $h_1 = 1.9$ μm and $h_2 = 2.1$ μm, and they have a thickness (depth) of 25 μm. In addition, the microstructure is subjected to an electrostatic force by a DC actuation voltage V_{dc} and an AC harmonic voltage V_{ac}, which actuates the second mode, through two electrodes. One electrode is placed on top of

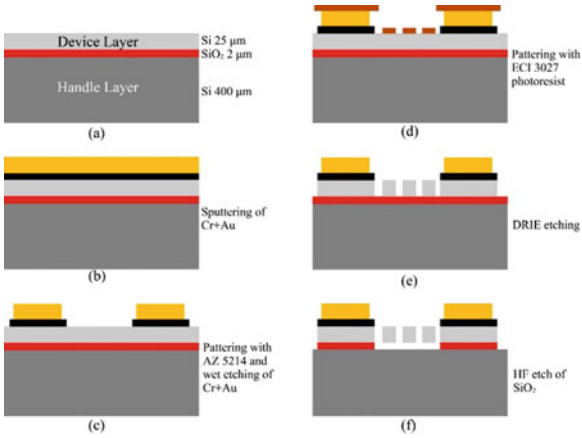

Fig. 1 The fabrication process flowchart of the in-plane resonator

the supported beam (Electrode B), and the other is placed on the column (Electrode A), which is used only for control purposes in the first mode direction. Control signals V_{cx} and V_{cy} are applied to electrodes A and B to control the first and second modes of vibration, respectively. The distances between the supported beam and columns from their electrodes are $d = 5$ μm and $g = 5$ μm, respectively.

2.2 Equations of Motion

To analytically study the dynamics and control of the micro portal frame, the equations of motion are derived from a finite element Rayleigh-Ritz procedure, accounting for the mode shapes of the complete portal frame derived through Hamilton's principle [3]. Accordingly, the nondimensional equations of motion for the first and second modes, neglecting the inertial nonlinearities, are given by

$$\begin{aligned} &\ddot{x} + 2\xi\dot{x} + x + k_{31}x^3 + \alpha_1 xy = \beta_1 \frac{V_{cx}^2}{(1-x)^2} \\ &\ddot{y} + 2\xi\dot{y} + \omega_{n2}^2 y + \alpha_2 x^2 + k_{32}y^3 = \beta_2 \frac{(V_{dc}+V_{ac}\cos\Omega t+V_{cy})^2}{(1-x)^2} \end{aligned} \tag{1}$$

where the nondimensional parameters are calculated as in the Supplementary Material in [3]. To yield numerical results, Eq. (1) is numerically integrated in time using the 4th order Runge-Kutta method.

2.3 Experimental Setup and Characterization

The in-plane resonance frequencies are measured through stroboscopic microscopy of the Micro System Analyzer (MSA) from Polytec, as shown in Fig. 3, using a ring-down measurement. The camera's targets are set on the end of a column,

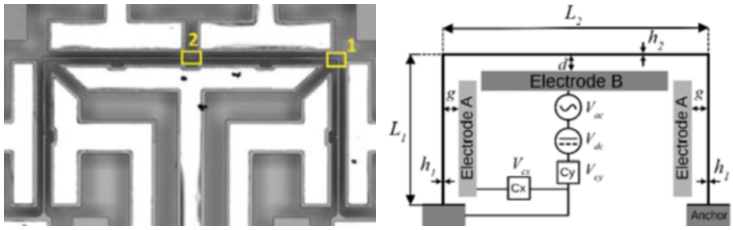

Fig. 2 (**a**) Picture of the top view of the fabricated micro portal frame made of silicon. (**b**) Schematic of the micro portal frame with the actuation electrodes

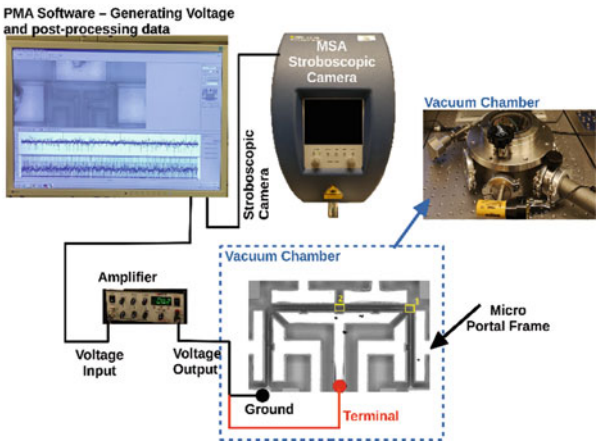

Fig. 3 Experimental setup for the data acquisition of the micro portal frame

square 1, and in the mid-span of the supported beam, square 2, as illustrated in Fig. 2a, to measure the response of the 1st (X-direction) and 2nd (Y-direction) modes, respectively. Due to the small gap between the resonator and the electrodes, a vacuum chamber is required to minimize the squeeze-film damping [9], with a pressure of 175 mTorr set throughout the experiments. The 1st and 2nd resonance frequencies are measured as 43.10 kHz and 90.42 kHz, respectively.

The frequency response curves are obtained using stroboscopic video microscopy with a Bode plot of the Planar Motion Analyzer (PMA) software of the MSA (Fig. 3).

2.4 The Linear Quadratic Regulator (LQR) Control

The Linear Quadratic Regulator (LQR) control is one of the most used controllers [10]. It provides optimum gains proportional to the cost of actuation and allowable error. However, to calculate the gains, it is needed to use a state-space notation such that

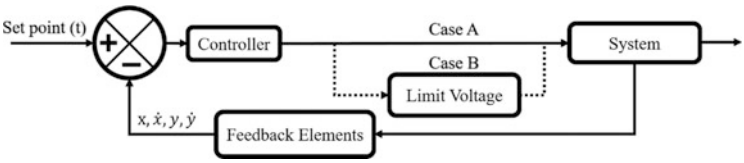

Fig. 4 Model for ideal and limit voltage controls

$$\dot{\mathbf{x}} = \mathbf{A}(\mathbf{x})\,\mathbf{x} + \mathbf{B}(\mathbf{x})\,\mathbf{u} \tag{2}$$

where **x** is the state vector, **A(x)** is the state matrix for the linear system, **B(x)** is the input matrix, and **u** is the control signal. However, for the ideal case, the state and input matrices are considered as constants to calculate the control signal. Hence, the control law is given by

$$\mathbf{u} = -\mathbf{R}^{-1}\mathbf{B}^{\mathbf{T}}\mathbf{P}\mathbf{e} = -\mathbf{k}\mathbf{e} \tag{3}$$

where $\mathbf{e} = (\mathbf{x} - \mathbf{s_p})$, and $\mathbf{s_p}$ is the desired state or set point. Defining **P** as a symmetric matrix, the algebraic Riccati equation is developed as:

$$\mathbf{P}\mathbf{A} + \mathbf{A}^{\mathbf{T}}\mathbf{P} - \mathbf{P}\mathbf{Q}\mathbf{R}^{-1}\mathbf{B}^{\mathbf{T}}\mathbf{P} + \mathbf{Q} = \mathbf{0} \tag{4}$$

where **Q** is a positive definite matrix.

The control input **u** is calculated based on the linearized state matrix **A** [8], using the cost function:

$$J = \int_0^\infty \left(\boldsymbol{e}^T \boldsymbol{Q}\boldsymbol{e} + \boldsymbol{u}^T \boldsymbol{R}\boldsymbol{u}\right) dt \tag{5}$$

where **R** is a positive definite matrix.

The control strategy to obtain a periodic orbit is based on the ideal LQR control. The efficiency of the controller is determined by the minimum required voltage of actuation to maintain a stable orbit. Figure 4 shows the control schematic for the ideal and limited voltage strategies. It shows that Case A is the ideal and unlimited voltage that can be applied to the electrodes, while for Case B, the LQR control is limited to actuate within a range of values.

However, the portal frame structure is highly nonlinear. Hence, the state and control matrices **A** and **B** must account for the nonlinear effects in it. Therefore, the matrices **A** and **B** are defined as:

$$\mathbf{A}(\mathbf{x}) = \begin{bmatrix} 0 & 1 & 0 & 0 \\ 1 + k_{31}x^2 & \mu_1 & \alpha_1 x & 0 \\ 0 & 0 & 0 & 1 \\ \alpha_2 x & \omega_{n2}^2 & k_{31}y^2 & \mu_2 \end{bmatrix}, \mathbf{B} = \begin{bmatrix} 0 \\ 1 \\ 0 \\ 1 \end{bmatrix} \tag{6}$$

where **A(x)** depends on the states, which accurately represents the nonlinearities of the system. However, the LQR control must have **A** and **B** constants. Thus, a few simplifications are needed. The state vector $x = [0.03\ 0\ 0.24\ 0]^T$ is selected to introduce some of the nonlinearities of the system to the controller. The **B** matrix also has low-order values, which increases the gains. Thus, for convenience, **B** is selected from Eq. (3), obtaining lower gains, and when applying the control on the MEMS resonator, it is converted to a voltage to become more realistic.

To calculate the set point, a stable orbit is used through long-time integration using the response of the system at the 2:1 internal resonance response as resonance frequencies. Thus, carrying out a linear regression, we establish a temporal function synchronized with the excitation force as the desired orbits for both modes of vibration, given by

$$\begin{cases} x = 0.9412 \sin(2\pi 47800t)\ [\mu m] \rightarrow R^2 = 0.9989 \\ \dot{x} = 0.3134 \cos(2\pi 47800t)\ \left[\frac{m}{s}\right] \rightarrow R^2 = 0.9989 \\ y = 0.2747 + 0.5565 \cos(4\pi 47800t)\ [\mu m] \rightarrow R^2 = 0.9981 \\ \dot{y} = -0.1853 \sin(4\pi 47800t)\ \left[\frac{m}{s}\right] \rightarrow R^2 = 0.9981 \end{cases} \tag{7}$$

In addition, for the control calculations, the matrices **Q** and **R** are used as:

$$\mathbf{Q} = \text{diag}\,[1] \qquad \mathbf{R} = 1 \tag{8}$$

3 Results and Discussion

3.1 Characterization and Experimental Data

First, the characterization of the fabricated device is carried out. Then, the mathematical model of Eq. (3) is validated. Figure 5a shows the frequency shift due to the DC actuation of the portal frame through (electrode B). Excellent agreement is observed between the experimental results and numerical simulations of Eq. (3). The experimental measurements are carried out until 50 V to avoid pull-in, which may cause device failure. Note that the second mode resonance frequency decreases while the first mode is almost constant. The pull-in voltage is around 87 V. It is also observed that a 2:1 ratio between the first and second modes is achieved at $V_{dc} = 44$ V, where the second mode resonance frequency is around 86.74 kHz.

Figure 5b shows the numerically simulated frequency response of the first and second modes when the portal frame is excited with $V_{ac} = 0.4$ V at $V_{dc} = 44$ V, sweeping around the second mode resonance frequency. It is observed that at a certain frequency in the upward direction, the first mode, which was inactive, is activated and dominates the response over the second mode, which is the excited mode. This is the saturation phenomenon due to the 2:1 internal resonance.

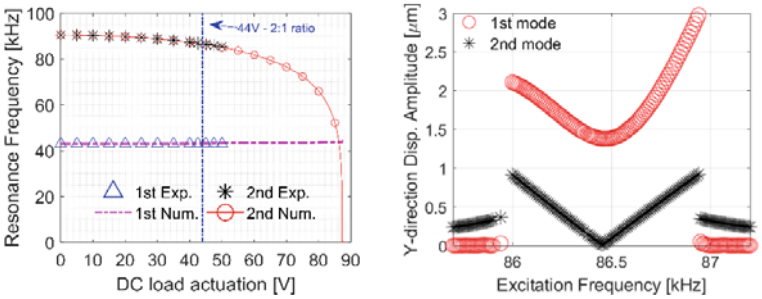

Fig. 5 (**a**) Frequency shift due to DC actuation through electrode B. (**b**) Numerically simulated frequency response swept around the shifted second mode at $V_{dc} = 44$ V and $V_{ac} = 0.4$ V

In addition to the 2:1 ratio, damping is also very important for the saturation phenomenon to occur, which is set at $\xi = 0.00057$.

Depending on the damping ratio, the phenomenon can be suppressed, or an irregular response can be seen, which is discussed in the next subsection.

3.2 Air-Damping Conditions Versus Saturation Phenomenon

According to Rocha and Younis [8], the 2:1 internal resonance can be activated at low damping, which is due to low air pressure. However, there is a range of pressure where the saturation phenomenon may occur. To assess the behavior of the first and second modes, a parametric variation of the damping at the range $0.00054 < \xi < 0.15$ is carried out related to the AC excitation amplitude, as shown in the contours of Fig. 6a (first mode response), b (second mode response). Note that there is a range of AC excitation where also the phenomenon is not observed. However, increasing the AC voltage, the internal resonance gets activated as seen through the response of the first mode. In addition, when $V_{ac} > 0.7$ V and $0.00054 < \xi < 0.003$, an unpredictable behavior is observed, which is noted in both modes.

To further characterize the behavior, the Lyapunov exponent is calculated. Figure 7 shows the maximum Lyapunov exponent map with variations in the damping coefficient ξ and the AC excitation where irregular behavior is observed. Note that at high AC and small damping ratio ξ, which represents low environmental pressure, evidence of quasiperiodic behavior is observed due to the positive Lyapunov exponent very close to zero [9–11]. To further illustrate this behavior, a Poincare map for different damping conditions is shown in Fig. 7. Note that it shows periodic (discrete points) to quasiperiodic behavior (closed curves). However, quasiperiodic behavior might lead to either noisy signal readouts or dynamic pull-in.

The appearance of irregular behaviors may yield noisy signal readout or sudden dynamic pull-in. Considering the case of $V_{ac} = 1.0$ V and $\xi = 0.00057$, the LQR

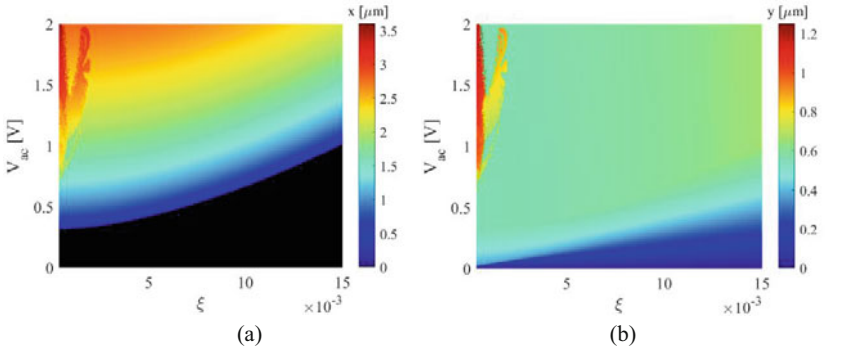

Fig. 6 Displacement amplitude due to changes in damping ξ and AC excitation voltage for (**a**) first mode and (**b**) second mode

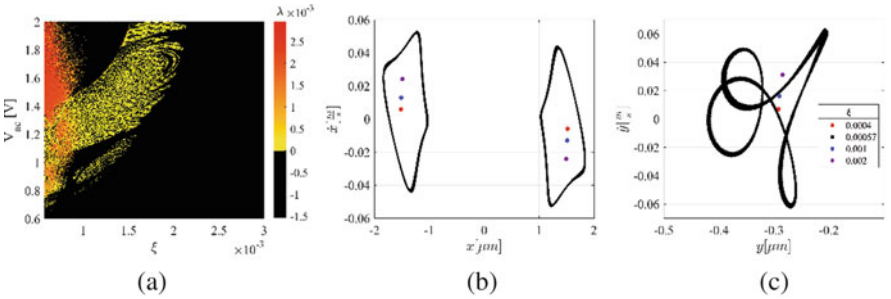

Fig. 7 Maximum Lyapunov exponent for different voltages and damping (**a**). Simulated Poincare map (**b**, **c**) for different damping at $V_{dc} = 44$ V and $V_{ac} = 1.0$ V

control, accounting for the ideal (Case A) and the limited voltage (Case B), is applied to suppress the irregular motion.

First, the ideal LQR control (Case A) is implemented. Figure 8a, b shows the phase portrait of the first and second modes, respectively, showing the uncontrolled response, the controlled one, and the desired set point. As expected, the LQR control converged very close to the desired orbit, resulting in a negligible steady-state error due to continuous excitation and the precision assumed by the mathematical modeling (Fig. 8).

Next, Case B is applied, which restricts the actuation for different voltages. Figure 9a, b shows the phase portrait of the first and second modes, respectively, showing the uncontrolled response, the desired set point, and the different controlled orbits for different applied voltages. Note that when the control is limited to a maximum of 5 V, it cannot bring the system close to the stable orbit or induce a single-period orbit, indicating that the actuation is not strong enough. When the control applies 10 V, it holds a periodic orbit, although very far from the desired set point. However, increasing the control voltage to 15 V and beyond, the response of

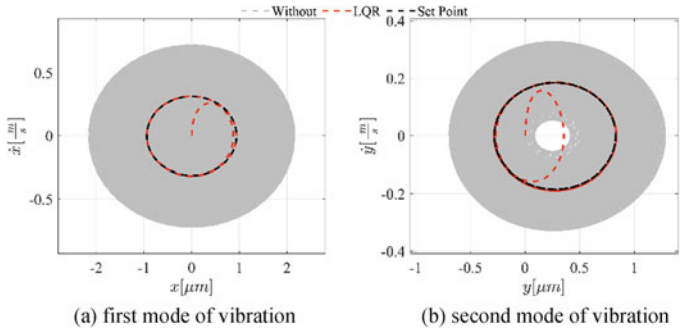

(a) first mode of vibration (b) second mode of vibration

Fig. 8 Phase portrait of an ideal control. Showing the invariance over time of the LQR in comparison with the desired set point and the uncontrolled system

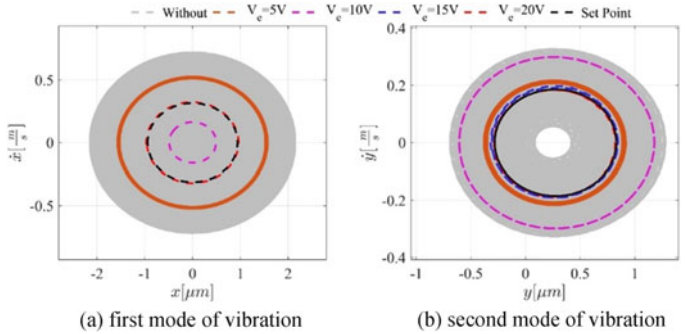

(a) first mode of vibration (b) second mode of vibration

Fig. 9 Phase portrait Case B: limited control voltage applied to the structure ($V_e = V_{cx} = V_{cy}$)

the system is finally led very close to the desired orbit, showing it to be sufficient to control the chaotic behavior and maintain a stable periodic orbit. This yields a clear signal that improves the readability of the electrical signal for sensing purposes and avoids sudden dynamic pull-in (Fig. 9).

4 Conclusions

The control of a micro U-shaped portal frame resonator at 2:1 internal resonance activation was presented. The microresonator was experimentally characterized and validated with the presented mathematical model. Due to low environmental pressure (low damping), the response of the micro portal frame presented quasiperiodic behavior, which might induce noisy signal readout and sudden dynamic pull-in due to unstable behavior.

To control the unstable behavior, the LQR control was designed accounting for two different implementation methods: an ideal control (Case A) and a limited

voltage actuation (Case B). Case A showed that the structure is controllable with unlimited power. For a more realistic and continuous regulation, Case B, the minimum required voltage in the selected damping and V_{ac} was 15 V. However, just to remove the undesirable orbit, the minimum significant actuation is 10 V. The addition of the controller proved to be efficient in controlling the unstable behaviors, leading them to a periodic orbit.

Acknowledgments The authors would like to thank KAUST for supporting this research.

References

1. Mestrom, R.M.C., et al.: Simulations and experiments of hardening and softening resonances in a clamped–clamped beam MEMS resonator. Sensors Actuators A Phys. **162**(2), 225–234 (2010)
2. Potekin, R., et al.: Multi-frequency atomic force microscopy based on enhanced internal resonance of an inner-paddled cantilever. Sensors Actuators A Phys. **273**, 206–220 (2018)
3. Karabalin, R.B., Cross, M.C., Roukes, M.L.: Nonlinear dynamics and chaos in two coupled nanomechanical resonators. Phys. Rev. B. **79**(16), 165309 (2009)
4. Westra, H.J.R., et al.: Nonlinear modal interactions in clamped-clamped mechanical resonators. Phys. Rev. Lett. **105**(11), 117205 (2010)
5. Molaei, S., Ganji, B.A.: Design and simulation of a novel RF MEMS shunt capacitive switch with low actuation voltage and high isolation. Microsyst. Technol. **23**(6), 1907–1912 (2017)
6. Rebeiz, G.M., Muldavin, J.B.: RF MEMS switches and switch circuits. IEEE Microw. Mag. **2**(4), 59–71 (2001)
7. Mazzilli, C.E.N., Brasil, R.M.L.R.F.: Effect of static loading on the nonlinear vibrations of a three-time redundant portal frame: analytical and numerical studies. Nonlinear Dyn. **8**(3), 347–366 (1995)
8. Lenz, W.B., et al.: Numerical simulations and control of offshore energy harvesting using piezoelectric materials in a portal frame structure. Shock. Vib. **2021**, 1–11 (2021)
9. Young, L.S.: Lyapunov exponents for some quasi-periodic cocycles. Ergodic Theory Dyn. Syst. **17**(2), 483–504 (1997)
10. de Souza, S.L.T., et al.: Characterization in bi-parameter space of a non-ideal oscillator. Phys. A Stat. Mech. Appl. **466**, 224–231 (2017)
11. Rocha, R.T., et al.: On a non-ideal magnetic levitation system: nonlinear dynamical behavior and energy harvesting analyses. Nonlinear Dynamics. **95**(4), 3423–3438 (2019)

Vibration Mitigation by Two Parametric Anti-resonances in High-Q Resonators: A Preliminary Case Study

Miguel Ramírez-Barrios and Fadi Dohnal

1 Introduction

Transient vibrations in mechanical systems are a common engineering problem. The concepts to mitigate or suppress vibrations can be classified as passive, semi-active, and active. A passive concept refers to the design of system parameters without change or feedback during operation. A semi-active concept involves an active change of one or more system parameters. An active concept realizes one or more forces acting on the system by real-time control during operation. The present contribution expands a known semi-active concept in MEMS by employing a multi-harmonic variation of the stiffness coefficients, an extension of mitigating transient vibrations by parametric excitation as investigated in, e.g., [1]. A parametrically excited two-degree-of-freedom system can be modeled, for instance, by a set of ordinary linear differential equations of the form $\ddot{\mathbf{y}} + \boldsymbol{D}\dot{\mathbf{y}} + \left(\boldsymbol{\Omega}^2 + \mathbf{B}p(t)\right)\mathbf{y} = 0$ with $\boldsymbol{D}, \boldsymbol{B} \in \mathbb{R}^{2\times 2}$, $\boldsymbol{\Omega}^2 = \text{diag}\{\omega_1^2, \omega_2^2\}$ where ω_i are the natural frequencies of the system and $p(t) = \cos\left(\omega_p t\right)$ as discussed lately in [2]. A parametric excitation in a multi-degree-of-freedom system can lead to a destabilizing parametric resonance (see, e.g., [2]), as well as to a parametric anti-resonance, an increase in the effective damping of the overall system (see, e.g., [1, 3]). This anti-resonance may occur when the frequency of the parametric excitation ω_p is tuned close to a parametric combination resonance frequency as defined by $\omega_p = \frac{|\omega_2 \mp \omega_1|}{n}$ with $n \in \mathbb{N}^+$.

M. Ramírez-Barrios (✉)
Instituto Politécnico Nacional, UPIBI, Mexico City, Mexico
e-mail: mlramirezb@ipn.mx

F. Dohnal
Research Centre for Microtechnology, Vorarlberg University of Applied Sciences, Dornbirn, Austria
e-mail: fadi.dohnal@fhv.at

© The Author(s), under exclusive license to Springer Nature Switzerland AG 2024

W. Lacarbonara (ed.), *Advances in Nonlinear Dynamics, Volume III*, NODYCON Conference Proceedings Series, https://doi.org/10.1007/978-3-031-50635-2_5

2 Problem Description

The simplified dynamic model of a high-Q micromechanical beam can be described by $\ddot{x_1} + \gamma_1 \dot{x_1} + \omega_1^2 x_1 = 0$, where x_1 represents the physical displacements, ω_1 its natural frequency, and γ_1 the damping of the first mode of the beam. Such a system configuration is usually used in sensor applications with a large quality factor $Q_1 = \omega_1/\gamma_1$. However, a large quality factor leads to a long settling time (t_s) which hinders its usage for fast applications. To reduce this settling time, it has been proposed in [4] to attach a second beam with similar dynamic properties, natural frequency $\omega_2 \approx \omega_1$, and damping $\gamma_1 \approx \gamma_2$. This second beam is attached to the same base but decoupled from the first beam. By employing a periodic signal $p_1(t) = \beta \cos(\omega_p t)$ tuned at the so-called parametric anti-resonance frequency $\omega_p = |\omega_2 - \omega_1|$, a transfer of the mechanical energy between the first beam and the second beam is enforced back and forth. If this periodic signal is activated only for a certain time period t_p, called the pulse of parametric excitation, the energy transfer becomes unidirectional. Such a pulsed $p_1(t)$ achieves a fast energy transfer from the first beam to the second one. Hence, the second beam acts as an energy sink from the perspective of the first beam, an equivalent dissipator. A formula for a proper choice for the pulse time for achieving a unidirectional energy transfer was derived in as reported in [5–7] and showed a reduction of the settling time down to approximately 9%. In the present contribution, we couple one more beam to create a triple-beam micromechanical sensor. The first beam is again the sensing beam. The second and the third beams are designed to become effective energy sinks. The second beam is driven by the pulsed periodic signal $p_1(t)$, while the third beam is driven by another pulsed signal $p_2(t)$. The equations of motion that describe the three coupled beams are given by

$$\ddot{\mathbf{x}} + \boldsymbol{\Gamma}\dot{\mathbf{x}} + \left(\boldsymbol{\Omega}^2 + \mathbf{B}_1 p_1(t) + \mathbf{B}_2 p_2(t)\right)\mathbf{x} = 0 \tag{1}$$

where

$$\boldsymbol{\Gamma} = \begin{bmatrix} \gamma_1 & 0 & 0 \\ 0 & \gamma_2 & 0 \\ 0 & 0 & \gamma_3 \end{bmatrix}, \ \boldsymbol{\Omega}^2 = \begin{bmatrix} \omega_1^2 & 0 & 0 \\ 0 & \omega_2^2 & 0 \\ 0 & 0 & \omega_3^2 \end{bmatrix}, \ \mathbf{B}_1 = \begin{bmatrix} 0 & b_{12} & 0 \\ b_{21} & 0 & 0 \\ 0 & 0 & 0 \end{bmatrix}, \ \mathbf{B}_2 = \begin{bmatrix} 0 & 0 & b_{13} \\ 0 & 0 & 0 \\ b_{31} & 0 & 0 \end{bmatrix},$$

$p_1(t) = \beta_1 \cos(\omega_{p_1} t)$ and $p_2(t) = \beta_2 \cos(\omega_{p_2} t)$. The system in Eq. (1) is a set of linear differential equations that is coupled by two parametric excitation signals at frequencies $\omega_{p_1} = \omega_2 - \omega_1$ and $\omega_{p_2} = \omega_3 - \omega_1$. In the following, the analysis of the parametric anti-resonance is discussed by using a singular perturbation. The derivation of the slow dynamics enables the computation of the pulse period t_p to reduce the settling time of the first beam.

3 Parametric Anti-resonance Analysis

The averaging technique in [8] is applied for analyzing the parametric anti-resonance. In the following, we present the averaging procedure for a subset of Eq. (1). Further details can be found in [1, 3, 5]. Consider the system

$$\ddot{\mathbf{x}} + \begin{bmatrix} \gamma_1 & 0 \\ 0 & \gamma_2 \end{bmatrix} \dot{\mathbf{x}} + \left(\begin{bmatrix} \omega_1^2 & 0 \\ 0 & \omega_2^2 \end{bmatrix} + \begin{bmatrix} b_{11} & b_{12} \\ b_{21} & b_{22} \end{bmatrix} p(t) \right) \mathbf{x} = 0 \tag{2}$$

with $\mathbf{x} = \begin{bmatrix} x_1 & x_2 \end{bmatrix}^T$ and $p(t) = \beta \cos \omega_p t$ the parametric excitation signal, $\beta \in \mathbb{R}$. Rewritten in index notation, where in the Einstein summation repeated indices are implicitly summed over, we obtain

$$\ddot{x}_i + \omega_i^2 x_i = -\beta \left(\gamma_i \dot{x}_j - b_{ij} x_j \cos \omega_p t \right) \tag{3}$$

with $i, j = 1, 2$. Normalizing the frequency through the variable change $\tau = \omega_p t$, the system (3) is transformed into

$$x_i'' + \nu_i^2 x_i = -\frac{\beta}{\omega_p^2} \left\{ \omega_p \gamma_i x_j' + b_{ij} x_j \cos(\tau) \right\} \tag{4}$$

where $\frac{d}{d\tau}() = ()'$ and $\nu_i = \omega_i / \omega_p$. Introducing the abbreviations $s_i = \sin(\nu_i \tau)$ and $c_i = \cos(\nu_i \tau)$, using the following amplitude and phase transformation:

$$x_i(\tau) = A_i(\tau) c_i + \phi_i(\tau) s_i, \tag{5}$$

$$x_i'(\tau) = -A_i(\tau) \nu_i s_i + \phi_i(\tau) \nu_i c_i \tag{6}$$

$$A_i' c_i + \phi_i' s_i = 0 \tag{7}$$

and differentiating Eq. (6), the following relation is obtained[1]

$$x_i'' = -A_i' \nu_i s_i - A_i \nu_i^2 c_i + \phi_i' \nu_i c_i - \phi_i \nu_i^2 s_i \tag{8}$$

Substituting Eq. (8) into Eq. (4) produces

$$-A_i' \nu_i s_i + \phi_i' \nu_i c_i = \frac{\beta}{\omega_p^2} \tilde{F}_i \tag{9}$$

where $\tilde{F}_i = \tilde{F}_i(A_1, A_2, \phi_1, \phi_2, \tau)$ is given by

[1] For simplicity in writing, the explicit time dependence is omitted: $A = A(\tau)$, $\phi = \phi(\tau)$.

$$\tilde{F}_i = -\left\{ \omega_p \sum_j \gamma_i \left[\left(-A_j \nu_j \right) s_j + \phi_j \nu_j c_j \right] + \sum_j b_{ij} \left(A_j c_j + \phi_j s_j \right) \cos(\tau) \right\}$$

Finally, introducing the vector $\mathbf{u} = \begin{bmatrix} A_1 & A_2 & \phi_1 & \phi_2 \end{bmatrix}^T$ and inserting the relation Eq. (7) into Eq. (9), the equations of motion are rewritten as

$$A_i' = -\frac{\beta}{\omega_p \omega_i} \tilde{F}_i(\mathbf{u}, t) s_i = \beta \tilde{G}_i(\mathbf{u}, \tau), \quad \phi_i' = \frac{\beta}{\omega_p \omega_i} \tilde{F}_i(\mathbf{u}, t) c_i = \beta \tilde{H}_i(\mathbf{u}, \tau) \quad (10)$$

with $i = 1, 2$. The functions $\tilde{G}_i(\mathbf{u}, \tau)$ and $\tilde{H}_i(\mathbf{u}, \tau)$ are quasiperiodic and can be written as a finite sum of periodic terms according to

$$\tilde{G}_i(\mathbf{u}, \tau) = \sum_{k=1}^{N} \tilde{G}_{i,k}(\mathbf{u}, \tau), \quad \tilde{H}_i(\mathbf{u}, \tau) = \sum_{k=1}^{N} \tilde{H}_{i,k}(\mathbf{u}, \tau)$$

where N is fixed and $\tilde{G}_{i,k}(u, \tau)$ and $\tilde{H}_{i,k}(u, \tau)$ are T_k periodic functions in τ.

Applying the *averaging* method following [8] to Eq. (10) results in

$$\hat{A}_i' = \beta \sum_{k=1}^{N} \frac{1}{T_k} \int_0^{T_k} \tilde{G}_{i,k}(\mathbf{u}, \tau) d\tau, \quad \hat{\phi}_i' = \beta \sum_{k=1}^{N} \frac{1}{T_k} \int_0^{T_k} \tilde{H}_{i,k}(\mathbf{u}, \tau) d\tau \quad (11)$$

where $\hat{}$ indicates time-averaged variables. For averaging the system, the periods of the right-hand sides of Eq. (10) must be determined using the trigonometric identities. The integrals in Eq. (11) over a basic trigonometric terms yield always zero with the exception for resonant terms, i.e., at frequencies $\omega_p = \frac{2\omega_i}{n}$ and $\omega_p = \frac{|\omega_2 \pm \omega_1|}{n}$ with $n \in \mathbb{N}^+$ [1, 8].

Averaging Eq. (10) at the parametric anti-resonance frequency $\omega_p = \omega_2 - \omega_1$ yields the slow dynamics with a constant coefficient matrix:

$$\hat{\mathbf{u}}' = \hat{\mathbf{A}} \hat{\mathbf{u}} \quad (12)$$

with

$$\hat{\mathbf{A}} = \frac{\beta}{\omega_p} \begin{bmatrix} -\frac{1}{2}\gamma_1 & 0 & 0 & \frac{1}{4\omega_1} b_{12} \\ 0 & -\frac{1}{2}\gamma_1 & -\frac{1}{4\omega_1} b_{12} & 0 \\ 0 & \frac{1}{4\omega_2} b_{21} & -\frac{1}{2}\gamma_2 & 0 \\ -\frac{1}{4\omega_2} b_{21} & 0 & 0 & -\frac{1}{2}\gamma_2 \end{bmatrix}$$

The averaged system in Eq. (12) is a linear time-invariant system, where the averaged solution $\hat{\mathbf{u}} = \left[\hat{A}_1\ \hat{A}_2\ \hat{\phi}_1\ \hat{\phi}_2\right]^T$ differs from the original solution $\mathbf{u} = \left[A_1\ A_2\ \phi_1\ \phi_2\right]^T$ as $\hat{\mathbf{u}}(\tau) - \mathbf{u}(\tau) = \mathcal{O}(\beta)$ on the time scale $1/\beta$ (see [8]).

At the frequency $\omega_p = \omega_2 - \omega_1$, the averaged equation in Eq. (12) becomes independent of the direct coefficients b_{11} and b_{22}. The coupling coefficients b_{12}, b_{21} describe the dynamics, at least in first-order approximation. In this case, the coefficient matrix $\mathbf{A}$ has the two repeated eigenvalues $\hat{\lambda}_1 = \hat{\lambda}_3$ and $\hat{\lambda}_2 = \hat{\lambda}_4$ given by

$$\hat{\lambda}_{1,2} = -\frac{\beta}{4\omega_p}\left((\gamma_1 + \gamma_2) \pm \sqrt{(\gamma_1 - \gamma_2)^2 - \frac{b_{12}b_{21}}{\omega_1\omega_2}}\right) \tag{13}$$

The slow dynamics in Eq. (12) describe the envelope of the response as visualized in Fig. 1. This envelope is characterized by the eigenvalues $\hat{\lambda}_i$ of the matrix $\hat{\mathbf{A}}$. If the condition

$$(\gamma_1 - \gamma_2)^2 > \frac{b_{12}b_{21}}{\omega_1\omega_2} \geq 0 \tag{14}$$

is satisfied, then the eigenvalues are real-valued and the envelope decreases exponentially in time as shown in Fig. 1b. Alternatively, if the condition in Eq. (14) is not fulfilled, then the eigenvalues are complex conjugate and the envelope is modulated as shown in Fig. 1a. Moreover, the imaginary part of $\hat{\lambda}_i$ corresponds to the frequency of envelope and is given by

$$\hat{\omega}_A = \pm\frac{\beta}{4\omega_p}\sqrt{\frac{b_{12}b_{21}}{\omega_1\omega_2} - (\gamma_1 - \gamma_2)^2} \tag{15}$$

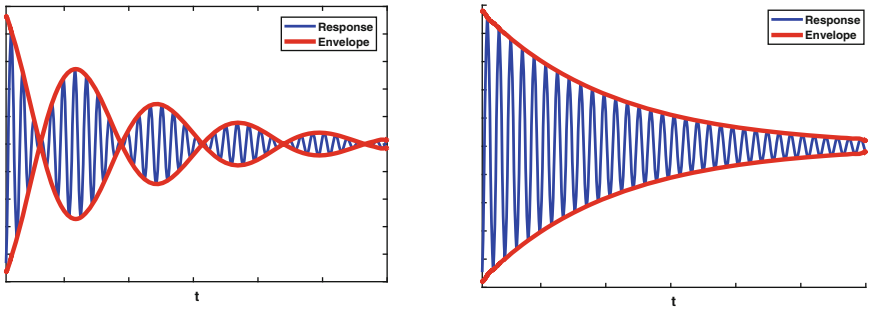

(a) $\frac{b_{12}b_{21}}{\omega_1\omega_2} > (\gamma_1 - \gamma_2)^2 \geq 0$ (b) $(\gamma_1 - \gamma_2)^2 > \frac{b_{12}b_{21}}{\omega_1\omega_2} > 0$

Fig. 1 Time response of the slow dynamics in Eq. (11): (**a**) exponentially decaying and beating envelope response and (**b**) exponentially decaying envelope

Table 1 Physical parameters for the system in Eq. (1)

Natural frequencies		
$\omega_1 = 1.8316 \times 10^6$ rad/s	$\omega_2 = 1.8344 \times 10^6$ rad/s	$\omega_3 = 1.8390 \times 10^6$ rad/s
Parametric anti-resonance frequencies		
$\omega_{p_1} = \omega_2 - \omega_1 = 2800$ rad/s		$\omega_{p_2} = \omega_3 - \omega_1 = 4600$ rad/s
Coupling coefficients		*Damping coefficients*
$b_{12} = b_{21} = 1.2 \times 10^9$ 1/s^2		$\gamma_1 = \gamma_2 = \gamma_3 = 39$ 1/s
$b_{13} = b_{31} = 1.2 \times 10^9$ 1/s^2		
Quality factors		
$Q_1 = \frac{\omega_1}{\gamma_1} = 46.96 \times 10^3$	$Q_2 = \frac{\omega_2}{\gamma_2} = 47.035 \times 10^3$	$Q_3 = \frac{\omega_3}{\gamma_3} = 47.15 \times 10^3$

There are two envelopes for x_1 and x_2 that correspond to the two frequencies $\pm\hat{\omega}_A$. Therefore, the envelopes are in antiphase. By rescaling time τ back to the physical time t, we obtain the period T_A of the envelope response:

$$T_A = \frac{4\pi}{\beta\sqrt{\frac{b_{12}b_{21}}{\omega_1\omega_2} - (\gamma_1 - \gamma_2)^2}} \tag{16}$$

4 Pulsed Parametric Excitation

A simulation is performed by numerical integration of the MEMS in Eq. (1) with the data listed in Table 1.[2] Firstly, the system behavior for deactivated parametric excitation is discussed by choosing $\beta_1 = 0$ and $\beta_2 = 0$ in Eq. (1). In this case, all modes are decoupled. Starting the system in its first modal deflection x_1, it decays with the corresponding modal damping. The time histories of the other two modal deflections remain zero because they are not excited for this special initial condition. The time histories of the envelope of all modal deflections are shown in Fig. 2a. The free response of x_1 possesses the settling time of approximately $t_{ss} = 150$ ms due to the high-quality factor.

Activating both parametric excitations continuously by choosing $\beta_1 = 1$ and $\beta_2 = 1$ and tuning each at a parametric anti-resonance frequencies $\omega_{p_1} = \omega_2 - \omega_1$ and $\omega_{p_2} = \omega_3 - \omega_1$ lead to the time histories shown in Fig. 2b. The modal energy is transferred back and forth between the mode x_1 and modes x_2 and x_3 due to the modal coupling employed by the two parametric excitations. The slow dynamics in Eq. (12) describe the transients of the modal response envelope of two-DOF system. For this specific three-DOF MEMS, the system modes are coupled only by the parametric excitations. More specifically, x_1 is coupled with x_2 and

[2] The numerical values listed in Table 1 are chosen similar to the experimental two-DOF MEMS reported in [9].

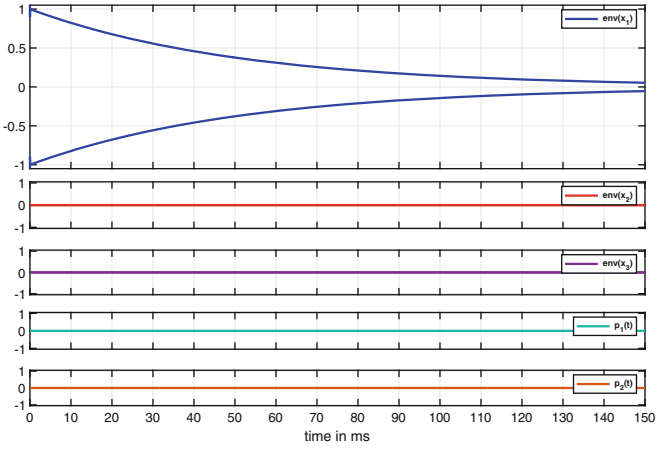

(a)

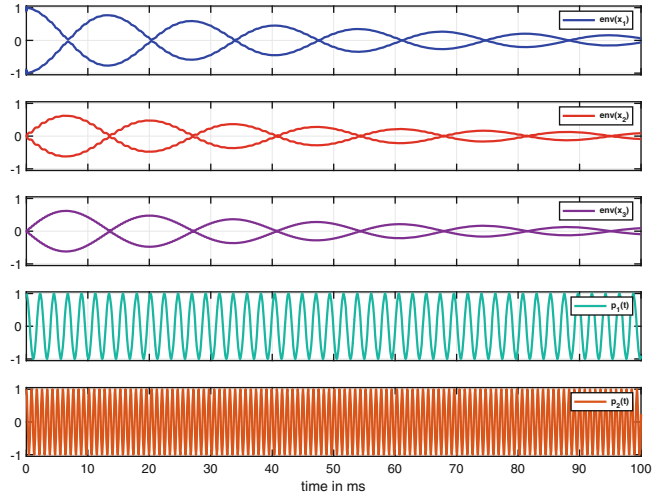

(b)

Fig. 2 Time histories of the individual modal envelopes of MEMS in Eq. (1) without and for a continuously activated multi-harmonic parametric excitation. (**a**) System without parametric excitation. (**b**) System at activated $p_1(t)$ and $p_2(t)$

x_1 with x_3. This system behavior can be described by two individual systems with two-DOF:

$$\begin{bmatrix} \ddot{x}_1 \\ \ddot{x}_2 \end{bmatrix} + \begin{bmatrix} \gamma_1 & 0 \\ 0 & \gamma_2 \end{bmatrix} \begin{bmatrix} \dot{x}_1 \\ \dot{x}_2 \end{bmatrix} + \left(\begin{bmatrix} \omega_1^2 & 0 \\ 0 & \omega_2^2 \end{bmatrix} + \begin{bmatrix} 0 & b_{12} \\ b_{21} & 0 \end{bmatrix} p_1(t) \right) \begin{bmatrix} x_1 \\ x_2 \end{bmatrix} = 0, \quad (17)$$

$$\begin{bmatrix} \ddot{x}_1 \\ \ddot{x}_3 \end{bmatrix} + \begin{bmatrix} \gamma_1 & 0 \\ 0 & \gamma_3 \end{bmatrix} \begin{bmatrix} \dot{x}_1 \\ \dot{x}_3 \end{bmatrix} + \left(\begin{bmatrix} \omega_1^2 & 0 \\ 0 & \omega_3^2 \end{bmatrix} + \begin{bmatrix} 0 & b_{13} \\ b_{31} & 0 \end{bmatrix} p_2(t) \right) \begin{bmatrix} x_1 \\ x_3 \end{bmatrix} = 0, \tag{18}$$

with $p_1(t) = \beta_1 \cos(\omega_{p_1} t)$ and $p_2(t) = \beta_2 \cos(\omega_{p_2} t)$. The transients in Fig. 2b show that the envelope of x_1 reaches a maximum or minimum when x_2 and x_3 are close to zero. Based on the analysis in the previous section for a generic two-DOF system, the periods of the modal envelopes in Fig. 2b can be estimated by Eq. (16). This provides the time after which the initial modal energy in x_1 is fully transferred to a higher mode. The pulse period for each parametric excitation at a parametric anti-resonance frequency becomes

$$t_{p_1} = \frac{2\pi}{\beta_1 \sqrt{\frac{b_{12} b_{21}}{\omega_1 \omega_2} - (\gamma_1 - \gamma_2)^2}} \qquad t_{p_2} = \frac{2\pi}{\beta_2 \sqrt{\frac{b_{13} b_{31}}{\omega_1 \omega_3} - (\gamma_1 - \gamma_3)^2}} \tag{19}$$

Knowing this upfront, the parametric excitation is only activated during t_{p_1} and t_{p_2} by choosing

$$\beta_1 = \begin{cases} 1 & \text{if} \quad 0 \leq t < t_{p_1} \\ 0 & \text{if} \quad t_{p_1} \leq t \end{cases} \qquad \beta_2 = \begin{cases} 1 & \text{if} \quad 0 \leq t < t_{p_2} \\ 0 & \text{if} \quad t_{p_2} \leq t \end{cases} \tag{20}$$

This results in pulsed parametric excitation $p_1(t)$ and $p_2(t)$, respectively. The effect of each individually pulsed parametric excitation is shown in Fig. 3. The effect of the coupling induced by $p_1(t)$ while $p_2(t)$ is not active as depicted in Fig. 3a. Figure 3b shows the change when the coupling with $p_2(t)$ is activated and $p_2(t)$ is deactivated. In both cases, the settling time was minimized by more than 93%. In the first case, t_{ss} reduced from 150 ms to 9.53 ms, and in the second case, from 150 ms to 9.6 ms. It clearly shows that in the slow dynamics, the second and third modes act as equivalent dissipators for transient dynamics. With Eq. (19), we can calculate the time length each pulse needs for reaching the maximum modal energy transfer to the dissipators x_2 and x_3. Considering the values in Table 1, the calculated time lengths become $t_{p_1} = 9.54$ ms and $t_{p_2} = 9.61$ ms matching the values found by numerical simulation in Fig. 3.

Finally, the transient dynamics in case of both pulsed parametric excitations $p_1(t)$ and $p_2(t)$ are being active for $t_p = 6.8$ ms in Fig. 4. This technique achieves a further significant reduction in settling time. Summarizing, adding an extra modal deflection and driving it at a pulsed parametric anti-resonance frequency reduces the settling time from 150 ms in the free transient response to 6.6 ms, which corresponds to a reduction of more than 95%.

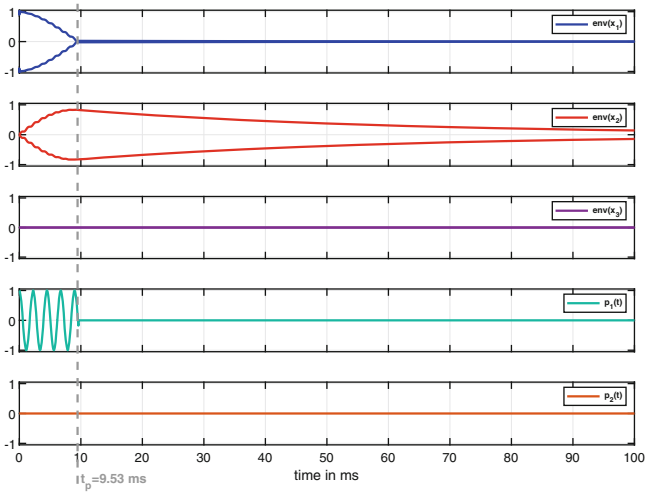

(a)

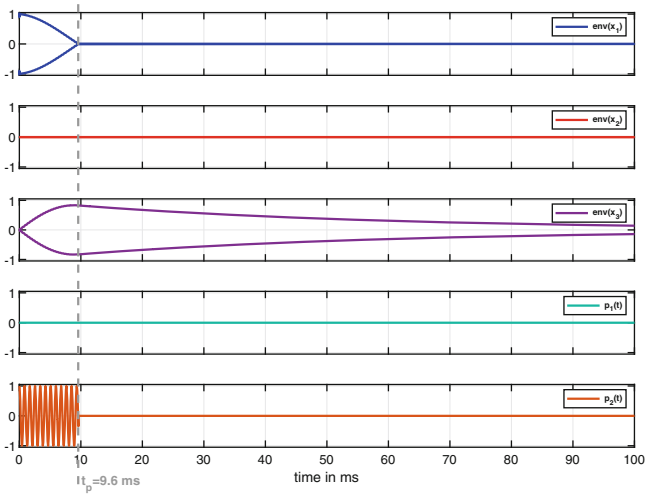

(b)

Fig. 3 Time histories of the individual modal envelopes of MEMS in Eq. (1) for individually pulsed harmonic parametric excitations. (**a**) System at activated $p_1(t)$ during t_{p_1} seconds. (**b**) System at activated $p_2(t)$ during t_{p_2} seconds

5 Conclusions

The transients of the slow dynamics of a specific three-DOF MEMS were analyzed numerically. The system is driven at two pulsed parametric anti-resonances. It is shown that the necessary pulse periods for achieving a parametric anti-resonance

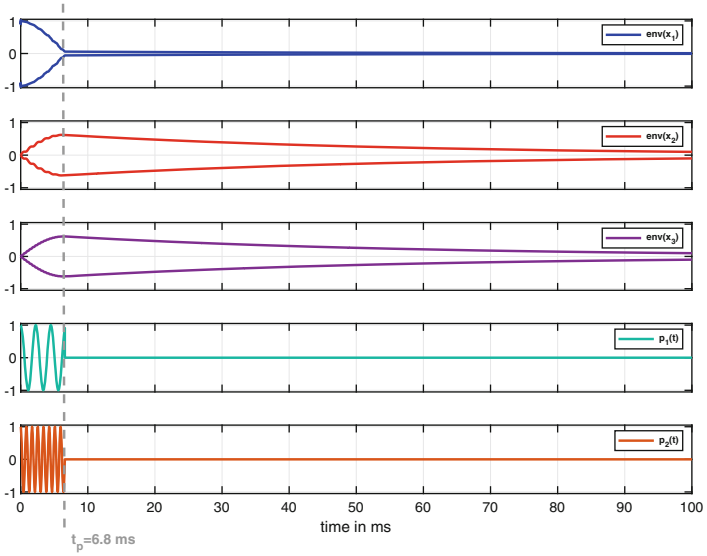

Fig. 4 Time histories of the individual modal envelopes of MEMS in Eq. (1) for a multi-harmonic parametric excitation with two simultaneously activated pulsed parametric excitations $p_1(t)$ and $p_2(t)$ during t_p seconds

can be predicted by an analytical approximation resulting from the application of the averaging method on the equations of motion. Driving the three-DOF MEMS with one pulsed parametric anti-resonance shows a coupling between the two modes defined by the parametric excitation frequency. This reduces the settling time, as shown already in a previous work. Adding a second pulsed parametric anti-resonance demonstrates the capability of a further reduction of the settling time. For this specific system, an overall reduction of at least 95% is achieved. The proposed technique is potentially applicable for operating MEMS arrays at a much higher speed.

References

1. Dohnal, F., Verhulst, F.: Averaging in vibration suppression by parametric stiffness excitation. Nonlinear Dyn. **54**(3), 231–248 (2008)
2. Ramírez-Barrios, M., Collado, J., Dohnal, F.: Stability of Coupled and Damped Mathieu Equations Utilizing Symplectic Properties. In: Lacarbonara, W., Balachandran, B., Ma, J., Tenreiro Machado, J., Stepan, G. (Eds.) Nonlinear Dynamics of Structures, Systems and Devices. Springer, Cham (2020)
3. Dohnal, F.: Damping by parametric stiffness excitation: resonance and anti-resonance. J. Vib. Control **14**(5), 669–688 (2008)
4. Okamoto, H., Gourgout, A., Chang, C.Y., et al.: Coherent phonon manipulation in coupled mechanical resonators. Nature Phys. **9**, 480–484 (2013)

5. Ramírez-Barrios, M., Dohnal, F. Collado, J.: Enhanced vibration decay in high-Q resonators by confined of parametric excitation. Arch. Appl. Mech. **90**, 1673–1684 (2020)
6. Ramírez-Barrios M., Dohnal, F.: Settling time reduction by open-loop control based on parametric anti-resonance. In: 2023 20th International Conference on Electrical Engineering, Computing Science and Automatic Control (CCE), Mexico City, Mexico (2023)
7. Ramírez-Barrios, M., Dohnal, F., Collado, J.: Transient vibrations suppression in parametrically excited resonators. In: Hernandez, E., Keshtkar, S., Valdez, S. (eds.) Industrial and Robotic Systems. LASIRS 2019. Mechanisms and Machine Science, vol 86. Springer, Cham (2020)
8. Verhulst, F.: Nonlinear Differential Equations and Dynamical Systems. Springer Science & Business Media, New York (2006)
9. Okamoto, H., Mahboob, I., Onomitsu, K., et al.: Rapid switching in high-Q mechanical resonators. Appl. Phys. Lett. **105**(8), 083114 (2014)

Part II
Chaotic Systems and Uncertainty

Self-supervised Contrastive Learning for Chaotic Time-Series Classification

Salama Hassona and Wieslaw Marszalek

1 Introduction

It is often crucial to compute bifurcation diagrams in order to assess the stability and effects of multiple parameters on the overall dynamical properties of nonlinear systems. The case of one-parameter bifurcation diagrams is fairly easy to deal with, but it is more difficult (due to computational requirements) to do so when two or more parameters change at once, as we need fairly advanced hardware and software resources for that purpose [1–4].

The problem of generating $n-$parameter bifurcation diagrams can be easily transformed into the time-series classification, whereby by applying the machine learning methods we can determine chaotic/quasi-periodic or periodic behaviour for the desired set of parameters or initial values of the dynamical system. Many studies have been published in recent years suggesting employing various machine learning techniques to handle such multi-parameter cases, for example, the Extreme Learning Machines [5], Time Series Forests with Entropy [6], LKCNN [7], LSTM-FCN [8] networks, and others. Although those models perform well on the training datasets, they have two major drawbacks: firstly, they need a large amount of labelled data and, secondly, they tend to overfit while tested on the new datasets as shown in [7, 8]. These drawbacks lead us to **the main objective of this work**, which is improving the generalization abilities of the machine learning models in order to make them applicable in real problems with a decreased amount of the labelled data needed to achieve satisfactory results. We achieved that by applying the Temporal and Contextual Contrasting (TS-TCC) framework [9], using the residual components, and scaling as the data augmentation techniques to train the TS-TCC framework.

S. Hassona (✉) · W. Marszalek
Faculty of Electrical Engineering, Automatic Control and Computer Science, Opole University of Technology, Opolskie, Poland

© The Author(s), under exclusive license to Springer Nature Switzerland AG 2024

W. Lacarbonara (ed.), *Advances in Nonlinear Dynamics, Volume III*, NODYCON Conference Proceedings Series, https://doi.org/10.1007/978-3-031-50635-2_6

The paper is organized as follows. In Sect. 2 we provide a TS-TCC Residual framework for classifying time-series and describe our chaotic dynamical system (electric arc model) used for testing purposes. The main results are presented in Sect. 3 with an extensive amount of illustrative material in the forms of two-parameter bifurcation diagrams and measures to evaluate the predictive performance of various ML algorithms. Comments on the obtained results are included in Sect. 4.

2 TS-TCC Framework, Dynamical System, and Decomposition Algorithm

2.1 Machine Learning Methods Applied and the TS-TCC Framework

In recent years, self-supervised learning became increasingly popular, for both contrastive and non-contrastive approaches. The main value that those methods are bringing is the ability to learn meaningful representations of unlabelled data and easily transfer them into supervised learning, trained on chunks of the labelled data. There are many state-of-the-art models designed for image representation learning [10–13], however, not that many when it comes to the time-series representation learning. In this paper, we applied the tuned TS-TCC framework which outperforms many state-of-the-art self-supervised time-series representation learning methods, like SimCLR [13], SSL-ECG [14], and CPC [15], to solve the reconstruction problem of two-parameter bifurcation diagrams.

The architecture of the TS-TCC framework is presented in Fig. 1. It is made of 4 parts: data augmentation, encoding, temporal contrasting, and contextual contrasting. Firstly, two different views are generated, using weak and strong augmentation. Weak augmentation consists of jittering and scaling. In the original

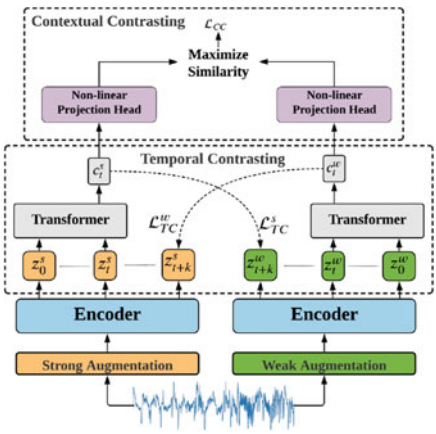

Fig. 1 TS-TCC framework architecture. From *Time-Series Representation Learning via Temporal and Contextual Contrasting* [9]

paper [9], strong augmentation was made of permutation and jittering, however, **in this paper** we use, instead of it, the residual component of the time-series and call it the **TS-TCC Residual**. More details of how the decomposition of time-series was performed can be found in Sect. 2.4. Secondly, both views of the original time-series are run through the encoder, which is the 3-block convolution architecture as proposed in [16]. Thirdly, the temporal contrasting module tries to extrapolate the temporal features of the data with an autoregressive model – Transformers [17]. The strong augmentation generates c_t^s token and the weak augmentation generates c_t^w. The cross-view prediction task is performed by using the context of the strong augmentation c_t^s to predict the future time steps of the weak augmentation z_{t+k}^w and vice versa. The contrastive loss tries to minimize the dot product between the predicted representation and the true one of the same sample while maximizing the dot product with the other samples $\mathcal{N}_{t,k}$ within the minibatch. Next, two losses $\mathcal{L}_{TC}^s$ and $\mathcal{L}_{TC}^w$ are calculated as follows

$$\mathcal{L}_{TC}^s = -\frac{1}{K}\sum_{k=1}^{K} log \frac{exp((\mathcal{W}_k(c_t^s))^T z_{t+k}^w)}{\sum_{n\in\mathcal{N}_{t,k}} exp((\mathcal{W}_k(c_t^s))^T z_n^w)}$$

$$\mathcal{L}_{TC}^w = -\frac{1}{K}\sum_{k=1}^{K} log \frac{exp((\mathcal{W}_k(c_t^w))^T z_{t+k}^s)}{\sum_{n\in\mathcal{N}_{t,k}} exp((\mathcal{W}_k(c_t^w))^T z_n^s)}$$

where $\mathcal{W}_k$ is a linear function that maps c_t^s and c_t^w to the same dimension as z_t^s and z_t^w have. Lastly, the contextual contrasting module is applied, which aims to learn more discriminative representations. It consists of a nonlinear transformation to the contexts using a nonlinear projection head [13]. The loss function $\mathcal{L}_{CC}$ of the projection head, which maximizes the similarity between the positive pair and minimizes the similarity between the negative pair, maps the contexts onto the space where the contextual contrasting is applied. We create $2N$ contexts from a batch of N input samples using two augmentation techniques on each sample. The positive sample of a context c_t^i that comes from the other augmented view of the same input is denoted as $c_t^{i^+}$, and as a result, $(c_t^i, c_t^{i^+})$ are regarded as a positive pair. The remaining $(2N-2)$ contexts from further inputs in the same batch are regarded as the negative samples of c_t^i. As a result, the final representations can be discriminative. The $\mathcal{L}_{CC}$ function is defined as follows

$$\mathcal{L}_{CC} = -\sum_{i=1}^{N} log \frac{exp(sim(c_t^i, c_t^{i^+})/\tau)}{\sum_{m=1}^{2N} \mathbb{1}_{[m\neq 1]} exp(sim(c_t^i, c_t^m)/\tau)}$$

where N is a batch size, $(c_t^i, c_t^{i^+})$ stands for the positive pair, sim is a ℓ_2 normalized dot product (i.e., cosine similarity), and τ is a temperature parameter.

The overall self-supervised loss is the combination of the two temporal contrasting losses and the contextual contrasting loss as follows

$$\mathcal{L} = \lambda_1 \cdot (\mathcal{L}_{TC}^{s} + \mathcal{L}_{TC}^{w}) + \lambda_2 \cdot \mathcal{L}_{CC}$$

where λ_1 and λ_2 are fixed scalar hyperparameters denoting the relative weight of each loss.

2.2 Dynamical System and Time-Series Data

For illustration purposes, we chose to study the oscillating electric arc RLC circuits described by a system of ordinary differential equations [8]

$$\frac{dx}{dt} = \frac{1}{L}(y - xz^{-1/3}), \quad \frac{dy}{dt} = \frac{1}{RC}(R + 1 - y - Rx), \quad \frac{dz}{dt} = x^2 - z \qquad (1)$$

The above ODE and the method used to obtain the original time-series responses (described below) are taken from [8]. For further analysis we consider three parameter spaces for parameters (a) $(R_1, R_2) \times (C_1, C_2) \times L = (6, 15.5) \times (2.8, 3.4) \times 1$, (b) $(R_1, R_2) \times (C_1, C_2) \times L = (6, 15.5) \times (2.8, 3.4) \times 1.1$, and (c) $(R_1, R_2) \times (C_1, C_2) \times L = (20, 29.5) \times (2.2, 2.8) \times 2$, and called them the *dataset* $L = 1$, *dataset* $L = 1.1$, and *dataset* $L = 2$, respectively. To solve the above system we used the 4th order explicit Runge–Kutta (RK-4) method with the time interval $0 \leq t \leq 2000$, integration step $dt = 0.01$ and initial conditions $[x(0), y(0), z(0)] = [0.5, 4.0, 1.0]$. After solving the above ODEs for the pair (C, R), we identify of local maximum points of the obtained oscillatory solution to classify each time-series as chaotic/quasi-periodic or periodic. Identification of the local maximum points for the obtained time-series was made in a time interval $[t_min, t_max]$, using a simple algorithm based on the three consecutive discrete values, say $x(t_{k-1})$, $x(t_k)$ and $x(t_{k+1})$, see [18]. The identification was done backwards from $t_max = 2000$ to $t_min = 1000$. The step size dt in the RK-4 solver was selected such that in the case of periodic solutions $dt \ll T$, where T was the minimum period of oscillations in the assumed rectangular area (R, C). The value of $dt = 0.01$ was proved to be small enough for the intervals of parameters R and C given above. Once the maximum points are identified for $t_min \leq t \leq t_max$, then the type of periodic response is established as period-n oscillations, $n = 1, 2, \ldots, 22$. In our examples in this paper, all responses with $n \geq 23$ are collected together as one class of responses and, making a rough assumption, given the status of the chaotic/quasi-periodic responses class. There is nothing special about the number 23, as one can easily consider a bigger value, say a few hundred or even a thousand. Examples of chaotic/quasi-periodic and steady-state periodic time-series are shown in Fig. 2. More on the method can be found in [18]. One run of the numerical solver in the above method results in 600,003 discrete time values for the three variables in the system. Data labels (with a colour attached to each pair of points (R, C)) were generated, as shown in Fig. 3a.

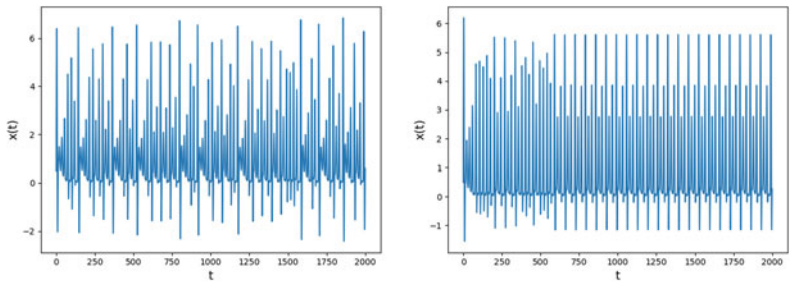

(a) Chaotic/quasi-periodic time-series (b) Periodic time-series for $t > 600$

Fig. 2 (**a**) chaotic/quasi-periodic time-series for $(R, C) = (15.484140, 3.279800)$, and (**b**) periodic time-series for $(R, C) = (6.570952, 3.312855)$. In both cases $L = 1$

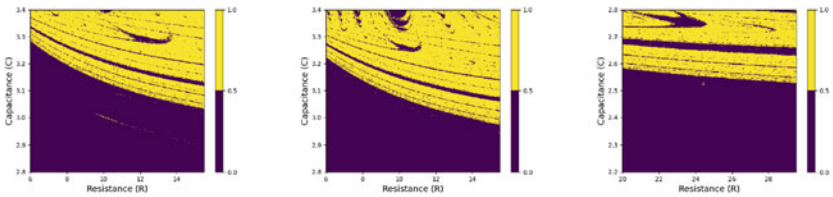

(a) (b) (c)

Fig. 3 Two-parameters bifurcation diagrams generated by the method described in [4] for datasets (**a**) $L = 1$, (**b**) $L = 1.1$, and (**c**) $L = 2$. Dark violet regions indicate periodic dynamics, whereas the yellow colour corresponds to chaotic/quasi-periodic ones

2.3 Training Data

The method mentioned in Sect. 2.2 results, for the given parameters, in 600,003 time values and labels for each of the three variables in (1). This method uses the specific properties of trajectories of the dynamical systems. The trajectories of the system evolve around the stationary point $(x, y, z) = (1, 1, 1)$. In the method, we project the trajectories to the XY plane and count the number of crossings of the line from the projected stationary point $(x, y) = (1, 1)$, see Fig. 4.

We used all three variables for our calculations (for each pair of 180,000 points (R_j, C_i) in the R and C parameter space), although to determine the chaotic behaviour, it is enough to study only one variable. As described earlier, we used a rather rough assumption that the identification process of periodic responses was done up to the number of local maximum points equal to 22. The number of local maximum points heavily depends on the integration step dt used to compute solutions of the system. If it is too big, the trajectories start to overlap each other, so it is impossible to correctly count the number of crossings. On the other hand, if it is too small, then the time of calculation drastically increases. In the assumed

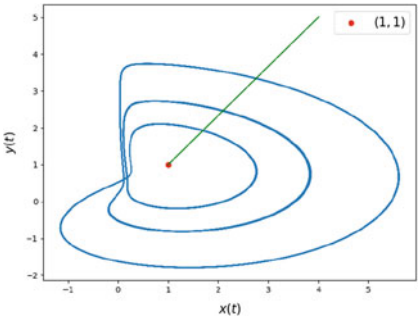

Fig. 4 The method used to calculate the labels for time-series. The blue curves denote the trajectories of the system and the red point is the projected stationary point. The green line is an auxiliary ray hooked at a stationary point. The number of crossings of the green line by the blue trajectories gives the number of local maximum of the examined time-series

parameter space for R and C there were neither unstable nor constant steady-state responses identified.

To train the TS-TCC framework we used time-series data in the interval of $1800 \leq t \leq 2000$, which results in 20,001 data points, but we took only every 8th point, so the final time-series had 2501 points.

2.4 Decomposition Algorithm

There are many decomposition algorithms but most of them require prior knowledge of the periodicity of the time-series, which in the case of chaotic dynamical systems is impossible to anticipate. In this paper, to estimate the period, we used periodogram averaging in our calculations. Firstly, one should detrend the data. We used the coarse-fitted cubic spline to do that. However, one could also use the mean or median filters or any other way to obtain the trend. In the next step, we estimate the range of likely periods for our time-series data by using the fast and robust periodogram averaging technique, developed by Welch [19]. Then we tested the obtained period values for the best fit to the detrended data, using the cross-validated residual errors and R^2 value of the leave-one-out cross-validation. Finally, we removed the seasonal variation of the dominant frequency using the estimated period. Once we remove the trend and seasonal components we obtain the residual component. In Fig. 5 we show the residual components of the time series presented in Fig. 2.

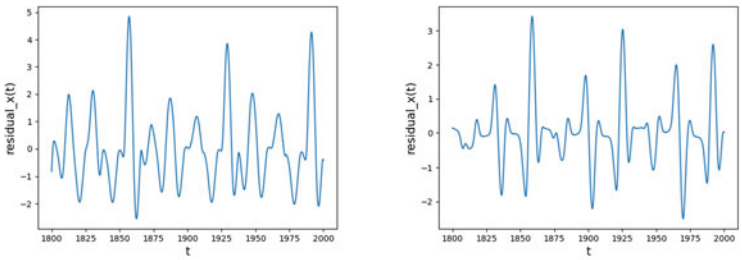

(a) Chaotic/quasi-periodic case (b) Periodic case

Fig. 5 Residual components of (**a**) chaotic/quasi-periodic time-series for $(R, C) = (15.484140, 3.279800)$, and (**b**) periodic time-series for $(R, C) = (6.570952, 3.312855)$ after preprocessing. In both cases $L = 1$

2.5 Training Setup

For training, validation, and testing datasets, the data was divided into 70%, 15% and 15% datasets, respectively. The pretraining and downstream tasks were carried out for 100 epochs each, and the best epoch was selected based on the lowest validation and training loss. A TS-TCC hyperparameters setup, similar to that described in [9], was used in this paper. We applied a batch size of 128, which was reduced to 32 in the few-labelled data experiments, as the data used can be less than 128. We used Adam optimizer with a learning rate of $3 \cdot 10^{-4}$, weight decay of $3 \cdot 10^{-4}$, $\beta_1 = 0.9$, and $\beta_2 = 0.99$. For the strong augmentation, we set the value of the maximum segment to 5, while for the weak augmentation, we set the scaling ratio to 2 for all three datasets. We set $\lambda_1 = 1$, and $\lambda_2 = 0.7$. In the Transformer model, we set the number of heads to 4, and the hidden dimensions value to 100. We also set its dropout to 0.1. In contextual contrasting, we set $\tau = 0.2$. The data generation, as well as the model training and classification, was performed on Tesla K80 GPU using Python framework PyTorch. As for time-series decomposition, we used library *seasonal* and performed calculations on the Intel(R) Xeon(R) CPU ES-2640 v2 processor at 2.00 GHz.

The code needed to reproduce our experiments and data is available at https://github.com/SalamaHassona/TS-TCC-Residual.

3 The Results

The TS-TCC Residual was compared to the following baselines: (1) Random Initialization – training a linear classifier on top of a randomly initialized encoder; (2) Supervised – supervised training of both encoder and classifier models; (3) TS-TCC proposed in [9]. The accuracy and F1-score are the two metrics we use to assess performance. We investigated the effectiveness of the TS-TCC Residual and

Table 1 Comparison between TS-TCC and TS-TCC Residual against baselines using linear evaluation experiments with 1% and 5% of labelled data. The best results are in bold and the second best is underlined

1% of labeled data						
	dataset $L = 1$		dataset $L = 1.1$		dataset $L = 2$	
Baseline	Accuracy	F1 Score	Accuracy	F1 Score	Accuracy	F1 Score
Random Initialization	61.82	10.08	79.27	75.73	67.45	0.00
Supervised	81.52	<u>72.17</u>	87.26	<u>87.63</u>	68.17	5.37
TS-TCC	<u>81.66</u>	72.00	<u>88.52</u>	87.58	<u>85.56</u>	<u>74.57</u>
TS-TCC Residual	**91.66**	**89.61**	**89.30**	**88.65**	**90.65**	**85.25**
5% of labeled data						
	dataset $L = 1$		dataset $L = 1.1$		dataset $L = 2$	
Baseline	Accuracy	F1 Score	Accuracy	F1 Score	Accuracy	F1 Score
Random Initialization	63.85	19.25	77.95	73.47	67.45	0.00
Supervised	<u>94.69</u>	<u>93.22</u>	<u>94.39</u>	<u>94.18</u>	**94.67**	**91.57**
TS-TCC	89.25	84.66	90.74	89.65	90.48	84.49
TS-TCC Residual	**95.52**	**94.35**	**94.59**	**94.50**	<u>93.86</u>	<u>90.49</u>

TS-TCC under the semi-supervised settings, by training the model with 1% and 5% of randomly selected instances of the training data. The linear evaluation results of our approach against all three baseline methods are shown in Table 1.

We obtained very high-performance metrics for both TS-TCC networks trained on only 1% and 5% of labelled data for all three sets of parameters. The TS-TCC Residual achieved around 89–91% of accuracy trained on 1% of labelled data, while TS-TCC achieved accuracy between 81–88%. Such results clearly show that training the TS-TCC framework on residual components for the nonlinear arc RLC circuit model is much more stable with varying the RLC parameters. Similar conclusions can be made for the training on 5% of labelled data. The reconstructed diagrams shown in Fig. 6 give a fairly good approximation of the original diagram.

4 Conclusions

We showed that:

1. TS-TCC Residual framework trained on the residual components of the dynamical systems' time-series achieves better accuracy than the original TS-TCC framework.
2. We proved that by taking only a chunk of labelled data, the self-supervised methods can perform very well and are more useful than the supervised machine learning methods for oscillatory time-series classification.

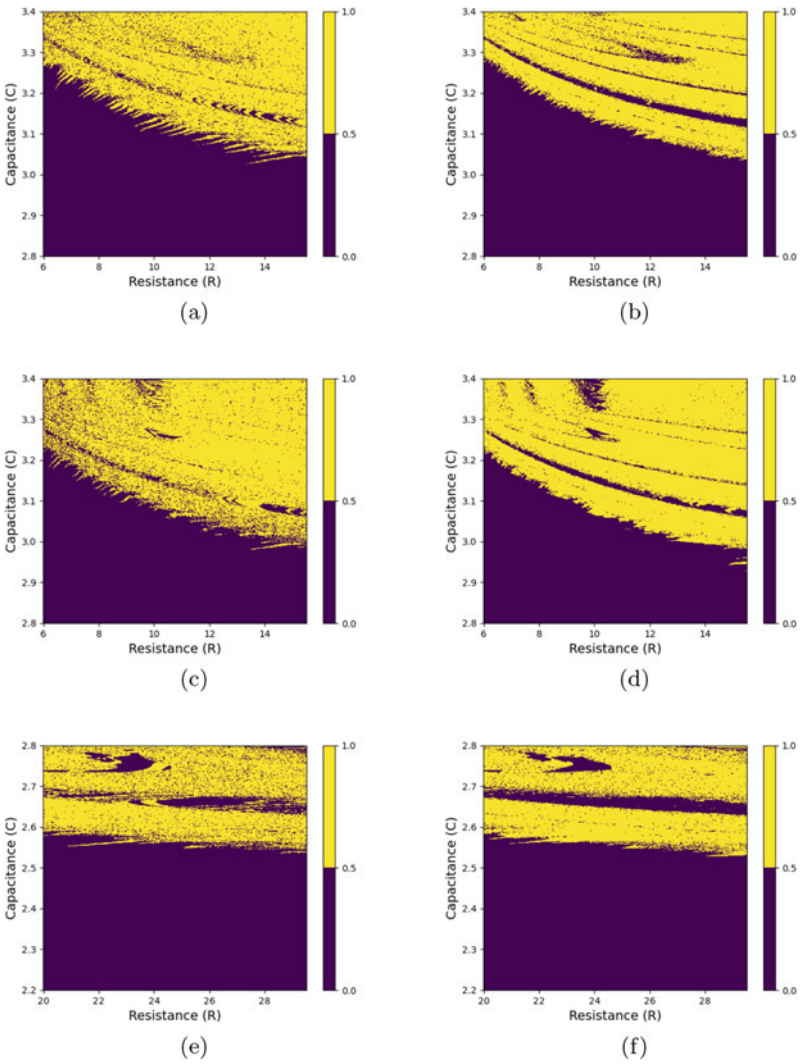

Fig. 6 Reconstructed bifurcation diagrams via TS-TCC Residual framework using 1% (left side) and 5% of labelled data (right side) for the datasets: (**a** and **b**) $L = 1$, (**c** and **d**) $L = 1.1$, and (**e** and **f**) $L = 2$. Regions in the reconstructed bifurcation diagrams with dark violet colour indicate periodic dynamics, whereas the yellow colour corresponds to chaotic/quasi-periodic ones

3. By improving the accuracy of the TS-TCC framework, we obtained the general method for the reconstruction of the n-parameter bifurcation diagrams that can compete with the currently used statistical methods.

References

1. Benettin, G., Galgani, L., Giorgilli, A., Strelcyn, J.-M.: Lyapunov Characteristic Exponents for smooth dynamical systems and for hamiltonian systems; A method for computing all of them. Part 2: Numerical application. Meccanica **15**, 21–30 (1980). https://doi.org/10.1007/BF02128237
2. Gottwald, G.A., Melbourne, I.: The 0–1 test for chaos: a review. Lect. Notes Phys. **915**, 221–247 (2016). https://doi.org/10.1007/978-3-662-48410-4_7
3. Pentegov, I.V., Sidorets, V.N.: Energy parameters in a mathematical model of a dynamic welding arc. Welding Int. **4**, 272–275 (1990). https://doi.org/10.1080/09507119009447722
4. Marszalek, W., Sadecki, J.: Complex two-parameter bifurcation diagrams of a simple oscillating circuit. IEEE Trans. Circuits Syst. II: Exp. Briefs **66**, 687–691 (2019). https://doi.org/10.1109/TCSII.2018.2871063
5. Itoh, Y., Uenohara, S., Adachi, M., Morie, T., Aihara, K.: Reconstructing bifurcation diagrams only from time-series data generated by electronic circuits in discrete-time dynamical systems. Chaos **30** (2020) https://doi.org/10.1063/1.5119187
6. Deng, H., Runger, G., Tuv, E., Vladimir, M.: A time series forest for classification and feature extraction. Inf. Sci. **239**, 142–153 (2013). https://doi.org/10.1016/j.ins.2013.02.030
7. Boullé, N., Dallas, V., Nakatsukasa, Y., Samaddar, D.: Classification of chaotic time series with deep learning. Phys. D: Nonl. Phenom. **403**, 132261 (2020). https://doi.org/10.1016/j.physd.2019.132261
8. Hassona, S., Marszalek, W., Sadecki, J.: Time series classification and creation of 2D bifurcation diagrams in nonlinear dynamical systems using supervised machine learning methods. Appl. Soft Comput. **113** (2021). https://doi.org/10.1016/j.asoc.2021.107874
9. Eldele, E., Ragab, M., Chen, Z., Wu, M., Kwoh, C.K., Li, X., Guan, C., et al.: Time-series representation learning via temporal and contextual contrasting. In: Proceedings of Thirtieth International Joint Conference on Artificial Intelligence, pp. 2352–2359 (2021). https://doi.org/10.24963/ijcai.2021/324
10. He, K., Fan, H., Wu, Y., Xie, S., Girshick, R.: Momentum contrast for unsupervised visual representation learning. In: CVPR'20, pp. 9726–9735 (2020). https://doi.org/10.1109/CVPR42600.2020.00975
11. Grill, J.-B., Strub, F., Altché, F., Tallec, C., Richemond, P.H., Buchatskaya, D.C., Pires, B.A., Guo, Z.D., Azar, M.G., Piot, B., Kavukcuoglu, K., Munos, R., Valko, M.: Bootstrap your own latent: a new approach to self-supervised learning. In: NIPS'20, vol. 1786, pp. 21271–21284 (2020). https://doi.org/10.5555/3495724.3497510
12. Chen, X., He, K.: Exploring simple siamese representation learning. In: CVPR'21, pp. 15745–15753 (2021). https://doi.org/10.1109/CVPR46437.2021.01549
13. Chen, T., Kornblith, S., Norouzi, M., Geoffrey, H.: A simple framework for contrastive learning of visual representations. In: ICML'20, vol. 149, pp. 1597–1607 (2020). https://doi.org/10.5555/3524938.3525087
14. Sarkar, P., Etemad, A.: Self-supervised ECG representation learning for emotion recognition. IEEE Trans. Affect. Comput. **13**, 1541–1554 (2020). https://doi.org/10.1109/TAFFC.2020.3014842
15. Oord, A., Li, Y., Vinyals, O.: Representation learning with contrastive predictive coding. arXiv:1807.03748 (2018). https://doi.org/10.48550/arXiv.1807.03748

16. Wang, Z., Yan, W., Oates, T.: Time series classification from scratch with deep neural networks: a strong baseline. In: IJCNN'17, pp. 1578–1585 (2017). https://doi.org/10.1109/IJCNN.2017.7966039
17. Vaswani, A., Shazeer, N., Parmar, N., Uszkoreit, J., Jones, L., Gomez, A.N., Kaiser, Ł., Polosukhin, I.: Attention is all you need. In: NIPS'17, pp. 6000–6010 (2017). https://doi.org/10.5555/3295222.3295349
18. Marszalek, W., Sadecki, J.: Parallel computing of 2-D bifurcation diagrams in circuits with electric arcs. IEEE Trans. Plasma Sci. **47**(1), 706–713 (2019). https://doi.org/10.1109/TPS.2018.2871576
19. Welch, P.D.: The use of fast fourier transform for the estimation of power spectra: a method based on time averaging over short, modified periodograms. IEEE Trans. Audio Electroacoust. **15**(2), 0–73 (1967). https://doi.org/10.1109/TAU.1967.1161901

Comprehensive Study of Electrical Power Grid Stability Issues Using Bifurcation and Chaos Theory

Ahmad Harb

1 Introduction

It is well known that the electric power system is a highly nonlinear system whose dynamics performance is influenced by a wide array of devices, with different response rates and characteristics. Under these stressful operating conditions, we are paying attention to two crucial instability problems called VC and SSR. These two main issues happen frequently in electric power systems all over the world. As power systems become more complex and more heavily loaded, voltage collapse becomes an increasingly serious problem. Also, to reduce the transmission line losses, we added series capacitors; however, these capacitors had a negative impact on the stability of the power system, with a phenomenon called SSR. Many investigators have linked these phenomena (VC and SSR) either to a static bifurcation [1–8], in particular, saddle-node bifurcation, or to a dynamic bifurcation [8]. The VC phenomenon could happen at any power system, any place, and time and this is due to either a high load demand on the power system or a sudden loss of power load. The SSR phenomenon happened back in 1970 and 1971 at Mohave Power Station, where there was a complete blackout in three states in America (Nevada, Arizona, and California) [8]. After extensive investigation, they found that the shaft of the turbine had broken down due to a new phenomenon named SSR. This phenomenon happens in the presence of the series capacitor bank in the power transmission line and is defined as the exchange of mechanical energy with electrical energy. So, in such phenomenon (SSR) in power system, a bifurcation and chaos theory can be applied to study the dynamics of the power system [8]. After heavily working on this phenomenon, we found that the most commonly

A. Harb (✉)
German Jordanian University, Amman, Jordan
e-mail: Ahmad.harb@gju.edu.jo

© The Author(s), under exclusive license to Springer Nature Switzerland AG 2024

W. Lacarbonara (ed.), *Advances in Nonlinear Dynamics, Volume III*, NODYCON Conference Proceedings Series, https://doi.org/10.1007/978-3-031-50635-2_7

encountered bifurcation is the dynamic bifurcation called Hopf bifurcation. So, the birth of a limit cycle from an equilibrium point gives rise to oscillations, and this might undergo complicated bifurcations such as period doubling, cyclic folds, or crises. Many researchers worked on this phenomenon [6] and used the Hopf bifurcation theorem to study an SMIB power system that experienced SSR. Nayfeh et al. [7] investigated the complex dynamics of a heavily loaded SMIB power system modeling the characteristics of the BOARDMAN generator with respect to the rest of the North-Western American Power System.

Recently, huge efforts have been directed toward control of bifurcation and chaos in the dynamical system. Thus, emphasis has been placed on design techniques that result in prescribed nonlinear dynamics for controlled processes. Bifurcation control deals with control input to modify the bifurcation characteristics of a parameterized system [8].

2 Mathematical Models and Results Discussion

2.1 Voltage Collapse Phenomenon (VC)

In this section, the first crucial issue in power systems named VC will be discussed. A three-bus power system shown in Fig. 1 will be used, and the mathematical model of this figure is given in Eqs. (1) as shown below. The power system has two generators feeding one comprehensive load represented by an induction motor in parallel with a capacitor and a PQ load [1].

$$\dot{V} = -66.66V \sin(\delta - 0.2094) - 16.66V \sin(\delta - \delta_m - 0.087266) - 6.996V^2 - V - 2.0 - 1.333\left(\dot{\delta}\right)$$

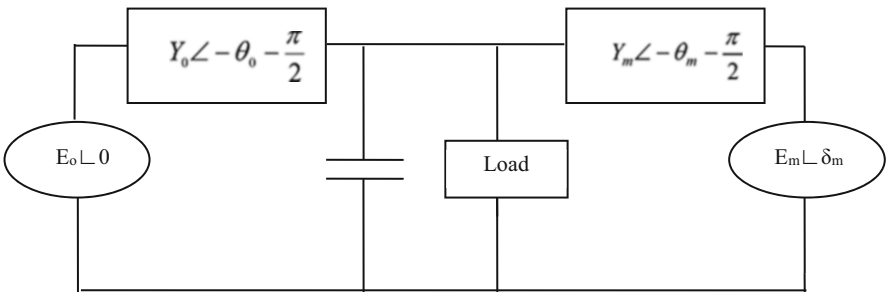

Fig. 1 Schematic diagram for three buses power system

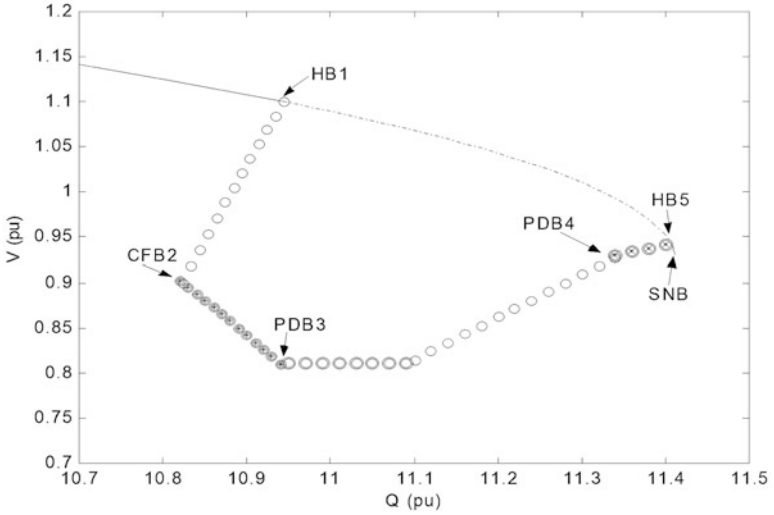

Fig. 2 Bifurcation diagram (constant and dynamic solutions)

$$\dot{\delta} = -666.66V\cos(\delta - 0.2094) - 16.66V\cos(\delta - \delta_m - 0.087266) + 496.863V^2 + 33.33\left(1 + V^2\right)Q + 136.66 \tag{1}$$

$$\dot{\delta}_m = \omega$$

$$\dot{\omega} = -0.1666\omega + 1.8777 + 16.66V\sin(\delta - \delta_m - 0.087266)$$

where the state variables of this system are given by δ_m, δ, V, ω, which are, respectively, the power angles for the generator and load buses, the load voltage, and the radian frequency of the generator. Q is the reactive power load used as a control parameter in this study of VC phenomenon.

After we found the equilibrium solutions, we chose one of these solutions and changed the control parameter Q to investigate if the system will lose stability or not. We found that the system lost its stability at a certain value of the control parameter Q as shown in Fig. 2. But, in the case of the periodic solutions, we were unable to study their stability in the same manner. So, the Floquet theory was used to study the stability of the periodic solutions [1, 7].

At this point, we used what Nayfeh et. al. [7] found in the bifurcation diagram shown in Fig. 2. There are two Hopf bifurcation points, HB1 at $Q = 10.9439$ and HB5 at $Q = 11.40675$, and a saddle-node bifurcation SN at $Q = 11.4109$. Using the method of multiple scales, we found the normal form near the two Hopf bifurcation points HB1 and HB5. The first Hopf bifurcation HB1 is found to be subcritical and the other Hopf bifurcation point HB5 is found to be supercritical. That means an

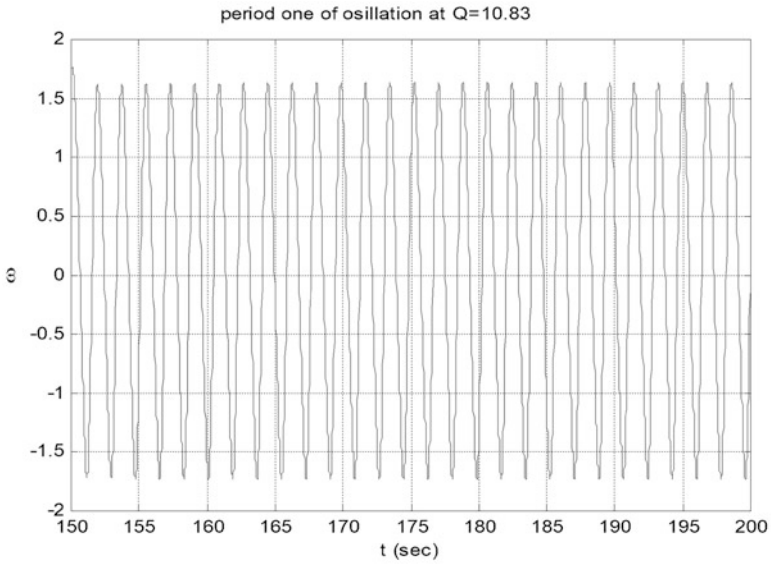

Fig. 3 A stable limit cycle (Period one) at $Q = 10.83$

unstable limit cycle will be born near HB1 and a stable limit cycle will be born near the second Hopf bifurcation HB5.

As mentioned earlier, the stability of limit cycles (periodic solutions) is studied by means of the Floquet theory. We found that the system experienced chaotic behaviors via period doubling as the control parameter changed as shown in Figs. 3 and 4. In power systems, this is considered a voltage collapse and needs to be controlled. Many control methods are used, and either linear, nonlinear, or fuzzy logic control can eliminate all chaotic oscillations. In this paper, we followed Harb et.al. [9] and used the fuzzy logic controller (FLC). As been mentioned earlier, the main concern of this study is to eliminate the chaotic oscillations to avoid voltage collapse. So, at certain value of the control parameter, say at $Q = 11$, which is considered a chaos point behavior, after the designed FLC was applied, all chaotic oscillations were controlled as shown in Fig. 5. So, such a controller shows that it possible to eliminate voltage collapse in a power system.

2.2 Subsynchronous Resonance Phenomenon (SSR)

In this section, the second crucial issue in power systems named Subsynchrous Resonance (SSR) will be discussed. So, we followed Harb & Widyan [8] and considered the first system of the IEEE second benchmark models of Subsynchronous Resonance. As shown in Fig. 6, it is an SMIB power system with two transmission

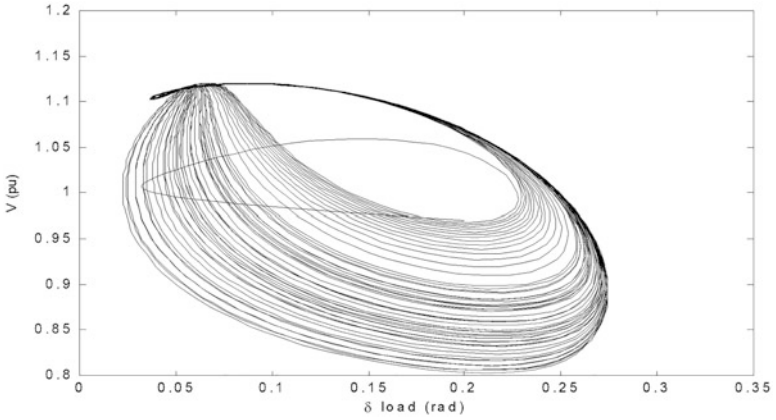

Fig. 4 Chaotic oscillations at $Q = 10.894$

lines, wherein one of them is compensated by a series capacitor. One can find the mathematical model of the whole system used in [8].

At this point, our study is carried out with a heavily loaded demand and at a variable compensation factor (μ) between 0 and 1. Again, we used the bifurcation and chaos theory to study the dynamics of the mentioned power system and followed Harb and Widyan [8]. The system consists of 15 differential nonlinear equations. Figure 7 shows the variation of real and imaginary parts of the eigenvalues with a compensation factor. As the control parameter (μ) increases, the two electrical modes start to move, one mode starts increasing and is called the super-frequency mode and the second mode starts decreasing and is called the sub-frequency mode. We ignore the first mode because it is not of our interest, rather we are interested in the second mode electrical frequency. As we increase the compensation factor, the second mode also decreases and might be self-excited and interact with the fixed torsional mechanical modes, and this may be dangerous. This interaction was strong enough to transversally move the real parts of the corresponding eigenvalues from left-to the right- half of the complex plane. Hence, a Hopf bifurcation had occurred.

The bifurcation diagram is shown in Fig. 8. It can be observed that, the power system has a stable operating point in the region, unstable operating point in the region and a Hopf bifurcation point at the compensation factor $\mu = 0.518428$. The Hopf bifurcation point is the point at which the constant solution is connected to that of the periodic solution; thus, at this point, a limit cycle is born, and this limit cycle is stable if the Hopf bifurcation is supercritical and unstable if the Hopf bifurcation is subcritical. The type of the Hopf bifurcation can be determined by either perturbation techniques based on the method of multiple scales or the numerical method based on the response of the perturbed system. Harb & Widyan [8] show that the Hopf bifurcation is supercritical. Figure 9 shows the time history of the system emanated near the Hopf bifurcation point and the two-dimensional projection at different compensation factors after the Hopf bifurcation value. It can

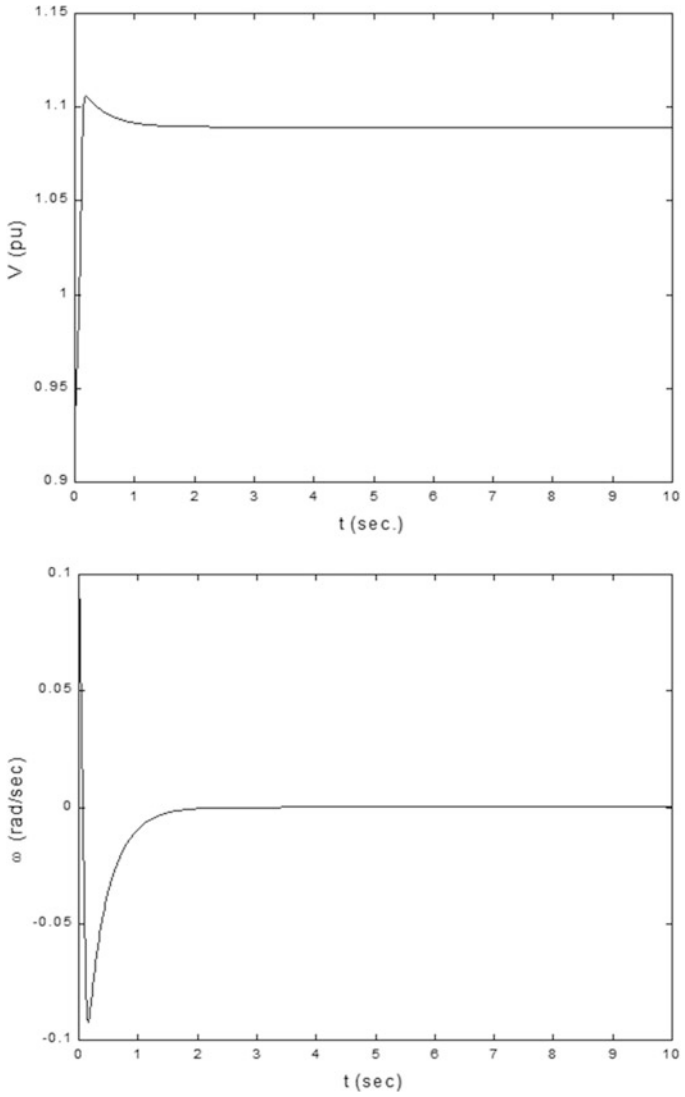

Fig. 5 Power system performance at $Q = 11$ using FLC

be observed that the system routes to chaos via torus breakdown intermittency. Also, in the case of a further increase of the compensation factor, the chaotic attractor collides with its basin boundary resulting in the destruction of both the attractor as well as the boundary in a dangerous discontinuous bifurcation called blue-sky catastrophe, so there is no bounded motion as shown in Fig. 10.

Again, such unwanted unstable oscillations need to be eliminated. So, a controller needs to be designed to eliminate such unwanted oscillations. The controller

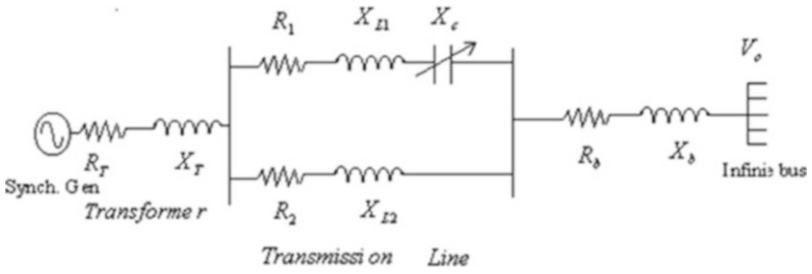

Fig. 6 IEEE second benchmark model of SSR

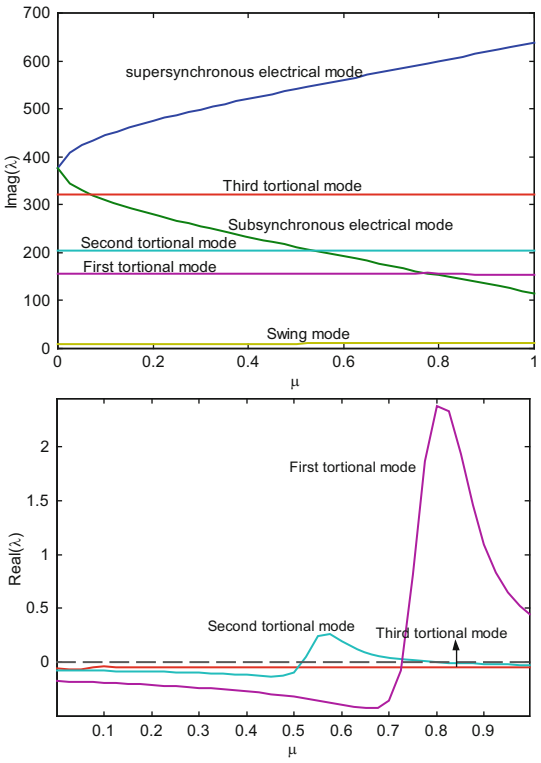

Fig. 7 Variation of real and imaginary parts of eigenvalues with the compensation factor μ

can be linear, nonlinear, or intelligent controllers. Many researchers used linear or nonlinear state-feedback controls [10, 11] and [12, 13].

The aim of this study is to use a linear controller to control bifurcation and chaos of SSR for the IEEE second benchmark model and to compare between these two types of controllers. Figure 11 shows the system with a designed linear controller and this controller was able to eliminate all unwanted unstable oscillations.

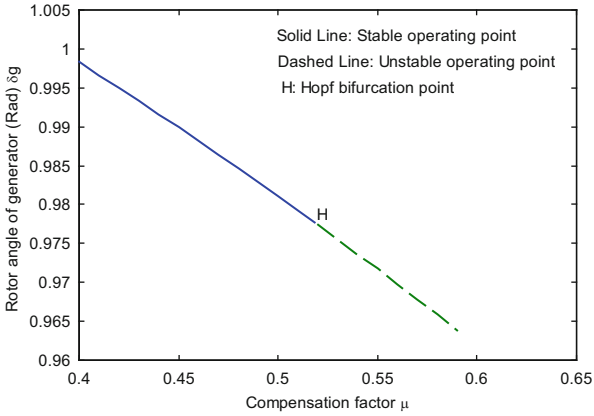

Fig. 8 Variation of rotor angle of generator (δ_g) with compensation factor μ (bifurcation diagram)

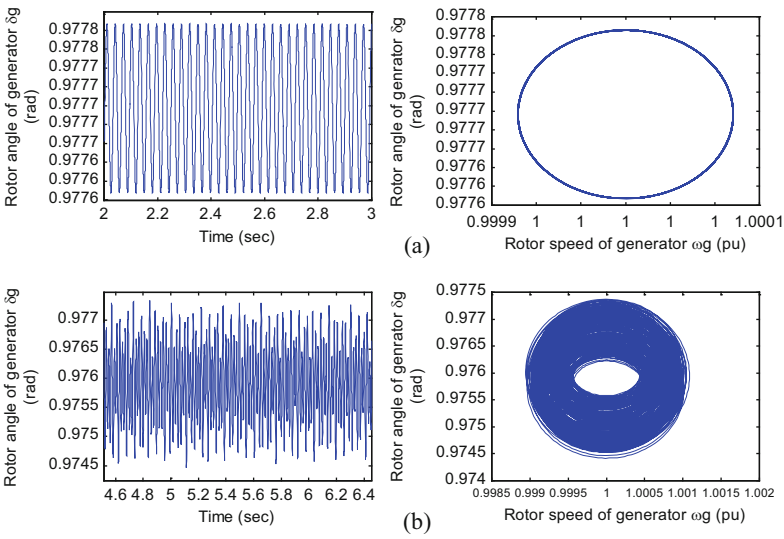

Fig. 9 (**a**) Time histories of the rotor angle of generator (left), the corresponding two-dimensional projections of the phase portrait into $\delta_g - \omega_g$plane (right) for the periodic solutions, and (**b**) the solution at chaotic attractor

3 Conclusions

In this chapter, a comprehensive study of two crucial issues in electric power systems has been conducted. The first one is the VC phenomenon, which happens frequently due to the high load demand on the power systems. The second one is the SSR phenomenon, which happened back in 1970 and 1971 at Mohave Power Station, Nevada, USA. We used the modern nonlinear theory (Bifurcation and Chaos) to analyze both phenomena. In the VC, as the control parameter (Q) increased, the system experienced unstable solutions via Hopf bifurcation all

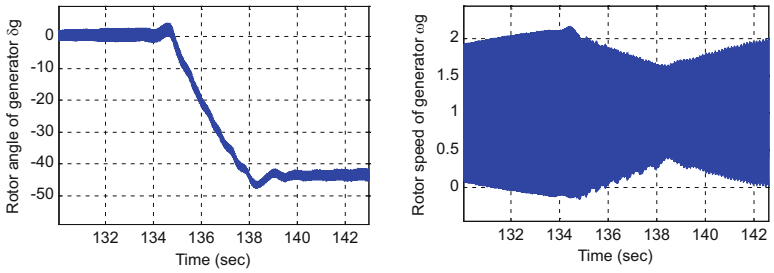

Fig. 10 Time history of (left) rotor angle of generator and (right) rotor speed of generator at $\mu = 0.528015$ (blue-sky catastrophe)

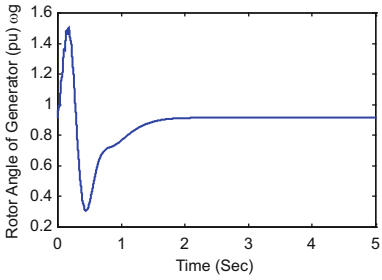

Fig. 11 Closed loop response of rotor angle with linear designed controller, at $\mu = 0.8$

the way to chaotic oscillations via the cyclic fold bifurcation. So, an intelligent control design (Fuzzy Logic Controller) has been designed to control and eliminate all unstable oscillations to avoid the voltage collapse. Similarly, in the second phenomenon, by using the Bifurcation and Chaos theory, we found the system loses stability as the control parameter (μ) increases. Therefore, a linear controller has been designed to eliminate all unstable oscillations and avoid the frequency collapse.

References

1. Nayfeh, A.H., Harb, A.M., Chin, C.-M.: Bifurcations in power system model. Int. J. Bifurcat. Chaos. **6**, 497–512 (1996)
2. Ajjarapu, V., Lee, B.: Theory and its application to nonlinear dynamical phenomena in an electrical power system. IEEE Trans. Power Syst. **7**(1), 424–431 (1992)
3. Kundur, P.: Power System Stability and Control. McGraw-Hill Inc. (1994)
4. IEEE SSR Working Group: Second benchmark model for computer simulation of subsynchronous resonance. IEEE Trans. Power Apparat. Syst. **104**(5), 1057–1064 (1985)
5. Anderson, P.M., Agrawal, B.L., Van Ness, J.E.: Subsynchronous Resonance in Power Systems. Wiley, New York (1990)
6. Zhu, W., Mohler, R.R., Spce, R., Mittelstadt, W.A., Maratukulman, D.: Hopf bifurcation in a SMIB power system with SSR. IEEE Trans. Power Syst. **11**(3), 1579–1584 (1996)

7. Nayfeh, A.H., Harb, A.M., Chin, C.-M., Hamdan, A.M., Mili, L.: Application of bifurcation theory to subsynchronous resonance in power systems. Int. J. Bifurcat. Chaos. **8**(1), 157–172 (1998)
8. Harb, A.M., Widyan, M.S.: Chaso and bifurcation as applied to subsynchronous resonance of the IEEE second benchmark model. Chaos Solitons Fractals. **21**(3), 537–552 (2004)
9. Harb, A.M., Smadi, I.A.: Tracking control of DC motors via mimo nonlinear fuzzy control. Chaos Solitons Fractals. **42**(2) (2009)
10. Chen, D., Wang, H.O., Chen, G.: Anti-Control of Hopf Bifurcations Through Washout Filters. Proc. 37th IEEE Conf. Decission and Control, Tampa, FL, Dec. 16–18, pp. 3040–3045 (1998)
11. Abed, E.H., Fu, J.H.: Local feedback stabilization and bifurcation control, I. Hopf bifurcation. Syst. Cont. Lett. **7**, 11–17 (1986)
12. Laufenberg, M.J., Pai, M.A., Padiyar, K.R.: Hopf bifurcation control in power systems with static VAR compensator. Int. J. Elect. Power Energy Syst. **19**, 339–347 (1997)
13. Abed, E.H., Wang, H.O., Chen, R.C.: Stabilization of period doubling bifurcations and implications for control of chaos. Physica. **D70**, 154–164 (1994)

Multidimensional Nonlinearity Time Series Forecasting Based on Multi-reservoir Echo State Network

Jingyu Sun, Lixiang Li, Haipeng Peng, and Shengyu Liu

1 Introduction

Echo state networks (ESNs) possess feedback connections between neurons and rich dynamic properties, allowing them to store partial information and exhibit instant memory. ESNs consist of three parts: input, hidden layer, and output [1]. The output weight is the only trainable part of the ESN and is the most important [2]. The hidden layer is composed of randomly and sparsely connected neurons, creating a high-dimensional, nonlinear representation of the input [3]. ESNs improve upon the inherent shortcomings of recurrent neural networks and find wide applications in time series prediction, pattern recognition, image processing, signal processing, and so on.

In recent years, ESNs have been widely applied in various fields, particularly in time series prediction. For example, Zhou et al. proposed an adaptive flow prediction method based on ESNs [4], while Sun et al. utilized an ESN model to predict stock prices [5]. Hu et al. developed a modified optimization model of bagged ESNs based on differential evolution algorithms to estimate energy consumption [6]. Additionally, there are many studies focused on improving the ESN model itself, such as Tian et al.'s improved fruit fly optimization algorithm [7] and Chen et al.'s optimization based on selective opposition gray wolf optimizer [8].

From above descriptions, it can be seen that the echo state network is used in sequence prediction in various fields. But researchers mostly focus on optimizing the single-layer echo state network and use different optimization algorithms to

J. Sun · L. Li (✉) · H. Peng
Information Security Center, State Key Laboratory of Networking and Switching Technology, Beijing University of Posts and Telecommunications, Beijing, China

S. Liu
National Engineering Laboratory for Disaster Backup and Recovery, Beijing University of Posts and Telecommunications, Beijing University of Posts and Telecommunications, Beijing, China

© The Author(s), under exclusive license to Springer Nature Switzerland AG 2024

W. Lacarbonara (ed.), *Advances in Nonlinear Dynamics, Volume III*, NODYCON Conference Proceedings Series, https://doi.org/10.1007/978-3-031-50635-2_8

achieve better prediction results. Generally speaking, the larger the number of nodes in the neural network, the more complex the system can be expressed. However, increasing the number of neurons in the reservoir of an ESN can lead to overfitting. Therefore, the addition of multiple reservoirs to an ESN can increase network complexity while preventing overfitting. Motivated by this, we propose a multi-reservoir echo state network (MESN) based on the fully connected output mode. We then apply the model to nonlinear prediction of chaotic systems with different dimensions and conduct simulation and comparative experiments to explore the significance of MESN.

2 Echo State Network

Echo state networks (ESNs) are a type of recurrent neural network that features feedback connections between neurons and rich dynamic characteristics [9]. They can simulate the function of the human brain, store information, and exhibit instant memory, making them similar to the information transmission of synapses in the human nervous system. ESNs are also a type of reservoir computing model, and unlike traditional neural networks, their training process is less complex and does not suffer from the issues of gradient disappearance or gradient explosion. ESNs improve upon the inherent shortcomings of cyclic neural network models, exhibiting faster learning speeds and better generalization abilities.

As a simple and efficient intelligent information processing model, echo state network has been widely used in various fields such as physics, chemistry, finance, and security. The traditional echo state network model is shown in Fig. 1. In a traditional echo state network, the state update process of the reservoir and the output weights are given as Eqs. (1)–(2).

$$x(t+1) = (1-\varrho)x(t) + \varrho \tan h(W_I\ i(t) + Wx(t) + \theta) \tag{1}$$

$$W_q' = AB^T \left(BB^T + \kappa C\right)^{-1} \tag{2}$$

where $x(t)$ is the state of the neurons at time t and $i(t)$ is the input at time t. W_I is the weight matrix between the input layer and the reservoir layer, and W is the weight matrix between the neurons in the reservoir layer. θ is the bias term, $\tan h$ is the activation function, and ϱ is the leaking rate or forgetting factor, which is a parameter that controls the influence of the previous state on the current state. Equation (2) is the calculation method of W_q, where A is the label sequence, B represents the state matrix of reservoir, C is set as the unit matrix and the size if it is same size as B, B^T is the inverse matrix of the B matrix, and κ is the ridge regression parameter.

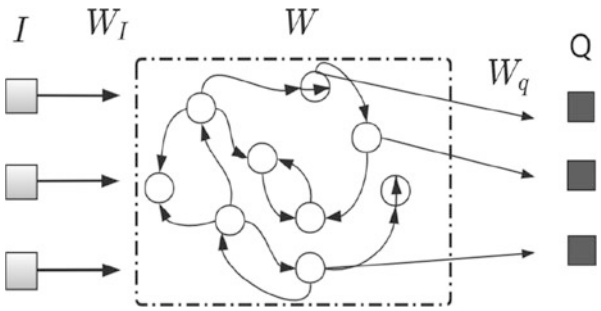

Fig. 1 Traditional model of echo state network consists of three parts: input layer, middle reservoir, and the output layer. W_I, W, W_q are the weight matrices of input, intermediate reservoir, and output separately. Its output weight W_q is the only thing needs to be trained

The reservoir is a crucial component of an echo state network (ESN), and its parameters play a critical role in the performance of network [10]. Parameters such as the connection weight spectral radius, sparsity, and leakage rate are all essential for effective network operation. The spectral radius is an important parameter for ensuring that the network exhibits echo state characteristics [11] and is also a necessary condition for ensuring the stability of the network cluster. The sparsity of the reservoir represents the connection density between neurons in the reservoir [12]. The greater the sparsity, the stronger the nonlinear approximation ability of the network. The leakage rate refers to the rate at which the reservoir state is updated [13] and is a parameter that needs to be adjusted through repeated testing [14].

3 Methods

Traditional echo state networks (ESNs) have a simple structure and achieve excellent results in many fields. However, increasing the number of neurons in the network can improve its processing power, but it can also lead to overfitting and increased computational burden. To address this issue, we propose increasing the number of reservoirs in the ESN, which effectively increases the number of neurons and enhances the model's performance. We construct a multi-reservoir echo state network based on the connection of input and output and use chaotic systems of different dimensions to explore the characteristics of our proposed model. The architecture of our model is depicted in Fig. 2.

The traditional multi-reservoir echo state network ignores the phenomenon that the input will disappear with the increase of the number of layers, so our multi-reservoir echo state network adds the input, and its update matrix equation is as Eq. (3)

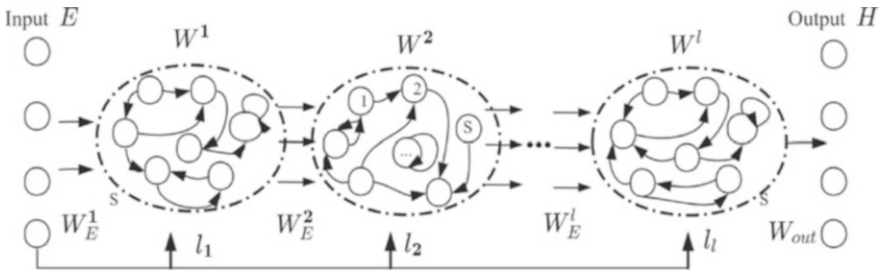

Fig. 2 The multi-reservoir echo state network model including input layer, reservoir, and output layer. There are l reservoir in total, and each reservoir is composed of S nodes. When $l \geq 2$, the composition of reservoir is the output of the previous reservoir and the initial input

$$\begin{Bmatrix} s_1^{(l)} \\ s_2^{(l)} \\ s_3^{(l)} \\ \vdots \\ s_S^{(l)} \end{Bmatrix} = (1-\alpha^l) \begin{Bmatrix} s*_1^{(l)} \\ s*_2^{(l)} \\ s*_3^{(l)} \\ \vdots \\ s*_S^{(l)} \end{Bmatrix} + \alpha^l \tan h$$

$$\left(\begin{Bmatrix} a_{1,1}^{(l)}, a_{1,2}^{(l)}, \ldots, a_{1,S}^{(l)} \\ a_{2,1}^{(l)}, a_{2,2}^{(l)}, \ldots, a_{2,S}^{(l)} \\ \ddots \\ a_{S,1}^{(l)}, a_{S,2}^{(l)}, \ldots, a_{S,S}^{(l)}, \end{Bmatrix} \begin{Bmatrix} s_1^{(l-1)} \\ s_2^{(l-1)} \\ s_3^{(l-1)} \\ \vdots \\ s_S^{(l-1)} \end{Bmatrix} + \right. \tag{3}$$

$$\left. \begin{Bmatrix} b_{1,1}^{(l)}, b_{1,2}^{(l)}, \ldots, b_{1,S}^{(l)} \\ b_{2,1}^{(l)}, b_{2,2}^{(l)}, \ldots, b_{2,S}^{(l)} \\ \ddots \\ b_{S,1}^{(l)}, b_{S,2}^{(l)}, \ldots, b_{S,S}^{(l)}, \end{Bmatrix} \begin{Bmatrix} s*_1^{(l)} \\ s*_2^{(l)} \\ s*_3^{(l)} \\ \vdots \\ s*_S^{(l)} \end{Bmatrix} + 1 \right)$$

where s is the state of the reservoir and $s*$ represents the state at last moment. $s^{(l-1)}$ is the previous layer state. Besides, a and b are the weights corresponding to the input and the reservoir matrix, respectively. ϱ and 1 still represent the leak rate and bias. When the layer $l = 1$ or $l > 1$, the input data e is represented as Eq. (4):

$$\begin{Bmatrix} e_1^{(l)} \\ e_2^{(l)} \\ e_3^{(l)} \\ \vdots \\ e_E^{(l)} \end{Bmatrix} = \begin{Bmatrix} E_1^{(1)} \\ E_2^{(1)} \\ E_3^{(1)} \\ \vdots \\ E_E^{(1)} \end{Bmatrix} or \begin{Bmatrix} s_1^{(l-1)} \\ s_2^{(l-1)} \\ s_3^{(l-1)} \\ \vdots \\ s_I^{(l-1)} \end{Bmatrix} \tag{4}$$

we find that the dimension of W_E is $S \times S$ rather than $S \times I$, and the input is the previous reservoir state $S^{(l-1)}$ in Eq. (3). Because we add input data, the size of the pool and the input weight will also change. We add the input method by merging the input matrix with the current reservoir matrix, at this time:

$$a_{size}^{(l)} = [S + I(l-1)] \times [1 + S + I(l-1)] \tag{5}$$

$$b_{size}^{(l)} = [S + I(l-1)] \times [S + I(l-1)] \tag{6}$$

where $a_{size}^{(l)}$ and $b_{size}^{(l)}$ are the size of input and reservoir matrix and I and S stand the dimension of initial data and the number of neurons of reservoir separately. Besides, 1 in Eq. (5) is the bias. Then the output of our MDESN model is calculated as follows:

$$\begin{aligned} Y(t) &= W'_{out} \times S + \theta \\ S &= [s_1, s_2, , s_l] \end{aligned} \tag{7}$$

where Y is the predicted value with the trained output weights W'_{out} and S is a matrix stacked by l reservoirs.

4 Experiment and Analysis

In the test part, we use one-dimensional Mackey-Glass and three-dimensional Lorenz chaotic systems to test the models respectively. Chaotic systems are sensitive to initial values and are considered to be systems that cannot be predicted in the long term but can be predicted in the short term [15]. These two models are as follows:

$$\dot{x}(t) = -px(t) + \frac{qx(t-\tau)}{1 + x^r(t-\tau)} \tag{8}$$

Equation (8) represents the Mackey-Glass system, where $x(t)$ is the state variable at time t; τ is the time delay; and q, r, and p are parameters that control the behavior of the system. When $q = 0.1$, $r = 10$, $p = 0.2$, $x(0) = 10$, and the time delay $\tau = 17$, the system generates chaotic behavior [16].

$$\begin{cases} \frac{dp}{dt} = \delta(q - p) \\ \frac{dq}{dt} = \eta p - q - pr \\ \frac{dr}{dt} = pq - \theta r \end{cases} \tag{9}$$

Equation (9) represents the Lorenz system, where p, q, and r are the state variables of the system and δ, η, and θ are parameters that determine the behavior of the system. When the value of η increases and greater 24.74, the system enters into the chaotic state [17].

To evaluate the performance of our model, we first measured the maximum prediction horizon that the model could accurately predict under different conditions. We then used the mean squared error (MSE) to assess the accuracy of the models. The equation for calculating the MSE is as follows:

$$MSE = \frac{1}{n}\sum_{i=1}^{n}(y_i - \hat{y}_i)^2 \tag{10}$$

where n is the number of samples, y_i is the true value of the i-th sample, and $\hat{y}_i$ is the predicted value of the i-th sample. In general, a smaller mean squared error (MSE) value indicates better performance of the model.

4.1 One-Dimensional Nonlinear System Prediction

First of all, we test it with a one-dimensional Mackey-Glass chaotic sequence. At the beginning of the training, the model needs to be initialized with a length of 100, the training length is 1000, and test length is 1500. We set the leak rate to be 0.2 and the sparsity to be 1, the layer of the reservoir is 1–5, and the size is 100–600.

Table 1 shows the relationship between the layers, reservoir size, and the prediction step in Mackey-Glass system. It can be seen from it that the best effect is achieved when the number of layers is 4 and the size of the reservoir is 400. And the minimum MSE value within the first 1000 prediction steps is obtained when the number of layers is 4. Figure 3 shows the relationship between the prediction step, number of layers, and size of the reservoir in the model (Fig. 4).

Table 1 Multi-reservoir echo state network in Mackey-Glass sequence

Layer/Size	100	200	300	400	500	600	MSE
Layer = 1	399	732	918	894	223	805	0.020
Layer = 2	202	306	402	576	511	400	0.019
Layer = 3	717	399	600	513	899	194	0.026
Layer = 4	560	518	399	**1307**	394	595	**0.011**
Layer = 5	396	401	305	264	35	6	0.070

The bold values represent situations where the prediction step size and the MSE value is the best

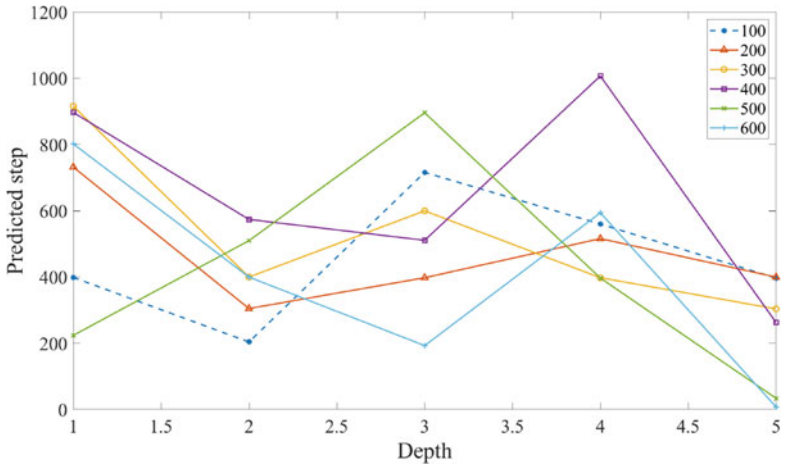

Fig. 3 The relationship between the depth of the model and the prediction horizon for different reservoir sizes using the Mackey-Glass sequence. We can observe that the model's performance is improved when the reservoir size is increased to 400. Furthermore, when the model is deepened to three layers, the overall prediction accuracy is further enhanced

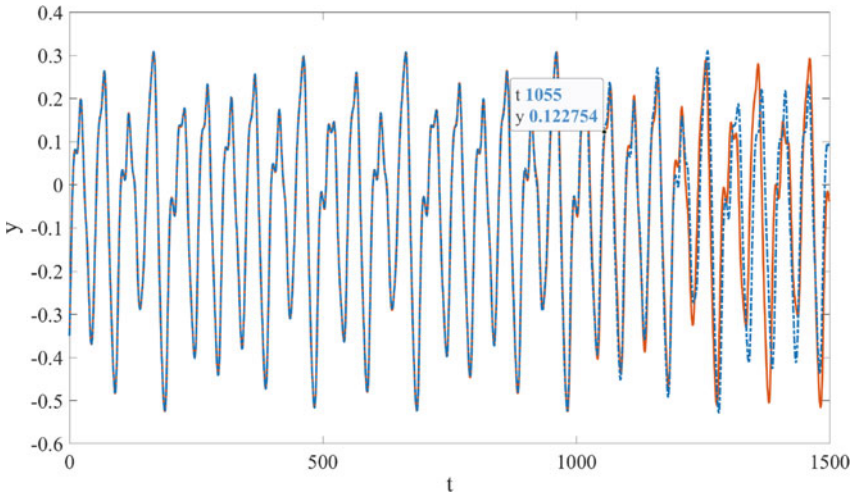

Fig. 4 MDESN model predicts the Mackey-Glass sequence: The solid line represents the original sequence, while the dashed line shows the sequence predicted by our model. We can observe that the model accurately predicts the first 1055 steps of the sequence, as indicated by the close alignment of the solid and dashed lines. However, some deviation between the predicted and actual values begins after the 1055th step

4.2 Multidimensional Nonlinear System Prediction

Then we used a three-dimensional Lorenz chaotic system to test the model. We set the initialization length to 100, the training length to 2000, and the test length to 1000. Besides, set the leakage rate to 0.01 and the sparsity to 0.682, the reservoir size increases from 100 to 600, and the layers is from 1 to 5.

Table 2 shows the relationship between the layers, reservoir size, and the prediction step in Lorenz system. It can be seen that the best effect is achieved when the number of layers is 4 and the size of the reservoir size is 500. And the minimum MSE value within the first 1000 prediction steps is obtained when the number of layers is 4. The following Fig. 5 shows the curve of the model's prediction of Lorenz system (Fig. 6).

Through experiments, we found that our multi-reservoir echo state network is better than the traditional one-reservoir echo state network. The optimal conditions for achieving both the highest average prediction accuracy and overall best per-

Table 2 Multi-reservoir echo state network in Lorenz system

Layer/Size	100	200	300	400	500	600	MSE
Layer = 1	668	798	810	919	958	888	0.218
Layer = 2	732	795	941	949	902	851	0.200
Layer = 3	744	**1011**	908	499	651	752	**0.001**
Layer = 4	441	671	759	621	**1029**	701	0.080
Layer = 5	538	751	602	571	648	522	0.124

The bold values represent situations where the prediction step size exceeds 1000, and the MSE value is the smallest

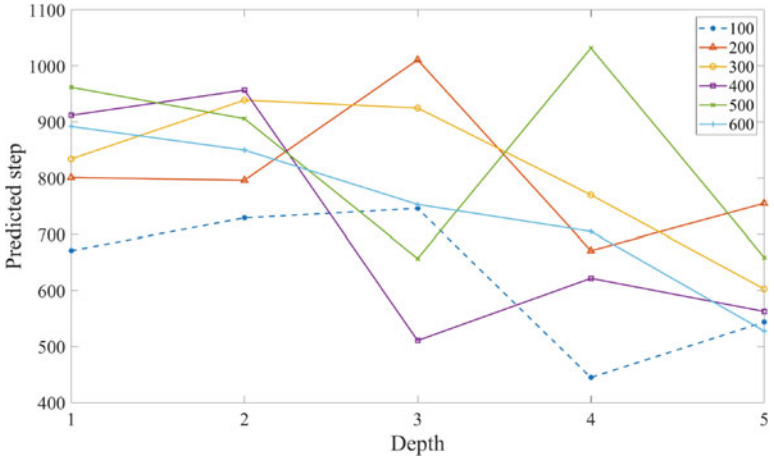

Fig. 5 The relationship between the depth of the model and the prediction horizon for different reservoir sizes using the Lorenz sequence. We can observe that the model's performance is improved when the reservoir size is increased to 300. Furthermore, when the model is deepened also to three layers, the overall prediction accuracy is further enhanced

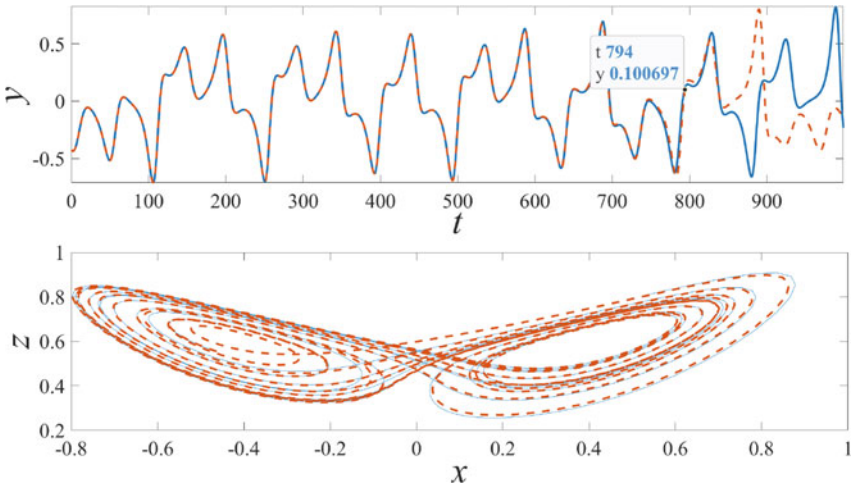

Fig. 6 MDESN model predicts the Lorenz system: This shows the prediction of y values over time, as well as the prediction on the x-z plane. We can observe that the model accurately predicts the first 794 steps of the sequence, as indicated by the close alignment of the solid and dashed lines. However, some deviation between the predicted and actual values begins after the 794th step

formance are observed when the number of layers is between three and four. And the increase of layer and the reservoir will have a positive impact on the model. However, neither the increase in the number of layers nor the size of the reservoir can promote the growth of the model endlessly. The results are not entirely stable, as we used uniform parameter settings for all configurations. However, different numbers of layers and reservoir sizes may require different parameter settings for optimal performance.

5 Conclusion

In this chapter, we constructed a new multi-reservoir echo state network to forecast multidimensional nonlinear time series. Besides, in order to avoid the disappearance of input, we add input to each reservoir by merging matrices. Then we use the complicated one-dimensional Mackey-Glass and three-dimensional Lorenz chaotic system to conduct experiments respectively. The comprehensive results show that increasing the reservoir size or depth can increase the prediction effect to a certain extent.

Besides, no matter how much the number of layers and the reservoir are increased, the network runs very fast. Therefore, the echo state network with multiple reservoir still has great advantages in structure and time. In addition to nonlinear time series prediction, echo state network is also used in artificial intelligence, brain-like computing, and so on. It needs more and further research.

Acknowledgments The National Key Research and Development Program of China (Grant No. 2020YFB1805403), the National Natural Science Foundation of China (Grant No. 62032002) and the 111 Project (Grant No. B21049).

References

1. Stefenon, S.F., Seman, L.O., Neto, N.F.S., Meyer, L.H., Nied, A., Yow, K.-C.: Echo state network applied for classification of medium voltage insulators. Int. J. Electr. Power Energy Syst. **134**, 107336 (2022)
2. Duggento, A., Guerrisi, M., Toschi, N.: Echo state network models for nonlinear granger causality. Phil. Trans. R. Soc. A **379**(2212), 20200256 (2021)
3. Silva, N.A., Ferreira, T.D., Guerreiro, A.: Reservoir computing with solitons. New J. Phys. **23**(2), 023013 (2021)
4. Zhou, J., Wang, H., Xiao, F., Yan, X., Sun, L.: Network traffic prediction method based on echo state network with adaptive reservoir. Softw.: Pract. Exper. **51**(11), 2238–2251 (2021)
5. Sun, G., Lin, J. Yang, C., Yin, X., Li, Z., Guo, P., Sun, J., Fan, X., Pan, B.: Stock price forecasting: an echo state network approach. Comput. Syst. Sci. Eng. **36**(3), 509–520 (2021)
6. Hu, H., Wang, L., Peng, L., Zeng, Y.-R.: Effective energy consumption forecasting using enhanced bagged echo state network. Energy **193**, 116778 (2020)
7. Tian, Z.: Echo state network based on improved fruit fly optimization algorithm for chaotic time series prediction. J. Ambient. Intell. Humaniz. Comput. **13**, 1–20 (2020)
8. Chen, H.-C., Wei, D.-Q.: Chaotic time series prediction using echo state network based on selective opposition grey wolf optimizer. Nonlinear Dyn. **104**(4), 3925–3935 (2021)
9. Nakajima, K., Fischer, I.: Reservoir Computing (2021)
10. Mansoor, M., Grimaccia, F., Leva, S., Mussetta, M.: Comparison of echo state network and feed-forward neural networks in electrical load forecasting for demand response programs. Math. Comput. Simul. **184**, 282–293 (2021)
11. Lu, Y., Liao, Y., Xu, L., Liu, Y., Liu, Y.: Laplacian deep echo state network optimized by genetic algorithm. In: 2021 IEEE International Conference on Information Communication and Software Engineering (ICICSE), pp. 107–111. IEEE, New York (2021)
12. He, Y., Zhang, L., Chen, Z., Li, C.Y.: A framework of structural damage detection for civil structures using a combined multi-scale convolutional neural network and echo state network. Eng. Comput. **39**(3), 1771–1789 (2022)
13. Steiner, P., Jalalvand, A., Birkholz, P.: Cluster-based input weight initialization for echo state networks. In: IEEE Transactions on Neural Networks and Learning Systems (2022)
14. Mahmoud, T.A., Elshenawy, L.M.: TSK fuzzy echo state neural network: a hybrid structure for black-box nonlinear systems identification. Neural Comput. Appl. **34**(9), 7033–7051 (2022)
15. Jafari, S., Kapitaniak, T.: Special Chaotic Systems (2020)
16. Pecora, L.M., Carroll, T.L.: Synchronization in chaotic systems. Phys. Rev. Lett. **64**(8), 821 (1990)
17. Lorenz, E.N.: The Essence of Chaos. University of Washington, Washington (1995)

Time-Periodic Perturbation Leading to Chaos in a Planar Memristor Oscillator Having a Bogdanov-Takens Bifurcation

Marcelo Messias and Paulo C. Rech

1 Introduction

The *memristor*, a nonlinear resistor with memory, is considered the fourth fundamental circuit element, besides the resistor, capacitor, and inductor. It was theoretically proposed in 1971 by Leon Chua [1], and its physical realization was possible only in 2007 [2]. Since then, the memristor attracts much interest from the academia and industry, due to its potential applications in several technological areas, like the construction of nonvolatile memories, logic operation circuits, artificial neural networks, and chaotic oscillations [3]. In 2008, Chua proposed the concept of active memristor [4], and nowadays, it is supposed that the complex behavior arising in memristive systems may be the result of its locally active characteristic [5–7], based on which, the memristor has the capability to amplify infinitesimally small signals and generate periodic and chaotic oscillations [8]. In [9] and [10], mathematical models of two kinds of active memristors were proposed, based on which, the simplest series and parallel memristor-inductor-capacitor circuits, respectively, were constructed to realize periodic and chaotic oscillations. However, no detailed analysis on the active characteristics of the memristors were given. At present, there are some researches on locally active memristors and its interaction with other fundamental circuit elements [5, 11, 12], but there is a lack of research on the mechanism creation of complex dynamics caused by them.

M. Messias (✉)
Faculdade de Ciências e Tecnologia, Departamento de Matemática e Computação, Universidade Estadual Paulista (UNESP), Presidente Prudente, Brasil
e-mail: marcelo.messias1@unesp.br

P. C. Rech
Departamento de Física, Universidade do Estado de Santa Catarina (UDESC), Joinville, Brasil
e-mail: paulo.rech@udesc.br

© The Author(s), under exclusive license to Springer Nature Switzerland AG 2024

W. Lacarbonara (ed.), *Advances in Nonlinear Dynamics, Volume III*, NODYCON Conference Proceedings Series, https://doi.org/10.1007/978-3-031-50635-2_9

In this chapter, we consider the periodic oscillator memristive circuit proposed by Gu et al. in [12], consisting of three elements: a locally active current-controlled memristor, a compensation inductor, and a bias resistor. The circuit is modeled by the following system of ordinary differential equations (for details, see [12])

$$\begin{aligned} \dot{x} &= 250\,[2x - x^2 - 2x^3 + x^4 + (5.4 - 2.8x)y], \\ \dot{y} &= \frac{1}{L}\,[(S - y)R + 1.5(x - 0.5)y]\,, \end{aligned} \tag{1}$$

where L, S and R are control parameters and x and y are state variables, which are proportional to the internal state of memristor and to the current in the circuit, respectively. The dynamics of system (1) was studied in [12], where the authors show the occurrence of periodic oscillations, arising at a Hopf bifurcation, when the parameter L is varied. Then, they added a capacitor to the circuit, generating another state equation in system (1), in order to obtain a chaotic three-dimensional autonomous differential system [12].

In this work, we show that the periodic oscillations of system (1) tend to a homoclinic orbit, showing a Bogdanov-Takens bifurcation-type scenario (see Sect. 2). Then, instead of adding a new element to the circuit as made in [12], in order to obtain complex behavior, we add into the system (1) a small external time-periodic excitation of the form $F(A, \omega, t) = A\cos(\omega t)$, obtaining a non-autonomous system. With this procedure, we show that chaotic dynamics and multistability can be obtained. To the best of our knowledge, it is the first time that time-periodic perturbation are considered in the study of memristive circuits and systems as a mechanism to generate complex dynamical behavior.

This chapter is organized as follows: in Sect. 2, we present the linear analysis and bifurcations of the system (1). In Sects. 3 and 4, we introduce a time-periodic perturbation into the system (1), showing numerically that the resulting nonautonomous system may present complex dynamical behavior, as quasiperiodic and chaotic oscillations and also multistability due to the coexistence of periodic and chaotic attractors.

2 Linear Analysis and Bifurcations of System (1)

Following what was made in [12], we consider system (1) with the fixed parameter values $S = -0.055$ and $R = 0.088$ and take the parameter $L > 0$ as the bifurcation parameter. In this case, system (1) has five equilibria, given by $S_1 = (-1.0028, -0.00021)$, $S_2 = (0.0161, -0.0059)$, $S_3 = (0.5362, -0.1434)$, $S_4 = (1.0092, 0.0072)$, and $S_5 = (2.0001, 0.0022)$. While the existence of these equilibria does not depend on the parameter L, their stability does. In fact, the Jacobian matrix of system (1) at a generic point (x, y) is given by

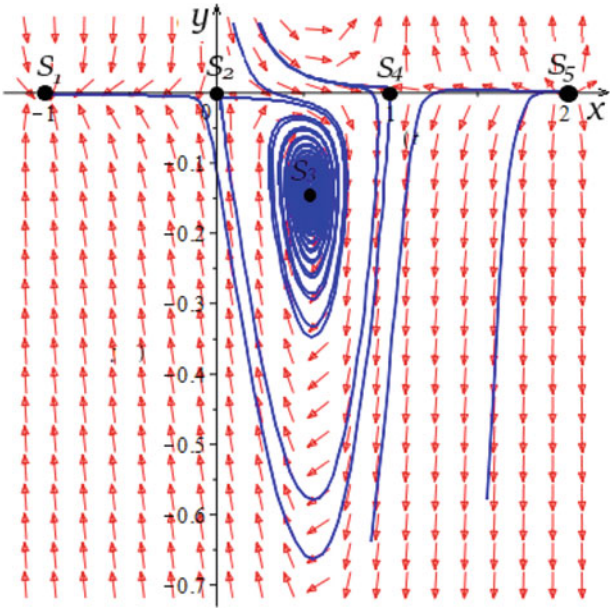

Fig. 1 Phase plane of system (1) with parameter values $S = -0.055$, $R = 0.088$ and $L = 0.0004$: there exist five equilibria, S_1 is a stable node, S_2 and S_4 are saddles, S_5 is an unstable node, and S_3 is a stable focus

$$J(x, y) = \begin{pmatrix} 250\,(2 - 2x - 6x^2 + 4x^3 - 2.8y) & 250\,(5.4 - 2.8x) \\ \dfrac{1.5\,y}{L} & \dfrac{-R + 1.5(x - 0.5)}{L} \end{pmatrix}. \tag{2}$$

Straightforward calculations of the eigenvalues of matrix (2) at the equilibria S_1 to S_5 show that for $R = 0.088$ and $L > 0$, the equilibrium point S_1 is an unstable node, S_2 and S_4 are saddles, and S_5 is an unstable node, while the equilibrium S_3 is a stable focus; as for $0 < L < 0.00061$, the eigenvalues of (2) at S_3 are complex conjugate with negative real part. In Fig. 1 is shown the phase plane of system (1) with parameter values $S = -0.055$, $R = 0.088$ and $L = 0.0004$.

Let us further analyze the local behavior of the equilibrium point S_3. The eigenvalues of matrix (2) at this equilibrium point are given by

$$\lambda_{1,2} = \frac{5 \times 10^{-5}}{L} \left(551770L - 337. \pm \sqrt{3.0445 \times 10^{11} L^2 - 8.3488 \times 10^{10} L + 113570}\right).$$

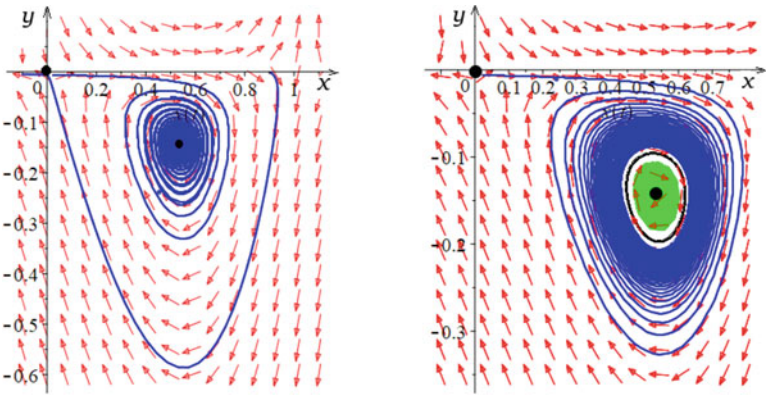

(a) $L = 0.0004 < 0.00061$. (b) $L = 0.00063 > 0.00061$.

Fig. 2 Hopf bifurcation in system (1) at the equilibrium point S_3, when the parameter L crosses the critical value $L_0 = 0.00061$: (**a**) for $L = 0.0004 < L_0$, the equilibrium S_3 is a stable focus; (**b**) for $L = 0.00063 > L_0$, S_3 is an unstable focus, and there exists a stable limit cycle (in black) around it

Hence, if $1.4 \times 10^{-6} < L < 0.2742$, then the eigenvalues of (2) at S_3 are complex conjugate, which implies that this equilibrium is a focus. Moreover, the real part of the eigenvalues is negative for $0 < L < 0.00061$ and positive for $L > 0.00061$. Hence, there is a change in the local stability of the focus, from stable to unstable, when the parameter L crosses the critical value $L_0 \approx 0.00061$, which suggests the occurrence of a Hopf bifurcation. We numerically verified that it does occur, leading to the creation of a stable limit cycle around S_3, as shown in Fig. 2.

By studying the continuation of the stable limit cycle for L growing from the critical value $L_0 = 0.00061$, we observe that the limit cycle tends to a homoclinic orbit, which tends to the saddle S_2 as $t \to \pm\infty$, when L approaches the critical value $L_1 \approx 0.00104$, as shown in Fig. 3a–c. This kind of dynamics resembles a slice of Bogdanov-Takens-type bifurcation scenario [13]. It is worth observing that the homoclinic orbit determines a region in the phase plane where the dynamic is bounded. For parameter values L bigger than the critical value $L_1 = 0.00104$, the homoclinic orbit is broken, and the solutions with initial condition near the unstable focus S_3 tend to the stable node S_1 (see Fig. 3d). Hence, for $0.00104 < L < 0.2742$, system (1) does not present periodic oscillations anymore, and the bounded solutions tend to the stable node S_1.

3 Time-Periodic Perturbation of System (1)

It is well-known from Melnikov theory [13] that periodic perturbations of homoclinic orbits on the plane can lead to complex dynamics. Based on this, we consider the following time-periodic perturbation of system (1):

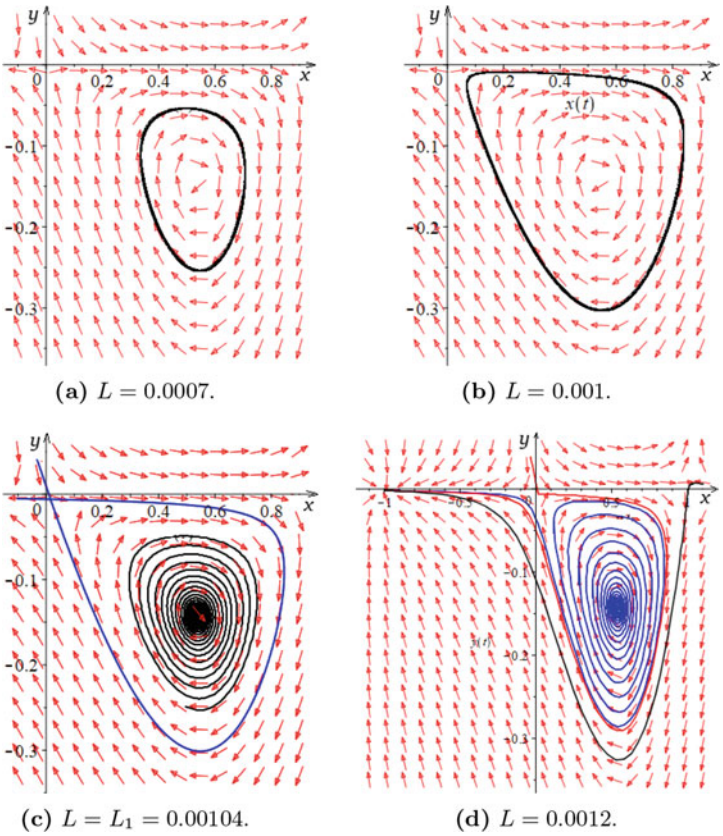

Fig. 3 Bogdanov-Takens-type bifurcation described by the solutions of system (1), when varying the parameter L: the limit cycle created in the Hopf bifurcation for $L_0 = 0.00061$, shown in (**a**) and (**b**), evolves into a homoclinic orbit, when L tends to the critical value $L_1 = 0.00104$ (see (**c**)) and disappears for $L > L_1$ (see (**d**))

$$\begin{aligned} \dot{x} &= 250\,[2x - x^2 - 2x^3 + x^4 + (5.4 - 2.8x)\,y] + A\cos(\omega t), \\ \dot{y} &= \frac{1}{L}\,[(S - y)R + 1.5(x - 0.5)\,y]\,, \end{aligned} \tag{3}$$

where the new parameters A and ω represent the amplitude and frequency of the periodic excitation, respectively. The aim in considering this perturbation is to obtain complex dynamics from the memristive circuit modeled by system (1) without add any new passive element to this circuit as made in Gu et al. [12]. Our main goal in this section is to investigate numerically the (A, ω) parameter plane related to system (3), seeking to delimit regions for which the solutions present

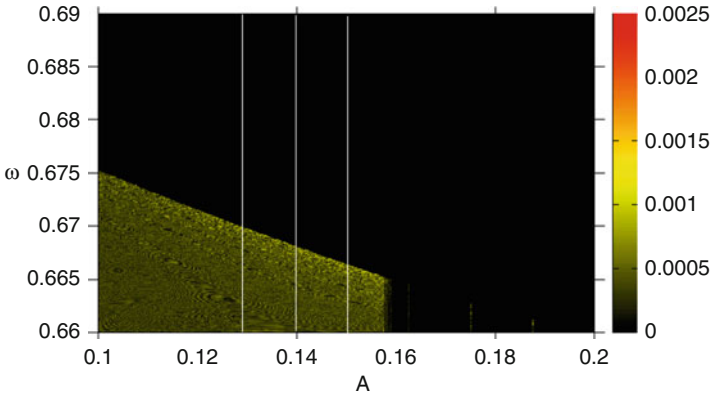

Fig. 4 Stability domains in (A, ω) parameter plane of the forced memristive system (3), for $S = -0.055$, $R = 0.088$, and $L = 0.0007$. Color is related with the magnitude of the largest Lyapunov exponent, according to the color bar at right side

regular behavior, that is, tend to periodic and quasiperiodic orbits, regions for which they have chaotic behavior, and also multistability regions. In order to do it, we started by generating a (A, ω) parameter plane in a diagram that considers 640×10^3 points, i.e., a mesh of 800×800 points.

The characterization of dynamical behavior for each region in the (A, ω) parameter plane, namely, chaos or regularity, will be done by the calculation of the respective Lyapunov exponents spectrum, computed by a FORTRAN code based on the one described by Wolf et al. in [14]. In Fig. 4 is presented a version of the (A, ω) parameter plane for system (3), obtained taking $S = -0.055$, $R = 0.088$, $L = 0.0007$, $0.1 \leq A \leq 0.2$, and $0.66 \leq \omega \leq 0.69$. The dynamical behavior of each of the 640×10^3 points considered in Fig. 4 was characterized by the magnitude of the largest Lyapunov exponent (LLE). The parameter plane diagram was obtained by following the attractor along lines of A kept fixed. More specifically, obtaining the diagram starts at $(A, \omega) = (0.1, 0.66)$, with a given arbitrary initial condition $(x_0, y_0) = (0.5, -0.2)$. Then system (3) was numerically integrated using the fourth-order Runge-Kutta algorithm, and the Lyapunov exponents spectrum associated to the obtained solution is calculated. Following, ω was incremented, and system (3) was initialized with the final point (x, y) in the time series for the anterior ω value. Then system (3) was numerically integrated for the new point (A, ω), and the respective Lyapunov exponents spectrum was calculated. The procedure of increasing ω was repeated until its highest value $\omega = 0.69$ is reached. Then A was incremented, with the procedure being repeated until the pair $(A, \omega) = (0.2, 0.69)$ was reached.

The diagram in Fig. 4 was discretized in a grid of 640×10^3 points equally spaced, i.e., the Lyapunov exponents spectrum was computed for 640×10^3 (A, ω) pairs of parameters. Color in diagram of Fig. 4 is related to the magnitude of the LLE, according to the scale shown in the color bar at right side. Therefore, yellow/red

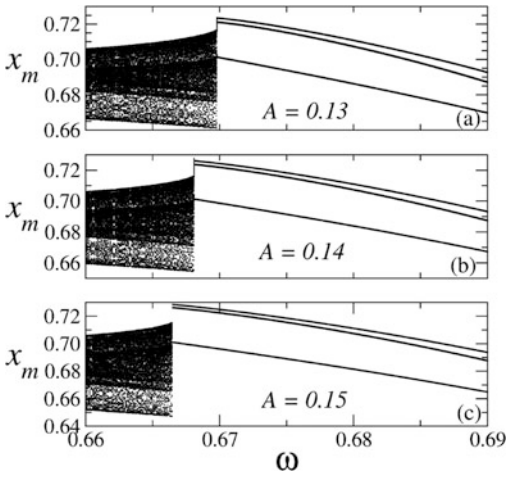

Fig. 5 Bifurcation diagrams related to the parameter plane in Fig. 4. The local maxima of x, as a function of the parameter ω, are plotted

color is associated to a positive LLE, while black color indicates a zero LLE. It can be seen that, in the considered cases, most of the region shown in Fig. 4 is dominated by parameters that correspond to periodic attractors of system (3), with a smaller yellow region at the bottom left of such a figure related to parameters corresponding to chaotic attractors. In order to corroborate the occurrence of chaotic dynamics in system (3), we generate three bifurcation diagrams, shown in Fig. 5, which show typical chaotic regions accompanied by a period-3 region and are consistent with Fig. 4. Each bifurcation diagram is related to a white vertical line, drawn in Fig. 4, which shows the variation of ω for a fixed value of parameter A. The bifurcation diagram in Fig. 5a was constructed considering the fixed value $A = 0.13$ and varying the parameter ω from 0.66 to 0.69, and the same was done in Fig. 5b and c, taking $A = 0.14$ and 0.15, respectively. The agreement between the diagrams in Figs. 4 and 5 is quite clear. In each of the bifurcation diagrams in Fig. 5 is plotted the local maxima (peaks) of the variable x, denoted by x_m, as a function of the parameter ω. We can clearly observe regions of chaotic and periodic behaviors, corresponding to the ones shown in Fig. 4, along the white lines.

4 Multistability in System (3)

Multistability is an interesting phenomenon related with nonlinear dynamics, meaning the coexistence of two or more attractors (stable equilibrium point, periodic, quasiperiodic, or chaotic) in the phase space, for a fixed set of parameters values [15]. The occurrence of multistability in nonlinear dynamical systems arises as a consequence of its sensitive dependence on initial conditions. The final state of multistable systems depends on the initial conditions, and the set of initial conditions that takes the system to a particular final state is called the basin of attraction of that

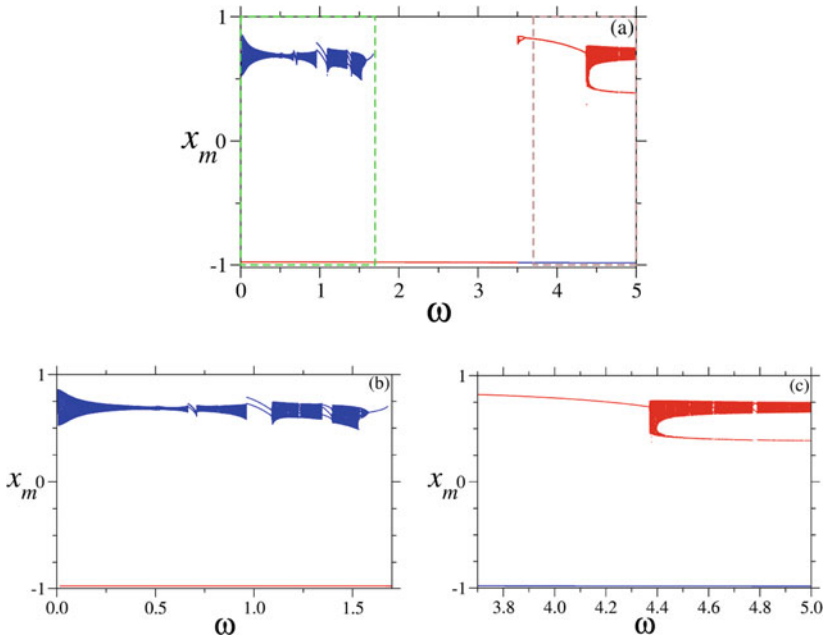

Fig. 6 (**a**) Two bifurcation diagrams for points along the vertical line segment $A = 0.15$ as in Fig. 4. Diagram in blue (red) considers the increase (decrease) of the parameter ω. Details of left and right regions of figure (**a**) are shown in (**b**) and (**c**)

state. In this section, we investigate the occurrence of multistability in system (3). We show that periodic attractors can coexist with chaotic ones for certain fixed sets of parameter values.

Figure 6a shows two bifurcation diagrams for system (3), one of them in blue, the other in red, both generated by following the attractor, for points along the vertical line segment $A = 0.15$ drawn in Fig. 4. Like the bifurcation diagrams in Fig. 5, in each of these two diagrams are shown the local maxima of the variable x, for each of one thousand values of the parameter ω. That in blue was generated considering the increase of the parameter ω from zero to 5, while that in red considers the decrease of ω from 5 to zero. At this point, it is important to remember that for the same ω value, all the parameters in system (3) are fixed as $S = -0.055$, $R = 0.088$, $L = 0.0007$, and $A = 0.15$. Even more important is the fact that the two bifurcation diagrams in Fig. 6a are clearly different, which evidences the occurrence of multistability. For example, in the right region, for $4.4 < \omega < 5.0$, we can observe the coexistence of a chaotic attractor, in red, and a period-1 attractor, in blue, while in the left region, for $0.0 < \omega < 1.7$, the coexistence consists of a chaotic attractor with some windows of periodicity, in blue, and a period-1 attractor, in red. The left and right regions in Fig. 6a are shown in detail in Fig. 6b and c, respectively.

In Fig. 7a are shown the basins of attraction on the plane (x, y), related to the chaotic attractor, in yellow, and related to the period-1 attractor, in black, for

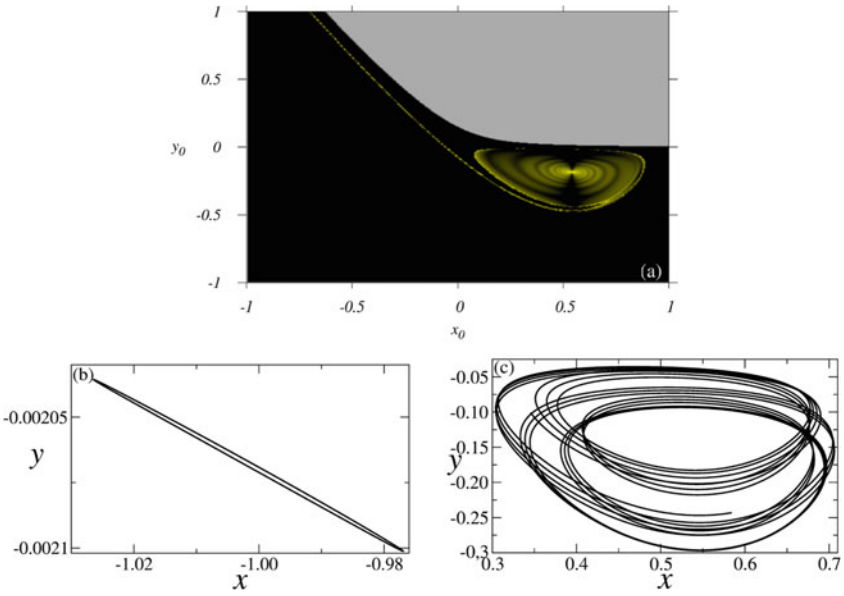

Fig. 7 (**a**) Basins of attraction for system (3), for $S = -0.055$, $R = 0.088$, $L = 0.0007$, $A = 0.15$, and $\omega = 0.4$. Black (yellow) is related to the period-1 (chaotic) attractor basin. In (**b**) and (**c**) are shown, respectively, a period-1 and a chaotic coexisting attractors of system (3) (see text)

solutions of system (3) with the parameters kept fixed as $S = -0.055$, $R = 0.088$, $L = 0.0007$, $A = 0.15$, and $\omega = 0.4$, which can be easily related to parameter values in Fig. 6. Consequently, as long as the parameters are thus fixed, any initial condition (x_0, y_0) chosen in the yellow region takes the system (3) solution to a chaotic attractor, whereas any initial condition (x_0, y_0) chosen in the black region takes the system's solution to a period-1 attractor. Figure 7b and c shows two coexisting attractors, respectively, a period-1 and a chaotic attractor, of system (3) with the abovementioned parameter values. In this figure, for the period-1 attractor, the chosen initial condition was $(x_0, y_0) = (-0.5, 0.5)$, while for the chaotic attractor, it was $(x_0, y_0) = (-0.580559, -0.170368)$, both points being easily located in Fig. 7a, the first one in the black region and the second in the yellow region. The solutions with initial conditions in the gray region of Fig. 7a tend to infinity.

Acknowledgments The first author was supported by the State of São Paulo Research Foundation (FAPESP) grant number 2019/10269-3.

References

1. Chua, L.O.: Memristor: the missing circuit element. IEEE Trans. Circuit Theory **18**, 507–519 (1971)
2. Strukov, D.B., Snider, G.S., Stewart, D.R., Williams, R.S.: The missing memristor found. Nature **453**, 80–83 (2008)
3. Tetzlaff, R. ed.: Memristors and Memristive Systems. Springer, New York (2014)
4. Itoh, M., Chua, L.O.: Memristor oscillators. Int. J. Bifurc. Chaos **18**, 3183–3206 (2008)
5. Ascoli, A., Slesazeck, S., Mähne, H., Tetzlaff, R., Mikolajick, T.: Nonlinear dynamics of a locally-active memristor. IEEE Trans. Circuits Syst. I **62**, 1165–1174 (2014)
6. Chua, L.O.: Local activity is the origin of complexity. Int. J. Bifurc. Chaos **15**, 3435–3456 (2005)
7. Dong, Y., Wang, G., Chen, G., Shen, Y., Ying, J.: A bistable nonvolatile locally-active memristor and its complex dynamics. Commun. Nonlinear Sci. Numer. Simulat. **84**, 105203 (2020)
8. Chua, L.O.: Resistance switching memories are memristors. Appl. Phys. A **102**, 765–783 (2011)
9. Muthuswamy, B., Chua, L.O.: Simplest chaotic circuit. Int. J. Bifurc. Chaos **20**, 1567–1580 (2010)
10. Xu, B.: A simplest parallel chaotic system of memristor. Acta Phys. Sin. **62**, 1–8 (2013)
11. Jin, P., Wang, G., Iu, H.H.C., Tyrone, F.: A locally-active memristor and its application in a chaotic circuit. IEEE Trans. Circuits Syst. II Exp. Briefs **65**, 246–250 (2018)
12. Gu, M., Wang, G., Liu, J., Liang, Y., Dong, Y., Ying, J.: Dynamics of a bistable current-controlled locally-active memristor. Int. J. Bifurc. Chaos **31**, 2130018 (20 pages) (2021)
13. Wiggins, S.: Introduction to Applied Nonlinear Dynamical Systems and Chaos. Springer, New York (2003)
14. Wolf, A., Swift, J.B., Swinney, H.L., Vastano, J.A.: Determining Lyapunov exponents from a time series. Phys. D **16**, 285–317 (1985)
15. Rech, P.C.: Multistability in a periodically forced brusselator. Braz. J. Phys. **51**, 144–147 (2021)

Structural Reliability Analysis Based on the Dynamic Integrity of an Attractor: Part I

Carlos Eduardo Nigro Mazzilli and Guilherme Rosa Franzini

1 Introduction

Stability, dynamic integrity, and reliability are essential properties of a dynamical system's attractor, for the purpose of a safe design in different branches of engineering and technology. The ideas and procedures discussed herewith are applicable to any dynamical system but will be illustrated within the context of structural stability, benefitting from the rich historical developments of classical elastic buckling analysis.

1.1 Determination of the Buckling Strength of a Structure: A Historical Perspective

The foundations of the elastic stability theory were established by Euler [1], by evaluating the buckling load of compressed rods (let's call it Euler's load) in the ideal scenario of "perfect" straight axis and in the absence of either lateral loading or axial load offsets. Extension to other slender structural systems, such as plates and shells, followed, as reported, for instance, by Timoshenko and Gere [2].

Nevertheless, it was noticed a long time ago that the theoretical estimates of the buckling strength could not always be confirmed experimentally, sometimes leading to values of the order of only 30% of the results evaluated for the so-called "perfect" system. That was the case of the experimental studies of von Kármán [3] with shells. Although the suspicion that small imperfections would be the cause for

C. E. N. Mazzilli (✉) · G. R. Franzini
University of São Paulo, São Paulo, Brazil
e-mail: cenmazzi@usp.br

© The Author(s), under exclusive license to Springer Nature Switzerland AG 2024

W. Lacarbonara (ed.), *Advances in Nonlinear Dynamics, Volume III*, NODYCON Conference Proceedings Series, https://doi.org/10.1007/978-3-031-50635-2_10

this unexpected result (how such minor deviations from the "perfect" model could explain such a large decrease in the buckling strength), it was necessary to wait for the advancements of nonlinear beam and shell theories, as proposed by Koiter [4] and Donnell and Wan [5] to fully understand it. As a matter of fact, although remaining unknown for a long time, the studies by Koiter, originally written in Dutch and only translated into English two decades later, are widely recognized as those that clearly established the concept of imperfection sensitivity of buckling loads (let's call them Koiter's load), showing its relationship with the patterns of unstable symmetric bifurcations (as in the case of cylindrical and spherical shells) and of asymmetric bifurcations (as in the case of framed asymmetric structures).

Thompson [6] and Roorda [7] anticipated that it was also important to consider the statistical variation of the buckling strengths as a consequence of the imperfections being a random variable, but perhaps Perry and Chilver [8] were the first to introduce the reliability analysis into the study of structural stability. They departed from the relation between the buckling strength and the imperfection parameter, as obtained from a deterministic model, yet taking into account the statistical properties of the imperfection (input variable), to evaluate the corresponding statistical properties of the buckling strength (output variable), thus characterizing its probability density function. Finally, they confronted the buckling strength's probability density function with that of the applied load, determining the probability of failure in the case the latter would overcome the former. It was indeed a pioneering work linking stability and reliability analysis.

A further important advancement came a few years later when Soliman and Thompson [9] introduced the concept of dynamic integrity of a dynamical system's attractor, expressing the need to somehow "measure" the compact and non-eroded part of its basin of attraction. In fact, it is not enough to know that a solution is stable (in other words, it is an attractor), if its basin of attraction is either too short or fractal, as it might happen in the case of a load just below the Koiter's load. Of course, to assess a measure of dynamic integrity, it was an absolute must to model the problem of structural buckling as a truly dynamical system, not just as a statical one, as usually done. Besides the dynamic-integrity measures proposed by Soliman and Thompson, namely, the *GIM* (global integrity measure), based on the "area" of the basin of attraction, and the *LIM* (local integrity measure), based on the largest radius of a hypersphere of the phase space centered in the attractor and tangent to the basin of attraction boundaries, Rega and Lenci [10] proposed still another measure called *IF* (integrity factor), similar to *LIM*, yet with the hypersphere not necessarily centered in the attractor, it henceforth being a property of the basin, as opposed to *LIM*, which is a property of the attractor.

Lenci and Rega [11] are among the first to connect the concepts of stability and dynamic integrity. They did that in a study of the buckling strength of an archetypal model. In this problem, they introduced what they called Thompson's load, as opposed to Euler's load (for the "perfect" model) and Koiter's load (for the "imperfect" model), by imposing a minimum "safe" *GIM*.

Yet, a reliability measure for Thompson's load was still missing, since the integrity measure may be affected by the statistical variation of Koiter's load, considered as a random variable, depending, on its turn, on the imperfection randomness. Hence, what is aimed in future works is something in the sequel, very similar to what Perry and Chilver have done with respect to Koiter's load, yet this time with Thompson's load. The probability that the integrity measure would be at least a safely chosen value is of course associated with the load not overcoming the associated "safely chosen" Thompson's load, which would be the buckling strength considering simultaneously structural stability, dynamic integrity, and reliability.

1.2 Integrity Measures and Erosion Profiles

As mentioned before, the usual dynamic-integrity measures are *GIM*, *LIM*, and *IF*. To calculate them, it is necessary to obtain the basin of attraction of the attractor of interest, which is still a computationally demanding task for systems with several degrees of freedom, and consequently with high-dimensional phase spaces.

It is supposed that some tool, such as the in-house code Poli BoA [12], is available for the purposes of both obtaining the basins of attraction and the associated dynamic-integrity measure chosen, generically referred to as I. This procedure is repeated for different values of a convenient system parameter A, within a convenient range. Typically, the graph $I(A)$ will indicate a decrease in the dynamic-integrity measure I as the parameter A increases, even with a steep gradient, thus justifying the nomenclature of an "erosion profile." Thompson refers to it as a "Dover Cliff" profile to the resemblance to the well-known English coastal topography (see Fig. 1).

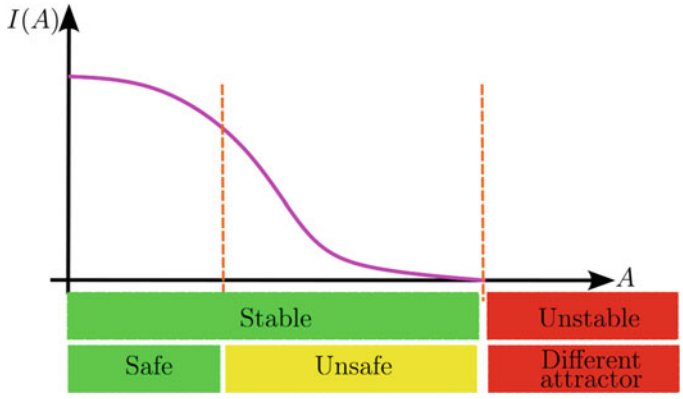

Fig. 1 Sketch of an erosion profile (Adapted from [13])

2 Statistical Properties and Probability Density Functions of Input and Output

Supposing that the "input" parameter A is a random variable, its statistical properties associated with its probability density function $f(A)$ can be communicated to the "output" dynamic-integrity measure's statistical properties and its associated probability density function $f(I)$.

From the fact that in usual applications the randomness of parameter A comes from multiple and independent factors, it is a reasonable assumption that an adequate probability density function is a normal distribution, resorting to the central limit theorem, as mentioned by Roorda [7]. Hence, for $f(A)$, it is written

$$f(A) = \frac{1}{\sigma_A \sqrt{2\pi}} e^{-\frac{(A-\bar{A})^2}{2\sigma_A^2}} \tag{1}$$

where $\bar{A}$ is the expected value and σ_A is the standard deviation of parameter A.

For $f(I)$, it is also reasonable to assume that it is a normal distribution, so that

$$f(I) = \frac{1}{\sigma_I \sqrt{2\pi}} e^{-\frac{(I-\bar{I})^2}{2\sigma_I^2}} \tag{2}$$

where $\bar{I}$ is the expected value and σ_I is the standard deviation of the dynamic-integrity measure I.

2.1 A Simplified Procedure to Evaluate the Dynamic Integrity Statistical Properties

A simplified methodology is proposed considering that the erosion profile $I(A)$ is known, so that $\tan\alpha = -dI/dA$ is the absolute value of its local slope. It is postulated that the output integrity measure standard deviation is given by $\sigma_I = \sigma_A \tan\alpha$ about the expected value $\bar{I}$. This assumption will be later discussed.

Hence, for every point $(\bar{A}, \bar{I})$ of the erosion profile, it can be defined the cutoff region for which the integrity measure complies with $I \geq I_{ref}$, provided $A \leq A_{ref}$, leading to the probability assigned to safety as a direct reliability measure.

For an illustrative example, the reader is referred to Sect. 3.

2.2 A Formal Procedure to Evaluate the Dynamic Integrity Statistical Properties

A more formal procedure for determining the statistical properties of the output distribution, using the moment-generating function [14], is now concisely presented. For such a procedure, auxiliary variables β and $\rho(\beta)$ are introduced such as

$$\beta = A - \bar{A} \tag{3}$$

$$\rho(\beta) = I(A) - I(\bar{A}) = I(\bar{A} + \beta) - I(\bar{A}) \tag{4}$$

For $\rho(\beta)$ a power series expansion can be written as

$$\rho(\beta) = \sum_{n=1}^{\infty} \frac{1}{n!} a_n \beta^n \tag{5}$$

Using the notation $E[x]$ for the expected value of a generic variable x and t for an auxiliary dummy variable, the moment-generating function can be concisely written as

$$M_\rho(t) = E[e^{\rho t}] = E\left[e^{t \sum_{n=1}^{\infty} \frac{1}{n!} a_n \beta^n} \right] = E\left[\prod_{n=1}^{\infty} e^{\frac{1}{n!} a_n \beta^n t} \right] \tag{6}$$

Equation 6 can be expanded in power series of the dummy variable t, so that

$$M_\rho(t) = 1 + t \sum_{n=2}^{\infty} \frac{1}{n!} a_n \mu_n + \\ + \frac{t^2}{2} \left(\sum_{n=1}^{\infty} \frac{1}{n!^2} a_n^2 \mu_{2n} + 2 \sum_{n=1}^{\infty} \sum_{m=n+1}^{\infty} \frac{1}{n!m!} a_n a_m \mu_{n+m} \right) + \ldots \tag{7}$$

where the central moments μ_n of the input random variable are defined by

$$\mu_n = E[\beta^n] \tag{8}$$

Notice that $\mu_1 = 0$ from Eq. 3. Now, the moment-generating function can be used to obtain the expected value $\bar{\rho}$ (first central moment η_1) and the other central moments η_r of the output distribution, as follows:

$$\bar{\rho} = \bar{I} - I(\bar{A}) = \left[\frac{\partial M_\rho}{\partial t} \right]_{t=0} = \sum_{n=2}^{\infty} \frac{1}{n!} a_n \mu_n \tag{9}$$

$$\eta_r = \left[\frac{\partial^r M_\rho}{\partial t^r}\right]_{t=0}, r = 2, 3, \ldots \tag{10}$$

From Eq. 9, the expected value of the output distribution comes out

$$\bar{I} = I(\bar{A}) + \bar{\rho} = I(\bar{A}) + \sum_{n=2}^{\infty} \frac{1}{n!} a_n \mu_n \tag{11}$$

From Eq. 10, the variance (second central moment) also comes out

$$\eta_2 = \sum_{n=1}^{\infty} \frac{1}{n!^2} a_n^2 + \mu_{2n} + 2 \sum_{n=1}^{\infty} \sum_{m=n+1}^{\infty} a_n a_m \mu_{n+m} - \left(\sum_{n=2}^{\infty} \frac{1}{n!} a_n \mu_n \right)^2 \tag{12}$$

Now, the procedure described in Sect. 2.1 can be recast, using an improved estimation for $\bar{I}$, as in Eq. 11, and for σ_I, taking the square root of η_2, as defined in Eq. 12.

3 Application to an Archetypal Model

The archetypal model discussed by Lenci and Rega [11] is addressed herewith (see Fig. 2). It is a rigid bar hinged at the bottom and constrained laterally by an inclined linear elastic spring. The buckling strength of the system under axial load (p) is sought in presence of an imperfection simulated by a small lateral load (q).[1]

Figure 3 depicts the erosion profile of the integrity measure $I = GIM$ in function of the axial load $A = p$, as found in [11], indicating a suggestion of Thompson's load to be $\bar{A} = p_T \approx 0.175$ and the corresponding $I(\bar{A}) = GIM_T \approx 0.100$ (this will be referred to as Scenario 2 in Table 1).

A cubic polynomial fitting for the curve $I(A) = GIM(p)$ is given by:

$$I(A) = b_0 + b_1 A + b_2 A^2 + b_3 A^3 \tag{13}$$

where $b_0 = 0.8500$, $b_1 = -6.0556$, $b_2 = 9.2479$, and $b_3 = 4.2930$. As for the local erosion profile slope in Scenario 2, from Eq. 13, it is found $\tan\alpha = -(dI/dA)(0.175) \approx 2.4244$. The simplified analysis is then carried out following the procedure presented in Sect. 2.1. Assuming, for the sake of an example, a standard deviation $\sigma_A = 0.020$, the estimated output standard deviation would be $\sigma_I = 0.049$, leading to a probability of 31.7% for GIM to be at least $GIM_T + \sigma_I = 0.149$, provided p is not larger than $p_T + \sigma_A = 0.195$; a probability of 50% for

[1] Uppercase parameters/variables are dimensional; lowercase parameters/variables are dimensionless.

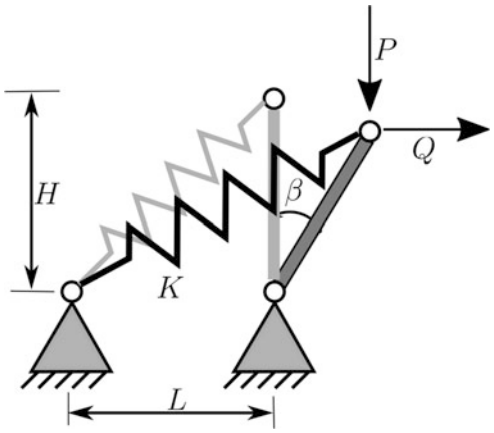

Fig. 2 Archetypal model (Adapted from [11])

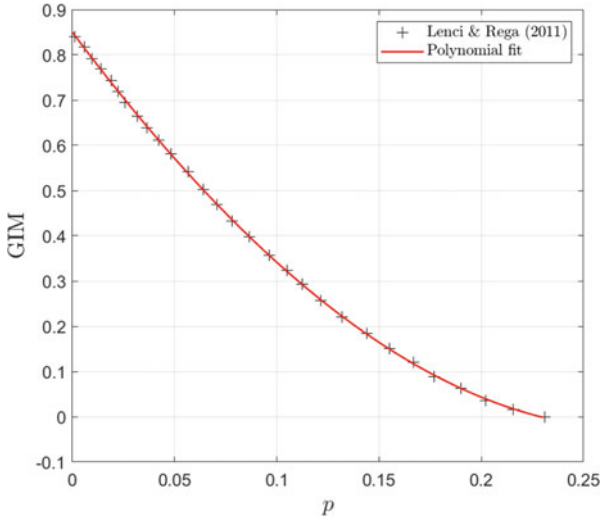

Fig. 3 Polynomial fitting for the erosion profile for $q = 0.03$ (Extracted from [11])

Table 1 Lower bounds of GIM and upper bounds of p for $\sigma_A = 0.040$

Prob. [%]	Scenario 1		Scenario 2		Scenario 3		Scenario 4		Scenario 5	
	$(\bar{p}; \overline{GIM})$		$(\bar{p}; \overline{GIM})$		$(\bar{p}; \overline{GIM})$		$(\bar{p}; \overline{GIM})$		$(\bar{p}; \overline{GIM})$	
	$(0.215; 0.018)$		$(0.175; 0.100)$		$(0.135; 0.208)$		$(0.095; 0.362)$		$(0.055; 0.546)$	
	$GIM \geq$	$p \leq$	$GIM \geq$	$p \leq$	$GIM \geq$	$p \leq$	$GIM \geq$	$p \leq$	$GIM \geq$	$p \leq$
31.73	0.092	0.215	0.149	0.195	0.208	0.175	0.279	0.155	0.357	0.135
50	0.053	0.195	0.100	0.175	0.150	0.155	0.212	0.135	0.282	0.115
68.27	0.004	0.175	0.051	0.155	0.092	0.135	0.145	0.115	0.207	0.095

GIM to be at least $GIM_T = 0.100$, provided p is not larger than $p_T = 0.175$; and a probability of 68.3% for *GIM* to be at least $GIM_T - \sigma_I = 0.051$, provided p is not larger than $p_T - \sigma_A = 0.155$. Table 1 displays other simulations for the probabilities of both lower bounds of *GIM* and upper bounds of p.

Notice that for $p \leq 0.175$, there is a 31.73% probability that $GIM \geq 0.208$ (Scenario 3) and 50% probability that $GIM \geq 0.100$ (Scenario 2), but a 31.73% probability that *GIM* would not be acceptable, since $GIM_T - \sigma_I$ is almost null (Scenario 1)! Alternatively, for $p \leq 0.155$, there is a 31.73% probability that $GIM \geq 0.279$ (Scenario 4), 50% probability that $GIM \geq 0.150$ (Scenario 3), and a 68.27% probability that $GIM \geq 0.051$ (Scenario 2). Finally, for $p \leq 0.135$, there is a 31.73% probability that *GIM* would be (anti-economically?) large (Scenario 5), a 50% probability that $GIM \geq 0.212$ (Scenario 4), and a 68.27% probability that $GIM \geq 0.092$. These results could be used to decide whether the choice of $p_T = 0.155$ or $p_T = 0.135$ would not be a better choice than $p_T = 0.175$ for a safe engineering design.

Next, the procedure presented in Sect. 2.2 is followed for the sake of a comparison with the simplified analysis just carried out. Only Scenario 2 is focused on what follows. Assuming a normal distribution for the input variable, due to its symmetry, it is clear that $\mu_3 = 0$. Hence, for the cubic polynomial fitting, the only non-null central moment to be considered is $\mu_2 = \sigma_A^2 = 0.0004$ for the example at hand. From Eq. 4, considering the cubic polynomial fitting of Eq. 13, it is straightforward to arrive at

$$\rho(\beta) = a_1\beta + a_2\beta^2 + a_3\beta^3 \tag{14}$$

where, for $\bar{A} = 0.175$, $a_1 = b_1 + 2b_2\bar{A} + 3b_3\bar{A}^2 = -2.4244$, $a_2 = b_2 + 3b_3\bar{A} = 11.5017$, and $a_3 = b_3 = 4.2930$, which is a particular case of Eq. 5. Hence, it follows from Eqs. 9 and 12 that $\bar{\rho} = (1/2)a_2\mu_2 \approx 0.002$ and $\eta_2 = a_1^2\mu_2 - (1/4)a_2^2\mu_2^2 = 0.002$. Finally, for the output variable $I = GIM$, the following statistical properties are found: $\bar{I} = I(\bar{A}) + \bar{\rho} \approx 0.102$, to be compared with $GIM_T \approx 0.100$, and $\sqrt{\eta_2} \approx 0.048$, to be compared with $\sigma_I = 0.049$, indicating a good agreement with the simplified method. Of course, if σ_A would be larger (i.e., a relative standard deviation larger than 11%), the simplified method might deviate too much from the formal procedure, and this latter would be more adequate to use in the analysis.

4 Concluding Remarks

This chapter proposes a simplified method to carry out a reliability analysis based on the dynamical integrity of a system, provided the statistical properties of the parameter used to define the erosion curve of the chosen integrity measure are known. A first try is simply based on the slope of the erosion curve to evaluate the

standard deviation of the integrity measure, giving the probability that a minimum reference value is attained, provided a threshold of the input system parameter is not surpassed. A more systematic procedure is then discussed, by which the statistical properties of the output variable (in this case, the dynamic integrity measure) are evaluated from those of the input variable (in this case, the system parameter used to obtain the erosion curve), as derivable from the moment-generating function. Both procedures are illustrated for an archetypal model in which a safe threshold is searched for the buckling load so as not to undergo a critical reduction (or fractalization) of the basin of attraction of the desired equilibrium configuration. A critical reasoning is raised about the choice of a safe, yet still economical, choice of Thompson's load for the problem at hand. The easiness of application of both the simpler and the more formal procedures, which closely agree with each other, gives hope to their adoption in the engineering design practice, although one should not underestimate the determination of the erosion curve stage, which still poses some difficulties for systems with large number of degrees of freedom, thus emphasizing the importance of reduced-order models.

Acknowledgments Both authors acknowledge the support from the São Paulo Research Foundation (FAPESP) through project 2022/00770-0 and the Brazilian Council for Scientifical and Technological Development (CNPq) for the grants 301050/2018-0 and 305945/2020-3. The second author acknowledges the support of BEPE scholarship 19/15046-2 from FAPESP .

References

1. Euler, L.: Methodus inveniendi lineas curvas maximi minimive proprietate gaudentes, sive solutio problematis isoperimetrici latissimo sensu accepti. Addentamentum 1: de curvis elasticis, Laussanae et Genevae. Apud Marcum-Michaelem, Bousquet et Socios, pp. 245–310 (1744)
2. Timoshenko, S.P., Gere, J.M.: Theory of Elastic Stability, 2nd edn. McGraw Hill, New York (1961)
3. von Kármán, T., Tsien, H.S.: The buckling of thin cylindrical shells under axial compression. J. Aeronaut. Sci. **8**(8), 303–312 (1941)
4. Koiter, W.T.: Over de stabiliteit van het elastisch evenwicht, Ph.D. thesis, Delft University, (1945). English translation: Koiter, W.T.: On the Stability of Elastic Equilibrium. NASA Technical Translation F-10, 833, Clearinghouse, US Department of Commerce/National Bureau of Standards N67–25033 (1967)
5. Donnell, L.H., Wan, C.C.: Effect of imperfections on buckling of thin cylinders and columns under axial compression. J. App. Mech. **17**, 73–83 (1950)
6. Thompson, J.M.T.: Towards a general statistical theory of imperfection-sensitivity in elastic post-buckling. J. Mech. Phys. Solids **15**, 403–417 (1967)
7. Roorda, J.: Some statistical aspects of the buckling of imperfection-sensitive structures. J. Mech. Phys. Solids **17**, 111–123 (1968)
8. Perry, S.H., Chilver, A.H.: The statistical variation of the buckling strengths of columns. Proc. Inst. Civil Eng. Part **2**(61), 109–125 (1976)
9. Soliman, M.S., Thompson, J.M.T.: Integrity measures quantifying the erosion of smooth and fractal basins of attraction. J. Sound Vib. **135**, 453–475 (1989)

10. Rega, G., Lenci, S.: Identifying, evaluating, and controlling dynamical integrity measures in nonlinear mechanical oscillators. Nonlin. Analysis **63**, 902–914 (2005)
11. Lenci, S., Rega, G.: Load carrying capacity of systems within a global safety perspective. Part I. Robustness of stable equilibria under imperfections. Int. J. Non-Linear Mech. **46**, 1232–1239 (2011)
12. Provasi, R., Maciel, V.S.F, Franzini G.R.: A Julia code for computing basins of attraction of one-degree-of-freedom systems. In: Proceedings of the 26th Int. Congress of Mech. Eng.—COBEM (2021)
13. Rega, G.: Achieving load-carrying capacity, Lecture Notes, PEF5737 Nonlinear Dynamics and Stability, Escola Politécnica, University of São Paulo (2018)
14. Mood, A.M., Graybill, F.A.: Introduction to the Theory of Statistics. McGraw Hill, Tokyo (1963)

Chaotic Dynamic Induced by PI Control in Offshore Oil Production Plants

Nayher A. Clavijo, Giovani G. Gerevini, Fabio C. Diehl, Príamo A. Melo, and José Carlos Pinto

1 Introduction

Brazil holds 3.9% of oil reserve in Latin America, being the second largest in the region with 12.25 billion barrels in offshore fields and 0.46 billion barrels in onshore fields. In 2019, pre-salt ultradeep fields production represented 58% of total oil production in Brazil [1]. Frequently, floating facilities used for offshore oil and gas production consist of tubing-pipeline-riser systems. Despite this production technology being widely used, it has been observed these production systems are susceptible to exhibiting slugging, a common and undesirable multi-phasic flow pattern phenomenon that causes periodic blockage of gas flow due to a large liquid slug accumulation through the riser and pipeline section. These slugging flow instabilities can generate harmful operating conditions leading to process safety losses, process production drop, and even plant shutdown [2]. Typically, the slugging flow emerges due to the pipeline-riser geometric structure of the production system [3]; low production rates related to the well production life; and gas-lift injection operating conditions that can favor the arise of flow instabilities [4].

Several approaches have been developed in order to avoid or remediate problems in pipeline-riser systems due to the slugging phenomenon, including automatic control strategies aimed to change the operating condition that favors the arise of the slugging flow [2]. Frequently, these control approaches are based on simulations of simplified low-dimensional models (usually based on mass conservation principles

N. A. Clavijo · G. G. Gerevini · P. A. Melo · J. C. Pinto (✉)
Programa de Engenharia Química/COPPE, Universidade Federal do Rio de Janeiro, Rio de Janeiro, Brazil
e-mail: pinto@peq.coppe.ufrj.br

F. C. Diehl
Centro de Pesquisas Leopoldo Americo Miguez de Mello—CENPES, PETROBRAS—Petróleo Brasileiro SA, Rio de Janeiro, Brazil

© The Author(s), under exclusive license to Springer Nature Switzerland AG 2024

W. Lacarbonara (ed.), *Advances in Nonlinear Dynamics, Volume III*, NODYCON Conference Proceedings Series, https://doi.org/10.1007/978-3-031-50635-2_11

and represented by ordinary differential equations) able to achieve acceptable prediction performance requiring low computational effort, allowing the use of these approaches in real-time applications [5, 6]. Some of these works and discussions about practical validation have been reviewed in the reference [7].

Severe slugging phenomena are characterized by the emergence of an oscillatory self-sustained dynamic behavior observed in the pressure and flow rate online measurements in the production plant [8]. The modeling and simulation works intended to describe these offshore oil and gas production processes have shown that the oscillatory dynamics arise due to the existence of a Hopf bifurcation. Particularly, it has been identified that changes in independent variables of the processes such as Choke valve opening and gas-lift injection flow rate are able to promote the emergence of instabilities in the system [9].

It is worth mentioning that the major part of slugging behaviors observed in industrial-scale processes and the corresponding phenomenological models described periodic oscillatory dynamics, and more complex dynamics have not been observed in these production scales [10].

Despite anti-slug control approaches being designed to suppress oscillatory behavior, it has been observed that feedback controllers can induce the development of complex dynamics [11]. The present work investigates the emergence of chaotic behavior in an upstream production facility described by the Fast Offshore Well Model (FOWM) model [5] when considering the effect of a feedback PI controller.

2 Mathematical Modelling

The FOWM was developed based on the production system architecture shown in Fig. 1, constituted for four subsystems: reservoir, annular, tubing, and flowline-riser. The system mass conservation equations can be given by:

$$\frac{dm_{ga}}{dt} = W_{gc} - W_{iv} \tag{1}$$

$$\frac{dm_{gt}}{dt} = W_r \alpha_{gr} + W_{iv} - W_{whg} \tag{2}$$

$$\frac{dm_{lt}}{dt} = W_r \left(1 - \alpha_{gr}\right) - W_{whl} \tag{3}$$

$$\frac{dm_{gb}}{dt} = (1 - E)\, W_{whg} - W_g \tag{4}$$

$$\frac{dm_{gr}}{dt} = E W_{whg} + W_g - W_{gout} \tag{5}$$

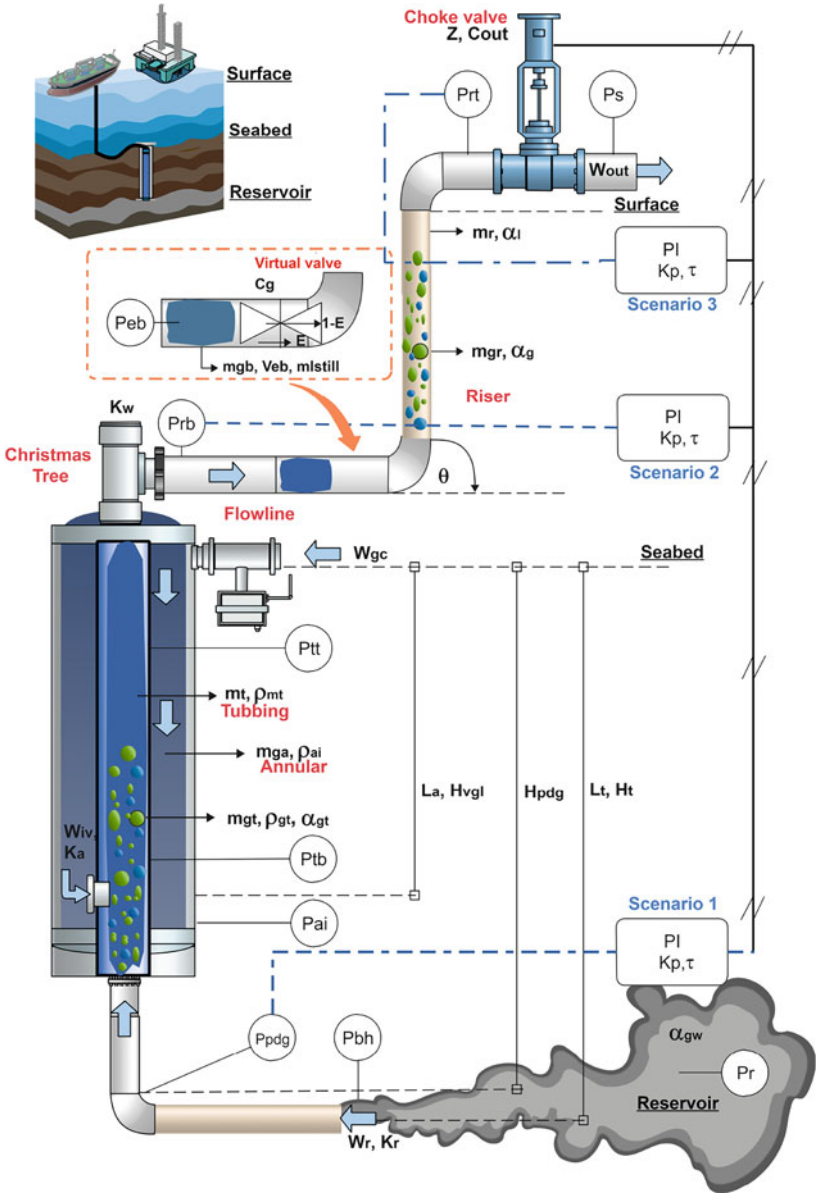

Fig. 1 Offshore oil and gas production system and PI control layout

$$\frac{dm_{lr}}{dt} = W_{whl} - W_{lout} \tag{6}$$

where the state variables correspond to m_{ga} the gas mass in the annular section, m_{gt} the gas mass in the tubing section, m_{lt} the liquid mass in the tubing section, m_{gb} the mass of gas in the bubble at the subsea production line, and m_{gr} and m_{lr},

respectively, the gas and liquid mass in the set flowline/riser section. E corresponds to the mass fraction of gas that bypasses the bubble in the subsea pipeline, and α_{gr} is the mass gas fraction at the reservoir pressure and temperature conditions.

In addition, the mass flow rates in the system are described by W_{gc} being the gas-lift mass flow rate entering the annular, W_{iv} corresponding to the gas mass flow rate from the annular to the tubing, and W_r being the multi-phase mass flow rate from the reservoir to the bottom hole. The gas and liquid mass flow rates through the Christmas tree are, respectively, W_{whg} and W_{whl}. The mechanism for modeling the slugging dynamics follows a virtual valve approach [12] where W_g is the flow rate at this proposed device and W_{gout} and W_{lout} are the gas and liquid flow rates through the topside choke valve. The complete model and parameters are presented in [5, 9].

Overall, the FOWM has nine estimable model parameters: $m_{l,still}$, C_g, C_{out}, V_{eb}, E, K_w, K_a, K_r and V_r. The parameters estimation procedure employs plant design and online measurements data from a real offshore well from PETROBRAS.

Figure 2 presents the production data of the studied actual well, where nP_{pdg}, nP_{rt}, and nz are the normalized pressures in the PDG position, at the top of the riser, and the normalized Choke valve opening, respectively. Additionally, Table 1 presents the fitting parameters obtained during the parameter estimation procedure.

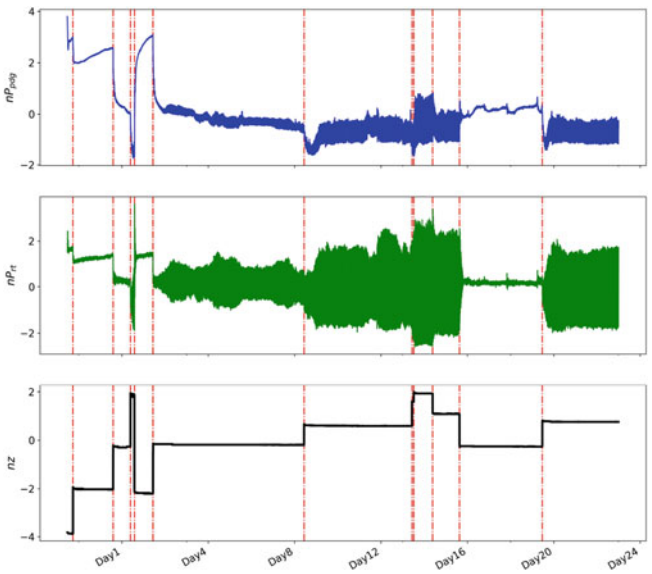

Fig. 2 Plant measured data as a function of Choke valve opening and the emergence of slugging

Table 1 FOWM fitting parameters

Parameter	Value
$m_{l,still}$	1.9656×10^{4}
C_g	2.0551×10^{-5}
C_{out}	6.8920×10^{-3}
V_{eb}	53.3003
E	0.9166
K_w	0.0347
K_a	6.6005×10^{-4}
K_r	691.2173
V_r	93.9425

2.1 PI Controller

The dynamics of the PI controller is described by the Eq. (7):

$$z(t) = z_{bias} + K_p \left[\left(\hat{P}(t) - \hat{P}_{sp} \right) + \frac{1}{\tau} \int_0^t \left(\hat{P}(t) - \hat{P}_{sp} \right) dt \right] \tag{7}$$

so that:

$$I = \frac{1}{\tau} \int_0^t \left(\hat{P}(t) - \hat{P}_{sp} \right) dt \tag{8}$$

then, the respective derivative is given by:

$$\frac{dI}{dt} = \frac{1}{\tau} \left(\hat{P}(t) - \hat{P}_{sp} \right) \tag{9}$$

The mathematical system that describes the dynamics of the production plant operating with the PI controller corresponds to the ODE system constituted by Eqs. (1)–(6) and Eqs. (7) and (9), where z_{bias} is the bias of the choke valve opening fraction, K_p is the controller proportional constant, τ is the integral time constant, and $\hat{P}(t)$ and $\hat{P}_{sp}$ correspond to the controlled pressure and its set point. Particularly, the present work considers the scenario when the controlled pressure is the pressure at the top of the riser P_{rt}. Other control scenarios are contemplated in the reference [9].

3 Results

The evaluation of the effect of the PI controller on the oil and gas production system considers the dynamic simulation of the previously presented process model. The evaluation of the effect of the PI controller on the oil and gas production system considers the dynamic simulation of the model constituted by the set of Eqs. The procedure includes the simulation of dynamical system in open-loop regime (i.e., excluding Eqs. (7) and (9) of the model) in order to determine the type response when applied perturbations in the manipulated variable. On the other hand, the simulation of the full model (in closed-loop regime) is performed, aiming to determine the PI controller effect on the dynamic behavior.

3.1 Open-Loop Responses in a Gas-Lift Well

Figure 3 shows the P_{rt} pressure response when a sequence of z step perturbations is applied. As it can be observed, a self-sustained oscillatory dynamic behavior emerges when the steps perturbations reach or exceed the corresponding value to the Hopf bifurcation. A special feature of the P_{rt} dynamics is the presence of inverse response when the perturbations were applied. This phenomenon is identified when the initial response of the variable goes in the opposite direction of the steady-state response leading to severe performance limitations of the feedback control scheme [13].

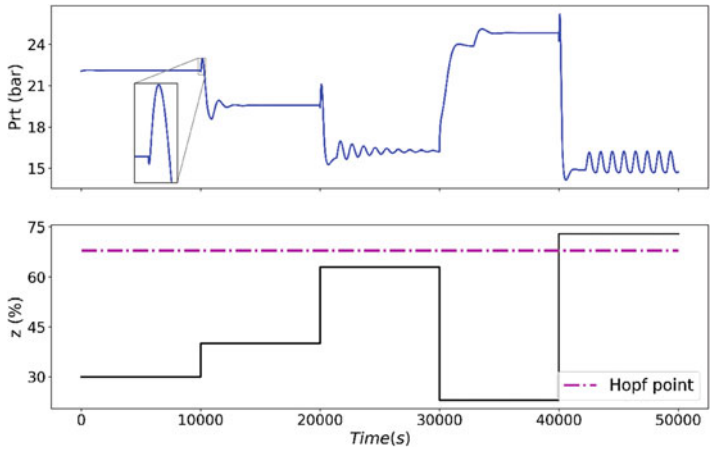

Fig. 3 Open-loop P_{rt} responses when z steps perturbations are applied. The zoom frame highlights an inverse response. The Hopf bifurcation point corresponds to $z \approx 68\%$, and it was estimated using parametric continuation analysis

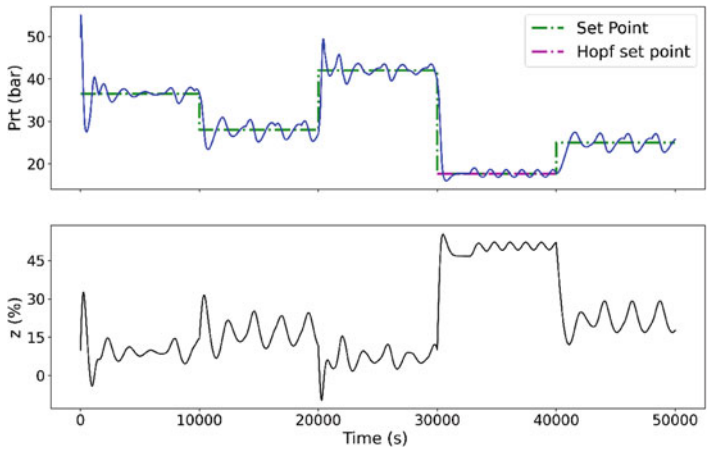

Fig. 4 Closed-loop P_{rt} responses for a sequence of set point values, where the tuning parameters correspond to $K_p = 1.0153e^{-7}(1/Pa)$, $\tau = 90.255(s)$, and $z_{bias} = 18.4865(\%)$

3.2 PI Control Dynamics in a Gas-Lift Well

On the other hand, Fig. 4 presents the P_{rt} response and the corresponding manipulated variable dynamics required to reach a determined sequence of set points. The PI control tuning parameters were set based on the pre-identification of the Hopf bifurcation points using parametric continuation analysis [9].

It has been observed that including a PI controller allows a shift of the Hopf bifurcation point with respect to the choke valve opening [7]. However, as one can see, when the P_{rt} is the controlled variable, the Hopf bifurcation point is shifted at lower choke valve opening values z than the Hopf bifurcation location observed in the open-loop regime. In particular, the presence of Hopf bifurcation points at low z values implies the increase of oscillatory dynamics for a wide range of operating plant conditions leading to low production rates in the system.

3.3 Induced Chaotic Behavior

Closed-loop simulations showed the appearance of oscillating responses of multiple periods indicating the existence of more complex dynamical behaviors. According to the mathematical model, the inverse response of the controlled variable adds an external source of positive feedback that enriches the variety of nonlinear dynamic behaviors in the system.

In order to determine the structural changes in the equilibrium stability of the system due to the variation of a control parameter, a set of simulations was

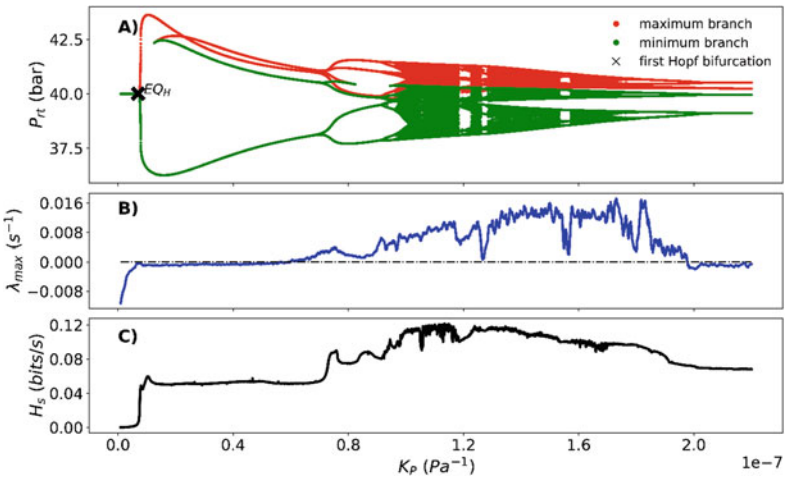

Fig. 5 Bifurcation diagram (**a**) and the representative metrics: Largest Lyapunov exponent (**b**) and Shannon entropy (**c**)

performed to build a bifurcation diagram taking the proportional constant K_p of the PI controller as the bifurcation parameter.

Figure 5 shows the bifurcation diagram depicting the local extrema of P_{rt}. In addition, representative metrics such as the largest Lyapunov exponent λ_{max} and Shannon entropy H_s are presented in order to characterize the emergence of the chaotic behavior. As one can see, the diagram exhibits a stable behavior up to $K_p \approx 0.078e^{-7}$, where a Hopf bifurcation EQ_H arises, generating single-period oscillations. Then, when increasing the parameter K_p, a period-doubling route to chaotic oscillations can be identified alternating with periodic windows. Furthermore, the chaotic behavior is considered properly identified by both positive largest Lyapunov exponent and entropy.

The computation of the largest Lyapunov exponent through a bi-parametric sweeping K_p—$u2$ allowed to identify a large variety of dynamic behaviors, as observed in Fig. 6. A plane region with $\lambda_{max} \approx 0$ for $u2 < 1e5$ can be observed, indicating that the dynamics in this parametric region is characterized by present oscillatory and periodic responses. Then, for $u2 > 1e5$, there are sequences of local regions with positive and negative values of λ_{max}, showing an alternation between chaotic and stable behaviors. Panels A-B in Fig. 6 exhibit two chaotic trajectories in the space state with $\lambda_{max} > 0$; panel C shows a periodic-oscillatory trajectory with $\lambda_{max} \approx 0$; and panel D presents a fixed point stable trajectory corresponding to $\lambda_{max} < 0$ case. Furthermore, each panel shows a heat map representing the recurrence rate (RR) of the trajectory, which is a density measure of the recurrence plots. As one can see, the trajectories are highly recurrent in regions that are close to the equilibrium point, showing the attractive pattern of this region. On the other hand, the outer orbits present a low density of recurrences, revealing

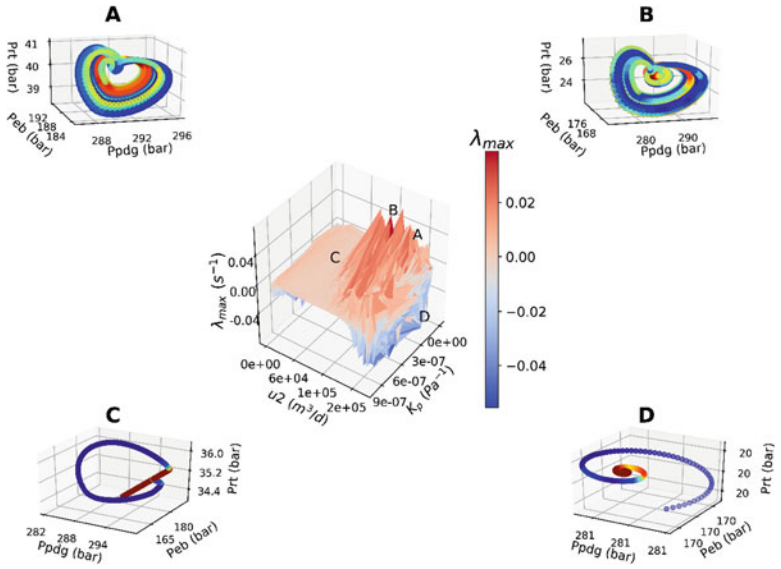

Fig. 6 Largest Lyapunov exponent λ_{max} for the $K_p - u2$ parametric space. The heat map and color bar indicate the λ_{max} value. Panels A-B exhibit chaotic trajectories, panel C shows an oscillatory periodic trajectory, and panel D a stable fixed point trajectory

that the trajectory lies in this region for short times. These RR patterns allow for distinguishing the flow expansion (repulsive-unstable) and flow contraction (attractive-stable) properties of the chaotic motion.

4 Conclusions

In the present work, an anti-slug scheme based on a PI feedback control was presented. The analysis was focused on the scenario when the pressure at the top of the riser P_{rt} was considered as the controlled variable. It has been observed that the shift of the Hopf bifurcation point lay at lower production rates than in the open-loop regime, constituting a plant operability limitation. Also, the emergence of chaotic dynamics was corroborated using quantitative metrics, such as Lyapunov exponents and Shanon entropy.

It is worth mentioning that the arising of chaotic behavior was directly related to the existence of inverse response of the controlled variable when steps perturbations are applied. This response offers an additional source of positive feedback to the system, enriching the variety of nonlinear behaviors that it can exhibit.

References

1. ANP—Agência Nacional do Petróleo, Gás Natural e Biocombustíveis: Anuário Estatístico 2020—Dados Abertos. ANP. Rio de Janeiro (2020). https://www.gov.br/anp/pt-br/centrais-de-conteudo/dados-abertos/anuario-estatistico-2020-dados-abertos
2. Pedersen, S., Durdevic, P., Yang, Z.: Challenges in slug modeling and control for offshore oil and gas productions: a review study. Int. J. Multiphase Flow **88**, 270–284 (2017). https://doi.org/10.1016/j.ijmultiphaseflow.2016.07.018
3. Taitel, Y: Stability of severe slugging. Int. J. Multiphase Flow **12**(2), 203–217 (1986). https://doi.org/10.1016/0301-9322(86)90026-1
4. Rashid, K., Bailey, W., Couët, B.: A survey of methods for gas-lift optimization. Model. Simul. Eng. **2012**, 24–24 (2012). https://doi.org/10.1155/2012/516807
5. Diehl, F.C., Anzai, T.K., Almeida, C.S., Von Meien, O.F., Neto, S.S., Rosa, V.R., Campos, M.C., Reolon, F., Gerevini, G., Ranzan, C., Farenzena, M., Trierweiler, J.O.: Fast Offshore Wells Model (FOWM): a practical dynamic model for multiphase oil production systems in deepwater and ultra-deepwater scenarios. Comput. Chem. Eng. **99**, 304–313 (2017)
6. Pedersen, S., Durdevic, P., Yang, Z.: Review of slug detection, modeling and control techniques for offshore oil and gas production processes. Ifac-papersonline **48**(6), 89–96 (2015). https://doi.org/10.1016/j.ifacol.2015.08.015
7. Diehl, F.C., Machado, T.O., Anzai, T.K., Almeida, C.S., Moreira, C.A., Nery Jr, G.A., Campos, M.C., Farenzena, M., Trierweiler, J.O.: 10% increase in oil production through a field applied APC in a Petrobras ultra-deepwater well. Control Eng. Pract. **91**, 104108 (2019). https://doi.org/10.1016/j.conengprac.2019.104108
8. Diehl, F.C., Gerevini, G.G., Machado, T.O., Quelhas, A.D., Anzai, T.K., Bitarelli, T., Serpentini F., Azambuja J., Jahanshahi E., Skogestad, S., Farenzena, M., Trierweiler, J.O.: Anti-slug control design: combining first principle modeling with a data-driven approach to obtain an easy-to-fit model-based control. J. Pet. Sci. Eng. **207**, 109096 (2021). https://doi.org/10.1016/j.petrol.2021.109096
9. Clavijo, N.A., Diehl, F.C., Gerevini, G.G., Melo, P.A., Lemos, T., Campos, L.F.D.O., Pinto, J.C.: Chaotic dynamics induced by anti-slug control in offshore oil production plants. J. Pet. Sci. Eng. **215**, 110716 (2022). https://doi.org/10.1016/j.petrol.2022.110716
10. Campos, M.,Takahashi, T., Ashikawa, F., Simões, S., Stender, A., Meien, O.: Advanced anti-slug control for offshore production plants. IFAC-PapersOnLine **48**, 83–88 (2015)
11. Pérez-Polo, M.F., Pérez-Molina, M.: Increasing the reactant conversion through induced oscillations in a continuous stirred tank reactor by using PI control. J. Process Control **23**(5), 778–792 (2013). https://doi.org/10.1016/j.jprocont.2013.03.007
12. Di Meglio, F., Kaasa, G.O., Petit, N.: A first principle model for multiphase slugging flow in vertical risers. In: Proceedings of the 48h IEEE Conference on Decision and Control, pp. 8244–8251. IEEE Press, New York (2009). https://doi.org/10.1109/CDC.2009.5400680
13. Skogestad, S., Postlethwaite, I.: Multivariable Feedback Control: Analysis and Design. Wiley, New York (2005)

The Jerk Dynamics of Lorenz Model

Jean-Marc Ginoux, Riccardo Meucci, Jaume Llibre, and Julien Clinton Sprott

1 Introduction

At the very beginning of the 1960s, Edward Norton Lorenz (1917–2008), a meteorologist from the famous MIT (Massachusetts Institute of Technology), succeeded in establishing a model for atmospheric convection comprising only three variables. The solution of this weather forecasting model that Lorenz [13] plotted in a three-dimensional phase space is compelled to evolve on a chaotic attractor which resembles the wings of a butterfly. It is probably this form that prompted Lorenz to call the "sensitivity to initial conditions" (described by the French mathematician Henri Poincaré as early as 1908 in his philosophical writings *Science and Method* [14]) the "butterfly effect." During these last two decades, the seminal works of Gottlieb [5] and Sprott [18–24] have triggered out an increasing interest in the study of chaotic oscillators based on jerk equations, that is, oscillators which can be completely described by third-order ordinary differential equations of the form $\dddot{x} = f(\ddot{x}, \dot{x}, x)$. In 1997, Stephan J. Linz [11] proposed in a very interesting paper an "exact transformation" enabling to obtain the jerk form of the Lorenz model and a nonlinear transformation "simplifying its jerky dynamics." Unfortunately, the third-order nonlinear differential equation he finally obtained precluded any

J.-M. Ginoux (✉)
Aix Marseille University, Université de Toulon, CNRS, CPT, Marseille, France
e-mail: ginoux@univ-tln.fr

R. Meucci
National Institute of Optics – CNR, Florence, Italy

J. Llibre
Departament de Matemàtiques, Universitat Autònoma de Barcelona, Barcelona, Spain

J. C. Sprott
University of Wisconsin, Madison, WI, USA

© The Author(s), under exclusive license to Springer Nature Switzerland AG 2024

W. Lacarbonara (ed.), *Advances in Nonlinear Dynamics, Volume III*, NODYCON Conference Proceedings Series, https://doi.org/10.1007/978-3-031-50635-2_12

mathematical analysis and made difficult numerical investigations since it contained exponential functions. Let's notice that the jerk form in x of the Lorenz model that we will provide below is exactly the same as those obtained by Linz but presented in a different way. In 2014, Buscarino et al. [2] used *linear combinations* of the three nonlinear ordinary differential equations modeling Chua's circuit to deduce its jerk forms in x and z. Recently, Xu and Cao [26] proposed to use the so-called controllable canonical form to provide all the jerk form dynamics of Chua's circuit. In this paper, following the method of *linear combinations* proposed by Buscarino et al. [2], we provide the jerk form in x of Lorenz model. Thus, by making a comparison of fixed points and their stability, eigenvalues, Lyapunov characteristic exponents (LCEs), and attractor shapes between the original three-order Lorenz model and its first jerk form in x, we demonstrate the *topological equivalence* of both systems.

The paper is organized as follows. In the next section, some introductive and historical materials on jerk equations are reported. Then, the set of three first-order nonlinear differential equations of Lorenz model and mathematical and numerical results concerning its main features (fixed points and their stability, Hopf bifurcation parameter, Lyapunov characteristic exponents, and Kaplan-Yorke dimension) are recalled. The mathematical demonstration leading to the Lorenz jerk system is then presented. A comparison with the original Lorenz model enables to show that they have of course exactly the same features. Phase portraits are also *topologically equivalent*, the only difference being the range of values of the y and z variables which is increased respectively by a factor 5 for y and 50 for z.

2 Preliminaries

At the end of the 1970s, Stephen H. Schot [15] published a very interesting paper in which he made a short history of the origin of the use of the concept of jerk, i.e., the time rate of change of the acceleration. He explained that:

> The French geometer Transon in 1845 was probably the first to consider the third time derivative of distance in mechanics and he uses the term virtualité for it. Transon computes the normal component of the jerk and expresses it in terms of what is now called the aberrancy (he uses the term déviation de courbure). Other early writers who treat the third derivative use neutral terms such as second acceleration or higher acceleration for it. Thus, Resal resolves the jerk along a space curve into tangential, normal, and binormal components and Somoff first establishes recursion formulas for these components of the higher-order accelerations in terms of those of the ordinary acceleration. Subsequently, the term jerk for the second acceleration seems to have gradually entered the literature of physics and without any explicit rational explanation for its use.

According to Pr. Christian Mira (personal communication), at the end of the nineteenth century, the French scientist Martin Haag (not to be confused with Jules Haag) made use of the concept of "over-acceleration" or jerk in a mathematical analysis [6]. Then, as recalled by Schot [15]:

> An unequivocal definition of the jerk as "the derivative of acceleration with respect to time" was given in 1928 by Melchior who justifies the use of the term by referring to the physiological sensation experienced by large changes in acceleration ... The term is now commonly used in mechanics and is being adopted in other areas of physics as well.

More than half a century later, Julian Clinton Sprott [17] found probably the simplest three-dimensional first-order system for chaos. Two years after, Hans Gottlieb [5] wondered "what is the simplest jerk function that gives chaos?", where the jerk function is of the form $\dddot{x} = f(x, \dot{x}, \ddot{x})$. According to Buscarino et al. [2]: "If a mechanical interpretation of the variable x in terms of displacement is given, the jerk equation can be viewed as an equation where the derivative of the acceleration is involved, that is, where a measure of the instantaneous variation of the acceleration is included." Since the question of the simplest jerk function is still open, in this work, we will only focus on the *topological equivalence* between the original model and its corresponding jerk equations. To this aim, we will use the Lyapunov characteristic exponents, the bifurcation diagram, and the shape of the attractor in the phase space to show that both laser's minimal universal model and its jerk equations in z are topologically equivalent. In general, given a nonlinear system of order n and considered one of its n state variables, say variable x_i, there is no guarantee that it can be rewritten in the equivalent form:

$$\frac{d^n x_i}{dt^n} = f\left(\frac{d^{(n-1)}x_i}{dt^{n-1}}, \frac{d^{(n-2)}x_i}{dt^{n-2}}, \ldots, x_i\right). \tag{1}$$

Although Xu and Cao [26] have proposed a scheme to implement the jerk form of the Chua system family using a controllable canonical form applied in linear systems, it does not seem (to our knowledge) that this scheme has been used for more general system such as laser's minimal universal model. So, we will follow in this work the method used by Buscarino et al. [2]. Thus, when it is possible to derive a jerk equation, the state space normal form of the system can be also written as follows:

$$\begin{aligned}
\frac{d\tilde{x}_1}{dt} &= \tilde{x}_2, \\
\frac{d\tilde{x}_2}{dt} &= \tilde{x}_3, \\
&\vdots \\
\frac{d\tilde{x}_n}{dt} &= f\left(\tilde{x}_1, \tilde{x}_2, \ldots, \tilde{x}_{n-1}\right),
\end{aligned} \tag{2}$$

with $\tilde{x}_1 = x_i$.

3 Lorenz Model

The purpose of the model established by Edward Lorenz [13] was in the beginning to analyze the unpredictable behavior of weather. After having developed nonlinear partial derivative equations starting from the thermal equation and Navier-Stokes equations, Lorenz truncated them to retain only three modes. The most widespread form of the Lorenz model is as follows:

$$\begin{aligned} \frac{dx}{dt} &= \sigma\,(y-x)\,, \\ \frac{dy}{dt} &= -xz + rx - y, \\ \frac{dz}{dt} &= xy - \beta z, \end{aligned} \tag{3}$$

where parameters represent respectively the Prandtl number (σ), the Rayleigh number (r), and the aspect ratio of the convection cylinders (β). In this study, we will use the following parameter values: $(\sigma, r, \beta) = (10, 28, 8/3)$. With this parameter set, numerical integration of Lorenz model (3) has led to the famous strange attractor in the shape of a butterfly (see Figs. 1a,c). Dynamics features of the Lorenz model have been completely analyzed for many years in many works, the most famous of which being that of Sparrow [16]. Lorenz model (3) has three *fixed points*:

$$\begin{aligned} O\,(0,0,0)\,, \quad I\left(-\sqrt{\beta(r-1)}, -\sqrt{\beta(r-1)}, r-1\right), \\ J\left(\sqrt{\beta(r-1)}, \sqrt{\beta(r-1)}, r-1\right), \end{aligned} \tag{4}$$

With this parameter set, eigenvalues corresponding to each of these fixed points are the following:

$$\begin{aligned} &(-22.8277, -8/3, 11.8277)\,, \\ &(-13.8546, 0.09395 - 10.1945, 0.09395 + 10.1945i)\,, \\ &(-13.8546, 0.09395 - 10.1945, 0.09395 + 10.1945i)\,. \end{aligned} \tag{5}$$

Thus, the origin O is a *saddle-node*, while I and J are *saddle-foci*. Then, according to Sparrow [16], a Hopf bifurcation [1, 7, 10, 12] occurs when the parameter r reaches the value:

$$r_H = \sigma \frac{\sigma + \beta + 3}{\sigma - \beta - 1} \tag{6}$$

With the original parameter set, i.e., with $\sigma = 10$ and $\beta = 8/3$, Sparrow [16] finds: $r_H = 470/19 \approx 24.74$. In order to complete the analysis of the

effects of the control parameter, value r changes on the topology of the attractor of the Lorenz model (3); the bifurcation diagram has been built and plotted in Fig. 2a for $r \in [20, 80]$. Then, by using the Lyapunov Exponents Toolbox (LET) developed by Steve Siu for MatLab® and involving the two algorithms proposed by Wolf et al. [25] and Eckmann and Ruelle [3] (see https://fr.mathworks.com/matlabcentral/fileexchange/233-let), we have obtained for this parameter set the following Lyapunov characteristic exponents (LCEs) for the Lorenz model:

$$(+0.906, 0, -14.572) \tag{7}$$

The Kaplan-Yorke conjecture [8] enabling to estimate the *fractal dimension* of a strange attractor is then equal to $d_{KY} \approx 2.062$. Thus, according to the classification of Klein and Baier [9] for (autonomous) continuous-time attractors of dynamical system, such LCEs (7) confirm the chaotic feature of the so-called Lorenz butterfly.

4 Lorenz Jerk System

Starting from the first equation of Lorenz model (3), we obtain:

$$y = \frac{\dot{x}}{\sigma} + x. \tag{8}$$

It follows that:

$$\dot{y} = \frac{\ddot{x}}{\sigma} + \dot{x}. \tag{9}$$

From the second equation of (3), we deduce that:

$$z = r - \frac{y + \dot{y}}{x}. \tag{10}$$

By replacing in this Eq. (10), y and $\dot{y}$ by their above expressions Eqs. (8 and 9), we have:

$$z = r - 1 - \frac{1}{\sigma x}\left[\ddot{x} + (\sigma + 1)\,\dot{x}\right]. \tag{11}$$

By taking the time derivative of Eq. (11), we find:

$$\dot{z} = \frac{\dot{x}}{\sigma x^2}\left[\ddot{x} + (\sigma + 1)\,\dot{x}\right] - \frac{1}{\sigma x}\left[\dddot{x} + (\sigma + 1)\,\ddot{x}\right]. \tag{12}$$

Then, by replacing equation (12) in the third equation of (3), we obtain finally:

$$\dddot{x} = -(\sigma+1)\,\ddot{x} + [\ddot{x} + (\sigma+1)\,\dot{x}]\,\frac{\dot{x}}{x} + \beta\,(r-1)\,\sigma x - \beta\,[\ddot{x} + (\sigma+1)\,\dot{x}] - x^2\,(\dot{x} + \sigma x)\,. \tag{13}$$

Then, the jerk form in x is obtained by posing:

$$\dot{x} = y, \quad \ddot{x} = z, \quad \dddot{x} = f(x, \dot{x}, \ddot{x})\,. \tag{14}$$

Considering the Lorenz model (3), we obtain the dynamics of the jerk system:

$$\begin{aligned} \frac{dx}{dt} &= y, \\ \frac{dy}{dt} &= z, \\ \frac{dz}{dt} &= \beta\,(r-1)\,\sigma x - \beta\,(\sigma+1)\,y - (\beta+\sigma+1)\,z \\ &\quad + [z + (\sigma+1)\,y]\,\frac{y}{x} - x^2\,(\sigma x + y)\,, \end{aligned} \tag{15}$$

Remark 1 Let's notice that Eq. (13) is identical to that obtained by Linz [11] (see his equation (18)), except for the fact that he has posed for unknown reasons $\dot{x}/x = \ln x$ and used a "Cole-Hopf-like transformation" to express his jerk equation. Thus, his resulting third-order nonlinear differential equation (20) contains exponential functions which preclude any mathematical analysis and made difficult numerical investigations.

Equations (15) represent in different state space representations Lorenz model (3) and thus maintain its same structural properties. The three-dimensional attractors for the previously defined parameters and for $(\sigma, r, \beta) = (10, 28, 8/3)$ are reported in the following figures. The original Lorenz model chaotic attractor is reported in Figs. 1a,c, and the attractor of the equivalent jerk system represented by Eqs. (15) is reported in Figs. 1b,d.

In order to state the topological equivalence between the original representation of the Lorenz model (3) and its jerk form in x (15), we have performed a stability analysis including the fixed points stability, the occurrence of Hopf bifurcation, the representation of the bifurcation diagram, and the computation of the Lyapunov characteristic exponents for the jerk form in x (15) that we have compared to the stability analysis of the Lorenz model (3).

By using the classical nullclines method, it can be shown that the Lorenz jerk system (15) admits exactly the same fixed points (4) as the Lorenz model (3). With this parameter set, we have verified that both eigenvalues corresponding to the fixed points I and J are exactly the same as the Lorenz model (3) but are different for the origin O which is a saddle-focus $(5.99248, -9.32958 \pm 5.57737i)$ for the Lorenz jerk system (15). We have also verified that a Hopf bifurcation occurs for the same

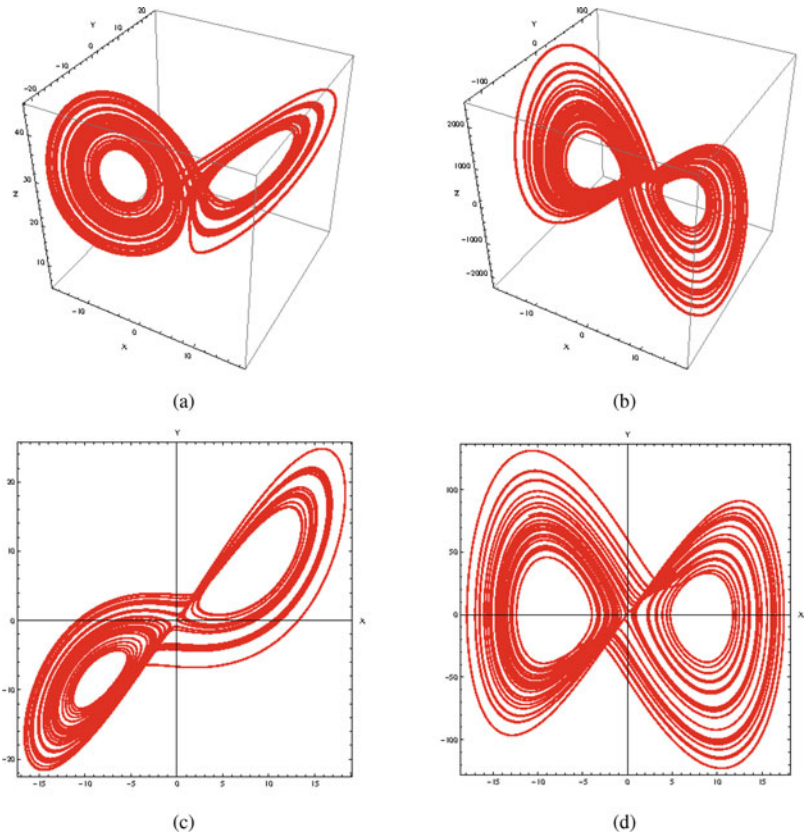

Fig. 1 Phase portraits of the Lorenz model (3) (left) and of its jerk form in x (15) (right)

value of parameter r (6). Then, in the next two Figs. 2a,b, we have plotted both bifurcation diagrams of the Lorenz model (3) and its corresponding jerk form (15). Figures 2a,b clearly demonstrate the equivalence of the two representations.

Finally, still using the Lyapunov Exponents Toolbox (LET) developed by Steve Siu for MatLab®, we have obtained for this parameter set exactly the same Lyapunov characteristic exponents (LCEs) as for the Lorenz model (7) and, of course, the same Kaplan-Yorke *fractal dimension* for the strange attractor of the Lorenz jerk system (15).

5 Discussion

In this paper, the jerk form in x of the Lorenz model has been derived following the method of *linear combinations* used by Buscarino et al. [2]. Then, a stability

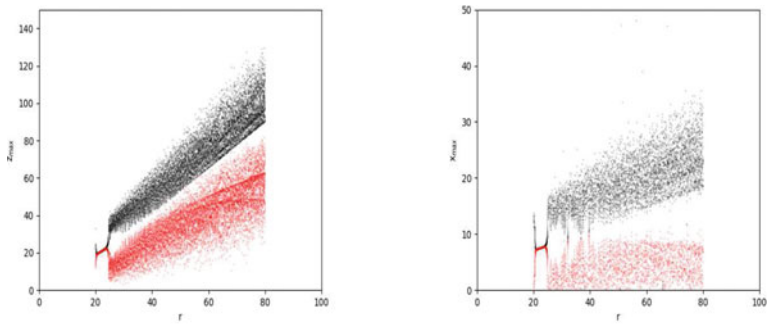

Fig. 2 Bifurcation diagrams of the Lorenz model (3) (left) and of its jerk form in x (15) (right)

analysis of the jerk dynamics of Lorenz model proves that fixed points and their stability, eigenvalues, Lyapunov characteristic exponents, and of course attractor shape are exactly the same as those of the original Lorenz model, the only difference being the range of values of the y and z variables which is increased respectively by a factor 5 for y and 50 for z as also highlighted on the above bifurcation diagrams (see Fig. 2a,b). Recently, Xu and Cao [26] proposed to use the so-called controllable canonical form to provide all the jerk form dynamics of Chua's circuit. So, two perspectives could be given to this work. The first would be to verify if the jerk form in x of the Lorenz model can be also obtained by making use of the controllable canonical form. The second would be an electronic realization of the jerk dynamics of Lorenz model. Concerning implications and applications of such results, let's recall that in a previous publication [4], by using the *flow curvature method*, we have been able to state a link between the *curvature* and *energy* of planar generalized Liénard systems. This has been made possible because this kind of system of two ordinary differential equations of order one can be transformed into a nonlinear second-order ordinary differential equation. The transformation of systems of three ordinary differential equations of order one into a third-order ordinary differential equation, i.e., a jerk equation, thus enables to open some promising developments for assessing the energy of nonlinear and chaotic three-dimensional dynamical systems.

References

1. Andronov, A., Leontovich, E., Gordon, I., Maier, A.: Theory of Bifurcations of Dynamical Systems on a Plane. Israel Program for Scientific Translations, Jerusalem (1971)
2. Buscarino, A., Fortuna, L., Frasca, M.: The Jerk dynamics of Chua's circuit. Int. J. Bifurcation Chaos **24**(06), 1450085 (2014)
3. Eckmann, J.P., Ruelle, D.: Ergodic theory of chaos and strange attractors. Rev. Mod. Phys. **57**, 617–656 (1985)

4. Ginoux, J.M., Lebiedz, D., Meucci, R., Llibre, J.: Flow curvature manifold and energy of generalized Liénard systems. Chaos Solitons Fractals **161**, 112354 (2022)
5. Gottlieb, H.P.W.: Question 38. What is the simplest jerk function that gives chaos? Amer. J. Phys. **64**, 525 (1996)
6. Haag, M.: Note sur les relations entre les éléments caractéristiques d'une courbe gauche et les accélérations du point qui la décrit. Bull. Soc. Math. Fran. **7**, 140–143 (1879)
7. Hopf, E.: Abzweigung einer periodischen Lösung von einer stationären Lösung eines Differentialsystems. In: Berichte der MathematischPhysikalischen Klasse der Sächsischen Akademie der Wissenschaften zu Leipzig, Band XCIV, Sitzung vom 19. Januar 1942, (1942), pp. 3–22. See L. N. Howard and N. Kopell, A Translation of Hopf's Original Paper, pp. 163–193 and Editorial Comments, pp. 194–205 in J. Marsden and M. McCracken
8. Kaplan, J., Yorke, J.A.: Chaotic behavior of multidimensional difference equations. In: Functional Differential Equations and Approximation of Fixed Points. Lecture Notes in Mathematics, vol. 730. Berlin, Springer (1979), pp. 204–227
9. Klein, M., Baier, G.: Hierarchies of dynamical systems. In: Baier, G., Klein, M. (eds.) A Chaotic Hierarchy. World Scientific, Singapore (1991)
10. Kuznetsov, Y.A.: Elements of Applied Bifurcation Theory. Springer, Berlin (1998)
11. Linz, S.J.: Nonlinear dynamical models and jerky motion. Am. J. Phys. **65**, 523–526 (1997)
12. Marsden, J.E., McCracken, M.: The Hopf Bifurcation and Its Applications. Springer, New York (1976)
13. Lorenz, E.N.: Deterministic nonperiodic flow. J. Atmos. Sci. **20**(7), 130–141 (1963)
14. Poincaré, H.: Science and Method. Thomas Nelson & Sons, London, Edinburgh, Dublin & New York (1914). (Translated from the first French edition: Science et Méthode, Ernest Flammarion, Paris, 1908)
15. Schot, H.S.: Jerk: the time rate of change of acceleration. Am. J. Phys. **46**, 1090–1094 (1978)
16. Sparrow, C.: The Lorenz Equations: Bifurcations, Chaos, and Strange Attractors. Springer, New York (1982)
17. Sprott, J.C.: Some simple chaotic flows. Phys. Rev. E **50**(2), R647–R650 (1994)
18. Sprott, J.C.: Some simple chaotic jerk functions. Am. J. Phys. **65**(6), 535–543 (1997)
19. Sprott, J.C.: A new class of chaotic circuits. Phys. Lett. A **266**, 19–23 (2000)
20. Sprott, J.C.: Simple chaotic systems and circuits. Am. J. Phys. **68**(8), 758–763 (2000)
21. Sprott, J.C.: Chaos and Time-Series Analysis, Oxford University Press, Oxford (2003)
22. Sprott, J.C.: Simplifications of the Lorenz attractor. Nonlinear Dyn. Psychol. Life Sci. **13**(3), 271–278 (2009)
23. Sprott, J.C.: Elegant Chaos: Algebraically Simple Chaotic Flows. World Scientific, Singapore (2010)
24. Sprott, J.C.: A new chaotic jerk circuit. IEEE Trans. Circ. Syst.-II: Exp. Briefs **58**, 240–243 (2011)
25. Wolf, A., Swift, J.B., Swinney, H.L., Vastano, J.A.: Determining Lyapunov exponents from a time series. Phys. D **16**, 285–317 (1985)
26. Xu, W., Cao, N.: Jerk forms dynamics of a Chua's family and their new unified circuit implementation. IET Circuits Devices Syst. **15**, 755–771 (2020)

Spiral Bevel Gears Nonlinear Dynamics: Chaotic Response Existence in Multi Degree of Freedom Systems

Moslem Molaie, Farhad S. Samani, Giovanni Iarriccio, Antonio Zippo, and Francesco Pellicano

List of Symbols

a_j, b_j	Fourier coefficients
b	Half of the gear backlash
C_m	Damping coefficient between the mesh gear teeth of the pairs
C_t^g	Material damping of the gear shaft
C_t^p	Material damping of the pinion shaft
$e(t)$	Time-varying circumferential no-load transmission error
F_n	The normal dynamic load for the driven gear
F_z	The Z-component of the normal dynamic load for the driven gear
G	Shear modulus of steel
I_p^x, I_g^y	Rotary inertia of pinion and gear
J	The second polar moment of shaft area
k_0	Average value of torsional MS of the gear pair
$K_m(t)$	The torsional MS of the gear pair
K_t^p	Rotational shaft stiffness of the pinion
K_t^g	Rotational shaft stiffness of the gear
m_{eq}	Equivalent mass
N_p, N_g	Teeth number of the pinion and gear
N_1	Number of samples for MS computation

M. Molaie (✉)
Department of Engineering "Enzo Ferrari", University of Modena and Reggio Emilia, Modena, Italy
e-mail: Moslem_molaie@unimore.it

F. S. Samani
Department of Engineering "Enzo Ferrari", University of Modena and Reggio Emilia, Modena, Italy
Department of Mechanical Engineering, Shahid Bahonar University of Kerman, Kerman, Iran

G. Iarriccio · A. Zippo · F. Pellicano
Department of Engineering "Enzo Ferrari", Centre InterMech MoRe, University of Modena and Reggio Emilia, Modena, Italy

© The Author(s), under exclusive license to Springer Nature Switzerland AG 2024

W. Lacarbonara (ed.), *Advances in Nonlinear Dynamics, Volume III*, NODYCON Conference Proceedings Series, https://doi.org/10.1007/978-3-031-50635-2_13

r_g	Mean radius at meshing point with respect to the gear
r_p	Mean radius at meshing point with respect to the pinion
S	Number of harmonics
T_m	Constant motor torque
T_l	Constant load torque
α	Normal pressure angle
β	The spiral angle
γ_s	Input shaft speed
ξ	Damping ratio
θ_g	Gear angular displacement
φ_p	Pinion angular displacement
θ_l	Load angular displacement
φ_m	Motor angular displacement
λ	Dynamic transmission error
τ	Non dimensional parameter for time
ω_m	Mesh frequency
ω_n	Natural mesh frequency

1 Introduction

Bevel gears are used for power transmission systems with limited space. Without bevel gears, the drive motor, gearbox, and driven equipment would locate in a linear position; consequently, the total space of the driving equipment would increase. For high-speed gearboxes, it is essential to use spiral bevel gears (SBGs) instead of straight bevel gears due to the high level of vibration magnitude. Bevel gears are applicable in different engineering fields, e.g., aerospace, terrestrial vehicles, and in heavy industries, wherever it is required to transmit a high load between nonparallel shafts [1, 2].

Li and Hu studied the dynamic analysis of a spiral bevel-geared rotor-bearing system [3]. The equation correlating the relationship between the generalized displacements of SBG pairs is derived and modeling of coupled axial–lateral–torsional vibration of the rotor system geared by SBGs is discussed in their research. An 8-DOF nonlinear dynamic model of an SBG pair, which involves time-varying mess stiffness, transmission error, backlash, and asymmetric mesh stiffness (MS) was investigated by Yinong et al. [4]. A 14-DOF nonlinear coupled vibration model was established by Jinli in 2016 [5] by employing the lumped mass method. Moreover, the engine's torque ripple, the alternating load from the universal joint, and the time-varying mesh parameters of the hypoid gear of the shaft-final drive system were also considered for accurate quantitative analysis. In Ref. [6], Samani et al. investigated the nonlinear vibration of the SBG with a novel tooth surface modification. However, they showed that the considered higher order transmission error method is not able to decrease the vibration level for the investigated frequency range. The effectiveness of squeeze film dampers for passive vibration control of SBGs was evaluated by Chen et al., [7]. Similarly, the radial and axial misalignments effects on the nonlinear response of SBG vibration were investigated by Molaie et

al. in Ref. [8]. Their results show that the spiral bevel gear with axial misalignment is more destructive compared to the cases with radial misalignment and the case with a combination of radial and axial misalignment. Nonlinear vibration of SBGs with periodic torque excitation and elastic bearing supports are considered in Ref. [9]. Cao et al. [10] studied the practical cases; the dynamics of SBGs of a helicopter's intermediate reducer with vibration error and lubrication was studied. They showed that the contact stiffness, when considering the oil film stiffness, reduced by 17.7% compared to the case without the effect of the oil film; moreover, the vibration amplitude increased by 18.5% with respect to the commercial software.

The main objective of the present paper is to delve into the influence of increasing the degree of freedom on chaos response by involving the rotational shaft stiffness of an SBG set that is used in the helicopter's transmission system. An accurate static analysis is done to obtain the system's MS by means of Transmission3D-Calyx, a finite element method-based software. Due to the mismatch between the teeth surfaces of the gear and the pinion, loaded tooth contact analysis (LTCA) and unloaded tooth contact analysis (UTCA) is conducted in both directions: forward and reverse motions. The governing equations are derived for the nonlinear and time-dependent system considering the possibility of backside contact. The dynamic behavior of the system is analyzed through the RMS and the bifurcation diagram. A comparison between the system with 2 DOF and the case with 4 DOF is carried out to show the influence of load and motor DOFs consideration, especially on the chaotic responses.

2 Dynamic model

Consider the spiral bevel gear pair of Fig. 1, the translational degrees of freedom for both driver and driven gears are constrained in all directions, as well as the rotations; the gears can rotate only around their axes. By considering the shaft rotational stiffness, the dynamic model becomes a 4-DOF system: two rotational DOF for the pinion and the gear, and two degrees of freedom for the load and the motor rotations. Table 1 presents the design parameters of the gear pair.

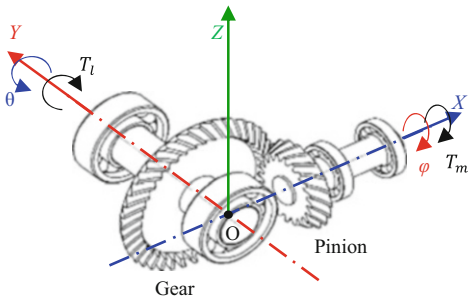

Fig. 1 The dynamic model of the gear system with rotational degrees of freedom

Table 1 Numerical parameters of the gear pair [1]

N_p and N_g, respectively	12	36
Face width, w [mm]	25.4	
Pressure angle, α	20°	
Mean spiral angle	35°	
Pinion teeth direction	Left-hand	
Shaft angle	90 Deg	
Pinion speed [rpm]	100	
Module [mm]	4.941	
Damping ratio, ξ [11]	0.01	
Material damping of shaft [N·s·m]	60	
Maximum shear stress [MPa]	50	
Shear modulus of steel [GPa]	77	
Input torque [N·m],	179.04	
Considered shaft parameter, $\frac{l}{d}$	5	
Motor inertia [kg•m^2]	1.49×10^{-5}	

Based on the Lagrange equation of motion, the dynamic equations of this system (see Figs. 1 and 4) are given by:

– In the "θ" direction for the gear:

$$I_g^y \ddot{\theta}_g = -r_g F_z - K_t^g \left(\theta_g - \theta_l\right) - C_t^g \left(\dot{\theta}_g - \dot{\theta}_l\right) \text{ where } K_t^g = \frac{G \cdot J}{l} \tag{1}$$

– In the "φ" direction for the pinion:

$$I_p^x \ddot{\varphi}_p = r_p F_z - K_t^p \left(\varphi_p - \varphi_m\right) - C_t^p \left(\dot{\varphi}_p - \dot{\varphi}_m\right) \text{where } K_t^p = \frac{G \cdot J}{l} \tag{2}$$

– In the "φ_{m}" and "θ_l" directions for the motor and load:

$$I_m \ddot{\varphi}_m = T_m - K_t^p \left(\varphi_m - \varphi_p\right) - C_t^p \left(\dot{\varphi}_m - \dot{\varphi}_p\right) \tag{3}$$

$$I_l \ddot{\theta}_l = -T_l - K_t^g \left(\theta_l - \theta_g\right) - C_t^g \left(\dot{\theta}_l - \dot{\theta}_g\right) \tag{4}$$

where, G is the shear modulus, and J is the second polar moment of shaft area, and C_t^p and C_t^g are material damping of the pinion and gear shafts. Due to mounting, manufacturing error, or teeth profile modifications, a local gap between mating teeth can appear, called geometric transmission error (GTE), $e(t)$; it can be calculated using UTCA. The linear dynamic transmission error (DTE) along the line of action is defined as:

$$\lambda = \left(r_p \varphi_p - r_g \theta_g\right) a \tag{5}$$

where

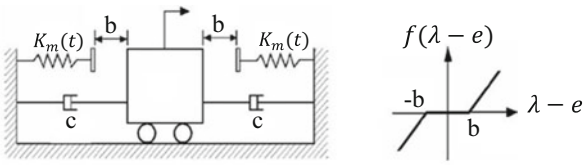

Fig. 2 Equivalent gear model and backlash function

$$a = \cos\alpha.\cos\beta;\ e(t) = \sum_{j=1}^{s} e_j \cos(j\omega_m t) \tag{6}$$

β is the spiral angle and α is the normal pressure angle.

The dynamic load of the pinion and its components along the line of action, F_n and along the $z-$axis F_z, can be calculated as:

$$F_z = -F_n a; \qquad F_n = K_m(t) f(\lambda - e) + C_m\left(\dot{\lambda} - \dot{e}\right) \tag{7}$$

where

$$f(\lambda - e) = \begin{cases} \lambda + b - e, & \lambda - e > b \\ 0, & -b \le \lambda - e \le b \\ \lambda - b - e, & \lambda - e < -b \end{cases} \tag{8}$$

$f(\lambda - e)$ is the function of the linear displacement (Fig. 2). This function with the multiplication of stiffness returns the restoring force function [6]. Whenever $\lambda - e$ is between $-b$ and $+b$, the contact loss happens (single-sided impact) [12, 13]. For $\lambda - e > b$, the mesh is expected to be in the forward contact (desired situation), while if $\lambda - e < -b$, undesired backside contact happens (double-sided impact); see Ref. [13].

The meshing stiffness of the gear pair is a time-varying periodic function, with the mesh frequency,$\omega_m = \frac{2\pi}{60} N_p \gamma_s$; the equivalent meshing stiffness Fourier series is given by:

$$\begin{cases} \omega_m = \frac{2\pi}{60} N_p \gamma_s \\ s = (N_1 - 1)/2 \end{cases} \quad \Rightarrow \quad K_m(t) = k_0 + \sum_{j=1}^{S} a_j \cos(j\omega_m t) + \sum_{j=1}^{S} b_j \sin(j\omega_m t) \tag{9}$$

From the pure elastic deformation obtained from the LTCA and UTCA, the meshing stiffness for both direction of motions is extracted (see Fig. 3); moreover, the geometric transmission error is regarded as the one mentioned in Ref. [1] (Fig. 4).

In order to normalize the governing equation, new parameters are introduced as follows:

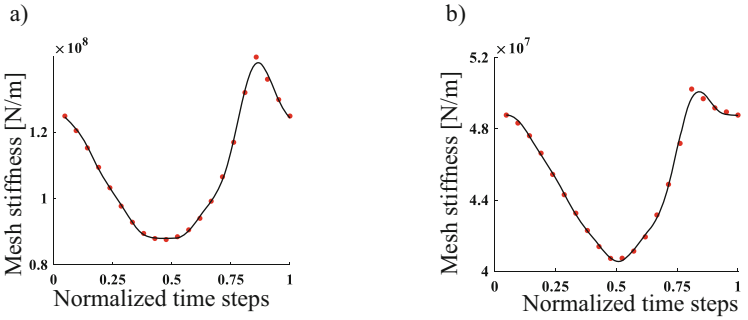

Fig. 3 MS diagram: (**a**) Forward motion, (**b**) Reverse motion; ♥ Fitted curve by Fourier series, ● FEM results

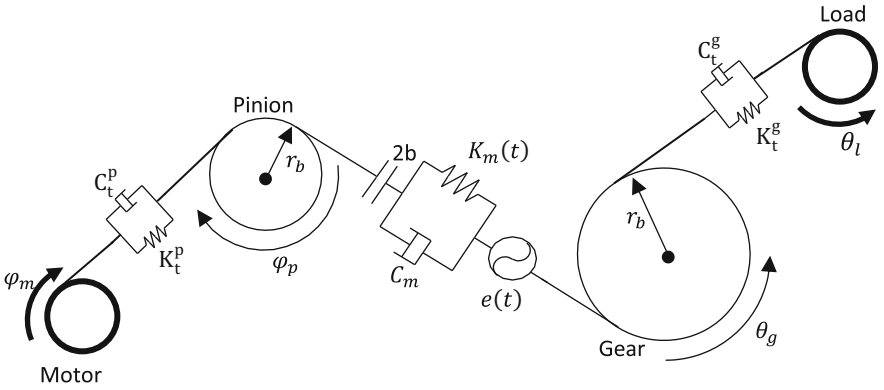

Fig. 4 Dynamic model of gear system with four DOF

$$\begin{aligned} \tau &= \omega_n t & \ddot{\theta} &= \omega_n^2 \theta'' \quad \dot{\theta} = \omega_n \theta' \\ \omega_n &= \sqrt{K_0/m_{\text{eq}}} & \ddot{\varphi} &= \omega_n^2 \varphi'' \quad \dot{\varphi} = \omega_n \varphi' \\ \omega_m &= 2\pi N_p \gamma_p / 60 & \overline{r}_p &= r_p/b \quad \overline{r}_g = r_g/b \\ \xi &= \frac{C_m}{2m_{\text{eq}}\omega_n} & m_{eq} &= \left(\frac{(r_p a)^2}{I_p^x} + \frac{(r_g a)^2}{I_g^y} \right)^{-1} \end{aligned} \tag{10}$$

Consequently, Eqs. (1, 2, 3, and 4) can be rewritten as follows:

$$f\left(\overline{\lambda} - \overline{e}\right) = \begin{cases} \overline{\lambda} - \overline{e} + 1, & \overline{\lambda} - \overline{e} > 1 \\ 0, & -1 \le \overline{\lambda} - \overline{e} \le 1 \\ \overline{\lambda} - \overline{e} - 1, & \overline{\lambda} - \overline{e} < -1 \end{cases} \tag{11}$$

$$\overline{K}_m(\tau) = 1 + \sum_{j=1}^{S} \frac{a_j}{m_{\text{eq}}{\omega_n}^2} \cos(j\omega_m \tau) + \sum_{j=1}^{S} \frac{b_j}{m_{\text{eq}}{\omega_n}^2} \sin(j\omega_m \tau) \tag{12}$$

$$\theta_g'' = \frac{m_{\text{eq}} b r_g a_3}{I_g^y}\left(\overline{K}_m(t) f\left(\overline{\lambda}\right) + 2\xi\overline{\lambda}'\right) + \overline{K}_t^g\left(\theta_l - \theta_g\right) + 2\overline{C}_t^g\left(\theta_l' - \theta_g'\right) \tag{13}$$

$$\overline{K}_t^g = \frac{K_t^g}{I_g^y \omega_n^2} \quad \overline{C}_t^g = \frac{C_t^g}{2 I_g^y \omega_n} \tag{14}$$

$$\varphi_p'' = \overline{K}_t^p\left(\varphi_m - \varphi_p\right) + 2\overline{C}_t^p\left(\varphi_m' - \varphi_p'\right) - \frac{m_{\text{eq}} b r_p a_3}{I_p^x}\left(\overline{K}_m(t) f\left(\overline{\lambda}\right) + 2\xi\overline{\lambda}'\right) \tag{15}$$

$$\overline{K}_t^p = \frac{K_t^p}{I_p^x \omega_n^2} \quad \overline{C}_t^p = \frac{C_t^p}{2 I_p^x \omega_n} \tag{16}$$

$$\varphi_m'' = \overline{T}_m + \overline{K}_t^m\left(\varphi_p - \varphi_m\right) + 2\overline{C}_t^m\left(\varphi_p' - \varphi_m'\right) \tag{17}$$

$$\overline{K}_t^m = \frac{K_t^p}{I_m \omega_n^2} \quad \overline{C}_t^m = \frac{C_t^p}{2 I_m \omega_n} \quad \overline{T}_m = \frac{T_m}{I_m \omega_n^2} \tag{18}$$

$$\theta_l'' = \overline{K}_t^l\left(\theta_g - \theta_l\right) + 2\overline{C}_t^l\left(\theta_g' - \theta_l'\right) - \overline{T}_l \tag{19}$$

$$\overline{K}_t^l = \frac{K_t^g}{I_l \omega_n^2} \quad \overline{C}_t^l = \frac{C_t^g}{2 I_l \omega_n} \quad \overline{T}_l = \frac{T_l}{I_l \omega_n^2} \tag{20}$$

The load rotational vibration θ_l is constrained to zero on the assumption that there is large output inertia (as is common); consequently, the rigid body mode is removed [14, 15]. Eqs. (13, 15, 17, and 19) are nonlinear differential equations with time-varying parameters. This equation is solved numerically based on an implicit fifth-order Runge-Kutta scheme (*RADAU*) coded in FORTRAN language; the algorithm is extremely stable and accurate, see e.g., Refs. [6, 16, 17]. Figure 5 represents the comparison of the developed code with experimental data [18] for single degree of freedom of spur gear model which is similar to the SBG dynamic model with single degree of freedom.

3 Numerical results

The time-varying coefficients besides the external torque excite the SBG system. The final solution is divided into two main parts: transient and steady-state responses. To analyze the dynamic behavior of the system, the transient part must

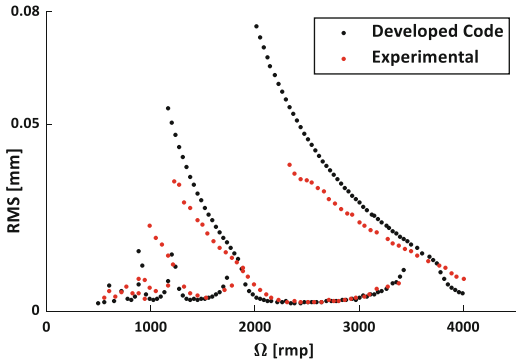

Fig. 5 Comparison between numerical simulation and experimental data from Ref. [18]

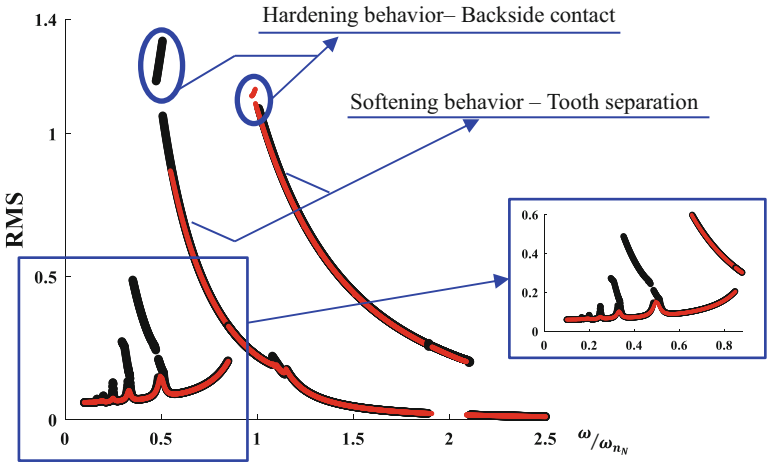

Fig. 6 RMS diagram, comparison between system with 2 DOF (•), and 4 DOF (●)

be skipped; therefore, the first 1000 periods are not recorded. The time history responses are utilized to plot the RMS and bifurcation diagrams by varying the excitation frequency, which is the pinion rotation speed.

Figure 6 represents the dynamic behavior, RMS, of the system with 2 DOF and 4 DOF. It should be noted that black dots indicate the responses of the system with 2 DOF and the red dots show the responses of the system with 4 DOF. Let us compare the responses of the 2-DOF system with the 4-DOF system; the main differences are found at low frequency and also at frequencies where the system experiences backside contact. At low frequencies, two main jumping phenomena occurred in the system with the 2 DOF due to the second and third super-harmonic of the meshing stiffness, i.e., $\frac{\omega_m}{\omega_n} \approx 0.34$ and $\frac{\omega_m}{\omega_n} = 0.5$, respectively. By comparing the low-frequency responses in both cases, it is observed that the system with 4-DOF does not experience tooth separation phenomenon. but it does not happen.

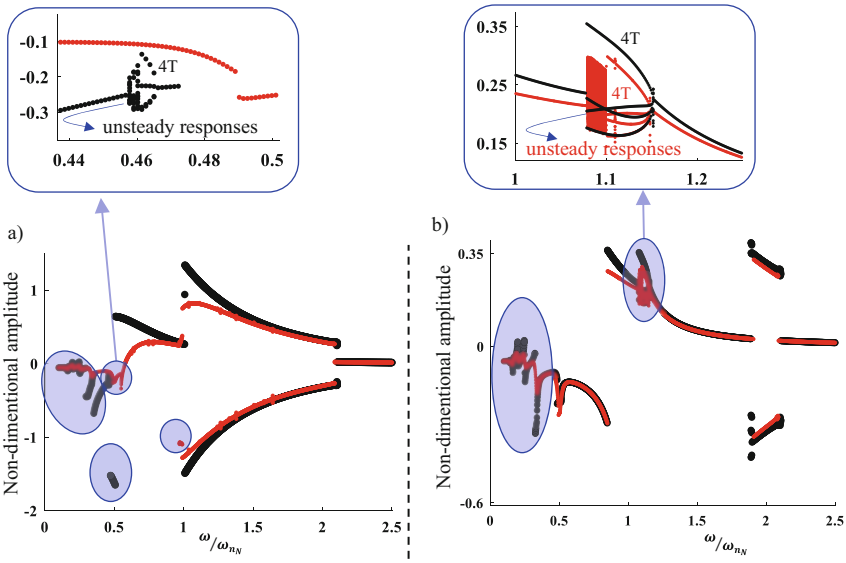

Fig. 7 Bifurcation diagram, comparison between system with 2 DOF (•), and 4 DOF (●): (**a**) backward simulation, (**b**) forward simulation

Both systems experience the main resonance close to $\frac{\omega_m}{\omega_n} = 1$, which is due to the fundamental harmonic; all resonances have a strong sub-harmonic character. Close to $\frac{\omega_m}{\omega_n} = 2$, an instability due to the principal parametric resonance is present; the parametric resonance branch shows a softening character due to loss of contact.

From the bifurcation diagram, the differences between the two systems, 2 DOF and 4 DOF, are highlighted in Fig. 7 for both backward and forward simulations (see Fig. 7a, b, respectively). The highlighted zone with the blue color specified the main differences between the two models.

4 Conclusion

This paper investigates the nonlinear dynamic behavior of a spiral bevel gear pair by analyzing the 2 DOF and 4 DOF vibrational models. Increasing the degree of freedom involves taking into account the rotational shaft stiffness. The first step of dynamic evaluation of system behavior is to calculate the accurate MS of the SBG set. To obtain the MS of the system, two different static simulations are carried out in forward and reverse rotational directions due to different teeth trace. The method to extract the MS results is Transmission3D-Calyx, an FEM-based software. The governing equations, which are nonlinear and time-dependent parametrically excited system, are solved by using an implicit Runge–Kutta algorithm.

The systems, regardless of the number of DOF, experienced three types of contact: drive-side contact, separation tooth, and undesirable backside contact. By comparing the response of the dynamic models with 2 DOF and 4 DOF, the dynamic behavior of the system altered. The vibration amplitude, RMS, with 2 DOF is higher than the system with 4 DOF at primary and super-harmonic frequency ratios. Besides, the maximum magnitude of vibration happens during backside contact. Vice versa, close to the primary resonance, the 4-DOF system represented chaotic response, while the 2-DOF system presents 4T harmonic response. At $\frac{\omega_m}{\omega_n} = 0.46$, the 2-DOF system presents chaotic response for a narrow range of frequency, while it is eliminated in the 4-DOF system.

References

1. Molaie, M., Samani, F.S., Zippo, A., Pellicano, F.: Spiral bevel gears: nonlinear dynamic model based on accurate static stiffness evaluation. J. Sound Vib. **544**, 117395 (2023)
2. Molaie, M., Zippo, A., Iarriccio, G., Bergamini, L., Pellicano, F.: Loaded and unloaded tooth contact analysis of spiral bevel gears in consideration of misalignments. Insight-Non-Destructive Test. Cond. Monitor. **64**(8), 442–446 (2022)
3. Li, M., Hu, H.: Dynamic analysis of a spiral bevel-geared rotor-bearing system. J. Sound Vib. **259**(3), 605–624 (2003)
4. Yinong, L., Guiyan, L., Shuen, Z.: Effect of asymmetric MS on vibration characteristics of spiral bevel gear transmission system. In: 2010 International Conference on Mechanic Automation and Control Engineering, pp. 2444–2447. IEEE, Wuhan (2010)
5. Jinli, X., Lei, W., Wenxin, L.: Influence of bearing stiffness on the nonlinear dynamics of a shaft-final drive system. Shock Vib. **2016** (2016)
6. Samani, F.S., Molaie, M., Pellicano, F.: Nonlinear vibration of the spiral bevel gear with a novel tooth surface modification method. Meccanica. **54**(7), 1071–1081 (2019)
7. Chen, W., Chen, S., Hu, Z., Tang, J., Li, H.: Dynamic analysis of a bevel gear system equipped with finite length squeeze film dampers for passive vibration control. Mech. Mach. Theory. **147**, 103779 (2020)
8. Molaie, M., Samani, F.S., Pellicano, F.: Spiral bevel gears nonlinear vibration having radial and axial misalignments effects. Vibration. **4**(3), 666–678 (2021)
9. Samani, F.S., Salajegheh, M., Molaie, M.: Nonlinear vibration of the spiral bevel gear under periodic torque considering multiple elastic deformation evaluations due to different bearing supports. SN Appl. Sci. **3**(9), 1–9 (2021)
10. Cao, X., Lu, F., Bao, H., Zhu, R.: Dynamic behavior analysis of spiral bevel gears of helicopter's intermediate reducer with vibration error and lubrication. Proc. Inst. Mech. Eng. Part K J. Multi-body Dyn. **236**(2), 291–307 (2022)
11. Blankenship, G., Kahraman, A.: Steady state forced response of a mechanical oscillator with combined parametric excitation and clearance type non-linearity. J. Sound Vib. **185**(5), 743–765 (1995)
12. Liu, G., Parker, R.G.: Nonlinear dynamics of idler gear systems. Nonlinear Dyn. **53**(4), 345–367 (2008)
13. Kahraman, A., Singh, R.: Non-linear dynamics of a spur gear pair. J. Sound Vib. **142**(1), 49–75 (1990)
14. Masoumi, A., Pellicano, F., Samani, F.S., Barbieri, M.: Symmetry breaking and chaos-induced imbalance in planetary gears. Nonlinear Dyn. **80**(1), 561–582 (2015)
15. Bahk, C.-J., Parker, R.G.: Analytical solution for the nonlinear dynamics of planetary gears. J. Comput. Nonlinear Dyn. **6**(2) (2011)

16. Molaie, M., Samani, F.S., Motahar, H.: Nonlinear vibration of crowned gear pairs considering the effect of Hertzian contact stiffness. SN Appl. Sci. **1**(5), 414 (2019)
17. Faggioni, M., Samani, F.S., Bertacchi, G., Pellicano, F.: Dynamic optimization of spur gears. Mech. Machine theory. **46**(4), 544–557 (2011)
18. Kahraman, A., Blankenship, G.: Experiments on nonlinear dynamic behaviour of an oscillator with clearance and periodically time-varying parameters. J. Appl. Mech. **64**, 217–226 (1997)

Coexistence of Hidden Attractor and Self-Excited Attractors on the Plane

Eric Campos-Cantón, R. de J. Escalante González, Hector E. Gilardi-Velázquez, and Guillermo Huerta-Cuellar

1 Introduction

Multistability is a phenomenon that refers to the coexistence of several possible eventual stable states for a given set of parameters. The final stable states converge to an attractor according to the given initial conditions. The phenomenon of multistability has been found in almost all areas of science and nature [1]. A pioneer study, which also coined the term multistability, was devoted to visual perception. Multistability has been identified in different classes of systems such as weakly dissipative systems, coupled systems, delayed feedback systems, parametrically excited systems, and stochastic systems [2].

There are three classes of attractors that can be generated in vector fields with or without equilibrium point. The first class is given by those classical attractors excited from unstable equilibria called *self-excited attractors* whose basin of attraction intersects at least a neighborhood of an equilibrium point, [3] and they are not difficult to find via numerical methods, and the second class is called *hidden*

E. Campos-Cantón (✉)
Division of Control and Dynamical Systems, Instituto Potosino de Investigacion Cientifica y Tecnologica, San Luis Potosí, Mexico
https://www.ipicyt.edu.mx/curricular/EricCamposCant%C3%B3n
e-mail: eric.campos@ipicyt.edu.mx

R. de J. Escalante González
Electrical, Electronic and Mechatronics Department, Technological Institute of San Luis Potosí, Soledad de Graciano Sánchez, San Luis Potosí, Mexico

H. E. Gilardi-Velázquez
Facultad de Ingeniería, Universidad Panamericana, Aguascalientes, Mexico

G. Huerta-Cuellar
Dynamical Systems Laboratory, Centro Universitario de los Lagos, Universidad de Guadalajara, Jalisco, Mexico

© The Author(s), under exclusive license to Springer Nature Switzerland AG 2024

W. Lacarbonara (ed.), *Advances in Nonlinear Dynamics, Volume III*, NODYCON Conference Proceedings Series, https://doi.org/10.1007/978-3-031-50635-2_14

attractors whose basin of attraction does not contain neighborhoods of equilibria. This type of attractor has been found by numerical methods and is sometimes not easy to find. The coexistence of a self-excited attractor and a hidden attractor was observed in Chua's circuit and reported in [4]. The last class is generated by vector fields without equilibria called *non-self-excited attractors* [5]. Notice that a non-self-excite attractor is given by a system without equilibria; therefore, it satisfies the definition of hidden attractors.

In multistability, two or more attractors coexist, and different multistability scenarios have been reported. For example, in [6], multistable behavior was generated via dissipative systems with unstable dynamics called the unstable dissipative systems. Then, in the aforementioned work, a PWL system was introduced, and the multistability of self-excited attractors was controlled through the linear part and a commutation function that depend on two parameters. The coexistence of hidden and self-excited attractors was given in [7], such that hidden attractors surround the self-excited attractors. The mechanism of generation consists of considering a vector field with an even number of equilibria, and then the self-excited attractor is generated by heteroclinic orbits and the hidden attractor is generated when the heteroclinic orbit is broken. In [8] multistability is studied by synchronization of coupled PWL systems, and the behavior is analyzed by Lyapunov functions of the different couplings and numerical simulations. In [9] in the same spirit as that of the previous work, multistability is found by coupled systems, jerk oscillators, and the theoretical analysis is carried out by using the PSpice simulation software. Recently, coexistence of attractors has been studied in the presence of noise. The approach considers intermittent noise to control the behavior of the system in a particular region of the state space [10]. The main result of this work is that the approach annihilates undesired attractors to control multistability.

Recently, in [11] a class of continuous time dynamical planar system was introduced and is generated by using hysteresis and at least two unstable foci. This class of system shows stretching and folding behavior due to hysteresis. In the same spirit as [11], we derive a class of planar systems through a three-dimensional piecewise linear (PWL) systems that have two manifolds, one stable and the other unstable, to generate heteroclinic chaos. Then, we present an approach to generate self-excited and hidden multiscroll attractors by defining a vector field on R^2 with an even number of equilibria. The vector field is defined by affine linear systems such that each equilibrium point is an unstable focus point. So the space is partitioned in hyperbolic set. We start by generating a self-excited multiscroll attractor based on heteroclinic orbits. Interesting phenomena appear when the equilibria are separated by pairs; firstly, the system presents only one basin of attraction which is divided accordingly with the separation of the equilibria, and the coexistence of different self-exited double-scroll attractors arises. At a certain separation of equilibria, a hidden multiscroll attractor emerges.

The rest of the manuscript is organized as follows: In Sect. 2, a dynamical system in R^3 is given to generate a four-scroll attractor. In Sect. 3, a planar system is derived. In Sect. 4, results of multistability are given. Lastly, conclusion is presented in Sect. 5.

2 PWL System in R^3

Consider a partition of the space $P = \{P_1, P_2, P_3, P_4\}$ where a PWL system is given as follows:

$$\dot{\mathbf{x}} = A\mathbf{x} + Bf(\mathbf{x}), \tag{1}$$

where $\mathbf{x} = (x, y, z)^T$ is the state vector, A is a linear operator whose entries are given in direct relation to its eigenvalues γ and $\alpha \pm i\beta$ as follows:

$$A = \begin{pmatrix} \alpha & \frac{2\beta}{3} & \frac{2\beta}{3} \\ -\beta & \frac{2\alpha+\gamma}{3} & \frac{2(\alpha-\gamma)}{3} \\ -\frac{\beta}{2} & \frac{\alpha-\gamma}{3} & \frac{\alpha+2\gamma}{3} \end{pmatrix}, \tag{2}$$

and B is a constant vector that defines the equilibria through the y-axis at $\mathbf{x}^*_{eq_1} = (0, 3, 0)^T \in P_1$, $\mathbf{x}^*_{eq_2} = (0, 1, 0)^T \in P_2$, $\mathbf{x}^*_{eq_3} = (0, -1, 0)^T \in P_3$ and $\mathbf{x}^*_{eq_1} = (0, -3, 0)^T \in P_4$. Then the vector $-B$ is given by the second column of A as follows:

$$B = \begin{pmatrix} -\frac{2\beta}{3} \\ -\frac{2\alpha+\gamma}{3} \\ -\frac{\alpha-\gamma}{3} \end{pmatrix} \tag{3}$$

and the functional $f(\mathbf{x})$ is given by

$$f(\mathbf{x}) = \begin{cases} 3 & \text{if} \quad \mathbf{x} \in P_1, \\ 1 & \text{if} \quad \mathbf{x} \in P_2, \\ -1 & \text{if} \quad \mathbf{x} \in P_3, \\ -3 & \text{if} \quad \mathbf{x} \in P_4. \end{cases} \tag{4}$$

For $\alpha = 0.2$, $\beta = 5$, and $\gamma = -3$, the eigenvectors of A are

$$v_1 = \begin{pmatrix} 1 \\ 0 \\ 0 \end{pmatrix}, \; v_2 = \begin{pmatrix} 0 \\ 1 \\ \frac{1}{2} \end{pmatrix}, \; v_3 = \begin{pmatrix} 0 \\ -1 \\ 1 \end{pmatrix}. \tag{5}$$

The switching surfaces are given by

$$SW_{12} = \{\mathbf{x} \in R^3 : -2y + z = -4\},$$

$$SW_{23} = \{\mathbf{x} \in R^3 : -2y + z = 0\},$$
$$SW_{34} = \{\mathbf{x} \in R^3 : -2y + z = 4\}.$$

The atoms of the partition P are given as follows:

$$\begin{aligned}
P_1 &= \{\mathbf{x} \in R^3 : -2y + z < -4\} \cup SW_{12}^{+}, \\
P_2 &= \{\mathbf{x} \in R^3 : -4 < -2y + z < 0\} \cup SW_{12}^{-} \cup SW_{23}^{+}, \\
P_3 &= \{\mathbf{x} \in R^3 : 0 < -2y + z < 4\} \cup SW_{23}^{-} \cup SW_{34}^{+}, \\
P_4 &= \{\mathbf{x} \in R^3 : 4 < -2y + z\} \cup SW_{34}^{-}.
\end{aligned}$$

The semiplanes SW_{ij}^{+} are the elements of SW_{ij} with $z \geq 0$, and the semiplanes SW_{ij}^{-} are the elements of SW_{ij} with $z < 0$, with $i, j = 1, \ldots, 4$.

Proposition 1 *The hyperbolic system given by (1)–(4) generates six heteroclinic orbits.*

Proof The unstable and stable manifolds are given by

$$W^{u}_{\mathbf{x}^*_{eq_i}} = \{\mathbf{x} + \mathbf{x}^*_{eq_i} \in P_i : \mathbf{x} \in span\{v_1, v_2\}\}$$

and

$$W^{s}_{\mathbf{x}^*_{eq_i}} = \{\mathbf{x} + \mathbf{x}^*_{eq_i} \in P_i : \mathbf{x} \in span\{v_3\}\},$$

with $i = 1, \ldots, 4$. The intersections given by the closure of the unstable and stable varieties are at the points

$$W^{s}_{\mathbf{x}^*_{eq_1}} \cap cl(W^{u}_{\mathbf{x}^*_{eq_2}}) = (0, 7/3, 2/3)^T \in SW_{12}^{+}, \tag{6}$$
$$W^{s}_{\mathbf{x}^*_{eq_2}} \cap cl(W^{u}_{\mathbf{x}^*_{eq_1}}) = (0, 5/3, -2/3)^T \in SW_{12}^{-}, \tag{7}$$
$$W^{s}_{\mathbf{x}^*_{eq_2}} \cap cl(W^{u}_{\mathbf{x}^*_{eq_3}}) = (0, 1/3, 2/3)^T \in SW_{23}^{+}, \tag{8}$$
$$W^{s}_{\mathbf{x}^*_{eq_3}} \cap cl(W^{u}_{\mathbf{x}^*_{eq_2}}) = (0, -1/3, -2/3)^T \in SW_{23}^{-}, \tag{9}$$
$$W^{s}_{\mathbf{x}^*_{eq_3}} \cap cl(W^{u}_{\mathbf{x}^*_{eq_4}}) = (0, -5/3, 2/3)^T \in SW_{34}^{+}, \tag{10}$$
$$W^{s}_{\mathbf{x}^*_{eq_4}} \cap cl(W^{u}_{\mathbf{x}^*_{eq_3}}) = (0, -7/3, -2/3)^T \in SW_{34}^{-}. \tag{11}$$

Note that the intersection points belong to a stable manifold, and then the trajectories with initial condition in the intersection points given by (6)–(11) converge to an equilibrium point. The trajectory with initial condition $\mathbf{x_0} = (0, 7/3, 2/3)^T \in W^{s}_{\mathbf{x}^*_{eq_1}}$

converges to $\mathbf{x}^*_{eq_1}$; therefore, there is a set $\Gamma_1^s \subset W^s_{\mathbf{x}^*_{eq_1}}$ generated by $\varphi(\mathbf{x}_0, t) \to \mathbf{x}^*_{eq_1}$ as $t \to \infty$.

On the other hand, there exists a set $\Gamma_2^u \subset W^u_{\mathbf{x}^*_{eq_2}}$ such that each trajectory with initial condition $\mathbf{x_0} \in \Gamma_2^u$ converges at the point $(0, 7/3, 2/3)^T$, and then each trajectory with initial condition $\mathbf{x_0} \in \Gamma_2^u$ converges to the equilibrium point $\mathbf{x}^*_{eq_2}$ in back time, i.e., $\varphi(\mathbf{x}_0, t) \to \mathbf{x}^*_{eq_2}$ as $t \to -\infty$. Therefore, each trajectory with initial condition $\mathbf{x_0} \in \Gamma_2^u$ converges at the point $(0, 7/3, 2/3)^T$ when $t \to \infty$, and the trajectory continues from this intersection point to the equilibrium point $\mathbf{x}^*_{eq_1}$. Then, the heteroclinic orbit HO_{21} from the equilibrium point $\mathbf{x}^*_{eq_2}$ to the equilibrium point $\mathbf{x}^*_{eq_1}$ is given by the set $\Gamma_1^s \cup \Gamma_2^u$.

Now, if we consider that the trajectory with initial condition $\mathbf{x_0} = (0, 5/3, -2/3)^T \in W^s_{\mathbf{x}^*_{eq_2}}$ converges to $\mathbf{x}^*_{eq_2}$, there is a set $\Gamma_2^s \subset W^s_{\mathbf{x}^*_{eq_2}}$ generated by $\varphi(\mathbf{x}_0, t) \to \mathbf{x}^*_{eq_2}$ as $t \to \infty$. Then, there exists a set $\Gamma_1^u \subset W^u_{\mathbf{x}^*_{eq_1}}$ such that each trajectory with initial condition $\mathbf{x_0} \in \Gamma_1^u$ converges at the point $(0, 5/3, -2/3)^T$, and then each trajectory with initial condition $\mathbf{x_0} \in \Gamma_1^u$ converges to the equilibrium point $\mathbf{x}^*_{eq_1}$ in back time, i.e., $\varphi(\mathbf{x}_0, t) \to \mathbf{x}^*_{eq_1}$ as $t \to -\infty$. Therefore, each trajectory with initial condition $\mathbf{x_0} \in \Gamma_1^u$ converges at the point $(0, 5/3, 2/3)^T$ when $t \to \infty$, and the trajectory continues from this intersection point to the equilibrium point $\mathbf{x}^*_{eq_2}$. Then, the heteroclinic orbit HO_{12} from the equilibrium point $\mathbf{x}^*_{eq_1}$ to the equilibrium point $\mathbf{x}^*_{eq_2}$ is given by the set $\Gamma_2^s \cup \Gamma_1^u$.

The other four heteroclinic orbits between the equilibrium points $\mathbf{x}^*_{eq_2}$ and $\mathbf{x}^*_{eq_3}$ and the equilibrium points $\mathbf{x}^*_{eq_3}$ and $\mathbf{x}^*_{eq_4}$ can be proved in a similar way that HO_{21} and HO_{12}.

3 Planar System

A PWL system in R^2 is derived from the affine linear system (1) by using the linear transformation of coordinates:

$$\mathbf{y} = Q^{-1}\mathbf{x},$$

$$\dot{\mathbf{y}} = E\mathbf{y} + Q^{-1} f(Q\mathbf{y})B, \tag{12}$$

where $\mathbf{y} = (x_1, x_2, x_3)^T \in R^3$ is the state vector of the uncoupled system and the linear operator E is given by

$$E = Q^{-1}AQ = \begin{pmatrix} \alpha & -\beta & 0 \\ \beta & \alpha & 0 \\ 0 & 0 & \gamma \end{pmatrix}, \tag{13}$$

where $Q = [v_1\ v_2\ v_3]$. A continuous time dynamic planar system with two unstable foci is derived from (13) by defining the linear operator $A_1 \in R^2$ from the block of Jordan form given by the complex eigenvalues $\lambda_{1,2} = \alpha \pm i\beta$ of $A \in R^3$. Then

$$A_1 = \begin{pmatrix} \alpha & -\beta \\ \beta & \alpha \end{pmatrix}. \tag{14}$$

Without loss of generality, the planar PWL system is given by

$$\dot{\mathbf{x}} = \begin{cases} A_1\mathbf{x} + B_1, \text{ while } \mathbf{x} \in D_1; \\ A_1\mathbf{x} + B_2, \text{ while } \mathbf{x} \in D_2; \\ A_1\mathbf{x} + B_3, \text{ while } \mathbf{x} \in D_3; \\ A_1\mathbf{x} + B_4, \text{ while } \mathbf{x} \in D_4; \end{cases} \tag{15}$$

where $\mathbf{x} = (x, y)^T$ is the state vector and $B_1, B_2, B_3, B_4 \in R^2$ are constant vectors. The equilibria of the system $\mathbf{x_i^*} = (x_i^*, y_i^*)^T \in D_i$ are determined by the components of the equilibria given by $\mathbf{y_{eqi}^*}$, with $i = 1, \ldots, 4$. In this case, the equilibria $\mathbf{x_1^*} = (0, 3)^T$, $\mathbf{x_2^*} = (0, 1)^T$, $\mathbf{x_3^*} = (0, -1)^T$, and $\mathbf{x_4^*} = (0, -3)^T$ are given by the first and the second components. The borders of the convex sets D_i, where subsystems are acting, are given by the lines $l_1 = 3$, $l_2 = 1$, $l_3 = -1$, and $l_4 = -3$ that pass through the equilibria $\mathbf{x_i^*}$, respectively:

$$\begin{aligned} D_1 &= \{\mathbf{x} \in R^2 : l_2 < y\}, \\ D_2 &= \{\mathbf{x} \in R^2 : l_3 < y < l_1\}, \\ D_3 &= \{\mathbf{x} \in R^2 : l_4 < y < l_2\}, \\ D_4 &= \{\mathbf{x} \in R^2 : y < l_3\}. \end{aligned}$$

Finally, the vectors $B_i = -A_1\mathbf{x}_i^*$; therefore, $B_1 = (15, -0.6)^T$, $B_2 = (5, -0.2)^T$, $B_3 = (-5, 0.2)^T$, and $B_4 = (-15, 0.6)^T$.

A four-scroll attractor is generated by (15) and initial condition $\mathbf{x}_0 = (0, 1.3)^T$; see Fig. 1. The initialization of the system is given by $x_0 \in D_1$, $x_0 \in D_2 - D_1 \cap D_2$, $x_0 \in D_3 - D_2 \cap D_3$, and $x_0 \in D_4 - D_3 \cap D_4$. The distance between equilibria is the same $d(\mathbf{x_1^*}, \mathbf{x_2^*}) = d(\mathbf{x_2^*}, \mathbf{x_3^*}) = d(\mathbf{x_3^*}, \mathbf{x_4^*}) = 2$.

4 Multistability

Now, we generate multistability by means of increasing the distance $d(\mathbf{x_2^*}, \mathbf{x_3^*}) > 2$ and keep the distances $d(\mathbf{x_1^*}, \mathbf{x_2^*}) = d(\mathbf{x_3^*}, \mathbf{x_4^*}) = 2$. The new equilibria of the system $\mathbf{x_i^*} = (x_i^*, y_i^*)^T \in D_i$ are given by $\mathbf{x_1^*} = (0, 55)^T$, $\mathbf{x_2^*} = (0, 53)^T$, $\mathbf{x_3^*} = (0, -53)^T$, and $\mathbf{x_4^*} = (0, -55)^T$. And the convex sets D_i, $i = 1, \ldots, 4$ are defined as

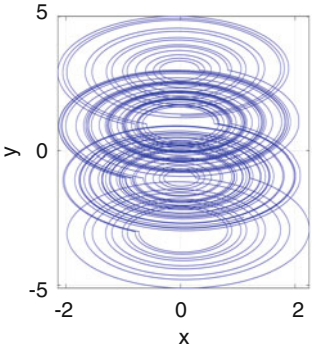

Fig. 1 A four-scroll attractor by using the following initial condition $\mathbf{x}_0 = (0, 1.3)^T$

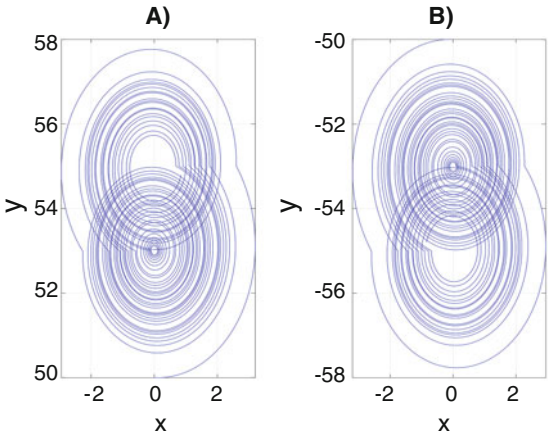

Fig. 2 Coexistence of two self-excited attractors: (**a**) A double-scroll attractor around equilibria $\mathbf{x}_1^*$ and $\mathbf{x}_2^*$, and initial condition $\mathbf{x_{01}} = (0, 50)$. (**b**) A double-scroll attractor around equilibria $\mathbf{x}_3^*$ and $\mathbf{x}_4^*$, and initial condition $\mathbf{x_{02}} = (0, -50)$

$$
\begin{aligned}
D_1 &= \{\mathbf{x} \in R^2 : \quad 53 \leq y\},\\
D_2 &= \{\mathbf{x} \in R^2 : -10 \leq y \leq 55\},\\
D_3 &= \{\mathbf{x} \in R^2 : -55 \leq y \leq 10\},\\
D_4 &= \{\mathbf{x} \in R^2 : \quad y \leq -53\}.
\end{aligned}
$$

The vectors $B_i = -A_1\mathbf{x}_i^*$, therefore, $B_1 = (275, -11)^T$, $B_2 = (265, -10.6)^T$, $B_3 = (-265, 10.6)^T$, and $B_4 = (-275, 11)^T$. Two double-scroll self-excited attractors are displayed around the equilibrium points, one of them around $\mathbf{x}_1^*$ and $\mathbf{x}_2^*$ and the other around $\mathbf{x}_3^*$ and $\mathbf{x}_4^*$. Figure 2 shows the coexistence of two double-scroll self-excited attractors: Fig. 2a shows an attractor around equilibria $\mathbf{x}_1^*$ and $\mathbf{x}_2^*$ for the initial condition $\mathbf{x_{01}} = (0, 50)$. Figure 2b shows an attractor around equilibria $\mathbf{x}_3^*$ and $\mathbf{x}_4^*$ for the initial condition $\mathbf{x_{02}} = (0, -50)$. The two initial conditions $\mathbf{x_{01}}$ and $\mathbf{x_{02}}$ belong to the basin of attraction, so the trajectories present transient states at the beginning.

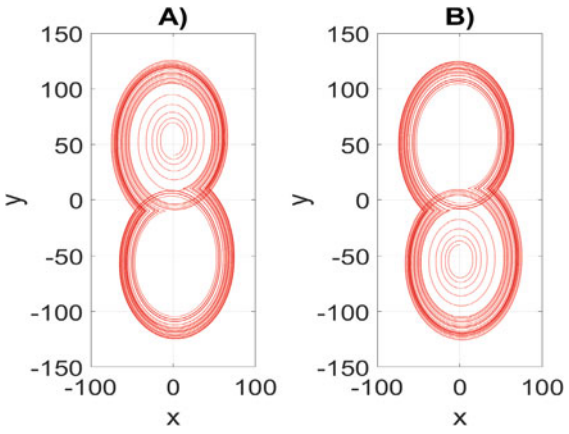

Fig. 3 A hidden attractor is generated for the initial conditions: (**a**) $\mathbf{x_{03}} = (0, 40)$. (**b**) $\mathbf{x_{04}} = (0, -40)$

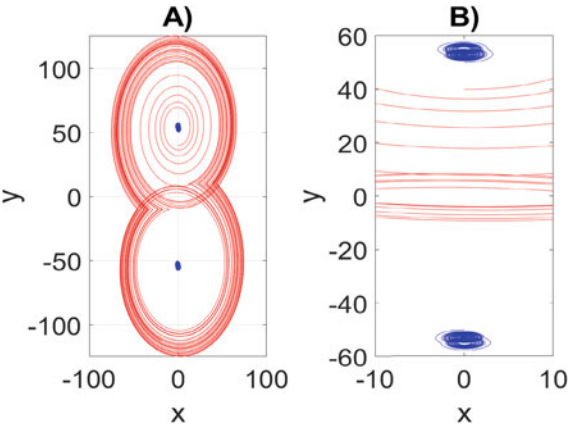

Fig. 4 Coexistence of two self-excited attractors and one hidden attractor: (**a**) Two double-scroll self-excited attractors are shown in color blue around equilibria $\mathbf{x}_1^*$ and $\mathbf{x}_2^*$ for the initial condition $\mathbf{x_{01}} = (0, 50)$ and around equilibria $\mathbf{x}_3^*$ and $\mathbf{x}_4^*$ for the initial condition $\mathbf{x_{02}} = (0, -50)$. And a hidden attractor is shown in color red for the initial condition $\mathbf{x_{03}} = (0, 40)$. (**b**) A zoom of figure (**a**)

Note that distances $d(\mathbf{x}_1^*, \mathbf{x}_2^*)$ and $d(\mathbf{x}_3^*, \mathbf{x}_4^*)$ remain equal to 2 and the distance $d(\mathbf{x}_2^*, \mathbf{x}_3^*) = 106$. Then this last distance is enough to let the generation of a hidden attractor around the two self-excited attractors as is shown in Fig. 3. Two initial conditions show that the same hidden attractor is generated: for Fig. 3a, the following initial was used $\mathbf{x_{03}} = (0, 40)$, and for Fig. 3b, the following initial condition $\mathbf{x_{04}} = (0, -40)$.

The system (15) is capable of generating coexistence of two double-scroll self-excited attractors and one hidden attractor; see Fig. 4. Figure 4a shows two double-scroll self-excited attractors in color blue around equilibria $\mathbf{x}_1^*$ and $\mathbf{x}_2^*$ for the initial condition $\mathbf{x_{01}} = (0, 50)$ and around equilibria $\mathbf{x}_3^*$ and $\mathbf{x}_4^*$ for the initial condition $\mathbf{x_{02}} = (0, -50)$. Also a hidden attractor is shown in color red for the initial condition $\mathbf{x_{03}} = (0, 40)$. Figure 4b shows a zoom of figure a. Figure 5a The basin of attraction of the hidden attractor is marked with red dots and the basins of attraction of the self-excited attractors are marked with blue dots. Figure 5b Zoom of the basin of attraction of a self-excited attractor.

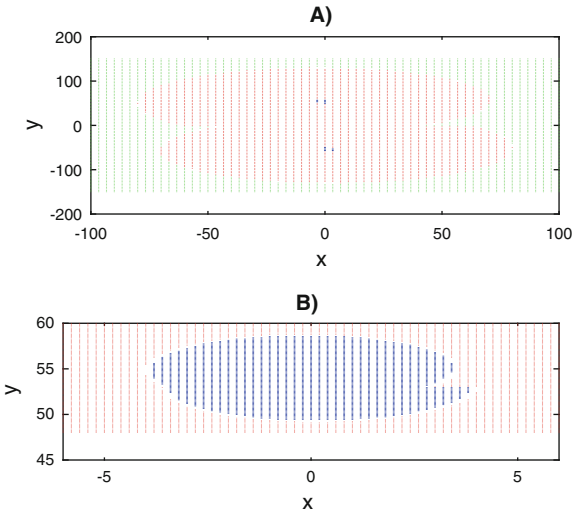

Fig. 5 (**a**) The basin of attraction of the hidden attractor is marked with red dots and the basins of attraction of the self-excited attractors are marked with blue dots. The green dots are initial conditions that escape to infinity. (**b**) Zoom of the basin of attraction of a self-excited attractor

5 Conclusion

We have introduced a continuous time planar system that presents the coexistence of a double-scroll hidden attractor and two double-scroll self-excited attractors. The hysteresis phenomenon was used to overcome the constraints on in-plane chaotic behavior, in order to obtain stretch-and-fold behavior. Then, it is possible to obtain chaos on the plane by using hysteresis. The class of planar system was derived from a three-dimensional PWL system.

The generation of a chaotic oscillator via heteroclinic chaos has some assumptions, and one of them is the relation between the real part α and imaginary part β of a complex eigenvalue. Usually, the ratio of $\beta/\alpha > 10$ to generate oscillations around the equilibrium point x^*. The future work is to apply the derived planar system to estimate the relation between the real part α and the imaginary part β of the complex eigenvalue. The idea is to be able to define an interval where the imaginary part β can take values given the value of the real part α.

Acknowledgments Eric Campos-Cantón acknowledges CONACYT for the financial support through Project no. A1-S-30433.

References

1. Pisarchik, A.N., Hramov, A.E.: Multistability in Physical and Living Systems, Characterization and Applications. Springer (2022). https://doi.org/10.1007/978-3-030-98396-3
2. Feudel, U.: Complex dynamics in multistable systems. Int. J. Bifurc. Chaos **18**, 1607–1626 (2008). https://doi.org/10.1142/S0218127408021233

3. Dudkowski, D., Jafari, S., Kapitaniak, T., Kuznetsov, N.V., Leonov, G.A., Prasad, A.: Hidden attractors in dynamical systems. Phys. Rep. **637**, 1–50 (2016). https://doi.org/10.1016/j.physrep.2016.05.002
4. Leonov, G.A., Kuznetsov, N.V., Vagaitsev, V.: Localization of hidden Chua's attractors. Phys. Lett. A **375**, 2230–2233 (2011). https://doi.org/10.1016/j.physleta.2011.04.037
5. Escalante-Gonzalez, R.de.J., Campos-Canton, E., Nicol, M.: Generation of multi-scroll attractors without equilibria via piecewise linear systems. Chaos Interdiscip. J. Nonlinear Sci. **27**, 053109 (2017). http://dx.doi.org/10.1063/1.4983523
6. Anzo-Hernandez, A., Gilardi-Velazquez, H.E., Campos-Canton, E.: On multistability behavior of unstable dissipative systems. Chaos Interdiscip. J. Nonlinear Sci. **28**, 033613 (2018). https://doi.org/10.1063/1.5016329
7. Escalante-González, R.J., Campos E.: Emergence of hidden attractors through the rupture of heteroclinic-like orbits of switched systems with self-excited attractors. Complexity **2021**, 5559913 (2021). https://doi.org/10.1155/2021/5559913
8. Ruiz-Silva, A., Cassal-Quiroga, B.B., Huerta-Cuellar, G., Gilardi-Velázquez, H.E.: On the behavior of bidirectionally coupled multistable systems. Eur. Phys. J. Spec. Top. **231**, 369–379 (2022). https://doi.org/10.1140/epjs/s11734-021-00406-4
9. Mekak-Egong, H.-D., Ramakrishnan, B., Nicole Kengnou Telem, A., Rajagopal, K., Kengne, J.: Multiscroll in bidirectionally coupled jerk oscillators: theoretical analysis and PSpice verification. Int. J. Bifurc. Chaos **32**(14), 2250211 (2022). https://doi.org/10.1142/S021812742250211X
10. Shajan, M., Shrimali, M.D.: Controlling multistability with intermittent noise. Chaos Solitons Fractals **160**, 112187 (2022). https://doi.org/10.1016/j.chaos.2022.112187
11. Campos, E.: Derivation of a continuous time dynamic planar system with two unstable foci from a three-dimensional chaotic piecewise linear system. Chaos Interdiscip. J. Nonlinear Sci. **30**, 053114 (2020). https://doi.org/10.1063/1.5144709

Compact Multiplier-less CORDIC-Based FPGA Implementation of Sine and Modified Sine Chaotic Maps

Hisham M. Elrefai, Sara S. Abou Zeid, Wafaa S. Sayed, Lobna A. Said, and Ahmed G. Radwan

1 Introduction

Many natural systems, such as fluid movement, rapid heartbeat, weather, and climate, exhibit chaotic behavior [1]. Additionally, it happens on its own in some artificially constructed systems, such as the movement of people in the streets and the movement of air. Implementing chaotic systems is crucial for various applications, such as robotics and encryption. The robotics field needs many scenarios for the trial-and-error process to learn how to interact with many use cases [2]. In encryption, [3], which is mainly based on the algorithm's unpredictability and output, requires a modified chaotic system to be reliable [4]. In addition, two image encryption applications based on the sine map were introduced in [5].

Many research works present chaotic maps with trigonometric nonlinearities, yet only a few implement them on hardware platforms. Zhongyun et al. implemented the sine chaotification model (SCM) on FPGA. SCM increases the chaotic range and improves the dynamic complexity of the one-dimensional (1D) chaotic maps. In addition, it widens the parameter range corresponding to chaotic behavior,

H. M. Elrefai · S. S. Abou Zeid · L. A. Said (✉)
Nanoelectronics Integrated Systems Center (NISC), Nile University, Giza, Egypt
e-mail: l.a.said@ieee.org

W. S. Sayed
Engineering Mathematics and Physics Department, Faculty of Engineering, Cairo University, Giza, Egypt

A. G. Radwan
Engineering Mathematics and Physics Department, Faculty of Engineering, Cairo University, Giza, Egypt

School of Engineering and Applied Sciences, Nile University, Giza, Egypt

© The Author(s), under exclusive license to Springer Nature Switzerland AG 2024

W. Lacarbonara (ed.), *Advances in Nonlinear Dynamics, Volume III*, NODYCON Conference Proceedings Series, https://doi.org/10.1007/978-3-031-50635-2_15

making the maps more suitable for pseudo-random number generators (PRNGs) [6]. The implementation of CORDIC for the sine function provides a significant improvement in the resource utilization of the FPGA. CORDIC only calculates the function using adders and shifters. CORDIC can also perform multiplication operations, resulting in a multiplier-less design that does not consume any DSPs [8].

This paper's objective is to propose a new modified sine chaotic map, and it implements both the conventional sine map and the new modified map on hardware. The organization of the paper is as follows: Sect. 2 reviews the sine map, and the modified sine map is proposed. The CORDIC algorithm is discussed in Sect. 3, as is the hardware implementation of both maps. Section 4 shows the comparison results against MATLAB and the used resources, followed by a conclusion in Sect. 5.

2 Chaotic Maps with Trigonometric Nonlinearities

This section reviews the sine map and introduces the modified sine map.

2.1 Sine Map

The sine map is described as follows [13]:

$$x_{n+1} = f(x_n) = \lambda \sin(\alpha \pi x_n). \tag{1}$$

where x_n is the iterated variable, α is the scaling parameter, and λ is the primary system parameter. The map produces a sine wave, which repeats periodically every $\frac{2}{\alpha}$. Since the period is inversely proportional to α, the frequency of the sine wave increases as the value of α increases. Figure 1a shows the resulting wave for $\lambda = \pi, and\ \alpha = 1$.

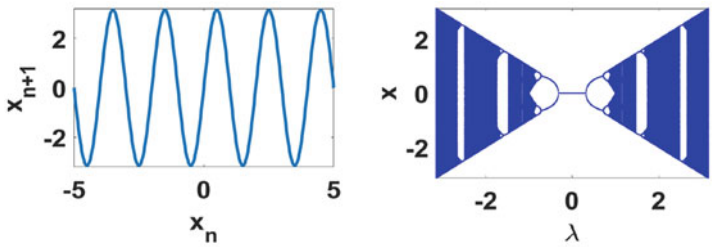

Fig. 1 (**a**) Graph of the generalized sine map (**b**) bifurcation diagram versus λ

The bifurcation diagram of the map against the parameter λ is shown in Fig. 1b, where the map exhibits a period-doubling bifurcation route to chaos with islands of stability in between. Modified maps exhibit chaotic behavior for all parameter values with no islands of stability or divergence [14]. They overcome the finite range of the control parameter and dynamical degradation problems of conventional chaotic maps. Generalized modified logistics, tent, and transition maps were presented, digitally implemented, and employed in speech encryption applications [15].

2.2 *Modified Sine Map*

A shifting parameter μ is added to the right-hand side of the iterative relation (1) resulting in

$$x_{n+1} = f(x_n) = \lambda \sin(\alpha\pi x_n) + \mu. \tag{2}$$

Another independent parameter, β, controls the output range. The modified output range can be either wider or narrower than the unmodified range by adding or subtracting β from the lower and upper bounds. The mathematical properties of one-dimensional maps are used to obtain the two dependent parameters λ and α in terms of β. The bifurcation diagram versus β can be either in range-shrinking or widening mode.

The analysis for the generalized modified sine map in the range-shrinking mode is presented as follows. The output x is confined to the interval $\frac{m}{\alpha} + \beta$ and $\frac{m+1}{\alpha} - \beta$, which corresponds to the function domain. The integer m corresponds to which period is considered. The maximum value of the function, at which the derivative with respect to x equals zero, occurs at $x = \frac{1}{2\alpha}$ and equals $\lambda + \mu$. The minimum value occurs at both bounds of the domain and equals $\lambda \sin(\alpha\pi\beta) + \mu$. Hence, the range of the function is given by the two equivalent intervals $[\beta, \frac{1}{\alpha} - \beta]$ and $[\lambda \sin\big(\alpha\pi(\frac{m}{\alpha} + \beta) + \mu\big), \lambda + \mu]$. Equating the bounds as follows:

$$\text{Lower bound :} \qquad \beta = \lambda \sin\left(\alpha\pi\left(\frac{m}{\alpha} + \beta.\right)\right) \tag{3a}$$

$$\text{Upper bound :} \qquad \frac{1}{\alpha} - \beta = \lambda + \mu, \tag{3b}$$

results in the expressions given in Table 1 for λ and μ. Figure 2 shows the bifurcation diagram for modes of modified sine map. The difference between range-shrinking and widening modes is further illustrated by the time series in Fig. 3.

Table 1 Modified sine map mods

	Widening	Shrinking
Parameters	$\mu = \frac{1}{2\alpha} + \beta - \lambda\ \lambda = \frac{2\beta - \frac{1}{\alpha}}{\sin(\alpha\pi(\frac{m}{\alpha}+\beta))-1}$	$\mu = \frac{1}{\alpha} - \beta - \lambda$ $\lambda = \frac{-2\beta}{\sin\left(\alpha\pi(\frac{2m+1}{2\alpha}-\beta)\right)-1}$
Range	$[\frac{1}{2\alpha} - \beta, \frac{1}{2\alpha} + \beta]$	$[\beta, \frac{1}{\alpha} - \beta]$
Domain	$[\lambda \sin\left(\alpha\pi(\frac{2m+1}{\alpha} - \beta) + \mu\right), \lambda + \mu]$	$[\lambda \sin(\alpha\pi(\frac{m}{\alpha} + \beta) + \mu), \lambda + \mu]$

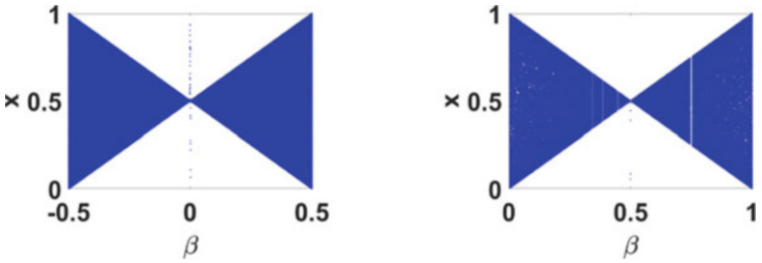

Fig. 2 Bifurcation diagram for modified sine map in (**a**) widening and (**b**) shrinking modes

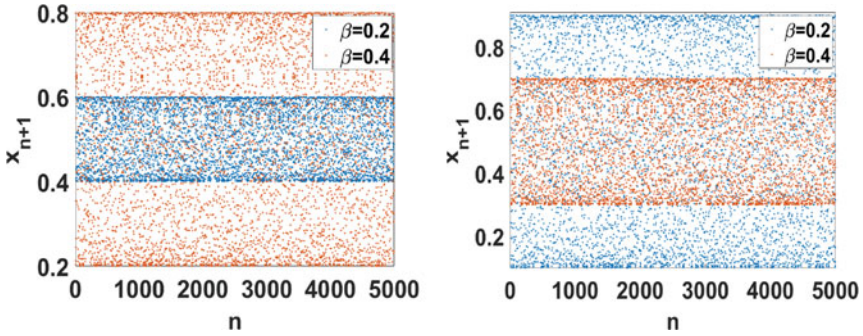

Fig. 3 Time series for modified sine map in (**a**) widening and (**b**) shrinking modes

3 Hardware Implementation

The proposed designs for the sine and modified sine maps are interpreted in the Verilog HDL language, Xilinx Vivado. After synthesis, the hardware is realized on the Xilinx Artix-7 FPGA board. In this design, a modified reconfigurable CORDIC calculates the sine function and multiplication operation. This section reviews the CORDIC algorithm and presents the hardware architecture.

3.1 CORDIC Algorithm

The CORDIC algorithm (modified reconfigurable CORDIC) is a subset of the reconfigurable CORDIC in [8]. The CORDIC algorithm eliminates the need for a look-up table for transcendental functions by performing vector rotation and directional operations. After vector rotation, the new vector's coordinate is determined by simply shifting, adding, and subtracting. The formulation of the modified reconfigurable CORDIC algorithm is as follows:

$$X_{i+1} = K_i(x_i - \mu\sigma 2^{-i} Y_i), \tag{4a}$$

$$Y_{i+1} = K_i(x_i + \mu\sigma 2^{-i} X_i), \tag{4b}$$

$$Z_{i+1} = \begin{cases} Z_i - \sigma_i(2^{-i}) \text{ if } m_0 = 0, \\ Z_i - \sigma_i(arctan(2^{-i}) \text{ if } m_0 = 1, \end{cases} \tag{4c}$$

where $m_0 = 0$ and 1 for linear and circular coordinate systems, respectively, $\sigma_i = sign(Z_i)$ or $-sign(Y_i)$ for rotation and vectoring modes, respectively, K the scale factor computed as follows:

$$K = \prod_{i=0}^{N-1} K_i = \prod_{i=0}^{N-1} \sqrt{1 + m_0 2^{-2i}}. \tag{5}$$

where N is the number of iterations. Table 2 shows the modified reconfigurable CORDIC configurations, m_1 represents the sign in X_{n+1} equation, and m_2 represent the $m_2 = arctan(2^{-i})$ or shift-right operation. Figure 4 shows the block diagram of the modified reconfigurable CORDIC.

Table 2 Modified CORDIC configurations

Function	Configuration	Initialization	Output
$\sin(\theta)$ $[-\pi : -\frac{\pi}{2}]$	C-RM Sel = 00	$X_0 = 1, Y_0 = -\frac{-1}{K_n}$ $Z_o = \theta + \frac{\pi}{2}, m_1 = 1$ $m_2 = arctan(2^{-i})$	$Y_n = \sin(\theta)$
$\sin(\theta)$ $[-\frac{\pi}{2} : \frac{\pi}{2}]$	C-RM Sel = 01	$X_0 = \gamma, Y_0 = 0$ $Z_0 = \theta, m_1 = 1$ $m_2 = arctan(2^{-i})$	$Y_n = \sin(\theta)$
$\sin(\theta)$ $[-\frac{\pi}{2} : \pi]$	C-Rm Sel = 10	$X_0 = 0, Y_0 = \frac{1}{K_n}$ $Z_0 = \theta - \frac{\pi}{2}, m_1 = 1$ $m_2 = arctan(2^{-i})$	$Y_n = \sin(\theta)$
$\theta\beta$	L-RM sel = 11	$X_0 = \theta, Y_0 = 0$ $Z_0 = \beta, m_1 = 0$ $m_2 = 2^{-i}$	$Z_n = \theta\beta$

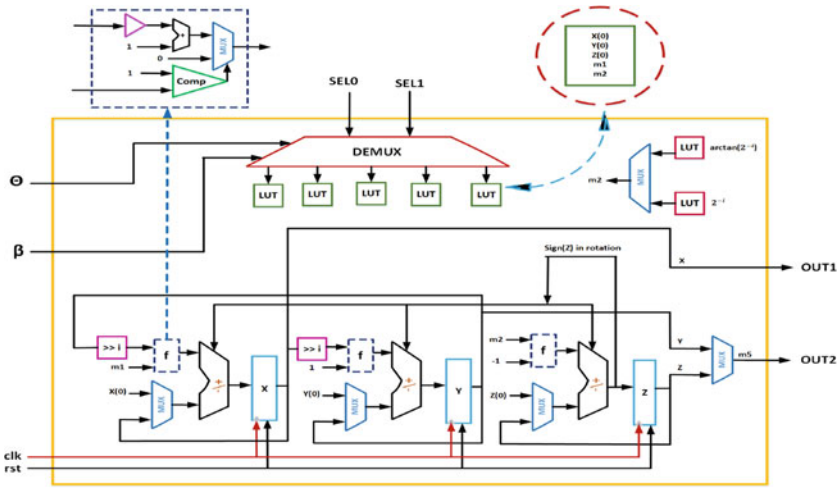

Fig. 4 Modified reconfigurable CORDIC

3.2 Hardware Architecture

The architecture of the design is shown in Fig. 4. The bit width for the input and the other system parameters is 42 in fixed point format, with 30 bits for the fractional part. SEL is used to choose the CORDIC configuration. For sine, SEL is 0, 1, or 2, depending on the angle value. For multiplication, the SEL value is 3. The control unit is responsible for using the correct mode and inputs to CORDIC and also choosing the correct destination for CORDIC output. The computation of the map output is done in three stages, as shown in Fig. 5: firstly, the sine angle is calculated, then the sine function is computed, and finally, λ is multiplied with $\sin(\alpha\pi x_n)$ and μ is added in case of the modified sine map.

4 Hardware Results

Table 3 summarizes the utilization of the FPGA resources. The designs achieve 5.276 and 5.043 MHz frequencies for sine and modified sine maps, respectively. The number of LUTs used in the case of the sine map is 6530, and for the modified sine map is 6735. The proposed architecture does not consume any DSPs, as it uses CORDIC in multiplication operations. The proposed architecture is compared to MATLAB floating-point results for $x \in [-1, 1]$ for both maps. The absolute relative error for both the sine and modified sine maps ranged from $[4 \times 10^{-6}, 2 \times 10^{-4}]$. Figure 6a shows the absolute relative error for the sine map for $\lambda = \pi$ and $\alpha = 1$. Modified sine map absolute relative error is shown in Fig. 6b for $\lambda = -1$, $\mu = 1$,

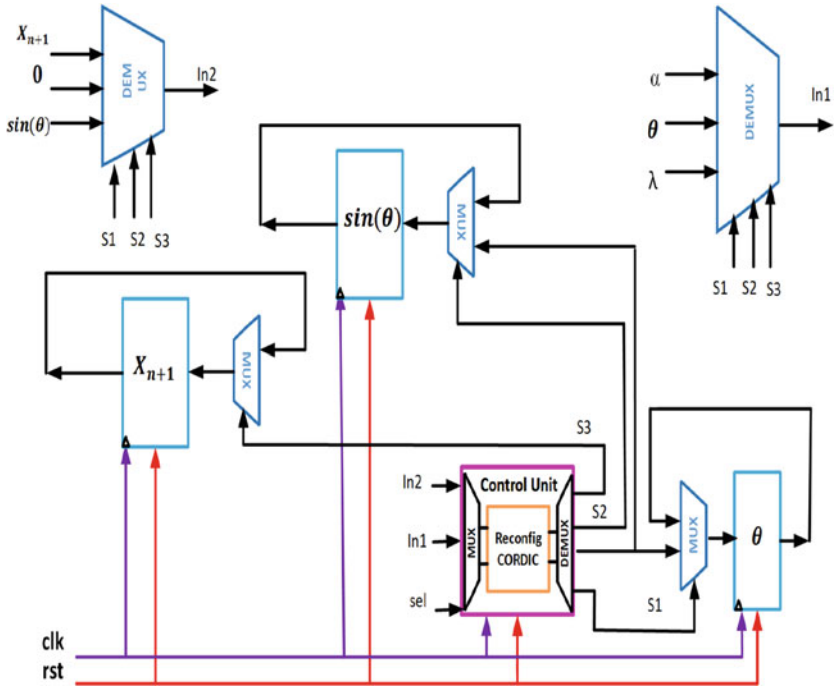

Fig. 5 Proposed map hardware architecture

Table 3 FPGA utilization for sine and modified sine maps

Logic utilization	Total no. of LUTS	Total no. of registers	Frequency (MHz)	Power (w)
Sine map	6530 (10.3%)	184	5.276	0.102
Modified sine map	6735 (10.7%)	187	5.043	

and $\alpha = 1$. In Figs. 7 and 8, the time series of sine and modified sine maps are plotted against MATLAB results, showing that the maps exhibit chaotic behavior.

5 Conclusion

This paper reviewed the sine map and proposed a modified one, studying its properties. Both maps were implemented in hardware using a modified reconfigurable multiplier-less CORDIC to compute the sine function and the multiplication operation. Consequently, the design does not consume any DSPs. The proposed hardware architecture was validated by comparing the hardware and software results. The maximum frequencies on the Xilinx Artix-7 FPGA board are 5.276 and 5.043 MHz for sine and modified sine maps, respectively.

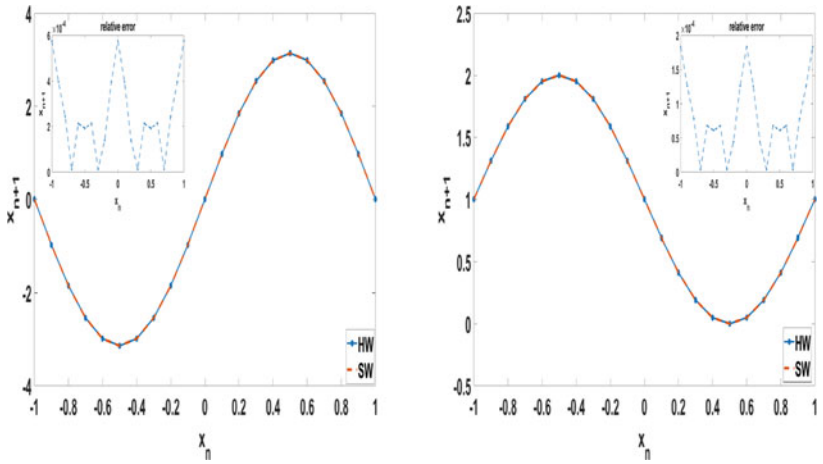

Fig. 6 Hardware vs software results. (**a**) Sine map, (**b**) modified sine map

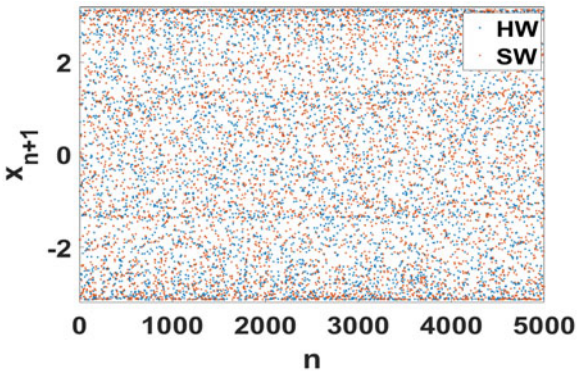

Fig. 7 Hardware vs software time series for sine map

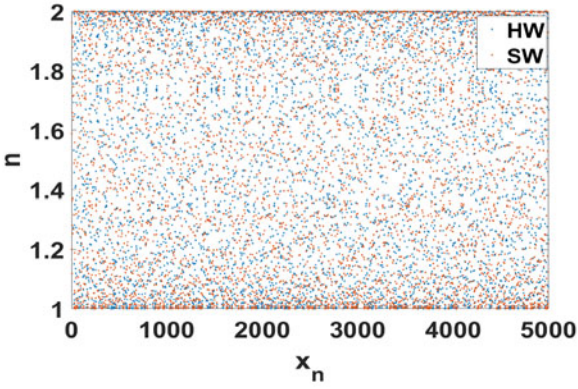

Fig. 8 Hardware vs software time series for modified sine map

Acknowledgments This paper is based upon the work supported by the Science, Technology, and Innovation Funding Authority (STIFA) under grant number(#38161).

References

1. Cao, J., Chugh, R.: Chaotic behavior of logistic map in superior orbit and an improved chaos-based traffic control model. Nonlinear Dyn. **94**(2), 959–975 (2018)
2. Zang, X., Iqbal, S., Zhu, Y., Liu, X., Zhao, J.: Applications of chaotic dynamics in robotics. Int. J. Adv. Robot. Syst. **13**(2), 60 (2016)
3. Sheu, L.J.: A speech encryption using fractional chaotic systems. Nonlinear Dyn. **65**(1), 103–108 (2011)
4. Mohamed, S.M., Sayed, W.S., Madian, A.H., Radwan, A.G., Said, L.A.: An encryption application and FPGA realization of a fractional memristive chaotic system. Electronics **12**(5), 1219 (2023)
5. Abd-El-Hafiz, S.K., Radwan, A.G., AbdEl-Haleem, S.H.: Encryption applications of a generalized chaotic map. Appl. Math. Inf. Sci. **9**(6), 3215 (2015)
6. Hua, Z., Zhou, B., Zhou, Y.: Sine chaotification model for enhancing chaos and its hardware implementation. IEEE Trans. Ind. Electron. **66**(2), 1273–1284 (2019)
7. Hua, Z., Zhou, B., Zhou, Y.: Sine-transform-based chaotic system with FPGA imple-mentation. IEEE Trans. Ind. Electron. **65**(3), 2557–2566 (2018)
8. Mohamed, S.M., Sayed, W.S., Radwan, A.G., Said, L.A.: FPGA implementation of reconfigurable CORDIC algorithm and a memristive chaotic system with transcendental nonlinearities. IEEE Trans. Circuits Syst. I Regul. Pap. **69**(7), 2885–2892 (2022)
9. Kumar, P.A.: FPGA implementation of the trigonometric functions using the CORDIC algorithm. In: Proceedings of the 2019 5th International Conference on Advanced Computing and Communication Systems (ICACCS), pp. 894–900 (2019). https://doi.org/10.1109/ICACCS.2019.8728315
10. Griffin, J.: The sine map. Retrieved May 4, 2018 (2013). https://people.maths.bris.ac.uk/~macpd/ads/sine.pdf
11. Sayed, W.S., Tolba, M.F., Radwan, A.G., Abd-El-Hafiz, S.K.: FPGA realization of a speech encryption system based on a generalized modified chaotic transition map and bit permutation. In: Multimedia Tools and Applications: Springer US, pp. 1–31 (2019)
12. Wiggins, S., Wiggins, S., Golubitsky, M.: Introduction to applied nonlinear dynamical systems and chaos, vol. 2(3). Springer, New York (2003)
13. Addison, P.S.: Fractals and chaos: an illustrated course. CRC Press, New York (1997)
14. Pande, A., Zambreno, J.: A chaotic encryption scheme for real-time embedded systems: design and implementation. Telecommun. Syst. **52**, 551–561 (2013)
15. Tolba, M.F., Sayed, W.S., Radwan, A.G., Abd-El-Hafiz, S.K.: FPGA realization of speech encryption based on modified chaotic logistic map. In: 19th International Conference on Industrial Technology (ICIT 2018). IEEE, New York (2018)
16. Alligood, K.T., Sauer, T.D., Yorke, J.A., Chillingworth, D.: Chaos: an introduc-tion to dynamical systems. SIAM Rev. **40**(3), 732–732 (1998)
17. Zhu, S., Wang, G., Zhu, C.: A secure and fast image encryption scheme based on double chaotic S-boxes. Entropy **21**(8), 790 (2019)

Fixed-Time Adaptive Neural Tracking Control for a Helicopter-Like Twin Rotor MIMO System

Aymene Bacha, Abdelghani Chelihi, and Chouki Sentouh

1 Introduction

The Twin Rotor MIMO System (TRMS) is an aerodynamic experimental setup whose behavior is similar to a helicopter. Its dynamics are characterized by complicated nonlinearity and a high coupling effect between two propellers. The two rotors are connected by a flexible link that moves in the vertical and horizontal planes which form an unstable open-loop system very sensitive to external disturbances [1]. The TRMS imposes challenging control problems due to its complex dynamics with the presence of unknown nonlinear functions. These features make it widely used in the control engineering field to test different control approaches where the objective is to achieve desired flight path tracking performance and ensure system stability.

In order to overcome the complexity of the system dynamics, various approaches have been proposed in the literature ranging from classic linear controllers to advance nonlinear and intelligent control techniques. Traditional synthesis algorithms such as proportional–integral–derivative (PID) [2], fractional order PID [3, 4], and optimal linear quadratic regulators [5] have been proposed to drive the TRMS. The model predictive controller in [6] and the robust H infinity controller in [7] are also control approaches discussed to improve the tracking performance of

A. Bacha (✉)
LI3CUB Laboratory, University of Biskra, Biskra, Algeria
e-mail: aymene.bacha@univ-biskra.dz

A. Chelihi
Department of Electronics, Faculty of Technology, Constantine 1 University, Constantine, Algeria
e-mail: chelihi.abdelghani@yahoo.fr

C. Sentouh
Department of Automatic Control, Hauts-de-France Polytechnic University, Valenciennes, France

© The Author(s), under exclusive license to Springer Nature Switzerland AG 2024

W. Lacarbonara (ed.), *Advances in Nonlinear Dynamics, Volume III*, NODYCON Conference Proceedings Series, https://doi.org/10.1007/978-3-031-50635-2_16

the twin rotors. However, linear control methods are not suitable for controlling the TRMS due to their limited ability to handle non-linearities and parameter uncertainties. Therefore, advanced control techniques such as backstepping control and sliding mode have been proposed to address this problem. In [8] a backstepping terminal sliding mode controller was presented and an adaptive fuzzy control was applied in [9, 10], in order to improve the robustness versus wind gusts, external disturbances, and uncertainties.

Since the system's initial values have a significant impact on how quickly these approaches converge, all of the synthesis procedures previously discussed become impractical without them. To overcome this gap and achieve finite-time convergence of the system dynamics regardless of the initial condition, the so-called fixed-time [11] control has been developed. This work is motivated by the paper [12], a fixed-time control for a class of uncertain nonstrict nonlinear systems is proposed, where the stability has a faster convergence speed and the settling time is bounded. Also, the convergence time does not rely on the initial information.

Radial basis function neural networks (RBF NNs) are powerful tools for unknown nonlinear function approximation, and they can provide accurate estimates of the system model. This allows for more accurate control of the TRMS using backstepping control. The effectiveness of the proposed control strategy is demonstrated by numerical simulations using the Matlab/Simulink software environment. The rest of the paper is arranged as follows: in Sect. 2, the TRMS description with dynamic modeling is adopted. Section 3 presents the FTANC design, and simulation results are provided in Sect. 4. Finally, the conclusion is given.

2 Modeling of Twin Rotor MIMO System

The TRMS configuration, as depicted in Fig. 1, consists of two rotor propellers that are perpendicular to each other. Direct current (DC) motors power their main and tail rotors, which are mounted on a beam. The pitch and yaw angles of the beam,

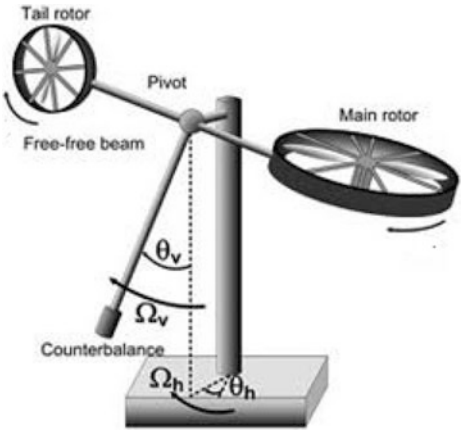

Fig. 1 Twin rotor MIMO system

θ_v and θ_h, respectively, allow the TRMS to revolve in both vertical and horizontal planes. The rotors' speed is ensured by their supply voltages denoted as u_v and u_h. The dynamic motion of the TRMS in both vertical and horizontal planes can be described respectively by the following equations [1]:

$$\begin{cases} \dot{\theta}_v = \Omega_v \\ J_v \dot{\Omega}_v = a_m u_{vv}^2 + b_m u_{vv} - M_g \sin\theta_v - B_v \Omega_v \\ T_{m_1} \dot{u}_{vv} = T_{m_0} u_{vv} + k_m u_v \end{cases} \tag{1}$$

$$\begin{cases} \dot{\theta}_h = \Omega_h \\ J_h \dot{\Omega}_h = a_t u_{hh} + b_t u_{hh} - B_h \Omega_h \\ T_{t_1} \dot{u}_{hh} = T_{t_0} u_{hh}^2 + k_t u_h \end{cases} \tag{2}$$

where Ω_v and Ω_h are the angular velocity around the vertical and horizontal axis respectively, u_{vv} and u_{hh} are the momentum of the main and tail DC motor respectively. The other TRMS constants and parameters with their numerical values are defined in Table 1.

From (1) and (2), the horizontal and vertical sub-models can be rewritten in a generalized state form as follows:

Table 1 TRMS model parameters

Symbol	Description	Value
$\mathbf{J_v}$	Moment of inertia of vertical rotor	0.068 kg.m^2
$\mathbf{J_h}$	Moment of inertia of horizontal rotor	0.02 kg $\cdot$ m^2
$\mathbf{a_m}$	Static characteristic parameter	0.0135
$\mathbf{b_m}$	Static characteristic parameter	0.0924
$\mathbf{a_t}$	Static characteristic parameter	0.02
$\mathbf{b_t}$	Static characteristic parameter	0.09
$\mathbf{M_g}$	Gravity momentum	0.32
$\mathbf{B_v}$	Friction momentum parameter	0.006 N.m.s/rad
$\mathbf{B_h}$	Friction momentum parameter	0.1 N.m.s/rad
$\mathbf{K_{g_y}}$	Gyroscopic momentum parameter	0.05 s/rad
$\mathbf{k_c}$	Cross-reaction momentum gain	-0.2
$\mathbf{T_0}$	Cross-reaction momentum parameter	3.5
$\mathbf{T_p}$	Cross-reaction momentum parameter	2
$\mathbf{k_m}$	Main motor gain	1.1
$\mathbf{T_{m_1}}$	Main motor denominator parameter	1.2
$\mathbf{T_{m_0}}$	Main motor denominator parameter	1
$\mathbf{k_t}$	Tail motor gain	0.8
$\mathbf{T_{t_1}}$	Tail motor denominator parameter	1
$\mathbf{T_{t_0}}$	Tail motor denominator parameter	1

$$\begin{cases} \dot{x}_{1,i} = x_{2,i} \\ \dot{x}_{2,i} = x_{3,i} + \alpha_i(x_i) + \mathcal{D}_i(x_i, t) \\ \dot{x}_{3,i} = u_i + \beta_i(x_i) \\ y_i = x_{1,i}, i \in v, h \end{cases} \tag{3}$$

where $x_i = [\theta_i, \Omega_i, u_{ii}]^T$ are the state vectors of the TRMS system, for $i \in \{v, h\}$, u_i and y_i are the corresponding control inputs and outputs, respectively, which represent the voltages supplied to the rotors and the beam angles. $\mathcal{D}_i(x_i, t)$ are the external disturbances added to describe the coupling effect and external perturbations. $\alpha_i(x_i)$ and $\beta_i(x_i)$ are unknown nonlinear functions with $x_{3,i} + \alpha_i(x_i) \neq 0$. Then, the objective is to design a control law $u_i(t)$ for the TRMS subsystems (3) so that the output signals y_i follow bounded and continuous reference signals $y_{d,i}$ and ensure the overall stability of the closed-loop system.

3 Fixed-Time Adaptive Neural Tracking Control

In this section, fixed-time adaptive neural control is designed for controlling the TRMS angles, θ_i, $i \in v, h$. For the controller design, let us define the following tracking errors:

$$e_{1,i} = y_i - y_{d,i} \tag{4}$$

$$e_{2,i} = x_{2,i} - \lambda_{1,i} \tag{5}$$

$$e_{3,i} = x_{3,i} - \lambda_{2,i} \tag{6}$$

where $\lambda_{1,i}$ and $\lambda_{2,i}$ are virtual commands that will be developed subsequently. According to the backstepping control algorithm, the control law with these two virtual controls is determined in three steps. Here, the control procedure introduces an adaptive neural network estimator to deal with the unknown functions in (3) and improve the TRMS performance. The synoptic scheme presented in Fig. 2 depicts the different steps to control the system.

Step 1
The derivative of (4) by considering the first equation of (3) gives

$$\dot{e}_{1,i} = x_{2,i} - \dot{y}_{d,i} = e_{2,i} + \lambda_{1,i} - \dot{y}_{d,i} \tag{7}$$

Then, let the Lyapunov function V_1 be given as [13]

$$V_1 = \sum_{i \in \{h,v\}} V_{1,i} = \sum_{i \in \{h,v\}} \frac{1}{2} e_{1,i}^2 \tag{8}$$

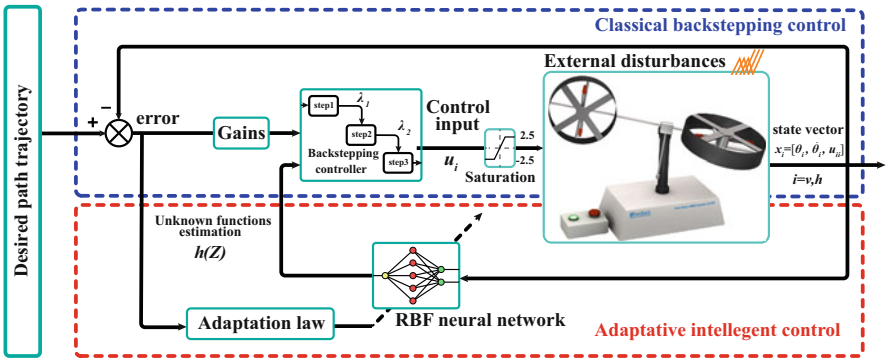

Fig. 2 Fixed-time adaptive neural control strategy

Time differentiation of (8) gives

$$\dot{V}_1 = \sum_{i\in\{h,v\}} e_{1,i}\left(e_{2,i} + \lambda_{1,i} - \dot{y}_{d,i}\right) \tag{9}$$

To stabilize $x_{1,i}$, we can now design the fixed-time virtual controller $\lambda_{1,i}$ as

$$\lambda_{i\,1} = -k_{i\,1,1}e_{1,i}^{2p-1} - k_{i\,2,1}e_{1,i}^{2q-1} + \dot{y}_{d,i} \tag{10}$$

where $k_{i_{1,1}} > 0, k_{i_{2,1}} > 0$ are design parameters, p and q are set by the user. Replacing (10) in (9), we can have

$$\dot{V}_1 \leq \sum_{i\in\{h,v\}} -k_{i\,1,1}e_{1,i}^{2p} - k_{i\,2,1}e_{1,i}^{2q} + e_{1,i}e_{2,i} \tag{11}$$

Step 2

Similarly, from (5) the derivative of $e_{2,i}$ is given by

$$\dot{e}_{2,i} = e_{3,i} + \lambda_{2,i} + \alpha_i(x) - \dot{\lambda}_{1,i} \tag{12}$$

The augmented Lyapunov function takes the form

$$V_2 = \sum_{i\in\{h,v\}} V_{1,i} + \frac{1}{2}e_{2,i}^2 + \frac{1}{2\gamma_{1,i}}\tilde{\Theta}_{1,i}^2 \tag{13}$$

where $\gamma_{1,i} = 2\rho_{1,i}/(2\rho_{1,i} - 1)$ with $\rho_{1,i} > 1/2$, and $\tilde{\Theta}_{1,i} = \Theta_{1,i} - \hat{\Theta}_{1,i}$ are the estimation errors of $\Theta_{1,i}$ by $\hat{\Theta}_{1,i}$ which will be determined to satisfy the stability conditions, $h_{1,i}(Z_{1,i})$ are unknown functions that take the following expression:

$$h_{1,i}\left(Z_{1,i}\right) = e_{1,i} + \alpha_i(x) - \dot{\lambda}_{1,i} + \frac{1}{2}e_{2,i} + k_{i\,2,2}e_{2,i}^{2q-1} \tag{14}$$

Using the RBF neural network, the unknown functions $h_{1,i}(Z_{1,i})$ can be approximated by

$$h_{1,i}\left(Z_{1,i}\right) = W_{1,i}^T\varphi_{1,i}\left(Z_{1,i}\right) + \delta_{1,i}\left(Z_{1,i}\right), \left\|\delta_{1,i}\left(Z_{1,i}\right)\right\| \leq \varepsilon_{1,i} \tag{15}$$

where $Z_{1,i} = [x_{1,i}, x_{2,i}, y_{d,i}, \dot{y}_{d,i}, \ddot{y}_{d,i}]^T$. According to completion squares theorem, we can write the following inequality:

$$\begin{aligned} e_{2,i}h_{1,i}\left(Z_{1,i}\right) &= e_{2,i}\left(W_{1,i}^T\varphi_{1,i}\left(Z_{1,i}\right) + \delta_{1,i}\left(Z_{1,i}\right)\right) \\ &\leq \frac{1}{2a_{1,i}^2}e_{2,i}^2\left\|W_{1,i}\right\|^2\varphi_{1,i}^T\left(Z_{1,i}\right)\varphi_{1,i}\left(Z_{1,i}\right) + \frac{a_{1,i}^2}{2} + \frac{e_{2,i}^2}{2} + \frac{\varepsilon_{1,i}^2}{2} \\ &\leq \frac{1}{2a_{1,i}^2}e_{2,i}^2\Theta_{1,i}\varphi_{1,i}^T\left(X_{1,i}\right)\varphi_{1,i}\left(X_{1,i}\right) + \frac{a_{1,i}^2}{2} + \frac{e_{2,i}^2}{2} + \frac{\varepsilon_{1,i}^2}{2} \end{aligned} \tag{16}$$

where $X_{1,i} = [x_{1,i}, x_{2,i}, y_{d,i}, \dot{y}_{d,i}, \ddot{y}_{d,i}]^T$ with $\Theta_{1,i} = \|W_{1,i}\|^2$ and $a_{1,i}$ are positive design parameters.

Thus, the virtual control $\lambda_{2,i}$ can be calculated as follows:

$$\lambda_{2,i} = -k_{i\,1,2}e_{2,i}^{2p-1} - \frac{1}{2a_{1,i}^2}e_{2,i}\hat{\Theta}_{1,i}\varphi_{1,i}^T\left(X_{1,i}\right)\varphi_{1,i}\left(X_{1,i}\right) \tag{17}$$

and the law of adaptation is given by the following expression:

$$\dot{\hat{\Theta}}_{1,i} = \frac{\gamma_{1,i}}{2a_{1,i}^2}e_{2,i}^2\varphi_{1,i}^T\left(X_{1,i}\right)\varphi_{1,i}\left(X_{1,i}\right) - \gamma_{1,i}\sigma_{1,i}\hat{\Theta}_{1,i} \tag{18}$$

where $k_{i_{1,2}} > 0$, $k_{i_{2,2}} > 0$, $\sigma_{1,i} > 0$ are design parameters. By replacing (17)–(18) in (13), we can have

$$\begin{aligned} \dot{V}_2 \leq \sum_{i\in\{h,v\}} &-k_{i\,1,1}e_1^{2p} - k_{i\,2,1}e_1^{2q} - k_{i\,1,2}e_2^{2p} - k_{i\,2,2}e_2^{2q} + e_{2,i}e_{3,i} \\ &+ \frac{\sigma_{1,i}}{\gamma_{1,i}}\tilde{\Theta}_{1,i}\hat{\Theta}_{1,i} + \frac{a_{1,i}^2}{2} + \frac{\varepsilon_{1,i}^2}{2} \end{aligned} \tag{19}$$

Step 3

Finally, using Eq. (6), the derivative of $e_{3,i}$ is expressed as follows:

$$\dot{e}_{3,i} = u_i + \beta_i(x) - \dot{\lambda}_{2,i} \tag{20}$$

Le us define the following Lyapunov function to stabilize $x_{3,i}$ and overall closed-loop system as

$$V_3 = \sum_{i\in\{h,v\}} V_{2,i} + \frac{1}{2}e_{3,i}^2 + \frac{1}{2\gamma_{2,i}}\tilde{\Theta}_{2,i}^2 \tag{21}$$

where $\gamma_{2,i} = 2\rho_{2,i}/(2\rho_{2,i} - 1)$ with $\rho_{2,i} > 1/2$, and $\tilde{\Theta}_{2,i} = \Theta_{2,i} - \hat{\Theta}_{2,i}$ are estimation errors of $\Theta_{2,i}$ by $\hat{\Theta}_{2,i}$. $h_{2,i}(Z_{2,i})$ are unknown functions take the following expression:

$$h_{2,i}(Z_{2,i}) = e_{2,i} + \beta_i(x) - \dot{\lambda}_{2,i} + \frac{1}{2}e_{3,i} + k_{i\,2,3}e_{3,i}^{2q-1} \tag{22}$$

Similar to the previous step, the nonlinear functions $h_{2,i}(Z_{2,i})$ are approximated by adaptive neural networks defined as follows:

$$h_{2,i}(Z_{2,i}) = W_{2,i}^T\varphi_{2,i}(Z_{2,i}) + \delta_{2,i}(Z_{2,i}),\ \left\|\delta_{2,i}\left(Z_{2,i}\right)\right\| \le \varepsilon_{2,i} \tag{23}$$

where $Z_{2,i} = [x_{1,i}, x_{2,i}, x_{3,i}, \Theta_{1,i}, y_{d,i}, \dot{y}_{d,i}, \ddot{y}_{d,i}, \dddot{y}_{d,i}]^T$, and the following inequality is written:

$$\begin{aligned} e_{3,i}h_{2,i}\left(Z_{2,i}\right) &= e_{3,i}\left(W_{2,i}^T\varphi_{2,i}\left(Z_{2,i}\right) + \delta_{2,i}\left(Z_{2,i}\right)\right) \\ &\le \frac{1}{2a_{2,i}^3}e_{3,i}^2\left\|W_{2,i}\right\|^2\varphi_{2,i}^T\left(Z_{2,i}\right)\varphi_{2,i}\left(Z_{2,i}\right) + \frac{a_{2,i}^2}{2} + \frac{e_{3,i}^2}{2} + \frac{\varepsilon_{2,i}^2}{2} \\ &\le \frac{1}{2a_{2,i}^2}e_{3,i}^2\Theta_{2,i}\varphi_{2,i}^T\left(X_{2,i}\right)\varphi_{2,i}\left(X_{2,i}\right) + \frac{a_{2,i}^2}{2} + \frac{e_{3,i}^2}{2} + \frac{\varepsilon_{2,i}^2}{2} \end{aligned} \tag{24}$$

where $X_{2,i} = [x_{1,i}, x_{2,i}, x_{3,i}, \Theta_{1,i}, y_{d,i}, \dot{y}_{d,i}, \ddot{y}_{d,i}, \dddot{y}_{d,i}]^T$ with $\Theta_{2,i} = \|W_{2,i}\|^2$ and $a_{2,i}$ are positive design parameters.

Now, we define the actual control law as:

$$u_i = -k_{i\,1,3}e_{3,i}^{2p-1} - \frac{1}{2a_{2,i}^2}e_{3,i}\hat{\Theta}_{2,i}\varphi_{2,i}^T\left(X_{2,i}\right)\varphi_{2,i}\left(X_{2,i}\right) \tag{25}$$

and the adaptation law as

$$\dot{\hat{\Theta}}_{2,i} = \frac{\gamma_{2,i}}{2a_{2,i}^2}e_{3,i}^2\varphi_{2,i}^T\left(X_{2,i}\right)\varphi_{2,i}\left(X_{2,i}\right) - \gamma_{2,i}\sigma_{2,i}\hat{\Theta}_{2,i} \tag{26}$$

where $k_{i_{1,3}} > 0$, $k_{i_{2,3}} > 0$, $\sigma_{2,i} > 0$ are design parameters.

By replacing (25)–(26) in (21), we can have

$$\dot{V}_3 \leq \sum_{i\in\{h,v\}} -k_{i\,1,1}e_1^{2p} - k_{i\,2,1}e_1^{2q} - k_{i\,1,2}e_2^{2p} - k_{i\,2,2}e_2^{2q} - k_{i\,1,3}e_3^{2p} - k_{i\,2,3}e_3^{2q}$$
$$+ \frac{\sigma_{1,i}}{\gamma_{1,i}}\tilde{\Theta}_{1,i}\hat{\Theta}_{1,i} + \frac{a_{1,i}^2}{2} + \frac{\varepsilon_{1,i}^2}{2} + \frac{\sigma_{2,i}}{\gamma_{2,i}}\tilde{\Theta}_{2,i}\hat{\Theta}_{2,i} + \frac{a_{2,i}^2}{2} + \frac{\varepsilon_{2,i}^2}{2} \tag{27}$$

From (25) and the result of [12], the stability TRMS closed-loop control system is guaranteed by using the virtual control laws (10) and (17), the actual controller (25) updated by (18) and (26). Furthermore, the tracking errors are bounded and the desired performance is established in a fixed time reliant on the appropriate selecting design parameters.

4 Simulation Results

Numerical simulation tests on the closed-loop TRMS system are performed for different reference signals, in regulation and tracking problems, to demonstrate the effectiveness of the proposed control method. The initial conditions are chosen the same in all tests as $x_v(0) = [0, 0, 0]$ and $x_h(0) = [0, 0, 0]$. The design parameters are selected as $a_1 = a_2 = a_3 = 1$, $p = 107/100$, $q = 97/101$, $k_{v\,1,1} = 2.4$, $k_{v\,2,1} = 28.3$, $k_{v\,3,1} = 18.8$, $k_{h\,1,1} = 9.8$, $k_{h\,2,1} = 20.8$, $k_{h\,3,1} = 52.2$.

The results are depicted in Figs. 3, 4, and 5. The performances of the yaw angle (θ_h) and pitch angle (θ_v) shown in Fig. 3 demonstrate the effectiveness of the developed control method in the regulation problem and effectively able to handle the change of references in both horizontal and vertical directions. We can conclude

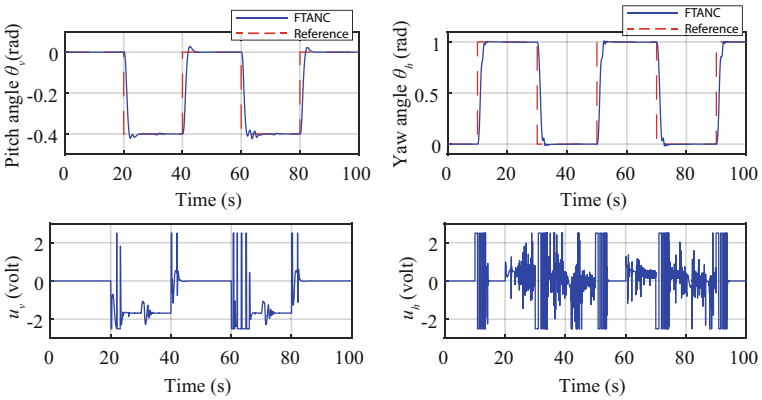

Fig. 3 TRMS response for square reference signals

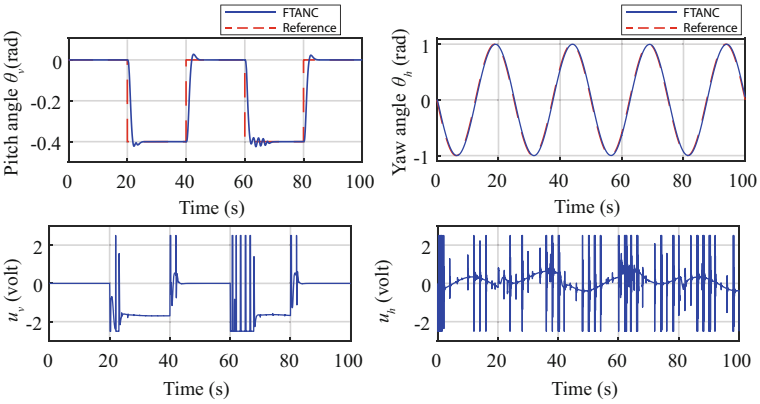

Fig. 4 TRMS response for different references signals

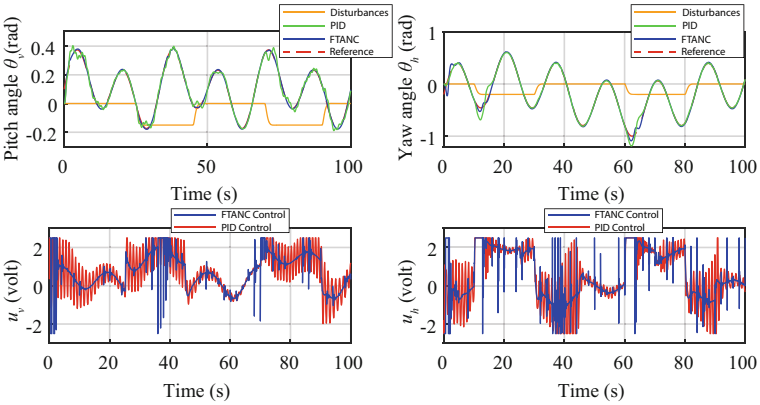

Fig. 5 TRMS response for sine wave reference signals under disturbances

that the proposed approach deals with coupling effects between the two rotors, i.e., horizontal and vertical subsystems.

Figure 4 depicts the dynamic performances of the TRMS with different references and frequencies. The square reference signal is selected for the vertical subsystem whilst the sine wave signal is chosen for the horizontal subsystem. The result demonstrates that the proposed controller has well compensated the aircraft motion maneuvers at times 20, 40, 60, and 80 seconds.

To test the robustness of the proposed control scheme against external disturbances, the TRMS with its controller is simulated for sine wave reference signals when an external force is applied in the flight moments [25, 45] and [70, 90] seconds for the vertical axis, and in [10, 30], [60, 80] seconds for the horizontal axis. Figure 5 shows the TRMS response with the control inputs in trajectory tracking. It is evident that the proposed controller has the best performance compared to the classical PID controller, especially in the presence of disturbance effects.

5 Conclusion

In this study, a radial basis function neural network (RBFNN) is combined with a backstepping control method to propose an intelligent adaptive control scheme for driving the TRMS. The RBFNN is introduced here to approximate all unknown nonlinear functions and disturbances, where the updating laws are derived using the rigorous Lyapunov proof. The proposed fixed-time controller has faster convergence and the upper bound of settling time can be estimated without any restriction on the initial conditions. The effectiveness and robustness of the proposed controller are demonstrated in a simulation environment. Our future research topics will aim to focus on the hardware implementation and the fault-tolerant control problem for the TRMS.

Acknowledgments The authors acknowledge the support of the University of Biskra. This work was supported also by the Algerian Ministry of Higher Education and Scientific Research.

References

1. Twin Rotor MIMO System Manual. Feedback Instruments Ltd., UK (2006)
2. Ramalakshmi, A.P.S., Manoharan, P.S.: Non-linear modeling and PID control of twin rotor MIMO system. In: 2012 IEEE International Conference on Advanced Communication Control and Computing Technologies (ICACCCT), pp. 366–369 2012. https://doi.org/10.1109/ICACCCT.2012.6320804
3. Saha, A., Chakraborty, S.: Genetic algorithm based I-PD controller design for Twin Rotor MIMO system. In: 2016 2nd International Conference on Control, Instrumentation, Energy & Communication (CIEC), pp. 15–19 2016. https://doi.org/10.1109/CIEC.2016.7513826
4. Azar, A.T., Sayed, A.S., Shahin, A.S., Elkholy, H.A., Ammar, H.H.: PID controller for 2-DOFs twin rotor MIMO system tuned with particle swarm optimization. In: Hassanien, A., Shaalan, K., Tolba, M. (eds.) Proceedings of the International Conference on Advanced Intelligent Systems and Informatics 2019. AISI 2019. Advances in Intelligent Systems and Computing, vol. 1058. Springer, Cham (2020). https://doi.org/10.1007/978-3-030-31129-2_22
5. Ranjan, K.V., Laxmi, V.: Design of an optimal controller for a twin rotor MIMO system (TRMS). In: 2022 International Conference on Sustainable Computing and Data Communication Systems (ICSCDS), pp. 950–959 2022. https://doi.org/10.1109/ICSCDS53736.2022.9760778
6. Nath, U.M., Dey, C., Mudi, R.K.: Controlling of twin rotor MIMO system (TRMS) based on multivariable model predictive control. In: Nath, V., Mandal, J. (eds.) Nanoelectronics, Circuits and Communication Systems. Lecture Notes in Electrical Engineering, vol. 692. Springer, Singapore (2021). https://doi.org/10.1007/978-981-15-7486-3_44
7. Pandey, S.K., Dey, J., Banerjee, S.: Design of H infinity (H8) controller for twin rotor MIMO system (TRMS) based on linear matrix inequalities. In: Bhattacharyya, S., Gandhi, T., Sharma, K., Dutta, P. (eds.) Advanced Computational and Communication Paradigms. Lecture Notes in Electrical Engineering, vol. 475. Springer, Singapore (2018). https://doi.org/10.1007/978-981-10-8240-5_52
8. Derakhshannia, M., Asl, S.B.F., Moosapour, S.S.: Backstepping terminal sliding mode control design for a TRMS. In: 2021 7th International Conference on Control, Instrumentation and Automation (ICCIA), pp. 1–5 (2021). https://doi.org/10.1109/ICCIA52082.2021.9403545

9. Chelihi, A., Perozzi, G., Sentouh, C.: Optimal Direct Adaptive Model-Free Controller for Twin Rotor MIMO System Using Legendre Polynomials and PSO Algorithm, pp. 83–93. https://doi.org/10.1007/978-3-030-81166-2_8
10. Zeghlache, S., Benyettou, L., Djerioui, A., Ghellab, M.Z.: Twin rotor MIMO system experimental validation of robust adaptive fuzzy control against wind effects. IEEE Syst. J. **16**(1), 409–419 (2022). https://doi.org/10.1109/JSYST.2020.3034993
11. Liu, Y., Li, H., Lu, R., Zuo, Z., Li, X.: An overview of finite/fixed-time control and its application in engineering systems. IEEE/CAA J. Autom. Sin. **9**(12), 2106–2120 (2022). https://doi.org/10.1109/JAS.2022.105413
12. Ba, D., Li, Y.-X., Tong, S.: Fixed-time adaptive neural tracking control for a class of uncertain nonstrict nonlinear systems. Neurocomputing **363**, 273–280 (2019). ISSN: 0925-2312. https://doi.org/10.1016/j.neucom.2019.06.063
13. Glida, H.E., Abdou, L., Chelihi, A., Sentouh, C., Perozzi, G.: Optimal model-free fuzzy logic control for autonomous unmanned aerial vehicle. Proc. Inst. Mech. Eng. G: J. Aerospace Eng. **236**(5), 952–967 (2022). https://doi.org/10.1177/09544100211025379

A New Key Generator Based on an Auto-Switched Hybrid Chaotic System and Its FPGA Implementation

Sid Hichem, Azzaz Mohamed Salah, and Sadoudi Saïd

1 Introduction

Currently, several chaotic generators have been studied and analyzed [1], some of them have only been simulated. Others have not been sufficiently optimized for cryptographic applications when they provide practical problems during hardware implementation. However, several chaotic generator implementations on FPGA technology have been carried out. Among the most famous generators, we find the generators of Lorenz, Chen, Chua and Lü, etc. [2–5]. Conversely, these main chaotic generators are easily identifiable by a simple visualization of their attractors, which can be used in cryptosystems [6]. Moreover, in today's digital communication systems, another important factor that we must take into consideration is finite precision [7].

When chaotic systems are implemented or implanted in digital form, a dynamic degradation of the response occurs. More precisely, the dynamic properties of digital chaotic systems can become non-ideal. The most well-known problem is the existence of many chaotic short-length orbits, which can weaken the desired statistical properties of chaotic evolving digital data, resulting in degradation of the security of the encryption process. In this context, it becomes important to mask or develop mechanisms associated with these generators in order to increase the complexity of a cryptanalysis from an identification of the chaotic signals of the key generator of a cryptosystem on one side and to solve the problem of precision during a digital implementation on the other hand.

S. Hichem (✉) · A. M. Salah
Laboratoire Systèmes Electroniques et Numériques, EMP, Algies, Algeria

S. Saïd
Laboratoire Télécommunications, EMP, Algies, Algeria

© The Author(s), under exclusive license to Springer Nature Switzerland AG 2024

W. Lacarbonara (ed.), *Advances in Nonlinear Dynamics, Volume III*, NODYCON Conference Proceedings Series, https://doi.org/10.1007/978-3-031-50635-2_17

In this chapter, we will use the principle of chaos in order to propose, design, and implement a new generator that better responds to the requirement of modern cryptography in terms of power consumption, speed, safety, and cost of production.

The interest of our solution is to propose a complex chaotic system allowing an unidentifiable cipher key generator by an analysis of its attractors, while proposing optimized architecture and hardware implementation giving a very useful and attractive compromise between high speed, low area cost and secure data communications for embedded applications. Our proposed logic Register Transfer Level (RTL) architecture is based on a pipelined numerical method to resolve several 3D chaotic differential equations characterizing some chaotic systems. Therefore, this proposed RTL architecture can be used as a more complex hard key chaotic generator in embedded self-synchronizing stream cipher encryptions. The rest of this chapter is organized as follows. In Sect. 2, a description of the chaotic auto-switched model is presented. In this section, the modeling of the presented auto-switched system and its hardware architecture to implement is proposed. The simulations result on Xsim of Vivado and the hardware implementation results on FPGA technology and performance evaluations are discussed in Sect. 3. At the end of this section, the random dynamical behaviors of our new scheme is evaluated through statistical tests in order to prove that the proposed hybrid generator exhibits truly random sequences suitable as cipher keys for data encryption. Finally, Sect. 4 concludes the chapter.

2 Methods

2.1 Modeling

The implementation of a three-dimensional continuous-time system requires a discretization of the latter and consequently the use of the methods of numerical resolution of the differential equations. To address the flow/cost problem of the implantation circuit, a comparative study was made between three numerical resolution methods: Runge Kutta of order 4 (RK4), Euler (EU), and Euler Modifier (EUM). In order to overcome the problem of finite precision, we adopted an approach based on the perturbation technique. Therefore, we used three continuous-time systems (Lorenz, Rôssler, and Chen) as a disturber and Henon Map's discrete-time system as a disturbance. The idea is to disrupt the trajectories of the Henon system by one of the outputs of the three disturbing generators, which is chosen by a multiplexer controlled by a switch based on the "X_{n+1}" output of the Henon Map (disturbed). The goal is to make the trajectories of the Henon system more complex and the length of the orbits generated longer. This technique is shown in Fig. 1. The Euler method (EU) can be built from a Taylor expansion of order 1. The Runge Kutta (RK4) and Euler Modifier (EUM) methods are built from a Taylor expansion of higher order [8] (Fig. 2).

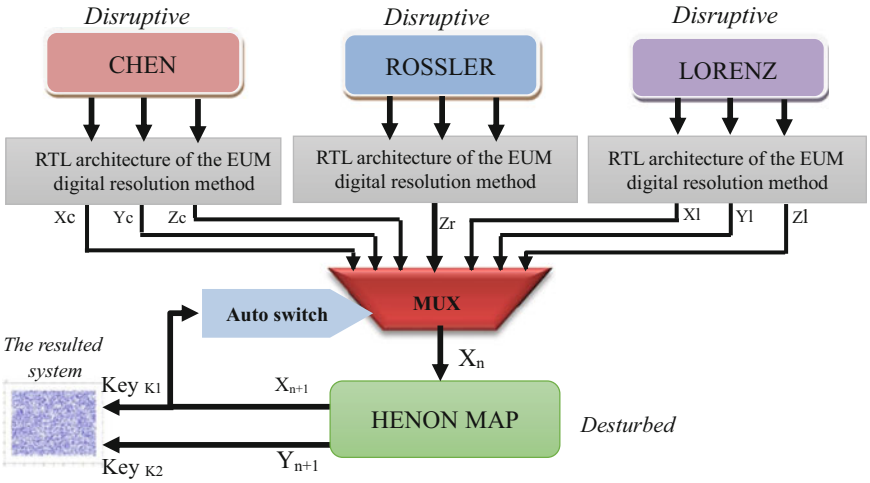

Fig. 1 The perturbation technique adopted for the modeling of the proposed generator

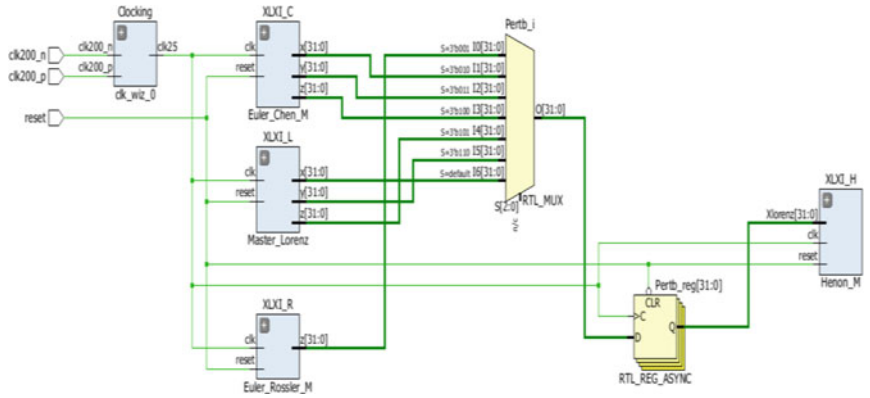

Fig. 2 RTL architecture of the proposed new generator

By comparing the results obtained by the three methods (these results are not presented in this work), we notice that the methods of EUM and RK4 give more precise results than those obtained by EU (we mean the precision, the accuracy of the trajectories, and the finity of the signals obtained). On the other hand, the RK4 method consumes more resources than the EUM, Therefore, we chose the EUM.

This subsection briefly describes our proposed auto-switched 3D systems based chaos for creating complex chaotic behaviors (complex attractors) with best statistical properties. We then consider the system of Lorenz, which is a famous example of a differential system with chaotic behavior parameter values [1]. This system is defined by the following equations:

$$\begin{cases} \dot{x} = \sigma\,(y - x) \\ \dot{y} = -xz + rx - y \\ \dot{z} = xy - bz \end{cases} \tag{1}$$

The standard parameter values for the Lorenz's chaotic attractor are: $\sigma = 10$; $r = 28$; $b = 8/3$. Similarly, we consider the Chen system introduced by Chen [3] described by:

$$\begin{cases} \dot{x}_2 = a\,(y_2 - x_2) \\ \dot{y_2} = (c - a)\,x_2 - x_2 z_2 + c y_2 \\ \dot{z_2} = x_2 y_2 - b z_2 \end{cases} \tag{2}$$

The Chen system presents chaotic behavior for the following value parameters: $a = 35$; $b = 3$; $c = 28$.

The Rössler System was proposed by Otto Rössler [9]. It is defined by the following system of equations (for a digital simulation, we take $a = b = 0.4$ and $c = 4$):

$$\begin{cases} \dot{x} = -\,(y + z) \\ \dot{y} = -x + ay \\ \dot{z} = b + z\,(x - c) \end{cases} \tag{3}$$

For the disturbed generator we chose Henon Map, which is a model proposed by the mathematician Michel Henon. This system introduces iterations into the plan [10]. These iterations are defined by the following relations with $a = 1.14$, $b = 0.3$:

$$\begin{cases} x_{k+1} = a - x_k^2 + b y_k \\ y_{k+} = x_k \end{cases} \tag{4}$$

We consider a first order differential equation:

$$F\,(x, y) = \frac{dy}{dx} \tag{5}$$

The EUM method uses several intermediate points of the initial value y_i by induction for the calculation of y_{i+1} according to a step 'h' of calculation of x. It defines two series. A first series, which defines the values of x from an initial value x_i, and a second series, which defines the values of y from an initial value y_0 and the following recurrence relation:

$$y_{i+1} = y_i + \frac{1}{2} \times (k_1 + k_2)$$

with:

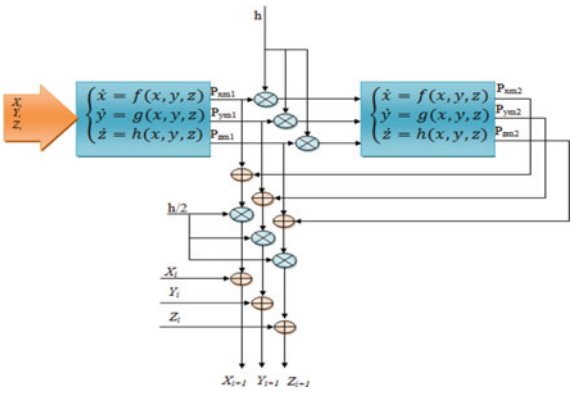

Fig. 3 RTL architecture of the EUM method

$$k_1 = h \times f\,(x_i, y_i)$$

$$k_2 = h \times f\,(t_i + h, y_i + k_1) \tag{6}$$

The RTL is a structural description of these methods by a VHDL hardware language. In (Fig. 3) we introduce our proposed RTL architecture of EUM.

For this auto-switched generator, the implemented switching rule varies with the parameter $sw = x_{n+1}(13 \text{ downto } 12)$.

(x_{n+1} is the first out of the Henon Map which is coded in 32 bits). "*sw*" is defined by the following logic conditions:

$$\begin{cases} x_n = x_c & \text{if } sw = "000" \\ x_n = y_c & \text{if } sw = "001" \\ x_n = z_c & \text{if } sw = "010" \\ x_n = x_r & \text{if } sw = "011" \\ x_n = x_l & \text{if } sw = "100" \\ x_n = y_l & \text{if } sw = "101" \\ x_n = z_l & \text{if } sw = "110" \end{cases} \tag{7}$$

3 Results and Discussion

3.1 Simulation Results

We coded the architecture of the new generator proposed in VHDL under Vivado16.2 using the RTL EUM architecture. For the proposed digital implementation, we have adopted a fixed-point representation of real data on 32 bits (16Q16), i.e., all data are fixed-point format with 16 bits integer and 16 bits

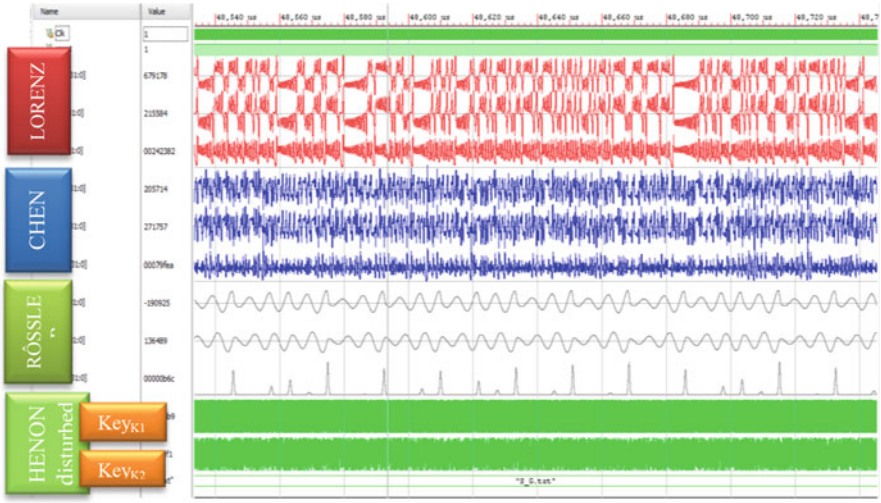

Fig. 4 XSilm simulation results of the perturbation technique adopted for the modeling of the proposed generator

fraction. To test the effectiveness of our solution, we simulated our RTL architecture with the integrated simulation module of Vivado. The results obtained are presented in Fig. 4. We observe that our hybrid generator based chaos has a complex chaotic behavior, much more complex than the four chaotic systems used (Lorenz, Rôssler, Chen and Henon).

3.2 Real-Time FPGA Implementation

The RTL description of the proposed architecture has been implemented on FPGA development platform Genesys2 with a Kintex-7 circuit type "xc7k325-0" from the Xilinx family using VHDL structural description. Vivado16.2 of Xilinx tool has been used for this digital implementation allowing to obtain the logic resource requirements and the associated real-time constraints. The synthesis results after place and route show the performance analysis of our implementation in Table 1. This table depicts the hardware resources in terms of the logic Slice or the Slice Flip-Flops and LUTs numbers and the power consumption. The performance of our RTL hardware architecture depends on the configured size of the fixed-point data. As a result, our logic implementation on a Xilinx Genesys2 requires only 0.84% CLB-Slices (LUT), a low power consumption (0.144 w) and a very low latency (1.10 ns). This very low use of the resources of our card is due, firstly, to the rich resources of the Genesys2 card and, secondly, to our working approach and the optimization of the codes developed.

Table 1 FPGA implementation results for the proposed auto-switched generator based chaos

Resource	Use (%)
LUT	0.84
FF	0.05
DSP	3.33
IO	6.80
BUFG	3.13
Power	0.144 w
Latency	1.10 ns

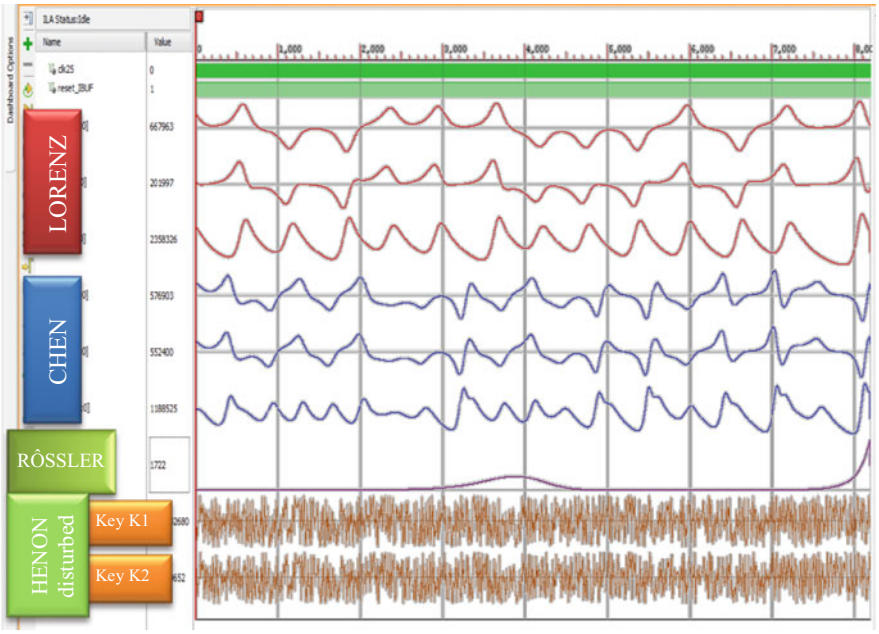

Fig. 5 Experimental ILA results of the perturbation technique adopted for the modeling of the proposed generator

3.3 Visualization of Implantation Results

To visualize the different signals of our generator in real time, we used an IP (Intellectual Property) under the name ILA (Integrated Logic Analyzer). The results obtained are presented in Fig. 4. We observe the similarity between the simulation results and the real-time implementation results of our new generator, which validates our hardware implementation approach based on the fixed-point representation and the use of numerical resolution methods (Fig. 5).

Table 2 NIST battery statistical test results for the "K1" encryption key

Tests	P-Value	
Frequency	0.350485	Success
Block frequency	0.000439	Success
Cumulative sums (Cusum)	0.739918	Success
Runs	0.066882	Success
Longest run of ones in a block	0.122325	Success
Binary matrix rank	0.534146	Success
Discrete fourier transform	0.534146	Success
Nonverlapping template	0.911413	Success
Overlapping template	0.122325	Success
Maurer's/universal statistical"	0.035174	Success
Approximate entropy	0.066882	Success
Random excursions	0.310483	Success
Random excursions variant	0.213309	Success
Serial	0.534146	Success
Linear complexity test	0.739918	Success

3.4 Statistical Tests

The generators of random keys or RNG (Random Number Generator) are the main basis of cryptography [11]. It is well known that the notion "random" is very important in the field of cryptography, especially for the generation of irreversible encryption keys. Chaotic systems are designed with a bare minimum of unpredictability and independence of random keys generated. The unpredictability of the keys in the security systems means the inability for anyone to observe, to duplicate, or manipulate the generator [12], even in a hostile environment. Yet it is very difficult to meet these conditions, and if it is not done correctly, it will be a disaster for the security systems. This is why RNG must satisfied very demanding conditions in the unpredictability and satisfaction of certain statistical properties. In addition, their robustness and resistance to external attacks must be proven by recent additional internal tests [13]. To quantify the random criterion of the generated keys, we performed a statistical analysis using the statistical test batteries of NIST, DIEHARD and ENT.

NIST TEST
We analyzed the recorded sequence in a binary file (.bin) of size 11 MB. Table 2 summarizes the results obtained (P-value). From this table, we can see that all NIST tests passed, so our encryption keys have good statistical properties.

DIEHARD TEST
Also, using the DIEHARD statistical test battery, we performed another statistical analysis on the encryption key. In order to obtain statistically correct results, it is necessary to perform tests on a sequence of size 3 million integers (of 32 bits). In our case, we used 144 million bits in a binary size file (11 MB). The battery of

Table 3 Diehard battery statistical test results for the "K1" encryption key

Tests	P-Value	
Birthday spacings test	0.995439	Success
Overlapping 5-permutation test	0.552539	Success
Binary rank test for 31 _ 31 matrices	0.342345	Success
Binary rank test for 32 _ 32 matrices	0.229764	Success
Binary rank test for 6 _ 8 matrices	0.413638	Success
Bitsream test	0.55821	Success
The tests OPSO, OQSO and DNA	0.84770.55620.8346	Success
COUNT-THE-1's test on a stream of bytes	0.810620	Success
Count the _1's test for specific bytes	0.822892	Success
A parking lot test	0.048881	Success
Minimum distance test	0.557088	Success
3d spheres test	0.012766	Success
Squeezee test	0.973124	Success
Overlapping sums test	0.782892	Success
Runs test	0.453939	Success
Craps test	0.89731	Success

Table 4 ENT battery statistical test results for the "K1" encryption key

Tests	P-Value
Entropy	7.999965 bits per byte = 8
Chi-square test	485.72 > 17.26
Arithmetic mean	127.5596 (127.5 = random)
Monte Carlo value for Pi	3.135361209 (error 0.02%)
Serial correlation coefficient	0.499928

DIEHARD tests consist of verifying the distribution of P-values for each test. The results of the tests obtained are presented in Table 3. It shows that all DIEHARD tests are passed successfully, which means our encryption keys were able to respond to safety requirements in terms of random properties.

ENT TEST

We notice that our results passed all the tests successfully. Now we can say that the generated keys have a random character, so they are robust, and they are ready to be used in cryptosystems (Table 4).

4 Conclusion

A new chaos-based encryption key generator is developed. The three dimensional chaotic system is resolved by the numerical resolution method (Euler-Modifier). The simulation and synthesis results allowed us to validate our hardware implementation approach based on the fixed-point representation and the use of numerical resolution

methods (in terms of cost / performance). Indeed, the implementation of this new generator on a Xilinx Genysis2 platform requires only 1% of CLB-Slices and allows a key generation rate of 7.43 Gbps (with a clock frequency of 237.7 MHz), a low power (0.144 W), and a low latency of 1.1 ns. Furthermore, we observed that our hybrid generator based chaos has a complex chaotic behavior, which make the identification of this generator by a simple visualization of his attractor very difficult. Moreover the generated keys respond to safety requirements in terms of random properties. Also, we solved the problem of precision which appears during a digital implementation (many chaotic short-length orbits).

Finally, this new key generator based on an auto-switched hybrid chaotic system is ready to be used in efficient embedded ciphering communication systems in terms of power consumption, speed, safety, and cost production.

References

1. Atzori, L., Iera, A., Morabito, G.: The internet of things: a survey. Comput. Netw. **54**, 2787–2805 (2010)
2. Lorenz, E.N.: Deterministic nonperiodic flow. Atmos. Sci. **20**, 130–141 (1963)
3. Chen, S., Yu, J., Lû, G.C., He, J.: Design and FPGA-based realization of a chaotic secure video communication system. IEEE Trans. Circuits Syst. Video Technol. **28**, 2359–2371 (2017)
4. Chua, L.O.: Chua's circuit 10 years later. Int. J. Circuit Theory Appl. **22**, 279–305 (1994)
5. Pande, A., Zambreno, J.: A chaotic encryption scheme for real-time embedded systems: design and implementation. Telecommun. Syst. **52**, 551–561 (2013)
6. Azzaz, M.S., Tanougast, C., Sadoudi, S., Fellah, R., Dandache, A.: A new auto-switched chaotic system and its fpga implementation. Commun. Nonlinear Sci. Numer. Simul. **18**, 1792–1804 (2013)
7. Azzaz, M.S.: Implantation paramétrable d'un nouvel algorithme de cryptage symétrique basé Chaos par inclusion au sein d'une architecture recongurable de type FPGA. PhD thesis, Cotutelle de thèse EMP Alger- Université de Lorraine-France (2012)
8. Azzaz, M.S., Tanougast, C., Maali, A., Benssalah, M.: An efficient and lightweight multi-scroll chaos-based hardware solution for protecting fingerprint biometric templates. Int. J. Commun. Syst. **33**, 4211 (2020)
9. Li, C., Chen, G.: Chaos and hyperchaos in the fractional-order Rôssler equations. Physica A Stat. Mech. Appl. **341**, 55–61 (2004)
10. Feit, M., Fleck Jr., J.: Wave packet dynamics and chaos in the hénon-heiles system. J. Chem. Phys. **80**, 2578–2584 (1984)
11. Patidar, V., Sud, K.: A novel pseudo random bit generator based on chaotic standard map and its testing. Electron. J. Theor. Phys. **6**, 327–344 (2009)
12. Lin, T., Chua, L.O.: A new class of pseudo-random number generator based on chaos in digital filters. Int. J. Circuit Theory Appl. **21**, 473–480 (1993)
13. Alvarez, G., Li, S.: Some basic cryptographic requirements for chaos-based cryptosys-tems. Int. J. Bifurcat. Chaos. **16**, 2129–2151 (2006)

Critical Dynamics of Kuramoto Model on Erdös–Rényi Random Graphs

Hai Chen

1 Introduction

Synchronization of interacting elements is ubiquitous in nature and has been widely investigated in many physical and biological systems, such as flashing fireflies, neurons in the brain, electric power grids, and Josephson junction arrays [1, 2]. Kuramoto introduced an analytically solvable model of coupled oscillators and thus inspired extensive studies on phase synchronization research since the 1980s [3–5]. In spite of its mature age, the theory of synchronization is still full of surprises, applications, and new features [6–8].

The synchronization of coupled oscillators depends on many factors, such as the coupling strength, the network topology, the natural frequency distribution, interaction time delay, etc. [9]. As these factors evolve and cross certain critical values, phase transition to or out of synchronization may occur in a smooth (second-order like) or abrupt (first-order like) way [10, 11]. Much attention has been focused on how the critical dynamics of these factors influence the result of synchronization. One of the key factors, the network topology, determines how interaction and information propagate among the elements. As the network topology's complexity increases, the evaluation of Kuramoto model's critical dynamics becomes very challenging [12–17]. The random graph model proposed by Paul Erdös and Alfred Rényi [18] is simple yet elegant and can be integrated into the Kuramoto model by connecting each pair of oscillators with a fixed link probability p. In spite of its limitations in simulating real-world networks that follow power-law degree distribution [19], it is the basis of many variations of random graph models and has important applications in statistical physics (e.g., percolation theory [20]).

H. Chen (✉)
Department of Physics, Zhejiang University, Hangzhou, China
e-mail: haichen@zju.edu.cn

© The Author(s), under exclusive license to Springer Nature Switzerland AG 2024

W. Lacarbonara (ed.), *Advances in Nonlinear Dynamics, Volume III*, NODYCON Conference Proceedings Series, https://doi.org/10.1007/978-3-031-50635-2_18

In this chapter, we apply the Erdös–Rényi (ER) random graph topology to Kuramoto model and aim to understand the two-dimensional critical behaviors with the graph link probability p and coupling strength K. This chapter is organized as follows: In Sect. 2, we first use semi-quantitative analysis to obtain the effective critical coupling K_{ec} and demonstrate the relation between link probability p and coupling strength K on the critical curve. Then we present the numerical simulations of large-scale Kuramoto systems with stochastic initial conditions and random graph topology in Sect. 3. The simulation results are compared with analytical prediction on the two-dimensional critical link probability p_c and critical coupling strength K_c. Finally, summary and discussion follow in Sect. 4.

2 Analysis

We start with the unweighted and undirected Kuramoto model, and the governing dynamic equation of the oscillators is [4]

$$\frac{d\theta_i}{dt} = \omega_i + \frac{K}{N}\sum_{j=1}^{N} W_{ij}\sin(\theta_j - \theta_i). \tag{1}$$

Here each oscillator's phase is denoted by θ_i, and its natural frequency ω_i follows a given distribution $g(\omega)$. For simplicity, we assume $g(\omega)$ to be a unimodal and symmetric function ($g(\omega) = g(-\omega)$), and in our study, a Gaussian distribution is utilized. K is the coupling strength, and we assume K to be homogeneous between all the connected oscillators pairs. W_{ij} is the adjacency matrix element to determine the connectivity between oscillators ($W_{ij} = W_{ji}$).

Kuramoto's conventional order parameter is defined by Strogatz [9]

$$Re^{i\Psi} = \frac{1}{N}\sum_{j=1}^{N} e^{i\theta_j}, \tag{2}$$

where R and Ψ represent the system's phase coherence and average phase, respectively, by taking the average of all the oscillators. For fully connected network ($W_{ij} = 1$), Eq. (1) can be simplified to

$$\frac{d\theta_i}{dt} = \omega_i + KR\sin(\Psi - \theta_i). \tag{3}$$

To visualize the outcome of Kuramoto model's synchronization, Fig. 1 shows the numerical simulation of $N = 500$ fully connected network's initial random states and final synchronized states after 1500 time steps (step size $dt = 0.1$ s). The Gaussian natural frequency distribution $g(\omega)$ has a standard deviation $\sigma = 0.1$. The

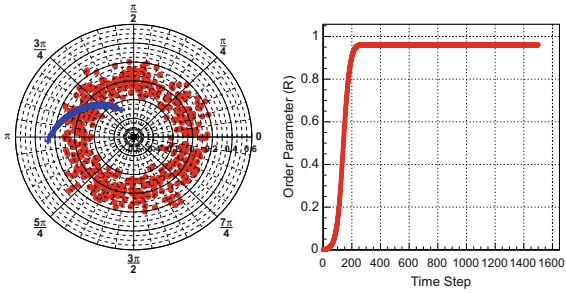

Fig. 1 Numerical simulation of $N = 500$ fully connected oscillators, with coupling strength $K = 1.0$. Left: initial(red) and final (blue, after 1500 time steps) distribution of oscillator phases, the radial axis represents natural frequency; right: the evolution of order parameter R as a function of time step

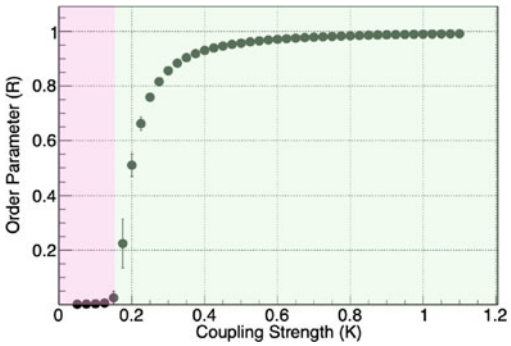

Fig. 2 Order parameter R as a function of coupling strength K for fully connected Kuramoto model

time evolution of order parameter R is displayed on the right, which shows a plateau curve when the system reaches synchronization.

For fully connected system, the one-dimensional phase transition diagram can be obtained by calculating R under different coupling strengths K, as shown in Fig. 2 for $0.05 \leq K \leq 1.1$. Clear phase separation between random states and synchronized states can be observed as K crosses the critical value K_c, which has been predicted to be $K_c = 2/\left[\pi g(0)\right] \approx 0.160$ in this case [9].

Then the question naturally arises that, for not fully connected system, how does the phase transition occurs according to the topology of the network? The adjacency matrix W determines the network structure, and thus its mathematical properties should govern the dynamics of the system. To date, a number of studies have attempted to evaluate the impact of network topology on the phase transition of synchronization [14, 21–23]. These examples include Erdös–Rényi graphs, Paley graphs, small-world networks, and other stochastic graphs. Erdös–Rényi random graph model is simple, yet it has useful applications, and it is closely related to other random discrete structures such as random surfaces, Ising model, and percolation theory. Figure 3 gives two examples of Erdös–Rényi random graph with 50 nodes and link probabilities $p = 0.2$ and $p = 0.5$. Intuitively for more connected random

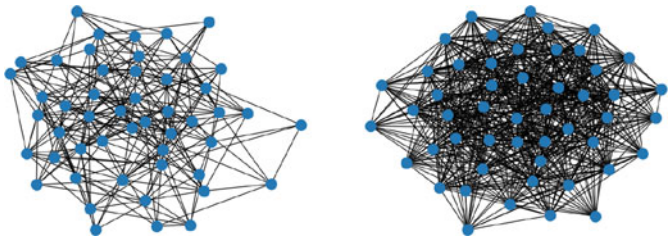

Fig. 3 Two examples of Erdös–Rényi random graph with 50 nodes and link probabilities $p = 0.2$ and $p = 0.5$

graphs, the interactions are easier to propagate over the network, and the critical phase transition requires less coupling strength. Chiba and Medvedev [22, 23] give a thorough investigation on Kuramoto model on graphs using the mean field analysis by calculating the eigenvalues of self-adjoint kernel operator from matrix W. Instead of deploying intimidating mathematical techniques, we aim to understand the critical dynamics by statistical and numerical analysis in this chapter.

Although it is impossible to directly solve the simultaneous equations (1) of all N oscillators due to the stochastic nature of ER random graph's W_{ij} elements and initial phase conditions, we can perform a statistical semi-quantitative analysis on how Kuramoto model evolves under this topology. We construct a total of M virtual copies of the system and denote the m-th copy's oscillator phases as $\theta_{m1}, \theta_{m2}, \cdots, \theta_{mN}$. For these virtual copies, we let each copy's oscillators to be identical, and the connection edges are generated according to ER random rules. As we aim to study the statistical average behaviors of all possible ensembles, we require that each copy's i-th oscillators are strongly coupled to their correspondences in other system copies, with virtual coupling strength $\Omega_{mn,i} \gg \omega_i$. The purpose of introducing the extra coupling term between layers is to study how these systems evolve collectively with only one different factor, the topology adjacency matrices. It is equivalent to require a coordinate transformation of θ_{mi} between layers so that all i-th oscillators will always be in the same phase. This also means the oscillators are glued together and form N tight virtual clusters, and the overall dynamics of these clusters are determined by the combination of all copies' topologies. Then the Kuramoto model of each oscillator can be rewritten to

$$\frac{d\theta_{mi}}{dt} = \sum_{n=1}^{n\neq m} \Omega_{mn,i} + \omega_i + \frac{K}{N} \sum_{j=1}^{N} W_{ij} \sin(\theta_{mj} - \theta_{mi}). \tag{4}$$

By this construction, there are in total $M \times N$ oscillators for all virtual copies, but the strong coupling terms $\Omega_{mn,i}$ give rise to the clusterization of $\theta_{mi} = \theta_{ni}$. Thus we can reduce the complexity by noting that the internal coupling terms will cancel out between m-th and n-th copy pairs when we add up their Eq. (4), which contain positive and negative contributions, respectively ($\Omega_{mn,i} = -\Omega_{nm,i}$). We can define

i-th oscillator's average phase as

$$\bar{\theta}_i = \frac{1}{M} \sum_{m=1}^{M} \theta_{mi}.$$

By taking sum of Eq. (4) for all the ensembles, we can obtain

$$\frac{d\bar{\theta}_i}{dt} = \omega_i + \frac{K}{MN} \sum_{j=1}^{N} W_{ij} \sum_{m=1}^{M} \sin(\bar{\theta}_j - \bar{\theta}_i). \tag{5}$$

For large ensemble number M, the edge number between each oscillator pairs, $W_{ij} \cdot M$, can be approximated to $p(M-1) \approx pM$, and Eq. (5) can be reduced to the average phase dynamic equation:

$$\frac{d\bar{\theta}_i}{dt} = \omega_i + \frac{K \cdot p}{N} \sum_{j=1}^{N} \sin(\bar{\theta}_j - \bar{\theta}_i). \tag{6}$$

With the above analysis, we convert the statistical average of Kuramoto model on ER random graph into its traditional version of fully connected oscillators, with the new effective coupling strength:

$$K_e = K \cdot p.$$

Following Kuramoto's self-consistent analysis [9], we can predict that under ER topology, there exists a similar effective critical coupling K_{ec}, beyond which synchronization phase transition will occur. Under unimodal frequency distribution $g(\omega)$, the effective critical coupling K_{ec} can be determined as [9]

$$K_{ec} = \frac{2}{\pi \cdot g(0)}. \tag{7}$$

Given by $K_e = K \cdot p$, we expect an inversely proportional relation between p and K at the critical condition. For example, the critical link probability p_c at certain coupling strength K is

$$p_c = \frac{2}{\pi \cdot g(0) \cdot K}. \tag{8}$$

This is exactly an example solution by Chiba and Medvedev's calculation in [22, 23]. In the following section, we will verify this prediction using large-scale numerical simulations.

3 Numerical Simulation

We perform the numerical simulation of Kuramoto model with $N = 1000$ oscillators. The oscillator number N is chosen based on the connectivity property that it is highly probable no isolated nodes exist when above the link threshold $\frac{\log(N)}{N}$. With $N = 1000$, we can explore the link probability region $p > 0.1$. The data samples are generated using the following procedure: (1) the initial phases $\theta_i(0)$ are randomly chosen from uniform distribution in $(0, 2\pi)$, and the natural frequencies ω_i are sampled from Gaussian distribution with $\sigma = 0.1$; (2) for each model parameter pair K and p, the random matrix elements W_{ij} are assigned according to the link probability p and a uniform variable λ:

$$W_{ij} = \begin{cases} 1 & \lambda \leq \mathrm{p} \\ 0 & \text{otherwise} \end{cases}$$

More than 2000 ER graphs are generated in the two-dimensional phase space grids of $K \in (0.05, 1.1)$ and $p \in (0.06, 1.0)$; (3) the Kuramoto model equation (1) is solved numerically using Runge–Kutta method for each ER graph, with time step $dt = 0.1$ s and total evolution time $T = 3000\,dt$; (4) the order parameter is calculated at each time step $R(t)$; (5) finally, $M = 250$ simulation ensembles are repeated for each grid point (K, p) to obtain a statistically significant number of samples.

In total we have numerically solved above 5×10^8 oscillator equations (1). This is achieved by the high-performance computing clusters. We use the average order parameter R in the last 500 time steps as the final stable value:

$$R = \frac{1}{500} \sum_{2500dt}^{3000dt} R(t).$$

Figure 4 shows the distribution of R for ensembles with coupling strength $K = 0.40$ and link probabilities from 0.34 to 0.82. We can clearly see that, as the link probability p increases, the order parameters shift gradually to synchronization states. To quantify their correlation, we evaluate R's dependence on link probability p for different coupling strengths K in Fig. 4. Like the fully connected situation in Fig. 2, there exists a critical link probability p_c, above which the oscillator system transits from random state to synchronized state. The value of p_c depends on the coupling strength K, and there will be no phase transition at any link probability for $K < K_c$.

To determine the critical curve of phase transition, we calculate the critical link probability p_c for each coupling strength K. p_c is obtained by a curve fitting to the data in Fig. 4, with fitting function in the following form using Kuramoto's analysis [9]:

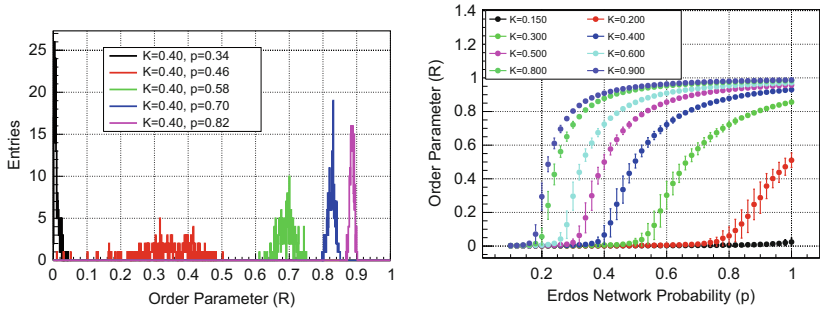

Fig. 4 Left: Histograms of order parameter R with ER link probabilities from 0.34 to 0.82 at coupling $K = 0.40$; right: Order parameter R vs. Erdös–Rényi link probability p under different coupling strengths K

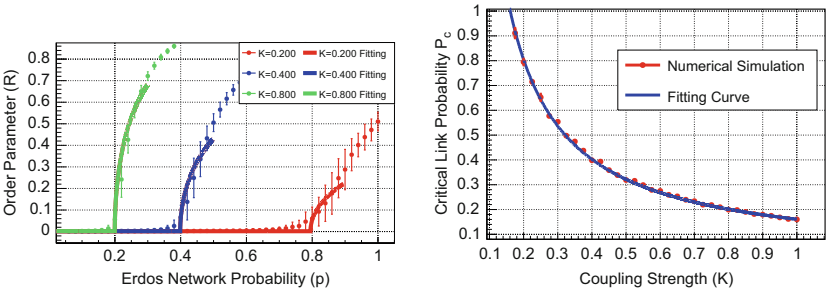

Fig. 5 Left: Examples of fitting to the simulation data of order parameter R and link probability p near the critical points; right: The critical link probability p_c vs. coupling strength K (red points), and fitting curve using inverse proportional function (blue curve)

$$R = \begin{cases} R(0) & \mathrm{p} \leq p_c \\ R(\infty) \cdot \sqrt{1 - \frac{p_c}{p}} & \text{otherwise} \end{cases},$$

where $R(0)$ and $R(\infty)$ are the random and synchronized order parameter constants. Figure 5 shows fitting examples in the vicinity of critical p_c. As can be seen, the fitting function can describe the phase transition features well. Finally, the critical link probability p_c as a function of coupling strength K is shown in Fig. 5. The inversely proportional relation between p_c and coupling strength K is in well agreement with previous analysis in Sect. 2. If expressed in $K_{ec} = p_c \cdot K$, the effective critical coupling K_{ec} is calculated to be 0.161 ± 0.001, close to the fully connected model's critical value $K_c = 0.160$ [9].

Similarly, under coupling strength's dimension, we can analyze the critical coupling K_c's dependence on link probability p. With the same procedure but switching the roles of K and p, we obtain the phase transition curves of order parameter R on K and determine the critical coupling strength K_c as illustrated

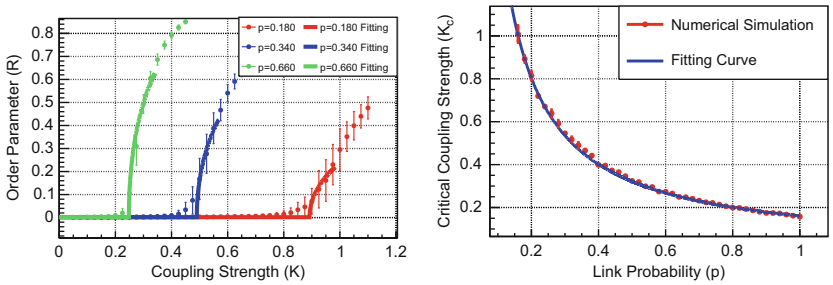

Fig. 6 Left: Order parameter R vs. coupling strength K and fitting curves at the critical points; right: The critical link probability K_c vs. link probability p (red points), and fitting curve using inverse proportional function (blue curve)

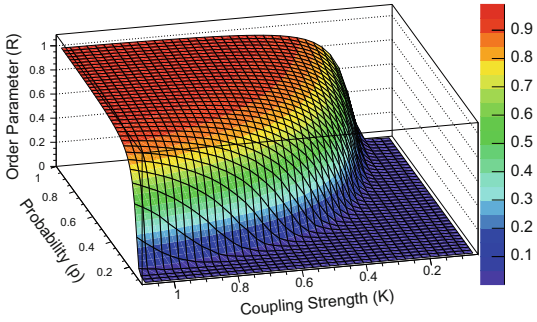

Fig. 7 Order parameter R with link probability p and coupling strength K in three dimensions

in Fig. 6. The resulting effective critical coupling $K_{ec} = K_c \cdot p$ in Fig. 6 is also 0.161 ± 0.001, which is consistent with the above analysis.

Figure 7 shows the three-dimensional distribution of order parameter R with K and p and reveals more details on the critical dynamics of Kuramoto model on the ER topology. We can see that the phase transition condition is jointly decided by K and p. The critical curve in the (K, p) plane follows inverse correlation that has been validated in the above two-dimensional projections.

To summarize, the numerical analysis demonstrates that the effective coupling strength, $K_e = K \cdot p$, can be used as the statistical measure of coupling between each oscillator pair no matter whether or not they are connected. The critical condition of phase transition is thus two dimensional in both K and p, and we can understand this result as follows: For topologically none-connected oscillator pairs, their interaction goes through other intermediate oscillators on the network, and thus the coupling strength K is reduced by a factor. As a special case, Erdös–Rényi topology's uniform link probability p ensures the effective coupling K_e is also statistically homogeneous in the system, and the reduction scaling factor is exactly $\sim p$ compared to the fully connected model.

4 Conclusions

With statistical analysis and extensive numerical simulation, the critical dynamics of Kuramoto model on Erdös–Rényi random graph have been resolved in this chapter. We first show that under ER topology it is statistically equivalent to the traditional fully connected form, with effective coupling strength K_e reduced according to the link probability p. The two-dimensional critical curve of phase transition reveals the simple inverse proportional relations between link probability p and coupling strength K. This leads to possibility of probing a physical system's intrinsic coupling strength if it follows ER random graphs topology. On the basis of this chapter, we will continue to investigate the critical behaviors under more complex network topology, such as small-world, scale-free, and other stochastic graphs. We will also extend the topology studies with the presence of noise, time delay, inertia, etc., to explore new features of Kuramoto model.

References

1. Winfree, A.T.: Biological rhythms and the behavior of populations of coupled oscillators. J. Theor. Biol. **16**(1), 15–42 (1967). https://doi.org/10.1016/0022-5193(67)90051-3
2. Pikovsky, A., Rosenblum, A., Kurths, J.: Synchronization: A Universal Concept in Nonlinear Sciences. Cambridge Nonlinear Science Series. Cambridge University Press, Cambridge (2001)
3. Kuramoto, Y.: Chemical Oscillations, Waves, and Turbulence, vols. 68–77. Springer, Berlin (1984)
4. Kuramoto, Y.: Cooperative dynamics of oscillator community. Prog. Theor. Phys. Suppl. **79**, 223 (1984) https://doi.org/10.1143/PTPS.79.223
5. Acebrón, J.A., Bonilla, L.L., Vicente, C.J.P., Ritort, F., Spigler, R.: The Kuramoto model: a simple paradigm for synchronization phenomena. Rev. Mod. Phys. **77**, 137–185 (2005). https://doi.org/10.1103/RevModPhys.77.137
6. Munyayev, V.O., Bolotov, M.I., Smirnov, L.A., Osipov, G.V., Belykh, I.V.: Stability of rotatory solitary states in Kuramoto networks with inertia. Phys. Rev. E **105**(2), 024203 (2022). https://doi.org/10.1103/PhysRevE.105.024203
7. Velasco, V., Silva Neto, M.B., Perali, A., Wimberger, S., Bishop, A.R., Conradson, S.D.: Kuramoto synchronization of quantum tunneling polarons for describing the dynamic structure in cuprate superconductors. Phys. Rev. B **105**(17), 74305 (2022). https://doi.org/10.1103/PhysRevB.105.174305
8. León, I., Pazó, D.: Enlarged Kuramoto model: secondary instability and transition to collective chaos. Phys. Rev. E **105**(4), L042201 (2022). https://doi.org/10.1103/PhysRevE.105.L042201
9. Strogatz, S.H.: From Kuramoto to Crawford: exploring the onset of synchronization in populations of coupled oscillators. Phys. D: Nonlinear Phenom. **143**, 1–20 (2000). https://doi.org/10.1016/S0167-2789(00)00094-4
10. Basnarkov, L., Urumov, V.: Phase transitions in the Kuramoto model. Phys. Rev. E **76**, 057201 (2007). https://doi.org/10.1103/PhysRevE.76.057201
11. Xu, C., Boccaletti, S., Zheng, Z., Guan, S.: Universal phase transitions to synchronization in Kuramoto-like models with heterogeneous coupling. New J. Phys. **21**, 113018 (2019). https://doi.org/10.1088/1367-2630/ab4f59

12. Strogatz, S.H.: Exploring complex networks. Nature **410**(6825), 268–276 (2001)https://doi.org/10.1038/35065725
13. Albert, R., Barabási, A.L.: Statistical mechanics of complex networks. Rev. Mod. Phys. **74**(1), 47–97 (2002). https://doi.org/10.1103/RevModPhys.74.47
14. Arenas, A., Díaz-Guilera, A., Kurths, J., Moreno, Y., Zhou, C.S.: Synchronization in complex networks. Phys. Rep. **469**, 93–153 (2008). https://doi.org/10.1016/j.physrep.2008.09.002
15. Kalloniatis, A.C., Roberts, D.O.: Synchronisation of networked Kuramoto oscillators under stable Lévy noise. Phys. A: Stat. Mech. Appl. **466**, 476–491 (2017). https://doi.org/10.1016/j.physa.2016.09.051
16. Hancock, E.J., Gottwald, G.A.: Model reduction for Kuramoto models with complex topologies. Phys. Rev. E **98**(1), 012307 (2018). https://doi.org/10.1103/PhysRevE.98.012307
17. Sokolov, Y., Bard Ermentrout, G.B.: When is sync globally stable in sparse networks of identical Kuramoto oscillators? Phys. A: Stat. Mech. Appl. **533**, 122070 (2019). https://doi.org/10.1016/j.physa.2019.122070
18. Erdős, P., Rényi, A.: On the existence of a factor of degree one of a connected random graph. Acta Mathematica Academiae Scientiarum Hungarica **17**(3), 359–368 (1966). https://doi.org/10.1007/BF01894879
19. Barabási, A., Albert, R.: Emergence of scaling in random networks. Science **286**(5439), 509–512 (1999). https://doi.org/10.1126/science.286.5439.509
20. Schmeltzer, C., Soriano, J., Sokolov, I.M., Rüdiger, S.: Percolation of spatially constrained Erdös–Rényi networks with degree correlations. Phys. Rev. E **89**, 012116 (2014). https://doi.org/10.1103/PhysRevE.89.012116
21. Chiba, H., Medvedev, G.S., Mizuhara, M.S.: Bifurcations in the Kuramoto model on graphs. Chaos: Interdiscip. J. Nonlinear Sci. **28**(7), 073109 (2018) https://doi.org/10.1063/1.5039609
22. Chiba, H., Medvedev, G.S.: The mean field analysis for the Kuramoto model on graphs I. The mean field equation and transition point formulas. Discrete Contin. Dyn. Syst. **39**, 131–155 (2019). https://doi.org/10.3934/dcds.2019006
23. Chiba, H., Medvedev, G.S.: The mean field analysis of the Kuramoto model on graphs II. Asymptotic stability of the incoherent state, center manifold reduction, and bifurcations. Discrete Contin. Dyn. Syst. **39**, 3897–3921 (2019). https://doi.org/10.3934/dcds.2019157

Part III
Energy Harvesting

Numerical Simulations of Energy Harvesting in a Portal Frame Coupled with a Nonlinear Energy Sink

Angelo M. Tusset, Alisson L. Agusti, Maria E. K. Fuziki, and Giane G. Lenzi

1 Introduction

It can be observed in recent years that the demand for more efficient and non-polluting renewable energy sources has grown, stimulating new products and an increasing number of research related to the subject. Among the energy sources, we can mention the sources from kinetic energy, which is a source of energy easily found in the environment and obtained from devices that convert kinetic energy into electrical energy and are being widely studied by many researchers, giving special attention to devices that use piezoelectric elements as a means of energy transduction or inductive systems [1, 2]. Among the research, we can mention those that use vibration sources that constantly produce kinetic energy, and these systems can be externally excited by a direct current motor with an unbalanced mass connected to its axis, which is found in several applications. The DC motor provides nonideal excitation, and its amplitude and frequency depend on the vibration of the structure [3]. The nonideal energy source can induce high levels of vibration in a structure, which becomes a promising source of kinetic energy [3–7]. The main advantage of nonlinear energy harvesters is the conversion of energy into a wider range of vibration frequencies [4, 8]. With the use of Nonlinear Energy Sink (NES), it is possible to passively control the vibration levels of a structure, as well as improve the levels of energy collection [2, 4]. NES is a lightweight device, which is coupled to a main system and has essential nonlinear coupling functions (generally a cubic nonlinear stiffness and a linear viscous damper) for localization of passive energy [2, 8–10]. The effectiveness of applying the NES as a passive vibration

A. M. Tusset (✉) · A. L. Agusti · G. G. Lenzi
Federal University of Technology – Parana, Ponta Grossa, PR, Brazil

M. E. K. Fuziki
State University of Maringa, Maringa, PR, Brazil

© The Author(s), under exclusive license to Springer Nature Switzerland AG 2024

W. Lacarbonara (ed.), *Advances in Nonlinear Dynamics, Volume III*, NODYCON Conference Proceedings Series, https://doi.org/10.1007/978-3-031-50635-2_19

control and as a source of energy harvesting is based on the same fundamental mechanism called directed energy transfer [11–13].

In this work, we investigate energy capture through a gantry structure that has a Nonlinear Energy Sink (NES) coupled to its structure. Furthermore, the structure is excited by a nonideal excitation source. The energy collection is analyzed considering the uses of the piezoelectric material considering a nonlinear electromechanical coupling model [4] and an inductive energy source obtained from the NES [2]. For numerical simulations, the parameters used in [3] are considered. The 0-1 test is used to distinguish between regular and chaotic behavior [14–18]. The main advantage of nonlinear energy harvesters is the conversion of energy over a wider range of frequencies of vibrations [1, 2].

2 Mathematical Model

Figure 1 illustrates the portal frame coupled with a nonlinear electromagnetic energy sink, excited by an unbalanced DC motor.

The equations of motion for Fig. 1 can be written as follows:

$$M\ddot{X}_1 + b\dot{X}_1 + b_1\left(\dot{X}_1 - \dot{X}_2\right) + C_e\left(\dot{X}_2 - \dot{X}_1\right) - kX_1 + k_{nl}{X_1}^3 + k_1(X_1 - X_2)^3 = \ldots$$
$$\ldots m_0 r\left(\ddot{\varphi}\sin(\varphi) + \dot{\varphi}^2\cos(\varphi)\right) + \frac{d(X_1)}{C}q \tag{1}$$

$$m_2\ddot{X}_2 - b_1\left(\dot{X}_1 - \dot{X}_2\right) - k_1(X_1 - X_2)^3 - C_e\left(\dot{X}_2 - \dot{X}_1\right) = 0 \tag{2}$$

$$\left(J + m_0 r^2\right)\ddot{\varphi} - m_0 r\ddot{X}\cos\varphi = V_1 - V_2\dot{\varphi} \tag{3}$$

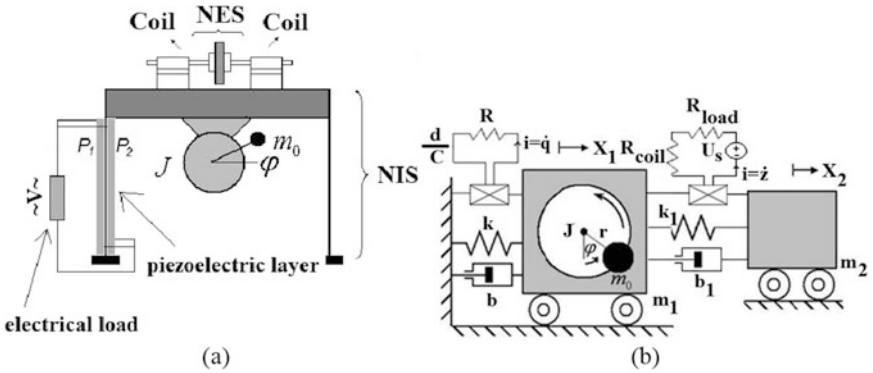

Fig. 1 (**a**) Portal frame energy harvester scheme with nonlinear energy sink. (**b**) Physical model of the oscillator with nonlinear energy sink

$$R\dot{q} - \frac{d(X)}{C}X + \frac{q}{C} = 0 \tag{4}$$

$$\dot{z} = C_c\left(\dot{X}_2 - \dot{X}_1\right) \tag{5}$$

where $M = m_1 + m_0$ is the total mass of the system, m_0 is the eccentric mass of the electric motor shaft, m_1 is the mass of the structure, X_1 is the vertical displacement of the system, c is the damping coefficient, k is the linear stiffness coefficient, k_{nl} is the nonlinear stiffness coefficient, $m_2$is the mass of the NES, $k_l$is the nonlinear stiffness of the NES, b_1 is the linear damping, and $X_2$is the displacement of the NES (oscillator),φ is the angular displacement of the rotor, $r$is the eccentricity, J is the moment of inertia of the motor, V_1 and V_2 are parameters of the DC motor, $d(X)$is a coupling coefficient between the structure and the PZT material, R is the electrical resistance, C is the capacitance, q is the electric charge, U_s is the induced electromotive force, R_{load} and R_{coil} are resistances, $C_e = k_t^2/(R_{\text{load}} + R_{\text{coil}})$and $C_e = k_t/(R_{\text{load}} + R_{\text{coil}})$, where $k_t$is a constant generally referred to as the transduction factor.

Equations (1), (2), (3), (4) and (5) can be written in state-space notation as follows:

$$\dot{x}_1 = x_2 \tag{6}$$

$$\dot{x}_2 = \frac{1}{\Delta}\begin{pmatrix} -\beta_1 x_1 - \alpha_1 x_2 - \alpha_2 (x_2 - x_4) - \beta_3 {x_1}^3 - \alpha_3 (x_1 - x_3)^3 - \varepsilon_4^2 \varepsilon_3 (x_2 - x_4) \\ +\theta x_7 (1 + \Theta |x_1|) + \delta_1 \cos(x_5)\, x_6^2 + \delta_1 \sin(x_5)(-\rho_3 x_3 + \rho_2) \end{pmatrix} \tag{7}$$

$$\dot{x}_3 = x_4 \tag{8}$$

$$\dot{x}_4 = e\left(\varepsilon_1 (x_2 - x_4) + \varepsilon_2 (x_1 - x_3)^3 + \varepsilon_4^2 \varepsilon_3 (x_2 - x_4)\right) \tag{9}$$

$$\dot{x}_5 = x_6 \tag{10}$$

$$\dot{x}_6 = \frac{1}{\Delta}\left(-\rho_3 x_6 + \rho_2 + \rho_1 \cos(x_5)\begin{pmatrix} -\beta_1 x_1 - \alpha_1 x_2 - \alpha_2 (x_2 - x_4) - \beta_3 {x_1}^3 - \\ -\alpha_3 (x_1 - x_3)^3 - \varepsilon_4^2 \varepsilon_3 (x_2 - x_4) + \\ +\theta x_7 (1 + \Theta |x_1|) + \delta_1 \cos(x_5)\, x_6^2 \end{pmatrix}\right) \tag{11}$$

$$\dot{x}_7 = \frac{\theta (1 + \Theta |x_1|)\, x_1}{\rho} - \frac{x_7}{\rho} \tag{12}$$

$$\dot{x}_8 = \varepsilon_4 \varepsilon_3 (x_2 - x_4) \tag{13}$$

where: $\Delta = 1 - \rho_1\delta_1 \cos(x_5) \sin(x_5)$, $\tau = \omega_1 t$, $x_1 = \frac{rX_1}{\omega_1^2}$, $x_3 = \frac{rX_2}{\omega_1^2}$, $\omega_1 = \sqrt{k/(m_1+m_0)}$, $\alpha_1 = \frac{b}{(m_1+m_0)\omega_1}$, $\beta_1 = \frac{k}{(m_1+m_0)\omega_1^2}$, $\beta_3 = \frac{k_{nl}r^2}{(m_1+m_0)\omega_1^6}$, $\delta_1 = \frac{m_0\omega_1^2}{(m_1+m_0)}$,$\varepsilon_3 = \frac{C_e}{m_2\omega_1}$, $\varepsilon_4 = k_t$, $\rho_1 = \frac{m_0 r^2}{(J+r^2m_0)\omega_1^2}$, $\rho_2 = \frac{V_1}{(J+r^2m_0)\omega_1^2}$, $\rho_3 = \frac{V_2}{(J+r^2m_0)\omega_1}$, $\alpha_2 = \frac{b_1}{m_2\omega_1}$, $\alpha_3 = \frac{k_1 r^2}{m_1}$, $\varepsilon_1 = \frac{m_1 b_1}{m_2\omega_1}$, $\varepsilon_2 = k_1 r^2$,$e = \frac{1}{m_2}$, $x_7 = \frac{q}{q_0}$, $\rho = RC\sqrt{k_l/(m_1+m_0)}$, $\hat{d}(x) = \left(\frac{r}{q_0}\right) d(r)$, $\theta\left(\frac{r}{q_0}\right) d_{lin}$, $\hat{d}(x) = \theta(1 + \Theta|x|)$.

The average harvested power is obtained through:

$$P_{\text{avg}} = \frac{1}{T}\int_0^T P_j(\tau)\, d\tau \tag{14}$$

where $j = 1:2$, and the instant power is computed using:

$$P_1 = x_7^2 \tag{15}$$

$$P_2 = x_8^2 \tag{16}$$

2.1 The 0-1 Test Method

Please note that the first paragraph of a section or subsection is not indented. The 0-1 test consists of estimating a single parameter κ by [16]:

$$\kappa = \frac{\text{cov}(Y, M(\overline{c}))}{\sqrt{\text{var}(Y)\,\text{var}(M(\overline{c}))}} \tag{17}$$

where: $\overline{c} \in (0, \pi)$, $M(\overline{c}) = [M(1, \overline{c}), M(2, \overline{c}), \ldots, M(n_{\max}\overline{c})]$and $Y = [1, 2, \ldots, n_{\max}]$.

If κ is close to "0," the system is periodic. On the other hand, if κ is close to "1," the system is chaotic. The test utilizes a system variable $x(j)$, where two new coordinates (p, q) are defined as follows [17, 18]:

$$p(n, \overline{c}) = \sum_{j=0}^{n} x(j)\cos(j\overline{c}) \tag{18}$$

$$q(n, \overline{c}) = \sum_{j=0}^{n} x(j)\sin(j\overline{c}) \tag{19}$$

The mean square displacement of the new variables $p(n, \overline{c})$ and $q(n, \overline{c})$ is given by [18]:

$$M(n,c) = \lim_{n\to\infty} \frac{1}{N} \sum_{j=1}^{N} \left[\left(p(j+n,\overline{c}) - p\left(j,\overline{c}\right) \right)^2 \ldots + \left(q(j+n,\overline{c}) - q\left(j,\overline{c}\right) \right)^2 \right] \tag{20}$$

where $n = 1, 2, \ldots, N$.

3 Numerical Simulations

The numerical simulations are carried out, accounting for the parameters proposed in [3]: $\alpha_1 = 0.1$, $\alpha_2 = 0.1$, $\alpha_3 = 0.5$, $\alpha_4 = 0.05$ $\beta_1 = -1$, $\beta_3 = 0.2$, $\rho_1 = 0.05$, $\rho_2 = 100$, $\rho_3 = 200$, $\delta_1 = 8.373$, $\theta = 0.20$, $\Theta = 0.60$,$\rho = 1.0$, $\varepsilon_1 = 1$, $\varepsilon_2 = 5$, $\varepsilon_4 = [0 : 1.5]$, $e = [0 : 5]$, with the initial conditions:$x_i(0) = 0$, where $i = 1{:}8$.

3.1 Numerical Analysis of the Influence of the Parameter ε_4

In this subsection, the influence of the parameter ε_4 is evaluated, a parameter that represents the transduction factor of the NES system.

Figure 2 shows the 0-1 test and average harvested power results sweeping the parameter ε_4 in the range $\varepsilon_4 = [0 : 1.5]$ with $e = 1$.

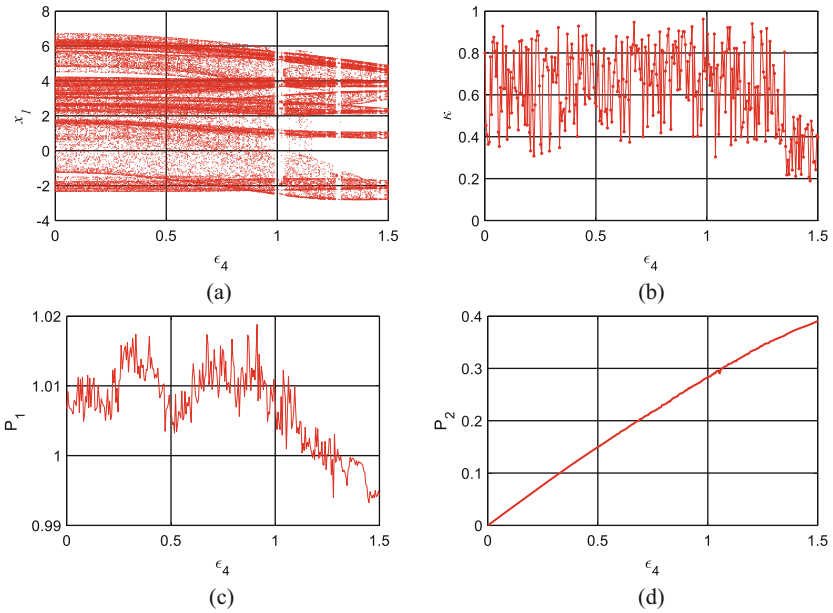

Fig. 2 Simulations for $\varepsilon_4 = [0 : 1.5]$ and $e = 1$. (**a**) Bifurcation diagram. (**b**) 0-1 test. (**c**) Power P_1. (**d**) Power P_2

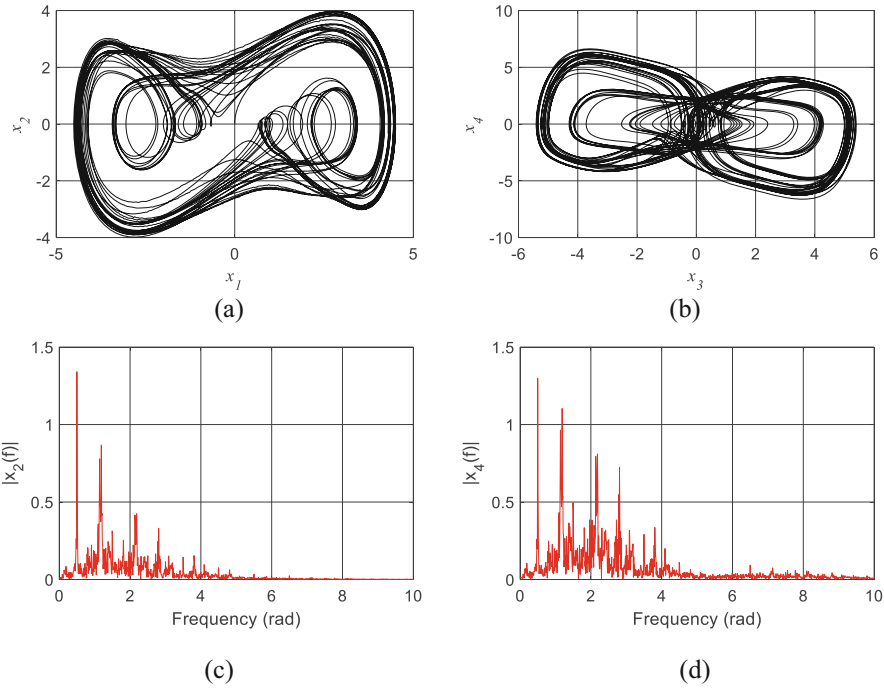

Fig. 3 Simulations for $\varepsilon_4 = 0.26$ and $e = 1$. (**a**) Phase diagram for x_1 versus x_2. (**b**) Phase diagram for x_3 versus x_4. (**c**) Power spectral density (FFT) for x_2. (**d**) Power spectral density (FFT) for x_4

It can be observed in Fig. 2 that as the value of the transduction factor of the NES (ε_4) is increased, we have a reduction in the displacement amplitude of the portal frame (Fig. 2a), thus reducing the average power of the PZT material (P_1), and an increase in the average power of the NES (P_2), with a slight reduction in the value of test 0-1, for values of ε_4 close to 1.5.

In Fig. 3, one can observe the behavior of the system for $\varepsilon_4 = 0.26$ and $e = 1$.

It can be observed in Fig. 3 that the system has a chaotic behavior, with $\kappa = 0.99$for x_1, average power for $P_1 = 1.0082$, and average power for $P_2 = 0.0799$.

3.2 Numerical Analysis of the Influence of the Parameter e

In this subsection, the influence of the parameter e is evaluated, a parameter that is related to the mass of the NES.

Figure 4 shows the 0-1 test and average harvested power results sweeping the parameter e in the range $e = [0.1 : 5]$ with $\varepsilon_4 = 0.26$.

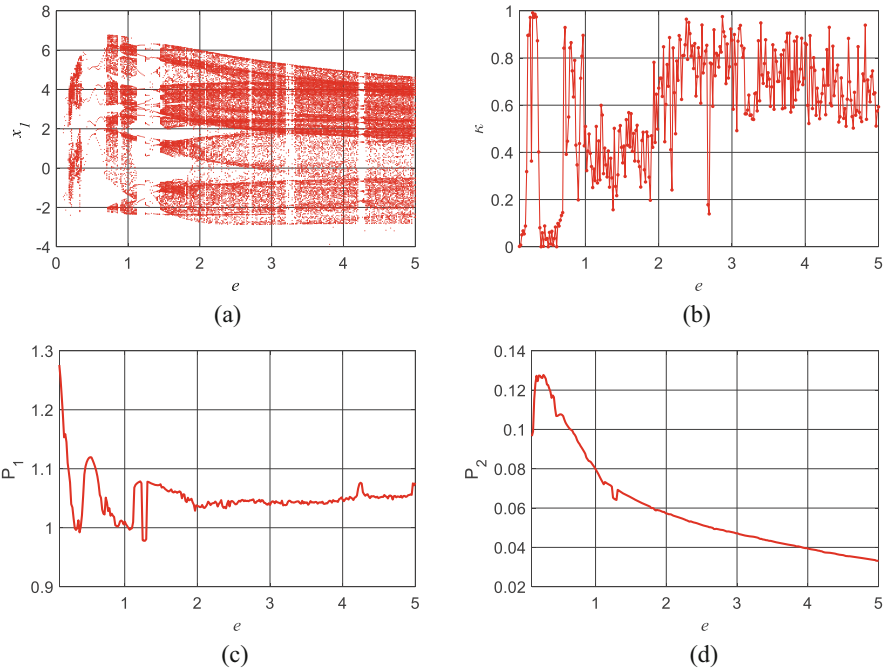

Fig. 4 Simulations for $\varepsilon_4 = 0.26$ and $e = [0.1 : 5]$. (**a**) Bifurcation diagram. (**b**) 0-1 test. (**c**) Power P_1. (**d**) Power P_2

We can observe in the results presented in Fig. 4 that for a few values of (e), the system has a periodic behavior, and its variation has a greater influence on the average power of the NES, for values greater than 1. We can also observe that for certain values of e, we have a reduction in the amplitude of displacement of the portal frame.

In Fig. 5, one can observe the chaotic behavior of the system (2) for $\varepsilon_4 = 0.26$ and $e = 0.5$.

It can be observed in Fig. 5a that the system has a periodic behavior, with $\kappa = 0.1$for x_1, average power for $P_1 = 1.119$, and average power for $P_2 = 0.1076$.

In Fig. 6, one can observe the chaotic behavior of the system (2) for $\varepsilon_4 = 0.26$ and $e = 2.5$.

It can be observed in Fig. 6 that the system has a chaotic behavior, with $\kappa = 0.99$for x_1, average power for $P_1 = 1.042$, and average power for $P_2 = 0.051$.

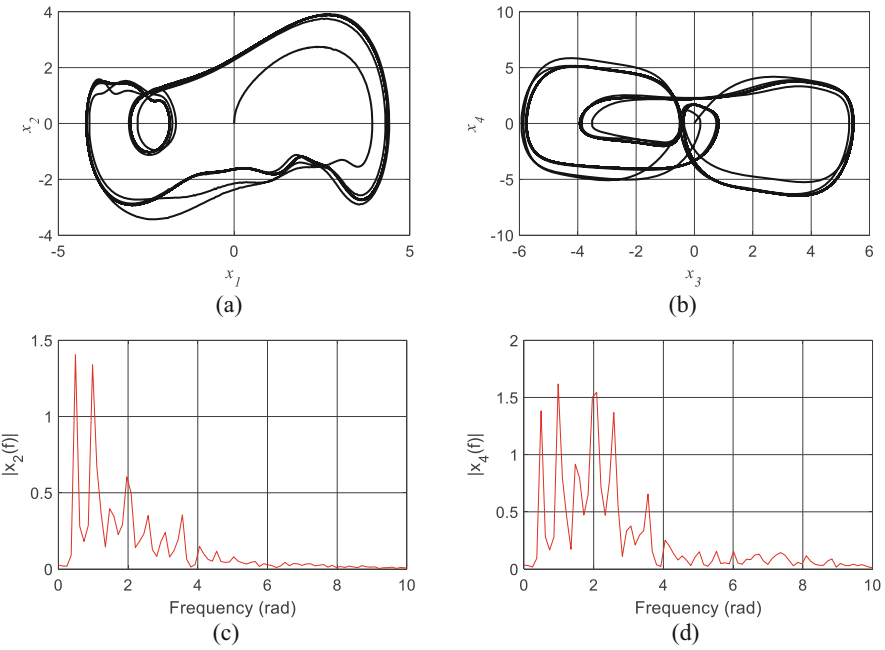

Fig. 5 Simulations for $\varepsilon_4 = 0.26$ and $e = 0.5$. (**a**) Phase diagram for x_1 versus x_2. (**b**) Phase diagram for x_3 versus x_4. (**c**) Power spectral density (FFT) for x_2 . (**d**) Power spectral density (FFT) for x_4

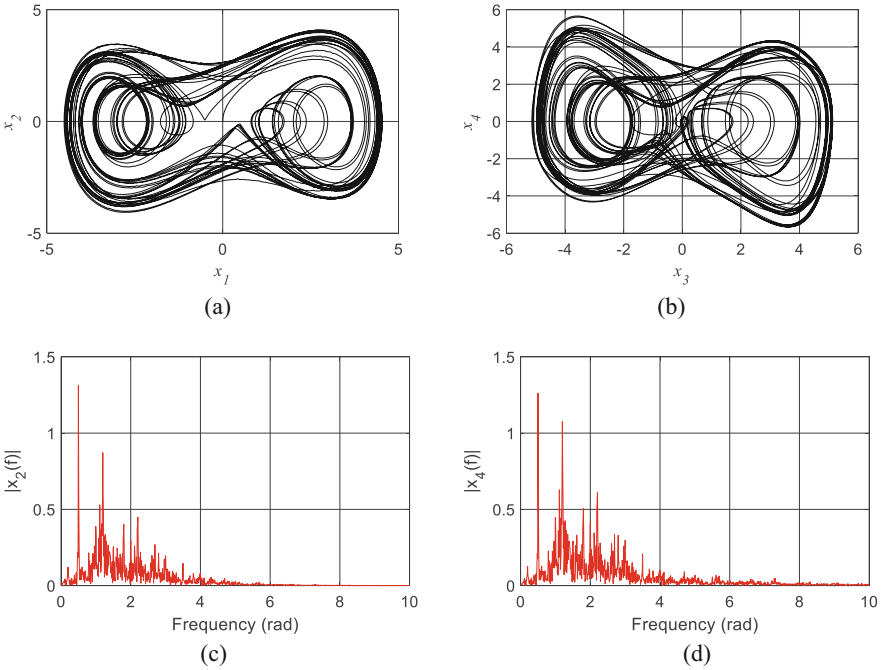

Fig. 6 Simulations for $\varepsilon_4 = 0.26$ and $e = 2.5$. (**a**) Phase diagram for x_1 versus x_2. (**b**) Phase diagram for x_3 versus x_4. (**c**) Power spectral density (FFT) for x_2. (**d**) Power spectral density (FFT) for x_4

4 Conclusions

The presented results demonstrate that the NES system can be used both as a passive vibration absorption system and as a power generation system. The presented results show that the parameter representing the transduction factor of the NES system has a greater influence on the average power of energy generation of the PZT material than on the behavior of the system. It was also observed that the mass of the NES is a parameter that can lead the system from a chaotic behavior to aperiodic one.

References

1. Lenz, W.B., Ribeiro, M.A., Rocha, R.T., Balthazar, J.M., Tusset, A.M.: Numerical simulations and control of offshore energy harvesting using piezoelectric materials in a portal frame structure. Shock. Vib. **2021**, 1–11 (2021)
2. Li, H., Li, A., Kong, X., Xiong, H.: Dynamics of an electromagnetic vibro-impact nonlinear energy sink, applications in energy harvesting and vibration absorption. Nonlinear Dyn. **108**, 1027–1043 (2022)
3. Balthazar, J.M., Tusset, A.M., Brasil, R.M.L.R.F., Felix, J.L.P., Rocha, R.T., Janzen, F.C., Nabarrete, A., Oliveira, C.: An overview on the appearance of the Sommerfeld effect and saturation phenomenon in non-ideal vibrating systems (NIS) in macro and MEMS scales. Nonlinear Dyn. **93**, 19–40 (2018)
4. Iliuk, I., Balthazar, J.M., Tusset, A.M., Piqueira, J.R.C., Pontes Jr., B.R., Felix, J.L.P., Bueno, A.M.: Application of passive control to energy harvester efficiency using a non-ideal portal frame structural support system. J. Intell. Mater. Syst. Struct. **25**, 417–429 (2014)
5. Rocha, R.T., Balthazar, J.M., Tusset, A.M., Piccirillo, V., Felix, J.L.P.: Comments on energy harvesting on a 2:1 internal resonance portal frame support structure, using a nonlinear-energy sink as a passive controller. Int. Rev. Mech. Eng. **10**, 147–156 (2016)
6. Rocha, R.T., Tusset, A.M., Ribeiro, M.A., Haura Jr., R., Jarzebowska, E., Balthazar, J.M.: On the positioning of a piezoelectric material in the energy harvesting from a non-ideally excited portal frame. J. Comput. Nonlinear Dyn. **15**, 121002–121012 (2020)
7. Felix, J.L.P., Balthazar, J.M., Rocha, R.T., Tusset, A.M., Janzen, F.C.: On vibration mitigation and energy harvesting of a non-ideal system with auto-parametric vibration absorber system. Meccanica. **53**, 3177–3188 (2018)
8. Triplett, A., Quinn, D.D.: The effect of nonlinear piezoelectric coupling on vibration-based energy harvesting. J. Intell. Mater. Syst. Struct. **20**, 1959–1967 (2009)
9. Li, H., Li, A., Kong, X.: Design criteria of bistable nonlinear energy sink in steady-state dynamics of beams and plates. Nonlinear Dyn. **103**(2), 1475–1497 (2021)
10. Qiu, D., Seguy, S., Paredes, M.: Design criteria for optimally tuned vibro-impact nonlinear energy sink. J. Sound Vib. **442**, 497–513 (2019)
11. Kopidakis, G., Aubry, S., Tsironis, G.P.: Targeted energy transfer through discrete breathers in nonlinear systems. Phys. Rev. Lett. **87**(16), 165501 (2001)
12. Tusset, A.M., Balthazar, J.M., Chavarette, F.R., Felix, J.L.P.: On energy transfer phenomena, in a nonlinear ideal and nonideal essential vibrating systems, coupled to a (MR) magneto-rheological damper. Nonlinear Dyn. **69**, 1859–1880 (2012)
13. Tusset, A.M., Balthazar, J.M., Felix, J.L.P.: On elimination of chaotic behavior in a non-ideal portal frame structural system, using both passive and active controls. J. Vib. Control. **19**, 803–813 (2013)
14. Tusset, A.M., Janzen, F.C., Rocha, R.T., Balthazar, J.M.: On an optimal control applied in MEMS oscillator with chaotic behavior including fractional order. Complexity. **2018**, 1–12 (2018)

15. Kudra, G., Balthazar, J.M., Tusset, A.M., Wasilewski, G., Sta'czyk, B., Awrejcewicz, J.: Dynamics analysis and control of a pendulum driven by a DC motor via a slider-crank mechanism. Mech. Syst. Signal Process. **166**, 108415 (2022)
16. Gottwald, G.A., Melbourne, I.: Testing for chaos in deterministic systems with noise. Physica D: Nonlinear Phenom. **212**, 100–110 (2005)
17. Bernardini, D., Rega, G., Litak, G., Syta, A.: Identification of regular and chaotic isothermal trajectories of a shape memory oscillator using the 0-1 test. Proc. Inst. Mech. Eng. Part K: J. Multi-body Dynamics. **227**, 17–22 (2013)
18. Bernardini, D., Litak, G.: An overview of 0-1 test for chaos. J. Braz. Soc. Mech. Sci. Eng. **38**, 1433–1450 (2016)

Leveraging 2:1 Parametric Resonance in a Notional Wave Energy Harvester

Giuseppe Giorgi

1 Introduction

The recent global energy crisis brings upfront a renovated sense of urgency for sustainability and energy self-sufficiency; this is woven over the background of climate crisis, so innovative measures should contribute to an overall decarbonization planning strategy [18]. Within this context, renewable energy harvesters are being developed extensively to contribute to the emancipation from fossil fuels [11]; one of the major form of still untapped renewable energy source is the ocean, whose waves can be used to produce clean energy, both at utility and small scales.

Wave energy harvesters (WEHs) are devices that respond to the external wave excitation force, typically with an oscillation motion, whose energy is converted via a power take-off (PTO) system. Although already technically viable, WEHs are required to improve their performance to become economically competitive with other more mature renewable energy sources. Efforts to this objective include holistic [21] or specific [22] optimization at a design stage, as well as control strategies including impedance-matching [6], linear time-invariant energy-maximization control [3], or time-varying system parameters [13]. However, such approaches are normally based on linear models, which are proven to become unrepresentative when large motions occur [20]; to circumvent such an issue, data-driven approaches are also investigated [10].

Although representative nonlinear models exist, they usually are too computationally demanding to be used in early stages of design or control. Another consequence of such a computational limitation is the usual way nonlinearity or instability is handled; in fact, floating objects may be prone to dynamic instability,

G. Giorgi (✉)
Marine Offshore Renewable Energy Lab (MOREnergy Lab), Department of Mechanical and Aerospace Engineering (DIMEAS), Politecnico di Torino, Turin, Italy
e-mail: giuseppe.giorgi@polito.it

© The Author(s), under exclusive license to Springer Nature Switzerland AG 2024

W. Lacarbonara (ed.), *Advances in Nonlinear Dynamics, Volume III*, NODYCON Conference Proceedings Series, https://doi.org/10.1007/978-3-031-50635-2_20

either in the yaw degree of freedom (DoF) [12, 19] or in the pitch and roll DoFs [15, 17]. Normally, such instability is discovered only after the preliminary design and effort is invested toward after-corrections or live-limitation [5]. However, having a representative and fast numerical model may enable to incorporate such instabilities already at the early stages of design. With this perspective, a few studies have proposed to embed parametric resonance into WEHs [1, 26], making it an enabling rather than a detrimental factor.

This chapter proposes a novel floating WEH that is purposely designed to be prone to parametric resonance; a 2:1 resonance condition is defined in a heaving-pitching device, assuming that the energy extraction will be performed in the rotation DoF. Although 2:1 resonance is often studied in vibration energy harvesters, it has never been considered as a performance enhancer in wave energy converters, to the best of the author's knowledge; this is due to the inherent difficulty of describing parametric resonance in a design-oriented way. In this chapter, parametric resonance is articulated and studied by means of a computationally efficient nonlinear Froude-Krylov (NLFK) force model [14]. The claim, herein demonstrated, is that parametric resonance can expand the operational bandwidth of the WEH. The remainder of the paper is organized as follows: Sect. 2 presents the mathematical model, and Sect. 3 shows some results, while concluding remarks are finally drawn in Sect. 4.

2 Mathematical Model

A generic heaving and pitching floater can be described via the following linear (LFK) and uncoupled equation of motion about the center of gravity, written in the frequency domain for compactness [9]:

$$\left[-\omega^2\left(\mathbf{M}+\mathbf{A}(\omega)\right)+j\omega\left(\mathbf{B}_v+\mathbf{B}(\omega)+\mathbf{B}_{PTO}\right)+\left(\mathbf{K}_h+\mathbf{K}_m+\mathbf{K}_{PTO}\right)\right]\boldsymbol{\xi}_2 = \\ =\mathbf{F}_d+\mathbf{F}_{FK_d}, \tag{1}$$

where $\boldsymbol{\xi}_2$ is the 2×1 state vector, composed of heave (z) and pitch (θ), $\mathbf{M}$ the diagonal inertia matrix, $\mathbf{A}(\omega)$ and $\mathbf{B}(\omega)$ the diagonal frequency-dependent added mass and radiation damping, $\mathbf{B}_v$ is the uncoupled linear viscous damping, $\mathbf{K}_m$ is the uncoupled linear mooring stiffness, $\mathbf{K}_h$ the diagonal linear hydrostatic stiffness, $\mathbf{F}_d$ and $\mathbf{F}_{FK_d}$ are the diffraction and linear dynamic FK forces, and $\mathbf{B}_{PTO}$ and $\mathbf{K}_{PTO}$ the diagonal PTO damping and stiffness. It is assumed that only the pitching motion is used to extract energy; however, the choice of the PTO coefficients is not trivial and is dependent on the model (either linear or nonlinear). Therefore, both for simplicity and to enable a meaningful first comparison of the inherent system nonlinear behavior, such PTO parameters are set to zero; then, the pitching angle,

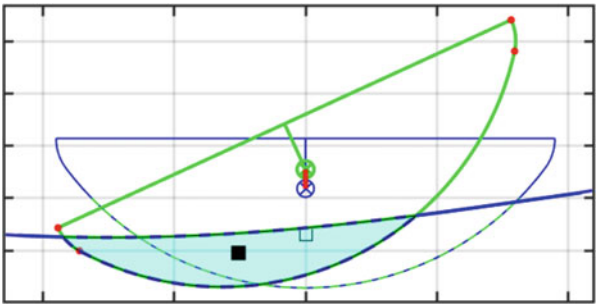

Fig. 1 Snapshot of a displaced hull, shown in green thick solid line, with instantaneous free surface elevation, shown in blue thick solid line, enclosing the instantaneous submerged volume (shaded area). The crossed-circle marker shows the position of the center of gravity, while the square shows the center of buoyancy (empty, LFK; full, NLFK). The rest position (LFK) is shown in thin line. Adapted from [14]

naturally a measurement of energy absorption by the hull, is also used as a proxy for power extraction ability.

The linear hydrodynamics is computed using a linear boundary element method (BEM) software, such as Nemoh [2] or WAMIT [24]. The characterizing quantities of interest are the radiation added mass, radiation damping, diffraction and dynamic Froude-Krylov forces, and hydrostatic stiffness. The computation is performed in frequency domain and considering the mean wetted surface, defined by the floater at rest and the still water level.

The NLFK version of (1) alternatively computes $\mathbf{F}_{FK_d} - \mathbf{K}_h \boldsymbol{\xi}_2$ in a nonlinear way, i.e., considering the actual instantaneous wetted surface, defined as the displaced floater with the free surface at each time step, as shown in Fig. 1.

Froude-Krylov generalized forces ($\mathbf{F}_{FK}$), divided into translational forces ($\mathbf{f}_{FK}$) and torques ($\boldsymbol{\tau}_{FK}$), integrate the undisturbed pressure field (p_u) on the instantaneous wetted surfaces (S_w) as follows:

$$\mathbf{f}_{FK}(t) = \mathbf{f}_g + \mathbf{f}_p = \mathbf{f}_g + \iint\limits_{S_w(t)} p_u(x, y, z, t)\ \mathbf{n}\, dS, \tag{2a}$$

$$\boldsymbol{\tau}_{FK}(t) = \boldsymbol{\tau}_g + \boldsymbol{\tau}_p = (\mathbf{r}_g - \mathbf{r}_R) \times \mathbf{f}_g + \iint\limits_{S_w(t)} p_u(x, y, z, t)\ (\mathbf{r} - \mathbf{r}_R) \times \mathbf{n}\, dS, \tag{2b}$$

where $\mathbf{f}_g$ is the gravity force, $\boldsymbol{\tau}_g$ its contribution to the torque, $\mathbf{n}$ is the unity vector normal to the surface, $\mathbf{r}$ is the generic position vector, $\mathbf{r}_R = (x_R, y_R, z_R)'$ is the reference point around which the torque is computed, and likewise $\mathbf{r}_g$ is the position vector of the center of gravity.

While generic NLFK solvers for arbitrary complex floaters must rely on a meshed representation of $S_w(t)$, which becomes the computational bottleneck [16, 23, 25], a

faster analytical representation is available for axisymmetric and prismatic floaters [14], which is herein implemented.

3 Results

The geometry of the floater is shown in Fig. 1. The rotational moment of inertia of the floater is chosen such that the natural frequency in the heaving DoF (ω_3) is twice the natural frequency in the pitching DoF (ω_5). Although real sea states are short-crested and multidirectional [4], long-crested waves are herein considered to clearly investigate the device attitude for different wave incoming frequency and highlight the parametric resonance response. A fine grid of wave periods (T_w) and wave heights (H_w) is simulated in both the linear (LFK) and nonlinear (NLFK) models. Simulations are run for long enough to reach steady state; the amplitude of the response, either in heave (z) or pitch (θ), is computed as half the distance from peak to trough of the last two wave periods, in order to consider the expected period doubling of the nonlinear response. Overall results are shown in Fig. 2, normalized with respect to the draft of the floater (D) and the pitching natural period (T_5).

According to the linear model, normally implemented in the field for design and control, the response is obviously proportional to the wave height. The heaving response reaches a peak at $T_w = T_3 = \frac{1}{2}T_w$ and remains about constant for

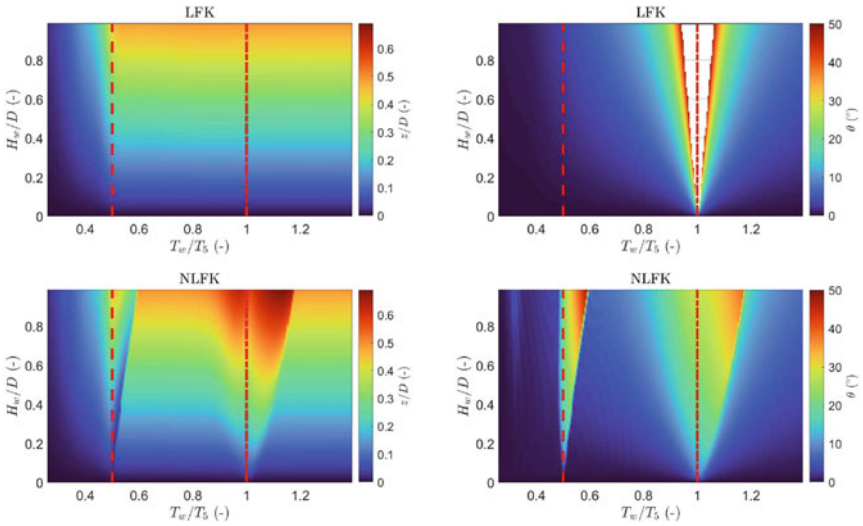

Fig. 2 Amplitude of response for heave (left) and pitch (right), according to the linear (top) and nonlinear (bottom) models. The dash-dot and dashed red lines highlight one or half of the pitching natural, respectively. The white region indicates capsizing, i.e., when the pitching angle is above the arbitrary threshold of 50°

higher periods; the pitching response sharply increases at $T_w = T_5$, well above physically meaningful values, due to the linearity assumption and the absence of viscous dissipation mechanisms: the white region in Fig. 2 represents capsizing of the hull, namely, when the pitching angle is above the arbitrary threshold of 50°. Note that the introduction of additional viscous damping may have averted the numerical capsizing; however, no artificial corrective mechanisms have been added in the LFK model in order to highlight that the NLFK model is inherently preventing unrealistic results, even without viscous damping. This is an evidence of how the NLFK model is more consistent to the physics of the wave-structure interaction.

Figure 2 clearly shows the region of parametric resonance: due to the 2:1 resonance, there is a sharp increase of the pitching motion around $T_w = \frac{1}{2}T_5$; the amplitude also presents a bending toward larger periods as the wave height increases, highlighting the nonlinearity of the response. Note that this bending behavior contributes to enlarge the operational bandwidth of the response, covering the region between $T_w = \frac{1}{2}T_5$ and $T_w = T_5$. In the same 2:1 resonance region, it is possible to appreciate a nonlinear coupling between the heaving and pitching DoFs, since there is a decrease of heaving motion as the pitching angle increases; this is usually detrimental for WEH that exploit heaving for the extraction [15], while it is beneficial for WEH working on the pitching DoF. Conversely, in the 1:1 parametric resonance region, the coupling between heave and pitch causes a significant increase in the heave motion, which drains energy from the pitching DoF.

To further investigate the buildup of the nonlinear response, Fig. 3a, b show the phase portraits of the time-series response at the 1:1 and 1:2 resonance conditions, respectively. Figure 3a presents a period doubling, where the amplitude of motion is similar in the two consecutive cycles. An asymmetric response can be noted, where the mean is shifted to positive values for both heave and pitch. Period doubling is also found in Fig. 3b, but the two amplitudes are significantly different; in addition, the asymmetric response is toward negative values for the largest amplitude, whereas the smallest oscillation is at the peak, i.e., at positive values.

Finally, a down-chirp signal is simulated to highlight the regions of instability and the interaction between the two DoFs. The frequency (ω) sweep shown is from $2.15\,\omega_5$ to $1.85\,\omega$, and about 10^4 wave periods have been simulated to ensure a smooth transition. Figure 4 shows the time-series response, highlighting the envelope of the peaks, which are also plotted in Fig. 5 against the related instantaneous frequency.

From Fig. 4, it can be noted that the pitch response is always essentially zero, apart from the abrupt rise caused by parametric resonance; once it kicks in, a substantial fall of the heave response is obtained, demonstrating an internal transfer of energy between the two degrees of freedom. The frequency range where parametric resonance appears is evident from Fig. 5: the 2:1 area is properly included within the pitching response region, but its extension is asymmetrically oriented toward lower frequencies; similarly, the peak of the response is found at $\omega \approx 1.91\,\omega_5$, hence lower than $2\,\omega_5$.

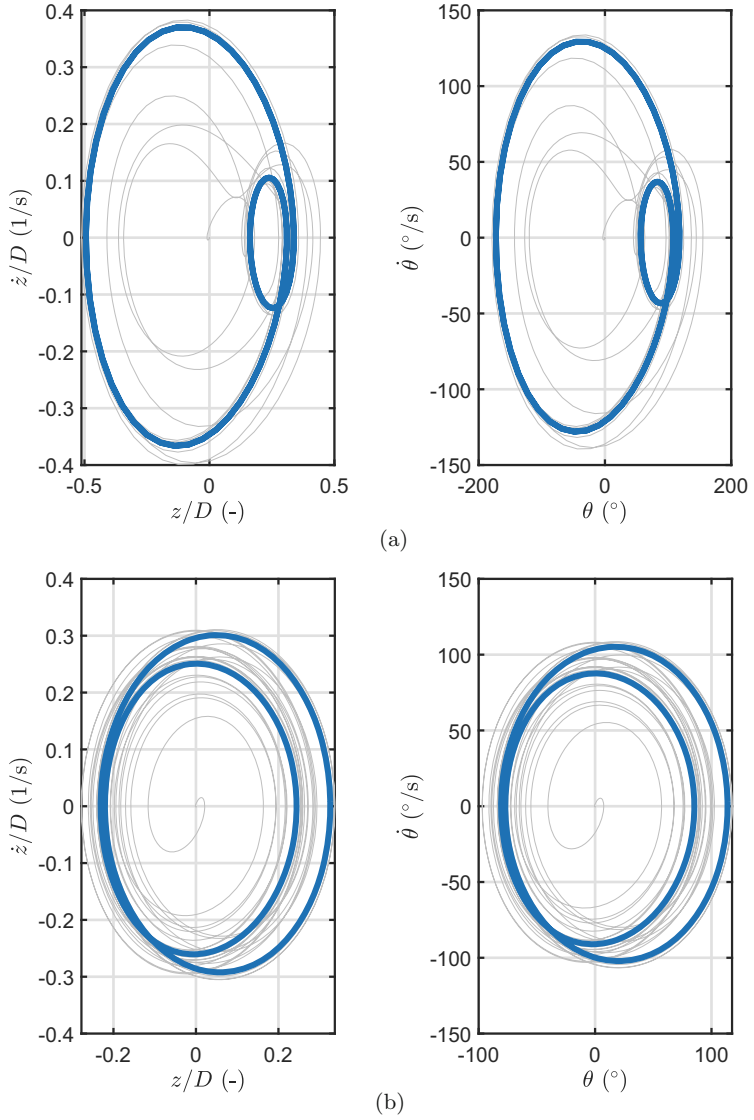

Fig. 3 Phase portraits. The full time series, hence comprising of the transient, is shown in thick-gray line, whereas the latest two periods of oscillation are highlighted in thick-blue line. (**a**) Phase portrait at $T_w = T_5$. (**b**) Phase portrait at $T_w = \frac{1}{2}T_5$

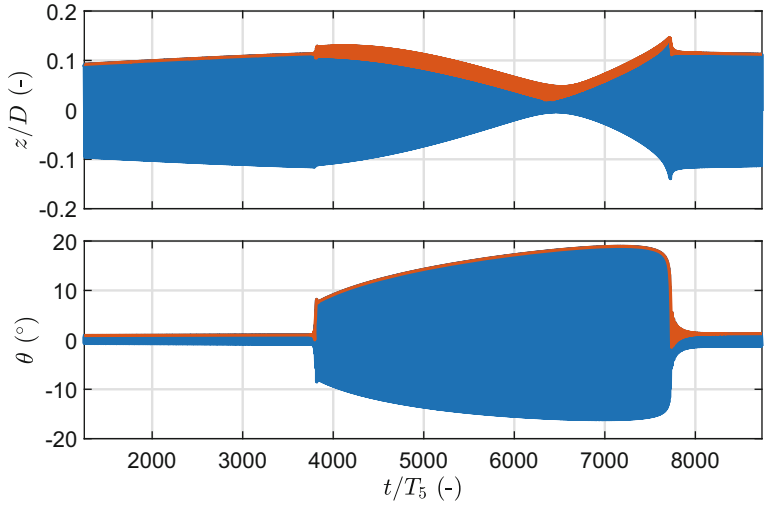

Fig. 4 Down-chirp time series response, with frequency (ω) sweep from 2.15 ω_5 to 1.85 ω

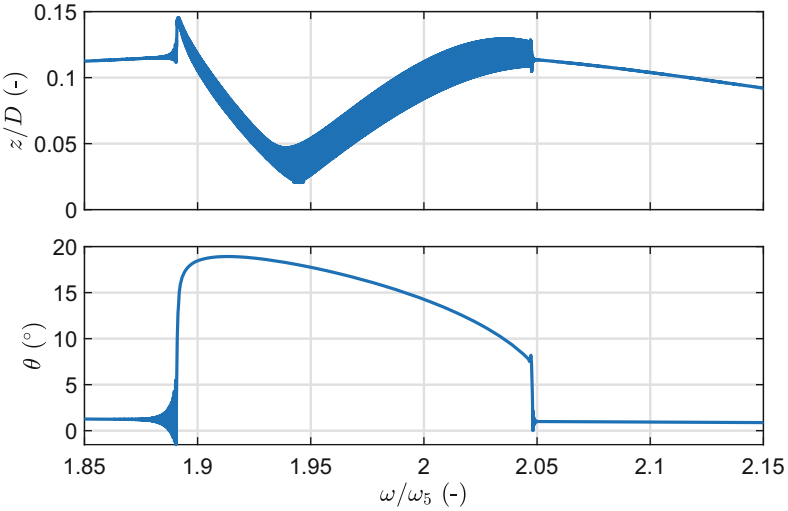

Fig. 5 Amplitude of the down-chirp response against instantaneous frequency

4 Conclusions

This chapter proposes to define at the design-stage a 2:1 resonance in a wave energy harvester in order to expand the operational bandwidth of the system, hence the ability to extract energy in a wider range of sea states. The response amplitude is demonstrated to be indeed increased in the targeted area of interest, i.e., at a wave

period half of the pitch natural period. Such a result is promising, since it confirms the potentiality of the approach; however, further steps are required to evaluate the practicality of the implementation. In particular, a power take-off system will be introduced and optimized, to quantify the improvement in power extraction, rather than power absorption (pithing angle). Finally, by framing the NLFK model into a control-oriented structure via model order reduction [7], it will be investigated the possibility to formulate an optimal control problem [8] to lead the system into parametric resonance condition and further enlarge the operational bandwidth.

References

1. Abdelkhalik, O., Zou, S., Robinett, R., Bacelli, G., Wilson, D., Coe, R.: Control of three degrees-of-freedom wave energy converters using pseudo-spectral methods. J. Dyn. Syst. Meas. Control. **140**(7), 074,501 (2018). https://doi.org/10.1115/1.4038860
2. Babarit, A., Delhommeau, G.: Theoretical and numerical aspects of the open source BEM solver NEMOH. In: Proceedings of the 11th European Wave and Tidal Energy Conference (September 2015), pp. 1–12 (2015). https://doi.org/hal-01198800
3. Carapellese, F., Pasta, E., Paduano, B., Faedo, N., Mattiazzo, G.: Intuitive LTI energy-maximising control for multi-degree of freedom wave energy converters: The PeWEC case. Ocean Eng. **256**, 111444 (2022). https://doi.org/10.1016/J.OCEANENG.2022.111444
4. Cervelli, G., Parrinello, L., Moscoloni, C., Giorgi, G.: Comparison of the ERA5 Wave Forecasting Dataset Against Buoy Record. Instrumentation Mesure Métrologie **21**(3), 87–95 (2022). https://doi.org/10.18280/i2m.210301
5. Davidson, J., Kalmár-Nagy, T.: A real-time detection system for the onset of parametric resonance in wave energy converters. J. Mar. Sci. Eng. **8**(10), 819 (2020). https://doi.org/10.3390/jmse8100819
6. Faedo, N., Carapellese, F., Pasta, E., Mattiazzo, G.: On the principle of impedance-matching for underactuated wave energy harvesting systems. Appl. Ocean Res. **118**, 102958 (2022). https://doi.org/10.1016/J.APOR.2021.102958
7. Faedo, N., Dores Piuma, F.J., Giorgi, G., Ringwood, J.V.: Nonlinear model reduction for wave energy systems: a moment-matching-based approach. Nonlinear Dyn. **102**(3), 1215–1237 (2020). https://doi.org/10.1007/S11071-020-06028-0
8. Faedo, N., Giorgi, G., Ringwood, J.V., Mattiazzo, G.: Optimal control of wave energy systems considering nonlinear Froude–Krylov effects: control-oriented modelling and moment-based control. Nonlinear Dyn. **109**(3), 1777–1804 (2022). https://doi.org/10.1007/s11071-022-07530-3
9. Fontana, M., Casalone, P., Sirigu, S.A., Giorgi, G., Bracco, G., Mattiazzo, G.: Viscous damping identification for a wave energy converter using CFD-URANS simulations. J. Mar. Sci. Eng. **8**(5), 355 (2020). https://doi.org/10.3390/JMSE8050355
10. Gioia, D.G., Pasta, E., Brandimarte, P., Mattiazzo, G.: Data-driven control of a pendulum wave energy converter: a gaussian process regression approach. Ocean Eng. **253**, 111191 (2022). https://doi.org/10.1016/J.OCEANENG.2022.111191
11. Giorgi, G.: Parametric resonance exploitation due to periodic damping in an electromechanical energy harvester. Int. J. Mech. Control **22**(01), 77–85 (2021)
12. Giorgi, G., Davidson, J., Habib, G., Bracco, G., Mattiazzo, G., Kalmár-Nagy, T.: Nonlinear Dynamic and Kinematic Model of a Spar-Buoy: parametric resonance and yaw numerical instability. J. Mar. Sci. Eng. **8**(7), 504 (2020). https://doi.org/10.3390/JMSE8070504
13. Giorgi, G., Faedo, N.: Performance enhancement of a vibration energy harvester via harmonic time-varying damping: a pseudospectral-based approach. Mech. Syst. Signal Process. **165**, 108331 (2022). https://doi.org/10.1016/J.YMSSP.2021.108331

14. Giorgi, G., Sirigu, S., Bonfanti, M., Bracco, G., Mattiazzo, G.: Fast nonlinear Froude–Krylov force calculation for prismatic floating platforms: a wave energy conversion application case. J. Ocean Eng. Mar. Energy **7**(4), 439–457 (2021). https://doi.org/10.1007/S40722-021-00212-Z
15. Gomes, R.P.F., Henriques, J.C., Gato, L.M., Falcao, A.F.d.O.: Experimental Tests of a 1:16th scale model of the spar-buoy OWC in a large scale wave flume in regular waves, pp. 1–10 (2018)
16. Guerinel, M., Zurkinden, A.S., Alves, M., Sarmento, A.: Validation of a partially nonlinear time domain model using instantaneous Froude-Krylov and hydrostatic forces. In: Proceedings of the 10th European Wave and Tidal Energy Conference: Technical Committee of the European Wave and Tidal Energy Conference, Aalborg (2013)
17. Habib, G., Giorgi, G., Davidson, J.: Coexisting attractors in floating body dynamics undergoing parametric resonance. Acta Mech. **233**(6), 2351–2367 (2022). https://doi.org/10.1007/S00707-022-03225-3
18. Novo, R., Marocco, P., Giorgi, G., Lanzini, A., Santarelli, M., Mattiazzo, G.: Planning the decarbonisation of energy systems: the importance of applying time series clustering to long-term models. Energy Convers. Manage.: X **15**(January), 100274 (2022). https://doi.org/10.1016/j.ecmx.2022.100274
19. Orszaghova, J., Wolgamot, H., Draper, S., Taylor, P.H., Rafiee, A.: Onset and limiting amplitude of yaw instability of a submerged three-tethered buoy. In: Proceedings of the Royal Society A: Mathematical, Physical and Engineering Sciences (2020). https://doi.org/10.1098/rspa.2019.0762
20. Ransley, E.J., Brown, S.A., Hann, M., Greaves, D.M., Windt, C., Ringwood, J., Davidson, J., Schmitt, P., Yan, S., Wang, J.X., Wang, J.H., Ma, Q., Xie, Z., Giorgi, G., Hughes, J., Williams, A., Masters, I., Lin, Z., Chen, H., Qian, L., Ma, Z., Chen, Q., Ding, H., Zang, J., van Rij, J., Yu, Y.H., Li, Z., Bouscasse, B., Ducrozet, G., Bingham, H.: Focused wave interactions with floating structures: a blind comparative study. Proc. Inst. Civ. Eng. Eng. Comput. Mech. **174**(1), 46–61 (2021). https://doi.org/10.1680/jencm.20.00006
21. Rava, M., Dafnakis, P., Martini, V., Giorgi, G., Orlando, V., Mattiazzo, G., Bracco, G., Gulisano, A.: Low-cost heaving single-buoy wave-energy point absorber optimization for Sardinia west coast. J. Mar. Sci. Eng. **10**(3),397 (2022). https://doi.org/10.3390/jmse10030397
22. Sirigu, S.A., Gallizio, F., Giorgi, G., Bonfanti, M., Bracco, G., Mattiazzo, G.: Numerical and experimental identification of the aerodynamic power losses of the ISWEC. J. Mar. Sci. Eng. **8**(1), 49 (2020). https://doi.org/10.3390/JMSE8010049
23. Tarrant, K.R., Meskell, C.: Investigation on parametrically excited motions of point absorbers in regular waves. Ocean Eng. **111**, 67–81 (2016). https://doi.org/10.1016/j.oceaneng.2015.10.041
24. Wamit, I.: WAMIT User Manual (2019). https://doi.org/10.1017/CBO9781107415324.004
25. Wolgamot, H.A., Fitzgerald, C.J.: Nonlinear hydrodynamic and real fluid effects on wave energy converters. Proc. Inst. Mech. Eng., Part A: J. Power Energy **229**(7), 772–794 (2015). https://doi.org/10.1177/0957650915570351
26. Zou, S.S., Abdelkhalik, O., Robinett, R., Korde, U., Bacelli, G., Wilson, D., Coe, R., Korde, U.: Model Predictive Control of parametric excited pitch-surge modes in wave energy converters. Int. J. Mar. Energy **19**, 32–46 (2017). https://doi.org/10.1016/j.ijome.2017.05.002

Experimental Testing of a Bi-stable Point Wave Energy Absorber Under Harmonic Waves

Mohammad A. Khasawneh and Mohammed F. Daqaq

1 Introduction

The potential to convert wave energy into usable energy has been researched for over two centuries [1]. Many devices and mechanisms have been proposed, constructed, and tested for this purpose. Such devices can be categorized based on their working principle and/or distance from shore. Based on their working principle, wave energy harvesters are categorized into oscillating water columns, overtopping devices, and point wave energy absorbers (PWAs) [2]. Based on their location of installation relative to the shore, they are categorized into onshore, nearshore, and offshore devices. Onshore devices are installed at the coast, nearshore devices utilize the seabed as an anchor, and offshore devices operate in very deep waters and are floating.

This chapter focuses on nearshore PWAs. They comprise of partially submerged body (buoy) that is connected to a power take-off unit (PTO) via a mooring mechanism. The PTO is usually a linear electromagnetic generator that is anchored to the seabed. Incident waves move the buoy, which pulls the mooring cable inducing relative motion between the PTO's stator and translator. The change in magnetic flux produces a current in the generator's coils following Faraday's law of induction.

PWAs operating based on the principle of linear resonance require that the frequency of the incident waves matches the natural frequency of the absorber in order to create the large-amplitude motions necessary to generate significant power

M. A. Khasawneh (✉) · M. F. Daqaq
Department of Mechanical Engineering, Tandon School of Engineering, New York University, New York, NY, USA

Division of Engineering, NYU Abu Dhabi, Abu Dhabi, UAE
e-mail: mak1011@nyu.edu

© The Author(s), under exclusive license to Springer Nature Switzerland AG 2024

W. Lacarbonara (ed.), *Advances in Nonlinear Dynamics, Volume III*, NODYCON Conference Proceedings Series, https://doi.org/10.1007/978-3-031-50635-2_21

levels. However, it is often difficult to find an overlap between the spectrum of the ocean waves and the PWA's resonance bandwidth for two reasons. First, the natural frequency of the absorber is dictated by the stiffness of the hydrostatic (buoyancy) restoring force, which is typically very high, resulting in a natural frequency that is much higher than the frequency associated with naturally occurring waves in energetic marine sites. Second, the frequency of the incident waves is stochastic in nature, resulting in a broadband energy spectrum that makes the resonance-based approach less than ideal for wave energy absorption [3].

A large body of research has focused on devising active methods to help maintain the PWA in proper tuning with the frequency of the incident energetic waves. Various linear and nonlinear active control schemes have been proposed to alter the natural frequency of the PWA in real time by tweaking the design parameters of the PTO [4]. Passive solutions have also been proposed and studied to pre-adjust the underlying dynamics of the buoy to unfold a more favorable response at known sea-state parameters including but not limited to increasing the total inertia of the buoy by incorporating a fully submerged mass, the utilization of nonlinear modal interactions via the placement of an auxiliary degree-of-freedom that exchanges energy with the buoy, and the intentional introduction of a bi-stable nonlinear restoring element [5–7]. The current work focuses on the latter scheme of solutions.

The main difference between the linear and bi-stable PWAs (B-PWAs) lies in the introduction of a nonlinear stiffness attachment in parallel with the PTO. This nonlinear attachment is specifically designed to obtain a restoring force with two stable equilibria (nodes). This arrangement allows the buoy to admit two types of motion. The first, less favorable, is called the *intra-well* motion, where the PWA oscillates around one of the stable nodes at low amplitude. The second, more favorable type of motion, is called the *inter-well* motion, which occurs at specific combinations of wave height and frequency. When the latter type of motion is activated, the buoy becomes capable of performing large-amplitude oscillations that span the two stable nodes. This type of motion typically occurs when the incident waves have a frequency lower than the natural frequency of the linear PWA, which is why bi-stable absorbers have been proposed to efficiently capture energy from the energetic long-period ocean waves.

Despite the significant amount of literature that has aimed at studying the response of B-PWAs under harmonic and random incident waves, the research is limited to theoretical investigations focusing on the design and optimization of the different mechanisms used to introduce bi-stability by utilizing numerical, and to a lesser extent, analytical means to assess the performance of B-PWAs. Very little attention, if any, has been dedicated to experimental studies investigating whether the improved responses observed theoretically can be replicated in an experimental setting, and if so, what challenges are associated with such an implementation. Therefore, the purpose of this paper is to experimentally study the performance of B-PWAs when subjected to harmonic incident waves, by designing, fabricating, and testing a small-scale B-PWA prototype in a narrow experimental wave flume.

2 Experimental Setup

Figure 1 shows the system that was developed and used to test the performance of the B-PWA under harmonic incident waves. The PWA consists of a cylindrical buoy with a diameter of 100 mm and a height of 150 mm. The diameter is one-third the width of the water basin to maintain enough distance from the walls. A linear rail is used to constrain the motion of the buoy to the vertical direction. The kinetic energy of the buoy is transformed into electrical energy by using a coreless two-stage, three-phase linear generator. The generator is fabricated by winding 250 turns of 36-AWG enameled copper wire around each stage. In the design, the translator carrying the windings moves with the buoy while the stator is fixed. The coil is wired to a three-phase bridge rectifier integrated with the signal conditioning circuit, which is designed to prevent destructive voltage interference. The load resistance is chosen to be 300 Ohms to match the impedance of the coil.

One of the challenging aspects of designing the experiment is creating a bi-stable restoring force. In our work, we choose to employ a set of attractive magnets such that a pair of magnets are mounted on a fixed frame, while a third one is mounted on the oscillating buoy. Such an arrangement creates a potential energy function of two stable equilibria (nodes), separated by an unstable saddle as shown in Fig. 1d.

The experimentally measured bi-stable restoring force resulting from the magnets arrangement shown earlier in Fig. 1 is depicted in Fig. 2a. The potential energy is shown in Fig. 2b.

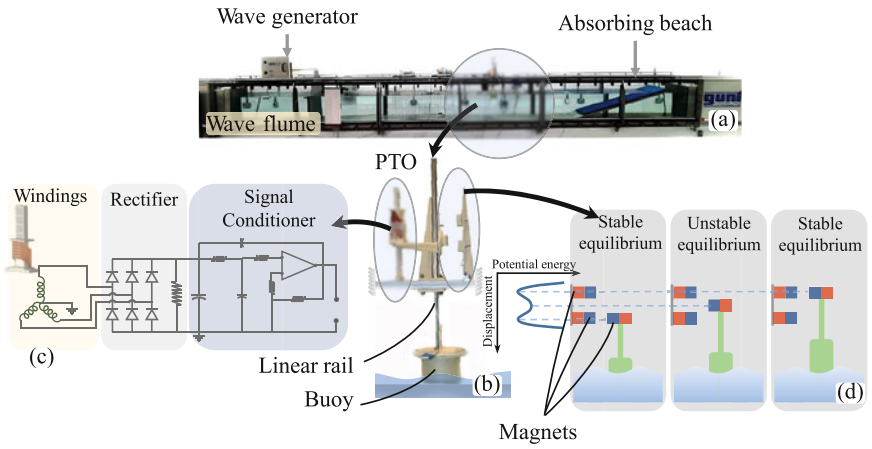

Fig. 1 An overview of the experiment. (**a**) Experimental wave flume. (**b**) B-PWA prototype. (**c**) Circuit diagram of the three-phase synchronous linear generator used in the experiments. (**d**) A schematic diagram of the mechanism used to induce bi-stability in the PWA motion

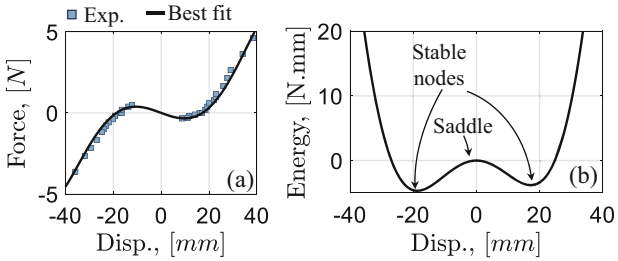

Fig. 2 (**a**) Bi-stable restoring force. (**b**) The resulting potential energy function

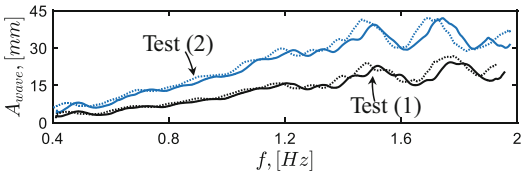

Fig. 3 Wave amplitude versus frequency for the two tests conducted in the current study. Solid lines: forward frequency sweep. Dotted lines: backward frequency sweep

3 Results

3.1 Description of the B-PWA Motion

Unlike the traditional linear PWA, the response of a B-PWA is very complex and highly nonlinear and can change qualitatively based on the frequency and/or amplitude of the incident waves. For example, under harmonic excitations, a linear PWA can only exhibit periodic responses at the frequency of excitation with an amplitude that increases linearly with the wave amplitude. However, a B-PWA can exhibit periodic responses at frequencies that are different from the frequency of the incident waves. They can also exhibit chaotic responses and has a response amplitude that does not necessarily increase linearly with the amplitude of the incident waves. Finally, depending on its initial state, a B-PWA can exhibit two or more qualitatively different responses for the same wave parameters. In this subsection, we describe such motions as observed in the experimental wave flume.

Two tests were conducted to understand the qualitative/quantitative changes in the response of the B-PWA when the frequency and amplitude of the incident wave are varied. Figure 3 shows variation of the amplitude of the incident waves as the frequency of the wave generating paddle is varied. In the first test, the wave amplitude remained bounded between 3 [mm] and 26 [mm], while in the second test, the B-PWA was subjected to higher wave amplitudes that ranged from 3.5 [mm] to 42 [mm]. Note that because of the kinematics of the wave generating paddle, it is impossible to change the frequency while maintaining a constant wave amplitude.

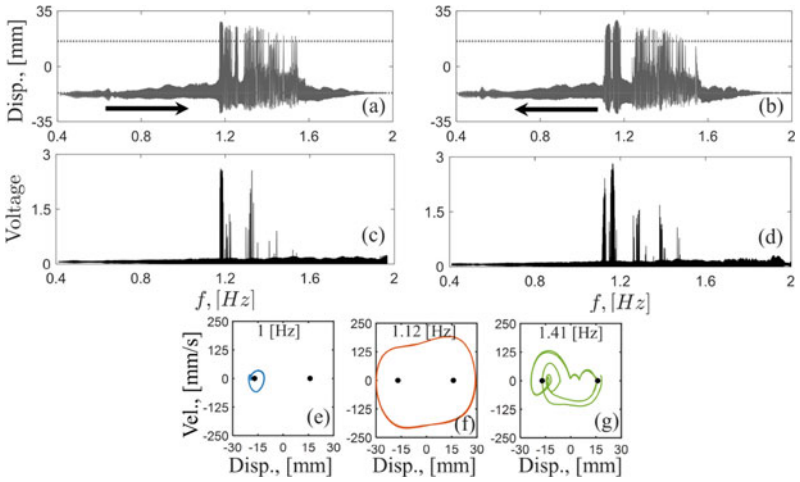

Fig. 4 Time histories showing the response if the B-PWA when subjected to harmonic incident waves correspond to test (1). (**a**,**b**) Buoy's displacement. (**c**,**d**) Induced voltage. (**e**–**g**) Phase portraits. The dashed lines in (**a**,**b**) and the dots in (**e**–**g**) correspond to the stable nodes

Figure 4 shows the response of the buoy as the excitation frequency is varied from 0.4 to 2 Hz in forward (a) and backward (b) directions. For frequencies below 1.18 Hz, the oscillations are of small amplitude and remain confined to a single potential well. Between 1.18 and 1.58 Hz, the buoy escapes the potential well and starts performing the desired large-amplitude inter-well oscillations, which are either periodic or chaotic. This behavior is seen in both directions of the frequency sweep. However, the large-amplitude oscillations are excited in a slightly different frequency bandwidth based on the direction of the frequency sweep, pointing to the non-unique nature of the response for some frequency bands. The phase portraits in Fig. 4e–g depict three different steady-state orbits that exist in the response. The largest orbit shown in Fig. 4f occurs at a frequency of 1.12 Hz and is an inter-well periodic orbit. The smallest orbit in Fig. 4e occurs at 1 Hz and is also periodic but represents motion within one of the potential wells, while the third orbit in Fig. 4g at a frequency of 1.41 Hz has an irregular shape typical of cross-well chaos. The resulting induced voltage is depicted in Fig. 4c,d. It can be seen that the voltage output is significant only inside the region where the PWA performs periodic large-amplitude inter-well motions, where the peak value of the induced voltage is around 2.8 V near a frequency of 1.2 Hz, and it drops elsewhere. Also, despite the fact the B-PWA is performing cross-well motion near a frequency of 1.4 Hz, the induced voltage is shown to be poor and intermittent due to the irregularity in the orbit topology. This is in agreement with the work of Daqaq et al. [8], who showed that chaotic responses of a vibratory energy harvester reduce the charging efficiency of a small battery.

As the wave excitation levels are increased to values corresponding to test (2) in Fig. 3, the region of large-amplitude motions expands significantly in both directions

of the frequency sweep, as shown in Figs. 5a and b. Comparing Figs. 5a and b, it is clear that the frequency bandwidth of large-amplitude oscillations is much larger in the forward frequency sweep. Thus, there is a region of coexisting responses (large and small) between 1.45 Hz and 1.55 Hz, where depending on the initial state of the buoy, it can either perform the desirable large-amplitude inter-well motions or the undesirable small-amplitude intra-well motions.

The induced voltage and average power levels resulting from the types of buoy motion seen in Fig. 5a,b are shown in Fig. 5c–e. A significant improvement in voltage induction and, therewith, in the power output is immediately noticeable when comparing the voltage levels and the size of the response bandwidth relative to Fig. 4. The vertical dotted lines in the figure mark the boundaries at which an abrupt rise or fall in the induced voltage values takes place. The vertical dotted line on the right corresponds to the frequency at which the buoy jumps up from intra- to inter-well motions in the forward frequency sweep. The second and third dotted vertical lines correspond to the points at which the buoy shifts from performing periodic inter-well oscillations to chaos, which results in a significant reduction in the output voltage. We performed an averaging based on a moving time window equal to the wave's period in order to compare the induced power. This is shown in Fig. 5e. The region bounded between the first two vertical dotted lines represents the *effective bandwidth* of the PWA, where the large-amplitude motions can be uniquely realized. Within this frequency bandwidth, we observe a monotonic increase in the induced power with increasing the frequency of the waves. The area between the second and third lines is where the large-amplitude periodic orbit is accompanied by chaotic solutions leading to very low power levels. In this region, depending on the initial conditions, the B-PWA can either be producing significant power levels or relatively none at all.

3.2 Effective Bandwidth

In Sect. 3.1, we demonstrated how the performance of the B-PWA varies with the incident wave height and frequency. By showing experimental time histories of the response, induced voltage, and average power, we were able to observe significant qualitative and quantitative changes in the behavior of the system as the frequency and amplitude of the incident waves are varied. In particular, we showed that there exists an *effective bandwidth* of the B-PWA whose size is very sensitive to the amplitude of the incident waves. In this section, we devise a criterion based on analyzing the FFT spectra of the experimental response to allow us to characterize the effective bandwidth of B-PWA such that, within the effective bandwidth, the response is unique and periodic with a period equal to that of the excitation. Outside this bandwidth, the response is generally more complex and sometimes chaotic, producing low output power levels.

Figure 6 shows a spectrogram of the time history from Fig. 5. The peaks of the response FFT and their power levels, as well as the average output power, are

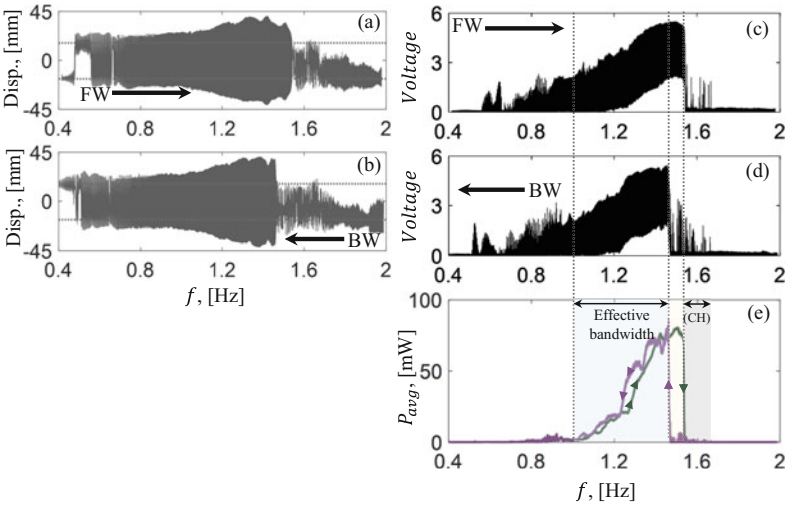

Fig. 5 Time histories showing the response of the B-PWA when subjected to harmonic incident waves correspond to test (2). (**a**,**b**) Buoy's displacement. (**c**,**d**) Induced voltage. (**e**) Average power

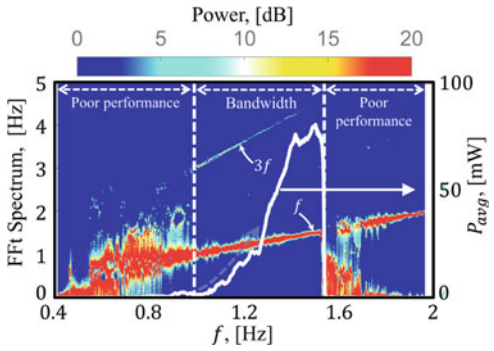

Fig. 6 A spectrogram plot for the displacement time history shown in Fig. 5a, where the x-axis represents the instantaneous wave frequency and the left y-axis represent the frequencies appearing in the FFT. The superimposed curve, right y-axis, represents the corresponding average output power

plotted against the excitation frequency. There are three distinct regions visible in the figure. In the lower frequency region, the frequencies of the response that create high power levels in the FFT are spread out over a wide bandwidth around the excitation frequency. The response is generally complex and sometimes chaotic in this region, which leads to low average power levels. In the central frequency region, there are two dominant frequencies in the response: one at the excitation frequency, f, and the other at three times the excitation frequency, $3f$. The higher frequency peak is present because of cubic nonlinearities in the stiffness of the B-PWA. The response is unique and periodic in this region, and the average power levels are high. In the higher frequency region, there is a dominant peak but also high power peaks at very low frequencies. The response is complex in this region, which causes the power to drop again.

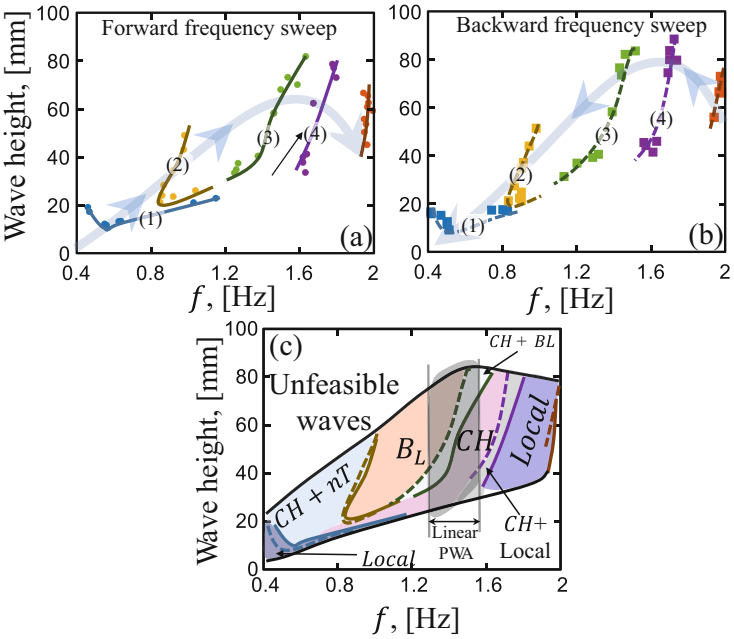

Fig. 7 Loci of the bifurcation points as a function of the wave amplitude and frequency. (**a**) Forward sweep, (**b**) backward sweep, and (**c**) a map that results from superimposing both sweeps. Circles and squares represent experimental data, while dashed and solid lines are best spline fits of the experimental data

By tracking the FFT of the response for multiple experimental time histories, we are able to generate a map that demarcates the parameter space of the wave amplitude and frequency into regions of different performance behavior. Such maps are shown in Fig. 7a and b for the forward and backward frequency sweeps of the B-PWA with the restoring force shown in Fig. 2. In the forward frequency sweep starting at $f = 0.4$ Hz, line (1) represents the loci of wave frequencies and amplitudes at which the response switches from small amplitude intra-well oscillations to a more complex periodic and aperiodic response leading sometimes to chaos (CH). Line (2) is when chaos disappears and the large-amplitude inter-well responses, B_L, become unique, i.e., the start of the effective bandwidth of the B-PWA. Line (3) is when B_L disappears and chaos appears again, i.e., the end of the effective bandwidth of the B-PWA. Line (4) is when chaos disappears and the response becomes of the small periodic intra-well type. The same set of lines is also generated for the backward frequency sweep as shown in Fig. 7b.

The bifurcation map shown in Fig. 7c, is generated by superimposing the lines in Fig. 7a and b into a single figure. The region denoted by B_L marks the most important region in the map, which represents the possible combinations of wave heights and frequencies that lead to periodic large-amplitude motions. When the B-PWA is operated outside this effective bandwidth, less favorable motions can

arise, including chaos, intra-well motions, n-period motions, and hysteresis. It is also important to notice that the effective bandwidth exists only when the height of the incident waves exceeds a critical value, (around 20 mm) on the figure. Below this amplitude, the B-PWA is not a good choice for harnessing wave energy. Moreover, when the incident wave heights are slightly above this activation threshold, the size of the effective bandwidth is sensitive to variations in the wave's height.

In order to compare the performance of the B-PWA with the linear counterpart, we conducted a set of tests on the same device in the absence of the magnets used to create bi-stability. To maintain a fair comparison, the total mass of both the linear and B-PWA is kept the same. The bandwidth of the linear PWA represents the frequency spectrum within which the buoy's displacement remains within $1/\sqrt{2}$ of the peak value during the test. The bandwidth of the linear PWA is also plotted in Fig. 7c. When compared to the B-PWA, we can notice that bi-stability does not seem to significantly improve the bandwidth size of the PWA, at least not for the bi-stable potential energy function tested in this paper. Nonetheless, a key advantage remains in the ability of the bi-stable restoring force to push the effective bandwidth of the PWA toward lower frequencies as can be clearly seen in Fig. 7c, without the need to incorporate additional bulky inertial elements.

4 Conclusion

This chapter presented an experimental investigation of the B-PWA response under harmonic wave excitations. A prototype of a B-PWA was designed, fabricated, and tested in an experimental wave flume. The complex dynamical features and different types of motion that the B-PWA undergoes when varying the incident wave frequency and amplitude were described. The B-PWA was subjected to a wide range of wave excitation conditions in order to experimentally generate a bifurcation map in the frequency and amplitude parameters space, which was used to define an effective bandwidth for the B-PWA. Within its effective bandwidth, the B-PWA produces significant power levels.

It was also shown that incorporating bi-stability to improve the steady-state effective bandwidth of the absorber and to reduce its sensitivity to variations in the wave frequency as demonstrated by previous researchers does not seem to translate experimentally, at least not for the bi-stable potential energy function used in our experiments. However, the merit of using a bi-stable restoring force in PWA applications remains in its ability to shift the effective bandwidth toward lower frequencies, where most of the incident wave energy is trapped, without the need to incorporate additional inertial elements.

References

1. Falnes, J.: A review of wave-energy extraction. Mar. Struct. **20**(4), 185–201 (2007)
2. Al Shami, E., Zhang, R., Wang, X.: Point absorber wave energy harvesters: A review of recent developments. Energies **12**(1), 47 (2018)
3. Falnes, J., Hals, J.: Heaving buoys, point absorbers and arrays. Philos. Trans. Royal Soc. A **370**(1959), 246–277 (2012)
4. Garcia-Teruel, A., Forehand, D.I.M.: A review of geometry optimisation of wave energy converters. Renew. Sust. Energ. Rev. **139**, 110593 (2021)
5. Piscopo, V., Benassai, G., Morte, R.D.m Scamardella, A.: Cost-based design and selection of point absorber devices for the mediterranean sea. Energies **11**(4), 946 (2018)
6. Khasawneh, M.A., Daqaq, M.F.: Internally-resonant broadband point wave energy absorber. Energy Convers. Manag. **247**, 114751 (2021)
7. Khasawneh, M.A., Daqaq, M.F.: Response behavior of bi-stable point wave energy absorbers under harmonic wave excitations. Nonlinear Dyn., 1–21 (2022)
8. Daqaq, M.F., Crespo, R.S., Ha, S.: On the efficacy of charging a battery using a chaotic energy harvester. Nonlinear Dyn. **99**(2), 1525–1537 (2020)

Optimization of Energy Harvesting from a Nonlinear Energy Sink

Pankaj Kumar and S. Narayanan

1 Introduction

Tuned mass damper (TMD) due to its structural similarity with linear vibration energy harvester has revived considerable research interest in recent years as a dual-function application to simultaneously absorb the vibration of primary structure and harvest energy using piezoelectric or electromagnetic devises [1, 2]. However, uncertainty in excitation and system parameters lead to detuning, which significantly reduces the performance of TMD as well as linear resonant energy harvesters [3]. Nonlinear energy sink (NES) due to its targeted energy character at multiple exciting frequencies has been gaining much research attention to overcome the problem of limited narrow-band effectiveness of linear vibration absorbers [4–6]. Theoretical studies have shown the benefits of an ideal NES to improve the EH [6]. However, it is difficult to realize a purely nonlinear stiffness in the harvester without a part of linear stiffness added to it [4]. Whether the secondary system of vibration absorber-energy harvester model has a linear spring or not, as long as it contains nonlinear elements, the system is nonlinear and hence can be treated as NES or a variant of NES [5]. In [4, 5], it was shown that a nonlinear energy harvester with linear spring and hardening nonlinear spring had better performance.

The vibration attenuation of the primary structure and effective energy harvesting often represent conflicting objectives [2–5], which poses a fundamental difficulty in optimization of system parameters. Nevertheless, design optimization of NES to

P. Kumar (✉)
Dynamic Analysis Group, Bharat Heavy Electricals Limited, Nagpur, India
e-mail: pk.mishra@bhel.in

S. Narayanan (Retired)
Mechanical Engineering, Indian Institute of Technology Madras, Chennai, India

© The Author(s), under exclusive license to Springer Nature Switzerland AG 2024

W. Lacarbonara (ed.), *Advances in Nonlinear Dynamics, Volume III*, NODYCON Conference Proceedings Series, https://doi.org/10.1007/978-3-031-50635-2_22

simultaneously achieve these two conflicting objectives under broadband excitation is challenging [4, 5].

This paper presents a numerical investigation to analyze the complex dynamic behavior of a single device exhibiting both vibration absorption and energy harvesting by employing passive vibration absorption and piezoelectric induction mechanism as a multi-objective optimization problem. Two types of energy harvesting are considered in a generic form: (i) TMD subjected to harmonic excitation and (ii) NES subjected to Gaussian white noise. The analysis of linear TMD subjected to harmonic excitation is undertaken as a preliminary study to highlight the conflicting requirements of vibration absorption and EH and to show that the nonlinear energy harvester under random loading may have opposite behavior with respect to system parameters. The vibration response and the voltage generated in the NES harvesting circuit are obtained using the equivalent linearization technique [7]. Optimum electrical as well as mechanical design parameters are obtained solving a multi-objective optimization problem of minimization of primary vibration response and maximization of the voltage using the dynamic weighted aggregation (DWA) technique [8] and construction of appropriate Pareto optimal fronts using particle swarm optimization scheme [9]. The problem is formulated as a min-max optimization problem [8].

2 Tuned Mass Damper-Energy Harvester Model

Consider a coupled two degree of freedom (DOF) electromechanical system as example of simultaneous energy harvesting dynamic vibration absorber (DVA) (Fig. 1a). The coupled equations of motion of the two DOF linear system and the electrical voltage in the circuit can be expressed as

$$m_1\ddot{x_1} + c_1\dot{x_1} + k_1x_1 - c_1(\dot{x_2} - \dot{x_1}) - k_2(x_2 - x_1) = F_0 \exp^{j\omega t},$$
$$m_2\ddot{x_2} + c_2(\dot{x_2} - \dot{x_1}) + k_2(x_2 - x_1) - \theta v = 0,$$

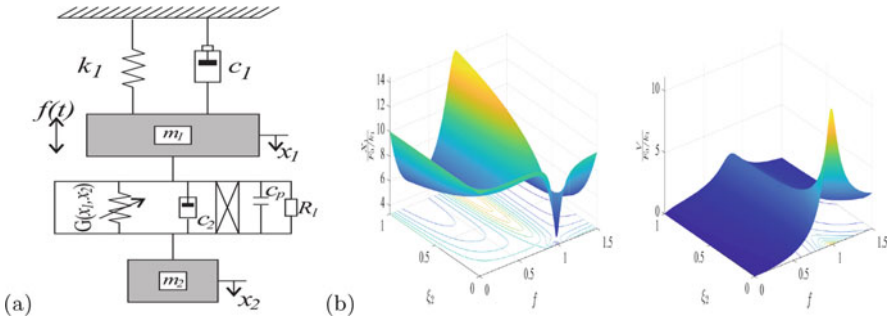

Fig. 1 (**a**) Schematic of energy harvesting with vibration absorber (**b**) surface of bi-objective functions in the space of $f - \xi_2$

$$C_p\dot{v} + \frac{v}{R_l} + \theta\dot{x_2} = 0, \tag{1}$$

where m_1, c_1, and k_1 are the mass, viscous damping coefficient, and stiffness of the primary system, respectively; m_2, c_2, and k_2 are the mass, viscous damping coefficient, and stiffness of the DVA, respectively; v is the voltage across the load resistance R_l; θ is the coupling coefficient between the electrical and mechanical parts of the harvester; C_p is capacitance; F_0 is the amplitude of harmonic force; and ω is the excitation frequency.

The solution for the displacement amplitude $x_1(p)$ and for the voltage amplitude $v(p)$ in the frequency domain can be given as (Fig. 1b)

$$\frac{x_1(p)}{F_0/k_1} = \frac{([f^2 - p^2 - 2\alpha f p^2 \xi_s] + j[\alpha f^2 p - \alpha p^3 + 2fp\xi_s + \alpha\beta\chi f^2 p])}{A + Bj} \tag{2}$$

$$\frac{v(p)}{F_0/k_1} = \frac{\alpha\beta p(2p\xi_s f - f^2 j)}{A + Bj} \tag{3}$$

where $\omega_1^2 = k_1/m_1$, $\omega_2^2 = k_2/m_2$, $\xi_1 = c_1/2\omega_1 m_1$, $\xi_2 = c_2/2\omega_2 m_2$, $\mu = m_2/m_1$, $p = \omega/\omega_1$, $f = \omega_2/\omega_1$, $\chi = \theta/k_s$, $\beta = \theta/c_p$, $\kappa^2 = \chi * \beta$, $A = (p^2-1)(p^2-f^2) - f^2p^2(\mu+2\alpha\xi_1) - 2\alpha f^2 p^2 \beta\chi(\xi_1 + f\mu\xi_2) + 2\alpha p^4(\xi_1 + f\xi_2(1+\mu)) - 2fp^2\xi_2(2\xi_1 + \alpha f p^2)$ and $B = (1-p^2)(\alpha p(f^2(1+\beta\chi) - p^2) + 2fp\xi_2) - fp^3(\mu(2\xi_2+\alpha f)+4\alpha\xi_1\xi_2)+2p\xi_1(f^2-p^2)+\alpha\beta\chi f^4 p\mu$. The optimization problem concerns the design variables f, μ, α, κ^2, ξ_2, which minimize the displacement of primary mass and at the same time maximize the voltage generated.

The frequency response curves of the primary mass displacement and the power harvested in terms of the square of the voltage for the variation in the harvester damping ξ_2, non-dimensional time constant α, and the non-dimensional coupling coefficient κ^2 are shown in Figs. 2 and 3, respectively. Here we observe that as the values of these design variables increase, after some threshold, the primary frequency response transforms from a two peaked curve to a single peaked curve, suggesting that at higher values, the system effectively behaves more like a single DOF system, indicating that the relative motion between the two masses decreases. Further, it is observed that the design value of these variables, which results in

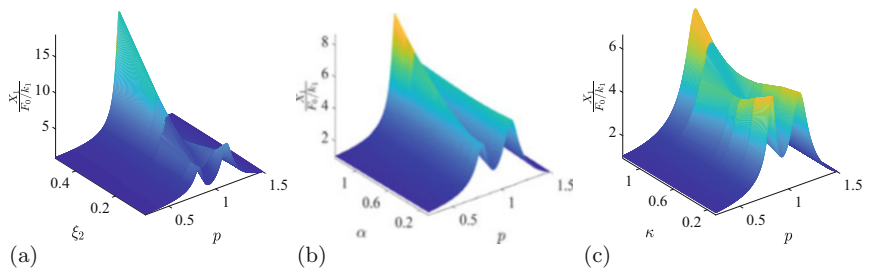

Fig. 2 Frequency response of the primary mass $\frac{X_1}{F_0/k_1}$ (**a**) ξ_2 (**b**) α (**c**) κ^2

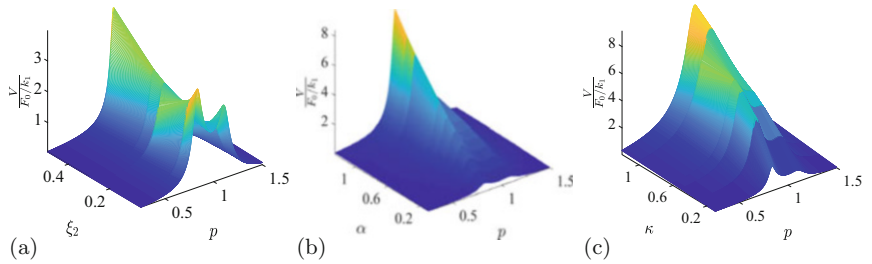

Fig. 3 Frequency response of the normalized voltage $\frac{V}{F_1/k_1}$ (**a**) ξ_2 (**b**) α (**c**) κ^2

the high-voltage generation, also escalates the peak primary displacement and vice versa. Hence, a twin objective optimization problem of determining optimum system parameters that minimizes the primary mass displacement and maximizes the energy harvested to the best possible extent is sought.

3 Bi-objective Optimization: Pareto Front Generation

For conflicting bi-objective functions, due to trade-offs between the two objectives, optimal solution results in a number of optimal solutions rather than a single optimal solution in the two-dimensional space known as Pareto optimal solution. One of the most widely used methods for solving a bi-objective optimization problem is to convert it as a single objective function (OF) optimization problem with a weighted objective function, which is to minimize as [8]

$$\text{Minimize} = OF = P_{norm} = w_1 f_1(x) - w_2 f_2(x), \tag{4}$$

where w_i are the weight of the i-th objective function $f_i(x)$, which can be parametrically varied among two OFs to obtain the Pareto optimal fronts. Moreover, in order to keep the solutions on the Pareto fronts and preventing premature convergence, during each iteration, weights can be gradually updated according to the following dynamic weighted aggregation (DWA) scheme [8]

$$w_1(n) = \left| \sin\left(\frac{2\pi n}{F}\right) \right|, \quad w_2(n) = 1 - w_1(n), \tag{5}$$

where F is the weights' change frequency and n is the iteration index. Evolutionary algorithms such as the particle swarm optimization (PSO) [9] or genetic algorithm can be used to obtain the Pareto optimal sets, because it maintains diversity and works simultaneously on a number of points resulting in well-distributed optimal solution.

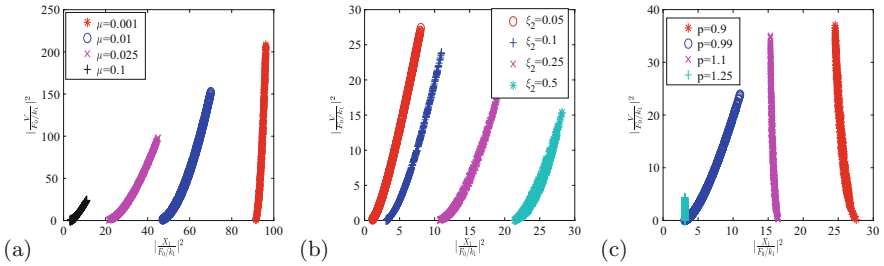

Fig. 4 Pareto front for different values of (**a**) μ (**b**) ξ_2 (**c**) p

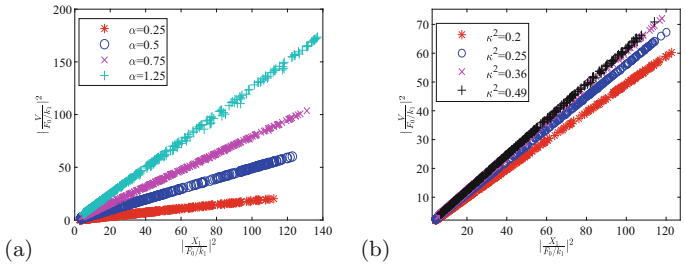

Fig. 5 Pareto front for different values of (**a**) α (**b**) κ^2

First, Pareto bi-objective optimization is formulated with respect to electrical design variables α and κ^2, and admissible domain of the design value is assumed to be $\Omega_{\mathbf{b}} = \{\alpha, \kappa^2 : 0.1 \leq \alpha \leq 0.8 \vee 0.1 \leq \kappa^2 \leq 0.6\}$. Figure 4a–c presents Pareto sets for different values of mass ratio μ, absorber damping ξ_2, and the non-dimensional input frequency ratio p respectively. As the absorber damping ξ_2 and mass ratio μ increase, the slope of the Pareto front decreases, resulting in reduced energy harvesting. Hence, the higher performance of the device is associated with the lower value of absorber damping ξ_2 as well as mass ratio μ. The effect of non-dimensional input frequency ratio p as shown in Fig. 4c, indicating that a good performance for linear 2-DOF EH under harmonic excitation is associated with resonant behavior.

Next, Pareto bi-objective optimization is formulated for the evaluation of optimum design space of mass ratio μ and non-dimensional tuning frequency f, and the admissible domain of the design values is assumed to $\Omega_{\mathbf{b}} = \{f, \mu : 0.9 \leq f \leq 1.1 \vee 0.001 \leq \mu \leq 0.1\}$. Figure 5a,b show different Pareto sets for different values of non-dimensional time constant α and non-dimensional coupling coefficient κ^2, respectively. It is evident from both the results that the higher performance can be attained by increasing the electrical design parameters α as well as κ^2. However, after some threshold value $\kappa^2 \approx 0.4$ benefits in harvesting power through increasing κ^2 gets somewhat saturated.

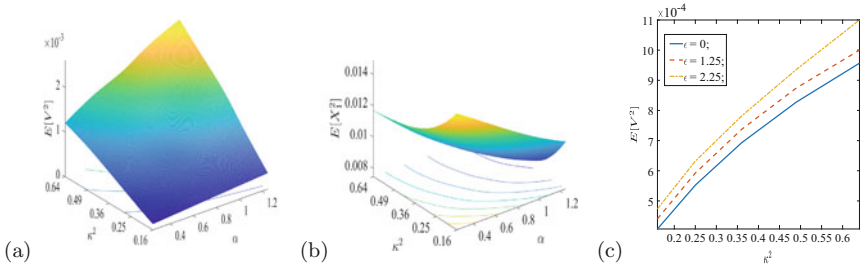

Fig. 6 Variation of (**a**) $E[V^2]$ (**b**) $E[X_1^2]$ with respect to α and κ^2; (**c**) effect of ϵ

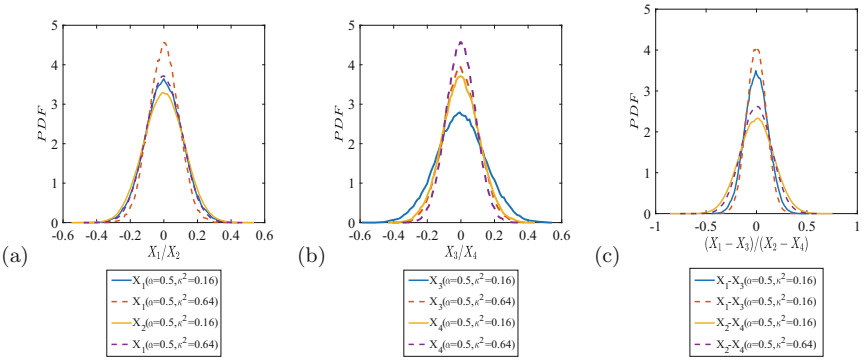

Fig. 7 Marginal pdf of X and $\dot{X}$ for (**a**) m_1 (**b**) m_2 (**c**) relative movement

4 Noisy Nonlinear Energy Sink-Energy Harvester

The equations of motion of a variant NES-based energy harvester when the primary structure is subjected to Gaussian white noise ($f(t) = W(t)$) can be expressed as

$$\begin{aligned} m_1\ddot{x_1} + c_1\dot{x_1} + k_1x_1 + c_2(\dot{x_1} - \dot{x_2}) + k_2(x_1 - x_2) + k_{nl2}(x_1 - x_2)^3 &= \sigma W(t), \\ m_2\ddot{x_2} - c_2(\dot{x_1} - \dot{x_2}) - k_2(x_1 - x_2) - k_{nl2}(x_1 - x_2)^3 - \theta v &= 0, \\ C_p\dot{v} + \frac{v}{R_l} + \theta\dot{x_2} &= 0; \end{aligned} \tag{6}$$

where k_{nl2} is nonlinear stiffness, σ is the noise intensity, and $W(t)$ is a random force, modeled as a stationary Gaussian white noise with zero mean and $E(W(t)W(t+\tau) = 2\pi S_0\delta(\tau)$. S_0 is two-sided power spectral density function, and $\delta(\tau)$ is the Dirac-delta function. A parametric investigation for the response statistics of NES-based energy harvester using Euler-Maruyama integration scheme is conducted for various design parameters $\mathbf{b} = (\mathbf{f}, \mu, \alpha, \kappa^2, \xi_2)$ in order to characterize system behavior and to obtain the associated response sensitivities to electro-mechanical design parameters.

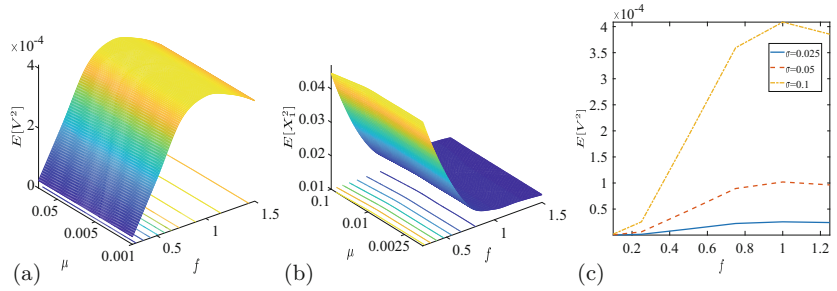

Fig. 8 Variation of (**a**) $E[V^2]$ (**b**) $E[X_1^2]$ with respect to f and μ, (**c**) effect of σ

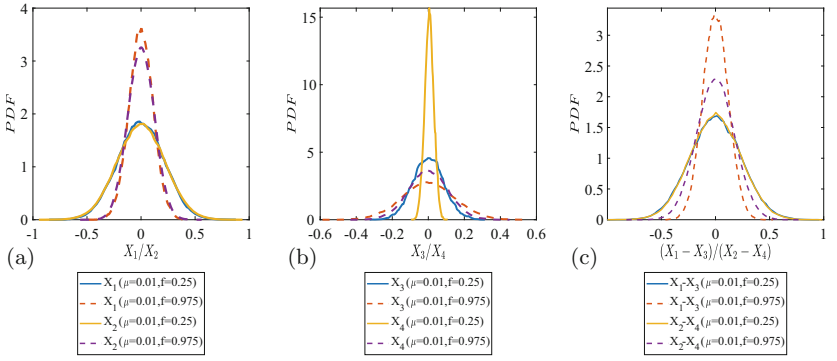

Fig. 9 Marginal pdf of X and $\dot{X}$ for (**a**) m_1 (**b**) m_2 (**c**) relative movement

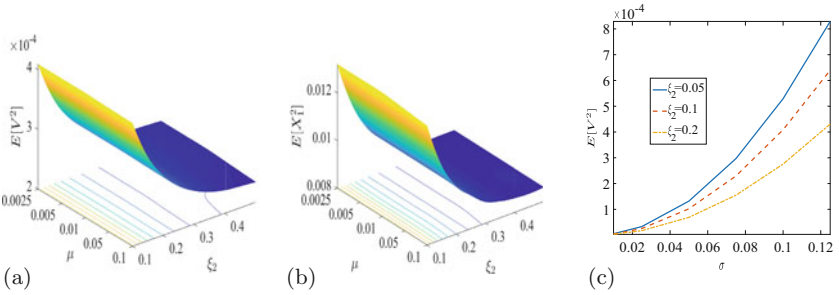

Fig. 10 Variation of (**a**) $E[V^2]$ (**b**) $E[X_1^2]$ with respect to μ and ξ_2, (**c**) effect of σ

In Fig. 6a,b, in the design space of $\alpha - \kappa^2$, as both these parameters increase, the mean square of voltage also increases. One can observe that simultaneously the mean square value of primary mass displacement decreases. Here, increase in $E[V^2]$ is directly linked with increase in electrical parameter because as shown in Fig. 7, marginal pdf of displacement and velocity of both m_1 and m_2 decrease with increase in coupling coefficient κ^2. Moreover as the nonlinearity coefficient ϵ increases, there is increase in power output (Fig. 6c).

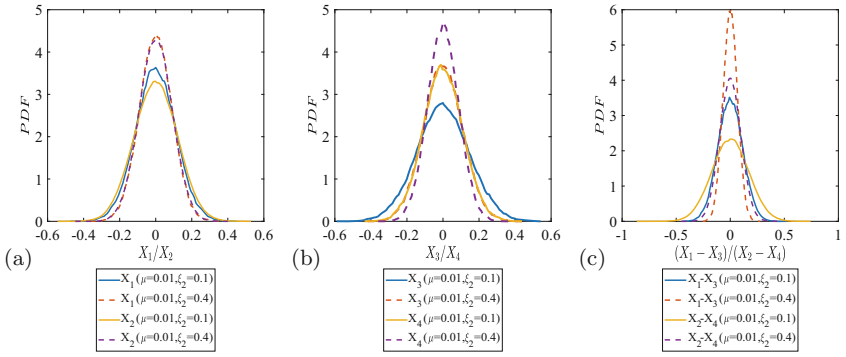

Fig. 11 Marginal pdf of X and $\dot{X}$ for (**a**) m_1 (**b**) m_2 (**c**) relative movement

Figure 8a,b shows that for a given mass ratio μ, maximum harvesting power occurs close to $f \approx 1$ and deviation to either side leads to a sharp reduction in energy harvesting. Figure 8 also indicates that in the space of $f - \mu$, the variations of mean square voltage and response of primary structure have conflicting behaviors. Even though marginal pdf of displacement and velocity of primary mass reduce with increase in tuning ratio f, the marginal pdf of velocity of m_2, which is coupled with electromechanical coupling coefficient θ, increases drastically (see Fig. 9), leading to increase in $E[V^2]$. Next, as shown in Fig. 8c, irrespective of tuning ratio f, mean square voltage increases steeply only after some threshold value of σ.

Figure 10a,b shows that in the design space of $\mu - \xi_2$, increasing harvester damping ξ_2 reduces the harvested power, but contrary to previous results, an increase or decrease in the amount of power harvested follows with an increase or decrease of the displacement of primary mass. This can be explained from Fig. 11a and b, which show the marginal pdfs of displacements and velocities of m_1 and m_2. Hence under random excitation, for certain cases, the nonlinear energy sink can be tuned in such a way that it is effective in both reducing the random response of the host structure and harvesting maximum vibrational energy. It can be seen from Fig. 10c that for a given harvester damping ξ_2, mean square voltage increases proportionally with noise intensity σ.

Next to investigate the optimal performance of the NES-based energy harvesting the two conflicting objectives, namely, $E[X_1^2]$ and $E[V^2]$ are obtained. Using equivalent linearization techniques, mean square value of displacement $E[X_1^2]$ of primary mass and voltage $E[V^2]$ are given by

$$E[X_1^2] = S_0 \int_{-\infty}^{\infty} \frac{[f^2 - p^2 - 2\alpha f p^2 \xi_{2e}]^2 + [2fp\xi_{2e} + \alpha f^2 p + \alpha\beta\chi f^2 p - \alpha p^3]^2}{\Delta(\omega)\Delta^*(\omega)} \mathrm{d}\omega \tag{7}$$

$$E[V^2] = S_0 \int_{-\infty}^{\infty} (\alpha\beta p)^2 \frac{[2p\xi_{2e} f]^2 + [-f^2]^2}{\Delta(\omega)\Delta^*(\omega)} \mathrm{d}\omega \tag{8}$$

Following Robert and Spanos [7], the $E[X_1^2]$ and $E[V^2]$ can be obtained as

$$E[X_1^2] = \frac{\pi S_0}{\lambda_5} \frac{det\begin{bmatrix} a_4 & a_3 & a_2 & a_1 & a_0 \\ -\lambda_5 & \lambda_3 & -\lambda_1 & 0 & 0 \\ -\lambda_5 & \lambda_3 & -\lambda_1 & 0 & 0 \\ 0 & -\lambda_4 & \lambda_2 & -\lambda_0 & 0 \\ 0 & \lambda_5 & -\lambda_3 & \lambda_1 & 0 \\ 0 & 0 & \lambda_4 & -\lambda_2 & \lambda_0 \end{bmatrix}}{det\begin{bmatrix} \lambda_4 & -\lambda_2 & \lambda_0 & 0 & 0 \\ -\lambda_5 & \lambda_3 & -\lambda_1 & 0 & 0 \\ 0 & -\lambda_4 & \lambda_2 & -\lambda_0 & 0 \\ 0 & \lambda_5 & -\lambda_3 & \lambda_1 & 0 \\ 0 & 0 & \lambda_4 & -\lambda_2 & \lambda_0 \end{bmatrix}};$$

$$E[V^2] = \frac{\pi S_0}{\lambda_5} \frac{det\begin{bmatrix} c_4 & c_3 & c_2 & c_1 & c_0 \\ -\lambda_5 & \lambda_3 & -\lambda_1 & 0 & 0 \\ -\lambda_5 & \lambda_3 & -\lambda_1 & 0 & 0 \\ 0 & -\lambda_4 & \lambda_2 & -\lambda_0 & 0 \\ 0 & \lambda_5 & -\lambda_3 & \lambda_1 & 0 \\ 0 & 0 & \lambda_4 & -\lambda_2 & \lambda_0 \end{bmatrix}}{det\begin{bmatrix} \lambda_4 & -\lambda_2 & \lambda_0 & 0 & 0 \\ -\lambda_5 & \lambda_3 & -\lambda_1 & 0 & 0 \\ 0 & -\lambda_4 & \lambda_2 & -\lambda_0 & 0 \\ 0 & \lambda_5 & -\lambda_3 & \lambda_1 & 0 \\ 0 & 0 & \lambda_4 & -\lambda_2 & \lambda_0 \end{bmatrix}} \tag{9}$$

where $a_0 = f^4$; $a_1 = \alpha^2 f^4 \kappa^4 - 2f^2 - 2\alpha^2 f^4 \kappa^2 - 4\alpha f^3 \kappa^2 \xi_s + \alpha^2 f^4 + 4\xi_s^2 f^2$; $a_2 = 4\alpha^2 \xi_s^2 f^2 + 1 + 2\alpha^2 f^2 \kappa^2 - 2\alpha^2 f^2$; $a_3 = \alpha^2$; $a_4 = 0$; $c_0 = 0$; $c_1 = \alpha^2 \beta^2 f^4$; $c_2 = 4\alpha^2 \beta^2 \xi_s^2 f^2$; , $\beta = \theta / c_p$, $c_3 = c_4 = 0$; and

$$\begin{aligned}
\lambda_0 &= f^2; \\
\lambda_1 &= 2f\xi_{2e} + \alpha f^2 + 2f^2\xi_1 + \alpha\beta\chi f^2 + \alpha\beta\chi f^4\mu; \\
\lambda_2 &= 1 + f^2 + f^2\mu + 2\alpha f\xi_{2e} + 4f\xi_1\xi_{2e} + 2\alpha f^2\xi_1 + 2\alpha\beta\chi f^2\xi_1 + 2\alpha\beta\chi f^3\mu\xi_{2e}; \\
\lambda_3 &= \alpha + 2\xi_1 + \alpha f^2 + 2f\xi_{2e} + 2f\mu\xi_{2e} + \alpha f^2\mu + 4\alpha f\xi_1\xi_{2e} + \alpha\beta\chi f^2; \\
\lambda_4 &= 1 + 2\alpha\xi_1 + 2\alpha f\xi_{2e} + 2\alpha f\mu\xi_{2e}; \\
\lambda_5 &= \alpha.
\end{aligned} \tag{10}$$

First, Pareto bi-objective optimization is formulated with respect to electrical design variables α and κ^2, and admissible domain of the design values is assumed to be $\Omega_{\mathbf{b}} = \{\alpha, \kappa^2 : 0.1 \leq \alpha \leq 0.8 \vee 0.1 \leq \kappa^2 \leq 0.6\}$. Figure 12a–c presents Pareto optimal fronts for different values of damping ξ_1, absorber damping ξ_2, and mass ratio μ, respectively. As these design variables increase, the slope of the Pareto optimal front decreases, which results in reduced energy harvesting. Hence, the higher performance of the device is associated with the lower values of ξ_1, ξ_2, and μ.

Next, Pareto multi-objectives optimization is formulated for the evaluation of the design vector $\mathbf{b} = \mathbf{f}$, μ, and the admissible domain of the design values is assumed to be $\Omega_{\mathbf{b}} = \{f, \mu : 0.9 \leq f \leq 1.1 \vee 0.001 \leq \mu \leq 0.1\}$.

Figure 13a,b shows non-dominant optimum design point as a Pareto front obtained for different values of non-dimensional time constant α and coupling strength κ^2.

5 Concluding Remarks

This chapter presents a comparative numerical analysis to examine the simultaneous vibration absorption and piezoelectric energy harvesting through the use of linear vibration absorber and nonlinear energy sink attached to a host structure. Two types of excitations are considered: harmonic and random. The system with optimal parameters shows considerable improvement both in terms of vibration absorption and energy harvesting compared to the non-optimal systems. It is found that electrical output is larger for decreased values of the system damping and mass ratio and for increased values of the non-dimensional time constant α and coupling strength κ^2. Under stochastic excitation, it is observed that both maximization of energy harvesting and attenuation of vibration of primary system can be achieved.

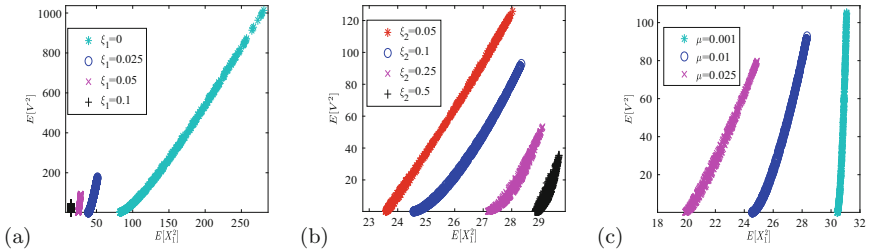

Fig. 12 Pareto front for different values of (**a**) ξ_1 (**b**) ξ_2 (**c**) μ

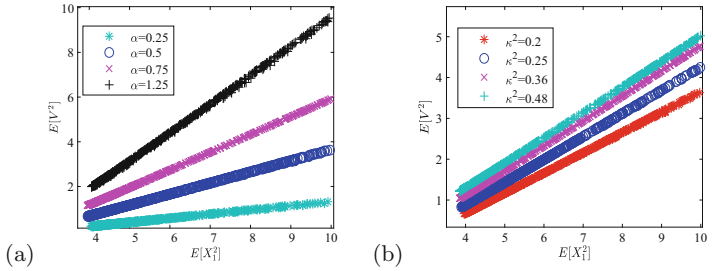

Fig. 13 Pareto front for different values of (**a**) α (**b**) κ^2

References

1. Brennan, M.J., Tang, B., Pechoto, G.M., Lopes, V.: An investigation into the simultaneous use of a resonator as an energy harvester and a vibration absorber. J. Sound Vib. **333**(5), 1331–1343 (2014)
2. Ali, S.F., Adhikari, S.: Energy harvesting dynamic vibration absorbers. J. Appl. Mech. **80**, 1–9 (2013)
3. Omer, F.T.: Optimum vibration absorber (tuned mass damper) design for linear damped systems subjected to random loads. J. Sound Vib. **331**(13), 3035–3049 (2012)
4. Zhang, Y., Tang, l., Liu, K.: Piezoelectric energy harvesting with a nonlinear energy sink. J. Intell. Mater. Syst. Struct. **28**(3), 307–322 (2017)
5. Kremer, D., Liu, K.: A nonlinear energy sink with an energy harvester: Transient responses. J. Sound Vib. **333**(20), 4859–4880 (2014)
6. Xue, J.R., Zhang, Y.W., Niu, M.Q., Chen, L.Q.: Harvesting electricity from random vibrations via a nonlinear energy sink. J. Vib. Control **0**(0), 1–15 (2022)
7. Roberts, J.B., Spanos, P.D.: Random Vibration and Statistical Linearization. Wiley, New York (1990)
8. Parsopoulos, K.E., Vrahatis, M.N.: Particle swarm optimization method in multi-objective problems. In: Proceedings of the 2002 ACM Symposium on Applied Computing, pp. 603–607 (2002)
9. Leung, A.Y.T., Zhang, H.: Particle swarm optimization of tuned mass dampers. Eng. Struct. **31**(3), 715–728 (2009)

Enhancing Aeroelastic Wind Energy Harvesting Using Quasi-Zero Stiffness

Shun Chen and Liya Zhao

1 Introduction

With the development of low-power microelectronics, wireless sensor networks, and Internet of Things, vast sensor nodes are deployed in remote and harsh circumstances for various monitoring purposes. However, how to provide a reliable and long-term power supply to these sensors is a big challenge. Currently, energy harvesting technology has attracted researchers' interests to solve this problem. Among various ambient energy sources, wind energy is a good alternative since it is ubiquitous in both indoor and outdoor environments. Wind-induced vibration can be converted to electricity using four main energy conversion mechanisms: piezoelectric [1], electromagnetic [2], electrostatic [3], and triboelectric [4] transduction. Piezoelectric energy harvesting shows good potential and has been widely investigated due to its high power density [5]. Wind-induced vibration resulting from different aeroelasticities has been utilized in piezoelectric energy harvesting, including vortex-induced vibration, galloping, and flutter. Wind energy harvesting based on galloping has been widely reported due to its unique advantage of large outputs in an infinite wind speed range [13].

In the literature, researchers have mainly focused on decreasing the cut-in wind speed, broadening the operational wind speed range, and improving the power output performance [7]. Efforts include adopting nonlinear techniques [8], dual vibration sources [9], and 2DOF system [10]. Because the cut-in wind speed is highly related to the oscillation frequency of the structure [7], manipulating the oscillation frequency is essential to decrease the cut-in wind speed and enhance the power extraction performance at low wind speeds for galloping energy harvesting.

S. Chen · L. Zhao (✉)
School of Mechanical and Manufacturing Engineering, University of New South Wales, Sydney, NSW, Australia
e-mail: liya.zhao2@unsw.edu.au

© The Author(s), under exclusive license to Springer Nature Switzerland AG 2024

W. Lacarbonara (ed.), *Advances in Nonlinear Dynamics, Volume III*, NODYCON Conference Proceedings Series, https://doi.org/10.1007/978-3-031-50635-2_23

2DOF systems provide more flexibility to adjust the galloping frequency for enhanced outputs by modifying the model frequencies [10, 12]. In a separate field of research, quasi-zero stiffness (QZS) nonlinearity has been found to provide a low dynamic resonance frequency at equilibrium [11]. We propose a 2DOF quasi-zero-stiffness galloping piezoelectric energy harvester (QZS-GPEH) for dramatically enhancing the wind power extraction performance at ultra-low wind speeds. A fully coupled aero-electro-mechanical distributed-parameter model is established to evaluate the performance of the proposed harvester. Numerical result shows that the 2DOF QZS-GPEH remarkably outperforms its linear and bistable counterparts. This paper is organized as follows. The conceptual design, working principle, and modeling process are presented in Sect. 2. Section 3 presents the results and discussion. The final section concludes the paper.

2 Design of 2DOF Quasi-Zero Stiffness Galloping Energy Harvester

2.1 Conceptual Schematic

Figure 1 shows the conceptual design of the 2DOF quasi-zero-stiffness galloping piezoelectric energy harvester (QZS-GPEH). A bluff body is elastically mounted as a primary oscillator, which can capture the kinetic energy in wind flows to induce galloping instability. M_1, K_3 and C_1 resent the mass, stiffness, and damping of the primary oscillator with the bluff body, respectively, and M_2, K_2 and C_2 are the mass, stiffness, and damping of the secondary oscillator, respectively. M_1 and M_2 undergo a displacement (relative to the ground) of Y_1 and Y_2, respectively. To achieve QZS, the primary oscillator has only a cubic nonlinear stiffness K_3, while its linear stiffness is zero and the total restoring force is $F_{K_3} = K_3 {Y_1}^3$. An energy conversion component is connected between the primary oscillator and the ground, which can convert kinetic vibration energy to electricity based on electromagnetic, piezoelectric, or electrostatic mechanisms. To realize the quasi-zero stiffness, Fig. 1b shows two conceptual designs, where the main structure (i.e., the bluff body with a payload mass of M_1) is supported by the vertical spring with positive linear stiffness, while the two horizontal springs or repulsively aligned magnets induce a negative linear stiffness as well as a positive cubic stiffness. The transduction component is a piezoelectric element with a capacitance C_p and the governing equation of the system is described as

$$\begin{aligned} &M_1\ddot{Y}_1 + C_1\dot{Y}_1 + K_1 Y_1 + K_3 {Y_1}^3 + C_2\left(\dot{Y}_1 - \dot{Y}_2\right) + K_2\left(Y_1 - Y_2\right) + \Theta V \\ &\quad = \tfrac{1}{2}\rho h L U^2 \sum_{j=1}^{3} A_j \left(\tfrac{\dot{Y}_1}{U}\right)^j \\ &M_2\ddot{Y}_2 + C_2\left(\dot{Y}_2 - \dot{Y}_1\right) + K_2\left(Y_2 - Y_1\right) = 0 \\ &\tfrac{V}{R} + C_p\dot{V} - \Theta\dot{Y}_1 = 0 \end{aligned} \tag{1}$$

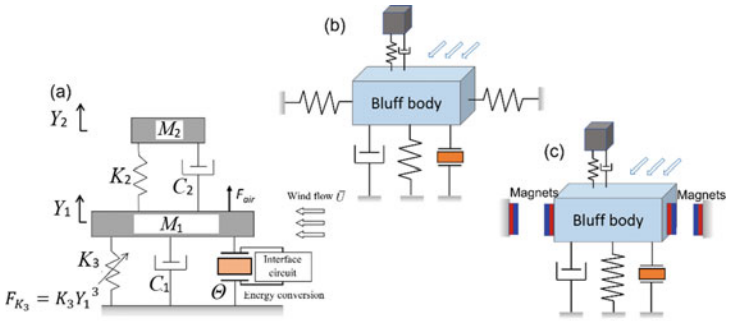

Fig. 1 (**a**) Mechanical representation and (**b**) conceptual schematic of 2DOF QZS-GPEH

where $K_1 = 0$, which is kept in the equation to facilitate the subsequent comparison between different configurations; Θ is the electromechanical coupling; ρ is the air density; h and L are the height and length of the bluff body, respectively; A_i are the empirical aerodynamic coefficients; and V is the generated piezoelectric voltage. The oscillation frequency of the harvester is ω. A simple AC circuit with a load R is connected to the piezoelectric element. We further nondimensionalize Eq. (1) as

$$\begin{aligned} &\ddot{y}_1 + 2\zeta_1 \dot{y}_1 + k_1 y_1 + k_3 {y_1}^3 + 2\zeta_2 \alpha\lambda\,(\dot{y}_1 - \dot{y}_2) + \alpha\lambda^2 (y_1 - y_2) + \kappa_e v \\ &\quad = f_1 u_a \dot{y}_1 + f_3 {u_a}^{-1} \dot{y}_1^3 \\ &\ddot{y}_2 + 2\zeta_2\lambda\,(\dot{y}_2 - \dot{y}_1) + \lambda^2 (y_2 - y_1) = 0 \\ &\tfrac{v}{r} + \dot{v} - \dot{y}_1 = 0 \end{aligned} \tag{2}$$

where the dimensionless parameters are $y_1 = \frac{Y_1}{h}$, $y_2 = \frac{Y_2}{h}$, $v = \frac{C_p V}{\Theta h}$, $\omega_n = \sqrt{\frac{K_0}{M_1}}$, $\omega_2 = \sqrt{\frac{K_2}{M_2}}$, $k_1 = \frac{K_1}{K_0}$, $k_3 = \frac{K_3 h^2}{K_0}$, $\zeta_1 = \frac{C_1}{2M_1\omega_n}$, $\zeta_2 = \frac{C_2}{2M_2\omega_2}$, $\alpha = \frac{M_2}{M_1}$, $\lambda = \frac{\omega_2}{\omega_n}$, $r = C_p R \omega_n$, $\kappa_e = \frac{\Theta^2}{C_p K_0}$, $m_{\text{air}} = \frac{M_1}{\rho h^2 L}$, $u_a = \frac{U}{\omega_n h}$, $f_1 = \frac{A_1}{2m_{\text{air}}}$, $f_3 = \frac{A_3}{2m_{\text{air}}}$, $\tau = \omega_n t$. The overdot in Eq. (2) denotes the derivative with respect to τ. We pre-set an arbitrary positive value K_0 which simply serves for the purpose of nondimensionalization. For a case study, the following parameters are assumed: ζ_1=0.0055, $\zeta_2 = 0.0055$, $\alpha = 1$, $\lambda = 2.828$, $r = 763.2$, $\kappa_e = 0.007766$, $f_1 = 0.007700$, $f_3 = -0.5263$. For the proposed 2DOF QZS-GPEH, we take $k_1 = 0$ and $k_3 = 2$ since the linear stiffness is zero; for the 1DOF and 2DOF linear GPEHs, $k_1 = 1$ and $k_3 = 0$; for a 2DOF monostable hardening GPEH, $k_1 = 1$ and $k_3 = 2$; and for a 2DOF bistable GPEH, $k_1 = -0.5$ and $k_3 = 2$. The voltage v and the oscillation frequency Ω ($\Omega = \omega/\omega_n$) responses for different configurations are compared in Fig. 2.

The proposed 2DOF QZS-GPEH outperforms the other configurations, especially at low wind speeds, with the lowest cut-in wind speed and highest voltage output from $u_a = 0.6$ to 2.6. Beyond $u_a = 2.6$, the bistable design overcomes the potential barrier and starts to produce voltage outputs that are comparable to those

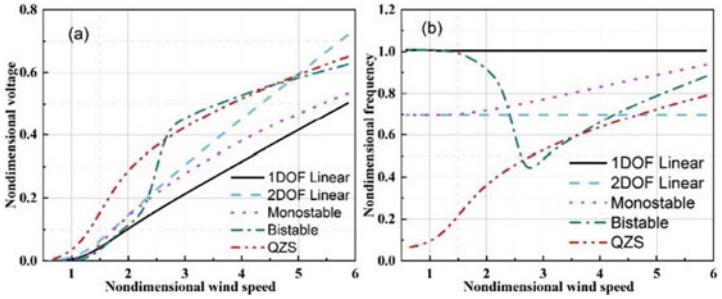

Fig. 2 (**a**) Voltage and (**b**) oscillation frequency as a function of wind speed for different configurations of GPEH

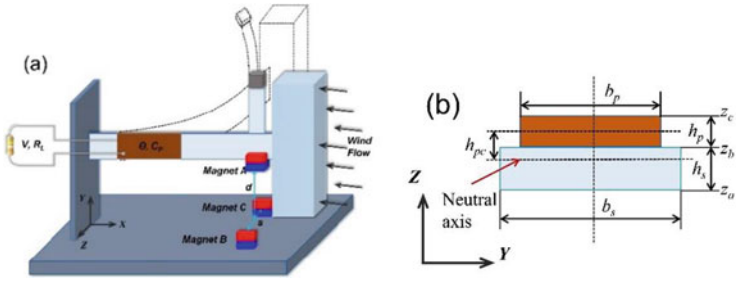

Fig. 3 (**a**) 2DOF QZS-GPEH prototype; (**b**) composite beam cross section for the segment with the transducer

of the QZS design. However, it is evident that the QZS mechanism eliminates the drawback of the potential barrier and provides robust performance over the entire considered wind speed range. It is worth noting that the voltage level appears to be inversely proportional to the harvester's oscillation frequency, as can be seen by comparing Fig. 2a with Fig. 2b. This further explains the outperformance of the 2DOF QZS-GPEH due to its low dynamic stiffness around equilibrium.

2.2 Configuration of the Prototype

We focus on the wind energy harvesting functionality in this study and ignore the payload support requirement in the vertical direction. Consequently, we design a practical prototype as shown in Fig. 3. The bluff body oscillates horizontally when subjected to the incoming flow. The piezoelectric transducer attached to the primary beam converts the strain energy during oscillation into electricity via piezoelectric transduction. A secondary beam with a tip mass is added at the free end of the primary beam as the second degree-of-freedom. The quasi-zero stiffness is achieved via magnetic interaction between magnets A, B and C. To achieve optimal galloping energy harvesting performance, a square-sectioned bluff body is employed in this study due to its superiority over other geometries [6, 9].

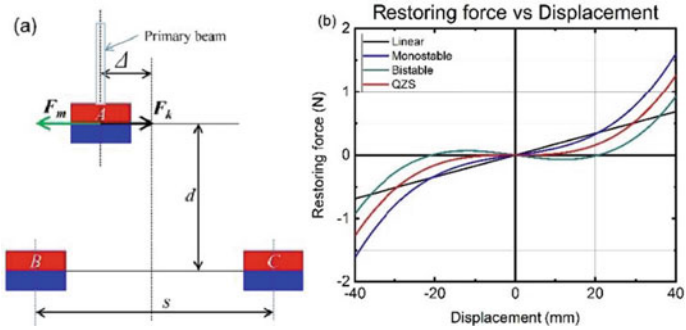

Fig. 4 (**a**) Schematic of magnets A, B and C, and (**b**) restoring force as a function of displacement

Figure 4a shows the deployment of three magnets. The magnetic force F_m on magnet A is described based on the dipole-to-dipole model [14], given in Eq. (3), where m_a and m_b are the magnetic moments; μ_0 is the vacuum permeability; and Δ is the horizontal deviation of magnet A from the center line. Equation (3) can be fitted as a cubic polynomial by $F_m = K_{m1}\Delta + K_{m3}\,\Delta^3$. Assuming K_0 is the original stiffness of the primary beam, it is possible to achieve that $K_{m1} - K_0 = 0$ by tuning s and d, making the resultant stiffness of the primary beam essentially nonlinear.

$$F_m = \frac{3\mu_0 m_a m_b}{4\pi}\left(\frac{-4(s-\Delta)}{\left((s-\Delta)^2+d^2\right)^{2.5}} + \frac{5(s-\Delta)^3}{\left((s-\Delta)^2+d^2\right)^{3.5}}\right) + \frac{3\mu_0 m_a m_b}{4\pi}\left(\frac{4(s+\Delta)}{\left((s+\Delta)^2+d^2\right)^{2.5}} - \frac{5(s+\Delta)^3}{\left((s+\Delta)^2+d^2\right)^{3.5}}\right) \tag{3}$$

For comparison, we also examine the performances of the linear 1DOF, linear 2DOF, and bistable 2DOF counterparts. The bistable configuration is achieved by decreasing d to buckle the beam; removing magnets B and C will degrade the system to a linear 2DOF design; further removing the secondary beam will yield a 1DOF linear design.

2.3 Modeling

The aero-electro-mechanically coupled model for the 2DOF QZS-GPEH consists of a Euler-Bernoulli distributed parameter model for the primary cantilever and a lumped parameter model for the secondary beam. The aerodynamic galloping force is modeled based on the quasi-steady hypothesis. The two beams are coupled by the reaction force at its free end of the primary beam, exerted by the secondary oscillator. The circuit model is established according to Gauss's law and constitutive

relationship of piezoelectric materials. The governing equations for the proposed system can be expressed as

$$\begin{aligned}&\left(E_{si}I_{si}+\delta_{2i}E_pI_p\right)\frac{\partial^4 w_i(x_i,t)}{\partial {x_i}^4}+c_{si}I_i\frac{\partial^5 w_i(x_i,t)}{\partial {x_i}^4\partial t}+c_{ai}\frac{\partial w_i(x_i,t)}{\partial t}+m_i\frac{\partial^2 w_i(x_i,t)}{\partial t^2}\\&+\delta_{2i}\theta V\left[\frac{d\delta(x_2)}{dx}-\frac{d\delta(x_2-L_2)}{dx}\right]=\delta_{3i}\left(F_{\text{air}}(t)+F_{\text{beam}}(t)+F_{\text{magnet}}(t)\right)\delta\left(x_3-L_3\right)\\&-\delta_{3i}M_{\text{air}}(t)\frac{d\delta(x_3-L_3)}{dx_3}\qquad\qquad(i=1,2,3)\end{aligned}\tag{4}$$

$$M_2\ddot{u}_2+C_2\left(\dot{u}_2-\frac{\partial w_3\left(L_3,t\right)}{\partial t}\right)+K_2\left(u_2-w_3\left(L_3,t\right)\right)=0\tag{5}$$

$$\frac{V(t)}{R}-\theta\frac{\partial^2 w_2\left(x_2,t\right)}{\partial x_2\partial t}\Bigg|_0^{L_2}+C_p\frac{dV(t)}{dt}=0\tag{6}$$

The primary beam is divided into three segments with $0<x_1<L_1$, $0<x_2<L_2$ and $0<x_3<L_3$, where L_i is the length of each segment. The second segment is covered by the transducer. $E_{si}I_{si}$ and E_pI_p are the bending stiffness of the substrate and piezoelectric layer (with respect to the neutral axis of the cross section); c_{si} is the strain rate damping; c_{ai} is the air damping; m_i is the distributed mass of the primary beam; δ is the Dirac delta function; $w(x_i, t)$ is the transversal displacement of the bluff body; u_2 is the absolute displacement of the tip mass of the secondary beam; M_2, C_2, K_2 are the equivalent mass, damping, and stiffness of the secondary beam, respectively; θ is the electromechanical term; C_p is the piezoelectric capacitance; F_{air} and M_{air} is the aerodynamic galloping force and moment; F_{magnet} is the nonlinear magnetic force; F_{beam} is the coupled reaction force applied by the secondary beam at the free end of the primary beam; V is the generated voltage of the transducer, and R is the load resistance.

The magnetic force F_{magnet} can be simplified as a cubic polynomial as

$$F_m(t)=K_{m1}w\left(L_3,t\right)+K_{m3}w^3\left(L_3,t\right)\tag{7}$$

The reaction force F_{beam} is calculated by

$$F_a(t)=C_2\left(\dot{u}_2-\frac{\partial w_3\left(L_3,t\right)}{\partial t}\right)+K_2\left(u_2-w_3\left(L_3,t\right)\right)\tag{8}$$

The aerodynamic galloping force and moment are expressed based on the quasi-steady hypothesis [6] as

$$F_{\text{air}}(t)=\frac{1}{2}\rho hlU^2\sum_{j=1}^{3}A_j\left\{\frac{1}{U}\left[\frac{\partial w_3\left(L_3,t\right)}{\partial t}+\frac{h}{2}\frac{\partial^2 w_3\left(L_3,t\right)}{\partial x_3\partial t}\right]+\frac{\partial w_3\left(L_3,t\right)}{\partial x_3}\right\}^j\tag{9}$$

$$M_{air}(t) = \frac{h}{2} F_{air}(t) \tag{10}$$

where, similar to those in Eq. (1), ρ is the air density; h and l are the width and length of the bluff body; U is the incoming air speed; and A_j are the aerodynamic coefficients. Applying the orthogonality relations, the aero-electro-mechanical governing equations can be written in modal coordinates as

$$\begin{cases} \ddot{\eta}_r(t) + 2\zeta_r\omega_r\dot{\eta}_r(t) + \omega_r^2\eta_r(t) + \chi_r V = f_{air} + f_a + f_m \\ M_2\ddot{u}_2 + C_2\left(\dot{u}_2 - \sum\limits_r \phi_{3r}(L_3)\,\dot{\eta}_r(t)\right) + K_2\left(u_2 - \sum\limits_r \phi_{3r}(L_3)\,\eta_r(t)\right) = 0 \\ I(t) - \sum\limits_r \chi_r\dot{\eta}_r(t) + C_p\dot{V}(t) = 0 \end{cases} \tag{11}$$

with

$$\begin{cases} f_{\text{air}} = \left[\phi_{3r}(L_3) + \frac{h}{2}\phi'_{3r}(L_3)\right]\frac{1}{2}\rho hlU^2 \sum\limits_{j=1}^{3} A_j \left\{\frac{1}{U}\sum\limits_r \left[\phi_{3r}(L_3) + \frac{h}{2}\phi'_{3r}(L_3)\right]\dot{\eta}_r(t) + \sum\limits_r \phi'_{3r}(L_3)\,\eta_r(t)\right\}^j \\ f_a = \phi_{3r}(L_3)\left[C_2\left(\dot{u}_2 - \sum\limits_r \phi_{3r}(L_3)\,\dot{\eta}_r(t)\right) + K_2\left(u_2 - \sum\limits_r \phi_{3r}(L_3)\,\eta_r(t)\right)\right] \\ f_m = \phi_{3r}(L_3)\left[K_{m1}\sum\limits_r \phi_{3r}(L_3)\,\eta_r(t) + K_{m3}\left(\sum\limits_r \phi_{3r}(L_3)\,\eta_r(t)\right)^3\right] \end{cases} \tag{12}$$

where $\phi_r(x)$ and $\eta_r(t)$ are the eigenfunction and modal coordinates for the rth mode, ζ_r is the damping ratio, and $\chi_r = \theta\left[\phi'_{2r}(L_2) - \phi'_{2r}(0)\right]$ is the modal electromechanical coupling coefficient.

3 Results and Discussions

Based on the developed theoretical model, Fig. 5 compares the RMS voltage versus wind speed for the four configurations, including 1DOF linear GPEH, 2DOF linear GPEH, 2DOF QZS-GPEH and 2DOF bistable GPEH. Firstly, the cut-in wind speed of the 2DOF QZS-GPEH is reduced to 1.5 m/s, smaller than that of the other three configurations. Besides, the output voltage is remarkably larger than that of the other three counterparts, especially at low wind speeds. For instance, at the wind speed of 2.0 m/s, the 2DOF QZS-GPEH increases the voltage amplitude by 95% in comparison to the 1DOF linear GPEH, and by 72% in comparison to the 2DOF linear GPEH. Moreover, below 2.4 m/s, the bistable GPEH is trapped into

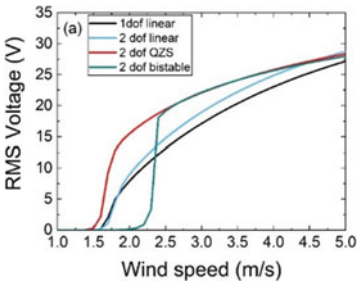

Fig. 5 Theoretically predicted RMS voltage as a function of wind speed

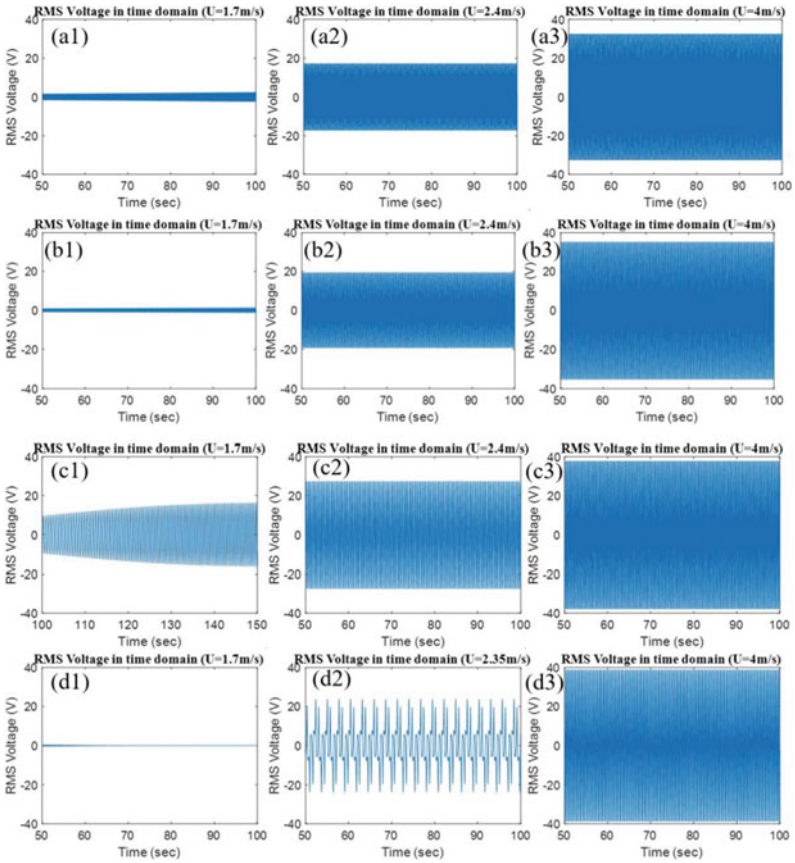

Fig. 6 Phase portraits for the four GPEHs at different wind speeds: (**a**) $U = 1.2$ m/s; (**b**) $U = 2.0$ m/s; (**c**) $U = 2.4$ m/s; (**d**) $U = 3.0$ m/s; (**e**) $U = 3.6$ m/s; (**f**) $U = 5$ m/s

the intrawell oscillation with very low voltage output. Apparently, the 2DOF QZS-GPEH has the best voltage output performance at low wind speeds, outperforming the other three counterparts.

Figure 6 shows the time history signals for the four configurations at different wind speeds. The voltage amplitude of the 2DOF QZS-GPEH is higher than that

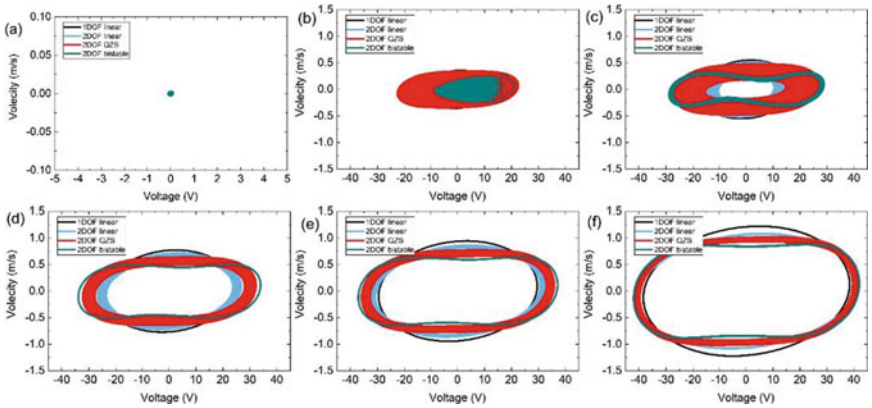

Fig. 7 Time history voltage for the four configurations: (a1)–(a3) 1DOF linear GPEH, (b1)–(b3) 2DOF linear GPEH, (c1)–(c3) 2DOF QZS-GPEH, (d1)–(d3) 2DOF bistable GPEH

of the other three counterparts, with the superiority being more remarkable at low wind speeds of 1.7 and 2.4 m/s. In addition, it is noted that the 2DOF bistable GPEH is trapped in the intrawell oscillation at 1.7 m/s and experiences interwell chaotic motion at 2.4 m/s, both of which are unfavorable for the purpose of wind power extraction.

Figure 7 plots the phase portraits of the four configurations under different wind speeds. At the low wind speed from 1.2 to 2.5 m/s, the cover area of the phase trajectory for the 2DOF QZS-GPEH is the largest among the four prototypes, indicating higher voltage generation capability than the other three counterparts. In particular, the phase trajectories of the 2DOF bistable GPEH is only a small dot below 2.0 m/s, which suggests that the input wind energy is not strong enough to overcome the potential barrier to initiate galloping oscillation and that the harvester is trapped to small-amplitude intrawell motion, either periodic or chaotic. On the contrary, the QZS mechanism is capable of providing robust performance over the whole considered wind speed range.

4 Conclusions

Inspired by the characteristic of the QZS nonlinearity with low dynamic natural frequency, we propose a 2DOF QZS-GPEH for wind power extraction at ultra-low wind speeds based on the galloping aeroelastic instability. The aero-electro-mechanically coupled model for the 2DOF QZS-GPEH consists of a Euler-Bernoulli distributed parameter model for the primary cantilever and a lumped parameter model for the secondary beam. The aerodynamic galloping force is modeled based on the quasi-steady hypothesis. The 2DOF QZS-GPEH has the best voltage output performance at low wind speeds, outperforming its 1DOF linear,

2DOF linear and 2DOF bistable counterparts. The proposed 2DOF QZS-GPEH is demonstrated to be a viable method for effectively harvesting wind energy at ultra-low wind speeds.

References

1. Wang, J., Zhou, S., Zhang, Z., Yurchenko, D.: High-performance piezoelectric wind energy harvester with Y-shaped attachments. Energy Convers. Manage. **181**, 645–652 (2019)
2. Dai, H., Abdelkefi, A., Javed, U., Wang, L.: Modeling and performance of electromagnetic energy harvesting from galloping oscillations. Smart Mater. Struct. **24**, 045012 (2015)
3. Nowakowska, H., Lackowski, M., Ochrymiuk, T., Szwaba, R.: Novel electrostatic wind energy converter: an overview. Task Q. **19**, 207–218 (2015)
4. Wang, M., Zhang, J., Tang, Y., Li, J., Zhang, B., Liang, E., et al.: Air-flow-driven triboelectric nanogenerators for self-powered real-time respiratory monitoring. ACS Nano. **12**, 6156–6162 (2018)
5. Li, H., Tian, C., Deng, Z.D.: Energy harvesting from low frequency applications using piezoelectric materials. Appl. Phys. Rev. **1** (2014)
6. Zhao, L., Tang, L., Yang, Y.: Comparison of modeling methods and parametric study for a piezoelectric wind energy harvester. Smart Mater. Struct. **22**, 125003 (2013)
7. Zhao, L., Yang, Y.: Analytical solutions for galloping-based piezoelectric energy harvesters with various interfacing circuits. Smart Mater. Struct. **24**(7), 075023 (2015)
8. Bibo, A., Alhadidi, A.H., Daqaq, M.F.: Exploiting a nonlinear restoring force to improve the performance of flow energy harvesters. J. Appl. Phys. **117**(4) (2015)
9. Zhao, L., Yang, Y.: An impact-based broadband aeroelastic energy harvester for concurrent wind and base vibration energy harvesting. Appl. Energy. **212**, 233–243 (2018)
10. Zhao, L., Tang, L., Yang, Y.: Enhanced piezoelectric galloping energy harvesting using 2 degree-of-freedom cut-out cantilever with magnetic interaction. Jpn. J. Appl. Phys. **53**(6) (2014)
11. Gatti, G.: Statics and dynamics of a nonlinear oscillator with quasi-zero stiffness behaviour for large deflections. Commun. Nonlinear Sci. Numer. Simul. **83** (2020)
12. Hu, G., Wang, J., Tang, L.: A comb-like beam based piezoelectric system for galloping energy harvesting. Mech. Syst. Signal Process. **150**, 107301 (2021)
13. Yang, Y., Zhao, L., Tang, L.: Comparative study of tip cross-sections for efficient galloping energy harvesting. Appl. Phys. Lett. **102**(6), 064105 (2013)
14. Yung, K.W., Landecker, P.B., Villani, D.D.: An analytic solution for the force between two magnetic dipoles. Magn. Electr. Sep. **9**, 39–52 (1970)

Part IV
Constitutive and Phenomenological Models

Stochastic Delay Modeling of Landslide Dynamics

Srđan Kostić and Nebojša Vasović

1 Introduction

Landslides represent slope instability processes that interact with everyday activities and are being constantly reported worldwide on a daily basis. Slope instability processes that could be activated due to engineering activities are usually mitigated by the adequate design of engineering works. However, if a landslide is active in real natural conditions (the so-called "creeping slides'"), then often no remediation measures could be applied to stabilize the slope. Such landslides are commonly reported; examples of these processes are found also in Serbia (landslide Umka, Duboko, Begaljičko brdo, Ražanj, Mramor et al.). Due to their long-term activity and complex affecting factors, these landslides require special attention, both from a purely theoretical aspect (when it comes to analysis and definition of basic mechanisms behind the process itself) and a practical viewpoint (design of cost-effective and time-efficient remediation measures). In engineering practice, the common way of theoretical modeling of landslide activity is conducted by invoking limit equilibrium methods or finite element methods [1]. Some recent approaches also include smooth-particle hydrodynamics mode, which especially enables the analysis of post-failure processes [2]. Although all of these approaches provide satisfying results, which either serve for further design or are comparable with the real observed displacements and velocities, none of them takes into account the occurrence of delay failure and the possible crucial effect of background noise, even though delay failure is considered as a feature of slope in overconsolidated

S. Kostić (✉)
Jaroslav Černi Water Institute, Belgrade, Serbia
e-mail: srdjan.kostic@jcerni.rs

N. Vasović
University of Belgrade Faculty of Mining and Geology, Belgrade, Serbia

© The Author(s), under exclusive license to Springer Nature Switzerland AG 2024

W. Lacarbonara (ed.), *Advances in Nonlinear Dynamics, Volume III*, NODYCON Conference Proceedings Series, https://doi.org/10.1007/978-3-031-50635-2_24

clays, where delays of the order of 50 years or more have been found in many slope failures. In this chapter, delayed failure is considered as a time-discontinuous failure of different parts of the slope, as suggested by Davis [3], who indicated the existence of a time period between the movement of feeder and accumulation parts of the slope. Regarding the presence of noise, there are three main types of natural background noise [4]: (1) long-period noise (<0.1 Hz), including earth tides, atmospheric pressure variations, winds and currents, tilt noise, single-frequency microseism peak, surface waves and long-period body waves, (2) short-period noise (>0.5 Hz), including short-period band microseisms, short-period noise on land, short-period noise on the sea floor and short-period body waves and (3) microseism peak (0.1–0.5 Hz). Up until our pioneer work [5], the dynamics of the spring-block model has been examined without the stochastic effect, which is in fact observed in nature and commonly originates from heterogeneous conditions along the seismogenic fault [6, 7].

In this chapter, we analyze the influence of these factors (background noise and delayed failure) on the dynamics of the mechanical model of a landslide, which we consider to exhibit qualitatively similar dynamics to the real observed recordings. Mechanical modeling of landslide dynamics has been the focus of research since the initially proposed model by Davis [3], who suggested the spring-block model composed of two blocks as a qualitative representative of surging and creeping. According to Petley and Allison [8], the main difficulty in the suggested model lies in the inability to characterize the interactions among the blocks properly. Singh and Singh [9] also examined the general form of the spring-slider-friction model, with special attention to the temperature and velocity effects, including the dependence of steady friction on the shear velocity and temperature of the sliding surface. The model they analyzed enables a prediction of the critical stiffness at which the sliding behavior changes, depending on the temperature of the sliding surface. The application of the model and the applied analyses in the case of a creeping rock slope or an earthquake fault are also shown.

One should note that mechanical spring-block models are convenient for the analysis of complex natural processes, such as landslide dynamics, since they enable the qualitative inquiry of the process, with an emphasis on the main controlling factors and conditions for transitions between different dynamical regimes, without the direct quantitative identity with the real observed recordings.

It should be emphasized that our analysis considers the cases of permanent creeping landslides, which exhibit displacements over the whole year with intermittent short-term occurrences of quick and large displacements. Creeping landslides have been the focus of contemporary research, primarily because of their scale, inability to stabilize completely and their impact on infrastructure and the urban environment [10–12].

The main novelties of this chapter are as follows:

– This is the first time the effect of noise on landslide dynamics is analyzed in the presence of delayed failure.

– For the first time, it is shown that the coupled effect of noise and delayed failure could lead to the occurrence of instability.
– It is confirmed that noise could have a crucial effect on the landslide activation when the slope (or creeping landslide) is on the verge of stability.

This chapter is organized as follows. In Sect. 2, we describe the applied methodology, while the results of the research are presented in Sect. 3. Section 4 is devoted to the main conclusions.

2 Applied Methodology

In the first phase of the research, surrogate data testing is invoked to examine the recorded background seismic noise [13]. We start with a null hypothesis that the data are independent random numbers drawn from some fixed but unknown distribution. For this purpose, we generate surrogates by randomly shuffling the data (without repetition), thus yielding surrogates with exactly the same distribution, but independent construction, and calculate zeroth-order prediction error γ for the original recording and for every generated surrogate. In the second step, we test the second null hypothesis that the recordings originate from a stationary linear stochastic process with Gaussian inputs. For this purpose, we randomize the phases of the Fourier transform of the original recording and then perform the inverse Fourier transform to obtain the desired temporal traces. The concept of zeroth-order prediction order is explained previously in [14].

In the second stage of the research, we start from the model initially proposed by Davis [7], who assumed that the dynamics of the accumulation slope could be qualitatively described by the interaction of the feeder and accumulation parts of the slope (Fig. 1).

Noise is proposed to be introduced as additive white noise as a part of the system of delay differential equations governing the dynamics of the spring-block model composed of n units with delayed failure, which is assumed to qualitatively mimic the landslide motion:

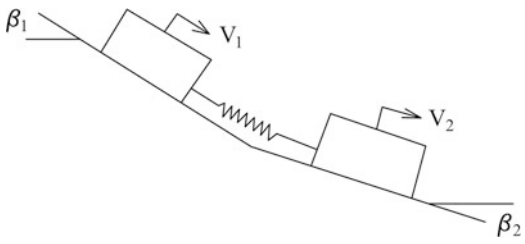

Fig. 1 Landslide mechanical model. β_1 and β_2 denote different slope inclinations, while V1 and V_2 denote different velocities of the blocks, as illustrated

$$\begin{aligned} dx_i(t) &= y_i(t)dt \\ dy_i(t) &= -\left[a(V+y_i(t))^3 - b(V+y_i(t))^2 + c\,(V+y_i(t))\right]dt \\ &+ \left(aV^3 - bV^2 + cV\right)dt + \sum_{i=1}^{N} k\,(x_{i-1}\,(t-\tau) - x_i(t))\,dt + \sqrt{2D}dW_i \end{aligned} \tag{1}$$

where x_i and y_i are the displacement and velocity of the i-th block, $V = 0.2$ is the constant background velocity of the system, τ is the introduced time delay and k is the spring stiffness. The terms $\sqrt{2D}\,dW_i$ represent stochastic increments of an independent Wiener process, i.e., dWi satisfies $E(dW_i) = 0$, E $(dW_i dW_j) = \delta_{ij}dt$, where $E(.)$ denotes the expectation over many realizations of the stochastic process, and D is the intensity of additive local noise. The friction law assumed in (1) represents the cubic friction force, with frictional parameters a, b and c as proposed in [15]. As it was shown in previous research [16], noise could represent the main trigger for instability to occur for certain initial conditions or dynamical regimes of the system under study. We examine the dynamics of the proposed model (1) for the following parameter values: $a = 3.2$, $b = 7.2$ and $c = 4.8$, $V = 0.1$, and for the following initial conditions: $x_{10} = 0.001$, $x_{20} = 0.0001$, $y_{10} = 0.05$, $y_{20} = 0.05$. The chosen initial values are close to the fixed point of the examined system.

The stochastic dynamical system (1) is analyzed by applying the mean-field approximation (MFA) method. In particular, a cumulant approach, together with a Gaussian approximation, allows us to analyze the behavior of an ensemble of coupled units driven by additive noise [17]. The use of a full set of cumulants or moments instead of a hierarchy of probability densities, is an alternative way to describe a stochastic process. Techniques based on cumulants are in many cases more convenient because they allow the use of several approximations. For instance, in a Gaussian stochastic process, only the first- and second-order cumulants are non-zero, while all moments may have finite values. When the original stochastic differential equations are nonlinear, the set of ordinary differential equations for cumulants appears to be unclosed: an equation for the n-th order cumulant may contain higher-order cumulants. In that case, several approximations can be used to truncate the series of cumulant equations. The cumulant approach within the Gaussian approximation is applied in the present research, since it has been successfully used to study the influence of noise on bifurcations in maps, colored noise-induced transitions in bistable systems [18], phase transitions and stochastic resonance in the globally coupled bistable elements' dynamics of noisy Fitzhugh-Hagumo neurons [19].

3 Results

Results of the surrogate data testing indicate that the zeroth-order prediction error for the examined time series does not follow the zeroth-order prediction error for 20

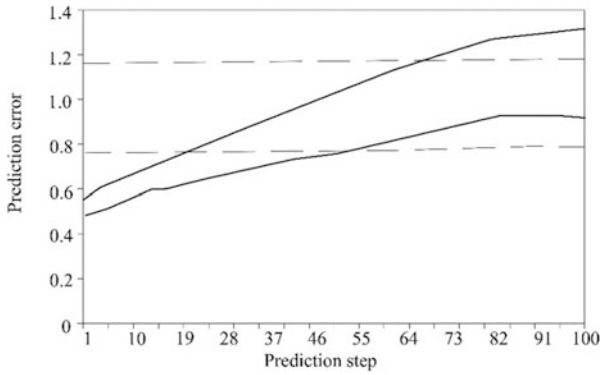

Fig. 2 Results of surrogate data testing—I hypothesis: black lines denote the limit envelopes of the evolution of zeroth-prediction error for the original data series, while dashed lines denote the zone of the zeroth-order prediction error evolution for the surrogate data series

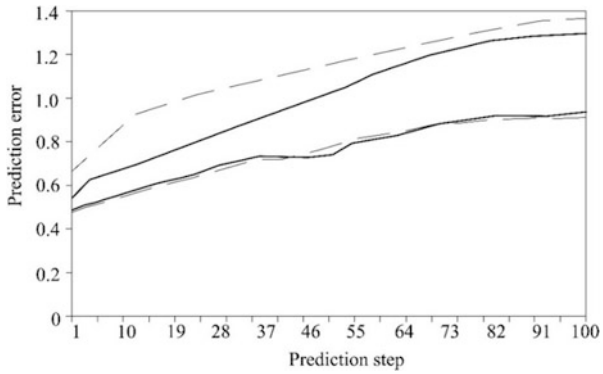

Fig. 3 Results of surrogate data testing—II hypothesis: black line denotes the limit envelopes of the evolution of zeroth-order prediction error for the original data series, while dashed lines denote the zone of the zeroth-order prediction error evolution for the surrogate data series

surrogate time series (for the first null hypothesis), which were obtained by random shuffling of the starting data, as shown in Fig. 2.

However, results of testing the second null hypothesis indicate that the zeroth-order prediction error for the original time series, γ_0, has the same trend as the prediction error evolution γ for surrogate time series, with $\gamma_0 < \gamma$, as shown in Fig. 3. In this way, we confirmed that recordings originate from a stationary linear stochastic process with Gaussian inputs, which justifies our introduction of random noise into the deterministic dynamic model of the landslide (1).

In the first step, we applied the mean-field approximation method to enable further conduct of standard bifurcation analysis for the following mean-field deterministic system:

$$\dot{m}_x(t) = m_y(t) \tag{2a}$$

$$\dot{m}_y(t) = \left(-3aV^2 + 2bV - c\right) m_y(t) + (b - 3aV)\left(s_y(t) + m_y^2(t)\right) - a\left(m_y^3(t) + 3m_y(t)s_y(t)\right) \tag{2b}$$

$$\frac{1}{2}\dot{s}_x(t) = U(t) \tag{2c}$$

$$\frac{1}{2}\dot{s}_y(t) = s_y(t)\left[\left(2bV - 3aV^2 - c\right) + 2(b - 3aV)\, m_y(t) - 3a\left(m_y^2(t) + s_y(t)\right)\right] - kU(t) + D \tag{2d}$$

$$\dot{U}(t) = U(t)\left[\left(2bV - 3aV^2 - c\right) + 2(b - 3aV)\, m_y(t) - 3a\left(s_y(t) + m_y^2(t)\right)\right] + s_y(t) - ks_x(t) \tag{2e}$$

where the first- and second-order cumulants are denoted in the following way: (a) the means $m_x(t) = \langle x(t)\rangle$, $mx(t-\tau) = \langle x(t-\tau)\rangle$, $m_y(t) = \langle y(t)\rangle$, (b) the mean square deviations $s_x(t) = \langle n_x^2(t)\rangle$, $s_y(t) = \langle n_y^2(t)\rangle$ and (c) the cross-cumulant $U(t) = \langle n_x n_y\rangle$. Noise intensity is denoted with D, V stands for the block velocity, while a, b and c denote cubic friction parameters. It can be easily shown that the mean-field approximated model exhibits the same qualitative dynamics as the starting stochastic model (1). Results of the bifurcation analysis of the mean-field model (2) indicate the following. Apparently, there is an Andronov-Hopf direct supercritical bifurcation occurring with an increase in time delay and spring stiffness, as shown in Fig. 4. This bifurcation indicates a transition from an equilibrium state, e.g., in this case, stable stationary motion with constant velocity (the creep stage), to regular periodic motion, which is considered to mimic the unstable phase of landslide displacement. The creep stage is the term used to denote the dynamical regime of the system (2) with constant mean-field velocity, while the occurrence of periodic oscillations is considered the onset of an unstable dynamical regime.

Figure 5 displays the stationary equilibrium state of the mean-field model (1), while periodic regular oscillations are shown in Fig. 6. The creep stage of landslide dynamics with stable constant mean-field velocity is clearly shown in Fig. 5 (on the right). One should note that the unstable regular periodic oscillations, shown in Fig. 6, only represent the qualitative image of the unstable phase of landslide dynamics. In real natural conditions, it is hardly expected to observe such frequent regular periodic oscillations. This is why we further increase the values of time delay and spring stiffness, which resulted in the occurrence of more realistic irregular dynamics, as shown in Figs. 7 and 8.

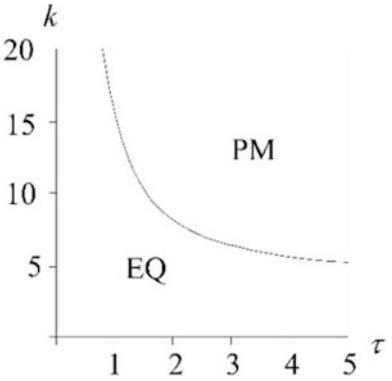

Fig. 4 Bifurcation diagram k-τ for the following fixed parameters: $a = 3.2$; $b = 7.2$, $c = 4.8$, $V = 0.1$, and the initial conditions: $x_{10} = 0.001$, $x_{20} = 0.0001$, $y_{10} = 0.05$, $y_{20} = 0.05$. EQ denotes the equilibrium regime—creep stage with constant mean-field velocity, while PM stands for regular periodic oscillations (unstable creep regime)

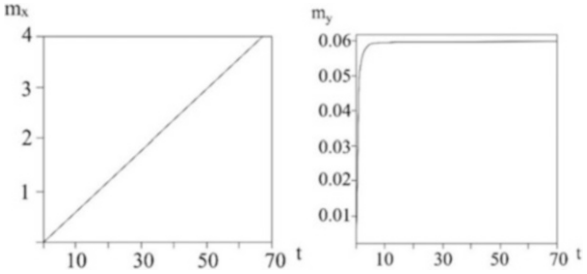

Fig. 5 Mean-field approximated displacements and velocities for $\tau = 0$, $k = 1$. Other parameters have the same values as for Fig. 4. τ is the introduced time delay, and k is the spring stiffness

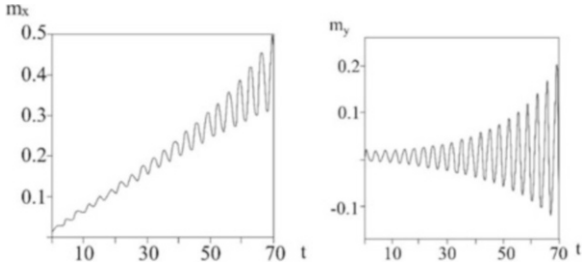

Fig. 6 Mean-field approximated displacements and velocities for $\tau = 3$, $k = 10$. Other parameters have the same values as for Fig. 4. τ is the introduced time delay, and k is the spring stiffness

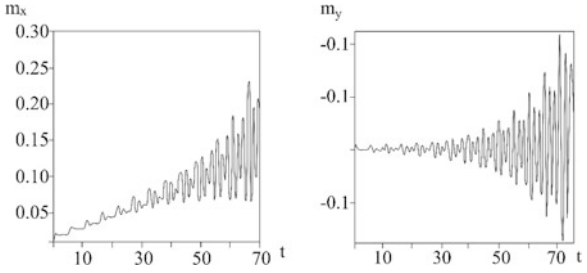

Fig. 7 Mean-field approximated displacements and velocities for $\tau = 5$, $k = 20$. Other parameters have the same values as for Fig. 4. τ is the introduced time delay, and k is the spring stiffness

In particular, with a further increase in spring stiffness and time delay, one can observe the occurrence of quasiperiodic behavior, which starts to resemble the real intermittent dynamics of landslides (Fig. 7). For very high values of delay and spring stiffness, one can indeed observe the real stick-slip behavior, as is

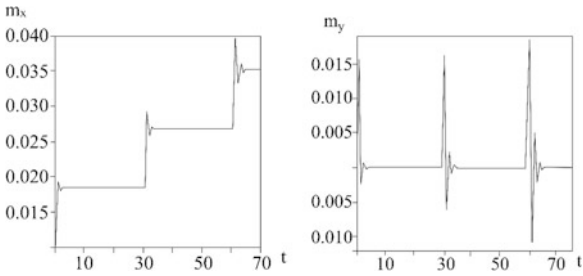

Fig. 8 Mean-field approximated displacements and velocities for $\tau = 30$, $k = 20$. Other parameters have the same values as for Fig. 4. τ is the introduced time delay, and k is the spring stiffness

commonly recorded in real practice (Fig. 8). As can be seen in Fig. 8, there are long "silent' 'periods with no displacement (dormant phase), followed by sudden bursts of movements (active phase). In real conditions, such activity of landslides could be prescribed to the predominant influence of rainfall or the river flow if the landslide is activated along the river bank. These results indicate that extremely high values of time delay could suppress the dynamics of the landslide with transition of the creep stage to the dormant stage of displacements along the slope.

It can be shown that background noise has a positive effect on the stability of landslide dynamics when the noise intensity D is changed near the bifurcation curve. In particular, noise has the same effect for slopes with rather low values of spring stiffness and high values of time delay, as well as for slopes with high values of spring stiffness and low values of time delay. In both cases, an increase in D "stabilizes" the landslide, and vice versa—a reduction of noise leads to the onset of slope instability. Such a stabilizing effect of the background noise confirms the significance of its effect, particularly near the bifurcation point, which is valid for creeping landslides.

4 Conclusions

In this chapter, we suggest a new model of landslide dynamics that includes the effect of random background noise and a delay between the motion of two neighboring parts of the slope. The presence of random noise is confirmed by the nonlinear time series analysis of the real recorded movements, whose results indicate that the observed time series belong to a group of stationary linear stochastic processes with Gaussian inputs. It should be noted that surrogate data testing ruled out the possibility that landslide displacements could be treated as completely random.

The stochastic model of landslide dynamics is represented as the system of three first-order delay differential equations, with included additive random noise. Such a system is, in the first phase of the research, represented as deterministic using the mean-field approximation. This approximated model is further examined numerically. Results obtained indicate the occurrence of a direct supercritical Hopf

bifurcation, which indicates a transition between the stable stationary motion (creep stage) and regular periodic oscillations (unstable stage). These results confirm the predominant impact of time delay on landslide dynamics, with delay as a possible trigger of excitable behavior. It should be noted that the occurrence of stick-slip behavior for high values of time delay could indicate the existence of another local bifurcation curve, or the occurrence of a global bifurcation (since $\tau = 30$ is outside the examined range of numerical analysis), which should be verified in further research. Additionally, further research could examine the sensitivity of the proposed landslide model to the change of initial conditions, which could also indicate the possible existence of a global bifurcation.

Considering the nature of the influence of time delay on the examined model, where only high values of delay have a significant impact, one could expect that background random noise in this case has an insignificant impact, or its impact could be crucial only for cases when the observed system is near the bifurcation point (taking into account low intensities of the background noise). Further research should examine the impact of random noise in such critical cases.

Acknowledgments This work is done in memory of the late Prof. Nikola Burić, who left invaluable results in the area of stochastic nonlinear dynamics.

References

1. Mebrahtu, T.K., Heinze, T., Wohnlich, S., Alber, M.: Slope stability analysis of deep-seated landslides using limit equilibrium and finite element methods in Debre Sina area, Ethiopia. Bull. Eng. Geol. Environ. **81**(10), 403 (2022)
2. Huang, C., Sun, Y., An, Y., Shi, C., Feng, C., Liu, Q., Yang, X., Wang, Z.: Three-dimensional simulations of large-scale long run-out landslides with a GPU-accelerated elasto-plastic SPH model. Eng. Anal. Bound. Elem. **145**, 132–148 (2022)
3. Davis, R.O.: Modelling stability and surging in accumulation slides. Eng. Geol. **33**, 1–9 (1992)
4. Webb, S.C.: Seismic noise on land and on the sea floor. In: Lee, W.H.K., Jennings, P., Kisslinger, C., Kanamori, H. (eds.) International Handbook of Earthquake and Engineering Seismology, pp. 305–318. Elsevier (2002)
5. Vasović, N., Kostić, S., Franović, I., Todorović, K.: Earthquake nucleation in a stochastic fault model of globally coupled units with interaction delays. Commun. Nonlinear Sci. Numer. Simul. **38**, 117–129 (2016)
6. Telford, W.M., Geldart, L.P., Sheriff, R.E.: Applied Geophysics, 2nd edn. Cambridge University Press, Cambridge (1990)
7. Ryabov, V.B., Correig, A.M., Urquizu, M., Zaikin, A.A.: Microseism oscillations: from deterministic to noise-driven models. Chaos, Solitons Fractals. **16**, 195–210 (2003)
8. Petley, D.N., Allison, R.J.: The mechanics of deep-seated landslides. Earth Surf. Process. Landf. **22**, 747–758 (1997)
9. Singh, A.K., Singh, T.N.: Stability of the rate, state and temperature dependent friction model and its applications. Geophys. J. Int. **205**, 636–647 (2016)
10. Marte, R., Hofmann, R.: Creeping large-scale landslides – characterisation and assessment of safety. Geomechanik und Tunnelbau. **13**(1), 32–51 (2020)
11. Palmer, J.: Creeping catastrophes: studies of slow landslides could unmask the mechanics of a worldwide scourge. Nature. **548**(7668), 384–386 (2017)

12. Oberender, P.W., Puzrin, A.M.: Observation-guided constitutive modelling for creeping landslides. Geotechnique. **66**(3), 232–247 (2016)
13. Perc, M., Green, A.K., Jane Dixon, C., Marhl, M.: Establishing the stochastic nature of intracellular calcium oscillations from experimental data. Biophys. Chem. **132**, 33–38 (2008)
14. Kantz, H., Schreiber, T.: Nonlinear Time Series Analysis. Cambridge University Press, Cambridge (1997)
15. Morales, J.E.M., James, G., Tonnelier, A.: Travelling waves in a spring-block chain sliding down a slope. Phys. Rev. E. **96**, 012227 (2017)
16. Bashkirtseva, I., Ryashko, L., Schurz, H.: Analysis of noise-induced transitions for Hopf system with additive and multiplicative random disturbances. Chaos, Solitons Fractals. **39**, 72–82 (2009)
17. Lindner, B., Garcia-Ojalvo, J., Neimand, A., Schimansky-Geiere, L.: Effects of noise in excitable systems. Phys. Rep. **392**, 321–424 (2004)
18. Anishchenko, V.S., Neiman, A.B.: Bifurcational analysis of bistable system excited by colored noise. Int. J. Bifurcation Chaos. **2**(4), 979–982 (1992)
19. Tanabe, S., Pakdaman, K.: Dynamics of moments of FitzHugh-Nagumo neuronal models and stochastic bifurcations. Phys. Rev. E. **63**, 031911 (2001)

A New Methodology for Nonlinear Analysis of Magneto-Rheological Elastomers Behavior Under Large Amplitude Oscillatory Axial (LAOA) Loadings

Hossein Vatandoost, Ramin Sedaghati, and Subhash Rakheja

1 Introduction

Composed of magnetically responsive particles embedded within a nonmagnetic soft polymeric medium, magneto-rheological (MR) elastomers (MREs) are multifunctional field-responsive smart materials, whose mechanical properties (e.g., stiffness and damping) can be adjusted on-demand via the application of an external magnetic field [1]. Characterization of MREs with highly complex behavior is fundamentally important for the development of material constitutive models and the design of smart MRE-based devices (e.g., vibration absorbers [2]).

The shear mode characterization of MREs has been extensively studied in the literature [3]. This is partly due to the ease of characterization as the mechanical and magnetic loadings are perpendicular to each other. On the contrary, tension/compression (T/C) dynamic characterization demands MRE samples to be subjected to unidirectional magnetic and mechanical loadings [4, 5]. This involves many challenges, such as the compensation of the magnetic force generated between two magnetic poles [6]. While several studies have confirmed a higher MR effect of MREs under C/T mode as compared to shear mode (e.g., [7]), much work is still needed to fully characterize, identify, and interpret their magneto-mechanical behavior particularly under large deformation for successful design development of MREs in T/C mode. Unlike the shear mode where the stress-strain characteristics are symmetric with respect to the origin even at large deformation [3], in T/C mode such properties are asymmetric. This implies that the material moduli possess different values in compression and extension cycles, where typically in

H. Vatandoost · R. Sedaghati (✉) · S. Rakheja
Concordia University, Montreal, QC, Canada
e-mail: h_vatand@encs.concordia.ca; ramin.sedaghati@concordia.ca

© The Author(s), under exclusive license to Springer Nature Switzerland AG 2024

W. Lacarbonara (ed.), *Advances in Nonlinear Dynamics, Volume III*, NODYCON Conference Proceedings Series, https://doi.org/10.1007/978-3-031-50635-2_25

the compression path, higher stress is generated as compared with the extension cycle [5].

The identification and interpretation of properties of viscoelastic materials, like MREs, under large amplitude oscillatory shear (LAOS) loadings, have been well established in the literature both in the time-domain and stress & strain-rate domain [8]. Due to the odd symmetry in the response of the viscoelastic in shear mode, the Fourier Transform (FT) of the stress possesses odd harmonics. This yielded a powerful approach, namely, stress-decomposition (SD), for quantifying the nonlinear response of materials under LAOS loadings. Cho et al. [9] introduced a novel methodology for decomposing the stress into elastic and viscous stresses. They approximated the stress response by using polynomial series to find the material moduli in the elastic and viscous stress components. However, the coefficients of the polynomials are not unique as they depend on the highest order of the considered polynomial series. Ewoldt et al. [10] employed Chebyshev orthogonal functions to predict the elastic and viscous stress components of nonlinear stress response. The coefficients of the elastic and viscous components are found to be unique due to the orthogonality characteristics of the Chebyshev functions. This method has been applied to MR materials in which Wang et al. [11] identified the nonlinear behavior of an MR grease using the SD method based on Chebyshev polynomials.

The orthogonal-based methods have been employed to a far lesser extent for the nonlinear identification of viscoelastic materials under large amplitude oscillatory tension/compression (LAOT/C) loadings or axial loadings [12], where the even harmonics unavoidably appear [8, 13]. The even harmonics are referred to as viscoelastic components and have not been uniquely identified yet [14]. Particularly, no study has been conducted on the nonlinear identification of MREs under large amplitude oscillatory axial (LAOA) loadings. Hence, in this study, the main objective is to provide a new methodology for identifying the nonlinear behavior of smart viscoelastic materials under LAOA loadings. In light of this, an experimental test bench was designed to perform experimental characterization of the MREs under LAOA loadings and wide ranges of magnetic field intensities. The stress-strain responses were analyzed to extract the elastic and viscous stress using the proposed decomposition method. Subsequently, the elastic and loss moduli of MREs at zero strain along with at the loading extremities were calculated.

2 Material and Method

2.1 Sample

A series of spatially isotropic and anisotropic MRE batches with three different particle volume fractions (15%, 30%, 45%) were fabricated in the laboratory, and subsequently, cylindrical MRE specimens with a diameter and height of 18 mm

and 8 mm, respectively, were cut and prepared for characterization purposes. The detailed explanation has been provided in previous studies [4, 15].

2.2 Dynamic Axial Test Bench

The experimental method is comprehensively explained in earlier works [4, 16]. Briefly, the test rig consists of an electromagnet unit, including a UI-shaped core and three coils, integrated into a material testing system. The lower part of the electromagnet unit is fixed to an electrodynamic actuator. The upper section of the electromagnet unit is connected to a load cell. The MRE samples were glued over the magnetic core and squeezed statically up to 21% to realize a practical pre-strain level [17]. Afterward, a series of displacement control oscillatory loadings were applied to the MRE specimens. The frequency of excitation was increased from 1 Hz to 50 Hz, while the strain amplitude varied from 2.5% up to 20%. The magnetic flux density was increased from zero to 750mT. Subsequently, the force and displacement for four consecutive cycles were collected. The force-displacement data were then averaged for each loading condition, and then the corresponding strain-stress response of MREs was calculated for the determination of axial compressive and tensile moduli, which are presented in the following section.

3 Methodology

3.1 Stress-Strain Hysteresis Response

The stress-strain characteristic of an isotropic MRE specimen is presented in Fig. 1. The result is presented for the loading frequency of 1 Hz and a magnetic flux density of 750mT. The result clearly demonstrates that the response of MREs under LAOA loadings is nonlinear and asymmetric. It can be observed that the elastic properties during the compression path are higher than that of the tension path. Moreover, the top-right of the figure shows a strong strain-stiffening effect. Such intra-cycle nonlinearity cannot be detected using the first harmonic modulus, which has been recommended by ASTM D5992-96 [18]. Besides, in contrast to LOAS loading, one material modulus cannot represent the elastic behavior for both the compression and extension cycles.

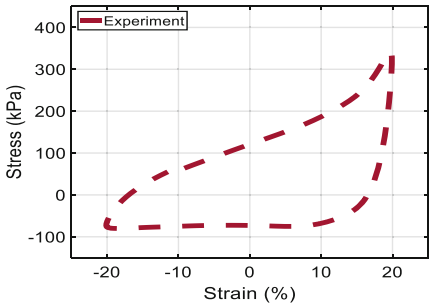

Fig. 1 The nonlinear asymmetric stress-strain characteristics of MREs under LAOA loadings

3.2 Quantification of Nonlinear Response

A methodology is presented to quantitatively analyze the MRE stress response under LAOA loadings. The input stress can be assumed as:

$$\varepsilon(t) = \varepsilon_0 \sin(\omega t) \tag{1}$$

where ω and ε_0 are the loading angular frequency and strain amplitude. Assuming periodic response, the stress response can be represented by a Fourier series as:

$$\sigma(t) = \sigma_m + \varepsilon_0 \left[\sum_{n=1}^{n=m} E'_n \sin(n\omega t) + E''_n \cos(n\omega t) \right] \tag{2}$$

where E'_n and E''_n are axial elastic and loss moduli at the nth harmonic. n does include both the even and odd harmonics due to the asymmetry in response. The nonzero mean stress (σ_m) has been removed from the stress response as it doesn't affect the dynamic moduli (instantaneous slope) of MRE under LAOA loadings. Using the Fourier approximation, the elastic, viscous, and viscoelastic stress components can be obtained as:

$$\sigma'_{Fe}(t) = \varepsilon_0 \left[\sum_{n=1}^{m} E'_{n_{\text{odd}}} \sin(n_{\text{odd}}\omega t) \right] \tag{3}$$

$$\sigma''_{Fv}(t) = \varepsilon_0 \left[\sum_{n}^{m} E''_{n_{\text{odd}}} \cos(n_{\text{odd}}\omega t) \right] \tag{4}$$

$$\sigma'''_{Fve}(t) = \varepsilon_0 \left[\sum_{n=1}^{m} E'_{n_{\text{even}}} \sin(\omega t) + E''_{n_{\text{even}}} \cos(\omega t) \right] \tag{5}$$

where $\sigma'_{Fe}(t)$, σ''_{Fv}, and $\sigma'''_{Fve}(t)$ are respectively elastic, viscous, and viscoelastic Fourier stress components. The coefficients of the Fourier approximation, which are related to material moduli, are highly sensitive to the number of harmonics considered. Using orthogonal functions, such as Chebyshev polynomials, alternatively, the stress response can be predicted with unique coefficients. Such an approximation permitted unique interpretation and nonlinear quantification of materials under LAOS loadings [10]. Similar quantification is yet to be established for LAOA. Using the Chebyshev polynomial of the first kind, the stress response can be approximated as:

$$\sigma_{T_e}(x) = \varepsilon_0 \left[\sum\nolimits_{n_{\text{odd}}} e_{n_{\text{odd}}} T_{n_{\text{odd}}}(x) \right] \tag{6}$$

$$\sigma_{T_v}(y) = \varepsilon_0 \omega \left[\sum\nolimits_{n_{\text{odd}}} v_{n_{\text{odd}}} T_{n_{\text{odd}}}(y) \right] \tag{7}$$

$$\sigma_{T_{ve}}(x, y) = \varepsilon_0 \left[\sum\nolimits_{n_{\text{even}}} e_{n_{\text{even}}} T_{n_{\text{even}}}(x) \right] + \varepsilon_0 \omega \left[\sum\nolimits_{n_{\text{even}}} v_{n_{\text{even}}} T_{n_{\text{even}}}(y) \right] \tag{8}$$

where σ_{T_e}, σ_{T_v}, and $\sigma_{T_{ve}}(t)$ are, respectively, the elastic, viscous, and viscoelastic stress components approximated by the Chebyshev polynomial. x and y are given as:

$$x = \frac{\varepsilon(t)}{\varepsilon_0} = \sin(\omega t)\,;\; y = \frac{\dot{\varepsilon}(t)}{\varepsilon_0 \omega} = \frac{\dot{\varepsilon}(t)}{\dot{\varepsilon}_0} \cos(\omega t) \tag{9}$$

Using the Fourier series and Chebyshev polynomial of the first kind, considering the first four harmonics ($n = 4$), the stress response of the MRE sample under LAOA loadings ($\varepsilon_0 = 21\%$, $\omega = 2\pi$, $B = 750$mT) can be decomposed into the elastic, viscous, and viscoelastic stress components as presented in Fig. 2. Results show the typical Lissajous-Bowditch curves of the stress response of the MRE sample under LAOA loading. Figure 2a, b shows that the viscoelastic stress component is an even function as expected. Likewise, the elastic stress approximated by Fourier series is not able to predict the asymmetry in the loading and unloading paths. In other words, the Fourier elastic stress relatively predicts the same slope/axial moduli ($E'^{-}_F \cong E'^{+}_F$) at the extreme strain amplitude (e.g., min. and max. strains). Similarly, the elastic stress approximated by the Chebyshev polynomial, presented in Eq. 6, is not able to estimate nonlinear asymmetry ($E'^{-}_T \cong E'^{+}_T$). However, in contrast to Fourier viscoelastic stress component, the Chebyshev viscoelastic stress component almost shows zero energy dissipation properties, thereby denoting that the viscoelastic component is more elastic-dominated rather than viscous-dominated. Hence, to properly estimate the asymmetry in the stress response, we propose to superimpose the elastic-dominated Chebyshev viscoelastic stress response to the Chebyshev elastic stress response, as schematically and mathematically presented in Fig. 3 and Eq. 9, respectively:

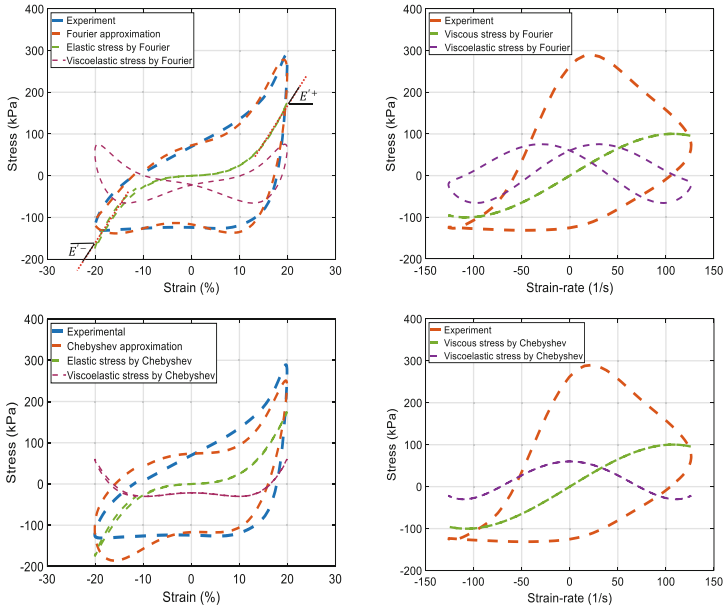

Fig. 2 The nonlinear asymmetric stress-strain characteristics of MREs under LAOA loadings

$$\sigma_{T_{e+ve}} = \varepsilon_0 \left[\sum\nolimits_n e_n T_n(x)\right] + \varepsilon_0 \omega \left[\sum\nolimits_{n_{\text{even}}} v_{n_{\text{even}}} T_{n_{\text{even}}}(y)\right] \tag{10}$$

To capture the nonlinear elastic response at large strain amplitudes, an instantaneous large strain elastic modulus is defined as:

$$E_L^{\pm} = \left.\frac{d\sigma_{T_{e+ve}}}{d\varepsilon}\right|_{\varepsilon=\pm\varepsilon_0} \tag{11}$$

The instantaneous elastic moduli $E_L^{\pm}$ at extreme loading (E_L^{+}) and unloading (E_L^{-}) were then calculated by taking the derivative of $\sigma_{T_{e+ve}}$ and summarized in Table 1. The instantaneous elastic moduli at loading extremities (Eq. 11) are different for compression and extension cycles.

The coefficients of the Fourier series and Chebyshev polynomial for the approximation of stress response of the MREs are summarized in Table 2.

Setting the highest harmonic as four, the stress response is also reconstructed via MITALOAS software, and the coefficients and results are presented in Table 2 and Fig. 4, respectively [19]. Table 2 reveals relatively the same values for the odd harmonics coefficients in this study and the results of MITLAOS software, as expected. Figure 5 presents results for the stress-strain curve based on the proposed superimposed elastic and viscoelastic via Chebyshev polynomials. As

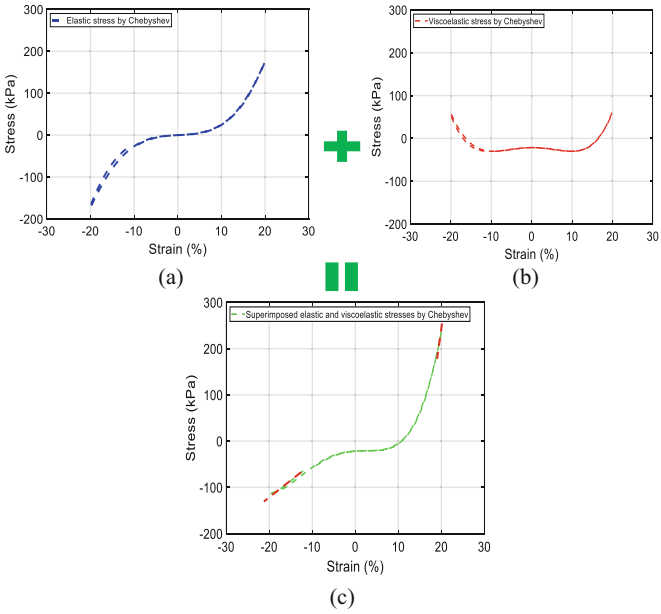

Fig. 3 The nonlinear asymmetric approximation of the MRE response under LAOA loading: (**a**) elastic, (**b**) viscoelastic, and (**c**) superimposed elastic and viscoelastic stress components

Table 1 Instantaneous elastic moduli at extreme loading and unloading

Extreme elastic moduli $E_L^{\pm}$(MPa)		
E_L^-	E_L^+	E_L^+/E_L^-
0.25	5.2	20.8

it can be realized, elastic moduli at extreme loading and unloading conditions agree well with those of the total stress. The results also compare the total stress with a linear stress approximation via Fourier series. This is called the first harmonic approximation recommended by ASTM D5992-96 [18], as an alternative approach for quantifying nonlinear stress response. It is clear that the first harmonic approximation lacks nonlinear stiffening and softening at the end of loading and unloading cycles. Further development of the current investigation would allow realizing the instantaneous/tangent elastic modulus at extreme loadings as functions of the linear elastic modulus.

4 Conclusion

Results showed that the stress response of MREs under LAOA loadings is nonlinear and asymmetric. The first harmonic approximation of the stress response cannot predict the intra-cycle nonlinearities (i.e., strain stiffening). Using Fourier series

Table 2 The coefficients of the Fourier series and Chebyshev polynomials for the approximation of stress response of the MREs

Fourier Series (kPa)							
E_1'	E_1''	E_2'	E_2''	E_3'	E_3''	E_4'	E_4''
669.7	578.4	222	−204.3	−205.6	−102	−47	96
Chebyshev polynomial (kPa)							
e_1	v_1	e_2	v_2	e_3	v_3	e_4	v_4
669.7	92.1	8.92	−31.1	205.6	−16.2	2.3	15.03
MITLAOS software (kPa)							
E_1'	E_1''	E_M	E_L	e_3	v_3	E_L/E_M	
666.2	575.3	53	870.7	204.5	−16.1	16.5	

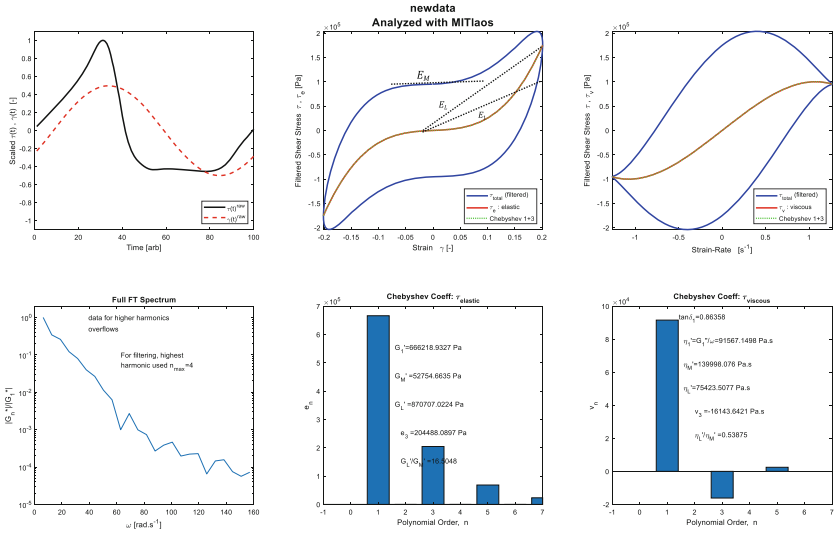

Fig. 4 Reconstruction of the total stress response using MITLAOS software considering only odd harmonics [19]

and Chebyshev Polynomials, the stress response of MREs was decomposed into elastic, viscous, and viscoelastic stress components. The stress decomposition using Chebyshev polynomials permitted the identification and quantification of asymmetric response in terms of elastic moduli. However, such quantification was not achieved using the Fourier series. In future studies, the proposed methodology will be applied to decompose the rheological constitutive models, thereby considering the nonlinear asymmetry in material modeling.

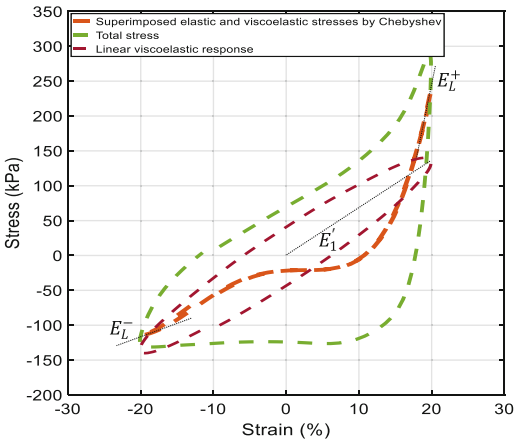

Fig. 5 Comparison between linear viscoelastic response by Fourier series (first harmonic moduli) and Chebyshev polynomial

References

1. Vatandoost, H., Sedaghati, R., Rakheja, S.: A novel methodology for accurate estimation of magnetic permeability of magnetorheological elastomers. J. Magn. Magn. Mater. **560**, 169669 (2022)
2. Choi, Y., Wereley, N.M.: Vibration isolation performance of an adaptive magnetorheological elastomer-based dynamic vibration absorber. Actuators. **11**(6), 157 (2022)
3. Norouzi, M., Sajjadi Alehashem, S.M., Vatandoost, H., Ni, Y.Q., Shahmardan, M.M.: A new approach for modeling of magnetorheological elastomers. J. Intell. Mater. Syst. Struct. **27**(8), 1121–1135 (2016)
4. Vatandoost, H., Hemmatian, M., Sedaghati, R., Rakheja, S.: Dynamic characterization of isotropic and anisotropic magnetorheological elastomers in the oscillatory squeeze mode superimposed on large static pre-strain. Compos. Part B Eng. **182**, 107648 (2020)
5. Vatandoost, H., Norouzi, M., Alehashem, S.M.S., Smoukov, S.K.: A novel phenomenological model for dynamic behavior of magnetorheological elastomers in tension–compression mode. Smart Mater. Struct. **26**(6), 065011 (2017)
6. Vatandoost, H., Rakheja, S., Sedaghati, R., Hemmatian, M.: Compensation of magnetic force of an electromagnet for compression mode characterization of magnetorheological elastomers. IEEE Trans. Magn. **57**(1), 1–14 (2021)
7. Gordaninejad, F., Wang, X., Mysore, P.: Behavior of thick magnetorheological elastomers. J. Intell. Mater. Syst. Struct. **23**(9), 1033–1039 (2012)
8. Hyun, K., Wilhelm, M., Klein, C.O., Cho, K.S., Nam, J.G., Ahn, K.H., et al.: A review of nonlinear oscillatory shear tests: analysis and application of large amplitude oscillatory shear (LAOS). Prog. Polym. Sci. **36**(12), 1697–1753 (2011)
9. Cho, K.S., Hyun, K., Ahn, K.H., Lee, S.J.: A geometrical interpretation of large amplitude oscillatory shear response. J. Rheol. **49**(3), 747 (2005)
10. Ewoldt, R.H., Hosoi, A., McKinley, G.H.: New measures for characterizing nonlinear viscoelasticity in large amplitude oscillatory shear. J. Rheol. **52**(6), 1427–1458 (2008)
11. Wang, H., Chang, T., Li, Y., Li, S., Zhang, G., Wang, J., et al.: Characterization of nonlinear viscoelasticity of magnetorheological grease under large oscillatory shear by using Fourier transform-Chebyshev analysis. J. Intell. Mater. Syst. Struct. **32**(6), 614–631 (2021)
12. Kim, J.H., Ahn, K.H.: Rheological characteristics of poly(ethylene oxide) aqueous solutions under large amplitude oscillatory squeeze flow. Korea-Australia Rheol. J. **24**(4), 257–266 (2012)

13. Kim, J.H., Ahn, K.H., Lee, S.J.: Model prediction of non-symmetric normal stresses under oscillatory squeeze flow. Korean J. Chem. Eng. **29**(8), 1010–1018 (2012)
14. Yu, W., Wang, P., Zhou, C.: General stress decomposition in nonlinear oscillatory shear flow. J. Rheol. **53**(1), 215–238 (2009)
15. Vatandoost, H., Rakheja, S., Sedaghati, R.: Effects of iron particles' volume fraction on compression mode properties of magnetorheological elastomers. J. Magn. Magn. Mater. **522**, 167552 (2021)
16. Vatandoost, H., Hemmatian, M., Sedaghati, R., Rakheja, S.: Effect of shape factor on compression mode dynamic properties of magnetorheological elastomers. J. Intell. Mater. Syst. Struct. **32**(15), 1678–1699 (2021)
17. Vatandoost, H., Sedaghati, R., Rakheja, S., Hemmatian, M.: Effect of pre-strain on compression mode properties of magnetorheological elastomers. Polym. Test. **93**, 106888 (2021)
18. Standard Guide for Dynamic Testing of Vulcanized Rubber and Rubber-Like Materials Using Vibratory Methods. ASTM D5992–D5996; (2011)
19. Ewoldt, R.H.: Nonlinear Viscoelastic Materials: Bioinspired Applications and New Characterization Measures [Ph.D.]: Massachusetts Institute of Technology (2009)

Magneto-Dynamic Characterization of a Silicone Filament Embedded with Magnetic Composite Microspheres

Luís Pedro Vieira Alexandrino, Alessandro Porrari, and Giulia Lanzara

1 Introduction

In the past two decades, there has been a growing interest in the use of smart materials or stimuli-responsive materials in high-tech industries and material science technology. These are a new generation of materials that can be controlled and/or act in a predicted manner [1]. These stimuli-responsive polymers can rapidly change their configuration, dimension, or physical properties with small changes in the appropriate stimuli such as heat [2, 3], pH [4], electricity [5], light [6], moisture/water [7], magnetic field [8], etc. One of the remarkable advantages of this new generation of materials is their capability to be actuated remotely when exposed to external triggering sources [9].

The use of magnetic fields seems to be promising since it allows accurate control of the deformation modes. It has also been proven to be safe and effective, especially in terms of response time. Magnetic actuation has the potential to lead to very fast response times and is very versatile in terms of the external magnetic field [10].

Stimuli-responsive materials with external magnetic properties can be achieved with a composition of particles of iron oxide, for example. Composites of polymers containing iron oxide were studied, using polymers such as poly(carbonate urethane) (PCU) [11], poly (vinyl chloride) (PVC) [12], polydimethylsiloxane (PDMS) [13], alginate [14], etc.

Alginate is a biopolymer that can be found in the cells of brown algae. It is composed of two residues: a 1,4-linked β-D-mannuronic acid (M) and a 1,4-linked α-L-guluronic acid (G). Alginate properties can be defined with the variation of these sugar residue ratios. Alginate is biocompatible, biodegradable,

L. P. V. Alexandrino · A. Porrari · G. Lanzara (✉)
Department of Civil Engineering, Computer Science and Aeronautical Technologies, Roma Tre University, Rome, Italy
e-mail: giulia.lanzara@uniroma3.it

© The Author(s), under exclusive license to Springer Nature Switzerland AG 2024

W. Lacarbonara (ed.), *Advances in Nonlinear Dynamics, Volume III*, NODYCON Conference Proceedings Series, https://doi.org/10.1007/978-3-031-50635-2_26

and easily available. For this reason, it is widely used in tissue engineering, drug delivery, wound dressing, food additives, and cell encapsulation. The formation of microspheres of alginate is created by the fast crosslinking of alginate with $CaCl_2$. The microspheres can be prepared depending on the intended application [15, 16].

In this work, a stimuli-responsive material, composed of silicone with embedded alginate microspheres with immobilized iron oxide particles, is investigated. The composite is shaped as a filament, and its frequency and damping ratio response are investigated using a laser vibrometer with and without increasing loads.

2 Fabrication and Test Setup

The spheres of calcium alginate with immobilized magnetite microparticles (Fe_3O_4) were previously produced using a solution of 20 mL of sodium alginate with a concentration of 28 g/L. Then, 5 g of magnetite was added to the solution. This solution was transferred to a syringe and extruded drop by drop using a needle of 21G to a solution of 2% $CaCl_2$ and were left to react for 2 h. Afterward, they were transferred to a solution of 0.5% $CaCl_2$ to stabilize the spheres. In the end, the spheres were dried in an oven at 60 °C and composite of spheres of calcium alginate loaded with magnetite was produced.

The alginate spheres loaded with Fe_3O_4 were placed at a 1 cm distance from each other on a 3D printed poly lactic acid (PLA) mold shaped as a guide (see Fig. 1a). The guide has a length of 7 cm with semi-holes of 1.6 mm in diameter. In this guide, a 10:1 ratio of silicon rubber and its hardener were roughly mixed, inserted in a syringe, and extruded manually. Finally, the mold was loaded in an oven and dried for 20 min at 60 °C.

The fabricated magnetic filament is placed on a specially designed testing rig (Figs. 1b and 3). The rig consists of two supports that hold the filament with a clamped-clamped configuration and allow the magnet to be inserted under the filament at 1.5 cm from its original position.

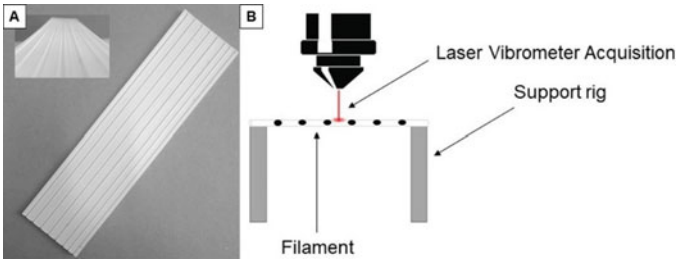

Fig. 1 (**a**) 3D printed guide with PLA to produce PDMS filaments and (**b**) schematics of the testing rig that holds the filament

Table 1 Weight applied to the filament each time

Weight	Mass (g)
1	0.0493
2	0.1002
3	0.1525

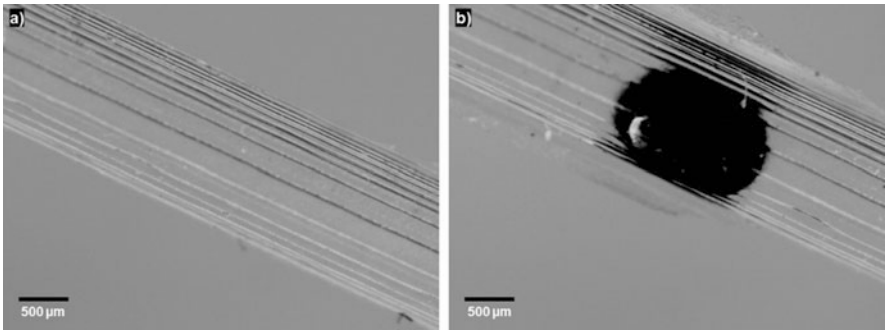

Fig. 2 (**a**) Images obtained with a lens on the filament without the composite of alginate embedded and (**b**) with the composite of alginate embedded

The composite filament is then tested dynamically with the support of a laser vibrometer focused on the filament. The vibrations of the suspended filaments were induced through the application of an impulsive force. The test is repeated both with and without the magnetic field under the influence of increasing loads (reported in Table 1).

3 Results and Discussion

The silicone filament, which embeds the composite microspheres of alginate loaded with magnetite particles, is shown in Fig. 2. The filament is formed by alternating portions of pure silicone and of microspheres embedded in the silicone matrix. An example of such portions can be observed in Fig. 2a, b, respectively. The filament shows a uniform striated structure, which is the result of the 3D printed mold that forms the desired shape via consecutive superimposed layers of material. Silicone is known to be a nanoscopic material and to reproduce patterns with high fidelity. Figure 2b on the other hand highlights a microscope image of a microsphere embedded in the silicone matrix. The spheres have an average area of (1.96 ± 0.33) mm^2. Since the spheres were a little bit oval, an analysis of the area was performed. The black color is representative of the magnetite particles that are homogeneously distributed in the cross-linked alginate matrix. The picture also highlights that the microsphere is not symmetrically placed with respect to the filament's central axis. This is due to the fabrication process according to which the

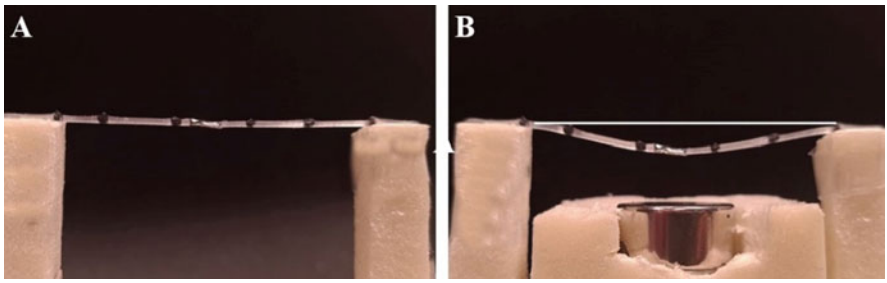

Fig. 3 Testing rig used for the measurements with the vibrometer. (**a**) Testing rig without a magnet. (**b**) Testing rig with a magnet placed at 1.5 cm

spheres are placed in the guide before the addition of the silicone matrix, which is then inhibited to fill in depth the space under the sphere.

The image in Fig. 3a shows the filament mounted on the support in a clamped-clamped configuration with a total free spam of 5 cm. The filament once exposed to a magnetic field plays the role of a "mechanical actuator" for morphing, rigidity, and damping modulation. An example of "morphing" action is shown in Fig. 3b in which the filament bends and indeed "morphs" on a large scale when a magnet is placed at a 1.5 cm distance from the mid-spam of the filament.

The tests were performed to identify the first flexural vibration mode of the filament. The resonance frequencies are identified by inducing a free vibration to the filament, which was done by applying an impulsive load. The result for the time-history acquisition for the vibration of the free filament (NM) and with the actuation of the magnet (M) is shown in Fig. 4. It is possible to observe that the vibration time is much longer when there is no actuation of the magnet (NM) than when there is a magnet actuation (M). This means that the damping is much higher when there is a magnetic actuation on the filament.

The fast Fourier transform (FFT) of the signal of the filament is reported along with the time history. The FFT signal obtained when a load is added and when a magnetic force is applied can be observed in Fig. 5. The exposure of the filament to a magnetic field (M curve in Fig. 5) increases the resonance frequency of the filament with respect to the unexposed case (NM curve in Fig. 5): a shift in frequency of 27.9% is recorded. This is due to an increase in rigidity given by the interaction of the magnetic field and the alginate microspheres. With increasing load applied to the filament, a decrease in resonance frequency is detected for both cases: with and without exposure to the magnetic field. The frequency decrease (NM case) is within a range of 51.2% for an unloaded filament and a filament with maximum load, respectively. Instead, a lower percentage variation for the loaded filament, 29.6%, is observed when the filament is exposed to a magnetic field.

These results can be interpreted by considering the balance between the stiffness, k, increase due to the interaction with the magnetic field and the increase in mass m

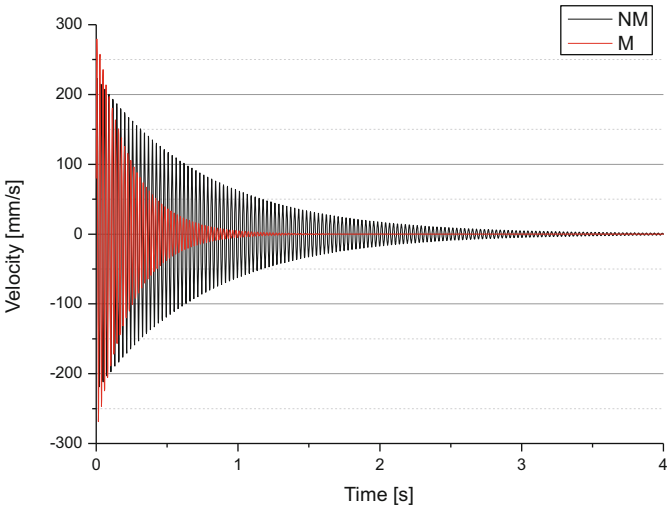

Fig. 4 Time-history acquisition of the vibration of the filament with magnet actuation (red line – M) and without (black line – NM). It is to be noted that the velocity on the graph is not to be considered, only the time that it takes for the vibration to be damped

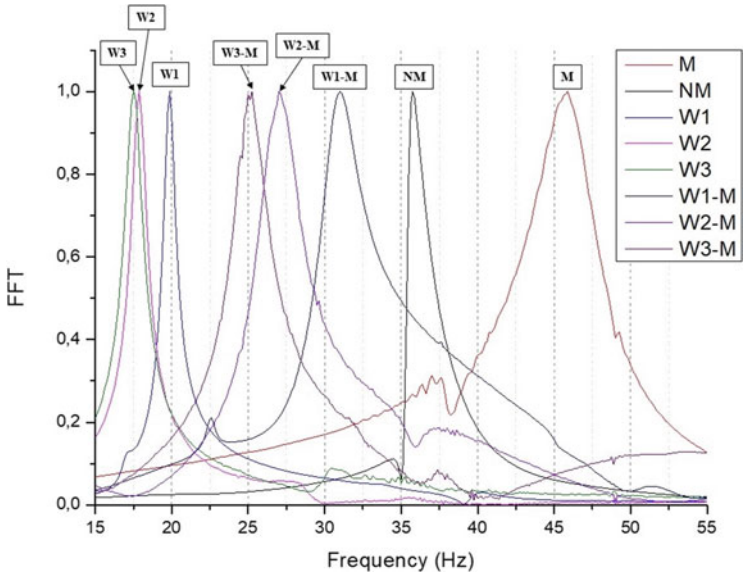

Fig. 5 Fast Fourier transform (FFT) of the filament exposed to different environments: when there is a magnetic field applied (M), when there is no magnetic field (NM), and with the respective weights (W1, W2, W3) added to these two environments

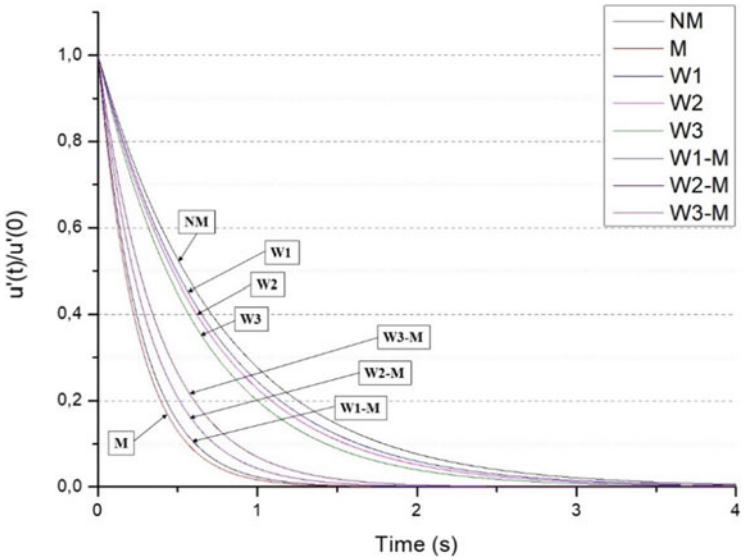

Fig. 6 Free vibration damping effect graph when a magnetic field is applied (m) and when there is no magnetic field applied (nm) (graph on the left). Exponential ratio calculation $u'(t)/u'(0)$ (graph on the right)

when the filament is loaded. The filament mass, m, is indirectly proportional to the frequency, f, as shown by the equation $\omega = 2\pi f = \sqrt{\frac{k}{m}}$.

The interaction of the filament with a magnetic field also influences the damping capability of the filament. Accordingly, the damping factor, ζ, is calculated from the velocity (U') vs. time response of the vibrating filaments. The decay of the time-domain response is reported in Fig. 6 in terms of $U'(t)/U'(0)$ to allow a direct comparison of all acquired data. With increasing weight on the filament, an increase in the slope of the curves, which results in a decrease in damping-time, is detected. It is also once again observed that the addition of the magnet (NM curve vs. M curve) results in a dramatic drop of the curve that decays even more rapidly over time with respect to all other tested cases. This is related to the attraction of the microspheres to the magnet that stabilizes the filament by absorbing the induced vibrations. However, the magnetic stabilization decreases with increasing applied mass. This is because the increase in added weight in the bottom part of the filament shields the interaction with the magnetic field.

The quantitative analysis of the damping factor calculated with the logarithmic decrement $\left(\xi = \frac{\delta}{2\pi n}\right)$ is reported in Fig. 7 for both M and NM cases and in which the magnetic field switches the damping factor from 5.7×10^{-3} to 1.42×10^{-2} for the unloaded filament. The increase of weight acts in terms of damping factor in agreement with the above discussion.

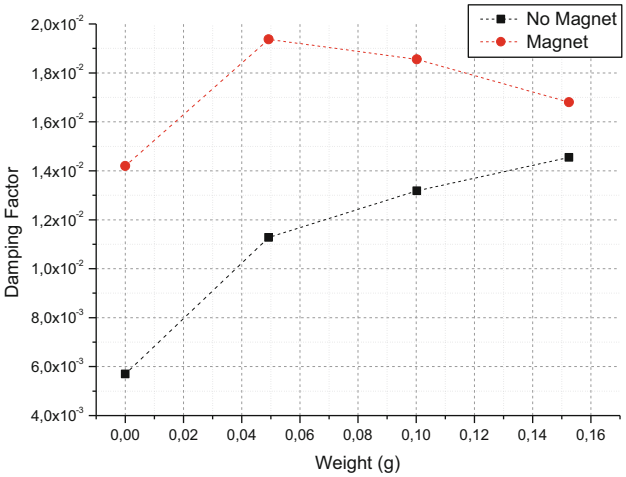

Fig. 7 Free vibration damping effect graph when a magnetic field is applied (m) and when there is no magnetic field applied (nm) (graph on the left). Exponential ratio calculation $u'(t)/u'(0)$ (graph on the right)

4 Conclusion

A novel magnetic filament is presented in this chapter. The filament is formed by a silicone matrix hosting an alginate magnetic microsphere. It is demonstrated that such spheres allow for modification of the filament performance in terms of frequency and damping response when exposed to a magnetic field. A higher damping factor and a lower resonance frequency are recorded when a magnetic field is applied. Most importantly, the study highlights the possibility of fine-tuning the material design to reach the desired dynamic response (vibration and damping).

Acknowledgments This research was funded by the Air Force Office of Scientific Research (AFOSR)/European Office of Aerospace Research and Development (EOARD), Award n. FA8655-20-1-7036 for which Dr. Les Lee is gratefully acknowledged.

References

1. Bhanushali, H., Amrutkar, S., Mestry, S., Mhaske, S.T.: Shape memory polymer nanocomposite: a review on structure–property relationship. Polym. Bull. **79**, 3437–3493 (2022)
2. Lendlein, A., Kelch, S.: Shape-memory polymers. Angew. Chemie Int. Ed. **41**, 2034 (2002)
3. Everhart, M.C., Nickerson, D.M., Hreha, R.D.: High-temperature reusable shape memory polymer mandrels. In: White, E.V. (ed.) International SAMPE Symposium and Exhibition, p. 61710K (2006)

4. Wang, X., Behl, M., Lendlein, A., Balk, M.: Responses to single and multiple temperature-, medium-, and pH-stimuli triggering reversible shape shifts in hydrogel actuators. Mater. Des. **225**, 111511 (2023)
5. Maksimkin, A.V., Dayyoub, T., Telyshev, D.V., Gerasimenko, A.Y.: Electroactive polymer-based composites for artificial muscle-like actuators: a review. Nanomaterials. **12**, 2272 (2022)
6. Lendlein, A., Jiang, H., Jünger, O., Langer, R.: Light-induced shape-memory polymers. Nature. **434**, 879–882 (2005)
7. Yang, B., Huang, W.M., Li, C., Li, L.: Effects of moisture on the thermomechanical properties of a polyurethane shape memory polymer. Polymer (Guildf). **47**, 1348–1356 (2006)
8. Riabchykov, M., Alexandrov, A., Trishch, R., Nikulina, A., Korolyova, N.: Prospects for the development of smart clothing with the use of textile materials with magnetic properties. Tekstilec. **65**, 36–43 (2022)
9. Ozair, H., Baluch, A.H., ur Rehman, M.A., Wadood, A.: Shape memory hybrid composites. ACS Omega. **7**, 36052–36069 (2022)
10. Kuhnt, T., Camarero-Espinosa, S., Takhsha Ghahfarokhi, M., Arreguín, M., Cabassi, R., Albertini, F., Nieto, D., Baker, M.B., Moroni, L.: 4D printed shape morphing biocompatible materials based on anisotropic ferromagnetic nanoparticles. Adv. Funct. Mater. **32**, 2202539 (2022)
11. Wei, W., Yang, J., Zhang, Z., Dai, Y., Li, W., Wu, X., Dai, H.: Biocompatible magnetic poly(carbonate urethane) microspheres for potential applications in aneurysm embolization. ACS Appl. Polym. Mater. **4**, 8847–8857 (2022)
12. Demirel, E., Zhang, B., Papakyriakou, M., Xia, S., Chen, Y.: Fe2O3 nanocomposite PVC membrane with enhanced properties and separation performance. J. Memb. Sci. **529**, 170–184 (2017)
13. Paknahad, A.A., Tahmasebipour, M.: An electromagnetic micro-actuator with PDMS-Fe3O4 nanocomposite magnetic membrane. Microelectron. Eng. **216**, 111031 (2019)
14. Shen, F., Li, A.A., Gong, Y.-K., Somers, S., Potter, M.A., Winnik, F.M., Chang, P.L.: Encapsulation of recombinant cells with a novel magnetized alginate for magnetic resonance imaging. Hum. Gene Ther. **16**, 971–984 (2005)
15. Jayachandran, V., Murugan, S.S., Dalavi, P.A., Gurushanthappa Vishalakshi, Y.D., Seong, G.H.: Alginate-based composite microspheres: preparations and applications for bone tissue engineering. Curr. Pharm. Des. **28**, 1067–1081 (2022)
16. Ismail, H., Irani, M., Ahmad, Z.: Starch-based hydrogels: present status and applications. Int. J. Polym. Mater. **62**, 411–420 (2013)

Modeling Asymmetric Hysteresis: Continuous Development Using Experimental Data

Jin-Song Pei, Biagio Carboni, and Walter Lacarbonara

1 Introduction

Sapienza University of Rome has a rich history of studying hysteresis through innovations in experimental test setups and mathematical modeling (e.g., [3–8, 12, 16]). As reported in [15], the precursor of this chapter, the investigated device herein exhibits asymmetric hysteresis due to coupled geometric nonlinearities and inter-wire frictional dissipation. Using a typical test in this study, the first half of Fig. 1a and b (up to $t \approx 352$ seconds) reveals the asymmetry of the restoring force, where a series of nearly symmetric cyclic displacement histories x (i.e., *input*) leads to a corresponding completely asymmetric response in terms of restoring force r (i.e., *output*). The obtained force-displacement data measurements show *hysteresis loops* as in Fig. 1c.

Asymmetric hysteretic responses, resulting from asymmetric material properties, boundary conditions, or geometry, have been studied, employing various modeling approaches [7, 9, 16, 17, 19, 20]. Asymmetric hysteresis is common in a variety of systems with material hysteresis due to the fact that there is often a pre-load that creates an initially deformed state about which the response is asymmetric. Reference [1] quantifies a measure for loading rate-dependency and concludes that the responses shown in Fig. 1 are *rate-independent*. The rate-independency hints to

J.-S. Pei (✉)
University of Oklahoma, Norman, OK, USA
e-mail: jspei@ou.edu
https://www.researchgate.net/profile/Jin-Song-Pei

B. Carboni
Sapienza University of Rome, Rome, Italy

W. Lacarbonara
Department of Structural and Geotechnical Engineering, Sapienza University of Rome, Rome, Italy

© The Author(s), under exclusive license to Springer Nature Switzerland AG 2024

W. Lacarbonara (ed.), *Advances in Nonlinear Dynamics, Volume III*, NODYCON Conference Proceedings Series, https://doi.org/10.1007/978-3-031-50635-2_27

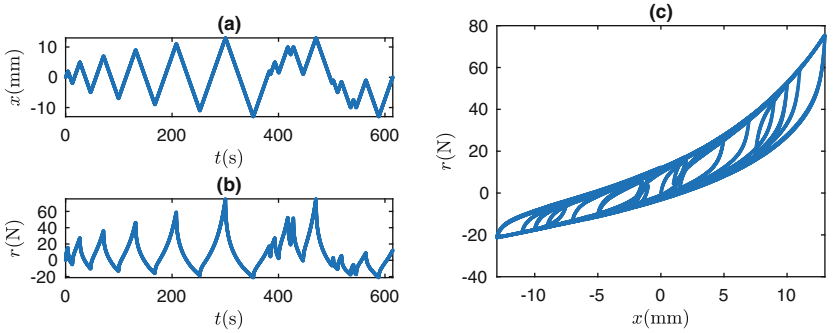

Fig. 1 Experimental (**a**) input, and (**b**) output time histories and (**c**) corresponding hysteresis loops for a typical test in this study

the possibility of applying the classical Preisach operator, the most general rate-independent hysteresis model. For computational efficiency, the extended Masing model [10, 11], a subset of the classical Preisach models [13], has been our focus. The extended Masing model has a compact model formulation for symmetric hysteresis; thus, we wondered if the same could be achieved for asymmetric hysteresis. The energy dissipation is different for the two loading directions. Reference [15] rules out the possibility of treating the asymmetric hysteresis as in the experimental data with a model assembly using a symmetric extended Masing model and an unsymmetrical one-to-one mapping (i.e., a nonlinear spring). We thus aim at generalizing the extended Masing model for improved computational efficiency.

The second half of Fig. 1a and b (after $t \approx 352$ seconds) displays the complex input and output relations investigated in this study, which allows us to question, propose, and validate all aspects involved in generalizing the extended Masing model. The rich information revealed in this study goes far beyond all test data combined in [15]. The original extended Masing model cannot be used to fit the data 100%. So, we will have to decide what to keep, what to adapt, and what to drop in the extended Masing model.

The experimental setup is discussed in Sect. 2. The extended Masing model for asymmetric hysteresis is reviewed in Sect. 3. All aspects of the proposed generalization of the extended Masing model are reported in Sect. 4, closely validated using the typical test data in this study. Section 5 summarizes concluding remarks.

2 Experimental Setup

Experimental data motivate, inspire, and validate this modeling work. The testing device is a wire rope isolator constituted by two plates connected by two curved continuous steel wire ropes. Figure 2a shows the undeformed configuration of the test apparatus, while Fig. 2b and c gives a snapshot of loading into negative and

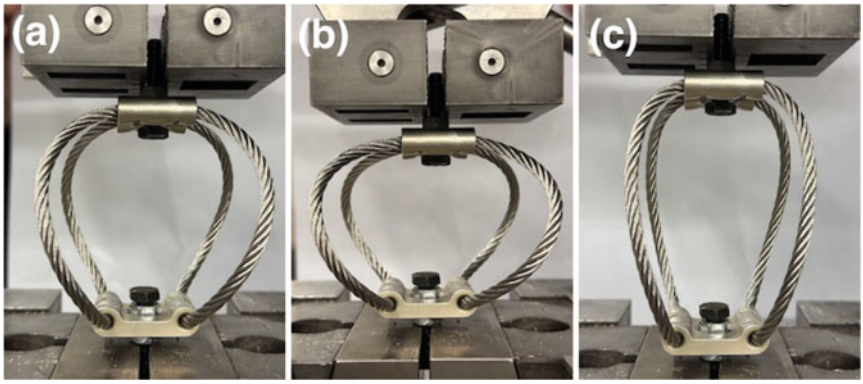

Fig. 2 Photos showing (**a**) neutral, (**b**) compressive, and (**c**) tensile states of the test setup

positive direction, respectively. The restoring force is acquired by means of a Zwick-Roell testing machine run in displacement control mode. One plate is cyclically moved with displacement histories at constant velocity, while the other plate is fixed. A load-cell measures the restoring force provided by the ropes assembly, which exhibits an asymmetric response for positive and negative displacements.

3 Extended Masing Model for Symmetric Hysteresis

For Masing models, the seminal paper [14] provided the inspiration for later developments of models for softening hysteretic systems, among which the so-called extended Masing model (EMM) from [10, 11] and as reviewed in [2] is the starting point for [15] and the current study. As proved in [13], Masing models are Preisach models, with a reduced number of parameters.

In [14], the *virgin loading (skeleton or backbone) curve* is in the general implicit form:

$$f(x, r) = 0 \tag{1}$$

Masing's model states that the *unloading* and *reloading branches* of the hysteresis loops are described by:

$$f\left(\frac{x - x_{[j]}}{2}, \frac{r - r_{[j]}}{2}\right) = 0 \tag{2}$$

where $(x_{[j]}, r_{[j]})$ is the jth *load reversal* point, i.e., $\dot{x}_{[j]} = 0$ and $\dot{r}_{[j]} = 0$. Masing assumed the *symmetry property*: $f(-x, -r) = f(x, r)$. Each reloading and unloading branch is monotonically increasing or decreasing, respectively, following the so-called *monotonicity*—as in the Preisach model—and leading to

a simultaneous occurrence of $\dot{x}_{[j]} = 0$ and $\dot{r}_{[j]} = 0$. For symmetric hysteresis, the extended Masing model class may use *explicit functions*, as developed in [10, 11].

References [10, 11] updated the original Masing rule for arbitrary loading. These rules are summarized in [2] as follows:

EMM Rule 1: The equation of any hysteretic force-deformation curve can be obtained by applying the original Masing rule to the virgin loading curve using the latest point of load reversal.

EMM Rule 2′: If an unloading or reloading curve described by Rule 1 meets either a previous loading curve or the virgin loading curve, the load-deformation curve switches to following that curve.

For efficient numerical implementation, hybrid dynamical system framework is introduced in [2], where the concepts of mode, domain, flow map, state event, event function, and reset map are employed to execute EMM Rules 1 and 2′. For example, there are three types of *state events*, where types 1 and 2 are associated with EMM Rule 2′ concerning minor loop closures, while type 3 refers to load reversal points. $x_{[j]}$ and $r_{[j]}$ are *pivoting values*, used in *event functions* to trigger the first two state events following EMM Rule 2′ and in *reset* right after every type of the state events also following EMM Rule 2′. Two *memory stacks*, for unloading and reloading brunches, are required following [18] to save the pivoting values, which are piecewise constant, i.e., as algebraic variables to complement state variables to make up a hybrid dynamical system.

4 Generalizing Extended Masing Model for Asymmetric Hysteresis

With the new experimental data in this study and using the typical test as an example, we first identify all load reversal points as shown in Fig. 3, where black up-pointing and red down-pointing triangles are used to mark the transitions from loading (or reloading) to unloading and from unloading to loading (or reloading), respectively. Monotonicity is clear aligning the input and output in Fig. 4a and b, respectively. As shown in Fig. 4a and b, virgin loading curves into the positive and negative directions are further identified and highlighted in cyan and green, respectively. Reloading and unloading branches are identified at the same time. This is a small step beyond [15], when virgin loading curves were not revealed from the tests in that context. Canceling out time t, Fig. 5a presents the virgin loading curves, which are not symmetrical about the origin, as expected. While the virgin loading curve into the negative direction is softening, the virgin loading into the positive direction is softening before quickly turning into hardening. Recall that EMM can only have softening virgin loading curves [2]. Monotonicity is once again prominent as shown in Fig. 5b using reloading and unloading branches. Assuming EMM Rule 2′ is applicable, we use the typical test in this study to identify the time evolution of all pivoting values. As shown in Fig. 4c and d, black and red are

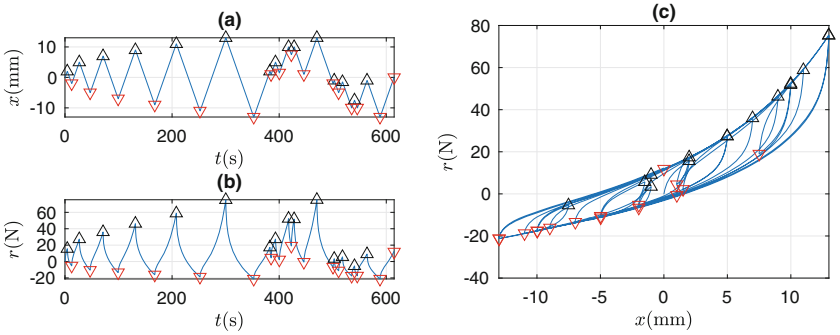

Fig. 3 Details showing identified load reversal points, i.e., state event type 3 as in [2]

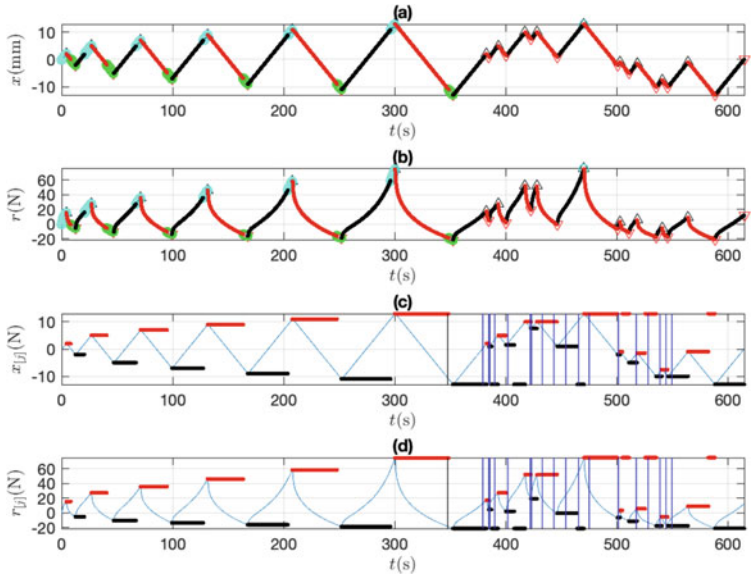

Fig. 4 Details showing (**a**) and (**b**) identified virgin loading curve, reloading and unloading curves, and (**c**) and (**d**) switching of displacement and restoring pivoting values, respectively, and the common beginning and 18 distinct ending time instants for Fig. 6 to further zoom into

assigned to show piecewise constant pivoting values for reloading and unloading branch, respectively. Up to $t \approx 352$ seconds, virgin loading appears at the end of every branch in either positive or negative directions, when the following load reversal point sees a reset of either an unloading or reloading pivoting value. This is a straightforward identification; however, the identification becomes far more complicated after $t \approx 352$ seconds, when minor loops occur together with one instance of virgin loading updating at $t \approx 470$ seconds. This identification is a major step accomplished in this study.

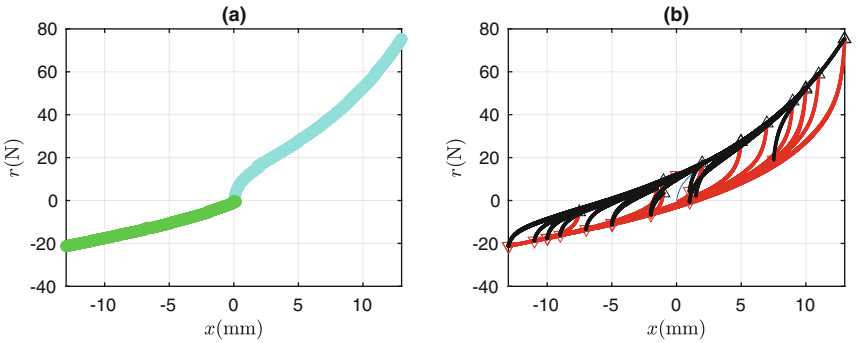

Fig. 5 Identified (**a**) virgin loading curve and (**b**) reloading (black) and unloading (red) curves

To explain and validate our work shown in Fig. 4c and d, we select one beginning time instant (shortly before $t \approx 352$ seconds) as marked in black, paired with 18 different ending time instants as marked in blue. A total of 18 segments—each defined with the common beginning time instant and a distinct ending time instant—are presented in Fig. 6. In each of the 18 panels, reloading and unloading branches are plotted in black and red, respectively. Current reloading and unloading pivoting points are marked in black diamond and red circle, respectively. Reloading and unloading memory stacks are presented in black and red fonts, respectively. Using jargons for Preisach model, the typical test in this study manifests second- and third-order load reversal.

In [15], we conjecture that for an asymmetric extended Masing model, we could have two *implicit functions*:

$$\text{All reloading curves:} \qquad f_l\left(\frac{x - x_{[j]}}{2}, \frac{r - r_{[j]}}{2}\right) = 0 \tag{3}$$

$$\text{All unloading curves:} \qquad f_u\left(\frac{x - x_{[j]}}{2}, \frac{r - r_{[j]}}{2}\right) = 0 \tag{4}$$

Using *explicit functions*, we can have the following *flow-controlled* formulations from the bond graph theory, meaning that the displacement x is natural to be solved first:

$$\text{All reloading curves:} \qquad r = r_l\left(x, x_{[j]}\right) \tag{5}$$

$$\text{All unloading curves:} \qquad r = r_u\left(x, x_{[j]}\right) \tag{6}$$

given that $r_{[j]}$ will be the starting or ending value of r of each branch, it thus can be dropped from the explicit functions. We can also have the following *effort-controlled explicit functions*:

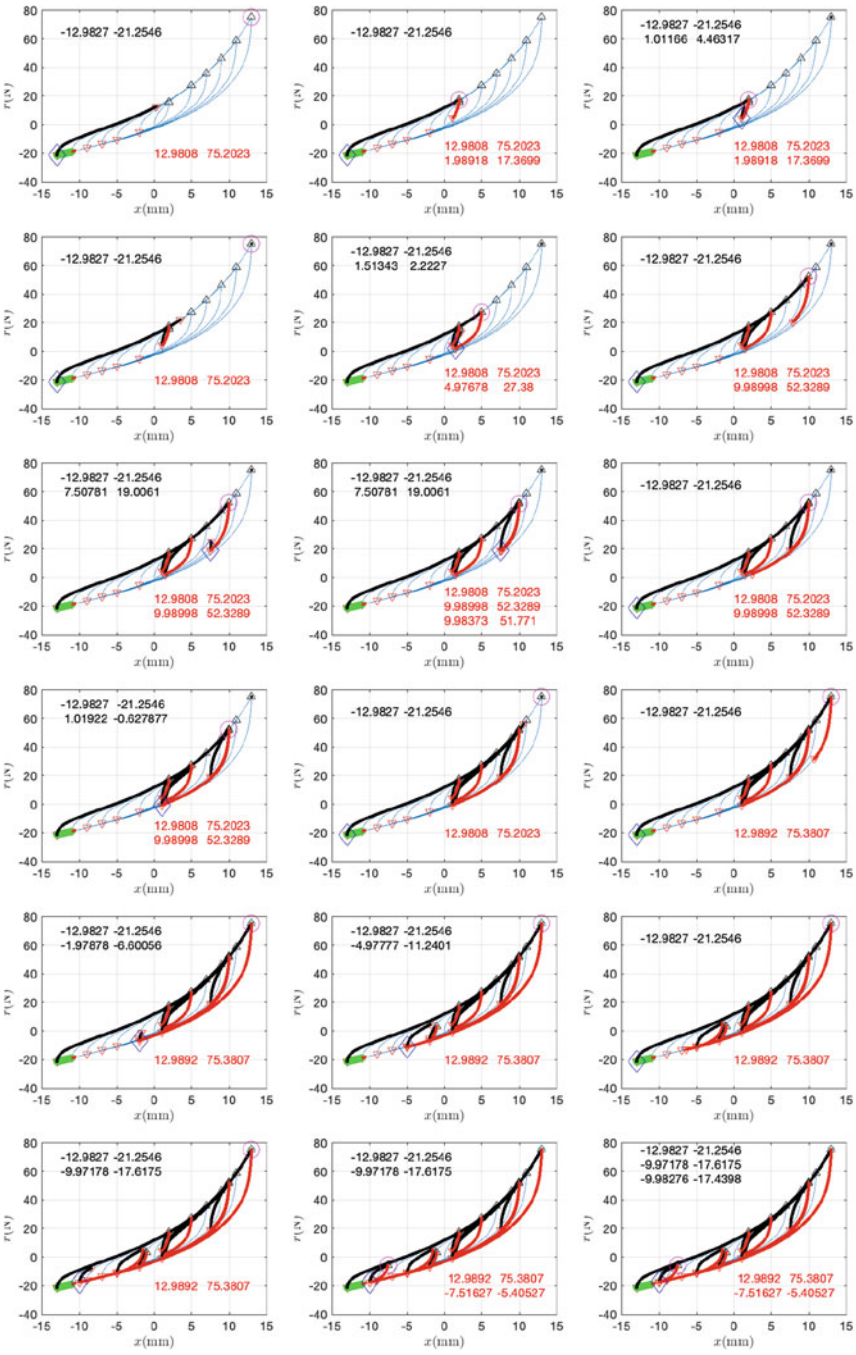

Fig. 6 Progression of reloading and unloading branches, their current pivoting points, and memory stacks with each panel defined by the common beginning and 18 distinct ending time instants marked in Fig. 4c and d

$$\text{All reloading curves:} \qquad x = x_l\left(r, r_{[j]}\right) \tag{7}$$

$$\text{All unloading curves:} \qquad x = x_u\left(r, r_{[j]}\right) \tag{8}$$

given that $x_{[j]}$ will be the starting or ending value of x of each branch, it thus can be dropped from the explicit functions.

To validate Eqs. (5)–(8) beyond [15], we have two research questions on the new results with minor loops and virgin loading curves as in Figs. 6 and 5a, respectively:

Research Question 1 (On Minor Loops) *If explicit functions can be used, do all reloading and unloading branches (including those with second- and third-order load reversal) satisfy Eqs.* (5) *(or* (7)*) and* (6) *(or* (8)*), respectively?*

Research Question 2 (On Virgin Loading Curve) *If explicit functions can be used, does a virgin loading curve into the positive and negative directions satisfy Eqs.* (5) *(or* (7)*) and* (6) *(or* (8)*), respectively, with* $x_{[j]} = 0$ *and* $r_{[j]} = 0$ *for the virgin loading curve?*

Using the typical test and identified minor loops and virgin loading curves as illustrated in Figs. 6 and 5a, respectively, Eqs. (5)–(8) are plotted in Fig. 7a–d, respectively. To further examine if each panel in Fig. 7 is a nice surface, MATLAB meshgrid command is used to approximate the surface before obtaining the contour

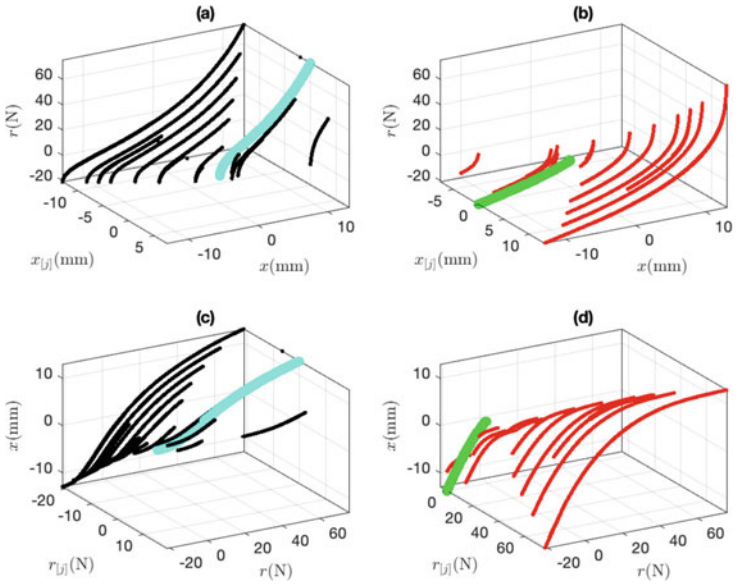

Fig. 7 Decomposed (**a**) reloading curves and virgin loading curve (cyan) in the positive direction and (**b**) unloading curves and virgin loading curve (green) in the negative direction following the flow-controlled formulation and (**c**) and (**d**) the counterparts of (**a**) and (**b**), respectively, following the effort-controlled formulation

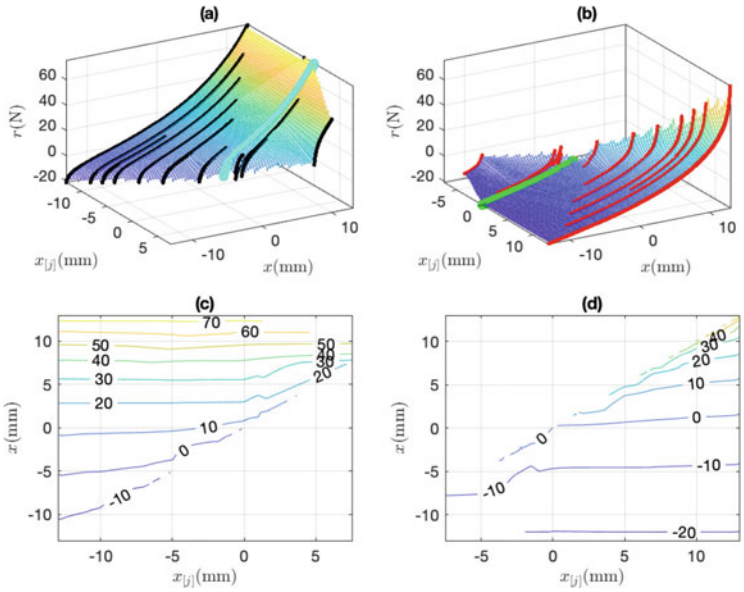

Fig. 8 Decomposed and fitted surfaces of (**a**) reloading curves and virgin loading curve in the positive direction and (**b**) unloading curves and virgin loading curve in the negative direction following the flow-controlled formulation and their contour plots in parts (**c**) and (**d**)

plot. For example, Fig. 8 is for Fig. 7a and b, i.e., for the flow-controlled formulation. A similar plot can be obtained for Fig. 7c and d, i.e., for the effort-controlled formulation. These analyses directly address Research Questions 1 and 2.

5 Concluding Remarks

We have generalized the extended Masing model for asymmetric hysteresis using data resulting from asymmetric geometry to address the following issues:

What can be kept: Monotonicity, EMM Rule 2′, and EMM Rule 1.
What can be adapted: Equations (2)–(3), and (4) (and their explicit functions).
What needs to be dropped: Equation (1), i.e., symmetry property.

Research Question 1 has been answered positively on minor loops in terms of EMM Rule 1; up to the third-order load reversal has been validated in this study. In response to Research Question 2 on virgin loading curve to replace Eqs. (1), (5) seems to fit well the positive virgin loading curve as in Fig. 8a, while the fit between Eq. (6) and the negative virgin loading curve needs a further study to be certain as shown in Fig. 8b.

References

1. Antonelli, M, Carboni, B, Lacarbonara, W, Bernardini, D, Kalmár-Nagy, T.: Quantifying rate-dependence of a nonlinear hysteretic device. In: Lacarbonara, W., Balachandran, B., Ma, J., Tenreiro Machado, J., Stepan, G. (eds) Nonlinear Dynamics of Structures, Systems and Devices. Springer, Berlin (2020)
2. Beck, J.L., Pei, J.S.: Demonstrating the power of extended masing models for hysteresis through model equivalencies and numerical investigation. Nonlinear Dyn. **108**(2), 827–856 (2022)
3. Brewick, P.T., Masri, S.F., Carboni, B., Lacarbonara, W.: Data-based nonlinear identification and constitutive modeling of hysteresis in NiTiNOL and steel strands. ASCE J. Eng. Mech. 142(12), 04016107 (2016)
4. Carboni, B., Lacarbonara, W.: Nonlinear dynamic characterization of a new hysteretic device: experiments and computations. Nonlinear Dyn. **83**(1–2), 23–39 (2016)
5. Carboni, B., Lacarbonara, W.: Nonlinear vibration absorber with pinched hysteresis: theory and experiments. ASCE J. Eng. Mech. 142(5), 04016023 (2016)
6. Carboni, B., Lacarbonara, W., Auricchio, F.: Hysteresis of multiconfiguation assemblies of nitinol and steel strands: experiments and phenomenological identification. ASCE J. Eng. Mech. **141**(3), 04014135 (2014)
7. Carboni, B, Lacarbonara, W., Brewick, P.T., Masri, S.F.: Dynamical response identification of a class of nonlinear hysteretic systems. J. Intell. Mater. Syst. Struct. **29**(13), 2795–2810 (2018)
8. Carpineto, N., Lacarbonara, W., Vestroni, F.: Hysteretic tuned mass dampers for structural vibration mitigation. J. Sound Vib. **333**, 1302–1318 (2014)
9. Dobson, S., Noori, M., Hou, Z., Dimentberg, M., Baber, T.: Modeling and random vibration analysis of SDOF systems with asymmetric hysteresis. Int. J. Non-Linear Mech. **32**(4), 669–680 (1997)
10. Jayakumar, P.: Modeling and identification in structural dynamics. Ph.D. Thesis, California Institute of Technology, Pasadena, CA (1987)
11. Jayakumar, P., Beck, J.L.: System identification using nonlinear structural models. In: Natke, H.G., Yao, J.T.P. (eds) Structural Safety Evaluation Based on System Identification Approaches, Friedr. Vieweg & Sohn Braunschweig/Wiesbaden, Vieweg International Scientific Book Series, vol Proceedings of the 1987 Workshop at Lambrecht/Pfalz, pp 82–102 (1988)
12. Lacarbonara, W., Verstroni, F.: Nonclassical responses of oscillators with hysteresis. Nonlinear Dyn. **32**, 235–258 (2003)
13. Lubarda, V.A., Sumarac, D., Krajcinovic, D.: Preisach model and hysteretic behaviour of ductile materials. Eur. J. Mech. A/Solids **12**(4), 445–470 (1993)
14. Masing, G.: Eigenspannungen und verfestigung beim messing. In: Proceedings of the 2nd International Congress for Applied Mechanics, Zurich, Switzerland, pp. 332–335 (1926). In German
15. Pei, J.S., Carboni, B., Lacarbonara, W.: Modeling asymmetric hysteresis inspired and validated by experimental data. In: Advances in Nonlinear Dynamics (2022)
16. Salvatore, A., Carboni, B., Chen, L.Q., Lacarbonara, W.: Experimental dynamic response of a nonlinear wire rope isolator. In: Nonlinear Dynamics and Control, pp 89–98 (2020)
17. Song, J., Der Kiureghian, A.: Generalized Bouc-Wen model for highly asymmetric hysteresis. ASCE J. Eng. Mech. **132**(6), 610–618 (2006)
18. Swevers, J., Al-Bender, F., Ganseman, C., Projogo, T.: An integrated friction model structure with improved presliding behavior for accurate friction compensation. IEEE Trans. Autom. Control **45**(4), 675–686 (2000)
19. Vaiana, N., Sessa, S., Rosati, L.: A generalized class of uniaxial rate-independent models for simulating asymmetric mechanical hysteresis phenomena. Mech. Syst. Signal Process. **146**, 106984 (2021)
20. Xie, S., Ren, G., Wang, B.: A modified asymmetric generalized Prandtl-Ishlinskii model for characterizing the irregular asymmetric hysteresis of self-made pneumatic muscle actuators. Mech. Mach. Theory **149**, 103836 (2020)

Preliminary Results on the Simulation of Pressurized Sand Dampers by Using the Vaiana-Rosati Model

Nicolò Vaiana, Luciano Rosati, Xenofon Palios, and Nicos Makris

1 Introduction

Passive energy dissipation is one of the most effective techniques for the vibration protection of structures [1–3]. This technique requires the use of devices, called *dampers*, which are characterized by a high energy dissipation capacity.

Dampers typically exhibit a complex hysteretic behavior. In particular, such a behavior is referred to as *rate-independent* if the device restoring force depends on the device displacement, whereas it is defined as *rate-dependent* when the device restoring force is a function of the device velocity [4].

Makris et al. [5] have recently proposed an innovative, low-cost, eco-friendly, long-stroke, fail-safe, rate-independent hysteretic device denominated *pressurized sand damper*. Its experimental response is characterized by symmetric and pinched force-displacement hysteresis loops.

The main aim of this work is to show that a recently formulated uniaxial hysteretic model [6, 7], belonging to a class formulated by Vaiana et al. [8–10], is sufficiently general to simulate the complex force-displacement hysteresis loops typically exhibited by such a novel device.

The proposed model, denominated *Vaiana-Rosati Model*, offers a series of advantages over other hysteretic models available in the literature, such as (i) the evaluation of the rate-independent hysteretic force and work in closed form; (ii) the

N. Vaiana (✉) · L. Rosati
University of Naples Federico II, Naples, Italy
e-mail: nicolo.vaiana@unina.it

X. Palios
University of Patras, Patras, Greece

N. Makris
Southern Methodist University, Dallas, TX, USA

© The Author(s), under exclusive license to Springer Nature Switzerland AG 2024

W. Lacarbonara (ed.), *Advances in Nonlinear Dynamics, Volume III*, NODYCON Conference Proceedings Series, https://doi.org/10.1007/978-3-031-50635-2_28

simulation of complex hysteresis loops; (iii) the use of two sets of eight parameters that govern, independently, the loading and unloading phases; (iv) the adoption of parameters having a clear theoretical and/or experimental meaning; and (v) an easy implementation in a computer program.

2 Pressurized Sand Damper

2.1 Properties of the Tested Device

Figure 1 illustrates the damper prototype that has been tested at the Structures Laboratory of the University of Patras, Greece. Such a device is made up of a steel cylinder, having a diameter of 18.9 cm and length of 62 cm, which is filled with dry sand pressured by adopting four external post-tensioned steel rods. A sphere with radius of 3 cm, attached to a piston rod having radius of 2 cm, moves along the damper axial direction.

2.2 Experimental Hysteretic Behavior

Figure 2a (b) shows the typical rate-independent hysteretic behavior exhibited by the above-described device when subjected to a sinusoidal axial displacement having amplitude of 40 mm and frequency of 0.2 Hz under the effect of a pressure p of 1 MPa (4 MPa). The experimentally derived symmetric and pinched hysteresis loops demonstrate the capability of the device to dissipate a large amount of mechanical energy.

3 Vaiana-Rosati Model

For the reader's convenience, this section briefly illustrates the formulation of the Vaiana-Rosati Model (VRM) recently proposed in [6]. In particular, we first describe

Fig. 1 Pressurized sand damper prototype

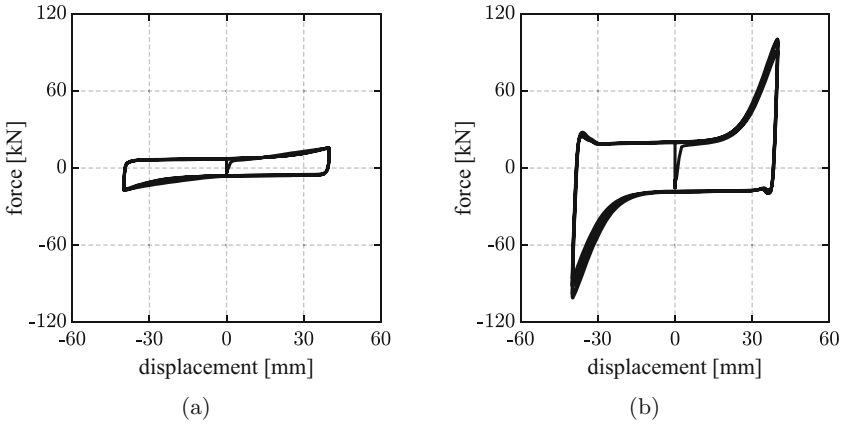

Fig. 2 Experimental responses obtained for $p = 1$ MPa (**a**) and $p = 4$ MPa (**b**)

the closed form expressions for the evaluation of the rate-independent hysteretic force (Sect. 3.1) and work (Sect. 3.2). Subsequently, we provide the closed form expression to compute the rate-independent hysteretic work associated with a single force-displacement hysteresis loop (Sect. 3.3), and finally, we show the influence of each model parameter on the hysteresis loop shape typical of the tested pressurized sand damper (Sect. 3.4).

3.1 Rate-Independent Hysteretic Force

Figure 3a illustrates a typical force-displacement hysteresis loop that can be simulated by the VRM. It can be observed that, during a generic loading phase ($\dot{u} > 0$), the rate-independent hysteretic force f_{ri} is evaluated as:

$$f_{ri}\left(u, u_j^+\right) = \begin{cases} c^+\left(u, u_j^+\right) & \text{when} \quad u < u_j^+ \quad (1a) \\ c_u\left(u\right) & \text{when} \quad u > u_j^+, \quad (1b) \end{cases}$$

whereas, during a generic unloading one ($\dot{u} < 0$), it is obtained as:

$$f_{ri}\left(u, u_j^-\right) = \begin{cases} c^-\left(u, u_j^-\right) & \text{when} \quad u > u_j^- \quad (2a) \\ c_l\left(u\right) & \text{when} \quad u < u_j^-, \quad (2b) \end{cases}$$

where u ($\dot{u}$) represents the displacement (velocity).

In the previous equations, c^+ and c^- are, respectively, the functions describing the generic loading and unloading curves, computed as:

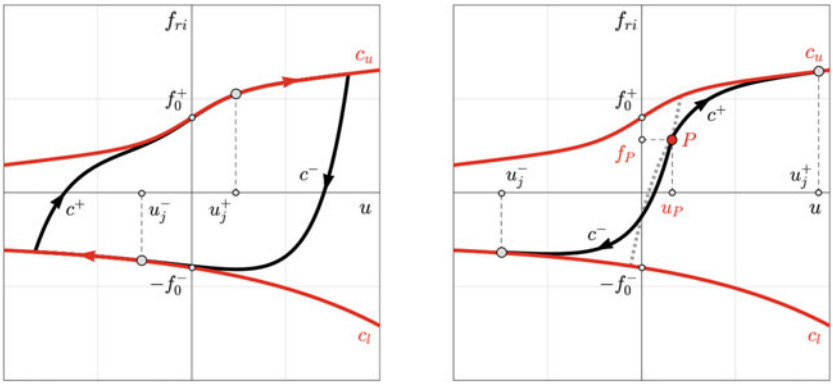

Fig. 3 Curves (**a**) and internal variables (**b**) characterizing a generic hysteresis loop reproduced by the VRM

$$c^+(u,u_j^+) = \beta_1^+ e^{\beta_2^+ u} - \beta_1^+ + \frac{4\gamma_1^+}{1+e^{-\gamma_2^+(u-\gamma_3^+)}} - 2\gamma_1^+ + k_b^+ u + f_0^+ - \frac{1}{\alpha^+}\left[e^{-\alpha^+\left(+u-u_j^+ +\bar{u}^+\right)} - e^{-\alpha^+\bar{u}^+}\right], \tag{3}$$

$$c^-(u,u_j^-) = \beta_1^- e^{\beta_2^- u} - \beta_1^- + \frac{4\gamma_1^-}{1+e^{-\gamma_2^-(u-\gamma_3^-)}} - 2\gamma_1^- + k_b^- u - f_0^- + \frac{1}{\alpha^-}\left[e^{-\alpha^-\left(-u+u_j^- +\bar{u}^-\right)} - e^{-\alpha^-\bar{u}^-}\right], \tag{4}$$

whereas c_u and c_l represent, respectively, the analogous functions associated with the upper and lower limiting curves; they are evaluated as:

$$c_u(u) = \beta_1^+ e^{\beta_2^+ u} - \beta_1^+ + \frac{4\gamma_1^+}{1+e^{-\gamma_2^+(u-\gamma_3^+)}} - 2\gamma_1^+ + k_b^+ u + f_0^+, \tag{5}$$

$$c_l(u) = \beta_1^- e^{\beta_2^- u} - \beta_1^- + \frac{4\gamma_1^-}{1+e^{-\gamma_2^-(u-\gamma_3^-)}} - 2\gamma_1^- + k_b^- u - f_0^-. \tag{6}$$

Finally, u_j^+ and u_j^- are internal variables having expressions:

$$u_j^+ = u_P + \bar{u}^+ + \frac{1}{\alpha^+}\ln\left\{+\alpha^+\left[\beta_1^+ e^{\beta_2^+ u_P} - \beta_1^+ + \frac{4\gamma_1^+}{1+e^{-\gamma_2^+(u_P-\gamma_3^+)}} - 2\gamma_1^+ + k_b^+ u_P + f_0^+ + \frac{1}{\alpha^+}e^{-\alpha^+\bar{u}^+} - f_P\right]\right\}, \tag{7}$$

$$u_j^- = u_P - \bar{u}^- - \frac{1}{\alpha^-}\ln\left\{-\alpha^-\left[\beta_1^- e^{\beta_2^- u_P} - \beta_1^- + \frac{4\gamma_1^-}{1+e^{-\gamma_2^-(u_P-\gamma_3^-)}} - 2\gamma_1^- + k_b^- u_P - f_0^- - \frac{1}{\alpha^-}e^{-\alpha^-\bar{u}^-} - f_P\right]\right\}, \tag{8}$$

where u_P and f_P are the coordinates of a generic point P belonging to c^+ or c^-, as illustrated in Fig. 3b.

Finally, the following quantities k_b^+, f_0^+, α^+, β_1^+, β_2^+, γ_1^+, γ_2^+, γ_3^+ (k_b^-, f_0^-, α^-, β_1^-, β_2^-, γ_1^-, γ_2^-, γ_3^-) are the eight model parameters governing the generic loading (unloading) phase, whereas $\bar{u}^+$ ($\bar{u}^-$) is an internal model parameter having expression:

$$\bar{u}^+ = -\frac{1}{\alpha^+}\ln(\delta_k^+), \tag{9}$$

$$\bar{u}^- = -\frac{1}{\alpha^-}\ln(\delta_k^-), \tag{10}$$

in which δ_k^+ (δ_k^-) is a quantity to be set equal to 10^{-20} for numerical purposes.

3.2 Rate-Independent Hysteretic Work

Figure 4 (Figure 5) presents an example of rate-independent hysteretic work W_{ri} computed over a displacement interval $[u_i, u_f]$ ($[u_f, u_i]$) during a generic loading (unloading) phase of a typical hysteresis loop reproduced by the VRM.

In particular, when $\dot{u} > 0$, such a work can be evaluated as:

$$W_{ri} = \begin{cases} W^+ & \text{when} \quad u < u_j^+ \quad \text{(11a)} \\ W_u & \text{when} \quad u > u_j^+, \quad \text{(11b)} \end{cases}$$

whereas, when $\dot{u} < 0$, it can be computed as:

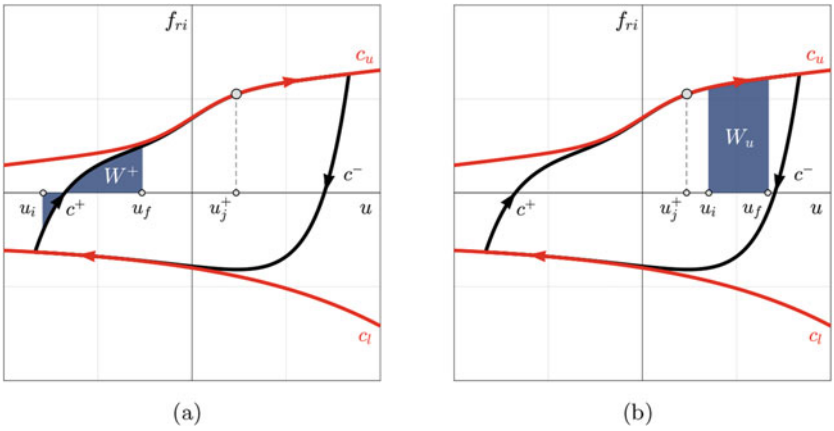

Fig. 4 Evaluation of the rate-independent hysteretic work during a generic loading phase when $u < u_j^+$ (**a**) and $u > u_j^+$ (**b**)

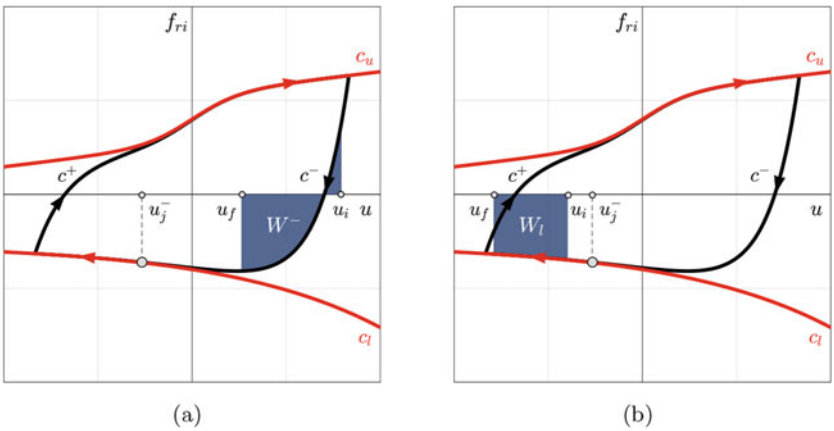

Fig. 5 Evaluation of the rate-independent hysteretic work during a generic unloading phase when $u > u_j^-$ (**a**) and $u < u_j^-$ (**b**)

$$W_{ri} = \begin{cases} W^- & \text{when} \quad u > u_j^- \quad (12a) \\ W_l & \text{when} \quad u < u_j^- . \quad (12b) \end{cases}$$

In the previous equations, W^+ and W^- are, respectively, the area under the curve c^+ over $[u_i, u_f]$, as illustrated in Fig. 4a and the area under the curve c^- over $[u_f, u_i]$, as shown in Fig. 5a.

Similarly, W_u and W_l represent, respectively, the area under the curve c_u over $[u_i, u_f]$, as illustrated in Fig. 4b, and the area under the curve c_l over $[u_f, u_i]$, as shown in Fig. 5b.

The terms W^+ and W^- are evaluated as:

$$W^+ = W_a^+ + W_b^+ + W_c^+ + W_d^+, \tag{13}$$

$$W^- = W_a^- + W_b^- + W_c^- + W_d^-, \tag{14}$$

whereas W_u and W_l are given by:

$$W_u = W_a^+ + W_b^+ + W_c^+, \tag{15}$$

$$W_l = W_a^- + W_b^- + W_c^-. \tag{16}$$

In turn, the expressions of W_a^+, W_b^+, W_c^+, and W_d^+ are:

$$W_a^+ = \frac{\beta_1^+}{\beta_2^+}\left(e^{\beta_2^+ u_f} - e^{\beta_2^+ u_i}\right) - \beta_1^+(u_f - u_i), \tag{17a}$$

$$W_b^+ = 2\gamma_1^+\left\{\frac{2\ln\left[e^{-\gamma_2^+(u_f-\gamma_3^+)}+1\right]}{\gamma_2^+} - \frac{2\ln\left[e^{-\gamma_2^+(u_i-\gamma_3^+)}+1\right]}{\gamma_2^+} + (u_f - u_i)\right\}, \tag{17b}$$

$$W_c^+ = \frac{k_b^+}{2}(u_f^2 - u_i^2) + f_0^+(u_f - u_i), \tag{17c}$$

$$W_d^+ = +\frac{1}{(\alpha^+)^2}\, e^{-\alpha^+(\bar{u}^+ - u_j^+)}\left[\alpha^+(u_f - u_i)e^{-\alpha^+ u_j^+} + e^{-\alpha^+ u_f} - e^{-\alpha^+ u_i}\right], \tag{17d}$$

whereas the expressions of W_a^-, W_b^-, W_c^-, and W_d^- are:

$$W_a^- = \frac{\beta_1^-}{\beta_2^-}\left(e^{\beta_2^- u_f} - e^{\beta_2^- u_i}\right) - \beta_1^-(u_f - u_i), \tag{18a}$$

$$W_b^- = 2\gamma_1^-\left\{\frac{2\ln\left[e^{-\gamma_2^-(u_f-\gamma_3^-)}+1\right]}{\gamma_2^-} - \frac{2\ln\left[e^{-\gamma_2^-(u_i-\gamma_3^-)}+1\right]}{\gamma_2^-} + (u_f - u_i)\right\}, \tag{18b}$$

$$W_c^- = \frac{k_b^-}{2}(u_f^2 - u_i^2) - f_0^-(u_f - u_i), \tag{18c}$$

$$W_d^- = -\frac{1}{(\alpha^-)^2}\, e^{-\alpha^-(\bar{u}^- + u_j^-)}\left[\alpha^-(u_f - u_i)e^{+\alpha^- u_j^-} - e^{+\alpha^- u_f} + e^{+\alpha^- u_i}\right]. \tag{18d}$$

It is important to note that $W_a^+ = 0$ and $W_a^- = 0$ ($W_b^+ = 0$ and $W_b^- = 0$) when the parameters β_2^+ and β_2^- (γ_2^+ and γ_2^-) are, respectively, set equal to zero, as it happens for specific shapes of the hysteresis loops [6, 7].

3.3 *Rate-Independent Hysteretic Work Associated with a Single Loop*

Figure 6a illustrates a symmetric and pinched hysteresis loop that is limited by two curves (dash red line) having no inflection point; such a hysteretic behavior is typical of the tested pressurized sand damper, as shown in Sect. 2.

In particular, the hysteresis loop in Fig. 6a has been obtained by applying a sinusoidal displacement, having unit amplitude and frequency, and by employing the VRM parameters listed in Table 1. Note that in such a table the parameters selected for the generic loading (unloading) phase are those belonging to the row associated with the + (−) sign of the velocity $\dot{u}$ specified in the first column.

The related rate-independent hysteretic work, representing the area enclosed by the hysteresis loop, as illustrated in Fig. 6b, has been computed as follows:

$$W_{ri} = W_a^+ + W_b^+ + W_c^+ + W_d^+ + W_a^- + W_b^- + W_c^- + W_d^-, \tag{19}$$

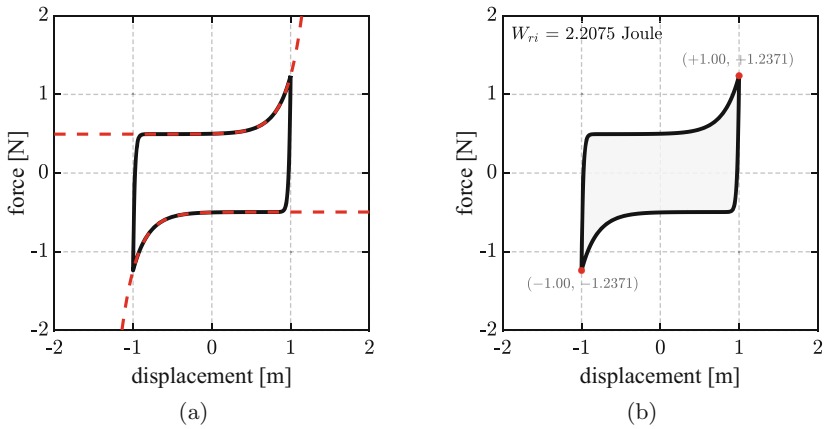

Fig. 6 Hysteresis loop simulated by using the VRM parameters in Table 1 (**a**) and related rate-independent hysteretic work (**b**)

Table 1 VRM parameters adopted for simulating the hysteresis loop in Fig. 6

	k_b	f_0	α	β_1	β_2	γ_1	γ_2	γ_3
sgn($\dot{u}$)	[N/m]	[N]	[1/m]	[N]	[1/m]	[N]	[1/m]	[m]
+	0	0.5	50	0.005	5	0	0	0
−	0	0.5	50	−0.005	−5	0	0	0

where W_a^+, W_b^+, W_c^+ (W_a^-, W_b^-, W_c^-) have been evaluated by using Eqs. (17a)–(17c) (Eqs. (18a)–(18c)) after setting $u_i = -1.00$ and $u_f = +1.00$ ($u_i = +1.00$ and $u_f = -1.00$), whereas W_d^+ (W_d^-) has been calculated by adopting Eq. (17d) (Eq. (18d)) after assuming $u_i = -1.00$ and $u_f = u_j^+$ ($u_i = +1.00$ and $u_f = u_j^-$). The abscissa u_j^+ (u_j^-) has been computed by employing Eq. (7) (Eq. (8)) with $u_P = -1.00$ and $f_P = -1.2371$ ($u_P = +1.00$ and $f_P = +1.2371$).

3.4 Parameter Sensitivity Analysis

Figure 7 shows how the shape of the reference hysteresis loop (Fig. 7a), simulated by adopting the parameters given in Table 1, changes as a function of the relevant nonzero model parameters, that is, f_0^+ (Fig. 7b), α^+ (Fig. 7c), β_1^+ and β_2^+ (Fig. 7d).

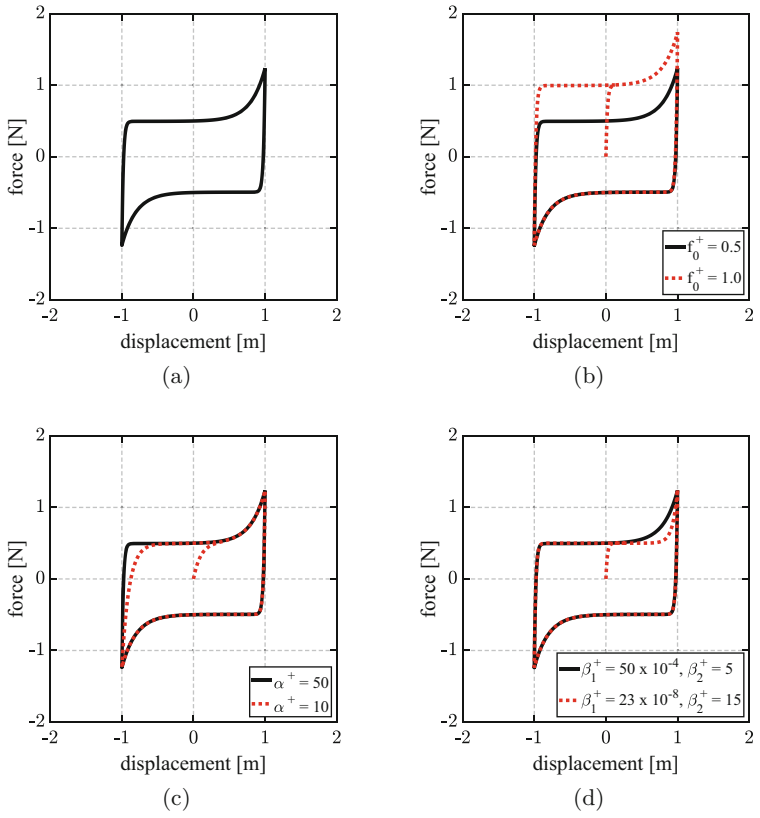

Fig. 7 Parameter sensitivity analysis: reference hysteresis loop (**a**) and its modifications as a function of the parameters f_0^+ (**b**), α^+ (**c**), β_1^+ and β_2^+ (**d**)

Since the influence of the model parameters f_0^-, α^-, β_1^-, and β_2^-, which characterize the generic unloading phase, is similar to the presented one, the related figures are omitted for brevity.

4 Simulation of Experimental Hysteresis Loops

Figure 8a (b) compares the symmetric and pinched experimental hysteresis loops, characterizing the cyclic response of the sand damper tested by applying a sinusoidal axial displacement having amplitude of 40 mm and frequency of 0.2 Hz under the effect of a pressure p of 1 MPa (4 MPa), with those simulated by using the VRM. The adopted model parameters are listed in Table 2.

The amount of work performed by the rate-independent hysteretic force in one cycle of applied harmonic displacement, evaluated by using Eq. (19), is equal to 1245.3 Joule (4231.9 Joule).

The very good agreement between analytical and experimental results demonstrates the capability of the VRM to accurately predict the experimental hysteresis loops exhibited by the tested device at different values of pressure.

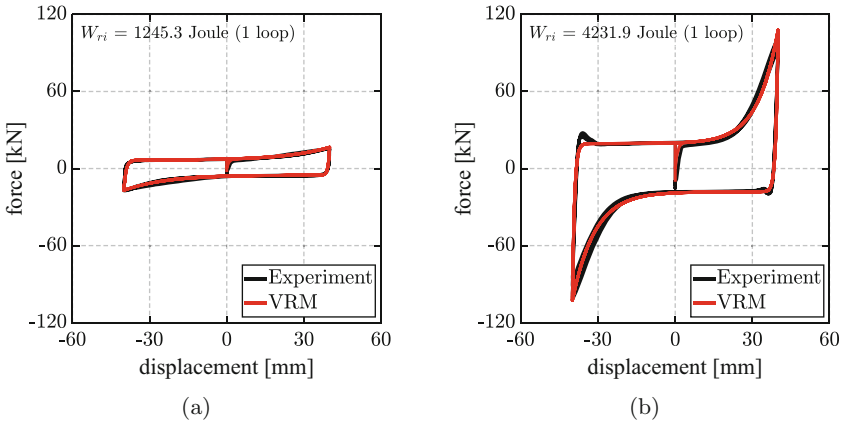

Fig. 8 Experimental hysteresis loops versus simulated ones obtained by using the VRM parameters given in Table 2: $p = 1$ MPa (**a**) and $p = 4$ MPa (**b**)

Table 2 VRM parameters adopted for simulating the hysteresis loops in Fig. 8

Fig.	sgn($\dot{u}$)	k_b [kN/mm]	f_0 [kN]	α [1/mm]	β_1 [kN]	β_2 [1/mm]	γ_1 [kN]	γ_2 [1/mm]	γ_3 [mm]
8a	+	0	7.4	1.2	1	0.058	0	0	0
	−	0	6.0	1.8	−1	−0.062	0	0	0
8b	+	0	20	1.2	0.55	0.127	0	0	0
	−	0	19	1.2	−0.85	−0.115	0	0	0

5 Conclusions

We have briefly presented the typical experimental response of a pressurized sand damper tested by Makris et al. [5].

To accurately reproduce its symmetric and pinched hysteresis loops, a recently formulated hysteresis model [6, 7] has been adopted.

The comparison between analytical and experimental hysteresis loops confirms the potentiality of the novel model and its capability of accurately simulating complex hysteresis loops.

References

1. Soong, T.T., Spencer, Jr. B.F.: Supplemental energy dissipation: state-of-the-art and state-of-the-practice. Eng. Struct. **24**(3), 243–259 (2002)
2. Nuzzo, I., Losanno, D., Caterino, N., Serino, G., Bozzo Rotondo, L.M.: Experimental and analytical characterization of steel shear links for seismic energy dissipation. Eng. Struct. **172**, 405–418 (2018)
3. Losanno, D., De Domenico, D., Madera-Sierra, I.E.: Experimental testing of full-scale fiber reinforced elastomeric isolators (FREIs) in unbounded configuration. Eng. Struct. **260**, 114234 (2022)
4. Vaiana, N., Napolitano, C., Rosati, L.: Some recent advances on the modeling of the hysteretic behavior of rate-independent passive energy dissipation devices. In: COMPDYN Proceedings (2021). https://doi.org/10.7712/120121.8648.18626
5. Makris, N., Palios, X., Moghimi, G., Bousias, S.: Pressurized sand damper for earthquake and wind engineering: Design, testing, and characterization. J. Eng. Mech. **147**(4), 04021014 (2021)
6. Vaiana, N., Rosati, L.: Classification and unified phenomenological modeling of complex uniaxial rate-independent hysteretic responses. Mech. Syst. Sig. Process. **182**, 109539 (2023)
7. Vaiana, N., Capuano, R., Rosati, L.: Evaluation of path-dependent work and internal energy change for hysteretic mechanical systems. Mech. Syst. Sig. Process. **186**, 109862 (2023)
8. Vaiana, N., Sessa, S., Marmo, F., Rosati, L.: A class of uniaxial phenomenological models for simulating hysteretic phenomena in rate-independent mechanical systems and materials. Nonlinear Dyn. **93**(3), 1647–1669 (2018)
9. Vaiana, N., Sessa, S., Rosati, L.: A generalized class of uniaxial rate-independent models for simulating asymmetric mechanical hysteresis phenomena. Mech. Syst. Sig. Process. **146**, 106984 (2021)
10. Vaiana, N., Losanno, D., Ravichandran, N.: A novel family of multiple springs models suitable for biaxial rate-independent hysteretic behavior. Comput. Struct. **244**, 106403 (2021)

Modified Bouc-Wen Model with Damage and Flexibility Increase for the Dynamic Analysis of Masonry Walls

Alessandra Paoloni, Domenico Liberatore, and Daniela Addessi

1 Introduction

A large part of the world's architectural heritage is built using traditional materials. Among these, masonry is the most widely spread and is still nowadays largely studied. Its fascinating and complex behavior, due to the coupling of bricks or blocks with mortar through interfaces, together with the high uncertainty caused by the failure mechanisms occurring during cyclic and dynamic actions, has deserved the application of numerous formulations to reproduce its strongly nonlinear mechanical response.

Many constitutive laws can be found in the literature to numerically reproduce masonry structural behavior [1]. Among many others, the hysteretic model proposed in first instance by Bouc [2], although it was formulated in the 1970s, and then modified by Wen [3], is still widely used to describe the cyclic response of various materials. This is especially due to its versatility and the capability of describing different behaviors through a reduced number of parameters, which also have a physical meaning [4]. However, a fundamental request in modern engineering is to be able to capture strength and stiffness degradation, especially when studying materials that are subjected to damaging processes during cyclic loadings (e.g., harmonic loadings, ground motion records), as masonry is. The Bouc-Wen hysteresis, in fact, has proven to be a reliable tool for the representation

A. Paoloni (✉) · D. Addessi
Department of Structural and Geotechnical Engineering, Sapienza University of Rome, Rome, RM, Italy
e-mail: alessandra.paoloni@uniroma1.it; daniela.addessi@uniroma1.it

D. Liberatore
Department of History, Representation and Restoration of Architecture, Sapienza University of Rome, Rome, RM, Italy
e-mail: domenico.liberatore@uniroma1.it

© The Author(s), under exclusive license to Springer Nature Switzerland AG 2024

W. Lacarbonara (ed.), *Advances in Nonlinear Dynamics, Volume III*, NODYCON Conference Proceedings Series, https://doi.org/10.1007/978-3-031-50635-2_29

of the cyclic response of masonry when modifications are introduced to account for the onset and propagation of damage [5, 6].

The formulation already presented in [5], which accounts for damage by means of a scalar variable depending on the dissipated energy, is here enriched by the introduction of a flexibility increase term. This latter also depends on the dissipated energy and is ruled by a scalar variable that regulates the rate of stiffness degradation, for a more accurate description of experimental tests. This model was proven to be thermodynamically admissible in the sense that the dissipated energy is a nondecreasing function. This condition is instead violated by similar models presented in the literature [7, 8].

A macroelement, originally formulated in [6], is then proposed, which uses the modified Bouc-Wen law to introduce the nonlinear mechanisms of masonry in a shear link and two lumped flexural hinges. To model the flexural behavior that characterizes slender panels, pinching is also taken into account thanks to the introduction of a dedicated device.

To investigate the dynamic behavior of masonry structures, considering that the evolution of damage definitely affects the structural dynamic properties [9], in this chapter, the formulation of the macroelement is enriched with the introduction of dynamic terms in the analysis. Regarding the dynamic formulation, the lumped mass matrix and classical Rayleigh damping are implemented consistently with the equilibrated force-based approach adopted for the formulation of the macroelement.

A slender panel is then analyzed to investigate the behavior of the proposed constitutive law in the dynamic field.

2 Bouc-Wen Hysteresis with Damage and Flexibility Increase

In the modified Bouc-Wen hysteresis proposed in [5], the presence of damage is taken into account thanks to the introduction of a scalar damage variable D, which affects the evaluation of the hysteretic force. This variable ranges between [0, 1), with 0 representing the initial undamaged state and 1 the fully damaged state [10]. The total restoring force is then evaluated as the composition of the elastic force, F^{el}, and the hysteretic force, F^{h}, as follows:

$$F = F^{el} + F^{h} = a\ k\ v_y\ u + (1–D)\ \ (1–a)\ \ k\ v_y\ z \tag{1}$$

where k is the system initial stiffness, a is the ratio between the asymptotic post-yielding stiffness and the initial tangent stiffness, v_y is the maximum absolute elastic displacement, u is the nondimensional displacement, and z is the hysteretic variable having the meaning of nondimensional elastic displacement. The evolution of this latter remains unchanged with respect to the classical Bouc-Wen hysteresis and is ruled through the following differential equation:

$$\frac{\mathrm{d}z}{\mathrm{d}u} = A - \left[\beta \,\mathrm{sign}\,(z\dot{u}) + \gamma\right] |z|^n \tag{2}$$

In this latter, A is a redundant parameter equal to 1, and n rules the passage from the elastic to the post-yielding part of the curve (the greater n, the more abrupt the transition), while β and γ affect the shape of the cycle, making it more bulged ($\beta > \gamma$) or S- shaped ($\beta < \gamma$). It can be shown that $\beta + \gamma = 1$, with $\beta \geq \gamma$ for thermodynamic admissibility [11], and $\beta \leq \gamma$ to satisfy Drucker's postulate, resulting in $\beta = \gamma = ½$, implying that the unloading branches must be linear elastic. The evolution of the damage variable depends on the dissipated energy, U^h, following the approach suggested by [7, 12], by means of a parameter δ_D that regulates the rate of degradation:

$$D = \delta_D \, U^h \tag{3}$$

As D is a nondimensional variable, δ_D has the dimension of the inverse of an energy.

The evaluation of the elastic displacement is also modified with the introduction of an additional term that depends on the dissipated energy and the parameter δ_K, increasing the value of the variable:

$$v = v_y \left[\left(1 + \delta_K \, U^h\right) z + u_p\right] \tag{4}$$

Also, δ_K has the dimension of the inverse of an energy. While δ_D can only assume positive values, δ_K can range from positive to the negative value of $-\delta_D$, representing pure strength degradation.

The evaluation of the dissipated energy U^h is modified with respect to that presented in [5] in order to account for δ_K. It governs the stiffness degradation, along with the parameter δ_D, but does not affect the term driving the strength decay:

$$U^h = \frac{1}{\delta_D}\left\{1 - \exp\left[-2c\delta_D \int_0^{u^p} \frac{z}{1 - c\,(\delta_D + \delta_K)\, z^2} d\tilde{u}^p\right]\right\} \tag{5}$$

where:

$$c = \frac{1}{2} \, k \, {v_y}^2 \;\; (1\text{–}a) \tag{6}$$

A more complete description of the flexibility increase formulation and the bounds of the parameters can be found in [13].

3 Macroelement Dynamic Formulation

The Bouc-Wen hysteresis modified with damage and flexibility increase (Fig. 1a) is introduced in a force-based beam macroelement, with the aim of describing the in-plane structural behavior of masonry walls. To achieve this, the beam element proposed in [14] and modified in [6] is considered, thanks to the possibility of implementing the constitutive law in a lumped hinges approach. The macroelement is composed of an elastic beam element in series with two lumped flexural hinges and a shear link, which use the modified Bouc-Wen model to describe the nonlinear mechanisms characterizing masonry response. To better describe the flexural mechanisms, a nonlinear elastic and an elastic negative device are considered in parallel and in series with the Bouc-Wen model, respectively, aiming to represent pinching and the high initial stiffness of flexural hinges, in order not to perturbate the flexural stiffness of the panel (Fig. 1b). Details of the formulation can be found in [6].

Since the existing model can describe only the cyclic static behavior, an enhancement of the formulation is made by introducing the possibility to reproduce the response to dynamic excitations. The discrete dynamic equilibrium equations governing the finite element solution are written as:

$$\mathbf{M}\ddot{\mathbf{u}} + \mathbf{C}\dot{\mathbf{u}} + \mathbf{P}^{\mathbf{int}}(\mathbf{u}) = \mathbf{P}^{\mathbf{ext}} \tag{7}$$

In Eq. (7), $\mathbf{u}$, $\dot{\mathbf{u}}$, and $\ddot{\mathbf{u}}$ are the global nodal displacement, velocity, and acceleration vectors, respectively, where the latter two are evaluated as the derivatives of the first vector with respect to time. $\mathbf{P}^{\text{ext}}$ is the external force vector, while $\mathbf{P}^{\text{int}}(\mathbf{u})$ is the internal force vector that represents the nonlinear structural response.

Consistently with the force-based approach, the global mass matrix $\mathbf{M}$ is evaluated by assembling the element mass matrix. This latter is a diagonal matrix that contains the contributions of the translational and rotational masses lumped at each node. The damping matrix $\mathbf{C}$ is evaluated through the Rayleigh formulation,

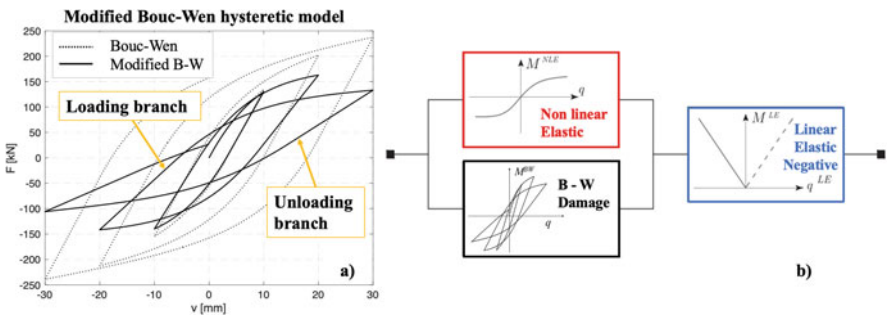

Fig. 1 Modified Bouc-Wen model with damage and flexibility increase compared to the classical Bouc-Wen hysteresis (**a**); structure of the flexural hinge of the macroelement (**b**)

being a linear combination of the mass and stiffness matrices by means of the coefficients a_0 and a_1, selected equal to 5.3 s^{-1} and 0.00019 s, respectively. These latter are calculated considering a 5% damping ratio and the elastic angular frequency of the system, with the panel being a single degree of freedom system.

The formulation is implemented in the finite element analysis program FEAP [15], where a Newmark algorithm, with adopted parameters of β equal to 0.25 and γ equal to 0.5 for an unconditionally stable integration procedure, is used to solve the dynamic equations integrated in time, together with a Newton-Raphson iterative procedure to solve the nonlinear problem at each time step.

4 Results and Discussion

The dynamic behavior of a slender unreinforced masonry wall is investigated using the model presented in the previous sections, considering different types of excitations. The wall is characterized by a height L_e equal to 3 m and a base length l equal to 1 m, giving an aspect ratio L_e/l equal to 3, while the thickness is equal to 0.25 m. Referring to the walls analyzed at the Joint Research Centre of Ispra [16], the masonry is considered to be made of bricks and lime mortar, and the wall is subjected to a vertical load of 150 kN. The mechanical parameters of the material, namely Young's modulus E, shear modulus G, compressive f_c and shear f_v strength of masonry, and the density mass ρ, reported in Table 1, are assumed from [16, 17], while the maximum absolute elastic displacement v_y required for the hinges is evaluated following the procedure described in [18, 19].

The parameters adopted for the flexural and shear hinges are reported in Table 2. Although the values are also reported for the shear link, the latter is not relevant for the analysis, as the major contributions for a slender wall are due to the flexural hinges.

To highlight the main characteristics of the dynamic response, sinusoidal horizontal excitations are applied at the base of the wall. These are derived from acceleration histories whose equation is:

$$\ddot{u}(t) = U \ \sin\left[\Omega(t)t\right] \tag{8}$$

Table 1 Mechanical parameters of the masonry wall

E	G	f_c	f_v	ρ
kN/m^2	kN/m^2	kN/m^2	kN/m^2	t/m^3
1700×10^3	300×10^3	6200	225	18

Table 2 Parameters of the Bouc-Wen model

Flexural hinges			Shear hinges		
a	δ_D	δ_K	a	δ_D	δ_K
–	kJ^{-1}	kJ^{-1}	–	kJ^{-1}	kJ^{-1}
0.05	10	10	0.05	10	10

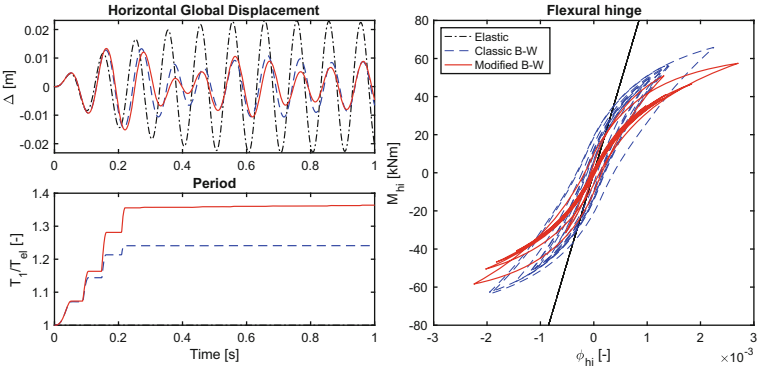

Fig. 2 Response of the slender panel to the excitation with a fixed ratio $\Omega/\omega_1 = 0.95$ and $U/g = 0.3$

Three different cases are analyzed. In the first one, the ratio between the frequency of the excitation, Ω, and the frequency of the wall, ω_1, is set equal to 0.95, close to the resonance condition. In the second and third cases, Ω is not fixed with respect to ω_1, but in one case increases, while in the other decreases, referred to as increasing and decreasing sweep respectively, and is evaluated considering that the period of the excitation varies between 0.2 and 1.5 times the period of the wall. The amplitude ratio of the three sinusoidal excitations is set to $U/g = 0.3$, where g is the gravity acceleration. For the evaluation of the Rayleigh damping matrix, a damping factor equal to 5% is assumed.

A modal analysis is performed at each step of the analysis in order to evaluate the variation of the period in the presence of damage and flexibility increase, calculating the period considering the secant stiffness at each time step.

The response of the wall clearly highlights how the presence of damage and flexibility increase modifies the hysteretic behavior. Figures 2, 3, 4, 5, and 6 show the global displacement of the panel and the variation of the period with respect to the elastic period in time and the behavior of the flexural hinge in terms of moment and rotation. In all the cases, as expected, the period of the case with degradation is greater than the period of the classical Bouc-Wen hysteresis.

Figure 2 shows the response to the excitation with a ratio Ω/ω_1 equal to 0.95, representing the global displacement, the period normalized with respect to the initial elastic period and the response of the flexural hinge at the base of the panel. The modified Bouc-Wen hysteresis (red) is compared to the classical Bouc-Wen (dashed blue) and the elastic case (dashed black). In the first cycles the maximum displacement of the case with degradation departs from the elastic displacement and consequently its period increases, reaching higher values than those of the classical Bouc-Wen. Considering that the period is evaluated from the secant stiffness, the maximum value of period is reached in correspondence of the maximum displacement experienced, while in the unloading branches the period remains constant. In the following cycles the displacement curves almost

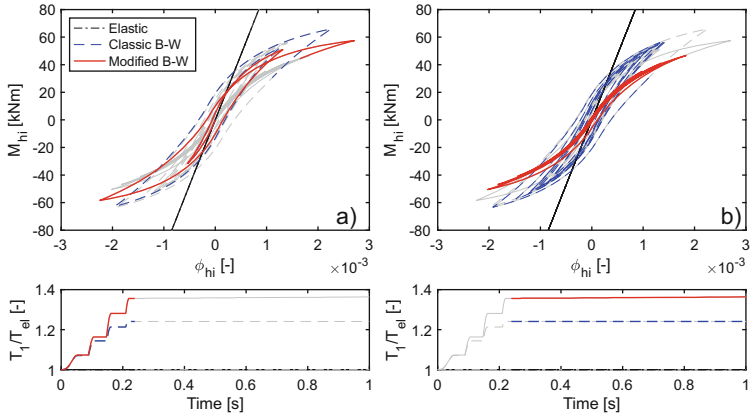

Fig. 3 Response of the slender panel to the excitation with fixed ratio $\Omega/\omega_1 = 0.95$ and $U/g = 0.3$. Zoom on the first cycles (left), zoom on the following cycles (right)

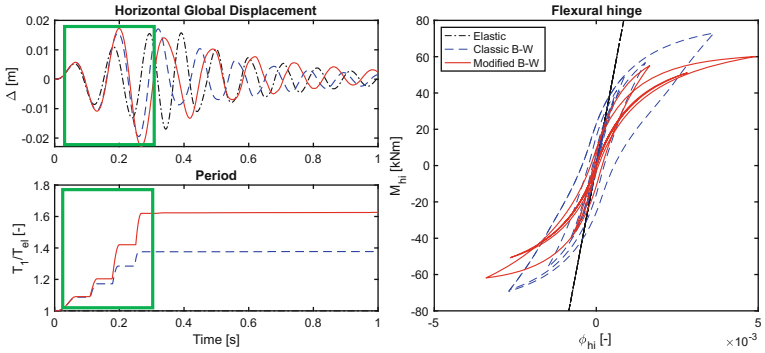

Fig. 4 Response of the slender panel to the sweep excitation with increasing ratio Ω/ω_1 and $U/g = 0.3$

reach the resonance condition in all the cases. In Fig. 3a, the first cycles of this analysis are highlighted. The case with damage and flexibility increase shows the effect of degradation in the hinge response: although the first cycle, in the third quadrant, is almost overlapped with the classical Bouc-Wen curve, from the second cycle on, both the strength and stiffness degradation affect the moment, increasing the rotation experienced at each cycle and consequently the period of the system, which reaches its highest value. The following cycles (Fig. 3b), which reach lower rotation, do not contribute to increasing the period, which, in fact, remains constant. The effect of flexibility increase is evident in the narrowing of the cycles, and the strength degradation can be recognized in the decreasing values of the moment.

Figures 4 and 5 show the results of the excitations with the sweep excitations increasing and decreasing the ratio Ω/ω_1, respectively. In the first case, damage is experienced in the first 0.3 s of the analysis and shows a rapid increase in a shorter

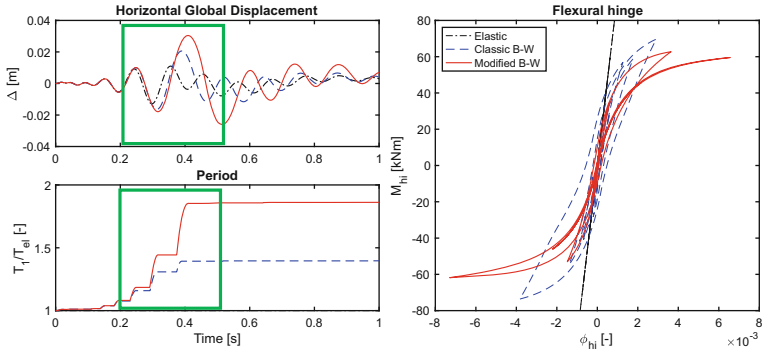

Fig. 5 Response of the slender panel to the sweep excitation with a decreasing ratio Ω/ω_1 and $U/g = 0.3$

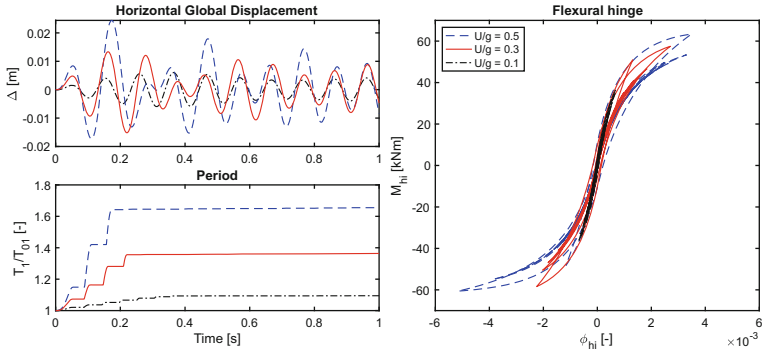

Fig. 6 Response of the slender panel to the excitation with a fixed ratio $\Omega/\omega_1 = 0.95$ and $U/g = 0.1, 0.3, 0.5$

lapse of time, as the widest cycles are experienced at the beginning of the analysis. The amplitude of the following cycles decreases gradually, keeping the period constant. In the flexural hinge response, both strength and stiffness degradation can clearly be distinguished. While the first cycle is almost overlapped with the classical Bouc-Wen model, the following ones are visibly thinner in both the loading and unloading branches. Moreover, the cycles with decreasing amplitude become almost nonlinear elastic, as the dissipation capacity of the hinge is depleted.

In the decreasing excitation, the wider cycles, as well as the damage, are experienced later in the analysis, between 0.3 and 0.5 s approximately. This allows to recognize how the flexibility increase shrinks the cycles compared to the classical Bouc-Wen model, reaching higher rotation and higher period, which is almost twice the elastic period.

In order to study how the amplitude of the excitation affects the evolution of damage, two additional sinusoidal acceleration histories are considered. Starting from the one with Ω/ω_1 equal to 0.95, the response of the system with both damage and flexibility increase to amplitude ratio U/g equal to 0.1 and 0.5, respectively, is evaluated and compared to the case with U/g equal to 0.3. The results show, as expected, that the response to the higher excitation reaches higher displacements. In addition, it is worth noting that when the ratio U/g is lower, even though the damaged period has smaller values compared to the other cases, the increase of the period is more spread over time.

This is caused by the circumstance that the maximum displacement experienced is reached by the system later, and more gradually, suggesting a more spread distribution of the damage over the wall. On the contrary, the case with amplitude $U/g = 0.5$ shows a more rapid increase in the period in a shorter time interval, as the maximum displacement is reached in the second cycle of the analysis.

5 Conclusions

In this chapter, the classic Bouc-Wen model, already modified with the introduction of damage, is enhanced with the addition of flexibility increase, which affects the loading and unloading branches of the response curve. This latter was described as an additional term in the evaluation of the elastic displacement which depends on the dissipated energy and increases the rate of stiffness degradation. The constitutive law formulated was then used in a force-based macroelement for the analysis of masonry panels. The macroelement was also modified, with respect to previously proposed formulations, allowing to perform dynamic analyses. A lumped mass approach and Rayleigh damping were considered.

The effect of damage and flexibility increase was investigated with respect to the classical Bouc-Wen model and the elastic case, with the aim of examining the performance of the model in the dynamic field, especially focusing on the influence of damage mechanisms on the dynamic characteristics of the structural response. Damage caused an increase in the period, while flexibility increase caused a thinning of the cycles experienced during the analysis. The variation of the amplitude of the acceleration history showed that the greater U/g, the more rapid the degradation, and the higher the period. On the opposite, the smaller U/g, the softer the degradation, and the smaller the period, which is more spread over time.

Ongoing developments are being carried out regarding the application of the presented macroelement for the analysis of masonry buildings under seismic actions, aiming at extending the macroelement to 3D structural cases in order to model both in-plane and out-of-plane failure mechanisms typical of masonry panels.

References

1. Sacco, E., Addessi, D., Sab, K.: New trends in mechanics of masonry. Meccanica. **53**(7), 1565–1569 (2018)
2. Bouc, R.: A mathematical model for hysteresis. Acta Acust. United Acust. **24**(1), 16–25 (1971)
3. Wen, Y.K.: Method for random vibration of hysteretic systems. J. Eng. Mech. Div. Proc. ASCE. **102**, 249–263 (1976)
4. Sivaselvan, M.V., Reinhorn, A.M.: Hysteretic models for deteriorating inelastic structures. J. Eng. Mech. **126**(6), 633–640 (2000)
5. Liberatore, D., Addessi, D., Sangirardi, M.: An enriched Bouc-Wen model with damage. Eur. J. Mech. A Solids. **77**, 103771 (2019)
6. Sangirardi, M., Liberatore, D., Addessi, D.: Equivalent frame modelling of masonry walls based on plasticity and damage. Int. J. Archit. Heritage. **13**(7), 1098–1109 (2019)
7. Baber, T.T., Noori, M.N.: Random vibration of degrading, pinching systems. J. Eng. Mech. **111**(8), 1010–1026 (1985)
8. Baber, T.T., Noori, M.N.: Modeling general hysteresis behavior and random vibration application. J. Vib. Acoust. Stress. Reliab. **108**(4), 411–420 (1986)
9. Gatta, C., Addessi, D., Vestroni, F.: Static and dynamic nonlinear response of masonry walls. Int. J. Solids Struct. **155**, 291–303 (2018)
10. Lemaitre, J., Chaboche, J.-L.: Mechanics of Solid Materials. Cambridge University Press (1994)
11. Charalampakis, A.E., Koumousis, V.K.: On the response and dissipated energy of Bouc – Wen hysteretic model. J. Sound Vib. **309**, 887–895 (2008)
12. Baber, T.T., Wen, Y.K.: Random vibration of hysteretic, degrading systems. J .Eng. Mech. Div. **107**(6), 1069–1087 (1981)
13. Liberatore, D., Addessi, D., Paoloni, A.: (Submitted) Hysteretic models with degradation
14. Addessi, D., Liberatore, D., Masiani, R.: Force-based beam finite element (FE) for the pushover analysis of masonry buildings. Int. J. Archit. Heritage. **9**, 231–243 (2015)
15. Taylor, R.L.: FEAP-A Finite Element Analysis Program, Version 8.5. Department of Civil and Environmental Engineering, University of California at Berkeley, California (2017)
16. Anthoine, A., Magonette, G., Magenes, G.: Shear-compression testing and analysis of brick masonry walls. In: Proceedings of the 10th European conference on earthquake engineering, Balkema, Rotterdam (The Netherlands), pp. 1657–1662 (1995)
17. Magenes, G., Calvi, G.M.: In-plane seismic response of brick masonry walls. Earthq. Eng. Struct. Dyn. **26**, 1091–1112 (1997)
18. Liberatore, D., Addessi, D., Sangirardi, M.: Nonlinear analysis of masonry walls based on a damage-plastic formulation. In: Aguilar, R., Torrealva, D., Moreira, S., Pando, M.A., Ramos, L.F. (eds.) Structural Analysis of Historical Constructions. RILEM Bookseries, vol. 18. Springer, Cham (2019)
19. NTC. 2018. Italian Building Code for Constructions. (Norme Tecniche per le Costruzioni). D.M. 17th January 2018 – S.O. n. 8, G.U. n. 42; 20th February 2018 [in Italian]

Constrained Green's Function for a Beam with Arbitrary Spring and Nonlinear Spring Foundation

X. Zhao, Q. Wang, W. D. Zhu, and Y. H. Li

1 Introduction

The study of dynamic properties of beams is an important issue [1–4], which has attracted many scholars from the beginning. Various methods have been proposed to study this problem. For example, the mainstream approach is the modal superposition method based on the infinite series expansion [5, 6]. However, the truncation method is inevitably used in the process of modal superposition. Therefore, the modal superposition method is essentially an approximation method. In order to obtain analytical solutions, Green's functions are applied as an analytical tool in various research fields.

Abu-Hilal [7] proposed a method for determining the dynamic response of Euler-Bernoulli beams subjected to distributed and concentrated loads by dynamic Green's functions, and also gave Green's functions for different boundary conditions. Li et al. [8] obtained dynamic Green's functions for forced vibration of Timoshenko beams with damping based on Abu-Hilal and compared classical beam models such as EB, RB, and TB. Han et al. [9] studied the bending-torsion coupled Timoshenko beam and discussed the effect of external load frequency and eccentricity on the Green's function of bending-torsion. Zhao et al. [10] used the Green's function method to study the forced vibration of a Timoshenko double

X. Zhao (✉) · Q. Wang
School of Civil Engineering and Architecture, Southwest Petroleum University, Chengdu, Sichuan, People's Republic of China

W. D. Zhu
Department of Mechanical Engineering, University of Maryland, Baltimore County, Baltimore, MD, USA

Y. H. Li
School of Mechanics and Engineering, Southwest Jiaotong University, Chengdu, Sichuan, People's Republic of China

© The Author(s), under exclusive license to Springer Nature Switzerland AG 2024

W. Lacarbonara (ed.), *Advances in Nonlinear Dynamics, Volume III*, NODYCON Conference Proceedings Series, https://doi.org/10.1007/978-3-031-50635-2_30

beam system under axial compressive loading and analyzed the interaction of the double beam structure and the effect of axial tension. Albassam [11] studied the vibration of flexible beams by dynamic Green's functions and found the steady-state vibration at the desired point could be eliminated using feedback control forces. Chen [12] studied the steady-state dynamics of axially forced Timoshenko beams with different boundary conditions.

In the coupled field, Kidawa-Kukla [13] studied the thermally induced vibration of beams by Green's function and analyzed the effect of moving heat sources on the transverse vibration of beams. Williams [14] studied the axisymmetric vibration of a tank filled with elastic fluid and discussed the frequency of ground excitation and the effect of various geometric and material parameters on the hydrodynamic pre-pressure distribution. Li et al. [15] proposed a Green's function solution for the forced vibration of a pipeline based on two parameter-based Green's function solutions for forced vibration of oil pipelines, and discussed the effects of boundary stiffness, foundation parameters, and geometric parameters on the natural frequency and critical flow velocity. Fan et al. [16] investigated the vibration characteristics of a drill pipe under rotational motion and multiple stabilizers by means of Green's functions, and discussed the effects of internal flow velocity, viscous damping coefficient, location of stabilizers, number of stabilizers, and stiffness coefficient of stabilizers on the system; Ghannadiasl [17] solved the dynamic Green's function of forced vibration of a multi-span cracked Euler-Bernoulli beam at the solution and evaluated the effect of the number and location of cracks on the dynamic response of the beam. Li et al. [18] presented the Green's function solution of coupled vibration of a wind turbine blade and analyzed the effects of modal coupling, centrifugal effect, and rotational speed on the natural frequency and mode shape.

In conclusion, the previous Green's function approach focused on the study of various forced vibration problems rather than the free vibration problems. To the authors' knowledge, there are no reports in the literature on constrained Green's functions for arbitrary springs and nonlinear foundation beams. In this chapter, based on the basic equations of forced vibration with and without springs, the corresponding Green's functions of forced vibration are solved by the variable separation technique and Laplace transform, and then the constrained Green's functions with springs are obtained by the superposition principle. The effectiveness of the scheme is verified by numerical calculation, and the influence of the spring on the dynamic characteristics is investigated. In this process, it is concluded that the springs and the foundation not only change the deflection of the beam but also affect the mode.

2 Solution of Green Function with Arbitrary Spring

The Green function method is usually an effective tool for solving forced vibrations. In order to use the superposition principle to obtain the constrained Green's function for any spring as shown in Fig. 1, it is necessary to find the Green's function for

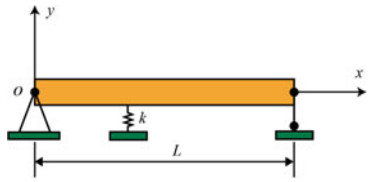

Fig. 1 Beam with arbitrary spring

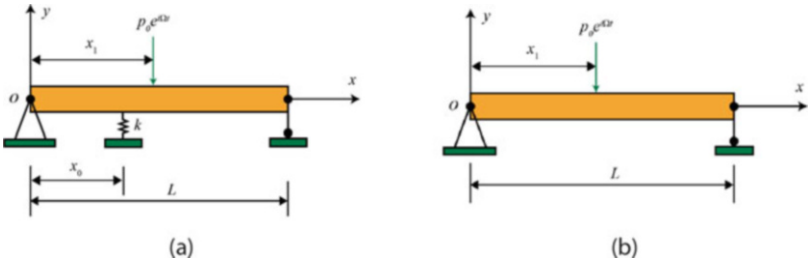

Fig. 2 Beams with spring (**a**) arbitrary and without spring (**b**) subjected to simple harmonic load

forced vibrations with arbitrary spring and the Green function for forced vibrations without a spring as shown in Fig. 2.

2.1 Control Equation with Spring Beam

First, we consider the forced vibration equation with arbitrary spring

$$EIw'''' + \rho A\ddot{w} + Kw\delta(x - x_0) = p(x,t), \tag{1}$$

where, EI and ρA represent the bending module and mass per unit length, $w(x,t)$ is the transverse displacement, K and $\delta(x - x_0)$ are spring stiffness and position, respectively. $p(x,t)$ denotes the load applied on the beam. In addition, the conventional differential symbols are used in (1), more precisely; The dot denotes a derivative with respect to time t, and the prime indicates a derivative with respect to the spatial coordinate x.

2.2 Green's Functions for Steady-State Dynamic Problems

Assume the beam is subjected to a simple harmonic load $p(x,t) = P(x)e^{i\Omega t}$, the corresponding displacement can be expressed as $w(x,t) = W(x)e^{i\Omega t}$. Bringing in Eq. (1) gives the following results

$$EIW'''' - \rho A\Omega^2 W + KW\delta(x - x_0) = p(x,t), \tag{2}$$

We can arrive at

$$W'''' - \frac{\rho A \Omega^2}{EI} W + \frac{K}{EI} \delta (x - x_0) W = \frac{1}{EI} p (x, t), \tag{3}$$

which can be symbolically presented as

$$W'''' + a_1 W + a_2 \delta (x - x_0) W = b_1 p (x, t), \tag{4}$$

Mathematically, $G(x, x_0, x_1)$ are the solutions of the following equations:

$$W'''' + a_1 W + a_2 \delta (x - x_0) W = b_1 \delta (x - x_1), \tag{5}$$

To obtain the corresponding Green's functions, we use the Laplace transform for Eq. (5) and obtain that

$$s^4 W - s^3 W(0) - s^2 W'(0) - s W''(0) - W'''(0) + a_1 W + a_2 e^{-s x_0} W = b_1 e^{-s x_1}, \tag{6}$$

After simple processing,

$$\hat{W} (s, x_0, x_1) = \frac{1}{\left(s^4 + a_1 + a_2 e^{-s x_0}\right)} \left[b_1 e^{-s x_1} + s^3 W(0) + s^2 W'(0) + s W''(0) + W'''(0) \right], \tag{7}$$

Let $e^{-s x_0} = 1 - x_0 s + \frac{1}{2} x_0^2 s^2$, which is a second-order power series expansion. Then we can derive $s^4 + a_1 + a_2 e^{-s x_0} = s^4 + \frac{1}{2} a_2 x_0^2 s^2 - a_2 x_0 s + a_1 + a_2$. To obtain the Laplace inverse transform of $\hat{W} (s, x_0, x_1)$, we assume that

$$s^4 + \frac{1}{2} a_2 x_0^2 s^2 - a_2 x_0 s + a_1 + a_2 = (s - s_1)(s - s_2)(s - s_3)(s - s_4) \tag{8}$$

Then the following result is derived

$$L^{-1} \left(\frac{b_1 e^{-s x_1}}{(s - s_1)(s - s_2)(s - s_3)(s - s_4)} \right) = H (x - x_1) \Big[A_1 (x - x_1) b_1 s_1 + A_2 (x - x_1) b_1 s_2 + A_3 (x - x_1) b_1 s_3 + A_4 (x - x_1) b_1 s_4, \tag{9a}$$

$$L^{-1} \left(\frac{s^3}{(s - s_1)(s - s_2)(s - s_3)(s - s_4)} \right) = A_1(x) s_1^3 + A_2 s_2^3 + A_3(x) s_3^3 + A_4(x) s_4^3, \tag{9b}$$

$$L^{-1}\left(\frac{s^2}{(s-s_1)\,(s-s_2)\,(s-s_3)\,(s-s_4)}\right)=A_1(x)s_1^2+A_2s_2^2+A_3(x)s_3^2+A_4(x)s_4^2, \tag{9c}$$

$$L^{-1}\left(\frac{s}{(s-s_1)\,(s-s_2)\,(s-s_3)\,(s-s_4)}\right)=A_1(x)s_1+A_2s_2+A_3(x)s_3+A_4(x)s_4, \tag{9d}$$

$$L^{-1}\left(\frac{1}{(s-s_1)\,(s-s_2)\,(s-s_3)\,(s-s_4)}\right)=A_1(x)+A_2+A_3(x)+A_4(x). \tag{9e}$$

where, $H(\cdot)$ the Heaviside function and $A_i(i=1,2,\cdots,4)$ are functions specified by

$$\begin{array}{l} A_1(x)=\frac{e^{s_1x}}{(s_1-s_2)(s_1-s_3)(s_1-s_4)},\ A_2(x)=\frac{e^{s_2x}}{(s_2-s_1)(s_2-s_3)(s_2-s_4)} \\ A_3(x)=\frac{e^{s_3x}}{(s_3-s_1)(s_3-s_2)(s_3-s_4)},\ A_4(x)=\frac{e^{s_4x}}{(s_4-s_1)(s_4-s_2)(s_4-s_3)} \end{array} \tag{10}$$

Green's function reads

$$\begin{array}{l} G\,(x,x_0,x_1)=L^{-1}\left(\frac{b_1e^{-sx_1}}{s^4+\frac{1}{2}a_2x_0^2s^2-a_2x_0s+a_1+a_2}\right)+L^{-1}\left(\frac{s_3}{s^4+\frac{1}{2}a_2x_0^2s^2-a_2x_0s+a_1+a_2}\right) \\ W(0)+L^{-1}\left(\frac{s^2}{s^4+\frac{1}{2}a_2x_0^2s^2-a_2x_0s+a_1+a_2}\right)W'(0)+L^{-1}\left(\frac{s}{s^4+\frac{1}{2}a_2x_0^2s^2-a_2x_0s+a_1+a_2}\right) \\ W''(0)+L^{-1}\left(\frac{1}{s^4+\frac{1}{2}a_2x_0^2s^2-a_2x_0s+a_1+a_2}\right)W'''(0) \end{array} \tag{11}$$

In Eq. (11), x_0 represents the spring position and x_1 is the external excitation position. Inserting (9) into (11) yields

$$\begin{array}{l} G\,(x,x_0,x_1)=H\,(x-x_1)\,\phi_1\,(x-x_1)+\phi_2(x)W(0)+\phi_3(x)W'(0) \\ \qquad\qquad +\phi_4(x)W''(0)+\phi_5(x)W'''(0) \end{array} \tag{12}$$

where, $\phi_i(x)(i=1,2,\cdots,5)$ are defined by

$$\begin{array}{l} \phi_1(x)=\sum_{i=4}^{4}A_i(x)b_1,\ \phi_2(x)=\sum_{i=4}^{4}A_i(x)s_i^3,\ \phi_3(x)=\sum_{i=4}^{4}A_i(x)s_i^2, \\ \phi_4(x)=\sum_{i=4}^{4}A_i(x)s_i,\ \phi_5(x)=\sum_{i=4}^{4}A_i(x), \end{array} \tag{13}$$

2.3 Determination of Constants

To determine the constants $W(0)$,$W^{'}(0)$,$W''(0)$ 和$W'''(0)$,it is necessary to calculate the various order derivatives of $\phi_i(x)(i = 1, 2, \cdots, 5)$. As a matter of fact, these derivatives turn out to be

$$\begin{aligned} &\phi_1^k(x) = \sum_{i=4}^{4} s_i^k A_i(x) b_1, \phi_2^k(x) = \sum_{i=4}^{4} A_i(x) s_i^3, \\ &\phi_3^k(x) = \sum_{i=4}^{4} s_i^k A_i(x) s_i^2, \phi_i^k(x) = \sum_{i=4}^{4} s_i^k A_i(x) s_i, \phi_i^k(x) = \sum_{i=4}^{4} s_i^k A_i(x) \end{aligned} \tag{14}$$

By taking the derivative of the Green function (12), the following matrix can be formed

$$\begin{bmatrix} \phi_2(L) & \phi_3(L) & \phi_4(L) & \phi_5(L) \\ \phi_2'(L) & \phi_3'(L) & \phi_4'(L) & \phi_5'(L) \\ \phi_2''(L) & \phi_3''(L) & \phi_4''(L) & \phi_5''(L) \\ \phi_2'''(L) & \phi_3'''(L) & \phi_4'''(L) & \phi_5'''(L) \end{bmatrix} \begin{bmatrix} W(0) \\ W'(0) \\ W''(0) \\ W'''(0) \end{bmatrix} = \begin{bmatrix} W(L) - \phi_1(L - x_1) \\ W'(L) - \phi_1'(L - x_1) \\ W''(L) - \phi_1''(L - x_1) \\ W'''(L) - \phi_1'''(L - x_1) \end{bmatrix} \tag{15}$$

Taking the simply supported boundary condition as an example, from the boundary conditions at $x = 0$, we determine that $W(0) = 0$ and $W''(0) = 0$. Then the coefficient matrix can be simplified as

$$\begin{bmatrix} \phi_3(L) & \phi_5(L) \\ \phi_3''(L) & \phi_5''(L) \end{bmatrix} \begin{bmatrix} W'(0) \\ W'''(0) \end{bmatrix} = \begin{bmatrix} \phi_1(L - x_1) \\ \phi_1''(L - x_1) \end{bmatrix} \tag{16}$$

From (16), we can obtain that

$$\begin{aligned} W'(0) &= \frac{\phi_5(L)\phi_1''(L-x_0) - \phi_1(L-x_0)\phi_5''(L)}{\phi_3(L)\phi_5''(L) - \phi_3''(L)\phi_5(L)} \\ W'''(0) &= \frac{\phi_1(L-x_0)\phi_3''(L) - \phi_1''(L-x_0)\phi_3(L)}{\phi_3(L)\phi_5''(L) - \phi_3''(L)\phi_5(L)} \end{aligned} \tag{17}$$

Thus, Green's function for forced vibration with an arbitrary spring is

$$G_1(x; , x_0, x_1) = H(x - x_1)\phi_{1-1}(x - x_1) + \phi_{3-1}(x) W_1'(0) + \phi_{5-1}(x) W_1'''(0) \tag{18}$$

Based on the literature [8], the springless forced vibration Green's function is found

$$G_2(x, x_1) = H(x - x_1)\phi_{1-2}(x - x_1) + \phi_{3-2}(x) W_2'(0) + \phi_{5-2}(x) W_2'''(0) \tag{19}$$

where,x_1 is still the external excitation position, and

$$\phi_{1-2}(x) = \sum_{i=4}^{4} A_i(x) b_1 s_i, \phi_{3-2}(x) = \sum_{i=4}^{4} A_i(x) s_i^2, \phi_{5-2}(x) = \sum_{i=4}^{4} A_i(x), \quad (20)$$

According to the linear superposition principle, the Constrained Green function with arbitrary spring is

$$G_3(x, x_0) = G_1(x, x_0, x_1) - G_2(x, x_1) = \phi_{3-1}(x) W'(0) + \phi_{5-1}(x) W'''(0) - \phi_{3-2}(x) W'(0) - \phi_{5-2}(x) W'''(0) \quad (21)$$

3 Green Function of Beam with Nonlinear Foundation

Equation (21) is the constrained Green's function with arbitrary spring, the constrained Green function for an equal stiffness base beam is obtained by integrating the spring stiffness K over the interval $[0, L]$.

In addition, if the spring stiffness K is a nonlinear function, as shown in Fig. 3, then Eq. (21) is the constrained Green's function for the nonlinear foundation beam

$$W(x) = \int_0^L K(\xi) G_3(x, \xi) d\xi \quad (22)$$

4 Numerical Results and Discussion

Consider a simply supported EB of height h and length L, who is supported by a spring,as shown in Fig. 1. For the sake of illustration, we introduce the following dimensionless quantities:

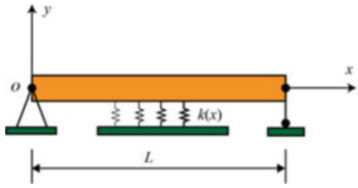

Fig. 3 Nonlinear foundation beam

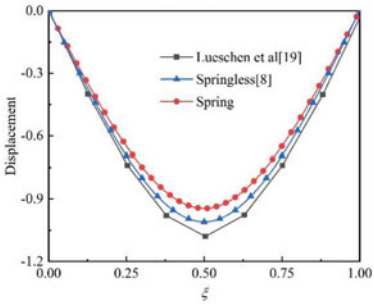

Fig. 4 Forced vibration Green's function with and without spring

$$\xi=\frac{x}{L},\ \Omega_1=\frac{\Omega}{\Omega_0},\ L'=\frac{x_0}{L},\ g_1(\xi,\xi_0,\xi_1)=\frac{G_1(x,x_0,x_1)}{w^s_{\max}},\ g_2(\xi,\xi_1)=\frac{G_2(x,x_1)}{w^s_{\max}},$$
$$g_3(\xi,\xi_0)=\frac{G_3(x,x_0)}{w^s_{\max}}. \tag{23}$$

where, $\Omega_0 = \pi^2\sqrt{EI/\rho A}/L^2$ is the first-order natural frequency of an EB, and $w^s_{\max} = L^3/(48EI)$ is the static deflection at the middle section $x_1 = L/2$. $L^{'}$ is the spring position. In this section, all the numerical calculations are made based on the parameters $E = 1.8 \times 10^{11}$.

4.1 Validity of the Present Solutions

To verify the present solution, the analytical solution is compared with the solutions of Lueschen et al [19] and Zhao et al [8]. As shown in Fig. 4, the solution in this paper agrees with the solution in Ref. and strongly verifies the validity of the present solution. In particular, it should be noted that the parameters involved in the data calculations such as Young's modulus, Poisson's ratio, and beam geometry are taken directly from the reference [8].

4.2 Effect of Arbitrary Spring

Figure 5 shows the forced vibration Green's function with and without spring and the constrained Green's function. Here, the forced vibration Green's function with springs $g_1(\xi, 1/3, 1/2)$ is called the entangled Green's function, which consists of the forced vibration Green's function without springs $g_2(\xi, 1/2)$ and the constrained Green's function $g_3(\xi, 1/3)$. It is worth noting that the constrained Green's function $g_3(\xi, 1/3)$ is the mode. As can be seen from the figure, the Green's function of

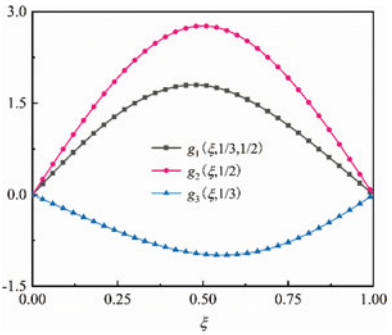

Fig. 5 Forced vibration Green's function and constrained Green's function

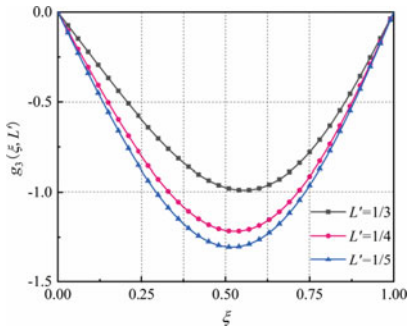

Fig. 6 Constrained Green's function for spring at different positions

forced vibration without spring is subjected to a point load at $L/2$ and the image is symmetric about $\xi = L/2$; however, the symmetry of the Green's function of the forced vibration with a spring is broken by the spring. In addition, once the forced vibration Green's functions with and without springs are determined, the constrained Green's functions are also unique, which serves as an alternative way to solve for the mode.

Figure 6 shows the constrained Green's function for the spring at different positions. It can be seen from the figure that the spring position at $L^{'} = 1/5$ has less effect on the mode of the constrained Green function $g_3(\xi, L^{'})$ and the image is still symmetric about the span; however, when the spring position is at$L^{'} = 1/3$, there is a significant shift, which indicates that the spring with a certain stiffness acts as a support and causes some changes in the mode of the constrained Green function $g_3(\xi, L^{'})$. The mode shape of the foundation beam can be modified by changing the spring position.

Figure 7 illustrates the constrained Green's function for different spring stiffness. It can be seen that when the spring stiffness is EI, the first order mode appears. At $K = 2EI$, the constrained Green's function $g_3(\xi, 2/3)$ exhibits a second-order mode. When $K = 3EI$, the constrained Green's function $g_3(\xi, 2/3)$ returns to the first-order mode again and no longer changes as K increases. This further suggests that the spring stiffness changes not only the shape of the mode, but also the mode order, which is an interesting phenomenon.

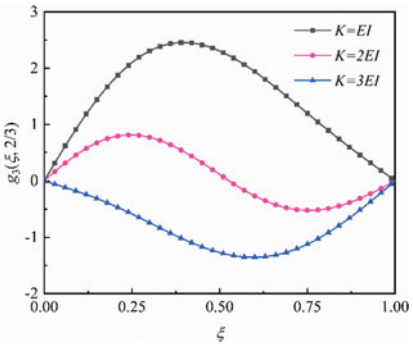

Fig. 7 Constrained Green's function for different spring stiffness

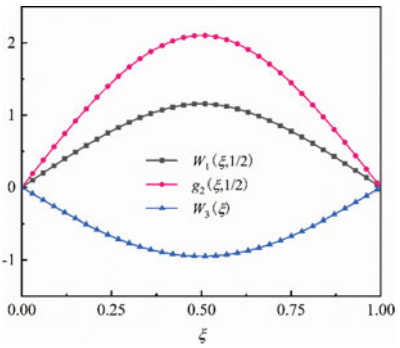

Fig. 8 Green's function for equal stiffness foundation

4.3 Effect of Linear Equal Stiffness Spring Foundation

Figure 8 shows the forced and constrained Green's functions for the equal stiffness spring foundation and the forced Green's function for the springless. From the figure, it can be seen that the springless forced vibration Green's function $g_2(\xi, 1/2)$ is larger than the equal stiffness spring foundation forced vibration Green's function $W_1(\xi)$, which is due to the effect of the equal stiffness spring. Furthermore, when the forced vibrational Green's with springs $W_1(\xi)$ and without springs are $g_2(\xi, 1/2)$ symmetric, the constrained Green's function $W_3(\xi)$ has the same result, which once again demonstrates the entanglement of the constrained Green's function.

4.4 Effect of Nonlinear Spring Foundation

Figure 9 shows the constrained Green's function for the polynomial function nonlinear foundation. In the picture, the second-order mode of the constrained Green's function is shown with variable stiffness spring. At $K = ax + b$, the basis is a linear foundation and the constrained Green's function $W_3(\xi)$ appears as a standard second-order mode. When $K = ax^2 + bx + c$, the foundation is nonlinear

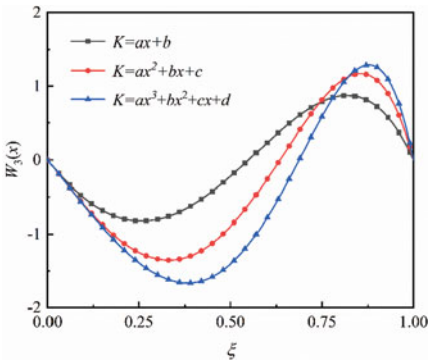

Fig. 9 Constrained Green's functions with polynomial function nonlinear foundation

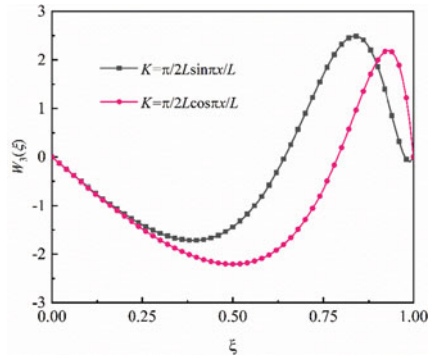

Fig. 10 Constrained Green's functions with trigonometric function nonlinear foundation

and constrains the Green's function $W_3(\xi)$ changes, especially more pronounced at $K = ax^3 + bx^2 + cx + d$, which indicates that the nonlinear foundation affects the mode. After that, there is no significant change in the constrained Green's function as the function order increases.

Figure 10 shows the constrained Green's function for the trigonometric function nonlinear foundation. It can be seen from the figure that the constrained Green's function $W_3(\xi)$ of the sine basis is about to complete the transition out of the third-order to the second-order mode; however, the cosine function presents the second-order mode, which is an interesting phenomenon. In other words,the constrained Green's function $W_3(\xi)$ of the sine function clearly lags behind the cosine function, which is due to the phase difference of the trigonometric function. In conclusion, the phase difference of the nonlinear basis of the trigonometric function has a significant effect on the modalities of the constrained Green's function.

Figure 11 shows the effect of height to length ratio on sinusoidal nonlinear foundation constraint Green's function. From the figure, it can be seen that the mode variation is caused by the height to length ratio on a sinusoidal nonlinear foundation. When the height to length ratio is $\beta = 1/3$, constraint Green's function $W_3(\xi)$ exhibits a first-order mode. At $\beta = 1/5$, $W_3(\xi)$ is a third-order mode. $W_3(\xi)$ shifts from the third mode to the second mode at $\beta = 1/8$. The whole process shows the influence of height to length ratio on the mode, indicating the special significance on the nonlinear foundation constraint Green's function.

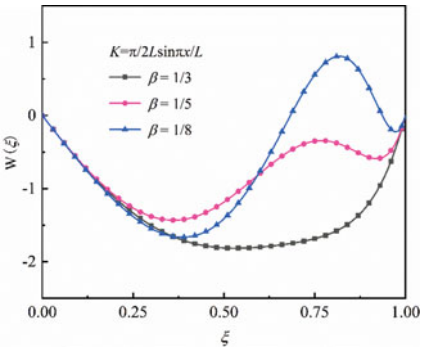

Fig. 11 Effect of height to length ratio on sinusoidal nonlinear foundation constraint Green's function

5 Conclusion

In this chapter, constrained Green's function for a beam with arbitrary spring and nonlinear spring foundation are systematically investigated by Laplace transform and the superposition principle. The solution was verified by numerical calculations. Some important physical parameters are investigated and the following conclusions are drawn

1. The spring has a significant effect on the amplitude reduction of the beam, and the deflection of the beam with the spring is significantly smaller than without the spring.
2. The mode of the constrained Green's function is changed by the stiffness and position of the spring.
3. The polynomial functions nonlinear foundation has significant influence on the constrained Green's function.
4. The phase difference exists in the nonlinear foundation of sine and cosine functions, and the high length ratio causes the mode transformation.

The current constrained Green's function can be applied to investigate a wider range of problems. For example, these results can provide some valuable references for the design of DNA composites and microbeam sensors [20]. In addition, applications in biomechanics [21] can be expected.

References

1. Stojanović, V., Kozić, P., Janevski, G.: Exact closed-form solutions for the natural frequencies and stability of elastically connected multiple beam system using Timoshenko and high-order shear deformation theory. J. Sound Vib. **332**, 563–576 (2013)
2. Piccardo, G., Tubino, F.: Dynamic response of Euler–Bernoulli beams to resonant harmonic moving loads. Struct. Eng. Mech. **44**, 681–704 (2012)
3. Hryniewicz, Z.: Dynamics of Rayleigh beam on nonlinear foundation due to moving load using Adomian decomposition and coiflet expansion. Soil Dyn. Earthq. Eng. **31**, 1123–1131 (2011)

4. Chen, W.R.: Closed-form solutions on bending of cantilever twisted Timoshenko beams under various bending loads. Struct. Eng. Mech. **35**, 261–264 (2010)
5. Thomson, W.T.: Theory of Vibration with Applications. Prentice Hall, Englewood Cliffs (1993)
6. Weaver Jr., W., Timoshenko, S.P., Young, D.H.: Vibration Problems in Engineering. Wiley, New York (1990)
7. Abu-Hilal, M.: Forced vibration of Euler–Bernoulli beams by means of dynamic green functions. J. Sound Vib. **267**, 191–207 (2003)
8. Li, X.Y., Zhao, X., Li, Y.H.: Green's functions of the forced vibration of Timoshenko beams with damping effect. J. Sound Vib. **333**, 1781–1795 (2014)
9. Han, H.S., Cao, D.Q., Liu, L.: Green's functions for forced vibration analysis of bending-torsion coupled Timoshenko beam. Appl. Math. Model. **45**, 621–635 (2017)
10. Zhao, X., Chen, B., Li, Y.H., Zhu, W.D., Nkiegaing, F.J., Shao, Y.B.: Forced vibration analysis of Timoshenko double-beam system under compressive axial load by means of Green's functions. J. Sound Vib. **464**, 115001 (2020)
11. Albassam, B.A.: Vibration control of a flexible beam structure utilizing dynamic Green's function. J. King Saud. Univ. Sci. **33**, 186–200 (2021)
12. Chen, T., Su, G.Y., Shen, Y.S., Gao, B., Li, X.Y., Müller, R.: Unified Green's functions of forced vibration of axially loaded Timoshenko beam: transition parameter. Int. J. Mech. Sci. **113**, 211–220 (2016)
13. Kidawa-Kukla, J.: Application of the Green functions to the problem of the thermally induced vibration of a beam. J. Sound Vib. **262**, 865–876 (2003)
14. Williams, A.N., Moubayed, W.I.: Green's function solution for axisymmetric vibration of flexible liquid-filled storage tanks. Eng. Struct. **12**, 49–59 (1990)
15. Li, M., Zhao, X., Li, X., Chang, X.P., Li, Y.H.: Stability analysis of oil-conveying pipes on two-parameter foundations with generalized boundary condition by means of Green's functions. Eng. Struct. **173**, 300–312 (2020)
16. Fan, J.M., Chang, X.P., Han, D.Z., Li, Y.H.: Vibration characteristics of the drill string subjected to spinning motion and multiple stabilizers by means of Green's functions. Eng. Anal. Bound Elem. **135**, 233–257 (2022)
17. Ghannadiasl, A., Ajirlou, S.K.: Forced vibration of multi-span cracked Euler–Bernoulli beams using dynamic Green function Formulation. Appl. Acoust. **148**, 484–494 (2019)
18. Li, L., Zhang, X.L., Li, Y.H.: Analysis of coupled vibration characteristics of wind turbine blade based on Green's functions. Acta Mech. Solida Sin. **29**, 620–630 (2016)
19. Lueschen, G.G.G., Bergman, L.A., McFarland, D.M.: Green's functions for uniform Timoshenko beams. J. Sound Vib. **194**, 93–102 (1996)
20. Zhang, N.H., Wu, C.X., Yang, Y., Wu, J.Z.: Adjustable frequency shift of laminated DNA microbeam under complex detection conditions by different packaging patterns. Compos. Struct. **292**, 115652 (2022)
21. Goda, I., Assidi, M., Belouettar, S., Ganghoffer, J.F.: A micropolar anisotropic constitutive model of cancellous bone from discrete homogenization. J. Mech. Behav. Biomed. Mater. **16**, 87–108 (2012)

Experimental Characterization and Identification of the Shear Hysteretic Behavior of a Helical Wire Rope Isolator

Raffaele Capuano, Nicolò Vaiana, and Biagio Carboni

1 Introduction

Helical wire rope isolators (HWRIs) are metal devices made up of a stainless steel cable and two aluminum alloy or steel retainer bars where the cable is embedded. They can be effectively adopted for the vibration control of museum artifacts, hospital equipment, electrical transformers, supercomputers, and intermodal containers [1].

To allow for their effective use in actual aerospace, civil, naval, and mechanical engineering applications, experimental campaigns, based on both static and dynamics tests, are typically necessary to fully investigate their complex behavior. The latter may be characterized by symmetric or asymmetric restoring force-displacement hysteresis loops [2–6]. In addition, accurate and computationally efficient hysteretic models are required when nonlinear time history analyses need to be performed, during the design stage, to verify the effectiveness of the adopted devices.

The main aim of this work is to study the experimental behavior exhibited by a HWRI when it is statically tested along one of its principal transverse directions, denominated shear direction. Two recently formulated hysteresis models [7, 8] are adopted to reproduce its complex response identifying the model parameters according to the experimental data and quantifying the accuracy with the mean square error (MSE). The two models are employed to compute the frequency

R. Capuano · N. Vaiana
Department of Structures for Engineering and Architecture, University of Naples Federico II, Naples, Italy

B. Carboni (✉)
Department of Structural and Geotechnical Engineering, Sapienza University of Rome, Rome, Italy
e-mail: biagio.carboni@uniroma1.it

© The Author(s), under exclusive license to Springer Nature Switzerland AG 2024

W. Lacarbonara (ed.), *Advances in Nonlinear Dynamics, Volume III*, NODYCON Conference Proceedings Series, https://doi.org/10.1007/978-3-031-50635-2_31

response curves (FRCs) of a one degree of freedom oscillator constituted by a mass connected to the excited ground by means of the identified HWRI. The FRCs are computed numerically for increasing levels of excitation showing the peculiar behavior of the isolator that exhibits a transition from softening to hardening. The results pave the way to an experimental validation based on dynamical tests.

2 Helical Wire Rope Isolator

Figure 1 shows the tested HWRI, which differs from similar devices, already studied in previous experimental campaigns [5, 9–11], because of the different way in which the stainless steel strands are mounted. Two different strands with helical shape are connected to a top and bottom steel plate. The helix angles of the two strands are different, and for this reason, the hysteretic behavior along the pitch direction is asymmetric. In several applications, a pair number of these HWRIs are used with a symmetric disposition with respect to a central axis in order to obtain a symmetric restoring force.

The force-displacement cycles for increasing amplitudes have been acquired in the Materials and Structures Laboratory of the Department of Structural and Geotechnical Engineering of the Sapienza University of Rome using a Zwick-Roell testing machine in displacement control. Figure 2a shows the acquired force versus time, while Fig. 2b reports the force-displacement cycles obtained for displacement ramps at constant velocity. We can observe a softening behavior for small displacements and a transition to hardening for larger amplitudes. The hardening is due to tensile forces arising in the strands when the bottom and top plates are relatively drifted, and here, it is more pronounced along the direction associated with negative displacements.

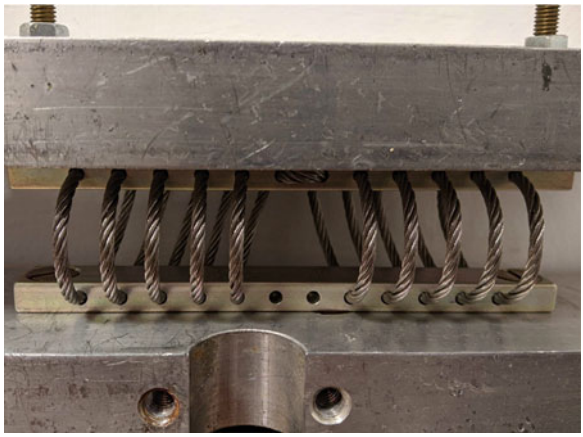

Fig. 1 Picture of the tested helical wire rope isolator

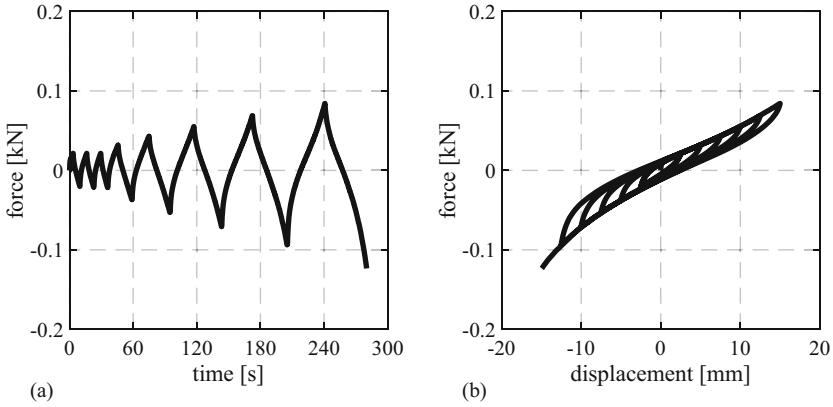

Fig. 2 Experimental responses: (**a**) restoring force time history and (**b**) force-displacement hysteresis loops

3 Hysteresis Models

In order to simulate the complex device response shown in Fig. 2, two hysteresis models are employed. The first one represents a Generalized Bouc–Wen model (GBWM), developed by Carboni et al. [7, 10], whereas the second one is the so-called Vaiana–Rosati model (VRM), recently formulated by Vaiana and Rosati [8, 12]. The GBWM is a differential model that adopts 18 parameters, whereas the VRM represents an exponential model based on two independent sets of 8 parameters that control, respectively, the loading and unloading phases. In particular, the GBWM may be adopted when the nonlinear equilibrium equations of the analyzed system equipped with HWRIs are rewritten in an equivalent set of first-order ordinary differential equations (ODEs), while the VRM may be employed when the second-order ODEs of motion are directly integrated.

3.1 Generalized Bouc–Wen Model

The GBWM was developed to identify a class of strongly nonlinear hysteretic behaviors characterized also by asymmetry [7, 10]. It is versatile and can reproduce very different shapes. Moreover, it can be efficiently employed for identifying static and dynamic responses within heuristic algorithms.

The total restoring force f is obtained by the sum of a linear elastic force, a cubic force, and a hysteretic force

$$f = k_e x + f_c + z, \tag{1}$$

respectively, where x denotes the displacement and k_e represents the linear elastic stiffness. The cubic force is also defined as the summation of a first symmetric cubic force and two cubic forces acting at the threshold displacements $x \geq x_0^+$ and $x \leq -x_0^-$,

$$f_c = k_3 x^3 + H^+ k_3^+ (x - x_0^+)^3 + H^- k_3^- (|x| - x_0^-)^3, \tag{2}$$

with k_3, k_3^+, and k_3^- indicating the cubic stiffnesses. The terms H^+ and H^- are support functions given by:

$$H^+ = \frac{1 + \text{sign}(x - x_0^+)}{2}, \quad H^- = \frac{-1 + \text{sign}(x + x_0^-)}{2}. \tag{3}$$

The cubic force can provide a hardening or softening behavior according to sign of the cubic stiffness. The evolution of the hysteretic force z is defined by the following generalized version of the Bouc–Wen law:

$$\dot{z} = [k_d h + k_d^+ h^+ + k_d^- h^- - (\gamma + \beta \text{sign}(z\dot{x}))\,|z|^n]\dot{x}, \tag{4}$$

$$h = 1 - \xi \mathrm{e}^{-\frac{x^2}{x_c}}, \tag{5}$$

where the dot indicates differentiation with respect to time and h is the pinching function with $\xi \in [0, 1)$ and $x_c > 0$. The term k_d denotes the hysteretic stiffness acting on the whole displacement range, while k_d^+ and k_d^- are the hysteretic stiffnesses working on the positive and negative displacement intervals over the threshold displacements x_b^+ and $-x_b^-$, respectively. The function h^+ and h^- read:

$$h^+ = 1 - \mathrm{e}^{-\frac{(|x| - x_b^+)^2}{x_c^+} L^+ L_v^+}, \quad h^- = 1 - \mathrm{e}^{-\frac{(|x| - x_b^-)^2}{x_c^-} L^- L_v^-}, \tag{6}$$

where x_c^+ and x_c^- are parameters greater than zero with the units of a squared displacement and

$$L^+ = \frac{1 + \text{sign}(x - x_b^+)}{2}, \quad L^- = \frac{1 - \text{sign}(x + x_b^-)}{2}, \tag{7}$$

$$L_v^+ = \frac{1 + \text{sign}(\dot{x})}{2}, \quad L_v^- = \frac{1 - \text{sign}(\dot{x})}{2}. \tag{8}$$

The terms k_e and k_d are the elastic and hysteretic stiffness of the classic Bouc–Wen model with $k_e + k_d$ representing the initial stiffness and k_e the post-elastic stiffness. The generalization of the Bouc–Wen model is provided by the parameters k_d^+ and k_d^- together with functions h^+ and h^-, which determine the asymmetric behavior of the hysteretic force z. This term introduces additional hysteretic

stiffness, which can be modulated along the cycle differently for positive and negative displacements. With respect to the Bouc–Wen model, two new asymptotes appear for the hysteretic force provided by the expressions $[(k_d + k_d^+)/(\gamma + \beta)]^{1/n}$ and $-[(k_d + k_d^-)/(\gamma + \beta)]^{1/n}$. The function h introduces a pinching in the cycle around the origin, and the parameters $\xi \in [0, 1)$ and x_c regulate the pinching severity and displacement-wise extension, respectively. A detailed description of the model can be found in [7].

3.2 Vaiana–Rosati Model

The VRM is a recently developed model that offers a series of advantages over other hysteretic models available in the literature. Indeed, it (i) allows for the evaluation of the generalized force in closed form, thus requiring a reduced computational effort; (ii) is capable of reproducing different types of complex hysteresis loops, ranging from the asymmetric, pinched, S-shaped, and flag-shaped ones to those obtained by their arbitrary combination; (iii) is based on two sets of eight parameters that allow one to manage, respectively, the loading and unloading phases independently; and (iv) adopts parameters describing specific theoretical and/or experimental properties of the hysteresis loops, thus simplifying the identification procedure.

During a generic loading phase ($\dot{u} > 0$), the rate-independent hysteretic force f_{ri} is evaluated as:

$$f_{ri}\left(u, u_j^+\right) = \begin{cases} c^+\left(u, u_j^+\right) & \text{when} \quad u < u_j^+ \quad \text{(9a)} \\ c_u\left(u\right) & \text{when} \quad u > u_j^+, \quad \text{(9b)} \end{cases}$$

whereas during a generic unloading one ($\dot{u} < 0$), it is obtained as:

$$f_{ri}\left(u, u_j^-\right) = \begin{cases} c^-\left(u, u_j^-\right) & \text{when} \quad u > u_j^- \quad \text{(10a)} \\ c_l\left(u\right) & \text{when} \quad u < u_j^-, \quad \text{(10b)} \end{cases}$$

where u ($\dot{u}$) represents the displacement (velocity).

In the previous equations, c^+ and c^- are, respectively, the functions describing the generic loading and unloading curves, computed as:

$$\begin{aligned} c^+(u, u_j^+) = \beta_1^+ e^{\beta_2^+ u} - \beta_1^+ + \frac{4\gamma_1^+}{1 + e^{-\gamma_2^+(u-\gamma_3^+)}} - 2\gamma_1^+ \\ + k_b^+ u + f_0^+ - \frac{1}{\alpha^+}\left[e^{-\alpha^+\left(+u-u_j^++\bar{u}^+\right)} - e^{-\alpha^+\bar{u}^+}\right], \end{aligned} \tag{11}$$

$$c^-(u,u_j^-) = \beta_1^- e^{\beta_2^- u} - \beta_1^- + \frac{4\gamma_1^-}{1+e^{-\gamma_2^-(u-\gamma_3^-)}} - 2\gamma_1^- + k_b^- u - f_0^- + \frac{1}{\alpha^-}\left[e^{-\alpha^-\left(-u+u_j^-+\bar{u}^-\right)} - e^{-\alpha^-\bar{u}^-}\right], \tag{12}$$

whereas c_u and c_l represent, respectively, the analogous functions associated with the upper and lower limiting curves; they are evaluated as:

$$c_u(u) = \beta_1^+ e^{\beta_2^+ u} - \beta_1^+ + \frac{4\gamma_1^+}{1+e^{-\gamma_2^+(u-\gamma_3^+)}} - 2\gamma_1^+ + k_b^+ u + f_0^+, \tag{13}$$

$$c_l(u) = \beta_1^- e^{\beta_2^- u} - \beta_1^- + \frac{4\gamma_1^-}{1+e^{-\gamma_2^-(u-\gamma_3^-)}} - 2\gamma_1^- + k_b^- u - f_0^-. \tag{14}$$

Finally, u_j^+ and u_j^- are internal variables having expressions:

$$u_j^+ = u_P + \bar{u}^+ + \frac{1}{\alpha^+}\ln\left\{+\alpha^+\left[\beta_1^+ e^{\beta_2^+ u_P} - \beta_1^+ + \frac{4\gamma_1^+}{1+e^{-\gamma_2^+(u_P-\gamma_3^+)}} - 2\gamma_1^+ + k_b^+ u_P + f_0^+ + \frac{1}{\alpha^+}e^{-\alpha^+\bar{u}^+} - f_P\right]\right\}, \tag{15}$$

$$u_j^- = u_P - \bar{u}^- - \frac{1}{\alpha^-}\ln\left\{-\alpha^-\left[\beta_1^- e^{\beta_2^- u_P} - \beta_1^- + \frac{4\gamma_1^-}{1+e^{-\gamma_2^-(u_P-\gamma_3^-)}} - 2\gamma_1^- + k_b^- u_P - f_0^- - \frac{1}{\alpha^-}e^{-\alpha^-\bar{u}^-} - f_P\right]\right\}, \tag{16}$$

where u_P and f_P are the coordinates of a generic point P belonging to c^+ or c^-.

Finally, the following quantities k_b^+, f_0^+, α^+, β_1^+, β_2^+, γ_1^+, γ_2^+, and γ_3^+ (k_b^-, f_0^-, α^-, β_1^-, β_2^-, γ_1^-, γ_2^-, γ_3^-) are the eight model parameters governing the generic loading (unloading) phase, whereas $\bar{u}^+$ ($\bar{u}^-$) is an internal model parameter having expression:

$$\bar{u}^+ = -\frac{1}{\alpha^+}\ln(\delta_k^+), \tag{17}$$

$$\bar{u}^- = -\frac{1}{\alpha^-}\ln(\delta_k^-), \tag{18}$$

in which δ_k^+ (δ_k^-) is a quantity to be set equal to 10^{-20} for numerical purposes.

The parameters k_b^+, f_0^+, and α^+ affect the slope of the upper limiting line, the ordinate of the intersection point between the upper limiting curve and the vertical

Table 1 GBWM parameters adopted for simulating the responses in Fig. 3

k_3^+	k_3^-	k_e	k_d	k_d^-	γ	β	n
$[\text{kN/mm}^3]$	$[\text{kN/mm}^3]$	[kN/mm]	[kN/mm]	[kN/mm]	[1/mm]	[1/mm]	[−]
5.377×10^{-7}	8.981×10^{-6}	4.614×10^{-3}	1.173×10^{-2}	8.758×10^{-2}	0.584	0.584	1

axis, and the curvature of the generic loading curve, respectively. In addition, β_1^+ and β_2^+ rule the curvature of the upper limiting curve, whereas parameters γ_1^+, γ_2^+, and γ_3^+ allow us to, respectively, modify the vertical distance between the two asymptotes of the upper limiting curve, vary the slope of the tangent to the upper limiting curve at its inflection point, and shift the upper limiting curve inflection point horizontally. The parameters associated with the unloading phase produce a similar effect on the generic loading and lower limiting curves, and their description is omitted for the sake of brevity.

4 Identifications and Dynamic Simulations

Figure 3 shows a comparison between the experimental data and the identified hysteresis cycles using the GBWM whose MSE is equal to 0.21%. The identified model parameters are reported in Table 1 and $x_c = x_c^+ = x_c- = 1000$, while all the other parameters not explicitly reported are equal to zero. The identification is performed by employing the differential evolution algorithm according to the minimization of the MSE defined as:

$$MSE(\mathbf{p}) = \frac{100}{N\sigma_{\mathbf{f}_e}} \sum_{j=0}^{N} (f_e(x_j, t_j) - f_n(x_j, t_j, \mathbf{p}))^2, \tag{19}$$

where $\mathbf{p}$ is the vector collecting the model parameters, N is the number of time instants t_j at which the restoring force $f_e(x_j, t_j)$ and the applied displacement x_j are recorded (i.e., $t_0 = 0$ and $t_N = T$), and $\sigma_{\mathbf{f}_e}$ indicates the variance of the acquired restoring force vector. The term $f_n(x_j, t_j, \mathbf{p})$ denotes the model-based restoring force at the time instant t_j for the displacement x_j and the parameters vector $\mathbf{p}$. A detailed description of the identification procedure can be found in [7].

Figure 4a and b compare, respectively, the experimental time history of the device restoring force as well as the force-displacement hysteresis loops with those simulated by using the VRM parameters listed in Table 2. The MSE evaluated according to (19) is equal to 0.17%.

Such parameters are identified by using a recently proposed procedure described in [13]. In particular, this identification strategy is based on the use of two optimization procedures, performed in sequence, in which a mean-square residual, between a target and a computed response, is minimized. The computation of

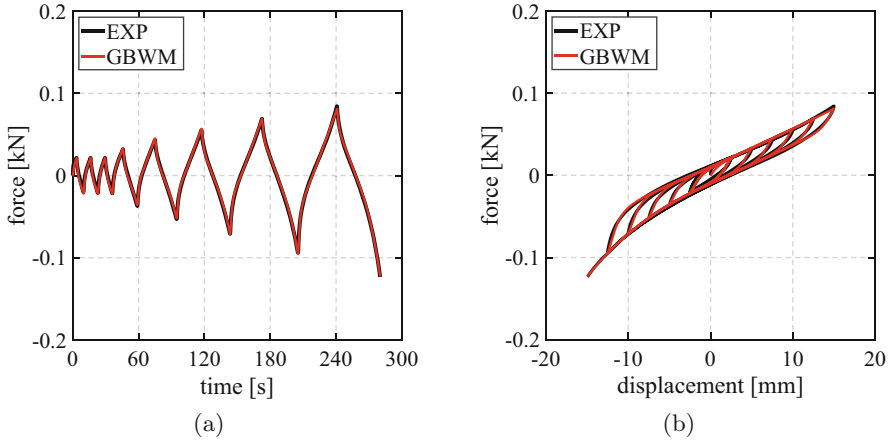

Fig. 3 Experimental versus simulated responses obtained by using the GBWM parameters in Table 1: (**a**) restoring force time history and (**b**) hysteresis loops

Table 2 VRM parameters adopted for simulating the responses in Fig. 4

	k_b	f_0	α	β_1	β_2	γ_1	γ_2	γ_3
sign($\dot{u}$)	[kN/mm]	[kN]	[1/mm]	[kN]	[1/mm]	[kN]	[1/mm]	[mm]
+	0.0042	0.007	0.70	+0.0001	+0.31	0	0	0
−	0.0046	0.016	0.75	−0.0017	−0.22	0	0	0

suitable first trials is performed by taking advantage of the fact that the model parameters correspond to physical and/or analytical properties of the experimental hysteresis loops.

By looking at Fig. 4a and b, we may note a good match between the experimental and numerical results; consequently, the capability of the model to accurately reproduce the device actual behavior is verified.

The FRCs of a mass equal to 0.767 kg connected to the excited ground by means of the investigated HWRI are numerically computed using the two identified hysteresis models. The curves are evaluated for increasing values of the base excitation in order to appreciate the nonlinear behavior of the device. The computations are performed integrating the ODEs governing the problem with the Runge–Kutta algorithm and assuming a step of 0.1 Hz for the forcing frequency. For each exciting frequency in the range $(10, 25)$ Hz, the maximum displacement of the stationary response is extracted to obtain the FRCs with the GBWM and the VRM shown in Fig. 5a and b, respectively. As expected, the device exhibits an initially softening trend followed by a hardening behavior when the oscillation amplitude becomes enough large. The FRCs obtained with the two models are very similar for the larger excitations, while differences in terms of displacement amplitude can be observed for low excitations. In conclusion, both models perform properly for the dynamic simulations and provide the expected softening-hardening behavior.

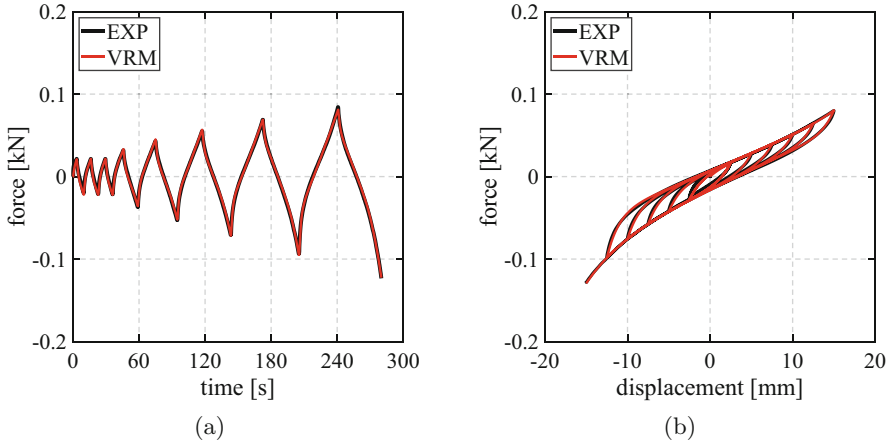

Fig. 4 Experimental versus simulated responses obtained by using the VRM parameters in Table 2: (**a**) restoring force time history and (**b**) hysteresis loops

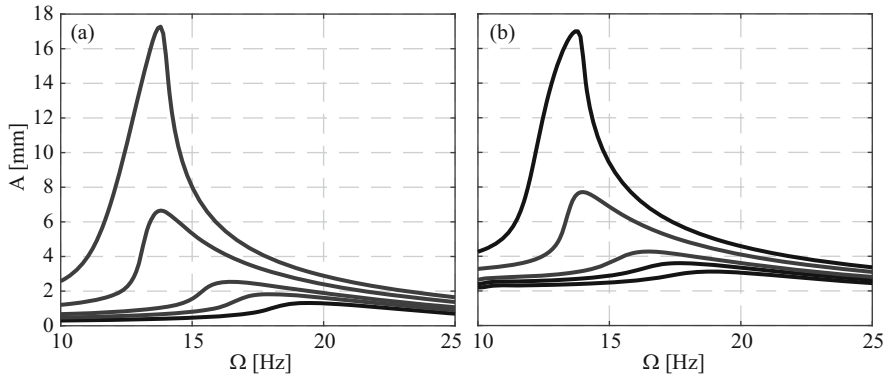

Fig. 5 The FRCs obtained with the (**a**) GBWM and (**b**) the VRM for base excitation levels equal to 0.5 g, 0.75 g, 1 g, 1.5 g, and 2.0 g where Ω and A represent the base excitation frequency and stationary response of the oscillators, respectively

5 Conclusions

The experimental investigation performed on the HWRI has revealed asymmetric force-displacement hysteresis loops along the shear direction, which are characterized by a softening behavior followed by hardening. This peculiar behavior has been identified by using two recently formulated hysteresis models, namely, the Generalized Bouc–Wen model and the Vaiana–Rosati model. Both models provide very accurate identifications considering the value of the mean square errors between the experimental and the simulated force-displacement cycles (0.21% and 0.17% for the GBWM and VRM, respectively). In order to confirm the capability

of the model to properly reproduce the dynamic response of the device, the FRCs of two oscillators connected to the ground by means of the restoring forces provided by the models are computed. The FRCs obtained with both models exhibit a softening behavior followed by hardening paving the way to a future experimental validation with respect to dynamical tests.

Acknowledgments This work was partially supported by Sapienza University of Rome under Grant RM1221816C52B759 "Progetti Medi 2021" (PI: B. Carboni).

References

1. Demetriades, G.F., Constantinou, M.C., Reinhorn, A.M.: Study of wire rope systems for seismic protection of equipment in buildings. Eng. Struct. **15**(5), 321–334 (1993)
2. Ni, Y.Q., Ko, J.M., Wong, C.W., Zhan, S.: Modelling and identification of a wire-cable vibration isolator via a cyclic loading test. Part 1: experiments and model development. J. Syst. Control Eng. **213**(3), 163–171 (1999)
3. Wang, H-X., Gong, X-S., Pan, F., Dang, X-J.: Experimental investigations on the dynamic behaviour of O-type wire-cable vibration isolators. Shock Vib. **2015**, 869325 (2015)
4. Vaiana, N., Marmo, F., Sessa, S., Rosati, L.: Modeling of the hysteretic behavior of wire rope isolators using a novel rate-independent model. In: Nonlinear Dynamics of Structures, Systems and Devices—Proceedings of the 1st International Nonlinear Dynamics Conference, NODYCON 2019, pp. 309–317 (2020)
5. Antonelli, M., Carboni, B., Lacarbonara, W., Bernardini, D., Kalmár-Nagy, T. Quantifying rate-dependence of a nonlinear hysteretic device. In: Nonlinear Dynamics of Structures, Systems and Devices, pp. 347–355. Springer, Cham (2020)
6. Pei, J-S., Carboni, B., Lacarbonara, W.: Modeling Asymmetric Hysteresis Inspired and Validated by Experimental Data. Advances in Nonlinear Dynamics, pp. 371–381. Springer, Cham (2022)
7. Carboni, B., Lacarbonara, W., Brewick, P.T., Masri, S.F. Dynamical response identification of a class of nonlinear hysteretic systems. J. Intell. Mater. Syst. Struct. **29**(13), 2795–2810 (2018)
8. Vaiana, N., Rosati, L.: Classification and unified phenomenological modeling of complex uniaxial rate-independent hysteretic responses. Mech. Syst. Signal Process. **182**, 109539 (2023)
9. Vaiana, N., Spizzuoco, M., Serino, G.: Wire rope isolators for seismically base-isolated lightweight structures: experimental characterization and mathematical modeling. Eng. Struct. **140**, 498–514 (2017)
10. Salvatore, A., Carboni, B., Chen, L.-Q., Lacarbonara, W.: Nonlinear dynamic response of a wire rope isolator: experiment, identification and validation. Eng. Struct. **238**, 112121 (2021)
11. Pellecchia, D., Vaiana, N., Spizzuoco, M., Serino, G., Rosati, L.: Axial hysteretic behaviour of wire rope isolators: experiments and modelling. Mater. Design **225**, 111436 (2023)
12. Vaiana, N., Capuano, R., Rosati, L.: Evaluation of path-dependent work and internal energy change for hysteretic mechanical systems. Mech. Syst. Signal Process. **186**, 109862 (2023)
13. Sessa, S., Vaiana, N., Paradiso, M., Rosati, L.: An inverse identification strategy for the mechanical parameters of a phenomenological hysteretic constitutive model. Mech. Syst. Signal Process. **139**, 106622 (2020)

Part V
Fractional-Order Systems

Reliability Problem of a Fractional Stochastic Dynamical System Based on Stochastic Averaging Method and Data-Driven Deep Learning Algorithm

Yu Guan, Wei Li, Dongmei Huang, and Natasa Trisovic

1 Introduction

Fractional calculus is an extension of traditional calculus and has been extensively studied in the fields of viscoelastic materials and piezoelectric energy.

In practical engineering, random incentives exist widely, especially Gaussian white noise excitation which is often used as the research focus. So scholars have studied random systems containing fractional orders. Spanos and Zeldin [1] proposed a frequency-domain approach for studying stochastic systems with fractional derivatives under the excitation of white Gaussian noise. Based on the LP method and the multiscale method, Xu et al. [2] established a new model for fractional-order systems with strong nonlinearity under random excitation. And the model is utilized to nonlinear dynamic system with fractional damping and viscoelastic term under random parameter excitation [3]. When studying complex nonlinear stochastic systems, we can apply the stochastic averaging method to reduce the dimensionality of the system under certain conditions, making the system characteristics easier to describe. Huang and Jin [4] used the stochastic averaging method for the first time to study a single-degree-of-freedom strongly nonlinear stochastic dynamical system modeled by fractional derivatives based on generalized harmonic functions and obtained the approximate stationary probability density and the maximum Lyapunov exponent of the system.

Due to the rapid development of machine learning, neural networks have been applied to stochastic dynamic systems in recent years, Zhai et al. [5] obtained a mesh free Fokker-Planck solver. LI and Zhang [6] applied artificial neural network

Y. Guan · W. Li (✉) · D. Huang · N. Trisovic
School of Mathematics and Statistics, Xidian University, Xian, China

Department of Mechanics, University of Belgrade, Belgrade, Serbia
e-mail: liweilw@mail.xidian.edu.cn

© The Author(s), under exclusive license to Springer Nature Switzerland AG 2024

W. Lacarbonara (ed.), *Advances in Nonlinear Dynamics, Volume III*, NODYCON Conference Proceedings Series, https://doi.org/10.1007/978-3-031-50635-2_32

algorithm for numerical simulation and studied tumor immune models excited by Gaussian white noise and Gaussian color noise, respectively. In the study of stochastic systems, the first crossing problem has always been a research hotspot, and the reliability function is one of the expressions for the first crossing problem. Li et al. [7] performed equivalent processing on a stochastic dynamical system with fractional order and then applied stochastic averaging to obtain the approximate reliability function of the system.

The purpose of this paper is to study the influence of fractional derivative value on the reliability function of the generalized Van Der Pol system with fractional derivative under the excitation of white Gaussian noise. The advantage of this paper is that the Monte Carlo sampling data is used as a reference point in the data-driven neural network algorithm to replace the boundary conditions and normalization conditions in the KBE and FPK equations to reduce data requirements.

2 VDP System with Fractional Derivatives Excited by White Gaussian Noise

2.1 Equivalent VDP Oscillator

In this chapter, we consider a generalized Van der Pol system with fractional derivatives excited by white Gaussian noise:

$$\ddot{x} + \left(\beta_1 - \beta_2 x^2 + \beta_3 x^4\right)\dot{x} + \omega_0^2 x + \varepsilon D^\alpha x(t) = W(t) \tag{1}$$

where ω_0 is the natural frequency of the generalized VDP system, $\beta_1, \beta_2, \beta_3$are constants, ε is a scalar parameter, $\alpha(0 < \alpha < 1)$ is the fractional derivative value, $W(t)$ is white Gaussian noise with zero mean and noise intensity D, and $D^\alpha x(t)$ is the fractional derivative defined in the Caputo sense:

$$D^\alpha x(t) = \begin{cases} \frac{1}{\Gamma(n-\alpha)} \int_0^t (t-\tau)^{n-\alpha-1} x^{(n)}(\tau) d\tau & n-1 < \alpha < n \\ x^{(n)}(t) & \alpha = n \in N \end{cases} \tag{2}$$

When $\beta_1, \beta_2, \beta_3$ and the intensity of Gaussian-noise excitation is the same order of scalar ε and is much smaller than 1, The system is a quasi-conservative system under the action of weak damping and weak excitation. Apply the generalized harmonic function:

$$\begin{cases} x(t) = A(t)\cos\varphi(t) \\ \dot{x}(t) = -A(t)\omega_0 \sin\varphi(t) \end{cases}, \varphi(t) = \omega_0 t + \theta(t) \tag{3}$$

According to the literature [7], it can be known that $D^{\alpha} = \int_0^{\infty} \Psi(y,t)dy$ and

$$\Psi(y,t) = \frac{\sin \pi\alpha}{\pi\alpha} A(t) \left[\frac{\omega_0^2 \cos\varphi(t) - \omega_0 y^{\frac{1}{\alpha}} \sin\varphi(t)}{\omega_0^2 + y^{\frac{2}{\alpha}}} \right] + c_1 e^{-ty^{\frac{1}{\alpha}}} \tag{4}$$

where the constant c_1 can be found by $\Psi(y,0) = 0$. Integrate to get the expression for $D^{\alpha}x(t)$, $D^{\alpha}x(t)$ can be expressed as

$$D^{\alpha}x(t) \approx \left(\omega_0^{\alpha} \cos\frac{\pi\alpha}{2}\right) x + \left(\omega_0^{\alpha-1} \sin\frac{\pi\alpha}{2}\right) \dot{x} \tag{5}$$

The generalized Van der Pol system with fractional derivatives can be equivalently transformed into:

$$\ddot{x} + \left(\beta_1 + \epsilon\omega_0^{\alpha-1} \sin\frac{\pi\alpha}{2} - \beta_2 x^2 + \beta_3 x^4\right) \dot{x} + \left(\omega_0^2 + \epsilon\omega_0^{\alpha} \cos\frac{\pi\alpha}{2}\right) x = W(t) \tag{6}$$

2.2 Stochastic Averaging

Consider the resulting equivalent system (6), and use the harmonic function to transform fast-varying variables into slow-varying variables.

Let

$$\begin{cases} x(t) = a(t)\cos\phi(t) \\ \dot{x} = -a(t)\omega\sin\phi(t) \end{cases}, \phi(t) = \omega_0 t + \delta(t)$$

In which $\omega^2 = \omega_0^2 + \epsilon\omega_0^{\alpha}\cos\frac{\pi\alpha}{2}$, $a(t)$ and $\phi(t)$ are random processes, $a(t)$ is the amplitude of the random response, which can be expressed as $a(t) = \sqrt{x^2 + \dot{x}/\omega^2}$, $\phi(t)$ is the random phase, after variable substitution, $a(t)$ and $\phi(t)$ are both slowly changing variables.

Substitute into the system (6) to get:

$$\begin{cases} \dot{a} = -\left(\beta_1 + \epsilon\omega_0^{\alpha-1}\sin\frac{\pi\alpha}{2}\right) a\sin^2\phi + \beta_2 a^3 \sin^2\phi\cos^2\phi - \beta_3 a^5 \sin^2\phi\cos^4\phi \\ \qquad\qquad -\frac{\sin\phi}{\omega} W(t) \\ \dot{\delta} = -\left(\beta_1 + \epsilon\omega_0^{\alpha-1}\sin\frac{\pi\alpha}{2}\right) \sin\phi\cos\phi + \beta_2 a^2 \sin\phi\cos^4\phi - \beta_3 a^4 \sin\phi\cos^5\phi \\ \qquad\qquad -\frac{\cos\phi}{a\omega} W(t) \end{cases} \tag{7}$$

In which

$$\begin{cases} f_{11} = -\left(\beta_1 + \epsilon\omega_0^{\alpha-1}\sin\dfrac{\pi\alpha}{2}\right) a\sin^2\phi + \beta_2 a^3\sin^2\phi\cos^2\phi - \beta_3 a^5\sin^2\phi\cos^4\phi \\ g_{11} = -\dfrac{\sin\phi}{\omega} \\ f_{22} = -\left(\beta_1 + \epsilon\omega_0^{\alpha-1}\sin\dfrac{\pi\alpha}{2}\right)\sin\phi\cos\phi + \beta_2 a^2\sin\phi\cos^4\phi - \beta_3 a^4\sin\phi\cos^5\phi \\ g_{21} = -\dfrac{\cos\phi}{a\omega} \end{cases}$$

It can be seen that $a(t)$ and $\delta(t)$ constitute a vector Markov diffusion process, and the expressions of the drift coefficient and diffusion coefficient are obtained as

$$\begin{aligned} m(a) &= \left\langle f_{11} + \int_{-\infty}^{0}\left(\frac{\partial g_{11}}{\partial a}|_t g_{11}|_{t+\tau} + \frac{\partial g_{11}}{\partial\phi}|_t g_{21}|_{t+\tau}\right) R_{11}(\tau)\,d\tau\right\rangle_t \\ \sigma^2(a) &= \left\langle \int_{-\infty}^{\infty}(g_{11}|_t g_{11}|_{t+\tau})\,R_{11}(\tau)\,d\tau\right\rangle_t \end{aligned} \tag{8}$$

Substitute to know,

$$\begin{aligned} m(a) &= \frac{\left(\beta_1 + \epsilon\omega_0^{\alpha-1}\sin\frac{\pi\alpha}{2}\right)a}{2} + \frac{\beta_2 a^3}{8} - \frac{\beta_3 a^5}{16} + \frac{D}{2a\omega^2} \\ \sigma^2(a) &= \frac{D}{\omega^2} \end{aligned} \tag{9}$$

Since the averaged $a(t)$ equation does not contain $\phi(t)$, the smoothed amplitude process $a(t)$ itself is a Markov diffusion process governed by the following Ito differential equation:

$$da = m(a)dt + \sigma(a)dB(t) \tag{10}$$

For a dynamic system with random excitation, the corresponding random diffusion occurs in the phase space. When the system responds to leave a certain safety domain for the first time, it is said that the system has passed through for the first time. The first crossing problem of the system can be described by the reliability function. The reliability function of the system is an important indicator to measure the stability of the system.

According to the system Hamiltonian function $g(a) = \omega^2 a$, $U(a) = \int_0^a g(u)du$, $H = \frac{1}{2}\omega^2 a^2$. Convert (10) to a one-dimensional diffusion process with respect to energy:

$$dH = m(H)dt + \sigma(H)dB(t) \tag{11}$$

In which,

$$\begin{aligned} m(H) &= \left[m(a)g(a) + \frac{1}{2}\sigma^2(a)g'(a) \right]_{a=U^{-1}(H)} \\ \sigma^2(H) &= \left[\sigma^2(a)g^2(a) \right]_{a=U^{-1}(H)} \end{aligned} \tag{12}$$

Substitute into the drift coefficient and diffusion coefficient can be obtained as:

$$\begin{aligned} m(H) &= -\left(\beta_1 + \epsilon\omega_0^{\alpha-1} \sin\frac{\pi\alpha}{2} \right) H + \frac{\beta_2 H^2}{2\omega^2} - \frac{\beta_3 H^3}{2\omega^4} + D \\ \sigma^2(H) &= 2HD \end{aligned} \tag{13}$$

The reliability function of the system with respect to energy satisfies the backward Kolmogorov equation as follows:

$$-\frac{\partial}{\partial t_0} R + m(H_0)\frac{\partial}{\partial H_0} R + \frac{1}{2}\sigma^2(H_0)\frac{\partial^2}{\partial H_0^2} R = 0 \tag{14}$$

The initial and boundary conditions are:

$$\begin{aligned} R(0, H_0) &= 1 \\ R(t, H_f) &= 0 \end{aligned} \tag{15}$$

3 Deep Learning

3.1 Selection of Training Data

The selection of training data based on data-driven neural network is one of the key points of the model. First, the training data is divided into two parts: one part is the sample point $X = \{x_i, i \in 1, \ldots, N_1\}$, and the other part is the reference point $Y = \{y_j, j \in 1, \ldots, N_2\}$. The reference point y_j has its corresponding reference value $v(y_j)$, which is obtained by applying Monte Carlo simulation and does not need to be very accurate. $10^4 \sim 10^5$ is generally the number of sample points N_1, and the number of reference points N_2 is usually $10^3 \sim 5 \times 10^3$.

For solving the reliability function, the reliability function is a two-dimensional function composed of initial energy H_0 and time t. Assuming that the safety domain of the energy function is $H_0 \in [0, H_f]$, time $t \in [0, t_m]$, where H_f and t_m are given right boundary values. When taking the sample points, divide the value range of (H_0, t) into grids with as small a length as possible, and the values on both sides are dH_0 and dt. Then apply uniform distribution sampling on these grid points to get the desired sample points. When taking the reference point, make dH_0 and dt larger to reduce the number of grids, and each grid point is used as the reference point.

After that, the Monte Carlo method is applied to obtain the reliability function value of each reference point as the reference value of the reliability function. Algorithm 1 details the steps for determining the reference value.

Algorithm 1 Determination of reliability function reference value

Input: Right boundary value H_f of energy, time length t, sampling times M, reference point Y.
Output: The corresponding reference value $V = v(y_j)$, $j = 1, ..., N_2$ of each reference point.

Construct grid points of $dH_0, dt, T = t/dt + 1$;
Set the array η of length N_2 and the matrix Q;
for $j = 1 : N_2$ **do**
    Compute $n_1 = y_j^1/dH_0, n_2 = y_j^2/dt$;
    Let $Q(n_1, n_2) = j$;
end for
for $H = 0 : dH_0 : H_f$ **do**
    while $k \leq M$ **do**
        Set the initial value $X(0)$;
        for $t = 1 : T$ **do**
            Apply Monte Carlo simulation to get $X(t)$ and $H(t)$;
            if $H(t) > H_f$ **then**
                $times = T, h_n = H/dH_0$;
                if $Q(times : end, h_n) > 0$ is not empty **then**
                    Find all $Q(times : end, h_n)$ non-zero value J;
                    $\eta(J) = \eta(J) + 1$;
                end if
                break;
            end if
        end for
        $k = k + 1$;
    end while
end for
return $v(y_j) = 1 - \eta(j)/M$.

3.2 Neural Networks

The basic neural network structure is shown in Fig. 1, which is divided into three parts, input layer, hidden layer, and output layer, with a total of L layers. For a two-dimensional stochastic dynamic system, x_1, x_2 are the input layers, y is the output layer, and H is the hidden layer, where $H_l = [h_1^l, h_2^l, \ldots, h_{n_l}^l]$, $(2 \leq l \leq L-1)$ is the output of the l layer, the output of the H_{l-1} layer is the input of the H_l layer, and n_l is the number of nodes in the hidden layer. $W = [\omega^1, \omega^2, \ldots, \omega^{L-1}]$ is the weight of the neural network. $Bias = [b^1, b^2, \ldots, n^{L-1}]$ is the bias of the network, $b^l = [b^{l1}, b^{l2}, \ldots, b^{ln_l}]^T$ is the bias of layer $l + 1$.

The activation function of the neural network is $f = [f_1, f_2, ..., F_{L-1}]$. The activation function usually uses functions such as sigmoid, tanh, RELU, etc. The output of the neural network can be expressed as $y = g(x; \theta)$, which is used to

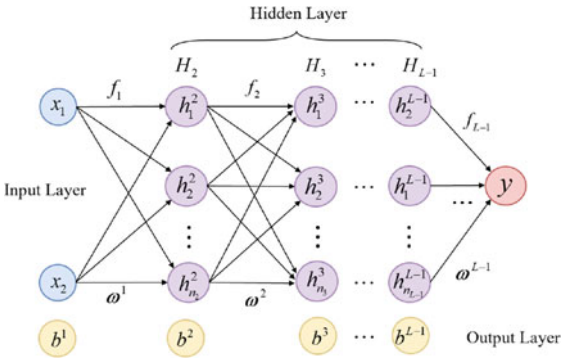

Fig. 1 Neural network structure

describe the reliability function and stationary probability density, g is a composite function composed of activation functions, and $\theta = [\omega, Bias]$ is used to represent the parameters of the neural network.

3.3 Loss Function

When selecting training data, we divided the data into two parts: sample point x_i and reference point y_j. Each reference point y_j has a reference value $v(y_j)$ for Monte Carlo simulation. The reference points are applied to replace the initial conditions of KBE, the normalized conditions of the FPK equation, and the boundary conditions of both. Based on this, the loss function is recorded as:

$$L(\boldsymbol{\theta}) = \frac{1}{N_1}\sum_{i=1}^{N_1}\left(\mathcal{L}\tilde{u}\left(x_i, \boldsymbol{\theta}\right)\right)^2 + \frac{1}{N_2}\sum_{j=1}^{N_2}\left(\tilde{u}\left(y_j, \boldsymbol{\theta}\right) - v\left(y_j\right)\right)^2 \tag{16}$$

in which, $\tilde{u}$ is the neural network solution, $\mathcal{L}\tilde{u} = \frac{\partial}{\partial t_0}\tilde{u} - m\left(H_0\right)\frac{\partial}{\partial H_0}\tilde{u} - \sigma^2\left(H_0\right)\frac{\partial^2}{\partial H_0^2}\tilde{u}/2$ when solving the backward Kolmogorov equation.

3.4 Adam

The Adam algorithm brings the first-order moment estimation and second-order moment estimation of the function gradient into the calculation and adaptively modifies the iterative step size of each parameter according to the gradient. In this chapter, Adam optimizer is used to iteratively update the parameters of the neural network, so that the value of the loss function is reduced, and finally the optimal

value of neural network parameters under the condition of minimizing the loss function is obtained to fit the required function.

Algorithm 2 is the implementation of the data-driven neural network algorithm, which is tested in Sect. 4.

Algorithm 2 Data-driven neural network algorithms

Input: Sample point $X = \{x_j, j = 1, 2, \cdots N_1\}$, reference point $Y = \{y_j, j = 1, 2, \cdots N_2\}$ and reference value $V = \{v(y_j), j = 1, 2, \cdots N_2\}$.

Output: Data-driven Neural Network Solutions $\tilde{u}$.

1: Initialize neural network weights and biases;
2: **for** $j = 1 : M$ **do**
3: Substitute the sample points X and reference points Y into the neural network, Obtain solution $\tilde{u}\left(X \mid \boldsymbol{\theta}_j\right)$ and $\tilde{u}\left(Y \mid \boldsymbol{\theta}_j\right)$;
4: Select a small number of sample points, the first and second derivative values of the reliability function can be obtained by applying the difference algorithm;
5: After substituting the derivative values into the equation, the first part of the loss function is obtained;
6: Select a small number of reference point, calculate the difference between the reference values V and $\tilde{u}\left(Y \mid \boldsymbol{\theta}_j\right)$ to get the second part of the loss function;
7: Calculate the loss function and update the neural network with the minimum loss function;

$$L(\boldsymbol{\theta}) = \frac{1}{N_1}\sum_{i=1}^{N_1}\left(\mathcal{L}\tilde{u}\left(x_i, \boldsymbol{\theta}\right)\right)^2 + \frac{1}{N_2}\sum_{j=1}^{N_2}\left(\tilde{u}\left(y_j, \boldsymbol{\theta}\right) - v\left(y_j\right)\right)^2$$

8: Obtained $\boldsymbol{\theta}_{j+1}$ using the adam algorithm;
9: **end for**
10: **return** $\tilde{u}$.

In fact, the data-driven neural network algorithm proposed by us has a wide range of applications, which can be utilized to various prediction problems on the basis of data driven. For example, we can use this approach to predict the price of a kind of American option in the future time. In particular, the method to collect the training data we used in this chapter is a general way, and it can be extended to solve partial differential equations with certain boundary conditions by simulation of uniform distribution.

4 Numerical Simulation

In Sect. 2, we analyze the system (1). Under the condition of weak damping and weak excitation, the backward Kolmogorov equation (14) is satisfied by the reliability function. In this section, we discuss the variation of the system reliability function of the energy under the influence of different fractional derivatives. For this reason, the parameter $\beta_1 = 0.1, \beta_2 = 0.3, \beta_3 = 0.1, \omega_0 = 2, \epsilon = 0.2, D = 0.2$

in the chapter remains unchanged; α is taken as $\alpha = 0.1, 0.9$ respectively; and the data-driven neural network proposed in Sect. 3 is used for simulation.

4.1 Reliability Function

Now, the exact solution of the backward Kolmogorov equation is difficult. According to the backward Kolmogorov equation (14) about energy obtained in Sect. 2, we introduce the numerical simulation method obtained by the chasing method and the MC simulation results as the criterion, compare the fitting solution of the reliability function of the neural network with it, and analyze the accuracy of the neural network solution. In addition, the influence of different fractional derivatives on the system reliability function should be studied. Setting the energy right boundary $H_f = 3$, the time range is $t \in [0, 10]$; the number of sampling points is 10,000; the number of reference points is 3000, the 3-layer neural network; and the number of nodes in each layer is 2, 15, 1.

The reliability function when the fractional derivative $\alpha = 0.1, 0.5$ is given by Figs. 2a and 3a is the reliability function graph obtained by the data-driven neural network. For different values of α, the fixed H_0 reliability function decreases monotonically from 1 with the increase of time, and the longer the time, the higher the probability of the first crossing. At the same time point, the greater the initial energy, the greater the probability of the first crossing. When the value of Alpha is small, the gradient of the reliability function in Fig. 2a is large, and the decline is rapid; when the value of alpha is large, the slope of the reliability function in Fig. 3a is small, and the decline is slow. (b) is the conditional reliability function $R(t)$ with $H_0 = 0.5, 2$. The red dotted line is the result of the catch-up method, and the blue solid line is the result of the data-driven neural network. The difference between the two is small.

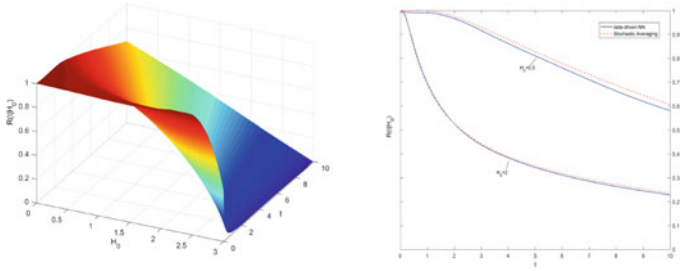

(a) (b)

Fig. 2 (**a**) Reliability function with $\alpha = 0.1$ for data-driven neural network simulation; (**b**) comparison of the neural network simulation solution and the chasing method simulation solution in the case of $H_0 = 0.5, 2$

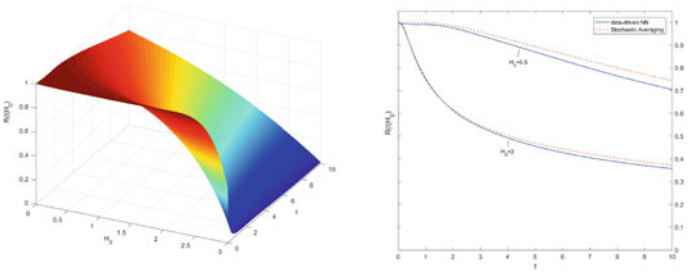

(a) (b)

Fig. 3 (**a**) Reliability function with $\alpha = 0.5$ for data-driven neural network simulation; (**b**) comparison of the neural network simulation solution and the chasing method simulation solution in the case of $H_0 = 0.5, 2$

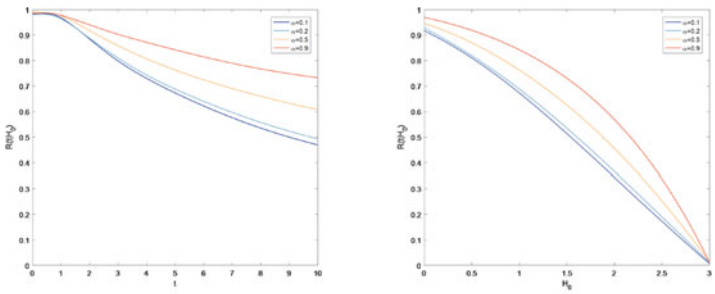

(a) (b)

Fig. 4 (**a**) Variation of conditional reliability function with $H_0 = 1$ under different fractional derivatives; (**b**) variation of conditional reliability function with $t = 5$ under different fractional derivatives

The cross-sectional view of the reliability function with different Alpha values is shown in Fig. 4a is the cross-sectional view of the reliability function obtained by the neural network with a fixed $H_0 = 1$. With the increase of α, the time required to obtain the same reliability function value becomes longer, the reliability function value becomes larger under the same time, and the probability of first crossing becomes smaller. When $t = 5$ is determined, the conditional reliability function diagram is shown in Fig. 4b. In the case of the same initial energy, the larger the alpha, the larger the value of the reliability function; for the same reliability function value, a larger alpha requires a larger initial energy.

5 Conclusions

In this chapter, the effects of fractional derivatives on the system reliability function in generalized van der pol systems with fractional derivatives under the excitation

of white Gaussian noise are studied. The fractional derivative is converted into the equivalent sum of restoring force and damping force, and the backward Kolmogorov equation of energy of the equivalent system is obtained by stochastic averaging method. In order to solve the reliability function, this chapter proposes a data-driven neural network algorithm using reference points instead of boundary points, which achieves high precision compared with the catch-up method. The conclusion is that the reliability function decreases monotonically with time. The larger the fractional derivative, the larger the reliability function value, and the smaller the first crossing probability. Since the data-driven neural network algorithm is a powerful tool to solve the partial differential equation with a certain boundary condition, as a following step, we are going to keep on studying the different case that the response of a FOPID (fractional order of proportion integration-derivative) system subjected to a Gaussian color noise by way of two methods of stochastic averaging method and data-driven neural network, in order to extend the application range of our presented method.

References

1. Spanos, P.D., Zeldin, B.A.: Random vibration of systems with frequency-dependent parameters or fractional derivatives. J. Eng. Mech. **123**(3), 290–292 (1997)
2. Xu, Y., Li, Y., Liu, D.: A method to stochastic dynamical systems with strong nonlinearity and fractional damping. Nonlinear Dyn. **83**(4), 2311–2321 (2016)
3. Xu, Y., Li, Y., Liu, D., Jia, W., Huang, H.: Responses of duffing oscillator with fractional damping and random phase. Nonlinear Dyn. **74**(3), 745–753 (2013)
4. Huang, Z.L., Jin, X.L.: Response and stability of a sdof strongly nonlinear stochastic system with light damping modeled by a fractional derivative. J. Sound Vib. **319**(3–5), 1121–1135 (2009)
5. Dobson, M., Li, Y., Zhai, J.: An efficient data-driven solver for Fokker-Planck equations: algorithm and analysis. Commun. Math. Sci. **20**, 803–827 (2022)
6. Li, W., Zhang, Y., Huang, D., Rajic, V.: Study on stationary probability density of a stochastic tumor-immune model with simulation by ann algorithm. Chaos, Solitons Fractals **159**, 112145 (2022). https://www.sciencedirect.com/science/article/pii/S0960077922003551
7. Li, W., Zhang, M., Zhao, J., Huang, D.: Reliability analysis of stochastic dynamical systems with fractional order pid controller. J. Dyn. Control. **17**(1), 65–72 (2019)

On the Dynamics Analysis of Fractional-Type Microresonator System

Tao Xi, Jin Xie, and Zhaohui Liu

1 Introduction

Microresonator, as a kind of micro-electromechanical systems (MEMS), is widely used in sensors, MEMS filters, and radio frequency MEMS. From the point of view of dynamics, it is a complicated nonlinear dynamic system. Many factors influence its performance, such as relatively large structural deformations and displacement-dependent excitations [1, 2], fringing field and viscoelasticity [3], working temperature [4], damping [5, 6], and squeeze-film phenomena [7].

In general, the dynamic system of a microresonator involves more intricate physical phenomena than that of a macro mechatronic. Researchers have been pursuing to establish a more accurate dynamics model of the microresonator, which is crucial not only for its analysis but also for its design [8, 9] and control [10, 11]. The fractional-order derivative, a recent surge of interest in science and technology, may be a new way to this end.

Compared with integer-order differential equations, the fractional-order derivative, or exactly non-integer-order derivative, takes any real number, rational or irrational, as its order, which provides more degrees of freedom in the model. Additionally, fractional-order derivative includes integral, which allows for taking the evolution of the system into consideration, not only local but the global correlation and characteristics as well [12, 13]. At present, some methods to identify the fractional-order from experimental or simulated data have been proposed. Then it is hopeful to establish a more accurate dynamic model for an individual microresonator with a different fractional-order derivative.

T. Xi · J. Xie (✉) · Z. Liu
Southwest Jiaotong University, Chengdu, People's Republic of China
e-mail: xj_6302@263.net

© The Author(s), under exclusive license to Springer Nature Switzerland AG 2024

W. Lacarbonara (ed.), *Advances in Nonlinear Dynamics, Volume III*, NODYCON Conference Proceedings Series, https://doi.org/10.1007/978-3-031-50635-2_33

Until now, many scholars have performed various studies on the fractional-order dynamic model concerning the physical properties of microresonator. Meral et al. proved by experiment that the fractional derivative model of viscoelasticity is more accurate than the integer derivative model for soft tissue-like materials [14]. Di Paola et al. showed that the fractional model has a good agreement with experimental tests on creep and relaxation, which means that the fractional model may easily capture both relaxation and creep of materials [15]. Kumar et al. utilized the fractional-order theory of thermoelasticity to derive the dynamic model for a thermo micro-electromechanical (MEM) and thermo nano-electromechanical (NEM) beam resonators [16]. Based on two different types of fractional derivative definitions, Youssef et al. constructed an analytical solution of a thermal model of a silicon microbeam resonator subjected to static prestress [17]. Aghababa investigated the existence of chaos in a non-autonomous fractional-order micro-electromechanical resonator system using the maximal Lyapunov exponent criterion and proposed a fractional finite-time controller to suppress the chaos [18].

In this paper, we do not focus on the accuracy of fractional-order dynamics equations but rather the analysis method of the fractional-order dynamics model for microresonator. Since the physical meaning of fractional-order derivative is not clear, and the analysis of fractional-order dynamics model also needs a high skill in using the theory of fractional calculus [19], we attempt to predict the behaviors of a fractional system by the theory and method of classical mechanics. To this end, based on the integer-order differential equations of the microresonator, the fractional-order one is obtained in the next section, and the prediction of its behavior is made in Sect. 3, and the motion of the microresonator with respect to the variation of the fractional-order is analyzed in Sect. 4. Then, conclusions are drawn in the last section.

2 Dynamic Model of Microresonator

2.1 Integer-Order Differential Equations of Microresonator

Figure 1 is the schematic diagram of an electrostatically actuated microresonator, in which the three microbeams are clamped at both their ends. Assuming that there exists squeeze-film damping between the microbeams.

In the microresonator, an electrical driving voltage, V_{AC} sin (Ωt), produces electrostatic excitation with a DC-bias voltage V_b between electrodes and the resonator, resulting in the vibration of the resonator.

By means of the Lagrangian equation and Rayleigh-Ritz method, one can obtain the dimensionless equation of the microresonator

$$\ddot{x} + \mu\dot{x} + x + \alpha x^3 = \gamma\left[\frac{1}{(1-x)^2} - \frac{1}{(1+x)^2}\right] + \frac{A}{(1-x)^2}\sin(\omega\tau) \tag{1}$$

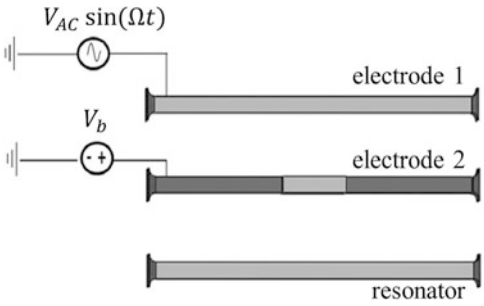

Fig. 1 Schematic representation of an electrically actuated microresonator

where x represents the vertical displacement of the resonator, μ and α represent squeeze-film damping and nonlinear stiffness of the resonator, respectively, γ represents the DC-bias voltage, and $\omega\tau = \Omega t$. For the details of the derivation of Eq. (1), please refer to Ref. [20].

2.2 *Fractional-Order Differential Equation of Microresonator*

There are three common definitions of fractional-order derivative [13]. Here, we employ the Caputo fractional-order derivative, exactly the left Caputo fractional-order derivative, because it allows for specifying inhomogeneous initial conditions. The left Caputo fractional-order derivative is

$$ {}_0{}^C D_t{}^p f(t) = \frac{1}{\Gamma(n-p)} \int_0^T (t-s)^{n-p-1} f^{(n)}(s) ds \tag{2} $$

where $\Gamma(\bullet)$ is the Gamma function, $n \in Z^+$is an integer, p is a non-integer, and we have $n-1 \le p < n$.

The operator ${}_0{}^C D_t^p$ represents the definition of the Caputo fractional-order derivative by the leading superscript C, and the fractional-order by the right superscript p, the upper and lower integral included in the definition by the right subscript t and leading subscript 0, respectively, which are differences from the right Caputo fractional-order derivative. The letter D signifies derivative.

Expressing the effect of viscoelasticity and thermal damping on the microresonator with fractional-order derivative, Eq. (1) becomes a fractional-order differential equation

$$ {}_0{}^C D_t^{p_1} x + \mu_0{}^C D_t^{p_2} x + x + \alpha x^3 = \gamma \left[\frac{1}{(1-x)^2} - \frac{1}{(1+x)^2} \right] + \frac{A}{(1-x)^2} \sin(\omega\tau) \tag{3} $$

where the fractional-order $p_1 \in [1,2]$ and $p_2 \in [0,1]$. Let ${}_0{}^C D_t^{p_2} x = y$, then we have

$$\begin{cases} {}_0{}^C D_t^{p_2} x = y \\ {}_0{}^C D_t^{p_1-p_2} y = -x - \alpha x^3 + \gamma \left[\frac{1}{(1-x)^2} - \frac{1}{(1+x)^2} \right] + \frac{A}{(1-x)^2} \sin(\omega\tau) \end{cases} \tag{4}$$

To solve Eq. (4), we employ the one-step Admas-Moulton algorithm [21], which is predictor-corrector approach. The predictor formula is

$$\begin{cases} x_h^{p_r}(t_{z+1}) = x_h(t_z) + h y_h(t_z) \\ y_h^{p_r}(t_{z+1}) = y_h(t_z) + h \Big[-x_h(t_z) - \alpha x_h(t_z)^3 + \\ \gamma \left[\frac{1}{(1-x_h(t_z))^2} - \frac{1}{(1+x_h(t_z))^2} \right] + \frac{A}{(1-x_h(t_z))^2} \sin(\omega\tau_z) \Big] \end{cases} \tag{5}$$

And corrector formula is

$$\begin{cases} x_{z+1} = x_0 + \frac{h^{p_2}}{\Gamma(p_2+2)} \left[y_{z+1}^{p_r} + \sum_{j=0}^{z} a_{j,z+1} (y_j) \right] \\ y_{z+1} = y_0 + \frac{h^{p_1-p_2}}{\Gamma(p_1-p_2+2)} \Big(-x_{z+1}^{p_r} - \alpha {x_{z+1}^{p_r}}^3 - \mu y_{z+1}^{p_r} + \\ \gamma \left[\frac{1}{\left(1-x_{z+1}^{p_r}\right)^2} - \frac{1}{\left(1+x_{z+1}^{p_r}\right)^2} \right] + \frac{A}{\left(1-x_{z+1}^{p_r}\right)^2} \sin(\omega\tau_{z+1}) + \\ \sum_{j=0}^{z} a_{j,z+1} \left(-x_j - \alpha {x_j}^3 - \mu y_j + \gamma \left[\frac{1}{(1-x_j)^2} - \frac{1}{(1+x_j)^2} \right] + \frac{A}{(1-x_j)^2} \sin(\omega\tau_j) \right) \end{cases} \tag{6}$$

where h is the step length, and $a_{j,\,z+1}$ is

$$a_{j,z+1} = \begin{cases} z^{p+1} - (z-p)(z+1)^p \text{ if } j = 0 \\ (z-j+2)^{p+1} + (z-i)^{p+1} - 2(z-j+1)^{p+1} \text{ if } 1 \le j \le z \\ 1 \text{ if } j = z+1 \end{cases} \tag{7}$$

3 Predicting the Behavior of the Fractional-Order Differential Equation

Because the physical meaning of fractional-order derivative is not as clear as that of integer-order derivative, there has not been the concept and definition of equilibrium point for a fractional-order dynamic model. Whereas in the field of integer-order dynamics, one can predict the behavior of a dynamic system through the analysis of equilibrium point and its stability.

In this section, we place the emphasis on the question of whether or not one can predict the behavior of a fractional-order dynamics by the analysis results of its counterpart, the integer-order dynamics. For this reason, we first analyze the

equilibrium points and their stabilities for the integer-order dynamic model, Eq. (1), and then using Eq. (5) through Eq. (7), carry out simulations. Based on the analysis and outcomes of simulation, the answers will be obtained.

3.1 *Analysis of Equilibrium Points and Their Stability for the Integer-Order Dynamics Model*

In the application of microresonator, the value of DC-bias voltage V_b is much larger than the amplitude of the AC driving voltage. So the last item in Eq. (1) can be regarded as a smaller disturbance to the system, as does the squeeze-film damping μ. Deleting these disturbances, we get a Hamiltonian equation

$$\begin{cases} \frac{dx}{dt} = y \\ \frac{dy}{dt} = -x - \alpha x^3 + \gamma \left[\frac{1}{(1-x)^2} - \frac{1}{(1+x)^2} \right] \end{cases} \tag{8}$$

According to the theory of nonlinear dynamics [22], the equilibrium point (x^*, y^*) should satisfy the condition that the right side of Eq. (8) is equal to zero, and their stabilities can be analyzed by the following potential function

$$V_x = \frac{1}{2}x^2 + \frac{1}{4}\alpha x^4 - \gamma \left[\frac{1}{1-x} + \frac{1}{1+x} \right] + 2\gamma \tag{9}$$

Obviously, the point (0, 0) is one of the equilibrium points, and the others are determined by the values of α and γ. The solutions for equilibrium points can be divided into seven cases, as displayed in Table 1.

Table 1 The number of equilibrium points versus the values of α and γ

	Value of α	Value of γ	Number of equilibrium points (stability)
Type I	$(0, +\infty)$	$\gamma > \frac{(\alpha+1)^3}{27\alpha^2}$	1 (unstable)
Type II	$(0, 2]$	$\gamma = \frac{(\alpha+1)^3}{27\alpha^2}$	1 (unstable)
Type III	$(2, +\infty)$	$\gamma = \frac{(\alpha+1)^3}{27\alpha^2}$	3 (unstable)
Type IV	$(0, +\infty)$	$(0, 0.25)$	3 (1stable, 2 unstable)
Type V	$(2, +\infty)$	0.25	3 (1stable, 2 unstable)
Type VI	$(0, 2)$	$\left[0.25, \frac{(\alpha+1)^3}{27\alpha^2}\right)$	1 (unstable)
Type VII	$(2, +\infty)$	$\left[0.25, \frac{(\alpha+1)^3}{27\alpha^2}\right)$	5 (2 stable, 3 unstable)

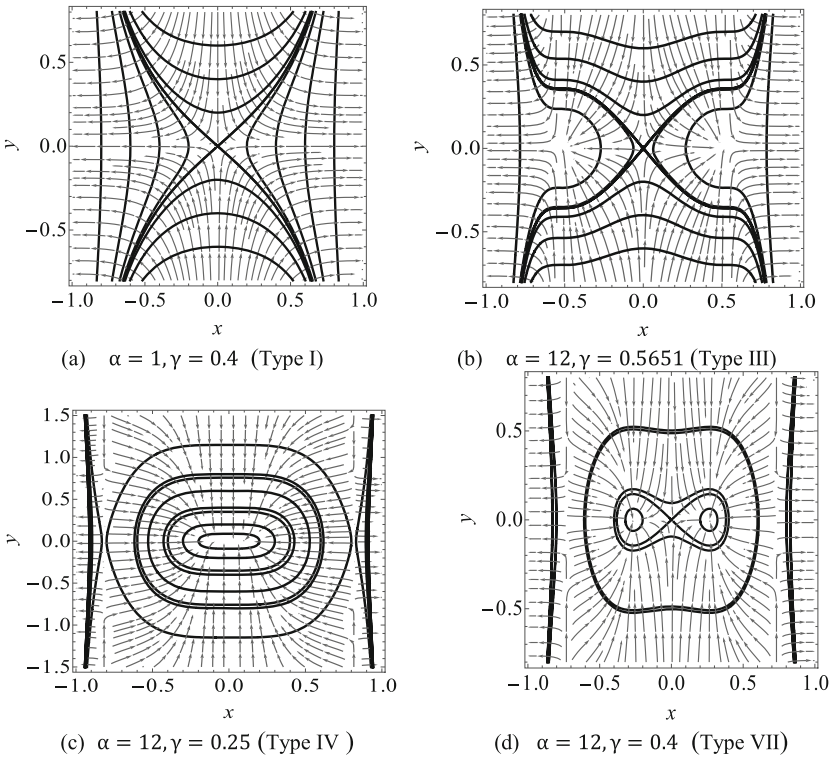

Fig. 2 Flow of some solutions around the equilibrium points

With the potential function, Eq. (9), we determine the stabilities for each type of equilibrium point. For Type I, Type II, and Type VI, there is only one equilibrium point at which the potential function is a local maximum, so the equilibrium point is unstable. For Type III, the potential function arrives at a local maximum at each of the three equilibrium points; all the equilibrium points are unstable. For Type IV and Type V, between the two unstable equilibrium points, there is a stable equilibrium point at which the potential function is a local minimum. Such stable equilibrium point forms a potential well. If the external excitation is not too large, the resonator will vibrate periodically in the well. In the same fashion, for Type VII, the two stable equilibrium points are embedded in the three equilibrium points; the resonator may vibrate periodically in a well, or out of the well, or jump from one well to the other well, depending upon the magnitude of the external excitation. When the latter case occurs, chaos appears.

Examples of flow for some solution types of equilibrium point are depicted in Fig. 2.

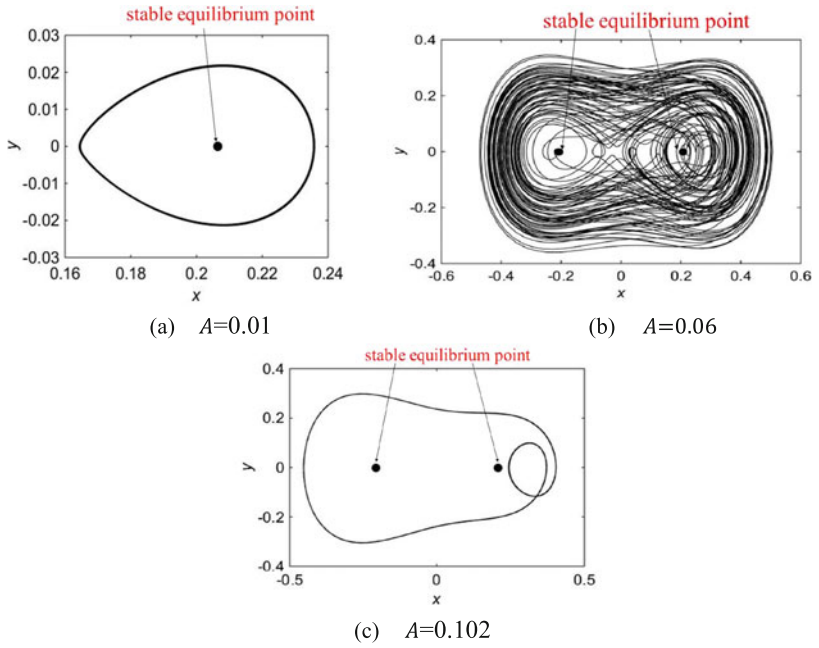

(a) A=0.01 (b) A=0.06

(c) A=0.102

Fig. 3 Phase portraits under different amplitude of driving voltage

3.2 Simulation of Fractional-Order Differential Equation for Microresonator

In the simulation, we set the fractional-orders in Eq. (4) as $p_1 = 1.995$ and $p_2 = 0.995$, and the parameters of microresonator $\alpha = 12$, $\mu = 0.01$, $\gamma = 0.338$, and $\omega = 0.5$.

From Table 1, we figure out that there will be three unstable equilibrium points and two stable equilibrium points, and the motion of the resonator is either periodic or chaotic.

Using Eq. (6) through Eq. (9), with the initial point [0, 0], we carry out simulation under the amplitude of the AC driving voltage, $A = \{0.01, 0.06, 0.102\}$, and the phase portraits of the dynamic model are shown in Fig. 3.

In Fig. 3, in the both cases, as $A = 0.01$ and $A = 0.102$, the trajectories are periodic, but for the case $A = 0.01$, the trajectory encircles only one stable equilibrium point. When A is increased to 0.102, more energy is inputted to the system, and the trajectory encircles two stable equilibrium points. While $A = 0.06$, the input energy is neither too less nor too much; therefore, the trajectory jumps from one potential well to the other, becoming chaotic. This situation is almost the same as that in integer-order dynamics Type VII described in the last section.

It should be noted that the differences between the fractional-orders and integer-orders are not great, not greater than 0.005 in this simulation, so it can be concluded that the behavior of a fractional-order dynamic model can be predicted by the rule of an integer-order dynamic model provided that the difference between the two orders is in a small interval.

4 The Effects of Varying the Fractional-Orders of Dynamics Model on the Motion of Microresonator

Figure 4 shows the bifurcation diagrams of the dimensionless parameter for the displacement of the resonator, x, with respect to the variations of fractional-orders, p_1 and p_2. The parameters of the microresonator are set as $\alpha = 12$, $\mu = 0.01$, $\gamma = 0.338$, $\omega = 0.5$ and $A = 0.0526$. From Fig. 4, it can be seen that the variations of both fractional-orders, p_1 and p_2, cause the motion of microresonator from periodic to chaotic or vice versa.

Figure 5 shows the changes in the motion state of the microresonator with respect to the simultaneous variation of p_1 and p_2, where the black "$_*$" indicates that at this point, i.e., taking the values of p_1 and p_2 at this point, the fractional-order dynamic model of the microresonator is in chaos.

As depicted in Fig. 5, when $p_1 = 2, p_2 = 1$, i.e., the integer-order dynamic model of Eq. (1), the dynamic system is in chaos, which is consistent with the discussion when A=0.06 in the last section, although here A=0.0526. It is also depicted in Fig. 5 that the motion of the resonator is most likely periodic as $p_1 \in [1, 2]$, $p_2 \in [0, 1]$. There are three bands in which the fractional-orders yield chaotic motion. They are nearby the point of p_1=1.2, interval (1.56, 1.7) and (1.93, 2) of p_1. And it can be seen that in the three bands, the values of p_2, whether large or small, almost have little effect on the chaotic motion of the resonator. So, as a whole, the fractional-order p_1 is more significant than the fractional-order p_2 in determining the motion state of the resonator.

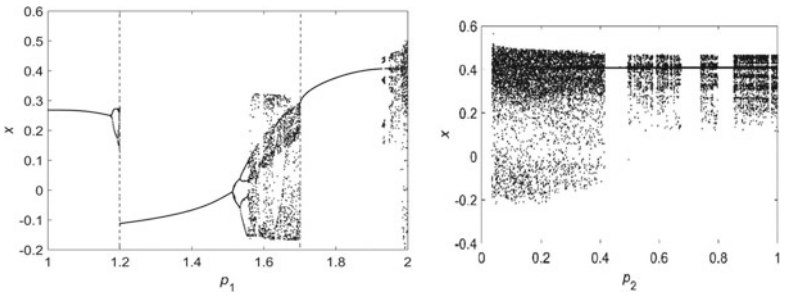

(a) as p_2=0.75 (b) as p_1=1.97

Fig. 4 The bifurcation diagram versus p_1 and p_2

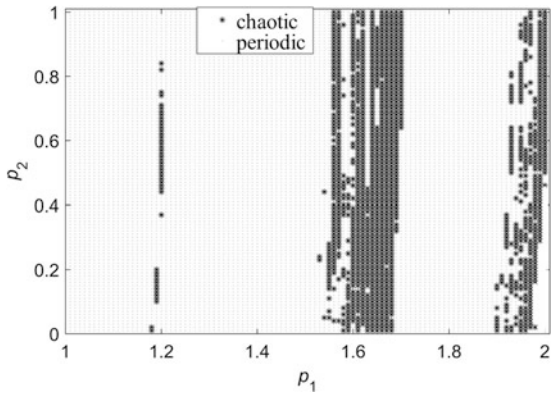

Fig. 5 The motion state of microresonator versus the variations of p_1 and p_2

5 Conclusions

Encouraged by the advantage of the fractional system, we analyze the dynamics of the microresonator with a fractional-order dynamic model, which is transformed from the integer-order dynamic model according to the definition of the Caputo fractional-order derivative. And the one-step Admas-Moulton algorithm is employed to carry out the simulation.

We apply the theory of equilibrium point and stability from integer-order dynamics to predict the behavior of fractional-order dynamic model. The results from simulation of fractional-order dynamic model confirm that this prediction is efficient under the condition that the difference between the fractional-order and integer-order is small enough. Using this way, the lack of physical meanings for the fractional-order derivative can be overcome.

By simulation of the fractional-order dynamic model, we obtain the bifurcation diagrams for the motion state of the microresonator. They show that the variation in fractional-order certainly causes some changes in the motion state of microresonator, maybe an alteration between periodic motion and chaotic motion. Whereas fractional-orders for different items in the same dynamic system have different significance for the determination of motion state.

With the results presented in this chapter, we will extend the research work to the analysis of a real microresonator and aim at finding the proper fractional-order for the microresonator.

Acknowledgments The authors would like to acknowledge the financial support of NSFC (National Natural Science Foundation of China) under the grants No. 51575457 and No. 52175031.

References

1. Liu, C.: Foundation of MEMS, 2nd edn. Pearson Education, Inc., London (2012)
2. Kempe, V.: Inertial MEMS: Principles and Practice. Cambridge University Press, New York (2011)

3. Farokhi, H., Ghayesh, M.H.: Electrically actuated MEMS resonators: effects of fringing field and viscoelasticity. Mech. Syst. Signal Process. **95**, 345–362 (2017)
4. Farokhi, H., Ghayesh, M.H.: Nonlinear thermo-mechanical behavior of MEMS resonators. Microsyst. Technol. **23**(12), 5303–5315 (2017)
5. Farokhi, H., Rocha, R.T., et al.: Nonlinear damping in micromachined bridge resonators. Nonlinear Dyn. (2022). https://doi.org/10.1007/s11071-022-07964-9
6. Wang, A., Sahandabadi, S., et al.: Modelling of air damping effect on the performance of encapsulated MEMS resonators. Microsyst. Technol. **28**, 2529–2539 (2022)
7. Jazar, R.N.: Nonlinear modeling of squeeze-film phenomena. In: Dai, W., Jazar, R.N. (eds.) Nonlinear Approaches in Engineering Applications. Springer, New York (2012)
8. Han, J., Zhang, Q., et al.: Design considerations on large amplitude vibration of a doubly clamped microresonator with two symmetrically located electrodes. Commun. Nonlinear Sci. Numer. Simul. **22**(1–3), 492–510 (2015)
9. Shoghmand, A., Ahmadian, M.T.: Dynamics and vibration analysis of an electrostatically actuated FGM microresonator involving flexural and torsional modes. Int. J. Mech. Sci. **148**, 422–441 (2018)
10. Guo, C., Fedder, G.K.: Bi-state control of a duffing microresonator on the falling edge of the instability. In: Morante, J.R., Hierold, C. (eds.) Transducers and Eurosensors 2013, pp. 1703–1706. IEEE Computer Society (2013)
11. Han, J., Zhang, Q., et al.: Stability and perturbation analysis of a one-degree-of-freedom doubly clamped microresonator with delayed velocity feedback control. J. Vib. Control. **24**(15), 3454–3470 (2018)
12. Almeida, R., Tavares, D., Torres, D.F.M.: The Variable-Order Fractional Calculus of Variations. Springer (2019)
13. Monje, C.A., Chen, Y., Vinagre, B.M., Xue, D., Feliu, V.: Fractional-Order Systems and Controls Fundamentals and Applications. Springer-Verlag London Limited, London (2010)
14. Meral, F.C., Royston, T.J., et al.: Fractional calculus in viscoelasticity: an experimental study. Commun. Nonlinear Sci. Numer. Simul. **15**, 939–945 (2010)
15. Di Paola, M., Pirrotta, A., et al.: Visco-elastic behaviour through fractional calculus: an easier method for best fitting experimental results. Mech. Mater. **43**, 799–806 (2011)
16. Kumar, R., Sharma, P.: Modelling of piezothermoelastic beam with fractional order derivative. Curved Layered Struct. **3**(1), 96–104 (2016)
17. Youssef, H.M., El-Bary, A.A., et al.: Characterization of the quality factor due to the static prestress in classical Caputo and Caputofabrizio fractional thermoelastic silicon microbeam. Polymers. **23**(1), 1–14 (2021)
18. Aghababa, M.P.: Chaos in a fractional-order micro-electro-mechanical resonator and its suppression. Chinese Phys. B. **21**(10), 100505 (2012)
19. (Stevanović) Hedrih, K.R, Machado, J.A.T., Discrete fractional order system vibrations: Int. J. Non-Linear Mech. **73**, 2–11 (2015)
20. Haghighi, H.S., Markazi, A.H.D.: Chaos prediction and control in MEMS resonators. Commun. Nonlinear Sci. Numer. Simul. **15**(10), 3091–3099 (2010)
21. Diethelm, K., Ford, N.J., et al.: A predictor-corrector approach for the numerical solution of fractional differential equations. Nonlinear Dyn. **29**(1), 3–22 (2002)
22. Robinson, R.C.: An Introduction to Dynamical System: Continuous and Discrete. Pearson Education, Inc., London (2004)

Bird-Like Trajectories in 6D Chaotic System Integrated with Fractional Order Derivative, Memristor, and Encryption

Muhammad Ali Qureshi

1 Introduction

Fractional order derivative calculus is currently playing a significant role in engineering and technological applications. The stable findings, complicated nature solution, memory effects, and heredity assets for many systems of the fractional derivative model over the integer derivative model are its advantages. In many fields of science, business, and engineering, fractional calculus has attracted significant interest and importance.

Nearly every branch of natural science, including physics, mathematics, biology, chemistry, genetics, economics, neurology, and ecology, includes chaos or nonlinear deterministic dynamical systems. Numerous research articles have exploited the continuous chaotic two-dimensional systems known as the Duffing oscillator and Van der Pol oscillator, respectively, proposed by George Duffing and Balthasar Van der Pol. Four-dimensional differential equations have also been used to create and study hyper-chaotic systems, such as the hyper-chaotic Newton-Leipnik system [1], etc.

Memristor chaotic systems (MCS) are a novel class of chaotic systems that have received a lot of attention lately. Memory resistance, often known as a memristor, is a fundamental part of a circuit system that Chua first outlined in 1971. The memristor's resistance varies with the amount of current flowing through the circuit while it is in operation, but when it is turned off, it does not vary. Memristors have nonlinear effects on voltage-ampere characteristics, which improve the performance of chaotic systems. Thus, it has been widely adopted by chaotic systems, leading to MCS [2].

M. A. Qureshi (✉)
Department of Physics, University of Karachi, Karachi, Pakistan
e-mail: maliqureshi@uok.edu.pk

© The Author(s), under exclusive license to Springer Nature Switzerland AG 2024

W. Lacarbonara (ed.), *Advances in Nonlinear Dynamics, Volume III*, NODYCON Conference Proceedings Series, https://doi.org/10.1007/978-3-031-50635-2_34

To the best of our knowledge, this study presents a novel six-dimensional chaotic system. The chaotic system is fused with a tangent hyperbolic memristor, and generated random numbers are utilized to encrypt images using an *amalgamated image encryption* scheme. The system dynamics are analyzed using different mathematical tools for different values of the fractional order q. The stability of the system is investigated with equilibrium points, Eigenvalues, Routh-Hurwitz stability criterion, Lyapunov exponents, Maximal Lyapunov, and Kaplan-Yorke dimension.

2 Fractional Derivative and Its Approximation

Definition 1 Fractional derivative definitions are of several forms, in which the Caputo fractional derivative is defined as [3]

$$D^{\alpha}\ y(x) = J^{m-\alpha}\ y^{m}\ (x), \qquad \alpha > 0 \tag{1}$$

where $m = [\alpha]$ is close to the integer order 1 and $y\ (m)$ is the ordinary derivative of y.

Definition 2 The Riemann-Liouville fractional derivative is defined as

$$\frac{d^{\alpha}\ f\ (t)}{dt^{\alpha}} = \frac{1}{\Gamma\ (n-\alpha)}\ \frac{d^{n}}{dt^{n}}\ \int_{\mathrm{a}}^{t} \frac{f\ (\tau)}{(t-\tau)^{\alpha-n+1}}\ d\tau, \tag{2}$$

for $n - 1 \leq \alpha < n$, where $\Gamma(\bullet)$ is the Gamma function.

The memristor emulator is applied to our novel system, which has a current–voltage relation as,

$$\begin{aligned} i &= W\ (v_0)\ v = [a - b\ \tanh\ (v_0)]\ v \\ \tau\ \tfrac{d\ v_0}{d\ t} &= f\ (v_0, v) = v_0 - v \end{aligned} \tag{3}$$

where i and v represent the current and voltage for the input and output of the memristor. v_0 is the inner state variable, and a, b are the positive constants. The integral time constant is τ, and $W\ (v_0)$ is the memductance, which is a nonlinear function defined as,

$$W\ (v_0) = a - b\ \tanh\ (v_0) \tag{4}$$

This implies that the memristor is a passive and voltage-controlled device [4].

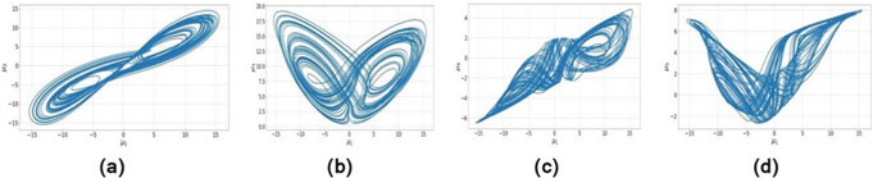

Fig. 1 The phase portraits of system (5) for $q = 1$ (**a**) (μ_1, μ_2), (**b**) (μ_1, μ_3), (**c**) (μ_1, μ_4), and (**d**) (μ_3, μ_4)

3 Novel Chaotic System Model

The developed system is a six-dimensional system with nineteen terms and state variables $(\mu_1, \mu_2, \mu_3, \mu_4, \mu_5, \mu_6)$, which is as follows:

$$\begin{aligned} D^q \dot{\mu}_1 &= a\ (\mu_2 - \mu_1) + \mu_2\mu_3 - h\mu_5\mu_4 - k\ (\varepsilon + \phi\ \ \tanh\ (\mu_6))\, \mu_2 \\ D^q \dot{\mu}_2 &= \ \ c\mu_2 - \mu_1\mu_3 \\ D^q \dot{\mu}_3 &= \ \ -b\mu_3 + \mu_1\mu_2 \\ D^q \dot{\mu}_4 &= \ \ \mu_2\mu_3 - c\mu_5 + \mu_3 - {\mu_4}^3 \\ D^q \dot{\mu}_5 &= \ \ \mu_2\,\mu_1 + d\mu_4 - \mu_5 - g\ e^{\mu_5} \\ D^q \dot{\mu}_6 &= \mu_2 \end{aligned} \tag{5}$$

Here, the values of constants are $a = 19$, $b = 5$, $c = 10$, $d = 15$, $g = 0.09$, $h = 3$, $k = 1$, $\varepsilon = 1$ and $\phi = 0.5$ with initial conditions $(1, 1, 1, 1, 1, 1)$ for our developed system. Through numerical simulation, we draw the chaotic trajectories of system (5) for $q = 0.99$, as shown in Fig. 1. Figure 1a–d illustrates the phase portraits (2D) graphs for (μ_1, μ_2), (μ_1, μ_3), (μ_1, μ_4), and (μ_1, μ_5), respectively.

4 Nonlinear Chaotic Dynamical System Analysis

4.1 Equilibrium Points and Stability Analysis

Firstly, the equilibrium points of system (5) are evaluated for different fractional order q values by solving the system in such a way that the right side of the equation is zero. The equilibrium points for integer and noninteger orders, i.e., $P_1\left(u_1^*, u_2^*, u_3^*, u_4^*, u_5^*, u_6^*\right)$, were calculated for different values of fractional order q, and are illustrated in Table 1. Further, the Jacobian matrix of system (5) for the equilibrium point $q = 1$ is calculated and its characteristic equation of the Jacobian matrix at $P_1$is

$$a_0\lambda^6 + a_1\lambda^5 + a_2\lambda^4 + a_3\lambda^3 + a_4\lambda^2 + a_5\lambda = 0 \tag{6}$$

Table 1 Equilibrium points for q values

q	μ_1^*	μ_2^*	μ_3^*	μ_4^*	μ_5^*	μ_6^*
1.00	0	0	0	0	0	253.528727
0.99	0	0	0	0	0	0
0.98	0	0	0	0	0	0
0.97	0	0	0	0	0	0

From Eq. (6), the coefficients of the polynomial can be obtained, which are

$$a_0 = 1, a_1 = a + b - c + 1.9, a_2 = ab - ac + 1.9a - bc + 1.09b + 13.1c,$$
$$a_3 = -abc + 1.09ab + 13.1ac + 13.1bc - 15c^2, a_4 = 13.1abc - 15ac^2 - 15bc^2,$$
$$a_5 = -15abc^2 \tag{7}$$

From Eq. (7), the calculated Eigenvalues are $\lambda_1 = 0$, $\lambda_{2,3} = -0.545 \pm 12.235\,j$, $\lambda_4 = -19$, $\lambda_5 = 10$ and $\lambda_6 = -5$. This shows that the Jacobian Matrix has three negative Eigenvalues, one zero Eigenvalues and two complex Eigenvalues, which clearly shows that the equilibrium points P_1 are saddle-focus points that are unstable.

4.2 *Lyapunov Exponent, Kaplan-Yorke, and Maximal Lyapunov*

The Lyapunov exponents (LE) values were calculated for different values of q for $a = 19$, $b = 5$, $c = 10$, $d = 15$, $g = 0.09$, $h = 3$, $k = 1$, $\varepsilon = 1$ and $\phi = 0.5$ for six-dimensional system $(\mu_1, \mu_2, \mu_3, \mu_4, \mu_5, \mu_6)$ with initial conditions [1, 1, 1, 1, 1, 1], results in three negative, two approximately approaching zero and are very small in magnitude as compared to other and one positive Lyapunov exponent. This suggests that the system is chaotic in nature. Further, the Kaplan-Yorke dimension of system (5) is calculated from the formula below:

$$D_{KY} = 5 + \frac{L_1 + L_2 + L_3 + L_4 + L_5}{\mid L_6 \mid} \tag{8}$$

Figure 2 illustrates the LEs of the system for $q = 1$, and for other fractional orders q, LEs are calculated and mentioned in Table 2 along with the Kaplan-Yorke dimension. Moreover, the stability and unstability of system (5) are determined by the largest/maximal Lyapunov. When $\lambda < 0$, the solution is almost stable, and when it is $\lambda > 0$, the solution is unstable, which means chaos [5]. The maximal Lyapunov are calculated for different values of q and are presented in Table 2.

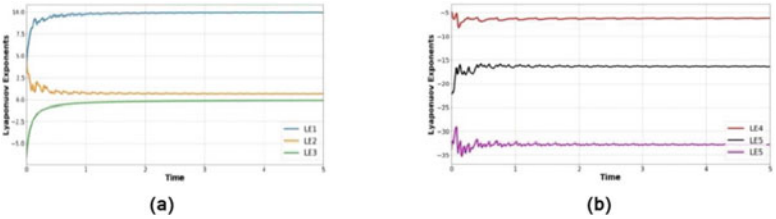

Fig. 2 Lyapunov exponents of the system (9) for $q = 1$ **(a)** LE_1, LE_2 and LE_3 **(b)** LE_4, LE_5 and LE_6

Table 2 Lyapunov exponents Kaplan-Yorke dimension and maximal Lyapunov for different q values

q	LE_1	LE_2	LE_3	LE_4	LE_5	LE_6	D_{KY}	Maximal LE
1.00	9.9012	0.6666	−0.2058	−6.7130	−15.8428	−32.7611	8.1653	0.00714
0.99	9.8537	0.6967	−0.2141	−6.2145	−16.4257	−32.7849	8.6208	0.01289
0.98	9.7907	0.7420	−0.2223	−6.0030	−16.7187	−32.7984	8.7975	0.01006
0.97	9.6969	0.8172	−0.2306	−5.9366	−16.8623	−32.8069	8.8329	0.00874

5 Chaotic System Circuit Implementation

In this section, we simulate the results of the fractional order memristor-based chaotic system (5) via active and passive electronic components. We first consider Eq. (5) and set circuital frequency to 1000 Hz with capacitors $C_1 = C_2 = C_3 = C_4 = C_5 = C_6 = C = 1\ nF$ than we applied Kirchhoff's law and the connection between the current and voltage of memristor described by Eq. (4), with given system parameters $a = 19$, $b = 5$, $c = 10$, $d = 15$, $g = 0.09$, $h = 3$, $k = 1$, $\varepsilon = 1$ and $\phi = 0.5$. For the fractional integrator, we consider an approximate transfer function at $q = 0.99$, which can take the approximate formula defined as follows [6]. This transfer function can be realized with analog components. The realized fractional order integrator for $q = 0.99$ is illustrated in Fig. 3 as a fractional order block (FO block) with normalized component values. Eq. (5) can be written in terms of circuit resistance and capacitor form as:

$$
\begin{aligned}
D^{0.99}\mu_1 &= \tfrac{1}{R_1C}\ \mu_2 - \tfrac{1}{R_2C}\mu_1 + \tfrac{1}{R_3C}\mu_2\mu_3 - \tfrac{1}{R_4C}\mu_5\mu_4 + \tfrac{1}{R_5C}\ \left(\tfrac{R_{45}}{R_{32}} + \tanh\ (\mu_6)\right)\ \mu_2 \\
D^{0.99}\mu_2 &= \tfrac{1}{R_6C}\mu_2 - \tfrac{1}{R_7C}\mu_1\mu_3 \\
D^{0.99}\mu_3 &= -\tfrac{1}{R_8C}\mu_3 - \tfrac{1}{R_9C}\ \mu_1\mu_2 \\
D^{0.99}\mu_4 &= \tfrac{1}{R_{10}C}\mu_2\ \mu_3 - \tfrac{1}{R_{11}C}\ \mu_5 + \tfrac{1}{R_{12}C}\ \mu_3 - \tfrac{1}{R_{13}C}\ {\mu_4}^3 \\
D^{0.99}\mu_5 &= \tfrac{1}{R_{14}C}\mu_2\ \mu_1 + \tfrac{1}{R_{15}C}\ \mu_4 - \tfrac{1}{R_{16}C}\ \mu_5 - \tfrac{1}{R_{17}C}\ e^{\mu_5} \\
D^{0.99}\mu_6 &= \tfrac{1}{R_{32}C}\mu_2
\end{aligned}
\tag{9}
$$

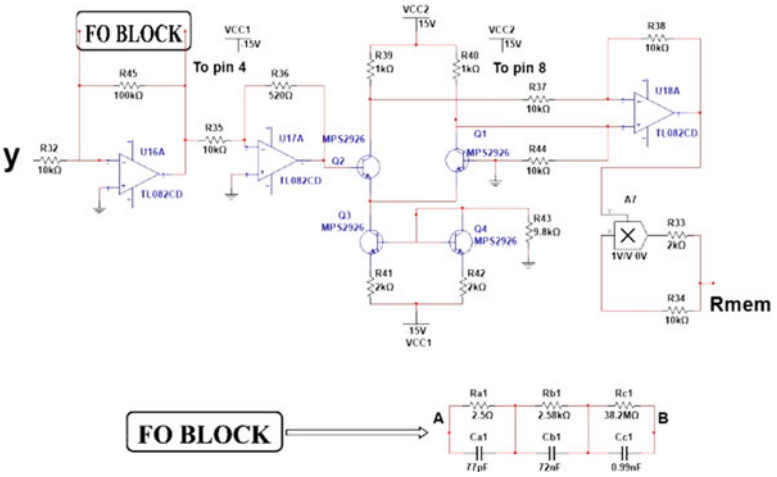

Fig. 3 Fractional order block and equivalent circuit of tangent hyperbolic memristor

The fractional order $q = 0.99$ electronic circuit is constructed using resistors, operational amplifiers TL082IP, multipliers and capacitors, four bipolar junction transistors MPS2926, along with a power supply for biasing voltage to amplifiers and transistors $\pm 15\ V$. For oscilloscopic results, we select the resistor and capacitor values shown in Figs. 3 and 4. The circuit-generated results are presented in Fig. 5. When the circuit system is simulated with an integer order $q = 0.99$, the fractional block (FO block) is attached to the operational amplifiers integrator to emulate the results with a tangential hyperbolic memristor. The electronically simulated results are illustrated in phase portraits, i.e., Fig. 5a for (μ_1, μ_2), Fig. 5b for (μ_1, μ_3), and Fig. 5c for (μ_1, μ_4) and Fig. 5c for (μ_1, μ_5). The realized circuit is generalized in a manner that if the fractional block is removed and the capacitor of $C = 1\ n\ F$ is attached, then the system works for an integer order, i.e., $q = 1$.

6 Amalgamated Image Encryption and Security Analysis

The random number generation (RNG) is the basic key for the encryption process. Chaotic data and a better algorithm scheme result in strong encryption, which is difficult to hack or third-party invasion. With immense modern applications in science and technology, cryptography (sound, image, video, PDF, Docx, digital watermarking, etc. [7–10] and cryptanalysis are the needs of the day. This section presents the application of chaotic image-data cryptography with amalgamated image encryption as our algorithm scheme. The encryption process is discussed

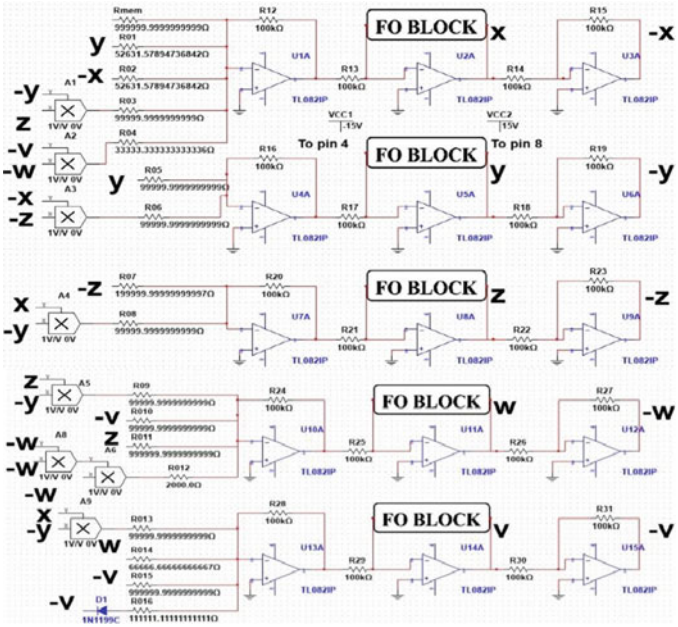

Fig. 4 Chaotic circuit by introducing tangent hyperbolic memristor with fractional order block

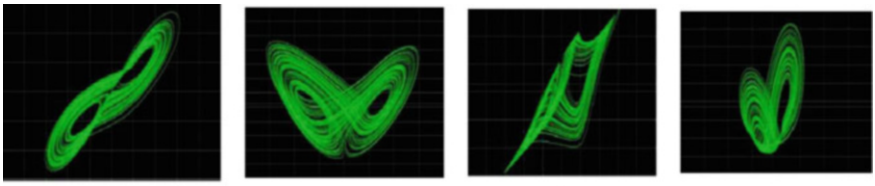

Fig. 5 Circuital generated results for system (8) at $q = 0.99$; (**a**) for (μ_1, μ_2), (**b**) for (μ_1, μ_3), and (**c**) for (μ_1, μ_4) and (**d**) for (μ_1, μ_5)

in detail and analyzed using image-security algorithms [11, 12]. Figure 6 shows the plain images utilized for doing the encryption process. Figure 7 illustrates the encryption and decryption process to be successful, as both the keys are correct, and Fig. 8 describes the encryption and decryption process with an incorrect key showing distortion in the decrypted portion. Figures 9 and 10 represent the histogram for Cat I and Cat II processes. Table 3 shows the security analysis of both Cat I and Cat II processes with PSNR, NPCR, UAIC, and Correlation Analysis.

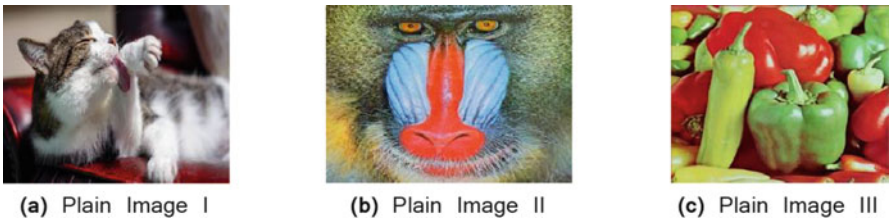

Fig. 6 Plain images utilized in encryption

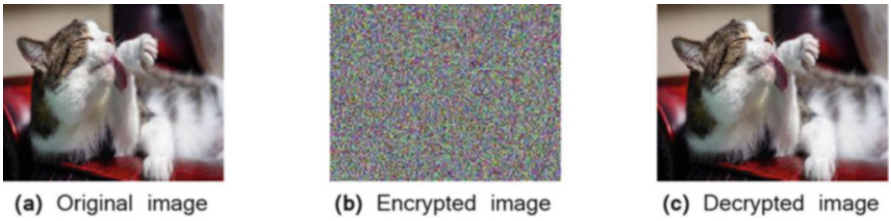

Fig. 7 Cat I (Encryption of Plain Image I with Plain Image II and decrypted through Plain Image II with chaotic data)

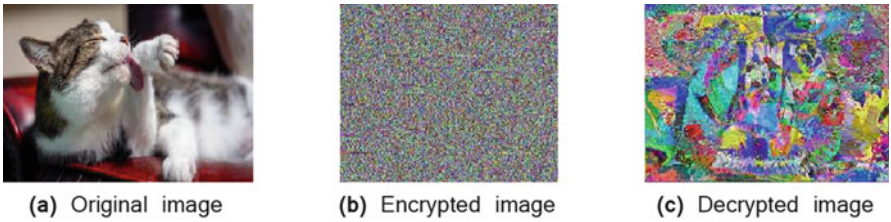

Fig. 8 Cat II (Encryption of Plain Image I with Plain Image II and decrypted through Plain Image III with chaotic data)

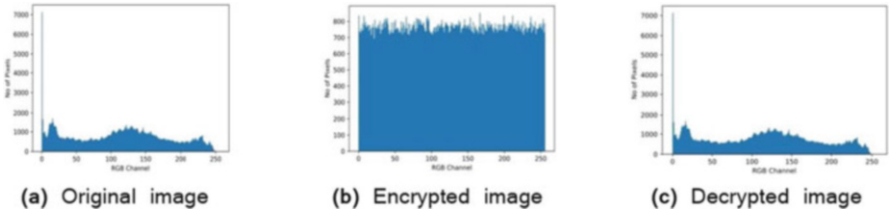

Fig. 9 Histogram of Plain Image I original, encryption and decryption for Cat I

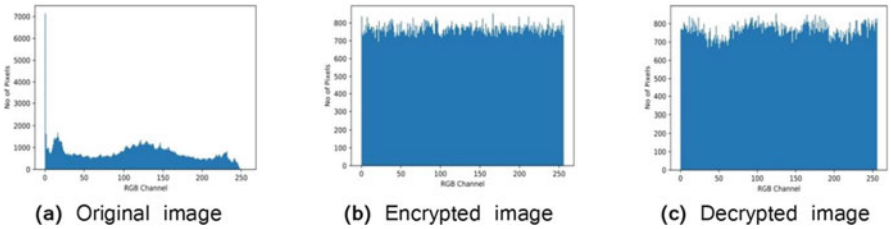

Fig. 10 Histogram of Plain Image I original, encryption and decryption for Cat II

7 Conclusion

To the best of our knowledge, this study presents a novel six-dimensional fractional order chaotic system, constructed using a tangent hyperbolic memristor. The dynamical system is analyzed using mathematical tools for different values of fractional order q. The analysis suggests that the system can generate chaos and is useful for cryptographic applications. Moreover, a graphical illustration of the characteristic curve generated by the system is presented in two-dimensional (2D), showing exciting new bird-like trajectories that have never been reported before. The circuit realization for a six-dimensional memristor-based system is carried out using *NI Multisim* with a fractional approximation transfer function technique for $q = 0.99$. Finally, complex dynamics are applied to perform image encryption with the idea of an image as a key, illustrated for both the outcomes when the key Plain Image is correctly or incorrectly inserted, and its encryption effectiveness is tested and analyzed using statistical image tools. The study has the following beneficial features:

- Many keys can be generated for securing communication in systems using FPGA (field programming gate array).
- Cryptography of voice, video, PDF, and Docx text files can be accomplished to ensure the security applications for this newly developed system.
- Biometric template protection, document watermarking, and other secret information stored in servers can be protected from potential attacks.

Table 3 Results of PSNR, NPCR, UAIC, and correlation analysis

Image	Dimension	MSE	PSNR	NPCR (%)	UAIC (%)	Correlation		
						Original image	Decrypted image	encrypted image
Cat I	256 × 256	0.00001	27.50464	99.5844	30.1688	0.96605	0.96605	0.20826
Cat II	256 × 256	388282274.2020	27.50464	99.5162	30.1688	0.96605	0.63848	0.20826

References

1. Vaidyanathan, S.V.: Adaptive control and synchronization of hyperchaotic Newton-Leipnik system. Int. J. Adv. Inform. Technol. **1**(3), 22–33 (2011)
2. Yang, S., et al.: Impulsive control and synchronization of memristor-based chaotic circuits. Int. J. Bifurcation Chaos. **24**(12), 1450162 (2014)
3. Caputo, M.: Linear models of dissipation whose Q is almost frequency independent—II. Geophys. J. R. Astron. Soc. **13**(5), 529–539 (1967)
4. Bao, B., et al.: Coexisting behaviors of asymmetric attractors in hyperbolic-type memristor based Hopfield neural network. Front. Comput. Neurosci. **11**, 81 (2017)
5. Li, J., Xu, W., Ren, Z., Lei, Y.: Maximal Lyapunov exponent and almost-sure stability for Stochastic Mathieu–Duffing systems. J. Sound Vib. **286**(1–2), 395–402 (2005)
6. Arıcıoğlu, B.: RNG and circuit implementation of a fractional order chaotic attractor based on two degrees of freedom nonlinear system. Analog Integr. Circ. Sig. Process. **112**(1), 49–63 (2022)
7. Khan, N.A., et al.: Emulate the chaotic flows of fractional jerk system to scramble the sound and image memo with circuit execution. Phys. Scr. **95**(6), 065217 (2020)
8. Khan, N.A., et al.: Behavioral effects of a four-wing attractor with circuit realization: a cryptographic perspective on immersion. Commun. Theor. Phys. **72**(12), 125004 (2020)
9. Qureshi, M.A.: Encryption-Python-Codes-0: Release of Video Encryption in Python. (Zenodo) (2021). https://doi.org/10.5281/zenodo.3693098
10. Qureshi, M.A.: Encryption-Python-Codes: Release of Voice and Image Encryption in Python. (Zenodo) (2020). https://doi.org/10.5281/zenodo.5499881
11. Khan, N.A., Qureshi, M.A., Akbar, S., Ara, A.: From chaos to encryption using fractional order Lorenz-Stenflo model with flux-controlled feedback memristor. Phys. Scr. **98**(1), 014002 (2022)
12. Qureshi, M.A.: Amalgamated Image Encryption, Circuit Realization for Lorenz-Stenflo Chaotic System. (Zenodo) (2022). https://doi.org/10.5281/zenodo.7046557

Generalized Fractional-Order Complex Logistic Map and Fractals on FPGA

Sara M. Mohamed, Wafaa S. Sayed, Lobna A. Said, and A. G. Radwan

1 Introduction

Chaotic systems are characterized by many interesting behaviors like randomness, unpredictability, aperiodicity, and sensitivity [1]. Chaotic systems are classified into discrete-time maps and continuous-time differential equations [2]. Figure 1 shows the classification of discrete maps with examples on each class. The logistic and tent map are integer-order maps and can be extended to fractional. Additionally, logistic and Gaussian are real maps and can be extended to complex, while Mandelbrot and Julia are complex maps by their nature. Realizations in digital hardware have become more practical for industrial use. When using fixed-point registers, FPGAs have many benefits, including ease of design, high speed, programmability, low hardware cost, noise immunity, rapid prototyping, reliability, reproducibility, and reconfigurability [3].

One of the most attractive chaotic characteristics is the fractal identity [4]. The term "fractal" was coined by Benoit Mandelbrot to describe the form produced by the following equation:

S. M. Mohamed · L. A. Said (✉)
Nanoelectronics Integrated Systems Center (NISC), Nile University, Giza, Egypt
e-mail: sara.mostafa@nu.edu.eg; l.a.said@ieee.org

W. S. Sayed
Engineering Mathematics and Physics Department Faculty of Engineering, Cairo University, Cairo, Egypt

A. G. Radwan
Engineering Mathematics and Physics Department Faculty of Engineering, Cairo University, Cairo, Egypt

School of Engineering and Applied Sciences, Nile University, Giza, Egypt

© The Author(s), under exclusive license to Springer Nature Switzerland AG 2024

W. Lacarbonara (ed.), *Advances in Nonlinear Dynamics, Volume III*, NODYCON Conference Proceedings Series, https://doi.org/10.1007/978-3-031-50635-2_35

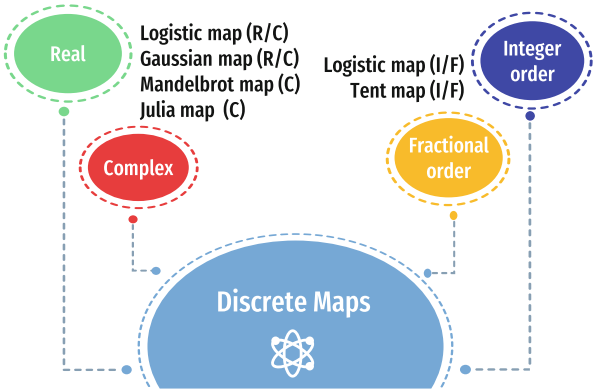

Fig. 1 Classification of discrete maps

$$z_{n+1} = z_n^2 + c, \tag{1}$$

where z and $c \in \mathbb{C}$, z_n is the system's iterated variable and can be assumed as $z_n = x_n + iy_n$. Several works introduced fractal generation from integer-order complex discrete maps including logistic and Gaussian maps [5–7].

In [5], the authors investigate the fractal-like activity demonstrated from the complex form of Gaussian chaotic map and its FPGA realization. In order to derive an explanation for the fractal behavior, the fractals emerging from the observed complex map are analyzed in comparison to various map coefficients for the highest chaotic periods. The work [6] studies the digital architecture's ability to mimic fractals generated from the generalized positive complex logistic map. To better comprehend the fractal behavior with various variations, the fractals generated from this system are linked to the outcomes of the mathematical analysis. In [7], a novel generalized complex logistic map is introduced, along with the FPGA implementation of an application for fractal production. The establishment of fractal limits is formulated from the relationship between mathematical analysis and fractal activity.

The generalization of conventional chaotic systems into the fractional-order domain increases the degree of freedom in design and enhances their dynamics and chaotic behaviors [8–10]. Many applications, including encryption [11], neural networks [12], synchronization [13], and multi-scroll generation [14], used discrete fractional-order chaotic maps. Among several fractional definitions [8, 9, 11], EL Raheem's definition is simple and suitable for hardware implementation [9].

This paper proposes a fractional-order complex logistic map, fractals, and their FPGA realization. The chaotic properties of the proposed map are studied using bifurcation and MLE diagrams. The proposed hardware implementation of the fractals based on the fractional-order complex logistic map utilizes simplified steps. The fractal behaviors are validated experimentally on an Artix-7 FPGA kit. The proposed implementation is compared to recent related works demonstrating its hardware efficiency and suitability for potential applications.

2 The Genesis of Generalized Fractional Complex Logistic Map

2.1 Literature Survey

The generalized complex logistic map, which was presented in [7], starts from:

$$z_{n+1} = r z_n \left(a - b z_n\right). \tag{2}$$

and follows a modification approach similar to [15] as follows:

$$z_{n+1} = \beta(r z_n(a - b z_n)) + (1 - \beta) z_n, \tag{3a}$$

Then, by decomposing the complex variable z_n, the real and imaginary components are given by:

$$x_{n+1} = \beta(r_x(a x_n - b x_n^2 + b y_n^2) - r_y(a y_n - 2b x_n y_n)) + (1 - \beta) x_n, \tag{3b}$$

$$y_{n+1} = \beta(r_x(a y_n - 2b x_n y_n) + r_y(a x_n - b x_n^2 + b y_n^2)) + (1 - \beta) y_n, \tag{3c}$$

where $r = r_x + i r_y$ and $\beta \in (0, 1]$.

The fractional counterpart of an integer real discrete map $x_{n+1} = f(x_n)$ is given by:

$$x_{n+1} = x_n + \frac{\mu^\alpha}{\Gamma(1 + \alpha)} f(x_n), \tag{4}$$

where α is the fractional-order and μ is a parameter.

2.2 Generalized Fractional Complex Logistic Map

A fractional complex discrete map can be obtained by substituting in (4) by z_n:

$$z_{n+1} = z_n + \frac{\mu^\alpha}{\Gamma(1 + \alpha)} f(z_n). \tag{5}$$

Thus, the generalized complex logistic map in (3) is extended to fractional domain as follows:

$$z_{n+1} = z_n + \frac{\mu^\alpha}{\Gamma(1 + \alpha)} (\beta(r z_n(a - b z_n)) + (1 - \beta) z_n), \tag{6a}$$

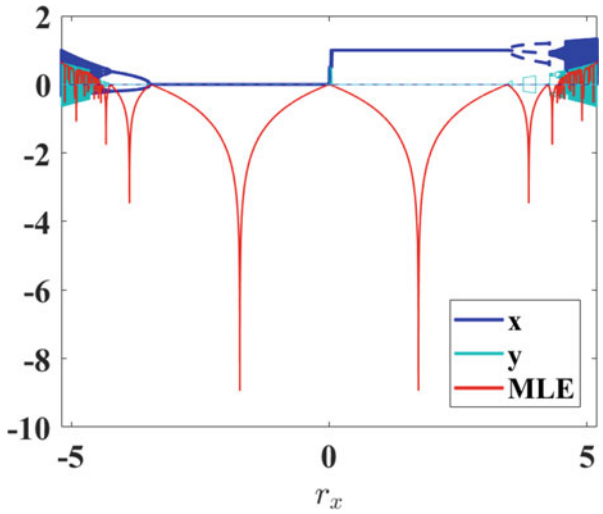

Fig. 2 Bifurcation and MLE of the generalized fractional complex logistic map at $a = 1$, $b = 1$, $r_y = 0$, $\beta = 1$, $\alpha = 1.25$, and $\mu = 0.712$

$$x_{n+1} = f_1(x_n, y_n) = x_n + \frac{\mu^\alpha}{\Gamma(1+\alpha)}(\beta(r_x(ax_n - bx_n^2 + by_n^2) - r_y(ay_n - 2bx_n y_n)) + (1-\beta)x_n), \tag{6b}$$

$$y_{n+1} = f_2(x_n, y_n) = y_n + \frac{\mu^\alpha}{\Gamma(1+\alpha)}(\beta(r_x(ay_n - 2bx_n y_n) + r_y(ax_n - bx_n^2 + by_n^2)) + (1-\beta)y_n). \tag{6c}$$

The bifurcation diagrams, one for the real part x and the other for the imaginary part y, and MLE of the generalized fractional complex logistic map at $a = 1$, $b = 1$, $r_y = 0$, $\beta = 1$, $\alpha = 1.25$, $\mu = 0.712$ are shown in Fig. 2. The chaotic range in the bifurcation is confirmed by the values of MLE, which exceed zero.

The bifurcation and MLE diagrams of the generalized fractional complex logistic map are shown in Fig. 3a at $a = 0.5$, 1, 2, 3 and 4, Fig. 3b at $b = 0.5$, 1, 2, 3 and 4, and Fig. 3c at $\alpha = 0.5$, 0.75, 1, 1.25 and 1.5 for $r_y = 0$, $\beta = 1$, $\alpha = 1.25$, $\mu = 0.25$. In Fig. 3a, as a increases, the r_x range corresponding to the bounded responses decreases, while the z range increases. In Fig. 3b, as b increases, the r_x range corresponding to the bounded responses remains fixed, while the z range decreases. In Fig. 3c, as α increases, the r_x range corresponding to the bounded responses increases, while the z range remains fixed.

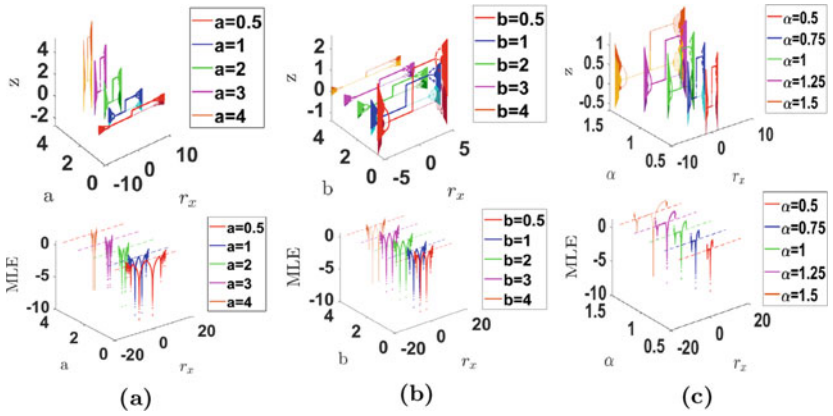

Fig. 3 Generalized fractional complex logistic map bifurcation and MLE diagrams with the changing (**a**) a, (**b**) b, and (**c**) α

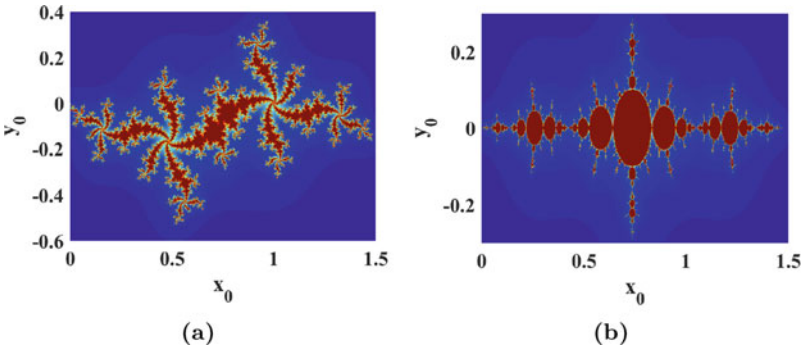

Fig. 4 Fractal generated based on fractional complex logistic map for $a = 1$, $b = 1$, $\alpha = 1.25$, $\mu = 0.712$ (**a**) $r_x = 3.2$, $r_y = 1.13$, $\beta = 1$ and (**b**) $r_x = 5.1$, $r_y = 0$, $\beta = 0.8$

3 Fractal Generation

Fractals can be generated based on the generalized fractional complex logistic map as shown in the two examples of Fig. 4 at different combinations of the parameters $a, b, \alpha, \mu, r_x, r_y$, and β of (6). The steps of fractal generation process are illustrated in the flowchart shown in Fig. 5, which extends the work in [7] to the fractional domain and is suitable for hardware realization. First, all parameters are initialized, where x_0, y_0 are the initial values of (6) and $\rho = \frac{\mu^{\alpha}}{\Gamma(1+\alpha)}$ is stored in a register for simplicity in hardware calculations. In addition, n_1, n_2 are the sizes of two-dimensional axes holding the fractal shape, δ is a step size, and λ is the number of iterations of the proposed map. Besides, s is the absolute squared of z, w is a register, d is the process counter, and j, m, k are counters. For $k > \lambda$, x_0 is increased by δ, j is incremented by 1, and k is set to 1. On the other hand, for $k < \lambda$, if $s < (\frac{2}{\beta})^2$,

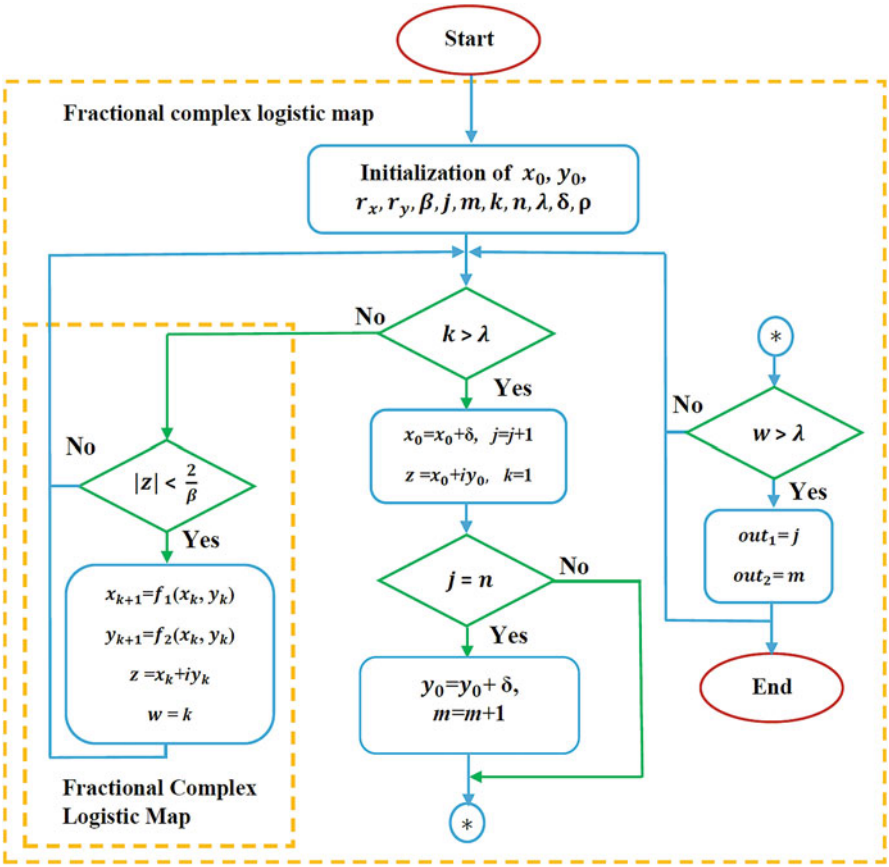

Fig. 5 Flowchart of fractal generation from fractional complex logistic map

which preserves the fractal connectivity [16], the equations (6) are executed and w stores the value of counter k. When $j = n_1$, y_0 is increased by δ, m is incremented by 1 and x_0 is set to x_{min}. Then, if $w > \lambda$, the values of j, m are out forming the fractal structure. Finally, this process is regenerated till getting the required fractal shape at $d > n_1 n_2 \lambda$.

4 FPGA Implementation and Results

The comprehensive hardware architecture that mimics the fractal generation process is shown in Fig. 6. The two registers for the initial values x_0 and y_0 are set to x_{min} and y_{min}, respectively, which vary depending on the target fractal temple. Besides, Fig. 6 clarifies the inner architecture of the fractional complex logistic map (6)

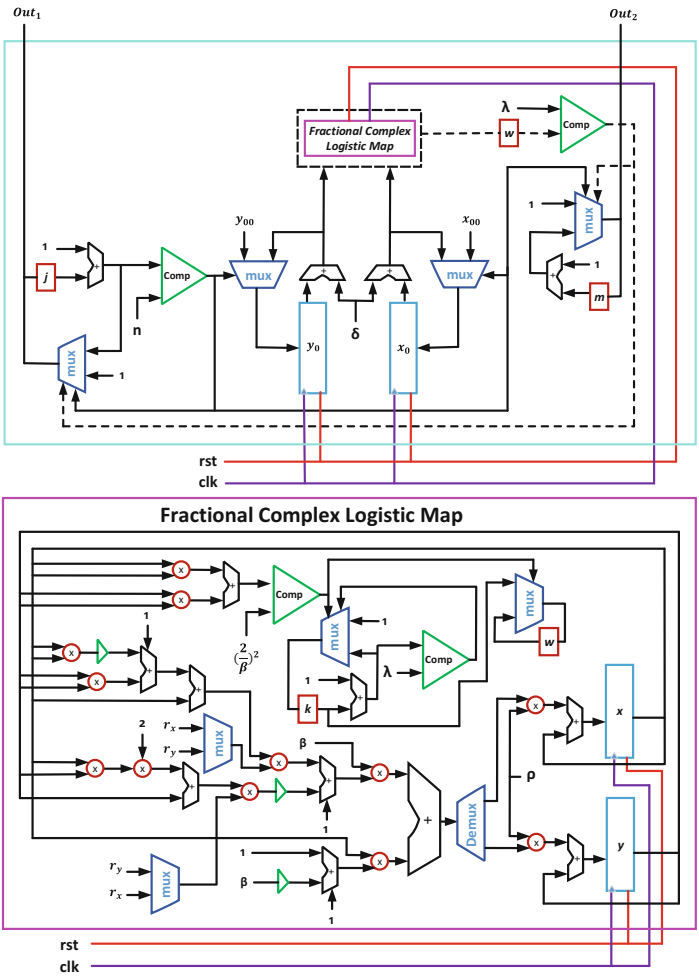

Fig. 6 Hardware architecture of the fractional complex logistic map-based fractal generation

module. The registers x_0, y_0, x, y are all represented in 32-bit fixed point, 8b for integer part and 24b for fractional part. The outputs j and m are represented in 12-bit.

The proposed design for fractals based on the generalized fractional complex logistic map was written in Verilog HDL with the simulation of Xilinx ISE 14.7 and implemented on Xilinx FPGA Artix-7 XC7A100TCSG324 by using Chip scope. The outputs j and m were wired to a 12-bit digital-to-analog converter, which is connected to a digital oscilloscope to display the fractal behavior. The example in Fig. 4b was realized and validated experimentally on FPGA. The design achieves a frequency of 24.34 MHz and a throughput of 0.292 Gbit/s.

Table 1 FPGA resources' summary of fractals based on fractional and integer complex maps

Logic utilization	Order	Complex map	FPGA device	Total no. of slice LUTs	Total no. of slice registers	Mult.	Add.	Comp.	Max freq (MHz)	Throughput (Gbit/s)
Proposed	Fractional	Eq. (6)	Artix-7	1087 (1%)	453 (1%)	18	16	8	24.34	0.292
[7]	Integer	Eq. (3)	Artix-7	969 (1%)	288 (1%)	14	11	6	31.979	0.384
[6]	Integer	Logistic	Virtex-5	977 (3%)	385 (1%)	6	6	10	52.280	0.627
[5]	Integer	Gaussian	Virtex-5	603 (2%)	21340 (74%)	130	106	49	7.955	0.095

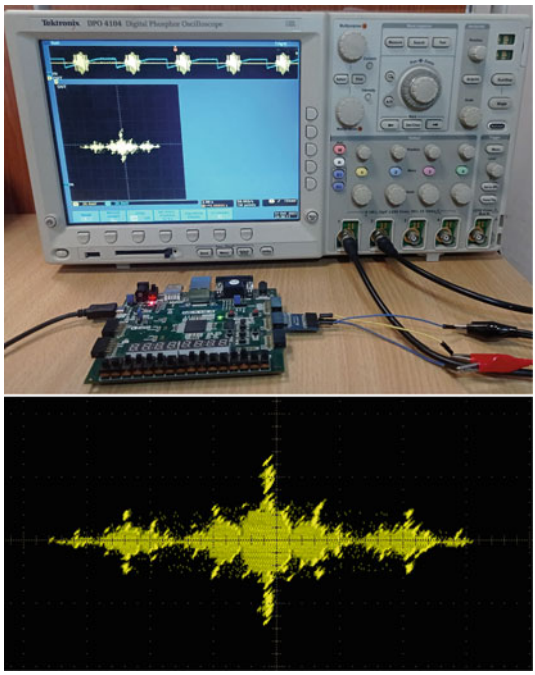

Fig. 7 FPGA experimental results of fractal based on fractional complex logistic map in Fig. 4b

Table 1 presents a summary of FPGA implementation results of this work and other implemented fractal works [5–7]. The proposed implementation consumes higher resources and lower frequency than [6, 7] due to the excessive arithmetic operations needed for the fractional domain. On the other hand, the proposed implementation achieves efficient hardware utilization and speed than [5] due to the simplicity of operations of the proposed map than Gaussian map.

Figure 7 shows the FPGA experimental results of the fractal realized based on the fractional complex logistic map. The proposed realization is considered a promising solution to increase the degrees of freedom in the design and enhance the performance in different applications such as multi-scroll generators, encryption schemes, image processing, and stochastic fractal search algorithm [17].

5 Conclusion

The paper proposed a generalized fractional-order complex logistic map and FPGA realization of fractals generated from it. The bifurcation and MLE of the proposed map were studied. A flowchart of an optimized fractal generation process and the corresponding hardware architecture were proposed. An example of fractal implementation is verified on Artix-7 FPGA board, yielding a frequency 24.34 MHz and a throughput of 0.292 Gbit/s. The proposed fractal generation hardware

with efficient utilization can be beneficial for several potential applications such as encryption schemes and multi-scroll generators.

Acknowledgments This paper is based upon the work supported by the Science, Technology, and Innovation Funding Authority (STIFA) under grant number (#38161).

References

1. Zidan, M.A., Radwan, A.G., Salama, K.N.: Random number generation based on digital differential chaos. In: 2011 IEEE 54th International Midwest Symposium on Circuits and Systems (MWSCAS), pp. 1–4. IEEE (2011)
2. Di Bernardo, M., Vasca, F.: Discrete-time maps for the analysis of bifurcations and chaos in dc/dc converters. IEEE Trans. Circuits Syst. I Fund. Theory Appl. **47**(2), 130–143 (2000)
3. Jiang, C.X., Carletta, J.E., Hartley, T.T., Veillette, R.J.: A systematic approach for implementing fractional-order operators and systems. IEEE J. Emerg. Sel. Top. Circuits Syst. **3**(3), 301–312 (2013).
4. Bouallegue, K., Chaari, A., Toumi, A.: Multi-scroll and multi-wing chaotic attractor generated with julia process fractal. Chaos Solitons Fractals **44**(1-3), 79–85 (2011)
5. AboAlNaga, B.M., Said, L.A., Madian, A.H., Radwan, A.G.: Analysis and fpga of semi-fractal shapes based on complex gaussian map. Chaos Solitons Fractals **142**, 110493 (2021)
6. Abo-Alnaga, B.-A. M., Said, L.A., Madian, A.H., Radwan, A.G.: Fpga realization of complex logistic map fractal behavior. Fractals **30**(01), 2250023 (2022)
7. Mohamed, S.M., Sayed, W.S., Said, L.A., Radwan, A.G.: Fpga realization of fractals based on a new generalized complex logistic map. Chaos Solitons Fractals **160**, 112215 (2022)
8. Wu, G.-C., Baleanu, D.: Discrete fractional logistic map and its chaos. Nonlinear Dyn. **75**(1), 283–287 (2014)
9. El Raheem, Z., Salman, S.: On a discretization process of fractional-order logistic differential equation. J. Egypt. Math. Soc. **22**(3), 407–412 (2014)
10. Munkhammar, J.: Chaos in a fractional order logistic map. Fract. Calculus Appl. Anal. **16**(3), 511–519 (2013)
11. Ismail, S.M., Said, L.A., Rezk, A.A., Radwan, A.G., Madian, A.H., Abu-Elyazeed, M.F., Soliman, A.M.: Generalized fractional logistic map encryption system based on fpga. AEU-Int. J. Electron. Commun. **80**, 114–126 (2017)
12. Chen, L., Yin, H., Huang, T., Yuan, L., Zheng, S., Yin, L.: Chaos in fractional-order discrete neural networks with application to image encryption. Neural Networks **125**, 174–184 (2020)
13. Khennaoui, A.-A., Ouannas, A., Bendoukha, S., Grassi, G., Lozi, R.P., Pham, V.-T.: On fractional-order discrete-time systems: Chaos, stabilization and synchronization. Chaos Solitons Fractals **119**, 150–162 (2019)
14. Ben Slimane, N., Bouallegue, K., Machhout, M.: Designing a multi-scroll chaotic system by operating logistic map with fractal process. Nonlinear Dyn. **88**(3), 1655–1675 (2017)
15. Rani, M., Agarwal, R.: Generation of fractals from complex logistic map. Chaos Solitons Fractals **42**(1), 447–452 (2009)
16. Peitgen, H.-O., Jürgens, H., Saupe, D.: Fractals for the Classroom: Part One Introduction to Fractals and Chaos. Springer Science & Business Media, New York (2013)
17. Banerjee, S., Hassan, M.K., Mukherjee, S., Gowrisankar, A.: Fractal Patterns in Nonlinear Dynamics and Applications. CRC Press, Boca Raton (2020)

Fractional Control Performance Assessment of the Nonlinear Mechanical Systems

Patryk Chaber and Paweł D. Domański

1 Introduction

Increasing interest in the Industry 4.0 transformation pushes industrial systems toward their technological edges. Production must be versatile, flexible, and sustainable supporting vertical and horizontal integration. The plant requires stringent control system operating close to the technological constraints. It's crucial to assess the quality of the control system with a reliable methodology. Therefore, a control performance assessment (CPA) plays a crucial role in good practices.

The CPA story started in the 1960s with the univariate PID-based loop assessment done for a pulp and paper plant using deviation benchmarking. Since those days, the assessment solutions have evolved in many directions and have successfully delivered mature approaches to the industry [1]. Current research covers many different areas [1, 2]. One may distinguish methods that require the plant experiment [3], methods that need the plant model [4], model-free approaches that directly use only the data [3, 5], and various hybrid techniques [6, 7]. It should be noted that the majority of those methods aim at linear and Gaussian systems, while undefined or unclear areas are rarely addressed. In contrary, industrial practice is complex and nonlinear and exhibits unknown stochastic properties. Thus, there is still a demand for new approaches that would address these issues.

Alternative nonlinear and non-Gaussian CPA approaches originate from the review and observations of industrial systems. Real process data exhibit significant nonlinearities impacted by frequent correlations between values at different time scales and with varying delays. Such a behavior might relate to the long-range dependence, non-stationarity, and persistence properties. Regression Box-Jenkins

P. Chaber · P. D. Domański (✉)
Institute of Control and Computation Engineering, Warsaw University of Technology, Warsaw, Poland
e-mail: Patryk.Chaber@pw.edu.pl; Pawel.Domanski@pw.edu.pl

© The Author(s), under exclusive license to Springer Nature Switzerland AG 2024

W. Lacarbonara (ed.), *Advances in Nonlinear Dynamics, Volume III*, NODYCON Conference Proceedings Series, https://doi.org/10.1007/978-3-031-50635-2_36

models are not enough as they are unable to capture all the phenomena reflected in the considered time series. Research shows that ARFIMA (autoregressive fractionally integrated moving average) models can take those effects into account [8]. The review of industrial data confirms the hypothesis that fractional-order approach enables to model such systems [9].

The goal of this research exploits the above. If the ARFIMA approach can model time series originating from the control of nonlinear processes, its coefficients, like the fractional order, could be used as a measure informing about the quality of the operation. This hypothesis is strengthened by the fact that previous research pointed out that the Hurst exponent (related to the fractional order), which measures data persistence, might be considered as the potential CPA index [10]. The research uses Geweke-Porter-Hudak (GPH) log periodogram regression (LPR) fractional-order estimator [11] d_{GPH} as the CPA index. It is shown that it represents the control quality of the real mechanical servomechanism system. The paper compares GPH fractional-order estimator with integral square error (ISE) and integral of absolute error (IAE).

The paper starts with the rationale for the research. CPA measures are described in Sect. 2 followed by the servomechanism stand and the experiments explained in Sect. 3. The results are summarized with their discussion in Sect. 4. Section 5 concludes the research and points out open issues.

2 Algorithms and Methods

Actually, three main areas are described: the α-stable fat tail distribution used as the disturbance, the CPA applied methods, and GPH fractional-order estimator.

2.1 The α-Stable Distribution

Stable functions deliver an alternative set of the statistical measures. α-stable distribution is expressed through the characteristic equation:

$$F^{\mathrm{stab}}_{\alpha,\beta,\delta,\gamma}(x) = \exp\left\{i\delta x - |\gamma x|^{\alpha}\left(1 - i\beta l(x)\right)\right\}, \tag{1}$$

with

$$l(x) = \begin{cases} \operatorname{sgn}(x)\tan\left(\frac{\pi\alpha}{2}\right) & \text{for } \alpha \neq 1 \\ \operatorname{sgn}(x)\frac{2}{\pi}\ln|x| & \text{for } \alpha = 1 \end{cases} \tag{2}$$

$0 < \alpha \leq 2$ is called the stability index, $|\beta| \leq 1$ a skewness factor, $\delta \in \mathbb{R}$ a shift coefficient, and $\gamma > 0$ a distribution scale.

2.2 Control Performance Assessment

The relationship between the process and the control system is direct. Better control means higher performance. Despite being obvious, a high share of industrial loops is neither well-tuned nor designed [12]. There are two types of CPA techniques [13, 14]: model-free and model-based. The distinction matters: model-based methods require a priori knowledge, while the other uses only the data. Our analysis uses model-free approach. Integrals ISE and IAE are benchmarks (N_p, the number of data; $y^\mathrm{sp}(k)$, setpoint; and $y(k)$, process variable):

$$\mathrm{ISE} = \frac{1}{N_\mathrm{p}} \sum_{k=1}^{N_\mathrm{p}} \left[y^\mathrm{sp}(k) - y(k) \right]^2, \quad \mathrm{IAE} = \frac{1}{N_\mathrm{p}} \sum_{k=1}^{N_\mathrm{p}} \left| y^\mathrm{sp}(k) - y(k) \right|. \tag{3}$$

The ISE penalizes errors with large values. The ISE used as a regression index exhibits 0% breakdown point [15]. The IAE is less conservative as it penalizes oscillations. Although its breakdown point is 0% as well, it protects regression against some outlying observations and is preferred over the ISE.

2.3 ARFIMA Models

ARFIMA time series are considered as an extension of classical ARIMA regression models [8]. The process x_k is denoted as ARFIMA(p, d, q) with

$$A_p(z^{-1}) \cdot x_k = B_q(z^{-1}) \cdot \left(1 - z^{-1}\right)^{-d} \epsilon_k, \tag{4}$$

where $A(z^{-1})$ and $B(z^{-1})$ are the polynomials in time delay operator z^{-1} and ϵ_k is a noise being a random variable with finite or infinite variance. Gaussian noise is selected in this work. Fractional order $-0.5 < d < 0.5$ refers to process memory.

For $d \in (0, 0.5)$, the process exhibits long memory or long-range positive dependence (persistence). The process has intermediate memory (anti-persistence) or long-range negative dependence, when $d \in (-0.5, 0)$. The process has short memory for $d = 0$; it is stationary and invertible ARMA. ARFIMA(p, d, q) time series is calculated by d-fractional integrating of a classical ARMA(p, q) process. The d-fractional integrating through the $\left(1 - z^{-1}\right)^{-d}$ operator causes the dependence between observations, even as they are far apart in time.

The **Geweke-Porter-Hudak (GPH)** estimator uses a semi-parametric procedure to estimate memory parameter d_GPH for ARFIMA process x_k [11]:

$$x_k = \left(1 - z^{-1}\right)^{-d} \epsilon_k, \tag{5}$$

Next, ordinary least squares (LS) are applied to estimate $\hat{d}$ from the

$$\log\left(I_x(\lambda_s)\right) = \hat{c} - \hat{d}\left|1 - e^{i\lambda_s}\right| + \text{residual}, \tag{6}$$

And evaluated for fundamental frequencies $\left\{\lambda_s = \frac{2\pi s}{n}, s = 1, \ldots, m,\ m < n\right\}$, m is the largest integer in $(n-1)/2$ and $\hat{c}$ is a constant. Discrete x_k Fourier transform is defined as

$$\omega_x(\lambda_s) = \frac{1}{\sqrt{2\pi n}} \sum_{k=1}^{n} x_k e^{ik\lambda_s}. \tag{7}$$

Application of the LS algorithm to Eq. (5) yields to the resulting formulation

$$\hat{d} = \frac{\sum_{s=1}^{m} x_s \log I_x(\lambda_s)}{2\sum_{s=1}^{m} x_s^2}, \tag{8}$$

where $I_x(\lambda_s) = \omega_x(\lambda_s)\omega_x(\lambda_s)^*$ being a periodogram and $x_s = \log\left|1 - e^{ik\lambda_s}\right|$. GPH evaluates d_{GPH} without explicit specification of the ARMA model polynomial orders. The research uses Beran's implementation [16].

2.4 Non-stationarity Tests

Dynamics may be tested by stationarity tests. The presence of a unit root indicates that the time series is non-stationary. Augmented Dickey-Fuller test (DF-GLS) assesses the null hypothesis of a unit root [17]. An alternative test, like Kwiatkowski-Phillips-Schmidt-Shin [18] (KPSS) test, is used to confirm the verdict of the DF-GLS. The following aspects are the results of using both tests:

1. DF-GLS and KPSS conclude non-stationarity.
2. DF-GLS and KPSS conclude that series is stationary.
3. DF-GLS concludes stationarity and KPSS the opposite.
4. DF-GLS concludes non-stationarity and KPSS the stationarity.

In the first and second case, the result and interpretation is straightforward. Case 3 implies that data is difference stationary and the differencing is needed to make data strictly stationary. The last case implies the need for detrending.

3 The Process and Experiments

The laboratory Modular Servo System with the INTECO digital servomechanism [19] is used during the experiments to visualize the method, as shown in Fig. 1.

The system allows to measure the speed in two ways: using the tachometer or the encoder. Each measurement unit has different properties. The first one is very noisy with the noise magnitude that depends on the speed, while the latter is very smooth. Therefore, the PID controller may use one of these two sensors to do control actions. Controller is equipped with the anti-windup mechanism to counteract the actuator saturation. Controller is tuned with seven sets of parameters to compare different types of PID tuning (SET) starting from the sluggish (SET1) to the most aggressive, denoted as SET7. Applied PID tuning parameters are shown in Table 1. Basic performance indexes of the overshoot κ and settling time T_s are added to the table to distinguish tuning properties.

Figure 2 shows the simulation environment. The experiments validate hypotheses with two configurations, i.e., the loop uses an encoder or a tachometer feedback. Setpoint is constant and the control is driven by disturbances: stochastic generated by the α-stable distribution $F^{\text{stab}}_{\alpha,\beta,\delta,\gamma}(x)$, $\alpha = 1.85$, $\beta = \delta = 0$ and $\gamma = 0.05$ and deterministic sinusoidal. Two PIDs are tested: with (PIDA) and without (PID) the anti-windup. The data are sampled with 10 ms interval. It must be noted that the real servo data are highly disturbed. In case of the tachometer, the measurement is significantly noisy, while in case of the encoder, the chattering and hunting once the speed stabilizes seriously reduces proper assessment.

Fig. 1 Laboratory servomechanism used during experiments

Table 1 Controllers' parameters with overshoot κ [%] and settling time T_s [sec]

Tuning	Kp	Ki	Kd	Kb	κ^{PID+A}	T_s^{PID+A}	κ^{PID}	T_s^{PID}
SET1	0.01	0.01	0.001	0.01	0.0	2.90	0.0	3.30
SET2	0.04	0.03	0.001	0.03	3.5	1.33	6.5	1.90
SET3	0.10	0.05	0.001	0.05	7.5	1.06	5.9	1.30
SET4	0.15	0.10	0.001	0.10	13.5	1.68	17.0	1.60
SET5	0.25	0.35	0.001	0.35	57.0	3.40	61.4	4.20
SET6	0.40	0.50	0.001	0.50	2.0	0.59	9.4	0.89
SET7	0.55	0.65	0.001	0.65	4.5	0.28	11.0	0.71

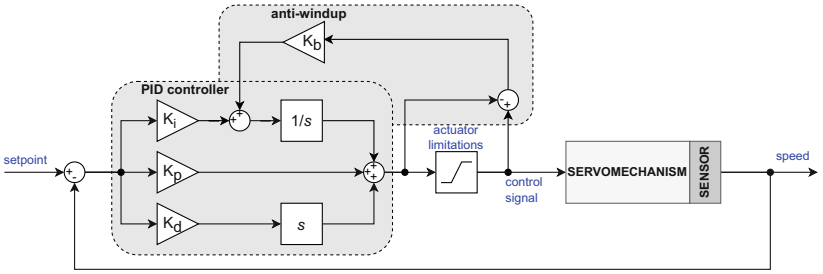

Fig. 2 Laboratory servomechanism used during experiments

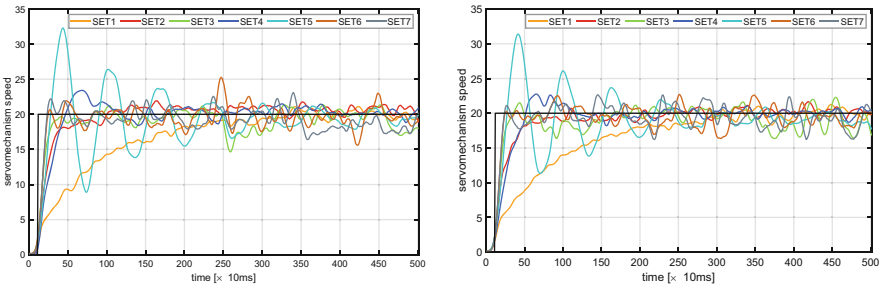

(a) PID controller (b) PID+A controller

Fig. 3 Control loop step responses smoothed with the moving average filter. (**a**) PID controller. (**b**) PID+A controller

4 Results

The analysis starts with comparison of the loop step response shown in Fig. 3. Data are smoothed with a Gaussian-weighted moving average filter ($N = 20$). Next, the stationarity tests are performed. The tests confirm that in all cases for the original control error time series and the incremented ones, all signals are stationary. Sample time series for control errors are sketched in Fig. 4.

Statistical properties for the obtained control errors have been reviewed as well. Sample time trends accompanied by the histogram and distribution fitting using normal and α-stable density functions are sketched in Fig. 5.

Finally, the CPA indexes are evaluated. Table 2 shows ISE and IAE for the original time series and Table 3 shows these indexes for the differentiated data. A review of the results for integral measures yields rather ambiguous observations. In case of the original time series, the analysis for encoder feedback indicates the SET1 tuning, while in case of the tachometer, the SET7 is pointed out. Contrasting these results with overshoot and settling time, we conclude that integral indexes favor conservative solutions that do not generate unnecessary oscillations.

Differentiated time series analysis yields different results. The indications are not as clear as before and the variations in index values are much more widely scattered.

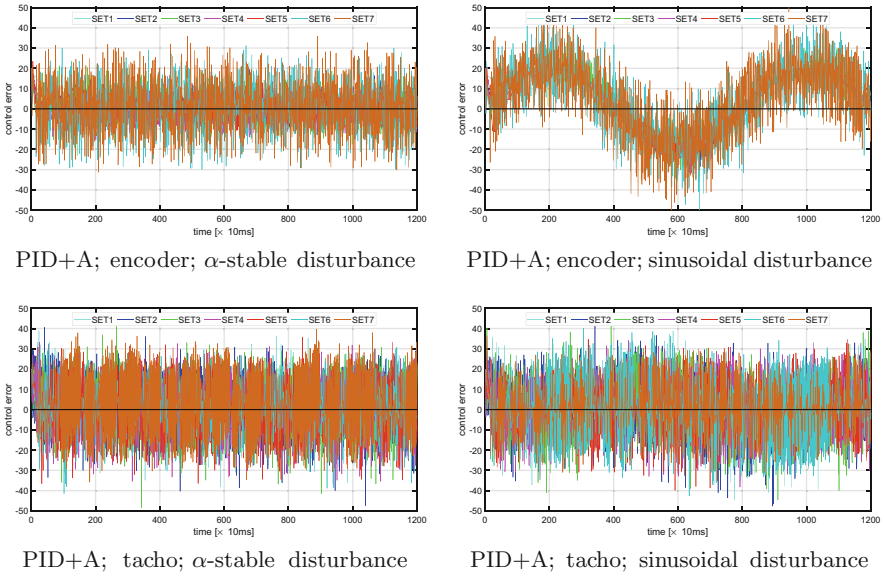

Fig. 4 Time series of control errors for selected scenarios

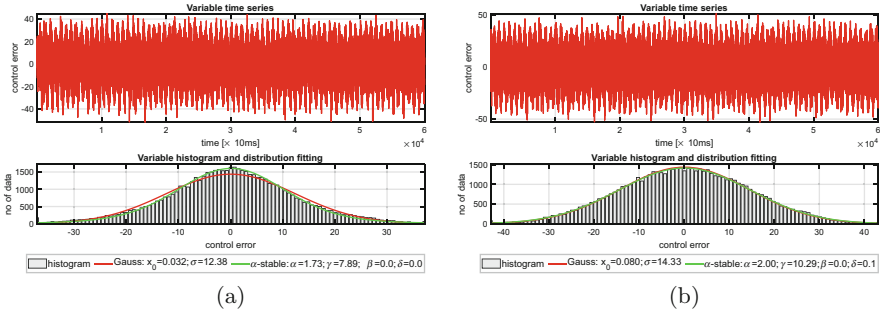

Fig. 5 Sample statistical review for SET1, tachometer, and sinusoidal disturbance. (**a**) PID control. (**b**) PID+A control

Interestingly, the ISE minimization often indicates a different controller than the IAE. Overall, the choice is much more difficult and less transparent. In addition to indicating conservative PID parameters with no overshoot (SET1 and SET7), the minimization of these indicators is able to select the SET5 tuning, which is the complete opposite of the previous ones, as it is characterized by far the highest overshoot, slowly fading oscillations, and a long, settling time.

It is expected that the fractional order should allow more constructive assessment. Fractional order is connected to the Hurst exponent with the $H = d + 0.5$ relationship. There exists a hypothesis that the best control is expected at $H \sim 0.5$ with smaller values indicating loop aggressiveness and higher ones pointing out

Table 2 Integral indexes ISE and IAE for the **original** control errors (bold numbers indicate the smallest values for the scenario, i.e., the row)

Control scenario			SET1		SET2		SET3		SET4		SET5		SET6		SET7	
			ISE	IAE	ISE	IAE	ISE	IAE	ISE	IAE	ISE	IAE	ISE	IAE	ISE	IAE
EN	PID	Stable	**25.0**	**4.06**	29.6	4.44	45.7	5.41	27.0	4.25	25.9	4.15	112.3	8.23	147.6	9.67
		Sine	**185.8**	**12.14**	205.4	12.74	209.8	12.60	209.3	12.88	200.6	12.63	292.4	14.21	304.6	14.55
	PIDA	Stable	**25.5**	**4.11**	33.1	4.68	49.9	5.67	32.0	4.64	29.1	4.40	139.2	9.54	180.9	11.04
		Sine	**179.6**	**11.94**	204.5	12.70	220.1	12.89	207.9	12.83	201.3	12.64	304.4	14.46	336.0	15.18
TA	PID	Stable	149.9	9.63	211.4	11.92	257.9	13.64	217.8	12.45	190.8	11.29	100.3	7.49	**59.9**	**5.81**
		Sine	153.3	9.62	191.1	10.83	249.1	12.97	188.7	11.01	167.4	10.10	76.5	6.46	**55.8**	**5.49**
	PIDA	Stable	191.4	11.45	236.0	13.02	225.0	12.87	191.7	11.61	**181.6**	**11.12**	197.1	10.64	203.3	11.20
		Sine	205.3	11.54	226.2	12.41	249.3	13.32	178.9	10.89	165.1	10.30	321.1	15.10	**118.7**	**7.92**

Table 3 Integral indexes ISE and IAE for the **differentiated** control errors (bold numbers indicate the smallest values for the scenario, i.e., the row)

Control scenario			SET1		SET2		SET3		SET4		SET5		SET6		SET7	
			ISE	IAE	ISE	IAE	ISE	IAE	ISE	IAE	ISE	IAE	ISE	IAE	ISE	IAE
EN	PID	Stable	**58.8**	13.24	66.4	16.79	89.9	20.67	64.0	17.15	60.8	14.97	221.6	11.95	316.5	**8.80**
		Sine	14.3	11.49	18.7	15.31	41.0	19.29	15.3	15.23	**13.6**	13.58	212.0	9.96	257.2	**8.22**
	PIDA	Stable	**59.3**	15.21	65.2	18.55	88.8	19.08	67.8	16.17	64.8	**15.15**	282.8	17.98	394.4	20.42
		Sine	14.2	14.64	17.2	17.51	44.2	19.68	14.8	15.15	**13.2**	13.96	244.9	28.63	325.9	**13.23**
TA	PID	Stable	286.0	**6.30**	439.3	6.71	616.4	7.65	439.4	6.56	356.9	6.39	239.1	11.94	**130.5**	14.40
		Sine	234.3	2.38	395.2	2.59	568.9	4.39	381.7	2.40	320.8	**2.31**	171.0	11.55	**119.7**	12.88
	PIDA	Stable	**353.1**	**6.31**	503.7	6.62	522.3	7.59	393.0	6.74	358.0	6.61	576.6	13.43	624.7	16.13
		Sine	333.6	2.42	469.8	2.47	560.1	4.54	364.4	2.33	322.6	**2.25**	1105.8	12.40	**298.5**	14.56

Table 4 Fractional order d_{GPH} for the **original** control errors (bold numbers indicate the values closest to zero)

Scenario			SET1	SET2	SET3	SET4	SET5	SET6	SET7
EN	PID	Stable	0.192	0.127	−0.022	−0.057	0.092	**0.018**	−0.025
		Sine	0.167	−0.096	0.043	−0.047	0.085	**−0.014**	−0.104
	PIDA	Stable	0.165	0.040	0.054	**0.028**	0.239	0.050	−0.043
		Sine	0.175	0.033	0.064	**−0.009**	0.260	0.012	0.114
TA	PID	Stable	**−0.159**	−0.428	**−0.159**	−0.798	−0.562	−0.496	−0.479
		Sine	**0.080**	−0.486	−0.174	−0.821	−0.645	−0.477	−0.415
	PIDA	Stable	−0.069	−0.402	−0.196	−0.602	−0.499	−0.100	**0.053**
		Sine	**−0.052**	−0.377	−0.151	−0.718	−0.348	−0.113	−0.143

Table 5 Fractional order d_{GPH} for the **differentiated** control errors (bold numbers indicate the values closest to zero)

Scenario			SET1	SET2	SET3	SET4	SET5	SET6	SET7
EN	PID	Stable	0.144	−0.129	−0.182	−0.046	**−0.014**	−0.380	−0.336
		Sine	0.210	−0.009	−0.100	−0.058	**−0.005**	−0.214	−0.482
	PIDA	Stable	0.079	**−0.012**	−0.046	−0.085	−0.095	−0.085	−0.122
		Sine	0.208	**0.008**	−0.159	−0.060	−0.015	−0.115	−0.234
TA	PID	Stable	−0.212	−0.085	−0.034	−0.159	**−0.011**	−0.210	−0.056
		Sine	**0.012**	−0.220	−0.249	−0.052	−0.013	−0.060	−0.060
	PIDA	Stable	−0.547	−0.285	−1.114	−0.168	**−0.013**	−0.070	−0.064
		Sine	**0.003**	−0.159	−0.027	−0.471	−0.025	−0.303	−0.050

sluggish tuning [1]. Thus, the $d = 0$ should indicate good control, $-0.5 > d > 0$ the aggressive and the $0 > d > 0.5$ the sluggish. Tables 4 and 5 show fractional orders d_{GPH} for the original and differentiated control errors.

Obtained results are not as clear as expected. At first, the assessment with the original time series is discussed. In case of the encoder feedback, the SET4 and SET6 are indicated to exhibit good quality. We observe the bias toward aggressive parameters, while on the contrary, the tachometer biases the results toward sluggish performance. The tendency that sluggish operation is associated with higher d_{GPH} values is observed. The bias may be caused by the simplification of $H = d + 0.5$. Actually, the $H = d + \frac{1}{\alpha}$ should be used. If we take into account observation of fat tails, the tachometer noises and the hunting/chattering effect may exhibit $\alpha < 2$, and the proper value of d_{GPH} is shifted toward the negative numbers with minor adjustments on the coefficients [20].

Once we consider the α-stable disturbance case and its stability exponent set to $\alpha = 1.85$, we obtain the optimal value $d = -0.04$. Shifted values change detection showing in case of the encoder mostly tuning SET3 and SET4. Simultaneously, sluggish control is more emphasized.

The above results show in a very explicit way that real process control assessment is seriously affected by the stochastic influence of the mostly unknown nature. In the considered case, it is the disturbance, the sensor noise, and other effects such

as the chattering and the encoder hunting. Control performance assessment should incorporate knowledge about fundamental processes behind the feedback control process itself, as the detection may be biased causing misleading conclusions.

5 Conclusions

Considered research investigates the hypothesis that the fractional-order long-memory GPH estimator $\boldsymbol{d_{\mathbf{GPH}}}$ can play the role of the control performance assessment indicator. It is shown that it works. Its effectiveness is confirmed using the laboratory mechanical servomechanism system. Its performance follows previous research observations, which state that the $d = 0$ indicates good control, the $-0.5 > d > 0$ the aggressive, and the $0 > d > 0.5$ the sluggish one, but with observed disclaimer. Theoretical relationship $\boldsymbol{H = d + \frac{1}{\alpha}}$ must take into account the unknown stability exponent α. Therefore, proper assessment should also consider the appropriate estimation of the stability index α, which biases the $\boldsymbol{d_{\mathbf{GPH}}}$ estimator value toward realistic representation of the control quality.

As the authors have not found any reports on that subject yet, this work plays the role of an initiator for further research. Consecutive analysis is required to better understand the issues observed during this study, as, for instance, how the estimated $\boldsymbol{d_{\mathbf{GPH}}}$ long-memory coefficients relate to the loop performance, its tuning, disturbances and noises, nonlinearity, MV constraints, sampling and the number of observations, chattering, hunting, and other real process effects.

References

1. Domański, P.D.: Control Performance Assessment: Theoretical Analyses and Industrial Practice. Springer International Publishing, Cham, Switzerland (2020)
2. O'Neill, Z., Li, Y., Williams, K.: HVAC control loop performance assessment: A critical review. Sci. Technol. Built Environ. **23**(4), 619–636 (2017)
3. Spinner T., Srinivasan, B., Rengaswamy, R.: Data-based automated diagnosis and iterative retuning of proportional-integral (PI) controllers. Control Eng. Pract. **29**, 23–41 (2014)
4. Harris, T.J., Seppala, C.T.: Recent Developments in Controller Performance Monitoring and Assessment Techniques. In: Proc. of the 6th International Conference on Chemical Process Control, pp. 199–207 (2001)
5. Domański, P.D.: Multifractal properties of process control variables. Int. J. Bifurc. Chaos **27**(6), 1750094 (2017)
6. Knierim-Dietz, N., Hanel, L., Lehner, J.: Definition and verification of the Control Loop Performance for Different Power Plant Types. Institute of Combustion and Power Plant Technology, University of Stutgart, Germany (2012)
7. Afshar Khamseh, S., Khaki Sedigh, A., Moshiri, B., Fatehi, A.: Control performance assessment based on sensor fusion techniques. Control Eng. Pract. **49**, 14–28 (2016)
8. Sheng, H., Chen, Y.Q., Qiu, T.S.: Fractional Processes and Fractional-Order Signal Processing, Techniques and Applications. Springer London Limited, London, UK (2012)

9. Liu, K., Chen, Y.Q., Domański, P.D.: Control Performance Assessment of the Disturbance with Fractional Order Dynamics. In: W. Lacarbonara, B. Balachandran, J. Ma, J.A. Tenreiro Machado, G. Stepan, (Eds.), Nonlinear Dynamics and Control, pp. 255–264. Springer International Publishing, Cham, Switzerland (2020)
10. Domański, P.D.: Control quality assessment using fractal persistence measures. ISA Trans. **90**, 226–234 (2019)
11. Geweke, J., Porter-Hudak, S.: The estimation and application of long memory time series models. J. Time Ser. Anal. **4**(4), 221–238 (1983)
12. Jelali, M.: Control Performance Management in Industrial Automation: Assessment, Diagnosis and Improvement of Control Loop Performance. Springer, London, UK (2013)
13. Ordys, A., Uduehi, D., Johnson, M.A.: Process Control Performance Assessment - From Theory to Implementation. Springer, London, UK (2007)
14. Domański, P.D.: Performance assessment of predictive control – a survey. Algorithms **13**(4), 97 (2020)
15. Rousseeuw, P.J., Leroy, A.M.: Robust Regression and Outlier Detection. Wiley, New York, NY (1987)
16. Beran, J.: Statistics for Long-Memory Processes (1st ed.). Routledge, New York, NY (1994)
17. Elliott, G., Rothenberg, T.J., Stock, J.H.: Efficient tests for an autoregressive unit root. Econometrica **64**(4), 813–836 (1996)
18. Kwiatkowski, D., Phillips, P.C.B., Schmidt, P., Shin, Y.: Testing the null hypothesis of stationarity against the alternative of a unit root. J. Econom. **54**(1–3), 159–178 (1992)
19. INTECO s. z o.o.: Modular Servo System (2007). User's Manual. http://www.inteco.com.pl/Docs/Servo_um.pdf
20. Ding, L., Luo, Y., Lin, Y., Yirong Huang, Y.: Revisiting the relations between Hurst exponent and fractional differencing parameter for long memory. Phys. A Stat. Mech. Appl. **566**, 125603 (2021)

Part VI
System Identification and SHM

Nonlinear System Identification of a Multi-story Building with Geometrical Nonlinearity Using a Deterministic Output-Only-Data Approach

Amirali Sadeqi, Dario Anastasio, and Stefano Marchesiello

1 Introduction

Nonlinear system identification is generally an input-output data-driven process since the nonlinear systems' input (load) and output (response) are not proportional. However, many real-world nonlinear structures are subjected to unmeasurable environmental or operational loads. Statistical approaches such as the Kalman filter and stochastic subspace identification (SSI) algorithms can be implemented using the vibration response of nonlinear structures excited by white Gaussian input. In such a case, a linearization in the domain with small steps, parameter updating, or additional terms for the basis function can be adopted for nonlinear parameter estimation [1–3]. Recently, other approaches have also been introduced based on a mass-change scheme [4] and an input location-change scheme [1].

In this chapter, the deterministic subspace identification algorithm recently used for the multi-degree of freedom (MDOF) system [1, 5] is applied to an experimental multi-story building with geometrical nonlinearity. It was demonstrated that when an MDOF is excited, the linear and nonlinear elements attached to DOFs away from the external force can be identified at a time using the response of the whole DOFs. Hence, to identify elements attached to the DOFs that directly experience external force, one more test by applying force to a different DOF is required. In other words, the necessary condition for using this approach is that the excitation and nonlinearity should not be at the same DOF. The objective of the present study is to extend the applicability range of the approach to the experimental identification of

A. Sadeqi (✉)
Department of Civil and Mechanical Engineering, Technical University of Denmark, Lyngby, Denmark
e-mail: amisa@dtu.dk

D. Anastasio · S. Marchesiello
Department of Mechanical and Aerospace Engineering, Politecnico di Torino, Italy

© The Author(s), under exclusive license to Springer Nature Switzerland AG 2024

W. Lacarbonara (ed.), *Advances in Nonlinear Dynamics, Volume III*, NODYCON Conference Proceedings Series, https://doi.org/10.1007/978-3-031-50635-2_37

structures with amplitude-dependent nonlinearity type based on vibration response only. Compared to the recent work, the present one is dedicated to simplifying the implementation of the algorithm for the users through the available system identification toolbox in MATLAB and using real vibration measurements.

In the first step of the nonlinear identification process, the velocity and displacement data are calculated from the first and second integrations of the acceleration records. The state-space phase diagrams and restoring force-state maps are commonly used to detect the existence of nonlinearity and its type [6, 7]. As the best fit for the detected nonlinearity, then the basis function is defined and utilized as the input in the data-driven subspace algorithm [8]. The idea is using the fact that the oblique projection of the response data onto the input data (i.e., in their Hankel matrix arrangements) removes the input contribution, which is the same nonlinear contribution here, from the response data. The remaining space corresponds to the underlying linear system response. If there is no external force at the location of the measured response, or the force has stochastic nature, the remaining space corresponds to the underlying linear modal response. However, the quality of the identified parameters depends on the user-defined basis function to capture the nonlinearity, matrix decomposition operation (i.e., Hankel matrix rows representing the over-determined model order and columns representing the signal length), and noise contamination in the acceleration records. The integration is carried out within detrending and filtering schemes to reduce the process error. In the following sections, the time-domain identification steps are listed, and the experimental testing results are presented.

2 Deterministic Nonlinear System Identification

Let u and y be the input (i.e., external force) and output (i.e., displacement) vectors of a q-DOF system with p nonlinearities, then the equation of motion can generally be stated as:

$$\begin{bmatrix} \dot{y}(t) \\ \ddot{y}(t) \end{bmatrix} = A_c \begin{bmatrix} y(t) \\ \dot{y}(t) \end{bmatrix} + B_c u(t) + N_c f\left(y(t), \dot{y}(t)\right) \tag{1}$$

where $\dot{y}$ and $\ddot{y}$ are the first and second derivatives of y, f is the nonlinear function, and the continuous-time state-space parameters have the following arrangement:

$$\begin{aligned} &A_c[1:2:2q;1:2:2q] = [0]_{q\times q},\ A_c[1:2:2q;2:2:2q] = [\mathrm{I}]_{q\times q} \\ &A_c[2:2:2q;1:2:2q] = -\left[M^{-1}K\right]_{q\times q}, \\ &\quad A_c[2:2:2q;2:2:2q] = \left[-M^{-1}C_d\right]_{q\times q} \\ &B_c[1:2:2q;1:m] = [0]_{q\times m},\ B_c[2:2:2q;1:m] = \left[M^{-1}\Gamma\right]_{q\times m} \\ &N_c[1:2:2q;1:p] = [0]_{q\times m},\ N_c[2:2:2q;1:p] = \left[M^{-1}\eta\right]_{q\times p} \end{aligned} \tag{2}$$

where m is the number of applied inputs, and M, K, C_d, and I are the mass, stiffness, damping, and identity matrices, respectively. Also, the components of Γ are one at DOFs under external inputs and zero elsewhere, and η contains the coefficient of nonlinearities attached to different DOFs. Assuming the applied input u is unknown but its location (i.e., excited DOFs) is known, the idea is to choose a basis function appropriate to f and then apply it to a deterministic (input-output) subspace identification algorithm instead of u. The process will lead to estimating A_c and N_c at DOFs with no external load or $\Gamma = 0$. If the applied load and the nonlinearity are not at the same location, N_c can be estimated by only one test, otherwise, one more test is required by applying load at another DOF. Hence, the representation and arrangement in Eqs. (1) and (2) aid in including or excluding the identified components concerning the excited DOF.

The conditions for implementing the oblique-projection-based nonlinear subspace algorithm have been presented in [1, 5]. Once the left singular and right matrices are calculated from SVD $(P) = L\,.\,S\,.\,R$, and P is the oblique projection of the future output Hankel matrix $Y_{r+1:2r}$ onto the past output-input Hankel block $\begin{bmatrix} Y_{1:r} \\ F_{1:r} \end{bmatrix}$ along the future input Hankel matrix $F_{r+1:2r}$, the observability matrix can be determined as:

$$O = L\,[1:lr;\,1:2q]\,(S\,[1:2q;\,1:2q])^{1/2} \tag{3}$$

Then A and N, the discrete-time counterparts of A_c and N_c, can be achieved by solving $X_f = AX_p + NF_p$, where $X_p = P^{\dagger}O$ is the past state, and $X_f = P[1:lr-l]^{\dagger}O[1:lr-l;1:n]$ is the future state, and '†' denotes the pseudo-inverse. In another fashion, one can directly obtain $A = (O[l+1:lr;1:n])^{\dagger}O[1:lr-l;1:n]$ and solve $L\,[1:lr;2q+1:lr]\,Y_f U_f^{\dagger} = L\,[1:lr;2q+1:lr]\,N$ to determine N.

In this chapter, to ease the implementation and comprehension of the algorithm, the N4SID command in MATLAB is called and performed to estimate the time-continuous deterministic state-space parameters. As the system output, the displacement data are integrated from the acceleration measurements. Such a linear deterministic process that normally estimates the state-space parameters A_c and B_c, now yields A_c and N_c, since instead of load measurements u, the nonlinear basis function f is used as the input. The flowchart of the simplified algorithm is presented in Fig. 1.

The 'n4sid' command can be set and performed as:

$$Sys = \mathbf{n4sid}\left(Data, Order, `Ts', 0, `form', `canonical', Option\right) \tag{4}$$

where *Data* is set as the input-output data through the 'iddata' command as:

$$Data = \mathbf{iddata}\,(y,\,f,\,dt) \tag{5}$$

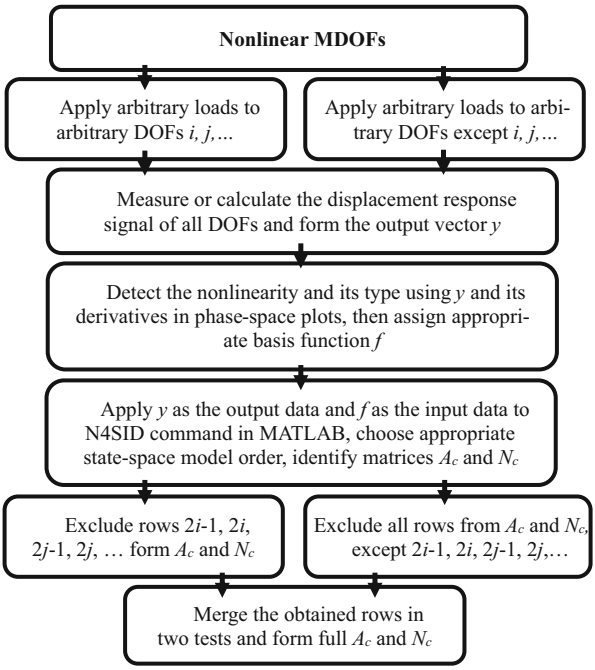

Fig. 1 Flowchart of the double-test deterministic nonlinear system identification algorithm

and *Option* accounts for the subspace weighting system that can be chosen, such as canonical variate analysis (CVA), via the 'n4sidOptions' command:

$$Option = \textbf{n4sidOptions}\left(`N4weight', `CVA'\right) \tag{6}$$

In Eq. (4), *Order* refers to the state-space model order that needs to be chosen by the user, either a priori if the DOFs are known (i.e., two times the DOFs, $Order = 2q$), or during the identification process by observing nonzero singular values (e.g., $Order = 1{:}4q$) or using a stabilization diagram. The next item '*Ts*' refers to the discrete/continuous-time model switch, and since the physical parameters such as stiffness and damping need to be estimated, the value of '*Ts*' is chosen as 0 to perform the continuous-time identification. The item '*form*' determines the arrangement of the estimated components, and following Eq. (2), it must be chosen as '*canonical*'. The identification results can be extracted as $A_c = Sys.\mathrm{A}$ and $N_c = Sys.\mathrm{B}$, and in discrete MDOFs with noisy output measurements, can be estimated accurately [1, 5].

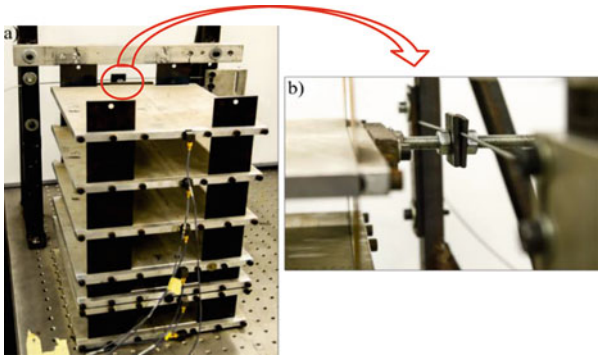

Fig. 2 (**a**) Multi-story building test setup, (**b**) thin wire attached to the last floor triggering geometrical nonlinearity

3 Experimental Testing

The structure under study has been frequently studied in [4, 9] for linear and nonlinear parameter estimation. Figure 2 displays the test setup, which consists of a lab-scale multi-story building with a thin elastic string at the last floor as the nonlinearity source when the vibration amplitude is high.

Within the new tests, the specimen has been excited at four elevations with different load levels simply using hammering tests. The acceleration responses have been recorded on four floors. The specimen can be deemed as an underlying linear structure with geometric nonlinearity localized at the last floor, and it is assumed not to be activated under low-level excitations. Hence, the response signals measured in four tests under high-level impulse trains are taken into the nonlinear identification process introduced in Fig. 1 for estimating both nonlinear and underlying linear parameters. Also, the free decay response signals measured in four other tests under low-level impulse are utilized in the stochastic subspace identification (SSI) process and the identified linear modal parameters are compared with those achieved from the underlying linear system in nonlinear tests.

4 Results and Discussion

4.1 Linear Modal Analysis

The modal parameters of the multi-story specimen are estimated using low-level responses in the SSI algorithm. Figure 3 depicts the stabilization of the identified natural frequencies and damping ratios associated with the first acceleration data set. The stabilization diagrams for the displacement data obtained using the Kalman filter integration scheme with a cut-off frequency of 3–200 Hz, follow almost the

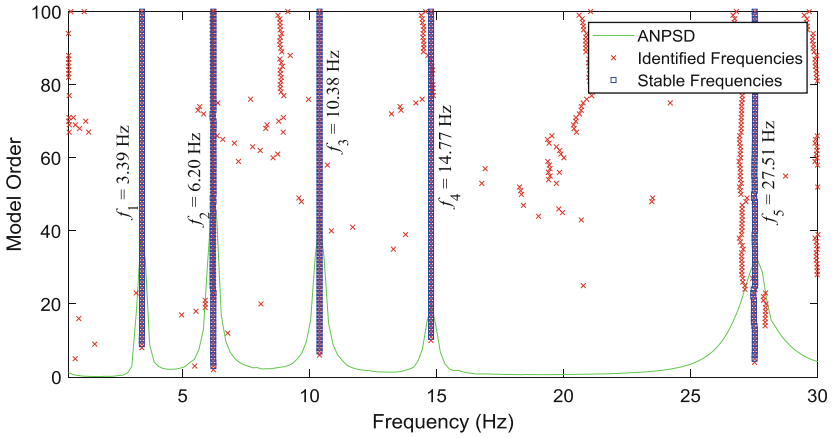

Fig. 3 Stabilization diagram of identified natural frequencies in a linear test

Table 1 Natural frequency and damping ratio estimated using four low-amplitude data sets

Data set	Natural frequency (Hz)					Damping ratio (%)				
1	3.41	6.20	10.40	14.70	27.41	0.37	0.29	0.42	1.12	0.86
2	3.41	6.20	10.40	14.28	27.46	0.24	0.30	0.40	1.48	1.08
3	3.41	6.19	10.37	14.76	27.70	0.26	0.32	0.37	0.52	0.84
4	3.41	6.20	10.38	14.77	27.88	0.55	0.34	0.32	0.49	0.84
Mean	3.41	6.20	10.39	14.63	27.61	0.36	0.31	0.38	0.90	0.91
CV($\times 10^{-4}$)	0.00	16	19	157	797	3889	645	11,316	5333	1209

same trend and values. Table 1 represents the linear modal parameters estimated based on displacement corresponding to four low-level tests. The mean and CV (coefficient of variation, which is standard deviation to mean) values in the last two rows indicate a limited uncertainty bound for the natural frequencies, whereas the damping ratios have a wider uncertainty bound. Figure 4 demonstrates the difference between the power spectral density (PSD) of the displacement data associated with two typical linear and nonlinear tests. The main harmonic (peak) shifts are observable in the nonlinear response of all floors, while for the fifth floor, the multi-harmonics are also significant due to the nonlinear element attached to this floor.

4.2 Nonlinear System Identification

In this section, the nonlinear system identification procedure introduced by Fig. 1 is implemented. The state-space phase diagrams are utilized to observe the nonlinearity and its type. In DOFs with no external force, the figure represents the nonlinear restoring force surface due to stiffness (acceleration-displacement) and

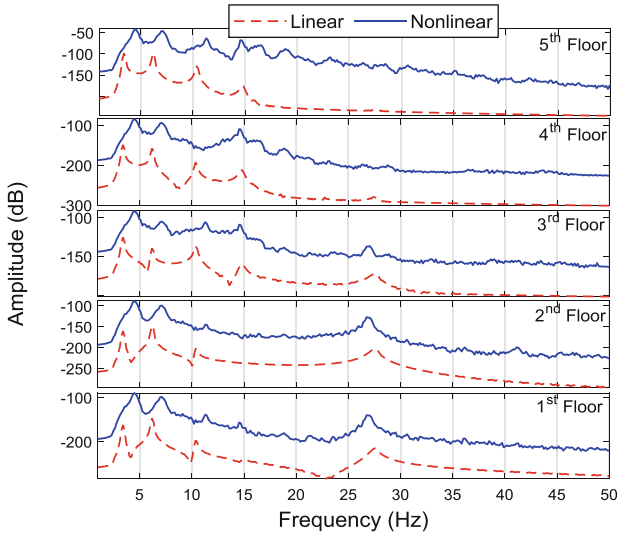

Fig. 4 PSD of measurements at five floors in two linear and nonlinear tests

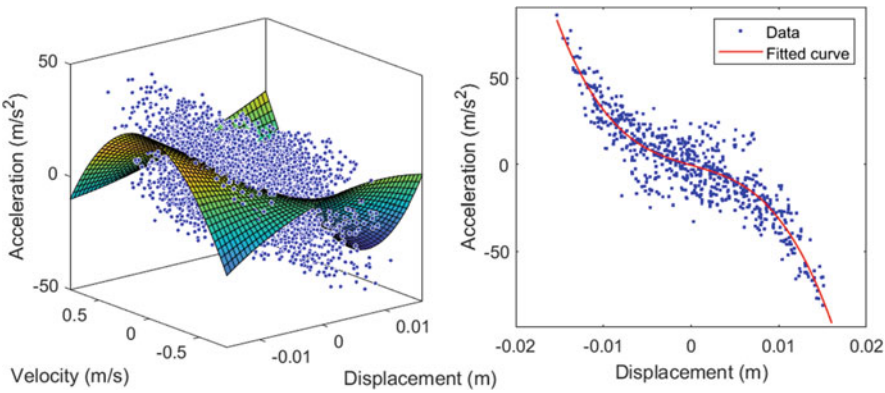

Fig. 5 Nonlinear behavior on the last floor, (**a**) restoring force surface, (**b**) zero-velocity section plot with cubic polynomial curve fitting

damping (acceleration-velocity) elements. Figure 5 displays the state-space phase plot of the fifth floor in a typical nonlinear test and the corresponding fitted surface and curve indicating cubic behavior. Hence, a polynomial-type basis function is used to characterize and estimate the nonlinear dynamics of the specimen.

The third order polynomial basis function $f = \left[y_5^2; y_5^3\right]$ is considered in terms of the fifth floor's displacement row-vector y_5, where the semicolon ';' separates two rows. Assuming Y and F are the Hankel matrices of $y = [y_1; \ldots; y_5]$ and f, respectively, then performing the oblique projection operation on the past-future splits of the mentioned matrices cancels the row-space of F from the response Y so

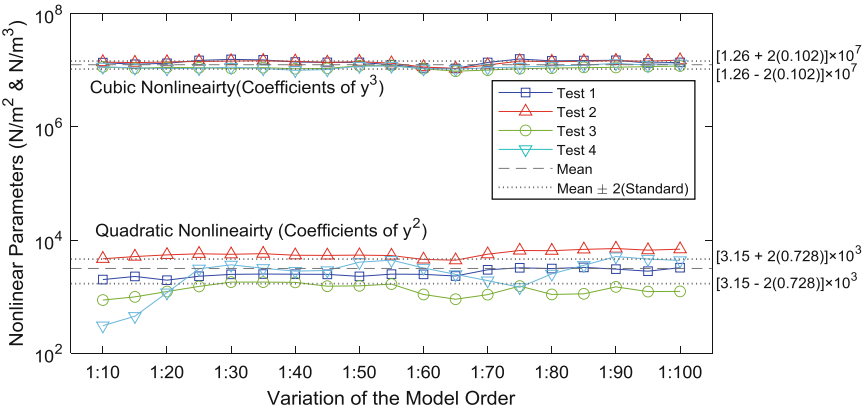

Fig. 6 Nonlinear parameters estimated in different tests vs the model order variation

that the resultant row space associates with the underlying linear system. In such a nonlinear state-space model identification process, both the dynamical matrix A (i.e., leading to modal parameters of the underlying linear system) and the nonlinear parameter N (i.e., coefficients of f) are simultaneously determined. In the present study, the N4SID command in MATLAB is implemented according to Eqs. (4), (5) and (6) using the displacement response y as the output data, the basis function f as the input data, and the state-space model order 10 chosen from variable Hankel matrix rows 10 to 100. The following figures represent the nonlinear identification results using displacement-only data measured under high-level excitation in four different tests. Figure 6 demonstrates the variation of the basis function coefficients estimated in different nonlinear tests. Figure 7 shows the underlying linear natural frequency estimates in four nonlinear tests compared to the mean of the natural frequency estimates previously obtained through the linear tests and presented in Table 1.

Figures 8 and 9 depict the corresponding mode shapes and their MAC diagrams. Utilizing the identified modal parameters, frequency response functions (FRFs) are obtained according to Eq. (10) in [4]. However, the mode shape vectors are not mass normalized here, and since the modal mass scale factor is unknown, it is assumed to be one. Figure 10 displays FRFs based on modal parameters obtained through linear and nonlinear tests.

5 Discussion

Regarding Fig. 6, almost all the estimates of the coefficient cubic term remain within the uncertainty bounds, whereas the quadratic term coefficient estimated through Test 2 and 3 is not acceptable. According to Fig. 7, the linear natural frequencies

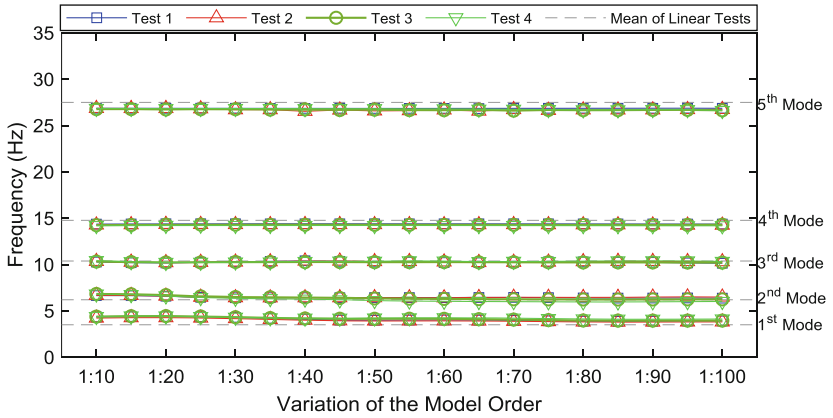

Fig. 7 Underlying linear frequencies estimated in different tests vs the model order variation

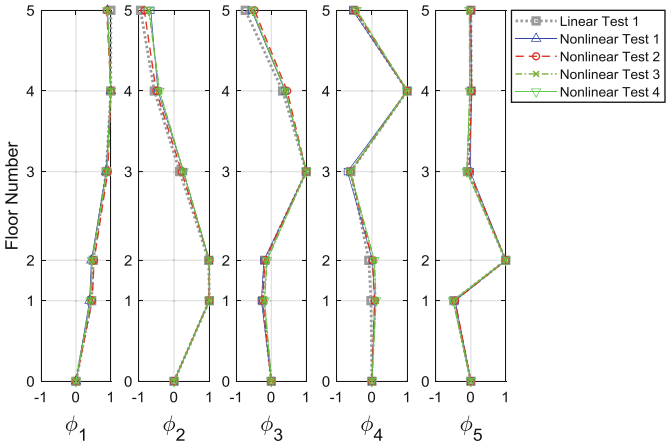

Fig. 8 Underlying linear system mode shapes compared to mode shapes in linear test 1

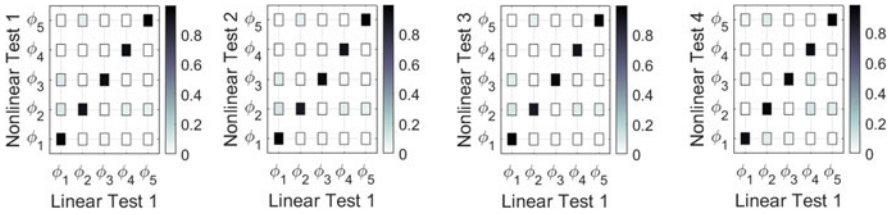

Fig. 9 MAC diagrams between underlying linear system mode shapes and mode shapes

estimated based on the nonlinear test data sets indicate a deviation (max 14%, in the first mode) from the linear test frequencies. The effect of high damping estimates is also observable within FRFs in Fig. 10. The mode shapes in Fig. 8 and their

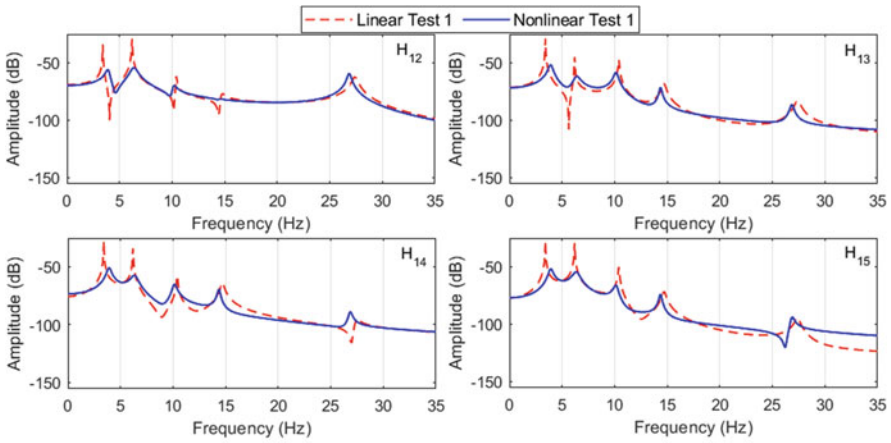

Fig. 10 FRFs based on modal parameters obtained from linear and nonlinear tests

MAC values in Fig. 9 indicate a minor discrepancy. It must be noticed that in each test, one floor (e.g., DOF) is excited, whose corresponding linear and nonlinear parameters must be excluded. Since the nonlinearity is observed only at the fifth floor, and in none of the present tests the excitation has not been applied to the fifth floor, the nonlinear parameter can correctly be estimated using the data of all tests. However, the underlying linear modal parameters are influenced because they are extracted here from a full-component dynamical system matrix of which rows/columns correspond to all floors, including the excited one. In other words, only the response data of floors with no external force must be taken into the identification process.

6 Conclusion

In this chapter, linear modal analysis and nonlinear system identification were carried out using vibration measurements of a multi-story building in laboratory conditions. The geometrical nonlinear behavior was observed on the fifth floor. Hence, the polynomial basis function was predicted and determined based on the displacement of the fifth floor. The basis function and displacement data were utilized as the input and output in a deterministic subspace identification algorithm to simultaneously estimate the nonlinear and underlying linear system parameters. The modal parameters of the underlying linear system were compared to those obtained from the linear test cases. The process error due to the integration operation and inclusion of the dynamical matrix components of the excited floor in each test caused a bias in the natural frequency and damping ratio. Meanwhile, the mode shapes properly match in linear and nonlinear tests. On the other hand,

the stability of the estimated nonlinear parameters verifies the capability of the simplified identification approach to be applied with MATLAB commands and experimental output-only measurements.

Acknowledgments The authors acknowledge Otto Mønsteds Fond, Denmark supported the chapter presentation.

References

1. Sadeqi, A., Moradi, S.: Nonlinear system identification based on force transmissibility of vibrating structures. Mech. Syst. Signal Process. **172**(1), 108978–108923 (2021)
2. Wan, E.A., van der Merwe, R.: The unscented Kalman filter for nonlinear estimation. In: Proceedings of the IEEE 2000 Adaptive Systems for Signal Processing, Communications, and Control Symposium (Cat. No.00EX373), pp. 153–158 (2000). https://doi.org/10.1109/ASSPCC.2000.882463
3. Marchesiello, S., Garibaldi, L.: A time domain approach for identifying nonlinear vibrating structures by subspace methods. Mech. Syst. Signal Process. **22**(1), 81–101 (2008)
4. Anastasio, D., Marchesiello, S.: Free-decay nonlinear system identification via mass-change scheme. Shock. Vib. **2019** (2019). https://doi.org/10.1155/2019/1759198
5. Sadeqi, A., Moradi, S., Shirazi, K.H.: Nonlinear subspace system identification based on output-only measurements. J. Frankl. Inst. **357**(17), 12904–12937 (2020)
6. Noël, J.P., Kerschen, G.: Nonlinear system identification in structural dynamics: 10 more years of progress. Mech. Syst. Signal Process. **83**, 2–35 (2017). https://doi.org/10.1016/J.YMSSP.2016.07.020
7. Worden, K.: Data processing and experiment design for the restoring force surface method, part II: choice of excitation signal. Mech. Syst. Signal Process. **4**(4), 321–344 (1990)
8. van Overschee, P., de Moor, B.: N4SID: subspace algorithms for the identification of combined deterministic-stochastic systems. Automatica. **30**(1), 75–93 (1994)
9. Marchesiello, S., Fasana, A., Garibaldi, L.: Modal contributions and effects of spurious poles in nonlinear subspace identification. Mech. Syst. Signal Process. **74**, 111–132 (2016)

An Approach to Monitor Bolt Faults in Two-Dimensional Structures Without Reference

Quankun Li, Qingzhou Zhao, Mingfu Liao, and Fali Yang

1 Introduction

For various two-dimensional engineering structures like satellite panels, engine casings and aircraft fuselages, bolts are widely applied to clamp different structural components together and to bear external loads because of their significant merits such as reusability and reliability [1, 2]. However, bolt connections easily encounter self-loosening faults since these two-dimensional engineering structures often work in dynamic environments and operations. Bolt self-loosening faults not only cause a decrease in clamping force but also lead to serious slip or separation between structural components. As a result, inspecting potential bolt self-loosening faults as early as possible is very important and meaningful to keep the normal and smooth operation of these two-dimensional engineering structures.

For this objective, a host of output spectrum-based methods have been presented [3, 4]. The use of artificial neural network (ANN) and features generated from output responses detected damages in a steel bridge [5]. To detect U-bolts in pipelines of steel bridges, authors [6] recently developed a method based on vibration output responses measured from girders of bridges. Apart from output spectrum, changes in the power spectrum of a plate were also measured by a scanning laser vibrometer to indicate loosening bolts [7]. Later, similar power spectrum-based features were applied to monitor bolt looseness in a clamping support structure under environmental random excitations [8]. These linear methods provide acceptable results for the detection of bolt self-loosening faults, while they

Q. Li (✉) · Q. Zhao · M. Liao
School of Power and Energy, Northwestern Polytechnical University, Xi'an, Shaanxi, China

F. Yang
Shenyang Engine Research Institute, Aero Engine Corporation of China, Shenyang, Liaoning, China

© The Author(s), under exclusive license to Springer Nature Switzerland AG 2024

W. Lacarbonara (ed.), *Advances in Nonlinear Dynamics, Volume III*, NODYCON Conference Proceedings Series, https://doi.org/10.1007/978-3-031-50635-2_38

may be more suitable for simple structures with very serious faults since they only consider changes in structural linear parameters.

To consider more real situations of bolt self-loosening faults and two-dimensional structures, methods based on nonlinear output spectrum have been proposed as well [9]. For the vehicle suspension system, changes in nonlinear output spectra at higher harmonic frequencies were used as features for detecting bolt loosening faults [10]. Based on the nonlinear subharmonic resonance analysis, bolted joint looseness was detected with piezoelectric active sensors and actuators [11]. Considering the effects of temperature fluctuations and ambient vibrations, changes in cross-spectral density function were applied to detect the state of a bolt in a composite plate [12]. Similar to this, the ratio of power spectra between higher frequency and excitation frequency was calculated for detecting loosening faults of a clamping system [13]. Apart from sub- and super-harmonic output spectra caused by faults, sideband output spectra were also applied as features. For example, the existence of components at sideband frequency was applied to indicate bolt loosening in a composite panel [14]. Changes in sideband output spectra were applied for weak loosening bolts [15].

Existing nonlinear output spectrum-based methods provide much more information on two-dimensional structures with potential bolt self-loosening faults. However, one obvious limitation is that fault features from basement structures are required during the diagnosis of faults. This condition would affect these methods' effectiveness if states of health structures are not known. To overcome this limitation, an improved method for inspecting bolt faults in two-dimensional structures without reference is proposed in this paper. The main contributions and novelties of this paper are: (1) Using nonlinear output spectra of damaged two-dimensional engineering structures only and the local structural modification method, local damage features are derived and analyzed; (2) With damage features, an improved method with sensitive damage indexes is proposed, and its effectiveness is illustrated through simulation cases on an MDOF model of two-dimensional engineering structures.

2 Dynamic Features

In this section, dynamics of two-dimensional structures including the discrete MDOF model, equation of motion and output spectrum are introduced.

2.1 The Model of Two-Dimensional Structures

As shown in Fig. 1, the MDOF model of two-dimensional structures uses the coordinate $x_{a,\,b}(t)(1 \leq a \leq n, 1 \leq b \leq q)$ to describe the vertical motion of each mass. Boundary constraints are applied to both sides of structures, and the single excitation

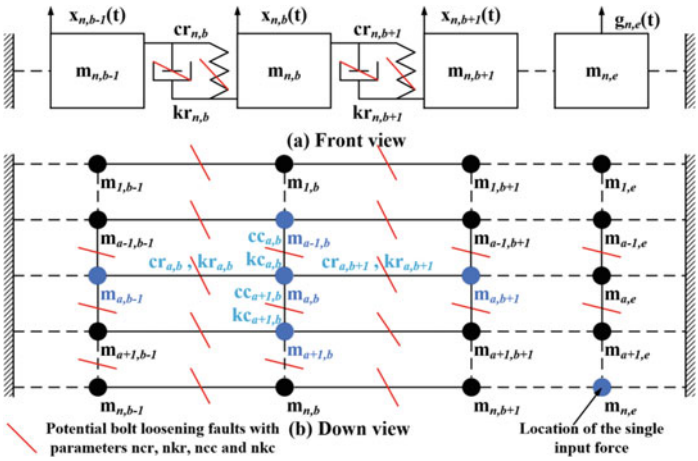

Fig. 1 Model of structures

is applied to mass $m_{n,\,e}(1 \le e \le q)$. Potential bolt self-loosening faults (marked by red slashes) are considered as nonlinear damper-spring components around each mass with nonlinear raw and column parameters [14, 15].

With Lagrange's equation method [16], the differential equation of motion of this model can be obtained, as

$$\begin{aligned}&[M]\left\{\ddot{x}_{a,b}(t)\right\} + [C]\left\{\dot{x}_{a,b}(t)\right\} + [K]\left\{x_{a,b}(t)\right\} \\ &\quad = \left\{g_{a,b}(t)\right\} + \left\{h_{a,b}(t)\right\},\ (1 \le a \le n,\ 1 \le b \le q)\end{aligned} \tag{1}$$

where $[M]$, $[C]$ and $[K]$ are model's mass, damping and stiffness matrices, respectively. $\left\{\ddot{x}_{a,b}(t)\right\}$, $\left\{\dot{x}_{a,b}(t)\right\}$ and $\{x_{a,\,b}(t)\}$ are the model's acceleration, velocity and displacement vectors, respectively. $\{g_{a,\,b}(t)\}$ and $\{h_{a,\,b}(t)\}$ are input and fault-induced nonlinear force vectors, respectively, in which the force element is applied to mass $m_{a,\,b}(1 \le a \le n, 1 \le b \le q)$.

In vector $\{g_{a,\,b}(t)\}$, only the term $g_{n,\,e}(t)$ is nonzero since the single excitation is applied to mass $m_{n,\,e}(1 \le e \le q)$. In vector $\{h_{a,\,b}(t)\}$, terms corresponding to potential bolt self-loosening faults can be expressed [14, 15], as

$$\begin{aligned}h_{a,b}(t) = &-\sum_{l=2}^{L}\left(ncr_{a,b}\dot{s}^{l}_{a,b-1,a,b}(t) + nkr_{a,b}s^{l}_{a,b-1,a,b}(t)\right) \\ &+\sum_{l=2}^{L}\left(ncr_{a,b+1}\dot{s}^{l}_{a,b,a,b+1}(t) + nkr_{a,b+1}s^{l}_{a,b,a,b+1}(t)\right) \\ &-\sum_{l=2}^{L}\left(ncc_{a,b}\dot{s}^{l}_{a-1,b,a,b}(t) + nkc_{a,b}s^{l}_{a-1,b,a,b}(t)\right) \\ &+\sum_{l=2}^{L}\left(ncc_{a+1,b}\dot{s}^{l}_{a,b,a+1,b}(t) + nkc_{a+1,b}s^{l}_{a,b,a+1,b}(t)\right)\end{aligned} \tag{2}$$

where

$$\begin{aligned}
\dot{s}^l_{a,b-1,a,b} &= \left(\dot{x}_{a,b}(t) - \dot{x}_{a,b-1}(t)\right)^l, s^l_{a,b-1,a,b} = \left(x_{a,b}(t) - x_{a,b-1}(t)\right)^l \\
\dot{s}^l_{a,b,a,b+1} &= \left(\dot{x}_{a,b}(t) - \dot{x}_{a,b+1}(t)\right)^l, s^l_{a,b-1,a,b} = \left(x_{a,b}(t) - x_{a,b+1}(t)\right)^l \\
\dot{s}^l_{a-1,b,a,b} &= \left(\dot{x}_{a,b}(t) - \dot{x}_{a-1,b}(t)\right)^l, s^l_{a,b-1,a,b} = \left(x_{a,b}(t) - x_{a-1,b}(t)\right)^l \\
\dot{s}^l_{a,b,a+1,b} &= \left(\dot{x}_{a,b}(t) - \dot{x}_{a+1,b}(t)\right)^l, s^l_{a,b-1,a,b} = \left(x_{a,b}(t) - x_{a+1,b}(t)\right)^l
\end{aligned}$$

ncr, *nkr*, *ncc* and *nkc* are nonlinear structural damping and stiffness parameters (r means row and c means column) respectively, L is the maximum order of nonlinear force. If there is no bolt self-loosening around mass $m_{a,b}$, corresponding nonlinear structural parameters and nonlinear force would be zero.

2.2 Output Spectra of the MDOF Model

If the excitation is $g_{n,e}(t) = \cos(\omega t)$, the output response of mass $m_{a,b}$ can be assumed based on the harmonic balance method [16], as

$$x_{a,b}(t) = \sum_{v=-\infty}^{\infty} A_v G^v_{a,b}(jv\omega)\, e^{jv\omega t} \tag{3}$$

where v is the order of harmonics, and $A_v G^v_{a,b}(jv\omega)$ is the vth order complex coefficient.

Substituting (3) into (1) and (2), and extracting the coefficients of $e^{jv\omega t}$, we obtain

$$\left[-(v\omega)^2 M + jv\omega C + K\right]\left\{G^v_{a,b}(jv\omega)\right\} = \left\{H^v_{a,b}(jv\omega)\right\}, (v \geq 2) \tag{4}$$

where $\{H_{a,b}(jv\omega)\}$ is the frequency-domain nonlinear fault-induced force vector, and condition $(v \geq 2)$ means that only nonlinear output spectra are considered.

With the inverse matrix, nonlinear output spectra can be computed, as

$$\left\{G^v_{a,b}(jv\omega)\right\} = \left[-(v\omega)^2 M + jv\omega C + K\right]^{-1}\left\{H^v_{a,b}(jv\omega)\right\}, (v \geq 2) \tag{5}$$

It is shown that the nonlinear output spectra of two-dimensional structures are just decided by nonlinear fault-induced forces and structural physical properties such that it could be applied for fault inspection.

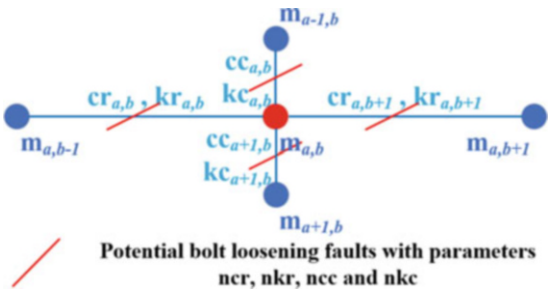

Fig. 2 Considered substructure

3 An Improved Inspecting Method

With the nonlinear output spectra in (5), an improved inspecting method with novel features and indexes is proposed for bolt self-loosening faults.

3.1 Damage Features and Indexes

Considering mass $m_{a,b}$ in the substructure as shown in Fig. 2 only, its differential equation of motion can be obtained from (4), as.

$$\begin{aligned}
&-(v\omega)^2 m_{a,b} G^{v}_{a,b}(jv\omega) + \left((jv\omega)\, cr_{a,b} + kr_{a,b}\right)\left(G^{v}_{a,b}(jv\omega) - G^{r}_{a,b-1}(jv\omega)\right) \\
&+ \left((jv\omega)\, cr_{a,b+1} + kr_{a,b+1}\right)\left(G^{v}_{a,b}(jr\omega) - G^{v}_{a,b+1}(jv\omega)\right) \\
&+ \left((jv\omega)\, cc_{a,b} + kc_{a,b}\right)\left(G^{v}_{a,b}(jv\omega) - G^{v}_{a-1,b}(jv\omega)\right) \\
&+ \left((jv\omega)\, cc_{a+1,b} + kc_{a+1,b}\right)\left(G^{v}_{a,b}(jv\omega) - G^{v}_{a+1,b}(jv\omega)\right) = H^{v}_{a,b}(jv\omega)
\end{aligned} \tag{6}$$

With the local structural modification method (i.e., adding masses m_r and m_u to masses $m_{1.1}$ and $m_{n,q}$ respectively) and exciting the structure with the same excitation, an equation similar to (6) could be obtained, as

$$\begin{aligned}
&-(v\omega)^2 m_{a,b} G^{v,1}_{a,b}(jv\omega) + \left((jv\omega)\, cr_{a,b} + kr_{a,b}\right)\left(G^{v,1}_{a,b}(jv\omega) - G^{v,1}_{a,b-1}(jv\omega)\right) \\
&+ \left((jv\omega)\, cr_{a,b+1} + kr_{a,b+1}\right)\left(G^{v,1}_{a,b}(jr\omega) - G^{v,1}_{a,b+1}(jv\omega)\right) \\
&+ \left((jv\omega)\, cc_{a,b} + kc_{a,b}\right)\left(G^{v,1}_{a,b}(jv\omega) - G^{v,1}_{a-1,b}(jv\omega)\right) \\
&+ \left((jv\omega)\, cc_{a+1,b} + kc_{a+1,b}\right)\left(G^{v,1}_{a,b}(jv\omega) - G^{v,1}_{a+1,b}(jv\omega)\right) = H^{v,1}_{a,b}(jv\omega)
\end{aligned} \tag{7}$$

Observing (6) and (7), it is shown that the change of values of masses $m_{1.1}$ and $m_{n,\,q}$ leads to changes in output spectra and fault-induced nonlinear force, while structural physical properties around mass $m_{a,\,b}$ are constant.

Repeating the local structural modification method three times, another three equations could be obtained as well. Writing all of them in matrix form, as

$$\left[G^{v,\varepsilon}\left(jv\omega\right)\right]_{5x5}\left\{B^{v}\left(jv\omega\right)\right\}_{5x1}=\left\{H_{a,b}^{v,\varepsilon}\left(jv\omega\right)\right\}_{5x1} \tag{8}$$

where

$$\left[G^{v}\left(jv\omega\right)\right]_{5x5}=\begin{bmatrix} G_{a,b}^{v,1}\left(jv\omega\right) & G_{a,b-1}^{v,1}\left(jv\omega\right) & G_{a,b+1}^{v,1}\left(jv\omega\right) & G_{a-1,b}^{v,1}\left(jv\omega\right) & G_{a+1,b}^{v,1}\left(jv\omega\right) \\ G_{a,b}^{v,2}\left(jv\omega\right) & G_{a,b}^{v,2}\left(jv\omega\right) & G_{a,b+1}^{v,2}\left(jv\omega\right) & G_{a-1,b}^{v,2}\left(jv\omega\right) & G_{a+1,b}^{v,2}\left(jv\omega\right) \\ G_{a,b}^{v,3}\left(jv\omega\right) & G_{a,b}^{v,3}\left(jv\omega\right) & G_{a,b+1}^{v,3}\left(jv\omega\right) & G_{a-1,b}^{v,3}\left(jv\omega\right) & G_{a+1,b}^{v,3}\left(jv\omega\right) \\ G_{a,b}^{v,4}\left(jv\omega\right) & G_{a,b}^{v,4}\left(jv\omega\right) & G_{a,b+1}^{v,4}\left(jv\omega\right) & G_{a-1,b}^{v,4}\left(jv\omega\right) & G_{a+1,b}^{v,4}\left(jv\omega\right) \\ G_{a,b}^{v,5}\left(jv\omega\right) & G_{a,b}^{v,5}\left(jv\omega\right) & G_{a,b+1}^{v,5}\left(jv\omega\right) & G_{a-1,b}^{v,5}\left(jv\omega\right) & G_{a+1,b}^{v,5}\left(jv\omega\right) \end{bmatrix}$$

$$\left\{B^{v}\left(jv\omega\right)\right\}_{4x1}=\begin{Bmatrix} \begin{pmatrix} -(v\omega)^{2}m_{a,b}+\left(jv\omega\right)cr_{a,b}+kr_{a,b} \\ +\left(jv\omega\right)cr_{a,b+1}+kr_{a,b+1}+\left(jv\omega\right)cc_{a,b}+kc_{a,b} \\ +\left(jv\omega\right)cc_{a+1,b}+kc_{a+1,b} \end{pmatrix} \\ \left(jv\omega\right)cr_{a,b}+kr_{a,b} \\ \left(jv\omega\right)cr_{a,b+1}+kr_{a,b+1} \\ \left(jv\omega\right)cc_{a,b}+kc_{a,b} \\ \left(jv\omega\right)cc_{a+1,b}+kc_{a+1,b} \end{Bmatrix},$$

$$\left\{H_{a,b}^{v}\left(jv\omega\right)\right\}_{5x1}=\begin{Bmatrix} H_{a,b}^{v,1}\left(jv\omega\right) \\ H_{a,b}^{v,2}\left(jv\omega\right) \\ H_{a,b}^{v,3}\left(jv\omega\right) \\ H_{a,b}^{v,4}\left(jv\omega\right) \\ H_{a,b}^{v,5}\left(jv\omega\right) \end{Bmatrix}.$$

It can be seen that if there is no bolt self-loosening fault around mass $m_{a,\,b}$, vector $\left\{H_{a,b}^{v}\left(jv\omega\right)\right\}$ would be zero, and the matrix $[G^{v}(jv\omega)]$ is singular. On the contrary, if there is a bolt self-loosening fault around mass $m_{a,\,b}$, vector $\left\{H_{a,b}^{v}\left(jv\omega\right)\right\}$ is nonzero, which in turn leads to a nonsingular matrix $[G^{v}(jv\omega)]$. As a result, the singularity of matrix $[G^{v}(jv\omega)]$ could be a sensitive and effective feature for inspecting potential bolt-loosening faults around mass $m_{a,\,b}$.

The rank of matrix is a useful algorithm to decide whether a matrix is singular or not. Therefore, a novel damage index can be defined, as

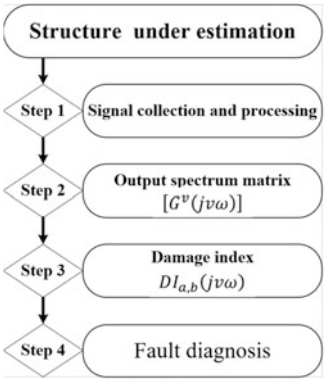

Fig. 3 Operating procedures

$$DI_{a,b}(jv\omega) = Rank\left(\left[G^v(jv\omega)\right]\right)(v \geq 2) \tag{9}$$

Based on the properties of matrix $[G^v(jv\omega)]$ and the above analysis, if $DI_{a,b}(jv\omega) = 5$ holds, results show that the matrix is full rank and potential bolt self-loosening faults may be located around mass $m_{a,b}$. On the contrary, if $DI_{a,b}(jv\omega) < 5$ holds, results reveal that the matrix is singular, and no bolt self-loosening fault exists around mass $m_{a,b}$.

3.2 Procedures of the Method

According to the derivation of the proposed features and indexes, an improved inspecting method can be developed accordingly. Its procedures are explained in detail below.

As shown in Fig. 3, the developed method has four main steps. Firstly, time domain data are collected from the two-dimensional structure to be inspected in step one. Then, data are transformed into the frequency domain to form matrix $[G^v(jv\omega)]$ in step two. Next, the rank of matrix $[G^v(jv\omega)]$ is calculated as the damage index in step three. Finally, potential bolt self-loosening faults are inspected based on the value of the damage index $DI_{a,b}(jv\omega)$.

4 Studies of Simulation Cases

In order to verify the effectiveness of the proposed method, three simulation cases on a two-dimensional structure with twelve masses are studied. In case one, one fault (red slash) is between masses $m_{2,4}$ and $m_{3,4}$ (Fig. 4a). Based on this, extra faults (red slashes) around mass $m_{2,2}$ exist in case two (Fig. 4b), and extra faults (red slashes)

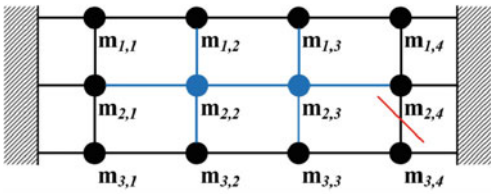

(a) Case one

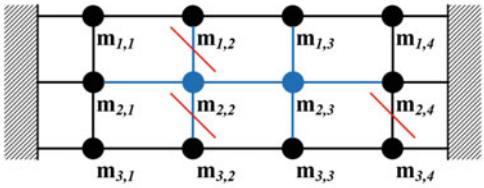

(b) Case two

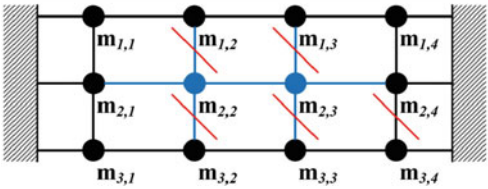

(c) Case three

Fig. 4 Schematic diagram of cases

Table 1 Structural mass

Terms	Values											
Coordinates (a,b)	1,1	1,2	1,3	1,4	2,1	2,2	2,3	2,4	3,1	3,2	3,3	3,4
Mass m	0.1	0.2	0.3	0.4	0.5	0.6	0.7	0.8	0.9	1.0	1.1	1.2

Table 2 Structural raw damping

Terms	Values							
Coordinates (a,b)	1,1	1,2	1,3	1,4	1,5	2,1	2,2	2,3
Damping (1e2)	0.57	0.93	1.29	1.65	2.01	2.37	2.73	3.09
Coordinates (a,b)	2,4	2,5	3,1	3,2	3,3	3,4	3,5	
Damping (1e2)	3.45	3.81	4.17	4.53	4.89	5.25	5.61	

around masses $m_{2,2}$ and $m_{2,3}$ exist in case three (Fig. 4b). All simulation cases are studied by using the Matlab software.

Corresponding structural parameters used in simulations are shown in the tables below (Tables 1, 2, 3, 4, 5 and 6).

According to (2), faults are simulated as nonlinear elements with nonlinear parameters. The input applied to mass $m_{3,4}$ is a cosine function $g(t) = \cos(2\pi ft)$ with a frequency of 16 Hz, and the local structural modification method with four groups of masses m_r and m_u is added to masses $m_{1,1}$ and $m_{3,4}$, respectively.

Table 3 Structural raw stiffness

Terms	Values							
Coordinates (a,b)	1,1	1,2	1,3	1,4	1,5	2,1	2,2	2,3
Stiffness (1e4)	1.03	1.68	2.33	2.98	3.62	4.27	4.92	5.57
Coordinates (a,b)	2,4	2,5	3,1	3,2	3,3	3,4	3,5	
Stiffness (1e4)	6.22	6.86	7.51	8.16	8.81	9.46	10.10	

Table 4 Structural column damping

Terms	Values							
Coordinates (a,b)	2,1	2,2	2,3	2,4	3,1	3,2	3,3	3,4
Damping (1e2)	0.39	0.75	1.11	1.47	1.83	2.19	2.55	2.91

Table 5 Structural column stiffness

Terms	Values							
Coordinates (a,b)	2,1	2,2	2,3	2,4	3,1	3,2	3,3	3,4
Stiffness (1e4)	0.47	0.90	1.33	1.77	2.20	2.63	3.06	3.49

Table 6 Structural nonlinear parameters

Terms	Values
Additional mass	(0.2,2.4); (0.8,9.6); (4.8,57.6); (38.4460.8); (384,4608);
Case one	ncc2,4 = 871.2; nkc2,4 = 148,104; Other nc and nk are zero
Case two	ncc2,4 = 871.2; nkc2,4 = 148,104; ncc1,2 = 655.2; nkc1,2 = 11,380; ncc2,2 = 799.2; nkc2,2 = 135,864; Other nc and nk are zero

Case two	ncc2,4 = 871.2; nkc2,4 = 148,104; ncc1,2 = 655.2; nkc1,2 = 11,380;
	ncc2,2 = 799.2; nkc2,2 = 135,864; ncc1,3 = 691.2; nkc1,3 = 117,500;
	ncc2,3 = 835.2; nkc2,3 = 141,984; Other nc and nk are zero

Table 7 Results of simulation studies

$DI_{a,\,b}(jv\omega)$	a,b = 2.2	a,b = 2.3
Case one	3	3
Case two	5	4
Case three	5	5

With the operating procedures in Fig. 3, the results of the damage index in each simulation case are shown in Table 7.

In case one, the results show that the values of both damage indexes are smaller than five, meaning that all matrices are singular and there is no fault around masses $m_{2,\,2}$ and $m_{2,\,3}$. In case two, the value of index $DI_{2,\,2}(jv\omega)$ is equal to five, while the value of index $DI_{2,\,3}(jv\omega)$ is less than five, which means that there is a fault around mass $m_{2,\,2}$ only. Compared with the results in the previous two cases, the values of both damage indexes are equal to five in case three, showing that there are faults around masses $m_{2,\,2}$ and $m_{2,\,3}$.

As a whole, the inspected results from the above simulations are consistent with the real situations of faults shown in Fig. 4. Therefore, the effectiveness and

reliability of the proposed method are verified and demonstrated by these three simulation cases.

5 Conclusion

In order to overcome the limitation in previous methods where benchmark features are required during fault diagnosis, an improved method for inspecting bolt self-loosening faults in two-dimensional structures without reference is proposed in this study. The main conclusions are given below.

1. By considering the impact of bolt self-loosening faults as nonlinear forces, a two-dimensional discrete MDOF model with nonlinear components could be built for the dynamic analysis of two-dimensional structures.
2. With the local structural modification method, five similar equations from the structure to be inspected could be used to form one matrix, whose rank could be a sensitive damage index for bolt loosening fault inspection.
3. Results from simulation studies on a two-dimensional model with multiple bolt self-loosening faults demonstrate that the proposed method could give precise states of bolt loosening faults in numerical structures.

In the further study, the extension of this method to other types of complex structures like rotors and experimental studies of this method on real two-dimensional engineering structures should be considered as well.

Acknowledgments This work is supported by the Fundamental Research Funds for the Central Universities project (No. 3102020OQD705).

References

1. Bickford, J. (ed.): Handbook of Bolts and Bolted Joints. CRC Press (1998)
2. Bickford, J.: An Introduction to the Design and Behavior of Bolted Joints, Revised and Expanded. Routledge, New York (2018)
3. Huang, J., Liu, J., Gong, H., Deng, X.: A comprehensive review of loosening detection methods for threaded fasteners. Mech. Syst. Signal Process. **168**, 108652 (2022)
4. Nikravesh, S.M.Y., Goudarzi, M.: A review paper on looseness detection methods in bolted structures. Latin Am. J. Solids Struct. **14**, 2153–2176 (2017)
5. Yeung, W.T., Smith, J.W.: Damage detection in bridges using neural networks for pattern recognition of vibration signatures. Eng. Struct. **27**(5), 685–698 (2005)
6. Yuta, I., Masafumi, N.: Vibration-based detection of loosened bolts on pipes attached to bridges. Mater. Res. Proc. **18**, 1–10 (1992)
7. Tashakori, S., Baghalian, A., Unal, M., Fekrmandi, H., McDaniel, D., Tansel, I.N.: Contact and non-contact approaches in load monitoring applications using surface response to excitation method. Measurement. **89**, 197–203 (2016)
8. Dong, G., Zhao, F., Zhang, X.: Experimental study on monitoring the bolt group looseness in a clamping support structure model. Adv. Mech. Eng. **9**(3), 1687814017695046 (2017)

9. Lei, Y., Lin, J., He, Z., Zuo, M.J.: A review on empirical mode decomposition in fault diagnosis of rotating machinery. Mech. Syst. Signal Process. **35**(1–2), 108–126 (2013)
10. Haroon, M., Adams, D.E.: Time and frequency domain nonlinear system characterization for mechanical fault identification. Nonlinear Dyn. **50**(3), 387–408 (2007)
11. Zhang, M., Shen, Y., Xiao, L., Qu, W.: Application of subharmonic resonance for the detection of bolted joint looseness. Nonlinear Dyn. **88**(3), 1643–1653 (2017)
12. Nichols, J.M., Trickey, S.T., Seaver, M., Motley, S.R., Eisner, E.D.: Using ambient vibrations to detect loosening of a composite-to-metal bolted joint in the presence of strong temperature fluctuations. J. Vib. Acoust. **21**, 1–16 (2007)
13. Amerini, F., Barbieri, E., Meo, M., Polimeno, U.: Detecting loosening/tightening of clamped structures using nonlinear vibration techniques. Smart Mater. Struct. **19**(8), 085013 (2010)
14. Zagrai, A.N., Doyle, D.T.: Exploring the Acoustic Nonlinearity for Monitoring Complex Aerospace Structures, vol. 14, pp. 21–36. New Mexico Institute of Mining and Technology Socorro Department of Mechanical Engineering (2008)
15. Amerini, F., Meo, M.: Structural health monitoring of bolted joints using linear and nonlinear acoustic/ultrasound methods. Struct. Health Monit. **10**(6), 659–672 (2007)
16. Liu, L., Thomas, J.P., Dowell, E.H., Attar, P., Hall, K.C.: A comparison of classical and high dimensional harmonic balance approaches for a Duffing oscillator. J. Comput. Phys. **215**(1), 298–320 (2016)

Physics-Informed Sparse Identification of a Bistable Nonlinear Energy Sink

Qinghua Liu and Junyi Cao

1 Introduction

Over the past few years, nonlinear energy sinks have been a subject of growing interest due to their wide application in the fields of energy harvesting and vibration absorption [1, 2]. Among various nonlinear energy sink devices, it seems that adding local bistable attachments may allow for efficient broad-band targeted energy transfer over a wide range of input energy levels [3, 4]. Therefore, the optimal design of a tuned bistable nonlinear energy sink has been widely studied [5, 6]. However, introducing bistability brings a great challenge for nonlinear elastic force identification in practical applications due to the snap-through characteristics.

For nonlinear elastic force identification in single-degree-of-freedom bistable vibrating structures, various methods have been proposed to address this issue [7]. Liu et al. comparatively investigated the acceleration and displacement measurement restoring force surface method for identifying nonlinear elastic force containing bistability [8]. Feldman proposed the Hilbert Vibration Decomposition combined with the "FREEVIB" algorithm to identify the nonlinear elastic force of the Duffing-Holmes bistable oscillator [9, 10]. Anastasio combined nonlinear subspace and restoring force surface methods to estimate the nonlinear elastic force of an asymmetric double-well Duffing oscillator and its damping characteristics [11, 12]. Liu et al. developed the two-stage nonlinear subspace method to identify the parameters of a nonlinear bistable piezoelectric cantilever beam in an energy harvesting system [13]. Zhu et al. employed the nonlinear subspace identification with the Bayesian probability method to select the best model and improve the accuracy of bistable oscillator identification [14]. For nonlinear elastic

Q. Liu · J. Cao (✉)
School of Mechanical Engineering, Xi'an Jiaotong University, Xi'an, China
e-mail: caojy@mail.xjtu.edu.cn

© The Author(s), under exclusive license to Springer Nature Switzerland AG 2024

W. Lacarbonara (ed.), *Advances in Nonlinear Dynamics, Volume III*, NODYCON Conference Proceedings Series, https://doi.org/10.1007/978-3-031-50635-2_39

force characterization in nonlinear energy sink structures, Wang et al. used the restoring force surface method to identify the nonlinear stiffness and damping of the piecewise linear nonlinear energy sink and a hyperbolic tangent function is adopted for characterization [15]. Lund et al. adopted an unscented Kalman filter for the identification of geometric nonlinear stiffness and Coulomb damping in a nonlinear energy sink device [16]. Moore proposed the characteristic nonlinear system identification method to identify the dynamics of local piecewise linear attachments [17]. These methods have typically been found to be accurate and reliable for their designed nonlinear energy sinks. However, they may encounter difficulties in obtaining nonlinear elastic force in a multi-degree-of-freedom system with local bistability.

2 Modeling and Identification

2.1 Modeling of a TBNES

The system of a Three-degree-of-freedom Bistable Nonlinear Energy Sink (TBNES) considered is schematically depicted in Fig. 1. It consists of two linear oscillators of primary mass m_1 and secondary mass m_2 with a bistable attachment m_3. Except for the bistable nonlinear elastic force in m_3 connected to m_2, the linear stiffness k_1, k_2 and viscous damping c_1, c_2 and c_3 are considered. It should be noted that the bistable attachment used here is a magnetically coupled cantilever beam. Therefore, the m_3, c_3, are equivalent lumped parameters. Besides, the polynomial-type nonlinear elastic force is adopted to characterize bistability.

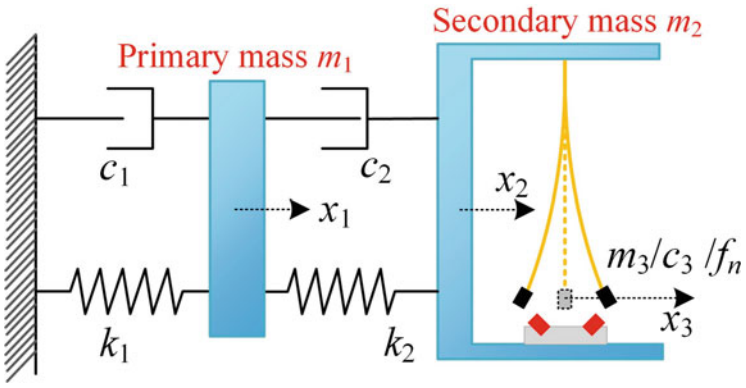

Fig. 1 Schematic view of a TBNES

The equations of motion of TBNES can be modeled as:

$$\begin{cases} m_1\ddot{x}_1 + c_1\dot{x}_1 + k_1x_1 + c_2\left(\dot{x}_1 - \dot{x}_2\right) + k_2\left(x_1 - x_2\right) = 0 \\ m_2\ddot{x}_2 + c_2\left(\dot{x}_2 - \dot{x}_1\right) + k_2\left(x_2 - x_1\right) + c_3\left(\dot{x}_2 - \dot{x}_3\right) + f_n\left(x_2 - x_3\right) = 0 \\ m_3\ddot{x}_3 + c_3\left(\dot{x}_3 - \dot{x}_2\right) + f_n\left(x_3 - x_2\right) = 0 \\ f_n(q) = \alpha_1 q + \alpha_2 q^3 \end{cases} \tag{1}$$

where q and α represent the relative displacement and polynomial fitting coefficients of the nonlinear stiffness force, respectively. And, f_n is the nonlinear stiffness force.

2.2 *Physics-Informed Sparse Identification of TBNES*

When the TBNES is described by Eq. (1), the parameters m_1, m_2, k_1, c_1 and c_2 can be easily measured or identified by linear parameter identification methods. However, the bistable nonlinear elastic force always has unknown models. Besides, the bistable nonlinear elastic force is strongly sensitive to installation uncertainties. Therefore, the nonparametric identification of nonlinear elastic force trajectories and the selection of an interpretable model are the first steps. Furthermore, the data-driven regression methods using the dynamic response of the oscillator need to be conducted for accurate parameter estimation.

For the local bistable attachment in TBNES, the nonlinear elastic force can be deduced once the absolute displacement of m_2 and m_3 is measured. The velocity and acceleration can be obtained by numerical differentiation of displacement. Then, the nonlinear elastic force can be described as:

$$f_n(q) = -m_3\ddot{x}_3 - c_3\left(\dot{x}_3 - \dot{x}_2\right) \tag{2}$$

The restoring force surface can be plotted using the triplets ($x_3 - x_2$, $\dot{x}_3 - \dot{x}_2$, $-m_3\ddot{x}_3$). The nonlinear elastic force can be extracted by assuming that the velocity is equal to zero. It is suggested that the two velocity planes in a quasi-zero range $[-\theta_1\ \theta_1]$ are used to intercept the restoring force surface. The nonlinear elastic force can be obtained by projecting the intercepted data set onto the real zero-velocity plane.

However, the construction of the restoring force surface and the intercepting procedure is sensitive to noise. Therefore, more accurate data-driven regression methods need to be conducted. For modern data-driven methods, the sparse identification of nonlinear dynamical systems may be a good technique [18, 19]. Based on the restoring force surface method, the basis functions in sparse identification can be physically informed. Eq. (1) can be rewritten as:

$$\frac{dx_k(t)}{dt} = \Theta(x)\xi_k + \sigma Z_k \tag{3}$$

where $\Theta(x)$ is the candidate library and ξ_k is the coefficient of the sparse vector. The σ is defined as the Signal-to-Noise Ratio (SNR), and Z_k is the root mean square of the measured data $x_k(t)$.

According to Eq. (2), the candidate library $\Theta(x)$ consists of polynomial terms; therefore:

$$\Theta(\mathbf{X}) = \begin{bmatrix} \boldsymbol{\theta}_1(\mathbf{X}) & \boldsymbol{\theta}_2(\mathbf{X}) & \cdots & \boldsymbol{\theta}_p(\mathbf{X}) \end{bmatrix} = \begin{bmatrix} \vdots & \vdots & \vdots & \vdots \\ \mathbf{X}^{P_1} & \mathbf{X}^{P_2} & \cdots & \mathbf{X}^{P_n} \\ \vdots & \vdots & \vdots & \vdots \end{bmatrix} \tag{4}$$

where $\mathbf{X}^{P_n}$ denotes the n-order polynomial nonlinearities in the state $\mathbf{X}$.

The coefficients ξ can be obtained by performing a standard regression. The L^1 regularization term needs to be added to the regression:

$$\boldsymbol{\xi} = \underset{\boldsymbol{\xi}'}{\operatorname{argmin}} \left\| \Theta \boldsymbol{\xi}' - \mathbf{x} \right\|_2 + \lambda \left\| \boldsymbol{\xi}' \right\|_1 \tag{5}$$

where λ weights the sparsity constraint. The formula is related to compressed sensing, which allows sparse vectors to be determined from relatively few noncoherent random measurements [20].

The specific identification processes can be summarized as follows:

1. Give the TBNES an impact.
2. Collect the displacement responses of each degree of freedom.
3. Obtain the velocity and acceleration by noise removal and numerical differentiation.
4. Arrange matrices of displacement, velocity and acceleration [18].
5. Construct the local restoring force surface using the X-axis of $(x_3 - x_2)$; Y-axis of $(\dot{x}_3 - \dot{x}_2)$ and Z-axis of $-m_3\ddot{x}_3$. Then, two quasi-zero velocity planes are selected to cut the restoring force surface. Finally, project the intercepted trajectories onto the real zero-velocity plane.
6. The trajectory of nonlinear elastic force can be fitted by a polynomial function.
7. Select an appropriate polynomial order based on the obtained nonlinear stiffness force and then construct the candidate function matrix in sparse regression.
8. Use the sequential thresholded least-squares algorithm to achieve sparse regression, and the coefficients ξ can be estimated.

3 Numerical Example

To verify the effectiveness and robustness of physics-informed sparse identification of the TBNES, the simulation selects the following parameters in Eq. (1): $m_1 = m_2 = 1$ kg; $c_1 = c_2 = 1$ N/(m/s); $m_3 = 0.02$ kg; $c_3 = 0.02$ N/(m/s);

$\alpha_1 = -100$ N/m; $\alpha_2 = 10^6$ N/m^3. The levels of SNR = 30 dB noise will be added to the displacement, velocity and acceleration responses of m_1, m_2 and m_3. The Eq. (1) can then be arranged in the following form:

$$\begin{cases} dy(1) = y(2) \\ dy(2) = -60000\mathrm{y}(1) - 3y(2) + 30000y(3) + y(4) \\ dy(3) = y(4) \\ dy(4) = 3000y(1) + y(2) - 29900y(3) - 1.01y(4) - 100y(5) - 10^6 y(3)^3 \\ \quad + 10^6 y(5)^3 + 3 * 10^6 y(3)^2 y(5) - 3 * 10^6 y(3) y(5)^2 \\ dy(5) = y(6); \\ dy(6) = 5000^* y(3) - 5000^* y(5) + y(4) - y(6) - 5^* 10^7 y(5)^3 \\ \quad + 1.5^* 10^8 y(5)^2 y(3) - 1.5^* 10^8 y(5) y(3)^2 + 5^* 10^7 y(3)^3 \end{cases} \tag{6}$$

The dynamic response of a TBNES is sensitive to nonlinear elastic force parameters and initial conditions due to strong nonlinear coupling. Therefore, the Normalized Mean Square Error (NMSE) of the nonlinear elastic force is defined here to evaluate identification accuracy:

$$J = \frac{100}{N\sigma_x^2} \sum_{i=1}^{N} \left(f_i - \widehat{f}_i \right)^2 \tag{7}$$

To obtain the data set for identification, the initial condition of Eq. (1) is chosen as [0.001 m; 0; 0.002 m; 0; 0.02 m; 0]. The sampling frequency of 1000 Hz in the time interval of $t = 0$ to $t = 600$ s is set. The displacement responses of m_1, m_2, m_3 are obtained by conducting an ode45 simulation. The 30 dB white Gaussian noise is added to the displacement responses. The three-point differential formula is used to solve the velocity and acceleration. Fig. 2 shows the displacement responses of each degree of freedom. Both m_1 and m_2 exhibit irregular free decay vibrations due to nonlinear coupling, as shown in Fig. 2a, b. It can be observed in Fig. 2c that the oscillator finally moves into the negative equilibrium point of -0.01 m.

Based on the above free vibration responses, the restoring force surface is constructed using the X-axis of $(x_3 - x_2)$, Y-axis of $(\dot{x}_3 - \dot{x}_2)$ and Z-axis of $-m3\ddot{x}_3$, as shown in Fig. 3a. The nonlinear elastic force trajectories are intercepted by assuming $\theta = 0.05$, as plotted using red asterisks. The final nonlinear elastic force can be fitted with a third polynomial with the function of $f_n = -119(x_3 - x_2) - 518(x_3 - x_2)^2 + 1.16 \times 10^6 (x_3 - x_2)^3$, as depicted in Fig. 4. The NMSE between the identified and theoretical nonlinear elastic force curves is 1.79% in the range of [−0.02 0.02].

From the above procedure, physical information about the nonlinear elastic force is obtained. Therefore, the nonlinear elastic force in the TBNES is a third-order polynomial function, which gives nonlinear basis functions in sparse regression prior knowledge. Furthermore, the sparse identification algorithm is conducted

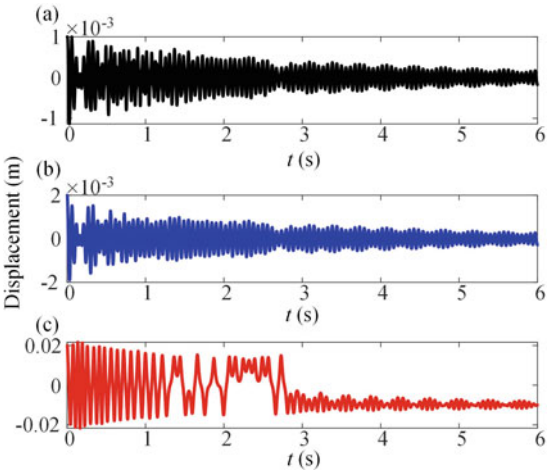

Fig. 2 Displacement responses of TBNES

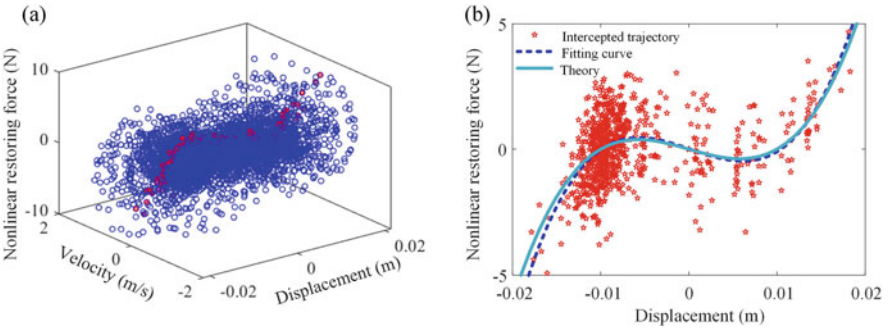

Fig. 3 Restoring force surface identification of TBNES: (**a**) construction of restoring force surface; (**b**) comparison between identified nonlinear elastic force and theory

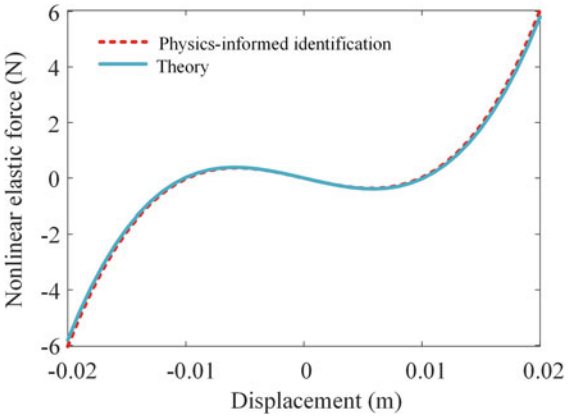

Fig. 4 Comparison of physics-informed identification result and theory

using the same free vibration responses. The final identified nonlinear elastic force is $f_n = -98.2(x_3 - x_2) + 999998(x_3 - x_2)^3$. The NMSE of the identified nonlinear elastic force is 0.18% in the range of [−0.02 0.02]. The results show that the restoring force surface-informed sparse identification improves the accuracy by 1.61%.

4 Experimental Validation

To verify the effectiveness of physics-informed sparse identification for the designed TBNES, an experimental setup is established, as shown in Fig. 5. The bistable cantilever beam is made of spring steel with a size of 150 × 20 × 0.8 mm. The tip magnets and the external rotatable magnets have dimensions of 20 × 10 × 3.5 mm and 20 × 5 × 5 mm, respectively. The designed first-floor mass and second-floor mass are made of 6061 aluminum alloy, and both are supported by four elastic beams. The supported beam has a dimension of 147.5 × 30 × 0.8 mm. The displacement response of the first floor is measured by the displacement sensor (HL-G103-A-C5, Keyence). The free vibration responses of the bistable cantilever beam and second-floor mass can be measured by the displacement sensors (HL-G112-A-C5, Keyence). The acceleration of the first floor and second floor is measured

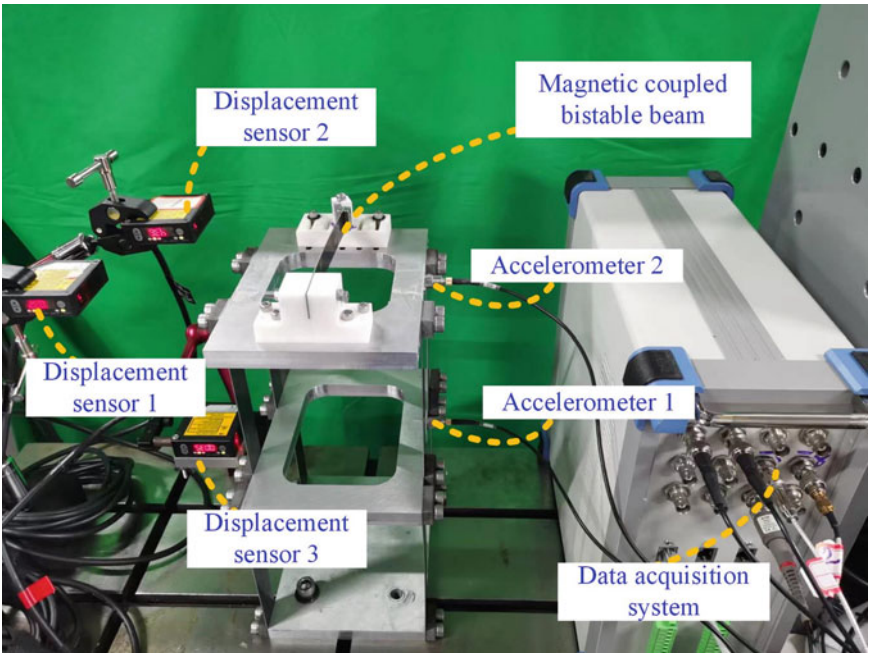

Fig. 5 Experimental setup

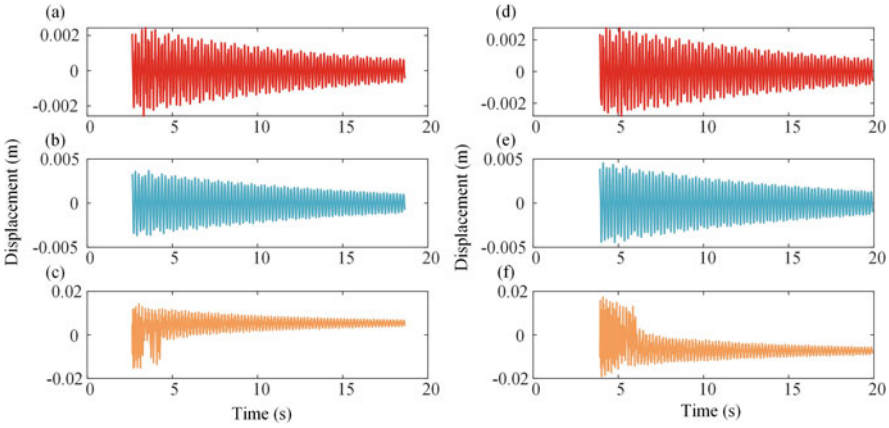

Fig. 6 The displacement responses of TBNES

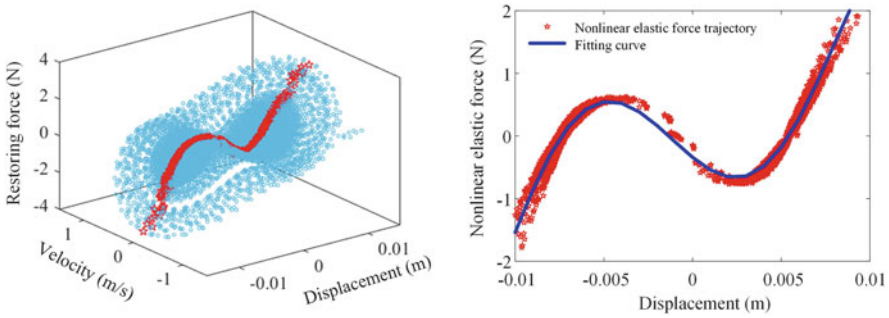

Fig. 7 Nonlinear elastic force identification: (**a**) construction of restoring force surface and extraction of nonlinear elastic force; (**b**) polynomial fitting of extracted nonlinear elastic force

by two accelerometers (EV4140, ECON Technologies Co., Ltd). The data sets are synchronously recorded in the data acquisition box.

The displacement responses of three masses are acquired by giving the bistable beam a large initial displacement, as shown in Fig. 6. The sampling frequency is 781.25 Hz, and the total acquisition time is 20 s. Fig. 6a–c shows the displacement response of the first floor x_1, second floor x_2 and bistable beam x_3, respectively. The bistable beam finally moves into the positive equilibrium point. When the bistable beam moves into the negative equilibrium point, the data sets are shown in Fig. 6d–f.

The relative displacement can be calculated by using $x_3 - x_2$. The acceleration of the bistable beam can be obtained by quadratic differentiation of x_3. The restoring force surface can be constructed using Eq. (2), as shown in Fig. 7a. The nonlinear elastic force can be intercepted by assuming $\theta_1 = 0.05$ m/s, as plotted using red asterisks. The nonlinear elastic force can be physically informed by conducting polynomial fitting, and the fifth order is suitable, as shown in Fig. 7b.

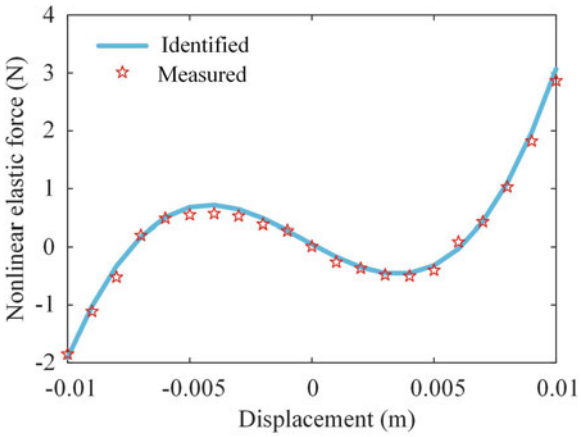

Fig. 8 Comparison of nonlinear elastic force using the proposed identification method and quasi-static measurement

The restoring force surface method and static fitting of intercepted nonlinear elastic force are often disturbed by noise. Therefore, sparse identification using sequential thresholded least-squares is conducted on Eq. (6). The identification data sets are the same as in the restoring force surface method. The sparsely identified nonlinear elastic force and quasi-static measured one are plotted using an aqua-green line and red asterisks, respectively, as shown in Fig. 8. The results show that there is good agreement, and the final NMSE is 0.97%.

5 Conclusions

This paper proposed a new physics-informed sparse identification method for parameter estimation of a three-degree-of-freedom bistable nonlinear energy sink. The restoring force surface is constructed on the local bistable structure, and the nonlinear elastic force trajectory is intercepted by assuming two quasi-zero velocity planes. Furthermore, the candidate functions can be physically informed in the sparse identification algorithm. Numerical simulation shows that the proposed method not only gives sparse identification physics information but also improves accuracy by 1.61% under a noise level of 30 dB. Experimental verification is performed on a two-story beam-type bistable energy sink structure. The results show that the identified nonlinear elastic force has good agreement with the measured one, and the NMSE is only 0.97%.

References

1. Vakakis, A.F., Gendelman, O.V., Bergman, L.A., Mojahed, A., Gzal, M.: Nonlinear targeted energy transfer: state of the art and new perspectives. Nonlinear Dyn. **108**, 1–31 (2022)

2. Ding, H., Chen, L.-Q.: Designs, analysis, and applications of nonlinear energy sinks. Nonlinear Dyn. **100**, 3061–3107 (2020)
3. Habib, G., Romeo, F.: The tuned bistable nonlinear energy sink. Nonlinear Dyn. **89**, 179–196 (2017)
4. Qiu, D., Li, T., Seguy, S., Paredes, M.: Efficient targeted energy transfer of bistable nonlinear energy sink: application to optimal design. Nonlinear Dyn. **92**, 443–461 (2018)
5. Fang, S., Chen, K., Xing, J., Zhou, S., Liao, W.-H.: Tuned bistable nonlinear energy sink for simultaneously improved vibration suppression and energy harvesting. Int. J. Mech. Sci. **212**, 106838 (2021)
6. Li, H., Li, A., Kong, X.: Design criteria of bistable nonlinear energy sink in steady-state dynamics of beams and plates. Nonlinear Dyn. **103**, 1475–1497 (2021)
7. Noël, J.-P., Kerschen, G.: Nonlinear system identification in structural dynamics: 10 more years of progress. Mech. Syst. Signal Process. **83**, 2–35 (2017)
8. Liu, Q., Hou, Z., Zhang, Y., Jing, X., Kerschen, G., Cao, J.: Nonlinear restoring force identification of strongly nonlinear structures by displacement measurement. ASME. J. Vib. Acoust. **144**(3), 031002 (2022)
9. Feldman, M.: Nonparametric identification of asymmetric nonlinear vibration systems with the Hilbert transform. J. Sound Vib. **331**, 3386–3396 (2012)
10. Feldman, M.: Hilbert transform in vibration analysis. Mech. Syst. Signal Process. **25**, 735–802 (2011)
11. Anastasio, D., Marchesiello, S.: Experimental characterization of friction in a negative stiffness nonlinear oscillator. Vibration. **3**, 132–148 (2020)
12. Anastasio, D., Fasana, A., Garibaldi, L., Marchesiello, S.: Nonlinear dynamics of a duffing-like negative stiffness oscillator: modeling and experimental characterization. Shock. Vib. **2020**, 1–13 (2020)
13. Liu, Q., Cao, J., Hu, F., Li, D., Jing, X., Hou, Z.: Parameter identification of nonlinear bistable piezoelectric structures by two-stage subspace method. Nonlinear Dyn. **105**, 2157–2172 (2021)
14. Zhu, R., Fei, Q., Jiang, D., Marchesiello, S., Anastasio, D.: Bayesian model selection in nonlinear subspace identification. AIAA J. **60**, 92–101 (2022)
15. Wang, X., Geng, X.-F., Mao, X.-Y., Ding, H., Jing, X.-J., Chen, L.-Q.: Theoretical and experimental analysis of vibration reduction for piecewise linear system by nonlinear energy sink. Mech. Syst. Signal Process. **172**, 109001 (2022)
16. Lund, A., Dyke, S.J., Song, W., Bilionis, I.: Identification of an experimental nonlinear energy sink device using the unscented Kalman filter. Mech. Syst. Signal Process. **136**, 106512 (2020)
17. Moore, K.J.: Characteristic nonlinear system identification: a data-driven approach for local nonlinear attachments. Mech. Syst. Signal Process. **131**, 335–347 (2019)
18. Brunton, S.L., Proctor, J.L., Kutz, J.N.: Discovering governing equations from data by sparse identification of nonlinear dynamical systems. Proc. Natl Acad. Sci. USA. **113**, 3932–3937 (2016)
19. Brunton, S.L., Kutz, J.N.: Data-Driven Science and Engineering: Machine Learning, Dynamical Systems, and Control. Cambridge University Press (2022)
20. Baraniuk, R.G.: Compressive sensing. IEEE Signal Process. Mag. **24**, 118–121 (2007)

Simultaneous Estimation of Multiple Backbone Curves Using Smooth Coordinate Tracking

Dalton L. Stein and David Chelidze

1 Introduction

In engineering design, data-driven analysis of nonlinear phenomena has become increasingly important, particularly with the development of complex lightweight structures and novel materials. Accurately quantifying active nonlinearities from output response data has become essential for reliable and efficient design. Nonlinearity is also intentionally introduced in the design of energy harvesters and sinks, making it necessary to use experimental methods to assess their capabilities in the field.

Several experimental methods are available for identifying nonlinear phenomena in mechanical systems. Techniques that identify changes in the frequency response functions for different forcing amplitudes and stepped-sine testing [1] are commonly used but can be time-consuming, even when automated. Recent research has focused on estimating the backbone curve to describe the frequency-amplitude relationship of a system's undamped and unforced response. The conservative backbone is theoretically distinct from that of the damped system [2], and resonant decay procedures aim to approximate the conservative backbone for weakly damped nonlinear mechanical systems. A seminal development was the application of the Hilbert transform (HT) for constructing these instantaneous frequency-amplitude pairs for single-mode identification [3]. In [4], a simple algorithm based on detecting the zero crossings of a single-mode free-decay response is described. The authors identify the instantaneous frequencies from the zero crossings and construct an instantaneous amplitude by finding the maxima for each complete oscillation cycle. However, these methods assume that the response contains only a single

D. L. Stein · D. Chelidze (✉)
University of Rhode Island, Kingston, RI, USA
e-mail: chelidze@uri.edu
https://web.uri.edu/nld/

© The Author(s), under exclusive license to Springer Nature Switzerland AG 2024

W. Lacarbonara (ed.), *Advances in Nonlinear Dynamics, Volume III*, NODYCON Conference Proceedings Series, https://doi.org/10.1007/978-3-031-50635-2_40

mode. Therefore, exhaustive experimental methods are needed for multi-degree-of-freedom systems to properly obtain a single mode responses [5, 6]. Furthermore, without proper guidance or insight into the nature of the nonlinearity, one can only rely on the assumed linear modal structure to guide these experimental procedures.

This chapter presents a simple and efficient algorithm for estimating the instantaneous frequency and amplitude from multivariate multi-mode decay responses. The algorithm uses *smooth coordinate decomposition* (SCD) [7] to separate the time series into approximate nonlinear modal coordinates or *smooth coordinate pairs* (SCPs) and filter out noise. This modal separation allows for treating each SCP as a single-mode oscillation if damping and nonlinearity are weak. A simple zero-crossing detection is used on each smooth coordinate pair to obtain the instantaneous frequency, and the orthogonality of the coordinates provides a convenient construction of the instantaneous amplitude. This enables the reconstruction of multiple backbone curves from a single decay response.

This chapter is organized into several sections. Section 2 reviews the SCD algorithm and introduces the concept of SCPs. Section 3 formulates the *smooth coordinate tracking algorithm* (SCTA) and illustrates its application using a multivariate non-stationary time series. Section 4 presents numerical and experimental case studies using the SCTA to reconstruct the backbone curves, followed by discussion and conclusions.

2 Smooth Coordinate Tracking

We begin with a sampled scalar field or a trajectory matrix, $X \in \mathbb{R}^{m\times n}$, where m is the number of snapshots in time recorded at n distinct spatial locations. A second matrix, denoted as $\hat{X}$, which is temporally correlated with X, is constructed and concatenated with X to construct the data matrix, $Y = [X\ \hat{X}] \in \mathbb{R}^{m\times 2n}$. Usually, $\hat{X}$ represents a time derivative of X and is constructed using a finite forward difference operator. In practice, one could also use a delay coordinate embedding to obtain the temporally correlated state measurements [8]. This would prevent additional noise from being introduced in the time-series data, especially since a second numerical derivative is introduced in Sect. 2.1. A filtering strategy is discussed in Sect. 3.1 to overcome this noise problem.

2.1 Smooth Coordinate Decomposition

The idea behind the SCD is to find the smoothest lower-dimensional approximation of a sampled scalar field, $Y \in \mathbb{R}^{m\times 2n}$, by minimizing the roughness in the corresponding time coordinates. To describe this smoothness, a velocity matrix, $\dot{Y}$, is constructed through a finite difference operator, $\mathcal{D}$, such that $\dot{Y} = \mathcal{D}Y$ [7]. The SOD problem is most aptly solved through a *generalized singular value decomposition* of the matrix pair Y and $\dot{Y}$,

$$Y = UC\Phi^T \quad \text{and} \quad \dot{Y} = VS\Phi^T \tag{1}$$

where $U \in \mathbb{R}^{m\times 2n}$ and $V \in \mathbb{R}^{m\times 2n}$ are orthogonal, $C = \text{diag}(c_i) \in \mathbb{R}^{2n\times 2n}$ and $S = \text{diag}(s_i) \in \mathbb{R}^{2n\times 2n}$ are diagonal, and the common basis of the decomposition, $\Phi \in \mathbb{R}^{2n\times 2n}$, are the *smooth modes*.

2.2 Smooth Coordinate Pairs

The *smooth coordinates* (SCs) are obtained by projecting the original trajectory matrix onto the adjoint modes of Φ,

$$Q = Y\Phi^{-T} = UC \tag{2}$$

where $Q \in \mathbb{R}^{m\times 2n}$ are the SCs. The SCs are conventionally sorted according to their frequency content. This degree of smoothness is characterized by $\lambda_i = c_i^2/s_i^2$, where $\lambda_1 \geq \lambda_2 \geq ... > \lambda_n$ are the *smooth values* (SVs). When decomposing a trajectory matrix of configuration states, these values were shown to be related to the natural frequencies of the undamped system via $\lambda_i = 1/\omega_i^2$ [7]. However, when decomposing a sampled scalar field containing state space measurements of an underdamped system, each i-th mode spans a two-dimensional subspace, and the corresponding SVs can be shown to be

$$\lambda_i^{-2} \approx \omega_i^2 + 2\zeta_i\omega_i^2 \quad \text{and} \quad \hat{\lambda}_i^{-2} \approx \omega_i^2 - 2\zeta_i\omega_i^2\,, \tag{3}$$

where λ_i and $\hat{\lambda}_i$ are the SVs and together form a *smooth value pair* (SVP). We have numerically validate this for values of $\zeta_i \in [0\ 0.05]$.

Each SVP will have a set of orthogonal temporal coordinates with the same oscillation tone (not necessarily a pure tone) since $U^TU = I$. The pairs of coordinates are called *smooth coordinate pairs* (SCPs) and have the following structure: $Q = [q_1(t), \hat{q}_1(t), \cdots, q_n(t), \hat{q}_n(t)]$, where $q_i, \hat{q}_i\ \forall\ i = 1, 2, ..., n$ form SCPs. This manuscript focuses on exploiting these SCPs to uncover the frequency-amplitude-dependent behavior in the response.

3 Tracking of Nonlinear System Backbone

The basic proposition is to make use of the properties within the SCPs to reconstruct the nonlinear backbone curves of multi-degree-of-freedom systems using data obtained from an arbitrary excitation method (e.g., impulse response or free decay). In this section, the proposed SCTA will be discussed and illustrated using a simple example. Consider the two continuous-time signals,

$$x_1(t) = e^{-0.01 f_i(t) t} \cos\left(2\pi f_i(t) t\right) + x x e^{-0.02t} \cos\left(\frac{2\pi}{3} t\right)$$
$$x_2(t) = \frac{2}{5} e^{-0.01 f_i(t) t} \cos\left(2\pi f_i(t) t\right) + e^{-0.02t} \cos\left(\frac{2\pi}{3} t\right) \tag{4}$$

where $f_i(t)$ is the instantaneous frequency of a logarithmic chirp function given by $f_i(t) = f_0 \beta^t$ with $\beta = (f_1/f_0)^{1/T}$. The start frequency is $f_0 = \frac{5}{2\pi} \frac{\text{rad}}{\text{s}}$, and the end frequency is $f_1 = \frac{5.5}{2\pi} \frac{\text{rad}}{\text{s}}$. The signals are sampled at uniform increments of $\triangle t = 0.02$ seconds for a total time of $T = 75$ seconds to create the vectors X_1 and X_2. Although the two signals can be analytically differentiated, numerical differentiation is used to construct $\dot{X}_1$ and $\dot{X}_2$ to replicate an experimental situation when the governing equations are unknown. Furthermore, -70 dB of White Gaussian Noise (WGN) is injected into both X_1 and X_2 before numerical differentiation, ultimately introducing more noise into $\dot{X}_1$ and $\dot{X}_2$. Finally, a trajectory matrix, $Y = [X_1\ X_2\ \dot{X}_1\ \dot{X}_2]$, containing the sampled signals and their numerical derivatives is formed.

3.1 Obtaining Clean SCPs

Pre-processing raw time series data to remove undesirable signal artifacts is a fundamental step in feature extraction and estimation. A few common techniques currently deployed are moving average and low-pass filters [3, 4]. Fortunately, SCD considers both *temporal and spatial* characteristics of the signals, ultimately separating the narrow-band and smooth, energetic signals (e.g., vibration responses) from wide-band, low-energy signals (e.g., measurement noise) [9, 10]. To accomplish this, the experimental trajectories are first embedded into a larger dimensional phase space using delay coordinate embedding [11, 12]. Formally, for a trajectory matrix Y this embedding is

$$Y_d = \left[Y_n, Y_{n-\tau}, \ldots, Y_{n-(d-1)\tau}\right]^T \tag{5}$$

where d is the embedding dimension and τ is the delay time. The authors suggest using the first minimum of the average mutual information to estimate the delay time τ [13]. In this work, the embedding dimension is chosen to be at least twice the expected signal dimension.

3.2 Instantaneous Frequency

Estimating a time-varying signal's attributes (e.g., phase and frequency) can be done using either *local* or *global* approaches. The instantaneous frequency obtained from

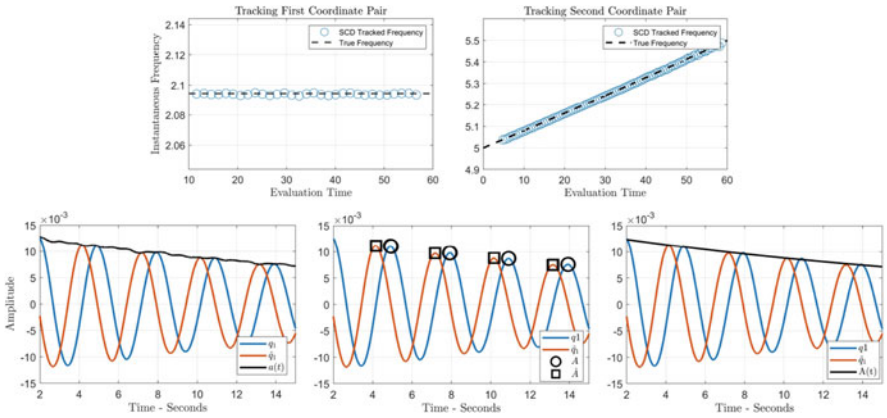

Fig. 1 Instantaneous frequency and amplitude tracking of each smooth coordinate pair (SCP). (Top Left) Tracking of the stationary harmonic term. (Top Right) Tracking of the non-stationary harmonic term. (Bottom left) Initial amplitude estimation from the magnitude of the components, q_1 within the smooth coordinate pair. (Bottom middle) Tangency points between the initial instantaneous amplitude estimation and the smooth coordinate pair components. (Bottom Right) Exponential function fitted to the tangency points

the HT uses the entire measured waveform and is thus a *global estimate* [14]. The detection of local properties such as extrema or zero-crossings is a *local estimate*. Local signal analysis can be highly sensitive to noise since it can hinder the estimation of local extrema in the signal. In the proposed algorithm, the trajectories are prefiltered using the delay-coordinate embedding procedure, and thus no low-pass or moving average filters are needed once the SCPs are obtained. A local estimation is used by finding the times in between the zero-crossing points, t_j^0, of each SCP. That is, $f_i(t_j^0) = \left(t_{j+1}^0 - t_{j-1}^0\right)^{-1}$, where $\left(t_j^0\right)$ is the estimated frequency in Hz for one complete period of oscillation. Applying the local estimation to the coordinate pairs $q_1(t), \hat{q}_1(t)$ and $q_2(t), \hat{q}_2(t)$ results in the two sequences $f_1\left(t_j^0\right)$ and $f_2\left(t_j^0\right)$. Figure 1 (Top) shows the two estimated instantaneous frequency sequences compared to the true signal frequencies.

3.3 Instantaneous Amplitude

The orthogonality of the smooth coordinates provides a convenient technique for estimating the instantaneous amplitude function. Consider a smooth coordinate pair $q_1, \hat{q}_1 \in \mathbb{R}^{m\times 1}$. One can then define,

$$a(t) = \sqrt{q_1(t)^2 + \hat{q}_1(t)^2} \tag{6}$$

where $a(t) \in \mathbb{R}^{m\times 1}$ is an initial estimate of the instantaneous amplitude function. The function $a(t)$ will be tangent to both $q_1(t)$ and $\hat{q}_1(t)$ near the local maxima (i.e., oscillation peaks) but will not intersect the signal. One can find these tangent points by finding the minima in the difference between $a(t)$ and the q_1, $\hat{q}_1$ pair within each evaluation window. A sequence of the tangent points is then constructed for both $q_1(t)$, $\hat{q}_1(t)$ through $A = |a(t) - q_1(t)|$ and $\hat{A} = |a(t) - \hat{q}_1(t)|$. It is assumed that the profile $A(t)$ will follow an exponential decay of the form $A(t) = ae^{-bt}$ for the slow-time coordinate pairs as the decay rates are assumed to have marginal amplitude dependence for a weakly nonlinear system. From this assumption, the exponential function, $A(t)$, is fit to the tangency points A and $\hat{A}$, which results in an analytical function, denoted as $A(t)$. This analytical amplitude function can be evaluated at the same evaluation times as the instantaneous frequency to construct the corresponding sequence $A(t_j^0)$. If needed, one can then use the smooth mode pair, Φ_i, in Eq. (1), to transform this evaluated amplitude function back into the physical coordinate space. That is, $A_c = \Phi_i A\left(t_j^0\right)$.

4 Mechanical Examples

In this section, we demonstrate the applicability of the proposed algorithm to identify the backbone curves for two numerical models and an experimental system. The first numerical model and physical experiment are single-degree-of-freedom systems, and thus no resonant decay procedures or mode separation is needed. However, as outlined in Sect. 3, there are advantages to the proposed algorithm for single-degree-of-freedom systems due to its simplicity and built-in noise reduction capabilities. The final example demonstrates the algorithm for obtaining multiple backbone curves of a multi-degree-of-freedom mechanical oscillator from a single decay response.

The mathematical models are numerically integrated using the RK45 method in MATLAB. The method of harmonic balance is used to construct the reference backbones and forced response curves using an ansatz solution containing seven harmonics. The purpose of these examples is to compare the numerical reference (i.e., harmonic balance) and experimental reference (i.e., stepped sine test) to those obtained empirically via the SCTA.

4.1 Numerical: Duffing Oscillator

In the first example, we explore the proposed algorithm to identify the backbone curve for the weakly nonlinear duffing equation. The governing differential equation is

$$\ddot{x} + \gamma\dot{x} + \omega_0^2 x + \beta x^3 = 0. \tag{7}$$

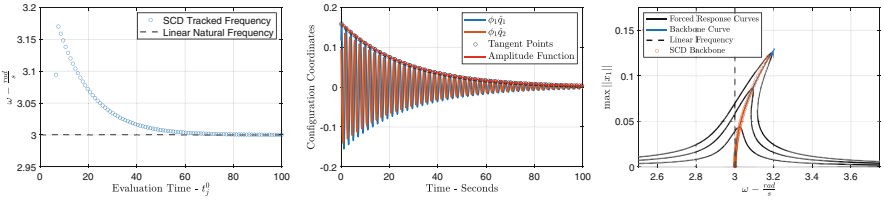

Fig. 2 Nonlinear backbone curve obtained via SCTA. (Left) Tracking of instantaneous frequency. (Middle) Construction of Instantaneous Amplitude Function. (Right) Estimated backbone compared with reference solutions

The parameters are set to $\gamma = 0.075,\ \omega_0 = 3, \beta = 100$, and the initial conditions are $[x(0), \dot{x}(0)]^T = [0.15,\ 0]^T$. The sampling frequency is set to $f_s = 100$ Hz for a total of $T = 100$ seconds. Although the velocity (i.e., $\dot{x}$) response is available, we numerically differentiate the position response to obtain an approximate velocity trajectory. The state-space trajectory matrix is then formed $Y = [X\ \dot{X}]$. The SCTA is applied directly to Y. The tracked hardening behavior in the natural frequency and corresponding amplitude are shown in the left and middle panels of Fig. 2, respectively. Pairing these two sequences together results in the reconstructed backbone curve shown in the right panel of Fig. 2.

4.2 Experiment: Large Pendulum Oscillations

A simple experimental study was performed to benchmark the proposed algorithm on real-world data. The schematic of the experimental setup shown in Fig. 3 (bottom middle) shows a simple pendulum that exhibits large amplitude oscillations. An incremental rotary encoder (CALT GHS38) serves as the pivot point and records the angular position of the pendulum with 0.1° resolution. The signals are decoded and converted to an analog output that was sampled at 1 kHz. The forced frequency response curve was constructed using a stepped-sine test at .005 Hz increments in both directions. Figure 3 (Bottom Right) shows the steady-state amplitudes at each forcing frequency. The hysteresis region is highlighted in gray bounded by the two jump frequencies occurring at roughly 7.5 $\frac{\text{rad}}{\text{s}}$ and 7.95 $\frac{\text{rad}}{\text{s}}$. The free decay response is obtained by rotating the pendulum roughly 80° and releasing it from rest. Similar to the Duffing oscillator example, the time series is numerically differentiated to obtain the state-space trajectory matrix $Y = [\theta\ \dot{\theta}]$. However, for this example, smooth coordinate filtering is performed to remove the measurement noise. Following Sect. 3.1, the trajectory matrix is first embedded into a six-dimensional phase-space, $Y_d \in \mathbb{R}^{m\times 6}$. Since only two state-variables are involved in the pendulum motion, one expects a two-dimensional signal subspace (i.e., a single smooth coordinate pair) and a four-dimensional noise subspace. The extracted smooth coordinate pair $q_1(t), \hat{q}_1(t)$ is shown on the top left panel in Fig. 3. The

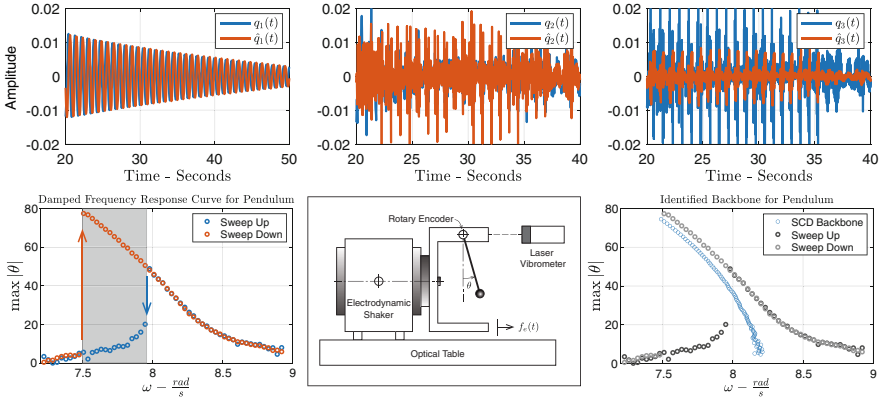

Fig. 3 (Top row) Separation of a SCPs and measurement noise from angular position time series. (Bottom middle) Experimental Schematic for large pendulum oscillations. (Bottom left) Steady-state amplitude for stepped-sine frequency sweeps. (Bottom right) Extracted SCD backbone curve

consequent middle and right panels correspond to mid-to-high-frequency noise that was removed from the signal via SCD.

4.3 Numerical: Mechanical Oscillator

Consider a two-degree-of-freedom mass damper spring system with a nonlinear cubic spring attached to the first mass and the fixed boundary. The system is governed by the system of differential equations

$$\begin{aligned} \ddot{x}_1 + 0.025\dot{x}_1 + 18x_1 - 9x_2 + k_{nl}x_1^3 &= 0 \\ \ddot{x}_2 + 0.025\dot{x}_2 + 18x_2 - 9x_1 &= 0 \end{aligned} \tag{8}$$

where system is sampled at $f_s = 100$ Hz.

The performance of the SCTA is evaluated for the following nonlinear spring constants, $k_{nl} = [0, \ 50, \ 100, \ 250]$. In this exploration, the initial conditions are a linear superposition of the two linear normal modes of the system: $x(0) = [0.06, \ 0, \ 0, \ 0]^T$. Top panels of Fig. 4 show the effect of nonlinear stiffness on the SCTA performance. We also explore the SCTA's performance for a variety of different initial conditions with the nonlinear spring constant set at $k_{nl} = 50$. We emphasize that there is no mode isolation excitation strategy, such as resonance decay methods [6], used here. Indeed, the initial conditions provided will in fact excite more than one mode in the response. Bottom panels of Fig. 4 show the identified frequency-amplitude behaviors for different combinations of the two linear normal modes.

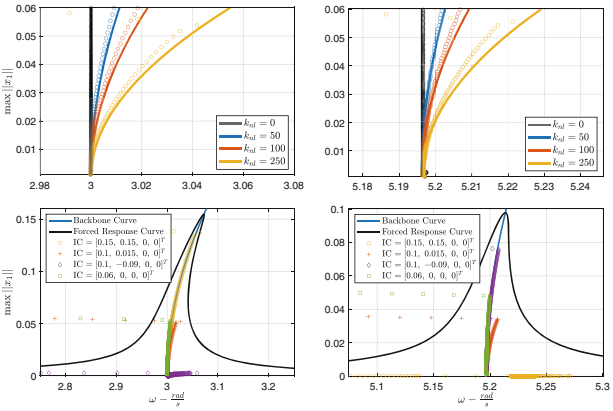

Fig. 4 (Top) Effect on nonlinear stiffness coefficient on the SCTA. (Bottom) Sensitivity of the SCTA for a variety of initial conditions

5 Discussion

The proposed SCTA effectively estimates backbone curves for single- and multi-degree-of-freedom (SDOF and MDOF) nonlinear mechanical systems under arbitrary decay conditions. With its applicability to weakly nonlinear MDOF systems, the method also benefits SDOF systems. As shown in Fig. 3, the algorithm allows separation of smooth deterministic signals from measurement noise, removes additional modes from contaminating single-mode decay response, and provides an initial estimate of the instantaneous envelope function.

The SCTA is well-suited for application in practical experimental settings as demonstrated in Sect. 4.2. The proposed algorithm would not only remove noise but also remove any extra modes from contaminating an assumed single-mode decay response. Due to their orthogonality, the SCPs provide a convenient first estimate of the instantaneous envelope function similar to the analytical signal representation used in the HT. In contrast with HT, Eq. (6) introduces zero ringing artifacts at the edges of the signal. However, both the HT and proposed SCTA are capable of making use of the tangent points, Fig. 1 (bottom middle), to fit a smooth envelope function as shown in Fig. 1 (bottom right). Aside from removing the troughs between adjacent peaks (see, e.g., Fig. 1), a significant advantage of fitting a function to the tangent points is that it allows a simple pairing between the amplitude and instantaneous frequency by evaluating the amplitude function at the corresponding instantaneous frequency.

The SCTA is suitable for initial inspection during nonlinear modal analysis tests, enabling practitioners to assess system nonlinearity before employing exhaustive experimental techniques.

The illustrative example used in Sect. 3 established the SCTA's capability in separating linear and nonlinear coordinate pairs. The continuous time signals

in Eq. (4) share similarities to a symmetrical two-degree-of-freedom mechanical oscillator, where one would have one linear normal mode with stationary oscillation frequency (see Fig. 1 (top left)), while the second mode contains frequency-amplitude dependence and exhibits non-stationary behavior (see Fig. 1 (Top Right)). Section 4.3 also demonstrated the capability of the algorithm to separate and track the instantaneous frequency of two nonlinear modal coordinate pairs. Figure 4 illustrates the algorithm's ability to track each backbone as the system transitions from linear to strongly nonlinear and identify the corresponding hardening behavior with moderate accuracy. Thus, the SCTA is suitable for initial inspection during nonlinear modal analysis tests, enabling practitioners to assess system nonlinearity before employing exhaustive experimental techniques.

However, the decomposition may fail to identify a mode's contribution if not excited adequately, preventing tracking of that mode's backbone as see in Fig. 4. The algorithm's success depends on sufficient modal participation for both modes. For arbitrary initial conditions, consistent trajectory paths to the origin are not guaranteed, suggesting the use of multiple trials of arbitrary free-decay data for validation.

6 Conclusion

The authors propose a *smooth coordinate tracking algorithm* (SCTA) for estimating frequency-amplitude dependence in nonlinear mechanical systems and time series. The multivariate signals are differentiated and embedded into an enlarged phase space using delay-coordinate embedding. Smooth coordinate decomposition is then used to separate the signals into approximate nonlinear modal coordinate pairs and filter out noise. These *smooth coordinate pairs* exhibit useful properties for estimating the instantaneous frequency and constructing an amplitude envelope of separated modal responses. Therefore, this algorithm provides noise reduction, modal coordinate separation, and instantaneous signal feature estimation in a single, physically interpretable process.

In summary, the SCTA is a valuable tool for estimating backbone curves and assessing nonlinearity in mechanical systems, particularly during initial inspection stages. It is essential to ensure sufficient input energy and appropriate initial conditions for accurate results, and using multiple trials can further validate the findings.

References

1. Worden, K.: Nonlinearity in Structural Dynamics: Detection, Identification and Modelling. CRC Press, Boca Raton (2019)

2. Cenedese, M., Haller, G.: How do conservative backbone curves perturb into forced responses? A Melnikov function analysis. Proc. Math. Phys. Eng. Sci. **476**(2234), 20190494 (2020)
3. Feldman, M.: Non-linear system vibration analysis using Hilbert transform—I. Free vibration analysis method 'Freevib'. Mech. Syst. Signal Process **8**(2), 119–127
4. Londono, J.M., Cooper, J.E., Neild, S.A.: Identification of systems containing nonlinear stiffnesses using backbone curves. Mech. Syst. Signal Process **84**, 116–135 (2017)
5. Peeters, M., Kerschen, G., Golinval, J.C.: Dynamic testing of nonlinear vibrating structures using nonlinear normal modes. J. Sound Vib. 330(3), 486–509 (2011)
6. Naylor, S., Platten, M.F., Wright, J.R., Cooper, J.E.: Identification of multi-degree of freedom systems with nonproportional damping using the resonant decay method. J. Vib. Acoust. **126**(2), 298–306 (2004)
7. Chelidze, D., Zhou, W.: Smooth orthogonal decomposition-based vibration mode identification. J. Sound Vib. **292**(3), 461–473 (2006)
8. Axås, J., Haller, G.: Model reduction for nonlinearizable dynamics via delay-embedded spectral submanifolds (2023). arXiv:2301.04560
9. Chelidze, D., Liu, M.: Reconstructing slow-time dynamics from fast-time measurements. Proc. Math. Phys. Eng. Sci. **366**(1866), 729–745 (2008)
10. Chelidze, D.: Smooth local subspace projection for nonlinear noise reduction. Chaos 013121 (2014)
11. Takens, F.: Detecting strange attractors in turbulence. In: Dynamical Systems and Turbulence, Warwick 1980: Proceedings of a Symposium Held at the University of Warwick 1979/1980, pp. 366–381. Springer, Berlin (2006)
12. Sauer, T., Yorke, J.A., Casdagli, M.: Embedol. J. Stat. Phys. **65**, 579–616 (1991)
13. Fraser, A.M., Swinney, H.L.: Independent coordinates for strange attractors from mutual information. Phys. Rev. A. **33**(2), 1134 (1986)
14. Feldman, M.: Hilbert Transform Applications in Mechanical Vibration. John Wiley & Sons, London (2011)

Optimizing Multilayer Perceptrons to Approximate Nonlinear Quaternion Functions

Arturo Buscarino, Luigi Fortuna, and Gabriele Puglisi

1 Introduction

In the last decades, the use of artificial neural networks has received a growing interest in a wide variety of scientific fields. Despite the fact that their theoretical foundations root in mathematical results of the last centuries [1], a recent revival for neural networks has been observed, with reference to the so-called deep neural networks [2]. Essentially, artificial neural networks are universal approximators of multivariable nonlinear functions and, thus, are effective in either modeling complex behavior for prediction or classifying complex patterns of data [3].

Among the possible configurations of neural networks, our interest in this contribution is focalized on multilayer perceptrons (MLPs) [1]. MLPs represent the most adopted and fascinating neural network structure as they embed many characteristics of their natural counterparts. MLPs are organized in hierarchically distributed layers of neurons with a dense network of interactions among layers, which constitute the basis of the knowledge. Interconnections, in fact, are opportunely weighted by coefficients that are obtained as the result of a learning phase, during which the network is trained with examples of inputs. The weights are, therefore, the results of a multivariable nonlinear optimization problem. If the network is provided also with the desired outputs, a supervised learning algorithm can be used, such as the backpropagation [1].

An extension, the real valued MLP are the so-called hypercomplex MLPs (HMLP), able to deal with quaternion algebra. Quaternions have been introduced in order to generalize complex number properties to a three-dimensional space and have been used in a wide variety of practical applications, including the

A. Buscarino (✉) · L. Fortuna · G. Puglisi
Universit degli studi di Catania, Catania, Italy
e-mail: arturo.buscarino@unict.it
https://www.dieei.unict.it/docenti/arturo.buscarino?eng

© The Author(s), under exclusive license to Springer Nature Switzerland AG 2024

W. Lacarbonara (ed.), *Advances in Nonlinear Dynamics, Volume III*, NODYCON Conference Proceedings Series, https://doi.org/10.1007/978-3-031-50635-2_41

reformulation of Maxwell equations, the analysis of stresses in three-dimensional objects, and in digital filter design. Moreover, applications can be found also in robotics, due to the possibility of representing rotations in the three-dimensional space with quaternions instead of matrices [4]. The idea of developing a MLP-ANN structure able to deal directly with quaternions to approach these problems more efficiently has been discussed in [5].

In this contribution, we aim at optimizing the MLP-ANN structure for quaternions in order to improve the approximation of complex valued nonlinear functions and the efficiency of the learning algorithm. To this latter aim, we will focus on a recent implementation based on parallel computing of generic MLP-ANNs [6]. The main idea is to exploit the parallel computing capabilities of modern microprocessors in embedded devices to instantiate a set of auxiliary networks devoted to the prediction of the learning algorithm output, thus sensibly reducing the time to get a robust and efficient learning error [7].

The work is organized as follows. In Sect. 2, mathematical preliminaries related to quaternion algebra are recalled, while the HMLP structure is outlined in Sect. 3. The auxiliary network paradigm to optimize the learning phase of HMLPs is described in Sect. 4, while the capabilities of HMLPs in modeling complex behavior is shown in Sect. 5. Conclusions are drawn in Sect. 6.

2 Quaternion Algebra

The fundamental operators defined in quaternion algebra are reported. A quaternion $\mathbf{q}$ is a generalized complex number composed of four real parameters (q_0, q_1, q_2, q_3) and of three imaginary units $(\mathbf{i}, \mathbf{j}, \mathbf{k})$, which represent the basis unit vectors of an orthogonal reference frame:

$$\mathbf{q} = q_0 + q_1\mathbf{i} + q_2\mathbf{j} + q_3\mathbf{k} \tag{1}$$

The role of the imaginary part in quaternion algebra is the same of unit $i = \sqrt{-1}$ in complex algebra.

A quaternion can be considered as the sum of a real number q and of a vector $\mathbf{q}$:

$$\mathbf{q} = q_0 + \mathbf{q} \tag{2}$$

In matrix form:

$$\mathbf{q} = [q_0, q_1, q_2, q_3]^T \tag{3}$$

The fundamental quaternion operators are:

– Conjugate

$$\mathbf{q}^* = q_0 - \mathbf{q} = q_0 - q_1\mathbf{i} - q_2\mathbf{j} - q_3\mathbf{k} \tag{4}$$

– Modulus

$$\left|\mathbf{q}^*\right| = q_0 - \mathbf{q} = q_0 - q_1\mathbf{i} - q_2\mathbf{j} - q_3\mathbf{k} \tag{5}$$

– Sum of quaternions

$$\mathbf{q} + \mathbf{p} = (q_0 + p_0) + (q_1 + p_1)\mathbf{i} + (q_2 + p_2)\mathbf{j} + (q_3 + p_3)\mathbf{k} \tag{6}$$

– Product of quaternions

$$\mathbf{q} \otimes \mathbf{p} = (q_0 + \mathbf{q}) \otimes (p_0 + \mathbf{p}) = q_0 p_0 - \mathbf{q} \cdot \mathbf{p} + q_0\mathbf{p} + p_0\mathbf{q} + \mathbf{q} \times \mathbf{p} \tag{7}$$

where "·" is the scalar product and "×" represents the vector product, as defined in vector algebra. The quaternion product is not commutative, but associative and distributive properties hold.

– inverse:

$$\mathbf{q}^{-1} = \frac{\mathbf{q}^*}{\mathbf{q}^* \otimes \mathbf{q}} \tag{8}$$

3 Hypercomplex Multilayer Perceptrons

A hypercomplex multilayer perceptron (HMLP) is a multilayer perceptron (MLP) in which input, output, weights, and biases are quaternions. Also the activation function in the neurons of the hidden layer is quaternion-valued sigmoidal functions. A HMLP with one hidden layer is considered a universal interpolator in quaternion algebra (H), and then, in the following, we will consider this kind of structure only [5].

Let n_o, n_h, n_i be the number of output, hidden, and input units, respectively. We will denote with:

– The superscript O, the quantities relative to the output layer
– The superscript H, the quantities relative to the hidden layer
– The superscript I, the quantities relative to the input layer

The weights and the biases are now defined:

– $\mathbf{W}_{nm}^{HO}$ is the weight connecting the mth hidden neuron to the nth output neuron:

$$\mathbf{W}_{nm}^{HO} = \mathbf{w}_{0nm}^{HO} + \mathbf{i}\mathbf{w}_{1nm}^{HO} + \mathbf{j}\mathbf{w}_{2nm}^{HO} + \mathbf{k}\mathbf{w}_{3nm}^{HO} \tag{9}$$

– $\mathbf{W}_{nm}^{IH}$ is the weight connecting the mth input neuron to the nth hidden neuron:

$$\mathbf{W}_{nm}^{IH} = \mathbf{w}_{0nm}^{IH} + \mathbf{i}\mathbf{w}_{1nm}^{IH} + \mathbf{j}\mathbf{w}_{2nm}^{IH} + \mathbf{k}\mathbf{w}_{3nm}^{IH} \tag{10}$$

– Θ_n^H is the nth hidden neuron bias:

$$\boldsymbol{\Theta}_n^H = \theta_{0n}^H + \mathbf{i}\theta_{1n}^H + \mathbf{j}\theta_{2n}^H + \mathbf{k}\theta_{3n}^H \tag{11}$$

The chosen activation function is the quaternion-valued sigmoidal function:

$$\mathbf{X}_n = \boldsymbol{\sigma}(\mathbf{S}_n) = \boldsymbol{\sigma}(S_{0n}) + \mathbf{i}\sigma(S_{1n}) + \mathbf{j}\sigma(S_{2n}) + \mathbf{k}\sigma(S_{3n}) \tag{12}$$

where:

$$\sigma(x) = \frac{1}{1+e^{-x}} \tag{13}$$

that is the usual sigmoidal real valued activation function. The activation function derivative is:

$$\dot{\boldsymbol{\sigma}}(\cdot) = \dot{\sigma}(\cdot) + \mathbf{i}\dot{\sigma}(\cdot) + \mathbf{j}\dot{\sigma}(\cdot) + \mathbf{k}\dot{\sigma}(\cdot) \tag{14}$$

where:

$$\dot{\sigma}(\cdot) = \sigma(\cdot)[1 - \sigma(\cdot)] \tag{15}$$

3.1 Feedforward Propagation

The feed-forward phase is shown in the following:

– The hidden unit activation value is computed in the following way:

$$\mathbf{S}_n^H = \sum_{m=1}^{n_i} (\mathbf{W}_{nm}^{IH} \otimes \mathbf{I}_m) + \boldsymbol{\Theta}_n^H \tag{16}$$

– The hidden unit output value will be:

$$\mathbf{X}_n^H = \boldsymbol{\sigma}(\mathbf{S}_n^H) = \boldsymbol{\sigma}(S_{0n}^H) + \mathbf{i}\sigma(S_{1n}^H) + \mathbf{j}\sigma(S_{2n}^H) + \mathbf{k}\sigma(S_{3n}^H) \tag{17}$$

– The output unit activation value is computed in the following way:

$$\mathbf{S}_n^O = \sum_{m=1}^{n_h} (\mathbf{W}_{nm}^{HO} \otimes \mathbf{X}_m^H) + \boldsymbol{\Theta}_n^O \tag{18}$$

– The nth output unit value will be:

$$\mathbf{Y}_n = \mathbf{X}_n^O = \boldsymbol{\sigma}(\mathbf{S}_n^O) = \boldsymbol{\sigma}(S_{0n}^O) + \mathbf{i}\sigma(S_{1n}^O) + \mathbf{j}\sigma(S_{2n}^O) + \mathbf{k}\sigma(S_{3n}^O) \tag{19}$$

3.2 Network Error Computation

The error function between the actual output of the network:

$$\mathbf{Y}_n = Y_{0n} + \mathbf{i}Y_{1n} + \mathbf{j}Y_{2n} + \mathbf{k}Y_{3n} \tag{20}$$

and the desired nth target:

$$\mathbf{t}_n = t_{0n} + \mathbf{i}t_{1n} + \mathbf{j}t_{2n} + \mathbf{k}t_{3n} \tag{21}$$

is defined as:

$$E = \frac{1}{2}\sum_{n=1}^{n_0}[(t_{0n} - Y_{0n})^2 + (t_{1n} - Y_{1n})^2 + (t_{2n} - Y_{2n})^2 + (t_{3n} - Y_{3n})^2] \tag{22}$$

3.3 Backpropagation and Corrections

The backpropagation algorithm for HMLPs is dual to the one adopted for classic MLPs.

First of all the output error is calculated:

$$\mathbf{e}_n^O = t_n - \mathbf{X}_n^O \tag{23}$$

where t_n is the target relative to the n pattern.

Then the propagation of the error from output layer to hidden one δ_h^{OH} is computed:

$$\delta_h^{OH} = e_{0n}^{OH}\dot{\sigma}(S_{0n}^O) + \mathbf{i}e_{1n}^{OH}\dot{\sigma}(S_{1n}^O) + \mathbf{j}e_{2n}^{OH}\dot{\sigma}(S_{2n}^O) + \mathbf{k}e_{3n}^{OH}\dot{\sigma}(S_{3n}^O) \tag{24}$$

where $h = 0, \ldots, N_O$ is the number of the neuron considered in the output layer.

The correction of the weights and biases of the hidden layer neurons is computed with the following formula:

$$\Delta\mathbf{W}_{hn}^{HO} = \eta\delta_n^H \otimes (\mathbf{X}_h^H)^* \tag{25}$$

$$\Delta\boldsymbol{\Theta}_n^H = \epsilon\delta_n^H \tag{26}$$

We get the error relative to the hidden layer from:

$$\mathbf{e}_n^H = \sum_{h=1}^{N_O}(\mathbf{W}_{hn}^{HO})^* \otimes \delta_h^{OH} \tag{27}$$

and then we can compute δ_h^{HI} as done in the hidden layer case:

$$\delta_h^{HI} = e_{0n}^{OH}\dot{\sigma}(S_{0n}^H) + \mathbf{i}e_{1n}^{OH}\dot{\sigma}(S_{1n}^H) + \mathbf{j}e_{2n}^{OH}\dot{\sigma}(S_{2n}^H) + \mathbf{k}e_{3n}^{OH}\dot{\sigma}(S_{3n}^H) \tag{28}$$

4 HMLP with Learning-on-Learning Optimization Algorithm

Since training is a time-consuming phase in neural networks, having an optimal predictive performance for the network in short times is one of the main goals of the research in this field [6].

It has been developed a strategy improving the convergence time based on the parallelization of the learning phase improving the convergence time. It is based on using the auxiliary networks to predict the trend of weights during the learning phase, with the aim of reducing the number of needed epochs [6].

It is possible to make faster the learning phase by increasing the learning rate η, but this approach could cause oscillation of the error gradient. To avoid this drawback, it is possible to adopt the following equation:

$$\Delta_p \mathbf{W}_{ij}(k) = \eta \boldsymbol{\delta}_{pj}(k)\mathbf{o}_{pi}(k) + \alpha \Delta_p \mathbf{W}_{ij}(k-1) \tag{29}$$

where constant α is called momentum, and it determines the effects of past changes in the weights on the current change.

From these considerations, we can build a dynamical system of the network weights evolution:

$$\mathbf{W}_{ij}(k) = \mathbf{W}_{ij}(k-1) + \Delta_p \mathbf{W}_{ij}(k) + \alpha \Delta_p \mathbf{W}_{ij}(k-1) \tag{30}$$

Neural network are optimal interpolator for discrete-time nonlinear system, and then we can exploit this features in order to predict the weight values at a given iteration, so that by predicting the optimal values of the weights, we will achieve a faster training phase.

The proposed idea is to use the capability of the actual multi-core processors in order to run other auxiliary neural networks able to find the almost optimal value of the weights.

The values of a given weight will be considered as time series:

$$\{\mathbf{W}_{ij}(k)\} \text{ with } k_{min} < k < k_{max} \tag{31}$$

The aim of the auxiliary networks is to estimate the value of the weight at a given discrete time k^*:

$$\{\mathbf{W}_{ij}(k)\} \text{ with } k_{min} < k^* < k_{max} \tag{32}$$

The auxiliary networks could be both HLMP with one input neuron and one output neuron, or MLP with one inputs and outputs neurons, since inputs are discrete time samples and outputs will be the 4 coefficients of the quaternionic weight. In order to have a greater speed in learning phase than the main network, it is necessary that they are very light in terms of neurons in the hidden layer. This consideration means that, when complex neural networks are considered, using several auxiliary networks instead of a single one is better.

When the learning of the main network overcomes the initial phase, the weights of the original network change very slowly in time; moreover, some weights change less than others. It follows that when

$$\eta \boldsymbol{\delta}_{pj}(k)\mathbf{o}_{pi}(k) + \alpha \Delta_p \mathbf{W}_{ij}(k-1) < \epsilon \tag{33}$$

where ϵ is a fixed real positive value, it can be assumed that the corresponding weight has reached the optimal value and no further correction is needed.

When the supervisor has discarded the weights satisfying condition (31), the patterns and targets necessary to train auxiliary networks are ready. These networks will immediately begin the learning phase on the available patterns and backpropagation is executed. Once that the weights are predicted, they are sent to the main network, substituted into the actual weight matrix, and finally the error provided them is computed. The new weight matrix is accepted only if the following condition is satisfied:

$$E(\mathbf{W}_{pred}) < E(\mathbf{W}_{prec}) \tag{34}$$

where $E(\mathbf{W}_{pred})$ represents the error associated with the predicted weight matrix and $E(\mathbf{W}_{prec})$ is the error associated with the weight matrix before the substitution.

It has been observed that when the estimated weights are sent to the main network, the error, in some cases, can assume large values, so that it is necessary to perform a certain number n of learning epochs, after which the error value reaches the expected value.

5 Numerical Results

In order to prove the greater performance of quaternion-valued HLMPs as respect to the MLPs in terms of output error and speed in convergence, we have performed different tests on the hyperchaotic Lorenz system:

$$\begin{cases} \dot{x} = \sigma(y - x) \\ \dot{y} = x(\rho - z) - \gamma y + w \\ \dot{z} = xy - \beta z \\ \dot{w} = -ky - rw \end{cases} \tag{35}$$

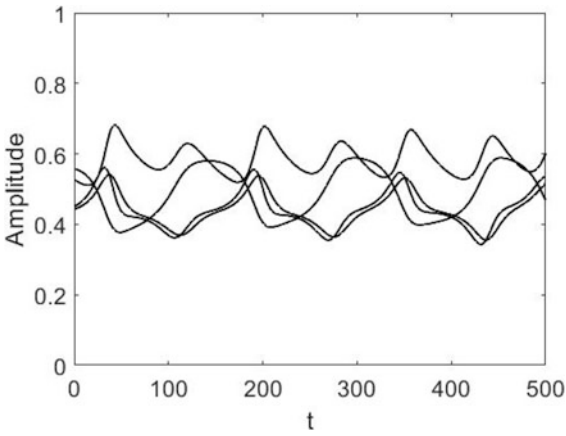

Fig. 1 The 4 signals of the hyperchaotic Lorenz system

with $\sigma = 12$, $\rho = 23$, $\gamma = 1$, $\beta = 2.1$, $k = 6$, $r = 0.2$, and initial conditions [0.1 10 $-$ 30 1]. In Fig. 1. the four signals are reported.

The complete Lorenz signals were previously normalized between [0.10.9] in order to fit the input requirements of the neural networks.

The networks were compared by performing a n-step prevision on the four hyperchaotic state variable signals, with $n = 1, 2, \ldots, 10$. This means that given the sample at the discrete time instant k, the two ANNs had to output the sample at the time $k + n$. Training and testing of the networks was performed by using as input the samples in the time window [501 1000] and consequently the samples in the time window [$501 + n$ $1000 + n$] as target in order to avoid the transitory part of the signal.

The training parameters of the networks were:

– 1-3-1 architecture for the HMPL, 4-12-4 for the MLP
– Learning rate 0.05 for the HMLP, while learning rate 0.1 for the MLP
– Momentum 0.1 for the HMLP, while momentum 0.9 for the MLP

With these results, we want to stress the capability of a HMLP to reach the same performance of an MLP in a lower number of epoch due to the simpler architecture of the quaternion-valued network and, consequently, to the reduced computational complexity. Both the networks exploit the learning-on-learning acceleration in order to make faster the learning process.

The graph in Fig. 2 shows the value of the ratio σ between the two nets employed epochs for each n-step prediction (as the value of n is reported in the x-axis). So that the 1.0 value means that the number of employed epoch in each one of the two different networks is the same. If the value $\sigma < 1.0$, it means that the proposed approach was faster than the traditional one and vice versa. The following equation formally explains what we said:

$$\sigma = \frac{n_{new}}{n_{old}} \tag{36}$$

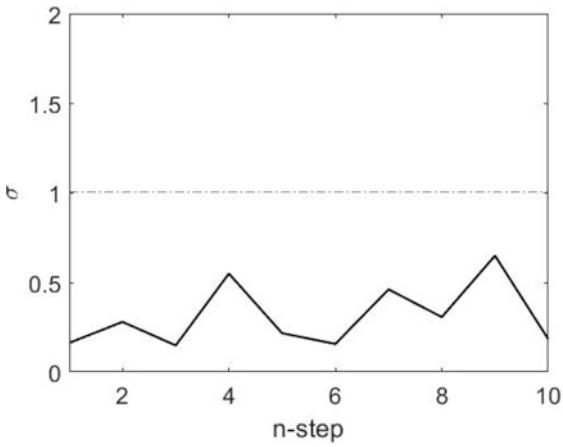

Fig. 2 Ratio between the employed epoch of the two networks for each n-step prediction

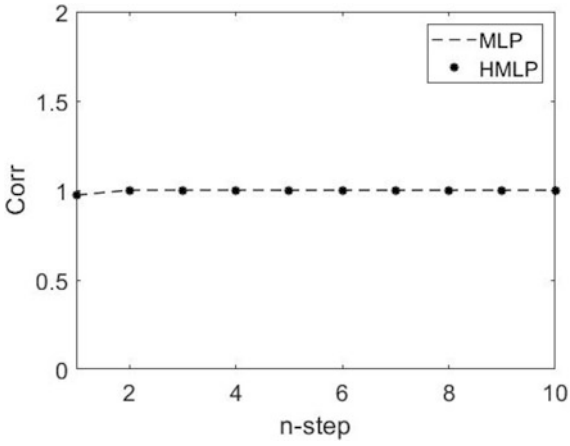

Fig. 3 Maximum values of the correlation for each n-step prediction

where n_{new} represents the number of epochs employed by the proposed neural network and n_{old} represents the number of epochs employed by the traditional backpropagation algorithm.

In order to prove also the performance equivalence, the maximum correlation values between the original signals and the output signals of the two proposed multilayer perceptrons have been computed for each n-step prediction and reported in the graph in Fig. 3.

The graph in Fig. 2 shows that the $sigma$ values represented by the curve are all less than 1.0. As a result, the HMLP under consideration achieves nearly the same performance as the MLP to which it has been compared by requiring fewer epochs in each of the cases (n-step) under consideration, although there is a difference in the number of hidden neurons between the two networks (3 for HMLP, 12 for MLP). As we can observe from the value of the maximum correlations (Fig. 3), the results are almost the same.

Another important aspect to stress is the difference between the respective learning rates (0.05 for HMLP, 0.1 for MLP) and momentums (0.1 for HMLP, 0.9 MLP), since it demonstrates how the HMLP is faster in gradient convergence than MLP. Indeed, after several tests, it was noted that with a greater η, the HMLP go into overlearning, and it was not able to overcome a certain minimum performance index.

6 Conclusions

The use of quaternion representations of complex phenomena is recently gaining a renewed interest. Hypercomplex neural networks provide surprising results for reducing the overall number of model parameters and the consequent energy consumption. However, in order to develop models that could be deployed on machines, the novel and efficient implementation outlined in this chapter can play a key role.

The possibility of exploiting the intrinsic parallel computing capabilities of modern microprocessors thus represents a fundamental advantage. The fast HMLS solution proposed in this paper is prone to the implementation on embedded devices, thus providing the basis for developing real-time identification toolboxes for nonlinear dynamics.

References

1. Haykin, S.: Neural Networks and Learning Machines, 3/E. Pearson Education India (2009)
2. LeCun, Y., Bengio, Y., Hinton, G.: Deep learning. Nature **521**(7553), 436–444 (2015)
3. Arena, P., Fortuna, L., Gallo, A., Graziani, S., Muscato, G.: Induction motor modelling using multi-layer perceptrons. IEICE Trans. Fund. Electron. Commun. Comput. Sci. **76**(5), 761–771 (1993)
4. Arena, P., Fortuna, L., Muscato, G., Xibilia, M.G.: Neural networks in multidimensional domains. Fundamentals and New Trends in Modelling and Control. Springer, Berlin (1998)
5. Arena, P., Fortuna, L., Muscato, G., Xibilia, M.G.: Multilayer perceptions to approximate functions quaternion valued. Neural Netw. **10**(2), 335–342 (1997)
6. Fortuna, L., Graziani, S., Lo Presti, M., Muscato, G.: Improving back-propagation learning using auxiliary neural networks. Int. J. Control **55**(4), 793–807 (1992)
7. Bucolo, M., Buscarino, A., Fortuna, L., Puglisi, G.: Learning-on-learning approach for modeling. In: 48th Annual Conference of the IEEE Industrial Electronics Society, IECON 2022 (2022)

Experimental Characterization and Phenomenological Modeling of Wire Rope Isolators

Paolo Neri and Jeremiah Holzbauer

1 Introduction

Many technological applications require the use of compliant devices to attenuate vibrations. In this field, wire rope isolators (WRI) are commonly adopted to reduce vibrations [1, 2]. These components are based on winded metal wires, whose friction can produce dissipation during deformation. For this reason, the component itself can produce a significant damping level, allowing for the design of compact suspension systems since additional dampers are not needed. Nevertheless, friction causes a non-linear behavior of the spring making the simple linear lumped spring-damper model unreliable. Manufacturers provide datasheets of the WRIs, but they focus on the quasi-static behavior only, generally providing two different equivalent stiffness values which represent static and dynamic regimes. These parameters, which can reasonably predict the deformation of the WRI under static loading, are not rigorously defined, do not precisely predict the component dynamic response, and their direct use in simulations is cumbersome and not accurate since they do not actually represent the physical phenomenon.

To overcome these limitations, more complex models are needed. Different modelling techniques are available in literature. A geometrical approach was studied in [1, 3, 4], analyzing the influence of dimensional parameters (e.g., rope diameter) on the hysteresis behavior along different directions. A different approach is presented in [5], where the force exerted by the WRI is modelled using two components: the elastic force due to the bending of the metallic wires summed with the damping

P. Neri (✉)
University of Pisa, DICI, Pisa, Italy
e-mail: paolo.neri@unipi.it

J. Holzbauer
Fermi National Accelerator Laboratory, Batavia, IL, USA

© The Author(s), under exclusive license to Springer Nature Switzerland AG 2024

W. Lacarbonara (ed.), *Advances in Nonlinear Dynamics, Volume III*, NODYCON Conference Proceedings Series, https://doi.org/10.1007/978-3-031-50635-2_42

force caused by strands friction (which depends on the deflection amplitude). On the other hand, other numerical methods can be found: a model based on the definition of four curves describing a hysteresis loop was proposed in [6], hybrid evolutionary algorithms were used in [7], and a neural network was developed in [8]. Nevertheless, the most widespread technique to model WRIs is based on the application of the so-called Bouc-Wen model, which represents the most general description of a hysteretic system [9–14]. The application of this model is well documented in literature. For example, this model was used to study asymmetric Stockbridge dampers in [15] or to investigate the general behavior of WRIs in [16–18]. Given the widespread diffusion of this model, the development of identification procedures able to relate the Bouc-Wen model parameters to the experimental data of a specific WRI is crucial. To this extent, the use of periodic vibration tests was proposed in [19–21]. In any case, the execution of dynamic testing can be cumbersome and is not trivial. Additionally, further research demonstrated that the WRI performance is not influenced by the loading frequency [22].

Thus, the estimation of the model parameters needed to represent the actual studied WRI is still a challenge. In this chapter, a systematic and simple experimental procedure is proposed to measure the data needed for the model identification. Additionally, the conventional Bouc-Wen model is further developed to emphasize the asymmetry of the hysteresis cycle between the compressive and tensile regions. Finally, an optimization procedure is discussed to retrieve the values of the model parameters and to represent a specific WRI. The proposed approach is then validated by comparing experimental and numerical results.

2 Experimental Characterization

2.1 Test Setup

This chapter is focused on the characterization of a specific WRI, i.e., H320-523-235-270 by Vibrostop, which will be used for the transportation of the 650 MHz cryomodules for the PIP-II Project at Fermilab [23]. The isolator was chosen to bear high loads in the range of 20 kN along each direction. The testing campaign on the WRI was performed by exploiting two different test benches: a conventional tensile testing machine (SCHENCK, 250 kN) and a hydraulic piston (MTS, 60 kN) on a customizable test bench. The former was used to test the spring axial direction and the latter to test the shear directions (i.e., longitudinal and transversal), which requires a more complex clamping setup. Figure 1 shows the WRI during test: Fig. 1a shows the axial direction testing, Fig. 1b shows the longitudinal direction testing, and Fig. 1c shows the transversal direction testing.

As can be seen, it was possible to clamp the WRI to the machine fixtures only during the axial direction tests. On the other hand, the two shear directions needed custom tooling and support brackets to hold the WRI in place, which also limited

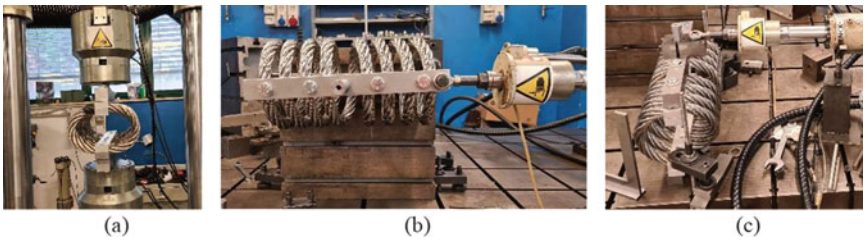

Fig. 1 WRI under testing along: (**a**) axial, (**b**) longitudinal, and (**c**) transversal directions

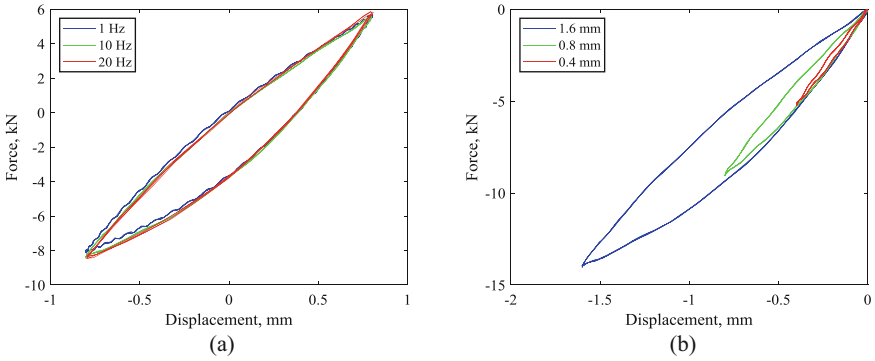

Fig. 2 Force-displacement curves in the case of sinusoidal loading: (**a**) fixed amplitude of 1.6 mm, variable frequency and (**b**) fixed frequency of 10 Hz, variable amplitude

the available measurement range. Additionally, it is worth noting that this family of isolators does not have a high geometrical precision since the support flanges are not parallel in any direction. Hence, it is not possible to strictly align the load direction along the defined WRI geometrical directions.

2.2 Testing Parameters' Influence

The first stage of the experimental characterization consisted in investigating the relevance of some testing parameters for the WRI behavior. In particular, the loading frequency and the loading amplitude were separately considered. This investigation was performed along all the three directions with similar outcomes, and the results obtained along the axial direction will be shown for brevity. A sinusoidal test was performed on the WRI by imposing a given amplitude of 1.6 mm peak-to-peak with three different frequencies: 1 Hz, 10 Hz, and 20 Hz. The results were analyzed in a force-displacement plot to assess if any difference would arise corresponding to different frequencies. As shown in Fig. 2a, the obtained cycles are perfectly overlapped despite the different excitation frequencies, thus demonstrating that the

WRI response, for a given amplitude, does not depend on the load frequency. This result confirmed that the WRI has a rate-independent behavior, which is in agreement with other research in the literature [6, 22].

Provided that the load frequency does not influence the WRI behavior, a test at a fixed frequency of 10 Hz was performed by gradually decreasing the load amplitude in the range 1.6 mm, 0.8 mm, and 0.4 mm (peak-to-peak). The results are shown in Fig. 2b. As can be noted, the compression arms of the curves are perfectly overlapped, meaning that the load amplitude itself does not change the WRI behavior. Indeed, if the ratio between the force variation and the amplitude variation is computed (i.e., equivalent stiffness of the linear spring model, or apparent stiffness), differences in the slope could be noted. Nevertheless, if a model is available which describes the non-linear curve, the same values of the parameters could be used to fit all the curve in Fig. 2b. In other words, even if the apparent stiffness of the linear model depends on the load amplitude, the actual values of an accurate non-linear model parameters should not depend on this variable. This confirms again the rate-independent behavior of the WRI.

This preliminary analysis allowed to simplify the testing condition which will be adopted to gain data for the model parameter optimization. Since neither the load frequency nor the load amplitude seems to affect the WRI behavior, in principle it is possible to perform quasi-static testing at any amplitude to fully characterize the WRI and to fit the underlying phenomenological model.

3 Phenomenological Model

The Bouc-Wen phenomenological model has already proven its potentiality in reproducing the physical behavior of WRIs. The model considers as input the displacement (x) and the speed ($\dot{x}$), and as output the produced force (F). The spring force is composed by three different contributions, as shown in Eq. 1:

$$F = F_2 \left(z + F_1\right) \tag{1}$$

The variable F_2 represents an exponential function in the form $F_2 = b^{cx}$. In this paper, the parameter b was set equal to the Euler number, thus $b = e$. On the other hand, the variable F_1 is a polynomial function of x in the form:

$$F_1 = k_1 x + k_2 \,\mathrm{sign}(x) x^2 + k_3 x^3 \tag{2}$$

Finally, the variable z represents the so-called hysteretic variable since it allows to replicate the amplitude of the hysteresis cycles. This variable can be computed by solving the differential equation:

$$\dot{z} = \dot{x} \left(\alpha - \left(\gamma + \beta \,\mathrm{sign}\left(\dot{x}\right) \mathrm{sign}(z)\right) |z|^n\right) \tag{3}$$

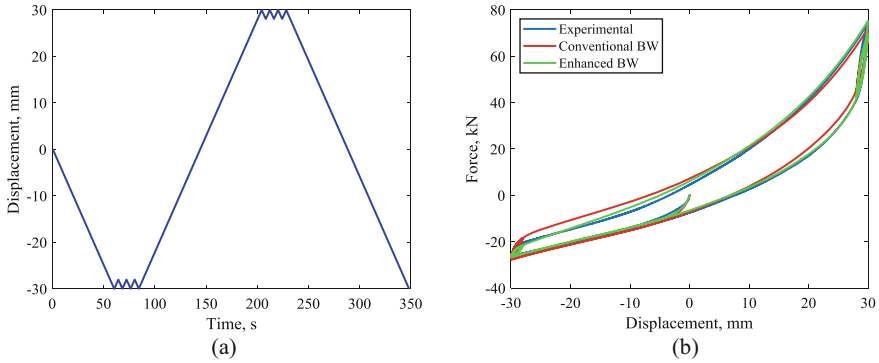

Fig. 3 Experimental test defined to characterize the WRI axial direction: (**a**) displacement profile and (**b**) force-displacement plot

The values of the different parameters in Eq. 3 can determine the shape of the hysteresis loop. In this chapter, Eq. 3 is numerically solved in Matlab environment through a numerical solver based on an explicit Runge-Kutta formula (*ode45* function) [24, 25]. The presented model is based on eight different parameters (since $b = e$ was chosen), which need to be determined for each specific WRI.

3.1 Improved Phenomenological Model

The conventional Bouc-Wen model was implemented and tested on the studied WRI by means of a comparison between numerical and experimental data. The results, which are reported in the following sections (red curve in Fig. 3b), confirmed the applicability of the model to the studied phenomenon. It is worth noting that the spring behavior is asymmetric in the compression and tensile region, especially along the axial direction. Indeed, along this direction the deformed shape is not symmetric with respect to the displacement sign. The conventional Bouc-Wen model can account for this asymmetry through the F_2 variable, which modulates the total force value differently when the displacement is positive or negative. Nevertheless, this variable does not directly influence the width of the hysteresis cycle, which indeed appeared to be different in the tensile and compression regions. Since the hysteresis loop in the model is defined by the hysteretic variable z and its width is dominated by the parameter α, a modification of the conventional model is proposed as reported in Eq. 4:

$$\dot{z} = \dot{x}\ \left((\alpha + \delta x) - (\gamma + \beta\,\mathrm{sign}\,(\dot{x})\,\mathrm{sign}(z))\,|z|^n\right) \tag{4}$$

The parameter δ allows to further emphasize the asymmetry in the width of the hysteresis cycle: positive values of δ determine wider cycles in the positive x region, and vice versa.

It is worth noting that the conventional Bouc-Wen model can be interpreted as a specific case of the proposed improved model where $\delta = 0$ is set. Thus, the proposed enhanced model represents a generalization of the conventional Bouc-Wen model. The performances of this improved model were compared with the conventional model in the following sections.

4 Parameters' Optimization

The application of the described models relies on the definition of the model parameters, which cannot be directly retrieved by the WRI geometrical characteristics, but needs to be determined with specific experimental testing. Thus, an optimization step is needed to determine the parameters set, which enhances the fitting between experimental and numerical data. In this paper, a non-linear least-square fitting procedure was adopted based on the Levenberg-Marquardt [26, 27] method (*lsqnonlin* function). The algorithm optimizes the parameters value in order to minimize the difference between the experimentally measured and the numerically computed force values.

As demonstrated in Sect. 2.2, neither the load amplitude nor the frequency has a direct influence on the parameter values, thus a simple quasi-static test can be used to feed the optimization. Figure 3 shows the experimental test which was defined to characterize the WRI behavior along the axial direction (similar loops, but with different amplitudes, were defined along the other two directions). Figure 3a shows the imposed displacement profile over time, while Fig. 3b shows the corresponding force-displacement diagram.

The maximum displacement amplitude was selected to be reasonably higher with respect to the expected static deflection due to the weight that the WRI will hold during operation. As can be noted, the force-displacement curve has a discontinuity every time that the sign of the speed is reverted. In order to enhance the effectiveness of the optimized parameters in describing these discontinuities, three motion reversals were performed in proximity of the maximum displacements, both in the tensile and in the compression regions. The optimization process was repeated, with the same experimental data, for both the conventional Bouc-Wen model and the enhanced Bouc-Wen model to obtain two sets of optimized parameters, as shown in Table 1.

The two parameter sets were then used to simulate the characterization test, and the results are shown in Fig. 3b. The blue line represents the experimental data, the red line represents the performance of the conventional Bouc-Wen model, while the green line represents the performance of the enhanced Bouc-Wen model. As can be noted, the overall matching between the blue and the red line is acceptable, meaning that the Bouc-Wen model is suitable to represent the studied

Table 1 Parameter sets for the conventional and the improved Bouc-Wen models

Parameter	Conventional BW	Enhanced BW
α	8.0	7.3
β	2.2	2.3
γ	1e-4	1e-4
n	0.64	0.63
δ	N.A.	9.8e-2
c	1.6e-2	1.45e-2
k_1	1.11	1.13
k_2	−1.1e-2	−8.7e-3
k_3	5e-4	5e-4

phenomenon. Nevertheless, the conventional formulation is not able to precisely catch the different width that can be noted in the hysteresis cycles corresponding to tensile and compressive loading. On the other hand, the green curve reflects the cycle asymmetry, providing much better matching results. The better performance of the enhanced Bouc-Wen model with respect to conventional model can be quantitatively assessed by computing the sum of the square differences between the experimental force and the results obtained with the two models, which provides the model error. This computation results in 179.1 N for the conventional model and 93.5 N for the enhanced model, meaning that the overall error of the enhanced model is almost half the error of the conventional model. Thus, only the parameters set corresponding to the enhanced model will be investigated in the rest of the chapter.

5 Model Validation

The results shown in Fig. 3b demonstrate that, after optimization, the developed model is able to reproduce the WRI non-linear behavior. Nevertheless, the comparison was performed on the same data which were used to run the optimization; thus, it cannot be considered as an external validation. In order to obtain a reliable validation of the proposed model and of the optimized parameters, two different independent tests were performed: a purely sinusoidal test at a frequency of 10 Hz and a random test with a white noise in the range 1–30 Hz. While the first test provides a clear view of the hysteresis cycles of the WRI, the second test is closer to the actual operational conditions of the WRI. Indeed, during transportation, the component is generally subject to random excitation spectra caused by road asperities, engine stroke, and other aleatory sources. A frequency limit of 30 Hz was considered because higher frequency components are generally drastically attenuated by other suspension stages, such as the track suspension system in the case of road transportation [2].

Figure 4 shows the results corresponding to the following testing condition: 10 Hz sinusoidal loading, 9 kN compression preload, peak-to-peak amplitude of 0.8 mm. The blue curve represents experimental data, while the green curve represents numerical data. As can be noted, the closed-loop testing machine requires

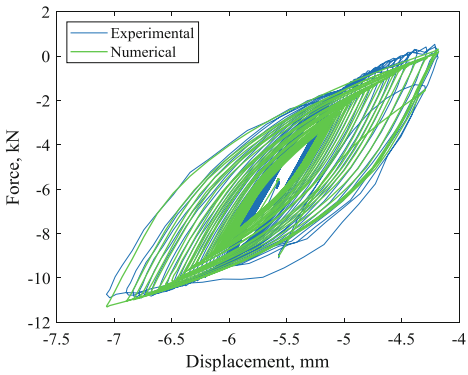

Fig. 4 Sinusoidal test: compression preload of 9 kN, amplitude 0.8 mm, frequency 10 Hz

some transient cycles to reach stationary regime conditions, and some overshoot is experienced. Nevertheless, the developed model allows to catch both the transient and the stationary regions of the test. It is worth noting that, when approaching the stationary region, the slope of the numerical curve is found to be slightly lower with respect to the experimental curve. Additionally, the model provides an accurate description of the hysteresis loop, thus guaranteeing a good estimation of the damping level.

Finally, the random test was performed under the following testing conditions: 9 kN compression preload, maximum peak-to-peak amplitude of 1.5 mm, 0.5–30 Hz white noise. Since the force-displacement curve is hardly readable for random test, the comparison between experimental and numerical results was performed on the force values over time. Figure 5 shows the obtained results: the blue curve represents experimental data, while the green curve represents numerical data. In Fig. 5a the comparison is shown in the time domain, proving that the model is able to capture the abrupt changes in force sign and the overall behavior of the spring. The Fast Fourier Transform of the data is shown in Fig. 5b and compares the results in the frequency domain.

The plot highlights that the whole investigated frequency range is properly represented by the proposed model in terms of frequency contributions. The numerical results slightly underestimate the experimental force amplitudes. Nevertheless, since the model is developed to estimate the WRI filtering capabilities, the discrepancy was considered acceptable.

6 Conclusions

This chapter exposes the definition, development, and implementation of a phenomenological model to represent the non-linear behavior of wire rope isolators. The proposed model is based on the Bouc-Wen model, where an additional

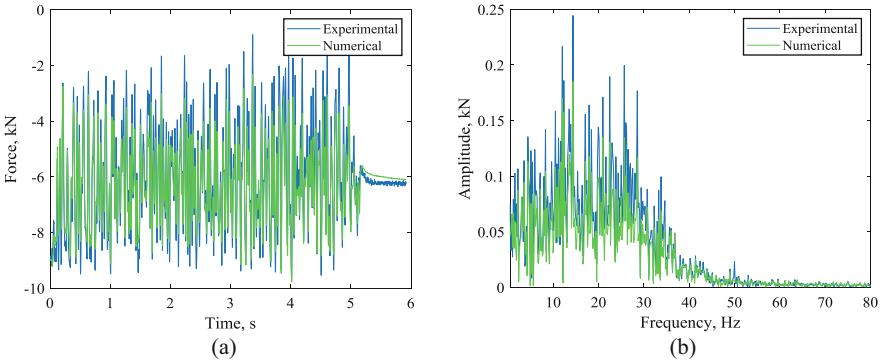

Fig. 5 Random test: compression preload of 9 kN, 0.5–30 Hz white noise, amplitude of 1.5 mm. Results in: (**a**) time domain and (**b**) frequency domain

parameter was used to emphasize the asymmetry which was experimentally noted between the compressive and tensile region of the spring hysteresis loop. The model parameters were optimized by the least square fitting of specific experimental data. An experimental characterization procedure with quasi-static loading was defined and used to fit the model parameters. The obtained parameter set was then used to simulate two independent experimental tests: a purely sinusoidal test and a random excitation test. The first test allowed to assess the performance of the proposed model in representing the hysteresis cycles of the spring, both in transient and stationary conditions. The second test allowed to investigate the performance of the model closer to operational conditions. The performed comparisons confirmed a good agreement between experimental and numerical results, proving the effectiveness of the developed model in simulating the WRI behavior.

Further development of the activity could be focused on the analysis of transportation data to assess the model performance in actual operational conditions. Also, other optimization approaches could be investigated for robustness assessment. Additionally, the spring was characterized along its three principal directions, with the aim of combining these three contributions to also describe any other possible direction. Nevertheless, due to the highly non-linear behavior, this hypothesis should be further investigated and validated through experimental testing along generic directions. Finally, the research should be extended to similar WRIs having different dimensions, in order to generalize the model and to investigate the possibility to derive at least a rough estimation of the Bouc-Wen parameters from the manufacturer's datasheet.

References

1. Balaji, P.S., Rahman, M., Moussa, L., Lau, H.H.: Wire rope isolators for vibration isolation of equipment and structures–a review. IOP Conf. Ser. Mater. Sci. Eng. **78**, 1–10 (2015)
2. Neri, P., Bucchi, F., Passarelli, D.: A multilevel finite element-multibody approach to design the suspension system for the road transportation of ssr1 cryomodule. Transport. Eng. **2**, 1–9 (2020)
3. Balaji, P.S., Moussa, L., Rahman, M., Ho, L.H.: An analytical study on the static vertical stiffness of wire rope isolators. J. Mech. Sci. Technol. **30**, 287–295 (2016)
4. Balaji, P.S., Moussa, L., Rahman, M., Vuia, L.T.: Experimental investigation on the hysteresis behavior of the wire rope isolators. J. Mech. Sci. Technol. **29**(4), 1527–1536 (2015)
5. Gerges, R.R.: Model for the force-displacement relationship of wire rope springs. J. Aerosp. Eng. **21**(1), 1–9 (2008)
6. Vaiana, N., Marmo, F., Sessa, S., Rosati, L.: Modeling of the hysteretic behavior of wire rope isolators using a novel rate-independent model. In: Nonlinear Dynamics of Structures, Systems and Devices, pp. 309–317 (2020) [R4]
7. Charalampakis, A., Koumousis, V.: Identification of Bouc–Wen hysteretic systems by a hybrid evolutionary algorithm. J. Sound Vib. **314**(3-5), 571–585 (2008)
8. Balaji, P.S., Leblouba, M., Rahman, M., Ho, L.H.: Static lateral stiffness of wire rope isolators. Mech. Based Design Struct. Mach. **44**(4), 462–475 (2016)
9. Bouc, R.: Forced vibrations of mechanical systems with hysteresis, Proceedings of the Fourth Conference on Nonlinear Oscillations, Prague (1967)
10. Carboni, B., Lacarbonara, W.: Nonlinear dynamic characterization of a new hysteretic device: experiments and computations. Nonlinear Dyn. **83**(1), 23–39 (2016)
11. Gao, H., Jézéquel, L., Cabrol, E., Vitry, B.: Characterization of a bouc-wen model-based damper model for automobile comfort simulation, Surveillance, Vishno and AVE conferences, INSA-Lyon, Université de Lyon, Lyon, France (2019)
12. Vaiana, N., Spizzuoco, M., Serino, G.: Wire rope isolators for seismically base-isolated lightweight structures: Experimental characterization and mathematical modeling. Eng. Struct. **140**, 498–514 (2017)
13. Bouc, R.: Modele mathematique d'hysteresis. Acustica. **24**, 16–25 (1971)
14. [R3] Wen, Y.K.: Method for random vibration of hysteretic systems. J. Eng. Mech. Div. ASCE. **102**(2), 249–263 (1976)
15. Barbieri, N., Marchi, M.E., Mannala, M.J., Barbieri, R.: Barbieri, LdSV, Barbieri, GdSV, Nonlinear dynamic analysis of a Stockbridge damper. Can. J. Civ. Eng. **46**(9), 828–835 (2016)
16. Carboni, B., Mancini, C., Lacarbonara, W.: Hysteretic beam model for steel wire ropes hysteresis identification. In: Structural Nonlinear Dynamics and Diagnosis, pp. 261–282. Springer, Cham (2015)
17. Leenen, R.: The modelling and identification of an hysteretic system: the wire as a nonlinear shock vibration isolator, DCT rapporten (2002)
18. Tyan, F., Tu, S.H., Wu, J.: An investigation on mathematical models of wire rope isolators, 30th National Conference on Theoretical and Applied Mechanics, Changhwa, Taiwan (2006)
19. Ni, Y., Ko, J., Wong, C.: Identification of non-linear hysteretic isolators from periodic vibration tests. J. Sound Vib. **217**(4), 737–756 (1998)
20. Ni, Y., Ko, J., Wong, C., Zhan, S.: Modelling and identification of a wire-cable vibration isolator via a cyclic loading test. Proc. Inst. Mech. Eng. Part I J. Syst. Control Eng. **213**(3), 163–172 (1999)
21. Ni, Y., Ko, J., Wong, C., Zhan, S.: Modelling and identification of a wire-cable vibration isolator via a cyclic loading test part 2: identification and response prediction. Proc. Inst. Mech. Eng. Part I J. Syst. Control Eng. **213**(3), 173–182 (1999)
22. Wang, H.X., Gong, X.S., Pan, F., Dang, X.J.: Experimental investigations on the dynamic behaviour of o-type wire-cable vibration isolators. Shock. Vib., 1–12 (2015)

23. Holzbauer, J.P., Cheban, S., Grimm, C., Helsper, J., Thiede, R., Wixson, A., Cubizolles, R., Kane, M.: Prototype HB650 transportation validation for the PIP-II project, 31st Linear Accelerator Conference (LINAC), Liverpool, UK (2022)
24. Dormand, J.R., Prince, P.J.: A family of embedded Runge-Kutta formulae. J. Comput. Appl. Math. **6**, 19–26 (1980)
25. Shampine, L.F., Reichelt, M.W.: The MATLAB ODE suite. SIAM J. Sci. Comput. **18**, 1–22 (1997)
26. Levenberg, K.: A method for the solution of certain problems in least-squares. Q. Appl. Math. **2**, 164–168 (1944)
27. Marquardt, D.: An algorithm for least-squares estimation of nonlinear parameters. SIAM J. Appl. Math. **11**, 431–441 (1963)

Multilayer Radical Morphing: Shape Transitions and Vibration

Ginevra Hausherr and Giulia Lanzara

1 Introduction

The development of materials with multiple functionalities is becoming essential not only in various engineering fields to improve performance of devices/structures but also to reduce environmental impact. Taking inspiration from nature, some materials are engineered in such a way as to respond to the surrounding environment [1]. For instance, morphing materials can have the intrinsic ability to adapt their shape due to different (even external) stimuli [2–5] such as: temperature, light, humidity [6], electricity and magnetic fields [7–9]. Among the existing morphing and smart materials, shape memory polymers (SMPs) are those capable of memorizing a temporary shape and recovering their permanent shape upon the occurrence of an external stimuli. Although this concept was known for half a century, recent progress has made it possible to transfer the usage of such materials in practical applications [10].

The fundamental limitation of SMPs is that they are not able to provide cyclic shape changes and that their morphing response can only be achieved under specific and unchangeable inputs. Moreover, in most cases external devices/power are required to provide the relevant stimulus to achieve the desired morphing shape (such as sources of heat, light, or humidity).

The most intriguing approach is seeking the spontaneous response of materials when the stimulus is directly provided by the surrounding environment. However, spontaneous cyclability and adaptability to different environmental conditions remain key challenges in the field together with the capability of the materials

G. Hausherr · G. Lanzara (✉)
Department of Civil Engineering, Computer Science and Aeronautical Technologies, University of Rome, Rome, Italy
e-mail: Giulia.Lanzara@uniroma3.it

© The Author(s), under exclusive license to Springer Nature Switzerland AG 2024

W. Lacarbonara (ed.), *Advances in Nonlinear Dynamics, Volume III*, NODYCON Conference Proceedings Series, https://doi.org/10.1007/978-3-031-50635-2_43

to maintain their mechanical and dynamic properties during and upon shape transitions.

With this in mind, a unique bimaterial structure that provides cyclic and indeed radical shape changes at a desired set triggering temperature is presented together with the vibrational response of the corresponding morphing modes.

2 Design of a Polymeric Film with Cyclic Memory

The strategic film design proposed in this paper consists of a textured commercial tape (American tape from TESA) sandwiched on its sticky side with an aluminum foil (10 μm thick). Once assembled, the system is strategically trained to carry out cyclic and radical shape changes. The key highlight of the proposed material design is that the cyclic response is the result of a special layup structure and not of a re-programming phase, which usually occurs after each single cycle for shape memory polymers. Such a unique response is due to two main factors: (1) the constituent materials (Fig. 1a, b); and (2) a one-time training session (Fig. 2). The key aspect of the constituent materials, a polyethylene film (PE- 80 μm thick) and a polyethylene terephthalate textile (PET- 70 μm thick), is that they are characterized by opposite glass transition temperatures (80 °C and –120 °C for PE and PET, respectively). The logic of the training session is schematically represented in Fig. 2. The process consists of "educating" the material to freeze its configuration in a desired shape at a set cooler temperature first (Step 1), and then to another shape at another warmer temperature (Step 2). The beauty is that the temperature settings and the desired shape can be fine-tuned depending on the specific application.

3 Experimental

Here the functionality of the material is proven for different temperature ranges $[T_{min}/T_{max}]$ [−5 °C/60 °C] and [20 °C/60 °C], and on samples characterized by different sizes in terms of width [W] and length L, namely [W/L] equal to [5 cm × 12 cm] and [2.5 cm × 6 cm]. Samples are trained and rolled up at 60 °C

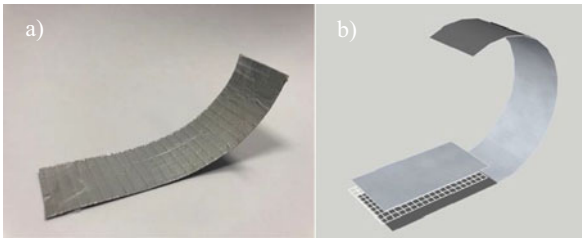

Fig. 1 (**a**) The constituent materials PE and PET with aluminum foil; (**b**) a schematic composition of the sample

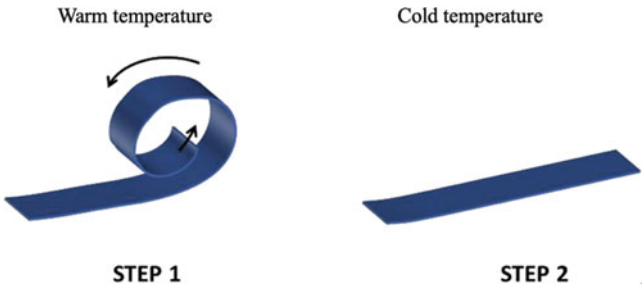

Fig. 2 Training steps of samples

with a bar (0.5 cm in diameter) and flat at $T = -5$ °C for 10 min. Functional tests are then carried out to verify the deformation modes over time with respect to the programming temperatures. Samples are finally tested under dynamic conditions to validate the stability of the programmed shapes under thermo-dynamic loading conditions. To this end, samples are analyzed with a Laser Vibrometer by Polytech, which allows to gather both time-domain and frequency domain responses when the system changes shape. The 6 cm × 2,5 cm sample trained at a $[T_{min}/T_{max}]$ value of [20 °C/60 °C] is used for this scope. The sample is mounted at one edge on a heating pad and is then placed under the laser. Data are collected in the two key configurations starting from the planar shape and following the rolled shape which is activated through the heating thermal pad.

4 Results and Discussions

4.1 Functional Response

An example of the functional response of the trained film and its capability in reaching and holding the objective shapes is shown in Fig. 4 that depicts pictures of the two extreme configurations: flat and rolled. The images refer to the evolution of the shape changes starting from the instant at which the cold film (at −5 °C temperature) is placed on the heating plate. It is observed that while the sample heats-up it deforms, reaching its maximum curvature when the film reaches 60 °C (set temperature) (Fig. 3a).

When the sample is removed from the heated plate, its shape goes back to the initial flat configuration. In other words, the film performs a rolling cycle at $T = 60$ °C and unrolling at $T = -5$ °C.

The images in Fig. 3 also highlight that the samples are able to hold the morphed shapes at each set temperature.

Fig. 3 Functional response at 60° (**a**) and −5° (**b**)

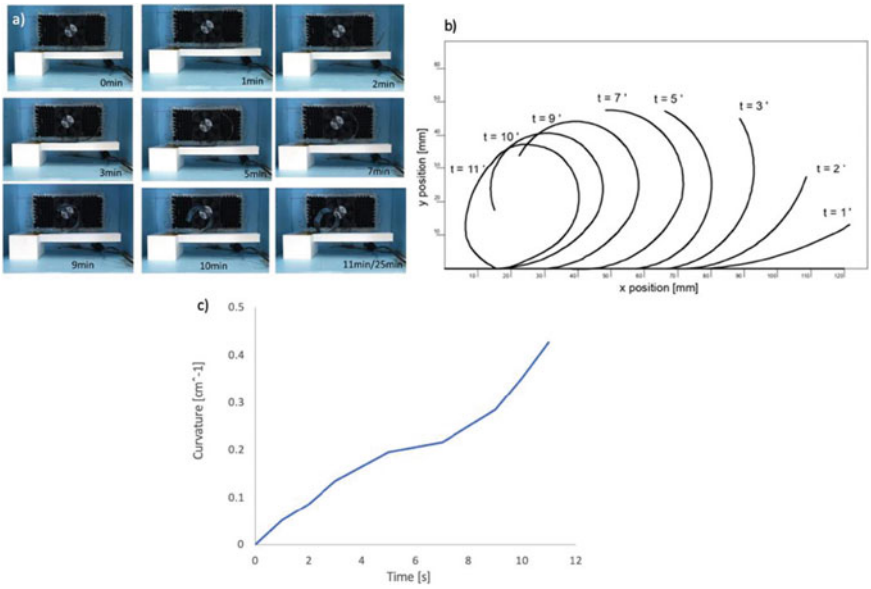

Fig. 4 A 5 cm × 12 cm sample; (**a**) Gradual transition of configuration; (**b**) Time-steps of the corresponding mode; (**c**) Curvature diagram

4.2 Time- and Frequency-Domain Analysis of the Functional Response

The trained sample is able to carry out these changes of shape (flat/rolled) when exposed to the aforementioned thermal gradients, cyclically and without the need to be re-educated. The gradual transition from a configuration to the other is investigated via a digital image correlation technique which allows to monitor the deformation modes as a function of time with increasing temperature (Fig. 4a). The maximum curvature reached by the sample is 0.4 cm^{-1} starting from the minimum "zero" curvature given by the initial flat configuration (Fig. 4c). It is worth noting that during programming the sample was rolled around a bar with a radius of 0.5 cm.

The corresponding modes, frozen at specific time-steps, can be viewed in Fig. 4b, in which the varying configurations of the 5 cm × 12 cm sample are analyzed.

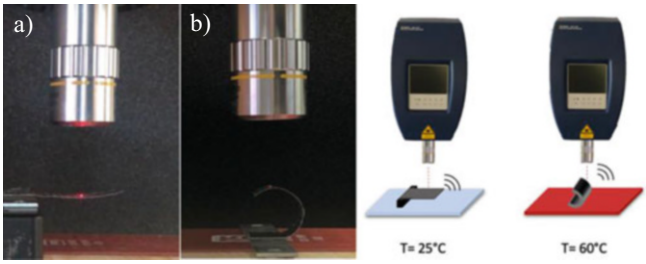

Fig. 5 Vibrational analysis of a 6 cm × 2.5 cm sample; (**a**) flat configuration at T_{amb}; (**b**) rolled configuration at 60 °C

The rolling/unrolling capability of the sample can be interpreted by the different degree of thermal expansion of each layer in the sandwich structure, which is amplified and guided by the stiffness changes of the layers with varying temperature that works in conjunction with the thermomechanical programming at specific set temperatures.

The vibrational analysis of the sample in its functional response is carried out with the support of a laser vibrometer (MSA-500 Polytec) and of a thermal pad. Two specific mode shapes are in particular investigated: (a) the flat configuration at T_{amb} and the rolled configuration at 60 °C (b). The corresponding mode shapes of the tested sample are captured and shown in Fig. 5, which also shows the role of the thermal pad and the selected laser spot to analyze the dynamic response of the sample. A small impulsive force is applied to the sample and the generated vibration is then captured in terms of velocity vs. time with the laser vibrometer.

The study highlights that when the sample moves from a mode shape to the other, its dynamic response changes.

Figure 6 shows both the frequency response of the sample for two distinct configurations and the signal in the time domain. The frequency response highlights a dominant peak at 13.25 Hz and at 12.24 Hz for the planar and rolled configurations, respectively. Such a counterintuitive response is related to the stiffness changes of the sample when heated. This effect is found to be dominant with respect to the expected geometrical stiffness increase due to the transition from a flat to a rolled shape. The influence of the stiffness variation due to thermal effects vs. that due to geometrical changes on the frequency response is then quantified with the support of an analytical analysis.

In order to compare the analyzed resonance frequency, the multilayered structure is then homogenized and its primary resonance frequency is calculated using the following equation for which the sample is approximated to a cantilever:

$$f_i = \sqrt{\frac{E_{Eq} J}{\rho A}} \frac{1}{L^2} (\chi L)^2$$

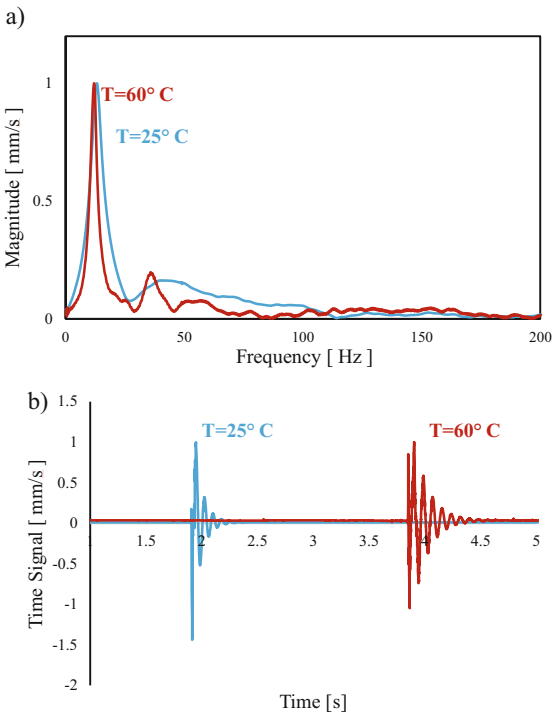

Fig. 6 (**a**) Frequency response of the sample for two distinct configurations and temperature; (**b**) time-signal domain

where f_i is the *resonance frequency,* E_{Eq} the equivalent *Young's modulus* $[8.7 \times 10^8\ N/m^2]$, J the *moment of inertia,* ρ the *density* $[1666\ Kg/m^3]$, χ the *mode of vibration's factor [1.875],* and finally L the *length [0.06 m].*

It is worth noting that the above value of the equivalent Young's modulus is calculated by taking advantage of the sample architecture. As mentioned earlier, in fact, the sample consists of a PE layer integrated with a grid of fibrous PET microwires. Thus, the equivalent Young's modulus can be calculated by applying the rule of mixture:

$$E_{Eq} = f_{mPE} E_{mPE} + f_{fPET} E_{fPET}$$

where f_m is the *matrix volumetric fraction and* f_f is the *fibers volumetric fraction*

The variation of the material stiffness, when switching from T_{amb} to $T = 60\ ^\circ\text{C}$, should then induce a 17,6% decrease in resonance frequency. However, it is expected that the system should be exposed to an increase in stiffness when switching from a flat to a rolled configuration (without considering material properties changes with temperature). The net of these two variations is 7% at the two investigated temperatures.

5 Conclusions

In this work it is shown that a bimaterial structure formed by a fiber reinforced composite layer and an aluminum foil has morphing ability when subjected to both positive and negative thermal gradients. This response can be associated with the opposite coefficients of thermal expansion and glass transition temperature between the forming layers as well as their stiffness variation with temperature and the multi-material plasticization during the "education" steps. The vibrational analysis shows that the resonance frequency is just slightly affected by the configuration changes, and this is due to the compensation of the loss in stiffness due to temperature variations with the increase in stiffness due to large-in-scale geometrical changes.

Acknowledgments The authors are grateful to the Air Force Office of Scientific Research (AFOSR)/European Office of Aerospace Research and Development (EOARD), Award n. FA8655-20-1-7036 for which Dr. Les Lee is gratefully acknowledged.

References

1. Athanasopoulos, N., Siakavellas, N.J.: Bioinspired temperature-responsive multilayer films and their performance under thermal fatigue. Biomimetics. **3** (2018)
2. Studart, A.R., Erb, R.M.: Bioinspired materials that self-shape through programmed microstructures (2014)
3. Lamri, A., Shirinbayan, M., Pereira, M., Truffault, L., Fitoussi, J., Lamouri, S., Bakir, F., Tcharkhtchi, A., Fi, J.: Effects of strain rate and temperature on the mechanical behavior of high-density polyethylene. J. Appl. Polym. Sci. (2020)
4. Liu, Y., Boyles, J.K., Genzer, J., Dickey, M.D.: Self-folding of polymer sheets using local light absorption. Soft Matter. **8**, 1764–1769 (2012)
5. Athanasopoulos, N., Siakavellas, N.J.: Programmable thermal emissivity structures based on bioinspired self-shape materials. Sci. Rep. **5** (2015)
6. Xie, T.: Recent advances in polymer shape memory (2011)
7. Khalid, S.A., Waterman, P.G., Erundan, M.F., Ch; Anderson, K.B., Winans, R.E., Evershed, R.P., Jerman, K., Eglinton, G., Mills, J., White, R.: 8. Crone, P. Meccan How Pines Cone Open (1997)
8. Oliver, K., Seddon, A., Trask, R.S.: Morphing in nature and beyond: a review of natural and synthetic shape-changing materials and mechanisms (2016)
9. Schleicher, S., Lienhard, J., Poppinga, S., Speck, T., Knippers, J.: A methodology for transferring principles of plant movements to elastic systems in architecture. CAD Comput. Aided Des. **60**, 105–117 (2015)
10. Burgert, I., Fratzl, P.: Actuation systems in plants as prototypes for bioinspired devices. Philos. Trans. R. Soc. A Math. Phys. Eng. Sci. **367**, 1541–1557 (2009)

A Novel Vibration Response-Based Approach to Monitor Faults in Bolted Complex Structures

Quankun Li, Qingzhou Zhao, Mingfu Liao, and Xiaobo Lei

1 Introduction

For complex structures like steel truss bridges in civil engineering applications, bolts are widely applied to clamp different structural elements together because of some advantages such as high strength and low cost [1]. However, they are easily subjected to fatigue crack/bolt loosening faults during their service since these complex structures often work with dynamic environmental loads. Fatigue crack/bolt loosening faults would lead to serious slip or separation between structural elements and seriously affect structures' safety and reliability. Therefore, monitoring potential faults at an early stage is an essential task to maintain the smooth operation of these bolted complex engineering structures.

For this objective, a host of vibration response-based methods have been proposed [2, 3]. Their fundamental principle is that vibration response-based features depend on structural physical properties; any change in properties due to bolt faults can thus be monitored by observing changes in vibration response-based indexes. For breathing cracks in structures, changes in the first few orders of natural frequencies were applied to detect the existence of cracks [4]. Similarly, changes in damping coefficients were monitored to detect nonlinear damages in frame structures [5]. Combining the frequency response function (FRF) and artificial neural network (ANN), bolt loosening faults in a plate were detected [6]. With the concept of the nonlinear output frequency response function (NOFRF), a new indicator based on information entropy was proposed for damages in rods [7]. In [8], higher harmonics of operational deflection shapes (ODSs) were estimated to

Q. Li (✉) · Q. Zhao · M. Liao
School of Power and Energy, Northwestern Polytechnical University, Xi'an, Shaanxi, China

X. Lei
Xi'an Aeronautical Institute, Xi'an, Shaanxi, China

© The Author(s), under exclusive license to Springer Nature Switzerland AG 2024

W. Lacarbonara (ed.), *Advances in Nonlinear Dynamics, Volume III*, NODYCON Conference Proceedings Series, https://doi.org/10.1007/978-3-031-50635-2_44

detect fatigue cracks in structures. Simulating effects of faults as nonlinear restoring forces, properties of transmissibility functions were analyzed and used to monitor loose fasteners in plates [9]. To improve diagnostic results, the natural logarithm was utilized to normalize transmissibility functions and related fault indexes [10]. To avoid the estimation of NOFRFs, nonlinear output spectra were directly applied to diagnose bolt loosening faults [11]. Recently, a systematic approach based on the second-order output spectra (SOOS) and local tuning approach (LTA) was proposed for monitoring bolt faults regardless of their severity, initial or serious [12].

Existing nonlinear vibration response-based approaches provide much more information about complex structures with bolt faults. However, one obvious limitation is that data from healthy structures are required during the implementation of these approaches. This would affect these approaches' effectiveness if data from healthy structures are not known. To consider this issue, a novel vibration response-based approach to monitor faults in bolted complex structures is proposed in this paper. The main novelties of this paper are: (1) stimulating the structure to be monitored only, and using nonlinear vibration responses, local fault features are derived; (2) with fault features, a novel approach with a sensitive fault index is proposed, and its availability is illustrated through experimental cases on a lab-bolted complex structure.

2 Dynamic Characteristics

In this section, the dynamics of extracted substructures, including the dynamic model, equation of motion, and vibration responses, are introduced.

2.1 The Model of Substructures

As shown in Fig. 1, bolted complex structures are usually assembled with a series of bolts, nuts, and chain-type beam-like structures, which can be further divided into some periodic substructures (marked by red arrows) according to structural configurations and vibration paths. By describing the dynamic behavior of chain-type beam-like structures with the general chain-type MDOF model, the dynamic model with coordinates $x_a(t)(a = i_l, i_o, i_r)$ of substructures can also be extracted and shown in Fig. 2. Boundary constraints and excitations are applied to other parts of the bolted complex structure, and potential bolt faults (marked by red slash) are considered as nonlinear damper-spring connections around the central mass [13].

With Newton's second law [14], the differential equation of motion for this model can be obtained as

Fig. 1 Bolted complex structures

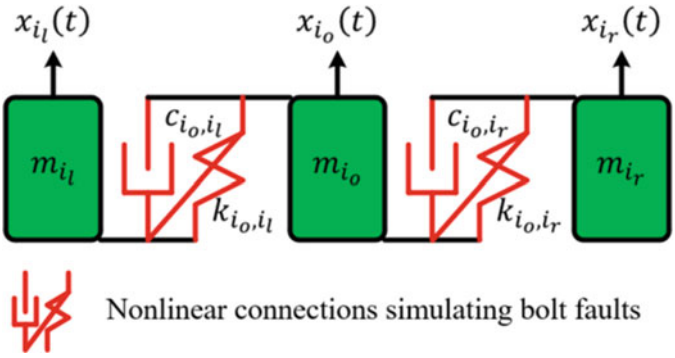

Fig. 2 Model of substructures

$$m_{i_o}\ddot{x}_{i_o}(t)+c_{i_o,i_l}\dot{\Delta}_{i_o,i_l}(t)+k_{i_o,i_l}\Delta_{i_o,i_l}(t)+c_{i_o,i_r}\dot{\Delta}_{i_o,i_r}(t)+k_{i_o,i_r}\Delta_{i_o,i_r}(t)=u_{i_o}^{\text{fau}}(t)$$
$$\left(\begin{array}{l}\dot{\Delta}_{i_o,i_l}(t)=\dot{x}_{i_o}(t)-\dot{x}_{i_l}(t),\ \Delta_{i_o,i_l}(t)=x_{i_o}(t)-x_{i_l}(t)\\ \dot{\Delta}_{i_o,i_r}(t)=\dot{x}_{i_o}(t)-\dot{x}_{i_r}(t),\ \Delta_{i_o,i_r}(t)=x_{i_o}(t)-x_{i_r}(t)\end{array}\right) \tag{1}$$

where m_{i_o}, c_{i_o,i_l}, c_{i_o,i_r}, k_{i_o,i_l}, and k_{i_o,i_r} are the model's mass, damping, and stiffness coefficients. $\ddot{x}_{i_o}(t)$, $\dot{x}_{i_o}(t)$, and $x_{i_o}(t)$ are the model's acceleration, velocity, and displacement. $u_{i_o}^{\text{fau}}(t)$ is the bolt fault force applied to the central mass m_{i_o}.

Since bolt faults usually affect structural damping and stiffness properties, they are simulated as nonlinear connections in the model, and their expressions can be expressed [13] as

$$u_{i_o}^{\text{fau}}(t)=\sum_{p=1}^{\infty}\left(c_{i_o,i_l,p}^{\text{fau}}\dot{\Delta}_{i_o,i_l}^{p}(t)+k_{i_o,i_l,p}^{\text{fau}}\Delta_{i_o,i_l}^{p}(t)+c_{i_o,i_r,p}^{\text{fau}}\dot{\Delta}_{i_o,i_r}^{p}(t)+k_{i_o,i_r,p}^{\text{fau}}\Delta_{i_o,i_r}^{p}(t)\right)$$
$$\left(\begin{array}{l}\dot{\Delta}_{i_o,i_l}^{p}(t)=\left(\dot{x}_{i_o}(t)-\dot{x}_{i_l}(t)\right)^{p},\ \Delta_{i_o,i_l}^{p}(t)=\left(x_{i_o}(t)-x_{i_l}(t)\right)^{p}\\ \dot{\Delta}_{i_o,i_r}^{p}(t)=\left(\dot{x}_{i_o}(t)-\dot{x}_{i_r}(t)\right)^{p},\ \Delta_{i_o,i_r}^{p}(t)=\left(x_{i_o}(t)-x_{i_r}(t)\right)^{p}\end{array}\right) \tag{2}$$

where subscript p is the polynomial function's order, and parameters $c^{\text{fau}}_{i_o,i_l,p}$, $c^{\text{fau}}_{i_o,i_r,p}$, $k^{\text{fau}}_{i_o,i_l,p}$, and $k^{\text{fau}}_{i_o,i_r,p}$ are nonlinear coefficients due to bolt faults. If there is no bolt fault around mass m_{i_o}, the related nonlinear coefficients and nonlinear bolt fault force will be zero.

2.2 Vibration Response of the Model

Application of the Fourier transform (FT), the frequency-domain differential equation of motion can be obtained as:

$$\begin{aligned}&\left(-v\omega^2 m_{i_o}+jv\omega c_{i_o,i_l}+k_{i_o,i_l}+jv\omega c_{i_o,i_r}+k_{i_o,i_r}\right)X^{v,A}_{i_o}(jv\omega)\\&-\left(jv\omega c_{i_o,i_l}+k_{i_o,i_l}\right)X^{v,A}_{i_l}(jv\omega)-\left(jv\omega c_{i_o,i_r}+k_{i_o,i_r}\right)X^{v,A}_{i_r}(jv\omega)\\&=U^{fau}_{i_o}(jv\omega),(v\geq 1)\end{aligned}\tag{3}$$

where ω and A are the excitation frequency and amplitude. $X^{v,A}_{i_o}(jv\omega)$, $X^{v,A}_{i_l}(jv\omega)$, and $X^{v,A}_{i_r}(jv\omega)$ are the v^{th} order output spectra, and $U^{\text{fau}}_{i_o}(jv\omega)$ is the frequency-domain bolt fault force.

It is shown that nonlinear vibration responses of the substructure are just decided by the nonlinear bolt fault force and structural linear properties, such that it can be applied for bolt fault monitoring.

3 A Novel Monitoring Approach

With the equation and nonlinear vibration responses in (3), a novel approach with fault features and an index is proposed in this section.

3.1 Fault Features and Index

If the structure is excited three times with different levels but the same frequency, equations similar to (3) can be obtained as

$$\begin{aligned}&\left(-v\omega^2 m_{i_o}+jv\omega c_{i_o,i_l}+k_{i_o,i_l}+jv\omega c_{i_o,i_r}+k_{i_o,i_r}\right)\\&-\left(jv\omega c_{i_o,i_l}+k_{i_o,i_l}\right)\frac{X^{v,A^\varepsilon}_{i_l}(jv\omega)}{X^{v,A^\varepsilon}_{i_o}(jv\omega)}-\left(jv\omega c_{i_o,i_r}+k_{i_o,i_r}\right)\frac{X^{v,A^\varepsilon}_{i_r}(jv\omega)}{X^{v,A^\varepsilon}_{i_o}(jv\omega)}\\&=\frac{L^{fau,\varepsilon}_{i_o}(jv\omega)}{X^{v,A^\varepsilon}_{i_o}(jv\omega)},(\varepsilon=1,2,3)\end{aligned}\tag{4}$$

or in a matrix form as

$$\begin{aligned}\left[G^{A^{12}}(jv\omega)\right]\begin{bmatrix}\left(jv\omega c_{i_o,i_l}+k_{i_o,i_l}\right)\\ \left(jv\omega c_{i_o,i_r}+k_{i_o,i_r}\right)\end{bmatrix}&=\left[B(jv\omega)\right]-\left[C^{A^{12}}(jv\omega)\right]\\ \left[G^{A^{23}}(jv\omega)\right]\begin{bmatrix}\left(jv\omega c_{i_o,i_l}+k_{i_o,i_l}\right)\\ \left(jv\omega c_{i_o,i_r}+k_{i_o,i_r}\right)\end{bmatrix}&=\left[B(jv\omega)\right]-\left[C^{A^{23}}(jv\omega)\right]\end{aligned}\tag{5}$$

where

$$\left[G^{A^{12}}(jv\omega)\right]=\begin{bmatrix}\frac{X_{i_l}^{v,A^1}(jv\omega)}{X_{i_o}^{v,A^1}(jv\omega)} & \frac{X_{i_r}^{v,A^1}(jv\omega)}{X_{i_o}^{v,A^1}(jv\omega)}\\ \frac{X_{i_l}^{v,A^2}(jv\omega)}{X_{i_o}^{v,A^2}(jv\omega)} & \frac{X_{i_r}^{v,A^2}(jv\omega)}{X_{i_o}^{v,A^2}(jv\omega)}\end{bmatrix},$$

$$\left[G^{A^{23}}(jv\omega)\right]=\begin{bmatrix}\frac{X_{i_l}^{v,A^2}(jv\omega)}{X_{i_o}^{v,A^2}(jv\omega)} & \frac{X_{i_r}^{v,A^2}(jv\omega)}{X_{i_o}^{v,A^2}(jv\omega)}\\ \frac{X_{i_l}^{v,A^3}(jv\omega)}{X_{i_o}^{v,A^3}(jv\omega)} & \frac{X_{i_r}^{v,A^3}(jv\omega)}{X_{i_o}^{v,A^3}(jv\omega)}\end{bmatrix},$$

$$\left[B(jv\omega)\right]=\begin{bmatrix}\left(-v\omega^2 m_{i_o}+jv\omega c_{i_o,i_l}+k_{i_o,i_l}+jv\omega c_{i_o,i_r}+k_{i_o,i_r}\right)\\ \left(-v\omega^2 m_{i_o}+jv\omega c_{i_o,i_l}+k_{i_o,i_l}+jv\omega c_{i_o,i_r}+k_{i_o,i_r}\right)\end{bmatrix},$$

$$\left[C^{A^{12}}(jv\omega)\right]=\begin{bmatrix}\frac{U_{i_o}^{fau,1}(jv\omega)}{X_{i_o}^{v,A^1}(jv\omega)}\\ \frac{U_{i_o}^{fau,2}(jv\omega)}{X_{i_o}^{v,A^2}(jv\omega)}\end{bmatrix},\left[C^{A^{23}}(jv\omega)\right]=\begin{bmatrix}\frac{U_{i_o}^{fau,2}(jv\omega)}{X_{i_o}^{v,A^2}(jv\omega)}\\ \frac{U_{i_o}^{fau,3}(jv\omega)}{X_{i_o}^{v,A^3}(jv\omega)}\end{bmatrix}.$$

With the inverse matrix $[G(jv\omega)]^{-1}=[Q(jv\omega)]$, structural properties in (5) can be calculated as

$$\begin{aligned}&jv\omega c_{i_o,i_l}+k_{i_o,i_l}=Q_{11}^{A^{12}}(jv\omega)B_{11}(jv\omega)+Q_{12}^{A^{12}}(jv\omega)B_{21}(jv\omega)\\&+Q_{11}^{A^{12}}(jv\omega)C_{11}^{A^{12}}(jv\omega)+Q_{12}^{A^{12}}(jv\omega)C_{21}^{A^{12}}(jv\omega)\\&jv\omega c_{i_o,i_r}+k_{i_o,i_r}=Q_{21}^{A^{12}}(jv\omega)B_{11}(jv\omega)+Q_{22}^{A^{12}}(jv\omega)B_{21}(jv\omega)\\&+Q_{21}^{A^{12}}(jv\omega)C_{11}^{A^{12}}(jv\omega)+Q_{22}^{A^{12}}(jv\omega)C_{21}^{A^{12}}(jv\omega)\end{aligned}\tag{6a}$$

$$\begin{aligned}&jv\omega c_{i_o,i_l}+k_{i_o,i_l}=Q_{11}^{A^{23}}(jv\omega)B_{11}(jv\omega)+Q_{12}^{A^{23}}(jv\omega)B_{21}(jv\omega)\\&+Q_{11}^{A^{23}}(jv\omega)C_{11}^{A^{23}}(jv\omega)+Q_{12}^{A^{23}}(jv\omega)C_{21}^{A^{23}}(jv\omega)\\&jv\omega c_{i_o,i_r}+k_{i_o,i_r}=Q_{21}^{A^{23}}(jv\omega)B_{11}(jv\omega)+Q_{22}^{A^{23}}(jv\omega)B_{21}(jv\omega)\\&+Q_{21}^{A^{23}}(jv\omega)C_{11}^{A^{23}}(jv\omega)+Q_{22}^{A^{23}}(jv\omega)C_{21}^{A^{23}}(jv\omega)\end{aligned}\tag{6b}$$

Then, novel vibration response-based features can be defined as

$$\lambda_{i_o}^{A^{12}}(jv\omega) = \frac{Q_{11}^{A^{12}}(jv\omega) + Q_{12}^{A^{12}}(jv\omega)}{Q_{21}^{A^{12}}(jv\omega) + Q_{22}^{A^{12}}(jv\omega)} = \frac{jv\omega c_{i_o,i_l} + k_{i_o,i_l}}{jv\omega c_{i_o,i_r} + k_{i_o,i_r}}$$
$$\frac{-Q_{11}^{A^{12}}(jv\omega)\, C_{11}^{A^{12}}(jv\omega) + Q_{12}^{A^{12}}(jv\omega)\, C_{21}^{A^{12}}(jv\omega)}{-Q_{21}^{A^{12}}(jv\omega)\, C_{11}^{A^{12}}(jv\omega) + Q_{22}^{A^{12}}(jv\omega)\, C_{21}^{A^{12}}(jv\omega)}$$
$$\lambda_{i_o}^{A^{23}}(jv\omega) = \frac{Q_{11}^{A^{23}}(jv\omega) + Q_{12}^{A^{23}}(jv\omega)}{Q_{21}^{A^{23}}(jv\omega) + Q_{22}^{A^{23}}(jv\omega)} = \frac{jv\omega c_{i_o,i_l} + k_{i_o,i_l}}{jv\omega c_{i_o,i_r} + k_{i_o,i_r}} \tag{7}$$
$$\frac{-Q_{11}^{A^{23}}(jv\omega)\, C_{11}^{A^{23}}(jv\omega) + Q_{12}^{A^{23}}(jv\omega)\, C_{21}^{A^{23}}(jv\omega)}{-Q_{21}^{A^{23}}(jv\omega)\, C_{11}^{A^{23}}(jv\omega) + Q_{22}^{A^{23}}(jv\omega)\, C_{21}^{A^{23}}(jv\omega)}$$

Observing (7), it is shown that the defined fault features are a function of the linear properties of the substructure and bolt fault force, meaning that they can be applied to monitoring potential bolt faults in the substructure.

With fault features in (7), a novel fault index can be proposed accordingly as

$$\Upsilon_{i_o}^{I,II}(j\omega) = \left| \frac{\left| \left| \sum_{v=1}^{V} \lambda_{i_o}^{A^{23}}(jv\omega) \right| - \left| \sum_{v=1}^{V} \lambda_{i_o}^{A^{12}}(jv\omega) \right| \right|}{\left| \sum_{v=1}^{V} \lambda_{i_o}^{A^{12}}(jv\omega) \right|} \right| * 100 \tag{8}$$

If there is no bolt fault in the substructure, the bolt fault force will be zero, which leads to two same fault features and zero fault index. On the contrary, if there is a bolt fault in the substructure, the nonlinear bolt fault force will cause different fault features and nonzero fault index. Therefore, the value of the fault index, whether zero or nonzero, can be applied to determine whether there is a bolt fault in the substructure or not.

3.2 *Procedures of the Approach*

According to fault features and the index, a novel monitoring approach is proposed accordingly. Its procedures are shown as follows.

As shown in Fig. 3, the novel approach has five main steps. Firstly, corresponding substructures to be monitored in bolted complex structures are found. Then, time domain data are collected from the substructure to be monitored. Next, data are transformed into frequency domain to compute fault features with (7). After that, fault index is computed with (8). Finally, potential bolt faults are monitored based on the value of the fault index.

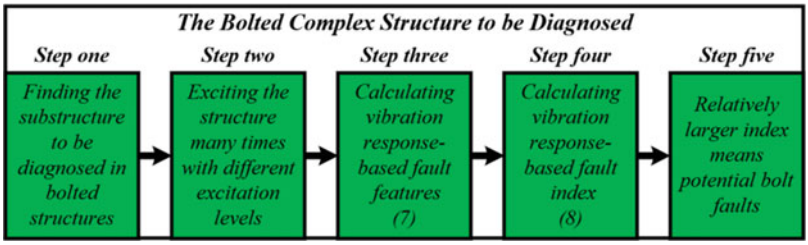

Fig. 3 Operating procedures

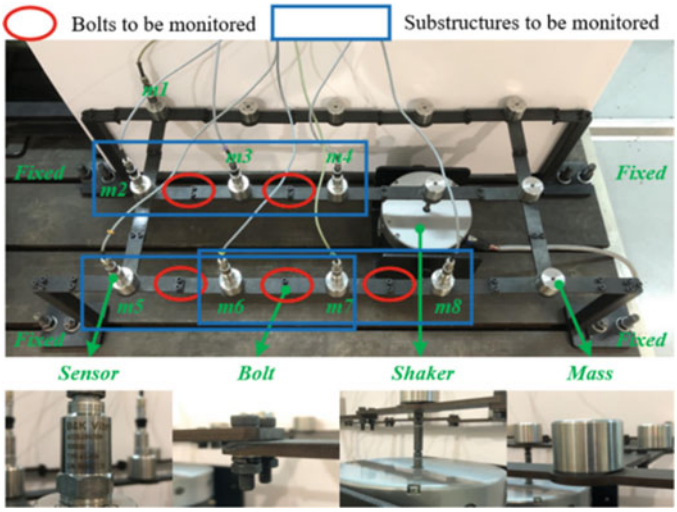

Fig. 4 Bolted structure for experiments

4 Studies of Experimental Cases

To verify the effectiveness of the proposed approach, experiments on a lab-bolted complex structure are studied (Fig. 4). The structure is connected by some bolts and rods, and its four corners are connected to the fixed ground. One modal exciter is used to excite the structure, and vibration data are collected by some accelerators. Three substructures are selected for bolt monitoring: (m2-m3-m4), (m5-m6-m7), and (m6-m7-m8). Since bolt faults often affect connections and generate nonlinearities in structures, they are simulated by loosening initially tightened bolts, whose torques are reduced from 4 Nm to about 1 Nm. As shown in Fig. 5, a total of two cases are considered. In case one (Fig. 5a), no fault exists in all substructures, meaning that all bolts are in a tightened state. In case two (Fig. 5b), only one fault is located between masses m7 and m8 in the substructure (m6-m7-m8).

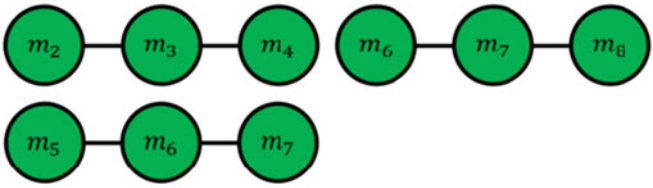

(a) Case one

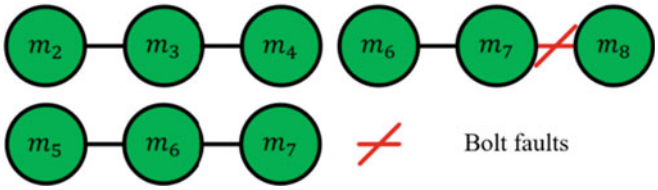

(b) Case two

Fig. 5 Experimental cases. (**a**) Case one. (**b**) Case two

Table 1 Excitation parameters

Case	Excitation	Parameter
Case one	Excitation one	Amplitude 7.97 V, phase 1.89 rad/s.
	Excitation two	Amplitude 5.98 V, phase 0.84 rad/s.
	Excitation three	Amplitude 9.97 V, phase 1.24 rad/s.
Case two	Excitation one	Amplitude 1.99 V, phase −1.89 rad/s.
	Excitation two	Amplitude 5.98 V, phase 0.84 rad/s.
	Excitation three	Amplitude 9.97 V, phase 1.24 rad/s.

According to the derivation of fault features and indexes, three excitations with different magnitudes and/or phases are required. In experiments, different cosine functions $u^i(t) = A^i \cos(2\pi ft + \varphi^i)$ with a frequency of 8 Hz are applied as inputs, and their detailed amplitudes and phases are shown in Table 1. In case one and case two, different excitations are applied. The purpose is to show the superiority of the proposed method that each case can be monitored independently.

With the procedures in Sect. 3.2, raw time-domain data are collected and processed with Matlab codes, and the final results of fault indexes in the experiments are shown in Fig. 6.

In case one (Fig. 6a), the results show that the values of all indexes are about zero, meaning that there is no bolt fault in any of the substructures. In case two (Fig. 6b), only the value of the fault index in substructure (m6-m7-m8) is relatively larger, which means that bolt fault occurs in this substructure and the other two substructures have no bolt fault.

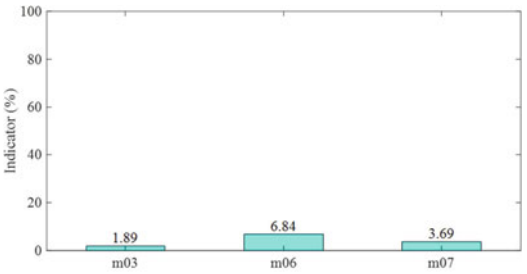

(a) Case one

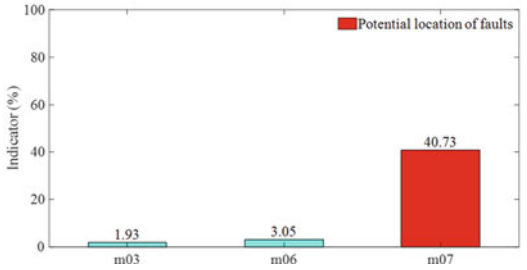

(b) Case two

Fig. 6 Experimental results. (**a**) Case one. (**b**) Case two

As a whole, the results from the above experiments are consistent with real situations of bolt faults shown in Fig. 5. Therefore, the effectiveness of the proposed approach is verified by these two experimental cases. Moreover, output responses will change in case two due to the generation of bolt faults, while it is very hard to know the precise position of faults since any bolt fault can cause variations in output responses. On the contrary, the fault index of the proposed method in substructure (m6-m7-m8) changes only, meaning that this approach can not only detect the existence of the fault but also localize the fault.

5 Conclusion

To overcome the limitation in existing approaches that data from healthy structures are required during the implementation of approaches, a novel vibration response-based approach to monitor faults in bolted complex structures is proposed in this paper. The main conclusions are as follows.

1. By considering the effects of faults as nonlinear restoring forces, a discrete MDOF model with nonlinear elements can be built for the dynamic analysis of bolted substructures.
2. By stimulating the structure many times, similar equations from the substructure to be monitored can be applied to form a local and sensitive vibration response-based fault index.

3. Results from experimental studies on a bolted complex structure with bolt loosening faults show that the novel approach can give correct location of faults in the substructure.

In further studies, the application of this approach to other types of bolted complex structures, such as rotor-bearing systems in aero engines and gas turbines, should be considered.

Acknowledgments This work was supported by the Fundamental Research Funds for the Central Universities project (No. 3102020OQD705).

References

1. Bickford, J.: An Introduction to the Design and Behavior of Bolted Joints, Revised and Expanded. Routledge, New York (2018)
2. Chang, F.K., Markmiller, J.F., Yang, J., Kim, Y.: Structural health monitoring. System Health Manage. **1**, 419–428 (2011)
3. Huang, J.Y., Liu, J.H., Gong, H., Deng, X.J.: A comprehensive review of loosening detection methods for threaded fasteners. Mech. Syst. Signal Process. **160**, 100652 (2022)
4. Yan, G., Stefano, A.D., Matta, E., Feng, R.: A novel approach to detecting breathing-fatigue cracks based on dynamic characteristics. J. Sound Vib. **332**(2), 407–422 (2013)
5. Curadelli, R.O., Riera, J.D., Ambrosini, D., Amani, M.G.: Damage detection by means of structural damping identification. Eng. Struct. **30**(12), 3497–3504 (2008)
6. Ondra, V., Sever, I.A., Schwingshackl, C.W.: A method for detection and characterisation of structural non-linearities using the Hilbert transform and neural networks. Mech. Syst. Signal Process. **83**, 210–227 (2017)
7. Huang, H., et al.: Study of cumulative fatigue damage detection for used parts with nonlinear output frequency response functions based on NARMAX modelling. J. Sound Vib. **411**, 75–87 (2017)
8. Asnaashari, E., Sinha, J.K.: Development of residual operational deflection shape for crack detection in structures. Mech. Syst. Signal Process. **43**(1–2), 113–123 (2014)
9. Johnson, T.J., Adams, D.E.: Transmissibility as a differential indicator of structural damage. J. Vib. Acoust. **124**(4), 634–641 (2002)
10. Johnson, T.J., Brown, R.L., Adams, D.E., Schiefer, M.: Distributed structural health monitoring with a smart sensor array. Mech. Syst. Signal Process. **18**(3), 555–572 (2004)
11. Zhao, X.Y., et al.: A new transmissibility analysis method for detection and location of damage via nonlinear features in MDOF structural systems. IEEE ASME Trans. Mechatron. **20**(4), 1933–1947 (2014)
12. Li, Q.K., Jing, X.J.: A systematic second-order output spectrum-based method for fault diagnosis with a local tuning approach. J. Sound Vib. **475**, 115283 (2020)
13. Chesné, S., Deraemaeker, A.: Damage localization using transmissibility functions: a critical review. Mech. Syst. Signal Process. **38**(2), 569–584 (2013)
14. Ewins, D.J.: Modal Testing: Theory, Practice and Application. John Wiley & Sons, New York (2009)

Data-Driven Delay Identification with SINDy

Ákos Tamás Köpeczi-Bócz, Henrik Sykora, and Dénes Takács

1 Introduction

Model construction based on data-driven techniques has gained considerable ground over the past years due to versatile measurement tools (such as image recognition, smartphone sensors, etc.) and a large amount of available data. The development of computer sciences and statistical and machine learning tools enables more efficient data processing and model discovery. The appearance of scientific machine learning [1] (SciML) made the model construction to be more sophisticated by opening a physics-informed toolset for researchers to discover unexplained phenomena in dynamic systems.

Although discovering governing equations of physical systems is a challenge, the wide availability of computers made it possible to have an extensive amount of data in our possession, together with the increasing computational power that opened the door for us to use data-driven techniques for model construction. Fitting linear models with data-driven techniques has been possible with dynamic mode decomposition [4], but constructing models with nonlinear structure is even a challenge today.

Á. T. Köpeczi-Bócz (✉)
Department of Applied Mechanics, Faculty of Mechanical Engineering, Budapest University of Technology and Economics, Budapest, Hungary
e-mail: kopeczi@mm.bme.hu

H. Sykora
Institute of Sound and Vibration Research, University of Southampton, Southampton, UK

D. Takács
ELKH-BME Dynamics of Machines Research Group, Budapest University of Technology and Economics, Budapest, Hungary

© The Author(s), under exclusive license to Springer Nature Switzerland AG 2024

W. Lacarbonara (ed.), *Advances in Nonlinear Dynamics, Volume III*, NODYCON Conference Proceedings Series, https://doi.org/10.1007/978-3-031-50635-2_45

Throughout this study, we investigate the *sparse identification of nonlinear dynamics* (SINDy) method. The core idea of the method was first presented by Brunton et al. in 2016 [2] to explore the nonlinear equations that describe the underlying physics of a dynamic system. Namely, the data-driven SINDy can be used to identify the key nonlinearities that may be implemented in the differential equations to describe the properties of the system. In this work, we extend the SINDy algorithm to find the underlying dynamics of systems with time delays. We investigate the limits and the prerequisites of this technique through numerical experiments using a dataset constructed by simulating dynamic systems with known parameters and time delays. We also include a stochastic effect to test the robustness of the method.

2 Sparse Identification of Nonlinear Dynamics for Time-Delay Identification

Let us consider a smooth dynamic system that is described by the differential equation of the form

$$\frac{\mathrm{d}}{\mathrm{d}t}\mathbf{x} = \mathbf{f}\left(\mathbf{x}(t), \mathbf{x}(t-\tau_1), \mathbf{x}(t-\tau_2), \ldots, t\right), \tag{1}$$

where $\mathbf{x}$ is the state of the system, $\dot{\mathbf{x}}$ denotes its derivative with respect to time t, and $\tau_1, \tau_2, \ldots, \tau_{N_\tau} > 0$ are the time delays. Suppose that we have measurements or any numerical data about the evolution of the solution in time. We arrange these time-series data of the system variables:

$$\underset{m\times s}{\mathbf{X}} = \left[\, \mathbf{x}(t_1)\ \mathbf{x}(t_2)\ \ldots\ \mathbf{x}(t_m) \,\right]^{\mathrm{T}}, \tag{2}$$

where $t_1, t_2, \ldots, t_m$ are the (not necessarily equidistant) sampling instances. The parameter s denotes the number of state variables. Similarly, we introduce the shifted state variables of the measurements as

$$\underset{m\times s}{\mathbf{X}_{\tau_j}} = \left[\, \mathbf{x}(t_1-\tau_j)\ \mathbf{x}(t_2-\tau_j)\ \ldots\ \mathbf{x}(t_m-\tau_j) \,\right]^{\mathrm{T}},\ j = 1, 2, \ldots, N_\tau. \tag{3}$$

We also collect the time derivative of the state variables in

$$\underset{m\times s}{\dot{\mathbf{X}}} = \left[\, \dot{\mathbf{x}}(t_1)\ \dot{\mathbf{x}}(t_2)\ \ldots\ \dot{\mathbf{x}}(t_m) \,\right]^{\mathrm{T}}. \tag{4}$$

In case $\mathbf{X}_\tau$ or $\dot{\mathbf{X}}$ are not available through direct measurements, we can obtain them through interpolation or numerical differential schemes, respectively.

Based on the core idea of SINDy, we can represent (1) using (2)–(4) as

$$\underset{m\times s}{\dot{\mathbf{X}}} = \underset{m\times p}{\boldsymbol{\Theta}}(\mathbf{X}, \mathbf{X}_{\tau_1}, \mathbf{X}_{\tau_2}, \ldots)\underset{p\times s}{\boldsymbol{\Xi}}, \tag{5}$$

where the matrix $\boldsymbol{\Theta}$ contains the candidate terms that may be used to construct the right-hand side of (1) and can be defined arbitrarily. Thus, dimension p is determined by the number of arbitrarily chosen candidate terms. The matrix $\boldsymbol{\Xi}$ determines the coefficients of the arbitrarily chosen candidate terms of $\boldsymbol{\Theta}$; ideally, it selects the terms that compose the differential equation (1). Thus, during the SINDy procedure, we determine the coefficient matrix $\boldsymbol{\Xi}$ using an optimization algorithm. We apply the SINDy with the sequentially thresholded least-squares algorithm (STLSQ) [3].

To obtain the k-th column $\boldsymbol{\xi}_k$ of the matrix $\boldsymbol{\Xi}$, we need to solve the following optimization problem:

$$\underset{p\times 1}{\boldsymbol{\xi}_k} = \text{argmin}_{\boldsymbol{\xi}'_k}\left(\left\|\dot{\mathbf{X}}_k - \boldsymbol{\Theta}(\mathbf{X}, \mathbf{X}_{\tau_1}, \mathbf{X}_{\tau_2}, \ldots)\boldsymbol{\xi}'_k\right\|_2 + \lambda\left\|\boldsymbol{\xi}'_k\right\|_1\right). \tag{6}$$

The norms are defined as in [3] and λ is a tuneable parameter that affects the sparsity and error tolerance of the dynamical system fitted on the measured data. During our implementation, we introduced an iteration for parameter λ and used the sequential thresholded least-squares (STLSQ) algorithm. In our investigation, we found that we were able to achieve a better fitting solution by favoring sparsity in many cases. In the following sections, we will show how this methodology can contribute to identifying the most prominent terms.

3 Time-Delay Identification of a System with Single Delay Using SINDy

We take a one-dimensional nonlinear delayed system

$$\dot{x}(t) = \alpha x^3(t-\tau) + \alpha x(t-\tau) + \beta\sin(t) \tag{7}$$

and simulate a dataset for given initial conditions and parameters. In our experiment, $\tau = 1.0$, $\alpha = -1.0$, and $\beta = 0.09$, while the initial condition is $x(\vartheta) = 0.6$ where $\vartheta \in [-\tau, 0]$ (Fig. 1).

The main characteristic of the system is provided by the term $\alpha x(t-\tau)$, while additional nonlinearity x^3 and excitation $\sin(t)$ are added in order to test out the sensitivity of the procedure. In order to highlight the capabilities and limitations of this method, the main focus is on the identification of the time delay in a partially known system. The candidate functions are chosen accordingly, so the algorithm has the chance to capture all details, but we are focused on the delayed state variables. Even with this setup, we can show later the limitations of the method and investigate the effectiveness in identifying the delayed terms. The candidate functions are

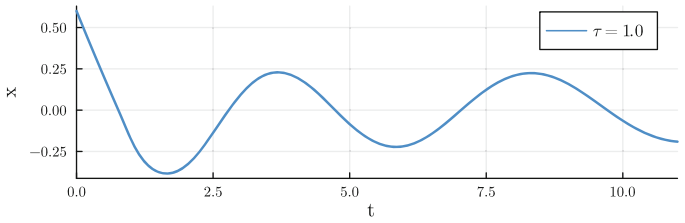

Fig. 1 Solution of (7) for $x(\vartheta) = 0.6$ where $\vartheta \in [-\tau, 0]$ and $\tau = 1.0$, $\alpha = -1.0$ and $\beta = 0.09$. Dataset for the SINDy operation is taken with 0.05 equidistant sampling. We take the samples from $t_0 = 0$ to $t_{220} = 11$

$$\underset{221\times 10}{\boldsymbol{\Theta}}(\mathbf{X}) = \left[\mathbf{1}\ \mathbf{X}\ \mathbf{X}^3\ \mathbf{X}_{1.0}\ \mathbf{X}_{1.0}^3\ \mathbf{X}_{1.5}\ \mathbf{X}_{1.5}^3\ \mathbf{X}_{2.0}\ \mathbf{X}_{2.0}^3\ \sin(\mathbf{t})\right], \tag{8}$$

where the operations (exponentiation, trigonometric function) are interpreted element-wise, meaning that $\boldsymbol{\Theta}(\mathbf{X})$ has the form

$$\underset{221\times 10}{\boldsymbol{\Theta}} = \begin{bmatrix} 1 & \mathrm{X}(t_0) & \mathrm{X}^3(t_0) & \mathrm{X}_{1.0}(t_0) & \mathrm{X}_{1.0}^3(t_0) & \mathrm{X}_{1.5}(t_0) & \mathrm{X}_{1.5}^3(t_0) & \mathrm{X}_{2.0}(t_0) & \mathrm{X}_{2.0}^3(t_0) & \sin(t_0) \\ 1 & \mathrm{X}(t_1) & \mathrm{X}^3(t_1) & \mathrm{X}_{1.0}(t_1) & \mathrm{X}_{1.0}^3(t_1) & \mathrm{X}_{1.5}(t_1) & \mathrm{X}_{1.5}^3(t_1) & \mathrm{X}_{2.0}(t_1) & \mathrm{X}_{2.0}^3(t_1) & \sin(t_1) \\ \vdots & \vdots & \vdots & \vdots & \vdots & \vdots & \vdots & \vdots & \vdots & \vdots \\ 1 & \mathrm{X}(t_n) & \mathrm{X}^3(t_n) & \mathrm{X}_{1.0}(t_n) & \mathrm{X}_{1.0}^3(t_n) & \mathrm{X}_{1.5}(t_n) & \mathrm{X}_{1.5}^3(t_n) & \mathrm{X}_{2.0}(t_n) & \mathrm{X}_{2.0}^3(t_n) & \sin(t_n) \end{bmatrix}, \tag{9}$$

where $\mathrm{X}_\tau(t) = \mathrm{X}(t-\tau)$ and $n = 220$ were used in our tests. Ideally, if differential equation (7) is represented as (5) with (9), then the coefficient matrix should be

$$\underset{10\times 1}{\boldsymbol{\Xi}} = \left[0\ 0\ 0\ \mathbf{-1.0}\ \mathbf{-1.0}\ 0\ 0\ 0\ 0\ \mathbf{0.09}\right]^{\mathrm{T}} \tag{10}$$

after the optimization. Applying the SINDy algorithm with a threshold value $\lambda = 0.1$, the identified coefficient matrix is

$$\underset{10\times 1}{\boldsymbol{\Xi}} = \left[0\ 0\ -0.9\ \mathbf{-1.17}\ \mathbf{-0.12}\ 0\ 0\ 0\ 0\ \mathbf{0}\right]^{\mathrm{T}}, \tag{11}$$

which translates to

$$\dot{x}(t) = -0.9x^3(t) - 1.17x(t-\tau) - 0.12x^3(t-\tau), \tag{12}$$

with $\tau = 1.0$. In Fig. 2, we can see that the identified system follows the characteristic of the original system and the identified delayed terms in (12) are the expected terms. The coefficients are different and there is a dominant misidentified term $x^3(t)$, while the $\sin(t)$ term is completely missing. We can see that the found system is following the main characteristic of the experiment. This can be misleading, since it is a possible outcome of an overfitted system. To improve confidence in the identified system, we will use parameter λ to explore the system's main behavior.

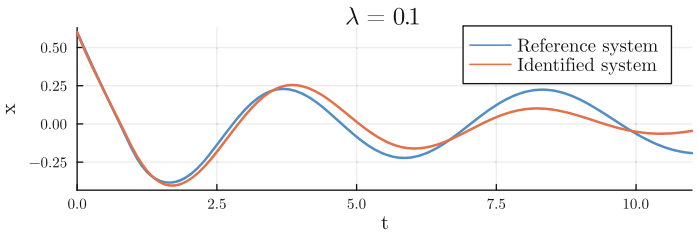

Fig. 2 Result of the SINDy operation on dataset generated with (7) using threshold $\lambda = 0.1$. Identified system (12) is presented along with the reference solution

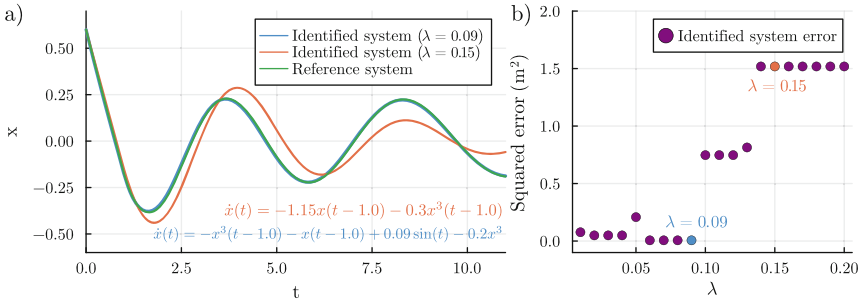

Fig. 3 (**a**) Two identified systems for different λ threshold values of the STLSQ algorithm. The reference system for this case was (7) with $\tau = 1.0$. By increasing the value of λ, we get a system with increased error on behalf of having less terms to describe it. (**b**) The errors of the identified systems are shown with respect to the λ values. Identification of the best fitting solution is possible this way. Two cases are highlighted with $\lambda = 0.09$ and $\lambda = 0.15$ thresholds in correspondence with panel a

Namely, there may be terms repeatedly appearing for different lambda values. Hence, we can be certain that those terms are strongly related to the behavior of the original system. In (6), by increasing the value of λ, we are promoting the identification of systems with fewer terms. Using an iteration for a range of λ values, we can store the mean squared error (MSE $= \frac{1}{n}\sum_{i=0}^{n}(x_{\text{ref}}(t_i) - x(t_i))^2$) of the system (by calculating the squared differences of the identified and reference system time histories) for each identified case and we can extract the delayed terms. We can find the best fitting solution that has the least error. Also, we will take the one with the highest λ value. Our goal is to find the optimum solution that has the least amount of error and contains as few terms as possible.

In Fig. 3a, the identified systems are shown for the best and worst fitting solutions. The coefficients are presented for these cases along with the reference system in Table 1.

Both systems contain the same delayed terms. The terms that influence the system can be easily identified with the method. On the other hand, with the higher $\lambda = 0.15$ value, we lost details like the time-dependent term $\sin(t)$. With the lower $\lambda = 0.09$ value, we caught the details of the system as well but there is a

Table 1 Identified coefficient values following the SINDy operation for the best and worst fitting cases with the respective mean squared errors. Reference system is (7) with $\tau = 1.0$. Results are shown visually in Fig. 3

	$x^3(t)$	$x(t-1.0)$	$x^3(t-1.0)$	$\sin(t)$	MSE
Reference	0	−1.0	−1.0	0.09	0
Fit 1 ($\lambda = 0.09$)	−0.2	−1.0	−1.0	0.09	0.006
Fit 2 ($\lambda = 0.15$)	0	−1.15	−0.3	0	1.518

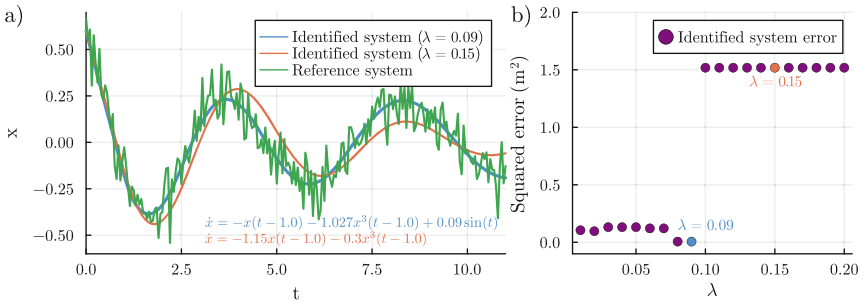

Fig. 4 (**a**) Two identified systems for different λ threshold values of the STLSQ algorithm. Same reference system as in Fig. 3a but with additional random noise with an amplitude of 0.08. (**b**) The errors of the identified systems are shown with respect to the λ values similar to Fig. 3b

Table 2 Identified coefficient values following the SINDy operation for the best and worst fitting cases with the respective mean squared errors (compared to the original system solution). Reference system is (7) with $\tau = 1.0$. Dataset is the reference system with added random noise of 0.08. Results are shown visually in Fig. 4

	$x(t-1.0)$	$x^3(t-1.0)$	$\sin(t)$	MSE
Reference	−1.0	−1.0	0.09	0
Fit 1 ($\lambda = 0.09$)	−1.0	−1.0	0.09	0.006
Fit 2 ($\lambda = 0.15$)	−1.15	−0.3	0	1.518

misidentified term x^3 appearing. All in all, the method was able to identify the most prominent terms and the identified delayed terms were correct in both cases.

In reality, this method may be used for measurement data that is often influenced by measurement noise. Hence, we also added a random noise with an amplitude of 0.08 to the input signal of our data-driven system identification; see Fig. 4. The coefficients are presented for these cases along with the reference system in Table 2.

Compared to the previous case, the identified system for $\lambda = 0.09$ is more accurate since there is only a small numerical difference in the coefficient of the $x^3(t-\tau)$ term, but the identified terms are the same as in the reference system. In the case of $\lambda = 0.15$, there is no difference compared to the case with no added noise. Additionally, we can see in Fig. 4b that the intermediate error showing up in the range from $\lambda = 0.1$ to $\lambda = 0.13$ of Fig. 3 has disappeared. All in all, the noise

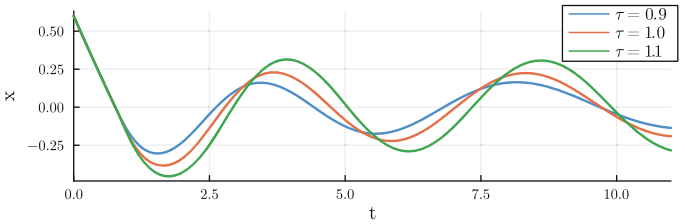

Fig. 5 Numerical solution of (7) for $\tau = 0.9$, 1.0, and 1.1 delays, with the same initial condition

Table 3 Identified coefficient values following the SINDy operation for the best and worst fitting cases with the respective mean squared errors. Reference system is (7) with $\tau = 1.0$. The candidate terms are with a tight delay distribution as (13). Here, $x_\tau^n(t) = x^n(t-\tau)$. Results are shown visually in Fig. 6

	$x(t)$	$x^3(t)$	$x_{0.9}(t)$	$x_{0.9}^3$	$x_{1.0}(t)$	$x_{1.0}^3(t)$	$x_{1.1}(t)$	$x_{1.1}^3(t)$	$\sin(t)$	MSE
Reference	0	0	0	0	−1.0	−1.0	0	0	0.09	0
Fit 1 ($\lambda = 0.03$)	0.04	−0.05	−0.9	0.29	0.3	−1.25	−0.5	0.29	0.09	0.089
Fit 2 ($\lambda = 0.16$)	0	0	−0.4	0	−0.6	−2.8	−0.16	2.5	0	0.951

had no negative impact on the identified system. This is mainly due to the fact that the system kept its main characteristic behavior.

In the previous cases, the base system defined in (8) helped in the identification since (7) shows characteristically different behavior for $\tau = 1.0$, 1.5, and 2.0. Now let us consider the base system

$$\underset{221\times 10}{\boldsymbol{\Theta}}(\mathbf{X}) = \left[\mathbf{1}\ \mathbf{X}\ \mathbf{X}^3\ \mathbf{X}_{0.9}\ \mathbf{X}_{0.9}^3\mathbf{X}_{1.0}\ \mathbf{X}_{1.0}^3\ \mathbf{X}_{1.1}\ \mathbf{X}_{1.1}^3\ \sin(\mathbf{t})\right], \tag{13}$$

i.e., select slightly different time delays for the candidate terms. The solutions of (7) for $\tau = 0.9$, 1.0, and 1.1 are shown in Fig. 5. The other parameters are set to $\alpha = 1.0$ and $\beta = 0.09$, as formerly.

The behavior of the systems for these three cases is similar and the values at each time point are close. In this case, it is expected that the algorithm will identify a system as an overfitted combination of the terms in the base system.

Based on Table 3, where the coefficients are presented for these cases along with the reference system, we can conclude that the identified systems are not close to the reference system with this tight delay distribution in the candidate terms.

According to the preliminary expectations, the algorithm constructed a system that is overfitted to the reference system in this time window.

We can improve the results by expanding the fitted dataset with a simulation from a different initial condition. This way the effect of overfitting can be reduced by providing a broader view of the behavior of the system. The solutions for two different initial conditions are shown in Fig. 7. The dataset provided for the SINDy algorithm is simply constructed by concatenation of the two cases. The resulting coefficients for this case are shown in Table 4.

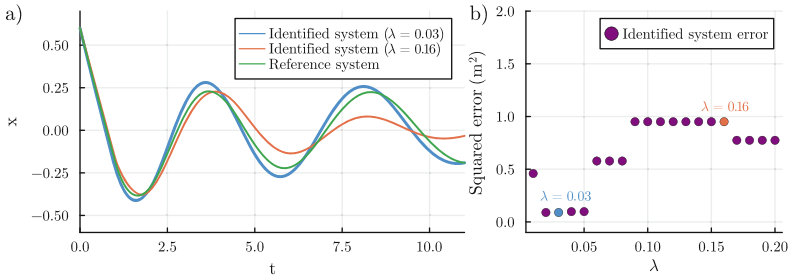

Fig. 6 (**a**) Two identified systems for the best and worst fitting cases following the SINDy operation. Reference system is (7) with $\tau = 1.0$. In this case, the SINDy operation uses tight delay distribution as the basis. (**b**) The errors of the identified systems are shown with respect to the λ values similarly to the previous cases

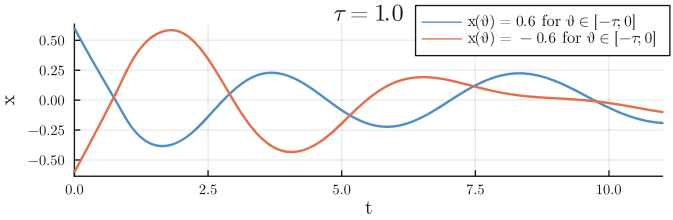

Fig. 7 Solution of (7) with $\tau = 1.0$ from two different initial conditions

Table 4 Identified coefficient values following the SINDy operation for the best and worst fitting cases with the respective mean squared errors. Reference system is (7) with $\tau = 1.0$. The candidate terms are with a tight delay distribution as (13) and dataset is based on two ICs. Results are shown visually in Fig. 8

	$x(t-0.9)$	$x(t-1.0)$	$x^3(t-1.0)$	$x(t-1.1)$	$x^3(t-1.1)$	$\sin(t)$	MSE
Reference	0	−1.0	−1.0	0	0	0.09	0
Fit 1 ($\lambda = 0.07$)	−0.6	0	−1.2	−0.4	0.21	0.09	0.078
Fit 2 ($\lambda = 0.26$)	0	−1.0	−1.07	0	0	0	3.532

In Fig. 8, the identified system for the best fitting case is still far from the reference system, but with a higher λ value, we were able to identify the proper delayed terms with the cost of losing the time-dependent $\sin(t)$ term. This is a small improvement compared to the case where the dataset was generated based on one initial condition, but it is still not trivial to identify the correct time delay with a tight delay distribution in the base system.

It is advised therefore to define a base system with sparse delay distribution. It is worth noting, however, that in both cases for the best fitting cases (Tables 3 and 4), if we sum the coefficients of the respective terms $(x(t-\tau), x^3(t-\tau))$, we obtain a close value of the original system coefficients.

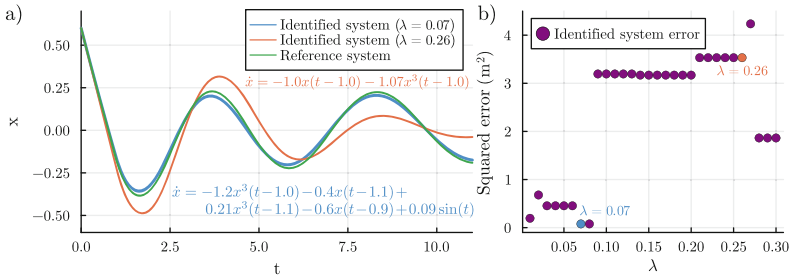

Fig. 8 (**a**) Two identified systems for the best and nearly the worst ($\lambda = 0.27$ considered as a single outlier) fitting cases following the SINDy operation. Reference system is (7) with $\tau = 1.0$ ran from two different initial conditions. (**b**) The errors of the identified systems are shown with respect to the λ values similarly to the previous cases

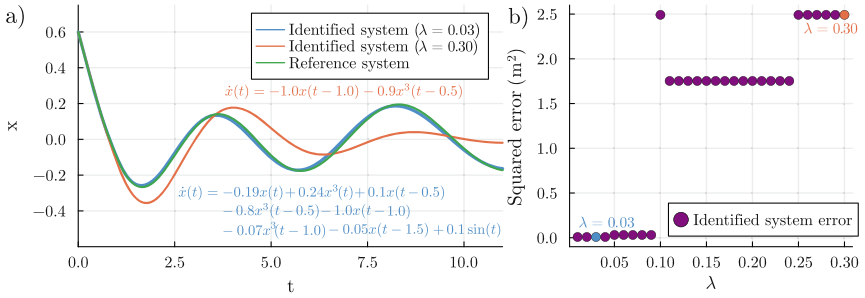

Fig. 9 (**a**) Two identified systems for the best and the worst fitting cases following the SINDy operation. Reference system is (14) with $\tau_1 = 1.0$ and $\tau_2 = 0.5$. (**b**) The errors of the identified systems are shown with respect to the λ values similarly to the previous cases

4 Time-Delay Identification of a System with Multiple Delays Using SINDy

One of the main advantages of this method is that it is applicable to systems containing multiple delays. We modify (7) and consider two separate delays:

$$\dot{x}(t) = \alpha x(t - \tau_1) + \alpha x^3(t - \tau_2) + \beta \sin(t), \tag{14}$$

where $\alpha = -1.0$, $\beta = 0.09$, $\tau_1 = 1.0$, and $\tau_2 = 0.5$. The dataset is generated based on this system for one initial condition of $x(\vartheta) = 0.6$ for $\vartheta \in [-\max\{\tau_1, \tau_2\}, 0]$. The candidate functions are

$$\underset{221\times 10}{\boldsymbol{\Theta}}(\mathbf{X}) = \left[\, \mathbf{1}\ \mathbf{X}\ \mathbf{X}^3\ \mathbf{X}_{0.5}\ \mathbf{X}^3_{0.5}\ \mathbf{X}_{1.0}\ \mathbf{X}^3_{1.0}\ \mathbf{X}_{1.5}\ \mathbf{X}^3_{1.5}\ \sin(\mathbf{t}) \,\right]. \tag{15}$$

The SINDy algorithm is performed as before. The results can be seen in Fig. 9. The resulting systems in Fig. 9a have successfully identified the time delay. In case

Table 5 Identified coefficient values following the SINDy operation for the best and worst fitting cases with the respective mean squared errors. Reference system is (14) with $\tau_1 = 1.0$ and $\tau_2 = 0.5$. Here, $x_\tau^n(t) = x^n(t-\tau)$. Results are shown visually in Fig. 9

	$x(t)$	$x^3(t)$	$x_{0.5}(t)$	$x_{0.5}^3$	$x_{1.0}(t)$	$x_{1.0}^3(t)$	$x_{1.5}(t)$	$\sin(t)$	MSE
Reference	0	0	0	−1.0	−1.0	0	0	0.09	0
Fit 1 ($\lambda = 0.03$)	−0.19	0.24	0.1	−0.8	−1.0	−0.07	−0.05	0.1	0.009
Fit 2 ($\lambda = 0.30$)	0	0	0	−0.9	−1.0	0	0	0	2.491

of $\lambda = 0.04$, there are a lot of misidentified terms, but the dominant terms are correct for the time delay. The $\lambda = 0.3$ case however was able to identify the correct and only the correct delayed terms, while the $\sin(t)$ term was completely missing. All in all, this method is able to identify multiple delays in a single system.

5 Conclusion

We have found that on simulated nonlinear systems, the SINDy algorithm worked well with the proposed method for delay identification. Our main focus was on the identification of the delayed terms. As it can be seen in Tables 1, 2, 4, and 5, the delayed terms were properly identified by simultaneously analyzing the best and worst fitting cases. Moreover, if we look at the best fitting cases, we find that the excitation (as a term that has smaller effect in our case) was captured in all cases. It should be noted, however, that the focus was not on the construction of the basis during our experiment. We introduced the excitation as a known part of the system. We did not introduce any other candidate terms, so we could focus on the capabilities of the delay identification. In our study, the physically meaningful range of delays had to be determined for the algorithm and the candidate terms had to be introduced with a sparse delay distribution. We experienced difficulties when the delays were closely separated and the found systems were often constructed as a linear combination of those terms. In this case, extracting data related to different initial conditions helped. The developed method is also capable of identifying multiple time delays in the same system which was also tested successfully.

Acknowledgments The research reported in this paper was partly supported by the János Bolyai Research Scholarship of the Hungarian Academy of Sciences and by the National Research, Development and Innovation Office under grant no. NKFI-128422 and under grant no. 2020-1.2.4-TÉT-IPARI-2021-00012.

References

1. Rackauckas, C., Ma, Y., Martensen, J., Warner, C., Zubov, K., Supekar, R., Skinner, D., Ramadhan, A., Edelman, A.: Universal Differential Equations for Scientific Machine Learning (2020). https://doi.org/10.48550/ARXIV.2001.04385
2. Brunton, S.L., Proctor, J.L., Nathan Kutz, J.: Discovering governing equations from data by sparse identification of nonlinear dynamical systems. Proc. Natl. Acad. Sci. **113**(15), 3932–3937 (2016)
3. Brunton, S.L., Nathan Kutz, J.: Data-Driven Science and Engineering: Machine Learning, Dynamical Systems, and Control. Cambridge University Press, University Printing House, Cambridge, UK (2019). ISBN: 9781108422093
4. Schmid, P.: Dynamic mode decomposition of numerical and experimental data. J. Fluid Mech. **656**, 5–28 (2010). https://doi.org/10.1017/S0022112010001217

Uncertainty Quantification in Parameter Estimation Using Physics-Integrated Machine Learning

Zihan Liu, Amirhassan Abbasi, Prashant N. Kambali, and C. Nataraj

1 Introduction

Physics-based modeling of dynamic systems is built upon two main components. The first component is model development in which an accurate abstraction of the dynamic system is obtained based on deductive reasoning and empirical data applied to well-established laws such as Newton's laws of motion or the laws of thermodynamics. The models usually are parameterized mathematically to represent the system's behavior in compliance with physical principles. This parametrization endows the models with reusability over the systems with the same underlying physics. Achieving this goal needs parameter estimation which is the focus of the second component of modeling. Accurate parameter estimation in addition to addressing the reusability of models can provide additional benefits. For instance, it can be informative about fundamental changes in the dynamics of the system owing to reasons such as system drift, incipient faults, and operational mode variation. It should be emphasized that reliable identification of these root causes depends on an assumption that the physics-based model remains accurate under changing conditions [1].

Traditional methods of parameter estimation aimed to minimize the deviation between model output and measured response data to estimate some specific parameters [2, 3]. The performance of these methods degrades in many engineering systems with complex, nonlinear, and multidimensional dynamics. In such systems, considering simplifying assumptions is unavoidable which expands the gap between reality and model prediction. The physics-based model would potentially be able to

Z. Liu · A. Abbasi · P. N. Kambali · C. Nataraj (✉)
Villanova Center for Analytics of Dynamic Systems, Villanova University, Villanova, PA, USA
e-mail: zliu5@villanova.edu; aabbasi@villanova.edu; prashant.kambali@villanova.edu; nataraj@villanova.edu
http://vcads.org

© The Author(s), under exclusive license to Springer Nature Switzerland AG 2024

W. Lacarbonara (ed.), *Advances in Nonlinear Dynamics, Volume III*, NODYCON Conference Proceedings Series, https://doi.org/10.1007/978-3-031-50635-2_46

capture generic behaviors in such cases but the lack of specifications is a major obstacle in parameter estimation. Therefore, the dynamics of systems and the interdependence of parameters are obscure in such cases.

Advancements in techniques of information mining from data have shown promising improvements in parameter estimations of dynamic systems. More recently, hybrid physics-machine learning methods have provided a unique opportunity for combining generic behaviors of systems captured by physics with its specification learned from data [4, 5]. Liu et al. [6] used proper orthogonal decomposition and smooth orthogonal decomposition methods to reduce the complexity of measured data and developed an artificial neural network to map processed data onto different gear defects. Laurain et al. [7] used least-squares support vector machines to identify nonlinear systems and employed instrumental variable-based estimation to find the optimal solution of parameter estimations. Mohamad et al. [8] proposed a long short-term memory conventional neural network to integrate dynamics information for the diagnosis of gear faults. Raissi and Karniadakis [9] introduced hidden physics models to leverage the underlying laws of physics for learning problems, system identification, or data-driven discovery of partial differential equations. Samadani et al. [10, 11] proposed the phase space topology (PST) method which quantifies the topological characteristics of a phase portrait of a dynamic system to extract appropriate features for training machine learning models. Mohamad et al. [12] discussed the applicability of the PST methods and extended this method to system identification, diagnostics, and health state estimation.

It should be noted that the root cause of variation in response to engineering systems is usually multifactorial or a combination of partial effects from different factors. For example, the health variation in the dynamic systems is under the effect of single or multiple degradation modes like age, fatigue, wear, etc. And the interactions between them lead to the variation of responses which is a combination of different reasons. Hence, probabilistic reasoning is an inevitable part of parameter estimation. In addition, uncertainty quantification carried out in this type of reasoning is critically important to guide decision-making that would need to follow. Also, from a practical point of view, it is important to evaluate the uncertainties of the estimated parameters to guarantee the stability or safety limitations of operations [13]. Therefore, more and more efforts have been expended recently toward probabilistic reasoning for parameter estimation. Tran et al. [14] employed the adaptive Markov chain Monte Carlo sampling to estimate the parameters of a biological system and quantified the uncertainty in the estimated parameters. Abbasi et al. [15] leveraged the Gaussian process model to quantify and reduce the uncertainties of the time response of a nonlinear pendulum. Ghani and Banazadeh [16] used the response characteristics in the frequency domain to identify the accurate model of quadcopters under the uncertainty of moment of inertia. Kwuimy and Nataraj [17] studied the horseshoes' chaos under the uncertainty of stiffness for active magnetic bearings.

This paper proposes a hybrid model which uses physics-based features extracted from analytical solutions obtained from the method of multiple scales. These features are fed into a Gaussian regression model (GPR) to estimate unknown parameters and the confidence interval over the estimations. Physics-based features are more informative which results in high accuracy, enhancement of generalization, robustness, and interpretability of the trained GPR model. Synthesizing data with the perturbation method (method of multiple scales in this paper) can boost the quality of physics-based features. Moreover, in the case of a system with complex dynamics and nonlinearity, numerical simulations fail to capture the whole response because of the choice of initial conditions, unstable solutions, etc. Additionally, in numerical simulation, one needs to extract each point from the stable time response, excite the system with different frequencies, choose the frequency resolution, change time of the transient response, etc. resulting in high computational cost. This further encourages one way to use analytical solutions to extract physics-based features.

2 Methodology

The flowchart of the proposed method and the comparison with data-based modeling is demonstrated in Fig. 1, assuming the governing equation of the target system is given and all parameters are identified accurately. Because of the variation of specific parameters from operational condition 1 to operational condition 2, deviations between the measured data from operational condition 2 and model output are observed. The proposed method aims to estimate changed parameters by incorporating measured data from operational condition 2 and quantify the uncertainty of the estimations. For data-based modeling, the obtained governing equations are simulated numerically to obtain time responses. By exciting the system with different frequencies, the frequency response is accessible and data-based features are able to be extracted from it. By varying the interest parameters and repeating the above process, feature sets corresponding to varying parameters are obtained to train a Gaussian process regression model which is marked as model 2 in Fig. 1. Then, the data-based features extracted from measured data are fed into the trained model 2 to estimate changed parameters. When it comes to the proposed hybrid modeling, the governing equation is analyzed by the perturbation method to derive the asymptotic solutions. Then, it is accessible to parameterize the system by varying different parameters and obtain corresponding frequency responses. Based on that, effective features can be extracted for training GPR models. By inputting physics-based features from measured data at operational condition 2 into the trained GPR model, we can obtain the estimations of target parameters and the confidence interval over it.

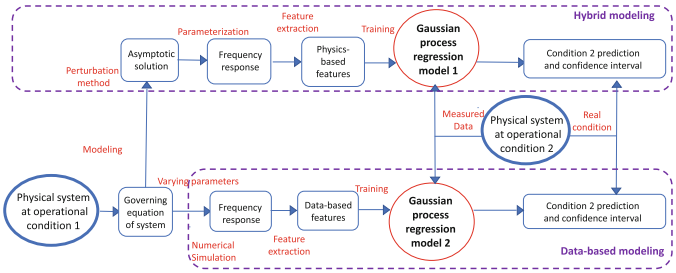

Fig. 1 Flowchart of the proposed method

3 Asymptotic Analysis

In this section, we consider a system of two linearly coupled Duffing oscillators with cosine excitation applied to the first oscillator. Such a model is an oft-used candidate for the description of various physical and electromechanical systems. Moreover, its dynamics has been widely studied by many previous works [18]. Equation 1 demonstrates the governing equation of the linearly coupled Duffing oscillator system with cosine excitation applied to the first oscillator:

$$\begin{aligned} x_1'' + w_0^2 x_1 + d x_1' + \beta x_1^3 + \delta(x_1 - x_2) &= F \cos \Omega t \\ x_2'' + w_0^2 x_2 + d x_2' + \beta x_2^3 + \delta(x_2 - x_1) &= 0 \end{aligned} \tag{1}$$

where x_1 is the displacement of the first oscillator and x_2 is the displacement of the second oscillator, $'$ indicates the first-order derivative with respect to time and $''$ denotes the second-order derivative with respect to time, ω_0^2 is the stiffness, d is the damping, δ is the coefficient of coupling, F is the amplitude of excitation, and Ω is the frequency of excitation.

The method of multiple scales (MMS) is leveraged here to solve Eq. 1 analytically [19]. Assuming displacements as functions of multiple time scales, $T_0 = t$, $T_1 = \epsilon t$ as below:

$$\begin{aligned} x_1 &= x_{10}(T_0, T_1) + \epsilon x_{11}(T_0, T_1) \\ x_2 &= x_{20}(T_0, T_1) + \epsilon x_{21}(T_0, T_1) \end{aligned} \tag{2}$$

where ϵ is a dimensionless small positive number.

The damping, excitation, and nonlinear term are then rescaled as $d = \epsilon d$, $F = \epsilon f$, $\beta = \epsilon \beta$. Substituting them into Eq. 1 and comparing different powers of ϵ up to the second order yields the following sets of equations:

$$
\begin{aligned}
&O(\epsilon^0): \\
&\qquad D_0^2 x_{10} + w_0^2 x_{10} + \delta x_{10} - \delta x_{20} = 0 \\
&\qquad D_0^2 x_{20} + w_0^2 x_{20} + \delta x_{20} - \delta x_{10} = 0
\end{aligned} \tag{3}
$$

$$
\begin{aligned}
&O(\epsilon^1): \\
&D_0^2 x_{11} + w_0^2 x_{11} + \delta x_{11} - \delta x_{21} \quad = -2D_0 D_1 x_{10} - d D_0 x_{10} - \beta x_{10}^3 + f \cos \Omega t \\
&D_0^2 x_{21} + w_0^2 x_{21} + \delta x_{21} - \delta x_{11} \quad = -2D_0 D_1 x_{20} - d D_0 x_{20} - \beta x_{20}^3
\end{aligned} \tag{4}
$$

The solution for homogeneous second-order differential equations in Eq. 3 is as follows:

$$
\begin{aligned}
x_{10} &= A_1 e^{i w_1 T_0} + A_2 e^{i w_2 T_0} + cc \\
x_{20} &= A_1 e^{i w_1 T_0} - A_2 e^{i w_2 T_0} + cc
\end{aligned} \tag{5}
$$

where cc denotes conjugate complex, w_1 and w_2 are the damped natural frequencies, $A_1 = \frac{1}{2} a_1 e^{i\beta_1}$, and $A_2 = \frac{1}{2} a_2 e^{i\beta_2}$. The expressions of w_1 and w_2 are shown as follows:

$$
w_1 = w_0, w_2 = \sqrt{w_0^2 + 2\delta} \tag{6}
$$

The detuning parameters σ_1, σ_2 are introduced into the analysis:

$$
\Omega = w_1 + \epsilon\sigma_1, w_2 = w_1 + \epsilon\sigma_2 \tag{7}
$$

Subsequently, we get the following set of autonomous forms of modulation equations as follows:

$$
\begin{aligned}
a_1' &= -\frac{1}{2} d a_1 + \frac{1}{4w_1} f \sin(\gamma_1) \\
\gamma_1' &= \sigma_1 - \frac{3}{8w_1} \beta a_1^2 - \frac{3}{4w_1} \beta a_2^2 + \frac{1}{4w_1 a_1} f \cos(\gamma_1) \\
a_2' &= -\frac{1}{2} d a_2 + \frac{1}{4w_2} f \sin(\gamma_2) \\
\gamma_2' &= \sigma_1 - \sigma_2 - \frac{3}{8w_2} \beta a_2^2 - \frac{3}{4w_2} \beta a_1^2 + \frac{1}{4w_2 a_2} f \cos(\gamma_2)
\end{aligned} \tag{8}
$$

where

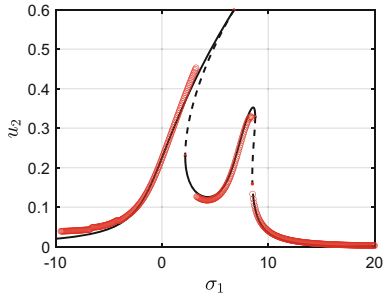

Fig. 2 Frequency response generated by the method of multiple scales (MMS) and numerical simulation

$$\gamma_1 = \sigma_1 T_1 - \beta_1, \gamma_2 = \sigma_1 T_1 - \sigma_2 T_1 - \beta_2 \tag{9}$$

By solving Eq. 8 and substituting the obtained $a_1, \gamma_1, a_2, \gamma_2$, Eq. 9, and Eq. 7 into Eq. 5, we obtained the following equation:

$$\begin{aligned} x_{10} &= a_1 \cos(w_1 t + \sigma_1 T_1 - \gamma_1) + a_2 \cos(w_1 t + \sigma_1 T_1 - \gamma_2) \\ x_{20} &= a_1 \cos(w_1 t + \sigma_1 T_1 - \gamma_1) - a_2 \cos(w_1 t + \sigma_1 T_1 - \gamma_2) \end{aligned} \tag{10}$$

In Eq. 10, x_{10} and x_{20} are expressed as two cosine functions with the same frequency but different phases. Therefore, they can be transferred into the following form:

$$\begin{aligned} x_{10} &= u_1 \cos((w_1 + \epsilon\sigma_1)t + \Gamma_1) \\ x_{20} &= u_2 \cos((w_1 + \epsilon\sigma_1)t + \Gamma_2) \end{aligned} \tag{11}$$

where u_1, u_2 are the amplitudes of x_{10} and x_{20} and Γ_1 and Γ_2 are the phases of x_{10} and x_{20}. They are determined by a_1, γ_1, a_2, and γ_2.

Choosing $w_0 = 1$, $f = 1$, $d = 1$, $\epsilon = 0.1$, $\beta = 70$, and $\delta = 1$, σ_2 is calculated as 7.3 according to Eq. 6 and Eq. 7; the frequency responses generated by both asymptotic analysis (solid line and dash line) and numerical simulation (red circles) are shown in Fig. 2. The comparison between asymptotic and numerical solutions is in good agreement as depicted in Fig. 2 except for high amplitude solutions, unstable solutions, and jump points.

4 Gaussian Process Regression Model

The Gaussian process model is a probabilistic supervised machine learning framework developed by computer science and statistics communities widely used for regression and classification tasks [20]. Based on this, a GPR model can make estimations incorporating prior knowledge (kernels) and provide uncertainty measures over these estimations [21].

The GPR model is based on some prior knowledge. The regression function modeled by a multivariate Gaussian is given as follows:

$$P(g|X) \sim \mathcal{N}(g|\mu, K) \tag{12}$$

where $X = [x_1, ..., x_n] \in \mathbb{R}^{d \times n}$, $g = [g(x_1), ..., g(x_n)]$, $\mu = [m(x_1), ..., m(x_n)]$, and $K_{ij} = k(x_i, x_j)$. X are the observed data points, m represents the mean function, and k represents a positive definite kernel function.

The process of conducting regressions by the Gaussian process model is that, given the observed data and a mean function g estimated by these observed data points, we make estimations at new points X^* as $g(X^*)$. The joint distribution of g and g^* is then expressed as follows:

$$\begin{bmatrix} g \\ g^* \end{bmatrix} \sim \mathcal{N}\left(\begin{bmatrix} m(X) \\ m(X^*) \end{bmatrix}, \begin{bmatrix} K & K^* \\ K^{*T} & K^{**} \end{bmatrix} \right) \tag{13}$$

In more realistic situations, we do not have access to true function values but noisy versions as $y = g(x) + \epsilon$. Assuming there is an additive independent and identically distributed Gaussian noise with variance σ_n^2, the prior on the noisy observations becomes $cov(y) = K + \sigma_n^2 I$. The joint distribution of the observed values and the function values at new testing points is obtained as follows:

$$\begin{bmatrix} y \\ g^* \end{bmatrix} \sim \mathcal{N}\left(0, \begin{bmatrix} K + \sigma_n^2 I & K^* \\ K^{*T} & K^{**} \end{bmatrix} \right) \tag{14}$$

5 Coupling Coefficient Estimations

The coupling coefficient usually plays a critical role in modeling, analyzing, and simulating a coupled system. It is also one of the root reasons for the complexity of a system due to the connection of multiple single simple systems. In this section, the proposed hybrid modeling method is designed to apply to the linearly coupled Duffing oscillator system for coupling coefficient estimation.

5.1 Physics-Based Features and Data-Based Features

Figure 3a depicts the feature extraction from nonlinear frequency response curves of oscillator two. The jump phenomena observed in nonlinear frequency response are the critical points where the bifurcation occurs and indicates the change in stability of the response. These points are indicated by numbers 1 and 2 for the jump down points and 3 and 4 for the jump up points separately. We select the amplitudes

and frequencies at these points as our features, and they are denoted by a_{ij} for amplitudes, fre_{ij} for frequencies where $i = 1, 2$ corresponds to oscillators one and two, and $j = 1, 2$ and $3, 4$ correspond to jump down and jump up points. Furthermore, the bending of the frequency response is a quantitative measure of the system's nonlinearity, as determined by slopes at bifurcation points. As a result, the slopes α_{ij} depicted in Fig. 3 are likewise chosen as features for our research, where $i = 1, 2$ corresponds to oscillators one and two and $j = 1, 2$ denote the bending of the first resonance and the second resonance.

Figure 3b demonstrates the data-based features extracted from numerical simulations. The general features like the two peaks, the locations of the two peaks, the minimum value, the medium value, the average, and the root mean square extracted here represent data-based features. We continue to use the first subscript $1, 2$ to denote oscillator one and oscillator two and use the second subscript to distinguish different resonance peaks. For example, loc_{22} represents the location of the second resonance peak in oscillator two. The choice of features for each method of analysis (data-based or physics-based) can be different in order to get optimal results. Therefore, please note that the data-based features from numerical simulations are necessarily different from physics-based features extracted from the method of multiple scales shown in Table 1.

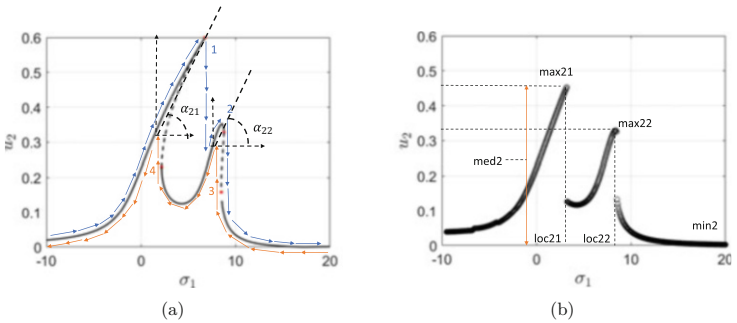

Fig. 3 Feature extraction: (**a**) physics-based features, (**b**) data-based features

Table 1 Features extracted from asymptotic solution and numerical simulation

Physics-based features	a_{11}	fre_{11}	a_{12}	fre_{12}	a_{13}	fre_{13}	a_{14}	fre_{14}	α_{11}	α_{12}
	a_{21}	fre_{21}	a_{22}	fre_{22}	a_{23}	fre_{23}	a_{24}	fre_{24}	α_{21}	α_{22}
Data-based features	max_{11}	loc_{11}	max_{12}	loc_{12}	min_1	med_1	$mean_1$	rms_1		
	max_{21}	loc_{21}	max_{22}	loc_{22}	min_2	med_2	$mean_2$	rms_2		

5.2 Development of the GPR Model

5.2.1 Data Generation

For data-based features, we randomly generated 100 coupling coefficients satisfying a normal distribution with expectation 1.5 and variance 0.3; these coupling coefficients are substituted into governing equations, Eq. 1, and the Runge-Kutta method is leveraged to solve it numerically. Then, other 30 coupling coefficients are generated to produce a test set. As for physics-based features, 100 coupling coefficients with the same norm distribution are also generated and substituted into modulation equations, Eq. 8, to generate frequency responses for extracting physics-based features. Similarly, another 30 coupling coefficients are generated for the test set.

5.2.2 Hyper-parameter Determination

In order to demonstrate the effectiveness of different features more directly, it is better to circumvent the complex construction of GPR models. Therefore, we choose a typical squared exponential kernel function. The ratio of the training set, validation set, and test set in the training process and the initial kernel parameters are determined by grid search technique estimated by the regression loss. The k-fold cross-validation technique is also used to guarantee the independence of different portions of the data.

5.3 Weak Nonlinear Scenario

In this case, the nonlinear coefficient β is chosen as 1. By substituting it in the asymptotic solutions, one of the related frequency responses is shown in Fig. 4a. Different sets of physics-based features are extracted with changing coupling coefficients from the generated frequency responses. Data-based features are available using the same nonlinear coefficient β and coupling coefficient with the same distribution as well. Two developed GPR models are trained and fine-tuned by feeding the extracted features. Then, the estimations of the coupling coefficient and related confidence interval obtained from the trained GPR models by inputting new data are shown in Fig. 5. The output of the GPR model trained by the physics-based model is displayed in Fig. 5a, and Fig. 5b demonstrates the output of the data-based GPR model. From Fig. 5a, it is observed that a better linear relationship between feature fre_{12} and the coupling coefficient and all real coupling parameters exists within the confidence interval. This demonstrates that the effectiveness of estimating confidence interval is better using a physics-based model compared to a data-based GPR model as shown in Fig. 5b.

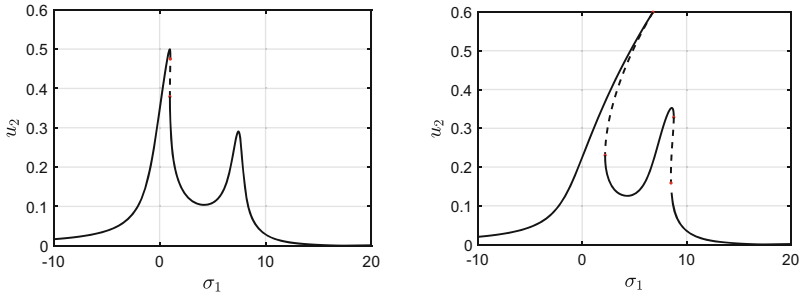

Fig. 4 Frequency response where the red points are the saddle node points, and the black dash line indicates the unstable solutions: (**a**) nonlinear coefficient $\beta = 1$ and (**b**) nonlinear coefficient $\beta = 7$

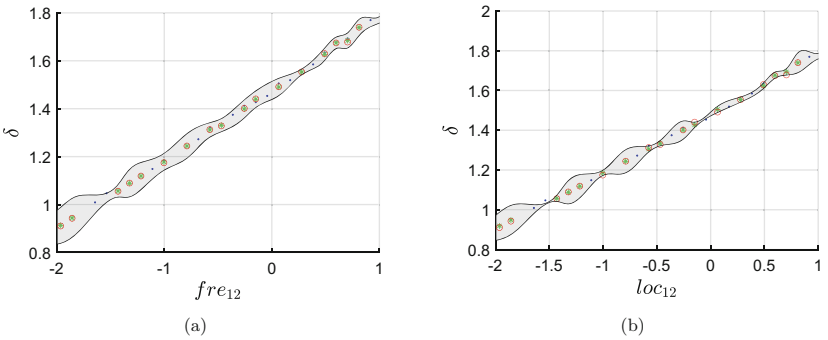

Fig. 5 Regression of extracted features and predicted coupling coefficients under weak nonlinearity where the black points are observed points, the green stars represent the estimations of the GPR model, the red circles demonstrate the real coupling parameters, and the gray area is the estimated confidence interval (**a**) using physics-based features and (**b**) using data-based features

The root mean square error (RMSE) of estimations and the regression loss are used to evaluate the performance of two GPR models. For the model developed with the physics-based features, the regression loss is found to be $6.69e^{-6}$ and the RMSE is 0.0025. For the GPR model trained with data-based features, the regression loss is calculated as $6.618e^{-6}$ and the RMSE is 0.0081. These results indicate the similar performance of the two models in the circumstance of weakly nonlinear systems. This is most likely because the bending of the resonance peak is relatively insignificant when the nonlinearity is weak. Therefore, the physical-based features and data-based features are close to some extent. We next explore if the physics-based features are indeed superior to data-based features in capturing nonlinear characteristics when the strength of the nonlinearity is increased.

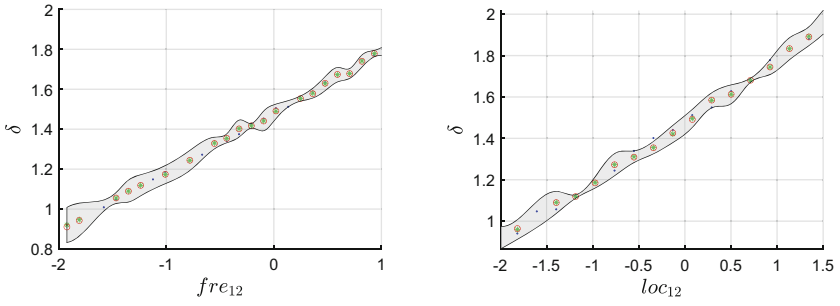

Fig. 6 Regression of extracted features and predicted coupling coefficients under strong nonlinearity where the black points are observed points, the green stars represent the estimations of the GPR model, the red circles demonstrate the real coupling parameters, and the gray area is the estimated confidence interval: (**a**) using physics-based features and (**b**) using data-based features

5.4 Strong Nonlinearity

In this case, the nonlinear coefficient is set as $\beta = 7$. We can observe pronounced bending and multiple solution phenomena in Fig. 4b. Based on these frequency responses with varying coupling coefficients, both physics-based features and data-based features are extracted to develop GPR models for coupling coefficient estimations.

The outputs of both physics-based and data-based GPR models are demonstrated in Fig. 6. Similarly, the black points are observed points, the green stars represent the estimations of the GPR model, the red circles demonstrate the real coupling parameters, and the gray area is the estimated confidence interval. Compared to the case with weak nonlinearity, larger deviations between prediction and targets are observed, which demonstrates the influence of strong nonlinearity.

In this case of strong nonlinearity, for the model developed with the physics-based model, we obtained regression loss as $1.0507e^{-5}$ and RMSE as 0.0032, while for the data-based GPR model, the regression loss is $3.7056e^{-4}$ and the RMSE is 0.0192. The dramatically increased regression loss and RMSE of the data-based GPR model validate the pronounced effect of nonlinearity in degrading the data-based features. This likewise indicates the robustness of physics-based features given that the regression loss and RMSE are similar to the case of weak nonlinearity.

5.5 Uncertain Parameter Scenario

The applicability of a model would largely depend on the uncertainty of parameters. Therefore, it is reasonable to take parameter uncertainties into account. In this scenario, we add uncertainties satisfying a normal distribution to the coupling

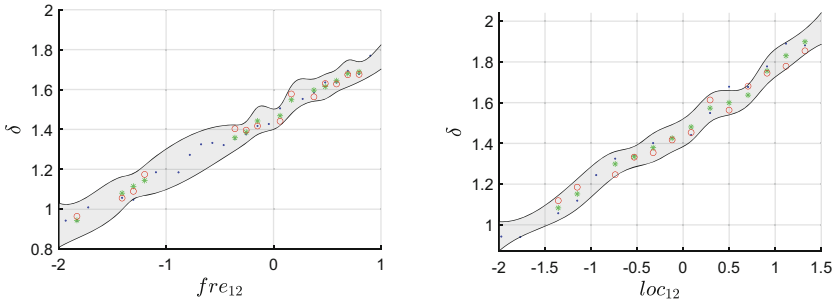

Fig. 7 Regression of extracted features and predicted coupling coefficients under parameter uncertainty where the black points are observed points, the green stars represent the estimations of the GPR model, the red circles demonstrate the real coupling parameters, and the gray area is the estimated confidence interval: (**a**) using physics-based features and (**b**) using data-based features

coefficient. The expectation of uncertainties is set at 10% of the real coefficients. We again use a weak nonlinear coefficient $\beta = 1$ to generate the frequency response for feature extraction. The outputs of the physics-based GPR model and the data-based GPR model are compared and plotted in Fig 7. In this case, the RMSE of the physics-based GPR model is 0.0261, and the corresponding regression loss is $6.8369e^{-4}$. For the data-based GPR model, we get an RMSE of 0.0339 and a regression loss of 0.00114.

To summarize, in the above analysis, the physics-based features are compared with data-based features under weak nonlinearity, strong nonlinearity, and uncertain parameter situations. In the case of weak nonlinearity, we observed similar results of estimation for both the physics-based GPR model and the data-based GPR model. However, with an increase in the nonlinearity of the system, the larger bending and increased complexity comprise the performance of data-based features, while the physics-based features are able to capture the nonlinear characteristics and achieve high accuracy of parameter estimation. The uncertain parameter scenario is a challenge for both GPR models discussed in this paper. In the situation with uncertain parameters, the increase in RMSE and regression loss is observed for both the physics-based GPR model and the data-based GPR. However, estimations using a physics-based model can still maintain higher accuracy than estimations using a data-based model.

6 Conclusion

This paper proposes a Gaussian process regression (GPR) model integrated with physics-based features to estimate unknown parameters and the uncertainty over these estimations. These physics-based features are extracted from asymptotic

solutions derived from the perturbation method. The typically nonlinear jump phenomenon is quantified using features such as amplitude and frequency at the saddle node point. A GPR model trained by these features is able to estimate unknown parameters and calculate the confidence interval over the estimations. A linearly coupled Duffing oscillator system is chosen in this paper to demonstrate the proposed method. Corresponding features are generated by changing the coupling coefficient of the system. These physics-based features are extracted under weak nonlinearity, strong nonlinearity, and uncertain parameter scenarios. Common data-based features like the maximum, minimum, average, RMSE, and median are employed to train a GPR model as a comparison. The final results show that the GPR model trained by physics-based features is superior to the data-based GPR model. Especially under a strong nonlinear situation, the proposed method has a significant advantage. This strongly suggests the effectiveness and robustness of the proposed method.

It is of course necessary to verify the effectiveness of the proposed method with a real experiment. The future work of the research focuses on extending this method to a designed experimental setup. The performances of estimating different parameters like damping, stiffness, and excitation need to be investigated and compared.

Acknowledgments This project was supported by research grants from the Office of Naval Research (Grant No. N00014-19-1-2070 and N00014-22-1-2480). We are grateful to ONR and Capt. Lynn Petersen, the program manager, for recognizing the importance of this work.

References

1. Chintha, H.P., Chatterjee, A.: Identification of nonpolynomial forms of damping nonlinearity in dynamic systems using harmonic probing and higher order frfs. In: Advances in Nonlinear Dynamics, pp. 357–368. Springer (2022)
2. Li, Y., O'Neill, Z., Zhang, L., Chen, J., Im, P., DeGraw, J.: Grey-box modeling and application for building energy simulations-a critical review. Renew. Sustain. Energy Rev. **146**, 111174 (2021)
3. Kristensen, N.R., Madsen, H., Jørgensen, S.B.: Parameter estimation in stochastic grey-box models. Automatica **40**(2), 225–237 (2004)
4. Pillonetto, G., Dinuzzo, F., Chen, T., De Nicolao, G., Ljung, L.: Kernel methods in system identification, machine learning and function estimation: A survey. Automatica **50**(3), 657–682 (2014)
5. Nataraj, C., Kappaganthu, K.: Vibration-based diagnostics of rolling element bearings: state of the art and challenges. In: 13th World Congress in Mechanism and Machine Science, Guanajuato, Mexico, June 19–25 (2011)
6. Liu, Z., Mohamad, T.H., Ilbeigi, S., Nataraj, C.: Early detection of cracks in a gear-train system using proper and smooth orthogonal decompositions. In: Advances in Nonlinear Dynamics, pp. 451–461. Springer (2022)
7. Laurain, V., Tóth, R., Piga, D., Zheng, W.X.: An instrumental least squares support vector machine for nonlinear system identification. Automatica **54**, 340–347 (2015)
8. Mohamad, T.H., Abbasi, A., Kim, E., Nataraj, C.: Application of deep cnn-lstm network to gear fault diagnostics. In: 2021 IEEE International Conference on Prognostics and Health Management (ICPHM), pp. 1–6. IEEE (2021)

9. Raissi, M., Karniadakis, G.E.: Hidden physics models: Machine learning of nonlinear partial differential equations. J. Comput. Phys. **357**, 125–141 (2018)
10. Samadani, M., Kwuimy, C.A., Nataraj, C.: Characterization of the nonlinear response of defective multi-dof oscillators using the method of phase space topology (pst). Nonlinear Dyn. **86**(3), 2023–2034 (2016)
11. Samadani, M., Kuimy, C.A.K., Nataraj, C.: Characterization of phase space topology using density: application to fault diagnosticsc. In: Annual Conference of the Prognostics and Health Management Society (2015)
12. Mohamad, T.H., Nazari, F., Nataraj, C.: A review of phase space topology methods for vibration-based fault diagnostics in nonlinear systems. J. Vib. Eng. Technol. **8**(3), 393–401 (2020)
13. Levi, D., Gispan, L., Giladi, N., Fetaya, E.: Evaluating and calibrating uncertainty prediction in regression tasks. Sensors **22**(15), 5540 (2022)
14. Tran, J.S., Schiavazzi, D.E., Ramachandra, A.B., Kahn, A.M., Marsden, A.L.: Automated tuning for parameter identification and uncertainty quantification in multi-scale coronary simulations. Comput. Fluids **142**, 128–138 (2017)
15. Abbasi, A., Nataraj, C.: Physics-informed machine learning for uncertainty reduction in time response reconstruction of a dynamic system. IEEE Internet Comput. **26**(4), 35–44 (2022)
16. Ghani, M., Banazadeh, A.: Accurate model identification of quadcopters with moments of inertia uncertainty and time delay. In: Advances in Nonlinear Dynamics, pp. 391–403. Springer (2022)
17. Kitio Kwuimy, C.A., Nataraj, C.: Prediction of horseshoes chaos in active magnetic bearings with time-varying stiffness. In: Proceedings of ASME 2011 International Design Engineering Technical Conferences & Computers and Information in Engineering Conference IDETC/CIE 2011, vol. DETC2011-48317, Washington, DC, USA, August 29–31, 2011. ASME
18. Jothimurugan, R., Thamilmaran, K., Rajasekar, S., Sanjuán, M.A.F.: Multiple resonance and anti-resonance in coupled duffing oscillators. Nonlinear Dyn. **83**(4), 1803–1814 (2016)
19. Kambali, P.N., Pandey, A.K.: Nonlinear coupling of transverse modes of a fixed–fixed microbeam under direct and parametric excitation. Nonlinear Dyn. **87**(2), 1271–1294 (2017)
20. Liu, H., Ong, Y.-S., Shen, X., Cai, J.: When gaussian process meets big data: A review of scalable gps. IEEE Trans. Neural Networks Learn. Syst. **31**(11), 4405–4423 (2020)
21. Seeger, M.: Gaussian processes for machine learning. Int. J. Neural Syst. **14**(02), 69–106 (2004)

Physics-Enhanced Sparse Identification of Nonlinear Oscillator with Coulomb Friction

Christos Lathourakis and Alice Cicirello

1 Introduction

The understanding of friction damping in structural dynamics is a key challenge in structural engineering. Frictional joints are present in most applications and fields, including aerospace, automotive, and buildings. The friction force identification in joints is difficult due to its nonlinear and non-smooth nature. To tackle this, alternative friction laws have been proposed [1, 2], and friction models have been validated by using experimental data [2–4]. An alternative is to take advantage of the rapid increase in data availability and of the newly developed techniques for identifying the underlying differential equations of physical problems based on noisy measurements. A promising framework called sparse identification of nonlinear dynamics (SINDy) was developed in [5] for deriving parsimonious solutions for nonlinear systems and has already been applied to the identification of smooth localized nonlinearities [6–8]. However, frictional problems might require the identification of non-smooth friction laws, often based on limited and noisy measurements obtained during stick-slip phenomena [9]. This paper investigates the applicability of state-of-the-art techniques based on SINDy (the so-called RK4-SINDy [10]) to identify the governing equation of a single degree of freedom (SDOF) system with a Coulomb friction contact. In particular, the inclusion of known physics in the identification process is going to be explored. Both synthetic and experimental noisy measurements will be considered for a continuous motion of the oscillator (no stick-slip).

C. Lathourakis · A. Cicirello (✉)
Faculty of Civil Engineering and Geosciences, Delft University of Technology, Delft, Netherlands
e-mail: ac685@cam.ac.uk

© The Author(s), under exclusive license to Springer Nature Switzerland AG 2024

W. Lacarbonara (ed.), *Advances in Nonlinear Dynamics, Volume III*, NODYCON Conference Proceedings Series, https://doi.org/10.1007/978-3-031-50635-2_47

2 Sparse Identification with Runge-Kutta Constraint (RK4-SINDy): A Review

Sparse identification aims at identifying a potentially nonlinear model with the fewest terms required to describe how the measurement data changes in time. The Runge-Kutta inspired sparse identification scheme, the so-called RK4-SINDy, was introduced in [10] and focuses on deriving the underlying nonlinear differential equations of dynamical systems based on corrupted and/or sparsely collected data. The two core concepts coupled in this framework are SINDy [5] and the fourth-order Runge-Kutta integration scheme applied to a mathematical model of the physical system expressed as a first-order differential equation.

Let us consider a dynamical system that is described by the following equation:

$$\dot{\mathbf{x}}(t) = \frac{\mathrm{d}}{\mathrm{d}t}\mathbf{x}(t) = \mathbf{f}(\mathbf{x}(t)) \tag{1}$$

where $\mathbf{x}(t) = \begin{bmatrix} x_1(t) & x_2(t) & \dots & x_n(t) \end{bmatrix}^{\mathrm{T}}$ corresponds to the time series data of the states of the system (e.g., displacement), and the function $\mathbf{f}(\mathbf{x}(t)) : \mathbb{R}^n \rightarrow \mathbb{R}^n$ defines the functional relationship between $\mathbf{x}(t)$ and its derivatives. This $\mathbf{f}(\mathbf{x}(t))$ is often referred to as the vector field, in other words, the set of candidate functions that formulate the equations of motion of the system. As stated in [5], the key observation is that for many systems of interest, the function $\mathbf{f}$ consists of only a few terms, making it sparse in the space of possible functions. Therefore, the sought vector fields can be expressed as the product of a dictionary of m candidate nonlinear features, $\boldsymbol{\Theta}(\mathbf{x})$, and a sparse matrix of coefficients, $\boldsymbol{\Xi} = \begin{bmatrix} \boldsymbol{\xi}_1 & \boldsymbol{\xi}_2 & \dots & \boldsymbol{\xi}_n \end{bmatrix}$, that determines which nonlinearities are active and what is their contribution to the final solution:

$$\mathbf{f}(\mathbf{x}(t)) = \boldsymbol{\Theta}(\mathbf{x}) \cdot \boldsymbol{\Xi} \tag{2}$$

Each $\boldsymbol{\xi_i}$ is an $m \times 1$ vector, where m is the number of the assumed features of the $\boldsymbol{\Theta}(\mathbf{x})$ dictionary, and refers exclusively to the i-th state of $\mathbf{x}(t)$. Thus, the dimensions of $\boldsymbol{\Theta}(\mathbf{x})$ and $\boldsymbol{\Xi}$ are $1 \times m$ and $m \times n$, respectively.

$\boldsymbol{\Theta}(\mathbf{x})$ can contain various nonlinear functions, e.g., polynomials, trigonometric, exponential, etc. For any given state vector $\mathbf{x}(t)$, it can take the following form:

$$\boldsymbol{\Theta} = \begin{bmatrix} 1, & \boldsymbol{x}, & \boldsymbol{x}^{\mathcal{P}_2}, & \boldsymbol{x}^{\mathcal{P}_3}, & \dots \cos(\boldsymbol{x}), & \cos(2\,\boldsymbol{x}), & \dots \mathrm{e}^{-\boldsymbol{x}}, & \mathrm{e}^{-2\,\boldsymbol{x}}, \dots \end{bmatrix} \tag{3}$$

in which $\boldsymbol{x}^{\mathcal{P}_i}$, $i \in 2, 3$, denote polynomials of the i-th order, for instance:

$$\boldsymbol{x}^{\mathcal{P}_2} = \begin{bmatrix} x_1^2, & x_1x_2, & x_1x_3, & \dots x_1x_n, & x_2^2, & x_2x_3, & \dots x_{n-1}x_n, & x_n^2 \end{bmatrix} \tag{4}$$

It is worth mentioning that by using polynomials, the training data changes in time might be well described. Nonetheless, this might lead to overfitting when a new data set is used, since the terms of the equation will not be generalizable.

The coefficients in each sparse column vector $\boldsymbol{\xi}_j$ act as weights for the candidate features that should be included in the right-hand side for the equation $\dot{x}_j = f_j(\mathbf{x}(t))$. $\boldsymbol{\Xi}$ is determined through a nonlinear and likely non-convex optimization leading to a sparse solution. This requires the definition of an appropriate loss function, usually including a sparsity-promoting parameter. Finally, each equation of the unknown vector field is:

$$\dot{x}_j = f_j(\mathbf{x}(t)) = \boldsymbol{\Theta}(\mathbf{x}) \cdot \boldsymbol{\xi}_j \tag{5}$$

Within the RK4-SINDy [10], the Runge-Kutta scheme is used to relate the measurement at t_{k+1} with the one at t_k via:

$$x_j(t_{k+1}) = x_j(t_k) + \int_{t_k}^{t_{k+1}} f_j(\mathbf{x}(\tau))\mathrm{d}\tau \tag{6}$$

Therefore, reducing the solution space, such that:

$$\mathbf{x}(t_{k+1}) \approx \mathbf{RK4}(\mathbf{f}, \mathbf{x}(t_k), h_k) \tag{7}$$

where **RK4** indicates:

$$\mathbf{RK4}(\mathbf{f}, \mathbf{x}(t_k), h_k) = \mathbf{x}(t_k) + \frac{1}{6} h_k \left(\mathbf{k}_1 + 2 \cdot \mathbf{k}_2 + 2 \cdot \mathbf{k}_3 + \mathbf{k}_4\right), \quad h_k = t_{k+1} - t_k \tag{8}$$

where

$$\mathbf{k}_1 = \mathbf{f}(\mathbf{x}(t_k)) \qquad \mathbf{k}_2 = \mathbf{f}\left(\mathbf{x}(t_k) + h_k \frac{\mathbf{k}_1}{2}\right)$$

$$\mathbf{k}_3 = \mathbf{f}\left(\mathbf{x}(t_k) + h_k \frac{\mathbf{k}_2}{2}\right) \qquad \mathbf{k}_4 = \mathbf{f}(\mathbf{x}(t_k) + h_k \mathbf{k}_3)$$

The RK4 scheme can propagate also backward in time, using a negative time step h_k, meaning that predictions both for $\mathbf{x}(t_{k+1})$ and $\mathbf{x}(t_{k-1})$ can be made.

To determine the $\boldsymbol{\Xi}$, a loss function, $\mathcal{L}$, can be formulated as the mean squared error, or any other loss criterion, between the measurements, $\mathbf{x}^*(t_{k+1})$ and the predicted values obtained by using Eq. (7), $\mathbf{x}^{\text{pred}}(t_{k+1})$:

$$\underset{\boldsymbol{\Xi}}{\operatorname{argmin}}\ \mathcal{L}\left(\mathbf{x}^*(t), \mathbf{x}^{\text{pred}}(t)\right) \tag{9}$$

For a parsimonious solution that will not account for redundant terms, sparsity needs to be promoted through an l_1-regularization term:

$$\underset{\boldsymbol{\Xi}}{\operatorname{argmin}} \mathcal{L}\left(\mathbf{x}^{*}(t), \mathbf{x}^{\text{pred}}(t)\right) + \alpha \ || \ \boldsymbol{\Xi} \ ||_{l_1} \tag{10}$$

where α is a regularizing parameter. However, as explained in [10], the optimization problem described by Eq. (10) is a non-convex one, so traditional approaches that exist for linear optimization problems, e.g., LASSO [11, 12], are not efficient. Thus, the fixed cutoff thresholding algorithm, introduced in [10], is used for the current project with slight modifications. To elaborate, the ξ coefficients are updated through a stochastic gradient descent (SGD) method to minimize the difference between predictions and measurements. In this process, a cutoff value λ is defined, and after each passing of a single time series containing both transient and steady-state responses, all the coefficients with an absolute value smaller less λ are set to zero, continuing in the next epoch with the nonzero ones. The step-by-step process is explained in Algorithm 1.

Algorithm 1: Fixed cutoff thresholding

Input: Measurement data $\mathbf{x}^{*}(t)$, Feature dictionary $\boldsymbol{\Theta}(\mathbf{x})$, Cutoff parameter λ, Number of training epochs M
Initialize coefficient matrix $\boldsymbol{\Xi}$ with 0 values
for $i = 1$ **to** M **do**
  $\mathbf{X}^{\text{pred}}(t) \leftarrow \mathbf{RK4}\left(\boldsymbol{\Theta}(\mathbf{x}) \cdot \boldsymbol{\Xi}, \mathbf{x}^{*}(t)\right)$
  Solve

$$\underset{\boldsymbol{\Xi}}{\operatorname{argmin}} \mathcal{L}\left(\mathbf{x}^{*}(t), \mathbf{x}^{\text{pred}}(t)\right)$$

  using SGD
  $inds = | \ \boldsymbol{\Xi} \ | < \lambda$ `// The indices of the coefficients smaller than λ`
  $\boldsymbol{\Xi}[inds] \leftarrow 0$
Output: The sparse coefficient matrix $\boldsymbol{\Xi}$

A drawback of such an approach constitutes the selection of the cutoff value. Ideally, an iterative procedure is needed, in which different values of λ are chosen and their corresponding performance is evaluated.

3 RK4-SINDy with Partially Known Governing Equations

As stated in [10], discovering governing equations can be made even more efficient by incorporating physics knowledge. However, this idea was not further explored and was left for future research. This is particularly important in structural dynamics when non-smooth nonlinearities are present since they cannot be appropriately captured with existing methodologies. Including physics would result in a more

generalizable solution, especially in cases with limited data availability. When performing the identification on corrupted and/or sparse data, including physics would overcome overfitting issues (which then reduce the predictive ability of the derived governing equation) observed with purely data-driven approaches. Physics knowledge can be included with three main strategies [13]:

– Providing training data that obey the underlying physics (observational bias)
– Include terms in the loss function that respect the physics (learning bias)
– Modify the algorithm architecture, e.g., physical constraints (inductive bias)

A modified version of RK4-SINDy is proposed in the current work, with a different algorithm architecture, where a part of the governing equation is assumed to be known in the identification process. Providing this inductive bias will shift the focus on the identification of the non-smooth terms.

4 Nonlinear Oscillator with Friction Case Study

Let us consider a laboratory setup [14] of an SDOF oscillator, consisting of a mass m, a spring of stiffness k, and a dashpot with a viscous damping coefficient c as shown in Fig. 1. The contact between the mass and the fixed wall of the Fig. 1 is characterized by the normal force N and the friction coefficient μ, while the mass is under harmonic excitation of frequency Ω and amplitude F_0. The governing equation, which describes the sliding phase of the oscillator, is:

$$m\,\ddot{x}(t) + c\,\dot{x}(t) + k\,x(t) + \mu\,N\,\mathrm{sgn}(\dot{x}(t)) = F_0\cos(\Omega\,t) \tag{11}$$

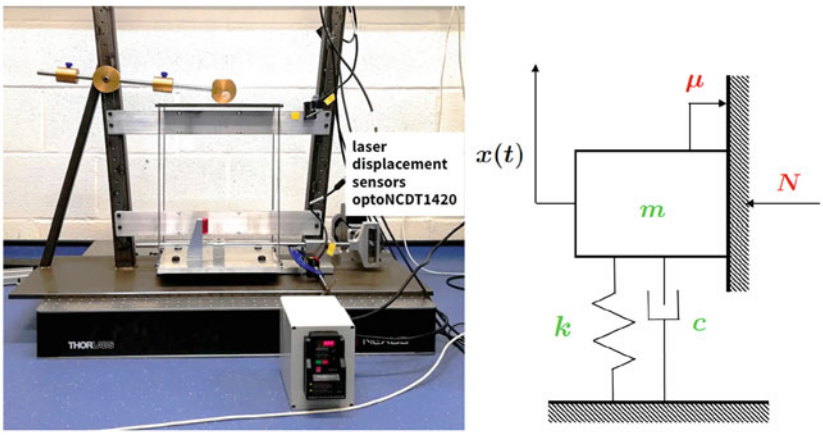

Fig. 1 Nonlinear SDOF with a Coulomb friction contact

$$\Rightarrow \ddot{x}(t) + 2\,\zeta\,\omega_n\,\dot{x}(t) + \omega_n^2\,x(t) + \frac{\mu\,N}{m}\,\mathrm{sgn}(\dot{x}(t)) = \frac{F_0}{m}\cos(\Omega\,t) \tag{12}$$

where $\zeta = c/(2\sqrt{k\,m})$ is the damping ratio and $\omega_n = \sqrt{k/m}$ the natural frequency. Equation (12) can be expressed in the state-space form as a coupled system of first-order differential equations:

$$\begin{cases} \dot{x}(t) = y(t) \\ \dot{y}(t) = -2\,\zeta\,\omega_n\,y(t) - \omega_n^2\,x(t) - \dfrac{\mu\,N}{m}\,\mathrm{sgn}(y(t)) + \dfrac{F_0}{m}\cos(\Omega\,t) \end{cases} \tag{13}$$

The true displacement and velocity time series are obtained with the explicit Runge-Kutta method of order 5(4) [15]. The noisy data needed for RK4-SINDy are generated according to a Gaussian distribution, with mean values the true time series, and standard deviation the noise level σ_{noise} multiplied by the mean:

$$\mathbf{x}^*(t) \sim \mathcal{N}(\mathbf{x}^{\text{true}}(t), \sigma_{\text{noise}} \cdot \mathbf{x}^{\text{true}}(t)) \tag{14}$$

The physics knowledge included in the identification process is the stiffness and viscous damping terms. The goal is the identification of the friction and forcing terms using synthetic data when known physics are included or otherwise, and for different noise levels. The properties that were used for the artificially generated measurements are summarized in Table 1. For each analysis, noisy values of the natural frequency and the damping ratio were considered, generated in a similar manner as the noisy measurements (Eq. (14)), using σ_{ω_n} and σ_ζ, respectively:

$$\omega_n^{\text{noisy}} \sim \mathcal{N}\left(\sqrt{k/m}, \sigma_{\omega_n}\right) \quad , \quad \zeta^{\text{noisy}} \sim \mathcal{N}\left(c/(2\sqrt{k\,m}), \sigma_\zeta\right) \tag{15}$$

Table 1 System's properties

Quantity	Description	Value	Units
m	Mass	1	kg
c	Viscous damping coefficient	0.1	Ns/m
k	Stiffness	1	N/m
F_0	Forcing amplitude	1	N
$\mu\,N/F_0$	Friction-to-forcing ratio	0.5	[-]
Ω	Forcing frequency	1.2	rad/s
T	Time horizon	50	s
Δt	Time step	0.01	s
σ_{ω_n}	Natural frequency noise	5%	[-]
σ_ζ	Damping ratio noise	20%	[-]
x_0	Initial displacement (at $t = 0$)	0.1	m
$\dot{x}_0$	Initial velocity (at $t = 0$)	0.1	m/s

Table 2 Experimental setup properties

Quantity	Description	Value	Units
m	Mass	3.080	kg
c	Viscous damping coefficient	0.264	Ns/m
k	Stiffness	1190	N/m
μ	Friction coefficient	0.274	[-]
M	Mass of sliding disc	0.150	kg
$N = M\,g$	Normal force	1.472	N

The examined case corresponds to a continuous motion of the oscillator. This is accomplished by considering a friction-to-forcing ratio of 0.5 and a ratio of the excitation frequency over the natural one Ω/ω_n of 1.2. More information on the values of these two quantities and the case of stick-slip are provided in [14].

While the numerical case can be easily tuned or modified, in reality, the terms of the governing equation might vary, and when the known physics is wrong, or not included at all, the differences from the real case will be encapsulated in the friction term. Therefore, in the experimental case, a slightly different problem is investigated, where instead of the analytical form of the forcing, the base excitation, $u(t)$, and the response to it, $x(t)$, both obtained with laser displacement sensors, are used. A smooth automatic differentiation scheme is applied to the two displacement histories to obtain the corresponding velocities. With the base excitation available, Eq. 12 is modified as follows:

$$\ddot{x}(t) = -2\,\zeta\,\omega_n\,\dot{x}(t) - \omega_n^2\,x(t) - \frac{\mu\,N}{m}\mathrm{sgn}(\dot{x}(t)) + 2\,\zeta\,\omega_n\,\dot{u}(t) + \omega_n^2\,u(t) \tag{16}$$

The system properties in this case (Fig. 1) are measured and summarized in Table 2. The more cumbersome to estimate damping and friction coefficients, c and μ, were derived by letting the system vibrate freely, with and without the contact on top, and measuring its decaying oscillation.

For the identification process, it is assumed that ζ and ω_n are known, to tackle directly the nonlinear friction term, $\frac{\mu\,N}{m}\mathrm{sgn}(\dot{x}(t))$.

5 Results

The hyperparameters used in both the synthetic and the experimental cases are summarized in Table 3.

Table 3 Hyperparameters

Quantity	Description	Value	
		Artificial	Experimental
M	Number of epochs	3000	6000
lr	Learning rate	1e–2	1e–1
λ	Cutoff threshold	5e–2	5e–2

Table 4 Normalized root mean squared error (NRMSE) for both knowing and not knowing part of the physics, for different noise levels

Noise	Unknown physics	Known physics
1e–2	0.0076	0.0010
5e–2	0.0163	0.0026
1e−1	0.0298	0.0072

5.1 Artificially Generated Data

According to [16], the feature dictionary, $\boldsymbol{\Theta}(\mathbf{x})$, should not include a large number of candidate functions. Their selection should be driven by the prior knowledge of the system at hand. Hence, second-order polynomial terms, signum terms of both $x(t)$ and $y(t)$, and cosine terms with frequencies ranging from 0.6 to 1.8 with a 0.2 step, were chosen. Various measurement noise levels were tested, both with known and unknown physics. For $\sigma_{\text{noise}} = 0.1$, the derived equations are:

$$\text{Ground truth:} \quad \dot{y} = -0.1\,y - x - 0.5\,\text{sgn}(y) + \cos(1.2\,t) \tag{17}$$

$$\text{Known Physics:} \quad \dot{y} = -0.1\,y - x - 0.492\,\text{sgn}(y) + 0.981\cos(1.2\,t) \tag{18}$$

$$\text{Unknown Physics:} \quad \dot{y} = -1.007\,x - 0.557\,\text{sgn}(y) + 0.941\cos(1.2\,t) \tag{19}$$

The learned governing equations are parsimonious and do not include redundant terms. However, it is evident that by including known physics, the derived solution is more generalizable, and its terms approach the ones of the ground truth. In the case of no prior system knowledge, the acceleration field is not correctly identified. The viscous damping term is omitted and the similarities with the coefficients of the remaining terms are smaller. The benefits of including known physics are highlighted even further in Table 4 where the normalized root mean squared errors (NRMSE) between the ground truth and the learned solution, for different noise levels, are summarized.

It can be observed in the displacement and velocity plots of Fig. 2 that when including known terms, RK4-SINDy is not trying to fit the solution on every point of the noisy measurements. This is because the algorithm tries to identify the complete vector field that would predict the system's behavior in every possible region and not just where data is available.

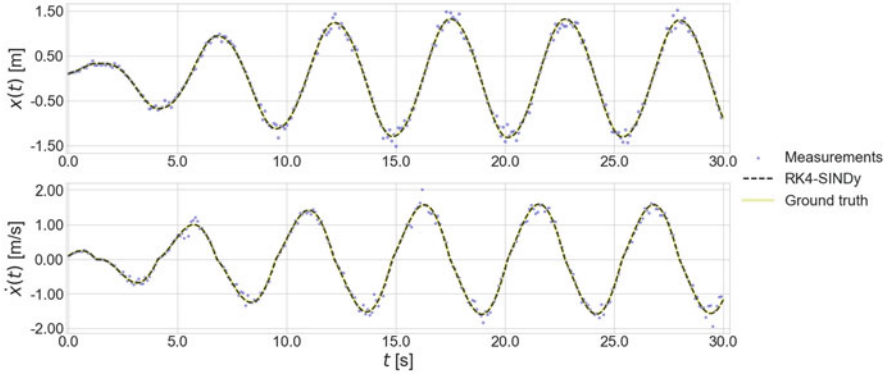

Fig. 2 Displacement and velocity identification: artificial data ($\sigma_{\text{noise}} = 0.1$)

5.2 Experimental Data

In this case, the candidate features employed are first-order polynomial terms, signum terms, and cosine terms with five different frequencies, surrounding the excitation one, which was derived using the fast Fourier transform. Three different cases of RK4-SINDy were examined to confirm the need of including the base excitation measurements, $u(t)$, i.e., (a) include the measured base displacements, (b) perform the identification without any knowledge of the forcing (purely data-driven approach), and (c) assume a perfect harmonic base excitation:

$$\begin{aligned} \text{Truth:} \quad & \dot{y} = -386.766\,x - 0.0658\,y - 0.131\,\text{sgn}(y) + 386.766\,u + 0.0658\,\dot{u} \\ \text{(a):} \quad & \dot{y} = -386.766\,x - 0.0658\,y - 0.125\,\text{sgn}(y) + 386.766\,u + 0.0658\,\dot{u} \end{aligned} \tag{20}$$

$$\text{(b):} \quad \dot{y} = -201.078\,x + 3.4602\,y + 0.158\cos(12.6\,t) \tag{21}$$

$$\text{(c):} \quad \dot{y} = -407.581\,x - 3.0138\,y + 0.109\cos(12.6\,t) \tag{22}$$

In all three cases, RK4-SINDy led to a parsimonious solution. Its performance is plotted together with the measurements and the ground truth in Fig. 3.

It is apparent that the best results were achieved when the exact $u(t)$ measurements are used. Redundant terms were dropped and the coefficient of the signum term approached the expected value. When no information about the excitation was included, and since low-order polynomial terms were used, RK4-SINDy did not converge to the ground truth. Moreover, a positive damping term is selected to fit the data. Lastly, if wrong assumptions are included, the results are close to the ground truth but the derived governing equation is not generalizable.

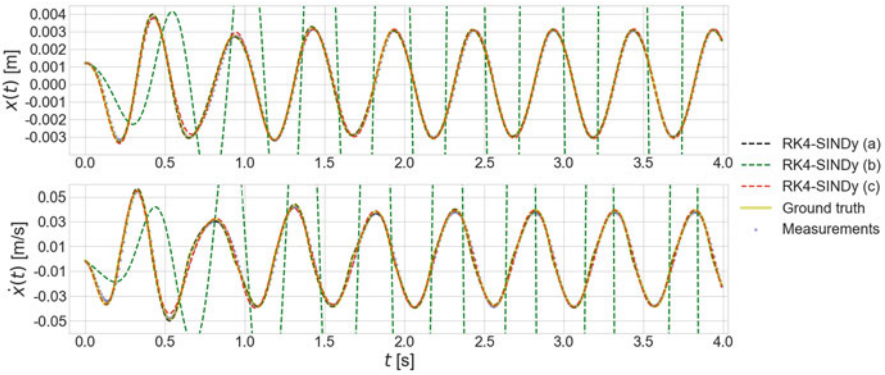

Fig. 3 Displacement and velocity identification: experimental data

6 Conclusions

RK4-SINDy has been explored for the identification of nonlinear dynamical systems with non-smooth nonlinearity. In particular, an SDOF oscillator with Coulomb friction damping has been investigated. The standard RK4-SINDy has been enhanced by including known physics about the system. The results obtained based on artificially generated data showed that the enhanced RK4-SINDy provides an improved identification of the unknown governing equation and a reduced NRMSE for various noise levels. Additionally, in the experimental case, the benefits of including excitation measurements in the identification process were highlighted, compared with approaches where wrong forcing terms were considered or no prior forcing knowledge at all. The aforementioned findings are limited to continuous motion. Preliminary studies have shown that measurements obtained during stick-slip phenomena might lead to the wrong identification of the differential equation. This is the subject of future investigations.

References

1. Mendez, B.C., Botero, E., Romo, M.P.: A new friction law for sliding rigid blocks under cyclic loading. Soil Dyn. Earthq. Eng. **29**(5), 874–882 (2009). https://doi.org/10.1016/j.soildyn.2008.09.004
2. Cabboi, A., Putelat, T., Woodhouse, J.: The frequency response of dynamic friction: enhanced rate-and-state models. J. Mech. Phys. Solids **92**, 210–236 (2016). https://doi.org/10.1016/j.jmps.2016.03.025
3. Green, P.L., Worden, K., Sims, N.D.: On the identification and modelling of friction in a randomly excited energy harvester. J. Sound Vib. **332**(19), 4696–4708 (2013). https://doi.org/10.1016/j.jsv.2013.04.024
4. Gutowski, P., Leus, M.: The effect of longitudinal tangential vibrations on friction and driving forces in sliding motion. Tribol. Int. **55**, 108–118 (2012). https://doi.org/10.1016/j.triboint.2012.05.023

5. Brunton, S.L., Proctor, J.L., Kutz, J.N.: Discovering governing equations from data by sparse identification of nonlinear dynamical systems. Proc. Natl. Acad. Sci. **113**(15), 3932–3937 (2016). https://doi.org/10.1073/pnas.1517384113
6. Fehr, J., Kargl, A., Eschmann, H.: Identification of Friction Models for MPC-based Control of a PowerCube Serial Robot (2022). arXiv preprint arXiv:2203.10896. https://doi.org/10.48550/arXiv.2203.10896
7. Didonna, M., Stender, M., Papangelo, A., Fontanela, F., Ciavarella, M., Hoffmann, N.: Reconstruction of governing equations from vibration measurements for geometrically nonlinear systems. Lubricants **7**(8), 64 (2019). https://doi.org/10.3390/lubricants7080064
8. Ren, Y., Adams, C., Melz, T.: Uncertainty analysis and experimental validation of identifying the governing equation of an oscillator using sparse regression. Appl. Sci. **12**(2), 747 (2022). https://doi.org/10.3390/app12020747
9. Cabboi, A., Marino, L., Cicirello, A.: A comparative study between Amontons–Coulomb and Dieterich–Ruina friction laws for the cyclic response of a single degree of freedom system. Eur. J. Mech. A. Solids **96**, 104737 (2022). https://doi.org/10.1016/j.euromechsol.2022.104737
10. Goyal, P., Benner, P.: Discovery of nonlinear dynamical systems using a Runge–Kutta inspired dictionary-based sparse regression approach. Proc. R. Soc. A **478**(2262), 20 210 883 (2022). https://doi.org/10.1098/rspa.2021.0883
11. Friedman, J., Hastie, T., Tibshirani, R.: The Elements of Statistical Learning, vol. 1. Springer, New York (2001)
12. Tibshirani, R.: Regression shrinkage and selection via the lasso. J. R. Stat. Soc. B (Methodological) **58**, 267–288 (1996). https://doi.org/10.1111/j.2517-6161.1996.tb02080.x
13. Karniadakis, G.E., Kevrekidis, I.G., Lu, L., Perdikaris, P., Wang, S., Yang, L.: Physics-informed machine learning. Nat. Rev. Phys. **3**(6), 422–440 (2021). https://doi.org/10.1038/s42254-021-00314-5
14. Marino, L., Cicirello, A.: Experimental investigation of a single-degree-of-freedom system with Coulomb friction. Nonlinear Dyn. **99**(3), 1781–1799 (2020). https://doi.org/10.1007/s11071-019-05443-2
15. Dormand, J.R., Prince, P.J.: A family of embedded Runge-Kutta formulae. J. Comput. Appl. Math. **6**(1), 19–26 (1980). https://doi.org/10.1016/0771-050X(80)90013-3
16. Corbetta, M.: Application of sparse identification of nonlinear dynamics for physics-informed learning. In: 2020 IEEE Aerospace Conference, pp. 1–8 (2020). https://doi.org/10.1109/AERO47225.2020.9172386

Recycled Smart Devices for Real-Time Monitoring of Civil Infrastructures

Arturo Buscarino, Carlo Famoso, and Luigi Fortuna

1 Introduction

The periodic collection of representative parameters of the overall behavior and state of health of an infrastructure constitutes that set of operations that flows into the structural monitoring process [1]. Structural monitoring, applied to buildings and infrastructures, can provide essential information especially for particularly complex structures or those affected by ongoing degradation phenomena [2]. However, monitoring is not only intended for a simple surveillance purpose. In the modern approach to the design, construction, and management of structures, monitoring aims to collect a series of data that allows to represent, possibly digitally, the physical and functional characteristics of the object they refer to [3]. This involves the acquisition of a series of interdisciplinary data (structural, physical, chemical, energy, safety) that must be conveyed to a single management entity that allows them to be used in view of analyses that are dynamic and multisectoral and whose results can flow toward a control action exercised on the system itself [4].

From this perspective, it is impossible to think of the control and monitoring of structures as two distinct and separate things. It is interesting to think, for monitoring/control, of a conceptual model that defines the way in which information can be collected, made available, processed, and the results exchanged between the numerous and heterogeneous actors who move around the creation, management, and maintenance of a building, and that they can act on it in view of the functional objective of the same.

A. Buscarino (✉) · C. Famoso · L. Fortuna
Università degli studi di Catania, Catania, Italy
e-mail: arturo.buscarino@unict.it

© The Author(s), under exclusive license to Springer Nature Switzerland AG 2024

W. Lacarbonara (ed.), *Advances in Nonlinear Dynamics, Volume III*, NODYCON Conference Proceedings Series, https://doi.org/10.1007/978-3-031-50635-2_48

In this communication, we report the results obtained in the design and implementation of monitoring device based solely on electronic waste [5]. Smart Devices and smartphones are among the most disposed electronic devices in the World. This occurs despite the fact that in many cases the disposed Smart Device is only partially damaged or simply outdated. The possibility of reusing these devices, therefore, would lead to significant advantages in terms of cost for the community, that is, decreasing the cost of the monitoring system itself and decreasing the impact of e-waste [6].

The monitoring device presented in this chapter has been tested on field to guarantee the reliability of the information collected even in the presence of low-end devices. Moreover, a preliminary analysis of the data collected in a public infrastructure has been carried out allowing to assess the health status of the building and recovering information related to mild intensity seismic events.

The communication is organized as follows. In Sect. 2, the fundamental problems in adopting the proposed strategy are outlined, while the conceived setup is described in Sect. 3. The results of on-field testing are described in Sect. 4. Finally, in Sect. 5 conclusions are drawn.

2 Monitoring Real-Time Data Using Recycled Smart Devices

One of the objectives of this chapter is to propose solutions capable of containing costs, referring to an extremely widespread technology, such as that present in smartphones, which has reached a technological maturity such as to be reliable both in the data provided and in the duration of operation. If we take into account that, according to reliable estimates, about 350,000 smartphones are thrown away every day, and of these the vast majority are still functional or barely damaged, we can think that, given the potential that each model offers in terms of sensors, connectivity, and the ability to process information on site, they represent the tools of choice for their use in the monitoring of buildings.

If properly placed in a point of the building, they allow to determine the acceleration of a certain point of the structure. The most common accelerometers in smartphones are capacitive ones, equipped with MEMS (Micro-Electro-Mechanical System) sensors. In some operating conditions, these accelerometers are more efficient than the more common piezoelectric accelerometers, allowing to measure constant accelerations linked to quasi-static phenomena.

Given the type of sensors most present in a smartphone, we can combine the accelerometers, for example, with the use of the video camera both for the simple monitoring of the brightness in an environment, and for the acquisition of images aimed at observing the crack in a structure, giving rise to a IoT system for monitoring the structural stability of buildings [7]. The GPS sensor also provides a reliable indication, within the system error margins, of the positioning of the sensor within the space to be monitored.

In addition, the subsequent processing of the raw data provided allows for the extrapolation of indirect information that helps to create a complete and comprehensive picture of the environment being monitored: speed, inclination, and subsidence. Hardware with which certain smartphone models are equipped is well documented in functional and structural terms, and this allows you to interact directly with the sensor of interest to obtain the performance that is closest to the needs of the project. By introducing these devices in the context of building monitoring, the software aspect should not be underestimated, without which it is not possible to attend to those features for which they are intended.

In recent years, the Android system has increasingly established itself in the heterogeneous world of smartphones, becoming the most popular operating system for mobile devices in the World. It is distributed under the terms of the free Apache 2.0 license and allows you to freely develop applications that make the mobile devices, that adopt it, extremely flexible tools and intended for the most diverse uses.

The performance of the smartphone, as a data acquisition device for acceleration measurements, was evaluated directly on the field, analyzing the performance obtained by the mobile device during its operation in order to obtain a unitary picture including both the hardware and software aspects.

The accelerometric sensor of the mobile device under consideration (Huawei Ascend G7 (L01)) is the LIS3DH an ultra-low-power three-axis linear accelerometer. The LIS3DH has dynamically user-selectable full scales of $\pm 2g$, $\pm 4g$, $\pm 8g$, $\pm 16g$ and is capable of measuring accelerations with output data rates from 1 Hz to 5.3 kHz.

In view of the previous considerations, it is expected that the parameter most affected by the degradation of performance is the sampling time of the device. This will store the new data at the end of the sensor reading and writing cycle on the file setup for information storage. This means that, compared to a minimum time of 10 ms offered by App2 for managing access to the accelerometer signals, this time interval must be multiplied by several units in relation to the data writing cycles on the storage device. Therefore, it is necessary to check whether the increase in the number of stored samples and the consequent increase in the size of the data file cause a degradation in performance, with a consequent increase in the sampling time.

To this analysis, we must add the evaluation if in the presence of stresses and peaks in the signal the system remains stable or shows a drift. To shed light on these conditions, the results that emerged from the comparison of the data obtained from two acquisition campaigns were examined, which resulted in two rows of 100,000 samples each. The signals examined showed values of the acceleration module as reported in Fig. 1.

The time intervals between one sample and another were obtained from each file, and the comparative examination was conducted on them. Examining these intervals, it is observed that no drifts are recorded in the sampling time between the case in which there are appreciable variations in the values of the samples and that in which the acceleration values remain around the value of g. Furthermore,

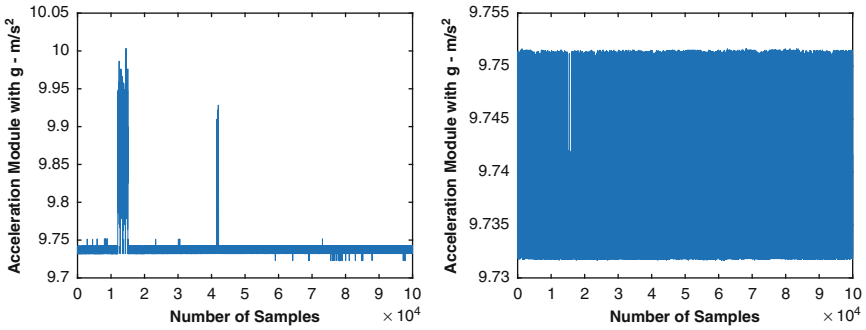

Fig. 1 Evaluation of the system. Test trends: (**a**) the presence of sudden changes in the acceleration; (**b**) action of the gravity only

no appreciable variation is recorded in the variation of the sampling interval as the number of samples grows. It clearly emerges that the dynamics of the signal and its duration do not affect the performance of the acquisition system in terms of sampling time.

3 The Hardware and Ad Hoc Apps

Assuming that the devices can be installed in places with difficult access, it is necessary to provide that an operating mode is implemented on it that ensures maximum autonomy over time. Furthermore, in the worst environmental conditions, excluding the possibility of energy harvesting, one must expect that the system, once positioned, will activate and manage itself, guaranteeing the maximum energy reserve for the entire expected operating time.

With this in mind, a stand-alone system has been developed in which ad hoc App ensures that the device starts up, operates, and a power reserve ensures that the system is powered for the intended period of time.

Inside a watertight container, we included the following sub-systems:

– A 12 V/20 Ah lead acid battery ensures stand-alone operation of the device for a very long time.
– The adjustable smartphone holder allows different models of smartphones to be housed inside the case, rigidly and integral to it, making it a multi-model configuration.
– Electrical power management is implemented locally through a series of electronic devices that manage the power delivered to the smartphone from the battery.

Fig. 2 Prototype monitoring device based on a partially damaged smartphone

– Recharging of the lead acid battery can be accomplished on site, as it is possible to connect, via an external connector, to a power source capable of delivering the required voltage and current.

The prototype box is shown in Fig. 2.

The system is designed and built to operate in open places exposed to solar irradiation. The control electronics keep the smartphone battery constantly under charge, which will use the energy directly produced by a solar panel during the day and under favorable irradiation conditions, while accessing the backup battery during the night hours and under conditions of no solar irradiation, such as temporary cloud cover or unfavorable weather conditions. The solar energy harvesting system was designed using parts from commercial and relatively widely used electronic circuits, in a way that allows for rapid replicability of the system itself at low cost.

From a software perspective, intervention on Android to disable the battery management service is necessary to ensure that the operating system constantly sees a source of power to ensure uninterrupted operation of the App and that the App is not detected as an energy-hungry App and as such automatically disabled.

In order to make the results of this project reachable by users, also not particularly expert in programming, the app was developed with the support of MIT App Inventor 2 [8]. MIT App Inventor is a free and open-source web application integrated development environment originally provided by Google and now maintained by the Massachusetts Institute of Technology (MIT). App2 gives the possibility to develop apps for mobile devices without writing a single line of code.

The ad hoc Apps allow the management of the various phases of monitoring, taking into account that the devices, once placed in the assigned points of the structure, may not be easy to access.

Two operating scenarios have been considered: The operating environment is accessible through a wireless network service, or no wireless network services can be implemented in the operating environment. In the first scenario, it was decided

to implement a whole series of procedures that allow the device, once started and connected to the network, to possibly be remotely controlled.

Through an on-board FTP server, the device can upload data files to a remote server. A user interface, via touchscreen if it is working, or via remote desktop, allows to initially configure the device according to the needs of the monitoring plan, assigning, among other things, the sampling frequency, the size of the data files, the frequency and the number of files with data to be sent to the remote server.

The system for sending data files to remote server has been implemented considering the possibility of using the device local memory as a buffer. The data files pass through the memory buffer according to the FIFO method, remaining in the buffer in relation to the number of recent files, which for safety you want to always be present in the buffer memory, and the successful sending of the file itself. Once the file sending phase has been positively concluded, this however remains in memory and the first of the files in the queue sent is deleted. If the file is not sent successfully, after a certain number of attempts, the device continues to collect data until the local memory made available to the process is saturated.

In the second scenario, the App that enables the operation of the device is designed so that the system can operate stand-alone, in what we can call a "place and forget" mode. In contrast to what we saw in the App defined for Scenario 1, where the possibility of local memory saturation was an event related to the permanent drop of the network connection, in this second scenario, as the "place and forget" mode applies, management of the external MicroSD is very important.

In both types of Apps, during the acquisition process, data are stored in a text file and then, after the acquisition campaign is completed, are processed offline.

Although modern smartphone models are equipped with substantial memory, in older ones this is not the case. To organize long observation campaigns, in the case of stand-alone operation of the device, it is necessary to ensure that there is a good supply of memory on which to carry out temporary data storage. In smartphone models equipped from Android 4.4 "KitKat" onward, it is possible to mount 32 GB external MicroSD, and, for newer ones, even a few hundred GBs.

Bearing in mind the limitations that direct writing to MicroSD entails in terms of security and data integrity, however, the use of very capacious MicroSDs allows for a twofold perspective: On the one hand, using smartphones that are at least nine years old, therefore already quite dated, while on the other hand, in terms of saved data, if not differently configured the system according to the items seen above, one has the possibility of implementing a long observation interval that the system will carry on until the complete saturation of the available memory.

4 Experimental Campaign

The building on which the measurements were made, impressive in terms of structure and architecture, is a Catholic church, built in masonry in the second half of the nineteenth century. The decision to consider it the subject of testing the

device was dictated by historical, structural, and geological reasons. Historically, the building represents a beautiful example of masonry construction, with gravity-bearing walls that at the base have a section that exceeds two meters and rise, without interruption, for more than 15 m, welcoming the trusses at their top. Moreover, the monitoring of churches and other relevant architectonic heritage is a topic of growing interest [9–11].

The point of the building where the sensor was placed is the top of the left bell tower, the one that supports the largest bells, among those present. Bells intended, according to Catholic custom, to indicate the beginning of important liturgical ceremonies, or to mark, with their tolling, certain moments of the day (noon, vespers, etc.). The left bell tower, or what remains of it today, appears on the top as a parallelepiped structure with a square base, rising just over 20 m from its lowest base plane.

It is certainly the part of the entire building most subject to vibrations and direct endogenous stresses (due to its function) and exogenous (due to the dynamics of the site in which it is located). In fact, due to the geotechnical characteristics of the construction site (lava and tuff), it is most affected by the unevenness of the ground on which the foundations of the entire construction rest.

The area in which the building is located is about 200 m above sea level, and it is affected by numerous active tectonic faults, attributable to the dynamics of the volcanic building of Etna. This territory is frequently subject to seismic phenomena, even of strong intensity, which in the past decades have caused serious damage to the structure and in some cases have compromised its stability, so much so as to require demolition and reconstruction of some of its parts.

The measuring system, as previously described, was positioned in the center of the floor at the top of the complex. The steel structure that currently supports the bells is anchored to this floor. This replaced a previous reinforced concrete structure, much heavier than the current one, which dynamically unbalanced the construction, and which, however, was damaged by an earthquake in 2002. The anchoring of the support structure for the bells to the top floor of the building ensures that the vibrations and stresses occurring on the bell system are transmitted to the building in a non-negligible manner, at least in the part of our interest.

The box containing the measurement setup, watertight in PVC, was firmly anchored to the floor with epoxy resin, thus becoming one with the reference plane.

Among the cyclical events that affect the structure, we must mention the chimes of the huts that mark the canonical hours, in particular noon and vespers. To these must be added the chimes that mark the beginning of liturgical activities, which generally have a daily cyclical nature, but sometimes appear as one-off phenomena. To exceptional events, we can ascribe all the stresses that come from the external environment, which can be traced back to human activities, or to natural phenomena (volcanic tremors, earthquakes, etc.).

As part of the cyclical events, attributable to the functionality of the structure, we can report the graphs of the accelerometric data obtained at a particular time of the day, shown in Fig. 3.

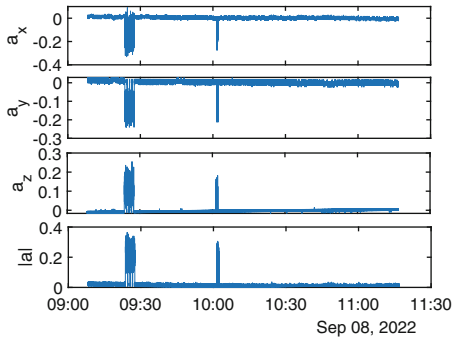

Fig. 3 Evaluation of the system: accelerometer recordings

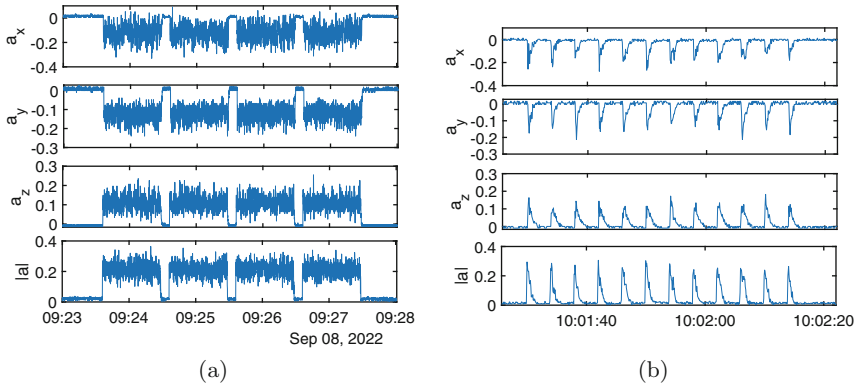

Fig. 4 Evaluation of the system. Experimental trends: (**a**) intense stress procured by bell tolling; (**b**) single-frequency event related to noon bell tollings

The sensor detected two events. The first is the chime for the beginning of a liturgical function. The building vibrates under the stresses transmitted to it by the steel structure that supports the bells. The zoom in Fig. 4a shows how the structure is subjected to fairly intense stresses that follow one another with a sustained frequency, typical of the bell, and that are repeated four times with short pauses. The second event observed at 11:00 UTC has the cadence of the striking of the hours, in particular the sensor recorded the twelve tones of noon. Each chime is presented as an impulse applied to the structure, of very short duration, as reported in Fig. 4b. The time interval between one strike and the next allows the structure to return to a condition of static equilibrium, and, where the sampling of the instrument allows it to be detected, the rapid decrease with exponential trend of the curve can be observed, a clear index of phenomena dissipative mechanics.

In both cases, observing the acceleration components, we note how the impulses stress the system that along the x and y axes give rise to accelerations with negative components. This gives us an indication of the location of the source of the stress relative to the sensing device. Taking into account what has been said about the arrangement of the reference axes for the accelerations of the smartphone, it appears

that the source of the stresses is to the right of the device (it urges it to its left) and in a slightly forward position with respect to it (it urges it toward its back).

Vertical stress causes the horizontal plane to oscillate around its equilibrium position. In all the cases examined, it can be seen that the structure, once subjected to an impulsive stress, returns quite quickly to the condition of equilibrium. This result is indicative of the fact that it is sufficiently rigid, such as not to allow, under the stresses of the tolling of the bells, large oscillations along the three directions of space.

5 Conclusions

Over 55 Mt of electronic waste are produced yearly, so that its impact on the quality of the environment is continuously increasing. The percentage of recycled electronic waste is still below the 20% per year. Many Smart Devices are currently disposed even if their electronics is mainly working properly. In this communication, we proved the efficiency of a monitoring device entirely based on electronic waste, in particular on partially damaged Smart Devices or on smartphones whose use has been discontinued.

The monitoring device has been conceived and tested to guarantee a reliable level of information related to the vibrations of buildings and civil infrastructures. Despite the low resolution of the accelerometers incorporated in low-end Smart Devices, they are capable of providing the necessary information even in the presence of external vibrational disturbances, such as mild seismic events.

Moreover, the Smart Devices are equipped also with magnetic sensors, sound sensors, high frame-rate cameras, and powerful microprocessing units whose operations are often preserved also in disposed devices. The sensible reduction of costs in adopting the proposed monitoring devices and its flexibility and reconfigurability provide key features that will be explored in the next future, allowing for low-cost reliable monitoring stations.

References

1. Monti, G., Fumagalli, F., Marano, G.C., Quaranta, G., Rea, R., Nazzaro, B.: Effects of ambient vibrations on heritage buildings: overview and wireless dynamic monitoring application. In: Proceedings of the 3rd International Workshop "Dynamic Interaction of Soil and Structures-Dynamic Interaction Between Soil, Monuments and Built Environment" (2013)
2. Athanasopoulos, G.A., Pelekis, P.C.: Ground vibrations from sheetpile driving in urban environment: measurements, analysis and effects on buildings and occupants. Soil Dyn. Earthq. Eng. **19**(5), 371–387 (2000)
3. Jornet-Monteverde, J.A., Galiana-Merino, J.J., Soler-Llorens, J.L.: Design and implementation of a wireless sensor network for seismic monitoring of buildings. Sensors **21**(11), 3875 (2021)

4. Azzara, R.M., Girardi, M., Occhipinti, M., Padovani, C., Pellegrini, D., Tanganelli, M.: Structural health monitoring for architectural heritage: case studies in Central Italy. In: European Workshop on Structural Health Monitoring, pp. 3–12. Springer, Cham (2023)
5. Van Yken, J., Boxall, N.J., Cheng, K.Y., Nikoloski, A.N., Moheimani, N.R., Kaksonen, A.H.: E-waste recycling and resource recovery: a review on technologies, barriers and enablers with a focus on Oceania. Metals **11**(8), 1313 (2021)
6. Pajunen, N., Holuszko, M.E.: Circular Economy in Electronics and the Future of e-Waste. Electronic Waste: Recycling and Reprocessing for a Sustainable Future, pp. 299–314 (2022)
7. Muttillo, M., Stornelli, V., Alaggio, R., Paolucci, R., Di Battista, L., de Rubeis, T., Ferri, G.: Structural health monitoring: an IoT sensor system for structural damage indicator evaluation. Sensors **20**(17), 4908 (2020)
8. Kamriani, F., Roy, K.: App Inventor 2 Essentials. Packt Publishing Ltd. (2016)
9. Alaggio, R., Aloisio, A., Antonacci, E., Cirella, R.: Two-years static and dynamic monitoring of the Santa Maria di Collemaggio Basilica. Constr. Build. Mater. **268**, 121069 (2021)
10. Clementi, F., Formisano, A., Milani, G., Ubertini, F.: Structural health monitoring of architectural heritage: from the past to the future advances. Int. J. Archit. Herit. **15**(1), 1–4 (2021)
11. Karanikoloudis, G., Lourenço, P.B., Mendes, N., Serra, J.B., Boroschek, R.: Monitoring of induced groundborne vibrations in cultural heritage buildings: miscellaneous errors and aliasing through integration and filtering. Int. J. Archit. Herit. **15**(1), 205–228 (2021)

Part VII
Nonlinear Wave Propagation

Excitations of Distorted Magnetosonic Lump Waves by Orbital Charged Space Debris Objects in Ionospheric Plasma

Siba Prasad Acharya, Abhik Mukherjee, and M. S. Janaki

1 Introduction

Space debris objects refer to various types of dead satellites, destroyed spacecrafts, meteoroids, etc. including many other inactive materials in space due to different hazardous phenomena [1]. These harmful objects are being levitated in the near-Earth space predominantly in the ionosphere. There are more than 21,000 debris objects having diameters larger than 10 cm, approximately 500,000 having diameters between 1 and 10 cm, and over 100 million with diameters less than 1 cm. One more important fact is that the number of space debris objects is increasing nowadays due to the increasing number of artificial space missions. The average orbital velocities of these charged debris objects are approximately 10 km/s in low earth orbit (LEO) region, whereas 3 km/s in geosynchronous earth orbit (GEO) region [2]. With such a high impact velocity of around 10 km/s in LEO region, even the smallest charged debris object can become potentially harmful for spacecrafts orbiting in this region [1, 2]. For instance, sub-centimeter debris objects can damage active spacecrafts about 100 times their sizes as demonstrated by Krag et al. [3].

Many remediation technologies have been proposed to address this space debris problem using different methods [4–8]. In the last decade, Ganguli and his coworkers [9] have formulated a novel concept for elimination of small-sized orbital debris objects with characteristic dimensions of 10 cm or less by injecting micron-sized dust grains in ionosphere to create a sweeping (snow-plow-like) effect on

S. P. Acharya (✉) · M. S. Janaki
Homi Bhabha National Institute, Mumbai, India

Saha Institute of Nuclear Physics, Kolkata, India
e-mail: siba.acharya@saha.ac.in

A. Mukherjee
Department of Physics, School of Basic Sciences, Manipal University Jaipur, Rajasthan, India

© The Author(s), under exclusive license to Springer Nature Switzerland AG 2024

W. Lacarbonara (ed.), *Advances in Nonlinear Dynamics, Volume III*, NODYCON Conference Proceedings Series, https://doi.org/10.1007/978-3-031-50635-2_49

them. This sweeping effect further facilitates deorbiting of these small-sized charged debris objects as desired. In addition, several plasma-based techniques have been reported as well for addressing space debris issues. For instance, a bidirectional plasma thruster to be mounted on a satellite can be used for ADR during satellite operations [10]. A directed ion beam ejected from this plasma thruster imparts a net force on a space debris object to decelerate it, which, in turn, facilitates its reentry into the Earth's atmosphere where it can burn out ultimately [10]. This bidirectional plasma thruster can also be used to accelerate or decelerate a satellite and remove space debris by altering magnetic field spatial profile in plasma expansion region [11].

Apart from this, certain indirect plasma-based detection methods have been proposed recently for orbital debris objects. The pioneering work of Sen et al. [12] has provided a different perspective for dealing with this space debris problem by deriving a forced Korteweg-de Vries (KdV) equation using reductive perturbation technique (RPT), which governs dynamics of debris-induced nonlinear wave excitations in ionospheric plasma. In particular, excitations of precursor ion acoustic solitons in upstream region moving ahead of the debris object as well as wake fields in downstream region moving behind them have been reported in their work [12]. They have proposed an indirect method of detection of charged space debris objects having characteristic dimensions less than 10 cm with the help of observations of precursor solitons by in situ or remote means; these small-sized debris objects are normally difficult to be observed by optical means. In recent years, Truitt and Hartzell [13, 14] have performed a detailed study on indirect detection methods for space debris objects as well as their mitigation techniques through observations of plasma solitons in their simulations using a pseudospectral scheme by considering the pioneering work of Sen et al. [12] as the main basis.

In our previous work [15], we have derived various exact as well as approximate analytical ion acoustic solitary wave solutions of the forced KdV equation, which had been derived by Sen et al. [12]. This, in turn, results in excitations of pinned accelerated solitary waves due to orbital charged debris objects for first time. In addition, an exact pinned accelerated soliton solution has also been derived in [15]. The pinned nature of these solutions indicates the fact that they move with the same velocity as debris objects; as such, they remain pinned during their motions to the debris objects. In another work [16], we have also included effects of static dust cloud in ionosphere in our formulation on space debris to yield dust-ion acoustic waves by extending [15] to $(2 + 1)$-dimensions. These are found to be governed by a forced Kadomtsev-Petviashvili II (KPII) equation using reductive perturbation technique (RPT) in plasma fluid equations [16]. In this work, certain novel accelerated and curved solitary waves solutions have been derived from the forced KPII equation. We have included effects of fluctuations in background magnetic field using Hall magnetohydrodynamic (MHD) framework in [17] to derive a forced KPI equation governing dynamics of slow and fast magnetosonic wave excitations due to debris objects. As such, inertial effects of electrons have been neglected in this work by assuming dominance of ion dynamics. Some novel exact as well as approximate pinned accelerated lump wave solutions have been derived in [17],

which represent dynamics of both slow and fast magnetosonic waves. Subsequently, the excitations of nonlinear magnetosonic waves by orbital motions of charged space debris objects have been investigated in inertial magnetohydrodynamics (MHD) framework by Acharya et al. [18]. These magnetosonic waves are found to be governed by a forced Kadomtsev-Petviashvili (KP) equation, where the forcing function interprets effects of charged space debris objects functioning as current density sources. In particular, nonlinear evolution of slow magnetosonic waves in entire parameter space and fast magnetosonic waves in a large region of parameter space has been shown to be governed by a forced KPI equation. Similarly, forced KPII equation governs dynamics in the remaining small region of parameter space for fast magnetosonic waves [18]. Therefore, accelerated lump waves become stable in the regions of parameter space that are governed by forced KPI equation along with normal lump waves; both curved and accelerated solitary waves gain stability in the remaining small region of parameter space governed by forced KPII equation in addition to normal solitary waves in $(2+1)$ dimensions excluding lump waves [16–18]. But the possibility of existence of lump wave solutions showing characteristic bending features or distortions cannot be avoided for forced KPI equation, which governs dynamics of space debris-induced magnetosonic waves in a large region of parameter space. Therefore, one important point in this context is that such distorted lump wave solutions for the forced KPI equation have not been analyzed in [16–18]. But such exotic magnetosonic wave structures can be of potential importance in designing indirect detection systems for space debris objects. This is because in realistic perturbative situations in ionospheric plasma in the presence of orbital charged debris objects, normal lump waves may have less possibility of occurrence as compared to distorted lump waves.

Inspired by this fact, we have derived a special exact pinned distorted lump wave solution of the forced KPI equation derived in [18] in Sect. 2 for a specific localized form of the forcing function for first time. The reason for choosing such a peculiar forcing function has been discussed in context of orbital space debris objects using [12, 14] as well in Sect. 2. Ultimately, some novel results of this work have been recapitulated along with comprehensive discussions and future research plans in Sect. 3. Some concluding remarks are provided in Sect. 4 followed by acknowledgments and bibliography.

2 Derivation of Novel Distorted Magnetosonic Lump Wave Solution of Forced KPI Equation

The normalized form of the forced KPI equation derived in the recent work of Acharya et al. [18] is given by

$$\frac{\partial}{\partial X}\left(\frac{\partial U}{\partial T}+6U\frac{\partial U}{\partial X}+\frac{\partial^3 U}{\partial X^3}\right)-3\frac{\partial^2 U}{\partial Z^2}=\frac{\partial J}{\partial X}. \tag{1}$$

In this Eq. (1), the normalizations used are given in [18]. In particular, X and Z denote normalized spatial variables, T is normalized temporal variable, U characterizes normalized plasma density that is fluctuating, and J stands for external forcing. The external forcing J in Eq. (1), in fact, represents a normalized current density source arising due to orbital motions of charged space debris objects in ionospheric plasma.

Now we are going to derive a special exact distorted magnetosonic lump wave solution for which the external forcing function J is taken to be of the form

$$\begin{aligned} J &= B_1(Z)\, U + B_2(Z)\, \tfrac{\partial U}{\partial X} + B_3(Z), \ X > 0, \\ J &= B_1(Z)\, U + B_2(Z)\, \tfrac{\partial U}{\partial X} - B_3(Z), \ X \le 0, \end{aligned} \tag{2}$$

where B_1, B_2, B_3 represent arbitrarily chosen localized functions of Z so that they vanish when $Z \longrightarrow \pm\infty$. In this forcing function J, the analytical solution U has also been used; this indicates a self-consistent forcing function that is similar to the special forcing function considered in our earlier work [16] to derive a novel curved solitary wave solution for dust-ion acoustic waves in the presence of space debris. The main requirement is that the function J in Eq. (2) should vanish as $X \longrightarrow \pm\infty$.

We introduce a new variable $\psi(X, Z, T)$ such that

$$U(X, Z, T) = U(\psi); \ \psi = X + A(Z) + T + \psi_0, \tag{3}$$

where ψ_0 is a constant responsible for phases of U and F and $A(Z)$ is another arbitrary function of Z. Using the above transformation Eq. (3), we get

$$\frac{\partial}{\partial X} = \frac{d}{d\psi}; \ \frac{\partial}{\partial Z} = \frac{dA}{dZ}\frac{d}{d\psi}; \ \frac{\partial^2}{\partial Z^2} = \frac{d^2A}{dZ^2}\frac{d}{d\psi} + \left(\frac{dA}{dZ}\right)^2 \frac{d^2}{d\psi^2}; \ \frac{\partial}{\partial T} = \frac{d}{d\psi}. \tag{4}$$

Equation (4) indicates that the partial derivatives have been transformed into normal derivatives as all the independent variables X, Z, and T are merged into a single new independent variable ψ after the transformation Eq. (3). Substituting Eq. (4) in Eq. (1), we obtain

$$\begin{aligned} &\left(\frac{d}{d\psi}\left(\frac{dU}{d\psi} + 6\,U\,\frac{dU}{d\psi} + \frac{d^3U}{d\psi^3}\right) - 3\frac{dA}{dZ^2}\frac{dU}{d\psi}\right. \\ &\left. - 3\left(\frac{dA}{dZ}\right)^2 \frac{d^2U}{d\psi^2} = B_1\,\frac{dU}{d\psi} + B_2\,\frac{d^2U}{d\psi^2}, \right. \end{aligned} \tag{5}$$

For simplicity, we have imposed the following restrictions among the arbitrary functions $B_1(Z)$, $B_2(Z)$, and $A(Z)$:

$$B_1 = -3\tfrac{d^2A}{dZ^2}, \quad B_2 = 3\left[1 - \left(\tfrac{dA}{dZ}\right)^2\right]. \tag{6}$$

Hence the function $A(Z)$ in Eq. (3) can be evaluated in terms of the arbitrarily chosen localized functions $B_1(Z)$ and $B_2(Z)$ taken in Eq. (2). As a result, Eq. (5) reduces to

$$\frac{d}{d\psi}\left(\frac{dU}{d\psi} + 6\,U\,\frac{dU}{d\psi} + \frac{d^3U}{d\psi^3}\right) - 3\frac{d^2U}{d\psi^2} = 0. \tag{7}$$

Equation (7) is nothing but an unforced KPI equation. Therefore, we have converted the forced KPI Eq. (1) into the unforced KPI Eq. (7) using the transformation Eq. (3) for the forcing function given in Eq. (2); this conversion is valid for specific constraints among $B_1(Z)$, $B_2(Z)$, and $A(Z)$ given in Eq. (6).

It is very well-known that the unforced KPI Eq. (7) admits an exact rational algebraic lump wave solution [19], which can be written as

$$U(\psi) = 4\frac{[-(1+m+3m^2-3n^2)^2 + n^2(1+6m)^2]\psi^2 + \frac{1}{n^2}}{\{[(1+m+3m^2-3n^2)^2 + n^2(1+6m)^2]\psi^2 + \frac{1}{n^2}\}^2}. \tag{8}$$

In terms of the original normalized variables X, Z, and T, the above lump wave solution (8) becomes

$$U(X,Z,T) = 4\frac{[-(1+m+3m^2-3n^2)^2 + n^2(1+6m)^2][X+A(Z)+T+\psi_0]^2 + \frac{1}{n^2}}{\{[(1+m+3m^2-3n^2)^2 + n^2(1+6m)^2][X+A(Z)+T+\psi_0]^2 + \frac{1}{n^2}\}^2}. \tag{9}$$

Equation (9) represents the desired special exact distorted magnetosonic lump wave solution of the forced KPI Eq. (1). Equation (9) has been referred to as special as it has been derived for a special choice of the forcing function J given in Eq. (2) of the forced KPI Eq. (1). The distortions in this lump wave solution can be modelled by different appropriate values of $A(Z)$ in view of Eq. (6). Therefore, this function $A(Z)$ is responsible for the distorted nature of the lump wave solution in Eq. (9).

3 Results and Discussions

The supreme finding of this work is the derivation of a novel exact distorted magnetosonic lump wave solution Eq. (9) in the previous section. One crucial feature of this solution is that its characteristic distortions have been modelled in our work with the arbitrary function $A(Z)$ satisfying a set of appropriate localization conditions given in Eq. (6). In accordance with this fact, different kinds of distortions in magnetosonic lump waves consistent with practical observations in ionospheric

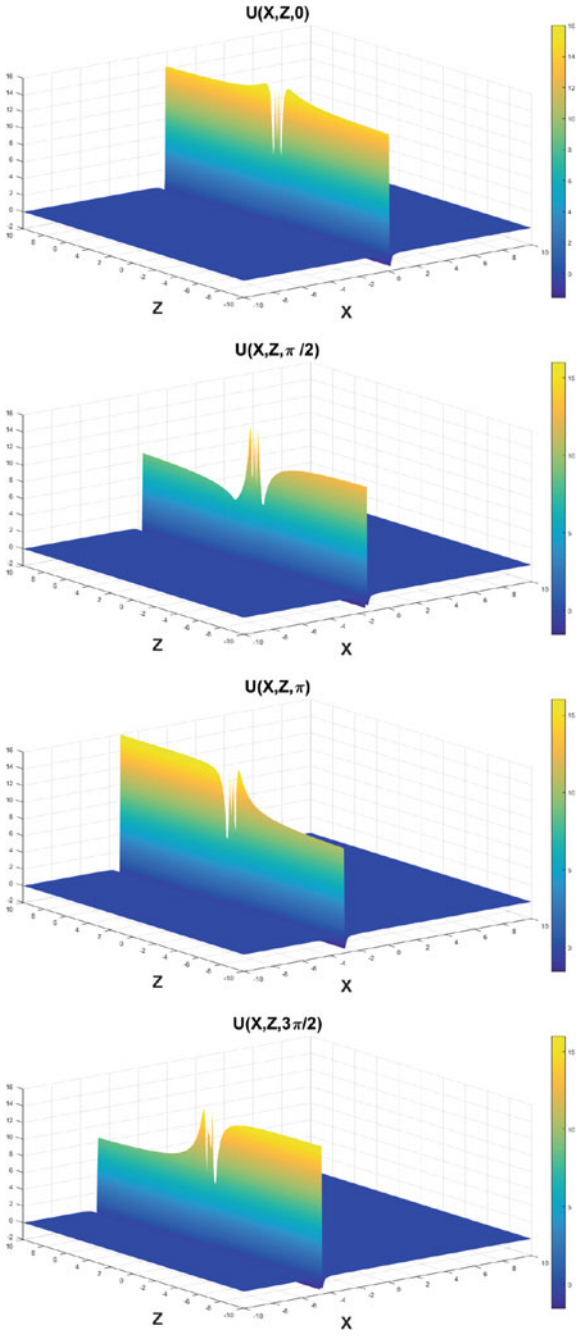

Fig. 1 Visualizations of the distorted magnetosonic lump wave solution in Eq. (9) at different times for the values of parameters given as: $m = 0.1,\ n = 2$ and $\psi_0 = 0$

plasma environment to be excited by orbital motions of charged space debris objects can be modelled by appropriate choices of the arbitrary function $A(Z)$, which is dependent on the two arbitrary localized functions $B_1(Z)$ and $B_2(Z)$.

Therefore, finally, the nature of the forcing function J defined in Eq. (2) determines the nature of distortions in the excited lump waves. This is physically consistent because the nature of the forcing function, in fact, is attributed to different characteristics of charged space debris objects as well as their associated orbital motions, which, of course, have implications on the nature of the excited magnetosonic lump waves due to debris objects. In this context, it is important to note that the work of Truitt and Hartzell [13, 14] has estimated the forcing function, in correspondence with orbital charged space debris objects, to be of Gaussian nature having dependences on size, shape, velocity, and surface potential of the charged debris object, Debye shielding effects, due to surrounding plasma and the distance of point of observation from the debris object. It is obvious that Gaussian functions are pictorially similar to $sech^2$ functions in one dimension and rational algebraic lump wave structures in two dimensions. Sen et al. [12] have considered forcing functions of $sech^2$ and $sech^4$ as well as Gaussian nature in their pioneering work on space debris. In our earlier studies [15–18], we have considered different localized forms of forcing functions involving expressions of hyperbolic as well as rational algebraic lump wave nature to interpret effects of charged space debris objects. In view of these facts, different localized functions similar to Gaussian or $sech^2$ functions at least in pictorial perspectives can be consolidated to represent effects of charged space debris objects along with their orbital motions in ionospheric plasma region in our model. The justifiability of the forcing function J in Eq. (2), in this regard, to represent the effects of charged space debris objects can be explained using the localization conditions specified in the previous section along with plots of J that have not been shown in this article for simplicity.

In order to explore the nature of the novel distorted magnetosonic lump wave solution Eq. (9), we have shown temporal evolution of $U(X, Z, T)$ against X and Z in Fig. 1 for following values of the free parameters: $m = 0.1$, $n = 2$, and $\psi_0 = 0$ at different times. From this Fig. 1, it is clear that this peculiar distorted lump wave solution Eq. (9) has some characteristics similar to planar solitary waves [16] as well. This is because we have chosen the arbitrary function $A(Z)$ to be of the form:

$$A(Z) = 0.069 \tan^{-1}(7.28Z) - 0.003 \sin[2 \tan^{-1}(7.28Z)]. \tag{10}$$

Equation (10) for $A(Z)$ is just an arbitrary selection from which $B_1(Z)$ and $B_2(Z)$ can be evaluated using Eq. (6) to visualize the nature of the forcing function Eq. (2) for another appropriate arbitrary value of $B_3(Z)$. For simplicity, this forcing function plot has not been shown here. One important aspect in this context is that this forcing function J in Eq. (2) moves with the same velocity as the distorted magnetosonic lump wave solution U given by Eq. (9), i.e., they are pinned in nature, which indicates the fact that the distorted magnetosonic lump waves excited by orbital charged space debris objects remain pinned to them during their

propagations. This pinned nature can be verified in an analogous way as done in our previous works [16, 17].

From Fig. 1, one obvious fact is that amplitudes of the contributions from planar solitary wave parts vary significantly, whereas those of lump wave parts remain more or less constant during propagation of the distorted magnetosonic lump wave solution Eq. (9). As such, dominance of contributions from lump wave parts is resulted; this special feature makes this kind of solution to be of immense interest. Various other appropriate forms of the arbitrary function $A(Z)$ in this solution Eq. (9) consistent with the localized arbitrary functions $B_1(Z)$, $B_2(Z)$ and $B_3(Z)$ in the forcing function Eq. (2) can be chosen to explore their dynamics. By observing Fig. 1 from pictorial viewpoint, one may also interpret this solution as a distorted or exotic planar wave solution. This nomenclature can create misconceptions as the mathematical expression of this solution Eq. (9) is of rational algebraic form having localized nature accompanied with distortions characterized by $A(Z)$; this is a typical characteristic of lump waves instead of planar waves. Therefore, our nomenclature to refer it as a distorted lump wave solution is justifiable.

One important characteristic feature of the distorted magnetosonic lump wave solution Eq. (9) is that $B_3(Z)$ does not appear in it, whereas it is present in the forcing function Eq. (2). The mere role of $B_3(Z)$ in Eq. (2) is to assist J in fulfilling the required localization condition. In certain cases, J may also satisfy the localization conditions with vanishing values of $B_3(Z)$. This means that the presence of $B_3(Z)$ in J as specified in Eq. (2) may not be needed in such cases. Such cases, in particular, correspond to some selections of arbitrary functions $B_1(Z)$, $B_2(Z)$, and $A(Z)$ satisfying the restrictions Eq. (6) for which the expression $B_1(Z)U + B_2(Z)\frac{\partial U}{\partial X} \longrightarrow 0$ as $X \longrightarrow \infty$. We have provided $B_3(Z)$ in Eq. (2) from a general perspective. One crucial point to be noted in this context is that we have not imposed the localization condition in $Z-$direction in both the distorted lump wave solution Eq. (9) and forcing function Eq. (2), i.e., U, $J \longrightarrow 0$ as $Z \longrightarrow \infty$, because the distortions in these self-consistent expressions have been modelled with the help of $A(Z)$ only.

The derivation of the distorted magnetosonic lump wave solution Eq. (9) from the forced KPI Eq. (1) in the previous section is similar to the derivation of a novel curved solitary wave solution in our earlier work [16] from a forced KPII equation including the nature of the forcing function. But this solution Eq. (9) is desirably novel and has not been reported till now as far as our knowledge goes.

4 Conclusions

In this work, we have derived an exact distorted lump wave solution of a forced KPI equation in context of magnetosonic wave excitations by orbital charged space debris objects in ionospheric plasma for a self-consistent forcing function. This typical solution has several special characteristics, which have been modelled using arbitrary functions in our work. Also, this solution remains pinned to the charged

debris object during its propagation in ionospheric plasma. As such, these distorted magnetosonic lump waves may not be helpful for indirect detection of charged space debris objects in ionosphere, but the distorted lump waves may be envisaged to have implications in ground-based detection systems for orbital debris objects serving as their indirect signatures. This is because these distorted magnetosonic lump waves have widths of order of ion inertial lengths as discussed in [18] for angles of propagations excluding nearly parallel angles; here, nearly parallel angles represent angles of propagations, which are nearly parallel to direction of ambient magnetic field in ionosphere. For nearly parallel propagations, they have widths of order of Debye lengths [18]. Distorted magnetosonic lump waves having such appreciable widths can be detected by various ground-based optical means, whereas sub-centimeter debris objects are very difficult to be detected from ground through optical means [12, 18]. In this perspective, the novel findings of the present investigation can be potentially very useful. This is because this work is applicable for sub-centimeter debris objects, which is discussed in the work of Acharya et al. [18]. This fact, in turn, can lead to many directions for further research in this interesting field to encounter different exotic solitary wave structures due to charged debris objects. Excitations of magnetosonic precursors as well as wakes by charged debris objects can be modelled in our work using numerical methods. This is planned to be carried out in the future.

Acknowledgments One of the authors Siba Prasad Acharya is thankful to Department of Atomic Energy (DAE) under the Government of India for financial assistance during this work through institute fellowship scheme.

References

1. Frequently Asked Questions [online database]. Orbital Debris Program Office, NASA (2018). https://orbitaldebris.jsc.nasa.gov/faq.html [retrieved 12 June 2019]
2. NASA's efforts to mitigate the risks posed by orbital debris (2021). In: Report no. IG-21-011, NASA Office of Inspector General, Office of Audits
3. Krag, H., Serrano, M., Braun, V., et al.: A 1 cm space debris impact onto the Sentinel-1A solar array. Acta Astronaut. **137**, 434–443 (2017). https://doi.org/10.1016/j.actaastro.2017.05.010
4. Missel, J., Mortari, D.: Path optimization for Space Sweeper with Sling-Sat: a method of active space debris removal. Adv. Space Res. **52**(7), 1339–1348 (2013)
5. ESA commissions world's first space debris removal, The European Space Agency (2019)
6. Si, J., Pang, Z., Du, Z., Cheng, C.: Dynamics modeling and simulation of self-collision of tether-net for space debris removal. Adv. Space Res. **64**(9), 1675–1687 (2019). https://doi.org/10.1016/j.asr.2019.08.006
7. Japan Aerospace Exploration Agency (JAXA). Press Release: JAXA concludes partnership-type contract for Phase I of its Commercial Removal of Debris Demonstration (CRD2) (2020)
8. Japan Aerospace Exploration Agency (JAXA). Press Release: Joint demonstration of J-SPARC initiated by ALE and JAXA, aimed at the commercialization of space debris prevention device (2020)
9. Ganguli, G., Crabtree, C., Rudakov, L., Chappie, S.: A concept for elimination of small orbital debris. Trans. Japan Soc. Aeronaut. Space Sci. Aerospace Technol. Japan 10(28), 23–27 (2012)

10. Takahasi, K., Charles, C., Boswell, R.W., Ando A.: Demonstrating a new technology for space debris removal using a bi-directional plasma thruster. Sci. Rep. **8**, 14417 (2018). https://doi.org/10.1038/s41598-018-32697-4
11. Saini, V., Ganesh, R.: Numerical simulation of a bi-directional plasma thruster for space debris removal. J. Plasma Phys. **88**(2), 905880203 (2022). https://doi.org/10.1017/S0022377822000174
12. Sen, A., Tiwari, S., Mishra, S., Kaw, P.: Nonlinear wave excitations by orbiting charged space debris objects. Adv. Space Res. **56**, 429–435 (2015). https://doi.org/10.1016/j.asr.2015.03.021
13. Truitt, A.S., Hartzell, C.M.: Simulating plasma solitons from orbital debris using the forced Korteweg-de Vries equation. J. Spacecrafts Rockets **57**, 5 (2020). https://doi.org/10.2514/1.A34652
14. Truitt, A.S., Hartzell, C.M.: Three-dimensional Kadomtsev-Petviashvili damped forced ion acoustic solitary waves from orbital debris. J. Spacecrafts Rockets **58**(3), 848–855 (2021). https://doi.org/10.2514/1.A34805
15. Mukherjee, A., Acharya, S.P., Janaki, M.S.: Dynamical study of nonlinear ion acoustic waves in presence of charged space debris at Low Earth Orbital (LEO) plasma region. Astrophys Space Sci. **366**, 7 (2021). https://doi.org/10.1007/s10509-020-03914-2
16. Acharya, S.P., Mukherjee, A., Janaki, M.S.: Bending of pinned dust-ion acoustic solitary waves in presence of charged space debris. Phys. Rev. E **104**, 014214 (2021). https://doi.org/10.1103/PhysRevE.104.014214
17. Acharya, S.P., Mukherjee, A., Janaki, M.S.: Accelerated magnetosonic lump wave solutions by orbiting charged space debris. Nonlinear Dyn. **105**, 671–689 (2021). https://doi.org/10.1007/s11071-021-06594-x
18. Acharya, S.P., Mukherjee, A., Janaki, M.S.: Charged space debris induced nonlinear magnetosonic waves using inertial magnetohydrodynamics. Adv. Space Res. **69**, 4045–4057 (2022). https://doi.org/10.1016/j.asr.2022.03.020
19. Ma, W.X.: Lump solutions to the Kadomtsev–Petviashvili equation. Phys. Lett. A **379**, 1975–1978 (2015). https://doi.org/10.1016/j.physleta.2015.06.061

Harmonic and Superharmonic Components in Periodic Waves Propagating Through Mechanical Metamaterials with Inertial Amplification

Marco Lepidi and Valeria Settimi

1 Introduction

The dispersion properties of microstructured periodic waveguides are a scientific topic of major interest in nonlinear dynamics. Particularly, the long-dating tradition of research studies concerning the propagation of nonlinear elastic waves in oscillator chains and other periodic structures [1, 2] is being catalyzed by the recent extraordinary development of microstructured materials and mechanical metamaterials [3, 4]. Specifically, a pressing technological demand is boosting the innovation in the emerging field of architected passive media. In order to broaden the existing range of achievable functionalities, the periodic cell of mechanical metamaterials can be enriched with auxiliary flexible microstructures inducing relevant linear and nonlinear dynamic phenomena. The micromechanisms of inertial amplification, in particular, have been theoretically conceived [5, 6], computationally and experimentally verified [7] to offer unprecedented possibilities in the functional design of efficient mechanical filters [8–11]. Within the class of inertially amplified metamaterials, the microstructural pantographic mechanisms of amplitude multiplication, accompanied by limited dissipation properties, constitute a natural scenario for the rise of important nonlinear dynamic phenomena [12]. The present paper analyzes the properties of superharmonic components in periodic waves propagating through inertially amplified metamaterials.

M. Lepidi (✉)
DICCA – Department of Civil, Chemical and Environmental Engineering, University of Genova, Genova, Italy
e-mail: marco.lepidi@unige.it

V. Settimi
DICEA – Department of Civil and Building Engineering, and Architecture, Polytechnic University of Marche, Ancona, Italy
e-mail: v.settimi@staff.univpm.it

© The Author(s), under exclusive license to Springer Nature Switzerland AG 2024

W. Lacarbonara (ed.), *Advances in Nonlinear Dynamics, Volume III*, NODYCON Conference Proceedings Series, https://doi.org/10.1007/978-3-031-50635-2_50

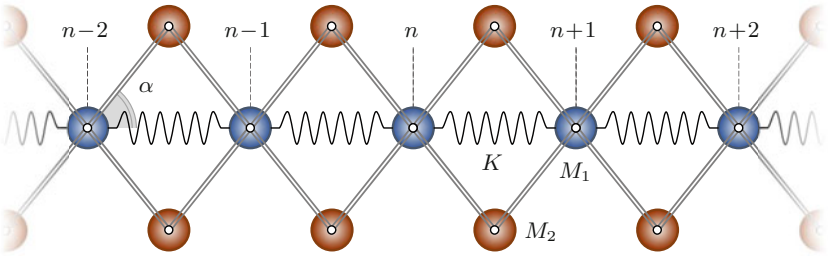

Fig. 1 Mechanical metamaterial with pantographic inertial amplification: primary atoms (blue) and secondary atoms (red)

2 Mechanical Metamaterial

The minimal mechanical metamaterial characterized by inertial amplification can be physically realized by assembling an infinite periodic one-dimensional chain of massive point particles, or *atoms*, interconnected by local pantographic mechanisms (Fig. 1). Within the repetitive pantographic mechanism, two adjacent point particles (*primary atoms*) are elastically coupled to each other and rigidly connected to a pair of eccentric point particles (*secondary atoms*).

The elastic coupling between each pair of primary atoms is described by a linear spring with stiffness K. The rigid connections between the primary and secondary atoms are modeled by indeformable massless truss (hinged-hinged) elements, namely, the *pantograph arms*, inclined by the same angle α with respect to the chain axis. The masses of the primary and secondary atoms are denoted by M_1 and M_2, respectively. The one-dimensional motion of the primary atom located at the n-th site (with $n \in \mathbb{Z}$) is described by the time-dependent displacement $U_n(t)$, collinear with the chain axis. Consequently, the displacements $U_{n-1}(t)$ and $U_{n+1}(t)$ indicate the displacements of the adjacent atoms at incremented $(n+1)$-th and decremented $(n-1)$-th sites. The pantographic mechanism makes the chain-orthogonal motion of the secondary atoms geometrically dependent on the differences of motion between the primary atoms.

A minimal set of independent dimensionless mechanical parameters, sufficient to completely describe the mechanical model, includes the *mass ratio* $\varrho^2 = M_2/M_1$, strictly positive by definition, and the *amplification angle* $\alpha \in (0, \pi/2)$.

2.1 Equation of Motion

The free undamped dynamics of the metamaterial can be analyzed by studying the equation of motion for the n-th site, by virtue of the periodicity. The dimensionless time $\tau = \Omega t$ and dimensionless displacements $u_n = U_n/L$, $u_{n-1} = U_{n-1}/L$,

$u_{n+1} = U_{n+1}/L$ can be defined, by selecting the ratio $\Omega^2 = K/M_1$ and the inter-site distance L as reference (square) frequency and length, respectively. First, an exact finite kinematic formulation for the indeformability constrain of the pantograph arms is adopted. Second, the hypothesis of small displacements is introduced by consistently expanding the constrained kinetic energy up to a suited order of the small displacements. Therefore, according to the Hamilton principle and retaining terms up to the third order, the equation of motion reads:

$$\begin{aligned}
&\varrho_n^2\ddot{u}_n + \varrho_a^2(\ddot{u}_{n-1} + \ddot{u}_{n+1}) + 2u_n - u_{n-1} - u_{n+1} + \\
&+ 2c_2\big[\ddot{u}_n(u_{n+1} - u_{n-1}) + \ddot{u}_{n-1}(u_{n-1} - u_n) + \ddot{u}_{n+1}(u_n - u_{n+1})\big] + \\
&+ c_2\big[\dot{u}_{n-1}^2 + 2\dot{u}_n(\dot{u}_{n+1} - \dot{u}_{n-1}) - \dot{u}_{n+1}^2\big] + \\
&+ c_3\ddot{u}_n\big[2u_n^2 + u_{n-1}^2 + u_{n+1}^2 - 2u_n(u_{n-1} + u_{n+1})\big] + \\
&- c_3\big[\ddot{u}_{n-1}(u_n - u_{n-1})^2 + \ddot{u}_{n+1}(u_n - u_{n+1})^2\big] + \\
&+ 2c_3\dot{u}_n\big[\dot{u}_{n-1}(u_{n-1} - u_n) + \dot{u}_{n+1}(u_{n+1} - u_n)\big] + \\
&+ c_3\big[\dot{u}_n^2(2u_n - u_{n-1} - u_{n+1}) + \dot{u}_{n-1}^2(u_n - u_{n-1}) + \dot{u}_{n+1}^2(u_n - u_{n+1})\big] = 0
\end{aligned} \tag{1}$$

where ϱ_n^2 is the amplified inertia at the n-th site and ϱ_a^2 is the linear inertial coupling, while c_2 and c_3 are the quadratic and cubic inertial coefficients. The inertial amplification ($\varrho_n^2 > 1$) is governed by the amplification angle α.

3 Wave Propagation

The equation of motion can be classified as a nonlinear second-order ordinary differential (in time τ) difference (in discrete space z) equation. In the absence of closed-form solutions and within the range of small oscillations, perturbation methods are powerful and efficient tools to achieve analytical solutions, suited to asymptotically approximate the exact solutions up the desired level of accuracy. Specifically, perturbation techniques like the method of ordered harmonic balance [13], the method of Lindstedt-Poincaré [14], the multiple scales method [15, 16], and the Hamiltonian perturbation theory [17] have been successfully exploited to analyze the weakly nonlinear wave dynamics in metamaterials. Based on these considerations, the real-valued solutions $u_n(\tau) = u(z,\tau)_{z=n}$ can be conveniently expressed in the form of the exponential infinite Fourier series:

$$u(z,\tau) = a_0 + \sum_{j=1}^{\infty} \epsilon^j \left(a_j + \imath b_j\right) \mathrm{e}^{-\imath(\beta z + j\omega\tau)} + \sum_{j=1}^{\infty} \epsilon^j \left(a_j - \imath b_j\right) \mathrm{e}^{\imath(\beta z + j\omega\tau)} \tag{2}$$

describing periodic waves oscillating harmonically in time with frequency ω and its multiples $j\omega$ while propagating in space with dimensionless wavenumber β.

According to a standard perturbation strategy, the real-valued amplitudes a_j and b_j of the j-th Fourier component, harmonically oscillating in time with frequency $j\omega$, are ordered in integer j-power series of the small perturbation parameter $\epsilon \ll 1$. From the physical viewpoint, this ordering postulates a priori that the amplitudes a_1 (of the harmonic ω component), $a_2, a_3,$, ... (of the superharmonic $2\omega, 3\omega$, ... components) are smaller than the quasistatic amplitude a_0 by one, two, three, ... ϵ-powers. Accordingly, the contribution of high harmonics becomes smaller and smaller for growing j, thus justifying the truncation of the Fourier series (up to a finite number $j = k$) on a physical ground.

Substituting the solution (2) for $k = 3$ into equation (1), expanding and collecting terms of the same ϵ-order, an ordered hierarchy of algebraic *perturbation equations* in the Fourier amplitudes a_j, b_j is carried out ($j = 1, 2, 3$). Specifically, the j-th order establishes a linear problem composed by a pair of independent, coupled equations in the unknown amplitudes a_j, b_j. If determinable, the problem solution is unique and generally depends on the solutions of all the lower-order problems. Accordingly, the lowest order rules the linear wave dynamics of the system, which is found to be participated only by the first harmonic ω component (unknown amplitudes a_1, b_1 of the *leading solution*). The higher orders govern the nonlinear wave dynamics, which is found to be participated *also* by the superharmonic $2\omega, 3\omega$ components (unknown amplitudes a_2, b_2, a_3, b_3). It may be noted that the quasistatic amplitude (constant shift a_0) remains undetermined and is unessential for the analysis of the wave propagation.

3.1 Linear Dynamics

At the lowest significant order ($j = 1$), the perturbation equations state a pair of algebraic linear eigenproblems in the amplitudes a_1, b_1 and frequency ω of the first harmonic component. The common eigensolution establishes that nontrivial – although undetermined – amplitudes (playing the role of eigenvectors) may exist if and only if the frequency (eigenvalue) satisfies a characteristic equation $F(\omega^2, \beta, \alpha, \varrho^2) = 0$. Its solution provides the dispersion relation:

$$\omega^2 = \frac{2(1 - \cos\beta)}{1 + \varrho^2 \left(2\cos\beta + \csc^2\alpha\,(1 - \cos\beta)\right)} \tag{3}$$

expressing the linear (amplitude-independent) frequency ω of the mono-harmonic waves freely forward-propagating through the metamaterial with wavenumber $\beta \in [0, \pi]$. The unique dispersion curve mapping the function (3) in the (β, ω)-plane (*metamaterial spectrum*) shows the dispersive nature of the metamaterial. Comprehensive parametric analyses of the dispersion curve can be carried out for different values of the mechanical parameters α, ϱ^2 (Fig. 2). The results show

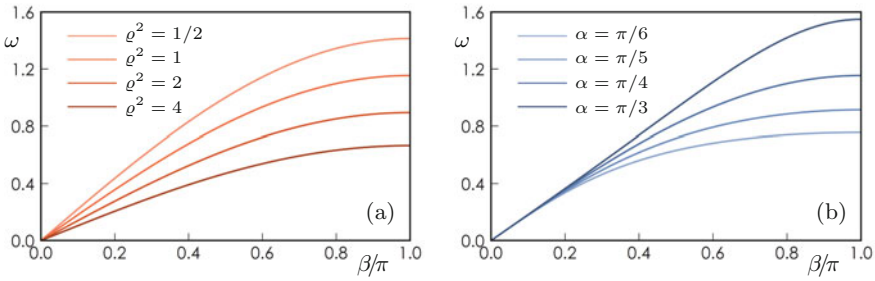

Fig. 2 Linear dispersion curves under variation of mechanical parameters: (**a**) different mass ratios ϱ^2 for fixed $\alpha = \pi/4$, (**b**) different amplification angles α for fixed $\varrho^2 = 1$

that increasing mass ratios ϱ^2 reduce the *pass-bandwidth*, covering the frequency range $\omega^2 \in [0, 4/(1 + 2\varrho^2(1 + \csc^2\alpha))]$. Growing mass ratios ϱ^2 also reduce the group velocity of wave propagation, especially in the range of long wavelengths (Fig. 2a). Differently, increments of the amplification angle α determine increasing pass-bandwidths and growing group velocities, especially in the range of mid wavelengths (Fig. 2b). From the functional viewpoint, this interesting scenario discloses that large mass ratios (realized, for instance, by light primary atoms connected with heavy secondary atoms), associated with small amplification angles, tend to minimize the pass-bandwidth, paving the way for the parametric design of efficient mechanical low-pass filters.

3.2 Nonlinear Dynamics

The higher orders of the perturbation equations leave the amplitudes a_1, b_1 of the first harmonic component undetermined (provided that the dispersion relation (3) is satisfied), whereas they state pairs of linear equations for the unknown amplitudes a_2, b_2 (at the second order $j = 2$) and a_3, b_3 (at the third order $j = 3$) of the superharmonic components. The respective solutions read:

$$\begin{aligned} a_2 &= \eta_2\, a_1 b_1 \\ b_2 &= \mu_2(a_1^2 - b_1^2) \\ a_3 &= \eta_3\left(a_1^3 - 3a_1 b_1^2\right) + \mu_3(a_1 b_2 + a_2 b_1) \\ b_3 &= \eta_3\left(3a_1^2 b_1 - b_1^3\right) + \mu_3(b_1 b_2 - a_1 a_2) \end{aligned} \tag{4}$$

where the parameter-dependent coefficients multiplying the polynomials are

$$\eta_2 = -2\omega^2\varrho^2 \cot^2\alpha\, \csc^2\alpha\, \sin\beta \tag{5}$$

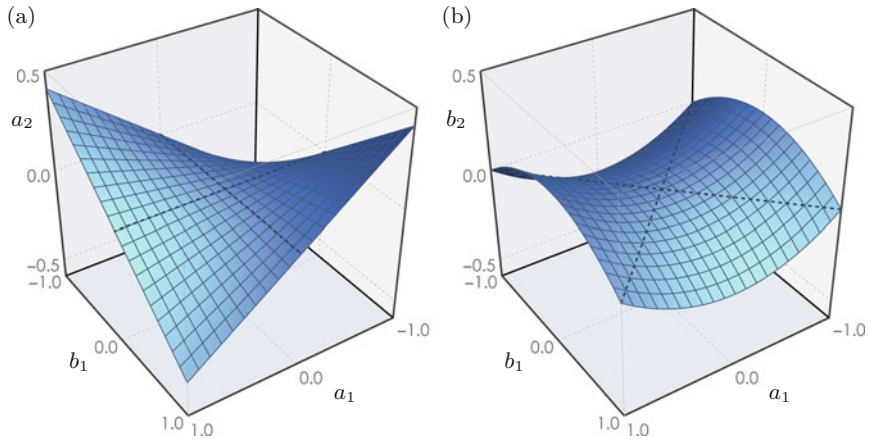

Fig. 3 Amplitude of the superharmonic 2ω components for $\varrho^2 = 1/2$, $\alpha = \pi/4$, $\beta = \pi/4$

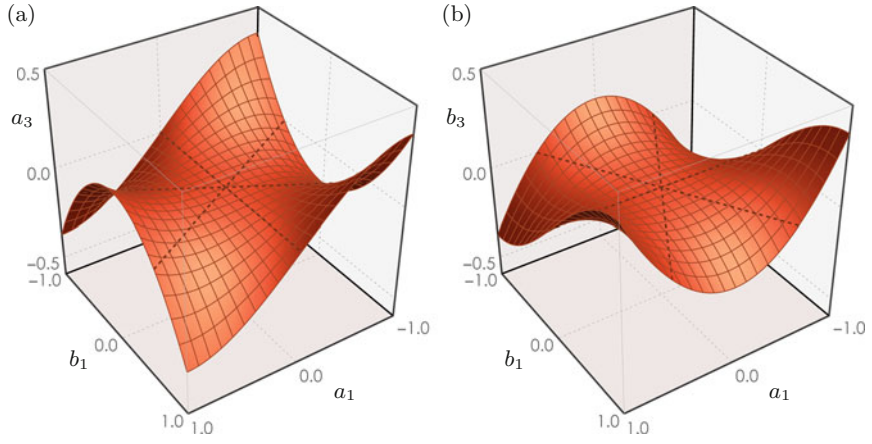

Fig. 4 Amplitude of the superharmonic 3ω components for $\varrho^2 = 1/2$, $\alpha = \pi/4$, $\beta = \pi/4$

$$\mu_2 = \omega^2 \varrho^2 \cot^2\alpha \ \csc^2\alpha \ \sin\beta$$

$$\eta_3 = \tfrac{1}{4}\omega^2 \varrho^2 \cot^2\alpha \csc^2\alpha (\csc^2\alpha + 3\cot^2\alpha)(1 - \cos\beta)(1 + 2\cos\beta)$$

$$\mu_3 = -\tfrac{7}{4}\omega^2 \varrho^2 \cot^2\alpha \csc^2\alpha \sin\beta$$

and ω is intended to satisfy equation (3). Consistently with the perturbation procedure, the superharmonic amplitudes a_2, b_2 and a_3, b_3 depend on the harmonic amplitudes a_1, b_1 according to quadratic and cubic functions, respectively.

The quadratic and cubic surfaces described by relations (4) over the (a_1, b_1)-domain are illustrated in Figs. 3 and 4 for a significant parameter set. The surface morphology shows that different combinations of the leading harmonic ampli-

Table 1 Analytical conditions for zeroing the wavenumber-dependent coefficients or the amplitude-dependent polynomials contributing to the superharmonic amplitudes

Coefficient	Condition
η_2	$\beta = 0 \,\|\|\, \beta = \pi$
μ_2	$\beta = 0 \,\|\|\, \beta = \pi$
η_3	$\beta = 0 \,\|\|\, \beta = 2/3\pi$
μ_3	$\beta = 0 \,\|\|\, \beta = \pi$

Polynomial	Condition
$a_1 b_1$	$a_1 = 0 \,\|\|\, b_1 = 0$
$a_1^2 - b_1^2$	$a_1 = \pm b_1$
$a_1^3 - 3a_1 b_1^2$	$a_1 = 0 \,\|\|\, a_1 = \pm\sqrt{3} b_1$
$a_1 b_2 + a_2 b_1$	$\beta = 0 \,\|\|\, \beta = \pi \,\|\|\, a_1 = 0 \,\|\|\, a_1 = \pm\sqrt{3} b_1$
$3a_1^2 b_1 - b_1^3$	$b_1 = 0 \,\|\|\, b_1 = \pm\sqrt{3} a_1$
$b_1 b_2 - a_1 a_2$	$\beta = 0 \,\|\|\, \beta = \pi \,\|\|\, b_1 = 0 \,\|\|\, b_1 = \pm\sqrt{3} a_1$

tudes a_1, b_1 can determine same-sign or opposite-sign superharmonic contributions a_2, a_3 and b_2, b_3 in the propagating multi-harmonic wave. Furthermore, it can be remarked that some loci in the wavenumber-extended space of harmonic amplitudes (a_1, b_1, β) systematically lead to null superharmonic amplitudes (dashed lines), independently of the mechanical parameter values. The analytical conditions describing these loci, which correspond to combinations of null coefficients and/or null polynomials in equations (4), are reported in Table 1. As significant remark, the conditions disclose that all the superharmonic components 2ω and 3ω vanish at the limit of long wavelengths (i.e., $a_2 = b_2 = a_3 = b_3 = 0$ for $\beta \to 0$). Differently, only the superharmonic 2ω components systematically vanish at the limit of short wavelengths (i.e., $a_2 = b_2 = 0$, but $a_3 \neq 0, b_3 \neq 0$ for $\beta \to \pi$ and generic a_1, b_1).

The higher orders of the perturbation equations provide also the nonlinear dispersion relation $\varpi(\beta)$, intended as the nonlinear (amplitude-dependent) frequency ϖ of the harmonic wave component oscillating with amplitudes a_1, b_1 and freely propagating with wavenumber β. Specifically, the third order perturbs the pair of linear eigenproblems obtained at the first order. Consequently, a pair of independent nonlinear eigenproblems rise up, whose common characteristic equation is satisfied by the nonlinear frequency:

$$\varpi^2 = \omega^2 + \kappa_2 \, \omega^2 (a_1^2 + b_1^2) \tag{6}$$

which consistently recovers the linear dispersion relation (3) for vanishing amplitudes. In this respect, it can be noted that the nonlinear correction of the linear frequency depends quadratically on the oscillation amplitudes. The parameter-dependent coefficient multiplying the square amplitudes is defined as

$$\kappa_2 = 2\omega^2 \varrho^2 \cot^2\alpha \csc^4\alpha \left(1 + 3\cos^2\alpha\right) (\cos\beta - 1) \tag{7}$$

and is commonly known as *effective nonlinearity coefficient*. From equation (7), it can be noted that $\kappa_2 \leq 0$ for any choice of the parameters, meaning that the effective nonlinearity coefficient determines a systematic softening behavior of the nonlinear frequency versus increasing oscillation amplitudes $r_1^2 = a_1^2 + b_1^2$. The softening behavior is qualitatively coherent with the amplitude-dependent reduction

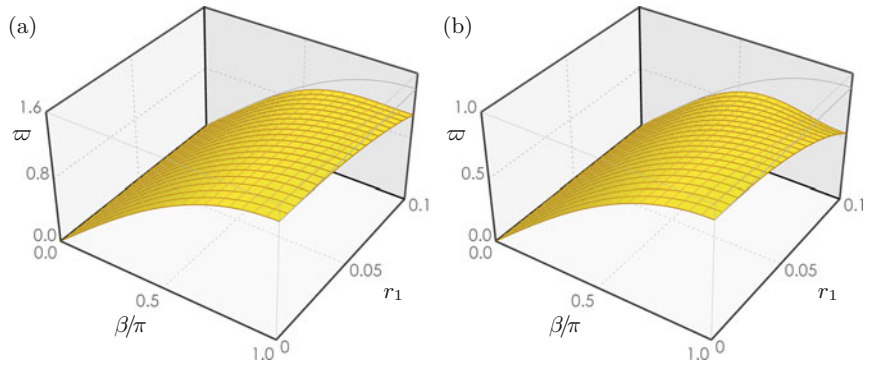

Fig. 5 Nonlinear dispersion curves versus amplitude: (**a**) $\varrho^2 = 1/2$, (**b**) $\varrho^2 = 2$

of the acoustic (lower) frequency characterizing inertially amplified metamaterials with biatomic periodic cell [12]. The nonlinear dispersion curves for increasing amplitudes r_1 are illustrated in Fig. 5 and compared for two different values of the mass ratio. The softening effect increases for larger mass ratios and becomes particularly significant in the range of short wavelengths, even at small vibration amplitudes.

Once the amplitudes of the superharmonic components are determined as a function of the undetermined amplitudes of the harmonic component, the multi-harmonic solution can be reconstructed and expressed in trigonometric form:

$$u_n(\tau) = a_0 + \sum_{j=1}^{k} 2\,\epsilon^j \left[a_j \cos(\beta n + j\omega\tau) + b_j \sin(\beta n + j\omega\tau) \right] \tag{8}$$

where the independent amplitudes a_j and b_j can be recognized to multiply orthogonal (in quadrature) components. The leading amplitudes a_1 and b_1 can be determined by imposing the initial conditions in the solution (8) in terms of displacement and velocity, if available for a certain site. The reconstruction of the multi-harmonic solution requires checking a posteriori the postulated ordering of the harmonic components, which is necessary for the mathematical consistency of the perturbation results. A viable parametric strategy to determine the consistency limits of the perturbation scheme, in terms of maximal leading amplitudes, is outlined and exemplified in the Appendix.

The multi-harmonic solution at the reference site ($n = 0$) is exemplified in Fig. 6. Two different solutions are shown in the phase plane $(u_0, \dot{u}_0)$ for fixed leading amplitudes $(a_1, b_1) = (5/100, 4/100)$ and the same mechanical parameters. The wavenumbers have been chosen to obtain three-harmonic $(\omega, 2\omega, 3\omega)$ solution (Fig. 6a) and bi-harmonic $(\omega, 3\omega)$ solution (Fig. 6b), according to the conditions reported in Table 1. It can be noted that the even (2ω) component breaks the double

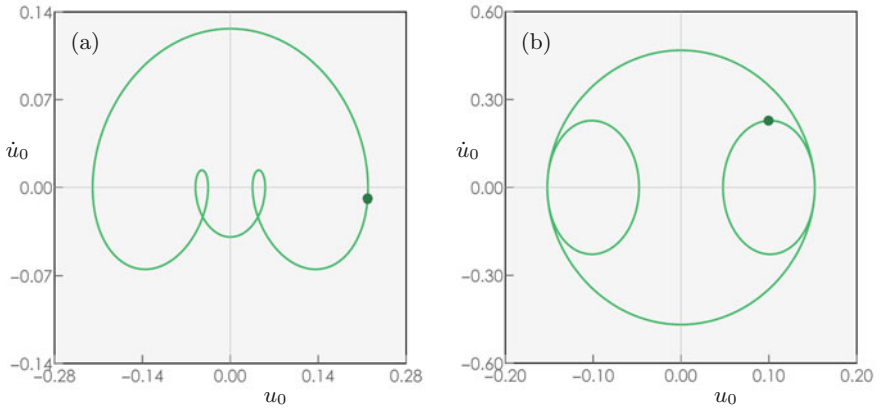

Fig. 6 Multi-harmonic solutions in the phase plane for $\alpha = \pi/8, \varrho^2 = 1$ and different wavenumbers: (**a**) $\beta = \pi/2$, (**b**) $\beta = \pi$

symmetry of the three-harmonic solution. The time periodicity of both solutions is confirmed by the Poincaré points.

4 Conclusions

The second-order differential difference equation governing the nonlinear dynamics of a one-dimensional mechanical metamaterial with inertial amplification has been presented. Within a weak nonlinear regime, a perturbation strategy has been adopted to achieve analytical – although asymptotically approximate – solutions, describing harmonically oscillating freely propagating periodic waves. Parametric expressions have been obtained for the nonlinear frequency, as well as for the amplitudes of the superharmonic components generated by quadratic and cubic nonlinearities. The consistency limits of the perturbation schemes have been discussed. Stronger nonlinear regimes, which can be expected to generate richer scenarios from a global dynamics perspective [18], are under investigation.

Appendix

Setting $b_1 = a_1$ for simplicity and excluding the meaningless case of null leading amplitude ($a_1 \neq 0$), the inherent validity limits of the perturbation method can be estimated by requiring the consistency conditions

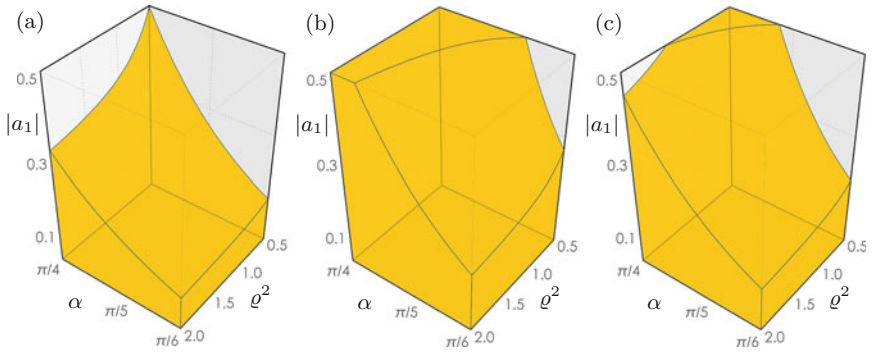

Fig. 7 Compatibility domains for the leading amplitude a_1 at the wavenumber $\beta = \pi/2$ satisfying the compatibility conditions: (**a**) $|a_2| < |a_1|$, (**b**) $|a_3| < |a_2|$, (**c**) $|b_3| < |b_1|$

$$
\begin{aligned}
|a_2| < |a_1| \quad &\rightarrow \quad |a_1| < -\eta_2^{-1} && && (9)\\
|a_3| < |a_2| \quad &\rightarrow \quad |a_1| < \eta_2(2\eta_3 - \eta_2\mu_3)^{-1} && \text{if} \quad 2\eta_3 < \eta_2\mu_3 \\
&\qquad\quad |a_1| < \eta_2(\eta_2\mu_3 - 2\eta_3)^{-1} && \text{iff} \quad \eta_2\mu_3 < 2\eta_3 \ \wedge \ 0 < \eta_3 \\
|b_3| < |b_1| \quad &\rightarrow \quad a_1^2 < (\eta_2\mu_3 - 2\eta_3)^{-1} && \text{if} \quad 2\eta_3 < \eta_2\mu_3 \\
&\qquad\quad a_1^2 < (2\eta_3 - \eta_2\mu_3)^{-1} && \text{iff} \quad \eta_2\mu_3 < 2\eta_3 \ \wedge \ 0 < \eta_3
\end{aligned}
$$

where the natural conditions $\eta_2 < 0$, $\mu_3 < 0$, descending from the definitions (5), have been taken into account. To exemplify, the consistency domains corresponding to inequalities (9) are reported in Fig. 7 over the parameter space.

References

1. Vakakis, A.F., King, M.E.: Nonlinear wave transmission in a monocoupled elastic periodic system. J. Acoust. Soc. Am. **98**(3), 1534–1546 (1995)
2. Romeo F., Rega G.: Wave propagation properties in oscillatory chains with cubic nonlinearities via nonlinear map approach. Chaos Solitons Fractals **27**(3), 606–617 (2006)
3. Hussein, M.I., Leamy, M.J., Ruzzene, M.: Dynamics of phononic materials and structures: Historical origins, recent progress, and future outlook. Appl. Mech. Rev. **66**(4), 040802 (2014)
4. Kadic, M., Milton, G.W., van Hecke, M., Wegener, M. 3D metamaterials. Nat. Rev. Phys. **1**(3), 198–210 (2019)
5. Yilmaz C., Hulbert G., Kikuchi N.: Phononic band gaps induced by inertial amplification in periodic media. Phys. Rev. B: Condens. Matter **76**(5), 054309 (2007)
6. Yilmaz, C., Hulbert, G.: Theory of phononic gaps induced by inertial amplification in finite structures. Phys. Lett. A **374**(34), 3576–3584 (2010)
7. Acar, G., Yilmaz, C.: Experimental and numerical evidence for the existence of wide and deep phononic gaps induced by inertial amplification in two-dimensional solid structures. J. Sound Vib. **332**(24), 6389–6404 (2013)

8. Frandsen N.M., Bilal O.R., Jensen J.S., Hussein M.I.: Inertial amplification of continuous structures: large band gaps from small masses. J. Appl. Phys. **119**(12), 124902 (2016)
9. Banerjee A., Adhikari S., Hussein M.I.: Inertial amplification band-gap generation by coupling a levered mass with a locally resonant mass. Int. J. Mech. Sci. **207**, 106630 (2021)
10. Yuksel O., Yilmaz C.: Realization of an ultrawide stop band in a 2-d elastic metamaterial with topologically optimized inertial amplification mechanisms. Int. J. Solids Struct. **203**, 138–150 (2020)
11. Settimi, V., Lepidi, M., Bacigalupo, A.: Analytical spectral design of mechanical metamaterials with inertia amplification. Eng. Struct. **274**, 115054 (2023)
12. Settimi V., Lepidi M., Bacigalupo A.: Nonlinear dispersion properties of one-dimensional mechanical metamaterials with inertia amplification. Int. J. Mech. Sci. **201**, 106461 (2021)
13. Narisetti, R.K., Ruzzene, M., Leamy, M.J.: Study of wave propagation in strongly nonlinear periodic lattices using a harmonic balance approach. Wave Motion **49**(2), 394–410 (2012)
14. Campana, M.A., Ouisse, M., Sadoulet-Reboul, E., Ruzzene, M., Neild, S., Scarpa, F.: Impact of non-linear resonators in periodic structures using a perturbation approach. Mech. Syst. Sig. Process. **135**, 106408 (2020)
15. Manktelow, K., Leamy, M.J., Ruzzene, M.: Multiple scales analysis of wave–wave interactions in a cubically nonlinear monoatomic chain. Nonlinear Dyn. **63**(1), 193–203 (2011)
16. Lepidi, M., Bacigalupo, A.: Wave propagation properties of one-dimensional acoustic metamaterials with nonlinear diatomic microstructure. Nonlinear Dyn. **98**(4), 2711–2735 (2019)
17. Fortunati, A., Bacigalupo, A., Lepidi, M., Arena, A., Lacarbonara, W.: Nonlinear wave propagation in locally dissipative metamaterials via Hamiltonian perturbation approach. Nonlinear Dyn. **108**(2), 765–787 (2022)
18. Rega, G., Settimi, V.: Global dynamics perspective on macro-to nano-mechanics. Nonlinear Dyn. **103**(2), 1259–1303 (2021)

Fast Numerical Solution to Nonlinear Shallow Water System

Mikhail Lavrentiev, Andrey Marchuk, Konstantin Oblaukhov, and Mikhail Shadrin

1 Introduction

After the Great Tohoku Earthquake of March 11, 2011 offshore Japan, it became clear that tsunami warning systems should be significantly improved. For the near field tsunami (in case tsunami source is close enough to the coast) it takes a wave nearly 20 min to propagate from the source to the nearest coast. There are several software packages which provide high accuracy simulation of the tsunami wave generation, propagation, and inundation of a dry land. First of all, MOST (Method of Splitting Tsunamis, NOAA Pacific Marine Environmental Laboratory, Seattle, WA USA) [1, 2], is widely used as a reference code in "tsunami research" community. In fact, it is the official instrument of the tsunami warning services of the USA. Among alternative instruments, it is necessary to mention the TUNAMI code (Tohoku University's Numerical Analysis Model for Investigation of Near field tsunamis, Tohoku University, Japan) [3, 4]. The improved version named NAMI-DANCE [5] was written in C++ using, in particular, the MPI (Message Passing Interface) and OpenMP (Open Multi-Processing) parallel programming methods. This parallel

M. Lavrentiev (✉)
Institute of Automation and Electrometry SB RAS, Novosibirsk, Russia

Sobolev Institute for Mathematics SB RAS, Novosibirsk, Russia

A. Marchuk
Institute of Automation and Electrometry SB RAS, Novosibirsk, Russia

Sobolev Institute for Mathematics SB RAS, Novosibirsk, Russia

Institute of Computational Mathematics and Mathematical Geophysics SB RAS, Novosibirsk, Russia

K. Oblaukhov · M. Shadrin
Institute of Automation and Electrometry SB RAS, Novosibirsk, Russia

© The Author(s), under exclusive license to Springer Nature Switzerland AG 2024

W. Lacarbonara (ed.), *Advances in Nonlinear Dynamics, Volume III*, NODYCON Conference Proceedings Series, https://doi.org/10.1007/978-3-031-50635-2_51

implementation makes it possible to achieve a very good performance on modern cluster supercomputer systems.

However, each of these tools requires extended computational resources and typically consumes valuable time. Moreover, one can hardly expect results of the required analysis in a few minutes even when relying on supercomputer processing. It should be also noted that disaster events, such as the one of March 11, 2011, may lead to power shutdowns.

At the same time, in order to evaluate possible negative tsunami wave implications (including infrastructure destruction and loss of human life), one does not need to know the exact wave amplitude at a particular populated coastal area or industrial site. There is no need to solve numerically a complete 3D Navier-Stokes system, to account bottom friction, dispersion, and some other physical phenomenon. Obviously, a wave with 2 m amplitude should be considered no dangerous even within 10–15% deviation. On the other hand, a 20 m wave is certainly dangerous, as well as waves of 17–23 m amplitude. So, a 10–15% error in predicting tsunami wave amplitude should be acceptable in tsunami warning services.

The desired tsunami warning system must (1) work very fast (within a few minutes), (2) be independent of power supply (in case of possible power supply shut down) and (3) provide a realistic approximation of tsunami wave height with a 10–15% accuracy. All these contradictory requirements could be achieved by using an ordinary modern personal computer (PC) with a specialized co-processor—the Field Programmable Gates Array (FPGA) based Calculator, proposed and tested [6].

Hardware devices, which allow structure adaptation according to a particular task, the so-called Programmable Logic Arrays (PLAs), appeared in the 1980s. The most popular were the Programmable Logic Devices (PLD) widely used to create autonomous devices and controllers, small in size and energy efficient. New generation hardware in this direction is called FPGA (Field-Programmable Gates Array), which has a much larger number of logic elements and enables reconfiguration. Due to these features of FPGA it is now possible to implement rather complicated mathematical algorithms for data processing and even perform prototyping of computation devices, including CPUs and GPUs.

To leverage the advantages of the FPGA microchip features, the stream processor architecture was proposed as an implementation of the numerical algorithm. The proposed Calculator contains several processor elements (PEs). Each of these elements forms a pipeline with a sequential data stream. The “onboard” memory contains all the necessary information. The acceleration of calculations by the FPGA architecture is due to the inner Block Random Access Memory (BRAM) for implementing the stencil buffer.

The Calculator architecture [6] makes it possible to process several nodes in parallel. At the same time, the user can connect a number of PEs to work on several time layers simultaneously. So, the computation pipeline could be optimized depending on the features of the FPGA microchip in use. MacCormack finite difference approximation fits very well with the Calculator architecture processing one node in one computer clock cycle.

In this chapter, the advantages of FPGA-based Calculator (parallel implementation of the MacCormack finite-difference scheme) for the numerical solution of the shallow water equation system are demonstrated by studying dependence of alongshore wave maximal heights on parameters of computational grid. To investigate the influence of the computational grid step length on the results, numerical simulations of tsunami propagation from a model ellipsoidal source were performed. The outlines and field of displacement of the water surface are not essential for qualitative conclusions on the influence of the grid resolution on the results. An acceleration of ~300 times (for one time step) was achieved compared to single-threaded computing. This comparison was made against a non-optimized, single-threaded reference MOST algorithm running on a 3 GHz CPU. Therefore, the use of such a model source in calculations is quite acceptable.

2 Problem Statement

2.1 Mathematical Model

Following most of the tsunami researchers, the nonlinear shallow water PDE system [7] was used to simulate the tsunami wave propagation. External forces such as sea bed friction, Coriolis force, and others were neglected. The effect of the Coriolis force on the dynamics of tsunami wave propagation can be observed only when it moves in the north-south direction for a long enough distance (10 geographic degrees or more). This force is taken into account in calculations of only transoceanic tsunamis. In our case, the size of the modeling area does not exceed a few degrees at fairly low latitudes (31–35 degrees NL), where the Coriolis force is weaker than at higher latitudes. The equivalent form of a shallow water system from [1] (not accounting the Coriolis force), namely the system (1), (2), and (3), was suitable for parallel implementation of finite-difference scheme: $\{f_k(t)\}$

$$H_t + (uH)_x + (vH)_y = 0 \tag{1}$$

$$u_t + uu_x + vu_y + gH_x = gD_x \tag{2}$$

$$v_t + uv_x + vv_y + gH_y = gD_y \tag{3}$$

where $H(x,y,t) = \eta(x,y,t) + D(x,y)$ is the entire height of the water column, η being the sea surface disturbance (wave height), $D(x,y)$ – depth profile (which is supposed to be known at all grid points), $u(x,y,t)$ and $v(x,y,t)$ components of velocity vector, g – acceleration of gravity. Subindexes t, x and y denote partial derivatives of the system unknowns with respect to the corresponding variables.

The following second order approximation finite difference Mac-Cormack scheme [8] was used for numerical experiments:

$$\frac{\widehat{H}_{ij}^{n+1}-H_{ij}^{n}}{\tau}+\frac{H_{ij}^{n}u_{ij}^{n}-H_{i-1j}^{n}u_{i-1j}^{n}}{\Delta x}+\frac{H_{ij}^{n}v_{ij}^{n}-H_{ij-1}^{n}v_{ij-1}^{n}}{\Delta y}=0$$

$$\frac{\widehat{u}_{ij}^{n+1}-u_{ij}^{n}}{\tau}+u_{ij}^{n}\frac{u_{ij}^{n}-u_{i-1j}^{n}}{\Delta x}+v_{ij}^{n}\frac{u_{ij}^{n}-u_{ij-1}^{n}}{\Delta y}+g\frac{\eta_{ij}^{n}-\eta_{i-1j}^{n}}{\Delta x}=0$$

$$\frac{\widehat{v}_{ij}^{n+1}-v_{ij}^{n}}{\tau}+u_{ij}^{n}\frac{v_{ij}^{n}-v_{i-1j}^{n}}{\Delta x}+v_{ij}^{n}\frac{v_{ij}^{n}-v_{ij-1}^{n}}{\Delta y}+g\frac{\eta_{ij}^{n}-\eta_{ij-1}^{n}}{\Delta y}=0$$

$$\frac{H_{ij}^{n+1}-\left(\widehat{H}_{ij}^{n+1}+H_{ij}^{n}\right)/2}{\tau/2}+\frac{\widehat{H}_{i+1j}^{n+1}\widehat{u}_{i+1j}^{n+1}-\widehat{H}_{ij}^{n+1}\widehat{u}_{ij}^{n+1}}{\Delta x}+\frac{\widehat{H}_{ij+1}^{n+1}\widehat{v}_{ij+1}^{n+1}-\widehat{H}_{ij}^{n+1}\widehat{v}_{ij}^{n+1}}{\Delta y}=0$$

$$\frac{u_{ij}^{n+1}-\left(\widehat{u}_{ij}^{n+1}+u_{ij}^{n}\right)/2}{\tau/2}+u_{ij}^{n}\frac{\widehat{u}_{i+1j}^{n+1}-\widehat{u}_{ij}^{n+1}}{\Delta x}+v_{ij}^{n}\frac{\widehat{u}_{ij+1}^{n+1}-\widehat{u}_{ij}^{n+1}}{\Delta y}+g\frac{\widehat{\eta}_{i+1j}^{n+1}-\widehat{\eta}_{ij}^{n+1}}{\Delta x}=0$$

$$\frac{v_{ij}^{n+1}-\left(\widehat{v}_{ij}^{n+1}+v_{ij}^{n}\right)/2}{\tau/2}+u_{ij}^{n}\frac{\widehat{v}_{i+1j}^{n+1}-\widehat{v}_{ij}^{n+1}}{\Delta x}+v_{ij}^{n}\frac{\widehat{v}_{ij+1}^{n+1}-\widehat{v}_{ij}^{n+1}}{\Delta y}+g\frac{\widehat{\eta}_{ij+1}^{n+1}-\widehat{\eta}_{ij}^{n+1}}{\Delta y}=0$$

Here, $H^{n}{}_{ij}$, $u^{n}{}_{ij}$, and $v^{n}{}_{ij}$ are the gridded variables which correspond to the H, u, and v functions in differential system (1), (2), and (3). The parameters τ, Δx, and Δy are the time step and spatial steps of the computational grid. In order to account for the sphericity of the Earth, a decreasing grid step with respect to longitude for larger values of latitude was used.

2.2 Hardware Solution for Computer Code Acceleration

To achieve expected performance of numerical simulation with regular personal computer PC) the specialized Calculator, based on Field Programmable Gates Array (FPGA) microchip, was designed [5, 9]. The McCormack scheme was very suitable for parallel implementation. Computation pipeline is based on the designed Processor Elements (PEs). Each of these PEs is responsible for a single step in the calculation algorithm. High-Level Synthesis (HLS) technology [10] was used, which makes it possible to significantly accelerate the development process. The main idea is that it is not necessary to wait a complete computation of the sought functions, H, u, v, at n-th time step to begin the computation for the $(n + 1)$-th time step. Having known the values of velocity vector and wave height just at space-neighboring grid points, the corresponding PE starts to deliver the values for the next time step. So, the special computation pipelines have been designed in the form of connections among the PEs' outputs and inputs. Depending on the particular parameters of the FPGA microchip in use, the above pipelines can have various lengths to meet the peculiarities of the given algorithm. For the considered problem, the inner memory of FPGA is enough to arrange a highly efficient implementation of McCormack finite-difference scheme for the grid size 6000×4000 nodes. Alternatively larger FPGA chip computational grids could be accepted as well as the other finite-difference schemes for a variety of mathematical models.

The best results were achieved at ZCU106 platform. This system is based on the Zynq Ultrascale+ SoC (system-on-chip). The proposed architecture is given in Fig. 1. The SoC is a 4-core ARM processor (Cortex-A53) combined with an FPGA.

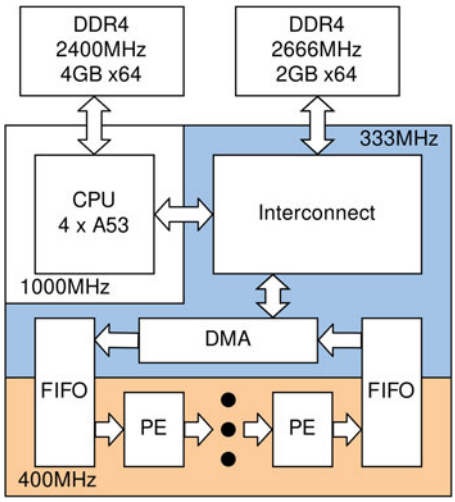

Fig. 1 A figure of Xilinx ZCU106-based implementation architecture

3 Numerical Experiments

3.1 Numerical Modeling Setup

To check the influence of the spatial resolution of the computational grid on the distribution of maximum wave heights along the coastline, a series of computational experiments simulating tsunami propagation in the same region from the identical model source were conducted using grid bathymetry with different step lengths of the spatial grid. The simulations were performed in the area south of the Japanese islands Shikoku and Honshu, bounded by latitudes 31.0° and 35.0° N and longitudes 131.0° and 140.0° E. In all three calculations, the time step of the difference scheme was equal to 0.3 s. Such a step quite satisfies the stability condition, which limits the wave propagation at any point in the region to one spatial step in one time step. At the maximum depth of 5000 m, the 0.3 s time step provides a stable calculation even on the most detailed grid with a step of 111 m.

As was observed [11], the quality of the bathymetry has valuable impact on the accuracy of tsunami computations. It is shown that modern digital bathymetry maps, for example, GEBCO, do not provide the adequate reproduction of the bottom topography in numerical models of the wave propagation, so it can lead to significant errors in estimating the maximum tsunami run-up on the coast.

Digital gridded bathymetry was developed based on depth measurements collected by JODC [12]. Three digital arrays of depth values with dimensions of 1500×1000, 3000×2000 and 6000×4000 nodes with spatial steps $\Delta x = 0.006°$, $\Delta y = 0.004°$ for the first array (1500×1000) and, respectively, two and four times smaller spatial steps for the second and third arrays were constructed. In the West-East direction this is equal to approximately 560 m, 280 m and 140 m, correspondingly. In the North-South direction, the step lengths are approximately 445 m, 223 m, and 111 m, respectively. Hereafter, we will denote these depth arrays by the numbers 1, 2, and 3. The geography and bathymetry of the modeling area is shown in Fig. 2.

In this area, according to the recurrence of major tsunamis, the next (after the Great Tohoku Tsunami 2011) catastrophic tsunami is expected [13]. The location of the tsunami source is expected opposite the Shikoku Island.

3.2 Computational Grid and Tsunami Source

The initial vertical displacement of the water surface in the form of an ellipse with axis lengths of 100 and 50 km was used as the tsunami source in the calculations. The maximum displacement η_0 in the source center was $+3$ m. The long axis of the ellipse is directed parallel to the axis of the deep Nankai trench (Fig. 3). The amplitude of the displacement of the water surface in the model source was set by the formula:

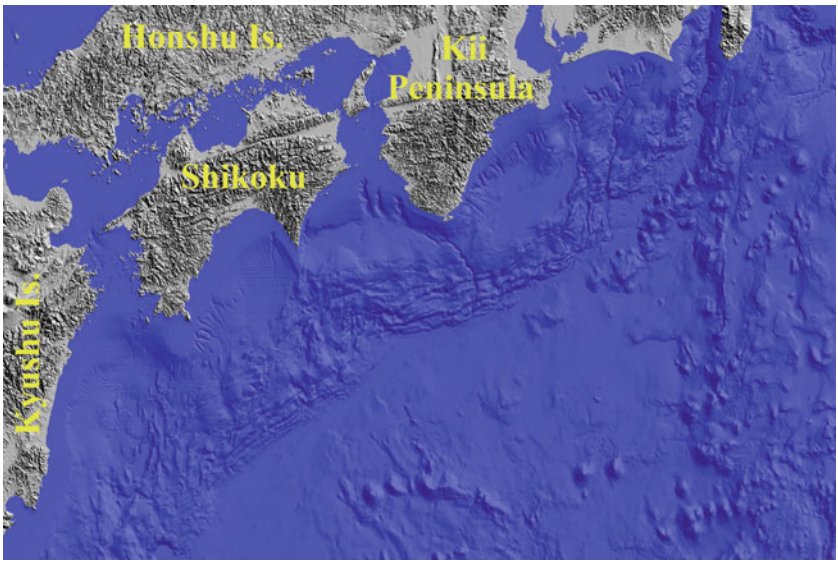

Fig. 2 The geography and the bottom relief of computation domain

$$\eta = \frac{\eta_0}{2}\left(1 + \cos\left(\sqrt{\frac{x^2}{r_1^2} + \frac{y^2}{r_2^2}}\right) \cdot \pi\right), 0 \le \frac{x^2}{r_1^2} + \frac{y^2}{r_2^2} \le 1.$$

At the center of the ellipsoidal source, the x and y coordinates are equal to zero. The lengths of the semi-axes of the ellipse r_1 and r_2 are 50 and 25 km, respectively.

3.3 Numerical Results

As mentioned above, three computational experiments were carried out to model tsunami propagation in the area under study from identical sources using grid bathymetry with different spatial steps along the parallels of 0.006°, 0.003° and 0.0015°. As a result, the distributions of maximum tsunami heights in all nodes of the three grids used for the calculations were obtained. Fig. 3 shows the distribution of maximum wave heights in the waters surrounding Shikoku Island and the Kii Peninsula, obtained by modeling grid number 1 (on the "coarsest" grid).

The calculation results in the form of maximum tsunami height distribution on more detailed grids 2 and 3 do not visually differ from those presented in Fig. 3. Detailed comparison of the calculated maximum heights along the Shikoku Island and Kii Peninsula shoreline, when modeling on different computational grids, is given in Fig. 4.

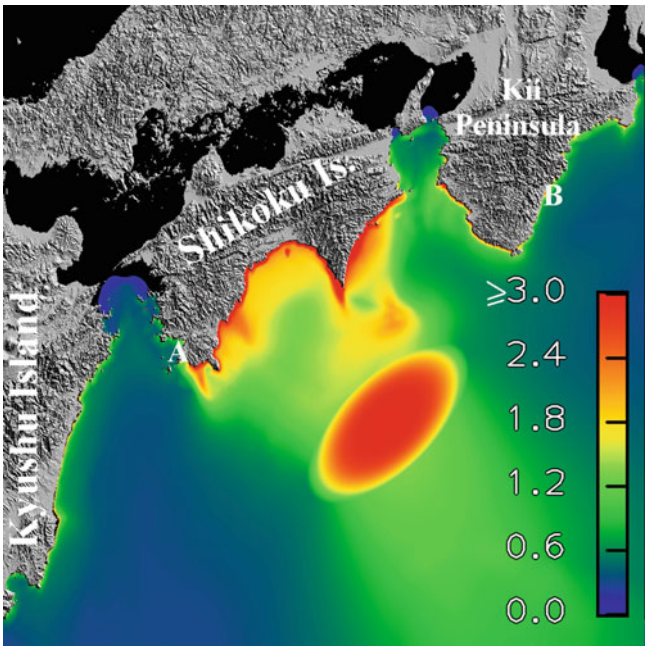

Fig. 3 Distribution of tsunami height maxima around Shikoku Island and Kii Peninsula as a result of tsunami modeling on a 1500 × 1000 knots computational grid

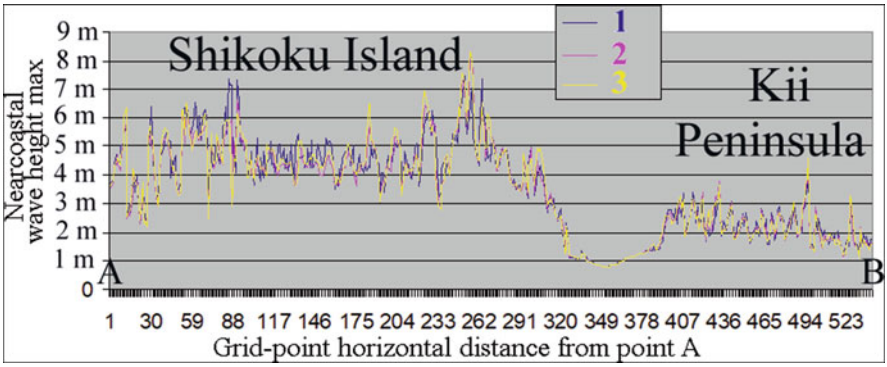

Fig. 4 Wave height maxima along the coastline of Shikoku Island and Kii Peninsula as a result of tsunami modeling using various computation grids. The shoreline segment is limited by points A and B (see Fig. 3)

Three lines of different colors show the distribution of tsunami height maxima along the segment of coastline from point A to point B (see Fig. 3). The color of the line correspondence to the number of the grid bathymetry used in the modeling is shown in the right part of the figure. Fig. 5 shows the difference of maximum tsunami heights between the results of calculation on grids 3 and 2 in the entire

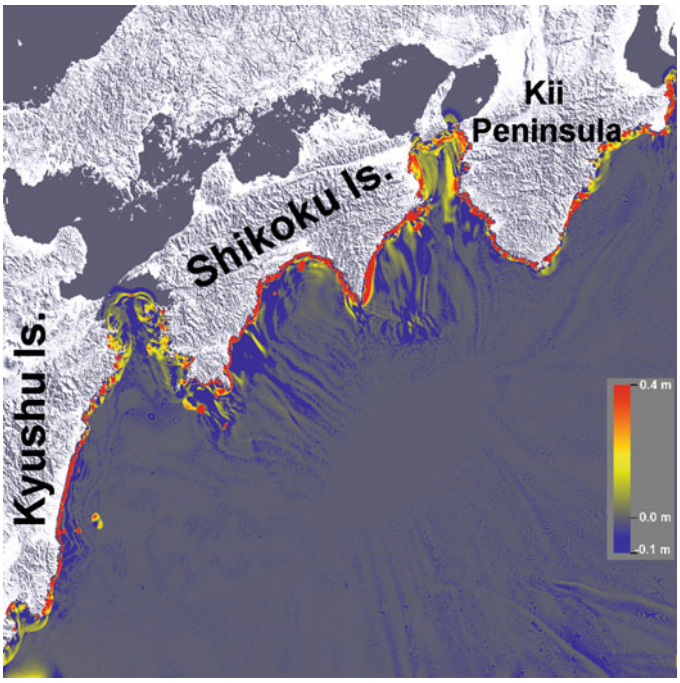

Fig. 5 Comparison of the maximum height distributions obtained by numerical simulation using computational grids #3 and #2

calculation area. When comparing the simulation results, one can see that near the shoreline, the wave heights obtained using a more detailed computational grid are greater than the wave heights obtained using a coarser grid (the points are colored in red). But at a distance from the shore, the wave calculated on the coarser grid is often higher than the tsunami calculated on the more detailed grid. In Fig. 5, these places are colored deep blue. The difference in the results of these two calculations does not exceed a few tens of centimeters (see the scale in the right part of Fig. 5).

4 Discussion

A series of numerical calculations of tsunami propagation in the ocean area south of Japan using FPGA computer architecture showed that the McCormack difference scheme implemented on the FPGA board allows speeding up significantly the numerical simulation of tsunami wave propagation over a nonlinear shallow water model. Testing of the algorithm on exact solutions together with a comparison with other software results [14] showed the satisfactory accuracy of the proposed

approach at high computational performance. For example, the computational experiments described above required:

Grid1: 1500 × 1000, 1 ms per iteration, 12 s for the complete test
Grid2: 3000 × 2000, 3.9 ms per iteration, 46.8 s for the complete test
Grid3: 6000 × 4000, 15.2 ms per iteration, 182 s for the complete test

In all calculations, the same time step is 0.3 s, the propagation time is 3600 s (12000 time steps).

The calculation results showed a weak dependence of the tsunami amplitude on the computational grid step length in the case when the wave length is about 100 spatial grid steps. For the model ellipsoidal source considered in the paper, this relation is satisfied for grids 2 and 3.

Using the hardware acceleration (FPGA-based Calculator), it is possible to determine "safe" and "dangerous" locations along the coast within a few minutes, calculating wave propagation over the several hundred kilometers wide water area. It is expected that in a few years tsunami warning systems will be able to save human lives and reduce economic loss even in cases of strong near field earthquakes.

Declaration The authors have no conflicts of interest to declare that are relevant to the content of this article.

Funding This study was funded under the state contract with IAE SB RAS (121041800012-8) and with ICMMG SB RAS (0315-2019-0004).

References

1. Titov, V.V., Gonzalez, F.I.: Implementation and testing of the method of splitting tsunami (MOST) model. NOAA Technical Memorandum ERL PMEL-112 (1997)
2. Gica, E., Spillane, M., Titov, V., Chamberlin, C., Newman, J.: Development of the forecast propagation database for NOAA's short-term inundation forecast for tsunamis (SIFT). NOAA Technical Memorandum (2008)
3. Goto, C., Ogawa, Y., Shuto, N., Imamura, F.: IUGG/IOC TIME Project: Numerical Method of Tsunami Simulation with the Leap-Frog Scheme. Manuals and Guides, p. 126. Intergovernmental Oceanographic Commission of UNESCO, No.35, Paris (1997)
4. Yalciner, A., Alpar, B., Altinok, Y., Ozbay, I., Imamura, F.: Tsunamis in the sea of Mar-mara: historical documents for past, models for future. Mar. Geol. **190**, 445–463 (2002)
5. Zaytsev, A., Kurkin, A., Pelinovsky, E., Yalciner, A.C.: Numerical Tsunami Model NAMI-DANCE. Sci. Tsunami Hazards. **38**(4), 151–168 (2019)
6. Lavrentiev, M.M., Lysakov, K.F., Marchuk, A.G., Oblaukhov, K.K., Shadrin, M.Y.: Hardware/software solution for low power evaluation of Tsunami danger. J. Low Power Electron. Appl. **12**(6), 1–16 (2022)
7. Stoker, J.J.: Water Waves. The Mathematical Theory with Applications. Interscience Publishers, New York (1957)
8. MacCormack, R.W., Paullay, A.J.: Computational efficiency achieved by time splitting of finite–difference operators. AIAA paper, 72-154 (1972)
9. Lavrentiev, M., Lysakov, K., Marchuk, A., Oblaukhov, K., Shadrin, M.: Hardware Acceleration of Tsunami Wave Propagation Modeling in the Southern Part of Japan. Appl. Sci. **10**(12), 4159 (2020)

10. Vitis High-Level Synthesis User Guide. https://www.xilinx.com/support/documentation/sw_manuals/xilinx2020_2/ug1399-vitis-hls.pdf. Last accessed 13 Jan 2023
11. Kulikov, E.A., Gusiakov, V.K., Ivanova, A.A., Baranov, B.V.: Numerical tsunami modeling and the bottom relief. Moscow Univ. Phys. Bull. **71**, 527–536 (2016)
12. J-DOSS|JODC. https://jdoss1.jodc.go.jp/vpage/depth500_file.html. Last accessed 18 July 2022
13. Hyodo, M., Hori, T., Ando, K., Baba, T.: The possibility of deeper or shallower extent of the source area of Nankai Trough earthquakes based on the 1707 Hoei tsunami heights along the Pacific and Seto Inland Sea coasts, southwest Japan. Earth Planets Space. **66**(123) (2014)
14. Lavrentiev, M.M., Marchuk, A.G., Oblaukhov, K.K., Romanenko, A.A.: Comparative testing of MOST and Mac-Cormack numerical schemes to calculate tsunami wave propagation. J. Phys. Conf. Ser. **1666**, 012028 (2020)

On the Asymptotical Description of Soliton Solutions to the Matrix Modified Korteweg-de Vries Equation

Sandra Carillo and Cornelia Schiebold

1 Introduction

This article is a sequel to [3, 4] on explicit solutions of the $\mathsf{d} \times \mathsf{d}$-matrix modified Korteweg-de Vries equation (matrix mKdV)

$$V_t = V_{xxx} + 3\{V^2, V_x\}. \tag{1}$$

The present work focuses on the interaction of two solitary waves, following the general philosophy that more complicated nonlinear superpositions locally behave like the 2-soliton case. The base is a general solution formula in Theorem 2, where the solitary waves combined in nonlinear superposition are encoded in matrix parameters. We consider the case $N = 2$, where the parameters in the solution formula (2) are two $\mathsf{d} \times \mathsf{d}$-matrices B_1, B_2, called *spectral matrices* as in [8], and in addition scalar parameters k_1, k_2. As for (2), these data can be chosen arbitrarily. Note that the resulting solutions may in general have singularities. In earlier work, the authors studied example classes where the spectral matrices are related in an algebraically simple way (e.g., B_1 and B_2 are multiples of each other) and lead nevertheless to intriguing solutions. In Sect. 2, we explore two examples of this kind in an essentially experimental spirit.

The main goal of the article is then to put these heuristic observations onto firm ground via the rigorous asymptotic description in Theorem 1, Sect. 3. The main

S. Carillo (✉)
Dipartimento SBAI, Sapienza Università di Roma, Rome, Italy

I.N.F.N. - Sez. Roma1, Gr. IV - Mathematical Methods in NonLinear Physics, Rome, Italy
e-mail: sandra.carillo@uniroma1.it

C. Schiebold
IMD, Mid Sweden University, Sundsvall, Sweden

© The Author(s), under exclusive license to Springer Nature Switzerland AG 2024

W. Lacarbonara (ed.), *Advances in Nonlinear Dynamics, Volume III*, NODYCON Conference Proceedings Series, https://doi.org/10.1007/978-3-031-50635-2_52

qualitative insight of our asymptotic analysis is that fairly generic assumptions imply that the collision only changes the lines on which the solitons travel by a phase shift, but neither their shape nor polarisation.

Compared to the motivating examples, where the spectral matrices are commuting, there is a considerable gain in generality. In fact, we prove the results for any pair of *invertible* matrices. In the sequel, we restrict to the case that both k_1, k_2 are positive since the other sign constellations can be treated similarly. However, in contrast to the scalar case, positivity cannot always be assumed without losing solutions, see [5].

Note, however, that the assumption that B_1, B_2 are invertible rules out interesting cases like the multisolitons of Goncharenko (for the matrix KdV) where B_1, B_2 are (sums of) projections, resulting in shifts both in shape and polarisation. We refer to [13] for an asymptotic discussion of 2-solitons of the matrix KdV in an even more general setting.

For a broad introduction to noncommutative integrable systems we refer to [10], and for recent results close in spirit to the present article to [6, 7, 9].

2 Collisions of 2-Soliton Solutions of the 2 × 2-Matrix Modified Korteweg-de Vries Equation

In previous work [3, 4], several examples of collisions of 2-soliton solutions to the matrix modified Korteweg-de Vries equation have been given, however, in some particularly intriguing cases without any deeper analysis. As one of the motivations of the present article is to provide an asymptotic explanation of those examples, we start with an experimental examination.

Example 1 In the solution formula in Theorem 2 with $N = 2$, we look at the choices

(a) ([4], Example 2) $k_1 = 1, k_2 = \sqrt{2}$ and $B_1 = \begin{pmatrix} 1 & 0 \\ 0 & 1 \end{pmatrix}$. $B_2 = \begin{pmatrix} 0 & 1 \\ 1 & 0 \end{pmatrix}$,

(b) ([3], 2nd Example) $k_1 = 1, k_2 = \sqrt{2}$ and $B_1 = B_2 = \begin{pmatrix} 1 & 1 \\ 0 & 1 \end{pmatrix}$.

Observe that the choices of parameters in [3] were slightly different (more precisely, we used $k_1 = -0.6$, $k_2 = 1$ in [3]).

The resulting solutions are plotted in Fig. 1.

To get an impression of the asymptotic behaviour, we plot the solution for sufficiently early and late times. More precisely, the solutions are plotted twice, in coordinates moving with each of their two solitons. This is done in Fig. 2 for Example 1(a) and in Fig. 3 for Example 1(b).

In both cases the plots indicate that the effect of the collision merely consists in a phase shift (meaning that the solution experiences an overall translation in space), and that their spectral matrices are not altered.

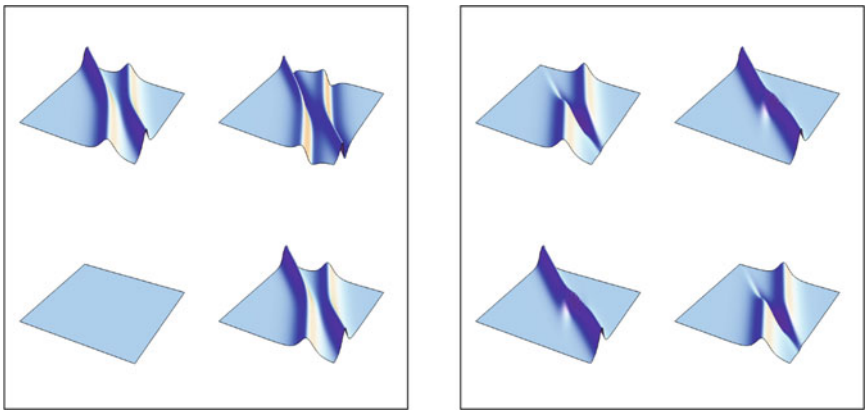

Fig. 1 The solutions in Example 1 are depicted for $-10 \leq x \leq 10$ and $-5 \leq t \leq 5$ with plot range between $-\sqrt{2}$ and $\sqrt{2}$, the solution in (**b**) to the left, the solution in (**a**) to the right

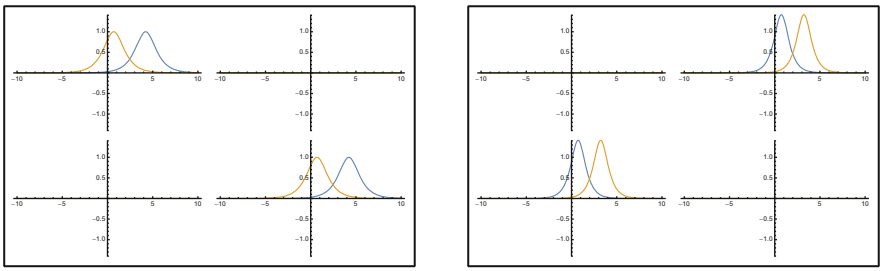

Fig. 2 The solution from Example 1(a) is plotted for $t = -20$ (the brown curve) and $t = 20$ (the blue curve). The plot to the left is plotted in the frame $(x - t, t)$, the plot to the right in $(x - 2t, t)$, both for $-10 \leq x \leq 10$ with plot range between $-\sqrt{2}$ and $\sqrt{2}$

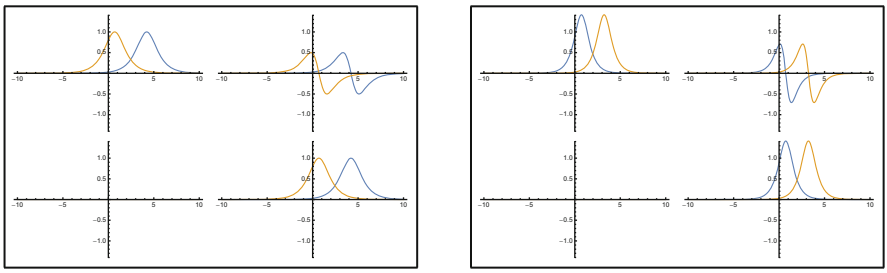

Fig. 3 The solution from Example 1(b) is plotted for $t = -20$ (the brown curve) and $t = 20$ (the blue curve). The plot to the left is plotted in the frame $(x - t, t)$, the plot to the right in $(x - 2t, t)$, both for $-10 \leq x \leq 10$ with plot range between $-\sqrt{2}$ and $\sqrt{2}$

Since this corresponds neatly to the well-known nonlinear superposition principle for soliton equations in the scalar case, it is natural to expect that the scalar phase-shift formula is also valid in our cases. This expectation can be easily confirmed using computer graphics.

Figure 4 is another visualization of Example 1(a). The upper row of the solution (containing to the left its diagonal and to the right its off-diagonal element) is plotted and compared to its expected asymptotic ingredients: the 1-soliton solutions $V_1^{\pm}(x,t)$, $V_2^{\pm}(x,t)$ corresponding to the input data

- $V_1^{\pm}(x,t)$: $k_1 = 1$, and $B_1^+ = A^2 B_1$, $B_1^- = B_1$ with $B_1 = \begin{pmatrix} 1 & 0 \\ 0 & 1 \end{pmatrix}$,
- $V_2^{\pm}(x,t)$: $k_2 = \sqrt{2}$, and $B_2^+ = B_2$, $B_2^- = A^2 B_2$ with $B_2 = \begin{pmatrix} 0 & 1 \\ 1 & 0 \end{pmatrix}$,

$A = \dfrac{k_1 - k_2}{k_1 + k_2} = \dfrac{1 - \sqrt{2}}{1 + \sqrt{2}}$, in Theorem 2.

The centre of the plot shows the upper row of the solution in Example 1(a).

Above, the upper left entry of the 1-soliton solution V_1^+ is depicted (to the left) and the upper right entry of V_2^+ (to the right), which are asymptotically expected at $t \approx +\infty$. Observe that both the upper right entry of V_1^+ and the upper left entry of V_2^+ are identically zero and are, therefore, not shown.

Below, the upper left entry of the 1-soliton solution V_1^- is depicted (to the left) and the upper right entry of V_2^- (to the right), which are asymptotically expected at $t \approx -\infty$. Again, the upper right entry of V_1^- and the upper left entry of V_2^- are not shown as they are identically zero.

Note also that it is V_1^+, V_2^- which are shifted.[1]

The resulting plot is shown in Fig. 4.

The asymptotic analysis in the next section confirms the experimental results for our examples and generalises them to the $\mathsf{d} \times \mathsf{d}$-matrix case with invertible spectral matrices.

3 Asymptotic Analysis

In this section we give an asymptotic analysis of the 2-soliton solutions of the $\mathsf{d} \times \mathsf{d}$-matrix mKdV (1) (in the sense that we use $N = 2$ in Theorem 2) under the assumption that the involved spectral matrices are *invertible*. This analysis is inspired by results on the matrix KdV in [13].

[1] As a remark, the fact that the unshifted 1-soliton solutions do not appear with geometric centre in $x + k^2 t = 0$ is due to an initial shift incorporated in Theorem 2 (for $N = 1$) by the factor $1/(2k)$ in the matrix function L.

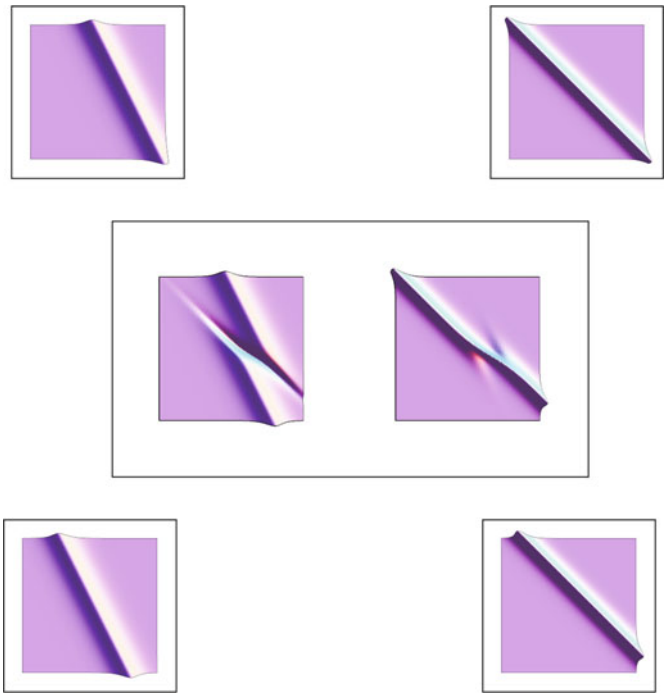

Fig. 4 The 2-soliton solution in Example 1(a) together with its asymptotic ingredients as described in Sect. 2. All plots are depicted for $-10 \le x \le 10$, $-5 \le t \le 5$ with plot range between $-\sqrt{2}$ and $\sqrt{2}$

Assumption 1 $0 < k_1 < k_2$.

Remark 1 Obviously we can take $k_1 < k_2$ without loss of generality. But the fact that, without loss of generality, k_1, k_2 can also be chosen positive is in general only true for the *scalar* mKdV [5].

We here restrict to this choice since the other cases can be treated similarly.

Assumption 2 *The spectral matrices B_1, B_2 are real and invertible.*

Remark 2 Note that the assumptions guarantee reality of the solutions.

As for regularity, we restrict to regions where $|t|$ is sufficiently large so that it is enough to look at the asymptotic solution, which consists of two 1-solitons. Those can be shown to be regular if one excludes purely imaginary eigenvalues of B_1, B_2 [5].

We now state our main result.

Theorem 1 *Let V be the solution of the $\mathsf{d} \times \mathsf{d}$-matrix mKdV (1) obtained from Theorem 2 for $N = 2$, and let Assumptions 1, 2 be satisfied. Then*

$$V(x,t) \approx V_1^{\pm}(x,t) + V_2^{\pm}(x,t), \qquad t \approx \pm\infty,$$

with the 1-soliton solutions

$$V_j^{\pm}(x,t) = L_j^{\pm}\Big(I + \big(\frac{1}{2k_j}L_j^{\pm}\big)^2\Big)^{-1},$$

where $L_j^{\pm} = L_j^{\pm}(x,t) = \exp\big(k_j x + k_j^3 t + \varphi_j^{\pm}\big)B_j$ *and*

$$\varphi_1^- = 0, \qquad \varphi_2^- = \log\Big(\frac{k_1-k_2}{k_1+k_2}\Big)^2,$$
$$\varphi_1^+ = \log\Big(\frac{k_1-k_2}{k_1+k_2}\Big)^2, \qquad \varphi_2^+ = 0.$$

The above theorem says that - for invertible spectral matrices - the asymptotic behaviour of 2-soliton solutions of the $\mathsf{d}\times\mathsf{d}$-matrix mKdV follows the same nonlinear superposition principle as in the scalar case: The solitons collide elastically with the only effect of an overall phase shift.

Remark 3 We would like to stress that the interaction behaviour of 2-soliton solutions becomes even richer if one does not restrict to invertible spectral matrices (see [13] for a rather complete asymptotic study in the case of the $\mathsf{d}\times\mathsf{d}$-matrix KdV).

We also mention the special case of 2-soliton solutions with (non-zero) spectral matrices satisfying $B_1B_2 = 0 = B_2B_1$ (implying in particular that none of B_1, B_2 are invertible) where solitons superpose linearly [4].

Before starting the proof, we introduce the notation

$$M_j = \frac{1}{2k_j}L_j \quad \text{and } \gamma_j = \frac{2k_j}{k_1+k_2},$$

so that our solution rewrites

$$V = \big(2k_1M_1\ 2k_2M_2\big)\Big(I_{2\mathsf{d}} + L^2\Big)^{-1}\begin{pmatrix} I_{\mathsf{d}} \\ I_{\mathsf{d}}\end{pmatrix} \text{ with } L = \begin{pmatrix} M_1 & \gamma_2M_2 \\ \gamma_1M_1 & M_2\end{pmatrix}.$$

Proof The arguments being symmetrical, we focus on straight lines $k_1x + k_1^3t = c$ in (x,t)-space. Observe that the resulting discussion is partially formal but can be extended to statements on uniform convergence by using techniques in [11, 12], even in the presence of poles. On such lines, we have that $k_2x + k_2^3t = k_2(x + k_1^2t) + k_2(k_2^2 - k_1^2)t$, and by Assumption 1, therefore,

$$\exp(k_2x + k_2^3t) \approx \begin{cases} 0 \\ \infty\end{cases} \text{ for } t \approx \begin{cases} -\infty \\ \infty\end{cases}.$$

Asymptotics in $-\infty$: Then M_2 asymptotically can be replaced by the zero-matrix, and we get

$$V \approx \begin{pmatrix} 2k_1 M_1 & 0 \end{pmatrix} \left(I_{2\mathsf{d}} + L^2 \right)^{-1} \begin{pmatrix} I_{\mathsf{d}} \\ I_{\mathsf{d}} \end{pmatrix} \text{ with } L \approx \begin{pmatrix} M_1 & 0 \\ \gamma_1 M_1 & 0, \end{pmatrix}.$$

From this and an explicit computation of the inverse,[2] we can directly evaluate the asymptotic approximation to be $2k_1 M_1 (I_{\mathsf{d}} + M_1^2)^{-1}$ as claimed.

Asymptotics in $+\infty$: Here we make use of a reformulation of the solution. Observe first that $(I + L^2)^{-1} = \frac{1}{2}\big((I + \mathrm{i}L)^{-1} + (I - \mathrm{i}L)^{-1}\big)$. Next, with $D = \operatorname{diag}\{I_{\mathsf{d}}, M_2\}$ we get

$$\begin{aligned} L &= \begin{pmatrix} M_1 & \gamma_2 M_2 \\ \gamma_1 M_1 & M_2 \end{pmatrix} = \begin{pmatrix} M_1 & \gamma_2 I_{\mathsf{d}} \\ \gamma_1 M_1 & I_{\mathsf{d}} \end{pmatrix} D =: T D, \\ \begin{pmatrix} 2k_1 M_1 & 2k_2 M_2 \end{pmatrix} &= \begin{pmatrix} 2k_1 M_1 & 2k_2 I_{\mathsf{d}} \end{pmatrix} D. \end{aligned}$$

Hence, $(I \pm \mathrm{i}L)^{-1} = D^{-1}(D^{-1} \pm \mathrm{i}T)^{-1}$, and

$$V = \begin{pmatrix} k_1 M_1 & k_2 I_{\mathsf{d}} \end{pmatrix} \left((D^{-1} + \mathrm{i}T)^{-1} + (D^{-1} - \mathrm{i}T)^{-1} \right) \begin{pmatrix} I_{\mathsf{d}} \\ I_{\mathsf{d}} \end{pmatrix}.$$

Now, asymptotically $D^{-1} \approx P$ for $P = \begin{pmatrix} I_{\mathsf{d}} & 0 \\ 0 & 0 \end{pmatrix}$.

Computing the inverses of $P \pm \mathrm{i}T$ directly,[3] and abbreviating $S = \begin{pmatrix} I_{\mathsf{d}} & -\gamma_2 I_{\mathsf{d}} \\ -\gamma_1 M_1 & M_1 \end{pmatrix}$, $\lambda = 1 - \gamma_1 \gamma_2$, we find

$$\begin{aligned} &(P + \mathrm{i}T)^{-1} + (P - \mathrm{i}T)^{-1} \\ &\quad = (\mathrm{i}I_{\mathsf{d}} - \lambda M_1)^{-1}(P^{\perp} + \mathrm{i}S) + (-\mathrm{i}I_{\mathsf{d}} - \lambda M_1)^{-1}(P^{\perp} - \mathrm{i}S) \\ &\quad = (\mathrm{i}I_{\mathsf{d}} - \lambda M_1)^{-1}(-\mathrm{i}I_{\mathsf{d}} - \lambda M_1)^{-1}\Big((-\mathrm{i}I_{\mathsf{d}} - \lambda M_1)(P^{\perp} + \mathrm{i}S) \\ &\qquad + (\mathrm{i}I_{\mathsf{d}} - \lambda M_1)(P^{\perp} - \mathrm{i}S)\Big) \end{aligned}$$

[2] **Lemma:** For a $\mathsf{d} \times \mathsf{d}$-block A such that $I_{\mathsf{d}} + A$ is invertible, it holds

$$\begin{pmatrix} I_{\mathsf{d}} + A & 0 \\ \alpha A & I_{\mathsf{d}} \end{pmatrix}^{-1} = (I_{\mathsf{d}} + A)^{-1} \begin{pmatrix} I_{\mathsf{d}} & 0 \\ -\alpha A & I_{\mathsf{d}} + A \end{pmatrix}$$

(by direct verification).

[3] **Lemma:** For a $\mathsf{d} \times \mathsf{d}$-block matrix A such that $\pm \mathrm{i}I_{\mathsf{d}} - (1 - \alpha_1 \alpha_2)A$ is invertible, it holds

$$\left(P \pm \mathrm{i} \begin{pmatrix} A & \alpha_2 I_{\mathsf{d}} \\ \alpha_1 A & I_{\mathsf{d}} \end{pmatrix} \right)^{-1} = \left(\pm \mathrm{i}I_{\mathsf{d}} - (1 - \alpha_1 \alpha_2)A \right)^{-1} \left(P^{\perp} \pm \mathrm{i} \begin{pmatrix} I_{\mathsf{d}} & -\alpha_2 I_{\mathsf{d}} \\ -\alpha_1 A & A \end{pmatrix} \right)$$

(by direct verification).

$$= 2\big(I_{\mathsf{d}} + (\lambda M_1)^2\big)^{-1}\big(S - \lambda M_1 P^{\perp}\big)$$
$$= 2\big(I_{\mathsf{d}} + (\lambda M_1)^2\big)^{-1} \begin{pmatrix} I_{\mathsf{d}} & -\gamma_2 I_{\mathsf{d}} \\ -\gamma_1 M_1 & (1-\lambda) M_1 \end{pmatrix}.$$

Hence for V it approximately holds that

$$V \approx \big(I_{\mathsf{d}} + (\lambda M_1)^2\big)^{-1} \begin{pmatrix} 2k_1 M_1 & 2k_2 I_{\mathsf{d}} \end{pmatrix} \begin{pmatrix} I_{\mathsf{d}} & -\gamma_2 I_{\mathsf{d}} \\ -\gamma_1 M_1 & (1-\lambda) M_1 \end{pmatrix} \begin{pmatrix} I_{\mathsf{d}} \\ I_{\mathsf{d}} \end{pmatrix}$$
$$= \big(I_{\mathsf{d}} + (\lambda M_1)^2\big)^{-1} \Big(2k_1(1-\gamma_2) + 2k_2(1-\gamma_1-\lambda)\Big) M_1.$$

Let $A_{12} = \dfrac{k_1 - k_2}{k_1 + k_2}$.

Note first that $1 - \gamma_2 = A_{12}$ such that $2k_1(1-\gamma_2) = 2k_1 A_{12}$.

Second, by definition of λ, we have $1 - \lambda = \gamma_1\gamma_2$ and $1 - \gamma_1 - \lambda = -(1-\gamma_2)\gamma_1$. Moreover, $k_2\gamma_1 = k_1\gamma_2$. Hence,

$$2k_2(1-\gamma_1-\lambda) = -2k_2\gamma_1(1-\gamma_2) = -2k_1\gamma_2(1-\gamma_2) = -2k_1\gamma_2 A_{12},$$

showing

$$2k_1(1-\gamma_2) + 2k_2(1-\gamma_1-\lambda) = 2k_1 A_{12} - 2k_1\gamma_2 A_{12} = 2k_1(1-\gamma_2)A_{12} = 2k_1 A_{12}^2.$$

To conclude, we observe that $\lambda = 1 - \gamma_1\gamma_2 = A_{12}^2$. In summary, this gives us the approximation

$$2k_1(A_{12}^2 M_1)\big(I_{\mathsf{d}} + (A_{12}^2 M_1)^2\big)^{-1}$$

as claimed.

We conclude by giving an example of a 2-soliton solution of the 2×2-matrix mKdV with *non-commuting* spectral matrices.

Example 2 $k_1 = 1$, $k_2 = \sqrt{2}$ and $B_1 = \begin{pmatrix} 1 & 2 \\ 3 & 4 \end{pmatrix}$, $B_2 = \begin{pmatrix} 4 & 3 \\ 2 & 1 \end{pmatrix}$.

The solution is plotted in Fig. 5, in the central row. For an empirical comparison to Theorem 1, the asymptotical ingredients for $t \approx \infty$ are plotted in the upper and for $t \approx -\infty$ in the bottom row. The soliton no. 1 (with input k_1, B_1) is plotted to the left, soliton no. 2 (with input k_2, B_2) to the right. Observe that the shifts, as predicted by Theorem 1, are attached to soliton no. 1 in $t \approx \infty$ and to soliton no. 2 in $t \approx -\infty$.

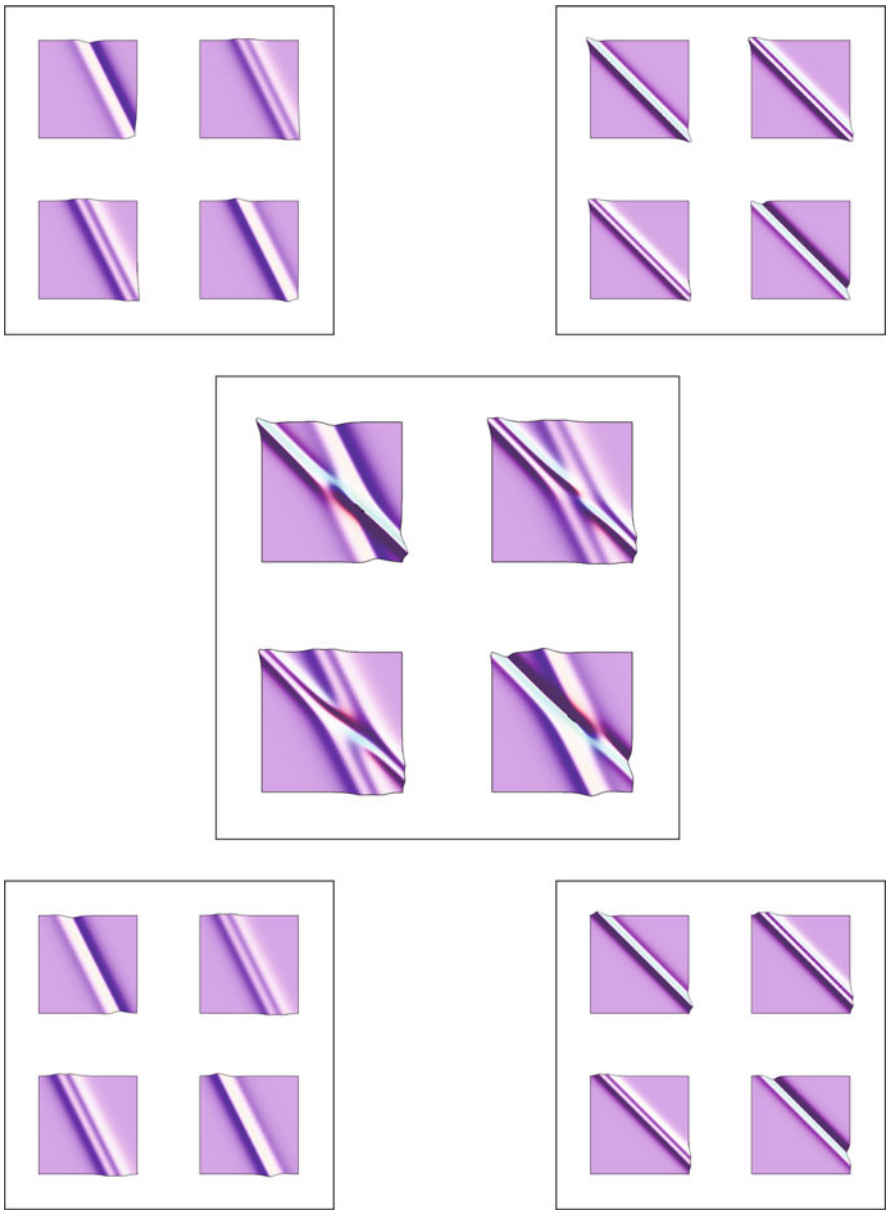

Fig. 5 The 2-soliton solution in Example 2 together with its asymptotic ingredients. All plots are depicted for $-10 \leq x \leq 10$, $-5 \leq t \leq 5$ with plot range between $-\sqrt{2}$ and $\sqrt{2}$. See Example 2 for more details

Appendix: An Explicit Formula for the N-Solitons of the $\mathsf{d} \times \mathsf{d}$-Matrix mKdV

A main ingredient for our asymptotic analysis is the following solution formula for the $\mathsf{d} \times \mathsf{d}$-matrix mKdV (1).

Theorem 2 *For $N \in \mathbb{N}$, let $k_1, \dots, k_N$ be complex numbers such that $k_i + k_j \neq 0$ for all i, j, and let $B_1, \dots, B_N$ be arbitrary $\mathsf{d} \times \mathsf{d}$-matrices.*

Define the $N\mathsf{d} \times N\mathsf{d}$-block matrix function $L = L(x,t)$ as

$$L = \Big(\frac{1}{k_i + k_j} L_j\Big)_{i,j=1}^{N}$$

with the $\mathsf{d} \times \mathsf{d}$-blocks $L_j = L_j(x,t) = \exp(k_j x + k_j^3 t) B_j$.

Then

$$V = \big(L_1 \dots L_N\big) \Big(I_{N\mathsf{d}} + L^2\Big)^{-1} \begin{pmatrix} I_{\mathsf{d}} \\ \vdots \\ I_{\mathsf{d}} \end{pmatrix} \tag{2}$$

is a solution of the matrix mKdV equation (1) with values in the $\mathsf{d} \times \mathsf{d}$-matrices on every domain Ω on which $\det(I_{N\mathsf{d}} + L^2) \neq 0$.

In fact, Theorem 2 is a reformulation of the solution formula presented in [4, Theorem 2.1]. For a rigorous proof (based on results in [1, 2]) we refer to [5].

Remark 4 For a justification for referring to the solutions in (2) as N-solitons solutions we refer to [13] where, for the corresponding solution class of the matrix KdV, the link to the multisolitons via the inverse scattering transform [8] is explained.

We conclude by indicating how to arrive at Theorem 2 from [4, Theorem 2.1].

Proof Starting from Theorem 2.1 in [4], and denoting by $D = \operatorname{diag}\{\ell_j I_{\mathsf{d}} | j\}$, $\ell_j = \ell_j(x,t) = \exp(k_j x + k_j^3 t)$, we derive the desired reformulation from

$$M := \Big(\frac{\ell_i}{k_i + k_j} B_j\Big)_{i,j=1}^{N} = DLD^{-1},$$

which implies

$$\begin{aligned} (I_{N\mathsf{d}} + M^2)^{-1} &= \big(I_{N\mathsf{d}} + (DLD^{-1})^2\big)^{-1} = \big(I_{N\mathsf{d}} + DL^2D^{-1}\big)^{-1} \\ &= D\big(I_{N\mathsf{d}} + L^2\big)^{-1} D^{-1} \end{aligned}$$

and

$$\begin{pmatrix} \ell_1 I_{\mathsf{d}} \\ \vdots \\ \ell_N I_{\mathsf{d}} \end{pmatrix} = D \begin{pmatrix} I_{\mathsf{d}} \\ \vdots \\ I_{\mathsf{d}} \end{pmatrix}, \qquad \big(B_1 \ \dots \ B_N\big) = \big(L_1 \ \dots \ L_N\big)\, D^{-1}.$$

References

1. Carillo, S., Schiebold, C.: Noncommutative Korteweg-de Vries and modified Korteweg-de Vries hierarchies via recursion methods. J. Math. Phys. **50**, 073510 (2009)
2. Carillo, S., Schiebold, C.: Matrix Korteweg-de Vries and modified Korteweg-de Vries hierarchies: noncommutative soliton solutions. J. Math. Phys. **52**, 053507 (2011)
3. Carillo, S., Lo Schiavo, M., Schiebold, C.: Matrix soliton solutions of the modified Korteweg-de Vries equation. In: Lacarbonara, W., Balachandran, B., Ma, J., Tenreiro Machado, J.A., Stepan, G. (eds.) Nonlinear Dynamics of Structures, Systems and Devices, pp. 75–83. Springer, Cham (2020)
4. Carillo, S., Schiebold, C.: Construction of soliton solutions of the matrix modified Korteweg-de Vries equation. In: Lacarbonara, W., Balachandran, B., Leamy, M.J., Ma, J., Tenreiro Machado, J.A., Stepan, G. (eds.) Advances in Nonlinear Dynamics, pp. 481–491. Springer, Cham (2022)
5. Carillo, S., Lo Schiavo, M., Schiebold, C.: N-soliton matrix mKdV solutions: a step towards their classification (2023). Preprint
6. Gilson, C.R., Nimmo, J.J.C., Sooman, C.M.: Matrix solutions of a noncommutative KP equation and a noncommutative mKP equation. Theor. Math. Phys. **159**, 796–805 (2009)
7. Gilson, C.R., Hamanaka, M., Huang, S.-C., Nimmo, J.J.C.: Soliton solutions of noncommutative anti-self-dual Yang–Mills equations. J. Phys. A **53**, 404002 (2020)
8. Goncharenko, V.M.: Multisoliton solutions of the matrix KdV equation. Theor. Math. Phys. **126**, 81–91 (2001)
9. Hamanaka, M., Okabe, H.: Soliton scattering in noncommutative spaces. Theor. Math. Phys. **197**, 1451–1468 (2018)
10. Kupershmidt, B.A.: KP or mKP: Noncommutative Mathematics of Lagrangian, Hamiltonian, and Integrable Systems. Mathematical Surveys and Monographs, vol. 78. AMS (2000)
11. Schiebold, C.: On negatons of the Toda lattice. J. Nonlinear Math. Phys. **10**, 181–193 (2003)
12. Schiebold, C.: Asymptotics for the multiple pole solutions of the Nonlinear Schrödinger equation. Nonlinearity **30**, 2930–2981 (2017)
13. Schiebold, C.: On the 2-soliton asymptotics for the $d \times d$-matrix Korteweg-de Vries equation. In: Walczak, S. (ed.) Proceedings of the Contemporary Mathematics in Kielce 2020, pp. 259–274. de Gruyter (Sciendo), Warsaw (2021)

Chirped Optical Solitons in Fiber Bragg Gratings with Dispersive Reflectivity

Khalil S. Al-Ghafri and Mani Sankar

1 Introduction

The data transmission through optical fiber optics for intercontinental distances is based on soliton propagation that arises due to delicate balance between chromatic dispersion (CD) and fiber nonlinearity [1–3]. However, the CD may have low count that leads to limit the transmission distances. Thus, Bragg gratings (BGs) is found to be one of the effective techniques to tackle this problem by introducing induced dispersion to compensate for low CD and subsequently ensure the existence of soliton transmission [4–7]. In literatures, many studies have been carried out using this technology to overcome the crisis of chromatic dispersion. For example, chirped and chirp-free optical solitons in fiber BGs with different forms of nonlinearity have been previously addressed by some authors [8–11].

The current study mainly discusses the dimensionless form of the coupled nonlinear Schrödinger equations in fiber BGs having polynomial law of nonlinearity given by [12, 13]

$$\begin{aligned} &iq_t + a_1 r_{xx} + (b_1|q|^2 + c_1|r|^2)q + (d_1|q|^4 + f_1|q|^2|r|^2 + g_1|r|^4)q \\ &+(l_1|q|^6 + m_1|q|^4|r|^2 + n_1|q|^2|r|^4 + p_1|r|^6)q + ih_1 q_x + k_1 r = 0, \end{aligned} \tag{1}$$

$$\begin{aligned} &ir_t + a_2 q_{xx} + (b_2|r|^2 + c_2|q|^2)r + (d_2|r|^4 + f_2|r|^2|q|^2 + g_2|q|^4)r \\ &+(l_2|r|^6 + m_2|r|^4|q|^2 + n_2|r|^2|q|^4 + p_2|q|^6)r + ih_2 r_x + k_2 q = 0, \end{aligned} \tag{2}$$

where the functions $q(x,t)$ and $r(x,t)$ stand for forward and backward propagating waves, respectively, whereas a_j for $j = 1, 2$ represent the coefficients of dispersive

K. S. Al-Ghafri (✉) · M. Sankar
University of Technology and Applied Sciences, Ibri, Oman
e-mail: khalil.alghafri@utas.edu.om

© The Author(s), under exclusive license to Springer Nature Switzerland AG 2024

W. Lacarbonara (ed.), *Advances in Nonlinear Dynamics, Volume III*, NODYCON Conference Proceedings Series, https://doi.org/10.1007/978-3-031-50635-2_53

reflectivity. In the coupled equations above, b_j indicate the coefficients of self-phase modulation (SPM) and c_j denote the cross-phase modulation (XPM) for cubic nonlinearity portion. For quintic nonlinear part, d_j are the coefficients of SPM while f_j and g_j are the coefficients of XPM. Regarding septic nonlinearity, l_j are the coefficients of SPM while m_j, n_j, and p_j are the coefficients of XPM. Finally, h_j accounts for inter-modal dispersion and k_j define detuning parameters. All of the coefficients are real valued constants and $i = \sqrt{-1}$.

It is worth mentioning that optical solitons with nonlinear chirping have a prominent performance in various applications such as the design of fiber-optic amplifiers, spread spectrum communications, photonic and optoelectronic devices. In contrast to the previous study [12] which retrieved solitons with linear chirping, herein we focus on deriving optical solitons with nonlinear chirping expressed in terms of the reciprocal of soliton intensity.

The objective of the present study is to investigate nonlinearly chirped optical solitons in fiber BGs. The system of Eqs. (1) and (2) is handled with the help of traveling wave transformation and then some specific conditions are assumed to ensure an integrable form for the coupled system. The generated traveling wave reduction is analytically solved by means of soliton ansatz method [14, 15] which yields various forms of chirped optical solitons.

2 Mathematical Analysis of Governing Model

In order to discuss chirped solitons, the model of the coupled NLSE (1) and (2) needs to be reduced to a simple form. Thus, we introduce the transformation given by

$$q(x,t) = v_1(\xi)e^{i(\varphi(\xi)-\omega t)}, \tag{3}$$

$$r(x,t) = v_2(\xi)e^{i(\varphi(\xi)-\omega t)}, \tag{4}$$

where $\xi = x - \nu t$. The functions $v_1(\xi)$ and $v_2(\xi)$ denote the amplitudes of the solitons while $\varphi(\xi)$ accounts for the phase function. The parameters ω and ν are real constants which represent the wave number and the soliton velocity. Applying the transformation given by (3) and (4) to the coupled Eqs. (1) and (2) and breaking down the resultant equations into real and imaginary parts, we reach the real parts in the form

$$\begin{aligned} &a_1 v_2'' - a_1 v_2 \varphi'^2 + (\nu - h_1) v_1 \varphi' + \omega v_1 + k_1 v_2 + b_1 v_1^3 + c_1 v_1 v_2^2 \\ &+ d_1 v_1^5 + f_1 v_1^3 v_2^2 + g_1 v_1 v_2^4 + l_1 v_1^7 + m_1 v_1^5 v_2^2 + n_1 v_1^3 v_2^4 + p_1 v_1 v_2^6 = 0, \end{aligned} \tag{5}$$

$$\begin{aligned} &a_2 v_1'' - a_2 v_1 \varphi'^2 + (\nu - h_2) v_2 \varphi' + \omega v_2 + k_2 v_1 + b_2 v_2^3 + c_2 v_2 v_1^2 \\ &+ d_2 v_2^5 + f_2 v_2^3 v_1^2 + g_2 v_2 v_1^4 + l_2 v_2^7 + m_2 v_2^5 v_1^2 + n_2 v_2^3 v_1^4 + p_2 v_2 v_1^6 = 0, \end{aligned} \tag{6}$$

and the imaginary parts in the form

$$(h_1 - v)v_1' + a_1(v_2\varphi'' + 2v_2\varphi') = 0, \tag{7}$$

$$(h_2 - v)v_2' + a_2(v_1\varphi'' + 2v_1\varphi') = 0. \tag{8}$$

We introduce the relation

$$v_2 = \sigma v_1, \tag{9}$$

where σ is a constant that is not equal to 1. Thus, the two Eqs. (5) and (6) are converted into

$$\begin{aligned}&\sigma a_1 v_1'' + [\omega + \sigma k_1 + (v - h_1)\varphi' - \sigma a_1 \varphi'^2]v_1 + (b_1 + \sigma^2 c_1)v_1^3 \\ &+ (d_1 + \sigma^2 f_1 + \sigma^4 g_1)v_1^5 + (l_1 + \sigma^2 m_1 + \sigma^4 n_1 + \sigma^6 p_1)v_1^7 = 0,\end{aligned} \tag{10}$$

$$\begin{aligned}&a_2 v_1'' + [\sigma\omega + k_2 + \sigma(v - h_2)\varphi' - a_2\varphi'^2]v_1 + (\sigma^3 b_2 + \sigma c_2)v_1^3 \\ &+ (\sigma^5 d_2 + \sigma^3 f_2 + \sigma g_2)v_1^5 + (\sigma^7 l_2 + \sigma^5 m_2 + \sigma^3 n_2 + \sigma p_2)v_1^7 = 0,\end{aligned} \tag{11}$$

whereas the two Eqs. (7) and (8) become as

$$(h_1 - v)v_1' + \sigma a_1(v_1\varphi'' + 2v_1\varphi') = 0, \tag{12}$$

$$\sigma(h_2 - v)v_1' + a_2(v_1\varphi'' + 2v_1\varphi') = 0. \tag{13}$$

The coupled Eqs. (12) and (13) can be integrated to induce the first integral given by

$$\varphi' = \frac{v - h_1}{2\sigma a_1} + \frac{\eta_1 v_1^{-2}}{\sigma a_1}, \tag{14}$$

$$\varphi' = \frac{\sigma(v - h_2)}{2a_2} + \frac{\eta_2 v_1^{-2}}{a_2}, \tag{15}$$

where η_1 and η_2 are the integration constants. These two equations impose the existence of the constraint condition given by

$$(a_2 - \sigma^2 a_1)v v_1^2 - (h_1 a_2 - h_2\sigma^2 a_1)v_1^2 + 2(\eta_1 a_2 - \eta_2\sigma a_1) = 0. \tag{16}$$

For convenience, we assume that

$$\eta_1 a_2 = \eta_2\sigma a_1, \tag{17}$$

which compel (16) to generate the expression for the velocity of the soliton as

$$v = \frac{h_1 a_2 - h_2\sigma^2 a_1}{a_2 - \sigma^2 a_1}. \tag{18}$$

Subsequently, the associated chirp can be presented as

$$\delta\omega(x,t) = -\left[\frac{\nu - h_1}{2\sigma a_1} + \frac{\eta_1 v_1^{-2}}{\sigma a_1}\right]. \tag{19}$$

Inserting (14) and (15) into Eqs. (10) and (11), respectively, we acquire coupled equations which are integrated once to yield

$$\sigma a_1 v_1'^2 - \frac{\eta_1^2}{\sigma a_1} v_1^{-2} + \left[\omega + \sigma k_1 + \frac{(\nu - h_1)^2}{4\sigma a_1}\right] v_1^2 + \frac{1}{2}(b_1 + \sigma^2 c_1) v_1^4$$
$$+ \frac{1}{3}(d_1 + \sigma^2 f_1 + \sigma^4 g_1) v_1^6 + \frac{1}{4}(l_1 + \sigma^2 m_1 + \sigma^4 n_1 + \sigma^6 p_1) v_1^8 = 0, \tag{20}$$

$$a_2 v_1'^2 - \frac{\eta_1^2 a_2}{\sigma^2 a_1^2} v_1^{-2} + \left[\sigma\omega + k_2 + \frac{\sigma^2(\nu - h_2)^2}{4a_2}\right] v_2 + \frac{1}{2}(\sigma^3 b_2 + \sigma c_2) v_1^4$$
$$+ \frac{1}{3}(\sigma^5 d_2 + \sigma^3 f_2 + \sigma g_2) v_1^6 + \frac{1}{4}(\sigma^7 l_2 + \sigma^5 m_2 + \sigma^3 n_2 + \sigma p_2) v_1^8 = 0, \tag{21}$$

where the constants of integration are taken to be zeros. It can be noted that Eqs. (20) and (21) are equivalent under the restrictions given as

$$a_2 = \sigma a_1, \tag{22}$$

$$\sigma\omega + k_2 + \frac{\sigma^2(\nu - h_2)^2}{4a_2} = \omega + \sigma k_1 + \frac{(\nu - h_1)^2}{4\sigma a_1}, \tag{23}$$

$$\sigma^3 b_2 + \sigma c_2 = b_1 + \sigma^2 c_1, \tag{24}$$

$$\sigma^5 d_2 + \sigma^3 f_2 + \sigma g_2 = d_1 + \sigma^2 f_1 + \sigma^4 g_1, \tag{25}$$

$$\sigma^7 l_2 + \sigma^5 m_2 + \sigma^3 n_2 + \sigma p_2 = l_1 + \sigma^2 m_1 + \sigma^4 n_1 + \sigma^6 p_1. \tag{26}$$

Based on the equivalency between (20) and (21), we deal with Eq. (20) to achieve our target. Making use of the variable transformation given by

$$v_1^2 = W, \tag{27}$$

Equation (20) reduces to an equation that can be manipulated to be in the form

$$\sigma a_1 W'' + 4\left[\omega + \sigma k_1 + \frac{(\nu - h_1)^2}{4\sigma a_1}\right] W + 3(b_1 + \sigma^2 c_1) W^2$$
$$+ \frac{8}{3}(d_1 + \sigma^2 f_1 + \sigma^4 g_1) W^3 + \frac{5}{2}(l_1 + \sigma^2 m_1 + \sigma^4 n_1 + \sigma^6 p_1) W^4 = 0. \tag{28}$$

3 Chirped Soliton Solutions

In what follows, we will apply the soliton ansatz to Eq. (28) and its extracted solutions will be plugged into the relation (27) together with (3) so as to derive chirped optical solitons for the discussed model.

Suppose that Eq. (28) has an exact optical soliton solution in the form

$$W(\xi) = \alpha - \frac{\beta \text{sech}^2(\rho\xi)}{4 - [1 - \tanh(\rho\xi)]^2} + \frac{\gamma \text{sech}^4(\rho\xi)}{(4 - [1 - \tanh(\rho\xi)]^2)^2}, \tag{29}$$

where α, β, γ, and ρ are constants to be identified. Plugging the ansatz (29) into Eq. (28) and equating all coefficients having the same order of $\text{sech}(\rho\xi)\tanh(\rho\xi)$ to zero leads a set of algebraic equations having distinct cases of solutions displayed as follows.

Case 1

$$\begin{aligned} \alpha &= -\frac{4\left(\omega + \sigma k_1 + \frac{(v-h_1)^2}{4\sigma a_1}\right)}{3(b_1 + \sigma^2 c_1)}, \quad \beta = \frac{16\left(\omega + \sigma k_1 + \frac{(v-h_1)^2}{4\sigma a_1}\right)}{(b_1 + \sigma^2 c_1)}, \\ \gamma &= -\frac{32\left(\omega + \sigma k_1 + \frac{(v-h_1)^2}{4\sigma a_1}\right)}{(b_1 + \sigma^2 c_1)}, \quad \rho = \sqrt{\frac{\omega + \sigma k_1 + \frac{(v-h_1)^2}{4\sigma a_1}}{\sigma a_1}}, \end{aligned} \tag{30}$$

under the constraint conditions

$$d_1 + \sigma^2 f_1 + \sigma^4 g_1 = 0, \tag{31}$$

$$l_1 + \sigma^2 m_1 + \sigma^4 n_1 + \sigma^6 p_1 = 0. \tag{32}$$

Substituting (30) into (29) and using the relations (27) and (9) along with (3) and (4), we extract a chirped soliton solution for the coupled system (2) and (3) in the form

$$\begin{aligned} q(x,t) = \Bigg[&-\frac{4\left(\omega + \sigma k_1 + \frac{(v-h_1)^2}{4\sigma a_1}\right)}{3(b_1 + \sigma^2 c_1)} \\ &\times \left\{ 1 - \frac{12\text{sech}^2(\rho\xi)}{4 - [1 - \tanh(\rho\xi)]^2} + \frac{24\text{sech}^4(\rho\xi)}{\left(4 - [1 - \tanh(\rho\xi)]^2\right)^2} \right\} \Bigg]^{\frac{1}{2}} e^{i(\varphi(\xi) - \omega t)}, \end{aligned} \tag{33}$$

$$r(x,t) = \sigma \left[-\frac{4\left(\omega + \sigma k_1 + \frac{(\nu - h_1)^2}{4\sigma a_1}\right)}{3(b_1 + \sigma^2 c_1)} \times \left\{ 1 - \frac{12\text{sech}^2(\rho\xi)}{4 - [1 - \tanh(\rho\xi)]^2} + \frac{24\text{sech}^4(\rho\xi)}{\left(4 - [1 - \tanh(\rho\xi)]^2\right)^2} \right\} \right]^{\frac{1}{2}} e^{i(\varphi(\xi) - \omega t)}, \tag{34}$$

where $(\omega + \sigma k_1 + \frac{(\nu - h_1)^2}{4\sigma a_1})(\sigma a_1) > 0$ and $(\omega + \sigma k_1 + \frac{(\nu - h_1)^2}{4\sigma a_1})(b_1 + \sigma^2 c_1) < 0$.

Case 2

$$\alpha = 0, \ \beta = -\frac{16\left(\omega + \sigma k_1 + \frac{(\nu - h_1)^2}{4\sigma a_1}\right)}{(b_1 + \sigma^2 c_1)}, \quad \gamma = \frac{32\left(\omega + \sigma k_1 + \frac{(\nu - h_1)^2}{4\sigma a_1}\right)}{(b_1 + \sigma^2 c_1)}, \ \rho = \sqrt{-\frac{\omega + \sigma k_1 + \frac{(\nu - h_1)^2}{4\sigma a_1}}{\sigma a_1}}, \tag{35}$$

under the constraint conditions (31) and (32). Substituting (35) into (29) and using the relations (27) and (9) along with (3) and (4), we derive a chirped bright soliton for the coupled system (2) and (3) in the form

$$q(x,t) = \left[-\frac{16\left(\omega + \sigma k_1 + \frac{(\nu - h_1)^2}{4\sigma a_1}\right)}{3(b_1 + \sigma^2 c_1)} \times \left\{ \frac{\text{sech}^2(\rho\xi)}{4 - [1 - \tanh(\rho\xi)]^2} - \frac{2\text{sech}^4(\rho\xi)}{\left(4 - [1 - \tanh(\rho\xi)]^2\right)^2} \right\} \right]^{\frac{1}{2}} e^{i(\varphi(\xi) - \omega t)}, \tag{36}$$

$$r(x,t) = \sigma \left[-\frac{16\left(\omega + \sigma k_1 + \frac{(\nu - h_1)^2}{4\sigma a_1}\right)}{3(b_1 + \sigma^2 c_1)} \times \left\{ \frac{\text{sech}^2(\rho\xi)}{4 - [1 - \tanh(\rho\xi)]^2} - \frac{2\text{sech}^4(\rho\xi)}{\left(4 - [1 - \tanh(\rho\xi)]^2\right)^2} \right\} \right]^{\frac{1}{2}} e^{i(\varphi(\xi) - \omega t)}, \tag{37}$$

where $(\omega + \sigma k_1 + \frac{(\nu - h_1)^2}{4\sigma a_1})(\sigma a_1) < 0$ and $(\omega + \sigma k_1 + \frac{(\nu - h_1)^2}{4\sigma a_1})(b_1 + \sigma^2 c_1) < 0$.

Case 3

$$\alpha = \frac{1}{2}\sqrt{-\frac{6\left(\omega+\sigma k_1+\frac{(\nu-h_1)^2}{4\sigma a_1}\right)}{(d_1+\sigma^2 f_1+\sigma^4 g_1)}},\ \beta = 2\sqrt{-\frac{6\left(\omega+\sigma k_1+\frac{(\nu-h_1)^2}{4\sigma a_1}\right)}{(d_1+\sigma^2 f_1+\sigma^4 g_1)}},$$
$$\gamma = 0,\ \rho = \sqrt{\frac{2(\omega+\sigma k_1+\frac{(\nu-h_1)^2}{4\sigma a_1})}{\sigma a_1}}, \tag{38}$$

under the constraint conditions (32) and

$$b_1 + \sigma^2 c_1 = 0. \tag{39}$$

Substituting (38) into (29) and using the relations (27) and (9) along with (3) and (4), we retrieve a chirped dark soliton for the coupled system (2) and (3) in the form

$$q(x,t) = \left[\frac{1}{2}\sqrt{-\frac{6\left(\omega+\sigma k_1+\frac{(\nu-h_1)^2}{4\sigma a_1}\right)}{(d_1+\sigma^2 f_1+\sigma^4 g_1)}}\left\{1-\frac{4\text{sech}^2(\rho\xi)}{4-[1-\tanh(\rho\xi)]^2}\right\}\right]^{\frac{1}{2}} e^{i(\varphi(\xi)-\omega t)}, \tag{40}$$

$$r(x,t) = \sigma\left[\frac{1}{2}\sqrt{-\frac{6\left(\omega+\sigma k_1+\frac{(\nu-h_1)^2}{4\sigma a_1}\right)}{(d_1+\sigma^2 f_1+\sigma^4 g_1)}}\left\{1-\frac{4\text{sech}^2(\rho\xi)}{4-[1-\tanh(\rho\xi)]^2}\right\}\right]^{\frac{1}{2}} e^{i(\varphi(\xi)-\omega t)}, \tag{41}$$

where $(\omega+\sigma k_1+\frac{(\nu-h_1)^2}{4\sigma a_1})(\sigma a_1) > 0$ and $(\omega+\sigma k_1+\frac{(\nu-h_1)^2}{4\sigma a_1})(d_1+\sigma^2 f_1+\sigma^4 g_1) < 0$.

Case 4

$$\alpha = -\frac{4\left(\omega+\sigma k_1+\frac{(\nu-h_1)^2}{4\sigma a_1}\right)}{(b_1+\sigma^2 c_1)},\ \beta = \frac{8\left(\omega+\sigma k_1+\frac{(\nu-h_1)^2}{4\sigma a_1}\right)}{(b_1+\sigma^2 c_1)},$$
$$\gamma = 0,\ \rho = \sqrt{-\frac{(\omega+\sigma k_1+\frac{(\nu-h_1)^2}{4\sigma a_1})}{\sigma a_1}}, \tag{42}$$

under the constraint conditions (32) and

$$16\left(\omega+\sigma k_1+\frac{(v-h_1)^2}{4\sigma a_1}\right)(d_1+\sigma^2 f_1+\sigma^4 g_1)=3(b_1+\sigma^2 c_1)^2. \tag{43}$$

Substituting (42) into (29) and using the relations (27) and (9) along with (3) and (4), we secure a chirped soliton solution for the coupled system (2) and (3) in the form

$$q(x,t)=\left[-\frac{4\left(\omega+\sigma k_1+\frac{(v-h_1)^2}{4\sigma a_1}\right)}{(b_1+\sigma^2 c_1)}\left\{1-\frac{2\text{sech}^2(\rho\xi)}{4-[1-\tanh(\rho\xi)]^2}\right\}\right]^{\frac{1}{2}} e^{i(\varphi(\xi)-\omega t)}, \tag{44}$$

$$r(x,t)=\sigma\left[-\frac{4\left(\omega+\sigma k_1+\frac{(v-h_1)^2}{4\sigma a_1}\right)}{(b_1+\sigma^2 c_1)}\left\{1-\frac{2\text{sech}^2(\rho\xi)}{4-[1-\tanh(\rho\xi)]^2}\right\}\right]^{\frac{1}{2}} e^{i(\varphi(\xi)-\omega t)}, \tag{45}$$

where $(\omega+\sigma k_1+\frac{(v-h_1)^2}{4\sigma a_1})(\sigma a_1)<0$ and $(\omega+\sigma k_1+\frac{(v-h_1)^2}{4\sigma a_1})(b_1+\sigma^2 c_1)<0$.

Case 5

$$\alpha=\gamma=0,\ \beta=-\frac{8\left(\omega+\sigma k_1+\frac{(v-h_1)^2}{4\sigma a_1}\right)}{(b_1+\sigma^2 c_1)},\ \rho=\sqrt{-\frac{(\omega+\sigma k_1+\frac{(v-h_1)^2}{4\sigma a_1})}{\sigma a_1}}, \tag{46}$$

under the constraint conditions (32) and (43). Substituting (46) into (29) and using the relations (27) and (9) along with (3) and (4), we extract a chirped soliton solution for the coupled system (2) and (3) in the form

$$q(x,t)=\left[-\frac{8\left(\omega+\sigma k_1+\frac{(v-h_1)^2}{4\sigma a_1}\right)}{(b_1+\sigma^2 c_1)}\frac{\text{sech}^2(\rho\xi)}{4-[1-\tanh(\rho\xi)]^2}\right]^{\frac{1}{2}} e^{i(\varphi(\xi)-\omega t)}, \tag{47}$$

$$r(x,t)=\sigma\left[-\frac{8\left(\omega+\sigma k_1+\frac{(v-h_1)^2}{4\sigma a_1}\right)}{(b_1+\sigma^2 c_1)}\frac{\text{sech}^2(\rho\xi)}{4-[1-\tanh(\rho\xi)]^2}\right]^{\frac{1}{2}} e^{i(\varphi(\xi)-\omega t)}, \tag{48}$$

where $(\omega+\sigma k_1+\frac{(v-h_1)^2}{4\sigma a_1})(\sigma a_1)<0$ and $(\omega+\sigma k_1+\frac{(v-h_1)^2}{4\sigma a_1})(b_1+\sigma^2 c_1)<0$.

4 Discussion and Remarks

The derived wave solutions above shows that the model of the coupled NLSE (1) and (2) possesses distinct chirped solitons having nonlinear phase functions in terms of the reciprocal of amplitude function which are entirely different from the previous studies in the literature. The model reduction and solution extraction are carried out under some assumptions and specific conditions. The obtained optical solitons include various forms such as W-shaped, bright, dark, kink, and anti-kink solitons.

To throw light on the behavior of chirped optical solitons, the graphical representations of the obtained solutions are displayed by taking suitable values for the model parameters. Figure 1 describes the evolution of chirped soliton solutions (33) and (34) which characterizes the W-shaped wave. The graph shown in Fig. 2 exhibits the profile of bright soliton wave for solutions (36) and (37). Furthermore, Fig. 3 depicts the plot of solutions (40) and (41) where the wave structure represents dark soliton. Obviously seen that Fig. 4 demonstrates soliton wave of kink shape for solutions (44) and (45). From Fig. 5, the behavior of solutions (47) and (48) illustrates anti-kink type soliton.

One can see from the figures that the intensity profiles of the derived optical solutions demonstrate various wave structures which are different from the ones obtained in the previous studies [12, 13]. In addition to this, the expression of the

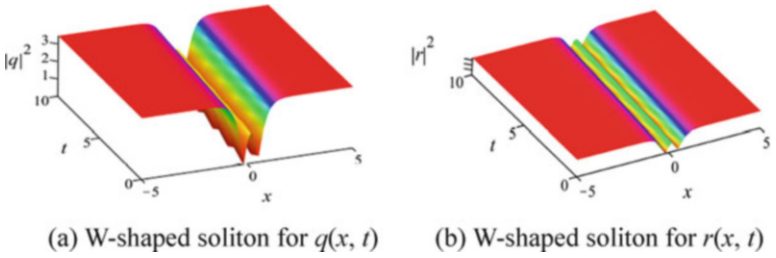

(a) W-shaped soliton for $q(x, t)$ (b) W-shaped soliton for $r(x, t)$

Fig. 1 The profile of W-shaped soliton

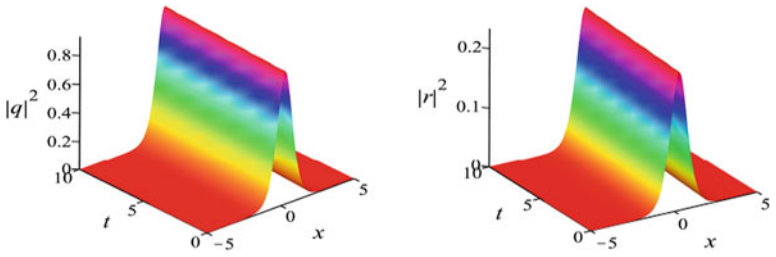

(a) Bright soliton for $q(x, t)$ (b) Bright soliton for $r(x, t)$

Fig. 2 The profile of bright soliton

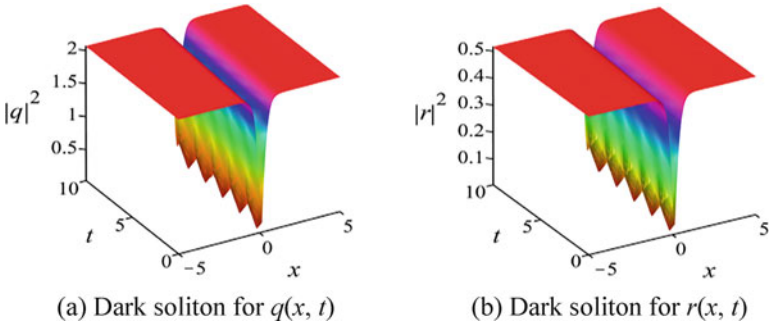

Fig. 3 The profile of dark soliton

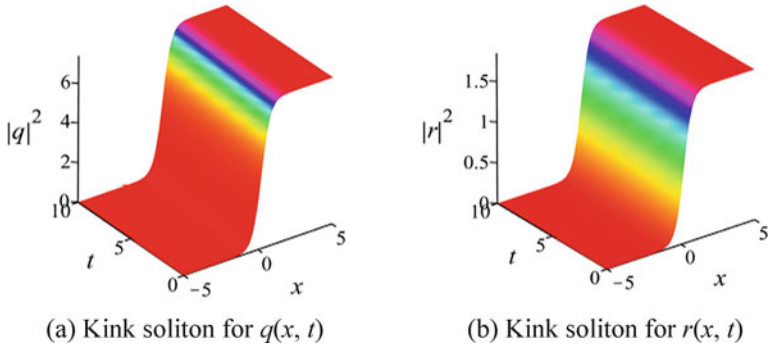

Fig. 4 The profile of kink-shaped soliton

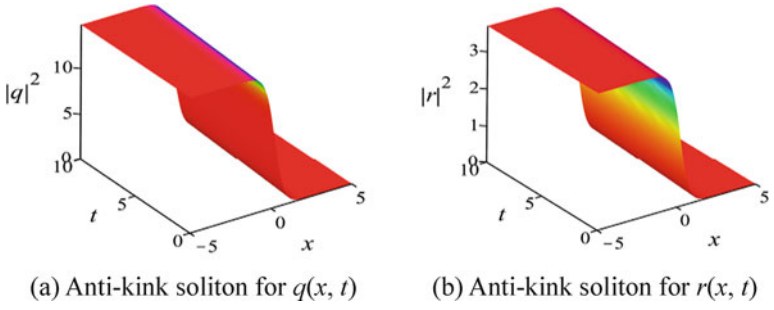

Fig. 5 The profile of anti-kink-shaped soliton

nonlinear chirp associated with each soliton solution can be extracted using (19). Besides, all cases of soliton solutions are induced under specific conditions as mentioned above.

5 Conclusion

This work has investigated the chirped optical solitons in fiber BGs with polynomial form of nonlinear refractive index. The associated chirp to the optical soliton is analytically induced in a form of nonlinear function. The discussed model is analyzed and reduced to an integrable form under specific conditions that ensure equivalence in the coupled equations of the system. The derived chirped soliton solutions have different structures such as W-shaped, bright, dark, kink, and anti-kink solitons. These soliton structures are entirely new compared to the previous studies that dealt with chirped and chirp-free optical solitons of the current model, where the associated chirp has a linear function in contrast to the more generalized form detected in the present work. The new results obtained here are expected to contribute in improving the experimental studies and engineering applications related to fiber BGs.

Acknowledgments The authors gratefully acknowledge support from University of Technology and Applied Sciences, Ibri, Oman through the Internal Research Funding Program, grant number 01-IRFP-IBRI-2023.

References

1. Willner, A.E., Hoanca, B.: Fixed and tunable management of fiber chromatic dispersion. In: Optical Fiber Telecommunications IV-B, pp. 642–724. Elsevier, Amsterdam (2002)
2. Xu, T., Jacobsen, G., Popov, S., Li, J., Vanin, E., Wang, K., Friberg, A.T., Zhang, Y.: Chromatic dispersion compensation in coherent transmission system using digital filters. Opt. Express **18**(15), 16243–16257 (2010)
3. Zhao, J., Ellis, A.: Transmission of 4-ASK optical fast OFDM with chromatic dispersion compensation. IEEE Photon. Technol. Lett. **24**(1), 34–36 (2011)
4. Li, H., Sheng, Y., Li, Y., Rothenberg, J.E.: Phased-only sampled fiber Bragg gratings for high-channel-count chromatic dispersion compensation. J. Light. Technol. **21**(9), 2074 (2003)
5. Dar, A.B., Jha, R.K.: Chromatic dispersion compensation techniques and characterization of fiber Bragg grating for dispersion compensation. Opt. Quantum Electron. **49**(3), 1–35 (2017)
6. Pan, Z., Song, Y., Yu, C., Wang, Y., Yu, Q., Popelek, J., Li, H., Li, Y., Willner, A.E.: Tunable chromatic dispersion compensation in 40-GB/s systems using nonlinearly chirped fiber Bragg gratings. J. Light. Technol. **20**(12), 2239–2246 (2002)
7. Amiri, I., Rashed, A.N.Z., Kader, H.M.A., Al-Awamry, A.A., Abd El-Aziz, I.A., Yupapin, P., Palai, G.: Optical communication transmission systems improvement based on chromatic and polarization mode dispersion compensation simulation management. Optik **207**, 163,853 (2020)
8. Biswas, A., Ekici, M., Sonmezoglu, A., Belic, M.R.: Optical solitons in fiber Bragg gratings with dispersive reflectivity for quadratic–cubic nonlinearity by extended trial function method. Optik **185**, 50–56 (2019)
9. Zayed, E., Alngar, M., Biswas, A., Ekici, M., Alzahrani, A., Belic, M.: Chirped and chirp-free optical solitons in fiber Bragg gratings with Kudryashov's model in presence of dispersive reflectivity. J. Commun. Technol. Electron. **65**(11), 1267–1287 (2020)
10. Yıldırım, Y., Biswas, A., Guggilla, P., Khan, S., Alshehri, H.M., Belic, M.R.: Optical solitons in fibre Bragg gratings with third-and fourth-order dispersive reflectivities. Ukr. J. Phys. Opt. **22**(4), 239–254 (2021)

11. Malik, S., Kumar, S., Biswas, A., Ekici, M., Dakova, A., Alzahrani, A.K., Belic, M.R.: Optical solitons and bifurcation analysis in fiber Bragg gratings with lie symmetry and Kudryashov's approach. Nonlinear Dyn. **105**(1), 735–751 (2021)
12. Zayed, E.M., Alngar, M.E., Biswas, A., Ekici, M., Triki, H., Alzahrani, A.K., Belic, M.R.: Chirped and chirp-free optical solitons in fiber Bragg gratings having dispersive reflectivity with polynomial form of nonlinearity using sub-ode approach. Optik **204**, 164,096 (2020)
13. Seadawy, A.R., Ahmed, H.M., Rabie, W.B., Biswas, A.: Chirp-free optical solitons in fiber Bragg gratings with dispersive reflectivity having polynomial law of nonlinearity. Optik **225**, 165,681 (2021)
14. Al-Ghafri, K., Krishnan, E., Biswas, A.: W-shaped and other solitons in optical nanofibers. Results Phys. **23**, 103973 (2021)
15. Al-Ghafri, K.S.: Soliton structures in optical fiber communications with Kundu–Mukherjee–Naskar model. Open Phys. **19**(1), 679–682 (2021)

Part VIII
Nonlinear Phenomena in Bio- and Eco-systems Dynamics

An Overview on Time-Frequency Effects of ECG Signals Using Synchroextracting Transform

Marcus Varanis, Sadra Hemmati, Murilo Cesar Filipus, Felipe Lima de Abreu, Jose M. Balthazar, and C. Nataraj

1 Introduction

Characterization and identification are a major goal in the study of complex dynamic systems. Unlike linear systems, for which system identification is well explored, nonlinear, real-world systems lack a comprehensive and universal theory. Techniques from digital signal processing (DSP) and time-frequency analysis (TFA) are commonly used in several areas of science and engineering to characterize and extract essential parameters (or features) from dynamic systems. DSP and TFA techniques, based on the Fourier transform (FT) and the continuous wavelet transform (CWT), have been applied successfully to the analysis of nonlinear systems and chaotic dynamics, helping the dynamicists to gain better understanding of the systems under study.

The discrete Fourier transform (DFT) has a very good resolution in the frequency domain but suffers from a poor resolution (if any) in the time domain (here, by "good resolution," we mean that the frequency domain information are well-resolved in the

M. Varanis (✉)
Physics Institute, Federal University of Mato Grosso do Sul (UFMS), Campo Grande, Brazil
e-mail: marcus.varanis@ufms.br
https://varanis.cc/

S. Hemmati · C. Nataraj
Villanova Center for Analytics of Dynamic Systems (VCADS), Villanova University, Villanova, PA, USA

M. C. Filipus · F. L. de Abreu
Faculty of Engineering, Federal University of Grande Dourados, Dourados, Brazil

J. M. Balthazar
Department of Electrical Engineering, Federal University of Technology– Parana, Curitiba, Brazil

Faculty of Mechanical Engineering, São Paulo State University, São Paulo, Brazil

© The Author(s), under exclusive license to Springer Nature Switzerland AG 2024

W. Lacarbonara (ed.), *Advances in Nonlinear Dynamics, Volume III*, NODYCON Conference Proceedings Series, https://doi.org/10.1007/978-3-031-50635-2_54

coefficients of DFT). To overcome this problem, the short time Fourier transform (STFT) was introduced as a modification of DFT, which, by performing Fourier transforms in time windows, contains information both in the frequency and time domains but loses resolution in both domains. Subsequently, CWT tries to overcome this problem by performing convolutions on the signal with waves of different amplitudes and lengths (i.e., wavelets), thus, representing the signal more effectively in both time and frequency domains, when compared to methods based on TF.

TFA techniques, such as CWT, are very efficient in parameter/feature extraction, and solving the fixed window size problem of STFT. However, their TFR presents a low resolution of the instantaneous frequency (IF) of the signal. To overcome this problem, new methods have been developed, including the Hilbert-Huang transform (HHT), which greatly improves the resolution of the IF. Another problem encountered in TFA is the energy dispersion in the TFR which can hide/offset some frequencies, and causing inaccuracy in TFA. Methods based on synchrosqueezing try to mitigate this problem as presented in [1, 2]. Emergent TFA techniques have been proposed in order to concentrate energy in the TFR, including the wavelet-based synchrosqueezing transform (WSST) and wavelet-based synchroextracting transform (WSET). In this work, WSET will be used, which is one of the emerging methods that has been used in the characterization of signals from mechanical systems [3]. A comprehensive discussion about synchroextracting transform (SET) formulation, with its applications and limitations, is presented in [4, 5]. It is important to note that these methods are eminently suitable for characterization of signals with nonstationary, nonlinear, and chaotic characteristics. It is well-known that ECG signals are strongly nonlinear: the ECG signal in healthy conditions presents quasi-periodic responses, while a signal containing a pathological condition, in general, presents chaotic or quasi-periodic responses [6–8].

The main objective of this paper is to present the use of techniques based on the WSET scheme to characterize abnormalities in ECG signals and also to perform a comparison between CWT scheme widely used in the literature, and the WSET method, from ECG signals with different clinical conditions, in order to present its unique features and potential advantages over other methods.

2 Methodology

The experimental and real-world data used in this study, including ECG signals, are from the PhysioNet [9], a database with different clinical conditions. In particular, we utilized ECG recordings from the MIT-BIH Arrhythmia dataset [10]. In Table 1, the conditions and the types of cardiac arrhythmias contained in the analyzed ECG signals are presented.

First, for comparison, slices of ECG signals at different clinical conditions, and at specific times, will be presented together, each of which was acquired using a time window of 1 minute. Then, all these signals are transformed to the frequency

Table 1 Clinical conditions in ECG signals

Symbol	Clinical condition
R	Right bundle branch block beat
L	Left bundle branch block beat
V	Premature ventricular contraction
VT	Ventricular tachycardia
VFL	Ventricular flutter

domain using CWT and WSET based techniques. The results are then analyzed using the TFR of each technique.

3 Time-Frequency Analysis Schemes

The CWT was proposed in order to overcome the limitations induced by a fixed window length in STFT. In general, the wavelet transform uses a variable window, where the resolutions vary along the time-frequency plane, so one can obtain all the information contained in the signal and is defined by Eq. (1).

$$W_f(t,a) = \frac{1}{\sqrt{a}} \int_{-\infty}^{+\infty} f(u) \overline{\left(\Psi \left(\frac{u-t}{a} \right) \right)} du \tag{1}$$

In Eq. (1), the term $\bar{\psi}(u)$ is the window prototype, known as the "mother wavelet." A long and in-depth study of various contexts and the formulation of CWT can be found in [11–13]. Next, the formulation of the CWT scheme in the Fourier domain is presented in order to demonstrate the construction of the TRF.

$$W_f(t,a) = \frac{1}{2\pi} \int_{-\infty}^{+\infty} \hat{f}(\xi) \sqrt{a} \hat{\Psi} e^{i\xi t} d\xi \tag{2}$$

In Eq. (2), the term $f(\epsilon)$ denotes the Fourier Transform of $f(u)$.

$$f(t) = A e^{i\omega_0 t} \tag{3}$$

Given that $f(u)$ is a purely harmonic signal with fundamental frequency ω_0 and constant amplitude, one can write:

$$\hat{f}(\xi) = 2\pi A \delta(\xi - \omega_0) \tag{4}$$

and the Fourier Transform of Eq. (4) as:

$$W_f(t,a) = \frac{1}{2\pi}\int_{-\infty}^{+\infty} 2\pi A\delta(\xi-\omega_0)\sqrt{a}\hat{\Psi}e^{i\xi t}d\xi = A\sqrt{a}\hat{\Psi}(a\omega_0)e^{i\omega_0 t} \tag{5}$$

Thus, from Eq. (5) it is possible to obtain the signal in the frequency domain and to compute the TFR of the $f(u)$ signal.

In [14] a new form of TFA, called wavelet Synchrosqueezed transform (WSST), is presented, which in general unites empirical mode decomposition (EMD) and CWT. This unification improves the analysis of instantaneous frequencies in the transformation process. The expression WSST is given by:

$$T_f(t,\omega) = \int_{-\infty}^{+\infty} W_f(t,a)a^{-\frac{3}{2}}\delta(\omega-\omega_0(t,a))da \tag{6}$$

Therefore, WSST can be characterized as a post-processing method based on CWT.

Analysis of real signals involves dealing with noise from several sources. The synchrosqueezed based process can present some problems in processing signals with added noise, which can result in a low resolution TFR. This problem can be overcome by synchroextraction (SET) based methods. The underlying principle of the SET procedure is that the maxima of the STFT coefficients are extracted from the IF trajectory. Therefore, SET can be written as follows:

$$S_e(t,\omega) = G_e(t,\omega)\delta(\omega-\omega_0(t,\omega)) \tag{7}$$

In Eq. (7), $G_e(t,\omega)$ denotes the STFT of the signal.

It should be noted that SET is a post-processing method based on STFT, with the result that limitations associated with STFT will be present in this approach as well.

In [3], a combination of SET and CWT is proposed, which results in a new TFA approach called wavelet-based Synchroextracting transform (WSET). This "combination process" involves manipulating the ω and $\omega_0(t,\omega)$ terms, replacing $G(t,\omega)$ with the a and a_ϕ scale terms and making $W_f(t,a).a^{(-3/2)}.\delta(a-a_\phi)$. Thus, the following expression is obtained:

$$\mathfrak{T}_f(t,a) = W_f(t,a).a^{-\frac{3}{2}}.\delta(a-a_\varphi). \tag{8}$$

We then redefine the operator $\delta(a-a_{varphi})$ in Eq. (8).

$$\delta(a-a_\varphi) = \begin{cases} 1, a = a_\varphi \\ 0, a \neq a_\varphi \end{cases} \tag{9}$$

In this way it is possible to rewrite $\mathfrak{T}_f(t,a)$ so that the expression for WSET has the form that follows.

$$\mathfrak{T}_f(t,a) = \begin{cases} W_f(t,a).a^{-\frac{3}{2}}, a = a_\varphi \\ 0, a \neq a_\varphi \end{cases} \tag{10}$$

Thus, we classify the WSET scheme as a post-processing method that merges SET and CWT [3], which makes the extraction of the FI more efficient. WSET preserves the main features of CWT that allows the analysis of signals with nonstationary and nonlinear characteristics.

4 Results

The results are presented as follows: in Figs. 1, 2, the signals in the time domain with different clinical conditions are presented. In Figs. 3, 4 the signals in the frequency domain obtained via TFR (CWT and WSET) are presented. These signals contain the isolated clinical conditions. In Fig. 5, we present a time-domain ECG signal that contains all the abnormalities described in Table 1. In addition, comparisons of the signal in the frequency domain through CWT and WSET are made. In Figs. 5, 6 we present an ECG signal in the time domain; note that it contains all the anomalies described in Table 1. In addition, a comparison of the signal in the frequency domain, through CWT and WSET, is made. Finally, in Fig. 7, representation of the ECG signal containing all anomalies is presented through a Waterfall plot making it possible to visualize and relate the amplitudes of energy to the most representative frequencies.

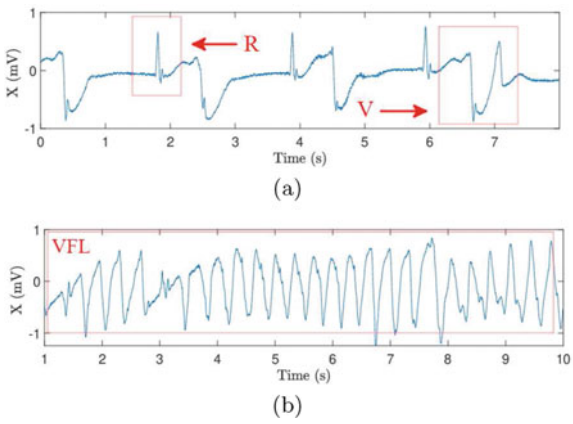

Fig. 1 ECG in time domain: (**a**) [R-V], (**b**) [VFL]

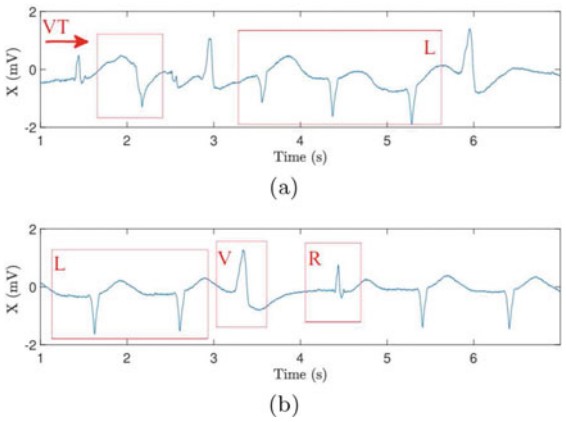

Fig. 2 ECG in time domain: (**a**) [VT-L], (**b**) [L-V-R]

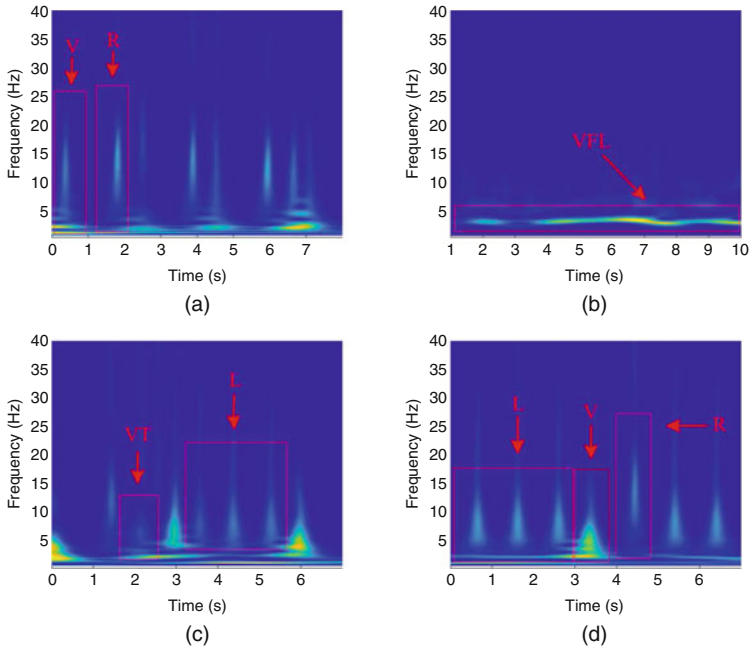

Fig. 3 ECG in frequency domain—CWT scheme: (**a**) [R-V], (**b**) CWT [VFL], (**c**) CWT [VT-L], (**d**) CWT [L-V-R]

5 Discussions

In this work, we propose the use of Wavelet-based Synchroextracting Transform (WSET) as a method for efficient and effective characterization of ECG signals in the frequency domain. The main justification for using WSET is its proven efficiency in the characterization of instantaneous frequency (IFs) and lower energy

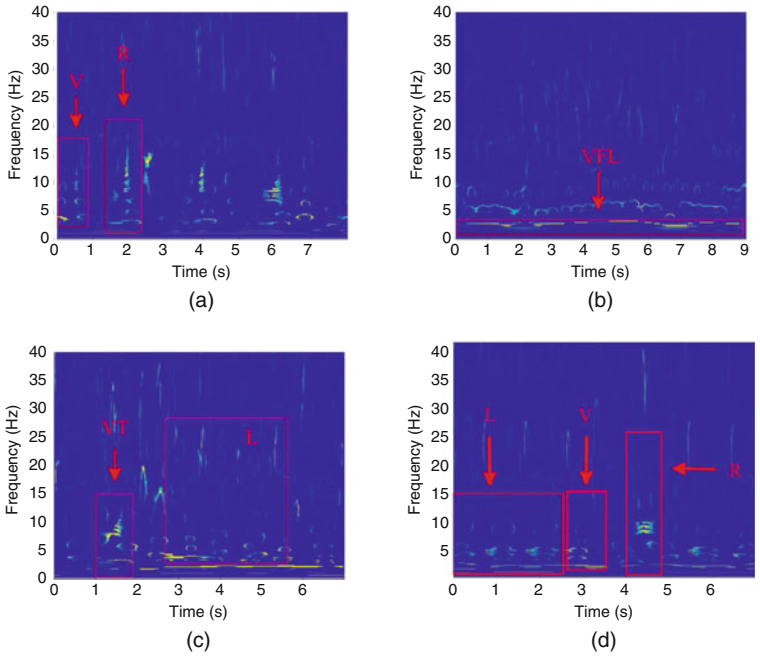

Fig. 4 WSET scheme: (**a**) WSET [R-V], (**b**) WSET [VFL], (**c**) WSET [VT-L], (**d**) WSET [L-V-R]

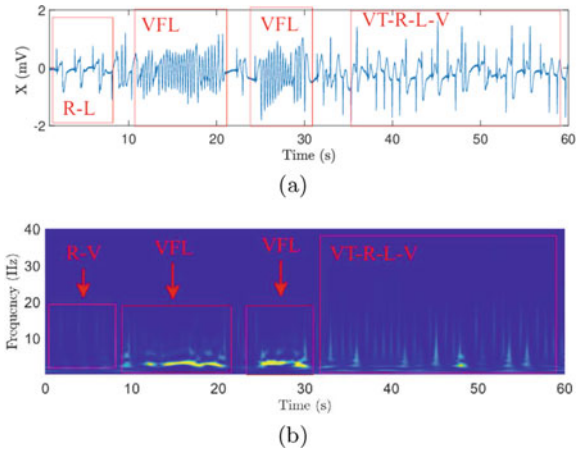

Fig. 5 ECG signal with all clinical conditions: (**a**) Time domain, (**b**) Frequency domain—CWT scheme

dispersion in the time-frequency representation compared to classical methods such as continuous wavelet transform (CWT) and short time Fourier transform (STFT).

Through the results presented in Fig. 3a and b, it can be seen that the signal in the frequency domain in the TFR obtained through the CWT scheme for four signals presented Figs. 1, 2, it is noted, different structures that appear due to each of the

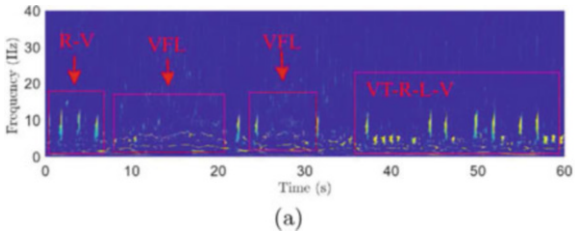

Fig. 6 Frequency domain—WSET scheme

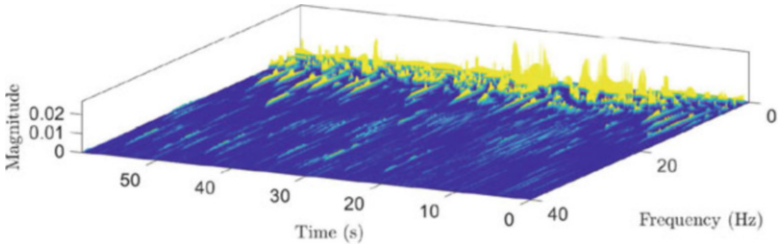

Fig. 7 ECG signal with all conditions: frequency domain—WSET scheme using waterfall representation

anomalies present in the signals. Such structures are well defined in the TFR, but some instantaneous frequencies of the ECG signal may not be identified (due to the fact that these structures scatter the energy in the TFR). However, it is interesting to note a pattern that defines the shape of the anomalies associated with the ECG signal.

When the WSET scheme is used, results of which are presented in Fig. 4, it is possible to see how the method characterizes the instantaneous frequencies throughout the signal, allowing better temporal localization of a different clinical condition. We also observe discontinuities in the main frequency. Due to the concentration of energy in the TFR it is possible to observe the strong variation in the frequency spectrum at the instants when the cardiac arrhythmias occur, and this variation is a qualitative indicator of occurrence of period doubling, quasi-periodicity and routes to chaos in nonstationary signals, as described in [15].

The abrupt variations in the frequency spectrum become even more evident when we compare different arrhythmias in Figs. 5, 6 which shows the responses of the ECG signal in the frequency domain. This is a signal with a longer time interval that shows all the clinical conditions cited. The results through the WSET scheme show the nonstationary and nonlinear characteristics of the signal more clearly when compared to the results through the CWT scheme.

Finally, in Fig. 7, it is possible to observe how the WSET scheme (waterfall representation) is processing the signal, where in the continuous region, one has a much larger amplitude with the noise concentrating at high frequencies with small energy intensity; one can also notice the strong variation of the IFs over time.

6 Final Remarks

In this paper, the emergent time-frequency analysis, the Wavelet-based Synchroextracting Transform, is presented for ECG signal analysis. It is compared qualitatively with continuous wavelet transform. The main advantage of the proposed method is the better characterization of instantaneous frequencies whose variation is associated with the clinical conditions presented. In addition, the method concentrates the energy in the time-frequency representation, showing better resolution.

ECG signals presenting different clinical conditions were used, which were given a good representation in the frequency domain by using WSET scheme, because the technique presents a good representation in the frequency domain for low frequencies, a characteristic present in cardiac systems.

This effective capturing of instantaneous frequencies and high energy concentration in the TFR, associated with the WSET scheme results, allows characterization of anomalies due to cardiac arrhythmias present in the ECG signals. In addition, it allows the characterization of abrupt variations in the frequency spectrum and nonlinearities in the signals.

The results show that the WSET procedure is a promising technique with compelling application potential in the analysis of signals from nonlinear systems. The results also indicate that the technique can be used to extract more effective features for machine learning and deep learning applications involving signal and system classification, especially ECG signals.

References

1. Yu, G., Wang, Z., Zhao, P., Li, Z.: Local maximum synchrosqueezing transform: an energy-concentrated time-frequency analysis tool. Mech. Syst. Signal Process. **117**, 537–552 (2019)
2. Varanis, M., Silva, A.L., Balthazar, J.M., Oliveira, C., Tusset, A. and Bavastri, C.A.:A short note on synchrosqueezed transforms for resonant capture, Sommerfeld effect and nonlinear jump characterization in mechanical systems. J. Vib. Eng. Technol. 1–6 (2021)
3. Shi, Z., Yang, X., Li, Y., Yu, G.: Wavelet-based synchroextracting transform: an effective TFA tool for machinery fault diagnosis. Control Eng. Practice **114**, 104884 (2021)
4. Li, Z., Gao, J., Li, H., Zhang, Z., Liu, N., Zhu, X.: Synchroextracting transform: The theory analysis and comparisons with the synchrosqueezing transform. Signal Process. **166**, 107–243 (2020)
5. Yuan, P.-P., Zhang, J., Feng, J.-Q., Wang, H.-H., Ren, W.-X., Wang, C.: An improved time-frequency analysis method for structural instantaneous frequency identification based on generalized S-transform and synchroextracting transform. Eng. Struct. **252**, 113657 (2022)
6. Grudzinski, K., Zebrowski, J.J.: Modeling cardiac pacemaker with relaxion oscillators. Phys. A **336**, 153–162 (2004)
7. Gois, S.R., Savi, M.A.: An analysis of heart rhythm dynamics using a three-coupled oscillator model. Chaos Solitons Fractals **41**, 553–2565 (2009)
8. Cheffer, A., Savi, M.A., Pereira, T.L., de Paula, A.S.: Heart rhythm analysis using a nonlinear dynamics perspective. Appl. Math. Model. **96**, 152–176 (2021)

9. Goldberger, A.L., Amaral, L.A.N., Glass, L., Hausdorff, J.M., Ivanov, P.Ch., Mark, R.G., Mietus, J.E., Moody, G.B., Peng, C.-K., Stanley, H.E.: PhysioBank, PhysioToolkit, PhysioNet: components of a new research resource for complex physiologic signals. Circulation **101**(23), e215–e220 2000. Circulation Electronic Pages http://circ.ahajournals.org/content/101/23/e215.full
10. Moody, G.B., Mark, R.G.: The impact of the MIT-BIH Arrhythmia Database. IEEE Eng. Med. Biol. **20**(3), 45–50 (2001). PMID: 11446209
11. Daubechies, I.: Ten Lectures on Wavelets. Society for Industrial and Applied Mathematics (1992)
12. Addison, P.S.: The Illustrated Wavelet Transform Handbook: Introductory Theory and Applications in Science, Engineering, Medicine and Finance. CRC Press, Boca Raton (2017)
13. Mallat, S.: A Wavelet Tour of Signal Processing. Elsevier, Amsterdam (1999)
14. Daubechies, I., Lu, J., Wu, H.T.: Synchrosqueezed wavelet transforms: an empirical mode decomposition-like tool. Appl. Comput. Harmon. Anal. **30**(2), 243–261 (2011)
15. Varanis, M.V., Tusset, A.M., Balthazar, J.M., Litak, G., Oliveira, C., Rocha, R.T., Nabarrete, A., Piccirillo, V.: Dynamics and control of periodic and non-periodic behavior of Duffing vibrating system with fractional damping and excited by a non-ideal motor. J. Frank. Inst. **357**(4), 2067–2082 (2020)

Hopf Bifurcation Analysis of the BVAM Model for Electrocardiogram

Ahsan Naseer, Imran Akhtar, and Muhammad R. Hajj

1 Introduction

Almost all of the natural phenomena are nonlinear in nature, applications ranging from population growth, chemical reactions, physiology of nerves, onset of turbulence, regulation of heartbeats and include many other [1]. A model can exhibit several qualitatively different solutions at different values of control parameters including fixed-point (FP) solution, limit cycle oscillations (LCO), quasi-periodic solution, or chaotic solution. Changing the control parameters can lead to qualitative variation in the response of a dynamical system due to bifurcation. These bifurcations are important in real-life applications, such as flutter in which the Hopf bifurcation induces self-oscillatory vibrations that sometimes accompanied with hysteresis [2]. Similarly, bifurcations occurring in BVAM model with linear control parameter lead to producing electrocardiograms (ECGs) of the human heart. It may further lead to the ECG of different arrhythmia, such as sinus tachycardia, atrial flutter, ventricular tachycardia [3] including ventricular fibrillation (VF) that if not treated promptly can result in sudden cardiac death [4].

There are different methods of determining bifurcations. Finding it through perturbation techniques allows us to know the normal form of bifurcation, and method of multiple scales (MMS) can be used to accomplish this [5]. Recent researches show that electrical dynamics of heart can be represented by nonlinear deterministic theory [3]. Action potential originating from the sinoatrial (SA) node

A. Naseer (✉) · I. Akhtar
Department of Mechanical Engineering, NUST College of Electrical and Mechanical Engineering, National University of Science and Technology, Islamabad, Pakistan
e-mail: anaseer.me19ceme@student.nust.edu.pk

M. R. Hajj
Department of Civil, Environmental and Ocean Engineering, Davidson Laboratory, Stevens Institute of Technology, Hoboken, NJ, USA

© The Author(s), under exclusive license to Springer Nature Switzerland AG 2024

W. Lacarbonara (ed.), *Advances in Nonlinear Dynamics, Volume III*, NODYCON Conference Proceedings Series, https://doi.org/10.1007/978-3-031-50635-2_55

initiates pumping function of the heart. The atrioventricular (AV) node receives this electrical signal that flows through the atrial muscles. Finally, electrical impulses travel along the His–Purkinje complex forcing the ventricular muscles to contract and thereby supplying blood to the whole human body [6]. The ECG represents normal or otherwise abnormal heart activities often referred to as arrhythmia [6].

Nonlinear dynamical systems theory is often employed as a valuable method for studying basic causes of abnormal arrhythmia and cardiac diseases [7]. Fibrillation is an arrhythmia that can be modeled showing how sinus rhythm bifurcates to chaos through Ruelle–Takens–Newhouse route [8]. In an earlier work [9], it was suggested that an ectopic pacemaker (EP) that activates the ventricular muscles and reproduces closely comparable ECG waveforms be added to the model to generate chaotic responses that are correlated with VF [10]. The suggestion that VF causes chaotic behavior may lead to new clinical insight in order to prevent it. In a recent work [3], a reaction–diffusion model capable of reproducing ECG of normal sinus rhythm and various arrhythmia was discretized. In this chapter, effort is made to find an analytic solution to the BVAM model near the Hopf bifurcation. Starting from the fixed points, critical control parameter is identified where Hopf bifurcation occurs and analytic solution is determined local to this region. This provides physical insight and can be employed to perform sensitivity analysis in a continuous fashion.

2 Mathematical Model

BVAM is a generic reaction–diffusion equation that can model a wide variety of biological phenomena [11]. It exhibits rich dynamics that include Turing patterns, traveling waves, temporal oscillations, and chaotic behavior [12]. The non-dimensionalized form of the BVAM model is given in Eq. (1) [12].

$$\begin{aligned} \frac{\partial u}{\partial t} &= D\nabla^2 u + \eta(u + av - Cuv - uv^2) \\ \frac{\partial v}{\partial t} &= \nabla^2 v + \eta(bv + Hu + Cuv + uv^2) \end{aligned} \tag{1}$$

where $u(x, t)$ and $v(x, t)$ are two interacting variable functions of time t and one-dimensional space component x. These variables can be interpreted as chemical substances or morphogens or any other quantity. Here, the values of these parameters are kept to be $\eta = 1, a = -1$ and $b = -3$. Equation (1) can be discretized at three different points to form six ordinary differential equations (ODEs) using the Newmann boundary conditions that imply zero flux or electrical insulated boundaries. The three pairs of ODEs can represent three nodes of Heart, namely SA node, AV node, and His–Purkinje Complex. Applying symmetry, six equations are reduced to four ODEs as given in Eq. (2) [3],

$$\begin{aligned}
\dot{x}_1 &= x_1 - x_2 - Cx_1x_2 - x_1{x_2}^2 \\
\dot{x}_2 &= Hx_1 - 3x_2 + Cx_1x_2 + x_1{x_2}^2 + \beta(x_4 - x_2) \\
\dot{x}_3 &= x_3 - x_4 - Cx_3x_4 - x_3{x_4}^2 \\
\dot{x}_4 &= Hx_3 - 3x_4 + Cx_3x_4 + x_3{x_4}^2 + 2\beta(x_2 - x_4)
\end{aligned} \tag{2}$$

where C is the ratio of quadratic to cubic non-linearity and is 1.35[3]. Here, $\beta = \frac{1}{\Delta x} = 4$, where Δx refers to the spacing between nodes, while H is the linear control parameter. The model has a diverse form of solutions. It has solutions ranging from fixed-point solution, periodic limit cycle solution, period two solution to quasi-periodic solution, and ultimately leading to chaos via Ruelle–Takens–Newhouse route [3].

3 Analytic Approach

Equation (2) undergoes several fixed-point (FP) bifurcations, as H is decreased, before moving into the periodic solution. At $H \approx 9$, the system has three FP solutions including the origin. For a general dynamical system represented by Eq. (3), where c is the set of general parameters and H can be one or multiple control parameters,

$$\dot{\mathbf{x}} = \mathbf{F}(\mathbf{x}, c, H) \tag{3}$$

The stability of solutions is analyzed at these FPs. After computing the eigenvalues of the Jacobian matrix, we find that the FP at origin is unstable, while the other two fixed points, as given in Table 1, are stable. As H is decreased further, one set of FP becomes nonhyperbolic at critical $H_c = 8.7793$ and undergoes Hopf bifurcation as eigenvalues become $\pm 5.82214\iota$. The numerical simulation confirms the occurrence of Hopf bifurcation. In the vicinity of $H \leq 8.7793$, there is one unstable trivial FP solution, one stable FP solution, and a branch of stable periodic solution that emerged as a result of Hopf bifurcation, and the other unstable FP that lost stability due to Hopf bifurcation. Other stable FP solution also becomes unstable as H is decreased past 7.9709 and experiences Hopf bifurcation that can be determined through the same aforementioned procedure. Table 2 shows the FPs and corresponding eigenvalues. Here, we intend to plot the bifurcation curve using the method of normal forms. The technique used is the MMS; however, before applying this perturbation technique, it is necessary to first transform the dynamics to center manifold.

Table 1 Stable FPs at $H \approx 9$

Serial No.	x_1	x_2	x_3	x_4
FP 1	−1.1975	−1.29	1.5284	0.4136
FP 2	0.8963	0.3546	−2.1215	−1.5315

Table 2 FPs and corresponding eigenvalues at critical H

H_c	FP	Eigenvalues
8.7793	FP1: 0.92, 0.36, −2.18, −1.54	$-7.36, -3.86, \pm 5.82\iota$
	FP2: −1.24, −1.31, 1.58, 0.42	$-8.59, -2.63, -0.22 \pm 5.42\iota$
7.9709	FP1: 1.03, 0.37, −2.44, −1.57	$0.16 \pm 5.90\iota, -5.38 \pm 0.68\iota$
	FP2: −1.41, −1.37, 1.79, 0.43	$-7.49, -3.35, \pm 5.56\iota$

3.1 Center Manifold Reduction

Manifolds are invariant sub-spaces whose dimensions m are less than the dimensions n of the entire system [13]. The control parameter is written as $H = H_c + \sigma$, where σ is the tuning parameter. The general representation in the y-coordinates takes the form of an Eq. (5).

$$\mathbf{x} = \mathbf{x_0} + \mathbf{y} \tag{4}$$

$$\dot{\mathbf{y}} = A\mathbf{y} + \sigma\mathbf{y} + \mathbf{F_2}(\mathbf{y}) + \mathbf{F_3}(\mathbf{y}) + O(||\mathbf{y}||^4) \tag{5}$$

Here, A is the Jacobian of the system of equation represented by Eq. (3). The eigenvectors of Jacobian matrix A, i.e., $\mathbf{p_1}, \mathbf{p_2}, \ldots, \mathbf{p_n}$, for a n-dimensional system are the local manifolds of the system. In center manifold analysis, coordinate axis of system is first translated to the fixed points using Eq. (4) and in its local region analysis is performed. If P is a matrix such that its columns are the eigenvectors of the Jacobian matrix A, i.e., $P = [\mathbf{p_1} \quad \mathbf{p_2} \quad \ldots \quad \mathbf{p_n}]$ and a transformation $\mathbf{y} = P\mathbf{v}$ transforms dynamics on the manifolds resulting in $\dot{\mathbf{v}} = J\mathbf{v} + P^{-1}\mathbf{F_2}(P\mathbf{v}) + P^{-1}\mathbf{F_3}(P\mathbf{v}) + O(||\mathbf{v}||^4)$, the matrix $J = P^{-1}AP$ is a diagonal matrix with the eigenvalues of matrix A as its diagonal entries. The vector functions $\mathbf{F_2}$ and $\mathbf{F_3}$ are the quadratic and cubic functions, respectively, of the variables $\mathbf{y}$ and $\mathbf{v}$ for Eq. (5) and most recent one. Since J is a diagonal matrix, therefore the system becomes linearly decoupled. Each component of $\mathbf{v}$ represents a distinct manifold if all of the eigenvalues are different. Equation (6) is the equation of manifolds of the form,

$$\begin{bmatrix} \dot{\mathbf{v_c}} \\ \dot{\mathbf{v_s}} \\ \dot{\mathbf{v_u}} \end{bmatrix} = \begin{bmatrix} J_c & 0 & 0 \\ 0 & J_s & 0 \\ 0 & 0 & J_u \end{bmatrix} \begin{bmatrix} \mathbf{v_c} \\ \mathbf{v_s} \\ \mathbf{v_u} \end{bmatrix} + \begin{bmatrix} \mathbf{G_2}(\mathbf{v_c}, \mathbf{v_s}, \mathbf{v_u}) + \mathbf{G_3}(\mathbf{v_c}, \mathbf{v_s}, \mathbf{v_u}) \\ \mathbf{H_2}(\mathbf{v_c}, \mathbf{v_s}, \mathbf{v_u}) + \mathbf{H_3}(\mathbf{v_c}, \mathbf{v_s}, \mathbf{v_u}) \\ \mathbf{K_2}(\mathbf{v_c}, \mathbf{v_s}) + \mathbf{K_3}(\mathbf{v_c}, \mathbf{v_s}, \mathbf{v_u}) \end{bmatrix}$$

$$+\sigma \begin{bmatrix} \mathbf{G_4}(\mathbf{v_c}, \mathbf{v_s}, \mathbf{v_u}) \\ \mathbf{H_4}(\mathbf{v_c}, \mathbf{v_s}, \mathbf{v_u}) \\ \mathbf{K_4}(\mathbf{v_c}, \mathbf{v_s}, \mathbf{v_u}) \end{bmatrix} \tag{6}$$

where $\mathbf{v_s}$ is the stable manifold, $\mathbf{v_u}$ is unstable manifold, and $\mathbf{v_c}$ is the center manifold. $\mathbf{G_2}, \mathbf{H_2}, \mathbf{K_2}$ represent quadratic nonlinear terms, while $\mathbf{G_3}, \mathbf{H_3}, \mathbf{K_3}$ are the cubic nonlinear terms. Primary concerned manifold is the center manifold, and it is required to see the center manifold equation (6) decoupled from the stable and unstable manifolds. For this reason, the stable and unstable manifolds are first approximated as power series in terms of center manifold variables and control parameter. This power series is shown in Eq. (7). Functions such as $\mathbf{f_2}$ and $\mathbf{f_3}$ represent the quadratic and cubic nonlinear terms, respectively. The first powers of the series are removed due to certain conditions associated with the manifolds such as $\mathbf{h}(\mathbf{0}, 0) = \mathbf{0}$, $\mathbf{g}(\mathbf{0}, 0) = \mathbf{0}$, $\frac{\partial \mathbf{h}}{\partial \mathbf{v_c}}(\mathbf{0}, 0) = \mathbf{0}$, and $\frac{\partial \mathbf{g}}{\partial \mathbf{v_c}}(\mathbf{0}, 0) = \mathbf{0}$.

$$\begin{aligned} \mathbf{v_s} &= \mathbf{h}(\mathbf{v_c}, \sigma) = \mathbf{c_1}\sigma + \mathbf{c_2}\sigma^2 + \cdots + \mathbf{c_3}\mathbf{f}_2(\mathbf{v_c}) + \mathbf{c_4}\mathbf{f}_3(\mathbf{v_c}) + \ldots \\ \mathbf{v_u} &= \mathbf{g}(\mathbf{v_c}, \sigma) = \mathbf{d_1}\sigma + \mathbf{d_2}\sigma^2 + \cdots + \mathbf{d_3}\mathbf{f}_2(\mathbf{v_c}) + \mathbf{d_4}\mathbf{f}_3(\mathbf{v_c}) + \ldots \end{aligned} \tag{7}$$

The power series approximation of manifolds in Eq. (7) has some unknown coefficients that can be determined using simple algebraic techniques. When the coefficients of power series for stable and unstable manifolds of Equation (7) are known, then using these approximations, one can have the equation of center manifolds (8) that is completely decoupled from the other manifolds. In this way, one can approximate the center manifold solution directly.

$$\dot{\mathbf{v}}_\mathbf{c} = J_c \mathbf{v_c} + \mathbf{G_2}(\mathbf{v_c}) + \mathbf{G_3}(\mathbf{v_c}) + \sigma \mathbf{G_4}(\mathbf{v_c}) \tag{8}$$

3.2 Application on BVAM Model

Center manifold reduction is performed around any type of stable or unstable fixed points to capture the dynamics in its local region [13]. Applying center manifold scheme on the main governing equations (2), the fixed points are moved to origin using the transformation given in Eq. (4) where $\mathbf{y} = [y_1 \quad y_2 \quad y_3 \quad y_4]^T$, $\mathbf{x} = [x_1 \quad x_2 \quad x_3 \quad x_4]^T$, and $\mathbf{x_0}$ is a four-component vector of fixed points. Using the fixed points from Table 2 for the critical control parameter where bifurcation is happening and applying this transformation in system of Eq. (2) gets us equation in the form of Eq. (5).

$$\dot{\mathbf{y}} = \begin{bmatrix} 0.969961 & -2.97135 & 0 & 0 \\ 8.0092 & -5.02865 & 0 & 4 \\ 0 & 0 & 0.238418 & -4.96362 \\ 0 & 8 & 8.73246 & -7.03638 \end{bmatrix} \cdot \begin{bmatrix} y_1 \\ y_2 \\ y_3 \\ y_4 \end{bmatrix} + \begin{bmatrix} 0 \\ -1.41438 + y_1 \\ 0 \\ 1.7963 + y_3 \end{bmatrix} \sigma + \begin{bmatrix} 1.39y_1y_2 + 1.41{y_2}^2 - y_1{y_2}^2 \\ -1.39y_1y_2 - 1.41{y_2}^2 + y_1{y_2}^2 \\ -2.21y_3y_4 - 1.80{y_4}^2 - y_3{y_4}^2 \\ 2.21y_3y_4 + 1.80{y_4}^2 + y_3{y_4}^2 \end{bmatrix} \tag{9}$$

This is Eq. (10) for the fixed points of Hopf bifurcation at $H \approx 7.97$.

$$\begin{bmatrix} \dot{\mathbf{v}}_\mathbf{c} \\ \dot{\mathbf{v}}_\mathbf{s} \end{bmatrix} = \begin{bmatrix} J_c & 0 \\ 0 & J_s \end{bmatrix} \begin{bmatrix} \mathbf{v_c} \\ \mathbf{v_s} \end{bmatrix} + \begin{bmatrix} \mathbf{G_2}(\mathbf{v_c}, \mathbf{v_s}) + \mathbf{G_3}(\mathbf{v_c}, \mathbf{v_s}) \\ \mathbf{H_2}(\mathbf{v_c}, \mathbf{v_s}) + \mathbf{H_3}(\mathbf{v_c}, \mathbf{v_s}) \end{bmatrix} + \sigma \begin{bmatrix} \mathbf{G_4}(\mathbf{v_c}, \mathbf{v_s}) \\ \mathbf{H_4}(\mathbf{v_c}, \mathbf{v_s}) \end{bmatrix} \tag{10}$$

The system thus obtained is nonlinearly coupled. The variables $\mathbf{v_c} = [v_2 \quad v_3]^T$ are the center manifold variables, while the variables $\mathbf{v_s} = [v_1 \quad v_4]^T$ are stable manifold that makes system decay to fixed point. Equation (10) is augmented with $\dot{\sigma} = 0$ to determine the dependence of center manifolds on the control parameter σ. The local manifold $\mathbf{v_s} = \mathbf{h}(\mathbf{v_c}, \sigma)$ can be found out in terms of polynomial expression (11) where the higher-order terms can be neglected.

$$\begin{aligned} v_1 &= h_1(v_2, v_3, \sigma) = a_1{v_2}^2 + a_2v_2v_3 + a_3{v_3}^2 + a_4\sigma \\ v_4 &= h_2(v_2, v_3, \sigma) = b_1{v_2}^2 + b_2v_2v_3 + b_3{v_3}^2 + b_4\sigma \end{aligned} \tag{11}$$

So following further steps of center manifold reduction, the coefficients of Eq. (11) can be easily determined and are given in Table 3. Inserting the polynomial function v_1 and v_4 from Eq. (11) for the center manifold equations (10) and ignoring the higher-order terms of more than one cubic non-linearity give the center manifold equations that are given in Eqs. (12) and (13).

$$\begin{aligned} \dot{v}_2(t) = {} & \iota\omega v_2(t) + c_0\sigma + (c_{132}\sigma + c_{131})\, v_2(t)^3 + (c_{122}\sigma + c_{121})\, v_2(t)^2 \\ & + (c_{322}\sigma + c_{321})\, v_3(t)v_2(t)^2 + (c_{332}\sigma + c_{331})\, v_3(t)^2v_2(t) + c_{112}\sigma\, v_2(t) \\ & + (c_{312}\sigma + c_{311})\, v_3(t)v_2(t) + (c_{232}\sigma + c_{231})\, v_3(t)^3 \\ & + (c_{222}\sigma + c_{221})\, v_3(t)^2 + c_{212}\sigma\, v_3(t) \end{aligned} \tag{12}$$

$$\begin{aligned} \dot{v}_3(t) = {} & -\iota\omega v_3(t) + d_0\sigma + (d_{232}\sigma + d_{231})\, v_2(t)^3 + (d_{222}\sigma + d_{221})\, v_2(t)^2 \\ & + (d_{332}\sigma + d_{331})\, v_3(t)v_2(t)^2 + (d_{322}\sigma + d_{321})\, v_3(t)^2v_2(t) + d_{212}\sigma\, v_2(t) \\ & + (d_{312}\sigma + d_{311})\, v_3(t)v_2(t) + (d_{132}\sigma + d_{131})\, v_3(t)^3 \\ & + (d_{122}\sigma + d_{121})\, v_3(t)^2 + d_{112}\sigma\, v_3(t). \end{aligned} \tag{13}$$

Table 3 Parameters for polynomial for manifold equation 11

Parameters	Values	Parameters	Values
a_1	$-0.26 + 0.17\iota$	b_1	$-0.20 - 0.27\iota$
a_2	0.99	b_2	2.099
a_3	$-0.26 - 0.17\iota$	b_3	$-0.20 + 0.27\iota$
a_4	-0.72	b_4	1.02

The center manifold variables v_2 and v_3 are complex conjugate of each other. The coefficients of Eqs. 12 and 13 are all known. All the coefficients are complex numbers, i.e., $c_a = \alpha_a + \beta_a\iota$ and $d_b = \alpha_b + \beta_b\iota$ where a and b are integers from 1 to 13.

3.3 Method of Multiple Scales

Analytical solution to the center manifold equations (12) and (13) can be obtained using the method of multiple scales. Full description of this technique can be referred to [14]. The variables become $v_2(t) = v_2(t, \varepsilon t, \varepsilon^2 t \ldots)$, $v_3(t) = v_3(t, \varepsilon t, \varepsilon^2 t \ldots)$ and for $T_0 = t, T_1 = \varepsilon t$ and $T_2 = \varepsilon^2 t$, and hence, $v_2(t) = v_2(T_0, T_1, T_2 \ldots)$ and $v_3(t) = v_2(T_0, T_1, T_2 \ldots)$ transforming dependence of variables from real time t to different fast-moving and slow-moving time scales $T_0, T_1, T_2, \ldots$. As a result, the ODE is transformed into a partial differential equation (PDE). The transformations specific to MMS are used as given in Eqs. (14) and (15):

$$v_k = v_{k0} + \varepsilon v_{k1} + \varepsilon^2 v_{k2} + O(\varepsilon^3) \tag{14}$$

$$\frac{d}{dt} = \frac{\partial}{\partial T_0} + \varepsilon \frac{\partial}{\partial T_1} + \varepsilon^2 \frac{\partial}{\partial T_2} + O(\varepsilon^3), \tag{15}$$

where $k = 2, 3$ and putting these Eqs. (14) and (15) in the center manifold equations (12) and (13) and comparing both sides of each equation for the same power of ε give a number of differential equations. At $\varepsilon = 0$, we have equations for state variables v_{20} and v_{30}, but these are actually the fixed points; therefore, we keep $v_{20} = v_{30} = 0$. For $\varepsilon = 1, 2$, and 3, these equations are enlisted for one of the conjugate variables v_2 in Eqs. (16), (17), and (18), respectively.

$$\frac{dv_{21}}{dT_0} = \iota\omega v_{21} \tag{16}$$

$$\frac{dv_{22}}{dT_0} - \iota\omega v_{22} = -\frac{dv_{21}}{dT_1} + c_0\sigma + c_{121}v_{21}^2 + c_{311}v_{21}v_{31} + c_{221}v_{31}^2 \tag{17}$$

$$\frac{dv_{23}}{dT_0} - \iota\omega v_{23} = F(v_{21}, v_{22}, v_{31}, v_{32}) \tag{18}$$

Solving the first linear equation (16) is possible, and its solution is given in Eq. (19). Similar to Eqs. (16), (17), and (18), there are other equations for variables v_{31}, v_{32}, and v_{33}, which are their conjugate. That is why the variable v_{31} that is complex conjugate of v_{21} has solution given in Eq. (20):

$$v_{21}(T_0, T_1, T_2) = A(T_1, T_2)e^{\iota\omega T_0} \tag{19}$$

$$v_{31}(T_0, T_1, T_2) = \bar{A}(T_1, T_2)e^{-\iota\omega T_0}. \tag{20}$$

Equation (17) is nonlinear equation of $O(\varepsilon^2)$, where v_{22} is unknown variable, while variables v_{21} and v_{31} are known from Eqs. (19) and (20), respectively. Therefore, Eq. (17) takes the form of Eq. (21):

$$\frac{\partial v_{22}}{\partial T_0} - \iota v_{22}\omega = c_{221}e^{-2\iota T_0\omega}\bar{A}\,(T_1, T_2)^{\,2} + c_{311}A\,(T_1, T_2)\,\bar{A}\,(T_1, T_2) - e^{\iota T_0\omega}\frac{\partial A}{\partial T_1}\,(T_1, T_2) + c_{121}e^{2\iota T_0\omega}A\,(T_1, T_2)^{\,2} + c_0\sigma. \tag{21}$$

The solution of Eq. (17) contains a term $T_0e^{\iota\omega T_0}\frac{dA(T_1,T_2)}{dT_1}$ that clearly indicates that the solution will blow up with time. It is therefore necessary to eliminate these secular terms that are the one containing frequency equal to the natural frequency of the system. For this purpose, the coefficients of secular terms are gathered and are placed equal to zero as shown in Equation $\frac{dA(T_1,T_2)}{dT_1} = 0$. Its solution is $A(T_1, T_2) = A(T_2)$. Eliminating secular term from Eq. (21) and solving for its solution give the form of function shown in (22). Next is Eq. (18) obtained at $O(\varepsilon^3)$ after applying MMS. This equation is first order with unknown variable v_{23} and the forcing function condensed in $F(v_{21}, v_{22}, v_{31}, v_{32})$. At this stage, the variables v_{21}, v_{22}, v_{31}, and v_{32} are known, and inserting these values in input function $F(v_{21}, v_{22}, v_{31}, v_{32})$ gives a linear forced ODE. The coefficients of now formed ODE after putting the values of v_{21}, v_{22}, v_{31} and v_{32} contain secular terms that when taken solution blow up the results. The coefficients of the secular terms "$e^{\iota\omega T_0}$" are combined and separated to form Eq. (23) that gives the steady-state amplitude of the system.

$$v_{22}\,(T_0, T_1, T_2) = \frac{\iota c_{311}A\,(T_1, T_2)\,\bar{A}\,(T_1, T_2)}{\omega} + \frac{\iota c_{221}e^{-2\iota T_0\omega}\bar{A}\,(T_1, T_2)^{\,2}}{3\omega} - \frac{\iota c_{121}e^{2\iota T_0\omega}A\,(T_1, T_2)^{\,2}}{\omega} + \frac{\iota c_0\sigma}{\omega} \tag{22}$$

The complex coefficient $A(T_2) = a(T_2)e^{\iota\beta(T_2)}$ is the function of the amplitude and phase of the response. When expanded this coefficient in Eq. (23), putting values of complex constants and separating the real and imaginary parts give amplitude equation (24) and phase equation (25).

$$A'(T_2) = -\frac{2\iota c_{221} d_{221} A(T_2)^2 \bar{A}(T_2)}{3\omega} - \frac{\iota c_{311} d_{311} A(T_2)^2 \bar{A}(T_2)}{\omega} + \frac{\iota c_{121} c_{311} A(T_2)^2 \bar{A}(T_2)}{\omega} + c_{321} A(T_2)^2 \bar{A}(T_2) - \frac{\iota c_{311} d_0 \sigma A(T_2)}{\omega} + \frac{2\iota c_0 c_{121} \sigma A(T_2)}{\omega} + c_{112} \sigma A(T_2) \tag{23}$$

The amplitude equation (24) is representing the normal form of Super critical Hopf bifurcation. Letting $a'(T_2) = 0$ gives a steady-state amplitude of $a = \pm 0.51\sqrt{-\sigma}$. This clearly means that the periodic solution will only happen when $\sigma < 0$ or in other words value of control parameter crosses the Hopf bifurcation point and its value is less than the critical control parameter.

$$a'(T_2) = -0.29\sigma a(T_2) - 1.13a(T_2)^3 \tag{24}$$

$$\gamma'(T_2) = -1.84a(T_2)^2 - 0.16\sigma \tag{25}$$

The amplitude equation (24) can be combined with Eqs. (14), (19), and (20) where $A = ae^{\iota\beta}$, and by neglecting v_{22} and v_{32} and keeping in mind the values of fixed points v_{20} and v_{30}, the solution to the manifold equations (12) and (13) can be found. But this is solution to the manifold equations (12) and (13), not to the governing equation of BVAM model (2). Following the same procedure for the other fixed point, finding first the center manifolds, and then applying method of multiple scales, equations similar to (24) and (25) are obtained. These equations given in Eqs. (26) and (27) are the normal forms of Hopf bifurcation at $H = 8.77$. It has the same form of super critical Hopf bifurcation where the periodic solution that forms for $H < 8.77$ is stable, while the branch of fixed points prior to bifurcation continues to be an unstable branch of fixed points. The steady-state amplitude of oscillation is $a = 0.47\sqrt{-\sigma}$.

$$a'(T_2) = -0.1832\sigma a(T_2) - 0.8387a(T_2)^3 \tag{26}$$

$$\gamma'(T_2) = -0.1019a(T_2)^2 - 1.9033\sigma \tag{27}$$

Following the normal forms given in Eqs. (24) and (25) at $H = 7.97$, in order to get the response for BVAM model given in Eq. (2) in local region of the Hopf bifurcation, reverse transformation to the one done in Sect. (3.2) of center manifolds reduction is needed to go from center manifolds to original system. Following that transformation, the analytic solution is obtained for the original BVAM model in the local region of the Hopf bifurcation in the vicinity of $H = 7.97$.

$$\mathbf{x} = \mathbf{x_0} + \mathbf{a_1}\sigma + \varepsilon^2 \mathbf{a_2}\sigma + \varepsilon \mathbf{a_3}\sqrt{\sigma} \sin[(\omega_1 + \varepsilon^2 c_1 \sigma)t + \boldsymbol{\beta_1}] + \varepsilon^2 \mathbf{a_4}\sigma \sin[(\omega_2 + \varepsilon^2 c_2 \sigma)t + \boldsymbol{\beta_2}] \tag{28}$$

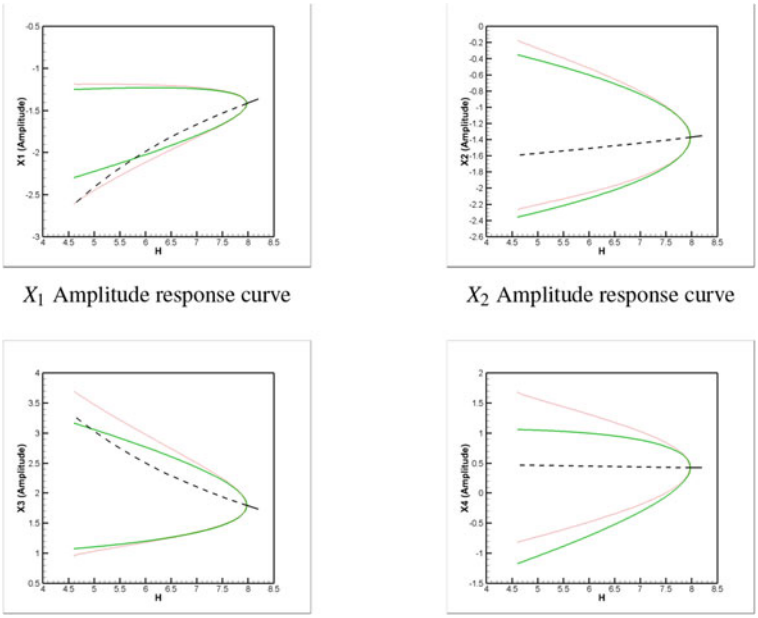

Fig. 1 Amplitude response curves in local region to Hopf bifurcation: stable fixed points (black solid line), unstable fixed points (black dashed line), analytic periodic solution (green solid line), numerical periodic solution (red dotted line)

4 Results and Discussion

Amplitude curves in the vicinity of $H \approx 7.97$ are plotted and compared with numerical solution as shown in Fig. (1). FPs are computed by keeping the first-order derivative equal to zero and solving for simultaneous algebraic equations, while the analytical solution is plotted by taking the amplitude of Eq. (28) where the coefficients are given in Eq. (29) and this solution is compared with the numerical solution. It can be observed that analytical solution matches well with the numerical solution near the bifurcation point. However, as the control parameter is varied, the agreement of two solutions diminishes. It is attributed to the linearization of the BVAM model in the vicinity of the bifurcation point. In addition, the higher-order terms are also ignored beyond cubic non-linearity. It is important to note that two frequencies in the analytical solution are correctly identified and have dependence on the control parameter. The solution is similar at the other bifurcation point $H \approx 8.77$.

$$\mathbf{a_1} = \begin{bmatrix} 0.212308 \\ 0.122757 \\ -0.342036 \\ 0.0214689 \end{bmatrix} \quad \mathbf{a_2} = \begin{bmatrix} 0.135121 \\ 0.131086 \\ -0.23636 \\ -0.0763403 \end{bmatrix} \quad \mathbf{a_3} = \begin{bmatrix} 0.281731 \\ 0.535615 \\ 0.540988 \\ 0.607102 \end{bmatrix}$$

$$\boldsymbol{a_4} = \begin{bmatrix} 0.0323221 \\ 0.0305694 \\ 0.051652 \\ 0.0461832 \end{bmatrix} \quad \boldsymbol{\beta_1} = \begin{bmatrix} 1.07987 \\ -0.318365 \\ 1.52798 \\ 0 \end{bmatrix} \quad \boldsymbol{\beta_2} = \begin{bmatrix} 0.310676 \\ -0.744948 \\ 0.128051 \\ 1.46583 \end{bmatrix}$$

$$c_1 = 0.307995 \quad c_2 = 0.615991 \quad \omega_1 = 5.56 \quad \omega_2 = 11.12 \tag{29}$$

5 Conclusion

BVAM model has the capability to mimic various natural phenomena. Its possible solutions range from equilibrium solution, periodic solution, quasi-periodic, and chaotic. In this chapter, we find the bifurcation point and then the fixed-point and period one solutions. We compute three fixed-point solutions at $H > 8.77$ including the origin that is unstable. The initial condition determines the solution. We observe supercritical Hopf bifurcation at each stable fixed point. There exist periodic solutions at $H \leq 8.77$ and at $H \leq 7.97$. These results are compared with the numerical solution, and it is shown that analytical solution matches with the numerical solution in local region to Hopf bifurcation. These analyses provide insight to understanding the mechanism to model ECG for sinus rhythm and arrhythmia.

References

1. Sinha, S.(auth.), In, V., Longhini, P., Palacios, A., Ditto, W.L., Murali, K. (eds.): Applications of Nonlinear Dynamics: Model and Design of Complex Systems, 1st edn. In: Understanding Complex Systems. Springer, Berlin/Heidelberg (2009)
2. Matsushita, H., Miyata, T., Christiansen, L.E., Lehn-Schioler, T., Mosekilde, E.: Nonlinear dynamics approach of modeling the bifurcation for aircraft wing flutter in transonic speed. In: Proceedings of the 41st SICE Annual Conference. SICE 2002., vol. 2, pp. 695–700 (2002)
3. Quiroz-Juárez, M.A., Jiménez-Ramírez, O., Vázquez-Medina, R., Breña-Medina, V., Aragón, J.L., Barrio, R.A.: Generation of ECG signals from a reaction-diffusion model spatially discretized. Sci. Rep. **9**(1), 1–10 (2019)
4. Gray, R.A., Pertsov, A.M., Jalife, J.: Spatial and temporal organization during cardiac fibrillation. Nature **392**(6671), 75–78 (1998)
5. Nayfeh, A.H.: Introduction to Perturbation Techniques. John Wiley & Sons, New York (2011)
6. Keener, J.P., Sneyd, J.: Mathematical Physiology, vol. 1. Springer, New York (1998)
7. Qu, Z., Hu, G., Garfinkel, A., Weiss, J.N.: Nonlinear and stochastic dynamics in the heart. Phys. Rep. **543**(2), 61–162 (2014)

8. Newhouse, S., Ruelle, D., Takens, F.: Occurrence of strange axiom a attractors near quasi periodic flows on T^m, $m \geqq 3$. Commun. Math. Phys. **64**(1), 35–40 (1978)
9. Quiroz-Juarez, M.A., Vázquez-Medina, R., Ryzhii, E., Ryzhii, M., Aragón, J.L.: Quasiperiodicity route to chaos in cardiac conduction model. Commun. Nonlinear Sci. Numer. Simul. **42**, 370–378 (2017)
10. Ryzhii, E., Ryzhii, M.: A heterogeneous coupled oscillator model for simulation of ECG signals. Comput. Methods Prog. Biomed. **117**(1), 40–49 (2014)
11. Barrio, R.A., Varea, C., Aragón, J.L., Maini, P.K.: A two-dimensional numerical study of spatial pattern formation in interacting Turing systems. Bull. Math. Biol. **61**(3), 483–505 (1999)
12. Toole, G., Hurdal, M.K.: Growth in a Turing model of cortical folding. Biomath **1**(1), ID–1209252 (2012)
13. Nayfeh, A.H., Balachandran, B.: Applied Nonlinear Dynamics: Analytical, Computational, and Experimental Methods. John Wiley & Sons, New York (2008)
14. Cole, J.D.: Perturbation Methods (Ali Hasan Nayfeh). Wiley (1976); WILEY-VCH Verlag GmbH & CO. KGaA, Weinheim (2004)

Stability and Instability of a Complex Biodynamical Discrete Structure on a Cantilever Coupled to Nonlinear Springs

Katica Hedrih [Stevanović] and Andjelka Hedrih

1 Introduction

Some seedlings are more, some less vulnerable to external biotic or abiotic factors [1]. First year of life is especially very important for young seedlings. When transplanted to a permanent place, the right method of staking is essential for proper rooting and stability of the seedling. Stability and instability of linear and nonlinear eigen modes in similar complex structures like tree stem with branches (with one and without nonlinear spring/tensioner) were studied in [2] and [3]. It was shown that in such systems, at least one linear nonstable hyperbolic eigen mode and one nonstable forced mode exist. Based on this research, a young seedling staked with a single, doubleor triple staking method (Fig. 1) is modeled as a complex discrete biodynamical structure on a cantilever coupled with one/two/three nonlinear elastic springs at 1/2 of cantilever (tree stem) height. Springs with cubic nonlinear properties oscillate in the horizontal plane. A methodology suitable for studying the stability and instability of four-frequency (one forced frequency and tree eigen own frequencies) nonlinear oscillations of these complex system under an external single frequency force is presented.

K. Hedrih [Stevanović]
Department of Mechanics, Mathematical Institute of Serbian Academy of Sciences and Arts (MI SANU), Belgrade, Serbia

Faculty of Mechanical Engineering, University of Niš, Niš, Serbia
e-mail: katicah@mi.sanu.ac.rs; khedrih@sbb.rs

A. Hedrih (✉)
Department of Mechanics, Mathematical Institute of Serbian Academy of Sciences and Arts (MI SANU), Belgrade, Serbia
e-mail: handjelka@hm.co.rs

© The Author(s), under exclusive license to Springer Nature Switzerland AG 2024

W. Lacarbonara (ed.), *Advances in Nonlinear Dynamics, Volume III*, NODYCON Conference Proceedings Series, https://doi.org/10.1007/978-3-031-50635-2_56

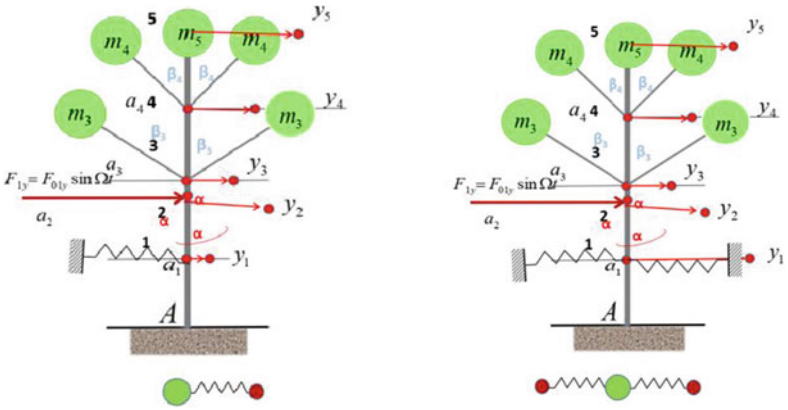

Fig. 1 Complex discrete structure on a cantilever: (**a**) One spring with nonlinear properties (**b**) Two springs with nonlinear properties

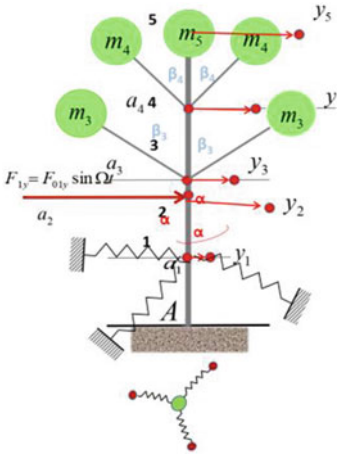

Fig. 2 Complex discrete structure on a cantilever with tree springs with nonlinear properties

2 Description of the Models

In practice, young seedlings are tied with ropes or more often with wide strips to prevent the unwanted effects of external perturbation load (wind, children, etc.) [4, 5]. A young seedling staked with a single, double (see Fig. 1a, b), or triple (see Fig. 2) staking method is modeled as a complex discrete biodynamical structure on a cantilever coupled with one/two/three nonlinear elastic springs at 1/2 of cantilever (tree stem height) length. Springs with cubic nonlinear properties oscillate in the horizontal plane.

The model consists of light massless elastic cantilever (represents seedlings' stem) with length ℓ fixed in point A to which are attached symmetrically (in cross-section 3 and 4) pairs of massless rigid rods with tip mass m on its ends (represent

branches) under certain angle (β_3 and β_4). Connections between elastic cantilever and massless rigid rods are rigid and of dynamical type, which means that the system is with dynamic connections. The dynamic connections are realized by means of the coupling of the forces of inertia of the material particles and the moments of those forces of inertia, reduced to the corresponding sections of the cantilever, and by means of the influential coefficients of displacement from the forces and moments of the forces of one section from the influence of the action in the other section. To wright the system of differential equations that will describe the forced oscillations of staked young seedlings, it is necessary to calculate the influential coefficients of the cantilever under unit momentum and under unit force. In this chapter, external single frequency force is applied in the cross-section 2 above the level where the staking is done (cross section 1). Other cases when external force acts: (a) in the same cross-section or beneath the cross-section where staking is done, can also be studied. Studying the oscillatory behavior in this case is important to confirm the right height of stacking which is usually empirically determined. The staking is done in cross-section 1 by one/two/three springs with cubic nonlinearity and each with rigidityc_0.

The system of differential equations for oscillations of a biodynamical system when coupled with one, two, or three nonlinear springs will be presented.

3 Results

3.1 System of Differential Equations for Oscillations of a Biodynamical System When Coupled with One or Two Nonlinear Springs

Each material point, of massm_k, $k = 3, 4, 5$ has two degrees of freedom of movement, x_k, and, y_k, $k = 1, 2, 3, 4, 5$ both in the horizontal plane and in directions orthogonal to the undeformed axis of the cantilever. We assume that these displacements are equal to the displacements of the points: the centers of the cantilever sections to which the masses are attached by rigid massless rods. By reducing those inertial forces to the point of rigid attachment of the corresponding pair of two rigid massless rods, we obtain in each corresponding section the inertial force perpendicular to the cantilever and the moment of inertia force. Using Wiliott's plan of compatible displacements and elongations of elastic tensions (elastic springs) for models presented in Fig. 1, the elongations or shortenings of the tensions (springs) and the force that acts on the console in section 1 are determined (see Fig. 3).

Assuming that the cantilever deflections are small, linear elastic tension force when section 1 of the cantilever, to which it is attached, moves in the horizontal direction for x_1 depends of elongation of elastic spring $\Delta\ell_0 \approx x_1 \cos \beta_{01}$ and its coefficient of rigidity c_0 and in direction of elastic tension is in the form:

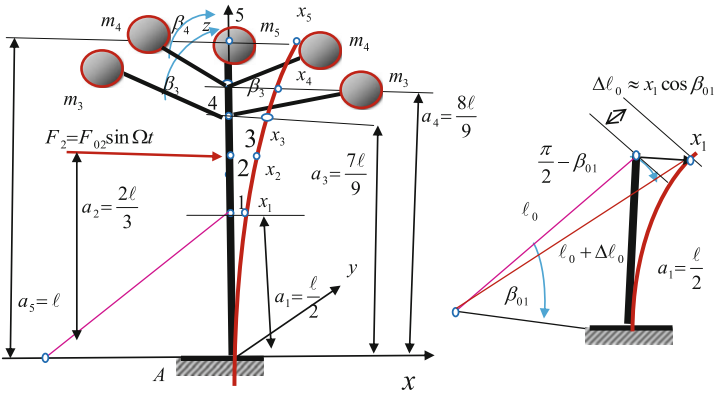

Fig. 3 Elastic tension force when section 1 of the cantilever, to which it is attached, moves in the horizontal direction

$$F_c = -c_0\Delta\ell_0 \approx -c_0 x_1 \cos\beta_{01} \tag{1}$$

The orthogonal component of linear elastic tension force is in the form:

$$F_{cx} = -c_0\Delta\ell_0 \cos\beta_{01} \approx -c_0 x_1 \cos^2\beta_{01} \tag{2}$$

The nonlinear elastic tension force with cubic nonlinearity is:

$$F_{cNx} = -\left[c_0\Delta\ell_0 + c_{0N}(\Delta\ell_0)^3\right]\cos\beta_{01} \approx -c_0 x_1\cos^2\beta_{01} - c_{0N}x_1^3\cos^4\beta_{01} \tag{3}$$

The first subsystem of differential equations for oscillations of a biodynamical system in x_k, $k = 1, 2, 3, 4, 5$ directions is:

$$\begin{aligned} x_k = {} & \alpha_{k1}\left(-c_0 x_1\cos^2\beta_{01} - c_{0N}x_1^3\cos^4\beta_{01}\right) + \alpha_{k2}F_{02x}\sin\Omega_x t + \\ & + \alpha_{k3}\left(-2m_3\ddot{x}_3\right) + \alpha_{k4}\left(-2m_4\ddot{x}_4\right) + \alpha_{k5}\left(-m_5\ddot{x}_5\right) + \\ & + \delta_{k3}\left(-2m_3\ddot{x}_3\ell_3\cos\beta_3\right) + \delta_{k4}\left(-2m_4\ddot{x}_4\ell_4\cos\beta_4\right) \end{aligned} \tag{4}$$

$$k = 1, 2, 3, 4, 5$$

The first subsystem of differential equations for oscillations of a biodynamical system in y_k, $k = 1, 2, 3, 4, 5$ directions is:

$$\begin{aligned} y_k = {} & \alpha_{k2}F_{02y}\sin\Omega_y t + \\ & + \alpha_{k3}\left(-2m_3\ddot{y}_3\right) + \alpha_{k4}\left(-2m_4\ddot{y}_4\right) + \alpha_{k5}\left(-m_5\ddot{y}_5\right) + \\ & + \delta_{k3}\left(-2m_3\ddot{y}_3\ell_3\cos\beta_3\right) + \delta_{k4}\left(-2m_4\ddot{y}_4\ell_4\cos\beta_4\right) \end{aligned} \tag{5}$$

$$k = 1, 2, 3, 4, 5$$

where α ($\alpha_{ik} = {f_{ik}}^{F_k=1}$, $i, k = 1, 2, 3, 4, 5$) is the coefficient of defection of the cantilever in cross-section "i" when the unit force is applied in cross-section "k" (see Table 1); $\delta(\delta_{ik} = {f_{ik}}^{M_k=1}$, $i = 1, 2, 3, 4, 5$; $k = 3, 4)$ is the coefficient of defection of the cantilever in cross-section "i" when the unit momentum is applied in cross-section "k" (see Table 2); c_0 is the coefficient of rigidity of the elastic spring; $c_{0N}$is the coefficient of rigidity that comes from the nonlinear component of the elastic spring; β_{01} is the angle between the elastic spring and the soil; β_3 and β_4 are angles between the cantilever (seedlings stem) and the branches (rigid massless rods); ℓ_3 and ℓ_4 are the lengths of the branches; F_{02x} is the amplitude of the external single frequency force applied in cross-section 2; and $\Omega_x$is the frequency of the external force.

B_x is the bending stiffness in the horizontal direction x. $B_x = B_y = EI_x = EI_y = E\frac{r^4\pi}{4}E$ is the Young module of elasticity of the cantilever, I is the axial moment of inertia for the corresponding cross-section.

Defection $\alpha_{ik} = {f_{ik}}^{F_k=1}$, $i, k = 1, 2, 3, 4, 5$ of the cantilever in cross-section "i" when the unit force F_k=1is applied in the cross-section "k", α_{ik} is calculated according to:

$$\alpha_{ik} = f_i^{F_k=1} = \frac{\ell^3}{6B_x}\left\{\left[3\left(\frac{a_k}{\ell}\right)\left(\frac{z_i}{\ell}\right)^2 - \left(\frac{z_i}{\ell}\right)^3\right] | + \left(\frac{z_i - a_k}{\ell}\right)^3\right\} \tag{6}$$

where a_k is the length of elastic cantilever from the ground to the corresponding cross-section.

Defection $\delta_{ik} = {f_{ik}}^{M_k=1}$, $i = 1, 2, 3, 4, 5$; $k = 3, 4$ of the cantilever in cross-section "i" when the unit moment $M_k = 1$is applied in cross-section "k", δ_{ik} is calculated according to the following:

$$\delta_{ik} = f_i^{M_k=1} = \frac{\ell^2}{2B_x}\left\{\left[\left(\frac{z_i}{\ell}\right)^2\right] | - \left(\frac{z_i - a_k}{\ell}\right)^2\right\} \tag{7}$$

The subsystem of differential equations for oscillations of a biodynamical system in y_k directions is analog to the subsystem of differential equations for oscillations in x_k.

The supposed solutions for each Eq. (4) are in the form:

$$x_i = A_i \sin \Omega_x t, \quad \ddot{x}_i = -\Omega_x^2 A_i \sin \Omega_x t, \quad i = 1, 2, 3, 4, 5 \tag{8}$$

Entering the proposed solutions and their second derivatives (8) in the linearized system of differential Eq (4), we obtain the system of nonhomogeneous algebra equations. Applying Cramer's rule to these nonhomogeneous algebra equations unknown amplitudes can be found. Solutins for unknown amplitudes are in the

Table 1 Table of coefficient of defection of the cantilever in cross-section "i" when the unit force is applied in cross-section 1. $p = \frac{\ell^3}{3^7 \cdot 2^4 B_x}$

α_{ik}	1	2	3	4	5
1	$\alpha_{11} = 3^6 \cdot 2^2 p$	$\alpha_{12} = 3^7 p$	$\alpha_{13} = 3^5 \cdot 11p$	$\alpha_{14} = 3^4 \cdot 3^2 \cdot 13p$	$\alpha_{15} = 3^6 \cdot 5p$
2	$\alpha_{21} = 3^7 p$	$\alpha_{22} = 3^3 \cdot 2^7 p$	$\alpha_{23} = 3^3 \cdot 2^5 \cdot 5p$	$\alpha_{24} = 3^4 \cdot 2^6 p$	$\alpha_{25} = 7 \cdot 3^4 \cdot 2^5 p$
3	$\alpha_{31} = 3^5 \cdot 11p$	$\alpha_{32} = 3^3 \cdot 2^5 \cdot 5p$	$\alpha_{33} = 43 \cdot 2^4 p$	$\alpha_{34} = 17 \cdot 49 \cdot 2^3 p$	$\alpha_{35} = 49 \cdot 5 \cdot 2^5 p$
4	$\alpha_{41} = 3^4 \cdot 3^2 \cdot 13p$	$\alpha_{42} = 3^4 \cdot 2^6 p$	$\alpha_{43} = 17 \cdot 49 \cdot 2^3 p$	$\alpha_{44} = 2^{13} p$	$\alpha_{45} = 19 \cdot 2^9 p$
5	$\alpha_{51} = 3^6 \cdot 5p$	$\alpha_{52} = 7 \cdot 3^4 \cdot 2^5 p$	$\alpha_{53} = 49 \cdot 5 \cdot 2^5 p$	$\alpha_{54} = 19 \cdot 2^9 p$	$\alpha_{55} = 3^6 \cdot 2^4 p$

Table 2 Table of coefficient of defection of the cantilever in cross-section "i" when the unit moment is applied in cross-section 1. $q = \frac{\ell^2}{2^3 \cdot 3^4 B_x}$

δ_{ik}	3	4
1	$\delta_{13} = 3^4 q$	$\delta_{14} = 3^4 q$
2	$\delta_{23} = 2^4 \cdot 3^2 q$	$\delta_{24} = 9 \cdot 3^4 q$
3	$\delta_{33} = 2^2 \cdot 49 q$	$\delta_{34} = 49 \cdot 2^2 q$
4	$\delta_{43} = 4 \cdot 63 q$	$\delta_{44} = 2^3 \cdot 32 q$
5	$\delta_{53} = 77 \cdot 4 q$	$\delta_{54} = 2^6 \cdot 5 q$

form: $A_i\left(\Omega_x^2\right) = \frac{\Delta_i(\Omega_x^2)}{\Delta(\Omega_x^2)}$, $i = 1, 2, 3, 4, 5$. The same procedure is followed for forced oscillations in y_k direction. The determinant of each subsystem should be different from zero. When the determinant of the subsystem is equal to zero the resonant frequencies, i.e., eigen circular frequencies are obtained.

3.2 *System of Differential Equations for Oscillations of a Biodynamical System When Coupled with Three Nonlinear Springs*

For the case from Fig. 2, when a young seedling is staked with three equal symmetrically distributed springs with nonlinear properties, the elongation of the third nonlinear spring is in the form:

$$\Delta\ell_{03} = \ell_0 \left[\sqrt{1 + \frac{r_1^2}{\ell_0^2} + \left(\frac{\left(x_1 \cos\beta_0 + y_1 \cos\beta_0 \sqrt{3} \right)}{\ell_0} \right)} - 1 \right] \tag{9}$$

As $\frac{r_1^2}{\ell_0^2} << 1$, we can neglect this term and with certain approximations we obtain:

$$\Delta\ell_{03} \approx \frac{\left(x_1 \cos\beta_0 + y_1 \cos\beta_0 \sqrt{3} \right)}{2} \tag{10}$$

The force in the third spring, for a linear case, is in the form:

$$F_{c3} = -c_0 \Delta\ell_{02} \approx -\frac{c_0}{2} \left(x_1 \cos\beta_0 + y_1 \cos\beta_0 \sqrt{3} \right) \tag{11}$$

Assuming that the deflection of the cross-section 1 is small, the changing of the direction of the spring can be neglected. Only the changing of the force amplitude in the spring can be taking into account. The components of the force along the coordinate axis in the third spring are:

$$F_{cx2} \approx -\frac{c_0}{4}\left(x_1 \cos\beta_0 + y_1 \cos\beta_0\sqrt{3}\right)\cos\beta_0 \tag{12}$$

$$F_{cy2} \approx -\frac{c_0\sqrt{3}}{4}\left(x_1 \cos\beta_0 + y_1 \cos\beta_0\sqrt{3}\right)\cos\beta_0 \tag{13}$$

The component in the direction of the cantilever axis stresses the cantilever to the axial stress and is of no importance for the oscillations of the biodynamic system.

The resultant forces in all three springs along the coordinate axis are:

$$F_{cx1} = -c_0\Delta\ell_{01}\cos\beta_0 \approx -c_0 x_1 \cos^2\beta_0 \tag{14}$$

$$F_{cx2} \approx -\frac{c_0}{4}\left(x_1 \cos\beta_0 - y_1 \cos\beta_0\sqrt{3}\right)\cos\beta_0 \tag{15}$$

$$F_{cx3} \approx -\frac{c_0}{4}\left(x_1 \cos\beta_0 + y_1 \cos\beta_0\sqrt{3}\right)\cos\beta_0 \tag{16}$$

$$F_{0x} = F_{cx1} + F_{cx2} + F_{cx2} \approx -\frac{3c_0}{2}x_1 \cos^2\beta_0 \tag{17}$$

According to Eq. (17), the resultant force of all horizontal displacements in the direction of *Ax*axis depends only on the displacement of cross-section 1 of the cantilever in the $x_1$direction. This means that the subsystem of differential equations related to the x_k direction can be independently solved from the subsystem of differential equations related to the in the y_k direction. Also, we can use all solutions obtained for the case with one and two nonlinear elastic springs by introducing in all previous equations and expressions the rigidity of elastic spring value of $c_0 \Rightarrow \frac{3c_0}{2}$:

$$F_{cy2} \approx -\frac{c_0\sqrt{3}}{4}\left(x_1 \cos\beta_0 - y_1 \cos\beta_0\sqrt{3}\right)\cos\beta_0 \tag{18}$$

$$F_{cy2} \approx -\frac{c_0\sqrt{3}}{4}\left(x_1 \cos\beta_0 + y_1 \cos\beta_0\sqrt{3}\right)\cos\beta_0 \tag{19}$$

$$F_{cy} = F_{cy2} + F_{cy2} \approx -\frac{c_0\sqrt{3}}{2}x_1 \cos^2\beta_0 \tag{20}$$

This fact, that the resultant of the component forces in the direction of the axis *Ay* depends on the displacement x_1, indicates that the subsystem of the differential equations of oscillation of the biodynamic system in addition to the five generalized coordinates y_k, $k = 1, 2, 3, 4, 5$ also contains the coordinate x_1 with which the

oscillations in two orthogonal directions Ay and Ax are coupled. This means that the first subsystem must be solved, and when a solution is found for x_1, solve the second subsystem.

We cannot look for the second subsystem of differential equations by y_k, it is dependently of the first one, because it contains an independent generalized coordinate x_1, and with it the circular frequency Ω_x from the first set of generalized coordinates x_k, $k = 3, 4, 5$. The independent generalized coordinate x_1 with a circular frequency Ω_x introduces a kinematic excitation of the frequency Ω_x in the direction Ay so that if a force in the cross-section 2 with frequency Ω_y is applied, a two-frequency forced mode of oscillations occurs, with all frequencies $\Omega_x$and Ω_y in the directions y_k, $k = 3, 4, 5$.

4 Concluding Remarks

Stability of forced oscillations of double and triple staking methods is analyzed using a modification of a previously developed model of a young seedling staked with one stake. The presented methodology is suitable to study the stability and instability of nonlinear oscillations of seedlings staked with double and triple staking method. The geometric nonlinearity of the system is introduced by a spring with cubic nonlinear properties that oscillates in the horizontal plane. The model used is much more complex than the basic model of oscillations of the stem with apical load presented in [6]. The methodology is suitable to analyze stability/instability of forced oscillations through the amplitude–frequency graphs: to analyze which canopy shapes are the most suitable for each particular staking method as well as proper stem height where staking should be done in order to prevent unwanted oscillations of the stem.

Acknowledgment Part of this research was supported by the Ministry of Sciences, Technological Development and Innovations of Republic of Serbia through the Mathematical Institute SANU, Belgrade.

References

1. Alvarez-Clare, S., Kitajima, K.: Susceptibility of tree seedlings to biotic and abiotic hazards in the understory of a moist tropical forest in Panama. Biotropica. **41**(1), 47–56 (2009)
2. Hedrih (Stevanović), K., Hedrih, A.: Mathematical modelling of nonlinear oscillations of a biodynamical system in the form of a complex cantilever. Appl. Math. Modell. **112**, 110–135 (2022)
3. Hedrih, A., Hedrih (Stevanović), K.: Oscillations and stability of dynamics of hybrid biostructure, has been accepted for publication. Eur. Phys. J. Special Topics. **230**(18–20), 3573–3580 (2021)

4. Author, F.: Article title. Journal 2(5), 99–110 (2016). Ramanujam, L. A.: Nonlinear Model for Wind-Induced Oscillations of Trees. Masters Theses 1911 – February 2014. 943. (2012). http://scholarworks.umass.edu/theses/943/
5. Yongmin, K., Harianto, R., Daryl, L.T.-T.: Stability analysis of laterally loaded trees based on tree-root-soil interaction. Urban For. Urban Green. **49**, 126639 (2020)
6. Spatz, H.C., Speck, O.: Oscillation frequencies of tapered plant stems. Am. J. Bot. **89**(1), 1–11 (2002)

Effects of Rising Sea Surface Temperature on the Dynamics of Coral-Algal Interactions

Sasanka Shekhar Maity, Joydeb Bhattacharyya, and Samares Pal

1 Introduction

Coral reefs are the most striking and different marine ecosystems in our globe. Productive and complex, coral reefs host hundreds of thousands of species, but few are described by science. Coral reefs are very well known for their biological diversity, beauty, and high productivity [1]. Coral reefs have the tendency to exist in alternate coral- or algae-dominated states [2, 3]. Faster-growing macroalgae always dominate coral reefs by making less the available space for the successful settlement of coral larvae [4, 5]. The growth rate of corals is approximately 2–185 mm per year, and the collective growth of many coral's colonies across a large area can return the area to coral dominance within a few years [6]. The coral reef is a rich and predominant oceanic ecosystem where one third of the total marine fish species and also thousands of other species are present. These ecosystems also provide six million tons of fish in a year and it plays a significant role in the national and international economy [7]. But now, this significant biodiversity is threatened due to increasing sea surface temperature [8]. As a result, the whole marine system as well as the coral reef ecosystem is in danger.

Coral's growth depends on a number of requirements: calcium carbonate saturation, temperature, irradiance, pH, turbidity, salinity, sedimentation, and nutrients [9]. Coral calcification rates and extension rates are highly dependent on sea surface temperature [10]. Another important fact due to increasing sea surface temperature is "coral bleaching." The term bleaching means loss of color that results when the coral-algae relationship breaks down and is caused by coral when it loses

S. S. Maity · S. Pal (✉)
Department of Mathematics, University of Kalyani, Kalyani, India

J. Bhattacharyya
Department of Mathematics, Karimpur Pannadevi College, Nadia, India

© The Author(s), under exclusive license to Springer Nature Switzerland AG 2024

W. Lacarbonara (ed.), *Advances in Nonlinear Dynamics, Volume III*, NODYCON Conference Proceedings Series, https://doi.org/10.1007/978-3-031-50635-2_57

zooxanthellae, a unicellular algae. Corals shelter zooxanthellae for their food which enables coral polyps to build reefs. They stop producing food when the sea surface temperature is above the seasonal maximum temperature. Photosynthetic pigments, which are found in zooxanthellae, are responsible for most of the coloration of corals. After losing zooxanthellae, it renders the tissue mostly transparent. As a result, the white skeleton of calcium carbonate is visible through the unpigmented tissue and making the corals bleached. Corals may die due to bleaching and it takes decades to recover partially or completely [11]. Most of the bleaching events occur when the temperature is at least 1° more than the temperature threshold [8, 12].

At first Mumby et al. [13] introduced a model on coral reef ecosystem to demonstrate the effects of grazing on coral-macroalgal phase shift. In this model, the basic assumption was a fraction of seabed settled by macroalgae, coral, and turf algae with the following facts: macroalgae growing on turf algae vegetatively, macroalgal overgrowth on corals, and grazing of herbivores on macroalgae. Blackwood et al.[14] modified the above model. They introduced the grazing of herbivore parrotfish to the system and investigated the grazing dynamics of parrotfish. Bhattacharyya et al.[15] introduced another fact, i.e., macroalgae produce toxin that prevents the growth of corals. They have also considered that macroalgae recruit externally from the surroundings of the ecosystem and have natural mortality.

In the present paper, the main emphasis will be placed on the dynamical behavior of coral reef ecosystem due to the increasing sea surface temperature. The model that we have considered in our study is an extension of the models proposed by [13, 14], but we have done a different work which is not a direct extension of any model on coral reef ecosystem. In our model, we have considered the effect of SST on the growth of corals. So we take the recruitment of adult corals in a temperature-dependent function.

Another important fact that we have introduced is Newton's law of cooling. According to the law, the rate of heat loss of a body is directly proportional to the difference in the temperatures between the body and its surroundings. The law is frequently qualified to include the condition that the temperature difference is small and the nature of heat transfer mechanism remains the same. As such, it is equivalent to a statement that the heat transfer coefficient, which mediates between heat losses and temperature differences, is a constant. Newton's law is more closely followed for fluid cooling, where the velocity of the fluid does not vary with temperature. Finally, in the case of heat transfer by thermal radiation, Newton's law of cooling holds only for very small temperature changes. We studied how the temperature can lid to shift of regime from coral-dominated state to macroalgae-dominated state.

2 The Basic Model

We study three benthic groups – corals, turf algae, and toxic macroalgae – competing for their space on the seabed. Here, we have considered that a fraction of seabed is available for their growth. In formulating the model, we assume that

macroalgae are always present in coral reef ecosystem irrespective of the abundance of corals in seabed. Let $M(t)$ be the proportion of seabed covered by macroalgae, $C(t)$ be the proportion of seabed covered by corals, and $A(t)$ represent the fraction of seabed occupied by algal turf so that $M(t) + C(t) + A(t) = c_0$ (constant) at any instant t. We consider $T(t)$ as the SST at time t. Corals grow effectively in between certain SST thresholds. We choose the recruitment rate $r(T)$ of adult corals on turf algae to be in the form

$$r(T) = \begin{cases} \left[1 - \left(\frac{T-z}{w}\right)^2\right] \nu_1 e^{\nu_2 T}, & \text{if } T_- < T < T_+ \\ 0, & \text{elsewhere} \end{cases}$$

where $T_\pm = z \pm w$ represents the thermal limits of corals, w is the temperature niche width, and the parameters z, ν_1, ν_2 have no specific biological meanings. The temperature T_{opt}, at which the recruitment rate $r(T)$ becomes maximum, is determined by the envelope function $\nu_1 e^{\nu_2 T}$ and is given by $T_{opt} = z + \frac{-1+w\sqrt{\nu_2^2 + \frac{1}{w^2}}}{b}$. For $\nu_2 = 0$, we have $T_{opt} = z$. Reef-building corals are stenothermic, having optimal growth at an SST closer to its upper thermal limit. However, the recruitment rate of corals decreases sharply with the increase in temperature once SST reaches T_{opt}. Therefore, to make the adopted recruitment function $r(T)$ to be more realistic, it is reasonable to take $\nu_2 > 0$. Corals have different thermal tolerance depending upon geographic differences and SST sets the limits on the latitudinal spread of corals throughout the world. Shallow-water coral reefs are almost exclusively found in tropical and subtropical waters across the globe, whereas corals in temperate zone exist at greater depths and at colder temperatures. The growth of temperate corals is slow than that of the tropical and subtropical corals. Experimental observations suggest that subtropical and tropical corals can withstand substantially higher SST than the corals in temperate zone, whereas the corals in temperate zone withstand potentially low SST. For fixed w and ν_2, T_{opt} is an increasing function of z and so, lowering the value of z will eventually lower T_{opt} and $T_\pm$ (cf. Fig. 1b). Therefore, z can be taken as a control parameter that determines the growth of corals at different geographic locations. Based on the curves as shown in Fig. 1b, representing recruitment rates of corals for different values of z, we choose $z > 20$, $18 \le z \le 20$ and $z < 18$ to determine tropical, subtropical, and temperate zones, respectively, to study the dynamics of our proposed model. Since macroalgae have a wide range of temperature tolerance for its optimal growth compared to that of corals, in our model, we consider the macroalgal growth to be independent of SST. Further, we make the following assumptions:

(H_1) Corals are overgrown by macroalgae at a rate α.
(H_2) Vegetative growth of macroalgae over algal turfs is at a rate a.
(H_3) The rate of colonization of newly immigrated macroalgae on turf algae is b.
(H_4) Natural mortality rate of corals is d.

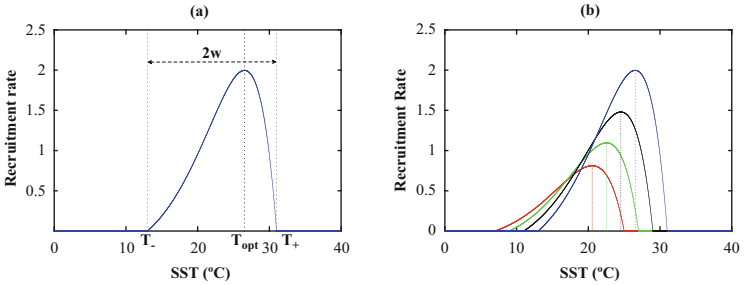

Fig. 1 (**a**) Recruitment rate of corals as a function of T (for $z = 22$, $w = 9$, $\nu_1 = 0.05$, $\nu_2 = 0.15$). (**b**) Recruitment rate of corals for $z = 22$ (blue), $z = 20$ (black), $z = 18$ (green), and $z = 16$ (red)

(H_5) Toxin-induced death rate of corals is $\frac{\gamma M}{\delta+M}$ per unit area of coral cover, where γ is the maximal toxicity rate and δ denotes the macroalgal area at which the toxicity rate is $\frac{\gamma}{2}$.

(H_6) The baseline herbivory encapsulates the loss of macroalgal cover due to grazing and other density-independent processes as well, whereas the supplementary herbivory depends on corals providing refuge to herbivorous fish. The total herbivory is based on the sum of the baseline herbivory h and supplementary herbivory $\frac{gC}{\omega+C}$ per unit area of macroalgal cover, where g is the maximal grazing rate of herbivorous fish and ω represents coral area for the settlement for herbivores at which grazing rate is half maximal.

Assuming that the grazing of herbivores is a dynamic process, the reef dynamics are thus described as a system of nonlinear differential equations:

$$\begin{aligned}
\frac{dM}{dt} &= M\left(\alpha C - \frac{gC}{\omega + C} - h\right) + (aM + b)A \\
\frac{dC}{dt} &= C\left\{Ar(T) - \left(\alpha + \frac{\gamma}{\delta + M}\right)M - d\right\} \\
\frac{dA}{dt} &= hM + dC + \left(\frac{g}{\omega + C} + \frac{\gamma}{\delta + M}\right)MC - A\{aM + Cr(T) + b\} \\
\frac{dT}{dt} &= \beta(T_a - T)
\end{aligned} \tag{1}$$

with the initial conditions $M(0) > 0$, $C(0) \geq 0$, $A(0) > 0$ and $T(0) \leq T_a$, where T_a is the normal average SST and β represents the coefficient of surface heat transfer.

Without any loss of generality, we assume that $c_0 = 1$. Then from (1), we obtain

$$\frac{dM}{dt} = M\left(\alpha C - \frac{gC}{\omega + C} - h\right) + (aM + b)(1 - M - C) \equiv f^1(M, C)$$

$$\frac{dC}{dt} = C\left\{(1-M-C)r(T) - \left(\alpha + \frac{\gamma}{\delta+M}\right)M - d\right\} \equiv Cf^2(M,C,T) \quad (2)$$
$$\frac{dT}{dt} = \beta(T_a - T) \equiv f^3(T)$$

with the initial conditions $M(0) > 0$, $C(0) \geq 0$ and $T(0) \leq T_a$.

From (2), we get

$$M(t) > M(0)e^{\int_0^t \left\{\alpha C(\tau) - \frac{gC(\tau)}{1+\omega C(\tau)} + a\{1-M(\tau)-C(\tau)\} - h\right\}d\tau}$$

and

$$C(t) \geq C(0)e^{\int_0^t \left\{\{1-M(\tau)-C(\tau)\}r(T) - \left(\alpha + \frac{\gamma}{1+\delta M(\tau)}\right)M(\tau) - d\right\}d\tau}$$

Therefore, for all $t \geq 0$, $M(t) > 0$ and $C(t) \geq 0$.

Also, we have $T(t) = T_a + \{T(0) - T_a\}e^{-\beta t}$ and so for all $t \geq 0$, we have $T(t) \geq 0$ whenever $T(0) \geq 0$.

The right-hand sides of the equations in system (2) are continuous, nonnegative smooth functions on $R_+^3 = \{(M, C, T) : M > 0, C \geq 0, T \geq 0\}$. Indeed, they are Lipschitzian on R_+^3 and so the solution of the system (2) exists and is unique. Therefore, R_+^3 is an invariant region.

2.1 Equilibria and Their Stability

In this section, we determine biologically feasible equilibrium solutions of the model and investigate the dependence of their stability on several key parameters.

The system (2) possesses the following equilibria:

(*i*) Coral-free equilibrium $E_0 = (M_0, 0, T_a)$, where $M_0 = \frac{a-b-h+\sqrt{(a-b-h)^2+4ab}}{2a}$. E_0 always exists;

(*ii*) Interior equilibria are given by the intersections of the two nontrivial nullclines $f^1(M, C) = 0$ and $f^2(M, C, T_a) = 0$ in the interior of the first quadrant on the plane $T = T_a$.

If we denote interior equilibria by $E_i^* = (M_i^*, C_i^*, T_a)$, then M_i^* is a positive root of the equation $F(M) \equiv \sum_{i=1}^{6} a_i M^{6-i} = 0$ and $C_i^* = 1 - M_i^* - \frac{1}{r(T_a)}\left\{\left(\alpha + \frac{\gamma}{\delta+M_i^*}\right)M_i^* + d\right\}$, where

$a_1 = p_1(\alpha p_1 + a p_2)$, $a_2 = p_1\{\alpha(2q_1+\omega) - g - h + bp_2 + aq_2\} + ap_2(q_1+\omega)$,
$a_3 = \alpha p_1(r_1+\delta\omega) + (\alpha q_1 - h)(q_1+\omega) + p_1\{\alpha r_1 - (g+h)\delta\} + b\{p_1 q_2 + p_2(q_1+\omega)\} + a\{p_1 r_2 + q_2(q_1+\omega) + p_2\delta\omega\}$,

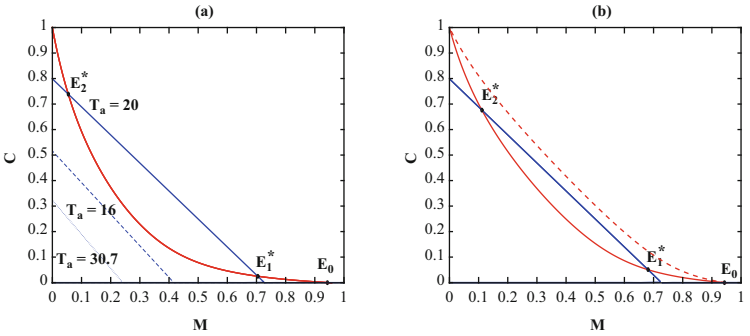

Fig. 2 Mutual positions of M-nullclines (red) and C-nullclines (blue) in $T = T_a$ plane. Possible number of equilibrium points for (**a**) $T_a = 20$ (solid), $T_a = 16$ (dashed), and $T_a = 30.7$ (dotted); (**b**) $g = 0.4$ (solid) and $g = 0.2$ (dashed)

$a_4 = (\alpha q_1 + a q_2 - h)(r_1 + \delta\omega) + (\alpha r_1 + a r_2 - h\delta)(q_1 + \omega) - g(q_1\delta + r_1) + b\{p_2 r_2 + q_2(q_1 + \omega) + p_2\delta\omega\}$,
$a_5 = (\alpha r_1 - h\delta + b q_2 + abr_2)(r_1 + \delta\omega) - g r_1\delta + b r_2(q_1 + \omega)$, $a_6 = b r_2(r_1 + \delta\omega)$,
$p_1 = -\left(1 + \frac{\alpha}{r(T_a)}\right)$, $q_1 = 1 - \delta - \frac{\alpha\delta + d + \gamma}{r(T_a)}$ and $r_1 = \delta\left(1 - \frac{d}{r(T_a)}\right)$.

For the existence of E^*, we must have $T_- < T_a < T_+$. It is difficult to derive analytically the number of feasible interior equilibria; however, the possible number of feasible interior equilibria can be explained from the relative positions and shapes of the nontrivial nullclines as presented in Fig. 2. The mutual positions of the macroalgae and corals nullclines are presented in Figs. 2a,b, showing the existence of a pair of interior equilibria $E_i^*(i = 1, 2)$ given by the intersection of the nullclines

$$M = \frac{(\alpha - a)C - \frac{gC}{\omega + C} + a - b - h + \sqrt{\left\{(\alpha - a)C - \frac{gC}{\omega + C} + a - b - h\right\}^2 + 4ab(1 - C)}}{2a}$$

$$C = 1 - M - \frac{1}{r(T_a)}\left\{\left(\alpha + \frac{\gamma}{\delta + M}\right)M + d\right\}$$

in the positive octant under certain conditions, whereas E_0 always exists. We first study the general nature of the two nullclines with direction of their vector fields and graphical Jacobian to find the nature of stability of the interior equilibria. From Fig. 3, it follows that one interior equilibrium (E_1^*) remains unstable and the other one (E_2^*) is stable whenever it exists. For the ease of notation, we denote E_2^* by E^*. We analyze the stability of system (2) by using eigenvalue analysis of the Jacobian matrix evaluated at the appropriate equilibrium.

At E_0, the eigenvalues of the Jacobian matrix of the system (2) are $-\sqrt{(a - b - h)^2 + 4ab}$, $(1 - M_0)r(T_a) - \left(\alpha + \frac{\gamma}{\delta + M_0}\right)M_0 - d$ and $-\beta$. Therefore,

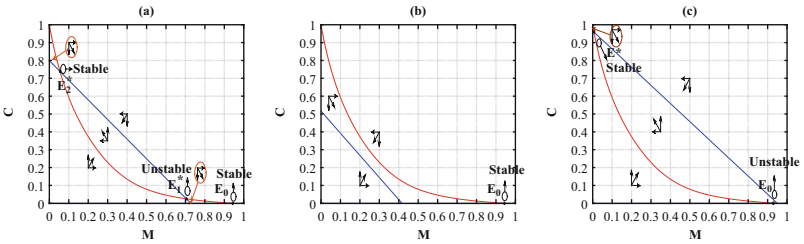

Fig. 3 Nature of stability of the equilibrium points using the direction of the flow field

all the eigenvalues of the Jacobian matrix are negative if $\gamma > \gamma_*$, where $\gamma_* = \left(\frac{\delta+M_0}{M_0}\right)\{(1-M_0)r(T_a) - \alpha M_0 - d\}$. This gives the following lemma:

Lemma 1 *The system* (2) *is locally asymptotically stable at* E_0 *if* $\gamma > \gamma_*$.

The Jacobian J^* of the system (2) evaluated at E^* is

$$J^* = \begin{pmatrix} -\frac{b(1-M^*-C^*)}{M^*} - aM^* - b & (\alpha-a)M^* - \frac{g\omega M^*}{(\omega+C^*)^2} - b & 0 \\ -\left\{r(T_a)+\alpha+\frac{\gamma\delta}{(\delta+M^*)^2}\right\}C^* & -C^*r(T_a) & C^*(1-M^*-C^*)r'(T_a) \\ 0 & 0 & -\beta \end{pmatrix}$$

where $r'(T_a) = \nu_1 e^{\nu_2 T_a}\left[\nu_2\left\{1-\left(\frac{T_a-z}{w}\right)^2\right\} - \frac{2(T_a-z)}{\omega^2}\right]$, $T_- < T_a < T_+$.

The characteristic equation of the Jacobian J^* of the system (2) is $(\lambda + \beta)\left(\lambda^2 + A\lambda^2 + B\right) = 0$, where

$A = \frac{b(1-M^*-C^*)}{M^*} + aM^* + b + C^*r(T_a) > 0$ and

$B = C^*\left[r(T_a)\left\{\frac{b(1-M^*-C^*)}{M^*} + aM^* + b\right\} + \left\{r(T_a) + \alpha + \frac{\gamma\delta}{(\delta+M^*)^2}\right\}\left\{(\alpha-a)M^* - \frac{g\omega M^*}{(\omega+M^*)^2} - b\right\}\right]$.

Therefore, the system is locally asymptotically stable at E^* if and only if $B > 0$.

Lemma 2 *If* $\alpha > a + \frac{g}{\omega} + \frac{b}{M_0}$, *the system* (2) *undergoes a transcritical bifurcation at* E_0 *when* γ *crosses* γ_*.

Proof At $\gamma = \gamma_*$, the Jacobian matrix of the system (2) at E_0 is

$$J_0 = \begin{pmatrix} -\sqrt{(a-b-h)^2+4ab}\left(\alpha - a - \frac{g}{\omega}\right)M_0 - b & 0 \\ 0 & 0 & 0 \\ 0 & 0 & -\beta \end{pmatrix}$$

Therefore, the zero eigenvalue of the Jacobian matrix is simple.

Let U_0 and V_0 be the eigenvectors corresponding to the zero eigenvalue for J_0 and J_0^T, respectively.

Then we obtain $U_0 = \begin{pmatrix} u_0 & 1 & 0 \end{pmatrix}^T$ and $V_0 = \begin{pmatrix} 0 & 1 & 0 \end{pmatrix}^T$, where $u_0 = \frac{(\alpha - a - \frac{g}{\omega})M_0 - b}{\sqrt{(a-b-h)^2+4ab}}$.

Let us express the system (2) in the form $\dot{X} = f(X;\gamma)$, where

$X = \begin{pmatrix} M & C & T \end{pmatrix}^T$ and $f(X;\gamma) = \begin{pmatrix} f^1 & Cf^2 & f^3 \end{pmatrix}^T$

Then $V_0^T f_\gamma(E_0;\gamma_*) = 0$ and so no saddle-node bifurcation occurs at E_0 when γ crosses γ_*.

Also, we obtain $V_0^T[Df_\gamma(E_0;\gamma_*)U_0] = \frac{-M_0}{\delta + M_0} < 0$.

Now, we have

$$D^2 f(E_0;\gamma_*)(U_0,U_0) = \begin{pmatrix} -2au_0^2 + 2u_0\left(\alpha - a - \frac{g}{\omega}\right) + \frac{2}{\omega^3} \\ -\left\{r(T_a) + \alpha + \frac{\gamma_* \delta}{(\delta + M_0)^2}\right\} u_0 - 2r(T_a) \\ 0 \end{pmatrix}$$

This gives $V_0^T[D^2 f(E_0;\gamma_*)(U_0,U_0)] = -\frac{\left\{r(T_a)+\alpha+\frac{\gamma_*\delta}{(\delta+M_0)^2}\right\}\{(\alpha-a-\frac{g}{\omega})M_0 - b\}}{\sqrt{(a-b-h)^2+4ab}} - 2r(T_a)$.

If $\alpha > a + \frac{g}{\omega} + \frac{b}{M_0}$ holds, then we have $V_0^T[D^2 f(E_0;\gamma_*)(U_0,U_0)] < 0$ and so, by the Sotomayor theorem [16], it follows that the system (2) undergoes a transcritical bifurcation at E_0 when γ crosses γ_*.

Thus, if the macroalgal growth on corals is high, there is a change in the stability of the system from E^* to E_0 at $\gamma = \gamma_*$ by means of a transcritical bifurcation.

Lemma 3 *If* $\eta \neq 0$ *and* $\delta \neq \frac{M_{sn}^* r(T_a) + \alpha + \frac{\gamma^* \delta}{(\delta + M_{sn}^*)^2}}{C_{sn}^* r(T_a) - M_{sn}^* \left\{r(T_a) + \alpha + \frac{\gamma^* \delta}{(\delta + M_{sn}^*)^2}\right\}}$, *the system* (2) *undergoes a saddle-node bifurcation at* E^* *when* γ *crosses* γ^*.

Proof In Sect. 2, the relative positions and shapes of the nullclines as given in Fig. 2 show the existence of two interior equilibria under certain parameter restrictions. Let M_{sn}^* be a double root of $F(M) = 0$ such that $0 < M_{sn}^* < 1$. Then we have $F(M_{sn}^*) = 0 = F'(M_{sn}^*)$ and $F''(M_{sn}^*) \neq 0$. In this case, the two nontrivial nullclines $f^1(M,C) = 0$ and $f^2(M,C,T_a) = 0$ touch each other at $E_{sn}^* = (M_{sn}^*, C_{sn}^*, T_a)$, where $C_{sn}^* = 1 - M_{sn}^* - \frac{1}{r(T_a)}\left\{\left(\alpha + \frac{\gamma}{\delta + M_{sn}^*}\right) M_{sn}^* + d\right\}$. Therefore, at E_{sn}^*, the slopes of the nontrivial nullclines $f^1 = 0$ and $f^2 = 0$ are equal. If $\frac{dC^{(f^1)}}{dM}|_{E_{sn}^*}$ and $\frac{dC^{(f^2)}}{dM}|_{E_{sn}^*}$ represent the slopes of $f^1 = 0$ and $f^2 = 0$, respectively, at E_{sn}^*, then we have $\frac{dC^{(f^1)}}{dM}|_{E_{sn}^*} = \frac{dC^{(f^2)}}{dM}|_{E_{sn}^*}$. This implies $\frac{\partial f^1/\partial M}{\partial f^1/\partial C}|_{E_{sn}^*} = \frac{\partial (Cf^2)/\partial M}{\partial (Cf^2)/\partial C}|_{E_{sn}^*}$ and consequently, $Det(J^*) = 0$. Let us denote the corresponding threshold for γ be γ^* so that $B(\gamma^*) = 0$. Then, at $\gamma = \gamma^*$, we have $Tr(J^*) > 0$ and $Det(J^*) = 0$ and so, the zero eigenvalue of the Jacobian matrix is simple. Let U^* and V^* be the eigenvectors corresponding to the zero eigenvalue for J^* and J^{*T}, respectively.

Then we obtain $U^* = \begin{pmatrix} u_1 & 1 & 0 \end{pmatrix}^T$ and $V^* = \begin{pmatrix} 1 & v_1 & v_2 \end{pmatrix}^T$, where $u_1 = \frac{-r(T_a)}{r(T_a)+\alpha+\frac{\gamma^*\delta}{(\delta+M^*_{sn})^2}}$, $v_1 = -\frac{b(1-M^*_{sn}-C^*_{sn})+M^*_{sn}(aM^*_{sn}+b)}{M^*_{sn}\{r(T_a)+\alpha\}+\frac{\gamma^*\delta M^*_{sn}}{(\delta+M^*_{sn})^2}}$ and $v_2 = \frac{v_1 C^*_{sn}(1-M^*_{sn}-C^*_{sn})r'(T_a)}{\beta}$.

We have $V^{*T} f_\gamma(E^*_{sn};\gamma^*) = -\frac{M^*_{sn}C^*_{sn}v_1}{\delta+M^*_{sn}} > 0$ and $V^{*T}[Df_\gamma(E^*_{sn};\gamma^*)U^*] = \frac{-v_1\{(C^*_{sn}u_1+M^*_{sn})\delta+M^{*2}_{sn}\}}{(\delta+M^*_{sn})^2} \neq 0$ if $\delta \neq \frac{M^*_{sn}r(T_a)+\alpha+\frac{\gamma^*\delta}{(\delta+M^*_{sn})^2}}{C^*_{sn}r(T_a)-M^*_{sn}\left\{r(T_a)+\alpha+\frac{\gamma^*\delta}{(\delta+M^*_{sn})^2}\right\}}$.

Also, we obtain

$$D^2 f(E^*_{sn};\gamma^*)(U^*,U^*) = \begin{pmatrix} -2au_1^2+2u_1\left(\alpha-a-\frac{g\omega}{(\omega+C^*_{sn})^2}\right)+\frac{2}{(\omega+C^*_{sn})^3} \\ \frac{2\gamma^*\delta C^*_{sn}u_1^2}{(\delta+M^*_{sn})^3}-2u_1\left\{r(T_a)+\alpha+\frac{\gamma_*\delta}{(\delta+M^*_{sn})^2}\right\}-2r(T_a) \\ 0 \end{pmatrix}$$

This gives $V^{*T}[D^2 f(E^*_{sn};\gamma^*)(U^*,U^*)] = \eta$, where $\eta = 2u_1^2\left\{\frac{\gamma^*\delta C^*_{sn}v_1}{(\delta+M^*_{sn})^3}-a\right\}+2u_1\left[\alpha-a-\frac{g\omega}{(\omega+C^*_{sn})^2}-v_1\left\{r(T_a)-\alpha-\frac{\gamma^*\delta}{(\delta+M^*_{sn})^2}\right\}\right]+\frac{2}{(\omega+C^*_{sn})^3}-2v_1r(T_a)$.

If $\eta \neq 0$ and $\delta \neq \frac{M^*_{sn}r(T_a)+\alpha+\frac{\gamma^*\delta}{(\delta+M^*_{sn})^2}}{C^*_{sn}r(T_a)-M^*_{sn}\left\{r(T_a)+\alpha+\frac{\gamma^*\delta}{(\delta+M^*_{sn})^2}\right\}}$, then by the Sotomayor theorem [16], it follows that the system (2) undergoes a saddle-node bifurcation at E^*_{sn} when γ crosses γ^*.

Triple roots $M^*_\pm$ of $F(M)=0$ are obtained from $F(M)=F'(M)=F''(M)=0$ and $F'''(M)\neq 0$, where $M^*_\pm = \frac{3(4a_2a_5-a_3a_4)\pm\sqrt{9(4a_2a_5-a_3a_4)^2-24(a_3^2-2a_2a_4)(a_3a_5-10a_2a_6)}}{6(a_3^2-2a_2a_4)}$ and $C^*_\pm = 1-M^*_\pm-\frac{1}{r(T_a)}\left\{\left(\alpha+\frac{\gamma}{\delta+M^*_\pm}\right)M^*_\pm+d\right\}$.

For the feasibility of the equilibria $(M^*_\pm, C^*_\pm, T_a)$, we must have $0 < M^*_\pm, C^*_\pm < 1$ and $9(4a_2a_5 - a_3a_4)^2 \geq 24(a_3^2 - 2a_2a_4)(a_3a_5 - 10a_2a_6)$. Now proceeding as above, it can be shown that the Jacobian matrix at $(M^*_\pm, C^*_\pm, T_a)$ has one zero eigenvalue. We use numerical simulations to verify that the quadratic normal form coefficient for the saddle-node bifurcation evaluated at $(M^*_\pm, C^*_\pm, T_a)$ is zero so that the system exhibits a cusp bifurcation when the parameters (T_a, g) cross the threshold (T_{cp}, g_{cp}), where T_{cp} and g_{cp} satisfy $2u_1^2\left\{\frac{\gamma^*\delta C^*_\pm v_1}{(\delta+M^*_\pm)^3}-a\right\}+2u_1\left[\alpha-a-\frac{g_{cp}\omega}{(\omega+C^*_\pm)^2}-v_1\left\{r(T_{cp})-\alpha-\frac{\gamma^*\delta}{(\delta+M^*_\pm)^2}\right\}\right]+\frac{2}{(\omega+C^*_\pm)^3}-2v_1r(T_{cp})=0$ and $\delta = \frac{M^*_\pm r(T_{cp})+\alpha+\frac{\gamma^*\delta}{(\delta+M^*_\pm)^2}}{C^*_\pm r(T_{cp})-M^*_\pm\left\{r(T_{cp})+\alpha+\frac{\gamma^*\delta}{(\delta+M^*_\pm)^2}\right\}}$.

To identify the effect of macroalgal toxicity on coral cover at different SST levels in tropical zone (viz., $z = 21$), in Fig. 4, we plot the solutions of the nullcline equations in the $CT_a\gamma$ space, yielding a bifurcation diagram. It is observed that the toxicity tolerance in corals increases due to the increase of SST up to a certain

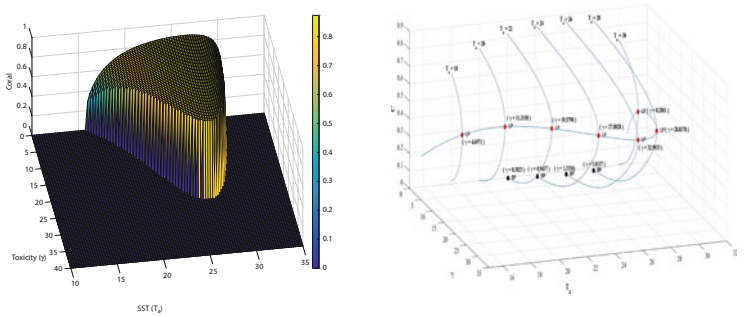

Fig. 4 Bifurcation diagram of γ versus the equilibrium value of coral cover for different SST in the zone determined by $z = 21$

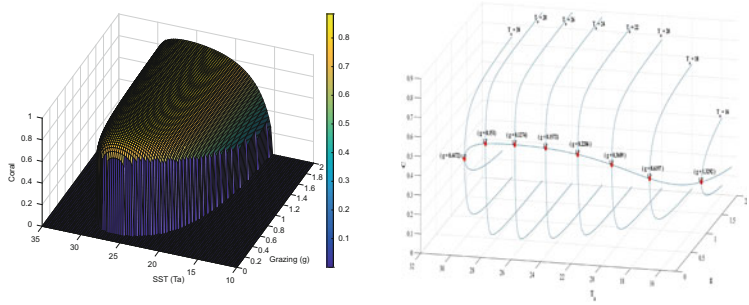

Fig. 5 Bifurcation diagram of g versus the equilibrium value of coral cover for different SST in the zone determined by $z = 21$

SST threshold. With high SST, the toxicity tolerance in corals reduces drastically followed by the mass mortality of corals.

Next, we identify the effect of grazing on coral cover for different SST levels in the same tropical zone determined by $z = 21$. In Fig. 5, we plot the solutions of the nullcline equations in the CT_ag space, yielding a bifurcation diagram. It is observed that, in this zone, higher rate of grazing of the herbivores is required for the corals to survive in the system when the SST is either low (less than $20°C$) or high (greater than $30°C$).

To identify the upper and lower SST tolerance thresholds for corals in tropical, subtropical, and temperate zones, in Fig. 6, we plot the solutions of the nullcline equations in the CT_az space, yielding a bifurcation diagram. It is observed that the difference in upper and lower SST thresholds for the survivability of corals is maximum when the corals are in the tropical region (viz., $z > 20$). The threshold difference becomes lower in the subtropical zone (viz., $18 \leq z \leq 20$) and is least at the temperate zone (viz., $z < 18$). The corresponding changes in the tolerance level of macroalgal toxicity is shown in Fig. 7a, with highest tolerance at the tropical region and lowest tolerance at the temperate region. The effect of macroalgal grazing

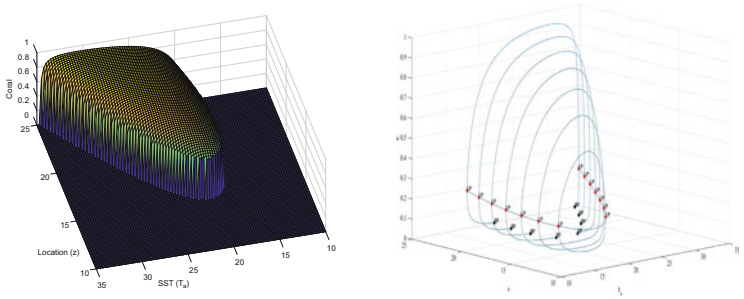

Fig. 6 Bifurcation diagram of T_a versus the equilibrium value of coral cover for different values of z

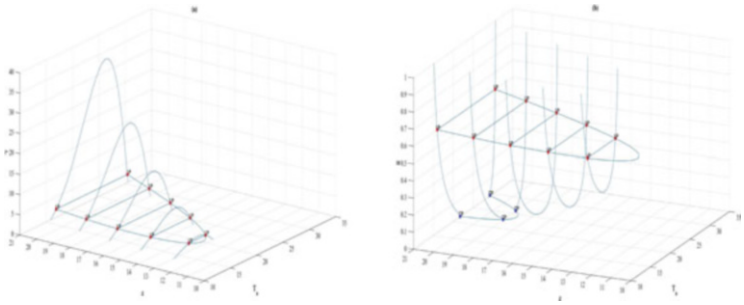

Fig. 7 Two parameter bifurcation diagrams with (**a**) T_a and γ as active parameters and (**b**) T_a and g as active parameters for different values of z

intensity by herbivores on coral cover is highest at the temperate region, where a marginal decrease of grazing rate has a substantial effect on coral cover compared to the corals at the tropical region (cf.Fig. 7b).

3 Results and Discussion

Coral reefs are the most ancient and dynamic ecosystem. In this paper, we model the dynamics of coral reef benthic system in which the effect of temperature plays a significant role in the system dynamics. We first perform equilibrium and stability analysis on our 3D nonlinear ODE model. We found that the system exhibits transcritical bifurcation at coral-free equilibrium point and saddle-node bifurcation at the coexistence equilibrium point when the toxicity crosses a certain threshold. Here, we have investigated and divided the whole coral reef ecosystem into three climate zones: tropical, subtropical, and temperate zones. In the tropical zone, we observed that the toxicity in corals increases due to the increase of SST up to a threshold value. In case of high SST, the toxicity tolerance in corals reduces

extremely followed by coral mortality. In the same tropical zone, we observed that higher rate of grazing of the herbivores is required for surviving corals in the system when the SST is either low or high. Also we have determined the upper and lower SST tolerance threshold for corals in three different climate zones. We observed that the difference of upper and lower SST threshold for surviving corals is maximum when they are in the tropical region. The threshold difference is minimum when corals are in the temperate zone, and it lies between maxima and minima when corals are in the subtropical zone. The corresponding changes of macroalgal toxicity becomes highest and lowest when corals are in tropical and temperate zones, respectively. Lastly, the macroalgal grazing intensity on coral cover is highest at the temperate region, and a marginal decrease of grazing rate on coral cover at the tropical zone.

Funding The research of Samares Pal is partially supported by the Science and Engineering Research Board, Government of India (Grant No. MTR/2020/000542).

Declarations

Conflict of interest The authors declare that there is no conflict of interests regarding the publication of this article.

Ethical approval The authors state that this research complies with ethical standards.

Human or animal rights This research does not involve either human participants or animals.

Data availability All data generated or analyzed during this study are included in this article.

References

1. Hoegh-Guldberg, O.: Climate change, coral bleaching and the future of the world's coral reefs. Marine Freshwater Res. **50**(8), 839–866 (1999)
2. Bruno, J.F., Sweatman, H., Precht, W.F., Selig, E.R., Schutte, V.G.: Assessing evidence of phase shifts from coral to macroalgal dominance on coral reefs. Ecology **90**(6), 1478–1484 (2009)
3. Albins, M.A., Hixon, M.A.: Invasive Indo-Pacific lionfish Pterois volitans reduce recruitment of Atlantic coral-reef fishes. Mar. Ecol. Prog. Ser. **367**, 233–238 (2008)
4. Birrell, C. L., McCook, L. J., Willis, B. L., Diaz-Pulido, G. A.: Effects of benthic algae on the replenishment of corals and the implications for the resilience of coral reefs. Oceanogr. Mar. Biol. Annu. Rev. **46**, 25–63 (2008)
5. Jompa, J., McCook, L.J.: Effects of competition and herbivory on interactions between a hard coral and a brown alga. J. Exp. Mar. Biol. Ecol. **271**(1), 25–39 (2002)
6. Harriott, V., Banks, S.: Latitudinal variation in coral communities in eastern Australia: a qualitative biophysical model of factors regulating coral reefs. Coral Reefs **21**(1), 83–94 (2002)
7. Crabbe, M.J.C.: Climate change, global warming and coral reefs: modelling the effects of temperature. Comput. Biol. Chem. **32**(5), 311–314 (2008)

8. Hughes, T.P., Baird, A.H., Bellwood, D.R., Card, M., Connolly, S.R., Folke, C., ... & Roughgarden, J.: Climate change, human impacts, and the resilience of coral reefs. Science **301**(5635), 929–933 (2003)
9. Crabbe, M.J.C.: Climate change and tropical marine agriculture. J. Exp. Botany **60**(10), 2839–2844 (2009)
10. Lough, J.M.: Coral calcification from skeletal records revisited. Mar. Ecol. Prog. Ser. **373**, 257–264 (2008)
11. Done, T.J.: Coral community adaptability to environmental change at the scales of regions, reefs and reef zones. Am. Zool. **39**(1), 66–79 (1999)
12. Lough, J.M.: 1997–98: Unprecedented thermal stress to coral reefs?. Geophys. Res. Lett. **27**(23), 3901–3904 (2000)
13. Mumby, P.J., Hastings, A., Edwards, H.J.: Thresholds and the resilience of Caribbean coral reefs. Nature **450**(7166), 98–101 (2007)
14. Blackwood, J.C., Hastings, A., Mumby, P.J.: The effect of fishing on hysteresis in Caribbean coral reefs. Theor. Ecol. **5**(1), 105–114 (2012)
15. Bhattacharyya, J., Pal, S.: Hysteresis in coral reefs under macroalgal toxicity and overfishing. J. Biol. Phys. **41**(2), 151–172 (2015)
16. Perko, L.: Differential equations and dynamical systems (Vol. 7). Springer Science & Business Media (2013)

Analysis and Bifurcations of Non-smooth Filippov Predator Prey System with Harvesting

U. Yadav, S. Gakkhar, and A. K. Nayak

1 Introduction

Over the years, mathematical modelling is used as a tool to understand the evolution of different species in the habitat. Continuous efforts are made in improving the models making them more realistic. Attempts are made to represent piece-wise continuous processes in mechanical and electrical systems as Filippov systems. Filippov process is also used to describe the epidemic systems [2, 7]. The therapy policy based on the threshold value for the treatment of HIV infection was investigated by De Carvalho et al. [5]. Recently, application of Filippov systems has been extended to ecological models. The dynamics of a non-smooth predator prey system characterized by density-dependent intermittent refuge protection of the prey was studied by [1]. When the level of apprehension of prey species is less than a threshold value, the existence of pair of pseudo-equilibrium was established. Cao et al. [4] studied ecological aspects of prey harvesting in Filippov competitive systems with threshold strategy depending upon the density of prey. Gupta and Gakkhar [3] investigated the dynamics of Filippov predator prey system with functional response varying with the threshold value depending on the ratio of prey to predator density.

In this paper, the Filippov predator prey is formulated ensuring the sustainable harvesting and coexistence of both the species in the habitat. When enough food (prey) is available to the predators, the coexistence of both the species is possible in the form of stable equilibrium point or stable limit cycle. However, when the prey to predator availability is below a threshold value, the pressure on predators to survive increases that may lead to extinction of predators. This pressure can be reduced either by providing additional food to the predators or by harvesting them.

U. Yadav (✉) · S. Gakkhar · A. K. Nayak
Indian Institute of Technology, Roorkee, India
e-mail: uyadav@ma.iitr.ac.in; ameeya.nayak@ma.iitr.ac.in

© The Author(s), under exclusive license to Springer Nature Switzerland AG 2024

W. Lacarbonara (ed.), *Advances in Nonlinear Dynamics, Volume III*, NODYCON Conference Proceedings Series, https://doi.org/10.1007/978-3-031-50635-2_58

With the assumption that the predators are of economic interest, its harvesting is adopted as a control measure. It is assumed that harvesting is permitted only when the ratio of prey to predator is below a threshold value. Whenever the ratio is above this threshold value, harvesting is not allowed. The predator prey system with the aim of controlling the predator population to the level that conserves prey species is considered. The hypothesis involved is that harvesting increases with predator abundance and decreases with their scarcity. From the investigation of the Filippov system it is concluded that the coexistence of the species is possible in two ways: the existence and stability of interior equilibrium state and the existence of limit cycle about the interior equilibrium state. The half saturation rate of predators plays a crucial role in determining this dynamical behaviour of the Filippov system. Since, origin exists as an unstable pseudo-equilibrium point of the Filippov system, it is claimed that the extinction of both the species is not viable for the system.

2 Model

A predator prey system with predator (y), logistically growing prey (x), and Holling type II functional response with usual parameters β, β_1, and a is considered. The positive parameter d is included as the predators mortality rate in the absence of prey. When the prey to predator availability is below a threshold value, the pressure on predators to survive increases. This pressure is decreased by harvesting the predators. Harvesting is not allowed above a threshold value μ for the availability of prey per predator. Predators are harvested below this threshold value. With the assumption that predators are of economic interest, harvesting seems a better option. To formulate this problem, the following regions S_1 and S_2 are used:

$$S_1 = \{Z = (x, y) \in \mathbb{R}^2_+, y \neq 0 \left| \frac{x}{y} > \mu, \quad i.e., \quad x - \mu y > 0 \right\}$$

$$S_2 = \{Z = (x, y) \in \mathbb{R}^2_+, y \neq 0 \left| \frac{x}{y} < \mu, \quad i.e., \quad x - \mu y < 0 \right. \}.$$

Let us introduce the parameter ϵ as,

$$\epsilon = \begin{cases} 0 & S_1 \\ 1 & S_2. \end{cases} \tag{1}$$

Then the Filippov system proposed for the combined two regions is given below:

$$\begin{aligned}\frac{dx}{dt} &= rx(1-\frac{x}{K}) - \frac{\beta xy}{a+x}\\ \frac{dy}{dt} &= -dy + \frac{\beta_1 xy}{a+x} - \epsilon q E y.\end{aligned} \tag{2}$$

Here, proportional harvesting is considered where q is the fraction of predators available for harvesting, E is effort incurred on harvesting.

Considering a smooth, scalar function $H : \mathbb{R}^2_+ \to \mathbb{R}$ as $H(Z) = x - \mu y$ and the boundary Σ as

$$\Sigma = \{Z \in \mathbb{R}^2_+ | H(Z) = 0\}.$$

Then clearly the boundary Σ is the splitting boundary between the two regions S_1 and S_2. As $F_{S_i} : \mathbb{R}^2_+ \to \mathbb{R}^2_+$ for $i = 1, 2$ are smooth vector fields corresponding to smooth subsystems. Accordingly, the Filippov system is given as below:

$$\dot{Z} = F(Z) = \begin{cases} F_{S_1}(Z), & Z \in S_1 \\ F_{S_2}(Z), & Z \in S_2. \end{cases} \tag{3}$$

3 Dynamics of Smooth Subsystems

The three equilibrium states of the subsystem F_{S_1} are:

1. The trivial equilibrium state $E^I_{00} = (0, 0)$ always exists.
2. The predator-free axial equilibrium state $E^I_{10} = (K, 0)$ always exists.
3. The coexistence equilibrium state $E^I_* = (x^I_*, y^1_*)$ defined as

$$x^I_* = \frac{ad}{\beta_1 - d}, \qquad y^I_* = \frac{r(K - x^I_*)(a + x^I_*)}{K\beta}. \tag{4}$$

The state E^I_* exists under the condition given below:

$$d < \beta_1, \qquad \text{and} \qquad x^I_* < K. \tag{5}$$

The three equilibrium state of the subsystem F_{S_2} are given as:

1. The always existing trivial equilibrium state $E^{II}_{00} = (0, 0)$ existing for all parametric values.
2. Another always existing predator-free equilibrium state $E^{II}_{10} = E^{II}_{10} = (K, 0)$.
3. The coexistence equilibrium point $E^{II}_* = (x^{II}_*, y^{II}_*)$ is given by:

$$x_*^{II} = \frac{(d+qE)a}{\beta_1 - (d+qE)}, \qquad y_*^{II} = \frac{r(K - x_*^{II})(a + x_*^{II})}{K\beta}. \tag{6}$$

The point E_*^{II} exists whenever the following condition is satisfied:

$$d + qE < \beta_1 \quad \text{and} \quad x_*^{II} < K. \tag{7}$$

3.1 Classification of Equilibrium States as Regular/Virtual

It is noticed that the switching boundary Σ passes through origin. Further, using the definition of regular and virtual equilibrium points [3], it is concluded that the point $(K, 0)$ is regular for subsystem F_{S_1} and virtual for subsystem F_{S_2}.

The point E_*^I is a regular equilibrium point E_{*R}^I for subsystem F_{S_1} whenever the following condition is satisfied:

$$\mu_1 = \frac{Kd\beta(\beta_1 - d)}{r\beta_1(K(\beta_1 - d) - ad)} > \mu. \tag{8}$$

Under the reversal condition of (8), the equilibrium state E_*^I becomes virtual as E_{*V}^I.

The equilibrium state E_*^{II} is regular equilibrium state E_{*R}^{II} for subsystem F_{S_1} whenever the following condition is satisfied:

$$\mu_2 = \frac{K\beta(d+qE)(\beta_1 - d - qE)}{r\beta_1(K(\beta_1 - d - qE) - ad - aqE)} < \mu. \tag{9}$$

Under the reversal condition of (9), the equilibrium state E_*^{II} becomes virtual as E_{*V}^{II}.

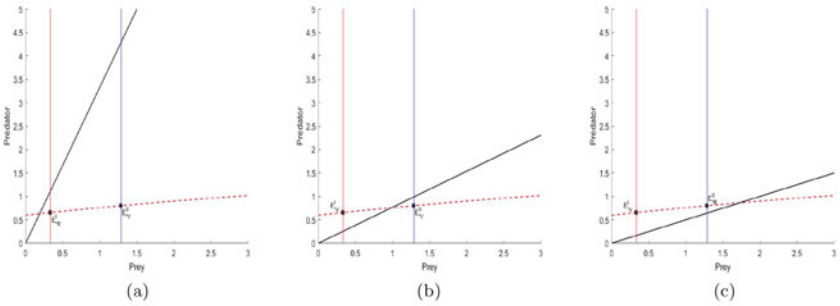

Fig. 1 Regular/Virtual Equilibrium $a = 3, d = 0.2, E = 2, K = 20, q = 0.2, r = 2, \beta = 10, \beta_1 = 2..$ (**a**) $\mu = 0.3$. (**b**) $\mu = 1.3$. (**c**) $\mu = 2$

3.1.1 Graphically Representation of Regular/Virtual Equilibrium

The existence of regular and virtual equilibrium of the subsystems F_{S_1} and F_{S_2} are shown graphically in the Fig. 1 with the help of nullclines. The curves for which

$$\frac{dx}{dt} = 0 \text{ and } \frac{dy}{dt} = 0$$

are the prey (x) and predator (y) nullclines, respectively. Using this, the respective non-zero x and y nullclines of Subsystem F_{S_1} are

$$y = \frac{r(K-x)(a+x)}{K\beta} \qquad x = \frac{da}{\beta_1 - d}. \tag{10}$$

Similarly, the respective non-zero x and y nullclines for Subsystem F_{S_2} are

$$y = \frac{r(K-x)(a+x)}{K\beta}, \qquad x = \frac{(d+qE)a}{\beta_1 - (d+qE)}. \tag{11}$$

In the Fig. 1, the common non-zero prey nullcline is represented by dotted red line whereas the non-zero predator nullclines for subsystem F_{S_1} is red and is blue for F_{S_2}. The boundary $H(Z)$ is shown in black. For the chosen parameters, it is be seen that $\mu_1 = 0.5021$, $\mu_2 = 1.5245$, for $\mu = 0.3 < \mu_1 < \mu_2$, the point E_*^1 is regular and the point E_*^2 is virtual as in Fig. 1a. In Fig. 1b, for $\mu_1 < \mu = 1.3 < \mu_2$ both the points E_*^1 and E_*^2 are virtual. Further in Fig. 1c, $\mu_1 < \mu_2 < \mu = 2$, the point E_*^1 is virtual whereas the point E_*^2 is regular. Also it can be noticed that for the chosen parameters, both the states E_*^1 and E_*^2 cannot be regular simultaneously.

3.2 Local Stability Analysis

The local stability of distinct equilibrium points for the smooth subsystems F_{S_1} and F_{S_2} are analysed using the eigenvalues of the Jacobian matrix computed at respective points. The following results are obtained from the analysis.

Theorem 1

1. *The equilibrium state* $E_{00}^I = E_{00}^{II} = (0,0)$ *is unstable equilibrium state with unstable manifold along* x*-direction and stable manifold along* y*-direction for both the subsystems.*
2. *The equilibrium state* $E_{10}^I = E_{10}^{II} = (K,0)$ *is stable whenever the following condition is satisfied:*

$$K < \frac{a(d+\epsilon qE)}{\beta_1 - (d+\epsilon qE)}. \tag{12}$$

3. *The coexistence equilibrium state is stable whenever the following condition is satisfied:*

$$\frac{K(\beta_1 - (d + \epsilon q E))}{\beta_1 + (d + \epsilon q E)} < a. \tag{13}$$

Note

1. For non-zero initial conditions, both the species will never get extinct simultaneously for the individual subsystems.
2. Whenever the carrying capacity of the ecosystem for prey is less than a threshold value which is dependent on the parameters of predator equation- their death rate, their half saturation level and the conversion rate of food (prey) then in both individual subsystems predator gets extinct.
3. It can be easily concluded that whenever the predator prey equilibrium state is stable, the interior equilibrium state would not exist in both the individual subsystem.

4 Sliding Mode

Definition 1 Let

$$\sigma(Z) = \langle H_Z(z), F_{S_1}(z)\rangle\langle H_Z(z), F_{S_2}(z)\rangle \quad \text{and} \quad H_Z(z) \neq 0. \tag{14}$$

Then sliding mode domain is defined as

$$\Sigma_s = \{Z \in \Sigma | \sigma(Z) < 0\} \tag{15}$$

and the crossing region is defined as

$$\Sigma_c = \{Z \in \Sigma | \sigma(Z) > 0\}. \tag{16}$$

The different types of region on the sliding region are:

– Sliding Region: The region $\Sigma_1 \in \Sigma$ is the sliding region for the following set of constraints:

$$\langle H_Z(z), F_{S_1}(z)\rangle < 0 \quad \text{and} \quad \langle H_Z(z), F_{S_2}(z)\rangle > 0. \tag{17}$$

– Escaping Region: The region $\Sigma_2 \in \Sigma$ is escaping region for the following set of constraints:

$$\langle H_Z(z), F_{S_1}(z)\rangle > 0 \quad \text{and} \quad \langle H_Z(z), F_{S_2}(z)\rangle < 0. \tag{18}$$

Then different regions on the boundary Σ for system (3) are found out as given below:

As, $H_Z(z) = (1, -\mu)$, $F_{S_1}(z)$ and $F_{S_2}(z)$as defined in (3).

The expression $\langle H_Z(z), F_{S_1}(z)\rangle = 0$ reduces to a quadratic equation in x given by

$$\mu r x^2 + x\big(K(\beta + \beta_1\mu) - \mu r(K - a) - dK\mu\big) - Ka\mu(r + d) = 0 \tag{19}$$

which in turn simplifies to

$$(x - x_{s_{11}})(x - x_{s_{12}}) = 0, \tag{20}$$

where $x_{s_{11}}, x_{s_{12}}$ are positive and negative root of (19), respectively.

Similarly, solving $\langle H_Z(z), F_{S_2}(z)\rangle = 0$ simplifies to quadratic equation in x as defined below:

$$\mu r x^2 + x(K(\beta + \beta_1\mu) - \mu r(K - a) - k\mu(d + qE)) - Ka\mu(r + d + qE) = 0 \tag{21}$$

which in turn reduces to

$$(x - x_{s_{21}})(x - x_{s_{22}}) = 0, \tag{22}$$

where $x_{s_{21}}, x_{s_{22}}$ are positive and negative root of (21), respectively.

Theorem 2 *The different regions are defined as below:*

- *The sliding region is given by the region*

$$\left\{\left(x, \frac{x}{\mu}\right)\middle| min\{x_{s_{11}}, x_{s_{21}}\} < x < max\{x_{s_{11}}, x_{s_{21}}\}\right\}.$$

- *There is no escaping region.*
- *The crossing region is given by the region*

$$\left\{\left(x, \frac{x}{\mu}\right)\middle| \{0 < x < min\{x_{s_{11}, x_{s_{21}}}\} \cup \{x > max\{x_{s_{11}}, x_{s_{21}}\}\right\}.$$

Proof Using the equations (20) and (22) and the defined definitions, the above theorems can be easily verified.

4.1 Boundary Equilibrium Point

The boundary equilibrium point is the equilibrium point that lies on the boundary Σ. The boundary Σ passes through the origin therefore the point $E_{00}^{I} = E_{00}^{II} = (0, 0)$ is the boundary equilibrium point. Also, the equilibrium point $E_{10}^{I} = E_{10}^{II} = (K, 0)$ can never be the boundary point. For subsystem F_{S_1}, the coexistence equilibrium state E_*^I becomes the boundary equilibrium B_1 if

$$\mu = \frac{Kd\beta(\beta_1 - d)}{r\beta_1(K(\beta_1 - d) - ad)}. \tag{23}$$

Similarly, for subsystem F_{S_2}, the coexistence equilibrium state becomes the boundary equilibrium B_2 whenever

$$\mu = \frac{K\beta(d + qE)(\beta_1 - (d + qE))}{r\beta_1(K(\beta_1 - (d + qE)) - a(d + qE))}. \tag{24}$$

The existence condition for the boundary points B_1 and B_2 is same as that of equilibrium state E_*^I and E_*^{II}, respectively.

4.2 Tangent Points

A state $E_T^i = (x_{Ti}, y_{Ti})$ is a tangent point for system 3 whenever

$$\langle H_Z(z), F_{S_i}(z)\rangle = F_{S_i} H(Z) = 0 \qquad \text{for i=1,2.} \tag{25}$$

Let $F_{S_i}^2 H(Z)$ for $i = 1, 2$ be the second directional derivative. Then, the tangent point E_T^I is visible whenever

$$F_{S_1}^2 H(Z) > 0.$$

Also, the tangent point E_T^{II} is visible whenever

$$F_{S_2}^2 H(Z) < 0.$$

For subsystem F_{S_1}, the x component of tangent point is the positive solution of the equation (19) which is given by

$$x_{T1} = \frac{-B + \sqrt{B^2 - 4AC}}{2A}, \tag{26}$$

where $A = \mu r, \quad B = r\mu a + \beta K + \beta_1 K\mu - dK\mu - rK\mu, \quad C = -Kda\mu - rKa\mu.$

It can be verified that x_{T1} is same as $x_{s_{11}}$ as in (20).

Now, for visibility of $E_T^1 = \left(x_{T1}, \frac{x_{T1}}{\mu}\right)$, we have

$$F_{S_1} H(Z) = rx(1 - \frac{x}{K}) - \frac{\beta x^2}{\mu(a+x)} + dx - \frac{\beta_1 x^2}{a+x}$$

$$\begin{aligned} F_{S_1}^2 H(Z) &= \left\langle \frac{\partial F_{S_1} H(Z)}{\partial z}, F_{S_1} \right\rangle \\ &= \left(r + d - \frac{2rx}{K} - \frac{2ax + x^2}{(a+x)^2}(\frac{\beta}{\mu} + \beta_1), 0\right) \\ &\quad \times \left(rx\left(1 - \frac{x}{K}\right) - \frac{\beta xy}{a+x}, -dy + \frac{\beta_1 xy}{a+x}\right) \\ &= x^2\left(\frac{r}{K} + \frac{a}{(a+x)^2}\right)\left(\frac{\beta}{\mu} + \beta_1\right)\left(-r(1 - \frac{x}{K}) + \frac{\beta x}{\mu(a+x)}\right) \\ &= x^2\left(\frac{r}{K} + \frac{a}{(a+x)^2}\right)\left(\frac{\beta}{\mu} + \beta_1\right) g_1(x) \end{aligned}$$

Now, E_T^1 is visible $\implies g_1(x) > 0$.

Similarly, for subsystem F_{S_2}, the x component of tangent point E_T^2 is the positive solution of the equation (21) which is given by

$$x_{T2} = \frac{-B_1 + \sqrt{B_1^2 - 4AC_1}}{2A}, \tag{27}$$

where $A = r\mu, \quad B_1 = r\mu a + \beta K + \beta_1 K\mu - dK\mu - rK\mu - qEK\mu, \quad C = -Kda\mu - rKa\mu - K\mu aqE$. It can be verified that x_{T2} is same as $x_{s_{21}}$ as in (22).

Now, for visibility of $E_T^2 = \left(x_{T2}, \frac{x_{T2}}{\mu}\right)$,

$$F_{S_2} H(Z) = rx\left(1 - \frac{x}{K}\right) - \frac{\beta x^2}{\mu(a+x)} + dx - \frac{\beta_1 x^2}{a+x} + qEx$$

$$
\begin{aligned}
F_{S_2}^2 H(Z) &= \left\langle \frac{\partial F_{S_2} H(Z)}{\partial z}, F_{S_2} \right\rangle \\
&= \left(r + d + qE - \frac{2rx}{K} - \frac{2ax + x^2}{(a+x)^2}\left(\frac{\beta}{\mu} + \beta_1\right), 0 \right) \\
&\quad \times \left(rx\left(1 - \frac{x}{K}\right) - \frac{\beta xy}{a+x}, -dy + \frac{\beta_1 xy}{a+x} - qEy \right) \\
&= x^2 \left(\frac{r}{K} + \frac{a}{(a+x)^2} \right) \left(\frac{\beta}{\mu} + \beta_1 \right) \left(-r(1 - \frac{x}{K}) + \frac{\beta x}{\mu(a+x)} \right) \\
&= x^2 \left(\frac{r}{K} + \frac{a}{(a+x)^2} \right) \left(\frac{\beta}{\mu} + \beta_1 \right) g_1(x).
\end{aligned}
$$

Now, tangent point E_T^2 is visible $\implies g_1(x) > 0$.

It can be concluded that visibility condition of E_T^1 and E_T^2 are same. Either both the tangent points will be visible or none will be visible.

4.3 Pseudo-equilibrium

From the sliding convex method, sliding vector field is governed by the equation given below:

$$
F_s(z) = \lambda F_{S_1}(z) + (1-\lambda) F_{S_2}(z), \quad \text{where } \lambda = \frac{\langle H_Z(z), F_{S_2}(z) \rangle}{\langle H_Z(z), F_{S_2}(z) - F_{S_1}(z) \rangle}. \tag{28}
$$

Now, $\langle H_Z(z), F_{S_2}(z) \rangle = rx\left(1 - \frac{x}{K}\right) + dx + qEx - \frac{x^2}{a+x}\left(\frac{\beta}{\mu} + \beta_1\right)$,

Also, $F_{S_2}(z) - F_{S_1}(z) = (0, -qEy)$ and $\langle H_Z(z), F_{S_2}(z) - F_{S_1}(z) \rangle = qEx$.

So,

$$
\lambda = \frac{r\left(1 - \frac{x}{K}\right) + d + qE - \frac{x}{a+x}\left(\frac{\beta}{\mu} + \beta_1\right)}{qE}.
$$

Hence, $F_S(z) = \left[rx\left(1 - \frac{x}{K}\right) - \frac{\beta xy}{a+x}, ry\left(1 - \frac{x}{K}\right) - \frac{\beta xy}{\mu(a+x)} \right]$.

It can be easily verified that $\langle H_Z(z), F_S(z) \rangle = 0$, which implies sliding motion is tangent to the switching surface. The sliding mode dynamics is guided by the equation

$$
\frac{dx}{dt} = rx\left(1 - \frac{x}{K}\right) - \frac{\beta x^2}{\mu(a+x)} = \psi(x), \qquad y = \frac{x}{\mu}. \tag{29}
$$

Theorem 3 *There are two pseudo-equilibrium points* $E_p^1 = (0, 0)$ *and* $E_p^2 = (x_p, \frac{x_p}{\mu})$. *Here,*

$$x_p = \frac{-\beta K + (a - K)\mu r + \sqrt{(\mu r(K - a) + \beta K)^2 + 4u^2 r^2 K a}}{2\mu r}. \tag{30}$$

The point E_p^1 *is always unstable and* E_p^2 *is stable under the following condition:*

$$r - \frac{2rx_p}{K} - \frac{2\beta\mu a x_p + \beta\mu}{\mu^2(a + x_p)^2} > 0. \tag{31}$$

Proof The singular points on the boundary Σ are the pseudo-equilibrium points. From equation (29), pseudo-equilibrium points are computed as E_p^1 and E_p^2 as defined above. For the analysis of stability of these pseudo-equilibrium points, $\phi'(x)$ is computed at respective points given as below

$$\phi'(E_p^1) = r > 0, \quad \phi'(E_p^2) = r - \frac{2rx_p}{K} - \frac{2\beta\mu a x_p + \beta\mu}{\mu^2(a + x_p)^2}. \tag{32}$$

The point E_p is stable whenever $\phi'(E_p) < 0$ which simplifies to equation (31).

5 Numerical Simulation

In this section, the bifurcation arising due to the Filippov system are illustrated diagrammatically with the help of numerical example. The numerical date is hypothetical with the sole purpose of illustrating the analytical results.

Global Sliding Bifurcation Global sliding bifurcation requires non-vanishing cycles, including sliding interference, touching bifurcation, buckling bifurcation, crossing bifurcation, bifurcation of a sliding homoclinic orbit, and heteroclinic orbit [6] Touching (or grazing) bifurcation indicates that a periodic solution can collide with the sliding segments.

Bifurcation with respect to parameter a, about the point E_*^I is shown in Fig. 2. The parameters are taken such that only the equilibrium state E_*^I exists as a stable state in both the domain about a. It can be seen in Fig. 2a, E_*^1 is stable for $a = 20$. Decreasing the value of a to 16 and then to 7, gazing limit cycle and crossing limit cycle exists about E_*^I as in Fig. 2b and c, respectively.

Similarly, bifurcation about the point E_*^{II} with respect to the parameter a is shown in the Fig. 3. For $a = 11$, the only equilibrium point which is stable is E_*^{II}. All the trajectories starting in either of the domain S_1 or S_2 tend to E_*^{II} as in Fig. 3a. In Fig. 3b, the portion of the limit cycle about the point E_*^{II} slides on the boundary for $a = 9$. With $a = 6$ the limit cycle expands in both the domains as in Fig. 3c.

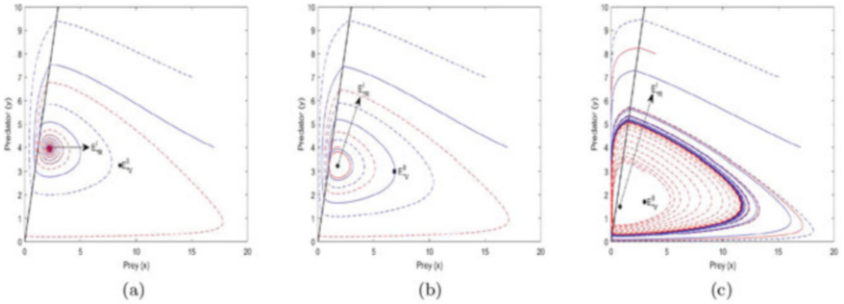

Fig. 2 Bifurcation about E_*^I $d = 2, q = 0.2, r = 2, E = 2, K = 20, \beta = 10, \beta_1 = 2, \mu = 0.3$.. (**a**) $a = 20$. (**b**) $a = 16$. (**c**) $a = 7$

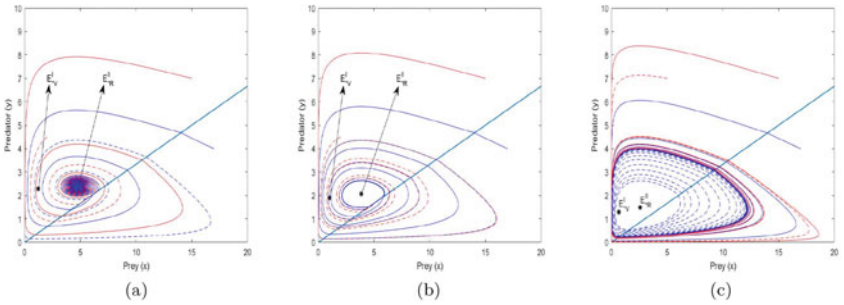

Fig. 3 Bifurcation about E_*^{II} $d = 0.2, q = 0.2, r = 2, E = 2, K = 20, \beta = 10, \beta_1 = 2, \mu = 3$. (**a**) $a = 11$. (**b**) $a = 9$. (**c**) $a = 6$

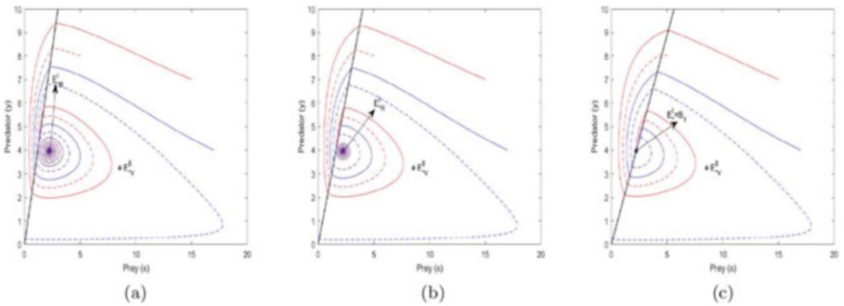

Fig. 4 Boundary Bifurcation for E_*^I $a = 20, d = 0.2, q = 0.2, r = 2, E = 2, K = 20, \beta = 10, \beta_1 = 2$. (**a**) $\mu = 0.3$. (**b**) $\mu = 0.4$. (**c**) $\mu = 0.5625$

Boundary Bifurcation Boundary Bifurcation occurs whenever any of the equilibrium state collides with the boundary Σ.

The boundary bifurcation with respect to parameter μ is demonstrated in Fig. 4. The threshold bifurcation value is computed as $\mu = 0.5625$. As the value of μ

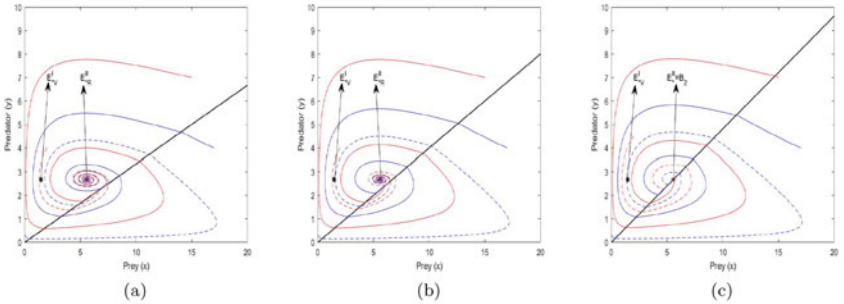

Fig. 5 Boundary Bifurcation for E_*^{II} $a = 13, d = 0.2, q = 0.2, r = 2, E = 2, K = 20, \beta = 10, \beta_1 = 2$. (**a**) $\mu = 3$. (**b**) $\mu = 2.5$. (**c**) $\mu = 2.0792$

moves towards 0.5625 Fig. 4b the stable regular equilibrium state E_*^I moves towards the boundary, finally colliding with the boundary when $= 0.5625$ as in Fig. 4c.

Similarly, $\mu = 0.0792$ is the bifurcation value for collision of stable regular equilibrium state E_*^{II} with the boundary Σ as shown in Fig. 5.

6 Conclusion

In this paper, Filippov predator prey system for selective predator harvesting is investigated. For the individual smooth subsystems, there is no possibility of bistability. From the analysis of Filippov system, it is proved that the splitting boundary has only crossing region and sliding region. There is no escaping region. This implies that the solution trajectory initiating in specific subregion of the Filippov system will never remain in the same subregion after hitting the boundary. Different equilibrium points such as boundary points, tangent points, pseudo-equilibrium points are found out for the boundary. It is established that there are two tangent points and either both will be visible or both will be invisible simultaneously. Also, origin exists as an unstable pseudo-equilibrium state. Bifurcation analysis of the Filippov system is carried out numerically. The existence of global sliding bifurcation of the limit cycle about the interior equilibrium states with half saturation rate of predators as a bifurcation parameter is illustrated. The transformation of stable interior equilibrium state to the boundary equilibrium state with the movement of boundary is elaborated with the help of numerical example.

References

1. Bhattacharyya, J., Chattopadhyay, J.: Non-smooth dynamics emerging from predator-driven discontinuous prey dispersal. Nonlinear Dyn. **106**(4), 3647–3668 (2021)

2. Zhou, H., Tang, S.: Bifurcation dynamics on the sliding vector field of a Filippov ecological system. Appl. Math. Comput. **424**, 127052 (2022)
3. Gupta, K., Gakkhar, S.: The Filippov approach for predator-prey system involving mixed type of functional responses. Differ. Equ. Dyn. Syst. **28**, 273–293 (2020)
4. Cao, N., Zhang, Y., Liu, X.: Dynamics and bifurcations in Filippov type of competitive and symbiosis systems. Int. J. Bifurcation Chaos **32**(13), 2250190 (2022)
5. de Carvalho, T., Cristiano, R., Goncalves, L.F., Tonon, D.J.: Global analysis of the dynamics of a mathematical model to intermittent HIV treatment. Nonlinear Dyn. **101**(1), 719–739 (2020)
6. Kuznetsov, Y.A., Rinaldi, S., Gragnani, A.: One-parameter bifurcations in planar Filippov systems. Int. J. Bifurcation Chaos **13**(08), 2157–2188 (2003)
7. Xiao, Y., Tang, S., Wu, J.: Media impact switching surface during an infectious disease outbreak. Sci. Rep. **5**(1), 1–9 (2015)

The Effect of Different Control Strategies on the Dynamics of a Dengue Model

Carla M. A. Pinto, Dumitru Baleanu, and Amin Jajarmi

1 Introduction

Dengue is a disease caused by the dengue virus (DENV) of the *Flaviviridae family*. It can appear in four different serotypes, and immunity is specific to each one of these [12]. We can distinguish three transmission modes in dengue disease, namely, mosquito-to-human (MtH), human-to-mosquito (HtM), and mother-to-child (MtC). In MtH mode, transmission to humans occurs, mainly, through the bite of infected *Aedes aegypti* mosquitoes. The reverse mode, the HtM, is characterized by the infection of a mosquito, after its blood meal from an infected human [8]. The infection by DENV may cause subclinical disease or develop, less commonly, to a severe flu-like pattern (severe dengue) [13]. Severe dengue is a potentially lethal complication of DENV infection.

Dengue affects human health, countries' economies, etc. Most of the burden is located in Asia and Latin America, due to natural weather conditions, fueling the infection. Treatment for dengue relies on fever reducers and painkillers, namely, acetaminophen or paracetamol. Severe dengue requires patients' hospitalization. Dengue prevention and control depends on effective vector control measures. These encompass combat mosquito vectors (e.g., preventing mosquito breeding),

C. M. A. Pinto (✉)
School of Engineering (ISEP), Polytechnic of Porto, Porto, Portugal

Center of Mathematics, University of Porto, Porto, Portugal
e-mail: cap@isep.ipp.pt

D. Baleanu
Faculty of Arts and Sciences, Cankaya University, Ankara, Türkiye

Institute of Space Sciences, Cankaya University, Magurele-Bucharest, Romania

A. Jajarmi
Department of Electrical Engineering, University of Bojnord, Bojnord, Iran

© The Author(s), under exclusive license to Springer Nature Switzerland AG 2024

W. Lacarbonara (ed.), *Advances in Nonlinear Dynamics, Volume III*, NODYCON Conference Proceedings Series, https://doi.org/10.1007/978-3-031-50635-2_59

community engagement, reactive vector control, active mosquito, and virus surveillance [11].

The literature on epidemiological models is extensive. Since the seminal Kermack-McKendrick compartmental model [6], a considerable number of papers describing the dynamics of various infections, namely, HIV, HCV, tuberculosis, malaria, Zika, dengue, and many others, have been surfaced [1–3, 9, 10]. In 2010, Pinho et al. [9] adapted a previous published model to analyze two dengue outbreaks in Salvador (1995–1996 and 2002), with and without vector control. They compared the patterns of both outbreaks to assess the role of vector control and susceptible population in the intensity and period of epidemics.

Bearing the referred ideas in mind, we propose a novel population model for dengue infection dynamics. We intend to assess the effectiveness of four control strategies, namely, vaccination, the release of sterilized male mosquitoes, and the spread of pesticides in aquatic environments and against adult mosquitoes. In Sect. 2, we describe the model. In Sect. 4, we debate the numerical outcomes. This is followed by the design of a vaccination protocol via optimal control theories in Sect. 5. Finally, we surmise this study in Sect. 6.

2 The Proposed Model

In this section, we describe the proposed compartmental model. It generalizes the model proposed in [9]. The mosquito population is divided into seven components: the aquatic phase (A_m), four winged female mosquitoes, and two winged male mosquitoes. The adult females are subdivided in four classes, the uninfected un-mated female (F_1), uninfected fertilized female (F_2), uninfected unfertilized female (F_3), and infected fertilized female (F_4). The male mosquitoes are split in susceptible mosquitoes (M_1) and susceptible sterilized mosquitoes (M_2). The human population, H, is assumed constant, with mortality rate given by μ_h, and includes four compartments, referring to susceptible (H_s), exposed (H_e), infectious (H_i), and recovered individuals (H_r). The parameters for the mosquito population are the aquatic mosquito recruitment rate (oviposition rate), ϕ_1, and the per capita mortality rates of adult mosquitoes and aquatic forms, μ_m and μ_a, respectively. The per capita rate at which female mosquitoes emerge from the aquatic phase and become adults is $p\sigma_A$, where $0 < p < 1$ is the fraction of female mosquitoes hatched from eggs. The parameter C represents the carrying capacity, and ϕ_2 is the recruitment rate of sterilized mosquitoes. The mating rate of mosquitoes is β. The transmission probabilities from mosquito to human and human to mosquito are denoted by β_h and β_m, respectively. Thus, the infection rates per susceptible human and per susceptible female mosquito are given by $\frac{b\beta_h F_4}{H+m}$ and $\frac{b\beta_m H_i}{H+m}$, respectively, where m represents the alternative (non-human) blood sources. The disease flow between the susceptible and infected classes of vectors and hosts is described as follows. The uninfected unfertilized females, F_1, mate with male mosquitoes or

with sterilized male mosquitoes at rate $\frac{\beta M_1}{M_1+M_2}$ or $\frac{\beta M_2}{M_1+M_2}$, respectively, and move to the F_2 or F_3 classes. An uninfected fertilized female mosquito, F_2, may be infected after biting an infectious human, H_i, and moves to the class F_4 at a rate $\frac{b\beta_m H_i}{H+m}$. A susceptible human H_s is exposed (infected but not infectious) to the dengue virus when he is bitten by an infectious female mosquito F_4 and moves to the class H_e. The exposed humans become infectious at a rate θ_h, where $1/\theta_h$ is the intrinsic period of virus replication in humans. The host recovers from dengue at a rate α_h, where $1/\alpha_h$ is the infectious period, and moves to the class H_r. These recovered individuals move at a rate η to the susceptible class since the conferred immunity is partial. The nonlinear system of ordinary differential equations, describing the dynamics of the model, is given below

$$
\begin{aligned}
A_m' &= \phi_1 \left(1 - \tfrac{A_m}{C}\right)(F_2 + F_4) - (\sigma_A + \mu_A) A_m, \\
F_1' &= p\sigma_A A_m - \tfrac{\beta}{M_1+M_2} F_1 M_1 - \tfrac{\beta}{M_1+M_2} F_1 M_2 - \mu_m F_1, \\
F_2' &= \tfrac{\beta}{M_1+M_2} F_1 M_1 - \tfrac{b\beta_m}{H+m} H_i F_2 - \mu_m F_2, \\
F_3' &= \tfrac{\beta}{M_1+M_2} F_1 M_2 - \mu_m F_3, \\
F_4' &= \tfrac{b\beta_m}{H+m} H_i F_2 - \mu_m F_4, \\
M_1' &= (1-p)\sigma_A A_m - \mu_m M_1, \\
M_2' &= \phi_2 - \mu_m M_2, \\
H_s' &= \mu_h (H - H_s) - \tfrac{b\beta_h}{H+m} H_s F_4 + \eta H_r, \\
H_e' &= \tfrac{b\beta_h}{H+m} H_s F_4 - (\theta_h + \mu_h) H_e, \\
H_i' &= \theta_h H_e - (\alpha_h + \mu_h) H_i, \\
H_r' &= \alpha_h H_i - (\eta + \mu_h) H_r.
\end{aligned}
\tag{1}
$$

The definitions of variables and parameters are also given in Tables 1 and 2, respectively.

3 Reproduction Number

In this section, we compute the reproduction number, R_0, of model (1), and prove the stability of the disease-free equilibrium state. Let $P_0 = \left(A_m^0, F1^0, F_2^0, 0, 0, M_1^0, 0, H_s^0, 0, 0, 0\right)$ be the disease-free equilibrium of model (1). We use the next-

Table 1 The variables of the model (1)

Variable	Definition
A_m	Mosquito's aquatic phase
F_1	Uninfected and unmated female mosquito
F_2	Uninfected fertilized female mosquito
F_3	Uninfected mated fertilized female
F_4	Infected mating fertilized female
M_1	Normal male mosquito
M_2	Sterile male mosquito
H_s	Susceptible human
H_e	Exposed human
H_i	Infectious human
H_r	Recovered human

Table 2 The description and the value of each parameter included in the model (1)

Parameter	Description	Value
ϕ_1	Aquatic mosquito recruitment rate	[0, 11.2] day
C	Carrying capacity of aquatic/adult mosquito	500
σ_A	Mosquitoes' transition rate from aquatic to adult stages	0.7
μ_A	Mosquitoes' aquatic form mortality rate	[0.01, 0.47] day
p	Proportion of female mosquitoes	0.5
β	Mosquitoes mating rate	0.7
μ_m	Mosquitoes' natural death rates	[0.02, 0.09] day
β_m	Contact rate from female mosquitoes to humans	0.75
b	Average bite per mosquito per day	[0, 1]
m	Alternative (non-human) blood sources	0
ϕ_2	Recruitment rate for sterile male mosquitoes	5
μ_h	Human natural death rate	[0.0143, 0.0167] year
β_h	Transmission rate from humans to mosquitoes	0.75
η	Partial immunity	[0, 1]
θ_h	Incubation rate	[0.083, 0.17] day
α_h	Recovering rate	[0.083, 0.25] day

generation method, described in [4]. The matrices for the new infection terms, F, and the other terms, V, are given below:

$$F = \begin{bmatrix} 0 & 0 & \frac{b\beta_m}{H} F_2^o \\ b\beta_h & 0 & 0 \\ 0 & 0 & 0 \end{bmatrix}$$

$$V = \begin{bmatrix} \mu_m & 0 & 0 \\ 0 & \theta_h + \mu_h & 0 \\ 0 & \theta_h & \alpha_h + \mu_h \end{bmatrix}$$

R_0 is the spectral radius of the matrix FV^{-1} and is computed to be:

$$R_0 = \frac{b^2 \beta_h \beta_m \theta_h}{\mu_m \left(\alpha_h + \mu_h\right)\left(\mu_h + \theta_h\right)} \frac{F_2^0}{H_s^0}$$

Thus, R_0 is dependent on the initial numbers of uninfected fertilized female mosquitoes and of the human population.

Theorem 1 ([4]) *The disease-free equilibrium P_0 is locally asymptotically stable for $R_0 < 1$.*

4 Simulations of the Model and the Control Strategies

We simulate the model (1) for epidemiological fair parameters' values (see Table 2) and for different control strategies. In Fig. 1, the positive impact of the male sterile mosquitoes is taken into account on the evolution of the state variables. It is observed a decrease in the number of larvae and infected mating fertilized females, in the case "with control" (e.g., when sterile male mosquitoes are released in the environment), when compared to the case "without control." Moreover, there is a reduction in the number of exposed humans.

Figure 2 displays the effect of pesticide in aquatic phase by including the control parameter $c_a(t)$ in the equation of $A_m(t)$ by the term $-c_a(t)A_m(t)$. As a result, higher numbers of infected mating fertilized females, male mosquitoes, and infected humans are observed in the case "without control," i.e., when the pesticide is not spread in the water.

We proceed similarly to reveal the effect of pesticide approach for all kinds of mosquitoes in the model (1). This is modeled by the control parameter $c_M(t)$, which is included in the equations of $F_1(t)$, $F_2(t)$, $F_3(t)$, $F_4(t)$, and $M_1(t)$. In the case "without control" (i.e., in the absence of pesticide), the numbers of infected mating

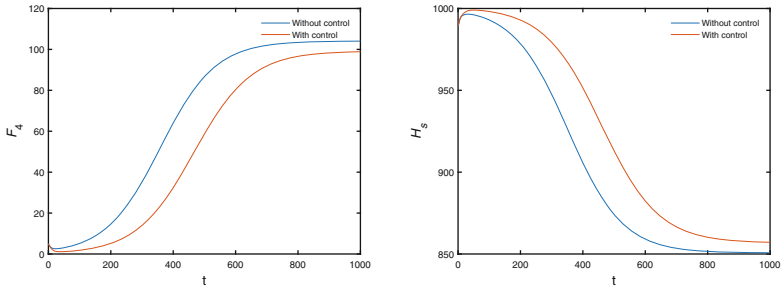

Fig. 1 The effect of male sterile mosquitoes on the dynamics of the dengue model (1)

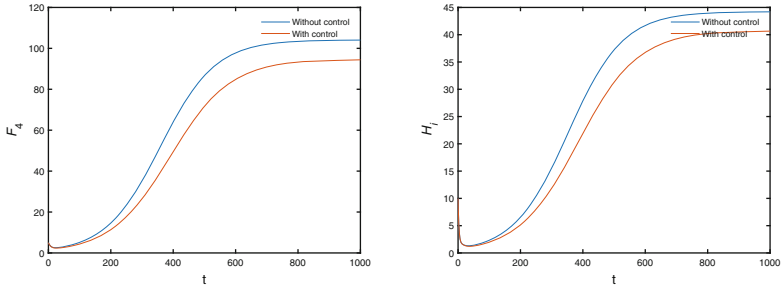

Fig. 2 The effect of pesticide (aquatic phase) on the dynamics of the dengue model (1)

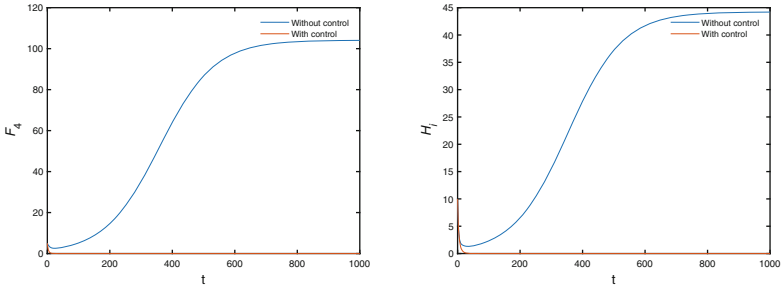

Fig. 3 The effect of pesticide on the dynamics of the dengue model (1)

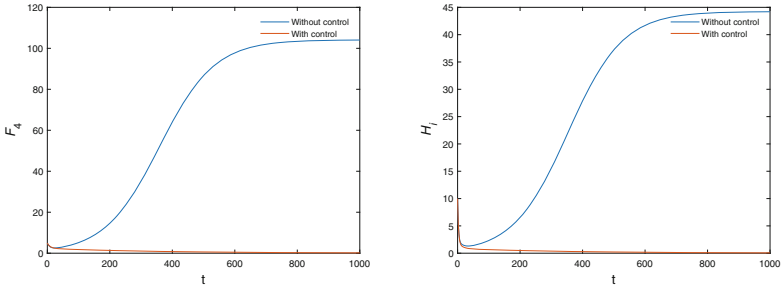

Fig. 4 The effect of vaccination on the dynamics of the dengue model (1)

fertilized female mosquitoes, normal male mosquitoes, and infected humans are higher than in the case "with control" (i.e., in the presence of pesticide) (Fig. 3).

Vaccination ($v(t)$) (Fig. 4) was added to the equations of $\dot{H}_s(t)$ and $\dot{H}_r(t)$ as follows. The term $-v(t)H_s(t) + kv(t)H_r(t)$ was included in $\dot{H}_s(t)$ and subtracted from $\dot{H}_r(t)$. The parameter k, associated with the control $v(t)$, represents the waning immunity process. Vaccination constitutes a valid control measure since it reduces the numbers of susceptible humans and infected mated female mosquitoes.

5 Vaccination via Optimal Control

This section designs a vaccination protocol via an optimal control scheme, to reduce the number of infected humans. We modify the model (1) into a control system by including the control parameter $v(t)$ as the vaccination strategy. As mentioned in the previous section, we add the term $-v(t)H_s(t) + kv(t)H_r(t)$ to $\dot{H}_s(t)$ and subtract it from $\dot{H}_r(t)$. The goal is to find $v(t)$, which minimizes the quadratic cost functional

$$J = \frac{1}{2}\int_0^T \left(q H_i^2(\tau) + r v^2(\tau)\right)\, d\tau, \tag{2}$$

where $q \geq 0$ and $r > 0$ are weighting coefficients for the state and control variables, respectively. To solve the abovementioned optimal control problem, the associated optimality conditions should be derived, so the following Hamiltonian function is formulated:

$$H(t) = m_0(t) + \sum_{1}^{11} p_i(t) m_i(t), \tag{3}$$

where $m_0(t)$ is the function inside the integral (2), $m_i(t)$ denotes the right-hand side of the ith equation in the state equations, and p_i is the costate variable also known as the Lagrange multiplier. Following [7], the costate equations are then obtained from

$$-p_i' = \frac{\partial H}{\partial x_i}, \quad i = 1, \ldots, 11, \tag{4}$$

where x_i is the ith state variable. Thus, the costate equations are formulated from (4) as

$$\begin{aligned}
-p_1' &= p_1(-\phi_1 \tfrac{F_2+F_4}{C} - \sigma_A - \mu_A) + p_2 p \sigma_A + p_6(1-p)\sigma_A,\\
-p_2' &= p_2(-\tfrac{\beta M_1}{M} - \tfrac{\beta M_2}{M} - \mu_m) + p_3 \tfrac{\beta M_1}{M} + p_4 \tfrac{\beta M_2}{M},\\
-p_3' &= p_1\phi_1(1 - \tfrac{A_m}{C}) + p_3(-\tfrac{b\beta_m H_i}{H+m} - \mu_m) + p_5 \tfrac{b\beta_m H_i}{H+m},\\
-p_4' &= -p_4\mu_m,\\
-p_5' &= p_1\phi_1(1 - \tfrac{A_m}{C}) - p_5\mu_m - p_8 \tfrac{b\beta_h H_s}{H+m} + p_9 \tfrac{b\beta_h H_s}{H+m},\\
-p_6' &= -p_2 \tfrac{\beta F_1}{M} + p_3 \tfrac{\beta F_1}{M} - p_6\mu_m,\\
-p_7' &= -p_2 \tfrac{\beta F_1}{M} + p_4 \tfrac{\beta F_1}{M} - p_7\mu_m,\\
-p_8' &= p_8(-\mu_h - \tfrac{b\beta_h F_4}{H+m} - v) + p_9 \tfrac{b\beta_h F_4}{H+m} + p_{11} v,\\
-p_9' &= p_9(-\theta_h - \mu_h) + p_{10}\theta_h,\\
-p_{10}' &= q H_i - p_3 \tfrac{b\beta_m F_2}{H+m} + p_5 \tfrac{b\beta_m F_2}{H+m} + p_{10}(-\alpha_h - \mu_h) + p_{11}\alpha_h,\\
-p_{11}' &= p_8(kv + \eta) + p_{11}(-kv - \eta - \mu_h).
\end{aligned} \tag{5}$$

The optimal vaccination control is also presented by

$$\begin{aligned} &\frac{\partial H}{\partial v} = rv + p_8(H_r k - H_s) + p_{11}(-H_r k + H_s) = 0 \\ &\Rightarrow \ v^*(t) = -\tfrac{1}{r}(p_8(H_r k - H_s) + p_{11}(-H_r k + H_s)). \end{aligned} \tag{6}$$

The initial conditions for the state variables are the same as the original system (1), while the terminal values of the costate variables are $p_i(T) = 0, i = 1, \ldots, 11$.

According to the abovementioned discussion, the necessary optimality conditions are obtained in the form of a boundary-value problem, which can be solved by various approximation schemes available in the previous literature. Here, we combined the standard predictor-corrector method (PECE) and a forward-backward sweep iterative algorithm in order to solve this problem effectively. The stability and convergence of this technique were discussed in [5]. We consider $X(t)$ and $P(t)$ as the vectors of the state and costate variables and take into account $X_i(t)$, $P_i(t)$, and J_i as the approximations of $X(t)$, $P(t)$, and the cost functional J at the ith iteration, respectively. Then we summarize the suggested algorithm as follows:

Algorithm:

- **Step 1.** Make an initial guess for the costate variable $P_0(t)$; then set $J_0 = \infty$ and $i = 1$.
- **Step 2.** Use $P_{i-1}(t)$ and calculate $X_i(t)$ forward in time from the state equations.
- **Step 3.** Use $X_i(t)$ from Step 2 and calculate $P_i(t)$ backward in time from the costate equations.
- **Step 4.** For a pre-defined error-bound $\varepsilon > 0$, if the condition $e_i = \left|\frac{J_i - J_{i-1}}{J_i}\right| < \varepsilon$ holds, stop the algorithm, else replace i by $i + 1$ and go to Step 2.

Figure 5 shows the simulations of the controlled and uncontrolled state variables; the results show that the vaccination strategy via the optimal control approach is efficient to reduce the number of infectious humans. Here, it is worth mentioning that the control scheme is focused on the state variable H_i, so the results are satisfactory in this regard. However, to improve the other states, they should be included in the cost functional J appropriately according to what we expect from

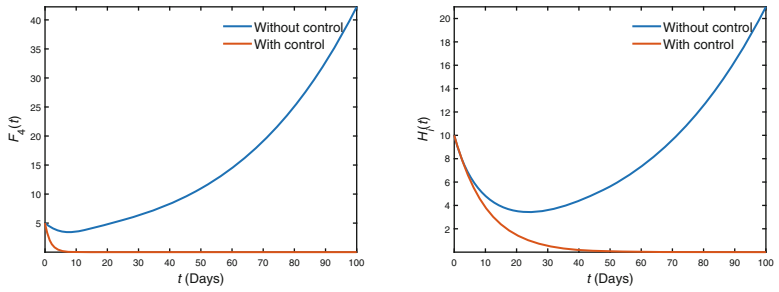

Fig. 5 The effect of vaccination via optimal control on the dynamics of the dengue model (1)

their behaviours, and suitable weighting coefficients should be selected based on the priority of each control objective.

6 Conclusions

Our priority in this chapter was to assess the effect of four control strategies, namely, the use of pesticides in the mosquitoes' aquatic phase, the use of pesticides against adult mosquitoes, vaccination, and the release of sterilized male mosquitoes in the dynamics of a new dengue infection model. The simulations of the model in the presence of various control measures combinations were presented. An efficient vaccination protocol was also designed by using optimal control theories. The reported results indicated that the model's patterns are epidemiologically well-posed, so future health policies can be extrapolated from the outputs of the current model. Dengue is still a major concern worldwide, with a 70% actual burden in Asia, so epidemiologists can provide substantial advice to policy makers by interpreting the predictions provided by mathematical models.

Acknowledgments The author Carla M.A. Pinto was partially supported by CMUP, which is financed by national funds through FCT—Fundação para a Ciência e a Tecnologia, I.P., under the project with reference UIDB/00144/2020.

References

1. Akın, E., Yeni, G., Perelson, A.S.: Continuous and discrete modeling of HIV-1 decline on therapy. J. Math. Biol. **81**(1), 1–24 (2020)
2. Cardozo, E.F., Ji, D., Lau, G., Schinazi, R.F., Chen, G.F., Ribeiro, R.M., Perelson, A.S.: Disentangling the lifespans of hepatitis C virus-infected cells and intracellular vRNA replication-complexes during direct acting anti-viral therapy. J. Viral Hepat. **27**(3), 261–269 (2020)
3. Chávez, J.P., Gürbüz, B., Pinto, C.M.: The effect of aggressive chemotherapy in a model for HIV/AIDS-cancer dynamics. Commun. Nonlinear Sci. Numer. Simul. **75**, 109–120 (2019)
4. Driessche, P., Watmough P.: Reproduction numbers and sub-threshold endemic equilibria for compartmental models of disease transmission. Math. Biosci. **180**, 29–48 (2002)
5. Hackbush, W.: A numerical method for solving parabolic equations with opposite orientations. Computing **20**(3), 229–240 (1978)
6. Kermack, W.O., McKendrick, A.G.: A contribution to the mathematical theory of epidemics. Proc. R. Soc. London, Ser. A Containing Pap. Math. Phys. Character **115**(772), 700–721 (1927)
7. Kirk, D.E.: Optimal Control Theory: An Introduction. Dover Publications, New York (1970)
8. Nguyen, N.M., Kien, D.T.H., Tuan, T.V., Quyen, N.T.H., Tran, C.N., Thi, L.V., Thi, D.L., Nguyen, H.L., Farrar, J.J., Holmes, E.C., Rabaa, M.A.: Host and viral features of human dengue cases shape the population of infected and infectious Aedes aegypti mosquitoes. Proc. Natl. Acad. Sci. **110**(22), 9072–9077 (2013)
9. Pinho, S.T.R., Ferreira, C.P., Esteva, L., Barreto, F.R., Morato e Silva, V.C., Teixeira, M.G.L.: Modelling the dynamics of dengue real epidemics. Philos. Trans. R. Soc. Lond. A Math. Phys. Eng. Sci. **368**(1933), 5679–5693 (2010)

10. Quaranta, G., Formica, G., Machado, J.T., Lacarbonara, W., Masri, S. F.: Understanding COVID-19 nonlinear multi-scale dynamic spreading in Italy. Nonlinear Dyn. **101**(3), 1583–1619 (2020)
11. Revised SAGE recommendation on use of dengue vaccine. https://www.who.int/immunization/diseases/dengue/revised_SAGE_recommendations_dengue_vaccines_apr2018/en/. Accessed September 19 2020
12. World Health Organization—Dengue and Dengue Fever. https://www.who.int/en/news-room/fact-sheets/detail/dengue-and-severe-dengue. Accessed September 16 2020.
13. World Health, O.: Dengue: Guidelines for Diagnosis, Treatment, Prevention and Control, pp. 1–147. World Health Organization, Geneva (2009)

Index

A
Alginate spheres, 272
Anti-symmetric modes, 25–33
Asymmetric hysteresis, 279–287
Asymmetric hysteresis behavior, 451
Asymptotic analysis, 496–498, 566, 568–573

B
Backbone curves, 429–438
Backside contact, 133, 135, 138, 140
Bifurcation, 15–23, 31–33, 59, 60, 63, 67, 71–79, 91–99, 102, 112, 116–119, 122–128, 133, 138, 139, 154–156, 224, 225, 254, 256–259, 356, 357, 372, 374, 379, 499, 500, 601–611, 629, 630, 632, 633, 637–649
Bifurcation and chaos, 71–79
Bifurcation-based sensing, 15, 16
Bifurcation theory, 71–79
Bi-stability, 218, 219, 225
Bistable nonlinear energy sink, 419–427
Bogdanov-Takens bifurcation, 91–99
Bolt fault, 407–416, 471–474, 476–479
Bouc–Wen constitutive law, 301–309, 327–329, 333, 452, 455–459

C
Chaos, 72, 74, 76–78, 91–99, 123, 140, 151, 155, 176, 177, 180, 184, 221, 222, 224, 350, 354, 356, 359, 367, 494, 598
Chaos theory, 71–79
Chaotic, 59–67, 74–76, 78, 82, 83, 85, 86, 89, 91, 92, 96, 117–119, 125, 131–140, 151, 153–160, 175–184, 198, 200, 202, 203, 220, 247, 355–357, 359–368, 371, 372, 374, 592, 601, 602, 611
Chaotic attractor, 76, 78, 92, 97–99, 121, 126, 178
Chaotic dynamics, 92, 97, 119, 591
Chirped solitons, 581–587
Collisions, 566–568, 649
Complex, 11, 49, 71, 72, 75, 82, 91–95, 112, 117, 148, 163, 176, 177, 180, 184, 193, 209, 220, 222–225, 228, 251, 252, 261, 289, 290, 299, 325, 329, 337, 362, 371–380, 410, 416, 429, 441, 447, 452, 471–480, 493, 495, 501, 519, 525, 591, 602, 607, 608, 613–621, 623
Complex discrete cantilever, 613–621
Complex hysteresis phenomena, 290, 299, 329
Complex structure, 416, 471–480, 519, 613
Computational geometry, 59, 103, 112, 207–209, 280, 325, 329, 481, 495, 541, 554–562
Constrained Green's function, 311–322
Controllable canonical form, 122, 123, 128
Control performance assessment (CPA), 381–391
Coral-algal interactions, 623–634
CORDIC, 153–161
Coulomb damping, 420
Critical dynamics, 185–193
Cryptography, 176, 182, 364, 367
Curved beam, 27–29

© The Editor(s) (if applicable) and The Author(s), under exclusive license to Springer Nature Switzerland AG 2024

W. Lacarbonara (ed.), *Advances in Nonlinear Dynamics, Volume III*, NODYCON Conference Proceedings Series, https://doi.org/10.1007/978-3-031-50635-2

D
Damage, 301–309, 407, 408, 411–413, 415, 416, 471, 520, 523, 525, 527, 531
Damping effect, 36, 276, 277
Data-driven and machine learning methods, 337
Degradation, 155, 175, 301–303, 306–309, 494, 519, 521
Differential difference equations, 549
Distorted magnetosonic lump wave solution, 531–539
Dynamic ecosystems, 633
Dynamic integrity, 101–109
Dynamic response, 27, 28, 33, 277, 305, 311, 312, 327, 334, 421, 423, 451, 467
Dynamical systems, 59–65, 72, 97, 101, 102, 116, 125, 128, 144, 254, 282, 337–347, 359, 361–363, 367, 404, 421, 446, 483, 508, 516, 601–603
Dynamics of MEMS, 35

E
Effort-controlled formulation, 286
Electrostatic MEMS, 16, 23, 26, 27, 31
Energy harvester, 197, 198, 207–214, 217, 221, 227–230, 232–237, 240–248, 429
Energy sink, 46, 197–205, 227–237, 419–427
Erdös-Rényi graph, 185–193
Euler, 101, 102, 176, 454
Experimental assessment, 21–22, 26–27, 37–38, 163, 217–225, 262, 279–287, 325–334, 350, 385–386, 399, 425–427, 430, 456, 513
Extended Masing model (EMM), 281–282

F
Fault monitoring, 474
Fiber Bragg gratings, 577–587
Field Programmable Gates Array (FPGA), 153–160, 175–184, 371–380, 554, 555, 557, 561, 562
Flexibility increase, 301–309
Flow-controlled formulation, 284, 286, 287
Force-based beam, 304
Forced Kadomtsev-Petviashvili I equation, 532, 533
Fractal, 102, 125, 127, 371–380
Fractional, 158, 337–341, 344–346, 350, 357, 360–361, 364, 373, 381–391
Fractional calculus, 337, 350, 359
Fractional order, 163, 337, 338, 347, 349–352, 356–357, 359–368, 371–380, 387, 390, 391
Fractional-order differential operator, 351–356
Fractional-type system, 349–357
Free vibrations, 423, 425
Friction, 5, 252, 254, 256, 279, 451, 452, 507–516, 554, 555

G
Galloping, 239–245
Gas sensor, 15, 16
Gaussian process regression model (GPR), 495, 498–499, 504
Gear mesh stiffness, 135
Generalized Bouc–Wen model (GBWM), 301–309
Geometrical nonlinearity, 395–405
Geometric nonlinearity, 399, 621
Geweke-Porter-Hudak estimator (GPH), 382, 383
Global sliding bifurcation, 647, 649
Graph theory, 284
Gravimeter, 3

H
Hamilton cycles, 37, 340, 353, 543, 657
Hardware code acceleration, 557
Hidden attractor, 143–151
Homoclinic orbit, 92, 94, 95, 647
Hysteresis, 144, 151, 225, 263–264, 279–287, 289–293, 296–299, 325, 331–333, 435, 451, 454–459, 601
Hysteresis model, 280, 299, 325, 327–331

I
Indirect excitation, 33
Inertial nonlinearities, 37
Internal resonance, 26, 35–44
Ionospheric plasma, 531–539

J
Jerk dynamics, 121–128

K
Key generator, 175–184
Korteweg-de Vries (KdV) equation, 532, 565–575
Kuramoto model, 185–193

L
Landslide, 251–259
Laplace transform, 312, 314, 322
Large amplitude oscillatory axial (LAOA) loadings, 261–269
Linear system, 39, 123, 144, 147, 228, 399, 402–404, 591
Logistic, 155, 371–380
Lorenz model, 121–128
Lyapunov characteristic exponents (LCEs), 122, 123, 125, 127, 128

M
Machine learning, 59–62, 337, 481, 493–505, 599
Magnetic composite, 271–277
Magnetite, 272, 273
Mechanical metamaterials, 541–550
Memristor oscillator, 91–99
Micro-electromechanical systems (MEMS), 15–23, 25–33, 35, 40, 45, 50, 51, 53, 54, 349, 520
Micromechanical torsion pendulum, 3–14
Microresonator, 33, 35, 36, 43, 349–357
Modal interaction, 25, 26, 29–33, 218
Modified sine map, 154–156, 158–160
Morphing materials, 463
Multi-degree of freedom (MDOF) model, 408, 410–411, 416, 472, 479
Multi-objective optimization, 228
Multistability, 92, 96–99, 143, 144, 148–151
Multi-story building, 395–405

N
Neural networks, 82, 337, 338, 341–347, 372, 441, 446–450, 452
NIST, 182
Noise, 3–14, 17–19, 30, 144, 193, 228, 232, 234, 251–256, 258, 259, 337–341, 347, 371, 383, 385, 390, 391, 396, 421–423, 427, 430, 432, 433, 435–438, 457–459, 486, 499, 512, 514, 516, 594, 598
Non-ideal excitation source, 198
Nonlinear control, 163
Nonlinear dynamics, 25, 36, 72, 97, 117, 131–140, 337, 349, 353, 401, 450, 482–483, 516, 541, 545–549
Non-linear electromagnetic energy sink, 198
Nonlinear foundation beam, 312, 317
Nonlinear Froude-Krylov force, 208
Nonlinear multi-degree-of-freedom mechanical systems, 420, 431
Nonlinear oscillations, 613, 621
Nonlinear quantification of moduli, 265
Nonlinear system identification, 395–405, 420
Nonlinear time-series classification, 59–68
Nonlinear vibration absorber, 236
Nonlinear waves, 532, 543, 544
Nullclines, 126, 628, 630, 631, 641

O
Off-shore well model, 114
Orbital charged space debris objects, 531–539
Output-only measurements, 395–405

P
Parallelization, 446
Parameters fitting, 114, 115, 459
Parametric anti-resonance, 45–54
Parametric excitation, 45–47, 50–54
Parametric resonance, 45, 139, 207–214
Periodic orbit, 39, 42–44, 221, 222
Perturbation methods, 495, 505, 543, 549
Physics-informed, 419–427, 481
Piezoelectric energy harvesting, 236, 239
Piezo-electricity, 197, 198, 227, 228, 236, 239–242, 244, 337, 408, 520
Planar system, 144, 147–148, 151
Point wave energy absorber (PWA), 217–219, 222, 225
Polymer's trained, 23, 271, 464
Polynomial law, 577
Power systems, 71, 72, 74–76, 78
Pressurized sand damper, 289–299
PWL system, 144–148, 151

Q
Quasi-zero stiffness (QZS), 239–248
Quaternions, 441–450

R
Random graph, 185–193
Random number generation (RNG), 182, 364
Real-time monitoring, 519–527
Recycled devices, 519–527
Regular/virtual, 640–641
Reliability analysis, 101–109
Reliability function, 338, 340–347
Restoring force surface, 400, 401, 419–424, 426, 427
Rotational shaft stiffness, 133, 139

S
Saturation phenomenon, 36, 40–43
Scientific machine learning, 481
Sea surface temperature (SST), 623–634
Self-exited attractor, 144
Self-supervised contrastive learning, 59–68
Servomechanism, 382, 385, 386, 391
Silicone, 271–277
Sine map, 153–160
Smooth coordinate decomposition (SCD), 430–432, 436, 438
Smooth coordinate pairs (SCPs), 430–433, 435–438
Smooth coordinate tracking algorithm (SCTA), 430, 431, 434–438
Sparse identification, 419–427, 507–516
Sparse identification of nonlinear dynamics (SINDy), 481–490, 507, 508
Sparse regression, 422, 423
Spectral matrices, 565, 566, 568–570, 572
Spiral bevel gears (SBGs), 131–140
Spring beam, 313
Stability of modes, 26
Stochastic averaging method, 337–347
Subsynchronous resonance (SSR), 71, 72, 74–78
Structural modification, 408, 411, 412, 414, 416
Structural stability, 101–103, 520
Subspace identification, 395, 397, 404, 419
Symmetric MEMS, 25–33
System identification, 395–405, 420, 486, 494, 591

T
Tangent hyperbolic memristor, 360, 364, 365, 367
Tangent point, 434, 437, 644–646, 649
Time delay, 85, 185, 193, 254, 256–259, 482, 483, 487–490
Time-delay identification, 482–489
Time-periodic perturbation, 91–99
Tsunami simulation, 553, 555, 561
Two degree-of-freedom (2DOFs), 36, 45, 133, 211, 228, 239–248, 436, 438, 615
Two-dimensional structure, 407–416
2-soliton solutions, 566–570, 572, 573

U
Uncertainty quantification, 493–505
U-shaped micro portal frame, 43

V
Vaiana-Rosati model (VRM), 289–299, 327, 329–333
VHDL, 179, 180
Vibration response, 228, 395, 396, 425, 432, 471–480
Vibrational control, 132, 325
Vivado, 156, 176, 180
Voltage collapse (VC), 71–74, 78, 79

W
Wave energy, 217, 225
Wave energy converter, 208
Wire rope isolators (WRI), 280, 451–459

X
Xilinx, 156, 159, 180, 184, 377, 557

Y
Young seedlings staking, 613–615, 619, 621